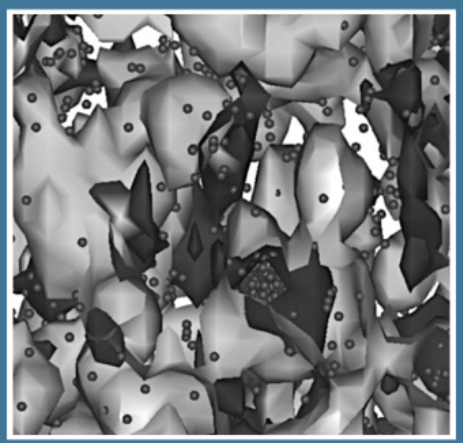
WOODHEAD PUBLISHING IN MATERIALS



Phase transformations in steels

Volume 2: Diffusionless transformations, high strength steels, modelling and advanced analytical techniques

Edited by Elena Pereloma and David V. Edmonds

WP
WOODHEAD PUBLISHING

Phase transformations in steels

© Woodhead Publishing Limited, 2012

Related titles:

Phase transformations in steels Volume 1: Fundamentals and diffusion-controlled transformations
(ISBN 978-1-84569-970-3)
Edited by two leading experts in the field, and with contributions from some of the most distinguished figures in steel research, this two-volume work summarises the vast amount of recent research on phase transformations in steels. The book covers both fundamental aspects (thermodynamics, diffusion, etc.) and more particular features (bainite, martensite, etc.). Volume 1 reviews fundamentals, diffusion-controlled, bainite and diffusional-displacive transformations.

Microstructure evolution in metal forming processes: Modelling and applications
(ISBN 978-0-85709-074-4)
Metal forming processes involve varying degrees of deformation to the metal substrate. This deformation results in changes to the microstructure of the metal. These microstructural changes need to be monitored and controlled. This book looks at the evolution of microstructure during metal forming processes and its modelling and control to produce steels and other metals with the right properties.

Nanostructured metals and alloys: Processing, microstructure, mechanical properties and applications
(ISBN 978-1-84569-670-2)
Nanostructured metals and alloys have enhanced tensile strength, fatigue strength and ductility and are suitable for use in applications where strength or strength-to-weight ratios are important. Part I of this important book reviews processing techniques for bulk nanostructured metals and alloys. Parts II and III discuss microstructure and mechanical properties, whilst Part IV outlines applications of this new class of material.

Details of these and other Woodhead Publishing materials books can be obtained by:

- visiting our web site at www.woodheadpublishing.com
- contacting Customer Services (e-mail: sales@woodheadpublishing.com; fax: +44 (0) 1223 832819; tel.: +44 (0) 1223 499140 ext. 130; address: Woodhead Publishing Limited, 80 High Street, Sawston, Cambridge CB22 3HJ, UK)
- contacting our US office (e-mail: usmarketing@woodheadpublishing.com; tel. (215) 928 9112; address: Woodhead Publishing, 1518 Walnut Street, Suite 1100, Philadelphia, PA 19102-3406, USA)

If you would like e-versions of our content, please visit our online platform: www.woodheadpublishingonline.com. Please recommend it to your librarian so that everyone in your institution can benefit from the wealth of content on the site.

© Woodhead Publishing Limited, 2012

Phase transformations in steels

Volume 2: Diffusionless transformations, high strength steels, modelling and advanced analytical techniques

---

Edited by

Elena Pereloma and David V. Edmonds



Oxford Cambridge Philadelphia New Delhi

© Woodhead Publishing Limited, 2012

Published by Woodhead Publishing Limited,
80 High Street, Sawston, Cambridge CB22 3HJ, UK
www.woodheadpublishing.com
www.woodheadpublishingonline.com

Woodhead Publishing, 1518 Walnut Street, Suite 1100, Philadelphia, PA 19102-3406, USA

Woodhead Publishing India Private Limited, G-2, Vardaan House, 7/28 Ansari Road,
Daryaganj, New Delhi – 110002, India
www.woodheadpublishingindia.com

First published 2012, Woodhead Publishing Limited
© Woodhead Publishing Limited. Chapter 17 was prepared by a US government employee and is therefore in the public domain and cannot be copyrighted.
The authors have asserted their moral rights.

This book contains information obtained from authentic and highly regarded sources. Reprinted material is quoted with permission, and sources are indicated. Reasonable efforts have been made to publish reliable data and information, but the authors and the publishers cannot assume responsibility for the validity of all materials. Neither the authors nor the publishers, nor anyone else associated with this publication, shall be liable for any loss, damage or liability directly or indirectly caused or alleged to be caused by this book.

Neither this book nor any part may be reproduced or transmitted in any form or by any means, electronic or mechanical, including photocopying, microfilming and recording, or by any information storage or retrieval system, without permission in writing from Woodhead Publishing Limited.

The consent of Woodhead Publishing Limited does not extend to copying for general distribution, for promotion, for creating new works, or for resale. Specific permission must be obtained in writing from Woodhead Publishing Limited for such copying.

Trademark notice: Product or corporate names may be trademarks or registered trademarks, and are used only for identification and explanation, without intent to infringe.

British Library Cataloguing in Publication Data
A catalogue record for this book is available from the British Library.

Library of Congress Control Number: 2012934585

ISBN 978-1-84569-971-0 (print)
ISBN 978-0-85709-611-1 (online)

The publisher's policy is to use permanent paper from mills that operate a sustainable forestry policy, and which has been manufactured from pulp which is processed using acid-free and elemental chlorine-free practices. Furthermore, the publisher ensures that the text paper and cover board used have met acceptable environmental accreditation standards.

Typeset by Replika Press Pvt Ltd, India
Printed by TJI Digital, Padstow, Cornwall, UK

© Woodhead Publishing Limited, 2012

Contents

Contributor contact details *xiii*
Foreword *xvii*
Introduction *xix*

Part I Diffusionless transformations 1

1 Crystallography of martensite transformations in steels 3
P. M. Kelly, The University of Queensland, Australia

1.1 Introduction 3
1.2 Martensite transformations in steels 4
1.3 Phenomenological theory of martensite crystallography (PTMC) 10
1.4 The post phenomenological theory of martensite crystallography (PTMC) period 18
1.5 Strain energy – the Eshelby/Christian model and the infinitesimal deformation (ID) approach 23
1.6 Interfacial dislocation models 25
1.7 Future trends 28
1.8 Conclusions 29
1.9 References 30

2 Morphology and substructure of martensite in steels 34
T. Maki, Kyoto University, Japan

2.1 Morphology and crystallographic features of martensite in ferrous alloys 34
2.2 Morphology and substructure of lath martensite 38
2.3 Morphology and substructure of lenticular martensite 46
2.4 Morphology and substructure of thin plate martensite 50
2.5 Conclusions 54
2.6 References 56

© Woodhead Publishing Limited, 2012

3 Kinetics of martensite transformations in steels 59
G. B. Olson and Z. D. Feinberg, Northwestern University, USA
3.1 Introduction 59
3.2 Mechanism and kinetics of martensitic transformation 60
3.3 Mechanically induced transformations 63
3.4 Transformation plasticity constitutive relations and applications 66
3.5 Conclusions 79
3.6 References 80

4 Shape memory in ferrous alloys 83
D. Dunne, University of Wollongong, Australia
4.1 Introduction 83
4.2 Fe-Pt alloys 89
4.3 Fe-Ni and Fe-Ni-C alloys 93
4.4 Fe-Ni-Co-based alloys 96
4.5 Austenitic stainless steels with low stacking fault energy (SFE) 99
4.6 Fe-Mn-based alloys 100
4.7 Summary 115
4.8 Acknowledgements 118
4.9 References 118

5 Tempering of martensite in carbon steels 126
G. Krauss, Colorado School of Mines, USA
5.1 Introduction 126
5.2 Martensitic microstructures prior to tempering heat treatments 127
5.3 Classification of aging and tempering stages: general considerations 130
5.4 Changes in martensitic fine structure due to aging 131
5.5 The stages of tempering 132
5.6 Conclusions 145
5.7 References 145

Part II Phase transformations in high strength steels 151

6 Phase transformations in microalloyed high strength low alloy (HSLA) steels 153
R. C. Cochrane, University of Leeds, UK
6.1 Introduction to microalloyed high strength low alloy (HSLA) steels 153

© Woodhead Publishing Limited, 2012

6.2 Brief historical review of the development of microalloyed steels 155
6.3 Solubility of microalloying elements in austenite and ferrite 157
6.4 Precipitation 161
6.5 Effects of microalloying on transformation kinetics 177
6.6 Phase transformations during high strength low alloy (HSLA) steels processing 185
6.7 Controlled processed ferrite/bainite and acicular ferrite steels 199
6.8 Conclusions and future trends 205
6.9 Acknowledgements 207
6.10 References 207

7 Phase transformations in transformation induced plasticity (TRIP)-assisted multiphase steels 213
P. J. Jacques, Université Catholique de Louvain (UCL), Belgium

7.1 Introduction 213
7.2 Historical perspectives on the emergence of transformation induced plasticity (TRIP)-assisted multiphase steels 215
7.3 Influence of parameters of the thermomechanical process on the formation of multiphase microstructures containing retained austenite 223
7.4 Conclusion and future trends 242
7.5 References 243

8 Phase transformations in quenched and partitioned steels 247
J. G. Speer, Colorado School of Mines, USA

8.1 Introduction to the quenching and partitioning concept 247
8.2 Microstructure development fundamentals and alloy designs 252
8.3 Mechanical behavior, potential applications, and implementation status 260
8.4 Conclusions 267
8.5 References 268

9 Phase transformations in advanced bainitic steels 271
F. G. Caballero and C. Garcia-Mateo, National Centre for Metallurgical Research (CENIM-CSIC), Spain

9.1 Introduction 271
9.2 Design of third generation of advanced high strength steels 273
9.3 Carbide-free bainitic steels: a material ready for the nanocentury 283

© Woodhead Publishing Limited, 2012

9.4 Conclusions and future trends 290
9.5 Acknowledgement 291
9.6 References 291

10 Phase transformations in high manganese twinning-induced plasticity (TWIP) steels 295
B. C. De Cooman, Pohang University of Science and Technology, South Korea

10.1 Introduction 295
10.2 Fe-Mn-X alloys 297
10.3 Strain-induced twinning 307
10.4 Twinning-induced plasticity (TWIP) industrialization 327
10.5 Conclusions 327
10.6 Acknowledgements 328
10.7 References 328

11 Phase transformations in maraging steels 332
W. Sha, Queen's University Belfast, UK, H. Leitner, University of Leoben, Austria, Z. Guo, Sente Software Ltd, UK and W. Xu, ArcelorMittal Global R&D Gent, Belgium

11.1 State of the art of ultra high strength steels 332
11.2 Types of maraging steels 334
11.3 Microstructure and precipitates in maraging steels 339
11.4 Reverted austenite and mechanical properties 342
11.5 Evolution of precipitates and the overall process 346
11.6 Precipitation kinetic theory in Fe-12Ni-6Mn maraging type alloy 349
11.7 Research trends 356
11.8 References 359

Part III Modelling phase transformations 363

12 First principles in modelling phase transformations in steels 365
M. H. F. Sluiter, Delft University of Technology, The Netherlands

12.1 Introduction 365
12.2 *Ab initio* description of phase stability of pure iron 370
12.3 *Ab initio* phase stability of iron carbides 374
12.4 Substitutional alloying elements 377
12.5 *Ab initio* description of diffusivity in bcc Fe 381
12.6 Future trends 384
12.7 References 385

© Woodhead Publishing Limited, 2012

13 Phase field modelling of phase transformations in steels 405
M. Militzer, The University of British Columbia, Canada

13.1 Introduction 405
13.2 Phase field methodology 406
13.3 Austenite formation 414
13.4 Austenite decomposition 418
13.5 Future trends 428
13.6 References 429

14 Molecular dynamics modeling of martensitic transformations in steels 433
H. M. Urbassek and L. Sandoval, Universität Kaiserslautern, Germany

14.1 Introduction 433
14.2 Interatomic interaction potentials 434
14.3 Martensitic transformations in iron: case studies 443
14.4 Transformations in ferrous nanosystems 449
14.5 Conclusions and future trends 459
14.6 Acknowledgement 460
14.7 References 460

15 Neural networks modeling of phase transformations in steels 464
C. Capdevila, National Centre for Metallurgical Research (CENIM-CSIC), Spain

15.1 Introduction 464
15.2 Essence of the method 465
15.3 On the quest of critical temperatures 472
15.4 Determining microstructural parameters 488
15.5 Development of continuous cooling transformation (CCT) diagrams 496
15.6 Conclusions and future trends 498
15.7 References 500

Part IV Advanced analytical techniques for studying phase transformations in steels 505

16 Application of modern transmission electron microscopy (TEM) techniques to the study of phase transformations in steels 507
D. Boyd and Z. Yao, Queen's University, Canada

© Woodhead Publishing Limited, 2012

16.1 Introduction 507
16.2 Transmission electron microscopy (TEM) sample preparation 508
16.3 Conventional transmission electron microscopy (CTEM) of steels 510
16.4 Modern transmission electron microscopy (TEM) of steels 513
16.5 *In-situ* transmission electron microscopy (TEM) 524
16.6 Future trends: emerging transmission electron microscopy (TEM) techniques 525
16.7 Sources of further information and advice 528
16.8 Conclusions 529
16.9 References 529

17 Atom probe tomography for studying phase transformations in steels 532
M. K. Miller, Oak Ridge National Laboratory, USA

17.1 Introduction 532
17.2 Outline of the technique 533
17.3 Specimen requirements 535
17.4 Recent developments 536
17.5 Interpretation of data 537
17.6 Characterizing and understanding phase transformations in various steels 538
17.7 Future trends 553
17.8 Conclusion 554
17.9 Acknowledgments 554
17.10 References 554

18 Electron backscatter diffraction (EBSD) techniques for studying phase transformations in steels 557
S. Zaefferer, N.-N. Elhami and P. Konijnenberg, Max Planck Institute for Iron Research, Germany

18.1 Introduction 557
18.2 Fundamentals of electron backscatter diffraction (3D-EBSD) technique 558
18.3 The current standard of 2D electron backscatter diffraction (EBSD) applications 561
18.4 3D electron backscatter diffraction (3D-EBSD) 569
18.5 Conclusions and future development of the technique 579
18.6 References 583

© Woodhead Publishing Limited, 2012

19 Application of synchrotron and neutron scattering techniques for tracking phase transformations in steels 588
S. S. Babu, The Ohio State University, USA

19.1 Introduction 588
19.2 X-ray and neutron scattering techniques 590
19.3 Measurements of phase transformation in steels 605
19.4 Conclusions and future trends 624
19.5 Acknowledgements 625
19.6 References 625

Index *634*

© Woodhead Publishing Limited, 2012

Contributor contact details

(* = main contact)

Editors

Professor Elena Pereloma*
Faculty of Engineering
University of Wollongong
Northfields Avenue
Wollongong
NSW 2522
Australia

E-mail: elenap@uow.edu.au

Professor David Edmonds
Institute for Materials Research
School of Process, Environmental and Materials Engineering
University of Leeds
Leeds LS2 9JT
UK

E-mail: d.v.edmonds@leeds.ac.uk

Chapter 1

Honorary Professor Patrick M. Kelly
Division of Materials
School of Mechanical and Mining Engineering
The University of Queensland
Brisbane
Queensland 4072
Australia

E-mail: patnkay86@bigpond.com

Chapter 2

Dr Tadashi Maki
Nippon Steel Corporation
20-1, Shintomi, Futtsu
Chiba 293-8511
Japan

E-mail: maki.tadashi@nsc.co.jp

© Woodhead Publishing Limited, 2012

Chapter 3

G. B. Olson* and Z. D. Feinberg
Department of Materials Science and Engineering
Northwestern University
2220 Campus Drive
Evanston, IL 60208
USA

E-mail: g-olson@northwestern.edu

Chapter 4

Emeritus Professor Druce Dunne
Faculty of Engineering
University of Wollongong
Northfields Avenue
Wollongong
NSW 2522
Australia

E-mail: druce@uow.edu.au

Chapter 5

Professor G. Krauss
Advanced Steel Processing and Products Research Center
The George S. Ansell Department of Metallurgical and Materials Engineering
Colorado School of Mines
Golden, CO 80401
USA

E-mail: gkrauss@mines.edu

Chapter 6

R. C. Cochrane
University of Leeds
Formerly British Steel Professor of Ferrous Metallurgy
UK

E-mail: r.cochrane.cochrane@btinternet.com

Chapter 7

Pascal J. Jacques
Université Catholique de Louvain (UCL)
Institute of Mechanics
Materials and Civil Engineering (iMMC)
Division of Engineering of Materials and Processes (IMAP)
Place Sainte Barbe, 2
B-1348 Louvain-la-Neuve
Belgium

E-mail: pascal.jacques@uclouvain.be

Chapter 8

J. G. Speer
Advanced Steel Processing and Products Research Center
The George S. Ansell Department of Metallurgical and Materials Engineering
Colorado School of Mines
Golden, CO 80401
USA

E-mail: jspeer@mines.edu

© Woodhead Publishing Limited, 2012

Chapter 9

F. G. Caballero* and C. Garcia-Mateo
National Centre for Metallurgical Research (CENIM-CSIC)
Av. Gregorio del Amo, 8
E-28040 Madrid
Spain

E-mail: fgc@cenim.csic.es

Chapter 10

B. C. De Cooman
Materials Design Laboratory
Graduate Institute of Ferrous Technology
Pohang University of Science and Technology
Pohang
South Korea

E-mail: decooman@postech.ac.kr

Chapter 11

Wei Sha*
School of Planning, Architecture and Civil Engineering
Queen's University Belfast
Belfast BT7 1NN
UK

E-mail: W.Sha@qub.ac.uk

Harald Leitner
Christian Doppler Laboratory for Early Stages of Precipitation
University of Leoben
Franz-Josef-Straße 18
A-8700 Leoben
Austria

Zhanli Guo
Sente Software Ltd
Surrey Technology Centre
40 Occam Road
Guildford GU2 7YG
UK

Wei Xu
OCAS
ArcelorMittal Global R&D Gent
BE-9060 Zelzate
Belgium

Chapter 12

Marcel H. F. Sluiter
Department of Materials Science and Engineering, 3ME
Delft University of Technology
Mekelweg 2
2628 CD Delft
The Netherlands

E-mail: M.H.F.Sluiter@tudelft.nl

Chapter 13

Matthias Militzer
The Centre for Metallurgical Process Engineering
The University of British Columbia
309-6350 Stores Road
Vancouver BC
Canada
V6T 1Z4

E-mail: matthias.militzer@ubc.ca

© Woodhead Publishing Limited, 2012

Chapter 14

Herbert M. Urbassek* and Luis Sandoval[†]
Fachbereich Physik und Forschungszentrum OPTIMAS
Universität Kaiserslautern
Erwin-Schrödinger-Straße
D-67663 Kaiserslautern
Germany

E-mail: urbassek@rhrk.uni-kl.de

Chapter 15

C. Capdevila
Materalia Group
Department of Physical Metallurgy
National Centre for Metallurgical Research (CENIM-CSIC)
Avda. Gregorio del Amo, 8
E-28040 Madrid
Spain

E-mail: ccm@cenim.csic.esm

Chapter 16

D. Boyd* and Z. Yao
Department of Mechanical and Materials Engineering
Queen's University
Kingston, ON
Canada
K7L 3N6

E-mail: boydjd@me.queensu.ca

Chapter 17

M. K. Miller
Materials Science and Technology Division
Oak Ridge National Laboratory
Oak Ridge, TN 37831-6136
USA

E-mail: millermk@ornl.gov

Chapter 18

Dr Stefan Zaefferer*, Nahid-Nora Elhami, Peter Konijnenberg
Department of Microstructure Physics and Alloy Design
Max Planck Institute for Iron Research
Max-Planck-Str. 1
D-40237 Duesseldorf
Germany

E-mail: s.zaefferer@mpie.de;
n.elhami@mpie.de;
p.konijnenberg@mpie.de

Chapter 19

Sudarsanam Suresh Babu
Department of Materials Science and Engineering
The Ohio State University
1248 Arthur E. Adams Drive
#130, Columbus, OH 43221
USA

E-mail: babu.13@osu.edu

[†] Currently at Lawrence Livermore National Laboratory

© Woodhead Publishing Limited, 2012

Foreword

A new and comprehensive book on phase transformations in steels is both timely and welcome. It is gratifying near the beginning of a new, technology-dominated, century to see a group of experts and well accomplished researchers, some of whom have devoted major parts of their professional activities to this area, as well as a group of younger researchers and steel users, all willing to assemble together a new two-volume publication on steels.

Strikingly, unlike many other groups of important metallic materials, it is the onset of transformations in steels resulting from the various thermal and mechanical treatments that make steels so special. This is possible mainly because of the unique properties of iron (Fe) which exhibits three different simple crystal structures; bcc, fcc and bcc again, as temperature rises. Even more unique is the fact that contrary to the usually observed order of the sequence of phase changes observed with temperature, the gamma phase at higher temperatures, is the 'more open' phase than the bcc alpha phase, and hence more able to absorb substantial amounts of alloying element additions. As a result, on quenching or cooling, and other heat treatments, all kinds of phase transformations can take place, and their understanding, manipulation, and utilization constitutes the essence of the importance that steels have exhibited in the past in the development of civilizations and related technologies.

The various chapters bring nicely up to date the vast assembled knowledge of steel transformations in the literature: from the more basic aspects (thermodynamics, diffusion, kinetics, etc.), through the more particular transformation features (nucleation and growth, bainite, martensite, massive, shape memory, etc.), to some aspects of the more recent and advanced analytical possibilities (synchrotron, atom probe, etc.).

Perhaps it is fitting also to mention that the bewildering role of magnetism in iron is the basis of much of this behavior. It is well documented that the ferromagnetic transition in the bcc-Fe phase makes the bcc phases more stable at lower temperatures than the fcc-gamma phase, but still too few people realize that it is the anti-ferromagnetic transition in the gamma phase at temperatures near 0 K that makes the crystalline closed-packed (therefore

© Woodhead Publishing Limited, 2012

'wrong') gamma phase return to stability on heating. Without these unusual features of iron, phase transformations in steels would not take place and the enormous versatility and benefits of steels in the progress of society would be lost.

It may also be time to admit that the ferromagnetic alpha phase has actually a bc-tetragonal symmetry due to the magnetic moments, if the more modern standards of phase definition are adopted, and so the bcc (and paramagnetic) beta phase which has been banished from the iron phase diagrams since the 1920s should be rightfully restored to its original position.

Undoubtedly, research on transformations in steels will continue in the future, as more sophisticated heat treatments are devised and more advanced techniques are brought into use to study the results, particularly at the micro and nano scales. The present book is likely to serve here as a good basis for future advances.

Ted Massalski
Professor of Materials Science, Engineering and Physics
Carnegie Mellon University

© Woodhead Publishing Limited, 2012

Introduction

Steel has been available as a high tonnage engineering material for nearly two centuries. During this time it has had a very creditable track record and one which is crucial to engineering progress, especially in providing the infrastructure in underdeveloped and developing parts of the world, which still dwarf in size and population the more developed nations. This is why the volume of steel production continues to increase, leading to the continual need to consider more economic ways of manufacturing using steel in order to minimise energy consumption and preserve natural resources.

Despite commendable efforts by scientists and engineers to understand fully the processing-microstructure-property relationships in steels, these continue to present new challenges to researchers because of the complexity of the phase transformation reactions and the wide spectrum of microstructures and properties achievable. Thus, an important theme and objective of this book is to follow the development of our understanding of phase transformations in iron alloys and steels through to the development of modern commercial steels, and in particular to highlight the clear connection between phase transformation studies, no matter how isolated and remote they may seem at the outset, to the emergence of new steels with enhanced engineering properties.

Unlike many other metals, the combination of several characteristics, such as magnetism, allotropic phase changes and the different solubility and diffusion behaviour of interstitial and substitutional elements, makes iron-based alloys unique and is responsible for a diversity of phase transformations. The first chapter of this book provides a historical perspective on the first pioneering attempts to gain insight into the complexity of these reactions. All aspects of phase transformations (thermodynamics, diffusion, kinetics and crystal structure) must be properly understood in order to develop a complete picture of the transformation reactions in steels. Thus it was deemed necessary to devote the first section of the book to the fundamental principles of thermodynamics, diffusion and kinetics, and in addition, owing to its growing importance in helping to understand transformations, the phase boundary interface separating parent and product, now much more amenable to observation and analysis using the increased power of modern metallographic instrumentation, as well as modelling.

© Woodhead Publishing Limited, 2012

Starting from the earliest studies on phase transformations in steels, a large number of theories and definitions have emerged leading to continual debates amongst researchers. Only with the development of more advanced experimental capabilities have some of these issues been satisfactorily resolved while others still provoke conflicting opinions. This book aims to represent the current status of knowledge on steel phase transformations whilst also highlighting the challenges facing future researchers in this field.

As mentioned in the Foreword, and demonstrating how the Fe-C system continues to generate important issues, magnetism plays an important role in the phase transformations of iron and steels due to the ferromagnetic and anti-ferromagnetic transitions that take place. Thus it is suggested that paramagnetic beta phase should be restored to the Fe-C phase diagram.

The most important transformations in steels, and the area where almost all research has been concentrated, are those which result in the final microstructure and properties. These involve decomposition of the high temperature γ-phase, austenite, which takes place on cooling and, dependent upon steel alloying and cooling conditions and also whether mechanical working occurs, could follow different paths resulting in a large diversity of lower temperature phase types and their mixtures. These phase transformations could be classified based upon microstructure, thermodynamics or mechanisms and in the present book the phase transformations are classified according to their mechanism. In this scheme the phase transformations in steels are customarily divided into two major groups, which are named according to whether long-range diffusion of atoms occurs or not, namely diffusional or non-diffusional (diffusionless). Each type of phase transformation is then characterised by a set of specific features, including but not limited to composition, crystal structure, shape change and carbon mobility.

It is generally accepted that the formation mechanisms of proeutectoid grain boundary allotriomorphs (of α-ferrite and cementite) and pearlite are diffusional. These reactions take place within the higher temperature region of the low temperature phase field with slow kinetics and generally do not require significant undercooling below the $\gamma \rightarrow \alpha$ transition temperature. In contrast, the formation of martensite with a structure change but composition inherited from parent austenite occurs by a diffusionless transformation at rapid cooling and/or large undercoolings. In-depth presentations of the current state of phase transformation theory for the former type of reactions are given in Volume 1, Part II, whereas the latter is addressed in Volume 2, Part I. These constitute the more traditional microstructures which have long been studied; Henry Clifton Sorby, for example, first identified pearlite around the middle of the 19th century. Moreover, they have long provided the properties of the high-tonnage carbon and alloy steels used in construction and many engineering applications. Nevertheless, as described in these sections, significant progress has been made in understanding their

© Woodhead Publishing Limited, 2012

formation, both for ferrite/pearlite and for basic martensite, in the latter case the *phenomenological theory of martensite crystallography* and, more recently, the proposals deriving from interface mechanics embodied in the so-called *topological model*, which attempt to describe the mechanistic aspects of the transformation. This demonstrates the rich variety of transformations in iron-based alloys, especially when one also adds the shape memory effect, which is of immense interest and commercialisation in non-ferrous systems.

Although significant advances have been made in developing a basic understanding of the nucleation and growth processes, and in validation of various theories, questions still remain due to the limitations of even the most powerful experimental techniques and the complexities of multiphase microstructures forming under a variety of conditions, generally at elevated temperatures. Examples include: elucidating the exact path for carbon diffusion; determining the embryo structure, location and evolution; measuring the effect of so-called 'solute drag' on interface migration; determining the diffusivities and binding energies of elements in multi-component systems; accurately measuring interfacial and strain energies; providing explanations on the differences between the predicted rates of diffusion of substitutional elements at low temperatures and the observed solute clustering. Proving again the complexity, even previously well-accepted ideal cases of partitioning of alloying elements under local equilibrium (LE) or paraequilibrium (PE) conditions for diffusional transformations are now challenged by assumption of negligible partitioning of substitutional elements under local equilibrium (NP-LE).

However, the issues most difficult to resolve, not unexpectedly, have been related to the intermediate products formed between the classical diffusional (e.g. ferrite/pearlite) and diffusionless (e.g. martensite) ones. A variety of morphologies of these products including Widmanstätten ferrite, upper bainite, lower bainite and carbide-free bainite, as well as granular bainite and the so-called 'acicular ferrite microstructures', are considered to exhibit a mixture of characteristics familiar to both classes of transformation, which has fuelled continuous debate regarding the exact formation mechanisms. Perhaps the main discord concerned with the fundamentals of the reaction mechanism has been related to the nature of the bainite transformation (Volume 1, Part III), which essentially reduces to the behaviour and location of carbon during the formation of the bainitic ferrite crystals. As mentioned above, better resolution of such questions might evolve from real-time measurement of carbon concentrations in parent austenite and product ferrite during transformation at elevated temperatures.

Nevertheless, there have been significant positive advances in these phase transformation studies. In this quest for greater understanding of the bainite reaction mechanism, experimental steels have been developed which contain untransformed austenite, useful for studying features of the transformation

© Woodhead Publishing Limited, 2012

mechanism, but which have subsequently been shown can impart valuable properties to a new generation of formable high strength steels for automotive use that has eventually led to commercialisation, e.g. transformation induced plasticity (TRIP) steels. Chapters on these new steels can be found in Volume 2, Part II, alongside comparative chapters on the new twinning induced plasticity (TWIP) steels and high alloyed maraging steels.

Almost all modern high-volume metal production processes are continuous, involving continuous cooling, often associated with mechanical forming, such that complex dynamic changes are more often the norm and sometimes even difficult to simulate in a laboratory environment. Thus, near-equilibrium microstructures are not always the ones which could lead to commercial success. Consequently, given the different industrial processes required in the production of steel in all its various forms, which are continually being updated or modified, a section dealing with parameters involved in transformation other than temperature was considered necessary. External factors, such as deformation, heating rate or application of electromagnetic field could either accelerate or retard the phase transformations depending upon the chosen set of conditions (Volume 1, Part IV). Although a significant body of evidence has been accumulated over time on the effects of these parameters, the underlying mechanisms are not yet fully understood. The phenomenon of restoration of prior austenite morphology and orientation at slow or fast heating rates and absence of it at intermediate heating rates continues to puzzle physical metallurgists. The explanations put forward for this structural inheritance also lack direct and comprehensive experimental evidence.

Many of the significant advances to our understanding of phase transformations in the evolution of steel microstructure during the last 50 years would not have been possible without the parallel development of higher resolution microscopes and related techniques. In the last two decades significant advances have been made in many characterisation techniques (Volume 2, Part IV) and microstructure observations have moved from only *ex-situ* to also *in-situ* ones. It is now possible using *in-situ* transmission electron microscopy, neutron and synchrotron scattering or electron backscattering diffraction coupled with energy dispersive X-ray spectroscopy, to observe the progress of phase transformations not only on heating or cooling, but under external load too. Recent leaps in the development of atom probes and aberration corrected transmission electron microscopes enable the collection of compositional and crystallographic information with atomic resolutions (<0.1 nm). The ability to gather microanalytical data at high resolutions has become increasingly important with the realisation that relatively low bulk concentrations of alloying elements can have disproportionately large effects on transformation behaviour. The exact structure of grain and interphase boundaries and solute segregation to them can now be revealed more clearly.

© Woodhead Publishing Limited, 2012

The improved resolution limit is especially valuable with the increased trend towards production of steels with ultrafine and nano-sized grains and precipitates. Perhaps it should be mentioned that more and more use of 3D techniques in addition to more customarily utilised 2D provides invaluable information on the morphology and distribution of various phases and their crystallography, which helps to fine-tune existing theories and indicates the route for other experiments. But whilst researchers should remain vigilant to artefacts related to each technique and continue to analyse data diligently, these newly developed techniques will allow gathering of the essential information for advancement or validation of existing theories and models, as well as provide the necessary input data for rapidly developing modelling methodologies.

However, we must remain mindful that these instruments and their applications, as will be evident from this section in the book, have become extremely specialised and expensive, and are not widely available, and consequently much of the metallographic work on commercial steel microstructures is still conducted at much lower resolutions by more conventional microscopy. This emphasises the need for consistent descriptions and classifications of microstructure and transformation behaviours across the length scales. As far as has been possible, we have tried to maintain a similar nomenclature throughout the book.

The major new inclusion in this book derives from probably the most significant and totally new topic or field of activity in phase transformations to emerge during the latter part of the main period covered, namely phase transformations modelling. A full section (Volume 2, Part III) has been devoted to this fairly embryonic but rapidly growing field, including all of the well-known approaches: first principles, phase field, molecular dynamics, neural networks. The models provide qualitative and semi-quantitative insight into phase transformations. Some good examples of the preliminary applications to ferrous transformations will be found, some of which have already produced useful advances whilst others are meeting the extensive challenges arising from the complexity of the subject. The hope exists that eventually steels may be designed from first principles taking into account the complexities of phase change associated with those of processing on a large scale, so often difficult to reproduce accurately in the laboratory, or alternatively to study during commercial production. However, it is clear that despite the progress made, the lack of reliable experimental data for input into the models hinders their development. For first principles models reliable experimental data are needed for validation of the potentials. As mentioned previously, quantitative interfacial and strain energy data, data on diffusivities and nucleation, are urgently required to further advance modelling and the theories of ferrous phase transformations.

© Woodhead Publishing Limited, 2012

Finally, the success of applying the knowledge of phase transformations to design of advanced high strength steels should be acknowledged (Volume 2 Part II). This part begins with a chapter on high strength low alloy (HSLA) or microalloyed steels which have probably been the category of steels that have seen the most resource-intensive development during the latter part of the period covered by this book, and still do, driven mainly by the ever more stringent engineering requirements for steels needed in the recovery and transmission of oil and gas. In the quest for greater strength and toughness combined with weldability, extensive data and understanding have been accumulated on the influence of alloying and controlled deformation processing and cooling on the phase transformation and precipitation reactions.

The pathway from the development of quenched and tempered steels and HSLA steels to dual phase, transformation-induced plasticity, nanostructured bainitic ('Nanobain'), twinning-induced plasticity and quenched and partitioned steels is marked by gradual increase in complexity of processing schedules and the microstructures formed. In the latter steels, the direct application of phase transformation sequences in the design of processing schedules led to either significant strength advantage or desirable combinations of high strength/high ductility in formable steels. These manipulations of steel microstructures also enable the achievement of cost savings due to leaner steel compositions and consequently the reduced use of natural resources, coupled with socio-economic benefits.

This project would not have been possible without support from Woodhead Publishing staff and the enthusiasm and co-operation of authors and co-authors in joining us in this task – which apart from confirming our inception of the idea, has made it a more worthwhile and also an enjoyable activity over the last two years. Our authors must also be congratulated on their efforts to produce comprehensive overviews of the topics, including fair and balanced treatments of various theories and models where appropriate. There can be no doubt that it has been an immense task and we can attest to the considerable work which has gone into the production of the manuscript for this book. It will always be a snapshot of where we have reached in this discipline by the year of publication, but it will also we hope, and because of the quality of the chapters provided, stand as a useful source for reference, advanced teaching and learning for a long time to come. In particular, it is hoped that this book will inspire a young generation of scientists and engineers to further advance the knowledge on phase transformations in steels, which remains a fascinating and significant field to explore.

Elena Pereloma
University of Wollongong
David Edmonds
University of Leeds

© Woodhead Publishing Limited, 2012

1

Crystallography of martensite transformations in steels

P. M. KELLY, The University of Queensland, Australia

Abstract: This chapter describes the unique features of martensitic transformations in steels. It covers the characteristics that serve to distinguish and identify the different types of ferrous martensite and then moves on to tackle the most impressive, but often complex and mathematically inscrutable, theory of phase transformations ever produced – the phenomenological theory of martensite crystallography (the PTMC). The approach concentrates on what the mathematics attempts to achieve and not on the mathematics itself. A general comparison between theory and experiment is included as well as attempts to identify features that have proved difficult to explain and hence led to subsequent improvements in the theory. Finally, the chapter identifies the need for further work, either to provide critical experimental evidence to test the theories or to suggest fruitful areas for future research.

Key words: martensite, crystallography, habit plane, orientation relationship, shape strain.

1.1 Introduction

As a solid state phase transformation, the formation of martensite in steels has some unique features. This chapter begins by describing these features and emphasising their importance in the crystallography of martensite. It deals briefly with some of the characteristics – the martensite plate habit plane in particular – that serve to distinguish and identify the different types of martensite found in steels. It then moves on to tackle the most impressive, but often complex and inscrutable, theory of phase transformations ever produced. The steps leading up to the development of the so-called phenomenological theory of martensite crystallography (the PTMC) are described and the various experimental and theoretical advances that provided critical ingredients for this theory are discussed.

The major portion of the chapter is then devoted to a description of the original versions of the PTMC and some of its progeny in the form of modifications or advanced variants. The biggest problem with describing the PTMC is its mathematics. The beautifully elegant matrix algebra employed in the PTMC is often sufficiently daunting and indigestible to permanently discourage the reader. Consequently the true value of this exceptional treatment

© Woodhead Publishing Limited, 2012

of the crystallography of martensite is often never fully appreciated. In this chapter the emphasis is on describing what the mathematics attempts to achieve and not on the mathematics itself. Wherever possible, the approach will be descriptive and will avoid becoming submerged in what is often regarded as incomprehensible mathematics. Important concepts that are essential foundation stones for the PTMC will be explained. The various alternative theoretical treatments and modifications to the PTMC will be discussed and compared with the original theory. However, because of its unsurpassed success as a predictive theory, the PTMC will receive the lion's share of attention and, in many cases, shown to be at least equivalent to the later models/theories.

The strength of any predictive theory rests on its ability to account for any experimental observations. Hence, the comparison between theory and experiment will be covered, but not in minute detail. There is an extensive amount of quite sophisticated experimental data on the crystallography of ferrous martensites in steels that has been collected over more than half a century, and it is impossible to cover all of this individual detail in a single chapter. Instead the emphasis will be on summaries that have appeared in textbooks or reviews and the reader is encouraged to go back to these sources for information on individual sets of observations. Wherever appropriate this comparison between theory and experiment will attempt to identify particular features that have proved difficult to explain via the PTMC. These examples have often led to developments/improvements in the theoretical treatment. Hence this theoretical/experimental comparison will serve not only to test the theories themselves, but also to provide a historical perspective on the development of our understanding of martensite crystallography in the last five decades. It is hoped it will also identify the need for further work, either to provide critical experimental evidence to test the theories or to suggest fruitful areas for future research.

Finally, the success of this chapter on the crystallography of martensite will depend on its ability to demonstrate the power of the PTMC and to encourage others to face the mathematical maelstrom of matrix algebra in the hope of appreciating its contribution to the understanding of a unique form of phase transformation in solids.

1.2 Martensite transformations in steels

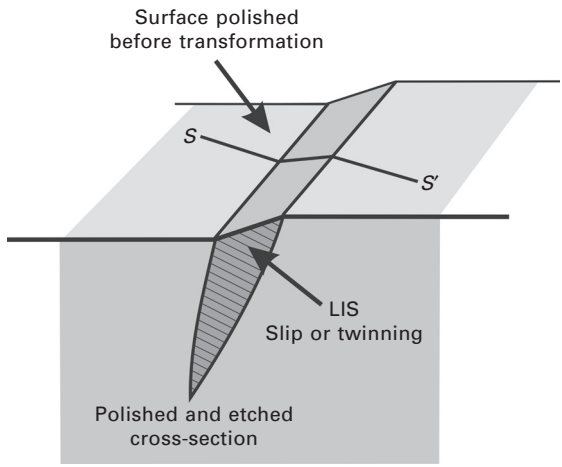
1.2.1 The characteristics of martensite transformations

The martensite transformation in steels is probably one of the earliest recognised examples of a phase transformation in the solid state. The ability to harden 'ignited iron' by quenching was referred to more than 3000 years ago in Homer's *Odyssey* (Homer, 900BC). The important characteristics of

© Woodhead Publishing Limited, 2012

this form of transformation are that it leads to a change in crystal structure that occurs in an athermal, diffusionless fashion involving the simultaneous, co-operative movement of atoms over distances less than an atomic diameter and is accompanied by a macroscopic change of shape of the transformed volume (Bilby and Christian, 1955; Christian, 1965, 1975, 1990; Petty, 1970; Nishiyama, 1978; Cohen *et al*., 1979). While the co-operative atom movements may involve some small 'shuffles' (Christian, 1990), there is no need to 'reconstruct' the crystal structure of the matrix, as there is in a conventional diffusional transformation (Christian, 1975).

From the point of view of the crystallography of the transformation, the displacive character is particularly important. The shape change that results from this displacive component is relatively large and dominated by shear, as opposed to the relatively small changes in volume that accompany the transformation. In a surface polished prior to the transformation, the shape change associated with the formation of a martensite plate leads to surface tilts and the change in direction of surface scratches, as illustrated in Fig. 1.1. The shape change, its magnitude and direction, therefore constitute the most important and defining features associated with a martensitic transformation.



1.1 The experimentally observable effects associated with a martensite transformation in steels. The shape strain, which is an invariant plane strain, causes tilts in a pre-polished surface and changes in direction of the initially straight surface scratch *SS′*. The polished and etched cross-section approximately normal to the pre-polished surface shows the lenticular martensite plate in section with possible evidence for the lattice invariant shear *L* in the form of slip or twinning, as well as the component of the tilt in the pre-polished surface. Adapted from fig. 2 of Zhang and Kelly (2009).

© Woodhead Publishing Limited, 2012

The other important crystallographic characteristics of martensite in steels are its morphology, the orientation relationship between the matrix and product martensite phases, the internal substructure of the martensite itself and the nature of the interface. These crystallographic features need to be referred to particular phases, such as the face centred cubic (fcc) parent phase austenite denoted by the subscript F, the body centred cubic (bcc) or tetragonal (bct) martensite phase denoted by the subscript B and the relatively rare hexagonal close-packed (hcp) epsilon (ε) martensite denoted by the subscript H.

Martensite in steels is often plate-like with a well-defined habit plane – the plane defined by the plate itself. Laths are another relatively common morphology. Martensite laths are ruler-shaped particles that have a habit plane, as well as a specific crystallographic long direction. On rare occasions, rod-like or multi-faceted lath shaped particles may form. The habit plane of a plate or the major facet plane of a lath is often used as a means of distinguishing between the various types of martensite formed in different steels, or in the same steel under differing conditions. The major types of ferrous martensite consist of the $\{259\}_F$ martensite plates formed in Fe-Ni alloys with more than 29% Ni, Fe-Ni-C, Fe-24.5at%Pt, and Fe-Al-C, the $\{225\}_F$ martensite plates formed in high carbon and/or high alloyed carbon steels, the $\{557\}_F$ lath martensite typical of low carbon steels and the $\{\bar{1}\,\bar{1}2\}_F$ bcc laths and $\{111\}_F$ hexagonal close-packed epsilon martensite formed in low stacking fault energy stainless steels (Nishiyama, 1978; McDougall and Wayman, 1992). It must be remembered that these so-called habit planes are generally 'irrational', i.e. they cannot strictly be represented by simple, single-digit Miller indices. However, rather than use a more complex system to represent the habit plane, they are usually, in the interests of brevity at the expense of precision, expressed in terms of the nearest low-index plane. The actual habit planes do not coincide exactly with these low-index planes – the so-called $\{225\}_F$ habit plane is more like $\{2\ 2\ 4.9\}_F$, the reported $\{259\}_F$ habit is closer to $\{3\ 10\ 15\}_F$ and $\{557\}_F$ is more accurately described as a plane close to, but not exactly of the form $\{hhl\}_F$ that is between 9° and 11° from $\{111\}_F$.

An orientation relationship (OR) expresses the relationship between planes and directions in one phase, such as the austenite matrix (F) with corresponding planes and directions in the other phase, i.e. the martensite (B). Typical austenite-martensite ORs are the Kurdjumov–Sachs (K-S) OR (Kurdjumov and Sachs, 1930):

$$(111)_F // (101)_B$$

$$[1\bar{1}0]_F // [11\bar{1}]_B$$

$$[1\bar{2}1]_F \text{ 5.26° from } [10\bar{1}]_B$$

the Nishiyama–Wasserman (N-W) OR (Nishiyama, 1934; Wassermann, 1935):

© Woodhead Publishing Limited, 2012

$(111)_F//(101)_B$

$[1\bar{1}0]_F$ 5.26° from $[11\bar{1}]_B$

$[1\bar{2}1]_F//[10\bar{1}]_B$

and the intermediate Greninger–Troiano (G-T) OR (Greninger and Troiano, 1949):

$(111)_F//(101)_B$

$[1\bar{1}0]_F$ 2.5° from $[11\bar{1}]_B$

$[1\bar{2}1]_F$ 2.5° from $[10\bar{1}]_B$

These three orientation relationships have been expressed in terms of the parallelism of the close-packed planes $(111)_F$ and $(101)_B$ and two sets of directions lying in these planes. This was done purposely to show the relationship between the three ORs. The N-W OR is merely rotated by 5.26° about the normal to the parallel planes $(111)_F$ and $(101)_B$, while the G-T OR is intermediate between these other two ORs. In fact, the close-packed planes $(111)_F$ and $(101)_B$ are often at a small angle of up to 1° to each other, and the parallelisms $[1\bar{1}0]_F//[11\bar{1}]_B$ in the K-S OR and $[1\bar{2}1]_F//[10\bar{1}]_B$ in the N-W OR are seldom exact. These small departures from the ideal are not merely the result of experimental scatter, but may be a combination of real deviations and the effects of the tetragonality of the body-centred martensite in high carbon content alloys.

The next crystallographic feature that is characteristic of a martensitic transformation is the presence of an internal substructure within the martensite plates. As will be discussed in the next section, one of the important aspects of most theoretical treatments of martensite transformations is that the strain represented by the shape change is not sufficient to achieve the required fcc to bcc (or bct) transformation. This was recognised by Greninger and Troiano (1949), who suggested that a second shear was required. In conjunction with the shape change, this second shear would produce the required change in crystal structure. However, this second shear could not contribute to the shape change, so it must be inhomogeneous or 'invisible' on a macroscopic scale. The way to accomplish this is for the second shear to be accompanied by a form of counteracting inhomogeneity, such as fine scale slip or twinning that does not result in any change in crystal structure. This compensating *lattice invariant shear* (LIS) should then be visible as internal substructure within the martensite plate, as shown in Fig. 1.1.

Finally, the interface between martensite and austenite must be extremely mobile. Martensite plates form instantaneously during rapid quenching and the austenite/martensite interface has been reported to move at speeds approaching the speed of sound in the metal—see section 4.4 in Nishiyama (1978). Any dislocations in the interface that accommodate coherency or

© Woodhead Publishing Limited, 2012

are responsible for the actual transformation from austenite to martensite must satisfy certain requirements. For a martensite transformation to occur, these interface dislocations must be completely mobile and capable of rapid movement as the interface propagates. Because of its diffusionless nature, any interface dislocation movement associated with the transformation must be conservative and not involve any net atom flux or the creation or destruction of lattice sites. In developing a dislocation model of the austenite/martensite interface or in postulating details of the transformation mechanism that may involve the creation of interface dislocations, all of these relatively strict conditions must be met. By comparison, in the case of a diffusion-controlled transformation, this interface dislocation movement criterion associated with no atom flux is not necessary, as non-conservative climb is possible and the interface dislocations merely have to satisfy geometric considerations.

The combination of these crystallographic characteristics has a pronounced impact on the development of a satisfactory theoretical model for a martensitic transformation. A successful theory must be capable of predicting a planar interface that corresponds to the habit plane of a martensite lath or plate, must derive the correct features of the OR and shape change, must be consistent with any internal substructure within the martensite plates, and finally, must only result in totally glissile arrangements of dislocations in the interface. How this is done is covered in the following sections.

1.2.2 Early theories of martensite crystallography

The earliest attempts to account for the fcc to bcc (or bct) transformation in steels involved looking at the similarities in the two structures and postulating a combination of strains, together with local atomic adjustments, that would be capable of converting the fcc austenite matrix to the bcc (or bct) martensite product. Kurdjumov and Sachs postulated a double shear mechanism that was consistent with their K-S orientation relationship (Kurdjumov and Sachs, 1930), and Nishiyama derived a mechanism involving a similar shear on a $\{111\}_F$ plane combined with a second distortion that led to his N-W orientation relationship (Nishiyama, 1934). Both these mechanisms are illustrated in fig. 6.5 of the English edition of Nishiyama's book (Nishiyama, 1978). The problem with both these mechanisms was that they predicted a $\{111\}_F$ habit plane and the observed habit planes in many steels were nowhere near $\{111\}_F$.

The next step in the development of a theory/model of martensitic transformations in steels was taken by Jaswon and Wheeler, who pointed out that, if some form of homogeneous deformation process was responsible for creating a martensite plate from the parent austenite, then the associated disturbance of the surrounding matrix would be intolerable, unless the austenite/martensite plate boundary was unrotated (Jaswon and Wheeler, 1948). Using

© Woodhead Publishing Limited, 2012

the Kurdjumov–Sachs double shears to generate the bcc martensite from fcc austenite, they searched for planes that remained unrotated after these strains had achieved the required transformation. For a cubic martensite product there were two unrotated planes that could become potential habit planes for a martensite plate: $\{111\}_F$ and a plane close to $\{225\}_F$. As the carbon content of the steel was increased and the product martensite became tetragonal, the unrotated $\{111\}_F$ habit plane remained, the one close to $\{225\}_F$ shifted slightly and a third unrotated plane close to $\{111\}_F$ appeared. Because there was already some evidence for the $\{225\}_F$ habit plane in high carbon plain carbon steels, this prediction was particularly significant. What was just as important was the emphasis on an unrotated habit plane, which would reappear as one of the ingredients of the invariant plane concept that formed the basis of the subsequent successful phenomenological theory of martensite crystallography (PTMC).

This emphasis on the strains associated with a martensite transformation aimed the theoretical developments in the right direction. The next significant step was due to Greninger and Troiano, who worked primarily on Fe-Ni and Fe-Ni-C steels where the martensite had an irrational habit plane close to $\{259\}_F$ (Greninger and Troiano, 1949). They concentrated on the observed shape strain and carried out the first measurements of the direction and magnitude of the shape strain. Even though they neglected the volume change and assumed that the shape strain was a simple shear, their measurements were done with sufficient precision to show that, on its own, the shape change was not capable of producing the required change of crystal structure from fcc to bcc (or bct). Hence, they suggested that *two* shears were required. The first was responsible for the observed change of shape, while the second shear would complete the required change in crystal structure, but would have no macroscopic consequences and so would not contribute to the observed shape strain. While this two shear mechanism was similar to the earlier Kurdjumov and Sachs proposal (Kurdjumov and Sachs, 1930), it introduced the important new concept that one of the shears would be 'invisible', and hence would be accompanied by some form of internal inhomogeneity, such as slip or twinning.

Bowles later showed that, for the $\{225\}_F$ transformation in high carbon steel, the Jaswon–Wheeler theoretical analysis was consistent with the Greninger–Troiano double shear proposal (Bowles, 1951). By measuring the shape strain and including the volume change, he was able to develop a mechanism that incorporated an inhomogeneous or 'invisible' shear on the same $(112)[11\bar{1}]_B$ twinning system in martensite that was used by Greninger and Troiano. More important, by including the volume change as an expansion normal to the habit plane, together with a shear on the habit plane, he introduced the important concept of an invariant plane strain (IPS) that was to become a key component of the subsequent PTMC.

© Woodhead Publishing Limited, 2012

Frank also considered the $\{225\}_F$ transformation and developed a model where the close-packed planes $(111)_F$ and $(10\bar{1})_B$ in the two phases met along the common close-packed directions $[1\bar{1}0]_F$ and $[11\bar{1}]_B$ lying in the $\{225\}_F$ habit plane interface (Frank, 1953). The spacing of the close-packed planes in the two phases differed slightly, and to achieve perfect matching a small rotation about their common intersection in the habit plane was necessary. In addition, a shear on the $(112)_B$ planes produced by an array of screw dislocations in the interface is needed to ensure that matching between successive planes remains 'in-step'. This is essentially the same as the inhomogeneous second shear proposed by Greninger and Troiano.

This two-dimensional model was criticised because it only applied to the $\{225\}_F$ transformation where the matching close-packed directions lie in the habit plane and it did not account for the $\{259\}_F$ habit plane. This was subsequently remedied when a three-dimensional prism matching theory was later developed (Bilby and Frank, 1960). The geometric matching conditions were obviously far more complex, but a second shear on $(112)_F$ was still required. This prism matching model predicted an elliptical locus of habit plane positions. The magnitude of the shape deformation varied along this habit plane locus and was a minimum at a position that corresponded to $\{259\}_F$. For the same set of lattice parameters this was identical with the predictions arrived at somewhat earlier using the PTMC.

1.3 Phenomenological theory of martensite crystallography (PTMC)

1.3.1 Key features of the PTMC

The most significant theoretical advance was undoubtedly the development of the PTMC. The first general version of the theory was published by Wechsler, Lieberman and Read (WLR) in 1953 (Wechsler *et al.*, 1953). A very similar theory was developed quite independently on the other side of the world by Bowles and Mackenzie (BM) (Bowles and Mackenzie, 1954a, 1954b; Mackenzie and Bowles, 1954). These two versions of what is now known as the phenomenological theory of martensite crystallography (PTMC) do differ slightly in their approach, but are essentially equivalent (Bilby and Christian, 1955; Christian, 1956). The essential input data required are the crystal structures and lattice parameters of the two phases, the correspondence between them and the elements of the lattice-invariant shear – the equivalent of the Greninger–Troiano 'invisible' or 'second' shear.

The PTMC involves three concepts that are often not fully appreciated. The first of these is the notion of a correspondence, the second is the involvement of an *invariant plane strain* that leaves the habit plane undistorted and unrotated and the third is the phenomenological nature of the theories. Each

© Woodhead Publishing Limited, 2012

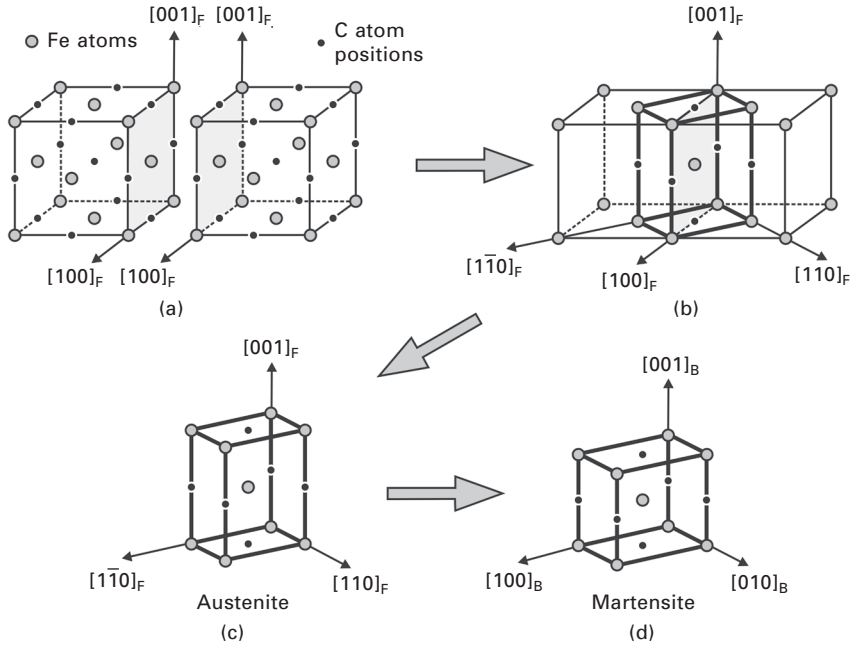
of these will be discussed before moving on to the detail of the theories themselves.

The *lattice correspondence* between the two phases is a particularly important concept. It describes how a set of labelled atoms (or atom sites) that define vectors, planes and unit cells of the matrix austenite lattice become the corresponding vectors, planes and unit cells of the product martensite lattice. One consequence of this correspondence is that there must be the same number of atoms in the 'unit' cell of the parent austenite as there is in the 'unit' cell of the product martensite. The atoms themselves do not have to be identical, but the atomic sites must correspond. The term 'lattice correspondence' therefore incorporates the meanings of both 'atomic site correspondence' (Howe, 1994) and 'atom correspondence' (Christian, 1997).

In the case of a correspondence between non-primitive unit cells containing more than one atom, the possibility of 'shuffles' must be recognised. The correspondence really only relates the positions of the atomic sites that define the corners of the parent and product unit cells, with any remaining atoms being regarded as occupying an interpenetrating equivalent lattice or as interior sites in the corresponding cells. In order to complete the structural transformation from parent to product, additional displacements in the form of 'shuffles' may be required (Christian, 1997). These shuffles are relative translations of certain subsets of atoms through less than an interatomic distance, do not affect the number of atoms in the corresponding unit cells and have no detectable influence on the shape change associated with the transformation.

The most appropriate correspondence for a particular martensitic transformation can often be selected by assuming that the correct correspondence is the one that leads to the smallest atomic displacements (Jaswon and Wheeler, 1948), but there is often no clear, direct experimental evidence that the selected correspondence is in fact correct. This is not the case with the fcc to bcc (or bct) transformation in steels. The Bain correspondence (Bain, 1924) used by Jaswon and Wheeler is illustrated in Fig. 1.2 and can be verified experimentally. In steels containing significant amounts of carbon, the martensitic product is not body centred cubic, but is distorted to body centred tetragonal, with the degree of tetragonality dependent on the carbon content of the steel – see fig. 2.2 of Nishiyama (1978). This distorted structure can be regarded as a body centred cubic iron (ferrite) lattice with carbon atoms occupying the octahedral interstitial sites in a very specific ordered arrangement. What is so unique about the Bain correspondence is that the ordered arrangement of interstitial carbon atoms in martensite can be produced from face centred cubic austenite that contains dissolved interstitial carbon atoms that are perfectly randomly arranged in the octahedral sites of the austenite matrix lattice. The selection of the bct

© Woodhead Publishing Limited, 2012



1.2 Schematic illustration of the Bain correspondence (Bain, 1924) for martensite in steels. Part (a) shows a pair of unit cells of the fcc austenite structure (F) with the octahedral interstitial carbon atom positions indicated by black circles. The number of these positions that are actually occupied at random by a carbon atom depends on the carbon content of the steel – approximately 5% occupancy per 1 wt% carbon. The two fcc unit cells can be joined on their $(010)_F$ planes (shaded) to give the arrangement shown in (b), where a body centred tetragonal (bct) unit cell outlined in bold can be identified. To avoid confusion, only the Fe atoms and the C atom positions of this bct austenite cell, together with the Fe atoms at the corners of the original fcc austenite unit cells are shown in (b). This bct austenite cell with a c/a ratio of $\sqrt{2}$ is shown on its own in (c). Note that the octahedral carbon atom positions are now in the centre of the (001) faces of this bct cell, but *not* in the (100) and (010) faces of this cell. Similarly, there are octahedral carbon atom positions in the centres of the cell edges parallel to [001], but *not* in the [100] or [010] cell edges. The bct austenite (F) cell in (c) can be converted to the bcc (or bct) martensite (B) unit cell, shown in (d), via a contraction approaching 25% along $[001]_F$, which becomes $[001]_B$, together with an expansion of around 13% along the directions $[1\bar{1}0]_F$ and $[110]_F$, which become $[100]_B$ and $[010]_B$, respectively.

austenite cell shown in Figs 1.2 (b) and (c) has the carbon atoms arranged in these very specific positions. Adding interstitial carbon atoms at random to this bct unit cell would result in it having a c/a ratio greater than unity. In other words, the interstitial carbon atoms in the martensite will make its

© Woodhead Publishing Limited, 2012

unit cell tetragonal, with the degree of tetragonality linearly proportional to the carbon content. This provides the experimental proof that completely justifies the choice of correspondence.

Figure 1.2 illustrates another important point. The variant of the correspondence shown in Fig. 1.2 is such that:

$[100]_F$ becomes $[110]_B$,

$[010]_F$ becomes $[\bar{1}10]_B$, and,

$[001]_F$ becomes $[001]_B$.

There are two other major variants of this correspondence, one with $[100]_F$ becoming $[001]_B$ and one with $[010]_F$ becoming $[001]_B$. This latter major variant is the one selected by Bowles and Mackenzie.

With the correspondence shown in Fig. 1.2 and the lattice parameters of the austenite and the martensite, the total strain necessary to convert the matrix austenite to the product martensite can be derived. This total strain is known as the Bain strain **B**. Note that throughout this chapter 'bold sans serif' type will be used to represent matrices (in capitals) and vectors (in lower case). If the fcc austenite lattice parameter is a_F and the lattice parameters of the bct martensite are a_B and c_B, then the Bain strain can be represented by three components η_1, η_2 and η_3 along the $[100]_F$, $[010]_F$ and $[001]_F$ directions in the austenite lattice, where:

$$\eta_1 = \eta_2 = \sqrt{2}(a_B/a_F),$$

and

$$\eta_3 = (c_B/a_F)$$

For ferrous martensite, both η_1 and η_2 are >1 (expansions), while η_3 is <1 (a contraction) and the total change in volume is given by $(\eta_1\eta_2\eta_3 - 1)$.

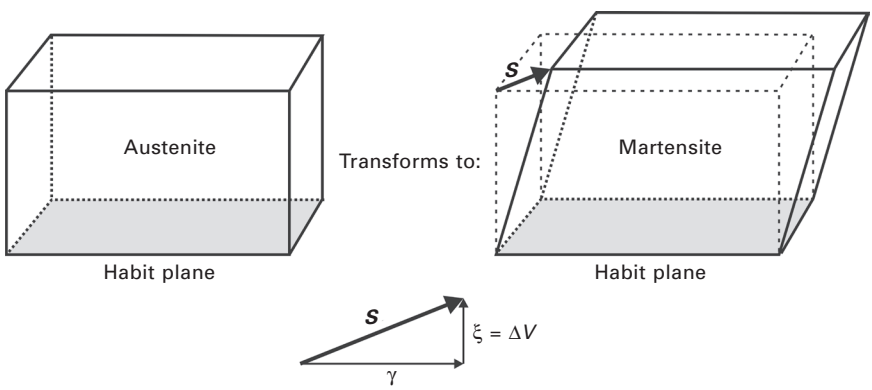
The second particularly important concept in the PTMC is the assumption that the planar interface of a plate-like martensite must be an *invariant* plane (Wayman, 1972). An invariant plane is a plane that is both undistorted and unrotated as a result of the total transformation strains. This is a much stricter geometric condition than the Jaswon–Wheeler unrotated plane (Jaswon and Wheeler, 1948), since none of the vectors lying in the invariant plane can be changed in length or rotated in any way. This assumption was consistent with the fact that the majority of ferrous martensites observed prior to the introduction of the PTMC were in the form of thin plates. A few years after the introduction of the PTMC, Eshelby's classic work on the strain energy associated with a constrained transformation (Eshelby, 1957) showed clearly that the strain energy of a transformed particle in the form of an infinitely thin oblate spheroid could be reduced to zero, if the strains associated with the transformation satisfied the conditions of an *invariant plane strain* (IPS)

© Woodhead Publishing Limited, 2012

(Christian, 1976). This concept meant that the shape strain associated with a martensite transformation had to be an invariant plane strain of the type illustrated in Fig. 1.3 – in other words a shear γ in a direction parallel to the habit plane, plus an expansion (or contraction) ξ normal to the habit plane.

The Bain strain **B** is sufficient to convert the matrix austenite crystal structure to that of the product martensite, but it seldom satisfies the two very stringent conditions required to produce an invariant plane strain. The first of these is that one of the principal strains must be zero and the second, equally important condition, is that the other two principal strains must be of opposite sign, i.e. one strain must be an expansion, while the other is a contraction (Bilby and Christian, 1955; Christian, 1956). If the strain involved in the martensite transformation can be made to satisfy these two conditions, then it will be possible to form a martensite plate where the habit plane of the plate is invariant. The two versions of the PTMC were both aimed at ensuring that the shape strain of the martensite transformation was an invariant plane strain.

The final point about the PTMC is that the WLR and BM theories are both *phenomenological*. This means that all the theories attempt to do is to relate the crystallographic features of the final transformed martensite product to those of the original matrix austenite. This is a purely 'before and after' description. Although governed by the very stringent conditions associated with the invariant plane concept, the PTMC does not pretend to offer any information about the actual mechanism of transformation. It is



1.3 A rectangular block of fcc austenite on the left is transformed to a block of bcc martensite via an invariant plane strain **S** that consists of a shear γ in a direction lying in the habit plane (shaded) and a dilatation ξ that is an expansion or contraction normal to the habit plane. Note that the dilatation component ξ is equal to the volume change ΔV that results from the austenite to martensite transformation. Adapted from fig. 3 of Zhang and Kelly (2009).

© Woodhead Publishing Limited, 2012

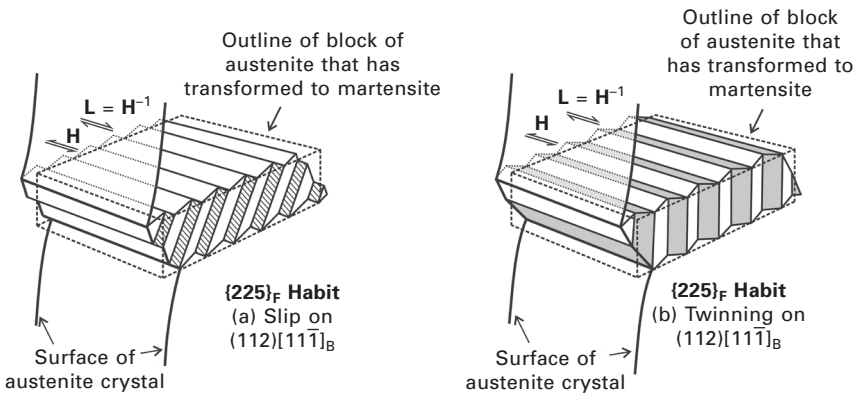
not a mechanistic model that describes individual atom movements. All the PTMC does is to specify, via an elegant analysis based on matrix algebra, the very strict geometrical conditions that must be met to get from the initial state to the final state. The mathematical steps taken in this process and the order in which they are carried out do not necessarily bear any particular relevance to the way the transformation actually occurs. This is pure mathematical manipulation, designed to go from 'before' to 'after'. The PTMC predictions of the habit plane, the orientation relationship between austenite and martensite and the magnitude and direction of the shape strain can then be compared with experimental observations.

1.3.2 How the PTMC works

The PTMC was based on the original observation in ferrous martensite that the experimentally measured shape strain on its own was not capable of transforming fcc austenite to bcc (or bct) martensite. Hence, an invisible second shear that did not contribute to the shape strain was required (Greninger and Troiano, 1949). The BM version of the PTMC followed this suggestion directly, while WLR adopted a slightly different approach. WLR recognised that the Bain strain **B**, which converts austenite to martensite, is unlikely to satisfy the rigorous conditions required for the shape strain to be an invariant plane strain. Hence, the problem to be solved was how to convert the strain **B** to an invariant plane strain without altering the crystal structure of the two phases, austenite and martensite.

This can be achieved by incorporating an additional strain that does not change the crystal structure of either phase. This *lattice invariant strain* (LIS) will of course alter the macroscopic shape of the transformed volume of martensite, but it must do so in a way that does not alter the crystal lattice of the phase in which it operates. The LIS cannot lead to a change in volume, because this would contribute to the shape change, so it is likely to be a simple shear. Regularly spaced slip on a series of parallel planes is a form of shear that would be an effective LIS. The other alternative is internal twinning where the relative thickness of the two twins would be equivalent to a simple shear. WLR followed Greninger and Troiano by selecting internal twinning to be the LIS. Simple slip and internal twinning as a LIS is illustrated in Fig. 1.4, and both are equivalent to a simple shear. If the LIS is represented by a shear **L**, then the total transformation strain is **BL**. Note that **L** is regarded as preceding **B** in the mathematical formulation, but this does *not* imply a real-time sequence. The magnitude **g** of the simple shear **L** is adjusted so that the product **BL** results in the formation of an invariant line lying in the plane of the LIS. This is the first condition necessary to produce a final invariant plane strain – one of the principal strains of the combination **BL** becoming zero. As the value of **g** is normally derived via the solution of a

© Woodhead Publishing Limited, 2012



1.4 The formation of a martensite plate in steels showing the two types of lattice invariant shear (LIS), slip on the left and twinning on the right. In both cases the LIS corresponds to a simple shear on $(112)[11\bar{1}]_B$ and the WLR lattice invariant shear **L** is the inverse of the Bowles/Mackenzie 'invisible' second shear **H**, i.e. $\mathbf{L} = \mathbf{H}^{-1}$. Adapted from the original fig. 5 of Kelly (1960).

quadratic equation, there will be two solutions for **g**, both of which lead to an invariant *line* strain (Wechsler *et al*., 1953). Normally, the smaller of the two is adopted on the grounds that this minimises the strain components of the LIS **L**.

To convert this invariant *line* strain **BL** to an invariant *plane* strain, the other two principal strains of **BL** must be opposite in sign. This is the second condition that must be satisfied and means that **BL** will generate at least one other undistorted line in addition to the original invariant line. This pair of undistorted lines defines an *undistorted* plane. However, only the original undistorted line is both undistorted and unrotated. The second undistorted line is not necessarily unrotated, but can be made completely invariant, i.e. undistorted *and* unrotated, via a rigid body rotation **R** about the original invariant line. This rigid body rotation has no effect on the morphological or crystallographic features of the 'rigid body' that is rotated. All it does is to ensure that there is now a pair of invariant lines that define an *invariant plane*. In other words the combination **RBL** is an *invariant plane strain*, which is exactly what is required by the theory to represent the shape strain **S**. The WLR formulation of the theory can therefore be represented via the matrix algebra 'short-hand' notation as:

$$\mathbf{S} = \mathbf{RBL} \qquad [1.1]$$

Because the theory is phenomenological, the mathematical steps taken to generate the shape strain **S** in Eq. [1.1] do not necessarily indicate actual physical processes that have occurred during the transformation. However, the resultant shape strain has real, physically measurable characteristics.

© Woodhead Publishing Limited, 2012

The habit plane corresponds to the invariant plane and, on a pre-polished surface, measurements of the surface tilts and change in direction of scratches illustrated in Fig. 1.1 can be used to determine the direction and magnitude of the shape strain **S**. Similarly, the orientation relationship between the austenite and the martensite depends on the correspondence, on which **B** is based, and the rotation **R**. The LIS **L** has no effect on the orientation relationship, but the shear that gives **L** its lattice invariant characteristics may be experimentally observable as regular slip or twinning, as shown in Figs 1.1 and 1.4.

The BM treatment of the PTMC follows directly from the original observation (Greninger and Troiano, 1949) that the shape strain **S** is, on its own, not capable of transforming fcc austenite to bcc (or bct) martensite. Hence the BM approach begins with the invariant plane strain **S** and combines this with an 'invisible' second shear **H**, which also deforms the crystal lattice. The total deformation that results from the BM combination **SH** must then be equal to the WLR total deformation **RB** and so the BM version of the PTMC can be represented as:

$$\mathbf{SH} = \mathbf{RB} \qquad [1.2]$$

In order to maintain the 'invisibility' of the 'second' shear **H** and to ensure that it cannot make up part of the shape change, the shape deformation **S** must equal $\mathbf{SHH}^{-1}$, where $\mathbf{H}^{-1}$ is the inverse of **H**. In other words, $\mathbf{H}^{-1}$ must be an equally opposite lattice invariant deformation that exactly balances any shape changes resulting from **H**. So, Eq. [1.2] can be written as:

$$\mathbf{SHH}^{-1} = \mathbf{S} = \mathbf{RBH}^{-1} \qquad [1.3]$$

Comparing the WLR equation [1.1] with the BM version of [1.3], it is clear that the LIS **L** is the same as $\mathbf{H}^{-1}$ or $\mathbf{H} = \mathbf{L}^{-1}$. The WLR 'lattice invariant shear' **L** is the inverse or mathematical opposite of the BM 'invisible' second shear **H**. Hence, although they appear to follow different approaches, the two versions of the theory are completely equivalent (Bilby and Christian, 1955; Christian, 1956).

The inputs to the PTMC were the lattice parameters of austenite and martensite, the correspondence between the two phases, usually the Bain correspondence, and the plane and direction of the LIS **L**, or its equivalent the 'invisible' second shear **H**. Initially, the only possible variables that could be changed to achieve agreement between theory and experiment were the correspondence, which was only very rarely attempted, and the elements of the LIS. In the mid-1950s, when the PTMC was developed, a reasonable amount of experimental data on habit planes and orientation relationships in ferrous martensite was already available. This showed clearly that there were two main types of truly plate-like martensite in steels, those with a $\{225\}_F$ habit plane primarily in plain carbon steels and those with a $\{259\}_F$

© Woodhead Publishing Limited, 2012

or $\{3\ 10\ 15\}_F$ habit plane in iron-nickel and iron-nickel carbon alloys with low martensite start (Ms) temperatures. The PTMC was able to explain all the crystallographic features of the $\{259\}_F$ martensite, which was not surprising, since Greninger and Trioiano's work on this type of martensite was the catalyst that lead to the development of the PTMC. However, there was a measure of marked disappointment when the PTMC appeared to have some difficulties in relation to the $\{225\}_F$ type of ferrous martensite. The need to account for $\{225\}_F$ martensite had always been recognised. It appears in Bowles initial introduction of the concept of an 'invisible' second shear (Bowles, 1951) and was the basis for Frank's original lattice matching model (Frank, 1953). Hence, it was not surprising to see a number of attempts to adapt the PTMC to the case of the $\{225\}_F$ transformation.

The first of these had already been incorporated in the BM version of the PTMC. Bowles and Mackenzie purposely permitted a small relaxation to the invariant plane condition by introducing a small dilatation (<2%) that allowed the distances in the habit plane to be slightly different in the two phases. So, the habit plane was *nearly* invariant, but it was still an unrotated plane in the two phases. This allowed the PTMC to be more versatile, and increasing the dilatation parameter δ from unity (an exactly invariant habit plane) to around 1.015 (1.5% strain allowed in the habit plane) the predicted habit plane moved from $\{259\}_F$ to $\{225\}_F$ (see, for example, fig. 2.11 in Petty, 1970, or fig. 5 in Bowles and Mackenzie, 1954b). No satisfactory physical explanation of the significance of this dilatation was put forward and consequently this explanation for $\{225\}_F$ martensite was occasionally regarded with some suspicion by other workers in the field.

Wechsler, Otte and Wechsler, Lieberman and Read all adopted a different approach in an attempt to account for the $\{225\}_F$ martensite habit plane. They tried different rational slip or twinning systems in the austenite or the martensite as the LIS (Wechsler, 1959; Otte, 1960; Wechsler *et al.*, 1960). These LIS systems were capable of predicting a variety of habit planes, but only a few came close to $\{225\}_F$ and even these possible solutions were not always really convincing. In some cases the variant of $\{225\}_F$ predicted was not correct and in others the magnitude **g** of the LIS was relatively large.

1.4 The post phenomenological theory of martensite crystallography (PTMC) period

1.4.1 Experiments and more trials of the theory

The advent of the PTMC and its obvious problems with accounting for the $\{225\}_F$ habit plane in steels led to a dramatic increase in research on martensite in the next couple of decades. This followed two main lines. The first was in using the PTMC to account for other forms of martensite in steels and the

© Woodhead Publishing Limited, 2012

second, more dominant, aspect was sophisticated experimental determinations of the morphological and crystallographic characteristics of martensite. An excellent summary of this very fruitful period of experimental work on ferrous martensite is available in a review by McDougall and Wayman (1992). Rather than repeat the content of this comprehensive review or go through the copious publications individually, this chapter will only highlight some of the experimental developments and the reader is encouraged to study the McDougall/Wayman review paper.

There was considerable emphasis on accurately measuring habit planes, orientation relationships and, in particular, the direction and magnitude of the shape strain. The other topic that received considerable attention was attempts to detect and measure the dilatation, if it was present. For the $\{259\}_F$ or $\{3\ 10\ 15\}_F$ martensite plates, all the accumulated experimental evidence was completely consistent with the predictions of the PTMC. The original observations of internal twinning in these martensite plates were confirmed and more detailed observations of the internal substructure were made. All of this merely confirmed the original selection of the $(110)[1\bar{1}0]_F$, i.e. $(112)[11\bar{1}]_B$, internal twinning as the operative LIS. Accurate measurements of the habit plane, orientation relationship and the direction and magnitude of the shape strain in a number of alloys all agreed completely with the predictions of the PTMC, as shown in table 1 in McDougall and Wayman (1992). This table also includes the results of attempts to measure the dilatation (if any) and these confirmed that the dilatation parameter δ in these alloys was essentially equal to 1.

The $\{225\}_F$ transformation was not such an obvious complete vindication of the PTMC. The internal substructure was more complex and variable compared with $\{259\}_F$ martensite, but it was clear that the same $(112)[11\bar{1}]_B$ internal twinning was present in the $\{225\}_F$ martensites. There was evidence suggesting that an additional LIS shear system was operative in $\{225\}_F$ martensite and this possibility will be explored later, when discussing the 'double-shear' theories. However, the predominance of internal twinning suggested that the alternative LIS approach to explaining the $\{225\}_F$ habit plane was not valid. Unfortunately, attempts to measure the dilatation suggested that any changes in length in the habit plane would have to be less than 0.2% or nearly 10 times too small to account for $\{225\}_F$ in this way. The final addition to the confusing saga of $\{225\}_F$ martensite was the obviously real, systematic variation in the measured shape strain direction by some 40° as shown in fig. 9 in McDougall and Wayman (1992). The section on 'Theories of the $(225)_F$ transformation' in this paper is an excellent summary of the various attempts to account for the $\{225\}_F$ transformation up to 1992.

The formation of bcc martensite, as well as hexagonal ε martensite, in highly alloyed steels with low stacking fault energy provided another example of the successful application of the PTMC (Kelly, 1965). The hexagonal ε

© Woodhead Publishing Limited, 2012

martensite forms as bands on the $\{111\}_F$ planes of the austenite and can be produced by a change in the stacking sequence from fcc to hcp via a shear of $a_{/6}<112>_F$ on every second $\{111\}_F$ plane, with no need for a LIS or 'second' shear. This shear can occur inhomogeneously by distributing the transformation shear over the three $<112>_F$ directions lying in the $\{111\}_F$ plane of a single band. This could lead to the fcc austenite to hcp ε transformation occurring with essentially no shape change.

The bcc α martensite can form within a band of hexagonal ε, via a single invariant plane strain, plus a slight 'shuffle' of atoms on adjacent $(000l)_\varepsilon$ planes. Alternatively, the fcc austenite to bcc martensite transformation can occur directly with a LIS on $(111)/[\bar{1}2\bar{1}]_F$ (Kelly, 1964, 1965). In this case the LIS corresponds to the formation of stacking faults within the parent austenite. Hence, the bcc martensite will always be associated with bands of faulting in the austenite and these faulted bands could be close to the hcp ε structure, so that the bcc martensite could appear as if it had formed from the hexagonal ε. The predicted habit plane for this bcc martensite is $(\bar{1}\bar{1}2)_F$ at a maximum dilatation ($\delta = 1.018$), and it is possible to form twin-related bcc martensite plates with this same habit plane arranged at right angles to the bands of faulting or hexagonal ε. In such situations the shape strains of the twin-related pair would have shear components that are exactly opposite and would effectively cancel each other (Kelly, 1965). For values of the dilatation parameter δ closer to unity, a habit plane of the type $\{225\}_F$ is predicted. But this habit plane is $(\bar{2}\bar{2}5)_F$ and is close to 90° from the close-packed fcc plane $(111)_F$ that is parallel to $(101)_B$. This is *not* the same as the normal $\{225\}_F$ martensite, where the habit plane is less than 30° away from the close-packed fcc plane $(111)_F$ that is parallel to $(101)_B$.

The orphan child in all of this burgeoning experimental work and further applications of the PTMC was the lath martensite formed primarily in low carbon steels. The main reason for the dearth of experimental attention devoted to what was subsequently to become known as the '$\{557\}_F$ lath transformation' was that it invariably formed at high temperatures and it was difficult to find any retained austenite matrix to use as the basis for measurements of the habit plane, orientation relationship or shape strain. In fact even now, nearly half a century later, there has never been a reliable measurement of the shape strain of lath martensite in steels. Little theoretical attention was devoted to lath martensite in the decade or two that followed the development of the PTMC, mainly because of the obsession with explaining the plate-like $\{225\}_F$ martensite that was much easier to deal with experimentally.

1.4.2 Alternative theories

The other area that did receive considerable attention during this post-PTMC period was the development of alternative or improved versions of

© Woodhead Publishing Limited, 2012

the theory. The driving force was primarily the attempt to come up with a more credible explanation for the $\{225\}_F$ martensite plates. For example, the Bilby/Frank prism matching method (Bilby and Frank, 1960) described in Section 1.2.2 was one of these proposed alternatives. It was able to predict a $\{225\}_F$ habit plane without incorporating a dilatation, but at the expense of a marked increase in the magnitude of the shape strain.

At about the same time as the PTMC was published, the first interface dislocation approach to martensite transformations was developed (Bullough and Bilby, 1956). The most important conclusion reached in this analysis was that it was essentially equivalent to the PTMC. This tended to dampen enthusiasm for this approach, despite the fact that it could, in principle, provide details of the actual mechanism of the transformation that was not available in the 'phenomenological' theory. The interface dislocation models were, however, revived in the late 1980s and again nearly two decades later, as discussed in Section 1.6.

The major theoretical developments that occupied the period following the publication of the PTMC tended to concentrate on alternative LIS systems. After trying LIS systems other than the $(112)[11\bar{1}]_B$ slip or twinning system used in the original PTMC, the next step was to relax the insistence that the LIS should be a rational slip or twinning system in either the matrix austenite or the product martensite. Initially the plane or direction of the LIS was allowed to become 'irrational' (Crocker and Bilby, 1961). An LIS with a 'rational' direction, but an 'irrational' plane, could be achieved quite simply by combining two shears with different rational shear planes and the same rational shear direction. Similarly, an LIS with a rational plane and an irrational direction could be produced via the combination of two shears with different rational shear directions that shared the same rational shear plane. This approach led to the prediction of a number of different habit planes, but did not achieve the original objective of satisfactorily accounting for the $\{225\}_F$ habit plane in steels. However, fig. 4 in Crocker and Bilby (1961) introduced a concept that was to prove valuable in subsequent applications of the PTMC, as a means of selecting the most likely LIS systems. For a particular rational LIS shear direction, a variable irrational shear plane could be represented in terms of the angle from some fixed starting position, and the same angle approach could be used to represent the position of an irrational shear direction lying in a rational shear plane. In both these cases the variation of the magnitude **g** of the LIS and the magnitude **s** of the shape strain could be plotted as a function of angle from the starting position for the various LIS systems being considered. Obviously the LIS which leads to the smallest values of **g** and **s** is likely to be favoured. In fig. 4 in Crocker and Bilby (1961), there are two such cases, namely $(112)[11\bar{1}]_B$ and $(111)[\bar{1}2\bar{1}]_F$. The first of these is the traditional twinning system first suggested by Greninger and Troiano and used as LIS in both the original versions of the

© Woodhead Publishing Limited, 2012

PTMC. The other corresponds to the LIS operating in the so-called System II transformation that is associated with profuse faulting or the formation of hexagonal ε in high alloy steels with low stacking fault energy. Figures 2 and 3 in Kelly (1964) show examples of these plots of **g** and **s** as a function of the angle of the irrational shear component from some fixed position for both the System I and System II transformations.

The next development in the 'double shear' approach was to make it even more general and not confine the LIS to a composite shear system with either a common rational shear plane or a common rational shear direction. Initially, this was achieved by using two shears that have the same 'plane of shear' (Crocker, 1965). This means that the shear plane normals for the two component shears, as well as their shear directions, all lie in the same plane. While this introduced a further degree of freedom in the selection of the LIS used in the PTMC, it was still not possible to produce a credible explanation for $\{225\}_F$ martensite. So the next step was to develop a completely generalised version of the PTMC that allowed the use of double LIS systems that were completely free of any crystallographic restrictions. Equivalent theoretical 'double shear' treatments were developed independently and essentially concurrently by Acton and Bevis (1969) and by Ross and Crocker (1970). This constituted a major step in generalising the PTMC and was largely aimed at accounting for the $\{225\}_F$ habit plane without having to invoke a dilatation. The publication of these two general versions of the 'double shear' theory coincided with some very reliable estimates of the dilatation parameter δ associated with a systematic series of experimental measurements of the shape strain magnitude and direction for both $\{225\}_F$ and $\{259\}_F$ martensite (Dunne and Bowles, 1969). This experimental work showed very convincingly that the dilatation parameter did not differ significantly from unity and that the observed shape strains could not be distinguished from a true invariant plane strain. Some direct measurements of length changes in the habit plane of $\{225\}_F$ martensite supported both the observation that δ was not significantly greater than unity (Krauklis and Bowles, 1969) and the earlier conclusion (Morton and Wayman, 1966) that a single shear LIS version of the PTMC could not account simultaneously for the measured shape strain results and the orientation relationship in $\{225\}_F$ martensite.

The accumulation of experimental evidence against the incorporation of a dilatation in the PTMC was a significant boost for the 'double shear' versions of the theory. Their success in adequately accounting for $\{225\}_F$ martensite was critically assessed by Dunne and Wayman, who concluded that 'the double shear theory results in improved predictions relative to the original single shear theory, but this does not provide a complete description of the crystallography of {225} martensite' (Dunne and Wayman, 1971). This comment relates to the difficulty of being able to correctly predict the habit plane, the shape strain and the orientation relationship simultaneously. At

© Woodhead Publishing Limited, 2012

the time this comment was made, the various published applications of the double shear theory had not been able to account for all of these observed crystallographic features of $\{225\}_F$ martensite. However, some two decades later an extended series of systematic double shear trials, where the larger of the two LIS shears incorporated a component of the twinning shear observed in $\{225\}_F$ martensite (Kelly, 1992c), led to a number of double shear combinations that simultaneously accounted for, not only the observed habit plane, orientation relationship and shape strain, but was also able to account for the previously observed real variation in shape strain direction of 40° or more (see Muddle *et al*., 1976, and fig. 9 in McDougall and Wayman, 1992). A similar application of the double shear theory (Kelly, 1992a, 1992b) was able to account for all the currently known crystallographic features of $\{557\}_F$ lath martensite, including the apparently large values of the shape strain, the orientation relationship and the observed array of $a_{/2}[1\overline{1}\,\overline{1}]_B$ dislocations in the austenite/martensite interface (Sandvik and Wayman, 1983). All of this is amply reviewed in the section on 'The $\{557\}_F$ lath transformation' in McDougall and Wayman (1992).

While the criticisms of the generalised double shear versions of the PTMC mentioned above are difficult to justify and, in this modified form, the theory appears to provide the required flexibility to account very well for the majority of the crystallographic features of martensite in steels and other materials, there is still room for doubt. One question often raised in informal discussions was whether or not such a double shear arrangement could still lead to an array of interface dislocations that were sufficiently mobile to permit the extremely rapid propagation of the austenite/martensite interface. Despite these niggling doubts about the mechanistic viability of the double shear versions of the theory, the PTMC has to be regarded as probably the best predictive, as opposed to explanatory, theory of phase transformations in crystalline solids. No other theory of martensitic or diffusional phase transformations would appear to even come close to the PTMC in this regard.

1.5 Strain energy – the Eshelby/Christian model and the infinitesimal deformation (ID) approach

Because martensite is often in the form of a thin lenticular plate, the Eshelby equations for the strain energy associated with the transformation of an oblate spheroid are particularly relevant (Eshelby, 1957, 1959). They can be used to explore a number of effects associated with the shape strain of ferrous martensite, including the work done by the shape strain while under the influence of an external stress (Patel and Cohen, 1953).

The Eshelby strain energy relationships can also be used to examine the effects on the overall strain energy of a transformed martensite plate that

© Woodhead Publishing Limited, 2012

result from the introduction of a dilatation parameter (Christian, 1958). For an oblate spheroid of semi-thickness t and radius R subjected to an invariant plane strain, when the ratio t/R approaches zero and the spheroid becomes infinitely thin, the strain energy associated with this planar feature reduces to zero. This is the justification for the use of the invariant plane strain concept in the PTMC. However, as Christian pointed out, the use of a dilatation parameter might be justified on the grounds that it led to a minimum strain energy per unit volume for *finite*, *non-zero* values of t/R (Christian, 1958). Some 25 years later, Hayakawa and Oka extended Christian's analysis, allowed for the possibility of an anisotropic dilatation and calculated the variation of strain energy per unit volume with habit plane position for a series of values of t/R (Hayakawa and Oka, 1984). Somewhat later, Ledbetter and Dunn derived similar results for the case of a uniform dilatation in the habit plane (Ledbetter and Dunn, 1999, 2000). Both these sets of calculations indicated that in steels, as the dilatation parameter δ was increased from unity to a value of 1.02, the martensite habit plane position moved from $\{259\}_F$ to $\{225\}_F$ as the value of t/R was increased from zero to over 0.1. This tends to offer a form of physical justification for the introduction of a dilatation parameter into the PTMC, but it is not entirely consistent with experimental observations. It does not adequately explain the fact that there appear to be two very distinct groups of habit planes, $\{225\}_F$ and $\{259\}_F$ with nothing in between (see, for example, fig. 2.11 in Petty, 1970, or fig. 5 in Bowles and Mackenzie, 1954b). There must be some additional factor, which accounts for this very discrete shift in habit plane position. A possible explanation will be put forward later in Section 1.7.

The role of the elastic strain energy in the Eshelby analysis provided an alternative basis for a crystallographic theory of martensite transformations. This was based on determining the conditions that led to a minimum in the strain energy of the lenticular transformed volume of martensite. When expressed in terms of *infinitesimal* strains, rather than the *finite* strains used in the PTMC, this led to calculating a strain matrix $\mathbf{T}^{\mathbf{i}}$, where the only non-zero terms correspond to those of an invariant plane strain (Shibata-Yanagisawa and Kato, 1990). So $\mathbf{T}^{\mathbf{i}}$ is the infinitesimal strain equivalent of the PTMC shape strain $\mathbf{S}$, i.e. $\mathbf{T}^{\mathbf{i}} = \mathbf{S}^{\mathbf{i}}$, where the superscript '**i**' denotes an infinitesimal strain. This was a very logical basis for a crystallographic theory of martensitic transformations. The Eshelby strain energy approach is a simpler, more understandable physical concept when compared with the more esoteric, but equivalent, geometric principle of an invariant plane that is the basis for the PTMC. In an attempt to capitalise on this conceptually simpler approach and, at the same time, avoid the complex matrix algebra of the PTMC, some authors adopted the infinitesimal strain approximation that neglects higher order strain terms, when they developed their version of the *infinitesimal deformation* (ID) analysis of martensite transformations

© Woodhead Publishing Limited, 2012

(Shibata-Yanagisawa and Kato, 1990; Navruz and Durlu, 1999; Navruz, 2001). If valid, the infinitesimal strain approximation allows strain and rotation matrices to be added, rather than multiplied, so that in ID terms the PTMC equation [1.1], namely $\mathbf{S} = \mathbf{RBL}$, becomes:

$$\mathbf{T}^{\mathbf{i}} = \mathbf{S}^{\mathbf{i}} = \mathbf{R}^{\mathbf{i}} + \mathbf{B}^{\mathbf{i}} + \mathbf{L}^{\mathbf{i}} \quad [1.4]$$

While this certainly simplifies the subsequent mathematical manipulation, unless at least two of the terms on the right-hand side of Eq. [1.4] satisfy the infinitesimal strain approximation by having strains that are less than 0.01, $\mathbf{T}^{\mathbf{i}}$ is not going to be equal to $\mathbf{S}^{\mathbf{i}}$ and the predictions of the ID theory will no longer be the same as those of the PTMC, as they should be. For example, in the case of $\{259\}_{\mathrm{F}}$ martensite, the strains in $\mathbf{B}^{\mathbf{i}}$ are in the range 0.13–0.24 and the magnitude of the LIS in $\mathbf{L}^{\mathbf{i}}$ is >0.2 (Wayman, 1964). These are clearly not infinitesimal strains by any stretch of the imagination and the predictions made by the matrix addition version of the ID theory in this case, and in any other application to martensite in steels for that matter, will not be consistent with those of the PTMC. If the infinitesimal strain approximation is not used when it is inappropriate and the ID analysis is conducted in a rigorous fashion with matrix multiplication where necessary, then the predictions will be exactly the same as those of the PTMC (Mura *et al*., 1976; Kato *et al*., 1977; Hayakawa and Oka, 1984; Ledbetter and Dunn, 1999, 2000; Kelly, 2003). Unfortunately, there is now little simplification in the mathematics of the rigorous ID approach.

1.6 Interfacial dislocation models

Both the PTMC and the ID theories are essentially phenomenological in that they do not claim to represent the actual atomic mechanism of the martensite transformation. An interface dislocation picture of the austenite/martensite boundary, on the other hand, could provide useful clues to the atomic mechanisms involved in the transformation (Bilby and Christian, 1955). An array of dislocations in the planar boundary of a martensite plate would have to satisfy certain conditions, if the habit plane interface is to be glissile and semi-coherent (Christian, 1976). The net Burgers vectors of the interface dislocations must be given by the equations of surface dislocations and individual dislocations must be free to move as an array into the lattices of either phase. As pointed out by Christian, referring to the first attempt at an interfacial dislocation model (Bullough and Bilby, 1956), 'these conditions lead to expressions for the martensite habit plane, the orientation relations and the shape strain identical with those derived from the formal crystallographic theories' (Christian, 1976). In a comprehensive paper, the dislocation theory of martensitic transformations was subsequently extended to include nucleation, thermoelastic behaviour, transformation plasticity, etc.

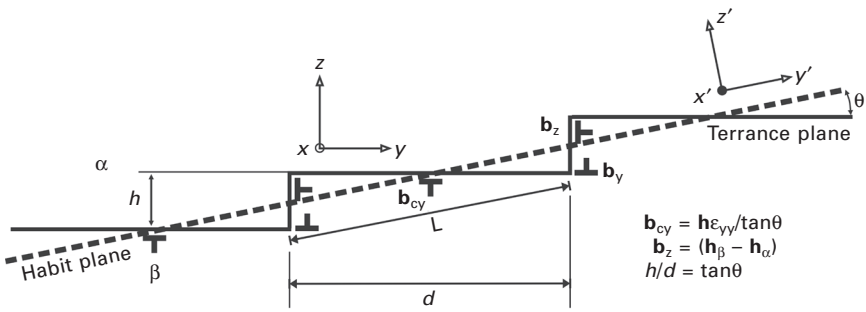
© Woodhead Publishing Limited, 2012

(Olson and Cohen, 1986). The emphasis on what was termed the 'topological' characteristics of interface dislocations has the potential to provide an atomistic mechanism for the martensite transformation that goes well beyond the purely phenomenological approach in theories like the PTMC.

Recently, Pond and co-workers have developed an interfacial dislocation theory termed the 'Topological Model' (TM) (Pond and Celotto, 2003; Pond *et al*., 2003, 2006, 2007). This was based on a habit plane made up of terraces and steps/disconnections, as shown in Fig. 1.5, and the martensitic transformation proceeds by the movement of the interface dislocations associated with these regularly spaced disconnections. The initial version was essentially two-dimensional and avoided the need to incorporate a lattice invariant shear. The mathematics was relatively simple compared with the PTMC and the TM offered considerable promise as a means of exploring the more mechanistic aspects of martensite formation. The determination of the overall interface habit plane orientation was based on the premise that the array of interface dislocations must lead to a situation where there is 'no long range strain' in the habit plane. The analysis in appendix B of Pond *et al*. (2003) and section 3.2 of Pond *et al*. (2007) led to the following equation for the angle θ of the habit plane to the terrace planes lying in the xy plane of Fig. 1.5:

$$\mathbf{b}_z\tan^2\theta + \mathbf{b}_y\tan\theta + \mathbf{h}\varepsilon_{yy} = 0 \qquad [1.5]$$

A martensite interface with no long range strain is in effect equivalent to the invariant plane strain concept used in the PTMC and it was to be expected



1.5 The stepped interface used in the Topological Model (TM). This consists of terrace planes with steps of height '*h*' separated by a spacing '*d*'. The interface incorporates three dislocations: $\mathbf{b}_z$ normal to the terrace planes, the shear dislocation $\mathbf{b}_y$ that is responsible for the shear component of the $\beta \rightarrow \alpha$ martensitic transformation and the coherency dislocation $\mathbf{b}_{cy}$ that is related to the atomic spacing mismatch ε_{yy} in the terrace plane. Adapted from fig. 15 of Pond *et al.* (2007).

© Woodhead Publishing Limited, 2012

that, like the earlier Bullough/Bilby interface dislocation theory, the TM predictions should agree with those of the PTMC. However, this was not the case and the TM predictions differed slightly from those of the PTMC, whenever the step heights in the two phases were not the same, i.e. when $|\mathbf{b}_z|$ was not equal to zero. These TM habit plane predictions were obtained by using the 'overlap step height', which is the smaller of the two step heights $\mathbf{h}_\alpha$ and $\mathbf{h}_\beta$, as the value of $\mathbf{h}$ in Eq. [1.5] (Pond *et al.*, 2003; Pond *et al.*, 2006, 2007). A minor modification to Eq. [1.5] where the value of $\mathbf{h}$ was put equal to the 'mean step height' $\langle\mathbf{h}\rangle = (\mathbf{h}_\alpha + \mathbf{h}_\beta)/2$ was put forward (Kelly, 2008b) and shown to give predictions that were now identical with those of the PTMC. However, this modification was not accepted (Hirth and Pond, 2008) and the disagreement over the appropriate value of $\mathbf{h}$ to use in Eq. [1.5] is still unresolved (Kelly, 2008a).

The two-dimensional version of the TM was not applied directly to ferrous martensite, but in subsequent papers attention turned to steels and in particular to the cases of $\{225\}_F$ and $\{557\}_F$ martensite (Ma and Pond, 2007, 2008; Pond *et al.*, 2008). This is particularly interesting, because this version of the TM is three-dimensional and includes a lattice invariant shear. It adopts a somewhat different approach that is mathematically more complex, but may not suffer from the same problems as the habit plane analysis in the two-dimensional TM. It also tends to start by assuming a major element in the orientation relationship by allowing the starting arrangement to vary from the N-W OR to the K-S OR and this has two consequences. It sacrifices a measure of predictability and it gives results that lead to a continuously variable habit plane position. To date the final habit plane structures have not been refined, so the results are somewhat preliminary. Consequently, the comparisons of the ferrous TM results with experiment and with the predictions of the PTMC, including the double-shear versions of this theory, have not been particularly extensive. To be really useful, this version of the TM should be extended to provide more refined habit plane calculations and to derive the shape strain magnitude and direction. While there is no reliable experimental data for the shape strain of $\{557\}_F$ lath martensite, considerable experimental data on the $\{225\}_F$ and $\{259\}_F$ transformations is available, including measurements of the direction and magnitude of the shape strain magnitude, and this would provide ample background against which to evaluate the TM. In principle, the application of the TM to ferrous martensite should be capable of providing some valuable insights into the atomic mechanism of martensite formation. For example, it might be possible to establish which double shear LIS systems would be the most appropriate in accounting for $\{225\}_F$ and $\{557\}_F$ martensite.

© Woodhead Publishing Limited, 2012

1.7 Future trends

Half a century after the development of the PTMC, the ability to predict and explain the vast majority of the crystallographic features of ferrous martensite is now very well established. The double shear versions of the PTMC have been able to account for $\{225\}_F$ and $\{557\}_F$ martensites, without having to invoke an arbitrary dilatation parameter or relax the strict invariant plane condition.

Interface dislocation models have made surprisingly little impact on the understanding of the atomistic mechanisms responsible for the crystallography of martensite in steels. This may in part be due to the fact that the current TM, at least in its two-dimensional form, does not agree with the predictions of the PTMC. In principle, an interfacial dislocation model like the TM should be able to cast some light on the few crystallographic features that do not fit absolutely comfortably with the PTMC, for example in providing insights into the most appropriate double shear systems, if any, that could be used to explain $\{225\}_F$ and $\{557\}_F$ martensites. To do this successfully, two things are necessary. The first is for the TM to be applied systematically to *all* the types of ferrous martensites and to make predictions about the shape strain magnitude and direction, as well as the habit plane and orientation relationship, for $\{259\}_F$, $\{225\}_F$, $\{557\}_F$ and $\{\bar{1}\,\bar{1}2\}_F$ martensites. Many of these crystallographic features have already been reliably measured and the results are available in the literature (see, for example, McDougall and Wayman, 1992). The missing items in this list of experimental data on ferrous martensites make up the second requirement for this comparison. There are no reliable experimental data on the direction and magnitude of the shape strain for $\{557\}_F$ lath martensite, or for that matter for the $\{\bar{1}\,\bar{1}2\}_F$ martensite in high alloy stainless steels. These experimental measurements are essential to provide a complete comparison with the theoretical predictions of both the PTMC and the TM. Finally, the recent emphasis on high-resolution transmission electron microscopy (HRTEM) examination of the details of the dislocation structure in ferrous martensite interfaces would be invaluable as a comparison with the theoretical outputs of the TM.

The PTMC is based on the premise that the shape strain of a martensite plate is an invariant plane strain. The Eshelby strain energy of a transformed oblate spheroid shows that such a martensite plate will have zero energy provided the plate is infinitely thin – a thickness to radius ratio t/R equal to zero. But infinitely thin martensite plates have never been observed! The plates may be thin, but they always have a finite t/R ratio in the range 0.01–0.1. So the strain energy of a 'real' martensite plate is never zero. As discussed in Section 1.5, the consequences of a finite t/R ratio have been explored a few times in the last 50 years, but have never really come up with any firm conclusions that have had a significant impact on our understanding of the

© Woodhead Publishing Limited, 2012

crystallographic features of martensite in steels. For example, although this type of analysis is capable of justifying the change in habit plane position from $\{259\}_F$ to $\{225\}_F$ as the t/R ratio increases from zero to ~0.1, it does not obviously account for the fact that there do not appear to be any martensite habit planes located between these two positions. Why the dramatic change in habit plane, with no evidence for a gradual movement from one to the other?

A recent possible explanation for this sudden transition introduces another important factor: the role of the interfacial surface energy in determining the crystallographic characteristics of martensite (Kelly, 2006). Why should the reduction of strain energy completely dominate the features of a displacive martensitic transformation? Is it not possible that the interfacial surface energy also plays a role? If so, how important are the relative influences of strain and surface energy in martensite transformations? Surely a strain energy dominated transformation can make some sacrifices in order to achieve a reduction in surface energy. Is this reduction in interfacial surface energy sufficient to compensate for the increase in strain energy associated with the change from the $\{259\}_F$ habit to the $\{225\}_F$ habit when the t/R ratio is increased to ~0.1? All this string of questions does is to highlight what would appear to be a promising area for future research, namely the role of interfacial surface energy in governing the crystallographic characteristics of martensite in steels. All the required theoretical and experimental tools are available for a concerted attack on this topic. On the theoretical side, interfacial dislocation models like the TM, combined with the elegant O-lattice formulation developed by Zhang and her co-workers (Zhang and Weatherly, 2005), should be able to make predictions that can be verified (or otherwise) by HRTEM examination of martensite interface dislocation structures. This particular aspect of martensitic transformations is crying out for further, more sophisticated analysis, verified by careful experiments.

1.8 Conclusions

The PTMC in all its versions has been extremely successful in accounting for the crystallographic features of martensite in steels. No other theoretical treatment of a phase transformation even comes close to the predictive abilities of the PTMC. We now have a very sound, comprehensive understanding of the crystallography of martensite transformations in steels. There are a few areas where the agreement between theory and experiment could be improved, and there are some gaps in the experimental data available and features, such as the role of interfacial surface energy, that should be investigated. Nevertheless, the PTMC has already demonstrated its superiority as the epitome of theoretical treatments of the crystallography of phase transformations in solids.

© Woodhead Publishing Limited, 2012

1.9 References

Acton, A F and Bevis, M (1969) 'A generalised martensite crystallography theory', *Mater. Sci. Eng.*, 5, 19–29.

Bain, E C (1924) 'The nature of martensite', *Trans. AIME*, 70, 25–35.

Bilby, B A and Christian, J W (1955) The mechanism of phase transformations in metals. In: *Martensitic Transformations*, London: The Institute of Metals, pp. 121–172.

Bilby, B A and Frank, F C (1960) 'The analysis of the crystallography of martensitic transformations by the method of prism matching', *Acta Metallurgica*, 8, 239–248.

Bowles, J S (1951) 'The crystallographic mechanism of the martensite reaction in iron-carbon alloys', *Acta Crystallographica*, 4, 162–171.

Bowles, J S and Mackenzie, J K (1954a) 'The crystallography of martensite transformations I', *Acta Metallurgica*, 2, 129–137.

Bowles, J S and Mackenzie, J K (1954b) 'The crystallography of martensite transformations III. Face-centred cubic to body-centred tetragonal transformations', *Acta Metallurgica*, 2, 224–234.

Bullough, R and Bilby, B A (1956) 'Continuous distributions of dislocations: surface dislocations and the crystallography of martensite transformations', *Proc. Phys. Soc. Lond.*, B69, 1276–1286.

Christian, J W (1956) 'Applications of the phenomenological theories of martensite – I–II', *J. Inst. Met.*, 84, 386–394.

Christian, J W (1958) 'Accommodation strains in martensite formation, and the use of a dilatation parameter', *Acta Metallurgica*, 6, 377–379.

Christian, J W (1965) Military transformations: an introductory survey. In: *Physical Properties of Martensite and Bainite*, London: The Iron and Steel Institute, pp. 1–19.

Christian, J W (1975) *The Theory of Transformations in Metals and Alloys*, 2nd edn, Oxford: Pergamon Press.

Christian, J W (1976) O-lattice, surface dislocation and elastic theories of martensite crystallography and martensitic nuclei. In: Suzuki, H, *New Aspects of Martensitic Transformation*, Kobe, Japan: Japan Institute of Metals, pp. 21–33.

Christian, J W (1990) 'Analyses of lattice and shape deformation and of atomic shuffles in martensitic transformation', *Materials Science and Engineering A*, 127, 215–227.

Christian, J W (1997) 'Lattice correspondence, atomic site correspondence and shape change in "diffusional-displacive" phase transformations', *Progress in Materials Science*, 42, 101–108.

Cohen, M, Olson, G B and Clapp, P C (1979) On the classification of displacive phase transformations. In: Owen, W. S., *International Conference on Martensitic Transformations*, *ICOMAT 1979*. Cambridge, MA: MIT, p. 1–11.

Crocker, A G (1965) 'Shear resolution applied to the martensite reaction in steel', *Acta Metallurgica*, 13, 815–825.

Crocker, A G and Bilby, B A (1961) 'The crystallography of the martensite reaction in steel', *Acta Metallurgica*, 9, 678–688.

Dunne, D P and Bowles, J S (1969) 'Measurement of the shape strain for the (225) and (259) martensitic transformations', *Acta Metallurgica*, 17, 201–212.

Dunne, D P and Wayman, C M (1971) 'An assessment of the double shear theory as applied to ferrous martensitic transformations', *Acta Metallurgica*, 19, 425–438.

Eshelby, J D (1957) 'The determination of the elastic field of an ellipsoidal inclusion, and related problems', *Proceedings of the Royal Society of London A*, 241, 376–396.

© Woodhead Publishing Limited, 2012

Eshelby, J D (1959) 'The elastic field outside an ellipsoidal inclusion', *Proceedings of the Royal Society of London A*, 252, 561–569.

Frank, F C (1953) 'Martensite', *Acta Metallurgica*, 1, 15–21.

Greninger, A B and Troiano, A R (1949) 'The mechanism of martensite formation', *Trans AIME*, 185, 590–598.

Hayakawa, M and Oka, M (1984) 'The calculation of elastic strain energy and the prediction of the habit plane for ferrous martensite', *Acta Metallurgica*, 32(9), 1415–1422.

Hirth, J P and Pond, R C (2008) Response to 'Phenomenological Theory of Martensite Crystallolgraphy (PTMC) Versus the Topological Method (TM)'. In: Olson, G B, Lieberman, D S and Saxena, A, *International Conference on Martensitic Transformations (ICOMAT-08)*. Santa Fe, New Mexico: TMS (The Minerals, Metals and Materials Society), pp. 123–128.

Homer (900BC) *The Odyssey*, IX, line 392.

Howe, J M (1994) 'Atomic site correspondence and surface relief in the formation of plate-shaped transformation products', *Metallurgical and Materials Transactions A*, 25A, 1917–1922.

Jaswon, M A and Wheeler, J A (1948) 'Atomic displacements in the austenite-martensite transformation', *Acta Crystallographica*, 1, 216–224.

Kato, M, Miyazaki, T and Sunaga, Y (1977) 'Re-examination of the minimization of elastic energy and the phenomenological crystallographic theory in a martensite transformation', *Scripta Metallurgica*, 11, 915–919.

Kelly, P M (1960) Metallography of the martensite transformation in plain carbon and alloy steels, PhD Thesis, University of Cambridge.

Kelly, P M (1964) Metallurgical developments in high-alloy steels. In: *Martensite Transformations in High-alloy Steels*, Scarborough: The Iron and Steel Institute, pp. 146–152.

Kelly, P M (1965) 'The martensite transformation in steels with low stacking fault energy', *Acta Metallurgica*, 13, 635–646.

Kelly, P M (1992a) 'Crystallography of lath martensite in steels', *Materials Transactions JIM*, 33(3), 235–242.

Kelly, P M (1992b) The crystallography of lath martensite in steels. In: Wayman, C M and Perkins, J, *International Conference on Martensitic Transformations (ICOMAT-92)*. Monterey, CA: Monterey Institute of Advanced Studies, pp. 299–304.

Kelly, P M (1992c) The crystallography of the $(225)_f$ martensite transformation in steels. In: Wayman, C M and Perkins, J, *International Conference on Martensitic Transformations (ICOMAT-92)*. Monterey, CA: Monterey Institute of Advanced Studies, pp. 293–298.

Kelly, P M (2003) 'Martensite crystallography – the apparent controversy between the infinitesimal deformation approach and the phenomenological theory of martensitic transformations', *Metallurgical and Materials Transactions A*, 34A, 1783–1786.

Kelly, P M (2006) 'Martensite crystallography – the role of the shape strain', *Materials Science and Engineering A*, 438–440, 43–47.

Kelly, P M (2008a) Comments on Response to 'The Phenomenological Theory of Martensite Crystallography (PTMC) versus the Topological Model (TM)'. In: Olson, G B, Lieberman, D S and Saxena, A, *International Conference on Martensitic Transformations (ICOMAT-08)*. Santa Fe, NM: TMS (The Minerals, Metals and Materials Society), pp. 129–133.

Kelly, P M (2008b) The phenomenological theory of martensite crystallography (PTMC) versus the topological model (TM). In: Olson, G B, Lieberman, D S and Saxena, A,

© Woodhead Publishing Limited, 2012

International Conference on Martensitic Transformations (ICOMAT-08). Santa Fe, NM: TMS (The Minerals, Metals and Materials Society), pp. 115–121.

Krauklis, P and Bowles, J S (1969) 'The direct measurement of length changes in the (225) martensite habit plane', *Acta Metallurgica*, 17, 997–1004.

Kurdjumov, G and Sachs, G (1930) 'Über den Mechanismus der Stahlhartung', *Zeitschrift für Physique*, 74, 325–343.

Ledbetter, H M and Dunn, M L (1999) 'Habit planes, inclusion theory, and twins', *Materials Science and Engineering A*, 273–275, 222–225.

Ledbetter, H M and Dunn, M L (2000) 'Equivalence of Eshelby inclusion theory and Wechsler–Lieberman–Read, Bowles–Mackenzie martensite-crystallography theories', *Materials Science and Engineering A*, 285, 180–185.

Ma, X and Pond, R C (2007) 'Parent–martensite interface structure in ferrous systems', *Journal of Nuclear Materials*, 361, 313–321.

Ma, X and Pond, R C (2008) 'Defect modelling of martensitic interfaces in plate martensite', *Materials Science and Engineering A*, A481–482, 404–408.

Mackenzie, J K and Bowles, J S (1954) 'The crystallography of martensite transformations II', *Acta Metallurgica*, 2, 137–147.

McDougall, P and Wayman, C M (1992) The crystallography and morphology of ferrous martensites. In: Olson, G B and Owen, W S (eds), *Martensite*, Warrendale, PA: ASM International, pp. 59–95.

Morton, A J and Wayman, C M (1966) 'Theoretical and experimental aspects of the (225) austenite-martensite transformation in iron alloys', *Acta Metallurgica*, 14, 1567–1581.

Muddle, B C, Krauklis, P and Bowles, J S (1976) 'The shape strain of the $(225)_f$ martensite transformation', *Acta Metallurgica*, 24, 371–380.

Mura, T, Mori, T and Kato, M (1976) 'The elastic field caused by a general ellipsoidal inclusion and the application to martensite formation', *Journal of the Mechanics and Physics of Solids*, 24, 305–318.

Navruz, N (2001) 'Determination of the crystallographic parameters of the cubic-to-tetragonal martensitic transformation using the infinitesimal deformation approach and Wechsler, Lieberman and Read theory', *Metallurgical and Materials Transactions A*, 32A(2), 247–250.

Navruz, N and Durlu, T N (1999) 'Application of the infinitesimal deformation approach to the fcc to bcc martensitic transformation for a Fe-%31Ni alloy', *Journal of Materials Science Letters*, 18, 959–961.

Nishiyama, Z (1934) 'X-ray investigation of the mechanism of the transformation from face-centered cubic to body-centered cubic', *Sci. Rep. Tohuku University*, 23, 637–664.

Nishiyama, Z (1978) *Martensitic Transformation*, *Materials Science and Technology*, New York: Academic Press.

Olson, G B and Cohen, M (1986) Dislocation theory of martensitic transformations. In: Nabarro, F R N (ed.), *Dislocations in Solids*, Amsterdam: North-Holland, pp. 295–407.

Otte, H M (1960) 'On the imperfections in martensite and their relation to the formation of martensite', *Trans. AIME*, 218, 342–351.

Patel, J R and Cohen, M (1953) 'Criterion for the action of the applied stress in the martensitic transformation', *Acta Metallurgica*, 1, 531–538.

Petty, E R (ed.) (1970) *Martensite – Fundamentals and Technology*, London: Longman.

© Woodhead Publishing Limited, 2012

Pond, R C and Celotto, S (2003) 'Special interfaces: military transformations', *International Materials Reviews*, 48(4), 225–245.

Pond, R C, Celotto, S and Hirth, J P (2003) 'A comparison of the phenomenological theory of martensite transformations with a model based on interfacial defects', *Acta Materialia*, 51, 5385–5398.

Pond, R C, Ma, X and Hirth, J P (2006) 'Kinematic and topological models of martensitic interfaces', *Materials Science and Engineering A*, 438–440, 109–112.

Pond, R C, Ma, X, Chai, Y W and Hirth, J P (2007) Topological modelling of martensitic transformations. In: Nabarro, F R N and Hirth, J P (eds), *Dislocations in Solids*, Amsterdam: North-Holland, pp. 225–261.

Pond, R C, Ma, X and Hirth, J P (2008) A dislocation model of parent-martensite interfaces. In: Olson, G B, Lieberman, D S and Saxena, A, *International Conference on Martensitic Transformations (ICOMAT-08)*. Santa Fe, NM: TMS (The Minerals, Metals and Materials Society), pp. 107–114.

Ross, N D H and Crocker, A G (1970) 'A generalised theory of martensite crystallography and its application to transformations in steels', *Acta Metallurgica*, 18, 405–418.

Sandvik, B P J and Wayman, C M (1983) 'Characteristics of lath martensite: Part I. Crystallographic and substructural features', *Metallurgical Transactions A*, 14A, 809–822.

Shibata-Yanagisawa, M and Kato, M (1990) 'Crystallographic analysis of cubic(tetragonal) to monoclinic martensitic transformations based on the infinitesimal deformation approach', *Materials Transactions JIM*, 31, 18–24.

Wassermann, G (1935) 'Über den Mechanismus der α–γ Umwandlung des Eisens', *Mitt K-Wilh-Inst Eisenforsch*, 17, 149–155.

Wayman, C M (1964) *Introduction to the Crystallography of Martensitic Transformations*, *Macmillan Series in Materials Science*, New York: Macmillan.

Wayman, C M (1972) 'Crystallographic theories of martensitic transformations', *Journal of the Less-Common Metals*, 28, 97–105.

Wechsler, M S (1959) 'On the theory of martensitic transformations. The generalized lattice invariant shear and the degeneracy of solutions for the cubic to tetragonal transformation', *Acta Metallurgica*, 7, 793–802.

Wechsler, M S, Lieberman, D S and Read, T A (1953) 'On the theory of the formation of martensite', *Trans. AIME*, 197, 1503–1515.

Wechsler, M S, Read, T A and Lieberman, D S (1960) 'The crystallography of the austenite-martensite transformation. The (111) shear solutions', *Trans. AIME*, 218, 202–207.

Zhang, M-X and Kelly, P M (2009) 'Crystallographic features of phase transformations in solids', *Progress in Materials Science*, 54, 1101–1170.

Zhang, W-Z and Weatherly, G C (2005) 'On the crystallography of precipitation', *Progress in Materials Science*, 50, 181–292.

© Woodhead Publishing Limited, 2012

2

Morphology and substructure of martensite in steels

T. MAKI, Kyoto University, Japan

Abstract: Martensite in ferrous alloys exhibits various morphologies, chiefly lath, lenticular and thin plate, depending on chemical compositions and M_s temperature. This chapter reviews crystallographic features and substructures for each of these specific forms. Furthermore, the chapter discusses crystallographic features of packet and block in lath martensite, the origin of dislocation structure in lath and lenticular martensites, and the origin of the midrib in lenticular martensite.

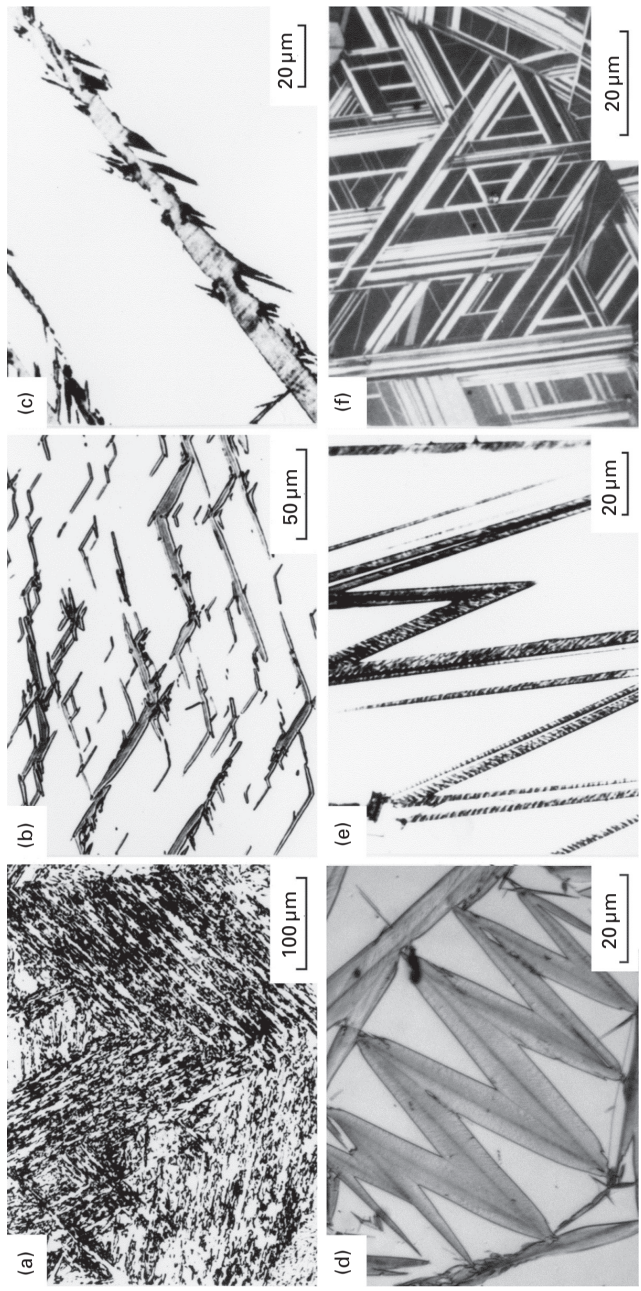
Key words: morphology of ferrous martensite, lath martensite, lenticular martensite, thin plate martensite, substructure of ferrous martensite.

2.1 Morphology and crystallographic features of martensite in ferrous alloys

In ferrous alloys, an FCC austenite (γ) phase is transformed into three kinds of martensites with different crystal structures, depending on alloying elements and compositions, i.e., (1) $\gamma \rightarrow \alpha'$ (BCC or BCT) martensite, (2) $\gamma \rightarrow \varepsilon$ (HCP) martensite, and (3) $\gamma \rightarrow$ FCT martensite. The α' type martensite is the most common in ferrous martensites, and is formed, for example, in Fe-C and Fe-Ni alloys. The ε martensite is formed only in ferrous alloys with low-austenite stacking fault energy, such as Fe-Cr-Ni and Fe-high Mn alloys. Lastly, FCT martensite is very rare and has been found only in Fe-~30at%Pd and Fe-~25at%Pt alloys (Sohmura *et al.*, 1980; Oshima *et al.*, 1985).

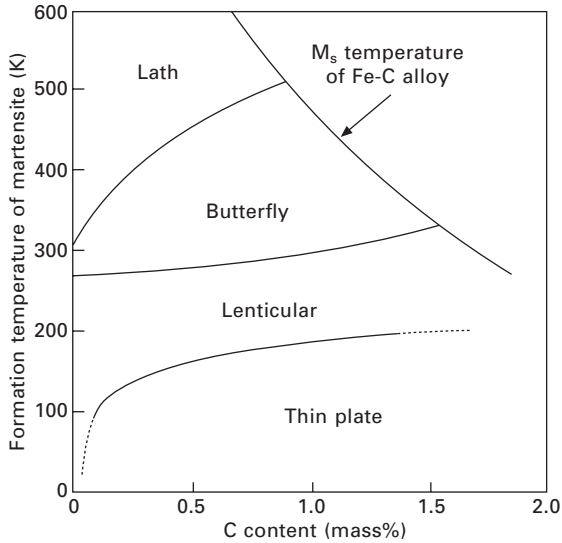
The morphology of ε and FCT martensite is of a parallel-sided thin plate-type with planar interfaces. However, in the case of α' martensite, five different types of morphologies have been reported, i.e., lath, butterfly, $\{225\}_\gamma$-plate type, lenticular, and thin plate. Figure 2.1 (Maki, 1990) shows optical micrographs of α' martensite with different morphologies (a)–(e), and ε martensite (f). These five types of α' martensites have their own formation temperature. Figure 2.2 (Maki and Tamura, 1984) shows the formation range of various types of α' martensite as a function of martensite start temperature (M_s) and carbon content in Fe-Ni-C alloys. In the case of Fe-Ni-C alloys, four types of α' martensite are formed; only $\{225\}_\gamma$-plate type martensite is not found. Lath martensite forms at the highest temperatures, whilst thin plate martensite forms at the lowest temperatures. The transition temperature

© Woodhead Publishing Limited, 2012



2.1 Optical micrographs of various types of martensites in ferrous alloys: (a) lath α' (Fe-7%Ni-0.22%C), (b) butterfly α' (Fe-20%Ni-0.73%C), (c) $(225)_\gamma$ plate type α'(Fe-8%Cr-0.9%C), (d) lenticular α' (Fe-29%Ni-0.26%C), (e) thin plate α' (Fe-31%Ni-0.23%C), (f) ε martensite (Fe-24%Mn) (Maki, 1990).

© Woodhead Publishing Limited, 2012



2.2 Formation range of various types of α' martensite (lath, butterfly, lenticular and thin plate) as a function of formation temperature (M_s) and carbon content in Fe-Ni-C alloys (Maki and Tamura, 1984).

of martensite morphology, from lenticular to thin plate, is increased with an increase in carbon content. For Fe-Ni binary alloys, the thin plate martensite does not form even at 77K. These α' martensites can be distinguished not only morphologically but also crystallographically. Thus, Table 2.1 (Maki, 1990) summarizes the substructures, habit planes (HP), and orientation relationships (OR) for the five types of α' martensite. With a decrease in M_s temperature, the substructure of α' martensite changes from dislocated (lath martensite) to twinned (thin plate martensite), and the habit plane changes from $\{111\}_\gamma$ to $\{225\}_\gamma$ and $\{3\ 15\ 10\}_\gamma$. Furthermore, the orientation relationship changes from K-S (Kurdjumov–Sachs) to N-W (Nishiyama–Wasserman) and G-T (Greninger–Troiano). Lath martensite nearly satisfies the K-S relationship with respect to austenite, and its habit plane is close to $\{111\}_\gamma$ or $\{557\}_\gamma$. Meanwhile, the habit plane of thin plate martensite is close to $\{3\ 15\ 10\}_\gamma$, and the orientation relationship approximates to the G-T relationship. These crystallographic features of thin plate martensites (Greninger and Troiano, 1949; Miyamoto *et al.*, 2009) are well explained by the phenomenological theory of martensite crystallography (Wechsler *et al.*, 1953; Bowles and Mackenzie, 1954) and are described in detail in Chapter 1 of this volume. The substructure and crystallography of lenticular martensite, which forms in the intermediate temperature range between lath and thin plate, is fairly complicated, compared with lath and thin plate martensite, as shown later.

The factors that determine the morphology and substructure of α' martensite

© Woodhead Publishing Limited, 2012

Table 2.1 Morphology, substructure, habit plane, and orientation relationship of five types of α′ martensites in ferrous alloys

	Morphology	Substructure	Habit plane	Orientation relationship	M_S	Alloy
1	Lath	Dislocations	$(111)_A$ or $(557)_A$	K–S	High	
2	Butterfly	Dislocations + Twins	$(225)_A$	K–S		Fe-Ni-(C) Fe-Ni-Cr-(C)
3	(225) type plate	Dislocations + Twins	$(225)_A$	K–S		Fe-7Cr-1C Fe-5Mn-1C Fe-3Mn-3Cr-1C
4	Lenticular	Dislocations + Twins (Mid-rib)	$(259)_A$ or $(3\ 10\ 15)_A$	N–W G–T		
5	Thin-plate	Twins	$(3\ 10\ 15)_A$	G–T	Low	Fe-high Ni-C Fe-7Al-2C Fe-25 at%Pt Fe-Ni-Co-Ti

Source: Maki (1990).
K–S OR $(111)_A//(011)_M$, $[\bar{1}01]_A//[\bar{1}\,\bar{1}1]_M$
N–W OR $(111)_A//(011)_M$, $[1\bar{1}0]_A//[100]_M$
G–T OR $(111)_A$ 1° from $(011)_M$, $[\bar{1}01]_A$ 2.5° from $[\bar{1}\,\bar{1}1]_M$

remain poorly defined. However, the M_s temperature, the strengths of parent austenite and product martensite, the critical resolved shear stress for slip and twinning in martensite, and the stacking fault energy of austenite are considered to be important factors (Davies and Magee, 1971; Krauss and Marder, 1971; Maki *et al.*, 1972; Carr *et al.*, 1978).

Lath and lenticular are the two major morphologies of α′ martensite (Reed, 1967; Marder and Krauss, 1967; Krauss and Marder, 1971). Lath martensite is formed in Fe-C (<0.6% C), Fe-Ni (<28% Ni), and Fe-Mn (<10% Mn) alloys, and most heat-treatable commercial steels, and has overwhelming industrial significance because it is a basic structure of high strength steels. Lenticular martensite appears in Fe-high C (0.8–1.8% C) and Fe-high Ni (29–33% Ni) alloys. The other three α′ martensites are not common in ferrous alloys. The butterfly martensite is formed in Fe-Ni, Fe-Ni-Cr alloys (Maki *et al.*, 1972; Umemoto *et al.*, 1984). The $\{225\}_\gamma$-plate type martensite is formed in Fe-Cr-C alloys with a low-stacking fault energy of the parent austenite (Shimizu *et al.*, 1970).

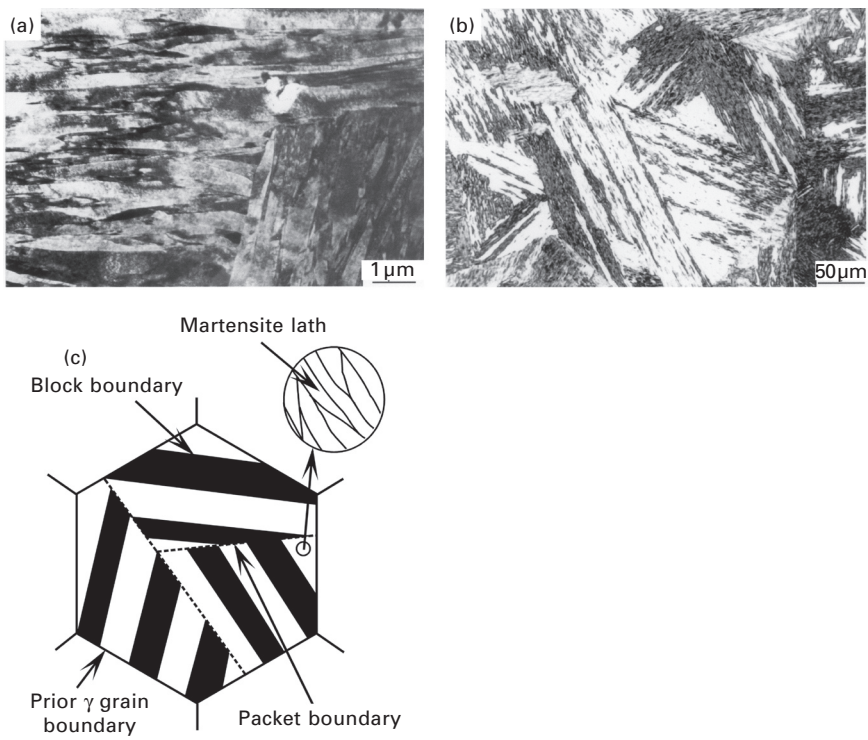
The ε martensite is formed in Fe-Mn (15–27% Mn) (Schumann, 1967) and austenitic stainless steels, such as Fe-18%Cr-8%Ni alloy. This martensite contains a high density of stacking faults. Amongst the various martensites in ferrous alloys, thin plate α′ martensite and ε martensite have the possibility to exhibit a shape memory effect which is discussed in Chapter 4 of this volume.

© Woodhead Publishing Limited, 2012

2.2 Morphology and substructure of lath martensite

2.2.1 Crystallographic features of lath martensite

The size of martensite laths is very small, e.g., the lath width is usually of the order of 0.2–0.5 μm and, thus, individual laths are not clearly observed in optical micrographs. However, since lath martensites have a tendency to become aligned parallel to one another in a large region of the austenite grain (Fig. 2.3(a)), lath martensite exhibits a characteristic microstructure at the optical microscopic scale (Fig. 2.3(b)). Thus, the current view held is that the austenite grain is divided into packets (a group of parallel laths with the same habit plane) and that each packet is further subdivided into blocks (a group of laths of the same orientation, i.e., the same variant of the K-S orientation relationship), as is shown in Fig. 2.3(c) (Marder and Marder, 1969; Inoue *et al.*, 1970; Matsuda *et al.*, 1972). These packet and block



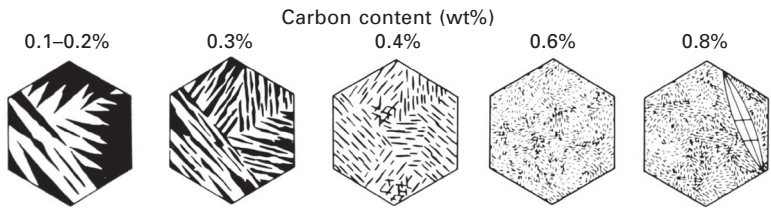
2.3 Transmission electron micrograph (a) and optical micrograph (b) of lath martensite in Fe-0.2%C alloy, and (c) schematic diagram showing characteristic morphology of lath martensite in an austenite grain (Marder and Marder, 1969; Inoue *et al.*, 1970; Matsuda *et al.*, 1972).

© Woodhead Publishing Limited, 2012

morphologies gradually change with carbon content, as shown schematically in Fig. 2.4 (Maki *et al.*, 1980). With an increase in carbon content of up to about 0.8%, the packet and blocks become finer, and are consequently more difficult to define in optical micrographs of high-carbon alloys. In the case of 0.8% C alloy, small amounts of lenticular martensite also form in addition to lath martensite.

Since the strength and toughness of martensitic steels are strongly related to packet and block sizes (the 'effective' grain size in a lath martensitic structure) (Inoue *et al.*, 1970; Matsuda *et al.*, 1972), the characteristics of the morphology and crystallography of lath martensite are of great importance and were studied extensively in the 1960s and 1970s. Recently, new and more accurate techniques for orientation measurement, with a margin of error less than 1°, such as Kikuchi diffraction patterns taken from a local area using the transmission electron microscope (TEM), and the electron back-scattered diffraction (EBSD) pattern from scanning electron microscopy (SEM), have been developed (Gourgues *et al.*, 2000; Zaefferer, 2003). Therefore, the crystallography of lath martensite in Fe-C alloys with different carbon contents has been re-examined using Kikuchi diffraction patterns and EBSD analysis (Morito *et al.*, 2003a, 2006).

As mentioned above, lath martensite has the K-S orientation relationship with respect to the austenite matrix. In the case of the K-S relationship, there are 24 variants as shown in Table 2.2. Laths with the same plane parallel relationship, e.g., V1–V6, have the same habit plane, e.g., $(111)_\gamma$ for V1–V6. As shown in Fig. 2.3(c), the packet consists of parallel laths with the same habit plane, and thus the same plane parallel relationship. Since there are four equivalent {111} austenite planes (i.e., (111), $(1\bar{1}1)$, $(\bar{1}11)$ and $(11\bar{1})$), there are four crystallographically different packets in any given austenite grain. In a packet, there are six variants (e.g., V1–V6) with different direction parallel relationships on the same conjugate parallel close-packed plane (e.g., $(111)_\gamma$ // $(011)_{\alpha'}$). Figure 2.5 shows the orientation relationship between austenite and the six K-S variants (V1–V6) within a packet. When V1 is taken as a reference, the orientation relationship between V1 and V2 is a twin relationship. Furthermore, variants 3, 5 or 6 are about 10–20° apart



2.4 Schematic diagram showing a change in microstructure at the scale of the optical microscope of lath martensite with carbon content in Fe-C alloys (Maki *et al.,* 1980).

© Woodhead Publishing Limited, 2012

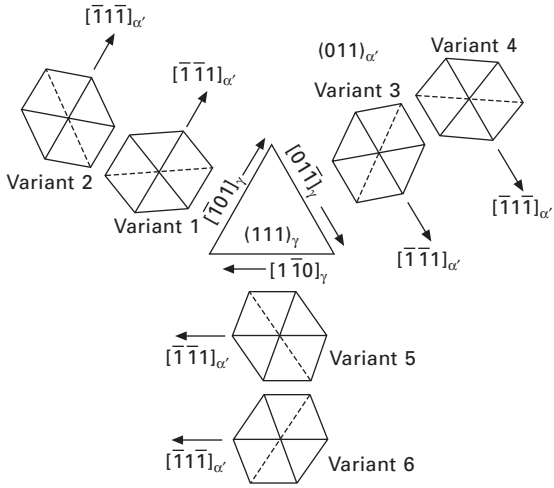
Table 2.2 Twenty-four variants in the K–S relationship

Variant no.	Plane parallel (Austenite)//(Martensite)	Direction parallel (Austenite)//(Martensite)
V1	$(111)_\gamma//(011)\alpha'$	$[\bar{1}01]_\gamma//[\bar{1}\,\bar{1}\,1]\alpha'$
V2	$(111)_\gamma//(011)\alpha'$	$[\bar{1}01]_\gamma//[\bar{1}1\bar{1}]\alpha'$
V3	$(111)_\gamma//(011)\alpha'$	$[01\bar{1}]_\gamma//[\bar{1}\,\bar{1}\,1]\alpha'$
V4	$(111)_\gamma//(011)\alpha'$	$[01\bar{1}]_\gamma//[\bar{1}1\bar{1}]\alpha'$
V5	$(111)_\gamma//(011)\alpha'$	$[1\bar{1}0]_\gamma//[\bar{1}\,\bar{1}\,1]\alpha'$
V6	$(111)_\gamma//(011)\alpha'$	$[1\bar{1}0]_\gamma//[\bar{1}1\bar{1}]\alpha'$
V7	$(1\bar{1}1)_\gamma//(011)\alpha'$	$[10\bar{1}]_\gamma//[\bar{1}\,\bar{1}\,1]\alpha'$
V8	$(1\bar{1}1)_\gamma//(011)\alpha'$	$[10\bar{1}]_\gamma//[\bar{1}1\bar{1}]\alpha'$
V9	$(1\bar{1}1)_\gamma//(011)\alpha'$	$[\bar{1}\,\bar{1}0]_\gamma//[\bar{1}\,\bar{1}\,1]\alpha'$
V10	$(1\bar{1}1)_\gamma//(011)\alpha'$	$[\bar{1}\,\bar{1}0]_\gamma//[\bar{1}1\bar{1}]\alpha'$
V11	$(1\bar{1}1)_\gamma//(011)\alpha'$	$[011]_\gamma//[\bar{1}\,\bar{1}\,1]\alpha'$
V12	$(1\bar{1}1)_\gamma//(011)\alpha'$	$[011]_\gamma//[\bar{1}1\bar{1}]\alpha'$
V13	$(\bar{1}11)_\gamma//(011)\alpha'$	$[0\bar{1}1]_\gamma//[\bar{1}\,\bar{1}\,1]\alpha'$
V14	$(\bar{1}11)_\gamma//(011)\alpha'$	$[0\bar{1}1]_\gamma//[\bar{1}1\bar{1}]\alpha'$
V15	$(\bar{1}11)_\gamma//(011)\alpha'$	$[\bar{1}0\bar{1}]_\gamma//[\bar{1}\,\bar{1}\,1]\alpha'$
V16	$(\bar{1}11)_\gamma//(011)\alpha'$	$[\bar{1}0\bar{1}]_\gamma//[\bar{1}1\bar{1}]\alpha'$
V17	$(\bar{1}11)_\gamma//(011)\alpha'$	$[110]_\gamma//[\bar{1}\,\bar{1}\,1]\alpha'$
V18	$(\bar{1}11)_\gamma//(011)\alpha'$	$[110]_\gamma//[\bar{1}1\bar{1}]\alpha'$
V19	$(11\bar{1})_\gamma//(011)\alpha'$	$[\bar{1}10]_\gamma//[\bar{1}\,\bar{1}\,1]\alpha'$
V20	$(11\bar{1})_\gamma//(011)\alpha'$	$[\bar{1}10]_\gamma//[\bar{1}1\bar{1}]\alpha'$
V21	$(11\bar{1})_\gamma//(011)\alpha'$	$[0\bar{1}\,\bar{1}]_\gamma//[\bar{1}\,\bar{1}\,1]\alpha'$
V22	$(11\bar{1})_\gamma//(011)\alpha'$	$[0\bar{1}\,\bar{1}]_\gamma//[\bar{1}1\bar{1}]\alpha'$
V23	$(11\bar{1})_\gamma//(011)\alpha'$	$[101]_\gamma//[\bar{1}\,\bar{1}\,1]\alpha'$
V24	$(11\bar{1})_\gamma//(011)\alpha'$	$[101]_\gamma//[\bar{1}1\bar{1}]\alpha'$

from a twin relation. These variants are high-angle with respect to V1. On the other hand, the misorientation between V1 and V4 is a low angle of about 10°. The V2/V5 and V3/V6 pairs are also combinations of low-angle misorientation.

Figures 2.6(a) and (b) (Morito *et al.*, 2003a) show a SEM image of a block structure within a packet of lath martensite in an ultra-low-carbon alloy, and the corresponding orientation image map obtained through EBSD analysis. Each block, with a little different contrast in SEM (Fig. 2.6(a)), corresponds to substantially different contrasts in the orientation image map (Fig. 2.6(b)). Blocks of B1, B2, and B3 with three different contrasts are formed repeatedly. It has been thought that the block consists of laths with a single variant, as shown in Fig. 2.3(c). However, Fig. 2.6(b) clearly shows that there are small regions showing slightly different contrasts, even in a given block, indicating that each block actually consists of two variants (termed sub-blocks), such as the combination of V1/V4, V3/V6 and V2/V5 with a small misorientation of about 10°. Figure 2.6(c) (Morito *et al.*, 2006) is an example of a TEM image showing that a block consists of two sets

© Woodhead Publishing Limited, 2012



Variant no.	Misorientation from Variant 1 (V1)
V2	twin relation (∑3)
V3	10.53° from twin relation
V4	10.53°
V5	10.53° from twin relation
V6	21.06° from twin relation (∑11)

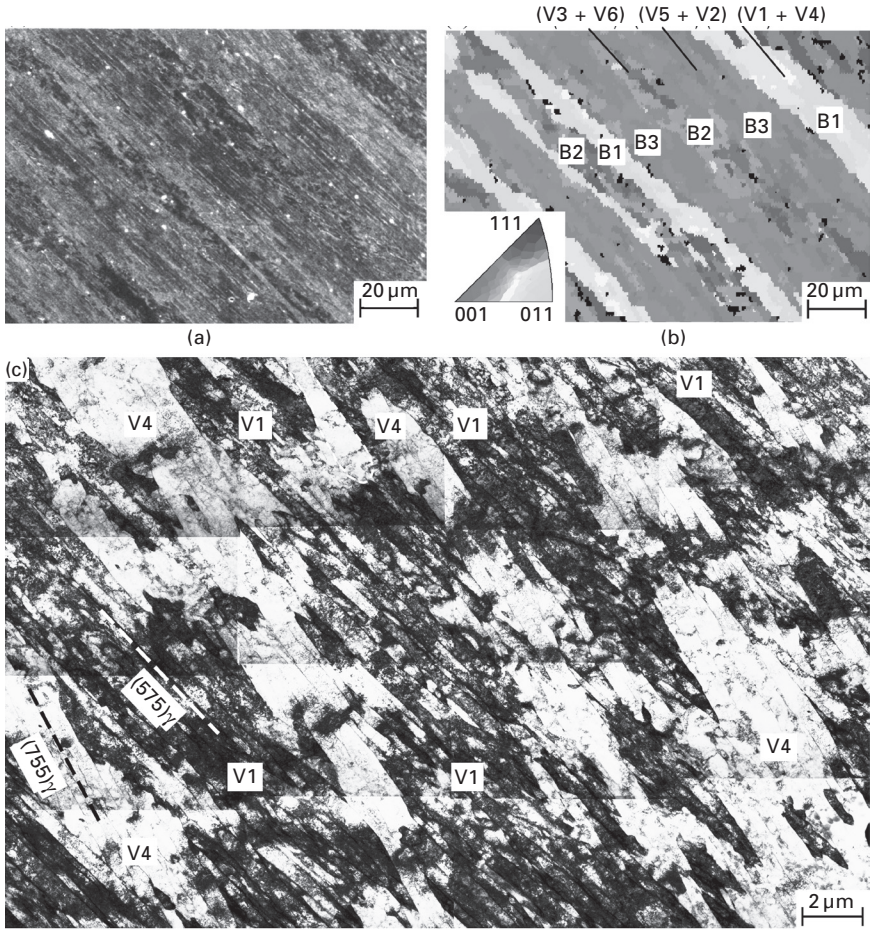
2.5 Orientation relationship between K-S variants (V1–V6) in a packet of lath martensite.

of sub-blocks. Two sets of parallel laths with V1 and V4 in a given block were observed. These variants are separated by a small misorientation of about 10°, and both variants can be distinguished by a slight difference in the habit plane, i.e., one is $(575)_\gamma$ and the other is $(755)_\gamma$, and both are close to the (111) austenite plane.

Figure 2.7 (Morito *et al.*, 2003a) shows a summary of the observations of a lath martensite structure in various Fe-C alloys. As carbon content increases, block and packet sizes decrease, as shown in Fig. 2.4. In low-carbon alloys (0–0.4% C, Fig. 2.7(a)), each packet consists of parallel blocks, and there are three blocks with different orientations in each packet. Furthermore, each block consists of laths of two specific variant groups (sub-blocks), which are misoriented by a small angle of about 10°. In high-carbon alloys (>0.6% C, Fig. 2.7(b)), packets consist of fine blocks in which the width is a few μm. The block consists of laths with a single variant, and six blocks with different orientations exist in a packet.

As shown above, blocks and packets are mostly surrounded by high-angle boundaries whereas lath boundaries in a block are of a low-angle type. Packets and blocks are important factors for both strengthening and toughening martensitic steels, as implied already. It is thus important that the size of the packets and blocks is shown to decrease as austenite grain

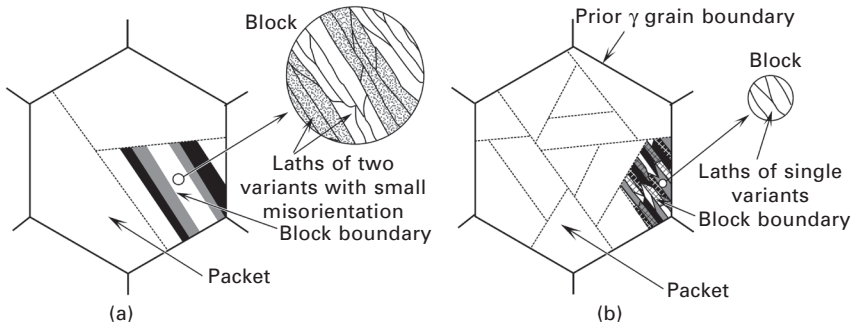
© Woodhead Publishing Limited, 2012



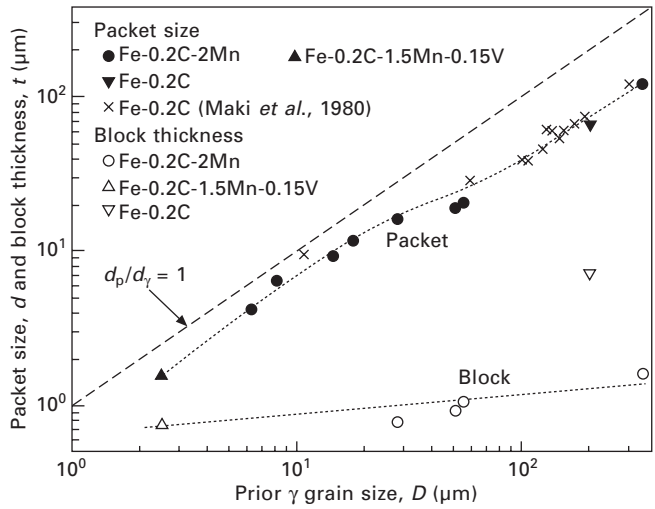
2.6 (a) Scanning electron micrograph of block structure within a packet of lath martensite in Fe-0.14%Mn-0.0026%C alloy, (b) corresponding crystal-orientation map measured by EBSD analysis, (c) transformation electron micrograph showing the block structure of lath martensite in Fe-3.1%Mn-0.004%C alloy. The block consists of two specific K-S variants (Morito *et al.*, 2003a).

size is refined, although the lath size is almost insensitive to changes in prior austenite grain size (Swarr and Krauss, 1976; Maki *et al.*, 1980; Morito *et al.*, 2005). Figure 2.8 (Furuhara *et al.*, 2008) is an example showing the relationship between prior austenite grain size and packet or block size in Fe-0.2%C alloys. Another way to decrease the packet and block sizes would be to increase the cooling rate (Tsuzaki and Maki, 1981), along with the partial formation of bainite before martensite transformation (Ohmori *et al.*, 1974). The bainite transformation effectively partitions the prior austenite

© Woodhead Publishing Limited, 2012



2.7 Schematic diagram showing lath martensite structure in (a) low-carbon (0–0.4% C) and (b) high-carbon (0.6% C) alloys (Morito *et al.*, 2003a).



2.8 Variation of packet size and block width of lath martensite with austenite grain size in various low-carbon (0.2% C) alloys (Furuhara *et al.*, 2008).

grain before martensite forms, resulting in refinement of the packets of lath martensites.

2.2.2 Dislocation density of lath martensite

It is known that lath martensite shows very high dislocation densities in the order of 10^{14} or 10^{15} m^{-2}, which is similar to those of very heavily cold-worked alloys. However, quantitative studies on dislocation density in martensite are very few. One of the difficulties in the measurement of dislocation density

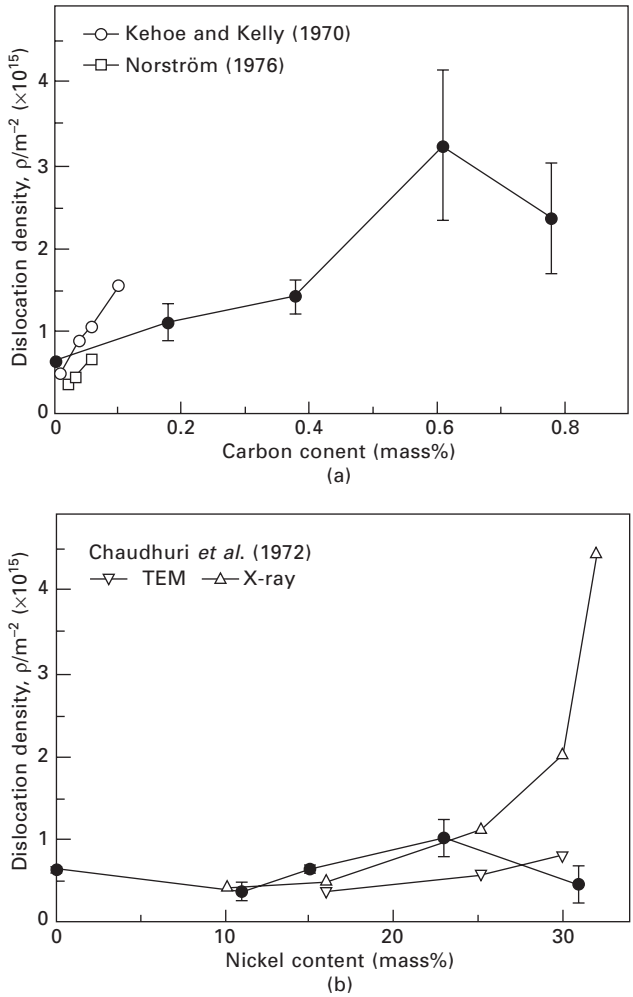
© Woodhead Publishing Limited, 2012

by TEM observation is the determination of thin foil thickness. Kehoe and Kelly (1970) determined foil thickness from extinction thickness fringes in an inclined boundary and measured the dislocation density in lath martensite of Fe-C alloys with carbon content from 0.01 to 0.1%. Thus it was shown that the dislocation density increases with carbon content. However, the effect of carbon content greater than 0.1% has not yet been made clear. Consequently, more recent measurements of dislocation density within lath martensite in Fe-C alloys (0–0.8% C) and Fe-Ni (0–23% Ni) alloys have been made by TEM, with precise determination of foil thickness using the convergent-beam electron diffraction (CBED) method (Morito *et al.*, 2003b).

Figure 2.9(a) (Morito *et al.*, 2003b) shows the change in dislocation density with carbon content in Fe-C alloys. As carbon content increases, the dislocation density increases. This tendency is similar to the results obtained by Kehoe and Kelly (1970) and subsequently also by Norström (1976) in low-carbon (0.01–0.1% C) martensites. It was also noted that the number of dislocations decreases slightly when carbon content increases from 0.6 to 0.8%. TEM observation revealed that laths in Fe-0.8%C alloys contained a higher fraction of fine transformation twins, whilst laths in Fe-0.6%C alloys also contained twins, but to a lesser extent. Therefore, it can be considered that the decrease in dislocation density is likely to be associated with this twinning, which occurs partly as a lattice invariant shear in the martensite transformation.

Figure 2.9(b) (Morito *et al.*, 2003b) shows the effect of Ni content on the dislocation density in Fe-Ni martensite. In this experiment, lath martensite is formed in the alloys with Ni contents of 0%, 11%, 15% and 23%, and lenticular martensite is formed in the Fe-31%Ni alloy. As the Ni content increases, the dislocation density in lath martensite increases slightly. However, this composition dependence in Fe-Ni alloys is very small, compared with Fe-C alloys. On the other hand, dislocation density in lenticular martensite in Fe-31%Ni alloys is lower than that of lath martensite in Fe-23%Ni alloy in the same way as for 0.8% C alloy in Fe-C alloys. This suggests that the occurrence of partial twinning results in the decrease of dislocation density in martensite. The composition dependence from 0 to 23% Ni on the dislocation density is similar to previous studies by Chaudhuri *et al.* (1972). However, they showed that dislocation density measured using X-ray diffraction increases sharply in the range of Ni content over 30%, which exhibits lenticular martensite, although the dislocation density measured using TEM is not so high. They concluded that this difference is caused by the loss of dislocations on thinning foils for TEM observation. If the effect of thin foil preparation exists, the dislocation density measured by TEM should always be lower than that measured using X-ray analysis. However, as shown in Fig. 2.9(b), their results regarding dislocation densities for lower Ni contents are nearly the same between X-ray and TEM measurements. Thus, it can be

© Woodhead Publishing Limited, 2012



2.9 Change in dislocation density (a) in lath martensite with carbon content in Fe-C alloys, and (b) in lath martensite (Fe-0–23%Ni) and lenticular martensite (Fe-31%Ni) with Ni content in Fe-Ni alloys (Morito *et al.*, 2003b).

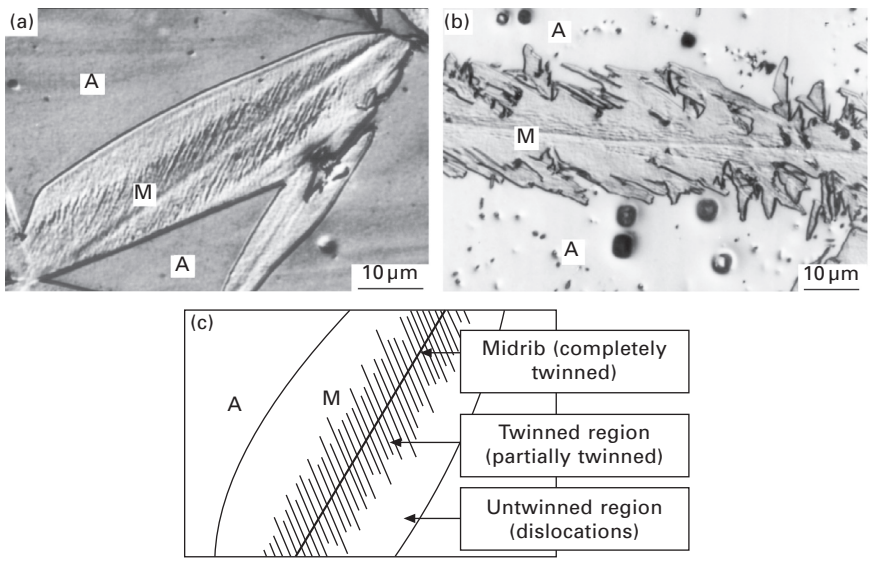
considered that the thin foil effect on dislocation density could be minimal. One of the possible reasons for this is the decrease in the mosaic particle size, due to the presence of fine transformation twins in lenticular martensite. This might result in the increase in the apparent dislocation density through the analysis of X-ray line-broadening.

© Woodhead Publishing Limited, 2012

2.3 Morphology and substructure of lenticular martensite

One of the features of lenticular martensite is the so-called 'burst' phenomenon, in which one martensite plate nucleates a sequence of plates, presumably as a result of stress concentrations set up when the first plate reaches an obstruction, such as a grain boundary or another martensite plate. As a result of burst transformation, lenticular martensite is formed as a zigzag array of plates, as shown in Fig. 2.1(d).

The shape of lenticular martensite varies with formation temperature, i.e., M_s temperature, as shown in Fig. 2.10(a) and (b) (Shibata *et al.*, 2009). The martensite (M)-austenite (A) interface in the Fe-32.9%Ni alloy (M_s = 171 K) is smooth. On the other hand, the M/A interface in the Fe-30.8%Ni alloy (M_s = 223 K) is quite irregular. Irrespective of boundary morphology, both martensites contain a straight line at the centre of the plate. This straight line (in reality, a plane) is called the 'midrib', and is considered to be the first part of a plate to form (Neuhauser and Pitsch, 1971; Kakeshita *et al.*, 1980). Since the M/A interface is not planar and does not have a definite habit plane, the midrib plane is usually taken as the habit plane of lenticular martensite, which is close to $\{2\ 5\ 9\}_\gamma$ or $\{3\ 10\ 15\}_\gamma$ (Reed, 1967; Krauss and Pitsch, 1965).

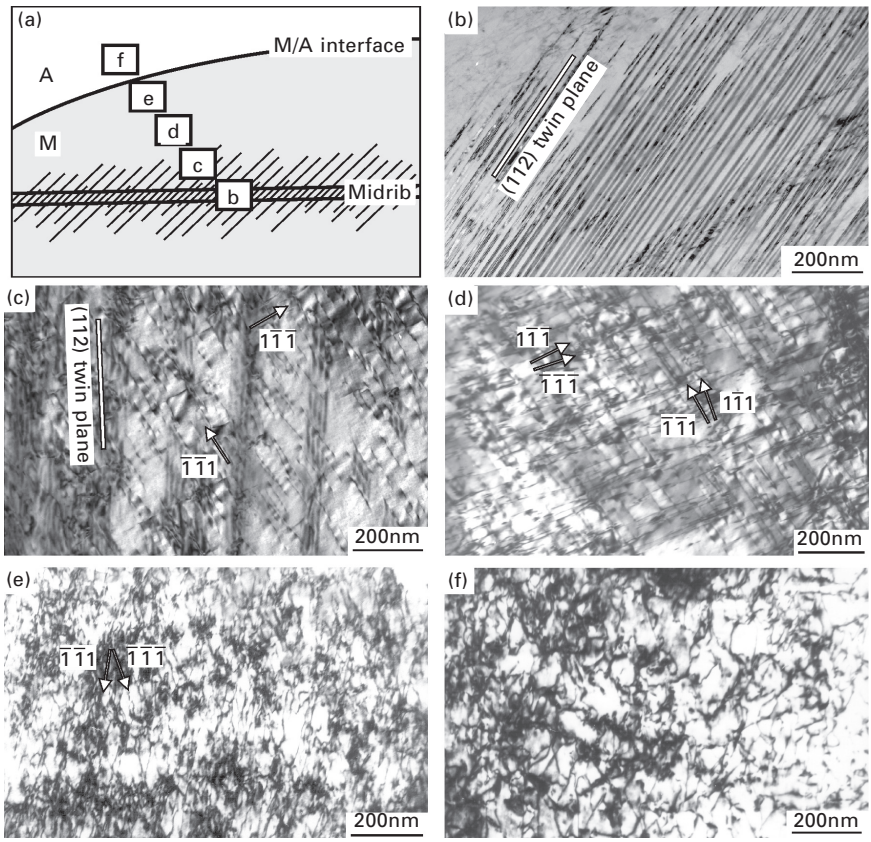


2.10 Optical micrographs of lenticular martensite in (a) Fe-32.9%Ni (M_s = 171 K), and (b) Fe-30.8%Ni (M_s = 223 K), and (c) schematic diagram of internal structure in lenticular martensite (Shibata *et al.*, 2009).

© Woodhead Publishing Limited, 2012

The substructure of lenticular martensite is more complicated compared with lath and thin plate martensite. As is shown schematically in Fig. 2.10(c), the lenticular martensite plate consists of three regions: (1) the 'midrib', which is completely twinned as thin plate martensite, (2) the 'twinned region', which partly consists of twins extending from the midrib, and (3) the 'untwinned (dislocated) region', which consists of a high density of dislocations. Even in an optical micrograph, the twinned regions can be recognized as a darkened area, as in Fig. 2.10(a), through suitable etching. It appears that the twinned region of lenticular martensite becomes thinner and the M/A interface more irregular when the M_s temperature increases.

Figure 2.11 (Shibata *et al.*, 2009) highlights TEM images showing the change in substructure from the midrib to the M/A interface in the

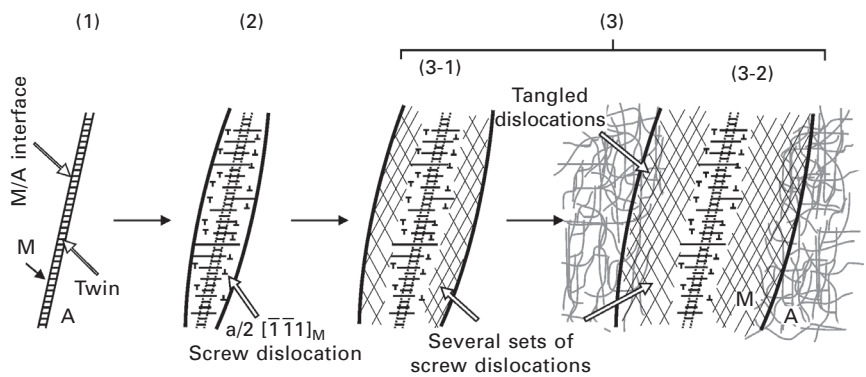


2.11 Transmission electron micrographs showing the substructure of lenticular martensite in Fe-32.9%Ni alloy: (a) schematic diagram describing the areas of observation, (b) midrib region, (c) twinned region, (d) untwinned region near the twinned region, (e) untwinned region near the M (martensite)/A (austenite) interface, and (f) surrounding austenite near the M/A interface (Shibata *et al.*, 2009).

© Woodhead Publishing Limited, 2012

lenticular martensite plate of an Fe-33%Ni alloy. The midrib region in Fig. 2.11(b), corresponding to 'b' in the schematic illustration in Fig. 2.11(a), is completely twinned. The twinning system is $(112)[\bar{1}\,\bar{1}1]_M$. In the twinned region corresponding to 'c' in Fig. 2.11(a), both fine twins and one set of screw dislocations, Burgers vector of which is parallel to the twinning shear direction, are observed as shown in Fig. 2.11(c). The structure in the untwinned region can be divided into two types, as shown in Figs 2.11(d) and 2.11(e). The area near the twinned region corresponding to 'd' in Fig. 2.11(a) contains several sets of screw dislocations (Fig. 2.11(d)). In contrast, the area near the M/A interface, corresponding to 'e' in Fig. 2.11(a), contains many tangled dislocations, in addition to straight dislocations (Fig. 2.11(e)). Figure 2.11(f) shows the dislocation structure in the surrounding austenite ('f' in Fig. 2.11(a)). The austenite contains a high density of tangled dislocations. These austenite dislocations might be introduced by the slip deformation for the accommodation of transformation strain. Because of the similarity of Figs 2.11(e) and (f), it can be considered that these austenite dislocations are inherited by the lenticular martensite during its growth.

The changes in the substructure of lenticular martensite in Fe-Ni alloys are shown by stages in Fig. 2.12 (1)→(2)→(3-1)→(3-2) (Shibata *et al.*, 2009). A midrib with a high density of $(112)[\bar{1}\,\bar{1}1]_M$ transformation twins is formed at the earliest stage of transformation (Fig. 2.12(1)). This is thin plate martensite itself, as is described later. In Fig. 2.12(2), the partial growth of twins in the midrib and the introduction of a set of screw dislocations with a Burgers vector of $a/2[\bar{1}\,\bar{1}1]_M$ accompanies the formation of the twinned region. These screw dislocations can be considered emissary dislocations decomposed from the transformation twins. The complete transition of lattice-invariant deformation, from twinning to slip during plate growth, results in the formation of an untwinned region (Fig. 2.12(3)). This untwinned region

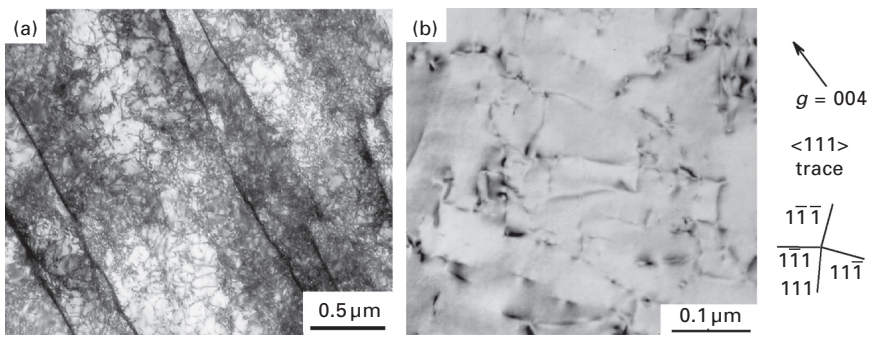


2.12 Schematic diagram showing the development of substructure during growth of lenticular martensite (Shibata *et al.*, 2009).

© Woodhead Publishing Limited, 2012

consists of two distinct regions with different substructures. At the growth stage ((3)-1), several sets of screw dislocations are observed that may result from lattice-invariant deformation. With further growth, plastic deformation also occurs in the surrounding austenite to accommodate the transformation strain. Because martensite inherits these accommodation dislocations in the parent austenite during growth, non-linear and tangled dislocations can be observed in the untwinned region near the M/A interface ((3)-2). The change in the lattice-invariant deformation mode from twinning to slip is likely to be caused by an increase in the local temperature produced by latent heat during martensite transformation, as proposed by Patterson and Wayman (1966).

It is common knowledge that the dislocation structure in an untwinned region of lenticular martensite consists of an array of uniformly distributed straight screw dislocations, as shown in Fig. 2.11(d). On the other hand, the dislocations in lath martensite are tangled and arranged in incipient dislocation cells as shown in Fig. 2.13(a). It has been considered that the dislocation tangles are a result of a plastic deformation mode consistent with the high M_s (a high-temperature range of formation) of low-carbon lath martensite. However, it should be emphasized that, even in lenticular martensite, the dislocation structure in an untwinned region close to the M/A interface is very similar to that of lath martensite. By careful observation, it has been confirmed that lath martensite definitely contains a set of straight screw dislocations, as shown in Fig. 2.13(b). Therefore, it can be considered that the dislocation structure in lath martensite consists of a set of screw dislocations, which are formed by the lattice invariant shear during transformation, along with tangled dislocations, which are inherited by martensite from the austenite matrix (Shibata *et al.*, 2009).



2.13 Transmission electron micrographs showing two types of dislocation structures in lath martensites (Fe-1.5%Mn-0.0026%C): (a) tangled dislocations, (dislocation cells) and (b) uniformly distributed straight dislocations.

© Woodhead Publishing Limited, 2012

2.4 Morphology and substructure of thin plate martensite

Figure 2.14 (Maki and Tamura, 1986) is a TEM image of thin plate martensite in Fe-Ni-C alloy. This martensite is characterized by a highly smooth and planar interface and the absence of a midrib, and (112) transformation twins in martensite extend completely from one interface to the other. In the case of α′ martensite with other types of morphologies, an A/M interface is not generally planar and no transformation twins exist in the martensite near an interface. Furthermore, it is characteristic that the parent austenite in the vicinity of thin plate martensite rarely contains dislocations. This indicates that no accommodation slip occurs there during martensitic transformation and that, therefore, the transformation strain is elastically accommodated by the austenite. This is in contrast to observations made regarding other types of α′ martensite (Miyamoto *et al*., 2009).

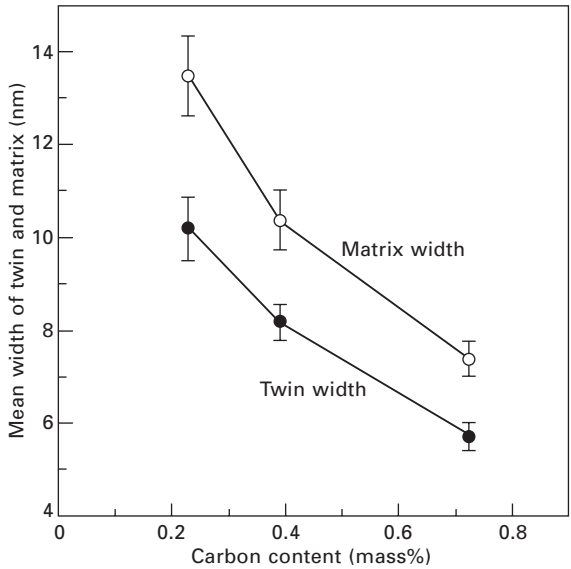
Each transformation twin in thin plate martensite extends completely, with uniform width, across the entire plate. On the other hand, the transformation twins in lenticular martensite are tapered, and thus the width of each twin decreases from the midrib as the M/A interface is approached (Maki and Wayman, 1976). Figure 2.15 (Maki and Wayman, 1976) shows the change in transformation twin width with carbon content in the thin plate martensite of Fe-Ni-C alloys. Although the designation of 'twin' vs. 'matrix' in the martensite is arbitrary, the narrower region was regarded as twin and the wider region as matrix. The width of transformation twins becomes finer with an increase in carbon content.

The most characteristic nature of thin plate martensite is that the M/A interface remains mobile. Figure 2.16 (Maki *et al*., 1989) shows

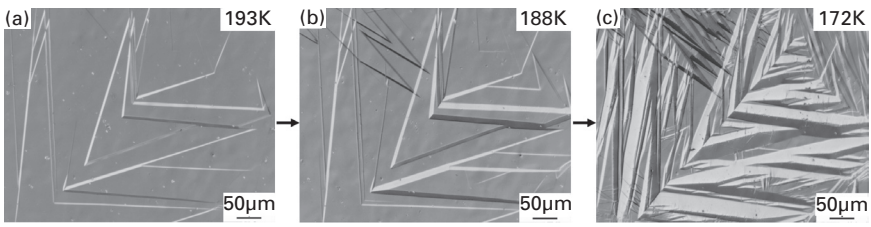


2.14 Transmission electron micrograph of thin plate martensite in Fe-30%Ni-0.39%C alloy (M_s = 133 K) (Maki and Tamura, 1986).

© Woodhead Publishing Limited, 2012



2.15 Change in twin width and matrix width in thin plate martensite with carbon content in Fe-Ni-C alloys (Maki and Wayman, 1976).



2.16 Optical micrographs showing transformation sequence of thin plate martensite during cooling in Fe-31%Ni-10%Co-3%Ti, ausaged at 873 K for 3.6 ks (M_s = 193 K) (Maki *et al.*, 1989).

the transformation sequence of thin plate martensite during cooling. It is evident that the thin plate martensite gradually thickens during cooling. This martensite also shrinks during heating by the backward movement of the A/M interface. This behaviour is not observed in other types of α' martensite. For example, in the case of lenticular martensite, each martensite plate attains the final size immediately when it forms, and no growth of the plate occurs by further cooling. Furthermore, the $\alpha' \rightarrow \gamma$ reverse transformation in lenticular martensite is always accomplished by the nucleation of austenite phase within a martensite plate rather than by the backward movement of interfaces (Kessler and Pitsch, 1965). The existence of fully extended transformation twins in martensite, and hence the smooth and planar interface, might thus be important for the reversible movement of the interface (Kajiwara and

© Woodhead Publishing Limited, 2012

Kikuchi, 1983). Because of this characteristic of interface movement during forward and reverse transformation, thin plate martensite has a possibility of exhibiting shape memory effect, such as in Fe-Pt (Wayman, 1971), Fe-Ni-Co-Ti (Maki *et al*., 1984), and Fe-Ni-Si (Himuro *et al*., 2002) alloys.

Judging from the characteristic of thin plate α' martensite, i.e., completely twinned and perfect elastic accommodation in the parent austenite, the following four factors might be favourable for the formation of thin plate martensite in ferrous alloys

1. high austenite strength;
2. small transformation volume change and small magnitude of transformation shape change;
3. low M_s temperature (a low formation range); and
4. high tetragonality of martensite.

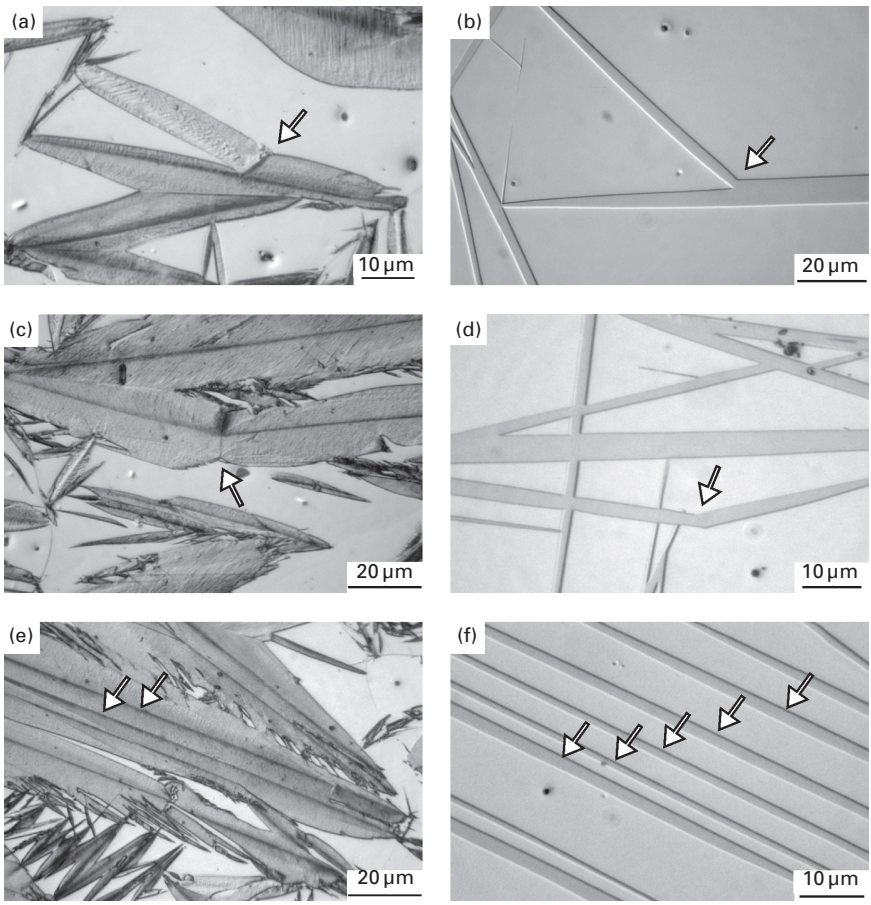
A high tetragonality of martensite corresponds to a small twinning shear, a low magnitude of shape strain, and low twin boundary energy (Kajiwara and Owen, 1977; Umemoto and Wayman, 1978). Thin plate α' martensite has been observed in some ferrous alloys, such as Fe-high Ni-C (Maki *et al*., 1972), Fe-Ni-Al (Hornbogen and Mayer, 1967), Fe-7%Al-2.0%C (Watanabe and Wayman, 1971), Fe-25at%Pt (Umemoto and Wayman, 1978), Fe-Ni-Co-Ti (Maki *et al*., 1989), and Fe-Ni-Si (Himuro *et al*., 2002). These alloys have, more or less, some of the factors described above favourable for the formation of thin plate martensite. For example, all of the thin plate martensites in the above alloys have a fairly high tetragonality, and austenite strength that is also fairly high.

Since the interface of thin plate martensite is mobile, such martensite possesses the necessary condition for thermoelastic martensite. However, thin plate α' martensite is not always thermoelastic, e.g., the thermal hysteresis (the temperature difference between M_s and A_s) of thin plate martensite in the Fe-Ni-C alloy shown in Fig. 2.14 is large, at about 600 K. Therefore, in order for thin plate α' martensite to become thermoelastic, the introduction of suitable factors for reducing its thermal hysteresis is necessary. Dunne and Wayman (1973) found that the thermal hysteresis of thin plate martensite in Fe-25at%Pt alloy is gradually decreased with increase in the degree of order of the parent austenite and, hence, martensite can become thermoelastic with a small thermal hysteresis through a proper ordering treatment. Maki *et al*. (1984) also found that the Fe-Ni-Co-Ti alloys exhibit a thermoelastic martensite with a small thermal hysteresis when the austenite is properly aged to give the precipitation of γ'–Ni_3Ti. Judging from various previous observations, it can be considered that the important condition for reducing the thermal hysteresis of thin plate martensite is to reduce the thickness of the transformation twins in the martensite. High austenite strength and a high tetragonality of BCT martensite seem to be favourable for reducing twin

© Woodhead Publishing Limited, 2012

thickness in martensites. A high tetragonality leads to a substantial reduction in the energy of a twin boundary (Kajiwara and Owen, 1977). In fact, Fe-25at%Pt alloy (Dunne and Wayman, 1973) and Fe-33%Ni-10%Co-4%Ti alloy (Maki *et al*., 1984), which exhibit thermoelastic martensites, satisfy the conditions described above.

As mentioned above, morphologies of thin plate martensite and lenticular martensite are completely different from each other. However, when only the midrib in lenticular martensite is given attention, the substructure and habit plane of the midrib are quite similar to those of thin plate martensite. The similarity of morphology of midrib in lenticular martensite and thin plate martensite is shown in Fig. 2.17 (Shibata *et al*., 2008). As mentioned



2.17 Optical micrographs showing various morphologies of lenticular martensite (Fe-29%Ni-0.2%C (M_s = 198 K)) (a, c and e), and thin plate martensite (Fe-31%Ni-10%Co-3%Ti (M_s = 83 K)) (b, d and e) (Shibata *et al*., 2008).

© Woodhead Publishing Limited, 2012

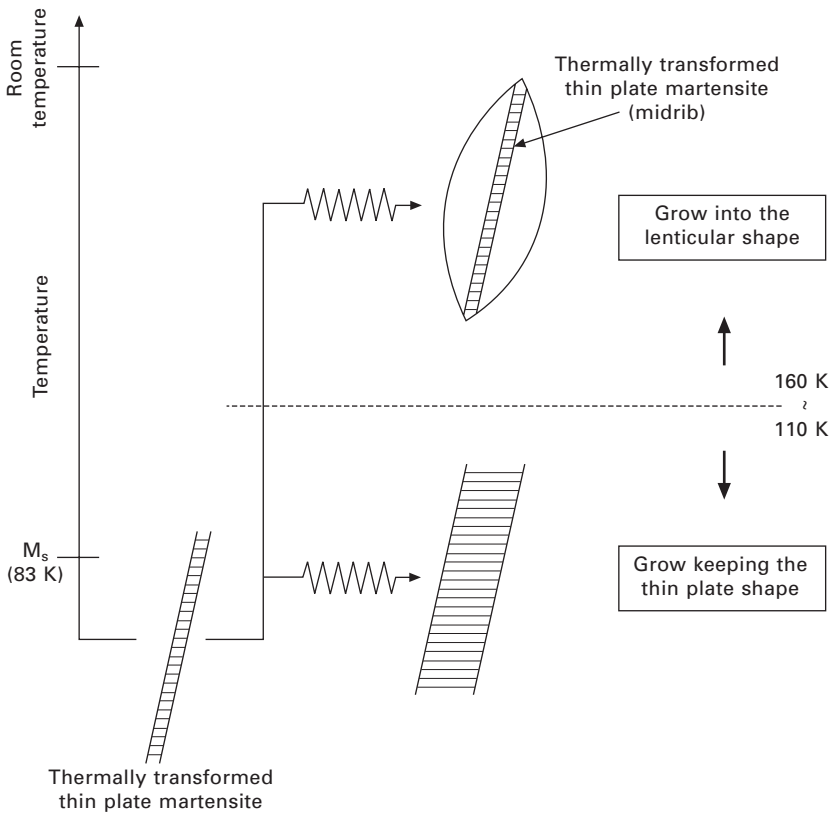
previously, lenticular martensite plates form in a group and exhibit a zigzag array (Fig. 2.1(d)). These arrays are quite similar to those of thin plate martensite (Fig. 2.1(e)). However, all lenticular martensite plates do not exhibit such a typical morphology, and some irregular morphologies often appear, as shown in Fig. 2.17(a), (c) and (e). The midrib in the lenticular martensite in Fig. 2.17(a) is branched, and that in Fig. 2.17(c) is kinked, as indicated by arrows. Unique morphologies such as these are often observed in thin plate martensite (Fig. 2.17(b) and (d)), as has been reported by Maki *et al*. (1973). Furthermore, single midrib does not always exist, and lenticular martensite plates with more than one midrib sometimes appear, as shown in Fig. 2.17(d). This configuration of midrib is quite similar to the morphology of thin plate martensite in Fig. 2.17(f), in which some martensite plates with the identical variant form closely with one another. Judging from the similarity of midrib and thin plate martensite, from the point of view of morphology, substructure and crystallographic features, it can be concluded that the midrib is thin plate martensite itself, and that the difference between lenticular martensite and thin plate martensite is only in their growth behaviour.

In order to confirm this consideration, the growth behaviour of thin plate martensite under applied stress at various temperatures was examined using an Fe-31%Ni-10%Co-3%Ti alloy (M_s = 83 K). Figure 2.18 (Shibata *et al*., 2008) summarizes the stress-induced growth behaviour of thin plate martensite by tensile deformation at various temperatures. The thermally transformed thin plate martensite grows whilst maintaining a thin plate shape when deformed below 110 K, but then grows into a lenticular shape above 160 K. In the temperature range between 110 and 160 K, both martensites with a thin plate shape or lenticular shape are observed. These results clearly indicate that the midrib in lenticular martensite is the thin plate martensite itself. Consequently, there is no difference between lenticular martensite at the earliest stage of martensite transformation (that is, the midrib) and thin plate martensite. When the formation temperature is quite low, martensite can grow whilst keeping a thin plate shape. On the other hand, when the formation temperature is relatively high, the change in deformation mode, from twinning to slip, results in the growth of martensite into a lenticular shape. This change in the lattice invariant deformation mode is due to the increase in the local temperature by latent heat during transformation. Although the local temperature is also raised in the case of thin plate martensite, the lattice invariant deformation mode remains twinning because of the relatively low formation temperature.

2.5 Conclusions

In this chapter, crystallographic features and substructure for various α' martensite with different morphologies, chiefly, lath, lenticular and thin plate,

© Woodhead Publishing Limited, 2012



2.18 Schematic illustration showing stress-induced growth behaviour of thin plate martensites by tensile deformation at various temperatures in Fe-31%Ni-10%Co-3%Ti (M_s = 83 K). Specimen was cooled to liquid nitrogen (77 K) to form thin plate martensite and then deformed in tension at various temperatures between 77 K and 200 K (Shibata *et al.,* 2008).

were reviewed. In particular, the crystallographic features of packet and block in lath martensite, the origin of dislocation structure in lath and lenticular martensite, the substructure change during growth of martensite plate in lenticular martensite and the origin of midrib in lenticular martensite were described based on the author's recent studies. Studies on ferrous martensite were carried out extensively in the 1960s and 1970s. Irrespective of many previous studies, it remains the case that little quantitative investigation of substructure, e.g., dislocation and twin densities, the size of martensite lath, etc., has been reported. Further detailed and systematic studies of the substructure of martensite are necessary to understand the transformation mechanism and also the mechanical properties of the ferrous martensite.

© Woodhead Publishing Limited, 2012

2.6 References

Bowles J S and Mackenzie J K (1954), 'The crystallography of martensite transformations I', *Acta Metall.*, 2, 129–137.

Carr M J, Strife J R and Ansell G S (1978), 'An investigation of the effect of austenite strength and austenite stacking fault energy on the morphology of martensite in Fe-Ni-Cr-0.3C alloys', *Metall. Trans., A*, 9A, 857–864.

Chaudhuri D K, Ravindran P A and Wert J J (1972), 'Comparative X-ray diffraction and electron microscopic study of the transformation-induced substructures in the iron-nickel martensites and their influence on the martensite properties', *J. Appl. Phys.*, 43, 778–788.

Davies R G and Magee C L (1971), 'Influence of austenite and martensite strength on martensite morphology', *Metall. Trans.*, 2, 1939–1947.

Dunne D P and Wayman C M (1973), 'The effect of austenite ordering on the martensite transformation in Fe-Pt alloys near the composition Fe_3Pt: morphology and transformation characteristic', *Metall. Trans.*, 4, 137–145.

Furuhara T, Kikumoto K, Saito H, Sekine T, Ogawa T, Morito S and Maki T (2008), 'Phase transformation from fine-grained austenite', *ISIJ Int.*, 48, 1038–1045.

Gourgues A F, Flower H M and Lindley T C (2000), 'Electron back scattering diffraction study of acicular ferrite, bainite, and martensite steel microstructures', *Mater. Sci. Tech.*, 16, 26–40.

Greninger A B and Troiano A R (1949), 'Mechanism of martensite formation', *Trans. AIME*, 185, 590–598.

Himuro Y, Kainuma R and Ishida K (2002), 'Martensitic transformation and shape memory effect in ausaged Fe-Ni-Si alloys', *ISIJ Int.*, 42, 184–190.

Hornbogen E and Mayer W A (1967), 'Gefüge und mechanische Eigenschaften von Legierungen auf Eisen-Nickel-Basis mit 12 at%Al nach verschiedener Wärmebehandlung', *Z. Metallk.*, 58, 372–380.

Inoue T, Matsuda S, Okamura Y and Aoki K (1970), 'The fracture of a low carbon tempered martensite', *Trans. JIM*, 11, 36–43.

Kajiwara S and Kikuchi T (1983), 'Reversible movement of the austenite-martensite interface and dislocation structures in reverse-transformed austenite in Fe-Ni-C alloys', *Phil. Mag. A*, 48, 509–526.

Kajiwara S and Owen W S (1977), 'The martensite-austenite interface and the thickness of twins in martensite in Fe_3Pt', *Scripta Metall.*, 11, 137–142.

Kakeshita T, Shimizu K, Maki T and Tamura I (1980), 'Growth behavior of lenticular and thin plate martensites in ferrous alloys and steels', *Scripta Metall.*, 14, 1067–1070.

Kehoe M and Kelly P M (1970), 'The role of carbon in the strength of ferrous martensite', *Scripta Metall.*, 4, 473–476.

Kessler H and Pitsch W (1965), 'Der Orientierungszusammenhang bei der Ruckumwandlung des Martensits in Austenit in Eisen-Nickel Legierungen', *Acta Metall.*, 13, 871–874.

Krauss G and Marder A R (1971), 'The morphology of martensite in iron alloys', *Metall. Trans.*, 2, 2343–2357.

Krauss G and Pitsch W (1965), 'Fine structure and habit planes of martensite in Fe-33wt% Ni single crystal', *Trans. AIME*, 233, 919–926.

Maki T (1990), 'Microstructure and mechanical behavior of ferrous martensite', *Mater. Sci. Forum*, 56–58, 157–168.

© Woodhead Publishing Limited, 2012

Maki T and Tamura I (1984), 'On the thin plate martensite in ferrous alloys and its various properties', *Bull. Japan Inst. Metals*, 23, 229–237.

Maki T and Tamura I (1986), 'Shape memory effect in ferrous alloys', *Proc. Int. Conf. on Martensitic Transformations (ICOMAT)*, JIM, pp. 963–970.

Maki T and Wayman C M (1976), 'Transformation twin width variation in Fe-Ni and Fe-Ni-C martensite', *Proc. 1st JIM Int. Symp. on New Aspects of Martensitic Transformation*, Kobe, JIM, pp. 69–74.

Maki T, Shimooka S, Umemoto M and Tamura I (1972), 'The morphology of strain-induced and thermally transformed martensite in Fe-Ni-C alloys', *Trans. JIM*, 13, 400–407.

Maki T, Shimooka S, Arimoto T and Tamura I (1973), 'The morphology of thin plate-like martensite in Fe-Ni-C alloys', *Trans. JIM*, 14, 62–67.

Maki T, Tsuzaki T and Tamura I (1980), 'The morphology of microstructure composed of lath martensite in steels', *Trans. ISIJ*, 20, 207–214.

Maki T, Kobayashi K, Minato M and Tamura I (1984), 'Thermoelastic martensite in an ausaged Fe-Ni-Ti-Co alloy', *Scripta Metall.*, 18, 1105–1109.

Maki T, Furutani S and Tamura I (1989), 'Shape memory effect related to thin plate martensite with large thermal hysteresis in ausaged Fe-Ni-Co-Ti alloy', *ISIJ Int.*, 29, 438–445.

Marder A R and Krauss G (1967), 'The morphology of martensite in iron-carbon alloys', *Trans ASM*, 60, 651–660.

Marder J M and Marder A R (1969), 'The morphology of iron-nickel massive martensite', *Trans. ASM*, 62, 1–10.

Matsuda S, Inoue T, Mimura H and Okamura Y (1972), 'Toughness and effective grain size in heat-treated low-alloy high strength steels', *Trans. ISIJ*, 12, 325–333.

Miyamoto G, Shibata A, Maki T and Furuhara T (2009), 'Precise measurement of strain accommodation in austenite matrix surrounding martensite in ferrous alloys by electron backscatter diffraction analysis', *Acta Mater.*, 57, 1120–1131.

Morito S, Tanaka H, Konishi R, Furuhara T and Maki T (2003a), 'The morphology and crystallography of lath martensite in Fe-C alloys', *Acta Mater.*, 51, 1789–1799.

Morito S, Nishikawa J and Maki T (2003b), 'Dislocation density within lath martensite in Fe-C and Fe-Ni alloys', *ISIJ Int.*, 43, 1475–1477.

Morito S, Saito H, Ogawa T, Furuhara T and Maki T (2005), 'Effect of austenite grain size on the morphology and crystallography of lath martensite in low carbon steels', *ISIJ Int.*, 45, 91–94.

Morito S, Huang X, Furuhara T, Maki T and Hansen N (2006), 'The morphology and crystallography of lath martensite in alloy steels', *Acta Mater.*, 54, 5323–5331.

Neuhauser H J and Pitsch W (1971), 'A new observation on the mechanism of martensitic transformations', *Acta Metall.*, 19, 337–344.

Norström L A (1976), 'On the yield strength of quenched low-carbon lath martensite', *Scand. J. Metall.*, 5, 159–165.

Ohmori Y, Ohtani H and Kunitake T (1974), 'Tempering of the bainite and the bainite/martensite duplex structure in a low-carbon low-alloy steel', *Met. Sci.*, 8, 357–366.

Oshima R, Sugimoto S, Sugiyama M, Hamada T and Fujita F E (1985), 'Shape memory effect in an ordered Fe_3Pt alloy associated with the FCC-FCT thermoelastic martensite transformation', *Trans. JIM*, 26, 523–524.

Patterson R L and Wayman C M (1966), 'The crystallography and growth of partially-twinned martensite plates in Fe-Ni alloys', *Acta Metall.*, 14, 347–369.

© Woodhead Publishing Limited, 2012

Reed R P (1967), 'The plate-like martensite transformation in Fe-Ni alloys', *Acta Metall.*, 15, 1287–1296.

Schumann H (1967), 'Die Martensitische Umwandlung in kohlenstoffarmen Manganstahlen', *Arch. Eisenfutt.*, 38, 647–656.

Shibata A, Murakami T, Morito S, Furuhara T and Maki T (2008), 'The origin of midrib in lenticular martensite', *Mater. Trans.*, 49, 1242–1248.

Shibata A, Morito S, Furuhara T and Maki T (2009), 'Substructures of lenticular martensites with different martensite start temperatures in ferrous alloys', *Acta Mater.*, 57, 483–492.

Shimizu K, Oka M and Wayman C M (1970), 'Transmission electron microscopy studies of $\{225\}_f$ martensite in an Fe-8%Cr-1%C alloy', *Acta Metall.*, 19, 1–6.

Sohmura T, Oshima R and Fujita F E (1980), 'Thermoelastic FCC-FCT martensitic transformation in Fe-Pd alloy', *Scripta Metall.*, 14, 855–856.

Swarr T E and Krauss G (1976), 'The effect of structure on the deformation of as-quenched and tempered martensite in an Fe-0.2%C alloy', *Metall. Trans. A*, 7A, 41–48.

Tsuzaki K and Maki T (1981), 'The effect of cooling rate on the morphology of lath martensite in Fe-Ni alloys', *J. Japan Inst. Metals.*, 45, 126–134.

Umemoto M and Wayman C M (1978), 'The effect of austenite ordering on the transformation temperature, transformation hysteresis, and thermoelastic behavior in Fe-Pt alloys', *Metall. Trans. A*, 9A, 891–897.

Umemoto M, Hyodo T, Maeda T and Tamura I (1984), 'Electron microscopy studies of butterfly martensite', *Acta Metall.*, 32, 1191–1203.

Watanabe M and Wayman C M (1971), 'Crystallography of the martensite transformation in Fe-Al-C alloys', *Metall. Trans.*, 2, 2229–2236.

Wayman C M (1971), 'On memory effect related to martensitic transformations and observations in b-brass and Fe_3Pt', *Scripta Metall.*, 5, 489–492.

Wechsler M S, Lieberman D S and Read T A (1953), 'On the theory of the formation of martensite', *Trans AIME*, 197, 1503–1515.

Zaefferer S (2003), 'Computer-aided crystallographic analysis in the TEM', *Adv. in Imaging and Electron Physics*, 125, 355–415.

© Woodhead Publishing Limited, 2012

3

Kinetics of martensite transformations in steels

G. B. OLSON and Z. D. FEINBERG,
Northwestern University, USA

Abstract: Dislocation theory of the mechanism and kinetics of martensitic transformation has provided a foundation for the prediction of constitutive relations for transformation plasiticity. Application to the control of stress-state dependent shaping of stress–strain behavior has demonstrated substantial improvements in uniform ductility and ductile fracture toughness. The advance of such predictive science continues to play a central role in the new enterprise of science-based materials design.

Key words: martensitic transformation, transformation kinetics, transformation plasticity, transformation toughening.

3.1 Introduction

A martensitic phase transformation can be considered as the spontaneous plastic deformation of a crystalline solid in response to internal chemical forces. It is no surprise, then, that the theory of dislocations, after incorporating the generalized forces of chemical thermodynamics and special constraints of crystalline interfaces, has provided the most useful basis for understanding the mechanism of these transformations. Martensitic transformations have been defined as a subset of diffusionless/displacive solid-state transformations in which the strain energy arising from a shear-dominant lattice distortion controls the kinetics and product morphology during transformation (Christian *et al*., 1995). Such transformations are first-order and heterogeneous in nature, proceeding by the propagation of relatively sharp interfaces. These characteristics make the approximations of traditional linear-elastic dislocation theory particularly appropriate, and it is for this reason that the application of the theory to martensitic transformations (Olson and Cohen, 1986a) has been so successful.

These same characteristics give rise to the high mobility of martensitic interfaces underlying the quench-hardening of steel and the precisely prescribable transformation kinematics predicting their interaction with applied stress exploited in transformation plasticity applications. The latter applications span not only modern TRIP (transformation-induced plasticity) steels, but the still emerging class of shape memory alloys.

© Woodhead Publishing Limited, 2012

3.2 Mechanism and kinetics of martensitic transformation

The application of classical nucleation theory to martensitic transformations, using both continuum-elastic and discrete-dislocation descriptions of a nucleus, has been extensively reviewed (Olson and Cohen, 1981, 1982, 1986a). The classical approach treats the energetics of formation of a nucleus along a 'path' of fixed structure and increasing size. The nucleus crystal structure is taken to be that of the fully formed transformation product, with relatively sharp interface; the specific interfacial energy is customarily assumed to be size independent.

The specific interfacial energy γ of a fully coherent particle will consist of a 'chemical' core energy, while the interfacial energy in the semi-coherent case will be dominated by a short-range elastic-energy contribution. If the nucleus transformation strain (IPS) is an invariant-plane strain, the strain energy per particle volume for a thin oblate spheroid of radius r and semi-thickness c is of the form Kc/r, where K is an elastic constant. When the transformation strain deviates from an exact invariant-plane strain, an additional shape-insensitive strain energy contribution g_p^{str} arises from distortions in the particle habit plane. Following Kaufman and Cohen (1958), the total free energy of an isolated martensitic particle can thus be described by:

$$\Delta G(r, c) = \frac{4}{3}\pi r^2 c(\Delta g^{ch} + g_p^{str}) + \frac{4}{3}\pi r^2 K + 2\pi r^2 \gamma \qquad [3.1]$$

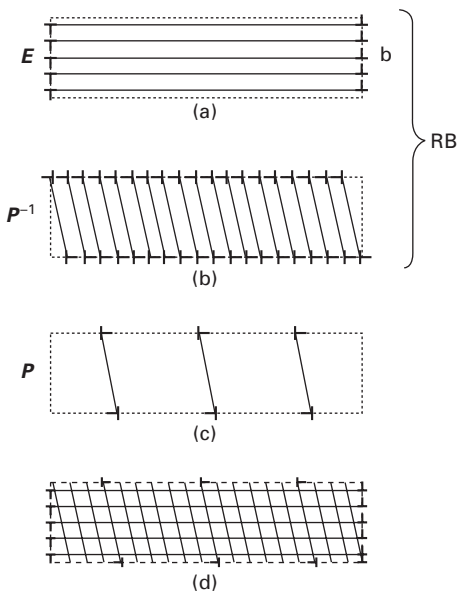
Under the thermodynamic conditions for which martensitic transformations are known to occur, the critical energy barrier is far too large to be thermally surmountable, and it can be safely concluded that classical homogeneous nucleation is not possible.

In an imperfect crystal, defect interactions can substantially alter the energy of a classical nucleus such that the free-energy barrier for heterogeneous nucleation is greatly diminished relative to the homogeneous case. Consistent with the strain-energy dominant character of martensitic transformations, it is generally assumed that the most important interaction in heterogeneous martensitic nucleation is with the defect stress field. It is now well established by quantitative calculations that classical nucleation via such interaction is indeed quite plausible at experimentally observed heterogeneous nucleation sites. While this interaction can be described by traditional continuum-elastic methods, the structurally equivalent discrete-dislocation description in terms of a defect-dissociation process leads most directly to the essential behavior, and is actually the method by which the first viable theory of heterogeneous martensitic nucleation was developed (Olson and Cohen, 1976a, 1976b).

© Woodhead Publishing Limited, 2012

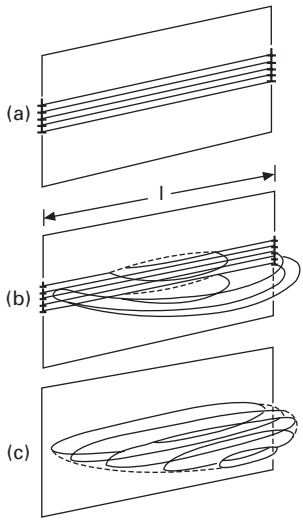
3.2.1 Heterogeneous nucleation by defect dissociation

Adopting the discrete-dislocation description of Fig. 3.1 for the interfacial structure of a classical martensitic embryo, the long-range stress field and volume strain energy of the embryo arise primarily from the array of transformation 'coherency' dislocations lying on crystal planes at a shallow angle to the embryo habit as represented schematically in Fig. 3.1(a). Clearly the free-energy barrier for nucleation is greatly diminished if the latter dislocation array is derived from the dissociation of an existing defect. A convenient defect model for this purpose is the extrinsic boundary defect represented by the array of 'excess' interfacial dislocation in Fig. 3.2(a), residing in an existing grain boundary or interphase boundary. The defect has a finite length and height, and a net Burgers vector content giving rise to a stress field of range comparable to its length, *l*. Embryo formation by dissociation of this defect is depicted in Figs 3.2(b) and (c). The interfacial motion producing such a particle involves both the motion of the array of Fig. 3.1(a) as shown in Fig. 3.2(b), and the sequential formation of the discrete loops in Figs 3.1(b) and (c) under the acting thermodynamic driving force, represented by Fig. 3.2(c).



3.1 Discrete-dislocation model of martensitic interface: (a) transformation 'coherency' dislocations producing macroscopic shape strain ***E***; (b) coherency dislocations producing complementary shear $\boldsymbol{P}^{-1}$; (c) anticoherency dislocations producing lattice-invariant deformation ***P***; (d) total interfacial structure (Olson and Cohen, 1981a).

© Woodhead Publishing Limited, 2012



3.2 Heterogeneous martensitic nucleation by defect dissociation: (a) nucleating defect; (b) dissociation to produce interfacial coherency dislocations of Fig. 3.1(a) in horizontal planes; (c) simultaneous generation of interfacial dislocation arrays of Figs 3.1(b) and (c) in nearly vertical planes (Olson and Cohen, 1981a).

Following prediction of interfacial structure theory that the most significant coherency dislocations will be associated with planes of closest packing, it is appropriate for the construction of the dislocation arrays of Figs 3.1(a) and (b) to decompose the transformation lattice deformation into invariant-plane strains on close-packed planes. For face-centered cubic (fcc) to body-centered cubic (bcc) transformation as in ferrous alloys, such a decomposition was proposed by Bogers and Burgers (1964) based on a hard-sphere deformation model. The resulting specific model for a martensitic nucleus provided the basis for the first detailed quantitative treatment of the energetics of classical heterogeneous nucleation. This model has predicted the essential characteristics of barrierless heterogeneous nucleation of martensitic transformations, with kinetic control by interfacial mobility. Combined with treatment of the composition dependence of solution hardening effects on the interfacial mobility, it has provided the framework for the most accurate prediction of the critical driving force for martensitic nucleation in complex alloys (Ghosh and Olson, 1994a, 1994b). Using a distribution of total Burgers vector content for 'superdislocation' defects of the type of Fig. 3.2(a) to describe potency distributions of both pre-existing defects and new 'autocatalytic' defects generated by martensite growth events, it has also provided the basis for a kinetic theory of the full evolution of martensitic transformations (Lin *et al.*, 1992). Incorporating both athermal and thermal components of the martensitic

© Woodhead Publishing Limited, 2012

interfacial mobility, the general theory accounts for both systems exhibiting 'athermal' (time-independent) behavior and the so-called 'isothermal' (time-dependent) mode of behavior, depending on the relative magnitude of the thermal terms in the interfacial mobility.

3.3 Mechanically induced transformations

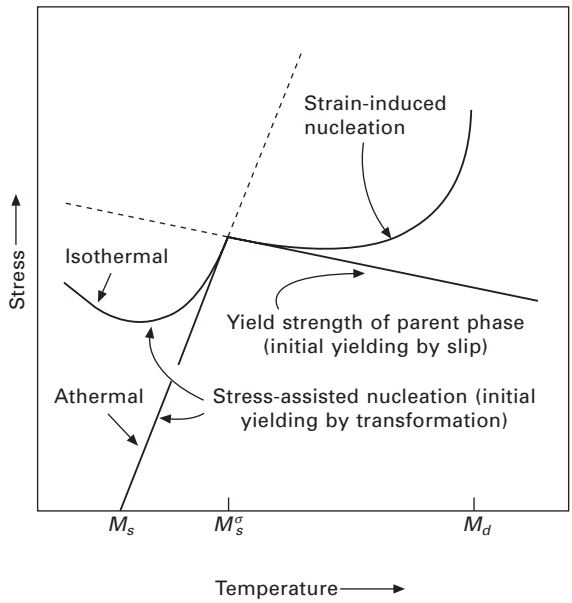
Applied stress can assist the operation of the same nucleation sites (with the same total critical driving force) responsible for the transformation on cooling; such stress-assisted nucleation can be described for any stress state by the thermodynamic effect of stress as first derived by Patel and Cohen (1953):

$$\Delta g^{\sigma} = \tau\gamma_T + \sigma_n\varepsilon_n, \qquad [3.2]$$

where τ and σ_n are the resolved shear and normal stresses in the planes and directions of the transformation shear (γ_T) and normal strain (ε_n). However, if the applied stress exceeds the yield stress of the parent phase, strain-induced nucleation can occur on new potent nucleation sites created by the plastic strain. Under these circumstances, nucleation sites are plentiful, and this has allowed numerous detailed observations of strain-induced sites, consisting primarily of various types of shear-band intersections, and including intersections with grain boundaries (Venables, 1962; Lagneborg, 1964; Manganon and Thomas, 1970; Lecroise and Pineau, 1972; Suzuki *et al*., 1977; Brooks *et al*., 1979). The shear bands may be mechanical twins, hexagonal close-packed (hcp) ε-martensite, bundles of stacking faults, or slip bands. In each case, the intersection can be interpreted as producing a dislocation stacking of the type illustrated in Fig. 3.2(a), and the relation of the active displacement to the orientation variant of the martensite being formed is consistent with the defect dissociation model (Lecroise and Pineau, 1972; Suzuki *et al*., 1977; Brooks *et al*., 1979). More potent defects can be generated in this way, compared to those existing in the annealed parent phase, and hence strain-induced nucleation can occur at lower driving forces.

The temperature regimes in which transformation initiates predominantly from either stress-assisted or strain-induced nucleation are depicted in the schematic stress–temperature diagram of Fig. 3.3. Spontaneous transformation triggered by existing nucleation sites occurs on cooling to the martensite start (M_s) temperature. Stress-assisted nucleation on the same sites will occur at the stress denoted by the solid line indicated. At a temperature designated M_s^{σ}, this stress reaches the yield stress σ_y for slip in the parent phase. Above M_s^{σ}, new potent nucleation sites introduced by plastic strain trigger strain-induced nucleation at the stress level depicted by the indicated solid curve. The temperature M_s^{σ} thus defines an approximate boundary between the temperature regimes where the two modes of nucleation dominate; near

© Woodhead Publishing Limited, 2012



3.3 Schematic representation of interrelationships between stress-assisted and strain-induced martensitic transformation (Olson and Cohen, 1972).

M_s^σ both modes will operate. Due to transformation plasticity, the observed yield stress follows the stress for stress-assisted transformation below M_s^σ. A reversal of the temperature dependence of the yield stress thus provides a convenient determination of the M_s^σ temperature. Above the temperature M_d, no transformation occurs on deformation to fracture. Figure 3.3 represents the behavior for a particular stress state.

3.3.1 Mechanism of stress-assisted transformations

Using the Patel–Cohen model (Patel and Cohen, 1953) of Eq. [3.2] for the work of applied stress computed for the most favorably oriented martensitic plate, the calculated driving force contribution of applied stress in uniaxial tension ($\partial\Delta G/\partial\sigma$) is in good agreement with the observed stress dependence of the M_s temperature in alloys exhibiting nominally athermal kinetic behavior (Patel and Cohen, 1953; Bolling and Richman, 1970; Fisher, 1974). In addition to the numerous studies of the stress dependence of the M_s temperature, the stimulating influence of applied stress on the rate of the time-dependent isothermal transformation was first demonstrated by Machlin and Cohen (1952).

The macroscopic transformation plasticity accompanying the transformation can arise in part from a biasing of the martensitic-plate variants which form

© Woodhead Publishing Limited, 2012

under stress, but in ferrous alloys (particularly when a strong autocatalytic effect operates), much of the transformation plasticity is attributable to stress biasing of the extensive accommodation slip which occurs around the plates as they grow. When this deformation takes place at stresses below that for general (slip) yielding of the parent phase (i.e., the temperature regime where stress-assisted transformation is dominant), the kinetics of the transformation paces the macroscopic deformation. The simultaneous measurement of plastic flow and transformation in TRIP steels (Olson and Azrin, 1978) verifies the existence of a temperature regime in which plastic flow is controlled by stress-assisted martensitic transformation. Under these conditions, the volume fraction of martensite (f) and the plastic strain (ε) are confirmed to be linearly related (Olson and Azrin, 1978):

$$f = k\varepsilon \qquad [3.3]$$

This, in turn, defines a linear relationship between transformation rate and plastic strain rate. Here plastic flow will occur at the applied stress for which the combined (chemical and mechanical) driving force is sufficient to make the rate of transformation plasticity match the imposed strain rate; yielding in a constant strain-rate tensile test then corresponds to an imposed rate of stress-assisted isothermal transformation, with kinetic behavior predictable from transformation kinetic theory.

3.3.2 Mechanism of strain-induced transformations

The kinetics of strain-induced martensitic nucleation at observed shear-band intersections can be adequately described by a simple relationship containing two temperature-dependent parameters and a fixed exponent (Olson and Cohen, 1975):

$$f^{\alpha'} = 1 - \exp\{-\beta[1 - \exp(-\alpha\varepsilon)]^n\} \qquad [3.4]$$

The first parameter (α) describes the rate of shear-band formation with respect to strain and is principally dependent on stacking-fault energy. The second parameter (β) is linearly related to the probability that a shear-band intersection will generate a martensitic embryo, and is governed by the chemical driving force for the martensitic reaction $\Delta G^{\gamma\to\alpha'}$, where γ refers to austenite and α' refers to the martensite. The transformation curve (volume fraction of martensite vs. plastic strain) is sigmoidal in shape and approaches a saturation value determined by the β parameter. The transformation rate (relative to plastic strain) is controlled by both parameters. The temperature sensitivity of these transformation kinetics arises largely through $\Delta G^{\gamma\to\alpha'}$ and the stacking-fault energy, and may be minimized by a reduction of the entropy differences, $\Delta S^{\gamma\to\alpha'}$ and $\Delta S^{\gamma\to\varepsilon}$.

© Woodhead Publishing Limited, 2012

3.4 Transformation plasticity constitutive relations and applications

The large transformation plasticity accompanying martensitic transformation allows substantial alteration of mechanical behavior under monotonic as well as cyclic loading conditions. A dramatic illustration of the potential of this is given by the original high-strength fully austenitic TRIP (transformation-induced plasticity) steels studied in the 1960s (Zackay *et al*., 1967), which exhibit an extraordinary combination of strength, ductility, and toughness.

Transformation plasticity provides a significant departure from the classical view of structure/property relationships in materials. The traditional role of transformation kinetics is in the control of materials processing to achieve desired properties associated with the structure of the transformation product. Via transformation plasticity, one can design metastable materials to exploit the properties of the transformation itself, i.e., properties of structural change. Under these circumstances, knowledge of transformation kinetics can be directly applied to the prediction of the constitutive flow relations underlying observed macroscopic mechanical behavior of materials during service as well as during processing.

3.4.1 Constitutive flow relations of transformation plasticity

Detailed comparison of stress vs. strain and fraction transformed martensite vs. strain curves of TRIP steels reveals two major factors controlling the plastic-flow behavior during deformation-induced martensitic transformation (Olson and Azrin, 1978). In addition to the well-known static hardening contribution of the transformation product, a dynamic softening contribution arises from the operation of the transformation as a deformation mechanism. The latter effect is most amenable to quantitative treatment in the case of the stress-assisted transformation at sufficiently low temperatures (stresses) where plastic flow is entirely controlled by the transformation kinetics.

For barrierless martensitic nucleation controlled by interfacial mobility, time-dependent isothermal transformation can be predicted from the aforementioned thermal component of solution hardening, for which the activation energy Q can be approximated as a linear function of the acting total thermodynamic driving force,

$$Q = A + B\Delta G \qquad [3.5]$$

Following the basic kinetic theory of Pati and Cohen (1969), the initial rate of transformation $\dot{f}$ can then be expressed as

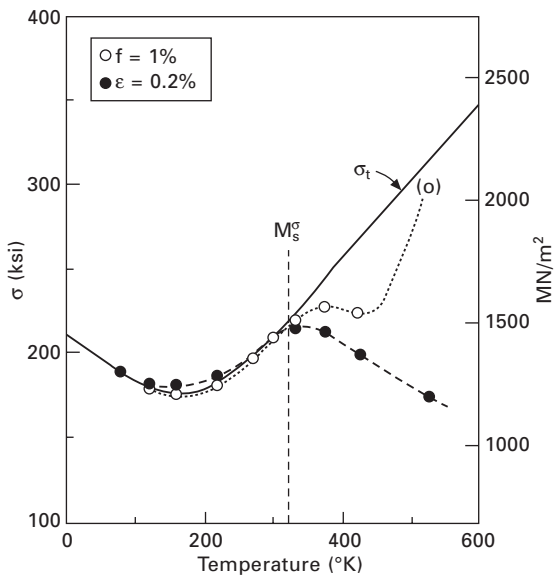
© Woodhead Publishing Limited, 2012

$$\dot{f} = n_s V v \exp\left(-\frac{A + B\Delta G}{RT}\right) \quad [3.6]$$

where n_s is the density of nucleation sites, V is the instantaneous mean martensitic volume, and v is the nucleation attempt frequency. The critical ΔG required to achieve a given $\dot{f}$ is then given by

$$\Delta G_{\text{crit}}(\dot{f}) = -\frac{1}{B}\left(A + RT \ln \frac{\dot{f}}{n_s V v}\right) \quad [3.7]$$

which shows a linear dependence on temperature, T. For stress-assisted transformation, where yielding occurs by the rate of transformation plasticity matching the imposed strain rate, this corresponds to an imposed transformation rate of $\dot{f} = k\dot{\varepsilon}$. Calculation of the total thermodynamic driving force (chemical plus stress contributions) at the yield stress observed (Olson and Azrin, 1978) at temperatures below M_s^σ for high-strength TRIP steels verifies the linear ΔG_{crit}(T) relation of Eq. [3.7] (Olson and Cohen, 1982). This linear relationship then predicts the critical stress for stress-assisted transformation σ_t determined by the solid curve of Fig. 3.4 where it is compared against measured stresses for 0.2% plastic strain and 1% transformation. In contrast to



3.4 Observed temperature dependence of 0.2% yield stress and stress at which 1% martensite is detected in high-strength TRIP steel (Olson and Azrin, 1978). Solid curve (σ_t) represents theoretical (tensile) stress for stress-assisted transformation (Olson and Cohen, 1982).

© Woodhead Publishing Limited, 2012

the linear behavior represented in Fig. 3.3, $\sigma_t(T)$ is in this case a curve which passes through a minimum at 158 K. The curvature arises from nonlinearity of $\Delta G_{ch}(T)$ at low temperatures, and the minimum is consistent with the behavior of relatively stable alloys which exhibit suppressible isothermal ('C-curve') transformation kinetics. In the stress-assisted regime, Eqs [3.3] and [3.7] also predict a strain-rate sensitivity of flow stress of the form (Olson and Cohen, 1982):

$$\frac{\partial \sigma}{\partial \ln \dot{\varepsilon}} = -\frac{RT}{B\dfrac{\partial \Delta G}{\partial \sigma}} \qquad [3.8]$$

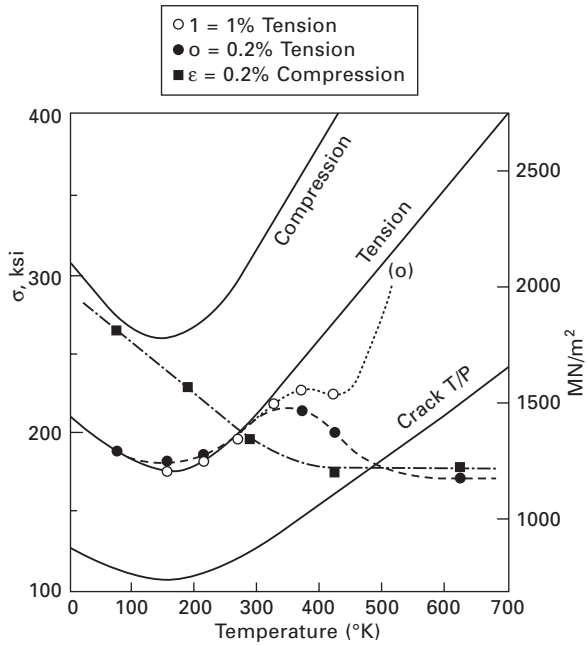
In line with the close relation between B and the activation volume for slip, the rate sensitivity of transformation plasticity is very similar to that for conventional plastic deformation.

Application of transformation plasticity to enhancement of uniform ductility and fracture toughness involves very different stress states, which must be taken into account in optimizing transformation stability for desired properties. A strong stress-state dependence of the Patel–Cohen work term (Patel and Cohen, 1953) arises from the transformation dilatation. Using the $\partial \Delta G/\partial \sigma$ values determined for uniaxial compression, uniaxial tension, and elastic crack tip, the corresponding σ_t curves calculated for the alloy of Fig. 3.4 are compared in Fig. 3.5. Also shown are 0.2% yield stress measurements for uniaxial compression. An unusually large strength-differential (S-D) effect, comparing flow stress in compression and tension, is expected in the stress-assisted regime. Although an anomalous reverse S-D effect is observed near 300 K, the expected effect is observed at low temperatures, suggesting that flow is controlled by transformation in tension and slip in compression. The prediction for the crack-tip case suggests that transformation will control flow over a wider temperature range and that the effective flow stress near 300 K is significantly reduced relative to uniaxial tension. As will be discussed further, this stress-state sensitivity is important to the achievement of improved strength/toughness combinations, allowing a high tensile strength material to benefit from the crack-tip plasticity of a softer material.

A knowledge of the kinetics of isothermal martensitic transformations can also be used to predict the shape of the σ-ε curve during stress-assisted transformation by taking into account the variation in the number of nucleation sites (n_s in Eq. [3.7]) with progress of the transformation (Olson and Cohen, 1982). The Pati–Cohen model, which satisfactorily accounts for the course of stress-free isothermal martensitic transformation, describes the nucleation-site density by an expression of the form (Pati and Cohen, 1969; Raghavan and Cohen, 1971):

$$n_s = (n_i + pf - N_v)(1 - f) \qquad [3.9]$$

© Woodhead Publishing Limited, 2012



3.5 Calculated transformation stresses and measured yield stresses for the TRIP steel of Fig. 3.4 under different stress states (Olson and Cohen, 1982).

Here n_i is the initial-site density, p is an 'autocatalytic factor' accounting for new sites produced during transformation, and N_v is the number of martensitic plates per unit volume (accounting for sites which have already operated); the $(1-f)$ factor takes into account potential sites which have been 'swept up' by transformation. While the p factor can cause n_s to increase in the initial stages of transformation, a decreasing average plate volume $\overline{V}$ due to 'partitioning' can cause the $-N_v$ term to reduce n_s at later stages. A saturation level of transformation is reached when $n_s \rightarrow 0$. Substituting Eq. [3.9] into Eq. [3.7], the flow stress during stress-assisted transformation can be expressed as (Olson and Cohen, 1982):

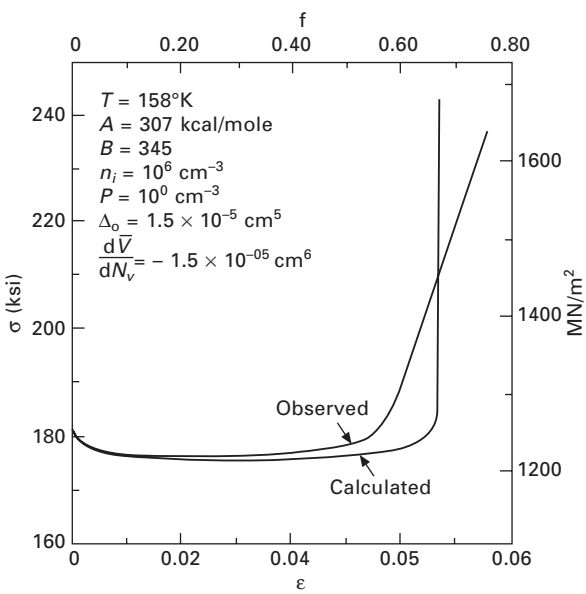
$$\sigma_t(f,\dot{f},T) = -\left(B\,\frac{\partial \Delta G}{\partial \sigma}\right)^{-1}\left\{A + B\Delta G_{ch} + RT\,\ln\left(\frac{\dot{f}}{(n_i + pf - N_v)(1-f)Vv}\right)\right\} \qquad [3.10]$$

Substitution of Eq. [3.3] then provides a complete constitutive relation for $\sigma_t(\varepsilon, \dot{\varepsilon}T)$. The shape of the σ-ε curve is determined by the behavior of the denominator in the last term of Eq. [3.13]. The yield stress is controlled by n_i, a stress drop is produced by the pf autocatalytic term, and approach to saturation

© Woodhead Publishing Limited, 2012

causes rapid hardening as site depletion brings the denominator toward zero. Using the A and B parameters defined by the temperature dependence of σ_t in Fig. 3.4, and typical experimental values of the other kinetic parameters, a calculated σ-ε curve is compared with that measured at 158 K for the same TRIP steel in Fig. 3.6. The yield drop and flat portions of the curves are in good agreement, but the calculated final hardening (saturation) stage is too abrupt. This arises from the approximation of a singly activated process. As described earlier, the distribution of nucleation-site potencies is known to give a distribution of nucleation activation energies (Magee, 1971; Lin *et al.*, 1992), and this can account for a more gradual approach to saturation. It is important to note that the flow stresses depicted in Fig. 3.6 are all well below the stress for general yielding by slip. Relative to the 'normal' slip-controlled flow behavior of this material, the phenomena thus far considered are entirely 'softening' contributions. The high strain hardening associated with the saturation stage is best understood as the cessation of a softening phenomenon rather than the onset of a hardening mechanism. Once the transformation plasticity phenomenon (dynamic softening) associated with stress-assisted transformation is essentially complete, the higher strength of the transformation product makes its 'static hardening' contribution to the flow stress.

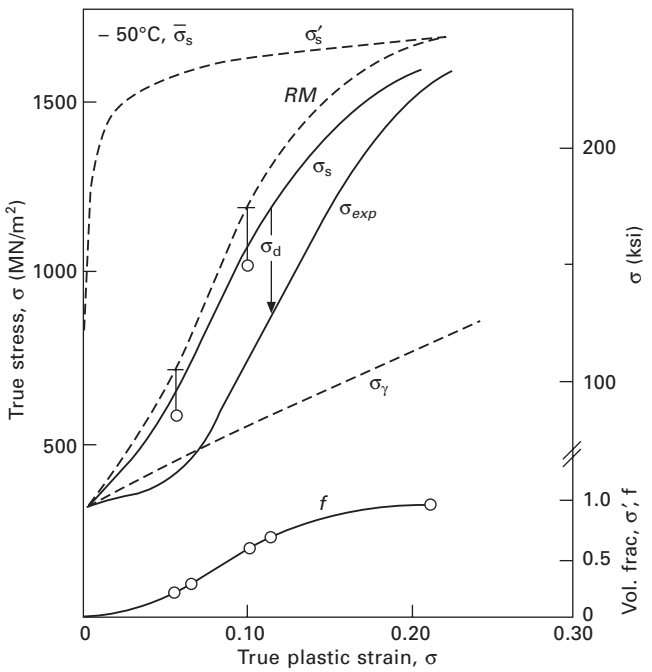
While control of plasticity by transformation kinetics allows rather precise prediction of flow behavior in the stress-assisted transformation regime, the



3.6 Comparison of calculated and observed (Olson and Azrin, 1978) true σ-ε curves for the TRIP steel of Fig. 3.4 (Olson and Cohen, 1982).

© Woodhead Publishing Limited, 2012

simultaneous operation of general slip and transformation in the strain-induced regime makes the quantitative treatment of flow behavior more difficult. Although much attention has been given to the static-hardening aspects of the two-phase mixture formed during strain-induced transformation, careful comparison of σ-ε curves has demonstrated that dynamic softening is also an important contribution. A detailed study of the transformation and flow behavior of a metastable austenitic stainless steel, summarized in Fig. 3.7, has allowed a quantitative separation of the static hardening and dynamic softening contributions during strain-induced transformation (Narutani *et al.*, 1982). The measured σ-ε curve of the metastable steel is labeled σ_{exp}. The dashed $\sigma_{\alpha'}$ and σ_γ curves represent the corresponding σ–ε curves of the martensite and stable austenite measured separately on specially designed similar steel compositions. One estimate of the static hardening behavior of the two-phase mixture is obtained from a simple 'rule of mixtures' using the $\sigma_{\alpha'}(\varepsilon)$, $\sigma_\gamma(\varepsilon)$ data and the measured $f(\varepsilon)$ curve shown at the bottom of the



3.7 Experimental flow stress, σ_{exp}, and volume fraction martensite, *f*, vs. plastic strain, ε, for metastable austenitic steel at –50°C, $\dot{\varepsilon}$, = 2.2×10^{-4} s^{-1}. Dashed curves represent the stable austenite flow stress, σ_γ, the martensite flow stress, σ_α', and the prediction of the rule of mixtures for two-phase hardening, *RM*. Solid curve, σ_s, is a prediction of strain-corrected rule-of-mixtures model (Narutani *et al.*, 1982).

© Woodhead Publishing Limited, 2012

figure; this estimate is depicted by the dashed curve labeled *RM*. Because the transformation plasticity contribution arising from biasing of the transformation shape strain does not contribute to the strain in either phase, the *RM* curve represents an upper limit to the static-hardening behavior. A strain-corrected rule of mixtures is obtained using $\sigma_{\alpha'}$ and σ_{γ} values at a strain of $\varepsilon - \alpha f$, where αf corrects for the shape-strain contribution to the measured ε. An upper-limit estimate of the α coefficient is $\alpha = k^{-1}$, taking k from the measured stress-assisted transformation behavior at low temperatures. This gives the solid curve depicted just below the dashed *RM* curve. The open points represent static flow-stress estimates determined by prestrain experiments. After the transforming material had been deformed to a particular strain, the static flow stress of the resulting two-phase mixture (in the absence of dynamic transformation softening) was determined from its flow stress subsequently measured at a higher temperature where the austenite is stable, correcting for its temperature dependence. These estimates and the *RM* estimate bracket the strain-corrected rule of mixtures estimate which is therefore taken as a reasonable approximation of the flow stress arising from static hardening, σ_s. This is expressed as:

$$\sigma_s = [1 - f] \cdot \sigma_{\gamma}(\varepsilon - \alpha f) + f \cdot \sigma_{\alpha'}(\varepsilon - \alpha f) \qquad [3.11]$$

As indicated in Fig. 3.7, the dynamic softening increment $\Delta\sigma_d$ is then taken as the difference between σ_s and σ_{exp}. Correlation of the $\Delta\sigma_d$ increment thus obtained with f-ε behavior observed over a wide temperature range indicates that the fractional softening increment is proportional to $\mathrm{d}f/\mathrm{d}\varepsilon$:

$$\frac{\Delta\sigma_d}{\sigma_s} = \beta \cdot \frac{\mathrm{d}f}{\mathrm{d}\varepsilon} \qquad [3.12]$$

where $\beta = 5.3 \times 10^{-2}$. This then gives a constitutive flow relation for strain-induced transformation of the form:

$$\sigma = \{[1 - f] \cdot \sigma_{\gamma}(\varepsilon - \alpha f) + f \cdot \sigma_{\alpha'}(\varepsilon - \alpha f)\} \cdot \left\lfloor 1 - \beta \cdot \frac{\mathrm{d}f}{\mathrm{d}\varepsilon} \right\rfloor \qquad [3.13]$$

Through Eq. [3.13], $\sigma(\varepsilon, \dot{\varepsilon}, T)$ can be predicted from a knowledge of f, σ_{γ} and $\sigma_{\alpha'}$ as functions of ε, $\dot{\varepsilon}$, and T.

As in the case of stress-assisted transformation, dynamic softening is the dominant factor at low strains, causing the flow stress σ_{exp} of the transforming material in Fig. 3.7 to fall below that of the stable austenite, σ_{γ}. The static hardening becomes dominant at high strains. The combined effect of these two factors delays the maximum hardening rate $\mathrm{d}\sigma/\mathrm{d}\varepsilon$ to a higher strain than that where $\mathrm{d}f/\mathrm{d}\varepsilon$ is maximum. The maximum $\mathrm{d}\sigma/\mathrm{d}\varepsilon$ arises from both the static hardening (proportional to $\mathrm{d}f/\mathrm{d}\varepsilon$) and the diminution of dynamic softening (proportional to $-\mathrm{d}^2f/\mathrm{d}\varepsilon^2$) as $\mathrm{d}f/\mathrm{d}\varepsilon$ decreases. Again, the cessation

© Woodhead Publishing Limited, 2012

of a softening phenomenon provides a major contribution to the net rate of hardening. The generalization of this constitutive law to three-dimensional deformation has been developed by Stringfellow *et al*. (1992).

3.4.2 Stability of plastic flow

With constitutive flow relations for transformation plasticity based on the transformation kinetics, we may now consider the associated macroscopic flow behavior as predicted by continuum plasticity theory. The ability of transformation plasticity to dramatically alter the shape of a σ-ε curve naturally raises the question of the optimum or 'ideal' curve shape for stability of plastic flow. The minimum strain-hardening rate required to maintain stable flow during tensile deformation is expressed by (Backofen, 1972):

$$\frac{\mathrm{d}\sigma}{d\varepsilon} = \sigma \qquad [3.14]$$

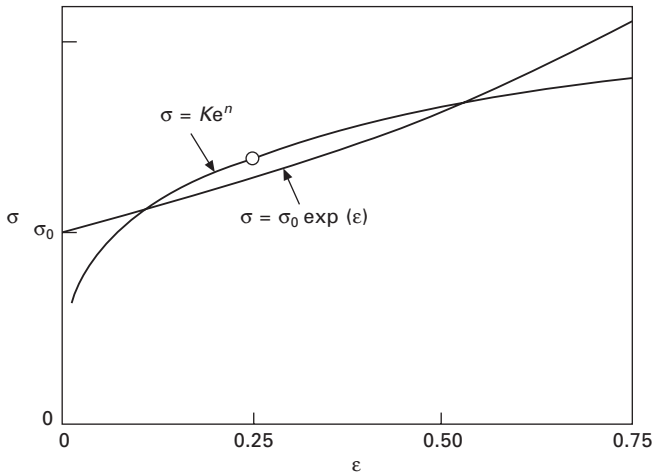
A consequence of strain hardening is that the hardening rate necessary to maintain stability is increased. Excessive hardening therefore makes it more difficult to maintain stability at higher strains. It follows that the most efficient use of a hardening increment $\Delta\sigma$ is to distribute it with respect to strain in such a way that $\mathrm{d}\sigma/\mathrm{d}\varepsilon$ increases with ε. The ideal hardening curve, which provides the minimum hardening rate necessary to maintain stability at all strains, is given by the solution of the differential equation represented by Eq. [3.15]:

$$\sigma = \sigma_y \exp(\varepsilon) \qquad [3.15]$$

where σ_y corresponds to the yield stress. In contrast to the usual downward curvature associated with the structural hardening and recovery processes controlling deformation by slip, the ideal flow relation of Eq. [3.15] possesses upward curvature (Kocks *et al*., 1979). The 'delayed hardening' behavior associated with the intersection of dynamic softening and static hardening phenomena in transformation plasticity provides an effective means of increasing $\mathrm{d}\sigma/\mathrm{d}\varepsilon$ with ε to achieve this curvature.

The ideal hardening behavior of Eq. [3.15] is contrasted with the conventional downward-curving behavior, approximated by a power law $\sigma = K\varepsilon^n$, in Fig. 3.8. The open circle indicates the point where the power-law curve reaches the condition for flow localization by tensile necking, i.e., where $\mathrm{d}\sigma/\mathrm{d}\varepsilon$ falls below σ (Eq. [3.14]). From a local viewpoint, which considers the conditions at the necking strain, one would attribute the necking to insufficient hardening, and would propose to increase uniform ductility by increasing the hardening exponent, n. From a perspective which considers the σ-ε curve as a whole, the necking can equally well be ascribed to excessive hardening at low strains. In the region where the $K\varepsilon^n$ curve lies above the $\sigma_0 \exp \varepsilon$ curve,

© Woodhead Publishing Limited, 2012



3.8 Comparison of ideal exponential hardening behavior with power-law hardening. Open point indicates necking strain.

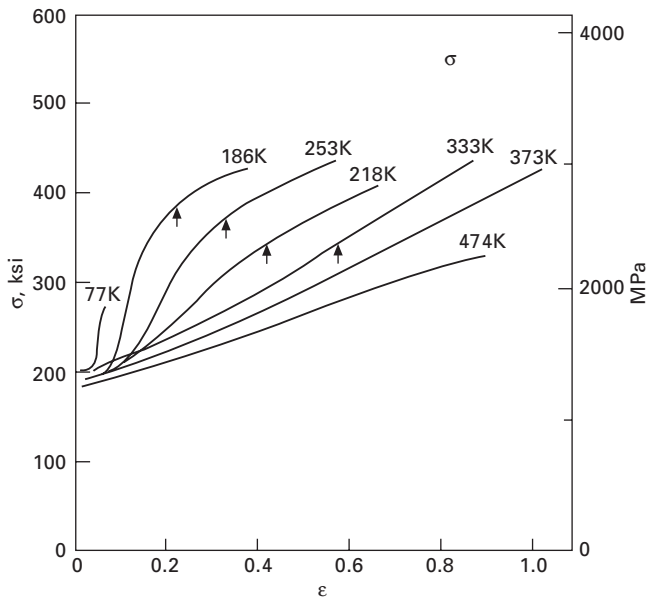
the superposition of a *softening* mechanism which lowers the flow stress to the $\sigma_0 \exp \varepsilon$ curve would double the uniform ductility for the case depicted in Fig. 3.8. This illustrates the potential of the dynamic softening phenomenon in transformation plasticity for the enhancement of flow stability. At higher strains, where the $K\varepsilon^n$ curve falls below the $\sigma_0 \exp \varepsilon$ curve, superposition of a hardening mechanism, such as the high-strain static hardening contribution in transformation plasticity, is required to further maintain stable flow. If the ideal $\sigma_0 \exp \varepsilon$ curve is followed, necking will never occur, and uniform ductility will be controlled by fracture rather than plastic instability. Figure 3.8 illustrates that the dynamic softening contribution to transformation plasticity at lower strains can be equally important as the high-strain static hardening contribution in promoting stability of plastic flow.

3.4.3 Applications of transformation plasticity to ductility

The flow-stabilizing influence of the σ-ε curve-shaping effects associated with transformation plasticity allows dramatic enhancement of uniform ductility under conditions of optimum thermodynamic stability, and this phenomenon is the most well-established transformation plasticity application. Although temperature sensitivity and Lüders-band behavior limit the useful ductility of the highest strength TRIP steels, which depend almost entirely on their transformation behavior for stability of flow, the flow-stabilizing contribution of a moderate rate of transformation in lower strength metastable austenitic steels has been practically applied for many years. Control of transformation plasticity has led to the development of numerous commercial high-formability stainless steels.

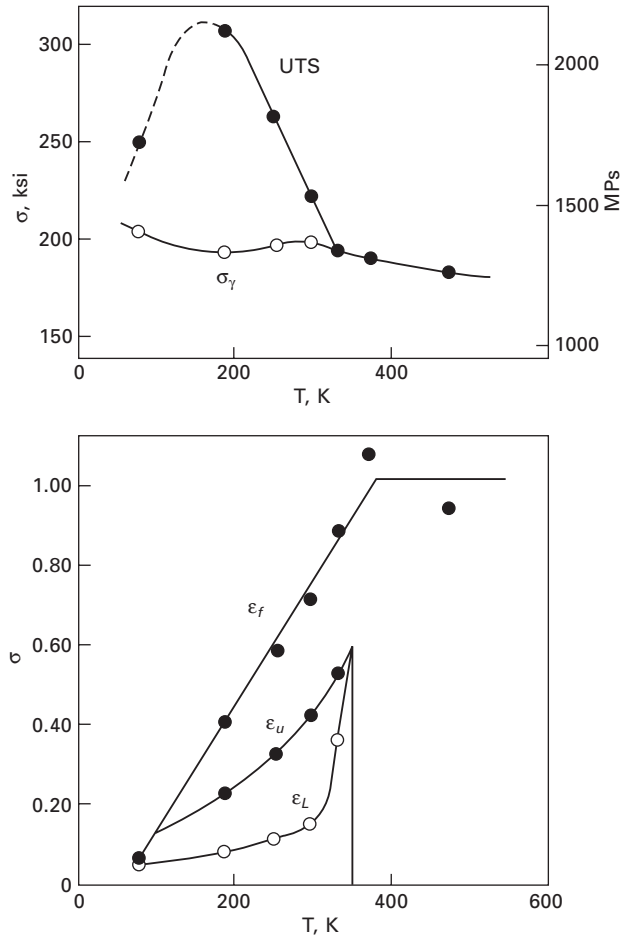
© Woodhead Publishing Limited, 2012

The enhancement of flow stability in metastable austentic steels via transformation plasticity has been extensively investigated (Krivobok and Talbot, 1950; Angel, 1954; Fiedler *et al.*, 1955; Powell *et al.*, 1958; Bressanelli and Moskowitz, 1966; Zackay *et al.*, 1967; Tamura *et al.*, 1970; Olson and Azrin, 1978; Zackay *et al.*, 1978; Hecker *et al.*, 1982), and analyzed in terms of Eq. [3.15] (Azrin *et al.*, 1976). A continuous local strain measurement technique allowed determination of true stress–true strain behavior of the original high-strength austenitic TRIP steels during both uniform and localized plastic flow under a variety of conditions (Azrin *et al.*, 1976; Olson and Azrin, 1978, unpublished research). Figure 3.9 summarizes such curves obtained for uniaxial tensile deformation of a fully austenitic TRIP steel of nominal composition Fe-9Cr-8Ni-4Mo-2Si-2Mn-0.3C strengthened by warm working to a 60% reduction at 450°C (Olson and Azrin, 1978). Arrows indicate the necking strain or uniform strain, ε_u. The temperature (stability) dependence of the strength and ductility properties is summarized in Fig. 3.10. Consistent with the constitutive model predictions, the true σ-ε curves in Fig. 3.9 have a characteristic sigmoidal shape. The temperature dependence of the 0.2% yield strength σ_y in Fig. 3.10 is similar to that of Fig. 3.4, indicating an M_s^σ temperature near 280 K. The ultimate tensile strength (UTS) reaches a maximum in the stress-assisted transformation regime, limited at lower temperatures by fracture. The latter effect is indicated by the intersection of uniform strain ε_u and the fracture strain ε_f at the lowest



3.9 True stress–strain curves of high-strength austenitic TRIP steel. Arrows indicate necking strain (Olson and Azrin, 1978).

© Woodhead Publishing Limited, 2012



3.10 Tensile properties of austenitic TRIP steel of Fig. 3.9, including Lüders strain ε_L, uniform (necking) strain ε_u, and fracture strain ε_f.

temperature. The uniform ductility ε_u reaches a maximum above M_s^σ at a temperature near 350 K, reflecting an optimum overall rate of deformation-induced transformation. As indicated by the shape of the σ-ε curves, early completion of transformation at lower temperatures leads to early necking in the downward-curving portion of the σ-ε behavior that follows. Above 350 K the strain hardening associated with a reduced degree of transformation is insufficient to maintain stable flow in this high-strength material, and the uniform ductility is negligible. The existence of such an optimum stability for maximum uniform ductility in metastable austenitic steels in general is well established (Bressanelli and Moskowitz, 1966; Tamura *et al.*, 1970; Zackay *et al.*, 1978). The shape of the optimum stability 333 K curve in

© Woodhead Publishing Limited, 2012

Fig. 3.9, giving a uniform ductility of 60% with a yield strength of 200 ksi (1.4 GPa), is quite close to the ideal exponential form.

3.4.4 Applications of transformation plasticity to fracture toughness

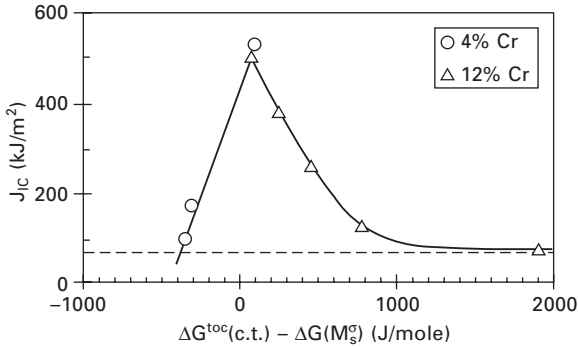
Transformation toughening in austenitic steels is complicated both by the greater complexity of the constitutive behavior of strain-induced as opposed to stress-assisted transformation, and the more complex processes of ductile fracture. The experimental study by Léal (1984) of the interaction of transformation with ductility and fracture toughness is reviewed in Olson and Cohen (1986b). A series of six precipitation-hardenable austenitic steels based on A286 steel were designed to have a constant 1300 MPa yield strength, varying stability with respect to transformation, and a varying transformation volume change. The alloys also had a fairly strong temperature dependence of phase stability to allow variation of stability over wide limits. The fracture ductility and J_{IC} toughness were found to peak at the M_s^σ of their respective stress states.

A subsequent study by Young (1988), reviewed in Olson (1990), involved a thorough evaluation of the transformation kinetics and constitutive relations of phosphocarbide-strengthened austenitic steels in which the transformation volume change and austenite-martensite hardness difference could both be varied. The measured enhancement of toughness and fracture ductility in these alloys was similar to that observed by Léal. In the regime of shear instability controlled ductile fracture, the increase in J_{IC} toughness varies linearly with the height of the transformation zone at the crack front. Correlation of the slope of this toughening response with transformation volume change $\delta V/V$, and austenite-martensite hardness differences δH_v (influencing strain hardening) shows that, in contrast to brittle solids, the toughening behavior is more dilatation sensitive, with the $\delta J/h$ scaling with the third power of $\delta V/V$. Higher δH_v also promotes more toughening.

The remarkable transformation toughening observed by Stavehaug (1990) in a more recent series of γ'-strengthened austenites is summarized in Fig. 3.11, which plots the measured room-temperature J_{IC} toughness vs. a thermodynamic stability parameter defined by the difference between the total acting thermodynamic driving force and its critical value at M_s^σ. Similar to the results of Léal and Young, the toughening is maximum at the M_s^σ condition, but in these experiments the apparent toughness enhancement over the stable austenite toughness indicated by the dashed line is significantly higher.

Quantitative modeling of the mechanics of the transformation toughening has addressed mechanisms on two length scales. As an analysis of interactions of transformation hardening and void softening induced localization at the

© Woodhead Publishing Limited, 2012

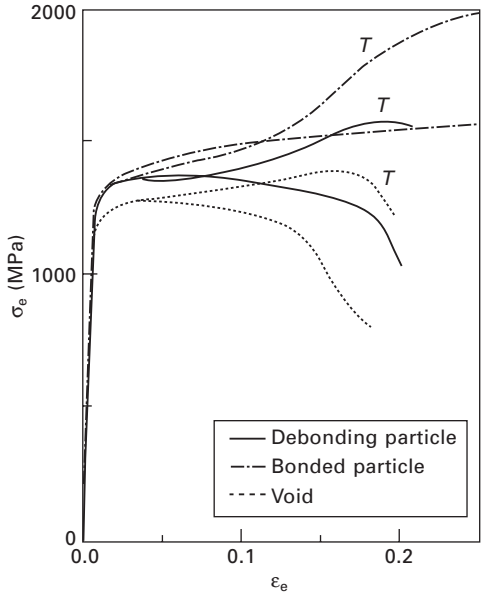


3.11 Measured J_{IC} fracture toughness of 12Cr and 4Cr austenitic alloy series (1380 MPa yield strength) as a function of thermodynamic austenite stability parameter (Stavehaug, 1990).

macroscopic level, Stringfellow and Parks (1991) and Stringfellow (1990) performed a series of model calculations incorporating a void softening model into the transformation constitutive model.

On a finer length scale, electron microscopy observations (Young, 1988) of the distribution of fine strain-induced martensite around 0.1 μm scale particles after straining to levels beyond the microvoid nucleation strain of non-transforming material indicate a more direct cross-interaction between transformation and the unit process of ductile fracture. Socrate and Parks (Socrate, 1995) have applied the transformation constitutive model in numerical simulations of microvoid nucleation, growth and coalescence employing a cohesive-zone model for interface debonding similar to that introduced by Needleman (1987). Using interfacial strength estimates for the TiC particles observed in the experimental alloys, Fig. 3.12 shows the computed stress–strain curves for a cell model of the crack-tip process zone with a remote stress state of $\sigma_h/\overline{\sigma} = 1.12$. Dotted, dashed, and solid curves represent material with (a) pre-existing void, (b) a permanently bonded particle, and (c) a debonding particle, respectively. The curves labeled with a T depict the effect of strain-induced transformation at a stability near that of the crack-tip M_s^σ temperature. Comparing the transforming and non-transforming behaviors for material with either a pre-existing void or a debonding particle, transformation greatly delays the onset of microvoid softening based negative strain hardening that drives shear localization fracture. Computed transformation fields prior to nucleation are in good agreement with the experimental observations. Simulations of interacting pairs of particles also demonstrate retardation of microvoid coalescence, but the largest toughening effect appears to be associated with delay of shear instability driven by void growth softening. The strain corresponding to the onset of terminal softening (stress maximum) in Fig. 3.12 increases

© Woodhead Publishing Limited, 2012



3.12 Computed stress–strain curves for crack tip cell model; curves labeled *T* represent transforming material while others represent non-transforming material (Socrate, 1995).

with transformation by a factor similar to the J_{IC} toughness enhancement of Fig. 3.11.

3.5 Conclusions

Building on dislocation-based theory of the mechanism and kinetics of heterogeneously nucleated martensitic transformations, quantitative models have been developed for the kinetics of stress-assisted and strain-induced martensitic transformations. Constitutive flow relations for transformation plasticity have been derived based on these kinetic models, incorporating the static hardening effect of the transformation product and the dynamic softening effect of the transformation as a deformation mechanism. The transformation softening and hardening effects can distort the stress–strain curve from the usual downward-curving shape to an upward-curving shape which approximates an ideal exponential hardening behavior promoting maximum uniform ductility. Numerical simulation of shear-instability-controlled ductile fracture demonstrates that the transformation plasticity behavior can also account for observed substantial enhancement of ductile fracture toughness.

The demonstrated behaviors in fully austenitic steels offer a foundation for predictive control of transformation plasticity in dispersed-phase systems.

© Woodhead Publishing Limited, 2012

More broadly, the application of predictive theory of transformation plasticity to enhance mechanical properties of advanced steels remains a vital avenue of steel research. Predictive control of the complexities of martensitic behavior has served as the foundation of a systems approach to science-based materials engineering. In this way, ferrous metallurgy has played a leading role in the new technology of materials design (Olson, 2006).

3.6 References

Angel, T. (1954). 'Formation of Martensite in Austenitic Stainless Steels'. *J. Iron Steel Inst*. **177**: 165–174.

Azrin, M., G. B. Olson, *et al*. (1976). 'Inhomogeneous Deformation and Strain-Rate Effects in High-Strength Trip Steels'. *Materials Science and Engineering* **23**(1): 33–41.

Backofen, W. A. (1972). *Deformation Processing*. Reading, MA: Addison-Wesley.

Bogers, A. J. and W. G. Burgers (1964). 'Partial Dislocations on the (110) Planes in the bcc Lattice and the Transition of the fcc into the bcc Lattice'. *Acta Metall*. **12**: 225–261.

Bolling, G. F. and R. H. Richman (1970). 'Influence of Stress of Martensite-Start Temperatures in Fe-Ni-C Alloys'. *Scripta Metallurgica* **4**(7): 539–544.

Bressanelli, J. P. and A. Moskowitz (1966). 'Effects of Strain Rate Temperature and Composition on Tensile Properties of Metastable Austenitic Stainless Steels.' *ASM Transactions Quarterly* **59**(2): 223–239.

Brooks, J. W., M. H. Loretto, *et al*. (1979). '*In-situ* Observations of the Formation of Martensite in Stainless-Steel'. *Acta Metallurgica* **27**(12): 1829–1838.

Christian, J.W., G. B. Olson, *et al*. (1995). 'Classification of Displacive Transformations: What is a Martensitic Transformation?', *Proc. ICOMAT 95*, supplement to *J. de Phys. III*, **5** Coll. C8: 3–10.

Fiedler, H. C., B. L. Averbach, *et al*. (1955). 'The Effect of Deformation on the Martensitic Transformation'. *Trans. ASM* **47**: 267–290.

Fisher, P. J. (1974). The Effects of Stress on the Martensite Transformation. PhD Thesis, University of New South Wales, Australia.

Ghosh, G. and G. B. Olson (1994a). 'Kinetics of Fcc→Bcc Heterogeneous Martensitic Nucleation. 1. The Critical Driving-Force for Athermal Nucleation'. *Acta Metallurgica et Materialia* **42**(10): 3361–3370.

Ghosh, G. and G. B. Olson (1994b). 'Kinetics of Fcc→Bcc Heterogeneous Martensitic Nucleation. 2. Thermal-Activation'. *Acta Metallurgica et Materialia* **42**(10): 3371–3379.

Hecker, S. S., M. G. Stout, *et al*. (1982). 'Effects of Strain State and Strain Rate on Deformation-Induced Transformation in 304 Stainless-Steel. 1. Magnetic Measurements and Mechanical-Behavior'. *Metallurgical Transactions A – Physical Metallurgy and Materials Science* **13**(4): 619–626.

Kaufman, L. and M. Cohen (1958). 'Thermodynamics and Kinetics of Martensitic Transformations'. *Prog. Metal Physics 1*: 165–246.

Kocks, U. F., J. J. Jonas, *et al*. (1979). 'The Development of Strain-Rate Gradients'. *Acta Metallurgica* **27**: 419–432.

Krivobok, V. N. and A. M. Talbot (1950). 'Effect of Temperature on the Mechanical Properties, Characteristics, and Processing of Austenitic Stainless Steels'. *Proceedings American Society for Testing and Materials* **50**: 895–930.

© Woodhead Publishing Limited, 2012

Lagneborg, R. (1964). 'Martensite Transformation in 18percent Cr-8percent Ni Steels'. *Acta Metallurgica* **12**(7): 823–843.

Léal, R. (1984). Transformation Toughening of Metastable Austenitic Steels. PhD Thesis, MIT.

Lecroise, F. and A. Pineau (1972). 'Martensitic Transformations Induced by Plastic-Deformation in Fe-Ni-Cr-C System'. *Metallurgical Transactions* **3**(2): 387–396.

Lin, M. F., G. B. Olson, *et al*. (1992). 'Distributed-Activation Kinetics of Heterogeneous Martensitic Nucleation'. *Metallurgical Transactions A – Physical Metallurgy and Materials Science* **23**(11): 2987–2998.

Machlin, E. S. and M. Cohen (1952). 'Isothermal Mode of the Martensitic Transformation'. *Transactions of the American Institute of Mining and Metallurgical Engineers* **194**(5): 489–500.

Magee, C. L. (1971). 'Kinetics of Martensite Formation in Small Particles'. *Metallurgical Transactions* **2**(9): 2419–2430.

Manganon, D. L. and G. Thomas (1970). 'The Martensite Phase in 304 Stainless Steel'. *Metall. Trans.* **1**: 1577–1586.

Narutani, T., G. B. Olson, *et al*. (1982). 'Constitutive Flow Relations for Austenitic Steels during Strain-induced Martensitic Transformations'. *J. de Physique* **43**(C4): 429–434.

Needleman, A. (1987). 'A Continuum Model for Void Nucleation by Inclusion Debonding'. *Journal of Applied Mechanics – Transactions of the ASME* **54**(3): 525–531.

Olson, G. B. (1990). *Science of Steel*. 34th Sagamore Army Materials Research Conference – Innovations in Ultrahigh-Strength Steel Technology, Lake George, NY.

Olson, G. B. (2006). 'Advances in Theory: Martensite by Design'. *Materials Science and Engineering A* **438**: 48–54.

Olson, G. B. and M. Azrin (unpublished research). AMMRC. Watertown, MA.

Olson, G. B. and M. Azrin (1978). 'Transformation Behavior of Trip Steels'. *Metallurgical Transactions A – Physical Metallurgy and Materials Science* **9**(5): 713–721.

Olson, G. B. and M. Cohen (1972). 'Mechanism for Strain-Induced Nucleation of Martensitic Transformations'. *Journal of the Less-Common Metals* **28**(1): 107–119.

Olson, G. B. and M. Cohen (1975). 'Kinetics of Strain-Induced Martensitic Nucleation'. *Metallurgical Transactions A* **6**(4): 791–795.

Olson, G. B. and M. Cohen (1976a). 'A General Mechanism of Martensitic Nucleation: Part II: FCC-BCC and Other Martensitic Transformations'. *Metall. Trans.* **7A**: 1905–1914.

Olson, G. B. and M. Cohen (1976b). 'Mechanism and Kinetics of Deformation-Induced Martensitic Transformations'. *JOM – Journal of Metals* **28**(12): A15.

Olson, G. B. and M. Cohen (1981). 'Dislocation Structure of Martensitic Interfaces'. *International Conference of Solid-Solid Phase Transformations*, Carnegie Mellon University.

Olson, G. B. and M. Cohen (1982). 'Stress-Assisted Isothermal Martensitic Transformation – Application to Trip Steels'. *Metallurgical Transactions A – Physical Metallurgy and Materials Science* **13**(11): 1907–1914.

Olson, G. B. and M. Cohen (1986a). 'Dislocation Theory of Martensitic Transformations'. in *Dislocations in Solids Vol. 7*, ed. F. R. N. Nabarro. Amsterdam: North-Holland, pp. 295–407.

Olson, G. B. and M. Cohen (1986b). *Mechanical Properties and Phase Transformations in Engineering Materials*. TMS-AIME, pp. 367–390.

© Woodhead Publishing Limited, 2012

Patel, J. R. and M. Cohen (1953). 'Criterion for the Action of Applied Stress in the Martensitic Transformation'. *Acta Metallurgica* **1**(5): 531–538.

Pati, S. R. and M. Cohen (1969). 'Nucleation of Isothermal Martensitic Transformation'. *Acta Metallurgica* **17**(3): 189–199.

Powell, G. W., E. R. Marshal, *et al*. (1958). 'Strain Hardening of Austenitic Stainless Steel'. *Trans. ASM* **50**: 478–479.

Raghavan, V. and M. Cohen (1971). 'Measurement and Interpretation of Isothermal Martensitic Kinetics'. *Metallurgical Transactions* **2**(9): 2409–2418.

Socrate, S. (1995). Mechanics of Microvoid Nucleation and Growth in High-Strength Metastable Austenitic Steels. PhD Thesis, MIT.

Stavehaug, F. (1990). Transformation Toughening of γ′ Strengthened Metastable Austenitic Steels. PhD Thesis, MIT.

Stringfellow, R. (1990). Mechanics of Strain-Induced Transformation Toughening in Metastable Austenitic Steels. PhD Thesis, MIT.

Stringfellow, R. G. and D. M. Parks (1991). 'A Self-Consistent Model of Isotropic Viscoplastic Behavior in Multiphase Materials'. *International Journal of Plasticity* **7**(6): 529–547.

Stringfellow, R. G., D. M. Parks, *et al*. (1992). 'A Constitutive Model for Transformation Plasticity Accompanying Strain-Induced Martensitic Transformations in Metastable Austenitic Steels'. *Acta Metallurgica et Materialia* **40**(7): 1703–1716.

Suzuki, T., H. Kojima, *et al*. (1977). 'Experimental-Study of Martensite Nucleation and Growth in 18-8 Stainless-Steel'. *Acta Metallurgica* **25**(10): 1151–1162.

Tamura, I., T. Maki, *et al*. (1970). 'On Morphology of Strain-Induced Martensite and Transformation-Induced Plasticity in Fe-Ni and Fe-Cr-Ni Alloys'. *Transactions of the Iron and Steel Institute of Japan* **10**(3): 163–172.

Venables, J. A. (1962). 'Martensite Transformation in Stainless Steel'. *Philosophical Magazine* **7**(73): 35–44.

Young, C. C. (1988). Transformation Toughening in Phosphocarbide-Strengthened Austenitic Steels. PhD Thesis, MIT.

Zackay, V. F., M. D. Bhandarkar, *et al*. (1978). *Advances in Deformation Processing*. New York: Plenum Press.

Zackay, V. F., E. R. Parker, *et al*. (1967). 'Enhancement of Ductility in High-Strength Steels'. *ASM Transactions Quarterly* **60**(2): 252–259.

© Woodhead Publishing Limited, 2012

4

Shape memory in ferrous alloys

D. DUNNE, University of Wollongong, Australia

Abstract: Iron-based shape memory alloys have been studied intensively over the last few decades by several research groups, notably those led by Maki (Kyoto University), Hsu (Shanghai Jiao Tong University), Sato (Tokyo Institute of Technology) and Kajiwara (NIMS, Tsukuba). These researchers have published authoritative reviews of this topic and the present contribution draws on these and other significant publications to analyse fundamental factors that are important in producing shape memory. Although steels have generally not matched the performance of non-ferrous alloys, design strategies are proposed in this review that could lead to improved ferrous shape memory alloys.

Key words: ferrous alloys, martensitic transformation, shape memory, stress-induced martensite, thermo-mechanical training, transformation reversibility, stacking fault energy.

4.1 Introduction

4.1.1 Steels and shape memory

Steels are highly versatile and cost-effective materials. The extensive knowledge and technical know-how that has been accumulated on steels over a long period of time is reflected currently in highly efficient and economical production processes. Therefore, the development of novel steels with the capacity for significant shape memory would certainly provide highly competitive alternatives to expensive commercial alloys based on NiTi and Cu. Although the attractive goal of developing effective shape memory steels has been pursued by many research groups, the outcomes so far have been somewhat below expectations, or the proposed alloys are too expensive to be viable relative to benchmark non-ferrous alloys.

The term ‘shape memory’ describes recovery of the shape that existed before application of a force to produce an apparently permanent strain. Recovery can be obtained by moderate heating (shape memory effect, SME) or by stress removal (pseudo-elasticity, PE).

Applications of shape memory alloys have been comprehensively reported (e.g. Shetky, 1994; Duerig *et al.*, 1999; Van Humbeeck, 1999) and include heat-shrink couplings, actuators, energy conversion devices, deployable antennas and medical and dental prostheses. One of the key drivers of

© Woodhead Publishing Limited, 2012

development of shape memory steels has been applications involving couplings and fasteners to obviate welding of steel tubes and pipes (Otsuka, 1992; Liu *et al.*, 1995).

Shape memory is associated with martensitic transformation – a diffusionless phase change that starts and finishes on cooling at the M_S and M_F temperatures; and reverts to austenite at A_S and A_F on heating.

The types of martensitic transformations that have been identified in steels are described in detail in Chapter 2. The dominant martensitic transformation in ferrous alloys is, in effect, the polymorphic transformation from the high temperature γ face-centred cubic (fcc, F) phase to the α' body-centred cubic (bcc, B) or body-centred tetragonal (bct, B) phase. A close-packed hexagonal (cph, H) martensite also occurs in austenitic iron alloys with a low stacking fault energy (SFE). Despite the wide variety of ferrous martensitic alloys, relatively few show the capacity for significant shape memory.

4.1.2 Defining 'steel'

Although the term 'steel' has been used since metallurgical antiquity to describe iron that has been hardened, or 'steeled', by the addition of carbon, it has been widened in scope in more recent times to include virtually carbon-free alloys of iron, such as maraging steels, stainless steels, and nickel- and/or manganese-bearing cryogenic steels. Similarly, a carbon-free Fe_3Pt alloy is considered to qualify as steel even though it is, in fact, Pt-rich on a weight percentage basis. Its inclusion is justified because the Fe-Pt phase diagram is similar to those of Fe-Ni and Fe-Mn and the familiar transformation of austenite to martensite lies at the core of the reported shape memory effect in this alloy (Wayman, 1971; Foos *et al.*, 1975).

Fe_3Pt is historically important as the first reported shape memory 'steel' (Wayman, 1971). Although Dunne and Wayman (1973) published results of research conducted in 1970 that demonstrated reversible martensitic transformation in Fe_3Pt, this was not the first observation of reversible martensitic transformation in steel. During the 1950s, Bowles (1971) recorded cold stage photomicrographs of Fe-Ni-C alloy that showed shrinking of thin martensite plates with rising temperature.

4.1.3 Defining 'shape memory behaviour'

Shape memory behaviour is exhibited when alloys with martensitic or pre-martensitic microstructures can respond to both force and temperature in such a way as to exhibit one or more of the related phenomena: SME (pseudo-plasticity), PE (pseudo-elasticity) and high vibration damping.

SME can be 'one-way' or 'two-way'. In the first case, the alloy 'remembers' and returns to the initial, pre-stressed shape on heating and, in the other, the

© Woodhead Publishing Limited, 2012

alloy is trained to 'remember' both the pre-stressed and the stressed shapes on thermal cycling, without the re-application of an external force by, for example, a bias spring.

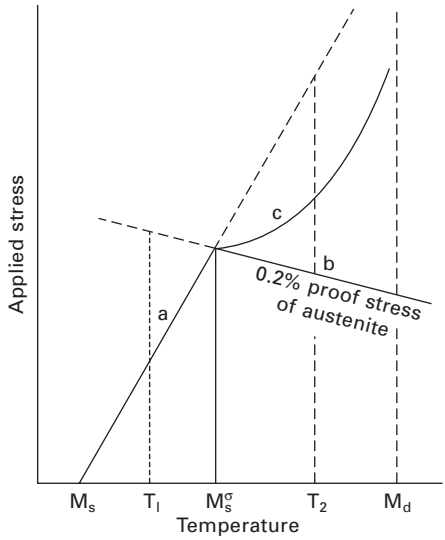
Two general conditions are necessary for an alloy to exhibit SME. Firstly, it must be able to respond to stress by undergoing a structure-based pseudo-strain, instead of irreversible plastic deformation by slip, faulting or twinning. Secondly, the original austenite structure and crystallographic orientation must be recoverable on heating above A_F. The original shape is set in the 'hot' austenitic condition and is substantially retained on cooling to ambient, whether or not the alloy remains austenitic or transforms fully or partially to martensite. The alloy shape is then changed by the application of a stress, which induces structural modifications that are reversible on subsequent heating.

Pseudo-elastic behaviour is manifest in non-linear elasticity that is about an order of magnitude higher than the linear elasticity exhibited by most metals. When this non-linear elasticity occurs in the austenitic condition, it is referred to, by convention, as 'super-elasticity' (Otsuka and Wayman, 1998b). For a completely martensitic alloy, the phenomenon is usually referred to as 'rubber-like behaviour'.

For a shape memory alloy that is austenitic at ambient temperature (T_{RT}), stress can induce the formation of martensite provided that M_D, the maximum temperature at which martensite can be induced by stress, is above T_{RT}. The competition between formation of stress-induced martensite (SIM) and plastic deformation of austenite is illustrated in Fig. 4.1. The stress required to form martensite increases with increasing temperature (curve a) up to the limiting temperature M_D, whereas the stress to produce plastic deformation of austenite (0.2% proof stress, curve b) decreases with increasing temperature. M_S^σ denotes the temperature at which these stresses are equal and deformation at a lower temperature (say T_1) provides a stress 'window' for formation of SIM that correlates with the extent of SME. Lowering the stress required to produce martensite and raising the flow stress of austenite will widen the window, and the latter effect, austenite strengthening, has been a major focus of attempts to improve shape memory (Dunne and Li, 1994; Maki, 1998b). For $M_S^\sigma < T_2 < M_D$, the stress to produce plastic flow in austenite is lower than that required for SIM, but martensite can be *strain-induced* (curve c) because its formation is catalysed by the dislocation structure generated in the austenite. If A_F is below M_S^σ, then super-elasticity can occur in some alloys on deformation at a temperature between A_F and M_S^σ, with combined SME and super-elasticity for temperatures between A_S and A_F (Otsuka and Wayman, 1998b).

At a structural level, shape memory phenomena are associated with *reversible* martensitic phase transformation, with *pseudo-strain* being produced by the motion of austenite/martensite interfaces, or inter-plate and transformation

© Woodhead Publishing Limited, 2012



4.1 Schematic diagram showing the variation with temperature of the stress to induce martensite (curve a); the 0.2% proof stress for austenite (curve b); and the stress required to strain-induce martensite (curve c) (after Tamura and Wayman, 1992).

twin interfaces within an originally martensitic structure. Reverse motion of these interfaces occurs on stress removal or heating to re-establish the *original* austenite grain or crystal in its *original* orientation.

All martensitic transformations are potentially reversible, but it is the type and ease of reversibility that determines whether or not significant shape memory can occur.

4.1.4 Martensitic transformation and shape memory

The mechanism of martensitic transformation involves consecutive rapid displacements of atoms to form a plate or lath-shaped product phase which can be characterised by a homogeneous strain (the shape strain, $\mathbf{P_1}$). This strain is an invariant plane strain (IPS) for which the interface or habit plane is a macroscopically invariant plane and the direction of the shape strain can be resolved into a displacement parallel to the invariant plane (a shear) and normal to it (an extension or contraction, corresponding to the increase or decrease in volume). This distinction is important, at least for polycrystalline alloys, because the shear displacements of thermally produced martensite plates can effectively be cancelled by the formation of groups of self-accommodating plate variants, whereas the volume change can only be accommodated by elastic and/or plastic strain. In the special case of a

© Woodhead Publishing Limited, 2012

monocrystalline alloy undergoing single interface transformation, the shear and volume strains are unconstrained.

In general, the homogeneous lattice strain **S** that defines the structural change is not equivalent to the homogeneous shape strain. The phenomenological theories of Bowles and Mackenzie (1954) and Wechsler *et al.* (1953) reconcile this difference by incorporating a lattice invariant shear (slip, twinning or stacking faults) in the martensite that allows a macroscopically invariant interface plane to be established. The matrix equation relating these strains is $\mathbf{S} = \mathbf{P_1P_2}$, where $\mathbf{P_2}$ is termed the complementary strain and its inverse $\mathbf{P_2^{-1}}$ is the lattice invariant shear. Written in terms of the shape strain, the expression becomes $\mathbf{P_1} = \mathbf{SP_2^{-1}}$.

The crystallography of the martensitic transformation is discussed in Chapter 1, but it is noted here that the crystallographic and physical characteristics of the transformation are critical in determining whether pronounced shape memory is possible.

The structural change on formation of martensite generally ensures that there is a volume change that must be accommodated by elastic and/or plastic strain in the austenite, martensite or in both phases. For shape memory alloys, the volume change, $\Delta V/V$, is typically less than about 0.5% (Shimizu and Otsuka, 1975), but for most ferrous alloys $\Delta V/V$ is significantly higher. Magee and Davies (1972) reported that the volume change at room temperature, $(\Delta V/V)_{RT}$, for Fe-C and low alloy steels lies in the range 3–4%, increasing slightly with C content and being relatively insensitive to substitutional alloying elements. Since the austenite has approximately twice the thermal expansion of ferrite, the effect of the transformation temperature range needs to be taken into account in estimating the volume change. Basinski *et al.* (1955) reported that for temperatures up to 1173 K, $(\Delta V/V)_T = 0.0375 - 3.1 \times 10^{-5}$ (T-273) (K), indicating that the volume change decreases with increasing temperature. Dilatometric results generally confirm this trend. For example, dilatometer curves for a high hardenability 9%Cr, 1%Mo steel* containing 0.1% C indicated that M_S was about 663 K and the volume change calculated from the length change at M_S was 2%, much smaller than the predicted $(\Delta V/V)_{RT}$ value of over 3% (Sulaiman, 2008). Similar low values have been reported for Fe-C alloys, e.g. Moyer and Ansell (1975) measured 2% transformation volume change for Fe-0.2%C.

Volume increases of about 2% recorded by dilatometry for a number of plain C and alloy steels with elevated transformation ranges are sufficiently large to require accommodating plastic strain. However, when the martensite is stress-induced by a tensile stress, a volume increase will provide a structural strain that contributes to accommodation of the external stress (Liu *et al.*, 2000). It should be noted, however, that the shear component

*All alloy compositions are given in wt% unless otherwise indicated.

© Woodhead Publishing Limited, 2012

of the shape strain is typically up to an order of magnitude higher than the normal component and contributes most of the structure-based pseudo-strain. Under a uniaxial stress, a given parent grain will select the martensite plate variant with a shear component of the shape strain which has the maximum Schmidt factor (Otsuka and Wayman, 1998b). In this way, the largest possible transformation strain is generated under the applied stress.

The relatively high volume change associated with the formation of ferrous martensites is relevant to shape memory because of the dislocation structure induced to plastically accommodate the change in specific volume. These dislocations can affect interfacial mobility and restrict reversion on heating.

For transformations that are reversible, there are degrees of transformation reversibility that can be measured by the thermal hysteresis of the forward and reverse transformations. The difference between the temperatures of a structure containing 50% martensite on cooling (M_{50}) and on heating (A_{50}) is one such measure. Highly reversible transformations are characterised by ΔT_{50} values < 50 K, whereas many reversible transformations have ΔT_{50} values > 300 K, implying that the frictional resistance to reverse interface motion requires superheating to provide sufficient chemical driving force to effect reverse transformation (Otsuka and Wayman, 1998a). Moreover, interfacial locking can be so strong that diffusionless transformation to austenite can occur by nucleation and growth of multi-variant austenite plates within the martensite (Kessler and Pitsch, 1967). In this case, an original austenite grain becomes polycrystalline and the transformation is not *crystallographically* reversible. Research on Fe alloys containing 30–35% Ni (Jana and Wayman, 1967), with ΔT_{50} values higher than 400 K, has demonstrated that reversion to austenite can occur by diffusion and by diffusionless transformation to austenite plates within martensite, depending on the heating rate. Alloys of this kind show only a limited or negligible capacity to accommodate stress by structure-based pseudo-strain. The austenite/martensite interface has limited mobility and requires a higher stress to move than defects that generate irreversible plastic strain.

In the case of C-bearing steels, tempering can intervene before reversion of martensite, producing a ferrite-carbide aggregate that can only transform to austenite by diffusional means. Therefore, shape memory is unlikely, except if the heating rate is high enough for reverse transformation to austenite to be induced in advance of significant tempering.

For the low hysteresis end of the spectrum, the term ‘thermoelastic martensitic transformation’ has been adopted, following Kurdjumov and Khandros (1949) who predicted, then proved, that martensite can form ‘elastically’, growing and shrinking freely in a Cu-Ni-Al alloy with small changes in temperature or stress. It is generally accepted that the high degree of interface reversibility associated with thermoelastic behaviour is central

© Woodhead Publishing Limited, 2012

to shape memory behaviour (Christian, 1965; Otsuka and Wayman, 1998b). However, it is important to note that transformation hysteresis is necessary for one- and two-way shape memory, and an alloy considered to be 'non-thermoelastic' because of a relatively large transformation hysteresis can still exhibit shape memory. Moreover, a wide hysteresis is considered to be advantageous for fastener applications (Melton *et al.*, 1986).

Therefore, the capacity for crystallographically reversible martensitic transformation is the essential condition for the shape memory effect, rather than the magnitude of the thermal hysteresis (Otsuka and Wayman, 1998b). Nevertheless, significant shape memory is usually associated with thermoelastic martensite transformation, which is characterised by a highly reversible (glissile) interface. Christian (1965) considered this type of transformation to be favoured by:

- small shear component of the shape strain;
- small volume change;
- low chemical driving force; and
- parent phase with a high elastic limit.

Ling and Owen (1981) proposed a more succinct, and largely equivalent, requirement that the macroscopic strains that accommodate the shape strain are 'essentially elastic'.

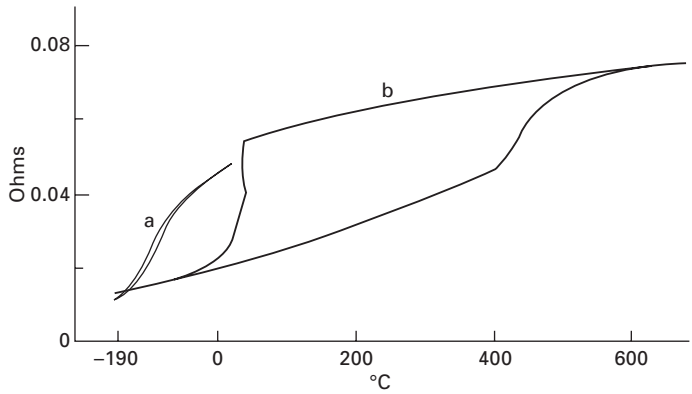
4.2 Fe-Pt alloys

Alloys close to the composition Fe_3Pt undergo martensitic transformation of γ to α' and have the fascinating attribute that they can exhibit a wide range of transformation hystereses, depending on the degree of order of the austenite. At the extremes, thermoelastic and non-thermoelastic martensitic transformation can be exhibited which correspond to significant and negligible shape memory. Figure 4.2 demonstrates the difference in transformation characteristics for two Fe_3Pt samples, one heat treated to produce $L1_2$ order in the austenite (a) and the other treated to obtain essentially disordered austenite (b). In both cases the martensitic transformation is reversible, but the thermal hystereses are starkly different: < 30 K for the ordered alloy and > 400 K for the disordered alloy. The smaller hysteresis indicates that the austenite/martensite interface is characterised by a high degree of atomic matching (coherence) and, consequently, 'glissile' motion can occur in both the forward and reverse directions.

Although a fcc to fct thermoelastic martensitic transformation has been reported in Fe-25 at% Pt and Fe-30 at% Pd (Oshima and Sugiyama, 1982), the dominant transformation in these alloys is fcc (γ) to bcc/bct (α').

The $\gamma \leftrightarrow \alpha'$ (bcc) transformation in disordered Fe_3Pt has similar characteristics to those of Fe~30%Ni alloys. Coarse lenticular plates are

© Woodhead Publishing Limited, 2012



4.2 Electrical resistance curves as a function of cooling and heating thermal cycles to produce the forward and reverse martensitic transformations in Fe_3Pt: (a) ordered sample $s \sim 0.8$; and (b) disordered sample $s \sim 0$ (after Dunne, 1974).

formed on cooling which cannot be easily manipulated by force and require significant heating for re-transformation to austenite. However, ordering of the γ phase brings about a series of remarkable changes in the nature of the martensitic transformation. Dunne and Wayman (1973) observed that the M_S temperature decreases steeply, the burst effect is suppressed, lenticular plates are replaced by thin plates, A_S drops below M_S and reversible transformation occurs with a small thermal hysteresis. The martensite also develops an ordered bct structure, *c*/*a* increases, the transformation twin spacing decreases (Tadaki and Shimizu, 1973; Tadaki *et al.*, 1976; Kajiwara and Owen, 1977); and the transformation volume change becomes negligibly small (Tadaki and Shimizu, 1973). Further, the austenite exhibits the Invar effect, the Curie temperature rises (Mizoguchi *et al.*, 1973; Dunne *et al.*, 1984), the shear modulus decreases (Grujicic *et al.*, 1992); and the strength (hardness) increases due to order (Dunne and Li, 1994) and magnetostrictive hardening (Grujicic *et al.*, 1992). The habit plane normal also shifts away from $\{3\ 10\ 15\}_F$ towards a plane of nearly two-fold symmetry (Dunne, 1998).

The multiplicity of changes has challenged the identification of the critical factors that are necessary for thermoelastic transformation. Umemoto and Wayman (1978) reported the results of a detailed investigation of binary alloys containing 23, 24 and 25 at% Pt. They varied the austenite order by heat treatment and assumed that the degree of order is proportional to *c*/*a*, which they measured, together with M_S, thermal hysteresis and the volume change. For a given hysteresis (say 50 K or 150 K), significantly different *c*/*a* values were obtained for the three alloys and so they concluded that tetragonality (and hence degree of order) does not control thermoelastic transformation. Although they failed to identify a unique factor controlling

© Woodhead Publishing Limited, 2012

thermoelastic behaviour, M_S values lower than 193 K were considered to be necessary for transformation to occur with a small hysteresis (20–30 K). The conclusion that *c/a* is not an essential factor is consistent with observations of $\{3\ 10\ 15\}_F$ martensites in FeNiC, FeAlC and other alloys with high *c/a* values, that do not transform thermoelastically. However, ordering of the austenite must be the global causative agent, and it is the confluence of a series of factors arising from ordering, none of which is sufficient *per se*, that results in thermoelastic transformation with a small hysteresis (Dunne, 1998).

In general, the austenite needs to be conditioned so that (1) the transformation strains are small and (2) the alloy has a high capacity to elastically accommodate these strains. Long range order (LRO) provides a means of achieving this conditioning, and both ausaging and ausforming can also be effective in other steels, as discussed later. In Fe_3Pt, ordering satisfies the first requirement by eliminating the volume change (the shape strain becomes a shear); reducing the magnitude of the shape strain, m_1, from 0.23 in the disordered alloy to 0.16 in austenite with an order parameter, *s*, of 0.8 (Dunne, 1998); and reducing the shear modulus and the chemical free energy change on transformation (Grujicic *et al.*, 1992). The second requirement is satisfied by an increase in the elastic limit associated with order and magnetostrictive strengthening of the austenite, and a reduction in the twinning shear magnitude, *k*. The magnitude *k* is given by $2(2 - x)/(2 + x)$, where $x = (c/a)^2$ (Bowles and Mackenzie, 1954; Dunne, 1977), and is 0.66 for disordered alloy with $c/a = 1$, and 0.49 for ordered alloy ($s = 0.8$) with $c/a = 1.1$. This last factor allows refinement of the transformation twins and more effective elastic accommodation of fine-scale interfacial strains (Kajiwara and Owen, 1974; Dunne, 1978).

Ordering stabilises the austenite structurally and magnetically as the Curie temperature is raised and the austenite becomes ferromagnetic. The martensite inherits atomic ordering from the austenite, resulting in an extended *c* axis because of the higher density of Pt atoms in this direction. The inherited order in the martensite does not correspond to the DO_3 type normally associated with bcc structures (Dunne and Wayman, 1973), an observation consistent with an increase in austenite stability relative to martensite and the marked decrease in M_S.

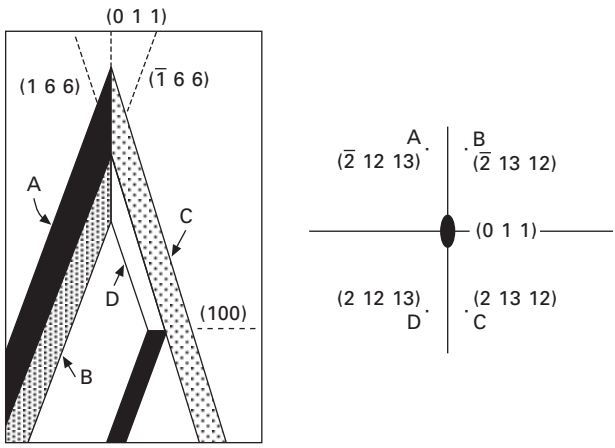
One characteristic of thermoelastic transformation in Fe_3Pt that is not accorded the significance that it deserves is the depression of A_S below M_S during the transformation thermal cycle (Dunne and Wayman, 1973). This effect is associated with 'constrained transformation': the accumulation of elastic energy in the austenite that moderates the growth of martensite plates and provides a back stress that contributes to the 'premature' reversion of martensite to austenite on heating (Kaufman and Cohen, 1958; Dunne and Wayman, 1973). This constrained transformation results in progressive,

© Woodhead Publishing Limited, 2012

moderated growth of plates as the temperature is lowered, in contrast to the burst transformation observed in disordered Fe_3Pt and to a lesser, but still significant extent, in partially ordered samples. The thin-plate morphology is a consequence of this form of transformation.

Another factor that is not widely appreciated is that the change in lattice parameters because of order and the Invar effect shifts the predicted habit plane normal closer to a plane of two-fold symmetry. For $s = 0.8$, the predicted habit plane is approximately $\{2, 12, 13.4\}_F$ or $\{1, 6, 6.7\}_F$ (Dunne, 1998), which is close to measured habit planes reported for β_1' martensite in Cu-based shape memory alloys: $\{2, 11, 12\}_B$ (Takezawa *et al.*, 1976) and $\{1\ 5\ 5\}_B$ (Otsuka *et al.*, 1974). This crystallography results in four habit plane variants distributed symmetrically about a $\{1\ 1\ 0\}_F$ pole, allowing six sets of four-plate groups to form, with each group being self-accommodating, in the sense that the shape strain directions, at least in part, cancel out any long-range shear strain. Figure 4.3 schematically shows the chevron-type morphology of one four-plate cluster in ordered Fe_3Pt, and identifies the junction planes between the plates.

Since the shape strain is a shear, there is no volume change to accommodate and, as the formation of plate groups counteracts much of the shear strain, the austenite can easily accommodate residual elastic shear strains. Furthermore, interfacial misfit strains are reduced by the fine-scale transformation twinning. Consequently, thermal cycling of well-ordered Fe_3Pt results in thermoelastic transformation with virtually no plastic strain. However, for the purposes of



4.3 Schematic diagram showing a four-plate self-accommodating group of martensite plates in Fe_3Pt and the corresponding stereographic projection of the habit plane normals distributed around $(0\ 1\ 1)_F$. The junction planes are $(0\ 1\ 1)_F$, $(1\ 0\ 0)_F$ and approximately $\{1\ 6\ 6\}_F$ and the habit plane normal is approximately $\{2\ 12\ 13\}_F$ (after Dunne, 1998).

© Woodhead Publishing Limited, 2012

shape memory, the application of a force pre-disposes the nucleation and/or the growth of the martensite variants that are best oriented to accommodate the applied stress. Permanent plastic strain then becomes possible, if the stress level is high enough or many stress cycles are applied.

4.3 Fe-Ni and Fe-Ni-C alloys

The fcc to bcc martensite transformation in Fe-~30Ni alloys has been extensively studied (Breedis and Wayman, 1962; Kessler and Pitsch, 1967; Jana and Wayman, 1967). The transformation is non-thermoelastic and characterised on cooling by burst formation of coarse lenticular plates, involving a sudden onset and the generation of a large volume fraction of martensite over a narrow temperature range. It is inferred that there is a nucleation problem that requires significant undercooling below the equilibrium temperature, T_0, to provide the chemical driving force necessary to overcome the opposing surface and strain energies. Once the initial plates form, nucleation of other plates, usually in a zig-zag pattern, can be induced in the strain fields and dislocation nucleating sites generated in the surrounding austenite (auto-catalysis). The coarse lenticular plates are resistant to reverse interface motion on heating. Transformation hysteresis is typically large and reversion occurs by nucleation of small austenite plates within the martensite (Kessler and Pitsch, 1967). Deformation of the martensitic structure is largely unrecoverable, because plastic strain dominates rather than structure-based pseudo-strain. Further, the original austenite orientation is not recovered on heating. However, Maki and Tamura (1986) reported partial shape memory for martensite that was stress-induced in austenite in Fe-32.7%Ni alloy at, or just above, M_S (168 K). They recorded 25% and 50% recovery of 2.5% bending strain for sheet specimens respectively subjected to solution treatment and ausforming by 40% rolling reduction at 373 K. The hardness of the austenite was 118 HV after solution treatment and 197 HV after ausforming. Therefore, work-hardening of the austenite effectively doubled the recoverable strain by promoting the formation of SIM and suppressing slip deformation during bending. In contrast, the interfacial mobility of thermal martensite is impaired by slip-induced dislocation barriers. Studies of martensitic surface relief in FeNi, FeNiC and other alloys by atomic force microscopy (Liu *et al.*, 2000) established that localized plastic accommodation occurs around thermal martensite plates, but is absent for SIM, because the transformation strain provides accommodation of the applied stress. Under tensile stress, the volume increase and the shear component of the shape strain contribute to 'plastic' extension of the test-piece, at least to a limited extent, without plastic deformation by slip. This type of behaviour is also referred to as transformation induced plasticity (TRIP).

Setsuo Kajiwara pursued the goal of developing shape memory steels

© Woodhead Publishing Limited, 2012

over several decades. He and his co-workers undertook an extensive research programme in the 1980s to develop carbon-bearing Fe-Ni alloys with shape memory capability (Kajiwara, 1985; Kajiwara and Kikuchi, 1983; Kajiwara *et al.*, 1986). The perceived advantages of C stem from its capacity to increase both the strength of the austenite and the martensite *c*/*a* ratio, as well as promoting the formation of non-burst, 'plate-type' martensite, which is equivalent to the 'thin-plate' martensite described previously.

High tetragonality results in refinement of the transformation twins and enhanced interfacial coherency – a necessary condition for reversible interface motion. Kikuchi and Kajiwara (1989) studied martensite tetragonality in Fe-Ni-C, Fe-Ni-Al-C and Fe-Ni-Al-Co-C alloys with 0.2–0.8 wt% C, aiming to elucidate the effect of *c*/*a* on the morphological and shape memory characteristics of these alloys. Lenticular martensites were generally associated with $c/a < 1.05$ and M_S temperatures higher than about 170 K. The addition of 6% Al to an alloy with 20% Ni and 0.8% C profoundly increased *c*/*a* from 1.045 to 1.086 at 100 K. Increasing Ni from 20 to 26% in 0.8% C alloys had a similar strong effect, increasing *c*/*a* from 1.043 to 1.088 at 100 K.

There was a significant drop in *c*/*a* by about 0.01 on heating from 100 K to ambient, but the presence of Al and Co tended to reduce the magnitude of the decrease. Previous work by Kajiwara and Kikuchi (1983) attributed the decrease in *c*/*a* of 'fresh' martensite in Fe-Ni-C on heating to a redistribution of C atoms from octahedral sites along the *c* axis to tetrahedral sites or octahedral sites along the *a* axis. Ullakko and Gavriljuk (1992) proposed a different explanation for the high tetragonality and its decrease on heating. Following work by Koval and Kokorin (1975), in which tetragonality in C-free, high Ni steels was attributed to coherency between the martensite and tetragonal clusters in the austenite, Ullakko and Gavriljuk (1992) proposed that short range ordering (SRO) of Ni atoms increases *c*/*a* of thin-plate martensite in FeNiC alloys. The highly coherent state allows interface mobility until the coherency breaks down, in company with a sharp drop in *c*/*a*. For example, a decrease in *c*/*a* from about 1.08 to 1.07 occurred in Fe-25Ni-0.7C alloy (M_S = 140 K) on heating above 170 K. Data for a carbon-free 33.5% Ni alloy showed a similar decrease in tetragonality on heating from 100 to 200 K, but the maximum *c*/*a* was only 1.018, falling to 1.004 above 160 K. Therefore, although most of the tetragonality in the FeNiC alloys is due to C, Ullakko and Gavriljuk (1992) considered the temperatures to be too low to account for the drop in tetragonality by C redistribution. Further, companion studies of a FeMnC alloy with low M_S, high *c*/*a* and fully twinned plates revealed no significant drop in *c*/*a* on heating and no coherency effects. This observation lends credence to the hypothesis of a breakdown in coherence due to loss of SRO in the austenite, but the reason for this change remains unclear. Of relevance to development of alloys capable of reversible transformation and shape memory, Ullakko and Gavriljuk (1992) concluded that a low M_S

© Woodhead Publishing Limited, 2012

temperature and fully twinned martensite are not sufficient to establish a coherent and mobile γ/α' interface.

A contribution by SRO of Ni atoms in FeNi alloys to tetragonality and interfacial coherence is consistent with the more profound effect of order in the related FePt system. Although the similarity of the atomic scattering factors for Fe and Ni militates against detection of order by X-ray diffraction, evidence of ordering in thin foils has been reported by Hausch and Warlimont (1971). Further, Hsu and Yan (1984) have inferred that ordering occurs in bulk alloys near the composition Fe_3Ni, on the basis of the presence of an 'M_S valley' at about 1073 K, when M_S is plotted against quenching temperature. This discontinuity was identified as the order-disorder temperature (Hsu and Yan, 1984). Increases in hardness and yield stress, considered to be due to ordering, were about 20 HV points and 20 MPa. Even if ordering does occur, these increases are relatively minor, as expected by the similarity of the atomic radii of Fe and Ni. A ramification is that significant tetragonal distortion of the martensitic crystal structure is unlikely. Nevertheless, SRO in austenite could play a part in the observed morphological transitions in FeNiC alloys (see Chapter 2).

Apart from LRO and SRO, pre-precipitate clusters or ordered precipitates in austenite (e.g. Ni_3Ti and Fe_3AlC in FeNiTi, FeNiTiC and FeAlC alloys) can be inherited by martensite, remain untransformed, bond coherently with the martensite structure and contribute a tetragonal distortion to it (Maki and Wayman, 1977).

A problem with C-bearing FeNi and FeNiX alloys is that the M_S temperature is usually well below 273 K, whereas it is of practical importance for M_S to be close to ambient so that pseudo-plastic strain at ambient can be recovered by moderate heating. Following this principle, Kikuchi and Kajiwara (1989) succeeded in producing thin-plate martensite in Fe-Ni-Al-Co-C alloys with M_S more closely approaching room temperature. For example, an alloy of Fe-22Ni-6Al-4Co-0.6C had an M_S of 226 K, and a *c/a* ratio of 1.07 that changed little on heating to 300 K. However, after bending at room temperature, samples were not fully reverse transformed after rapid heating to 1270 K; and reversion, by formation of thin austenite plates parallel to the habit plane, resulted in only about 35% shape recovery. The researchers attributed the large transformation hysteresis, not to C, but to stabilisation of the martensite by Perovskite-type precipitates of Ni_3AlC. However, it appears likely that precipitation of Fe-rich carbides (tempering) would occur rapidly at the high temperatures involved, exacerbating any initial stabilisation by Ni_3AlC. There are obvious practical difficulties with alloys of this kind for shape memory applications.

This extensive work has highlighted the limitations of FeNi alloys and C-bearing high Ni steels, with and without Al and/or Co, for shape memory applications. However, it serves to demonstrate, as concluded by Ullakko

© Woodhead Publishing Limited, 2012

and Gavriljuk (1992), that formation of fully twinned thin-plate martensite with high tetragonality, either at low or higher temperatures, is not sufficient to ensure thermoelastic transformation, or reversible transformation with a relatively small hysteresis – the general condition considered to be necessary for significant shape memory.

So, what factors preclude thermoelastic transformation in FeNiC alloys and those containing Al and/or Co? Although carbon increases austenite strength, lowers M_S, raises *c*/*a* and promotes formation of twinned thin-plate martensite, it may be detrimental in terms of interfacial mobility. Despite the conclusion of Ullakko and Gavriljuk (1992) that there is no uniform redistribution of carbon at low temperatures that causes the sharp drop in *c*/*a* on heating to ambient, it remains possible that C atoms can relax into interfacial interstices at low temperatures, thereby stabilising the interface (Dunne, 1978). The shrinkage of thin-plate martensite in FeNiC observed by Bowles (1971) on heating from a low temperature could have occurred prior to interface stabilisation.

4.4 Fe-Ni-Co-based alloys

Magee and Davies (1972) studied FeNi alloys with Co added to induce the Invar effect in the austenite, and to reduce the transformation volume change. This work and subsequent studies (Shibata *et al.*, 2006) confirmed that the combinations of about 20%Co/28%Ni and 24%Co/30%Ni produce partially twinned, lenticular $\{259\}_F$ martensite plates, with small $\Delta V/V$ and low M_S (80–180 K). Since thin-plate martensite and thermoelastic transformation were not obtained, it was concluded that a low volume change and a low transformation temperature are not sufficient to produce thermoelastic transformation.

In analysing the necessary conditions for thermoelastic transformation, Shimizu and Otsuka (1975) suggested that an ordered parent phase is required, as well as a small driving force and a low volume change. In relation to austenite order, studies by Koval *et al.* (1981) have established that thermoelastic transformation can occur in disordered FeNiCoTi alloys after conditioning the austenite with coherent precipitate particles of the ordered γ' $L1_2$ (Ni_3Ti) phase.

Koval *et al.* (1981) reported the formation of thermoelastic thin-plate martensite in FeNiCoTi alloy that had been appropriately aged before subzero cooling. Further detailed work on this alloy system has been conducted by Maki *et al.* (1989) to assess its capacity for shape memory. They reported that, although the hysteresis can be much higher than that considered typical of thermoelastic transformation, perfect shape memory can be exhibited. For example, an alloy of Fe-31Ni-10Co-3Ti was ausaged at 873 K for 3.6 ks, subjected to 2.5% bending strain between 77 K and 293 K, and reverse

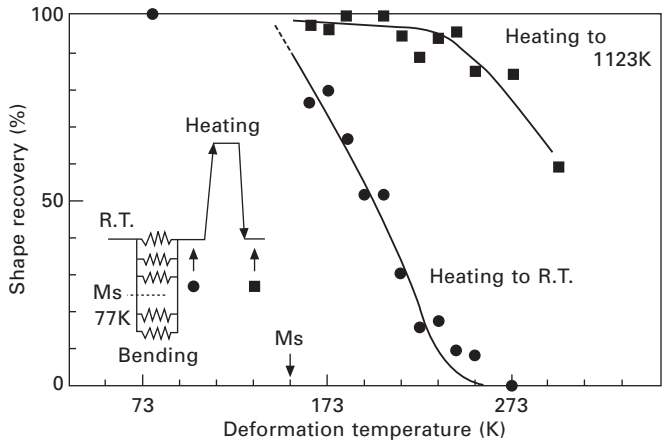
© Woodhead Publishing Limited, 2012

transformed by heating above A_F (508 K). Complete strain recovery was obtained for samples deformed at temperatures within ±10 K of M_S (193 K), but it decreased to 83% recovery for 77 K and fell steeply to about 20% for deformation at ambient (293 K). Full shape memory was obtained despite a hysteresis of about 200 K (Maki *et al.*, 1989). In addition, when the same alloy was pre-cooled to 77 K to produce about 70% of thermal, thin-plate martensite before bend testing, about 85% recovery was obtained over a wide temperature range of 77–293 K. It is inferred that, as well as pseudo-strain due to formation of SIM, existing martensite plates can also contribute pseudo-strain by variant coalescence and/or martensite twin boundary motion. The martensite *c*/*a* value for this alloy after ausaging was 1.08 (Maki, 1989), similar to values reported for ordered Fe_3Pt (Tadaki and Shimizu, 1973), which are associated with full transformation twinning and reduced twin spacing. However, the corresponding volume change $\Delta V/V$ was 1.7%, much higher than that typical of thermoelastic transformation. Therefore, the large hysteresis probably relates to reduced interfacial mobility due to dislocations generated in accommodating this volume change.

However, careful selection of alloy composition and ageing treatment resulted in thin-plate martensite that reverted to austenite on heating with a hysteresis < 30 K (Maki, 1989). After ausaging at 973 K for 3.6 ks, samples of the alloy Fe-33Ni-10Co-3.5Ti-1.5Al showed low hysteresis martensitic transformation (M_S = 155 K, A_S = 126 K, A_F = 204 K). When deformed by bending at 77 K, perfect shape memory occurred on heating to room temperature (see Fig. 4.4). However, for deformation between M_S (155 K) and 273 K, two types of thin-plate martensite were formed that were distinguished by small and large transformation hystereses (thermoelastic and non-thermoelastic transformations). Shape recovery, due to reversion of the thermoelastic martensite decreased to zero at 273 K, but close to complete recovery was achieved for deformation at temperatures between 155 K and 273 K, then heating to 1123 K. Maki (1989) pointed out that the ausaged alloy exhibits shape memory at both low and high temperatures. The sensitivity of transformation hysteresis to deformation temperature is intriguing and reflects variation in the interfacial coherence of thin-plate martensite induced at different temperatures. The lattice parameters of the austenite and martensite will change as a function of temperature and the capacity of the austenite to elastically accommodate the martensite shape strain could decrease with rising temperature, introducing slip dislocations that compromise reversibility of the γ/α' interface. Martensite plate thickness could also affect reversibility of martensite formed on isothermal bending between 155 and 273 K, with thinner plates remaining in thermoelastic equilibrium and thicker plates resulting in plastic accommodation strains.

These studies of Fe-Ni-Co-Ti alloys have demonstrated that the austenite does not have to be ordered for reversible transformation to occur. The

© Woodhead Publishing Limited, 2012



4.4 Effect of deformation (bending) temperature on percentage shape recovery in ausaged Fe-33Ni-10Co-3.5Ti-1.5Al alloy on heating to room temperature or to 1123 K (after Maki, 1990).

dispersion of fine coherent precipitates produces a tetragonal distortion of the martensite structure and promotes shape memory (Maki, 1998a).

Co-free ternary alloys capable of precipitating ordered γ' $L1_2$ particles typically transform to lenticular martensites and show only limited shape recovery. For example, ausaging of FeNiSi alloys (Himuro *et al.*, 2002) can produce ordered γ' $L1_2$ particles of Ni_3Si without significant enhancement of shape recovery. However, the addition of about 10% Co to this alloy resulted in a marked improvement in shape memory. In the case of aged Fe-28%Ni-10%Co-6%Si alloy, increased shape memory is associated with a rise in the Curie temperature, a decrease in the transformation temperature, the formation of thin-plate martensite, a decrease in the volume change, intensification of γ' precipitation and an increase in the hardness of the austenite (Tanaka *et al.*, 2006). Nevertheless, the transformation hysteresis remains high, the martensite tetragonality increases only marginally (from 1.00 to 1.01) and the strain recovery is only about 50% of 2% bending strain. On these measures, this alloy system is clearly inferior to FeNiCoTi.

Although Co appears to be an important element for improving shape memory, a Co-free alloy, Fe-31%Ni-7%Nb, has been reported by Koval and Monastyrsky (1993) to exhibit nearly perfect shape memory after ausaging to produce fine plates of coherent γ'' Ni_3Nb particles with DO_{22} type order. Shape memory was obtained even though the martensite tetragonality was moderate (1.048) and the hysteresis was relatively high (250 K). Tetragonality in Fe-Ni-Ti and Fe-Ni-Nb martensites was initially reported by Honorat *et al.* (1965). Winchell and Speich (1970) subsequently proposed that 'point defects' consisting of Ni_3Ti and Ni_3Nb atom clusters in austenite are responsible for the observed martensite tetragonality. However, for ausaged alloys,

© Woodhead Publishing Limited, 2012

small coherent *precipitates* are produced in austenite, and it is clear that for fine particles with specific crystallographic orientations, the homogeneous lattice strain can result in a tetragonal martensite, just as C and N atoms in octahedral interstices in austenite produce tetragonal martensite. Koval and Monastyrsky (1993) similarly concluded that the particles promote tetragonality and function as 'memory elements' that induce shape memory by providing uniformly distributed 'counteractive' forces due to aligned dislocation loops and/or stored elastic energy.

An Fe-Ni-Co alloy containing Al and B, with a strong $\{035\}<100>_F$ texture, has been reported recently by Tanaka *et al.* (2010) to show exceptional superelasticity (13.5%) at ambient temperature, albeit with 4% irreversible plastic strain. The alloy (Fe-28Ni-17Co-11.5Al-2.5Ta-0.05B, in at%) has a high tensile strength of about 1200 MPa after ageing to produce intense γ'-$(Ni,Fe,Co)_3(Al,Ti)$ precipitation. After ageing, the alloy exhibits a low transformation hysteresis (24 K), low M_S (187 K) and high c/a (1.11) – values very similar to those measured for ordered Fe_3Pt. Also like Fe_3Pt, the wt% of alloying elements exceeds that of Fe. However, the reported volume change of +0.68% is surprisingly large (0% for ordered Fe_3Pt), possibly reflecting a high elastic limit and an enhanced capacity of the alloy to elastically accommodate the transformation strains.

4.5 Austenitic stainless steels with low stacking fault energy (SFE)

Thus far, alloys considered have medium to high SFEs and the formation of α' martensite is favoured over ε-martensite which has a cph structure. However, lowering SFE below a threshold level results in preferential formation of ε.

Estimating SFE remains problematic as the fundamental equations proposed by Noskova and Pavlov (1962) and Reed and Schramm (1974) are subject to large errors (Jiang *et al.*, 1998). The equations are similar and specify an inverse relationship between SFE and the stacking fault probability, P_{SF}. The Noskova–Pavlov equation is:

$$\text{SFE} = (G \cdot a_o^2 \cdot d \cdot \rho)/(24\pi \cdot P_{SF})$$

where G is the shear modulus, a_o is the austenite lattice parameter, d is the spacing of the fault plane, ρ is dislocation density and P_{SF} is the stacking fault probability. Therefore, SFE is directly proportional to dislocation density and varies with composition through its effect on the lattice parameters and elastic constants. Because of the low SFE of austenitic steels, the determination of SFE by dislocation node radii measurements by TEM is difficult, and X-ray line broadening techniques have been developed to measure P_{SF} (Jiang *et al.*, 1998). However, estimates of P_{SF} are about 10 times lower than those

© Woodhead Publishing Limited, 2012

subsequently determined using an X-ray peak shift method (Rong *et al*., 2002; Stanford *et al*., 2007). Therefore, P_{SF} appears to provide a useful ranking parameter rather than a rigorous measure of probability. Moreover, from a mechanistic view of the transformation and its shape memory performance, the orientation and density of stacking fault (SF) nuclei generated by thermo-mechanical conditioning of the austenite would seem to be more relevant factors than P_{SF}.

Gallagher (1970) studied the transformation of austenite in stainless steel to ε and α′ martensites and observed limited shape memory. Enami *et al*. (1971) confirmed this result for 304 stainless steel and attributed the modest shape memory capacity to reverse transformation of stress-induced ε martensite. Brook *et al*. (1975) concluded that shape memory is promoted by increasing the concentrations of elements that decrease SFE: Cr, Co, Mn and Si, and that the degree of strain recovery varies inversely with the amount of ferromagnetic (α′) martensite. Further, they observed that the highest shape recovery was obtained for deformation above M_S, but at as low a temperature as possible.

4.6 Fe-Mn-based alloys

4.6.1 Alloy development

Research on FeMn, FeMnSi and FeMnSi-based alloys has been copious, reflecting a widespread conviction that this system has the potential for significant commercial applications. Research output has been largely directed towards improved understanding of the fundamental aspects of shape memory, and also vibration damping, as well as fine tuning of alloy design and processing methods to enhance performance.

Enami *et al*. (1975) discovered a weak shape memory effect in Fe-Mn alloys that peaked at about 20% Mn. This maximum has been attributed to a rise in the Néel temperature (T_N) above M_S for >20% Mn, thus producing anti-ferromagnetic austenite that is stabilised against martensitic transformation (Sato *et al*., 1982). More than about 20% Mn also causes SFE to rise steeply, as opposed to a marked decrease with increasing Mn from 0 to 20% (Volosevich *et al*., 1976). Lee and Choi (2000) developed a thermodynamic model which gave a lower prediction of the Mn content associated with minimum SFE (about 13%) which is closer to the 15% Mn reported by Schumann (1967). Regardless of the exact trend of SFE with Mn content, its adverse effect on both T_N and SFE can be countered by the addition of Si, which strongly lowers T_N and SFE, resulting in improved shape memory (Sato *et al*., 1982; Murakami *et al*., 1987).

Sato *et al*. (1984) were the first to demonstrate nearly complete shape memory in FeMnSi. They applied a tensile stress to a single crystal of Fe-

© Woodhead Publishing Limited, 2012

30Mn-1Si alloy, oriented to induce transformation to a specific martensite plate variant. Murakami *et al*. (1987), conducted detailed investigations of the effect of composition on shape memory in polycrystalline FeMnSi alloys and identified the composition ranges that lead to almost complete shape recovery (30–32% Mn, 5.5–6.5% Si). Consequently, an alloy with a composition close to Fe-30%Mn-6%Si provides an excellent benchmark for exploring the effects of other alloying additions. Modified compositions include a 'stainless' shape memory alloy based on substitution of Cr and Ni for Mn (Otsuka *et al*., 1990), FeMnSi alloys containing 0.024% rare earth elements (Zhou *et al*., 1998) and Co-bearing alloys (Hamers and Wayman, 1991).

Complete strain recovery in polycrystalline FeMnSi-based alloys is typically limited to about 2.5% strain, but much higher strain recoveries are possible in association with permanent plastic strain. Therefore, the percentage of the applied strain that is recovered should be quoted as well as the absolute strain, to reflect the shape memory capacity of the alloy.

The shape memory properties of Fe-Mn, Fe-Mn-Si and alloy variants are due to the forward and reverse martensitic transformations between the fcc austenite phase (γ) and cph martensite (ε). The habit plane, $\{111\}_F$ or $(0001)_H$, and the orientation relationship are both rational and the transformation is often considered to be 'degenerate' in terms of the phenomenological theory, because the lattice strain **S** is equivalent to the shape strain $\mathbf{P_1}$ (McDougall and Wayman, 1992). The forward transformation occurs by the overlap of SFs formed by motion of $a/6\langle 112\rangle_F$ Shockley partial dislocations on alternate close-packed planes. Reverse transformation involves backward motion of the partials and/or growth of γ stacking faults within the martensite (Ogawa and Kajiwara, 1993), as the SFE rises with increasing temperature and the free energy balance favours re-formation of austenite (Hsu, 2000). Each $\{111\}_F$ habit plane can be associated with Shockley partial dislocations that produce a transformation shear in one of three $\langle 112\rangle_F$ directions, allowing self-accommodation in thermally-induced ε martensite by formation of the three variants within the one parallel band of plates (Gaunt and Christian, 1959). When the martensite is stress-induced, a specific variant is selected that is favoured by the applied stress (Sato *et al*., 1984). These characteristics are therefore common with those of the α' shape memory martensites and, indeed, shape memory alloys in general, as pointed out by Yang and Wayman (1992).

Although α' martensite does not form directly from austenite under stress in Fe-Mn-Si alloys, it can form within ε-martensite, particularly at plate intersections (Jang *et al*., 1991). The formation of α' increases with increasing strain and, since α' reverts to γ directly at high temperatures (>773 K), its presence is considered to impede reverse transformation of ε (Gu, 1994; Jang *et al*., 1995), with more than 5% pre-strain limiting shape memory.

© Woodhead Publishing Limited, 2012

From a practical viewpoint, it is advantageous to control the alloy composition and processing conditions so that M_S is close to room temperature and SIM can be produced by deformation at ambient. There is evidence that shape memory is optimized for deformation at about 10–30 K below M_S when some thermal martensite is present (Ghosh *et al.*, 1989; Gu, 1994; Stanford and Dunne, 2006a). In addition to the formation of SIM oriented to maximise strain in the stress direction, it is likely that the pre-existing thermal martensite undergoes variant coalescence to contribute to the pseudo-strain (Yang and Wayman, 1992). It is also possible that the small volume fraction of thermal martensite partitions the austenite grains and effectively decreases the austenite 'grain size' and the diameters of the plates of SIM. Gu (1994) observed that 13–26% thermal martensite had negligible effect on the amount of SIM and maximised the recovery strain for a series of FeMnSiCr and FeMnSiCrNi alloys subjected to 5.5% compressive strain. This effect was considered to be due to transformation hardening of the austenite and creation of nucleating sites for SIM.

Normally, only moderate heating is required to produce shape recovery, as the hysteresis is typically in the range 100–200 K. Nevertheless, the transformation is usually considered to be non-thermoelastic and only suitable for 'one-way' shape memory applications, such as couplings. However, there is evidence that both super-elasticity and two-way memory effects are possible (Yang *et al.*, 1992).

As well as composition control, Fe-Mn-Si-based alloys can be thermo-mechanically treated to optimise performance. Otsuka *et al.* (1989) were the first to report that a 'training' schedule consisting of a series of deformation and annealing cycles substantially increased the magnitude of strain recovery. Since this procedure is practically complex and costly, much research effort has since been directed towards simpler and cheaper treatments, as well as more unusual processing methods that could generate a large improvement in shape memory capacity. Various alloying strategies have also been pursued with the aim of eliminating training by strengthening the austenite, reducing SFE and lowering the Néel temperature. Proposed methods for austenite strengthening include grain refinement (Tan *et al.*, 1991), the use of dispersed NbC and other coherent precipitates to increase the recovery stress and strain (Kajiwara *et al.*, 2001); the addition of rare earth elements (Zhou *et al.*, 1998); and alloying with carbon (Tsuzaki *et al.*, 1992) and nitrogen (Ullakko *et al.*, 1996; Jiang *et al.*, 1996).

Tsuzaki *et al.* (1992) demonstrated a positive effect of C on shape memory in Fe-16.9Mn-6.03Si-0.3C, in comparison with a carbon-free reference alloy: Fe-33Mn-6Si. The M_S temperatures were similar and just below room temperature, so that pre-straining for shape memory testing was conducted for an initial austenitic condition. The beneficial effect of C was amplified by training, producing 100% recovery of 2.5% tensile strain for between two

© Woodhead Publishing Limited, 2012

and five cycles of 2.5% strain and recovery annealing at 873 K for 600 s. In comparison, the reference alloy showed 90% recovery after five training cycles. Dunne and Liu (1999) confirmed these results for Fe-19Mn-6Si-0.3C alloy and Jiang *et al*. (1996) reported a similar favourable effect. However, these findings are contrary to other work that indicates C and/or N are detrimental when present as interstitial solutes (Ariapour *et al*., 2001; Wen *et al*., 2004; Stanford *et al*., 2007). Since C exerts an adverse effect on the reversibility of α′ martensites (Section 4.3), it is plausible that growth and shrinkage of ε martensite can be restricted by interstitial atom segregation to, and locking of, SFs and/or by repulsive strain field interactions between interstitial atom clusters and transformation partial dislocations.

These apparently conflicting data highlight the importance of the precise thermal-mechanical history of a given alloy and its M_S relative to the deformation temperature for shape memory testing. If, for example, carbon and/or nitrogen have been largely removed from solution by pre-precipitation in austenite, then shape memory may be enhanced both by the reduced solute content and particle-stimulated nucleation. Improvement or otherwise in shape memory should also be measured in relation to a reference alloy that is devoid of the variable of interest (a particular alloying element or precipitate species), has similar transformation temperatures to the test alloy and has been identically treated (Stanford *et al*., 2008).

The effect of grain refinement of austenite is uncertain, with claims of both negligible and significant improvement in shape memory. Matsuya *et al*. (2000) reported that reduction in the recrystallised austenite grain size from 100 to 5 μm resulted in austenite strengthening in accordance with the Hall–Petch relationship, but did not strongly affect shape memory. In contrast, Tan *et al*. (1991) found that with increasing holding time at 1375 K, shape recovery decreased as grain size increased from 10 to 60 μm. It is not clear, however, if the trend was due to grain size or to progressive restoration of the hot-rolled starting structure. Grain size reduction strengthens the austenite and should therefore have a favourable effect on shape recovery. However, each grain in a polycrystalline aggregate will respond to a uniaxial stress by a pseudo-strain of magnitude that depends on its crystallographic orientation. Differential strain between grains could therefore lead to localised tri-axial stresses that result in permanent strain, compromising reverse transformation. This effect would be expected to become more pronounced with decreasing grain size and counteract the positive effect of austenite strengthening.

Recent work has been concentrated on effective refinement by precipitate networks, which result in martensite formation in a ‘domain-specific manner’ (DSM) (Wen *et al*., 2007). These researchers subjected deformed austenite to aging to form domains of approximate ‘diameter’ of 1–2 microns, based on an aligned $Cr_{23}C_6$ precipitate network. It was claimed that these small domains resulted in formation of non-intersecting plates of a single variant

© Woodhead Publishing Limited, 2012

under stress and were responsible for improved shape recovery. However, the authors did not adequately assess the effect of thermo-mechanical processing, the contribution of precipitation to austenite strengthening and martensite nucleation, and M_S relative to the temperature of bending deformation.

4.6.2 Effect of silicon

Silicon is established as an essential ingredient for good shape memory in FeMnSi-based alloys, and the presence of 5–6% Si has become *de rigueur* in alloy design. In a more modest way, Si performs an enabling role like that of LRO in Fe_3Pt alloys, but detailed explanations are lacking for the mechanisms by which it enhances shape memory. Reasons proposed for its beneficial effect include:

1. lowering T_N (Sato *et al.*, 1982);
2. reducing SFE (Gallagher, 1970; Sato *et al.*, 1982);
3. solid solution strengthening of austenite (Murakami *et al.*, 1987; Ghosh *et al.*, 1989);
4. reducing plate thickness (facilitating reversibility) (Maki and Tsuzaki, 1992; Kajiwara *et al.*, 2001);
5. promoting SRO in austenite (Sade *et al.*, 1988; Bliznuk *et al.*, 2004);
6. increasing *c/a* in the cph structure (Sato *et al.*, 1986); and
7. improving interfacial matching and reducing the volume change (Stanford and Dunne, 2010).

The austenite strengthening factor (3) is undisputed and fits the formulaic aim of increasing the flow resistance of austenite to increase the gap between the stress to induce martensite and that required for austenite slip (Fig. 4.1). Si is considered to increase the resistance of austenite to irreversible plastic strain during straining to produce martensite (Maki and Tsuzaki, 1992); and increases the amount of reversible pseudo-plastic strain by generation of an increased volume fraction of reversible martensite (Chung *et al.*, 1996). However, there are more potent austenite strengtheners than Si. Prominent examples are precipitate particles (carbides, nitrides and intermetallics) and solute C and N. Ullakko *et al.* (1996) reported major strengthening by alloying FeMnSi with N, but this did not translate into a commensurate improvement in shape memory. Moreover, a training routine was applied to enhance shape memory.

Maki and Tsuzaki (1992) studied the role of Si in FeMnSi alloys and concluded that it enhances the reversibility of both thermally- and stress-induced ε martensite. They proposed that this effect originates from factors (1), (2) and (3). Reduction in SFE (2) decreases the thermodynamic driving force for $\gamma \rightarrow \varepsilon$ transformation, as well as promoting martensite nucleation through an increase in stacking fault density. However, this is not a unique

© Woodhead Publishing Limited, 2012

feature of Si and other elements can also lower the SFE: e.g. Cr and small concentrations of rare earth elements (Zhou *et al*., 1998); and even N and C, which raise SFE, can produce a net reduction when they replace a significant concentration of Mn (Dunne and Liu, 1999; Hsu, 2000). Despite such trends, recent experiments by Stanford *et al*. (2007) showed no clear correlation between SFE and SME in alloys for which SFE was modified by alloying with Cr and Ni. It was concluded that if the SFE is low enough to promote ε and inhibit α′, further decreases in SFE by alloying have only a marginal effect on SME. A contrary view was expressed by Li *et al*. (2000) who measured SFE by dislocation node analysis for a series of FeMnSi(Cr)(Ni) alloys and associated the best shape memory with the alloy of lowest SFE. However, the Cr-Ni stainless alloys showed significantly better SME than the FeMnSi alloys, despite similar SFEs. Furthermore, no M_S measurements were reported to indicate differences from the ambient bend testing temperature. Therefore, the correlation should be treated with circumspection. From their dislocation mode measurements, Li *et al*. (2000) derived the regression equation: SFE = 28.87 + 1.64Ni – 1.1Cr + 0.21Mn – 4.45Si, which indicates that Si and Cr decrease SFE, and Ni and Mn raise it. Therefore, the presence of about 6% Si produces a low SFE baseline, calculated by this equation to be 8.5 mJ/m^2 for Fe-30Mn-6Si alloy, whereas Guo *et al*. (1999) estimated about 3 mJ/m^2.

Depressing T_N below M_S factor (1) is believed to ensure that SIM forms from paramagnetic austenite, rather than with a higher thermodynamic driving force from the more stable anti-ferromagnetic state. However, Stanford *et al*. (2007) claimed that there was no significant decrease in SME for alloys with both M_S and the selected deformation temperature below T_N. It was concluded that T_N had little effect on shape recovery, consistent with earlier work by Yang *et al*. (1992), which showed that anti-ferromagnetic austenite does not inhibit formation of SIM. Wu and Hsu (1999) provided qualified support through their report that $\gamma \rightarrow \varepsilon$ transformation is only partly suppressed in anti-ferromagnetic austenite. Although the formation of thermal martensite may be inhibited when the austenite is anti-ferromagnetic, this restriction may not apply to SIM. Moreover, the higher stability of the austenite could facilitate reverse transformation of SIM on heating up to T_N. Therefore, factor (1) does not appear to be as important as originally thought.

There is strong experimental evidence that Si decreases the width of martensite plates (factor (4)) (Maki and Tsuzaki, 1992). Thinner SIM plates have been associated with improved reversibility and shape memory (Dunne and Li, 1995; Kajiwara and Ogawa, 2000). It is likely that the high P_{SF} for Si-bearing alloys provides a high density of stacking fault nuclei and limited growth of large numbers of martensite plates.

Bliznuk *et al*. (2004) reported that small angle scattering and polarised neutron diffraction data indicate that Si significantly improves the chemical

© Woodhead Publishing Limited, 2012

homogeneity of FeMnSi alloys, providing support for the proposal by Sade *et al*. (1988) that Si and N induce SRO (factor (5)). Bliznuk *et al*. (2004) claimed a direct correlation between chemical homogeneity and shape recovery and explained it on the basis that reversible motion of transformation partials is favoured because their forward motion disturbs the SRO and raises the austenite free energy. However, SRO in FeMnSi alloys remains speculative and requires more complete experimental verification.

Factor (6) is based on data reported by Sato *et al*. (1986) that alloys with enhanced shape memory have relatively high *c*/*a* ratios, and *c*/*a* increases with increasing Si content. This result is related to factor (7), which is based on recent work by Stanford and Dunne (2010). They found that Si increases the *c*/*a* ratio by about 27×10^{-4} per wt% Si, being about 25 times more effective than Mn. A consequence of the higher *c*/*a* ratio is that $\Delta V/V$ is reduced by a factor of about 2 for an increase in Si from 0 to 6 wt%. For a Fe-30Mn-6Si alloy, a volume contraction of about 1% still occurs, as well as atomic mismatch in the interface (habit) plane. These experimental findings are inconsistent with the assumption that the lattice strain **S** is an invariant plane strain (IPS), identical to the macroscopic shape strain $\mathbf{P_1}$. The orientation relationship is described by parallelism of the close-packed planes, $(111)\gamma$ and $(0001)\varepsilon$, which comprise the habit plane, and parallelism of the close-packed directions, $[1,\bar{1},0]\gamma$ and $[1,\bar{2},1,0]\varepsilon$, which lie in the habit plane. However, lattice parameter data (Martínez *et al*., 2006; Stanford and Dunne, 2010) indicate that the atomic spacing along $[1,\bar{1},0]\gamma$ is consistently larger than that along $[1,\bar{2},1,0]\varepsilon$, but decreases from about 0.08 nm at 0% Si to 0.04 nm for 6% Si.

Stanford and Dunne (2010) reported approximately linear relationships between the percentage strain recovery and both *c*/*a* and $\Delta V/V$. They therefore concluded that the improvement in strain recovery with increasing Si is due, at least in part, to decreasing $\Delta V/V$ and improved atomic matching in the interface, i.e. the macroscopic shape strain more closely approaches a shear with increasing Si content, reducing the levels of elastic and/or plastic strain required to accommodate the volume change. In the limit, for ideal close-packing, $c/a = 1.633$, $\Delta V/V = 0$ and the IPS is a shear strain.

Although $\Delta V/V$ decreases for a higher Si content, it remains relatively large (1% for 6% Si) and could induce dislocations in austenite that can impede reverse transformation. Furthermore, misfit dislocations are likely to be required to accommodate cumulative spacing mismatch in the γ/ε interface (Stanford and Dunne, 2010).

All of the Si factors, with the possible exception of (5), are plausible as contributors, at least in a minor way, to improved shape memory. However, the more important factors are considered to be those relevant to the two essential requirements for reversible transformation with low hysteresis: the transformation strains should be small: factors (2), (4) and (7); and the alloy

© Woodhead Publishing Limited, 2012

should have a high capacity to elastically accommodate these strains: factor (3).

The favourable effect of Si on shape memory can be amplified substantially by thermo-mechanical treatment (TMT) of austenite to increase the density of SF nuclei. The importance of TMT is illustrated by internal friction measurements by Chung *et al.* (1996) for Fe-33.7Mn-5.22Si alloy. They found that the internal friction peak corresponding to reverse transformation of martensite, which relates to the volume fraction of reversible martensite, is more than 10 times larger after thermo-mechanical training than for the annealed condition.

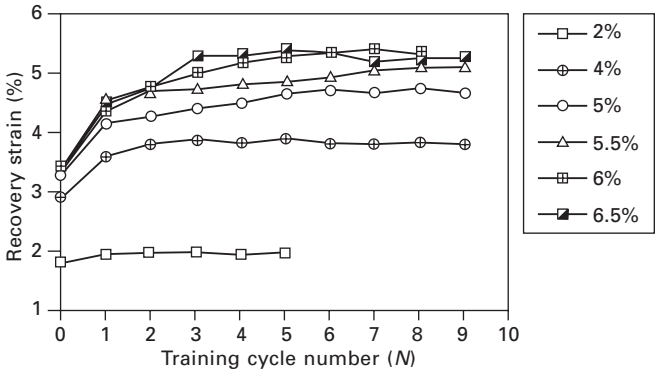
4.6.3 Thermo-mechanical treatment

The training process developed by Otsuka *et al.* (1989) consists of the repeated application of a small amount of strain (1–4%), followed by recovery annealing at a temperature above A_F. This procedure can result in a significant increase in shape recovery, particularly if the stress state associated with training is the same as that used ultimately to test the shape recovery (e.g. bending or uniaxial tension). The training process results in SIM and dislocations that produce plastic strain. Recovery annealing serves to reverse transform the martensite and annihilate some of the excess dislocations, leaving behind stacking fault nuclei for subsequent martensite formation. The residual dislocation structure also serves to strain harden the austenite. The density of stacking fault nuclei can evidently be optimised for specific training conditions. Moreover, the nuclei are likely to be 'oriented', i.e. nuclei for martensite variants that are best oriented to accommodate the applied stress. In contrast, conditioning by hot or cold rolling and annealing is likely to result in a distribution of nuclei that are suited to compressive deformation, rather than tensile or bending deformation. Therefore, SME testing by tensile or bending stress, after TMT by rolling and annealing, is likely to result in a somewhat lower strain recovery than that achievable if the stress state during training is the same for the testing procedure.

Training is capable of doubling the recovered strain, typically from about 2% to 4% (e.g. Otsuka *et al.*, 1989; Gu *et al.*, 1994). The beneficial effects of training include suppression of α' martensite formation and production of a high density of short segment stacking faults, which act as nuclei for formation of SIM (Gu *et al.*, 1994).

An investigation of the effect of training by Dunne and Li (1995) showed that 5.4% tensile strain could be recovered for Fe-20Mn-5.5Si-7.7Cr-1.0Cu after seven training cycles of 6% tensile strain and recovery annealing at 873 K for 600 s (Fig. 4.5). Special enhancement of SME by addition of Cu was investigated, but the obvious possibilities of solid solution strengthening and lowered SFE were eliminated. Rather, it was concluded that the alloy

© Woodhead Publishing Limited, 2012



4.5 Effect of number of training cycles (2–6.5% tensile strain and recovery annealing at 873 K for 600 s) on the recovery of tensile strain for Fe-20Mn-6Si-7Cr-1Cu alloy (after Dunne and Li, 1995).

fortuitously has an M_S temperature (311 K) that is highly appropriate for pre-deformation at ambient following training (Stanford and Dunne, 2006a).

Tomota and Maki (2000) compared trained samples of Fe-24Mn and Fe-24Mn-6Si alloys using TEM. The latter alloy contained nano-scale lamellae of ε and an internal (elastic) stress field that assisted reverse transformation on heating to produce excellent shape memory. An internal stress field was largely absent in the reference alloy, which displayed poor shape memory.

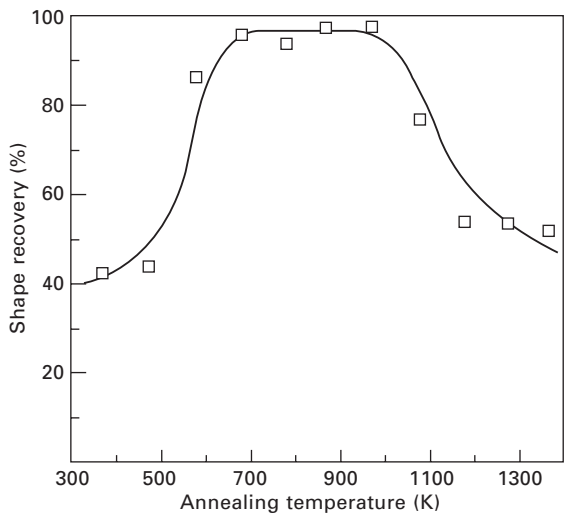
Earlier TEM studies by Ogawa and Kajiwara (1993) were based on trained samples of Fe-14Mn-6Si-9Cr-5Ni alloy, with the aim of clarifying the mechanism by which training enhances SME. They found that the ε plates contained γ stacking faults and proposed that these faults provide nucleation sites for reverse transformation on heating, facilitating austenite formation and shape recovery. A later report on the same alloy by Kajiwara and Ogawa (2000) revealed that, after training, high densities of very thin stress-induced martensite plates were formed that were characterised by elastic strain fields at their tips, associated with Shockley partial dislocations. It was concluded that these thin plates easily revert to austenite on heating by reverse motion of the partials. The two proposed mechanisms for reversion are consistent with internal friction studies by Wu and Hsu (1999), who detected an asymmetry between the internal friction behaviours of the forward and reverse transformations. They concluded that the ε to γ transformation occurs by two modes: reverse movement of partial dislocations and growth of γ SFs in the ε plates.

Simpler processing treatments than training have been developed: direct hot rolling, hot rolling and recovery annealing, warm rolling/working (ausforming) and cold rolling and recovery annealing, but in most cases shape recovery is inferior to that obtained by training.

© Woodhead Publishing Limited, 2012

Ghosh *et al*. (1989) reported an early study on the effect of hot rolling and recovery annealing on shape memory of high purity FeMnSi alloys. Hot rolling was performed at 1375 K followed by vacuum annealing at temperatures in the range 400–1300 K. The best performing alloy contained the highest Mn (32.05%) and Si (5.48%) contents (M_S = 327 K and T_N = 293 K). This alloy exhibited 95% recovery of 5% bending strain after annealing at temperatures in the range 700–950 K (Fig. 4.6). The percentage shape recovery dropped steeply for lower temperatures due to unreverted strain-induced martensite and an inadequately recovered dislocation substructure; and at higher temperatures because of full restoration and softening of the austenite. For intermediate temperatures, pronounced strain recovery occurred despite bending at ambient, some 35 K below M_S, with the structure consisting of austenite and thermal martensite. More recent investigations of hot rolling and annealing of a series of four FeMnSiCr(Cu)(Ni)(Ti) alloys confirmed similar shape recoveries (about 90% recovery of 5% bending strain) provided the rolling temperature, recovery annealing treatment and deformation temperature for shape memory testing were appropriate for the alloy (Stanford and Dunne, 2006a).

After annealing Fe-33Mn-6Si alloy at 1273 K, Tsuzaki *et al*. (1994) used warm tensile working at 573 K (above A_F) as a pre-straining process before re-heating to 573 K to recover 2.5% tensile strain applied at 290 K. They found that pre-strains of 1–7% resulted in similar shape recovery (about 85% of 2.5% strain), and concluded that a small pre-strain (1–2%) is sufficient to



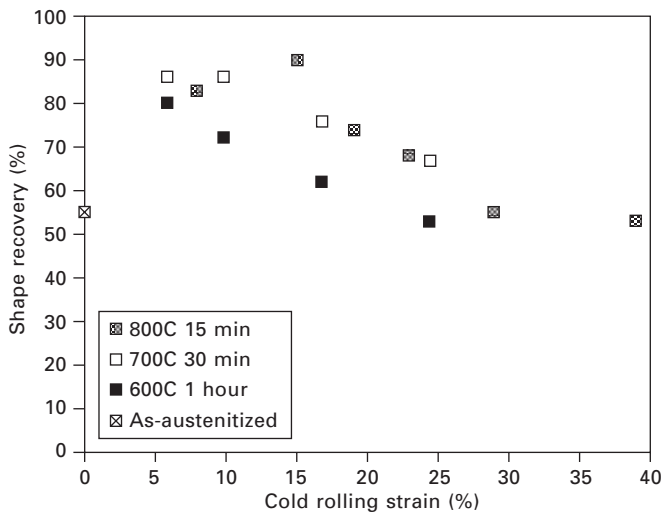
4.6 Effect of recovery annealing temperature, following hot rolling at 1375 K, on the recovery of 5% bending strain in Fe-32.05Mn-5.48Si alloy (after Ghosh *et al.*, 1989).

© Woodhead Publishing Limited, 2012

raise the strength of the austenite and improve shape memory compared to an annealed sample with no pre-strain. However, the strain recovery was modest compared to that measured by Ghosh *et al*. (1989) for a similar alloy and it is possible that the deformation temperature of 290 K was inappropriately high in relation to the M_S of 264 K.

Other systematic studies of the effect of ausforming temperature and strain have been reported. For example, Wang *et al*. (2000) investigated ausforming above M_D for Fe-28Mn-6Si-5Cr. They found that the improvement in shape memory peaked for 9% tensile strain at 973 K and they attributed this effect to dynamic restoration of austenite to a dislocation substructure of uniformly distributed SFs and dislocations that provided both martensite nuclei and austenite work hardening. It is clear that thermo-mechanical processing designed to optimize shape memory has to be tuned to the composition and transformation characteristics of the alloy of interest.

The effectiveness of cold rolling and recovery annealing on SME is illustrated in Fig. 4.7, which shows that maximum SME was achieved for Fe-13.5Mn-5.5Si-7.7Cr-7.1Ni alloy after cold rolling to 15% strain, followed by annealing for 900 s at 1073 K (Stanford and Dunne, 2006b). The effect of hot rolling conditions on SME was also examined for the same alloy after hot rolling at the optimum temperature of 1373 K and recovery annealing at 873 K for 1.8 ks. For both processing methods: cold rolling and annealing, and hot rolling and annealing, 70–80% recovery of 5% bending strain was obtained, despite different microstructures.



4.7 Effect of cold rolling strain and heat treatment on the percentage shape (strain) recovery of 4% bending strain in Fe-13.5Mn-5.5Si-7.7Cr-7.1Ni alloy (after Stanford and Dunne, 2006b).

© Woodhead Publishing Limited, 2012

Sato *et al*. (1982) reported that a single crystal of FeMnSi deformed in tension in the direction <414>, showed a recovered true strain of over 8%, because the crystal was oriented to induce a single variant of martensite with a shear direction close to 45° from the stress axis. The potential therefore exists for improved shape memory in polycrystalline alloys if a <110> texture can be developed along the tensile axis, since this is only about 10° from <414> (Matsumura *et al*. 1996). Stanford and Dunne (2006a) conducted texture studies for a series of FeMnSiCr(Cu)(Ni)(Ti) alloys and found that the strongest texture was only about four times random intensity and was consistent with the recrystallisation texture normally found in low SFE fcc metals. The results were similar to those of Matsumura *et al*. (1996) and it was concluded that the hot rolled texture was not significantly altered by the rolling conditions and that shape memory is relatively insensitive to the textures produced. Similar conclusions were drawn for treatments involving cold rolling and annealing. More recently, Li *et al*. (2008) investigated texture evolution on warm rolling of Fe-28Mn-6Si-5Cr alloy and mapped the texture transitions as a function of rolling reduction at 873 and 573 K. For rolling reductions up to 57% at 873 K, it was found that the Goss texture component $\{011\}\langle 100\rangle_F$ was dominant, but the effect of texture on shape recovery was not reported.

More complex working processes, such as high strain deformation by dropped weight and projectile penetration (Matsuya *et al*., 2000); and high speed sandwich rolling (Yoneyama *et al*., 2003) have been reported. In the latter case, rolling generated cph and bcc nanophases within deformation bands containing fine cells. After annealing at 1073 K, this structure transformed into fine, highly twinned austenite grains with a twin band thickness of about 1 μm. Although shape recovery was demonstrated, it was improved by subsequent 'training' and so this processing method does not appear to offer any distinct advantage.

TMT is an important means of manipulating the microstructure of the austenite to enhance the capacity of the alloy for shape memory. Another well-researched strategy is precipitation of fine particles in the austenite.

4.6.4 Effect of precipitate particles

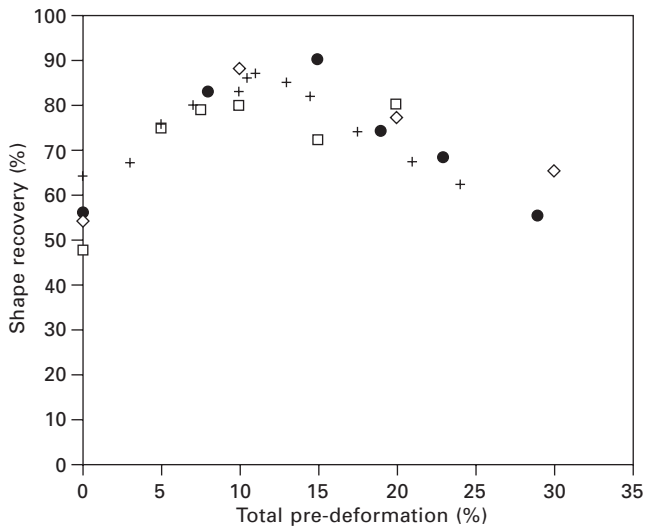
Kajiwara *et al*. (2001) reported that NbC precipitates in Fe-Mn-Si alloys have a beneficial effect on shape recovery. Two standard shape memory alloy compositions (with C and Nb) were solution treated and isothermally aged to produce 0.5–1.5 vol% NbC. Precipitation was shown to markedly increase the shape recovery of the alloys compared to those without precipitates after identical treatments. For fully recrystallised alloys, martensite formation is nucleation limited (Stanford *et al*., 2007), as the low dislocation density does not provide a significant number of nucleation sites for SIM. However,

© Woodhead Publishing Limited, 2012

precipitates can provide extra nucleation sites for SIM, increasing the volume fraction of martensite and improving SME relative to a precipitate-free reference alloy.

Results subsequently reported by Baruj *et al*. (2002, 2004) for precipitate-containing, thermo-mechanically processed alloys were less straightforward. Since the processing history affects SME (Otsuka *et al*., 1989), the origin of any improvement must be carefully compared to a particle-free reference alloy before conclusions can be drawn on the effect of the precipitates.

The data in Fig. 4.7 for a particle-free FeMnSiCrNi alloy has been used in Fig. 4.8 as a benchmark to examine other work on alloys that contain precipitates (Baruj *et al*., 2002, 2004; Dong *et al*., 2005; Wang *et al*., 2007). It can be seen from Fig. 4.8 that the data for alloys containing NbC particles,



	Author/ref	Alloy comp.	Alloy type	Deformation mode	Annealing cond.	SME PS
•	Stanford and Dunne (2006b)	Fe-Mn-Si-Cr-Ni	Particle-free	Room temp. rolling	800 C, 15 min.	4%
+	Dong *et al*. (2005)	Fe-Mn-Si-Cr-Ni-NbC	1% NbC	Room temp. tension	797 C, 10 min.	4%
◇	Baruj *et al*. (2004)	Fe-Mn-Si-Cr-NbC	0.5% NbC	Room temp. rolling	797 C, 10 min.	4%
□	Wang *et al*. (2007)	Fe-Mn-Si-Cr-Ni-NbC	0.08% NbC	Room temp. tension	800 C, 15 min.	5.33%

4.8 Percentage shape recovery of particle-free and particle-containing alloys with prior deformation followed by heat treatment. SME PS is the pre-strain prior to SME testing (Stanford *et al.*, 2008). The SME PS was applied by bending by Stanford *et al.* and by tension in the other cases (after Stanford *et al.*, 2008).

© Woodhead Publishing Limited, 2012

and the data for the particle-free alloy are almost identical when the results are plotted on the same scale. This plot suggests that the increase in SME that was attributed to the particles was due mainly to the deformation and heat treatment given prior to shape memory testing.

Cold rolling and annealing of particle-containing alloys showed that those with fine particles actually had lower shape memory than particle-free reference alloys (Stanford and Dunne, 2006b), in disagreement with previously published work (e.g. Baruj *et al*., 2004). To elucidate why particles exerted a negative effect in some cases and a positive effect in others, the parameter, ΔSME, was introduced (Stanford and Dunne, 2007) which represents the percentage difference in shape memory between particle-containing and particle-free alloys that have been given identical treatments. A negative value of ΔSME indicates that the particles have an adverse effect on SME, and a positive ΔSME represents improved SME. In general, positive parameters were obtained for coarser particles and negative values for fine particles with diameters less than about 50 nm. Enhancement of shape memory in the presence of coarser particles is considered to be due to additional martensite nuclei created in dislocation-rich regions around the particles, whereas inhibition of SME occurs for fine particles because they act as barriers that restrict martensite growth – effectively reducing both the volume fraction of SIM and the SME.

Dunne and Li (1994) reached the same conclusion for intermetallic precipitation in Fe-Mn-Si-based alloys. The precipitates were coherent with the parent austenite, and about 5 nm in diameter. X-ray diffraction was used to demonstrate that for the same strain level, samples with fine particles showed significantly less SIM than a particle-free reference alloy, with markedly decreased shape recovery. Further, Ullakko *et al*. (1996) found that VN precipitation in one of a series of N-bearing FeMnSi-based alloys resulted in poorer shape recovery than the precipitate-free alloys. Kubo *et al*. (2004) also investigated VN precipitation in FeMnSiCr alloy and claimed that they obtained 'a large amount of shape recovery strain' in the presence of high densities of 'large size' (unquantified) coherent particles of VN. The quoted shape recovery was relatively modest: about 70% of 5% tensile strain, and required a training step of 7.5% tensile deformation and recovery annealing at 873 K. It therefore remains uncertain what role the precipitates played. Additional evidence for an adverse effect of precipitation on γ to ε transformation is provided by Ono *et al*. (1997) who studied Fe-22Mn alloys containing 0.5 and 1 vol% NbC. They reported that martensitic transformation was significantly suppressed by fine NbC particles. These observations collectively add weight to the hypothesis that fine particles pin martensite, restrict its growth, and reduce the volume fraction of SIM, compared with particle-free microstructures.

Although fine precipitates certainly raise the flow stress of the austenite, it

© Woodhead Publishing Limited, 2012

is also likely that they raise the stress to induce martensite, with little or no increase in the stress window shown in Fig. 4.1. Therefore, any improvement in recovery strain due to the presence of fine precipitates is at best marginal. Nevertheless, Dong *et al*. (2009) have demonstrated that for a stainless type alloy containing VC, the recovery stress is well in excess of 300 MPa. This result confirms an earlier report by Baruj *et al*. (2004) that NbC-containing alloys, 20–30% pre-rolled at room temperature and aged at 1070 K, can exhibit a recovery stress of about 300 MPa, compared to 150 MPa for a trained sample of the same alloy, measured at the same recovery strain.

The presence of about 6% Si in FeMn-based alloys has proved to be highly beneficial to shape memory because of the physical, morphological and crystallographic reasons discussed. However, the presence of Si, *per se*, is not sufficient to ensure significant shape recovery and, in order to optimise shape memory, appropriate, alloy-specific, thermo-mechanical processing is essential. The same reservation applies to alloy variants that contain precipitates or other alloying additions designed to lower SFE and increase austenite strength.

4.6.5 Applications

For the application of shape memory alloys as heat recoverable fasteners, sufficient force must be developed under constrained recovery to develop a pressure-tight, high-integrity joint. The total movement (shrinkage) must be large enough to account for dimensional tolerances in the ring and substrate, to allow for installation clearance and to compress the substrate sufficiently to develop a high recovery stress (Bordon, 1990). Therefore, the typical 3–4% recovery strain for FeMnSi-based alloys is marginal and underscores the substantial research effort to increase the recovery strain as well as the recovery stress.

Liu *et al*. (1995) reported the application of Fe-29Mn-5.9Si alloy for couplings to join pipelines in the oil and chemical engineering industries in China. Steel pipes with outer diameters of 60 to 114 mm, joined by shape memory steel couplings, had given trouble-free service for three years. Although Liu *et al*. measured a recovery strain of 3.2% and a stress of 150 MPa in laboratory tensile tests, the contractions of the internal diameters of 60 mm and 114 mm couplings on heating above A_F (573 K) showed actual strain recoveries of about 2%. A recovery strain of this magnitude does not seem to provide sufficient latitude for easy installation, but the joints were able to sustain 40 MPa of hydrostatic pressure without leaking.

A novel method for pipe joining has been proposed by Jee *et al*. (2006) which allows the full recovery stress to be utilised in making the joint, with either internal SM ferrules (that expand on heating) or external ferrules (that contract). The external (internal) pipe diameter in the region of the joint is

© Woodhead Publishing Limited, 2012

reduced (increased) by machining to accommodate the ferrule and, with the ferrule in place, the pipe is locally expanded (compressed) mechanically to eliminate the clearance with the SM fitting. Heating to 623 K produces constrained recovery with no free motion to accommodate clearances. Practical drawbacks are the need to machine, then deform the pipe at the site of the joint.

The New Materials Group of Nippon Steel has actively investigated commercial applications of FeMnSi-based alloys since the 1980s. This group has contributed strongly to alloy development, training and fundamental understanding (Murakami *et al.*, 1987; Otsuka *et al.*, 1989, 1990; Otsuka, 1992). Applications reported include a C-shaped locking ring, constructed from Fe-28Mn-6Si-5Cr, for assembling bicycle frame components; and stainless alloy ferrules for joining steel water pipes up to about 43 mm outer diameter (Otsuka, 1992). In both cases the joint includes an adhesive sealant that cures during heating to effect shape memory. Otsuka (1992) reported that the locking rings are being successfully used in bicycle manufacture, eliminating the need for welding; and 22 mm pipe joints were found to be trouble-free after one year in service.

There is little doubt that FeMnSi-based shape memory alloys are suitable for a range of specific applications that are compatible with their properties. One limitation is a shape recovery strain of not more than about 4%. Another is restriction to one-way applications (such as clamping and fastening), as reversible operation using (say) a bias spring requires a relatively high force to counteract the recovery force and reform SIM (Otsuka, 1992). Further, the temperature response is slow and the recovery temperature range is relatively wide.

4.7 Summary

Yang and Wayman (1992) analysed the shape memory effect in FeMnSi alloys in terms of the general framework developed to explain shape memory in Cu-based and Ti-Ni-based alloys. They concluded that, in common with other shape memory alloys, thermally-induced martensite in FeMnSi-based alloys forms in self-accommodating plate groups and responds to an applied stress by variant coalescence and re-orientation. Further, the stress-induced martensite has similar characteristics to those formed in other shape memory alloys.

The unique features of the γ to ε transformation are crystallographic. In particular, the rational habit plane halves the number of crystallographic variants and reduces the number of self-accommodating variants from four to three. The transformation is also mechanistically simple in the sense that it involves a change in stacking sequence of the close-packed planes by the propagation of Shockley partial dislocations. Although a twinned martensite

© Woodhead Publishing Limited, 2012

substructure (the LIS) is characteristic of α′ shape memory alloys, it is absent in FeMnSi-based alloys and, instead of refining the transformation twins to enhance elastic accommodation of interfacial strains, improved interfacial coherence can only be effected by reducing the atomic mismatch between the γ and ε phases in the interface.

There is no conclusive evidence of SRO in austenitic FeMnSi. Order is a pervasive feature of shape memory alloys and it is considered to be important in constraining the path of reverse transformation on heating to produce the original austenite grain orientation and to obtain complete shape recovery (Otsuka and Wayman, 1998b). Yang and Wayman (1992) theoretically analysed the reverse transformation of a single crystal of ε martensite produced by application of a stress to an austenite single crystal. Three reverse paths are possible through the motion of the a/6<112> partial dislocations. For reverse transformation to follow the unique path that produces the original austenite orientation, Yang and Wayman (1992) hypothesised that an internal 'reforming' stress is present that pre-determines the operation of a specific partial dislocation. They considered that thermo-mechanical treatment plays an important role in establishing the internal stress field, consistent with the resulting improvement in shape recovery. In practice, however, deformation of polycrystalline FeMnSi alloys does not produce 100% martensite and, as observed by Kajiwara and Ogawa (2000) and Tomota and Maki (2000), partial dislocations remain at the tips of the plates and establish an internal elastic stress field that drives the reverse transformation to the original austenite grain orientation on heating.

Kajiwara (1999) pointed out that thermo-mechanical processing should achieve a high density of uniformly distributed SFs on the primary slip plane of each grain in the polycrystalline aggregate, so that these nuclei are activated during pre-strain. The desirable result is formation of a high volume fraction of very fine ε plates of the same variant with no or few plate intersections. This ideal microstructure is unlikely to be achieved in polycrystalline samples because, just as complex slip is normally required for a grain to change its shape to accommodate plastic strain of surrounding grains, multiple variants of SIM are expected to be activated during pre-strain of shape memory alloys. This factor may not be detrimental if the multiple variants are reversible, but reverse transformation could be impeded if α′ forms at plate intersections and/or plastic strain occurs.

Considering the basic factors that influence shape memory (Christian, 1965), there appears to be scope for enhancing shape memory in FeMnSi alloys by alloy design to reduce the volume change and improving interfacial atomic matching whilst maintaining a low SFE. Further, since the key role of thermo-mechanical processing has been clearly demonstrated, SME could potentially be improved by closer control and optimisation of the austenite defect structure.

© Woodhead Publishing Limited, 2012

For significant shape memory to be exhibited in alloys undergoing the γ to α′ transformation, the martensite tetragonality must be high (≥ 1.08) to lower the twin boundary energy and refine the twin spacing (Kajiwara, 1999). This condition and a small volume change are certainly *necessary* conditions for thermoelastic transformation, and when present in company with a deformation-resistant austenite, they are probably *sufficient* conditions. However, either condition alone is not sufficient, as demonstrated by a high *c/a* in FeNiC alloys and low ΔV/V values in FeNiCo that do not produce thermoelastic transformation. Therefore, as for ordered Fe_3Pt, a series of factors must simultaneously apply that generate low transformation strains and a high capacity for their elastic accommodation. The α′ martensitic alloys based on Fe_3Pt, FeNiC and FeNiCoTi currently appear to have limited commercial potential as shape memory alloys because the Pt- and Co-bearing alloys are expensive and C-bearing high Ni alloys are beset with problems of very high hysteresis and limited shape recovery. Although 100% shape recovery has been demonstrated for ausaged FeNiCoTi alloys, it was only 2% bending strain and fuller investigation of its potential is required. Furthermore, this 'perfect' shape memory is associated with either sub-zero temperatures or a wide range from ambient to over 1100 K (Maki, 1998a). These characteristics are limiting in terms of engineering applications.

Magnetically-induced martensitic transformation has not been considered because it is still in a relatively early stage of exploration. Kakeshita *et al.* (2003) reported the effect of a magnetic field on Fe-based shape memory alloys and demonstrated an increase in transformation temperature above the thermal M_S of up to 70 K in an Invar Fe-31.7 at%Ni alloy, as well as magneto-elastic transformation in ausaged FeNiCoTi alloy. The effect of magnetic field on rearrangement of twin variants within martensite in ferromagnetic Fe-Pd and Fe_3Pt alloys has also been reported (Kakeshita *et al.*, 2006) with the conclusion that the magnetic shear stress required for variant re-arrangement is higher than the mechanical shear stress.

The enhanced damping capacity arising from hysteretic movement of interfaces generated by martensitic transformation was also considered to be outside the scope of this treatment. However, there is little doubt that ferrous shape memory alloys have potential for vibration damping applications (Jee *et al.*, 1994, 1999; Van Humbeeck, 1999).

In conclusion, this analysis indicates that the crystallographic factors of low ΔV/V and good interfacial matching are essential to ensure reversible transformation with a relatively low hysteresis. Another key factor is austenite strengthening to increase the elastic limit, provided it can be achieved without compromising the formation and reversion of martensite. These principles should be at the forefront of attempts to design improved ferrous shape memory alloys.

© Woodhead Publishing Limited, 2012

4.8 Acknowledgements

The valuable and indeed, essential, contributions of Drs Nicole Stanford and Huijun Li to research work on Fe-based shape memory alloys conducted at the University of Wollongong are gratefully acknowledged.

4.9 References

Ariapour, A., Yakubstov, I. and Perovic, D.D. (2001): 'Shape-memory effect and strengthening mechanism in a Nb and N-doped Fe-Mn-Si alloy', *Metall. Trans.*, **32A**, 1621–1628.

Baruj, A., Kikuchi, T., Kajiwara, S. and Shinya, N. (2002): 'Effect of pre-deformation of austenite on shape memory properties in Fe-Mn-Si based alloys containing Nb and C', *Mater. Trans.*, **43**, 585–588.

Baruj, A., Kikuchi, T., Kajiwara, S. and Shinya, N. (2004): 'Improvement of shape memory properties of NbC containing Fe-Mn-Si based shape memory alloys by simple thermomechanical treatment', *Mat. Sci. & Eng. A*, **378**, 333–336.

Basinski, R.S., Hume-Rothery, W. and Sutton, A.L. (1955): 'The lattice expansion of iron', *Proc. Roy. Soc.*, **A229**, 459–467.

Bliznuk, V.V., Gavriljuk, V.G., Kopitsa, G.P., Grigoriev, S.V. and Runov, V.V. (2004): 'Fluctuations of chemical composition of austenite and their consequence on shape memory effect in Fe-Mn-(Si,Cr,Ni,C,N) alloys', *Acta Mater.*, **52**(16), 4791–4799.

Bordon, T. (1990): 'Shape memory alloy fastener rings', in *Engineering Aspects of Shape Memory Alloys*, T. Duerig *et al.* (eds.), Butterworth-Heinemann, London, 158–169.

Bowles, J.S. (1971): Personal communication.

Bowles, J.S. and Mackenzie, J. (1954): 'The crystallography of martensitic transformations I, II and III', *Acta Metall.*, **2**, 129–137, 138–147, 224–234.

Breedis, J.F. and Wayman, C.M. (1962): 'The martensitic transformation in Fe-31 wt pct Ni', *Trans. AIME*, **224**, 1128–1133.

Brook, G.B., Iles, R.F. and Brooks, P.L. (1975): 'The relationship between stacking fault energy and shape memory in primary solid solutions', in *Shape Memory Effects in Alloys*, J. Perkins (ed.), Met. Soc. AIME, Plenum Press, New York, 477–486.

Christian, J.W. (1965): in *The Theory of Phase Transformations in Metals and Alloys*, Pergamon Press, Oxford.

Chung, C.Y., Chen, S. and Hsu, T.Y. (1996): 'Thermomechanical training behaviour and its dynamic mechanical analysis in an Fe-Mn-Si shape memory alloy', *Mater. Characterization*, **37**, 227–236.

Dong, Z.Z., Kajiwara, S., Kikuchi, T. and Sawaguchi, T. (2005): 'Effect of pre-deformation at room temperature on shape memory properties of stainless type Fe-15Mn-5Si-9Cr-5Ni-(0.5-1.5NbC)', *Acta Mater.*, **53**, 4009–4018.

Dong, Z.Z, Klotz, U.E., Leinenbach, C., Bergamin, A., Czaderski, C. and Motavalli, M. (2009): 'A novel Fe-Mn-Si shape memory alloy with improved shape recovery properties by VC precipitation', *Adv. Eng. Materials*, **11**, 40–44.

Duerig, T., Pelton, A. and Stockel, D. (1999): 'An overview of nitinol medical applications', *Proc. ICOMAT'98*, Bariloche, Argentina, M. Ahlers, G. Kostorz and M. Sade (eds.), *Mat. Sci. & Eng. A*, **273–275**, 149–160.

Dunne, D.P. (1974): 'Transformation-induced anelasticity', *J. Australian Institute of Metals*, Metallurgical Forum on Martensite, **19**(1), 28–34.

© Woodhead Publishing Limited, 2012

Dunne, D.P. (1977): 'A model for the interface of $(3, 15, 10)_F$ martensite in steel', *Scripta Metall.*, **11**, 1017–1021.

Dunne, D.P. (1978): 'The interface structure of martensite in Fe_3Pt', *Scripta Metall.*, **12**, 143–146.

Dunne, D.P. (1998): 'Martensitic iron-platinum alloys', *Proc. Int. Conf. on Displacive Transformations and their Applications in Materials Engineering*, Urbana, IL, K. Inoue, K. Mukherjee, K. Otsuka and H. Chen (eds.), TMS, Warrendale, PA, 133–140.

Dunne, D.P. and Li, H. (1994): 'The effect of parent phase strengthening on shape memory behaviour of ferrous alloys', *Proc. Advanced Materials '93*, Vol. 18B, Shape Memory and Hydrides, K. Otsuka and Y. Fukai (eds.), Elsevier, Oxford, 995–960.

Dunne, D.P. and Li, H. (1995): 'The mechanism of thermomechanical training of a newly developed Fe-Mn-Si-Cr-Mn shape memory alloy', *Proc. ICOMAT 95*, Lausanne, R. Gotthardt and J. Van Humbeeck (eds.), *Journal de Physique IV*, C8, 415–420.

Dunne, D.P. and Liu, H. (1999): 'Influence of carbon on the shape memory effect in Fe-Mn-Si alloys', *Proc. Int. Conf. on Solid-Solid Phase Transformations '99*, ed. by M. Koiwa, K. Otsuka and T. Miyazaki, The Japan Institute of Metals, Sendai, 997–1003.

Dunne, D.P. and Wayman, C.M. (1973): 'The effect of austenite ordering on the martensite transformation in Fe-Pt near the composition Fe_3Pt: I. Morphology and transformation characteristics; II. Crystallography and general features', *Metall. Trans.*, **4**, 137–146, 147–152.

Dunne, D.P., Stobbs, M. and Kennon, N.F. (1984): 'The effect of order on the martensitic transformation in Fe_3Pt', *Proc. Mat. Res. Soc. Symp.*, **21**, 675–680.

Enami, K., Nenno, S. and Minato, Y. (1971): 'Shape memory effect associated with the martensitic transformation in 304 type stainless steel', *Scripta Metall.*, **5**, 663–667.

Enami, K., Nagasawa, A. and Nenno, S. (1975): 'Reversible shape memory effect in Fe-base alloys', *Scripta Metall.*, **9**, 941–948.

Foos, M., Frantz, C. and Gantois, M. (1975): 'Shape memory effect and anelasticity associated with martensitic transformation in the stoichiometric Fe_3Pt alloy', in *Shape Memory Effects in Alloys*, J. Perkins (ed.), Met. Soc. AIME, Plenum Press, New York, 407–417.

Gallagher, P.J.C. (1970): 'Influence of alloying, temperature, and related effects on stacking fault energy', *Metall. Trans.*, 1, 2429–2461.

Gaunt, P. and Christian, J.W. (1959): 'The cubic-hexagonal transformation in single crystals of cobalt and cobalt-nickel alloys', *Acta Metall.*, **7**, 529–533.

Ghosh, G., Vanderveken, Y., Van Humbeeck, J., Chandrasekaran, M., Delaey, L. and Vanmoorleghem, W. (1989): 'Influence of cycling, aging and heat treatment on the martensite transformation and shape recovery of Fe-Mn-Si alloys', *Proc. MRS Int. Meeting on Advanced Materials*, Ikebukuro, Japan, Vol. 9, 'Shape Memory Materials', ed. by M. Doyama, S. Somiya, R. Chang, MRS, Pittsburgh, PA, 457.

Grujicic, G.R., Ling, H.C., Haezebrouck, D.M. and Owen, W.S. (1992): 'Growth of martensite', in *Martensite*, G.B. Olsen and W.S. Owen (eds.), ASM Int. Pub., Metals Park, OH, 175–196.

Gu, Q. (1994): 'Martensitic Transformation and Shape Memory Effect in Fe-Mn-Si Based Shape Memory Alloys', PhD Thesis, Catholic University Leuven, Belgium.

Gu, Q., Van Humbeeck, J. and Delaey, L. (1994): 'On the improvement of shape memory effect in Fe-16Mn-5Si-9Cr-4Ni alloys by thermomechanical treatment', *Scripta Metall. & Mater.*, **30**, 1587–1592.

Guo, Z., Rong, Y., Chen, S., Hsu, T.Y., Hong, J. and Zhao, X. (1999): 'Reverse

© Woodhead Publishing Limited, 2012

transformation characteristics of thermally induced ε (hcp) martensite in an Fe-Mn-Si based alloy', *Materials Trans. JIM*, **40**, 193–198.
Hamers, A.A.H. and Wayman, C.M. (1991): 'Shape memory behaviour in Fe-Mn-Co alloys', *Scripta Metall. & Mater.*, **25**, 2723–2728.
Hausch, G. and Warlimont, H. (1971): 'Structural inhomogeneity in Fe-Ni invar alloys studied by electron diffraction', *Phys. Lett.*, **36A**, 415–416.
Himuro, Y., Ikeda, O., Kainuma, R. and Ishida, K. (2002): 'Martensitic transformation and shape memory effect in ausaged Fe-Ni-Si alloys', *ISIJ Int.*, **42**, 184–190.
Honorat, Y., Henry, G. and Munenc, J. (1965): *Mém. Sci. Revue Métall.*, 429.
Hsu, T.Y. (2000): 'Fe-Mn-Si based shape memory alloys', *Materials Sci. Forum*, **327–328**, 199–206.
Hsu, T.Y. and Yan, L. (1984): 'The effect of austenite ordering on the martensitic transformation in Fe-Ni alloys', *Metallography*, **17**, 397–409.
Jana, S. and Wayman, C.M. (1967): 'Martensite to fcc reverse transformation in an Fe-Ni alloy', *Metall. Trans.*, **239**, 1187–1193.
Jang, W.Y., Jee, K.K., Shin, M.C. and Hong, J.H. (1991): 'Transformation behaviour and shape memory effect in Fe-15Mn-5Cr-5Co-3Si alloy', *Korean Inst. Metals J.*, **29**, 398.
Jang, W.Y., Gu, Q., Van Humbeeck, J. and Delaey, L. (1995): 'Microscopic observation of γ-phase and ε and α′ martensite in Fe-Mn-Si-based shape memory alloys', *Materials Characterization*, **34**, 67–72.
Jee, K.K., Ito, K. and Shin, M.C. (1994): 'Damping capacity of Fe-27Mn-3.5Si alloy', *ISIJ Int.*, **34**, 912–916.
Jee, K.K., Jang, W.Y., Baik, S.H. and Shin, M.C. (1999): 'Damping mechanism and application of Fe-Mn based alloys', *Mater. Sci. & Eng. A*, **235–237**, 538–542.
Jee, K.K., Han, J.H. and Jang, W.Y. (2006): 'A method of pipe joining using shape memory alloys', *Mater. Sci. & Eng. A*, **438–440**, 1110–1112.
Jiang, B., Qi, X., Zhou, W., Xi, Z.L. and Hsu, T.Y. (1996): 'Effect of nitrogen on shape memory effect in Fe-Mn-Si alloys', *Scripta Mater.*, **34**, 1437–1441.
Jiang, B., Qi, X., Yang, S., Zhou, W. and Hsu, T.Y. (1998): 'Effect of stacking fault probability on γ→ε martensitic transformation and shape memory effect in Fe-Mn-Si alloys', *Acta Mater.*, **46**, 501–510.
Kajiwara, S. (1985): 'Nearly perfect shape memory effect in Fe-Ni-C alloys', *Trans. Jap. Inst. Metals*, **26**, 595–596.
Kajiwara, S. (1999): 'Characteristic features of shape memory effect and related transformation behaviour of Fe-based alloys', *Mater. Sci. & Eng. A*, **273–275**, 67–88.
Kajiwara, S. and Kikuchi, T. (1983): 'Reversible movement of the austenite-martensite interface and dislocation structures in reverse-transformed austenite in Fe-Ni-C alloys', *Phil. Mag. A*, **48**, 509–526.
Kajiwara, S. and Ogawa, K. (2000): 'Mechanism of improvement of shape memory effect by training in Fe-Mn-Si-based alloys', *Materials Sci. Forum*, **327–328**, 211–214.
Kajiwara, S. and Owen, W.S. (1974): 'The reversible martensite transformation in iron-platinum alloys near Fe_3Pt', *Metall. Trans.*, **5**, 2047–2061.
Kajiwara, S. and Owen, W.S. (1977): 'The martensite-austenite interface and the thickness of twins in Fe_3Pt', *Scripta Metall.*, **11**, 137–142.
Kajiwara, S., Kikuchi, T. and Sakuma, N. (1986): 'Shape memory effect in high nickel steels', *Proc. ICOMAT'86*, Nara, Japan, Japan Institute of Metals, 991–996.
Kajiwara, S., Liu, D., Kikuchi, T. and Shinya, N. (2001): 'Remarkable improvement

© Woodhead Publishing Limited, 2012

of shape memory effect in Fe-Mn-Si based alloys by producing NbC precipitates', *Scripta Mater*., **44**, 2809–2814.

Kakeshita, T., Fukuda, T., Terai, T., Takeuchi, T. and Kishio, K. (2003): 'Martensitic transformation in Fe-based shape memory alloys under magnetic field', *J. Phys. IV France*, **112**, 93–100.

Kakeshita, T., Fukuda, T. and Takeuchi, T. (2006): 'Magneto-mechanical evaluation for twinning plane movement driven by magnetic field in ferromagnetic shape memory alloys', *Mater. Sci & Eng. A*, **438–440**, 12–17.

Kaufman, L. and Cohen, M. (1958): 'Thermodynamics and kinetics of martensitic transformations', *Prog. Met. Phys*., **7**(3), 165–246.

Kessler, H. and Pitsch, W. (1967): 'On the nature of reverse martensite to austenite transformation', *Acta Metall*., **15**, 401–405.

Kikuchi, T. and Kajiwara, S. (1989): 'Relationships between martensite tetragonality, morphology and shape memory in Fe-Ni based alloys', *Proc. of MRS Int. Meeting on Advanced Materials*, Ikebukuro, Japan, Vol. 9, 'Shape Memory Materials', M. Doyama, S. Somiya, R. Chang (eds.), MRS, Pittsburgh, PA, 463–468.

Koval, Yu. N. and Kokorin, K.K. (1975): *Phys. Met. Metallogr*., **39**, 129–133.

Koval, Yu. N. and Monastyrsky, G.E. (1993): 'Reversible martensite transformation and shape memory effect in Fe-Ni-Nb alloys', *Scripta Metall*., **28**, 41–46.

Koval, Yu. N., Kokorin, K.K. and Khandros, L.G. (1981): *Phys. Met. Metallogr*., **48**(6), 162.

Kubo, H., Nakamura, K., Farjami, S. and Maruyama, T. (2004): 'Characterization of Fe-Mn-Si-Cr shape memory alloys containing VN precipitates', *Mater. Sci. & Eng. A*, **378**, 343–348.

Kurdjumov, G.V. and Khandros, L.G. (1949): *Dokl. Akad. Nauk SSSR*, **66**, 211–221.

Lee, Y-K. and Choi, C-S. (2000): 'Driving force for $\gamma \rightarrow \varepsilon$ martensitic transformation and stacking fault energy of γ in Fe-Mn binary system', *Metall. Mater. Trans. A*, **31A**, 355–360.

Li, H., Yin, F., Sawaguchi, T., Ogawa, K., Zhao, X. and Tsuzaki, K. (2008): 'Texture evolution analysis in warm-rolled Fe-28Mn-6Si-5Cr shape memory alloy', *Mater. Sci. & Eng. A*, **494**, 217–226.

Li, J.C., Zhao, M. and Jiang, Q. (2000): 'Alloy design of FeMnSiCrNi shape-memory alloys related to stacking-fault energy', *Metall. Mater. Trans. A*, **31A**, 581–584.

Ling, H.C. and Owen, W.S. (1981): 'A model of the thermoelastic growth of martensite', *Acta Metall*., **29**, 1721–1736.

Liu, D.Z., Liu, W.X. and Gong, F.Y. (1995): 'Engineering application of Fe-based shape memory alloy on connecting pipe line', *Proc. ICOMAT 95*, Lausanne, R. Gotthardt and J. Van Humbeeck (eds.), *Journal de Physique IV*, C8, 1241–1246.

Liu, D.Z., Bergeon, N., Kikuchi, T., Kajiwara S. and N. Shinya N. (2000): 'Observation on plastic accommodation of shape strain in martensitic transformation in Fe-Ni-C shape memory alloys', *Materials Sci. Forum*, **327–328**, 405–408.

McDougall, P.G. and Wayman, C.M. (1992): 'The crystallography and morphology of ferrous martensites', in *Martensite*, G.B. Olsen and W.S. Owen (eds.), ASM Int., Metals Park, OH, 59–95.

Magee, C.L. and Davies, R.G. (1972): 'On the volume expansion accompanying f.c.c. to b.c.c. transformation in ferrous alloys', *Acta Metall*., **20**, 1031–1043.

Maki, T. (1989): 'Martensitic transformation and shape memory effect in ausaged Fe-Ni-Co-Ti alloys', *Proc. MRS Int. Meeting on Advanced Materials*, Ikebukuro, Japan, Vol. 9, 'Shape Memory Materials', M. Doyama, S. Somiya, R. Chang (eds.), MRS, Pittsburgh, PA, 415–429.

© Woodhead Publishing Limited, 2012

Maki, T. (1990): 'Microstructure and mechanical behaviour of ferrous martensite', *Proc. Int. Conf. on Martensitic Transformations (ICOMAT'89)*, B.C. Muddle (ed.), *Materials Sci. Forum*, **56–58**, 157–168.

Maki, T. (1998a): 'Ferrous shape memory alloys,' in *Shape Memory Materials*, K. Otsuka and C.M. Wayman (eds.), Cambridge University Press, Cambridge, 117–132.

Maki, T. (1998b): 'Improvement of shape memory effect in Fe-Mn-Si alloys by strengthening of austenitic matrix', *Proc. Int. Conf. on Displacive Phase Transformations and their Applications in Materials Engineering*, Urbana. IL, K. Inoue, K. Mukherjee, K. Otsuka and H. Chen (eds.), TMS, Warrendale, PA, 111–117.

Maki, T. and Tamura, I. (1986): 'Shape memory effect in ferrous alloys', *Proc. ICOMAT'86*, Nara, Japan, The Japan Institute of Metals, Sendai, 963–970.

Maki, T. and Tsuzaki, K. (1992): 'Transformation behaviour of ε-martensite in Fe-Mn-Si shape memory alloys', *Proc. Int. Conf. on Martensitic Transformations (ICOMAT'92)*, 1992, Monterey, CA, C.M. Wayman and J. Perkins (eds.), Monterey Institute of Advanced Studies, 1151–1162.

Maki, T. and Wayman, C.M. (1977): 'Effect of coherent precipitates in austenite on the martensitic substructure in an Fe-Ni-Ti-C alloy', *Acta Metall.*, **25**, 695–710.

Maki, T., Furutani, S. and Tamura, I. (1989): 'Shape memory effect related to thin plate martensite with large thermal hysteresis in ausaged Fe-Ni-Co-Ti alloy', *ISIJ Int.*, **29**, 438–445.

Martínez, J., Aurelio, G., Cuello, G.J., Cotes, S.M. and Desimoni, J. (2006): 'Structural properties of FCC and HCP phases in FeMnSi alloys: a neutron diffraction experiment', *Mater. Sci. & Eng. A*, **437**, 323–327.

Matsumura, O., Furusako, S., Furukawa, T. and Otsuka, H. (1996): 'Formation of surface texture and anisotropy of shape memory effect in Fe-Mn-Si alloy', *ISIJ Int.*, **36**, 1103–1108.

Matsuya, T., Yoneyama, N., Kumai, S. and Sato, A. (2000): 'Grain size effect on the microstructure of deformed Fe-Mn-Si based shape memory alloys', *Materials Sci. Forum*, **327–328**, 267–270.

Melton, K.N., Simpson, J. and Duerig, T.W. (1986): 'A new wide hysteresis NiTi based shape memory alloy and its application', *Proc. ICOMAT'86*, Nara, Japan, The Japan Institute of Metals, Sendai, 1053–1058.

Mizoguchi, T., Akimisu, M. and Chikazumi, S. (1973): *J. Phys. Soc. Japan*, **34**, 932–938.

Moyer, J.M. and Ansell, G.S. (1975): 'The volume expansion accompanying the martensite transformation in iron-carbon alloys', *Metall. Mater. Trans.*, **6**(9), 1785–1791.

Murakami, M., Otsuka, H., Suzuki, H.G. and Matsuda, S. (1987): 'Complete shape memory effect in polycrystalline Fe-Mn-Si alloys', *Proc. ICOMAT-86*, Japan Institute of Metals, Sendai, 985–990.

Noskova, N.I. and Pavlov, V.A. (1962): *Physics Metals Metallogr.*, **14**, 87–92.

Ogawa, K. and Kajiwara, S. (1993): 'HREM study of stress-induced transformation structures in an Fe-Mn-Si-Cr-Ni shape memory alloy', *Mater. Trans. JIM*, **34**, 1169–1176.

Ono, Y., Nakatshu, H. and Takaki, S. (1997): 'Effect of NbC particles on $\gamma \rightarrow \varepsilon$ transformation in Fe-22 mass% Mn alloys', *Nippon Kinzoku Gakkaishi*, **61**, 580–585.

Oshima, R. and Sugiyama, M. (1982): 'Martensite transformation in Fe-Pd alloys', *Proc. Int. Conf. on Martensitic Transformations*, Leuven, Belgium, *J. de Physique*, C-4, No. 12, C4–383.

Otsuka, H. (1992): 'Fe-Mn-Si based shape memory alloys', *Mat. Res. Soc. Symp. Proc.*, **246**, 309–320.

© Woodhead Publishing Limited, 2012

Otsuka, H., Murakami, M. and Matsuda, S. (1989): 'Improvement in shape memory effect of Fe-Mn-Si alloys by thermomechanical treatment', *Proc. MRS Int. Meeting on Advanced Materials*, Ikebukuro, Japan, Vol. 9, M. Doyama, S. Somiya, R. Chang (eds.), MRS, Pittsburgh, PA, 451–456.

Otsuka, H., Yamada H., Tanahashi, H. and Maruyama, T. (1990): 'Shape memory effects in Fe-Mn-Si-Cr-Ni polycrystalline alloys', *Proc. Int. Conf. on Martensitic Transformations (ICOMAT'89)*, B.C. Muddle (ed.), *Materials Sci. Forum*, **56–58**, 655–660.

Otsuka K. and Wayman, C.M. (1998a): 'Martensitic transformations: crystallography', in *Shape Memory Materials*, K. Otsuka and C.M. Wayman (eds.), Cambridge University Press, Cambridge, 5–21.

Otsuka K. and Wayman, C.M. (1998b): 'Mechanism of shape memory and superelasticity' in *Shape Memory Materials*, K. Otsuka and C.M. Wayman (eds.), Cambridge University Press, Cambridge, 27–48.

Otsuka, K., Nakamura, T. and Shimizu, K. (1974): 'Electron microscopy study of stress-induced acicular β_1' martensite in CuAlNi alloy', *Trans. JIM*, **15**, 201–210.

Reed, R.P. and Schramm, R.E. (1974): 'Relationship between stacking-fault energy and x-ray measurements of stacking-fault probability and microstrain', *J. Applied Physics*, **45**(11), 4705–4711.

Rong, Y., He, G., Guo, Z., Chen, S. and Hsu, T.Y. (2002): 'X-ray peak shift determination of deformation fault probability in Fe-Mn-Si alloys', *J. Mater. Sci. Technol.*, **18**, 459–461.

Sade, M., Halter, K. and Hornbogen, E. (1988): 'The effect of thermal cycling on the transformation behaviour of Fe-Mn-Si shape memory alloys', *Z. Metallk.*, **79**, 487–491.

Sato, A., Chisima, E., Soma, K. and Mori, T. (1982): 'Shape memory effect in $\gamma \leftrightarrow \varepsilon$ transformation in Fe-30Mn-1Si alloy single crystals', *Acta Metall.*, **30**, 1177–1183.

Sato, A., Chisima, E., Yamaji, Y. and Mori, T. (1984): 'Orientation and composition dependencies of shape memory effect in Fe-Mn-Si alloys', *Acta Metall.*, **32**, 539–547.

Sato, A., Yamaji, E. and Mori, T. (1986): 'Physical properties controlling shape memory effect in Fe-Mn-Si alloys', *Acta Metall.*, **34**, 287–294.

Schetky, L. McD. (1994): 'The current staus on industrial applications for shape memory alloys', *Proc. Advanced Materials '93*, *Vol. 18B*, *Shape Memory and Hydrides*, K. Otsuka and Y. Fukai (eds.), Elsevier, Oxford, 1131–1141.

Schumann, H. (1967): *Arch. Eisenhutt.*, **38**, 647–656.

Shibata, A., Yonezawa, H., Yabuuchi, K., Morito, S., Furuhara, T. and Maki, T. (2006): 'Relation between martensite morphology and volume change accompanying fcc to bcc martensitic transformation in Fe-Ni-Co alloys', *Mater. Sci. & Eng. A*, *Structural Materials: Properties*, *Microstructure and Processing*, **438–440**, 241–245.

Shimizu, K. and Otsuka, K. (1975): 'Optical and electron microscope observations of transformation and deformation characteristics in Cu-Al-Ni Marmem alloys', in *Shape Memory Effects in Alloys*, J. Perkins (ed.), Met. Soc. AIME, Plenum Press, New York, 59–87.

Stanford, N. and Dunne, D. (2006a): 'Optimisation of alloy design and hot rolling conditions for shape memory in Fe-Mn-Si-based alloys', *ISIJ Int.*, **46**, 1703–1711.

Stanford, N. and Dunne, D. (2006b): 'Effect of NbC and TiC precipitation on shape memory in an iron-based alloy', *J. Mater. Sci.*, **41,** 4883–4891.

Stanford, N. and Dunne, D. (2010): 'Effect of Si on the reversibility of stress-induced martensite in Fe-Mn-Si shape memory alloys', *Acta Mater.*, **58**, 6752–6762.

© Woodhead Publishing Limited, 2012

Stanford, N., Chen, K., Dunne, D. and Jin, X. (2007): 'Effect of alloying additions on the SFE, Néel temperature and shape memory effect in Fe-Mn-Si alloys', *ISIJ Int.*, **47**, 883–889.

Stanford, N., Dunne, D.P. and Li, H. (2008): 'Re-examination of the effect of NbC precipitation on shape memory in Fe-Mn-Si-based alloys', *Scripta Mater.*, **58**, 583–586.

Sulaiman, S. (2008): 'Structure and properties of the heat affected zone of P91 creep resistant steel', PhD Thesis, University of Wollongong, NSW, Australia.

Tadaki, T. and Shimizu, K. (1973): 'High tetragonality of the thermoelastic Fe_3Pt martensite and small volume change during transformation', *Scripta Metall.*, **9**, 771–776.

Tadaki, T., Katsuki, K. and Shimizu, K. (1976): *Suppl. Trans. Jpn Inst. Met.*, **17**, 187.

Takezawa, K., Shindo, T. and Sato, S. (1976): 'Shape memory effect in β_1 CuZnAl', *Scripta Metall.*, **10**, 13–18.

Tamura, I. and Wayman, C.M. (1992): 'Martensitic transformations and mechanical effects', in *Martensite*, G.B. Olsen and W.S. Owen (eds.), ASM Int., Metals Park, OH, 227–242.

Tan, S., Lao, J. and Yang, S. (1991): 'Influence of grain size on shape memory effect of polycrystalline Fe-Mn-Si alloys', *Scripta Metall.*, **25**, 2613–2615.

Tanaka, Y., Himuro, Y., Omori, T., Sutou, Y., Kainuma R. and Ishida, K. (2006): 'Martensitic transformation and shape memory effect in ausaged Fe-Ni-Si-Co alloys', *Mater. Sci. and Eng. A*, *Structural Materials: Properties*, *Microstructure and Processing*, **438–440**, 1030–1035.

Tanaka, Y., Himuro, Y., Kainuma, R., Sutou, Y., Omori, T. and Ishida, K. (2010): 'Ferrous polycrystalline shape-memory alloy showing huge superelasticity', *Science*, **327**, 1488–1490.

Tomota, Y. and Maki, T. (2000): 'Reversibility in martensitic transformation and shape memory in high Mn ferrous alloys', *Materials Sci. Forum*, **327–328**, 191–198.

Tsuzaki, K., Natsume, Y., Kurokawa, Y. and Maki, T. (1992): 'Improvement of the shape memory effect in Fe-Mn-Si alloys by the addition of carbon', *Scripta Metall.*, **27**, 471–473.

Tsuzaki, K., Murakami, Y., Natsume, Y. and Maki, T. (1994): 'Role of pre-straining of austenite in the improvement of shape memory effect in Fe-33Mn-6Si alloy', *Advanced Materials '93*, *Vol. B*, *Shape Memory Materials and Hydrides*, K. Otsuka and Y. Fukai (eds.), Elsevier Science, Amsterdam, 961–970.

Ullakko, K.M. and Gavriljuk, V.G. (1992): 'Mobility of coherent interfaces in freshly formed highly-tetragonal Fe-Ni and Fe-Ni-C martensites', *Proc. Int. Conf. on Martensitic Transformations*, Monterey, CA, C.M. Wayman and J. Perkins (eds.), Monterey Institute of Advanced Studies, 463–468.

Ullakko, K., Jakovenko, P. and Gavriljuk, V. (1996): 'High strength shape memory steels alloyed with nitrogen', *Scripta Mater.*, **35**, 473–478.

Umemoto, M. and Wayman, C.M. (1978): 'Effect of austenite ordering on the transformation temperature, transformation hysteresis and thermoelastic behaviour of Fe-Pt alloys', *Metall. Trans.*, **9A**, 891–897.

Van Humbeeck, J. (1999): 'Non-medical applications of shape memory alloys', *Mater. Sci. & Eng. A*, **273–275**, 134–148.

Volosevich, P.Yu., Gridnev, V.N. and Petrov, Yu.N. (1976): *Phys. Met. Metallogr.*, **42**, 126.

Wang, D., Ji, W., Han, M., Jia, D. and Liu, W. (2000): 'Influence of ausforming on substructures and shape memory behaviour in Fe-28Mn-6Si-5Cr alloy', *Mater. Sci. Forum*, **327–328**, 263–266.

© Woodhead Publishing Limited, 2012

Wang, S.H., Wen, Y.H., Zhang, W. and Li, N. (2007): 'Improvement of shape memory effect in an Fe-Mn-Si-Cr-Ni-Nb-C alloy through ageing after pre-deformation', *J. Alloys & Compds*, **437**, 208–210.

Wayman, C.M. (1971): 'On memory effects related to martensitic transformations and observations in β brass and Fe_3Pt', *Scripta Metall.*, **5**, 489–492.

Wechsler, M.S., Lieberman, D.S. and Read, T.A. (1953): 'On the theory of formation of martensite', *Trans. AIME*, **197**, 1503–1515.

Wen, Y.H., Yan, M. and Li, N. (2004): 'Effects of carbon addition and aging on the shape memory effect of Fe-Mn-Si-Cr-Ni alloys', *Scripta Mater.*, **50**, 441–444.

Wen, Y.H., Zhang, W., Li, N., Peng, H.B. and Xiong, L.R. (2007): 'Principle and realization of improving shape memory effect in Fe-Mn-Si-Cr-Ni alloy through aligned precipitations of second phase particles', *Acta Mater.*, **55**, 6526–6534.

Winchell, P.G. and Speich, G.K. (1970): 'Point-defect-supported martensite tetragonality', *Acta Metall.*, **18**, 53–62.

Wu, X. and Hsu, T.Y. (1999): 'Audio-frequency internal friction characteristics associated with the γ→ε martensitic transformation in Fe-Mn-Si based alloys', *Mater. Trans. JIM*, **40**, 112–117.

Yang, J.H. and Wayman, C.M. (1992): 'Self-accommodation and shape memory mechanism of ε-martensite – II. Theoretical considerations', *Materials Characterization*, **28**, 37–47.

Yang, J.H., Chen, H. and Wayman, C.M. (1992): 'Development of Fe-based shape memory alloys associated with face-centred cubic–hexagonal close-packed martensitic transformation. Part I. Shape memory behaviour', *Met. Trans.*, **23A**, 1431–1437.

Yoneyama, N., Setoda, T., Kumai, S., Sato, A., Komatsu, M. and Kiritani, M. (2003): 'Structural refinement and strengthening of an Fe-Mn-Si-Cr-Ni shape memory alloy by high speed rolling', *Mater. Sci. & Eng. A*, **350**, 125–132.

Zhou, W., Jiang, B., Qi, X. and Hsu, T.Y. (1998): 'The influence of rare earths elements on shape memory effect in Fe-Mn-Si alloys', *Scripta Mater.*, **39**, 1483–1487.

© Woodhead Publishing Limited, 2012

5
Tempering of martensite in carbon steels

G. KRAUSS, Colorado School of Mines, USA

Abstract: The changes in microstructure and substructure produced by tempering martensitic microstructures in carbon steels are described and are divided into aging and tempering phenomena. Aging phenomena occur prior to carbide formation, and tempering phenomena are classified primarily by carbide reactions, including eta or epsilon transition carbide formation at low tempering temperatures, cementite and chi carbide formation at higher temperatures in martensitic crystals or by transformation of retained austenite, and alloy carbide formation at the highest tempering temperatures. Changes in the matrix martensitic microstructures produced by recovery, recrystallization, and grain boundary rearrangement are also described, and carbon- and alloying-element-dependent changes in structure are noted.

Key words: martensite, carbon steel, alloy steel, tempering of martensite, transition carbides, carbide formation, alloy carbides, tempered martensite recovery, tempered martensite recrystallization, tempered martensite grain boundary changes.

5.1 Introduction

Tempering as discussed in this chapter is defined as the heating of a ferrous microstructure, most commonly produced by martensitic phase transformation, to any temperature below the lower critical (Ac_1) temperature, the temperature at which austenite forms in a given steel. In view of the latter rather broad definition, a wide range of microstructures and mechanical properties can be produced by tempering, depending on steel composition and intensity of the tempering heat treatment. Almost always an object of tempering is to increase ductility, fracture resistance, and toughness, a benefit that is accompanied by reduced but useable strength for a given application. However, in some temperature ranges, embrittlement phenomena can be introduced, reducing fracture resistance. The mechanical property changes and embrittlements caused by tempering are discussed in detail elsewhere (Krauss, 2005). The purpose of this chapter is to review the phase transformations, namely the transformation of retained austenite and carbide precipitation reactions, and other substructural and microstructural changes produced by tempering of carbon steels cooled or quenched to martensitic microstructures.

In view of its scientific and practical importance, tempering has received considerable attention in the literature: several conferences have been held

© Woodhead Publishing Limited, 2012

and a number of review articles have been written about tempering (Speich and Leslie, 1972; Speich, 1973; Imai, 1975; TMS, 1983; Krauss, 1984; ISS, 1992; Speich and Taylor, 1992). This chapter reviews this information and incorporates the results from other references to amplify the existing knowledge base regarding structural changes produced by tempering of carbon steels with starting martensitic microstructures.

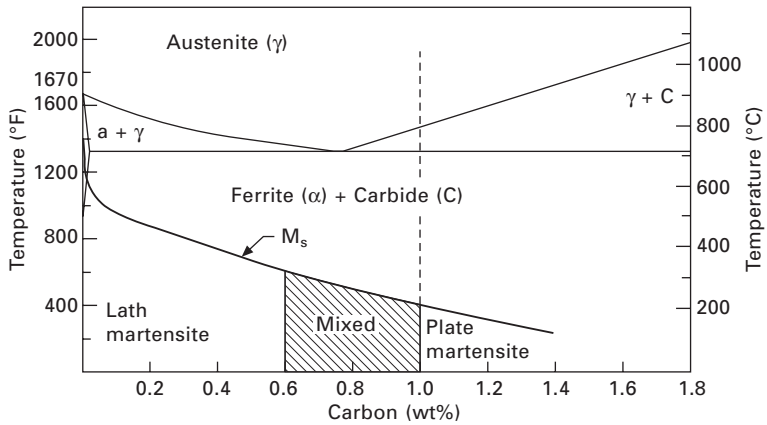
5.2 Martensitic microstructures prior to tempering heat treatments

Ferrous martensitic microstructures, by virtue of the diffusionless, shear transformation of austenite, are highly unstable during subsequent aging and tempering. The shear transformation requires a lattice deformation from fcc austenite to bct martensite and a lattice invariant deformation to maintain an undistorted and unrotated habit plane (Bilby and Christian, 1961; Wayman, 1964). The lattice invariant deformation is accomplished by dislocation slip or fine twinning, and together with the volume expansion from fcc to bct crystal lattices, creates a high density of imperfections within martensite crystals. The dislocation density in low-carbon lath martensite has been determined to be on the order of 10^{12} per square centimeter (Speich, 1969), and several investigations show that dislocation densities in martensite increase with increased steel carbon content (Norstrom, 1976; Kelly and Kehoe, 1976; Morito *et al.*, 2003).

The instability of martensite and martensitic microstructures is due to many features characteristic of the as-quenched condition. The very high density of dislocations in as-quenched martensite creates sites for carbon atom segregation and carbide precipitation, and a driving force for recovery and recrystallization. The absence of diffusion causes carbon and alloying element supersaturation within martensite crystals and a driving force for segregation and carbide precipitation. Austenite that is retained as part of almost all martensitic microstructures in carbon steels is unstable below Ac_1, and must transform during tempering. Martensite crystals are very fine, and the high density of martensite crystal interfaces provides a driving force for boundary rearrangement by recovery or grain growth mechanisms during tempering.

Figure 5.1 shows martensite morphology and M_S temperatures as a function of steel carbon content (Marder and Krauss, 1967; Krauss and Marder, 1971; Krauss, 2005). In steels with lath martensite morphology, the martensite crystals form parallel to one another in blocks and packets, and in steels with plate martensite morpholgy the martensite crystals form non-parallel to one another. The decrease in M_S with increasing carbon content affects two phenomena relative to tempering. First, the high M_S temperatures of low-carbon steels, and the associated large range of cooling

© Woodhead Publishing Limited, 2012



5.1 M_S temperatures and morphologies of martensite as a function of carbon content superimposed on the iron–carbon diagram (Krauss, 2005).

to room temperature, sometimes causes microstructural changes and carbon atom rearrangement to occur during quenching or cooling prior to applied tempering heat treatments. Second, the low M_S temperatures of higher carbon steels causes large volume fractions of austenite to be retained, and limits diffusional changes during quenching. Alloying elements lower M_S temperatures, and high-Ni alloys with subzero M_S temperatures have been used to study the effect of tempering in martensitic structures that have not been affected by changes produced by diffusion during quenching or room temperature aging (Winchell and Cohen, 1962; Chen and Winchell, 1980).

5.2.1 Cementite formation during quenching

The high M_S temperatures of low carbon steels make possible the formation of cementite in martensite crystals during quenching, a process referred to as autotempering or quench tempering (Aborn, 1956). Large section sizes that reduce cooling rates as well as high temperatures below M_S permit the necessary carbon atom diffusion for cementite formation (Speich, 1969; Foley *et al.*, 1993). The cementite particles are plate-shaped and are present in high density in larger crystals of martensite that form closest to M_S.

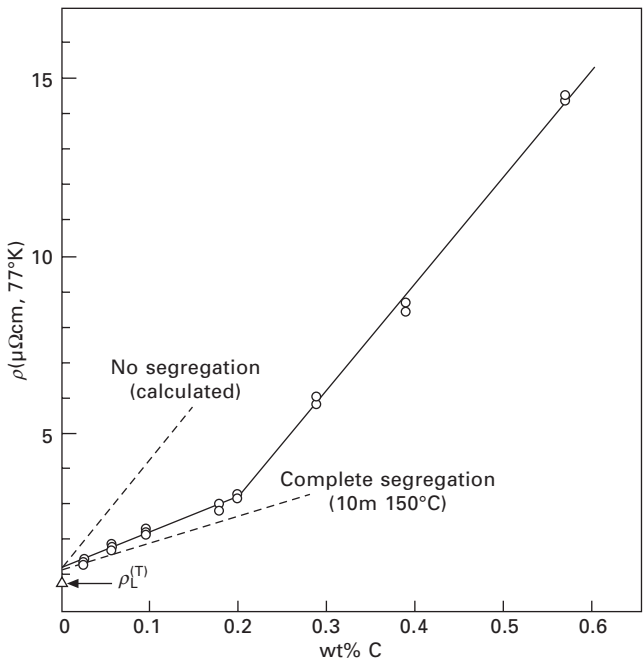
5.2.2 Carbon atom segregation during quenching and room temperature aging

The diffusionless transformation of austenite to martensite in steels requires that carbon atoms dissolved in the interstitial octahedral sites of austenite are trapped in c-axis interstitial octahedral sites that produce the tetragonality of

© Woodhead Publishing Limited, 2012

bct martensite. However, the high diffusivity of carbon atoms and the high density of dislocations in martensite crystals make it almost impossible to prevent redistribution of carbon to dislocation strain fields during quenching and room temperature aging. Almost complete segregation of the carbon to dislocations and lath boundaries in martenstic steels containing up to 0.2% carbon has been proposed based on the electrical resistivity measurements shown in Fig. 5.2 (Speich, 1969). The lower slope of the resistivity curve for martensite containing less than 0.2% carbon was attributed to the absence of carbon-filled octahedral sites that serve as electron scattering centers; above 0.2% carbon, with saturation of imperfections with segregated carbon atoms, octahedral scattering centers containing carbon increase the slope of the electrical resistivity curve. A significant contribution to the strength of as-quenched hardenable steels such as SAE 4340, a low-alloy, medium-carbon steel, containing nominally 0.40% carbon, 1.80% nickel, 0.65% chromium, and 0.25% molybdenum, has been attributed to rearrangement of carbon atoms during quenching (Leslie and Sober, 1967).

Field ion/atom probe microscopy has made possible direct evidence for carbon atom segregation to dislocation strain fields in martensite (Miller *et al.*, 1981; Chang *et al.*, 1992). Carbon atom distribution around screw dislocations in martensite appears to have three-fold symmetry consistent



5.2 Electrical resistivity of as-quenched martensite measured at 77°K as a function of carbon content (Speich, 1969).

© Woodhead Publishing Limited, 2012

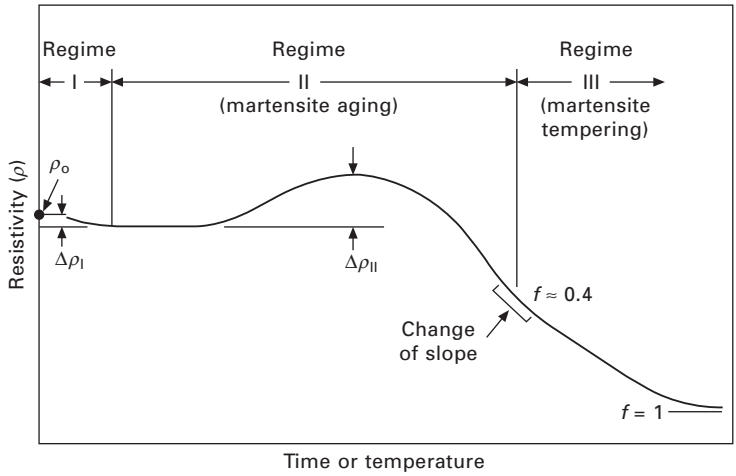
with proposed interstitial atom distribution in the strain field around screw dislocations (Cochardt *et al.*, 1955). The atom probe studies confirm Speich's conclusion that about 90% of the carbon atoms in as-quenched low-carbon steel are segregated to dislocations. The experimental studies that show substantial segregation of carbon atoms to dislocations are supported by a theoretical statistical mechanics study based on a generalized perfect lattice gas model that shows 85% of carbon atoms in an untempered, martensitic, low-carbon steel are segregated to dislocations at equilibrium (Kalish and Roberts, 1971).

5.3 Classification of aging and tempering stages: general considerations

A framework for the classification of the various stages of tempering, driven by the need to understand the practical effects of tempering, was developed in the 1950s by Morris Cohen, his students and colleagues (Roberts *et al.*, 1953; Lement *et al.*, 1954, 1955; Werner *et al.*, 1957). Other investigators in that period also identified and characterized the microstructures in various stages of tempering in the Cohen system (Hyam and Nutting, 1956). That classification system was based on the identification of the carbide phases and the changes in carbide distributions that were formed and evolved during the typically used commercial ranges of temperatures used for tempering. The substructural and microstructural changes produced in the various stages of tempering have been more completely described as further research and advanced instrumentation have been applied, but the basic framework established by Cohen remains valid and will be used in this review.

In addition to the classification of the stages of tempering based largely on carbide formation, a number of changes in martensitic fine structure that precede carbide formation have been identified. Certainly the segregation of carbon atoms to dislocations in martensite during quenching and room temperature aging of low-carbon and medium-carbon steels as described above falls into this category of change. Other changes based on carbon atom rearrangement have been documented, primarily in alloys with high nickel content and high carbon content with M_S temperatures close to or below room temperature. In the latter alloys, the initial changes in martensitic microstructures can be studied without the complications of carbon atom diffusion during quenching. Figure 5.3 shows schematically changes in electrical resistivity as a function of holding time or temperature in iron-nickel-carbon martensite (Sherman *et al.*, 1983). Early stages of change are attributed to aging reactions and later changes to tempering. Following this suggestion, the non-carbide-forming early changes in martensitic structure are classified as aging stages, and the carbide-forming stages, as before, are classified as the stages of tempering.

© Woodhead Publishing Limited, 2012



5.3 Schematic curve of resistivity related to aging and tempering stages of martensite in an iron-nickel-carbon alloy as a function of time and temperature (Sherman *et al.,* 1983).

5.4 Changes in martensitic fine structure due to aging

In addition to carbon atom segregation and clustering, a number of other changes in fine structure have been observed when martensite is aged or heated at temperatures from –40 to 100°C. These changes have been documented by electrical resistivity, x-ray diffraction, Mössbauer spectroscopy, and transmission electron microscopy (TEM), and have been reviewed in several references (Olson and Cohen, 1983; Krauss, 1984; Speich and Taylor, 1992).

One type of structural change has been identified as a modulation of the martensitic fine structure on {102} planes due to clusters of atoms about 1 nm in size spaced at 1–2 nm on the {102} planes (Kusunoki and Nagakura, 1981; Nagakura *et al.*, 1983). Satellite spots around the fundamental spots in electron diffraction patterns are associated with the modulated structure. Spinodal decomposition has been suggested as a mechanism for the formation of the modulated structure (Taylor, 1985; Speich and Taylor, 1992). Another structural change induced by aging, identified by superlattice spots in electron diffraction patterns, is a long period ordered phase with an orthorhombic crystal structure (Nagakura and Toyoshima, 1979; Nagakura *et al.*, 1983).

© Woodhead Publishing Limited, 2012

5.5 The stages of tempering

5.5.1 The first stage of tempering

This stage of tempering is characterized by the precipitation of very fine transition carbides in crystals of martensite at temperatures approximately between 100 and 200°C. The carbide was first identified as having a hexagonal crystal structure with a chemistry of $Fe_{2.4}C$ and was designated epsilon (ε) carbide (Jack, 1951). Kinetic studies showed that the transition carbide formation was dependent on the diffusion of carbon in martensite with an activation energy of 16,000 cal/mol (Roberts *et al.*, 1953). More recently the transition carbide has been identified as having an orthorhombic crystal structure isomorphous with transition-metal carbides of the type M_2C and designated eta (η) carbide (Hirotsu and Nagakura, 1972, 1974).

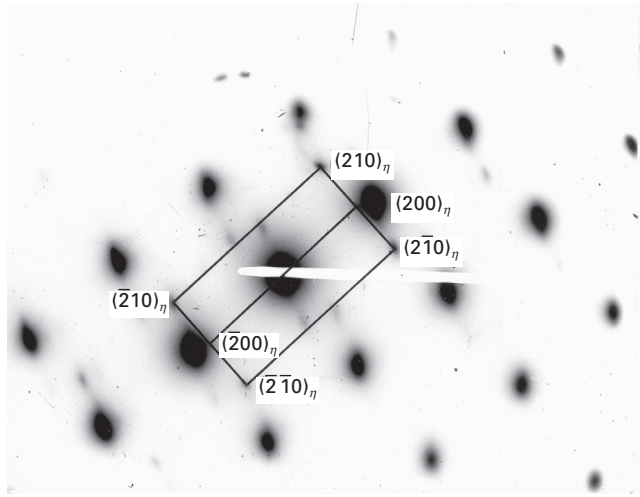
Figure 5.4 shows an electron diffraction pattern from a crystal of plate martensite in an iron 1.22% carbon alloy tempered at 150°C (Williamson *et al.*, 1979a). The crystal contained transition carbides present as rows of fine particles 2–4 nm in size. The diffraction patterns from the transition carbides are indexed assuming the hexagonal lattice of epsilon or the orthorhombic lattice of eta carbide, as shown in Figs 5.4(a) and (b). The indexing of the pattern assuming eta carbide is somewhat better than that assuming epsilon carbide, but the issue of the actual crystal structure of the transition carbides remains (Ohmori and Tamura, 1992).

The first identification of the eta transition carbide was made in high carbon martensite, but since then eta carbide has been identified in steels containing 0.79% carbon (Shimizo and Okamoto, 1974), 0.50% carbon (Lee and Krauss, 1992), 0.45% carbon (Hirotsu and Nagakura, 1974), 0.30% carbon (Baozhu *et al.*, 1986), and 0.14% carbon (Okamoto, 1990). Figure 5.5 shows the distribution of eta transition carbides in a crystal of lath martensite in AISI 4130 steel, a low-alloy, medium-carbon steel, containing nominally 0.30% carbon, 0.80% chromium, and 0.20% molybdenum, tempered at 150°C.

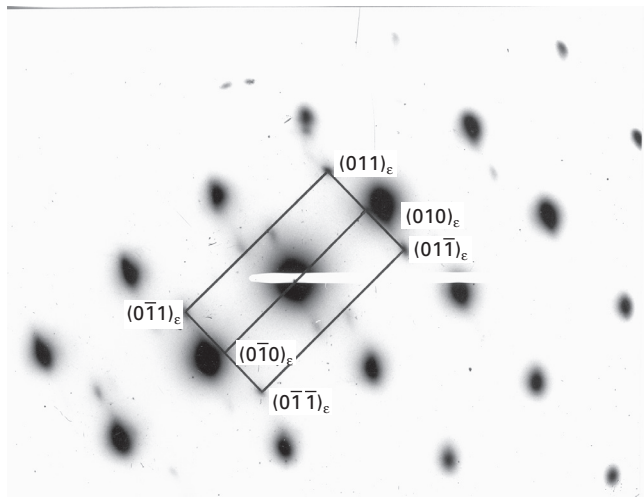
5.5.2 The second stage of tempering

Carbon steels are typically divided into three groups depending on their carbon content: low-carbon steels, containing up to 0.20% carbon, medium-carbon steels, containing between 0.20 and 0.5% carbon, and high-carbon steels, containing more than 0.5% carbon (Krauss, 2005). Untransformed or retained austenite is present in all groups of carbon steels quenched to martensite, and despite the high M_S temperatures of low-carbon steels, retained austenite has been found in the martensitic microstructures of steels containing as little as 0.14% carbon (Okamoto, 1990). As indicated in Fig. 5.1, as M_S decreases with increasing carbon content, the amount of austenite untransformed or

© Woodhead Publishing Limited, 2012



(a)

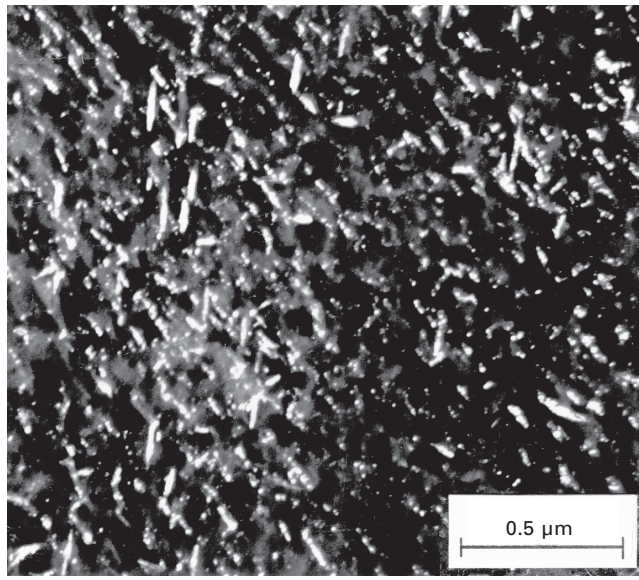


(b)

5.4 Electron diffraction pattern of the transition carbide formed in a crystal of martensite in an iron-1.22% carbon alloy indexed as (a) eta carbide, and (b) as epsilon carbide (Williamson *et al.*, 1979a.

retained at room temperature increases. In low- and medium-carbon steels the austenite is retained between parallel crystals of lath martensite, and in high-carbon steels the austenite is present in large volumes between non-parallel plates of martensite. Retained austenite is unstable below A_{C1} for a given steel and the transformation of retained austenite to a mixture of cementite and ferrite at temperatures typically between 200 and 300°C has been designated the second stage of tempering.

© Woodhead Publishing Limited, 2012

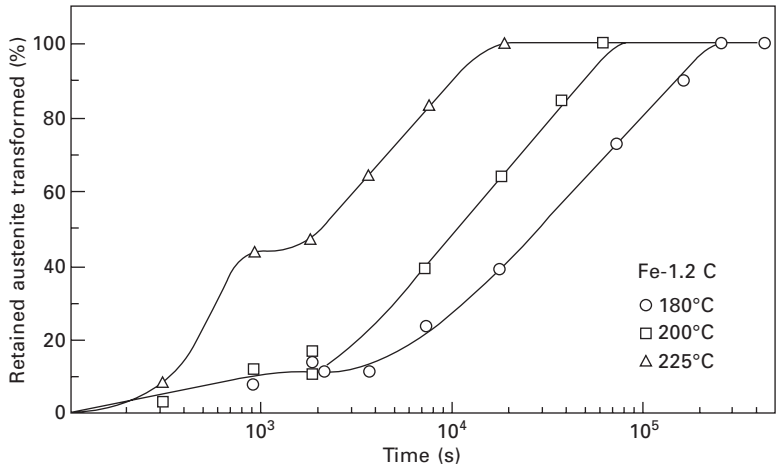


5.5 Eta transition carbides, the small nano-sized round white features, in a crystal of lath martensite in 4130 steel tempered at 150°C. Darkfield transmission electron micrograph taken with a transition carbide diffracted beam (courtesy of J.M.B. Losz while at the Colorado School of Mines).

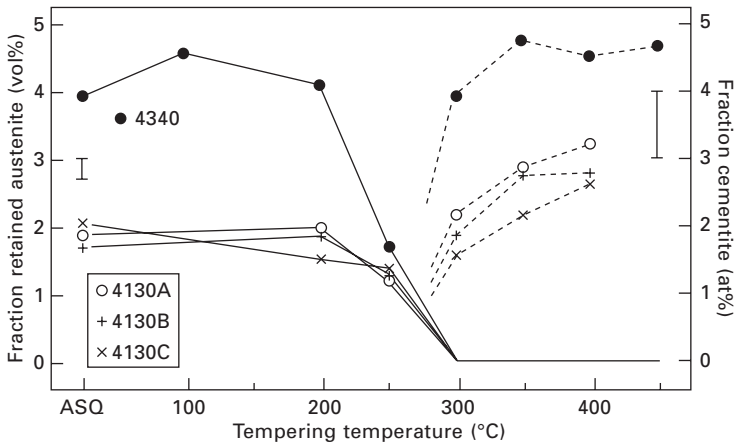
Figure 5.6 shows the transformation of retained austenite, determined by x-ray diffraction, in an iron-1.2% C alloy as a function of time at three temperatures (Balliett and Krauss, 1976). The samples contained 19% retained austenite in the starting as-quenched microstructure of plate martensite and retained austenite. From these curves, an activation energy of 27.5 kcal/mol for the transformation of retained austenite was determined, slightly less than the 29 kcal/mol determined earlier for the second stage of tempering by length change measurements (Roberts *et al.*, 1953). These values of activation energy are close to that for carbon diffusion in high-carbon austenite (Wells *et al.*, 1950), and show that the transformation of retained austenite during tempering is dependent on carbon diffusion in austenite. In high-carbon steels with large volume fractions of austenite, the product of the austenite transformation has been typically identified as various mixtures of bainitic ferrite and cementite (Roberts *et al.*, 1953; Balliett and Krauss, 1976; Nakamura and Nagakura, 1987; Kaputkin *et al.*, 2003).

Figure 5.7 shows the transformation of retained austenite, determined by Mössbauer spectroscopy, as a function of temperature in several medium-carbon steels (Williamson *et al.*, 1979b). The small amounts of retained austenite are stable until 200°C and the transformation is complete at

© Woodhead Publishing Limited, 2012



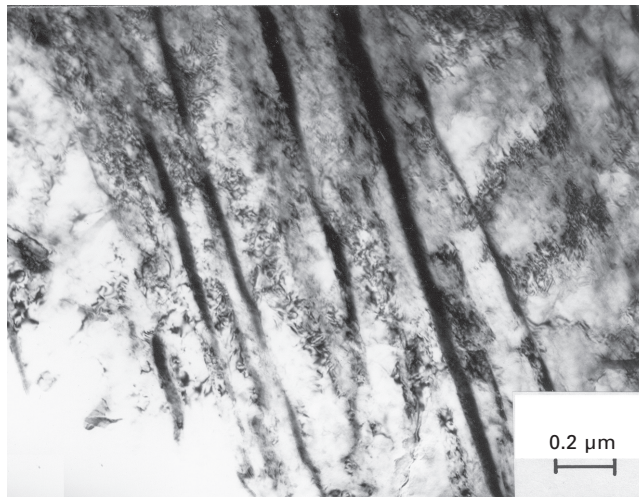
5.6 Transformation of retained austenite in the martensitic microstructure of an iron-1.22% carbon alloy as a function of time at various tempering temperatures (Balliett and Krauss, 1976).



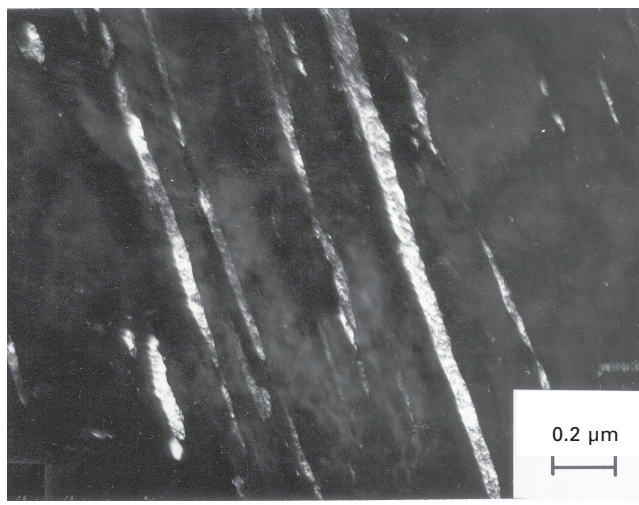
5.7 Retained austenite and cementite in various as-quenched medium-carbon steels as a function of tempering for 1 h at temperatures shown (Williamson *et al.,* 1979b).

300°C. The resulting microstructure now contains coarse interlath plates of cementite, as shown in Fig. 5.8, and is responsible for a form of reduced fracture toughness termed tempered martensite embrittlement (Materkowski and Krauss, 1979; Krauss, 2005).

© Woodhead Publishing Limited, 2012



(a)



(b)

5.8 Interlath cementite formed in the martensitic microstructure of AISI 4340 steel quench and tempered at 350°C: (a) bright-field transmisson electron micrograph (cementite appears black), and (b) dark-field transmission electron micrograph taken with a cementite diffracted beam (cementite appears white) (Materkowski and Krauss, 1979).

5.5.3 The third stage of tempering: general considerations

This stage of tempering effectively starts when the transition carbide is replaced by cementite or theta carbide (θ), Fe_3C, and in plain carbon steels

© Woodhead Publishing Limited, 2012

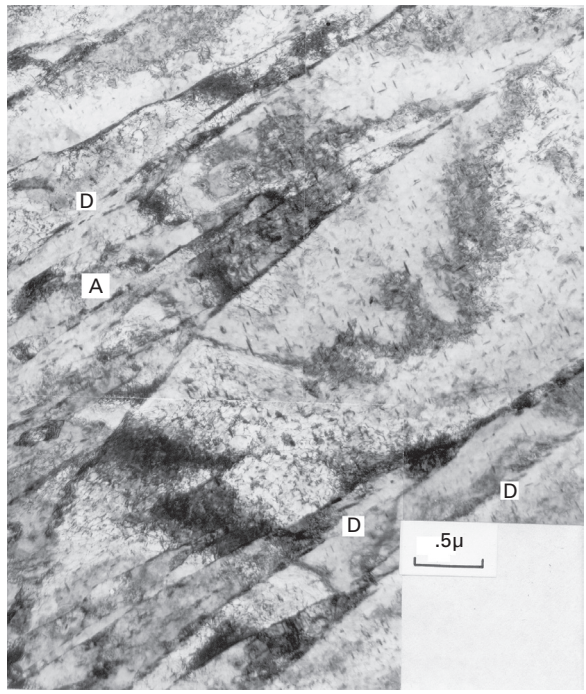
and iron-carbon alloys is considered to extend to the A_{C1} temperature. The microstructural changes within this range of tempering are dramatic, not only from the standpoint of the cementite particle size, morphology, and distribution, but also from the changes in the microstructure of the parent martensitic matrix, now ferrite because carbon supersaturation has been completely relieved by cementite formation. Despite the fact that the phases in steels tempered in the third stage are ferrite and cementite, the microstructure is still referred to as tempered martensite, because it originates from martensitic microstructures, and retains some of the morphological features of martensite. The microstructural changes are highly influenced by alloying elements, as discussed below, and to some extent, carbon content, in view of the fact that the first carbide to form in high-carbon martensite might be chi carbide (χ). The large number of microstructural changes that occur within the presently recognized third stage of tempering might warrant future classification changes, but this chapter will accept, as current state-of-the-art, the term third stage. Carbide and matrix changes within the third stage, although interdependent, are described separately in the following sections.

5.5.4 The third stage of tempering: carbide considerations

The beginning of the third stage of tempering begins with the formation of cementite, θ carbide, with a stoichiometry of Fe_3C, within martensite crystals, at martensite crystal boundaries, and at prior austenitic grain boundaries, and proceeds in parallel with the second stage formation of cementite from the transformation of austenite. Within martensitic crystals the transition carbides are replaced by intralath cementite crystals that nucleate at the transition carbides but grow from the eta carbide particles rather than forming *in-situ* with the transition carbides because of different habit plane requirements (Nakamura and Nagakura, 1986; Lee and Krauss, 1992). The cementite crystals grow as fine platelets with $\{110\}_m$ habit planes (Sarikaya *et al.*, 1983), as shown in Fig. 5.9 and similar to those in autotempered martensite (Aborn, 1956; Foley *et al.*, 1993). With increasing tempering temperature, the cementite particles coarsen, spheroidize, and eventually grow by Ostwald ripening, a mechanism by which small particles dissolve and large particles grow in order to minimize surface to volume ratios (Oriani, 1964). Rapid heating to tempering temperatures has been shown to produce more uniform and finer dispersions of cementite than slower heating (Furuhara *et al.*, 2004, 2009).

In high-carbon steels there is strong evidence that the first carbide that forms during the third stage of tempering is chi (χ) carbide with a stoichiometry of M_5C_2. The carbides form within martensite crystals and at martensite crystal interfaces and have been identified as χ carbide by electron diffraction and

© Woodhead Publishing Limited, 2012



5.9 Transmission electron micrograph of tempered martensite with intralath distributions of fine cementite plates (short, dark linear features) in an iron-0.2% carbon alloy tempered at 400°C for 1 min (Swarr and Krauss, 1976).

Mössbauer spectroscopy (Ma *et al.*, 1983). Some of the carbides form as a result of the transformation of retained austentite. High resolution electron microscope imaging of the carbides formed early in the third stage of tempering in high-carbon steels shows that carbide particles consist of a mixture of χ carbide and higher order carbides (Nagakura *et al.*, 1981). The intergrowth of the various carbides was referred to as microsyntactic growth. At higher tempering temperatures the χ carbide is replaced by cementite (Ohmori, 1972; Ma *et al.*, 1983).

5.5.5 The third stage of tempering: matrix considerations

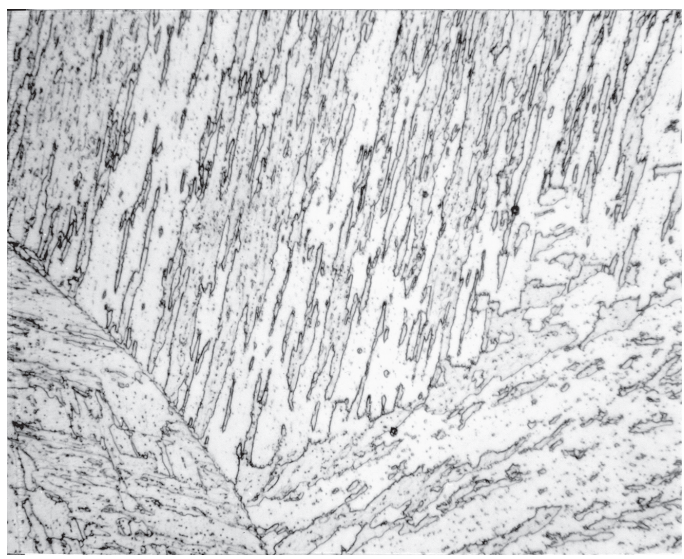
As described above, the matrix structure of as-quenched martensite is highly unstable, not only because of carbon supersaturation and unstable retained austenite, but also because of high intra-crystal dislocation density and large areas of interfaces bounding the fine martensite crystals of lath martensite. The latter characteristics of a martensitic microstructure create the driving forces for recovery, recrystallization and grain growth of the martensitic

© Woodhead Publishing Limited, 2012

microstructure during tempering. The kinetics and mechanisms of the matrix microstructural changes are highly dependent on alloying, and in general are significantly slowed by alloying effects.

Changes in the matrix of as-quenched martensite have been systematically studied in an iron-0.2% carbon alloy. The parent austenite grains are subdivided by transformation to martensite into blocks or packets of roughly parallel martensitic crystals, many of which are very fine and not resolvable in the light microscope. There is a very high martensite lath boundary area per unit volume of martensitic microstructure, on the order of 65,000 cm^{-1} (Apple *et al.*, 1974; Swarr and Krauss, 1976). Some of these boundaries are low angle where adjacent crystals of martensite have the same crystallographic orientation, and some are high angle where adjacent crystals have different orientations. On tempering into the third stage, the lath boundary area drops significantly. For example, in the iron-0.2% carbon alloy, after tempering for only one minute at 400°C, the martensite boundary area per unit volume decreases to 40,500 cm^{-1}. Similar drastic decreases in boundary area were measured over a range of tempering temperatures, and have been shown to be largely a result of the disappearance of low angle boundaries (Caron and Krauss, 1972).

Figure 5.10 shows the microstructure of an iron-0.2% carbon alloy after tempering at 700°C for 2 hours. Spheroidized cementite particles



5.10 Light micrograph, nital etch of microstructure of lath martensite in an iron-0.2% carbon alloy after tempering at 700°C for 2h. The packet structure of lath martensite with parallel crystals is still present, but the remnant martensitic crystals are significantly coarsened (Caron and Krauss, 1972).

© Woodhead Publishing Limited, 2012

can be resolved in the light microscope, and coarse blocks of structure, differentiated by etching differences, still in the parallel packet alignment of lath martensite, characterize the microstructure. The fine martensitic crystals within the blocks have been eliminated, a change in microstructure attributed to recovery mechanisms associated with the low angle dislocation boundaries that separated parallel martensite crystals with the same orientation. With increased tempering, the large angle parallel boundaries rearrange to form equiaxed ferritic grains to minimize grain boundary energy. Thus the equilibrium microstructure of spheroidized carbides and equiaxed ferrite grains in highly tempered high purity iron-carbon alloys and low-alloy steels may be a result of a sequence of recovery and grain growth mechanisms (Caron and Krauss, 1972; Hobbs *et al.*, 1972). Recovery mechanisms, involved not only in the elimination of the low angle martensite interfaces but also in the reduction of intracrystal dislocation densities, apparently lower strain energy to below the critical amount necessary for recrystallization.

In contrast to the above development of highly tempered microstructures, recrystallization by the nucleation and growth of new grains within a tempered lath martensitic microstructure has also been documented (Galibois and Dube, 1964, 1967; Tua *et al.*, 1992). Unrecrystallized lath martensitic microstructures around recrystallized grains are characterized by high dislocation densities, and recrystallized grains grow through retained distributions of spheroidized cementite particles. Thus sufficient strain energy to drive recrystallization is available, perhaps as a result of alloying-element suppression of dislocation substructure recovery in the martensite. The latter explanation has been proposed for the role that cobalt, a weak carbide-forming element, plays in the achievement of super-hard high-speed tool steels during secondary hardening (Speich, 1990). Recrystallization of lath martensite has also been documented in ultra-low-carbon steels (Tsuchiyama *et al.*, 2001, 2010). In these steels recystallization occurs by nucleation at prior austenite grain boundaries, creating bulges that grow into the martensitic matrix, as effectively shown by electron back scattered diffraction (EBSD) analysis.

5.5.6 The fourth stage of tempering: alloying element effects

The fourth stage of tempering is roughly defined as the alloy-dependent stage of tempering that overlaps the high-temperature tempering range of the third stage of tempering. Quench and tempered steels are alloyed for two major reasons:

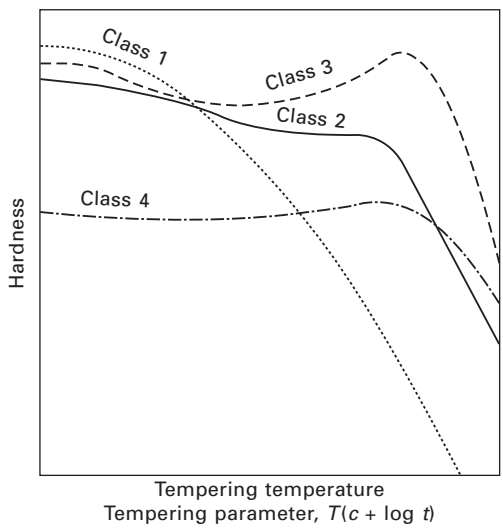
1. to provide hardenability and make martensite formation possible in various section sizes and various quenching media, and
2. to control microstructural and mechanical property changes during the higher temperature ranges of tempering.

© Woodhead Publishing Limited, 2012

At low tempering temperatures, roughly up to 200 or 300°C, structural changes are caused primarily by carbon atom rearrangement and recovery mechanisms. At higher tempering temperatures, the effects of alloying-element-dependent microstructural changes range from a retardation of softening during the third stage of tempering in low-alloy steels to alloy carbide precipitation and secondary hardening in highly alloyed steels.

Figure 5.11 shows schematically, based on hardness changes as a function of tempering intensity, four classes of alloy-dependent tempering behavior in steels quenched to martensite and tempered (Roberts *et al.*, 1998). Class 1 is characteristic of plain carbon and low alloy steels in which hardness decreases continuously; alloying elements slow the hardness decrease. Class 2 represents steels sufficiently alloyed for carbide precipitation but short of the amount needed for secondary hardening. Class 4 may be classified similarly but with a lower carbon concentration that produces a lower as-quenched hardness. Class 3 behavior is typical of highly alloyed tool steels capable of fine alloy carbide precipitation that provides a peak in hardness, termed secondary hardening, after tempering at high temperatures. Secondary hardening by carbide forming elements is extensively characterized in the tool steel literature (Roberts *et al.*, 1998); the effects of non-carbide-forming elements have also been evaluated (Garrison, 2006).

Many of the alloying elements added to steels, especially the transition elements as shown in Table 5.1 (Toth, 1971), are strong carbide-forming elements, and elements such as Cr, Mo, W, V, and Nb are added to slow



5.11 Schematic classification of tempering response to alloying, based on changes in hardness, as a function of tempering intensity (Roberts *et al.*, 1998).

© Woodhead Publishing Limited, 2012

Table 5.1 Transition metal carbides. The elements of Group VIII are weak-carbide forming elements or do not form carbides

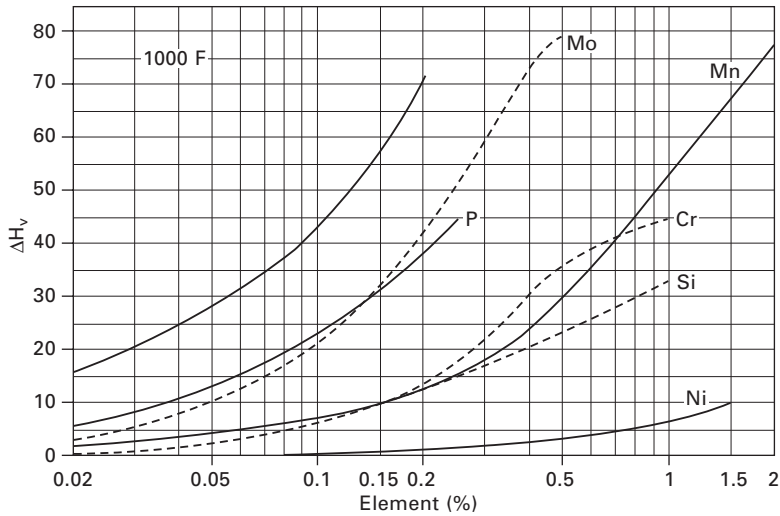
III	IV	V	VI	VII	VIII		
$Sc_{2-3}C$ ScC_2 Sc_2C_3	TiC	V_2C VC	$Cr_{23}C_6$ Cr_7C_3 Cr_3C_2	$Mn_{23}C_6$ Mn_3C MN_5C_2 Mn_7C_3	Fe_3C	Co_3C Co_2C	Ni_3C
Y_2C Y_2C_3 YC_2	ZrC	Nb_2C NbC	Mo_2C Mo_3C_2 MoC_{1-x}	TcC	Ru	Rh	Pd
LaC_2	HfC	Ta_2C TaC	W_2C W_3C_2 WC	ReC	OsC	Ir	Pt

Source: Toth, 1971

hardness decreases or even increase hardness during tempering or service depending on heat treatment and amounts. The binary element carbides shown in Table 5.1 often incorporate other carbide-forming elements that contribute to the precipitation kinetics and stability of the carbides (Roberts *et al.*, 1998). Also, in a given steel with multiple alloying elements, several different carbides might precipitate. For example, in a 2.25% chromium-1.0% molybdenum steel, tempering at temperatures above 500°C with increasing tempering intensity successively produces carbide dispersions of Fe_3C + Mo_2C, Fe_3C + Mo_2C + Cr_7C_3, $M_{23}C_6$ + Cr_7C_3, and $M_{23}C_6$ + M_6C, where M indicates combinations of Cr and Mo in a given type of carbide (Baker and Nutting, 1959). In steels highly alloyed with chromium and containing boron, the boron may be incorporated into the boro-carbides $M_{23}(B\text{-}C)_6$ and $M_7(B\text{-}C)_3$ (Kobayashi *et al.*, 2002). Alloy carbides may form by nucleation at pre-existing cementite particles, by nucleation in the ferritic matrix on dislocations, or at prior austenite grain boundaries and martensite lath boundaries (Honeycombe and Bhadeshia, 1995).

Austenitizing treatments place alloying elements in solution, and therefore to create dispersions of alloy carbides during tempering, the diffusion of substitutional elements to nucleating carbide particles is necessary. In contrast to carbon, an interstitial alloying element, the diffusion of the substitutional carbide-forming elements is sluggish, and higher tempering temperatures are necessary to drive the substitutional atom rearrangement. Coarsening of the as-quenched martensitc microstructures is retarded and incipient carbide formation slows the hardness decreasing characteristic of iron-carbon alloys and plain carbon steels. Figure 5.12 shows the retardation of hardness loss associated with various alloying elements relative to that in unalloyed steel after tempering at 540°C for 1 h (Grange *et al.*, 1977). By virtue of increased diffusivity at high tempering temperatures, the strong carbide-forming elements create and maintain fine substructures as well as fine carbide precipitate dispersions that resist coarsening and softening. Increasingly, electron back scattered diffraction (EBSD), in combination with

© Woodhead Publishing Limited, 2012



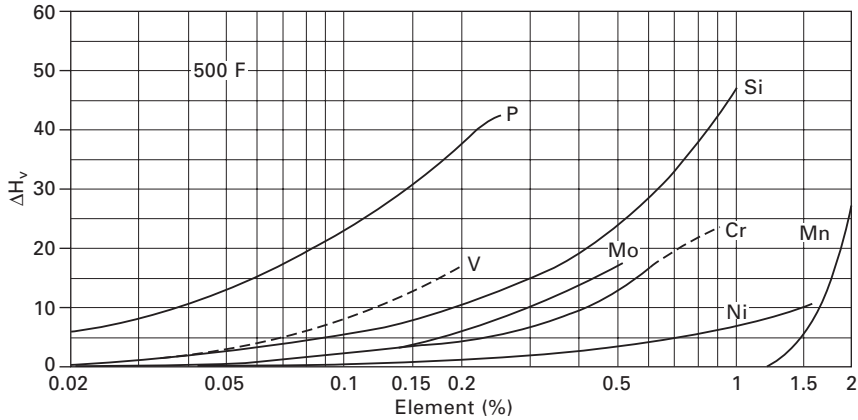
5.12 Effect of alloying elements on the retardation of softening relative to iron-carbon alloys after tempering at 540°C for 1 h (Grange *et al.,* 1977).

other experimental techniques, is being used to characterize martensitic matrix changes as well as alloy carbide formation in high alloy steels (Kitahara *et al*., 2006; Tamura *et al*., 2006).

In contrast to high tempering temperature behavior, during low temperature tempering treatments characteristic of the first stage of tempering, substitutional carbide-forming elements cannot effectively diffuse (Zhu *et al*., 2007), and alloying elements have quite different effects on microstructural and mechanical property changes. Figure 5.13 shows the effect that various elements have on the retention of hardness after tempering at 260°C, a temperature in the transition between the first and third stages of tempering. The carbide-forming substitutional elements, Mn, Mo, V and Cr are at the very beginning stages of diffusing into cementite, and Ni, a non-carbide-forming element is just beginning to be rejected from cementite (Zhu *et al*., 2007). As a result those alloying elements have a minimal effect on microstructural and hardness changes during low temperature tempering.

However, as shown in Fig. 5.13, silicon, a non-carbide-forming element, has a strong effect on maintaining hardness during tempering at temperatures where in low alloy steels cementite is beginning to replace transition carbides and contribute to softening in low-silicon steels. Silicon has long been known to provide resistance to softening in alloy steels during tempering when added at high levels, 1.0% or greater, above those typically produced during steelmaking of alloy steels (Allten and Payson, 1953; Owen, 1954; Altstetter *et al*., 1962). The kinetics of the first stage of tempering, when

© Woodhead Publishing Limited, 2012



5.13 Effect of alloying elements on retardation of softening relative to iron-carbon alloys after tempering at 260°C for 1 h (Grange *et al.,* 1977).

stable dispersions of transition carbides are produced, are unaffected by silicon, but the kinetics of the second and third stages, both of which require the formation of cementite, are significantly reduced and require higher tempering temperatures to activate. Similar to the suppression of cementite formation by silicon in the second stage of tempering, cementite formation in upper bainite is suppressed, and bainitic microstructures of ferrite and austenite are produced instead of those of ferrite and cementite in low silicon steels (Bhadeshia and Edmonds, 1979).

Atom probe analysis of silicon steel shows that the solubility of silicon in cementite is very low, inhibiting cementite formation and requiring that silicon be rejected from cementite, concentrating silicon adjacent to cementite interfaces (Barnard *et al*., 1982; Zhu *et al*., 2007). The diffusion of silicon away from enriched regions adjacent to cementite further contributes to reduced rates of cementite formation. In contrast, transition carbides incorporate the silicon content of the parent martensite. Thus the strong effect of silicon shown in Fig. 5.13 is due to the retention of the hardness associated with fine dispersions of transition carbides and the prevention of the formation of coarse dispersions of cementite that lower hardness in low silicon steels. In commercial low alloy steels, high silicon additions not only maintain high strength and hardness produced by transition carbide dispersions, but raise the temperatures necessary to prevent tempered martensite embrittlement due to the formation of cementite during the beginning third and second stages of tempering (Altstetter *et al*., 1962; Youngblood and Raghavan, 1977).

© Woodhead Publishing Limited, 2012

5.6 Conclusions

This chapter has shown that considerable scientific and technical knowledge regarding the effects of tempering of carbon steels quenched to martensitic microstructures has been acquired. Nevertheless, in order to predict and optimize microstructural and substructural changes, systematic studies of all phases of tempering would be warranted based on questions that remain in the current state-of-the-art database. Future studies should incorporate the many well-established analytical techniques such as transmission electon microscopy and electron diffraction for the characterization of substructural features such as nanometer-sized carbide precipitates and dislocation configurations, as well as newer techniques such as EBSD and three-dimensional atom probe characterization for changes in matrix crystal morphologies, chemistries, and orientation.

The effects of tempering are very much alloy dependent, as shown in the discussion of alloying effects during high temperature tempering, and therefore classifying those effects into the single category of Stage four may require further classification or dropping the little-used term from the literature. Classification is difficult in view of the facts that structure changes continuously with increasing tempering time and temperature, and that many of the mechanisms of microstructural change occur simultaneously.

The driving force for the evaluation of structural changes produced by tempering of martensitic steels has always been to produce structures that produce the best combination of strength and fracture resistance for a given application. By design, this text concentrates on phase transformations, so this chapter has made little reference to the mechanical properties that couple to the effects of tempering on structure. Nevertheless, it is the correlation of mechanical behavior to structure that is a critically important aspect of the selection of steel chemistry and heat treatment processing of hardened steels. Questions remain about the response of tempered microstructures to stress, specifically about the interaction of dislocations, dislocation multiplication, strain hardening, and embrittlement phenomena during deformation. Also, all of the structural features that have been discussed are either reversible or irreversible traps for hydrogen, and identifying the effects of tempering that produce microstructures that minimize susceptibility to hydrogen embrittlement requires attention (Wei and Tsuzaki, 2005). Answers to such questions will evolve by building on the considerable knowledge base about tempered steel structures that already exists as described in this chapter.

5.7 References

Aborn R H (1956), 'Low Carbon Martensites', *Transactions ASM*, 48, 51–85.

Allten A G, Payson P (1953), 'The Effect of Silicon on the Tempering of Martensite', *Transactions ASM*, 45, 498–532.

© Woodhead Publishing Limited, 2012

Altstetter C J, Cohen M, Averbach B L (1962), 'Effect of Silicon on the Tempering of AISI 43xx Steels', *Transactions ASM*, 55, 287–300.

Apple C A, Caron R N, Krauss G (1974), 'Packet Microstructure in an Fe-0.2% C Martensite', *Metallurgical Transactions*, 5, 593–599.

Baker R G, Nutting J (1959), 'The Tempering of 2 1/4 Cr-1 Mo Steel after Quenching and Normalizing', *Journal of the Iron and Steel Institute*, 192, 257–268.

Balliett T, Krauss G (1976), 'The Effect of the First and Second Stages of Tempering on Microcracking in Martensite of an Fe-1.22 Alloy', *Metallurgical Transactions A*, 7A, 81–86.

Baozhu G, Losz J M B, Krauss G (1986), 'Substructure and Flow Strength of Low-Temperature Tempered Medium Carbon Martensite', *Proceedings of the International Conference on Martensitic Transformations*, Sendai, The Japan Institute of Metals, 367–374.

Barnard S J, Smith G D W, Garrat-Reed A J, Vander Sande J (1982), 'Atom Probe Studies: 1) Role of Silicon in Tempering of Steel and 2) Low Temperature Chromium Diffusivity in Bainite', in *Solid – Solid Phase Transformations*, Warrendale, PA, TMS-AIME, 881–885.

Bhadeshia H K D H, Edmonds D V (1979), 'The Bainite Transformation in a Silicon Steel', *Metallurgical Transactions A*, 10A, 895–907.

Bilby B A, Christian J W (1961), 'The Crystallography of Martensite Transformations', *Journal of the Iron and Steel Institute*, 197, 122–131.

Caron R N, Krauss G (1972), 'The Tempering of Fe-C Lath Martensite', *Metallurgical Transactions*, 3, 2381–2389.

Chang L, Barnard S J, Smith G D W (1992), 'The Segregation of Carbon Atoms to Dislocations in Low-Carbon Martensites: Studies by Field Ion Microscopy and Atom Probe Microanalysis', in Krauss G and Repas P E, *Fundamentals of Aging and Tempering in Bainitic and Martenstic Steel Products*, Warrendale, PA, ISS, 19–28.

Chen P C, Winchell P G (1980), 'Martensite Lattice Changes During Tempering', *Metallurgical Transactions A*, 11A, 1333–1339.

Cochardt A W, Schoek G, Wiedersich H (1955), 'Interaction between Dislocations and Interstitial Atoms in Body Centered Cubic Metals', *Acta Metallurgica*, 3, 533–537.

Foley R P, Weiss R K, Thompson S W, Krauss G (1993), 'Tempering Behavior of Martensitic Plate Steels Produced by Direct-Quench and Reaustenitize-and-Quench Processing', in Asfahani R and Tither G, *International Symposium on Low-Carbon Steels for the 90's*, Warrendale, PA, TMS, 243–256.

Furuhara T, Kobayashi K, Maki T (2004), 'Control of Cementite Precipitation in Lath Martensite by Rapid Heating and Tempering', *ISIJ International*, 44 (11), 1937–1944.

Furuhara T, Miyamoto G, Maki T (2009), 'Refinement of Cementite in Tempered Lath Martensite', Proceedings of the 17th IFHTSE Congress, *The Japan Society for Heat Treatment*, 49, Special Issue, 423–429.

Galibois A, Dube A (1964), 'Recrystallization Kinetics of Martensitic Extra-Low Carbon Steels', *Canadian Metallugical Quarterly*, 3 (4), 321–343.

Galibois A, Dube A (1967), 'Similarities between the Martensitic and Cold-Worked Structures of Steels', *Canadian Metallurgical Quarterly*, 6 (2), 121–136.

Garrison W M Jr (2006), 'A Comparison of the Effects of Cobalt, Silicon, Nickel and Aluminum on the Tempering Response of a Medium Chromium Secondary Hardening Steel', *ISIJ International*, 46(5), 782–784.

© Woodhead Publishing Limited, 2012

Grange R A, Hribal C R, Porter L F (1977), 'Hardness of Tempered Martensite in Carbon and Low-Alloy Steels', *Metallurgical Transactions A*, 8A, 1775–1785.

Hirotsu Y, Nagakura S (1972), 'Crystal Structure and Morphology of the Carbide Precipitated from Martensitic High Carbon Steel during the First Stage of Tempering', *Acta Metallurgica*, 20, 645–655.

Hirotsu Y, Nagakura S (1974), 'Electron Microscopy and Diffraction Study of the Carbide Precipitated at the First Stage of Tempering of Martenstic Medium Carbon Steel', *Transactions JIM*, 15, 129–134.

Hobbs R M, Lorimer G W, Ridley N (1972), 'Effect of Silicon on the Microstructure of Quenched and Tempered Medium-Carbon Steels', *JISI*, 210, 757–764.

Honeycombe R W K, Bhadeshia H K D H (1995), *Steels Microstructure and Properties*, 2nd edn, London, Edward Arnold.

Hyam E D, Nutting J (1956), 'The Tempering of Plain Carbon Steels', *Journal of the Iron and Steel Institute*, 179, 148–165.

Imai Y (1975), 'Phases in Quenched and Tempered Steels', *Transactions Japan Institute of Metals*, 16, 721–734.

ISS (1992), *Proceedings Gilbert R. Speich Symposium: Fundamentals of Aging and Tempering in Bainitic and Martensitc Steel Products*, Warrendale, PA, ISS.

Jack K H (1951), 'Structural Transformations in the Tempering of High Carbon Martensitic Steel', *JISI*, 169, 26–36.

Kalish D, Roberts E M (1971), 'On the Distribution of Carbon in Martensite', *Metallurgical Transactions*, 2, 2783–2790.

Kaputkin D E, Kaputkina L M, Prokoshkin S D (2003), 'Transformation of Retained Austenite during Tempering of High Carbon Steel', *Journal de Physique IV*, 112, 275–278.

Kelly P M, Kehoe M (1976), 'The Role of Dislocations and Interstitial Solute on the Strength of Ferrous Martensite', *Supplement to Transactions JIM*, 17, 399–404.

Kitahara H, Ueji R, Tsuji N, Minamino Y (2006), 'Crystallographic Features of Lath Martensite in Low-Carbon Steel', *Acta Materialia*, 54, 1279–1288.

Kobayashi S, Toshimori K, Nakai K, Ohmori Y, Asahi H, Muraki T (2002), 'Effects of Boron Addition on Tempering Processes in an Fe–9Cr–0.1C Alloy Martensite', *ISIJ International Supplement*, 42, S72–S76.

Krauss G (1984), 'Tempering and Structural Change in Ferrous Martensitic Structures', in Marder A R and Goldstein J I, *Phase Transformations in Ferrous Alloys*, Warrendale, PA, TMS, 101–123.

Krauss G (2005), *Steels: Processing*, *Structure*, *and Performance*, Materials Park, OH, ASM International.

Krauss G, Marder A R (1971), 'The Morphology of Martensite in Iron Alloys', *Metallurgical Transactions*, 2, 2343–2357.

Kusunoki M, Nagakura S (1981), 'Modulated Structure of Iron-Carbon Martensite Studied by Electron Microscopy and Diffraction', *Journal of Applied Crystallography*, 14, 329–336.

Lee H-C, Krauss G (1992), 'Intralath Carbide Transitions in Martensitic Medium-Carbon Steels Tempered between 200 and 300°C', in *Fundamentals of Aging and Tempering in Bainitic and Martensitic Steel Products*, Warrendale, PA, ISS, 39–43.

Lement B S, Averbach B L, Cohen M (1954), 'Microstructural Changes on Tempering Iron-Carbon Alloys', *Transactions ASM*, 46, 851–881.

Lement B S, Averbach B L Cohen M (1955), 'Further Study of Mircostructural Changes on Tempering Iron-Carbon Alloys', *Transactions ASM*, 47, 291–319.

© Woodhead Publishing Limited, 2012

Leslie W C, Sober R J (1967), 'The Strength of Ferrite and Martensite as Functions of Composition, Temperature, and Strain Rate', *Transactions ASM*, 60, 459–484.
Ma C-B, Ando T, Williamson D L, Krauss G (1983), 'Chi-Carbide in Tempered High Carbon Martensite', *Metallurgical Transactions A*, 14A, 1033–1045.
Marder A R, Krauss G (1967), 'The Morphology of Martensite in Iron Carbon Alloys', *Transactions ASM*, 60, 651–660.
Materkowski J P, Krauss G (1979), 'Tempered Martensite Embrittlement in SAE 4340 Steel', *Metallurgical Transactions A*, 10A, 1643–1651.
Miller M K, Beaven P A, Smith G D W (1981), 'A Study of the Early Stages of Tempering of Iron-Carbon Martensites by Atom Probe Field Ion Microscopy', *Metallurgical Transactions A*, 12A, 1197–1204.
Morito S, Nishikawa J, Maki T (2003), 'Dislocation Density Within Lath Martensite in Fe-C and Fe-Ni Alloys', *ISIJ International*, 43 (9), 1475–1477.
Nagakura S, Toyoshima M (1979), 'Crystal Structure and Morphology of the Ordered Phase in Iron-Carbon Martensite', *Transactions JIM*, 20, 110–119.
Nagakura S, Suzuki T, Kusunoki M (1981), 'Structure of the Precipitated Particles at the Third Stage of Tempering of Martensitic Iron-Carbon Steel Studied by High Resolution Electron Microscopy', *Transactions Japan Institute of Metals*, 22, 699–709.
Nagakura S, Hirotsu Y, Kusunoki M, Suzuki T, Nakamura Y (1983), 'Crystallographic Study of the Tempering of Martensitic Carbon Steel by Electron Microscopy and Diffraction', *Metallurgical Transactions A*, 14A, 1025–1031.
Nakamura Y, Nagakura S (1986), 'Structure of Iron-Carbide Martensite in the Transition Stage from the First to Third Stage of Tempering Studied by Electron Microscopy and Diffraction', *Transactions Japan Institute of Metals*, 27, 842–848.
Nakamura Y, Nagakura S (1987), 'Decomposition of Retained Austenite during the Tempering of Martensitic High Carbon Steel Studied by *in situ* Electron Microscopy', in *Proceedings of the International Conference on Martensitic Transformations*, Sendai, The Japan Institute of Metals, 386–391.
Norstrom L-A (1976), 'On the Yield Strength of Quenched Low-Carbon Lath Martensite', *Scandinavian Journal of Metallurgy*, 5, 159–165.
Ohmori Y (1972), 'χ-Carbide Formation and Its Transformation into Cementite During the Tempering of Martensite', *Transactions Japan Institute of Metals*, 13, 119–127.
Ohmori Y, Tamura I (1992), 'Epsilon Carbide Precipitation during Tempering of Plain Carbon Martensite', *Metallurgical Transactions A*, 23A, 2738–2751.
Okamoto S (1990), 'Strain Rate and Temperature Effects on Deformation Behavior and Mechanical Properties of As-Quenched Low-Carbon Martensite', MSc Thesis, Colorado School of Mines, Golden, CO.
Olson G B, Cohen M (1983), 'Early Stages of Aging and Tempering of Ferrous Martensite', *Metallurgical Transactions A*, 14A, 1057–1065.
Oriani R A (1964), 'Ostwald Ripening of Precipitates in Solid Matrices', *Acta Metallurgica*, 12, 1399–1409.
Owen W S (1954), 'The Effect of Silicon on the Kinetics of Tempering', *Transactions ASM*, 46, 812–829.
Roberts C S, Averbach B L, Cohen M (1953), 'The Mechanism and Kinetics of the First Stage of Tempering', *Transactions ASM*, 45, 576–604.
Roberts G, Krauss G, Kennedy R (1998), *Tool Steels*, 5th edn, Materials Park, OH, ASM International.
Sarikaya M, Jhingan A K, Thomas G (1983), 'Retained Austenite and Tempered Martensite Embrittlement in Medium Carbon Steels', *Metallurgical Transactions A*, 14A, 1121–1133.

© Woodhead Publishing Limited, 2012

Sherman A M, Eldis G T, Cohen M (1983), 'The Aging and Tempring of Iron-Nickel-Carbon Martensite', *Metallurgical Transactions A*, 14A, 995–1005.

Shimizo K, Okamoto H (1974), 'High Voltage Electron Microscopy Study of the Metastable Iron Carbide in a Eutectoid Fe-C Alloy', *Transactions of the Japan Institute of Metals*, 15, 193–199.

Speich G R (1969), 'Tempering of Low-Carbon Martensite', *Transactions TMS-AIME*, 245, 2552–2564.

Speich G R (1973), 'Tempered Ferrous Martensitic Structures' in *Metals Handbook*, *Vol. 8*, 8th edition, Materials Park, OH, American Society for Metals, 202–204.

Speich G R (1990), 'Secondary Hardening Ultrahigh Strength Steels', in Olson G B, Azrin M, Wright E S, *Innovations in Ultra-high Strength Steel Technology*, US Army Materials Technology Laboratory, 89–111.

Speich G R, Leslie W C (1972), 'Tempering of Steel', *Metallurgical Transactions*, 3, 1043–1054.

Speich G R, Taylor K A (1992), 'Tempering of Ferrous Martensites', in Olson G B and Owen W S, *Martensite*, Materials Park, OH, ASM International, 243–275.

Swarr T, Krauss G (1976), 'The Effect of Structure on the Deformation of As-Quenched and Tempered Martensite in an Fe-0.2 Pct C Alloy', *Metallurgical Transactions A*, 7A, 41–48.

Tamura M, Haruguchi Y, Yamashita M, Nagaoka Y, Ohinata K, Ohnishi K, Itoh E, Ito H, Shinozuka Y, Esaka H (2006), 'Tempering Behavior of 9%Cr-1%Mo-0.2%V Steel', *ISIJ International*, 46 (11), 1693–1702.

Taylor K A (1985), 'Aging Phenomena in Ferrous Materials', Sc.D. Thesis, Massachusetts Institute of Technology.

TMS (1983), 'The Peter G. Winchell Symposium on the Tempering of Steel', *Metallurgical Transactions A*, 14A, 991–1145.

Toth L E (1971), *Transition Metal Carbides and Nitrides*, New York, Academic Press.

Tsuchiyama T, Miyamoto Y, Takaki S (2001), 'Recrystallization of Lath Martensite with Bulge Nucleation and Growth Mechanism', *ISIJ International*, 41 (9), 1047–1052.

Tsuchiyama T, Natori M, Nakada N, Takaki S (2010), 'Conditions for Grain Boundary Bulging during Tempering of Lath Martensite in Ultra-low Carbon Steel', *ISIJ International*, 50 (5), 771–773.

Tua S J, Weiss R K, Krauss G, Thompson S W (1992), 'Structural Changes Induced by High-Temperature Tempering of Martensitic Plate Steels and a Mechanism for the Recrystallization of Martensite', in *Fundamentals of Aging and Tempering in Bainitic and Martensitic Steel Products*, Warrendale, PA, ISS, 53–66.

Wayman C M (1964), *Introduction to the Crystallography of Martensite Transformations,* New York, Macmillan.

Wei F-G, Tsuzaki K (2005), 'Response of Hydrogen Trapping Capability to Microstructural Change in Tempered Fe-0.2 C Martensite', *Scripta Materialia*, 52, 467–472.

Wells C, Batz W, Mehl R F (1950), 'Diffusion Coefficient of Carbon in Austenite', *Transactions AIME*, 188, 553–560.

Werner F E, Averbach B L, Cohen M (1957), 'The Tempering of Iron-Carbon Martensite Crystals', *Transactions ASM*, 49, 823–841.

Williamson D L, Nakazawa K, Krauss G (1979a), 'A Study of the Early Stages of Tempering in an Fe-1.2 Pct C Alloy', *Metallurgical Transactions A*, 10A, 1351–1362.

Williamson D L, Schupmann J P, Materkowski J P, Krauss G (1979b), 'Determination of Small Amounts of Austenite and Carbide in Hardened Medium Carbon Steel', *Metallurgical Transactions A*, 10A, 379–382.

© Woodhead Publishing Limited, 2012

Winchell P G, Cohen M (1962), 'The Strength of Martensite', *Transactions ASM*, 55, 347–361.

Youngblood J L, Raghavan M (1977), 'Correlation of Microstructure with Mechanical Properties of 300M Steel', *Metallurgical Transactions A*, 8A, 1439–1448.

Zhu C, Xiong X Y, Cerezo A, Hardwicke R, Krauss G, Smith G D W (2007), 'Three-dimensional Atom Probe Characterization of Alloy Element Partitioning in Cementite during Tempering of Alloy Steel', *Ultramicroscopy*, 107, 808–812.

© Woodhead Publishing Limited, 2012

6

Phase transformations in microalloyed high strength low alloy (HSLA) steels

R. C. COCHRANE, University of Leeds, UK

Abstract: The addition of small amounts of Nb, Ti or V singly or in combination has been the key to producing high strength low alloy (HSLA) steels with greatly improved mechanical properties. Such microalloyed HSLA steels are now commonplace in a huge variety of applications. The combinations of strength, toughness and formability that are possible are directly related to the way in which the steel is processed from the as-cast slab (usually) to the final plate or strip dimensions. The effects of microalloying result principally from three main effects on the austenite to ferrite transformation. Firstly, the microalloying additions form precipitates in both austenite and ferrite; this factor alone can be exploited in various ways to control the microstructure, hence mechanical properties, of the steel. Secondly, although present in relatively small quantities, there are discernible effects on ferrite transformations in terms of the hardenability of the steel. Finally, there are interactions between the various deformation sequences used in steel production and the presence of microalloying elements as solutes or precipitates which can be exploited to control microstructure. The interactions between processing, microstructural development and the effect of microalloying additions on the austenite-ferrite transformations are the topic of this chapter. A brief history of the use of microalloying is also given as is some indication of the range of mechanical properties that result from the current understanding of the role of microalloying additions.

Key words: phase transformations, microalloying, controlled processing, rolling, strain induced, precipitation, interphase, inclusions, acicular ferrite, ferrite, bainite, austenite grain size.

6.1 Introduction to microalloyed high strength low alloy (HSLA) steels

High strength low alloy (HSLA) steels are a broad group ranging in carbon content from 'ultra-low', typically between 0.02 and 0.04% up to ~0.2%. Any intentional alloying additions of elements such as Ni, Cr, Cu and Mo are limited to less than 1.5% in total whereas Mn ranges from 1 to 2% and Si up to ~0.5%. Within the confines of these compositional limits, such steels are little different from conventional C-Mn ferrite/pearlite steels and yield strengths greater than around 350 MPa are only achieved by making use of the martensite reaction followed by tempering. When, however, these steels are

© Woodhead Publishing Limited, 2012

alloyed with small additions of, principally, Nb, Ti and V, but occasionally Zr or Ta, a wide range of mechanical properties is possible. Such additions are used in a manner which can raise strength disproportionately to the amount added, for example, addition of 0.02%Nb can raise yield strength by as much as 200 MPa in comparison to the effect of, say, 1% Ni, which raises yield strength by 38 MPa. Thus the reason for the term usually used to denote these additions as 'microalloyed' becomes self-evident. Deliberate microalloying additions can range from 0.008% to above 0.1%. The former figure is set by residual elements from ores used in steelmaking; for example, Ti varies significantly from source to source, but typically, the trace amounts of Nb, V or Zr and Ta are below 0.005%. Some steels have been manufactured to deliberately exploit some of the beneficial influence of microallloying on mechanical properties through their effects on transformation behaviour. Such steels may use Nb additions up to 0.15% or V up to 0.45%.

Yield strengths obtainable can range up to approximately 500 MPa with a ferrite/pearlite microstructure and, potentially, up to 890 MPa for microstructures variously described as 'quasi-polygonal' ferrite, bainite or 'acicular ferrite'. An example of such a HSLA steel would be that used for current oil and gas transmission pipelines from Arctic regions; the specification of such a steel requires a yield strength in excess of 690 MPa coupled with a Charpy impact toughness in excess of 50 Joules at –50°C. Coupled with a need for economical welding and a moderate resistance to corrosion, the specification can only be met by careful attention to details of composition and processing control. In turn, this has necessitated a thorough understanding of how the transformation from austenite to ferrite and the other morphologies is influenced by microalloying additions, singly or in combination.

Microalloyed HSLA steels have been adopted and adapted for a huge variety of applications ranging from thin hot-rolled sheet for car body pressing through to structural steels for ship construction to sections for earthquake resistant buildings and high strength strip for domestic use, garden tools and the like. An extremely large tonnage has been and is being used for oil/gas extraction and transmission where extremely low S, <0.002%, and P, <0.01%, are essential. As mentioned above, such steels make use of sophisticated metallurgical concepts and closely controlled processing to achieve combinations of mechanical properties unheard of prior to the use of microalloying. The understanding of the role of microalloying elements in this respect has been an important reason for the now widespread, even ubiquitous, use of this class of steel.

This chapter will attempt to illustrate the developments in microalloyed steels outlined above in the light of the phase transformations taking place.

The effect of microalloying additions on the austenite/ferrite transformation can be broadly classified into three areas. Firstly, microalloying elements form carbides or nitrides with variable solubility in both ferrite and austenite. The

© Woodhead Publishing Limited, 2012

interaction between steel processing and precipitation of these compounds form the basis for the utility of microalloying additions. Secondly, they can act purely as alloying additions; however, as concentrations are small, there can be correspondingly modest changes in hardenability or transformation characteristics. An exception to this is during transformation in the weld heat affected zones (HAZ) around structural steel joints. Finally, the presence of microalloying elements in solid solution or as precipitates and their interactions with dislocation substructures produced during rolling in the austenite phase field has a marked influence on the subsequent development of the ferrite. The former effect is, historically, the more important, but the latter increasingly is of interest in the recent development of higher strength ferrite/'bainite' steels.

6.2 Brief historical review of the development of microalloyed steels

The principles from which this class of steel evolved were at first (as with most metallurgical principles) entirely empirically based on observations of the effect of alloying additions on the mechanical properties of steel. Thus, it was demonstrated in the 1930s that aluminium improved the mechanical properties of steels, although this had probably been known to the 'Sheffield little meisters' or steelmakers from the latter part of the 19th century but rejected as 'leading to poor steel cleanness'. Around the same time vanadium was shown to strengthen steels with carbon contents up to around 0.4%. Somewhat later titanium and niobium were used and again improvements in mechanical properties were demonstrated, but in this case improvements appeared to be confined to steels with carbon contents less than around 0.2%. Much of this historical development has been detailed by Morrison (2009) for Nb additions, Baker (2009) for V additions and, in more general terms, Gladman (1997), whereas some, particularly for Ti additions, has yet to be documented. A major development during the late 1950s and 1960s was the use of microalloying principally by aluminium, vanadium, titanium and especially niobium, to enhance the mechanical properties of low carbon, <0.2%, structural steels, although the use of Zr or Ta was occasionally suggested.

Some idea of the scale of these developments comes from reflecting on the volume of published literature on microalloyed steels. Over the past 40 years, a major international conference with the theme of microalloyed HSLA steels has taken place somewhere in the world every two to three years. HSLA steels also feature prominently in a multitude of national and international conferences on specific product areas such as steels for oil and gas transmission pipelines, steels for shipbuilding, general construction or strip steels for automotive products. Hence, there is a vast resource detailing the

© Woodhead Publishing Limited, 2012

effects of microalloying elements on the processing, heat treatment, mechanical behaviour and weldability of this class of steel. Some of the literature was documented in a review by Edmonds (2004) but no comprehensive listing has been compiled to the author's knowledge since that time.

A quantum jump in understanding came about in the 1950s following the work by Petch and co-workers (Armstrong *et al*., 1962) on the role of grain size in controlling yield strength. The later detailed studies during the late 1950s and early 1960s by many steel companies, particularly the United Steel Companies in the UK, built on this principle and identified the strengthening mechanisms controlling the mechanical properties of C-Mn steels. These (Irvine *et al*., 1967, 1970) and many other studies (see, for example, Pickering, 1978; Tamura *et al*., 1988; DeArdo, 2003) clarified the separate roles, grain refinement and precipitation, played by the microalloying additions in modifying mechanical properties. Both of these roles are a result of the changing solubility of the relevant carbides and/or nitrides as a function of temperature, as will be described in more detail later.

The first role to be identified was the realisation that a dispersion of fine particles of AlN, and later NbC, could be used to control austenite grain size in heat-treated or normalised steels. Simultaneously, the contribution to yield strength made by precipitation of microalloyed nitrides and/or carbides was identified and the differing behaviour of microalloying additions in rolled steels compared to that in the heat-treated or normalised (N) condition was clarified.

There followed a period where improvements in the properties of rolled steels appeared to be erratic but linked to aspects of the rolling schedule. The first observations of a duplex ferrite grain size distribution were made at this time and it was eventually deduced that this was due to the presence of both deformed and recrystallised austenite prior to ferrite transformation. In turn, this led to the identification of the role of Nb, in particular, and other microalloying additions (V, Ti) in retarding austenite recrystallisation rate. By introducing a delay during rolling over a restricted temperature range (the so-called hold temperature) and controlling the defomation sequence in terms of reduction at each rolling pass, major improvements in consistency of mechanical properties were made possible. Such controlled rolled (CR) steel grades were introduced by most steel producers.

Over the period between 1970 and 1985, details of the kinetics of Nb precipitation in austenite became well understood and formed the basis for design of controlled rolling schedules. The realisation that a combination of Nb precipitation and deformed austenite was essential to producing ferrite grain refinement also led to the widespread adaptation of rolling mills capable of withstanding the increased loads due to higher steel strength in the relevant temperature range. The term thermomechanical controlled rolling (TMCR) was widely used for such processing, emphasising the importance

© Woodhead Publishing Limited, 2012

of temperature and strain control during the rolling process. By the early 1980s, high strength, up to 550 MPa, and excellent toughness, were attainable from microalloyed HSLA CR or TMCR steels of much lower CEV (carbon equivalent value, usually given by C+Mn/6+(Cu+Ni)/15+V/5) compared to conventional heat-treated (normalised) low alloyed steels and at lower cost. In part, this reduced CEV was due to improvements in understanding the role of microalloying elements but, also, the demonstration that weldability was greatly improved as a consequence of the lower CEV. In particular, great strides were made in establishing the reasons for poor HAZ toughness associated with multiple microalloying additions for welded structural steelwork. Attempts were made at this time to produce TMCR steels with yield strength greater than 550 MPa by changes to the alloy content; these so-called 'acicular ferrite' Nb-Mo steels had the desirable attribute that the sharp yield point was suppressed which reduces the stresses needed for pipe forming.

Progressively, in the decades which followed, further improvements in terms of strength/toughness balance coupled with excellent weldability were made possible by the introduction of improved rolling and accelerated cooling technologies, termed thermomechanical controlled processing (TMCP). The introduction of a range of 'ultra-low', generally below 0.04%, carbon steels alloyed principally with Mn, Si or Ni and Cu additions, further extended the range of applicability of the principles behind microalloying additions to ferrite/bainite microstructures. These TMCP steels currently exemplify the 'state of the art'.

Current processing routes now exploit a range of microstructures, from conventional fine grained ferrite/pearlite steels to 'bainitic' (sometimes used as a generic reference to a range of ferritic microstructures, such as 'acicular' ferrite, apolygonal or quasi-polygonal ferrite or granular bainite) as well as quasi-polygonal ferrite steels capable of meeting specifications requiring strength levels up to 690 MPa (X100 grade) and toughness levels better than 100 J at –30°C. Throughout this development of HSLA microalloyed steels, the various technologies used to achieve steel specification requirements have been based on an understanding of how microalloying additions influence the austenite to ferrite and, latterly, bainite transformations.

6.3 Solubility of microalloying elements in austenite and ferrite

The major microalloying additions are Nb, V and Ti, all of which form carbides or nitrides with a cubic NaCl crystal structure with lattice parameters in the range 0.415–0.455 nm. The usual assumption is that the carbides or nitrides are stoichiometric, that is V:N is 1:1 in atomic terms or 54:14 in mass. Deviations from stoichiometry are common, for example 'VC' is more

© Woodhead Publishing Limited, 2012

likely to be closer to V_4C_3 in most steels (Baker, 2009; Goldschmidt, 1967) and NbC is also known to exhibit variable stoichiometry (Gladman, 1997; Goldschmidt, 1967). The formation of microalloy compounds in austenite or ferrite is usually written as an equation whose rate constant is termed the solubility product:

$$[X] + [\text{C or N}] = X(\text{C or N}) \qquad [6.1]$$

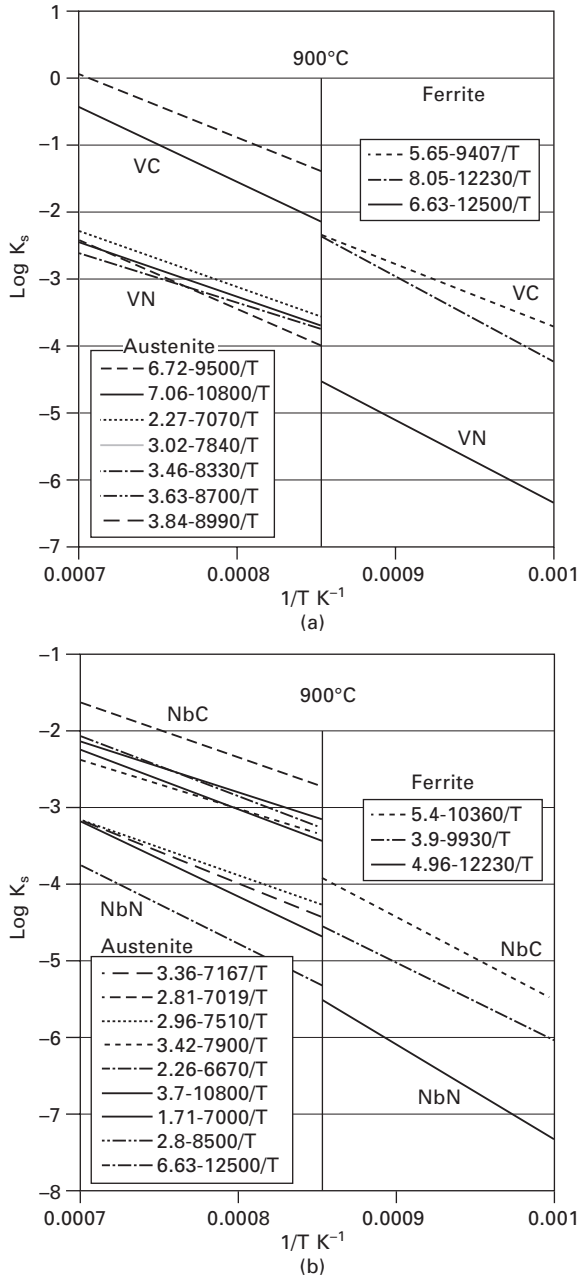
where $[X]$ is the amount of soluble Nb, V, Ti or Al in equilibrium with dissolved [C] or [N], at temperature T (K). (Note that Al does not form a stable carbide in iron alloys.) The solubility in either ferrite or austenite has the general form (see Gladman (1997) for a comprehensive treatment of this topic):

$$\text{Log } [X] [\text{C or N}] = A - B/T \qquad [6.2]$$

and Fig. 6.1 shows changes in solubility for some microalloy compounds taken from the review by Lagneborg *et al*. (1999). Other sources are quoted in the reviews by Morrison (2009), Baker (2009), Gladman (1997) and Narita (1975). The difference in solubility of the microalloy carbides and nitrides in austenite compared to that in ferrite is clearly illustrated. Given that the crystal structures are isomorphous, mutual intersolubility between the carbides and nitrides of Nb, V and Ti can be anticipated. In many cases it has been established that XC_yN_{1-y} compounds are formed, particularly for between Nb and V (Speer *et al*., 1987) or Nb and Ti; examples are given later. More recently, particle compositions have been confirmed directly by high resolution transmission electron microscopy (HRTEM) and electron energy loss spectroscopy (EELS) for a wide range of microalloyed steels.

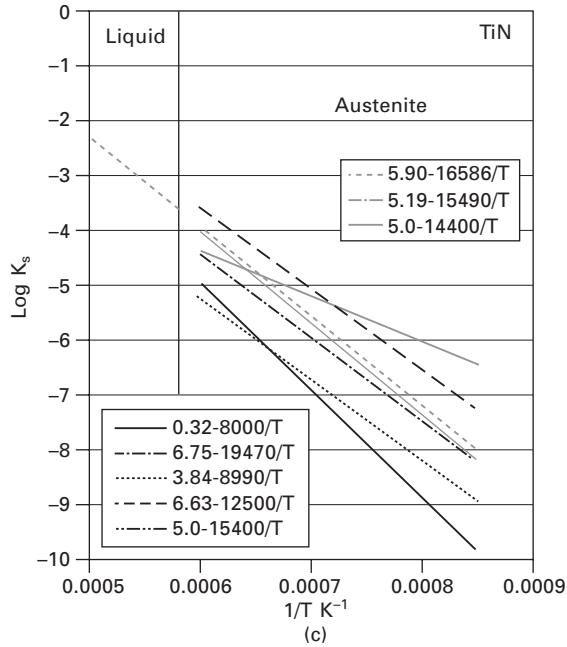
Al, which is unavoidably present as a result of steelmaking, and is not generally considered to be a microalloying addition in its own right, forms a hexagonal nitride with N with limited intersolubility with microalloy compounds. In almost all modern steelmaking, Al is present in excess of that needed for deoxidation purposes for clean steel production and, consequently, soluble Al is present and the stability of AlN with respect to other microalloy species can influence, or dictate, the precipitation sequences. Similarly, the use of Ti, which is a stronger nitride former than Al, can significantly change precipitation behaviour. Likewise,when B is added to raise hardenability to some HSLA steels where either Ti or Al (occasionally Zr) are also present, the competing reactions between BN and other more stable nitirides, AlN or TiN, demand careful consideration in order to optimise microstructure and mechanical properties. As an example, if sufficient soluble Al is present in V-N normalised steels, there is a change in the solubility of VC and VN as a result of the interactions between AlN, VN and VC given from the equations below and the solubility product for each reaction:

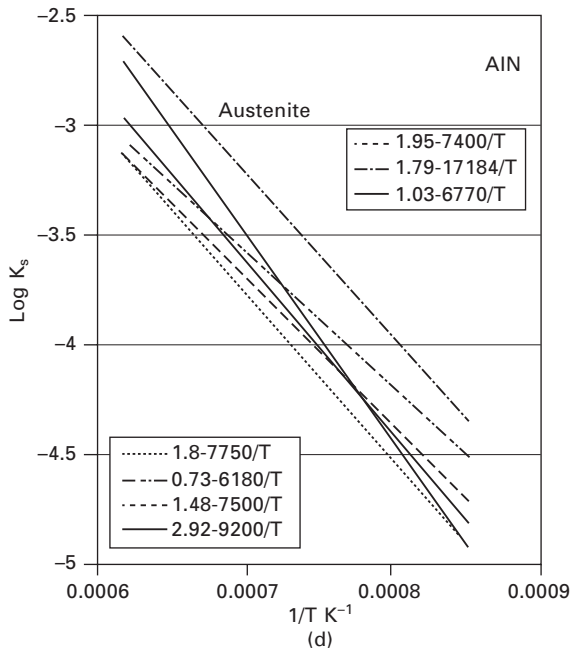
© Woodhead Publishing Limited, 2012



6.1 Relative solubilities of microalloy carbides and nitrides, the figures correspond to *A* and *B* constants in the text. Adapted from Lagneborg *et al.* (1999).

© Woodhead Publishing Limited, 2012





6.1 Continued

© Woodhead Publishing Limited, 2012

$$[V] + [N] = VN$$
$$[V] + [C] = VC \quad [6.3]$$
$$[Al] + [N] = AlN$$

where [N] is the amount of N in solution in equilibrium with either VN or AlN, whilst simultaneously satisfying the condition that [V] must also be in equilibrium with [C]. By solving the relevant simultaneous equations, the equilibrium amounts of [Al], [V], [C] and [N] can be derived.

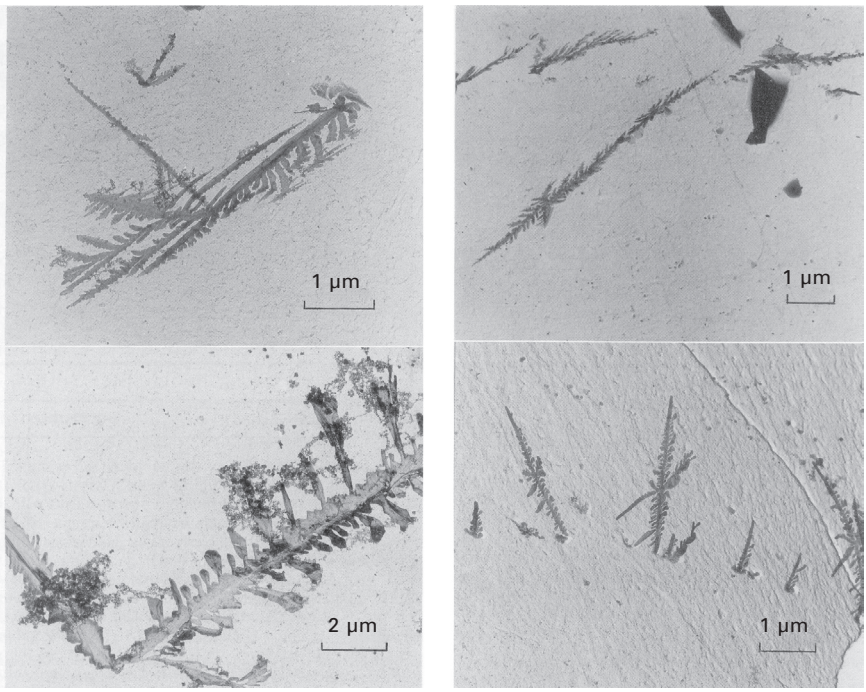
Many microalloyed HSLA steels contain multiple additions; typically these might be Nb-V, Nb-V-Ti or V-Ti with or without deliberate N additions as well as soluble Al. In the early work by Hudd *et al.* (1971) on such systems, it was generally assumed that each carbide or nitride precipitated independently of the others, the precipitation sequence starting with the least soluble compound, usually AlN, unless Ti has been added. Extensions of the simple example given above have been made to more complex systems such as Al-treated Nb-V-Ti-N C-Mn steels. Adrian (1992) and Houghton (1993) were amongst the first to attempt a thermodynamic evaluation of multiple microalloyed systems, concluding that complete equilibrium was rarely achieved in most steels and compounds of variable stoichiometry in terms of metal and interstitial content (C or N) can be expected. Modelling the precipitation sequence using ThermoCalc, Chemsage, MTDATA or similar thermodynamic software is now widely used to establish the amounts and composition of the phases present at equilibrium following the method devised by Hillert and Staffanson (1970). Nevertheless, there is a danger that excessive reliance on such tools for alloy design may underestimate the effects of non-equilibrium steel solidification conditions and subsequent rolling operations on precipitation sequences and, therefore, on the development of the desired ferrite structures needed for optimum mechanical properties.

6.4 Precipitation

6.4.1 Precipitation in cast steels

The increasing use of HRTEM, energy dispersive X-ray analysis (EDX) and EELS techniques is revealing that precipitation is more complex than that which might be expected from equilibrium conditions. In continuous cast slab, not only may some of the larger precipitates be cored in terms of the major microalloying additions but, depending on location in the slab, and therefore cooling rate, others may be more complex, consisting of two or more phases. Several different morphologies have been identified in Nb-Ti-V microalloyed steels (Raison, 1982; Chen *et al.*, 1987; Houghton *et al.*, 1982). Some examples are shown in Fig. 6.2, the 'dendritic' types are found mainly at grain boundaries whereas the 'star' morphology (Fig. 6.3) is more common

© Woodhead Publishing Limited, 2012

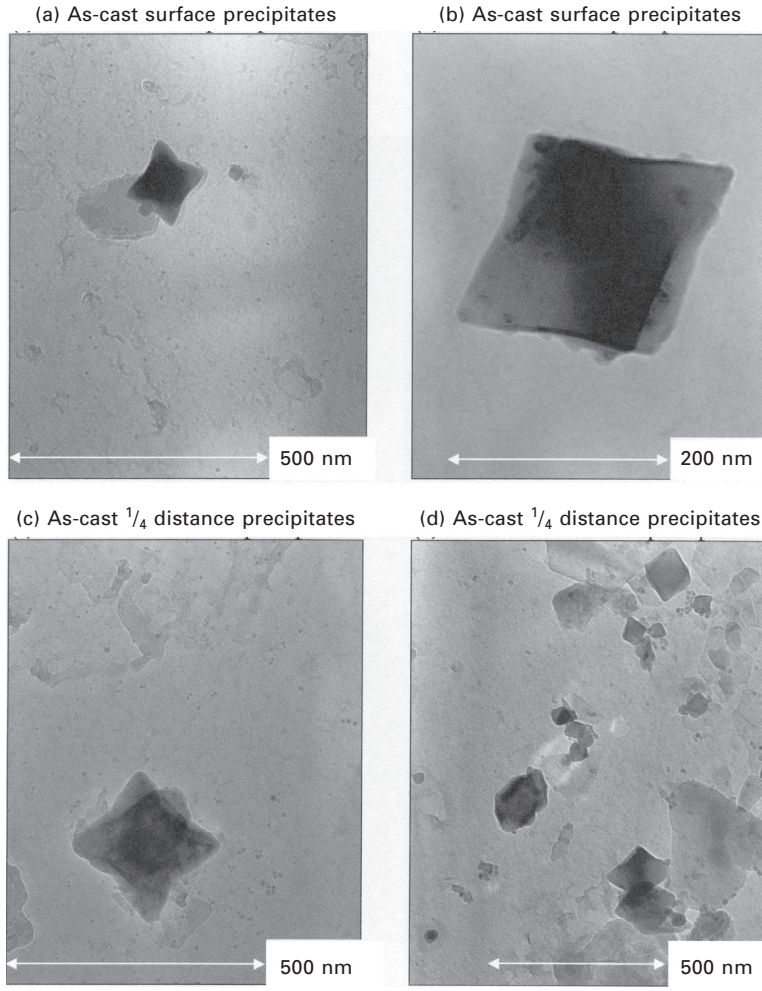


6.2 Examples of dendritic Nb-Ti-V particles in as-cast steel illustrating their persistence after heat treatment at 1050°C. Taken from Chen *et al.* (1987). Used with permission from Maney Publishing.

in the grain interiors or in locations closer to the centre of the slab where cooling and solidification structures are markedly different from those near the slab surface (Figs 6.3a and b) (Couch, 2001). Given the thermal history of the slab, these morphologies have yet to be explained in any detail and are believed to be a consequence of micro-segregation during solidification. It seems likely that the size of the particles found can only have formed in the interdendritic liquid during the later stages of solidification (Raison, 1982; Chen *et al.*, 1987). As the solidification sequences depend on steel composition (Davies and Strangwood, 2009), particularly for carbon contents between the peritectic, ~0.04%C, where solidification begins as δ-ferrite, and C contents greater than approximately 0.09%C when austenite forms first, significant differences in the size, composition and morphology of precipitates can be anticipated. The resulting size, type and distribution can then be important factors in the development of the austenite grain structure during reheating of the slab prior to rolling.

The diffusion distances for the microalloying elements for typical slab reheating temperatures and times are small in relation to the interdendrite spacing, which is of the order of 100s of microns where microsegregation of

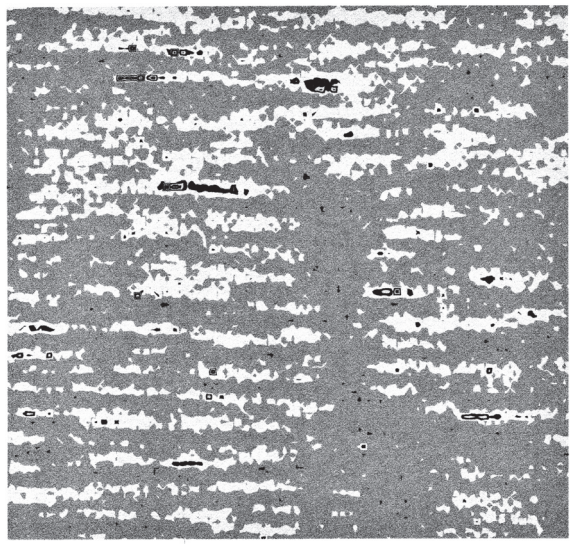
© Woodhead Publishing Limited, 2012



6.3 'Star' shaped particles in as-cast Nb-V-Ti steels: (a) and (b) are from a region approximately 10 mm beneath the as-cast slab surface, whilst (c) and (d) are 75 mm from the as-cast surface some 400 mm from the slab edge. After Couch (2001).

Nb, etc., is found. Hence, the austenite is likely to remain inhomogeneous. An example is shown in Fig. 6.4 taken from the study by Couch (2001), and this illustrates that microsegregated regions of high Nb present in the slab are not entirely eliminated even after times considerably longer than would be used for commercial slab reheating before rolling. The consequences of this type of study have yet to be explored fully but would have implications for the development of austenite grain structure before rolling; should this grain size be too large (of the order of 500 μm and above) or the initial

© Woodhead Publishing Limited, 2012



6.4 Nb microsegregation mapping of a 0.042Nb-0.05%V obtained by laser ablation mass spectroscopy at a spatial resolution of 50 μm illustrating the as-cast distribution, top, compared to that after heat treatment of 18 h at 1250°C. Note that there are peak segregation levels of >0.08%Nb in the as-cast condition. Areas above 0.06%Nb remain after heat treatment, bottom. After Couch (2001).

© Woodhead Publishing Limited, 2012

rolling reductions too small, little or no grain refinement is possible unless impracticably large rolling reductions are made (Cuddy, 1984). Similar considerations may apply to some of the newer thin slab casting direct charging processes being studied as alternative lower energy ('greener') approaches to steel production, the work of Baker and co-workers (Li *et al.*, 2007; Wilson *et al.*, 2009) being relevant in this context.

6.4.2 Precipitation in controlled rolled steels

Figure 6.5 shows typical regions of precipitation in a controlled rolled Nb plate steel, Fig. 6.5(a), and a V treated strip steel, Fig. 6.5(b), illustrating the complexity of particle size distribution in typical commercial steels and, hence, the difficulty of assigning an origin to the various types and sizes of particle. The largest particles are arranged in chains traversing ferrite grain boundaries and it can be deduced that these have formed in the austenite. By using dark field techniques, Fig. 6.6, it can be confirmed that these chains are consistent with formation on prior austenite grain boundaries, in this case for V treated steel. From examples such as these, a hierarchy of nucleation sites in austenite can be inferred. Groups of smaller particles appear to be associated with sub-grains or migrating boundaries in the austenite, area B in Fig. 6.5(a), but the finest particle forming in the austenite appear to be nucleated on dislocation networks in both steels. Also present in the Nb steel are fine particles aligned in rows, Fig. 6.5(a) area C. Similar morphologies are also found in V or Ti treated steels; an example is shown in Fig. 6.7. Analysis of the orientation relationship between the particles and ferrite has confirmed that this type of precipitation is confined to a single ferrite grain implying that the 'row' morphology forms in ferrite. The unique feature of 'row' (Gray and Yeo, 1968) or interphase precipitation, as it was alternatively named, is the presence of only one of the possible variants of the Baker/Nutting orientation relationship:

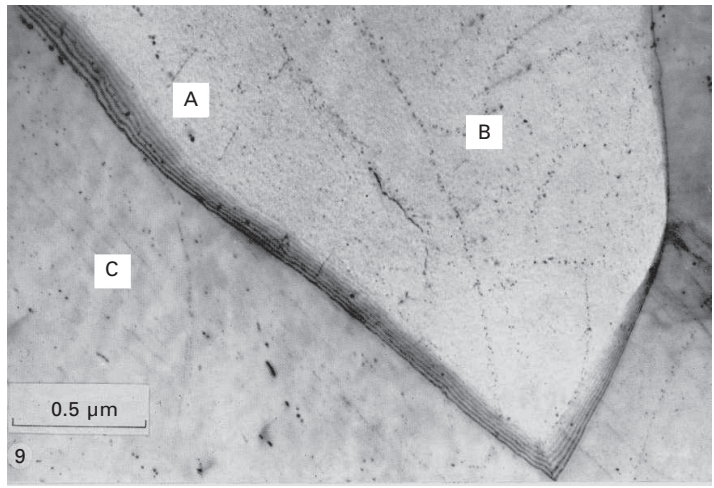
$(100)\alpha//(100)$carbide

$\langle 011\rangle\alpha//\langle 010\rangle$carbide

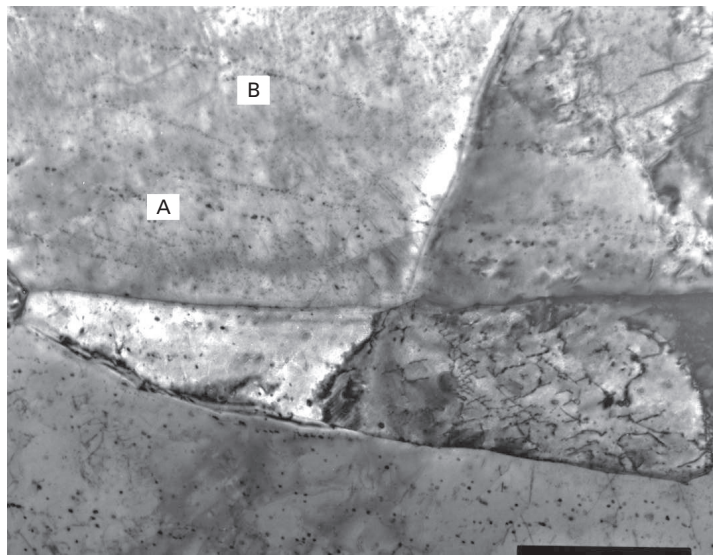
between ferrite, α, and fcc carbides (Baker and Nutting, 1959) in any particular region of precipitates.

An alternative mode of $X(C_yN_{1-y})$ precipitation in ferrite is an apparently random distribution of particles within the ferrite matrix, hence the term 'random' precipitation. The distinguishing feature of this type of precipitation is that the crystallography is given by the Baker–Nutting relationship (Baker and Nutting, 1959; Baker, 2009) with all variants of this being visible within a single region. Some examples of this type of precipitation in V steels are shown in Fig. 6.8. Both types of ferrite precipitation are responsible

© Woodhead Publishing Limited, 2012



(a)



(b)

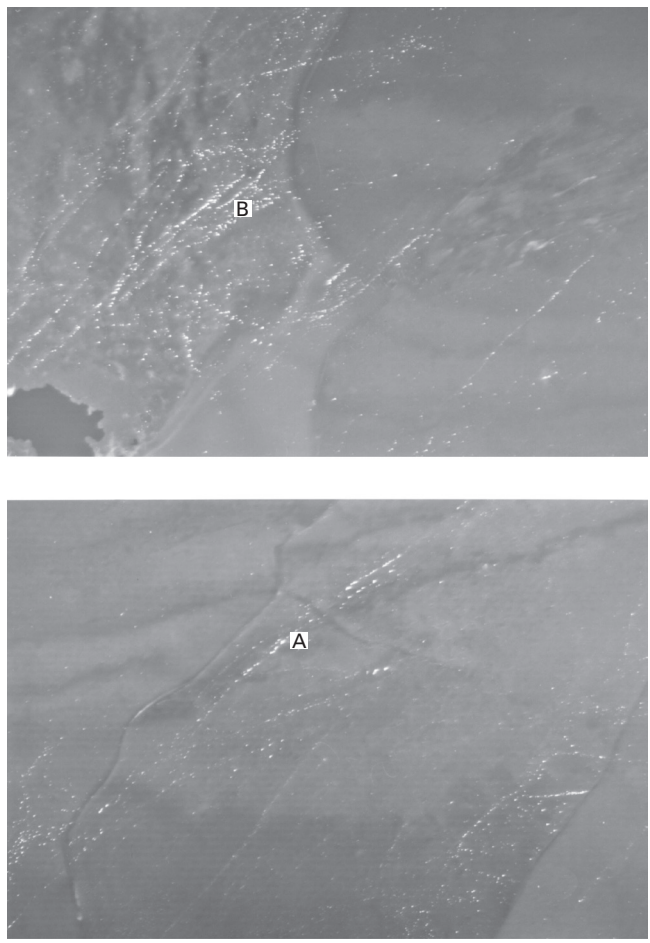
6.5 (a) Typical precipitate distribution in a commercial C-Mn-Nb controlled rolled steel. A: particles aligned along prior austenite boundaries; B: coarse particles formed on sub-structures on the austenite; and C: a region of 'row' precipitates formed in ferrite. After Cochrane unpublished, based on Morrison W B, Chapman J A (1975), Rosenhain Centenary Conference, Royal Society, London, pp. 196–207. (b) Precipitation in a controlled rolled C-Mn-V steel containing 0.2%V. Chains of particles can be noted to traverse ferrite grain boundaries in regions marked A and B corresponding to austenite grain boundaries and austenite sub-structure respectively.

© Woodhead Publishing Limited, 2012

for part of the strength increase in microalloyed steels. A further type of microalloy precipitation in the form of rods or fibres occurs in steels with larger additions of V or Ti, but this type is comparatively rare in commercial HSLA steels.

6.4.3 Precipitation kinetics in austenite and strain induced precipitation

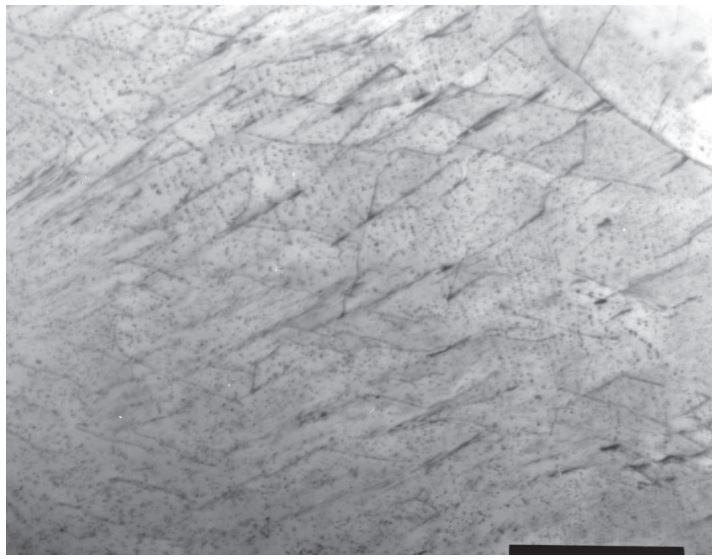
Precipitation kinetics of $X(C_yN_{1-y})$ in austenite are difficult to measure experimentally and a variety of indirect techniques have been used. Early studies relied on electrolytic dissolution of the iron matrix and X-ray analysis



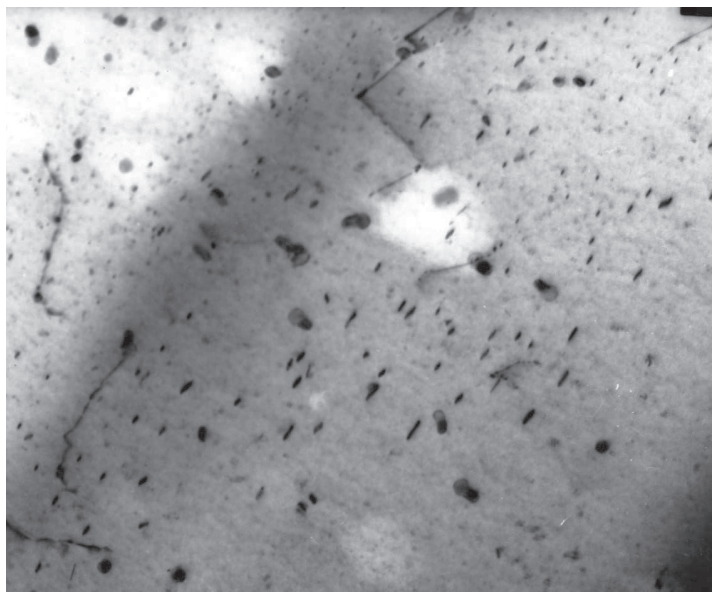
6.6 Unfocused dark field images centred on $\{010\}_{VC}$ precipitates in a controlled rolled V steel illustrating chains of particles outlining prior austenite grain boundaries and sub-structures.

© Woodhead Publishing Limited, 2012

of the residue to derive information on the amount of microalloy precipitated. One such study (LeBon *et al.*, 1975) showed the effect of deformation was to increase the Nb precipitation rate by more than an order of magnitude



6.7 'Row' or interphase precipitation in a 0.45%V steel.



6.8 Region of 'random' VC precipitation in normalised C-Mn-V-N steel showing typical disc-like particles.

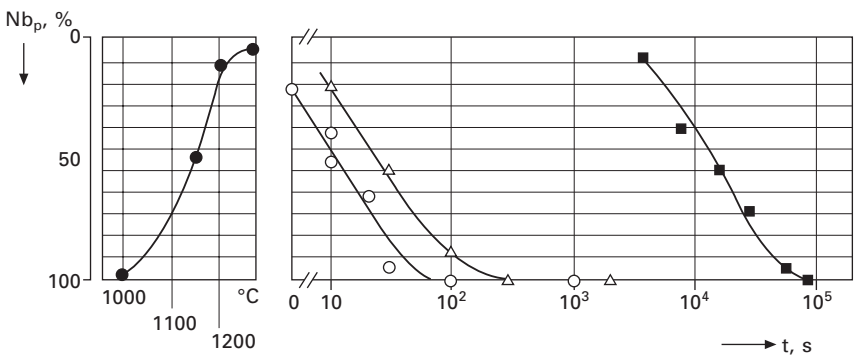
© Woodhead Publishing Limited, 2012

(Fig. 6.9). Since that time most of the kinetic data for $Nb_y(CN_{1-y})$ has been derived from changes in the yield strength of austenite during a variety of deformation processes, for example the increase in rolling load (Trowsdale, 1999) or the increase in flow stress during torsion or compression testing (Weiss and Jonas, 1980; Medina and Mancilla, 1994; Medina, 1997; Gomez *et al.*, 2005).

More recently other techniques such as electrical resistivity have been used (Park and Lee, 2007; Park *et al.*, 2009). Typical of the recent data obtained are results shown in Fig. 6.10 (Park *et al.*, 2009) which display the classical 'C' curve expected for precipitation; the effect of deformation can clearly be seen.

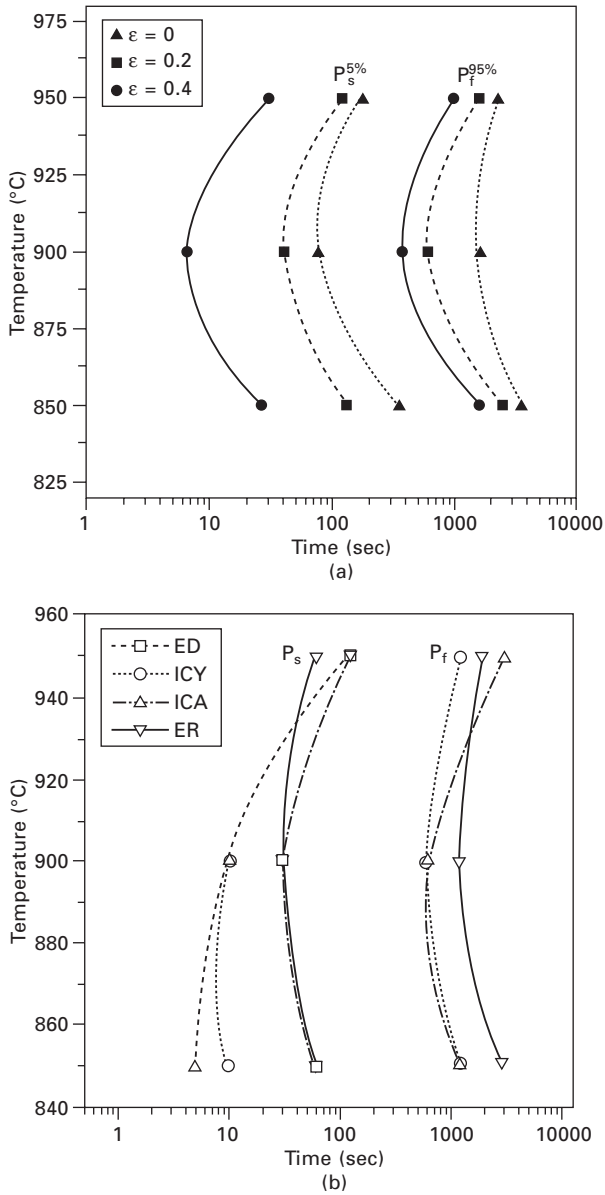
Examination of rolling loads in commercial operations generally corroborates experimental studies of precipitation kinetics in austenite. The acceleration of precipitation by deformation can be explained in terms of higher density of, or increase, in the number of heterogeneous nucleation sites, such as dislocation substructures, shear bands, twin boundaries and the creation of vacancies by deformation.

Much of the recent work has focused on developing models of the precipitation behaviour in austenite based on classical nucleation theories and assumptions about precipitate nucleation, for example, that by Turnbull and Fisher (1949). Such models make the assumption that nucleation is mainly on the austenite sub-structures as the larger particles at boundaries and sub-boundaries are not thought to contribute to control of recrystallisation. The early models concentrated on single pass deformation (Dutta *et al.*, 1992; Abad *et al.*, 2001; Pereloma *et al.*, 2001; Dutta and Palmiere, 2003). They



6.9 Precipitation kinetics of NbC obtained by electrolytic extraction illustrating the acceleration in kinetics by about two orders of magnitude; closed points are for undeformed austenite, open points for two levels of applied torsional strain. The vertical axis corresponds to Nb in solution, and the left-hand diagram shows the dissolution of Nb(CN) as a function of austenitising temperature. Adapted from LeBon *et al.* (1975). Used with permission from Maney Publishing.

© Woodhead Publishing Limited, 2012



6.10 Precipitation kinetics of NbCN in a 0.08%C-0.039%Nb steel measured by a variety of techniques. (a) shows the effect of strains of ε = 0, 0.2 and 0.4. (b) compares the kinetics measured using different techniques: ICY and ICA are interrupted compression tests, ED is from electrolytic dissolution methods and ER electrical resistivity. Adapted from Park *et al.* (2009).

© Woodhead Publishing Limited, 2012

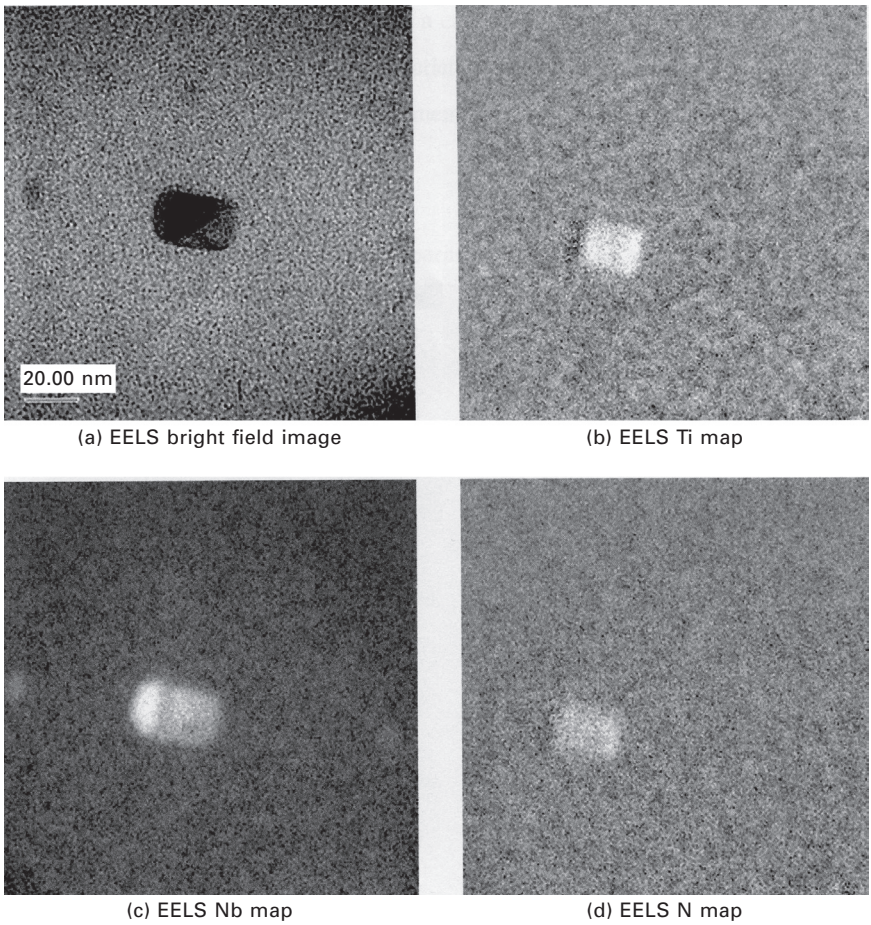
are increasingly being refined to include multiple deformation steps (Sellars and Palmiere, 2005; Nagarajan *et al.*, 2009) and are in general agreement with measured kinetics. For example, Nb precipitation on the austenite deformations sub-structure, so-called 'microbands', have been modelled in a Fe-30%Ni alloy (Nagarajan *et al.*, 2009) which remains fully austenitic down to room temperature, the results being closely comparable to the kinetics inferred from analysis of rolling loads in conventional Nb steels (Randerson, 1994; Trowsdale, 1999).

There is some evidence that precipitation kinetics are altered by the presence of other solute elements or other more stable precipitates, such as AlN or TiN. In some cases there is a direct effect of solutes on chemical activity of C or N, as in the case of Mo additions (Andrade *et al.*, 1983), but in others the effects are observed more indirectly, for example, of P (Cochrane, 1979) and Ti (Dutta and Sellars, 1987). In these studies systematic effects on the level of precipitation hardening were observed and were correlated with direct observations of precipitate distribution. An interpretation in terms of solute-vacancy interactions has been proposed, in agreement with similar effects noted in austenitic stainless steels (Faulkner, 1985; Faulkner *et al.*, 1996), implying that vacancy trapping by solutes other than the microalloy addition may play a part in precipitate development. In this context it is noteworthy that recent detailed HRTEM studies of precipitates appear to suggest that in some cases there may be a 'halo' of other solute atoms surrounding the particles (Craven *et al.*, 2008). Frequent observations of duplex precipitates have been made in many TMCR and TMCP steels (see, for example, Pereloma *et al.*, 1996) but more particularly in the weld heat affected zone (HAZ) (Egner *et al.*, 1999; Moon and Lee, 2009), indicating that the presence of TiN acts as a heterogeneous substrate for Nb(C,N) (Fig. 6.11). Such effects may explain some of the discrepancies in precipitation behaviour in commercial steels from different process routes observed over recent decades.

6.4.4 Precipitation during austenite/ferrite transformation, 'row' or interphase precipitation

The cooling conditions for 'row' precipitation were first characterised in commercial microalloyed steels by Gray and Yeo (1968), who established a direct correlation between plate cooling rate, row spacing and particle size (Fig. 6.12). Later studies showed 'row' or interphase precipitation was characterised by bands or sheets of aligned particles which form parallel to the advancing austenite/ferrite interface. Subsequent work has confirmed this, but the inter-row (or band) spacing and particle size is more non-uniform than was originally envisaged as cooling rates were increased to those more typical of hot strip or coiled plate mill processing.

© Woodhead Publishing Limited, 2012



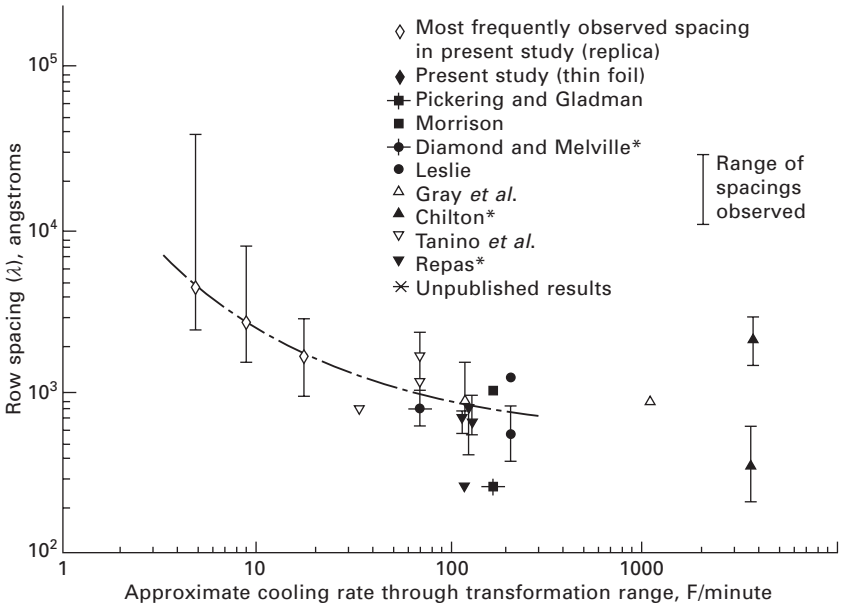
(a) EELS bright field image (b) EELS Ti map

(c) EELS Nb map (d) EELS N map

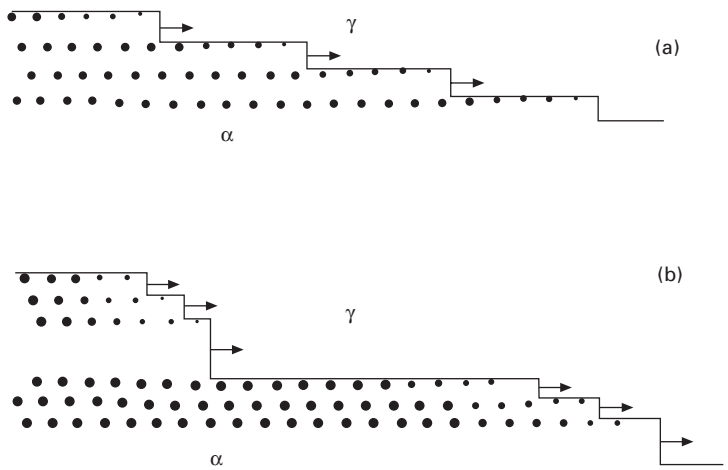
6.11 Complex Ti-Nb-N in a simulated weld heat affected zone of a laboratory controlled rolled 0.04%C-0.3%Si-1.4%Mn-0.014%V-0.026%Nb-0.014%Ti steel. Taken from Egner (1999), see also Egner *et al.* (1999).

Extensive work by Honeycombe and co-workers (as in, for example, Davenport and Honeycombe, 1971; Dippenaar and Honeycombe, 1973; Barbacki and Honeycombe, 1976; Honeycombe, 1976; Ricks and Howell, 1983; Law *et al.*, 1987) revealed the essential features of the mechanism and kinetics of this transformation using simple alloy systems. In particular, precipitation was consistent with sideways migration of ledges on $\{111\}\gamma//\{110\}\alpha$ planes accounting for the selection of a single crystallographic variant for the particles. It is clear that where there is a large supersaturation of the microalloying addition, conditions for precipitation occur at the austenite/ferrite interfaces because of the C rejection by the growing ferrite,

© Woodhead Publishing Limited, 2012



6.12 Relationship between 'row' spacing and cooling rate for a number of commercial Nb treated steels. After Gray and Yeo (1968).



6.13 Schematic diagram showing formation of interphase precipitates by ledge migration tranverse to the direction of interface movement. Adapted from Honeycombe (1976).

as illustrated in Fig. 6.13. As the ferrite/austenite interface migrates into the austenite, solute enrichment also occurs in the disordered interphase boundary as envisaged by Hillert (1999). When a sufficient supersaturation is reached, particles form along the interface causing migration to cease. The

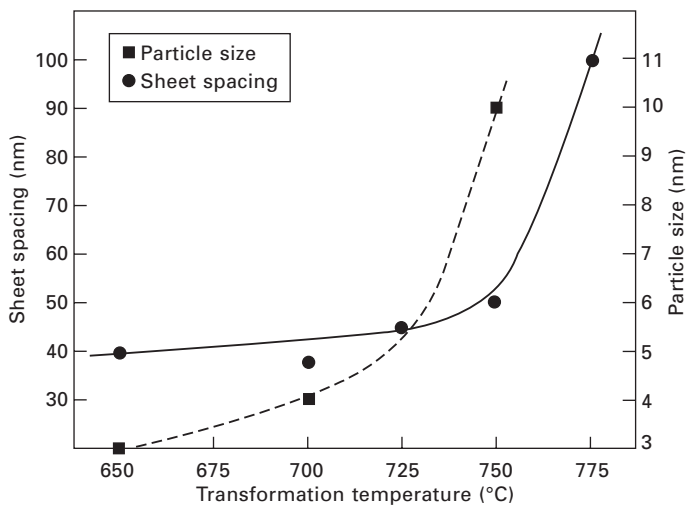
© Woodhead Publishing Limited, 2012

interface then moves forward by migration of ledges across the interface, thereby creating a new solute-free region; the process then repeats until the supersaturation is reduced sufficiently that precipitation is no longer possible. It follows from this type of model that 'row' precipitation cannot take place when the mobility of the ferrite/austenite interface is high, hence, at more rapid cooling rates the extent of 'row' precipitation begins to decrease as transformation temperature decreases (Figs 6.14 and 6.15). More rigorous treatments of interphase precipitation have been proposed by Todd *et al.* (1988), Rios (1995) and Okamoto *et al.* (2010), elaborating on the mechanism outlined above. The theoretical predictions by Okamoto and Ågren (2010) were shown to be consistent with directly comparable isothermal experimental data (Okamoto *et al.*, 2010).

Other forms of interphase precipitation in medium to high carbon steels with larger amounts of Nb or V (Mannerkoski, 1964) can occur in the form of rods or fibres at the growing interface. This structure has many similarities to precipitation in high Cr or Mo steels (Jachym *et al.*, 1978). As yet these structures have not been used in practical microalloyed steels, although in some Nb/Mo controlled rolled pipeline steels rather similar precipitate morphologies have been noted (Fig. 6.16).

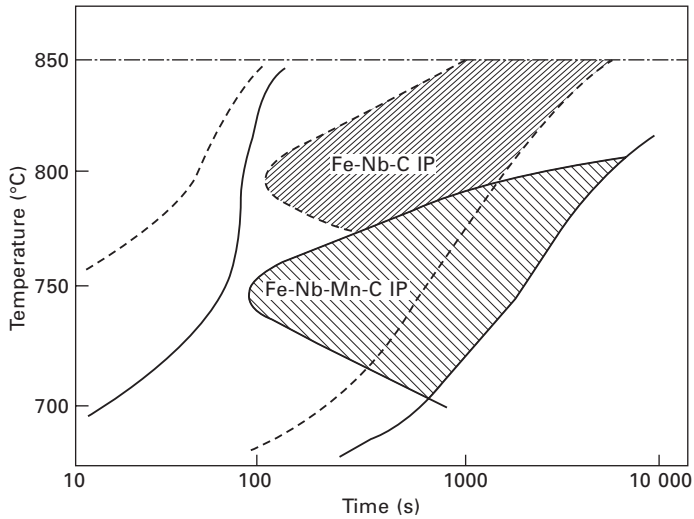
6.4.5 Precipitation in ferrite

In commercial steels it is only the contribution to strength which is of importance and, because of the relevance of this precipitation mode to

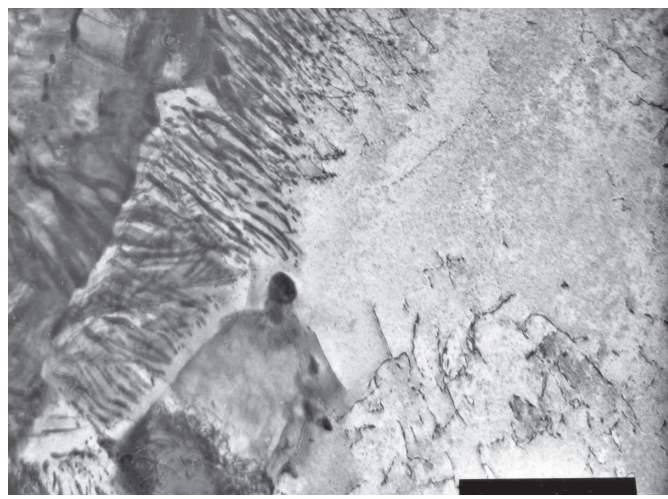


6.14 Relationship between transformation temperature, particle size and sheet ('row') spacing for stoichiometric V alloys. Adapted from Honeycombe (1976).

© Woodhead Publishing Limited, 2012



6.15 Isothermal Nb precipitation kinetics illustrating the effect of manganese, dashed lines and solid lines respectively; the hatched regions show where interphase precipitation predominates. Adapted from DeArdo (2009), based on the study by Sakuma and Honeycombe (1985). Used with permission from Maney Publishing.



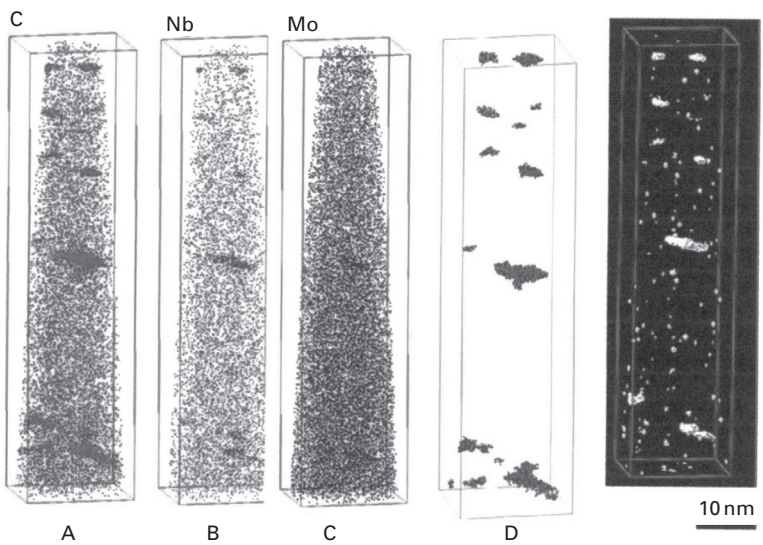
6.16 Complex fibrous carbide morphologies in a Nb-Mo X80 controlled rolled steel.

commercial steels subjected to accelerated cooling regimes, the kinetics of precipitation and systematic studies of 'random' NbCN precipitation has received some recent attention. There is appreciable evidence from TEM studies that precipitation can take place on dislocations in ferrite

© Woodhead Publishing Limited, 2012

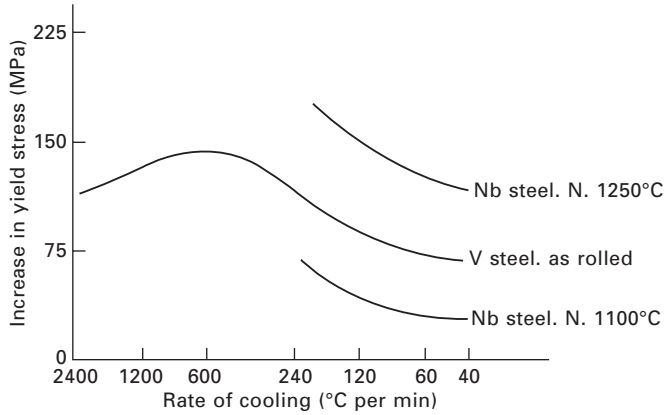
and the expected sequence of segregation to heterogeneous sites preceding precipitation has been simulated in Monte Carlo models of NbC precipitation in ferrite. These studies have confirmed assumptions about nucleation sites (Fujita and Bhadeshia, 2001; Hin *et al.*, 2008a, 2008b). At sufficiently large supersaturations, there is evidence, reviewed by Baker (2009) for V steels, that 'zones', similar to those in Al alloys, may be present at the early stages of precipitation. The zones are thought to be due to clustering of solute atoms on $\{100\}_\alpha$ planes causing coherency strain in the surrounding lattice leading to the typical platelet or disc-shaped particles found in many microalloyed steels. Recent studies using atom probe tomography have confirmed the presence of clusters in various microalloyed steels (Fig. 6.17) (Pereloma *et al.*, 2006; Timokhina *et al.*, 2007, 2011) and suggest that these may be present in the ferrite immediately after transformation. Much of this new information will have an impact on current models for nucleation of microalloy particles.

Precipitation of V compounds has been studied extensively in commercial steels because cooling rate and transformation temperature have a more pronounced effect than in Nb steels (Fig. 6.18). These effects are used to control VC or VN particle size in the design of steels as diverse as hot rolled strip or accelerated cooled thermomechanically rolled steels for pipelines. Shercliff and Ashby (1990) have proposed a parametric approach to predict the extent of precipitation for a range of times and temperatures and this has been applied to coiled strip production (Nakata and Militzer, 2005).



6.17 Elemental maps of C, Mo and Nb at A, B and C, illustrating the presence of clusters of these elements at D, in a Nb-Mo steel. After Pereloma *et al.* (2006).

© Woodhead Publishing Limited, 2012



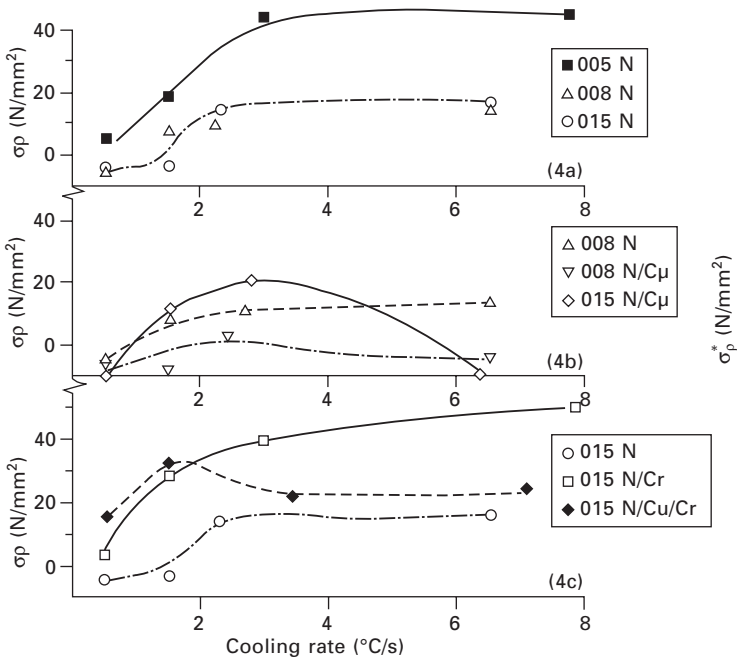
6.18 Effect of cooling rate and transformation temperature on precipitation strengthening in commercial V treated steels. N indicates a normalising heat treatment temperature. Adapted from Pickering (1978).

Precipitation in V treated steels can also be influenced by other solute additions. Suzuki *et al*. (1971) first reported effects of Ni, Mn and, later, Tanino (1974) showed the effects of Mo and Cu. Cochrane and Morrison (1979a) confirmed differences in precipitation hardening in a range of V steels alloyed with Cr, Cu or Mn (Fig. 6.19). The effect of cooling rate for Cu containing steels (Fig. 6.19) shows a distinct peak in the extent of precipitation inferred from mechanical properties and differences in particle size as revealed by TEM examination. It is likely, therefore, that increasing cooling rate can retain a supersaturation of microalloying elements down to ambient temperature leading to the possibility of substitutional/interstitial dynamic strain hardening effects (Cochrane, 1976). That a supersaturation of microalloying element can be retained, even after cooling rates as low as 0.5°C/sec, is apparent from the 're-appearance' of particles in annealed or stress relieved normalised V-Al-N steels. In some cases, particles in the 'row' morphology become more obvious after stress relieving heat treatment (tempering) (Fig. 6.20) (Cochrane, 2000). Such observations appear to be confirmed by the more recent HRTEM observations of 'pre-precipitation' clusters and consistent with observations made in early studies where no precipitation was detected yet an increase in strength was measurable.

6.5 Effects of microalloying on transformation kinetics

As with all alloying elements, some effect of microalloying on transformation might be expected. However, the amounts added are small and in most normalised HSLA steels there is relatively little evidence for a direct effect

© Woodhead Publishing Limited, 2012

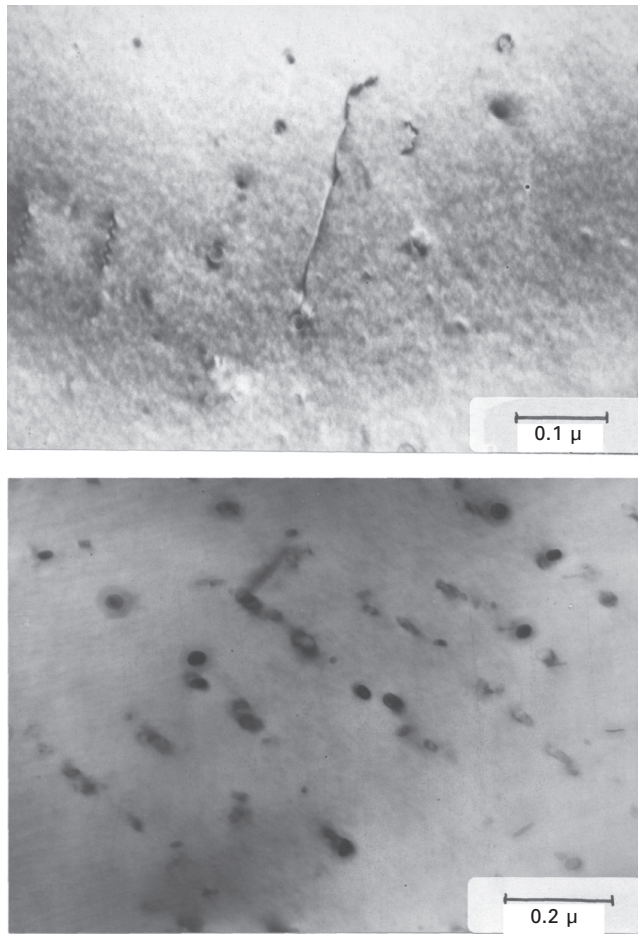


6.19 Precipitation strengthening in normalised V steels containing deliberate additions of Cu, Cr and N. Note the effect of Cu is to inhibit precipitation of V_4C_3. Adapted from Cochrane and Morrison (1979a).

on either conventional measures of hardenability (for example, Jominy tests) or continuous cooling transformation (CCT) diagrams, since austenite grain refinement occurs and, therefore, for most normalised HSLA steels the hardenability is decreased. For rolled steels, there is no doubt that Nb and V retard ferrite transformation either singly, Fig. 6.21(a), or in combination, Fig. 6.21(b), when the precipitate solvus is exceeded (summarised by Morrison, 2009; Cochrane and Morrison, 1981a). The principal microalloying additions, Nb, V and Ti, are all ferrite stabilisers; the predicted rise in the equilibrium austenite to ferrite transformation temperature, Ae_3 (Uhrenius, 1978) can be significant but not easy to determine (Kirkaldy and Baganis, 1978) unless near identical austenite grain size can be achieved and precipitation in austenite avoided. The temperatures at which the austenite to ferrite transformation takes place on cooling, Ar_3, is depressed by an average of ~8°C/0.01%Nb at plate cooling rates but there is a greater effect at cooling rates typically used for TMCP steels, as shown in Fig. 6.22 (Eldis and Hagel, 1978; DeArdo, 2003).

Many studies have shown a greater tendency to form bainite, indicated by a shift in the CCT diagram to longer times although direct comparisons

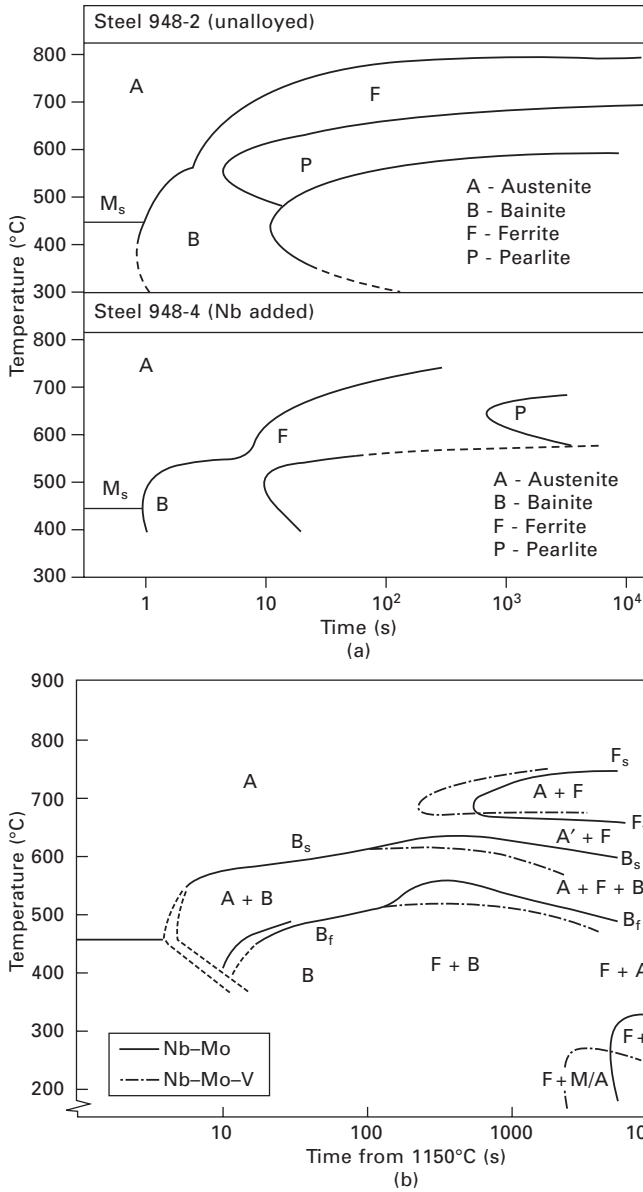
© Woodhead Publishing Limited, 2012



6.20 Additional precipitation after a stress relief heat treatment of 8 h at 600°C, normalised V-Al-N steel (Cochrane, 1976).

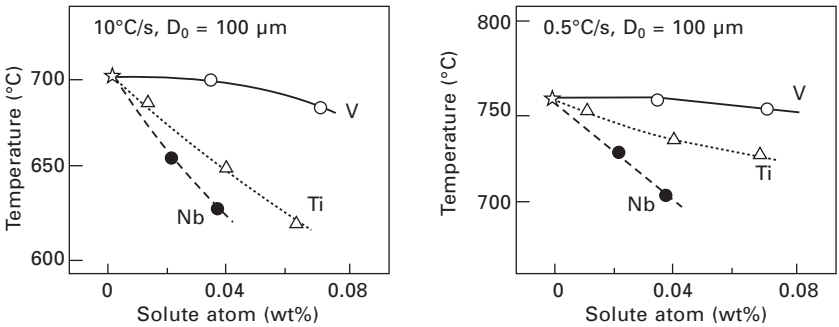
are difficult because of differences in overall steel composition and austenite grain size. For example, the effect of increasing the reheating temperature from 1150 to 1250°C is to decrease the cooling rate needed to form ferrite by about a factor of 2, ~11°C/s to ~7°C/s (Fig. 6.23) (Hulka *et al.*, 1990). This contrasts with a steel of a similar C content but lower Mn which shows no ferrite forms in this range of cooling rate despite a lower austenitising temperature and finer grain size, 65 μm (Fig. 6.24) (Xu *et al.*, 2009). These discrepancies are not easily explained, but given the comments made on precipitation sequences in cast steel and laboratory cast steel, from the work of Couch (2001) and Davies and Strangwood (2009), such changes might be expected. One method of compensating for these differences is to choose austenitising temperatures to give similar grain sizes, then calculate the Nb

© Woodhead Publishing Limited, 2012



6.21 (a) Effect of Nb on the transformation behaviour of a C-Mn steel, adapted from the review by Morrison (2009). Originally published by DeKazinczy K *et al.* (1963). Used with permission from Maney Publishing. (b) Effect of V on the transformation behaviour of a Nb-Mo steel (Cochrane and Morrison, 1981a). Used with permission from Maney Publishing. Phase field as designated, A: Austenite, A′: retained austenite, B: Bainite, F: Ferrite, M/A: phases consisting of high carbon martensite together with other phases including retained austenite. B_s, B_f and F_s, F_f are transformation start and finish for bainite and martensite, respectively.

© Woodhead Publishing Limited, 2012



6.22 Changes in Ar_3 temperatures for microalloying additions at two different cooling rates, 0.5°C/s is typical of 19 mm plate cooling in air whereas 10°C/s is more relevant to accelerated cooling. From DeArdo (2009). Used with permission from Maney Publishing.

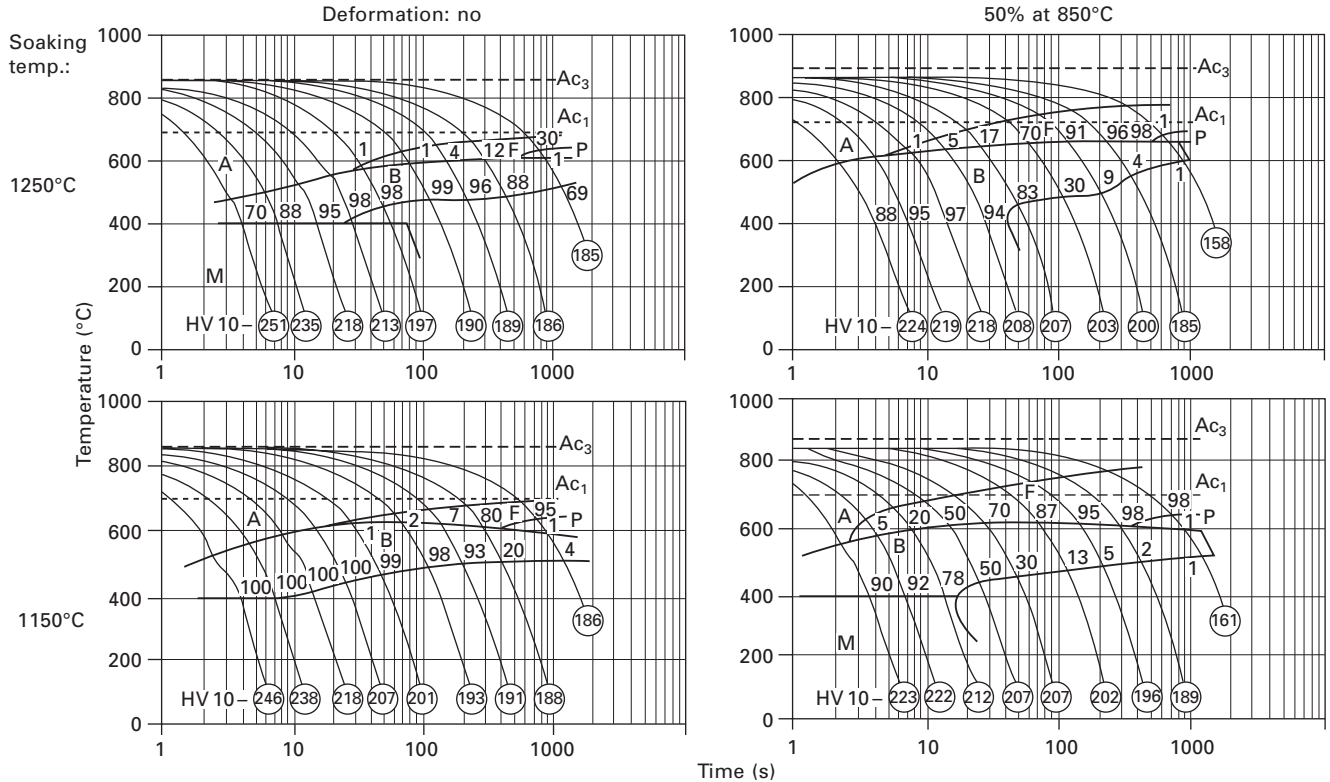
(or V as appropriate) and compare volume fraction transformed per unit surface area of austenite; an example is shown in Fig. 6.25 (from Cochrane and Morrison, 1981a). Here, the acceleration of ferrite formation by V and retardation by Mo is evident.

There is a marked effect of 0.4%V when added to 0.06%C steels (Fig. 6.26) (Cochrane and Morrison, 1981b). Likewise, Nb above 0.1% decreases transformation temperature although for the reasons given this is difficult to illustrate directly. The addition of Ti has been studied less comprehensively but Liu and Zhang (1990) and Garcia de Andres *et al*. (1998) indicated that 0.1%Ti retarded ferrite formation.

Deformation dilatometry or Gleeble simulation has been used in several studies to obtain CCT information more relevant to controlled rolling or TMCP processing; examples of these are data shown in Figs 6.23 and 6.24. The effect of retained deformation (as opposed to recrystallisation controlled rolling (RCR) type processing) is to accelerate ferrite formation. These effects are discussed more fully in a later section dealing with transformation from austenite containing retained deformation.

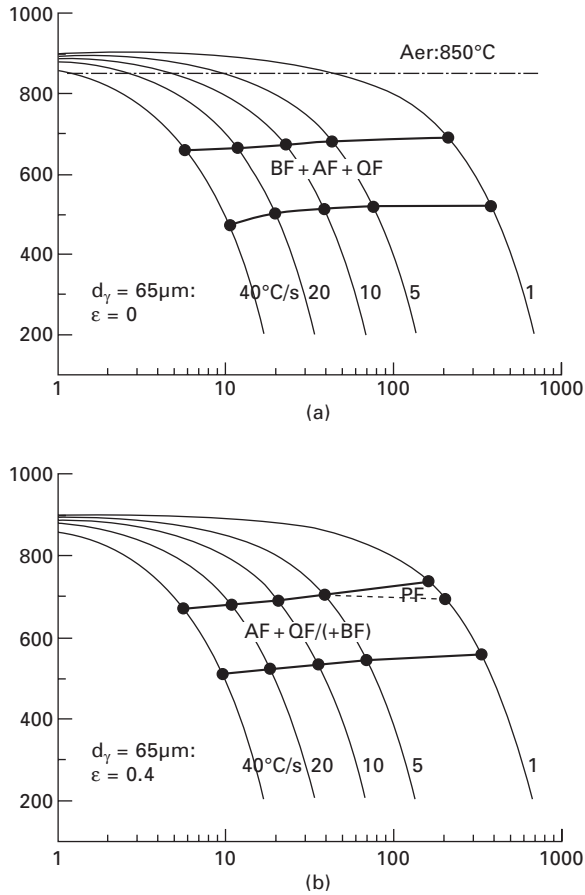
Microalloying also modifies the transformation of austenite remaining at the end of ferrite transformation; this carbon enriched austenite would normally transform to pearlite and in most C-Mn-Nb steels this occurs. However, when higher Mn or Si contents are used or deliberate additions of Mo, Cr, Cu or Ni are made, the austenite may be retained to room temperature and/or a range of microstructures from bainite to twinned martensite may be present. These phases, termed martensite/austenite 'micro-constituents' or M/A, are desirable for pipe forming as their presence suppresses the yield point making forming easier. A similar strategy accounts for the strain hardening capacity of other types of steels intended for high formability applications (termed transformation-induced plasticity, TRIP) and Nb or V has been used

© Woodhead Publishing Limited, 2012



6.23 CCT diagrams for a 0.03%C-1.78%Mn-0.26%Cu-0.17%Ni-0.29%Cr steel. Austenitised for 6 minutes at the temperatures indicated, after Hulka *et al.* (1990). A: Austenite, B: Bainite, F: Ferrite, M: Martensite, P: Pearlite. The figures at the end of the cooling curves are the hardness of the microstructure produced after cooling.

© Woodhead Publishing Limited, 2012



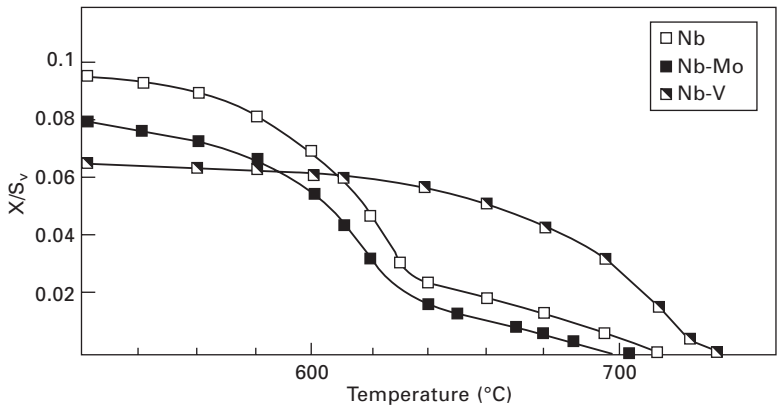
6.24 Effect of deformation on the CCT transformation behaviour of a 0.03%C-0.17%Si-1.49%Mn-0.1%Nb-0.26%Cu-0.15%Ni steel. CCT diagram (a), austenitised at 1200°C for 15 min, shows the absence of ferrite compared to CCT diagram (b). After Xu *et al.* (2009).

to modify transformation behaviour in this way by the use of high Si or Al contents (De Meyer *et al.*, 2000).

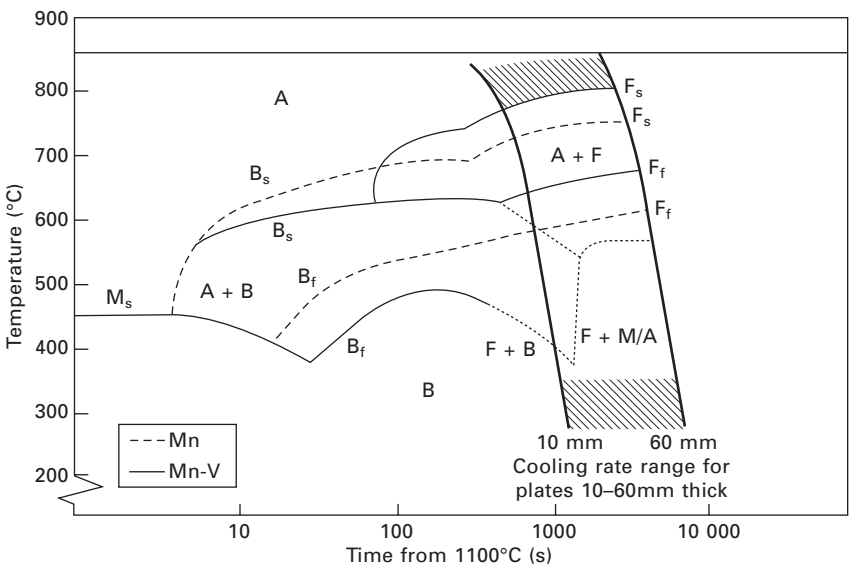
In the context of weld thermal cycles, changes in CCT behaviour can lead to significant differences in ferrite morphology which are thought to be linked to changes in weld HAZ mechanical properties. Nb appears to make a bainitic microstructure more likely at a given cooling rate and together with precipitation leads to embrittlement of the weld HAZ. In contrast, V additions can lead to a specific morphology of generally tough intragranularly nucleated ferrite consisting of intersecting plates, or 'basketweave structures', with different variants of the Kurdjumov–Sachs relationship. In studies of weld metal microstructure, such ferrite morphologies became known as 'acicular

© Woodhead Publishing Limited, 2012

ferrite', the formation of which can also improve HAZ toughness under some conditions. This effect has been shown to occur in a variety of weld HAZ ranging from those typical of submerged arc welding to those found



6.25 Effects of Mo and V on the ferrite transformation in a 0.10%C-0.3%Si-1.45%Mn-0.028%Nb steel. X/Sv is the volume fraction ferrite formed on unit area of austenite grain boundary. The acceleration of transformation by V contrasts with the retardation by Mo (Cochrane and Morrison, 1981a). Used with permission from Maney Publishing.



6.26 Effect of near-stoichiometric additions of V (0.45%) to a 0.08%C-1.9%Mn steel, after Cochrane and Morrison (1981b). A: Austenite, B: Bainite, F: Ferrite, M: Martensite, P: Pearlite, M/A: mixtures of high carbon martensite and retained austenite. M_s is the martensite start temperature. Used with permission from Maney Publishing.

© Woodhead Publishing Limited, 2012

around laser welds. The mechanism leading to acicular ferrite is obscure. Unlike weld metals, there is no obvious substrate on which AF can nucleate. He and Edmonds (2002) considered the role of a number of potential sites and concluded that V may lead to a reduction in the energy needed for formation of a ferrite nucleus possibly by Fe-V clustering in austenite (He and Edmonds, 2002). The observation of coherency strains surrounding twins at transformation interfaces in V steels would also suggest some form of local clustering at the interface which hinders migration of the α/γ interface (Heikkinen, 1974; Baker, 2009). As well as modifying the morphology of the transformation products, there is a change in the transformation behaviour of the austenite remaining at the end of the bainite or acicular ferrite transformations (Axelsen *et al.*, 1987; Lee *et al.*, 1992), leads to the formation of M/A regions which have a more block-like appearance in Nb steels compared to V steels (Axelsen *et al.*, 1987). While the M/A phase can be explained in terms of increased austenite hardenability, its morphology is less easily explained and may be related to the effect of microalloying on plate-like ferrite growth.

6.6 Phase transformations during high strength low alloy (HSLA) steels processing

6.6.1 Austenite to ferrite transformation

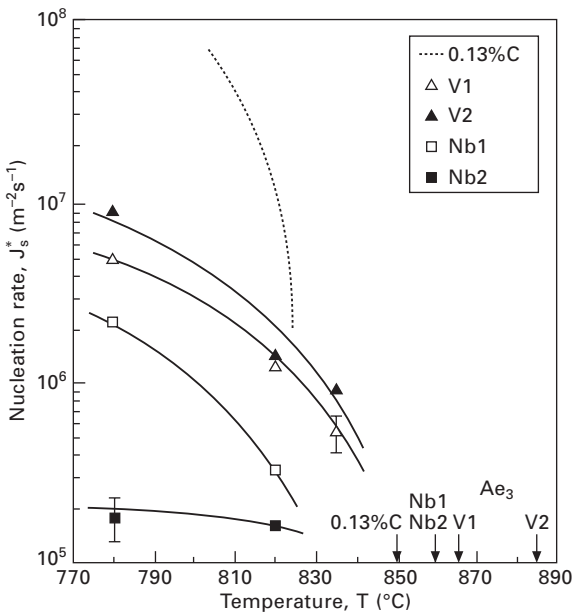
Put in the simplest of terms, the goal of processing microalloyed HSLA steels is to achieve the maximum number of ferrite grains from a single austenite grain, in other words, to raise the ferrite nucleation rate. Cahn (1956) showed that for a given grain size, nucleation first occurs at corner sites, the junctions between four grains, followed by edge sites where three grains meet and finally at grain surfaces between two adjacent grains. The contribution made by intragranular sites was considered negligible in the absence of suitable heterogeneous sites. However, such sites may contribute to so-called 'acicular ferrite' nucleation as in the case of ferritic weld metals or via dislocation sub-structures in controlled rolled steels as will be discussed in a later section. The topic of nucleation and growth is covered in detail in Volume 1, Chapter 6, but it should be noted that steel development based on the principles outlined below increasingly makes use of models of the austenite to ferrite phase transformation (see, for example, the work of Militzer and co-workers (Militzer *et al.*, 2000; Sarkar and Miller 2009), Hodgson (Hodgson and Gibbs, 1992; Hodgson *et al.*, 1996) or Sellars and co-workers (Sellars and Whiteman, 1979; Beynon and Sellars, 1992)). Most of these models make use of the Johnson–Mehl–Avrami equation (Avrami, 1939, 1940, 1941) to predict kinetics, but there are rather fewer attempts to predict ferrite grain size except by empirical relationships derived from

© Woodhead Publishing Limited, 2012

experimental studies (see, for example, Hutchinson, 2000). It is not intended to discuss the use of, nor the assumptions behind, such models as many steel producers have tailored similar metallurgical models and adjusted parameters to best fit their particular processing capabilities and thus detailed information on current development is frequently withheld on commercial grounds.

6.6.2 Nucleation and growth of ferrite

Much of the information on ferrite nucleation rates has been derived from classical treatments of nucleation, whereby an embryo becomes stable only when the energy required to form a new interface is greater than the free energy available. The classical theory is then used to derive the ferrite nucleation rate from measurements of the numbers of particles nucleated at grain boundaries. Such studies have shown that Nb has a greater effect in reducing ferrite nucleation rates at austenite grain boundaries than V (Enomoto *et al.*, 1994) (Fig. 6.27). Similarly, Nb/V additions were found to reduce nucleation rates relative to both plain C and Mo containing steels (Essadiqi and Jonas, 1989). This effect was ascribed to segregation of Nb to austenite grain boundaries (Ouchi *et al.*, 1982; Tomita *et al.*, 1994; Fosseart *et al.*, 1995; Fujita and Bhadeshia, 2001; Hin *et al.*, 2008a) leading to changes in



6.27 Relative effects of Nb and V on ferrite nucleation in 0.13%C steels with additions of 0.016%Nb (Nb1), 0.082%Nb (Nb2), 0.092%V (V1) and 0.46%V (V2), respectively. The Ae_3 temperature for each steel is indicated by the arrows. Adapted from Enomoto *et al.* (1994).

© Woodhead Publishing Limited, 2012

the interfacial energy balance associated with nucleus formation (Enomoto *et al*., 1994). The alternative scenario, whereby microalloy particles can act as heterogeneous nucleation sites at grain boundaries, has also been vigorously debated but lacks direct evidence from studies of partially transformed samples. For example, Cochrane and Morrison (1981a) linked the change in ferrite formation with particles precipitated by holding in the austenite phase field. The situation is less clear for Ti, although given the similarity to V and the propensity for interphase precipitation in all common microalloyed steels, retardation of ferrite formation is likely. Eldridge (2000) suggested that Ti reduced nucleation rates. In a recent treatment of nucleation kinetics in steels (Van Dijk *et al*., 2007), the classical view of embryo formation leading to nucleation was questioned. By using dynamic observations of ferrite nucleation in medium carbon steels using X-ray techniques, van Dijk *et al*. (2007) concluded that there is, essentially, no barrier to ferrite formation and analysis of the cluster dynamics may form a better basis for estimating ferrite nucleation behaviour. The implications of this are discussed later in relation to ferrite growth in CR and TMCP steels.

Growth of ferrite in studies to date has shown that ferrite, at least in the early stages, follows a parabolic law indicative of carbon diffusion control. When Nb and Mo have been used, ferrite growth appears somewhat slower than in plain C steels (Essadiqi and Jonas, 1989) possibly as a consequence of solute partitioning at the interface. The presence of clusters referred to earlier is evidence for this and, perhaps, alters the interface mobility. Of the few studies of the effects of Nb on ferrite growth, the evidence is contradictory, some showing little or no effect (Gupta, 1993).

6.6.3 Normalised steels

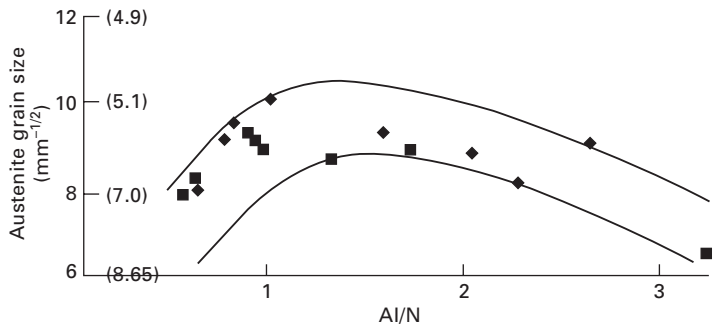
As alluded to in the historical review above, the first use of Nb (and V) was to provide grain refinement in normalised steels, normalised being the heat treatment of steels at temperatures between 880 and 950°C followed by cooling in still air. There are surprisingly few data on the relationship between austenite, l_γ, and the resultant ferrite grain size, l_α, for this class of steels. However, the link between austenite grain size and the size and volume fraction of any class of particle was made by Gladman in a seminal paper (1966) in which it was shown that austenite grain size, l_γ, is related to a critical particle size, r, and volume fraction, f, by the expression:

$$r = 6l_\gamma f/\pi(3/2 - 2/Z)^{-1}$$

Z being a measure of the heterogeneity of the austenite grain structure, typically between 1.414 and 2. Similar expressions have been given more recently taking into account factors such as the particle size distribution and nature of the grain boundary interaction with particles of differing surface

© Woodhead Publishing Limited, 2012

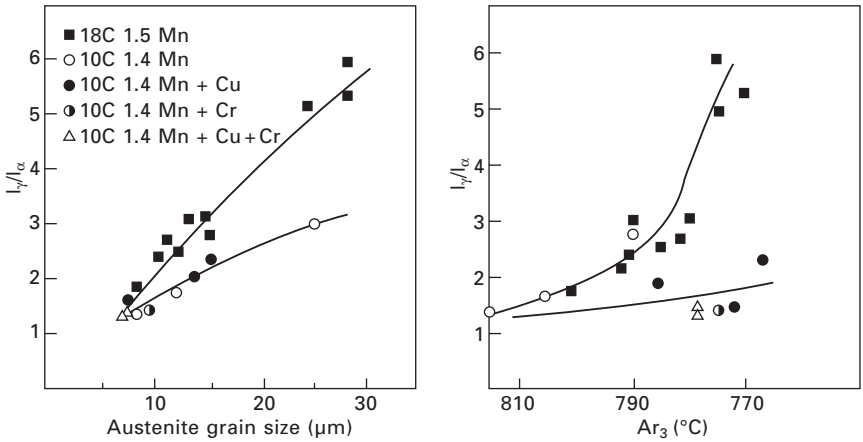
energy. Whilst these treatments have refined this relationship (Hillert, 1965, 1988; Hellman and Hillert, 1975; Rios, 1987), there are few direct measurements of such parameters which improve predictions of austenite grain size in the presence of particles. Refinement of ferrite grain size (hence improved mechanical properties) of normalised steels, therefore, results from the use of either a greater volume fraction of particles, as in the range of normalised V-Al-N steels capable of yield strength in the range 450–550 MPa, or alternatively, closer control of the Al/N ratio in the case of normalised C-Mn-Nb steels for specifications requiring 355 MPa (Cochrane, 2000) giving more consistent properties (Fig. 6.28). Whilst it is self-evident that a refined austenite grain size will lead to a refined ferrite grain size, the effects of alloying or cooling rate have only a minor effect on the final ferrite grain size. Of more importance here is the role of the prior processing on the l_γ/l_α ratio, first exploited by the use of double normalising heat treatments. Consideration of the nucleation processes in a fine austenite grain size leads to the conclusion that, when corner site saturation occurs, then there is a limit to the ferrite grain size that can be obtained. Consequently, controlling the austenite grain size prior to transformation up to this limit can improve ferrite grain refinement. An example of this is shown in Fig. 6.29, taken from the study of Cochrane and Morrison (1979b), which also illustrates the effect of transformation temperature. A practical extension of this was used to produce greater consistency during production of a normalised C-Mn-Nb steel for oil extraction platforms by 'controlling' the plate rolling process so that a more reproducible ferrite grain size, hence austenite grain size, resulted prior to normalising (Fig. 6.30) (Cochrane *et al.*, 1989). The use of forced air or air mist cooling showed some promise for further refinement in ferrite grain size but the technology was expensive and soon replaced by controlled rolled alternatives. Normalised steels have been largely superseded by lower CEV controlled rolled steels but as a class they represent the probable limit



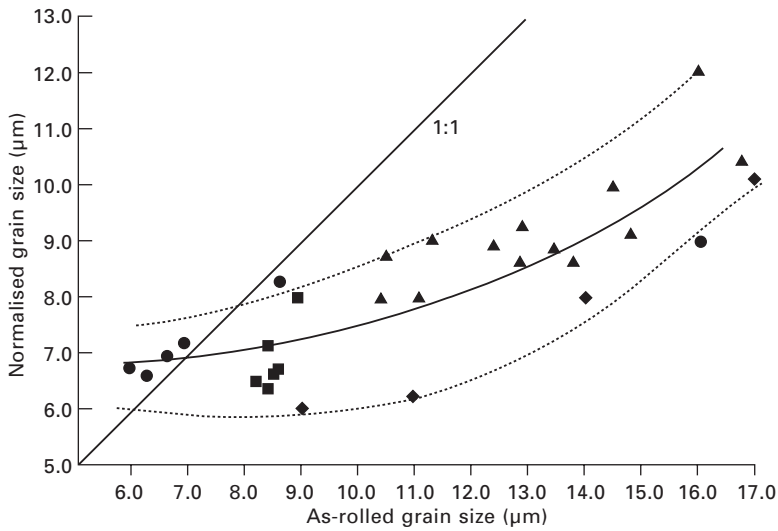
Figures in parentheses are ferrite grain size in microns.

6.28 Influence of soluble Al/N ratio on the effectiveness of grain refinement of normalised Nb steels (Cochrane, 2000).

© Woodhead Publishing Limited, 2012



6.29 Effect of transformation temperature on the efficiency of austenite grain boundaries in nucleating ferrite grain as measured by the I_γ/I_α ratio for some normalised V-N steels (Cochrane and Morrison, 1979b).



6.30 Effect of prior as-rolled ferrite grain size on the final ferrite grain size in normalised C-Mn-Nb steels (Cochrane *et al.*, 1989).

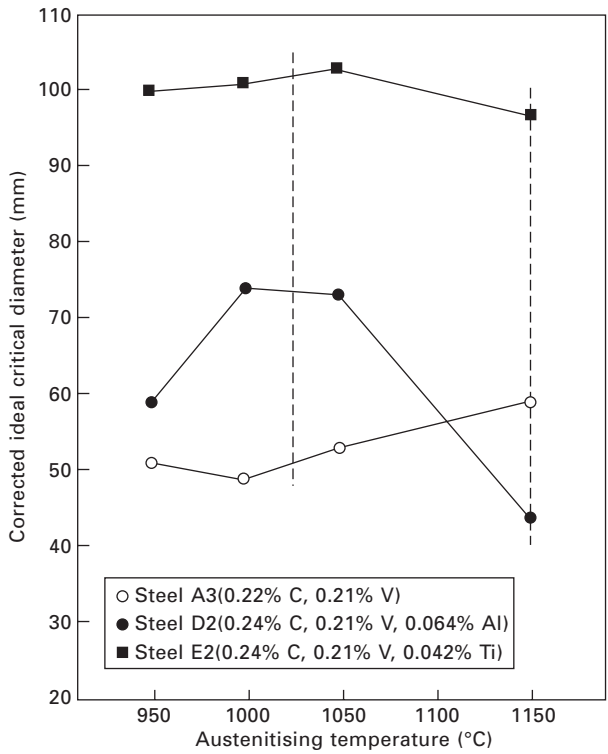
of grain refinement by heat treatment. However, as Grange (1971) showed some 40 years ago, rapid heating into the austenite phase field can further refine the steel, although there has been little or no practical application of the technique.

One unexplained consequence of microalloying additions is that thicker grain boundary or filamentary carbides form more easily when Nb or Ti is

© Woodhead Publishing Limited, 2012

used in both normalised and quenched and tempered steels. Whilst there is a measurable effect on impact properties of normalised steels (Mintz *et al.*, 1979), no mechanism has been proposed apart from suggestions that the interfacial energies between cementite and ferrite grain boundaries are changed possibly due to segregation.

In normalised steels the amount of microalloying element remaining in solid solution is only significant for V and Ti, consequently hardenability changes are small. However, in V-Al-N steels, there is evidence that the Jominy hardenability varies significantly with austenitising temperature (or time) because the relative amounts of V and Al in solution vary as equilibrium between VN and AlN is approached (Garbarz and Pickering, 1988) (Fig. 6.31). Similar effects have been observed in normalised V-N steels and B treated HSLA steels if Ti additions are used to protect the B addition, particularly if Al is present in excess (Martin, 1983).



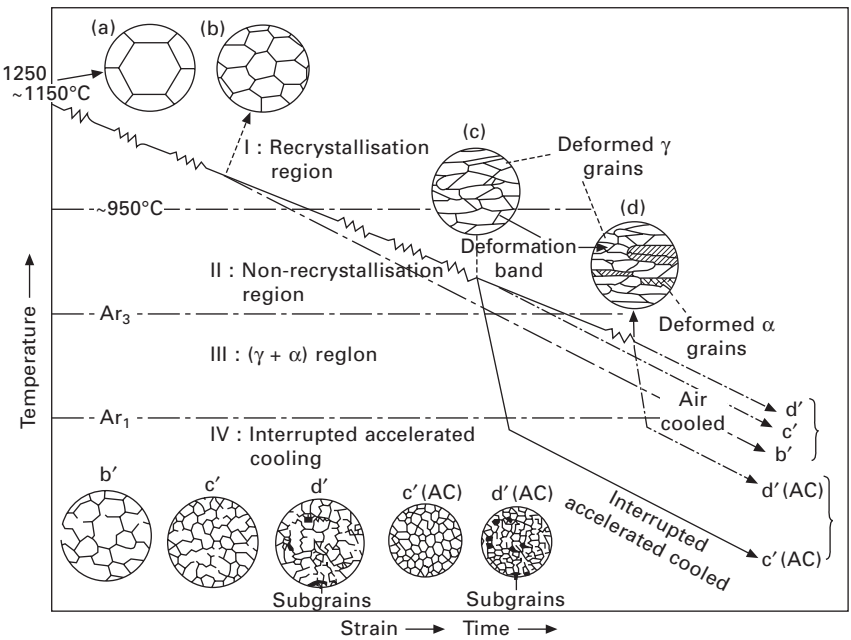
6.31 Changes in Jominy hardenability of a V-Al-N steel as a function of austenitising temperature, after Garbarz and Pickering (1988). Used with permission from Maney Publishing.

© Woodhead Publishing Limited, 2012

6.6.4 Controlled rolled ferrite/pearlite steels

Almost all microalloyed HSLA steels are now produced by variants of controlled rolling and, as already stated, a key finding has been that, in order to produce uniform ferrite refinement, the austenite must be 'conditioned' before transformation to ferrite takes place. Some typical rolling sequences for the development of the 'conditioned' austenite illustrating the various stages of microstructural development are shown in Fig. 6.32 (Kozasu *et al*., 1980). In the main, the technology was developed for 'reversing' plate mills and later the principles were extended to other types of rolling mill such as coiled plate or 'Steckel' mills where rolling is more of a continuous process and interpass times shorter, allowing less time for recovery processes in the austenite to take place.

The austenite 'conditioning' has three main stages. The first of these occurs during the early stages of rolling where the objective is to grain-refine the austenite by recrystallisation. In some Ti-V(-N) HSLA steel types, this



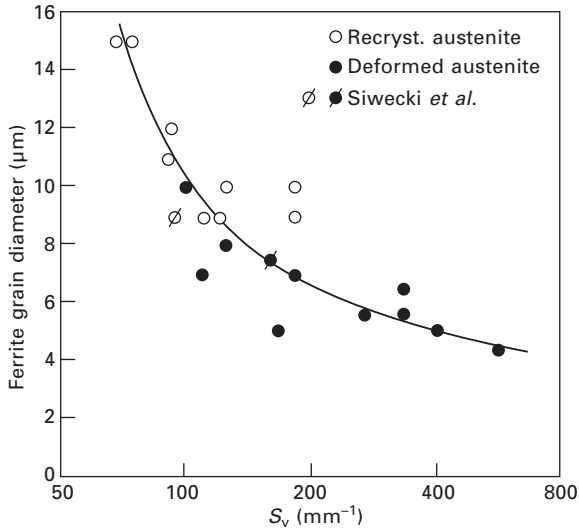
6.32 Schematic diagram comparing the changes in relative austenite grain size and shape on the final ferrite grain size after different types of controlled processing. Typically the ferrite grain sizes for b′: air cooled from RCR schedule, 6–12 μm; c′: air cooled from deformed austenite normal TMCR(1) schedule 5–10 μm; d′: TMCR(2) schedule with greater reduction after hold temperature, air cooled, 4–6 μm; c′(AC): TMCR(1) schedule plus accelerated cooling 4–8 μm. Adapted from Kosazu *et al.* (1980).

© Woodhead Publishing Limited, 2012

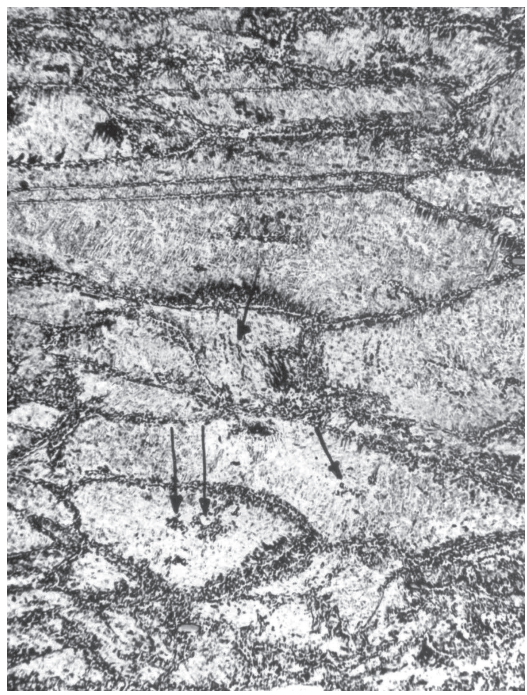
rolling sequence makes use of stable TiN particles to restrict grain growth at the slab reheating temperature and during recrystallisation, so maintaining a fine austenite structure throughout the entire rolling operation; such rolling schedules are referred to as RCR (Zajac *et al.*, 1991; Lagneborg *et al.*, 1999). Particularly for Nb HSLA steels, the second stage is one in which the microalloying addition(s) in the austenite interact with the presence of vacancies and dislocations inhibiting recovery and recrystallisation. There has been considerable discussion as to whether strain-induced precipitation of the microalloying element(s) is solely responsible for inhibiting recovery/recrystallisation or whether solute drag effects dominate at particular stages in austenite deformation. Much of this debate has been summarised in many reviews over the decades (Pickering, 1978; Tamura *et al.*, 1988; Gladman, 1997; DeArdo, 2003; Baker, 2009; Morrison, 2009). The final stage is one in which recrystallisation is almost completely inhibited by the microalloying additions and as deformation progresses no recrystallisation is allowed to take place by controlling the steel temperature within defined limits, the 'hold' temperature range. Thereafter, the austenite grain boundary surface area increases monotonically with the total rolling strain until the finish rolling temperature (FRT) is reached, the grains elongating and becoming thinner, so-called 'pancaking'. Ferrite transformation then takes place as the steel cools below the Ae_3 and is accelerated by the retained deformation (Tanaka, 1981). Additional grain refinement takes place through control of the cooling cycle, for example, on the run out table of hot strip mills or air mist cooling of reversing mill plate.

Viewed from a phase transformation aspect, the ferrite grain size is then determined by the extra nucleation sites available at the austenite grain boundaries. That there should be a relationship, as shown in Fig. 6.33, between the ferrite grain size and austenite surface area per unit volume is unsurprising. Detailed studies later inferred that not all controlled rolled steels obeyed this relationship and it was demonstrated that with suitable combinations of prior austenite grain size and rolling strain, intra-granular ferrite nucleation, an example of which is shown in Fig. 6.34, could make a significant contribution to grain refinement. Identification of these additional nucleation sites is difficult but some studies, on partially transformed and quenched laboratory rolled steels, have shown that deformation substructures in the austenite, particularly twins, shear bands and/or sub-boundaries are effective sites. Since the ferrite transformation is induced by retained strain in the austenite (Priestner and de los Rios, 1980; Choquet *et al.*, 1990; Kwon and DeArdo, 1991; Palmiere *et al.*, 1994; Quispe *et al.*, 1997), this process has been termed static strain-induced ferrite transformation (SSIT). Figure 6.35 shows an example of the change in transformation, Figs 6.35(a) and (b), and microstructure after deformation, Figs 6.35 (c) and (d) (Isasti *et al.*, 2011). Whilst, for most commercially rolled reversing plate mill steels, there

© Woodhead Publishing Limited, 2012



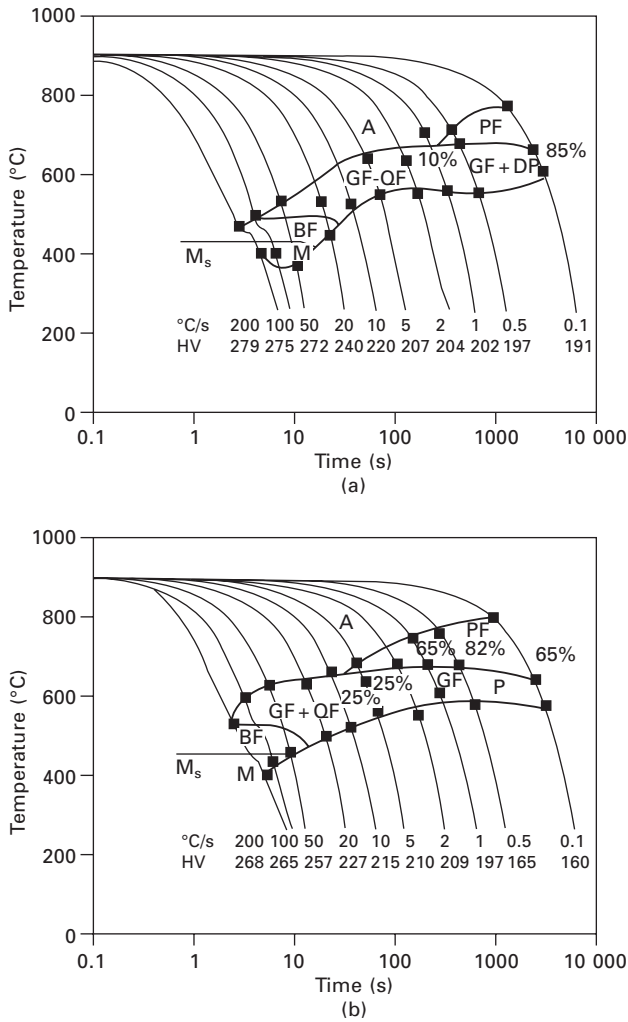
6.33 Relationship between ferrite grain size and the surface area/unit volume, S_v, for recrystallised austenite and 'pancaked' austenite, after Zajac *et al.* (1991).



6.34 Example of ferrite formation at intragranular sites in austenite. Quenched at 100°C/s directly after the end of rolling 0.13%C-1.25%Mn-0.022%Nb.

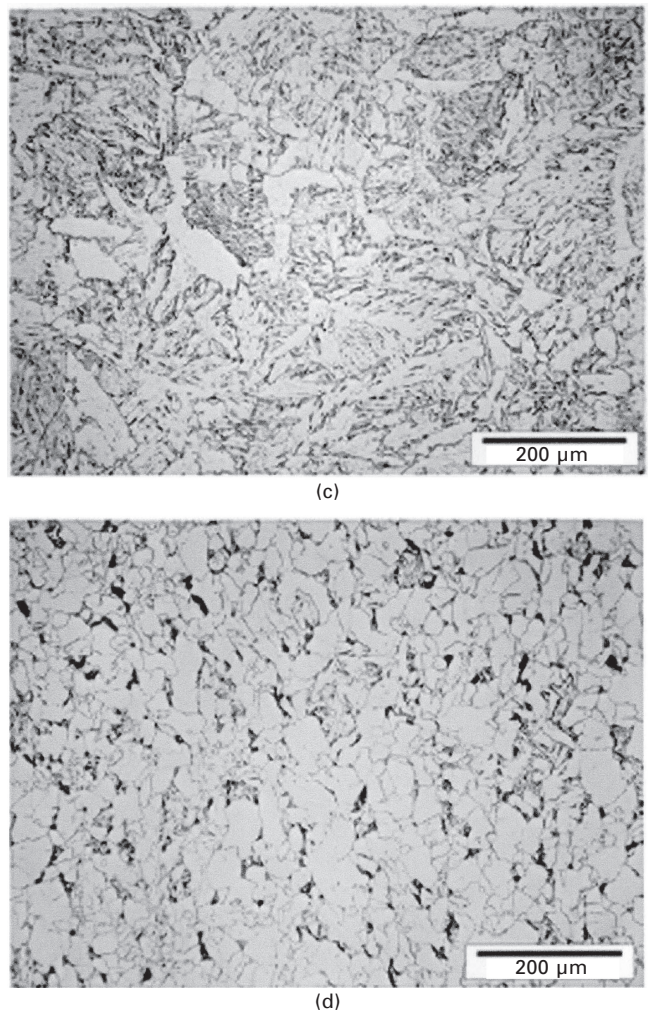
© Woodhead Publishing Limited, 2012

is reasonable agreement that the ferrite grain size is related to 'pancaking' of the austenite when deformation accumulates more gradually, as in coiled plate or hot strip mill processing, the role of stored energy in the austenite appears to be the more important nucleation event. The smaller interpass times in these later processes limits the time available for recovery processes



6.35 (a) and (b) CCT diagrams for Nb steel, undeformed and deformed, respectively, composition 0.05%C-0.05%Si-1.56%Mn-0.06%Nb. A: austenite, BF: bainitic ferrite, GF: grain boundary nucleated ferrite, QF: quasipolygonal ferrite, DP: dual phase regions consisting of mixtures of high carbon ferrite, martensite and other phases. M_s: martensite start temperature. (c) and (d) Micrographs for Nb steel transformed from (c) recrystallised, and (d) deformed austenite.

© Woodhead Publishing Limited, 2012



6.35 Continued

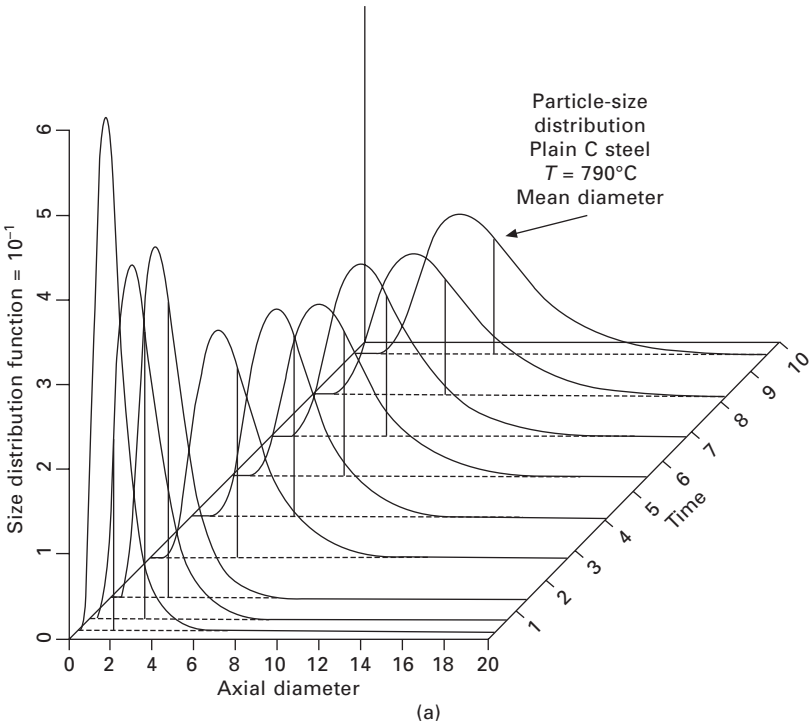
in the deformed austenite and presumably retains more active nucleation sites from which ferrite develops.

Whilst the development of the ferrite grain size from the deformed austenite structure is fairly well documented, there are aspects of the development of the ferrite which do not correspond to the simple idea of ferrite nucleation followed by growth into austenite. Several studies (e.g., those by Choquet *et al.*, 1990; Kwon and DeArdo, 1991) have concluded that nucleation at deformed austenite grain boundaries is on an extremely fine scale (Priestner and de los Rios, 1980; Priestner and Ali, 1993). The decrease in the number of ferrite grains as the ferrite structure develops is striking. Other attempts

© Woodhead Publishing Limited, 2012

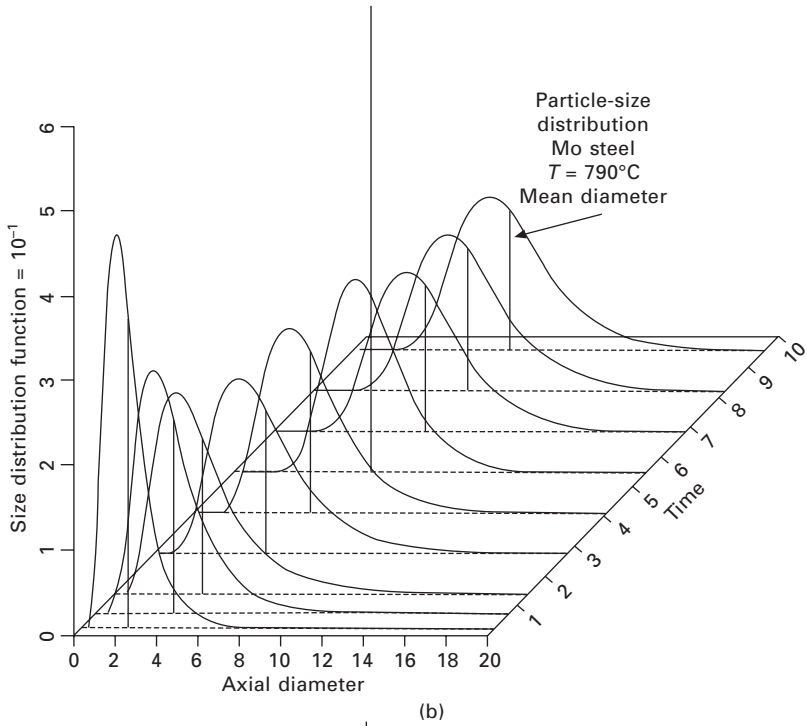
to track the changes in ferrite microstructure have shown similar trends (Priestner and Ali, 1993). The most obvious conclusion drawn from such studies is that the ferrite structure develops initially by amalgamation of groups of grains or sub-grains with very similar orientations, as envisaged in the later stages of recovery, simultaneous with growth of the 'surviving' grains into austenite. This mode of ferrite formation has been termed 'ferrite coarsening'. Measurements of ferrite grain size after quenching during ferrite growth confirms that the number of ferrite grains decreases and size increases continuously with time from the end of rolling (Cotrina *et al.*, 2000, 2004). Isothermal studies on undeformed steels (that is, in austenite which has simply been recrystallised by heat treatment) also show this effect albeit to a much less marked degree (Essadiqi and Jonas 1989; Cotrina *et al.*, 2004) (Fig. 6.36).

More recent studies using EBSD have shown that grain coalescence is the likely mechanisms through which ferrite coarsening takes place but there

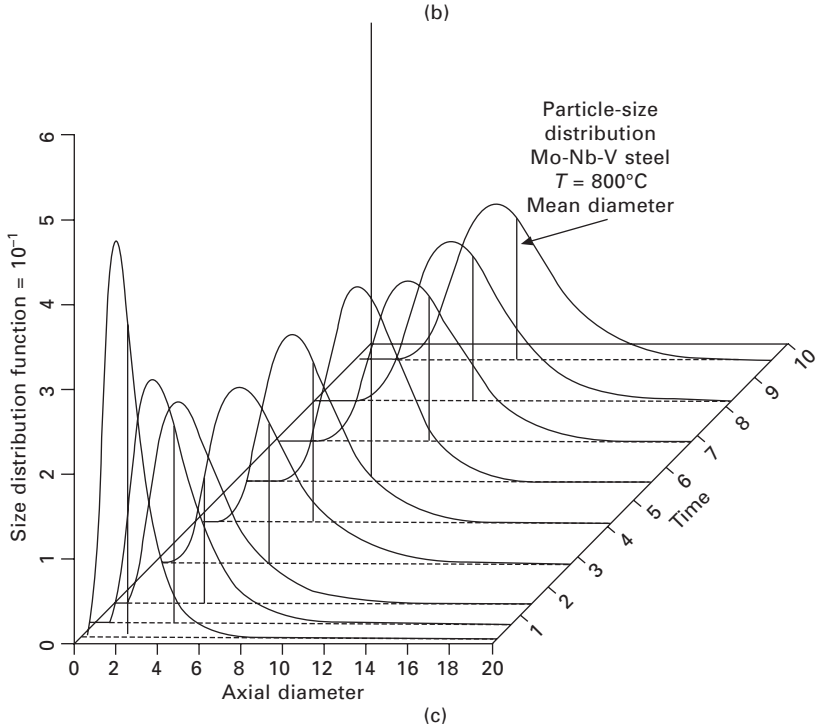


6.36 Changes in ferrite grain numbers in unit volume as transformation progresses for plain C, C-Mo and C-Mo-Nb-V, showing a gradual coarsening of ferrite grain size and a widening of the grain size distribution, from Essadiqi and Jonas (1989).

© Woodhead Publishing Limited, 2012



(b)



(c)

6.36 Continued

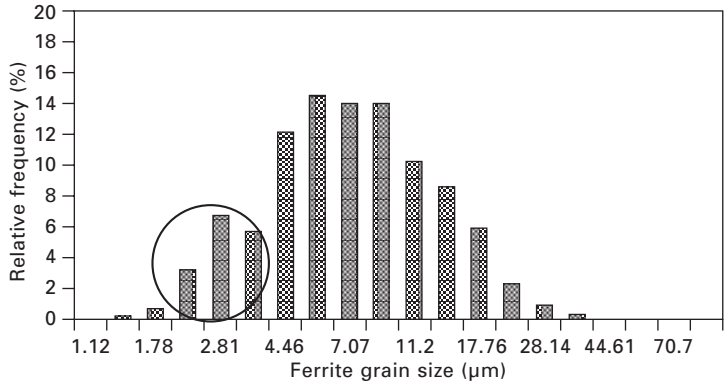
© Woodhead Publishing Limited, 2012

appears to be two stages to the process (Cotrina *et al*., 2004). The first is related to impingement of ferrite grains in the plane of prior austenite grain boundaries; the second appears to take place at comparatively high volume fractions of ferrite transformed where impingement takes place across the austenite grains as the ferrite grains become larger. The first stage appears to result in the elimination of low angle boundaries (<15°) whereas in the second higher angle boundaries are also lost. The generality of this effect suggests that this is a feature of the austenite/ferrite transformation, but the presence of sub-structures in the parent austenite is considered to aid the grain coalescence process. In most modelling studies to date, these effects are subsumed into the empirical relationship used to derive ferrite grain size from that of the parent austenite (see Sellars and Whiteman, 1979; Hodgson and Gibbs, 1992; Hodgson *et al*., 1996; Hutchinson, 2000; Sarkar and Militzer, 2009). Should the observations by Van Dijk *et al*. (2007) that ferrite nucleation may be best described by the dynamics of clustering and the lack of a barrier to nucleation, if repeated for microalloyed steels, prove correct, then the very high density of ferrite nuclei observed in the early stages of transformation in CR and TMCR steels might imply the ferrite coarsening process leading to evolution of the final ferrite grain size has more significance than previously considered.

6.6.5 Role of deformed austenite in ferrite formation and 'dynamic strain-induced' ferrite

At higher applied strains and/or in the case when FRT is at or close to the Ae_3, then a further mechanism is invoked to explain the formation of extremely fine grained ferrite, termed dynamic strain-induced transformation (DSIT) ferrite (Beladi *et al*., 2007; Basabe and Jonas, 2010). The key differences between this form of ferrite and the more usual ferrite grain development, SSIT, from austenite grain boundaries appear to relate to the presence of additional ferrite nucleation sites or, rather, that a larger number of sites are active because the interval between austenite deformation and the start of ferrite transformation is shorter. The role of microalloying elements is yet to be fully clarified, conceivably the presence of microalloy carbides could act as a substrate for nucleation. At least one study (Shokouchi and Hodgson, 2009) implies that the increase in Ae_3 associated with such additions may be important and therefore together with Si, also a ferrite stabiliser, may make an important contribution to grain refinement. An example of DSIT at temperatures close to the para-equilibrium Ae_3 for the steel in question is shown in Fig. 6.37 (Shokouchi and Hodgson, 2009) illustrating the appearance of a separate group of fine grains developing from dynamically created nucleation sites not eliminated by recovery. The mechanism by which dynamically strain-induced ferrite is formed remains controversial (Hickson

© Woodhead Publishing Limited, 2012



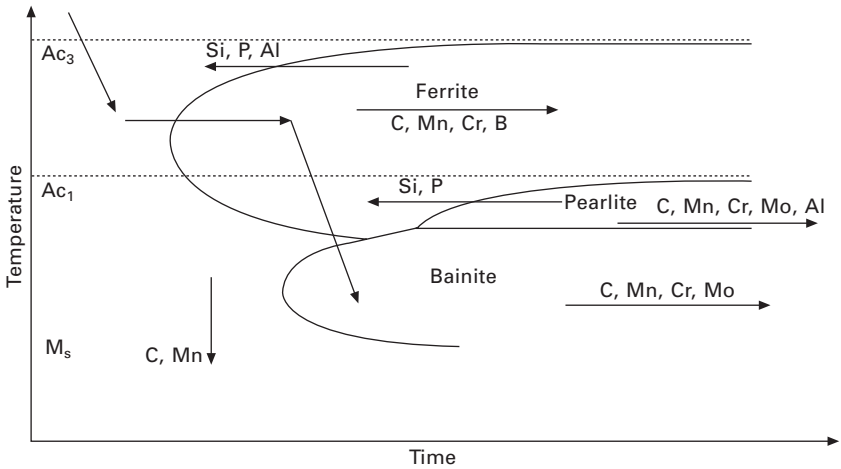
6.37 Presence of an additional size group of ferrite grains after DSIT treatment close to the Ae_3 of a C-Mn-Nb steel, after Shokouchi and Hodgson (2009).

et al., 1999; Hong *et al*., 2003; Shokouchi and Hodgson, 2009). Nevertheless, there is clear evidence that ferrite formation by such mechanisms increases with applied strain such that grain sizes less than 2 μm can be obtained at very high strains. One consequence of this has led to the development of laboratory scale processing of 'ultra-fine' ferrite structures where the final grain size is in the range 1 to 2.5 microns. The state of the art for this type of processing was recently reviewed by Howe (2009).

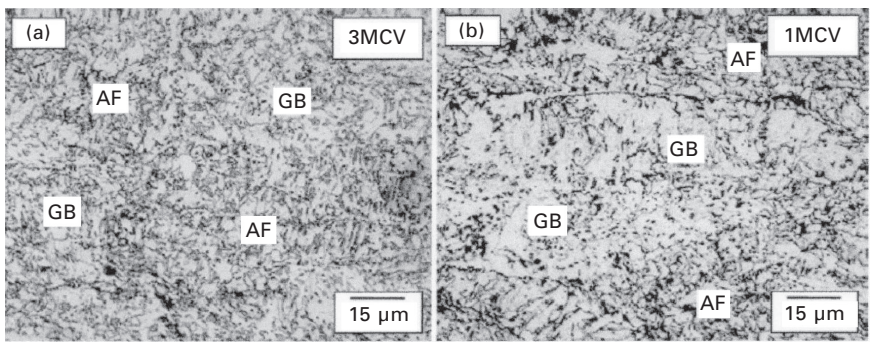
6.7 Controlled processed ferrite/bainite and acicular ferrite steels

The need for greater yield strength, in excess of about 550 MPa coupled with exceptional levels of impact toughness, particularly for oil/gas transmission pipeline steels, has led to the utilisation of 'bainitic' microstructures. For this to be achieved requires alloying additions which delay the onset of the ferrite transformation, elements such as Mo, Cr and B are effective and their role is shown schematically in Fig. 6.38. An early example of this approach was the so-called 'acicular ferrite' class of Nb-Mo steels introduced in the early 1980s. These steels were characterised by an irregular apolygonal ferrite microstructure containing islands of high carbon austenite/martensite. Later developments used additional alloying, principally Mn but also Mo, Cu and Ni and, in some cases B, which decreased the transformation temperature further and produced structures termed 'granular' bainite but which more closely resemble mixed microstructures of bainitic laths and quasi-polygonal ferrite grains (Fig. 6.39) (Han *et al*., 2009). The ferrite morphology has been variously described as 'acicular', 'quasi-polygonal', 'apolygonal' or 'bainitic'. Space precludes a detailed discussion of the growth mechanism

© Woodhead Publishing Limited, 2012



6.38 Schematic diagram illustrating the role of alloying on transformation characteristics. Note that elements such as Si, Al and P promote the ferrite reaction whereas C, Mn, Cr and B retard ferrite formation. Adapted from fig. 5 in Heller *et al.* (2000).



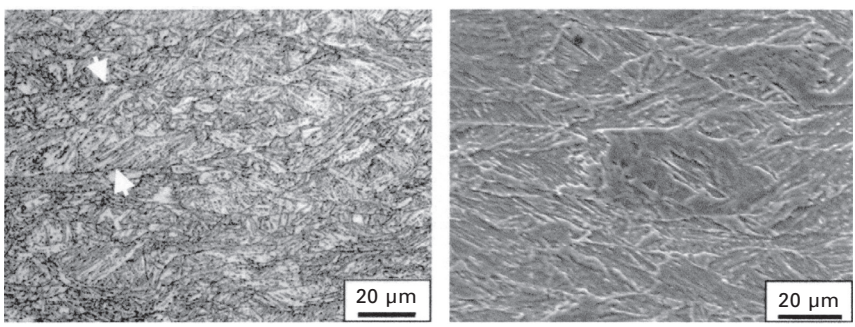
6.39 Microstructure of X80 type HSLA steels, 0.08%C-0.26%Si-1.9%Mn with additions of Mo, Cr and V. 3MCV, 0.3%Mo-0.3%Cr-0.06%V. 1MCV, 0.1%Mo-0.3%Cr-0.06%V. AF: acicular ferrite, GB: granular bainite. After Han *et al.* (2009).

responsible for the range of ferritic microstructures observed in this class of steels, but quasi-polygonal ferrite (QF) structures are characterised by irregular grain boundaries corresponding to groups of ferrite sub-grains with similar orientations (Kim *et al.*, 2008) whereas the 'acicular' structures, whilst implying a needle morphology, are generally applied to groups of ferrite plates or laths with mis-orientations greater than 15°. There is a general trend for the ferrite to become more lath-like or 'bainitic' in character as the alloy content increases. The balance of evidence from TEM observations suggests that the 'acicular' ferrite in these steels is dissimilar to the range

© Woodhead Publishing Limited, 2012

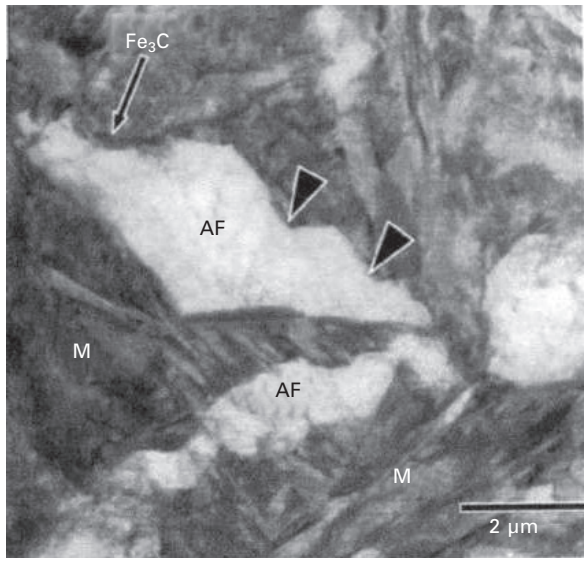
of characteristic intragranularly nucleated 'acicular ferrite' microstructures, found primarily in weld metals, which consist of interlocking or 'basket-weave' ferrite plates nucleated at intragranular sites within austenite. The detailed structure of the particular type of acicular ferrite morphology found in the higher strength HSLA TMCP steels suggests that the mis-orientation between sub-units is smaller than found for acicular ferrite in weld metals, indicative of a different origin (Wang *et al.*, 2008).

More recently, the use of higher Nb content, in the range 0.06–0.1%, coupled with reduced C contents in the range 0.02–0.06%, has allowed inhibition of recrystallisation by precipitation to begin at significantly higher rolling temperatures. The Nb remaining in solution then reduces transformation temperature. By increasing the Mn content, up to 2% in some cases, as well as other additions, for example Si, Ni, Cu or Mo, the bulk of transformation takes place close to or below the bainite start temperature, B_s. When processed via a severe controlled rolling schedule and accelerated cooling, such steels have extremely fine microstructures which have proved difficult to categorise. The effective ferrite grain size (EFG), has been estimated as ~1.9 μm in one study (Guo *et al.*, 2010). EBSD and TEM studies show structures with similarities to carbide-containing or carbide-free bainite, for example, thin carbide or retained austenite films between laths with rather small mis-orientation of the order of 5–10° (Guo *et al.*, 2010) (Fig. 6.40). The presence of other groups of laths, EFG around 3 μm, with larger mis-orientation, ~15°, may be indicative of acicular ferrite formation (Guo *et al.*, 2010) (Fig. 6.41). More commonly, similar microstructures in 'ultra-low' carbon steels are essentially carbide-free although, based on very limited CCT information, consistent with transformation in the bainitic temperature range (Bojarski and Bold, 1974; Jun *et al.*, 2006).



6.40 Elongated 'bainitic' microstructure of a controlled rolled 890 MPa linepipe steel of nominal composition 0.04%C-0.3%Si-1.8%Mn-0.2%Cr-0.08%Nb-0.015%Ti with unstated Ni and Mo additions in the range 0.2–0.7. Arrows indicate prior austenite boundaries. Adapted from Guo *et al.* (2010).

© Woodhead Publishing Limited, 2012



6.41 Details of a partially transformed acicular ferrite (AF) microstructure quenched after transformation at 600°C. M is martensite formed from the prior austenite and the arrows show sub-unit boundaries. Nominal composition 0.05%C-1.79%Mn-0.05%Nb+Ti. After Kim *et al.* (2008).

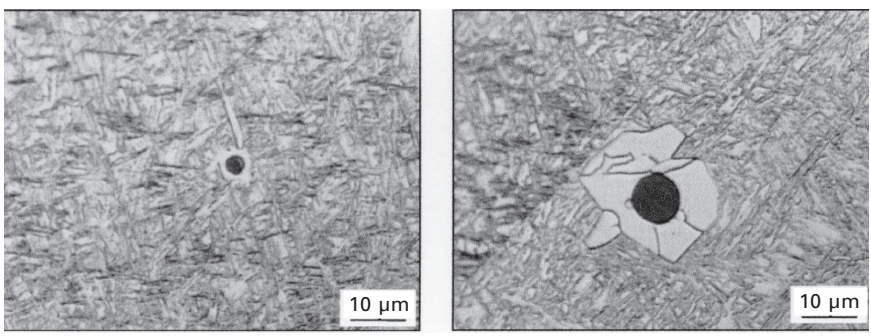
6.7.1 Acicular ferrite steels

Given the attractive combination of mechanical properties provided by a fully acicular ferrite microstructure, some weld metals can exhibit yield strengths of about 690 MPa coupled with 54 J impact transition temperature below –100°C and, consequently, several attempts have been made to promote this mode of transformation either directly to optimise mechanical properties in plate or strip steel compositions or to modify the weld HAZ microstructure. In weld metals where such structures can be readily obtained, there is little doubt as to the effectiveness of the inclusion population which is some 10 times that of a commercial steel (weld metal oxygen contents range from ~200 to 450 ppm compared to <10–50 ppm for steels). While the effectiveness of the various inclusion substrates continues to be debated, some features are well recognised. There needs to be at least one set of crystallographic planes with a close match to ferrite; 'TiO' (Mills *et al.*, 1987; Lee, 1994), galaxite ($MnO{\cdot}Al_2O_3$) (Mills *et al.*, 1987), TiN (Ilman, 2001; Ilman *et al.*, 2011) or BN (Ilman, 2001) have all been proposed. To form acicular ferrite in a steel, three conditions appear to be necessary. Firstly, Ti deoxidation appears to be beneficial; the role of Ti appears to be due to epitaxial ferrite nucleation on 'TiO'-rich inclusions or TiN particles or inclusions. Secondly, there needs to be a critical volume fraction and size of inclusions for ferrite nucleation to

© Woodhead Publishing Limited, 2012

be effective (Grong *et al.*, 1995). Finally, displacive transformation to ferrite must take place below or close to the B_s temperature (Barbaro *et al.*, 1989). Although weld metals are characterised by relatively coarse austenite grain size and therefore the ratio of austenite grain boundary surface area to total inclusion surface area approaches 1, this does not necessarily preclude the formation of acicular ferrite in steels provided the intragranular nucleation rate is enhanced by adding active substrates, such as 'TiO' (Shim *et al.*, 1999), MnS (Tomita *et al.*, 1994) (Fig. 6.42), or rare earth oxides (Thewlis, 2006).

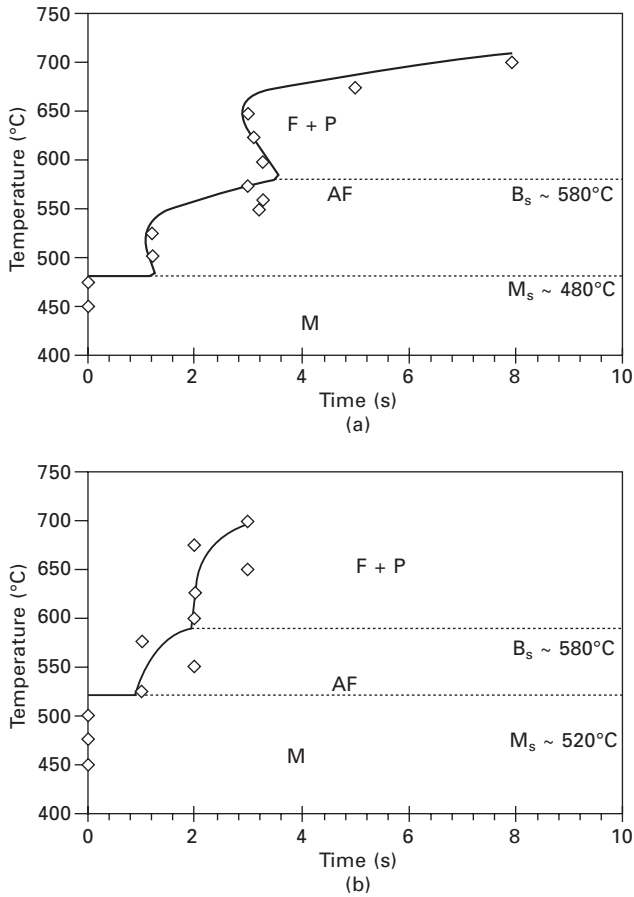
Several attempts have been made to produce AF microstructures in steels or in the weld HAZ by doping with suitable inclusions of an appropriate size; between 0.25 and 2.5 μm appears to be optimal from studies on welds and/or by lowering the transformation temperature by alloying (Al-Hajeri *et al.*, 2006). Ensuring sufficient oxide particles are present means that the oxygen content must be above some minimum value, estimated to be 50–80 ppm. At this level, Al deoxidation is not desirable and to some degree, this also mitigates against using Nb since Nb_2O_5 is formed and would reduce O below that desired at steelmaking temperatures. Hence, V additions seem to be more appropriate. Whilst some success in promoting AF has been achieved on a laboratory scale for Nb steels, prospects for scaling to commercial production appear limited by the need to control, firstly, the state of deoxidation as this requires a departure from conventional steelmaking; secondly, the cooling rate needed to form inclusions of an appropriate size is unobtainable with conventional continuous casting, except by the thin slab process route. Although some commercial steels have been promoted as having improved HAZ properties as a result of promoting acicular ferrite formation (Hart and Mitchell, 1995), only V treated steels appear to give rise to a fully AF microstructure (He and Edmonds, 2002; Jun *et al.*, 2006) under HAZ conditions. However, a recent study by Garcia and co-workers (Garcia-Mateo *et al.*, 2008a, 2008b) strongly implicates VN formed in



6.42 Examples of ferrite plates nucleating at 'TiO' inclusions in a simulated heavy steel section. After Al-Hajeri *et al.* (2006).

© Woodhead Publishing Limited, 2012

austenite as a nucleant for AF (Fig. 6.43). However, given that little or no precipitation would be expected during a typical weld HAZ thermal cycle, such an interpretation seems contrary to the work of He and Edmonds (2002) and the balance of studies on welded structures. It seems probable that all these observations can be reconciled in terms of a sequence of segregation, clustering followed by precipitation with the dominant mechanism being dependent on steel composition and/or processing.



6.43 Acceleration of acicular ferrite formation in a V-N steel after a deliberate heat treatment to precipitate VN in austenite after holding at 900°C for 2500 s (b), compared to simply cooling from the re-heating temperature of 1125°C for 120 s. The solid lines correspond to the start of transformation. Note the broadening of the AF range and depression of martensite start temperature, M_s, on the CCT diagram (a), compared to that in (b). Steel composition, 0.08%C-1.46%Mn-0.25%V-0.018%N. Adapted from Garcia-Mateo *et al.* (2008a, 2008b).

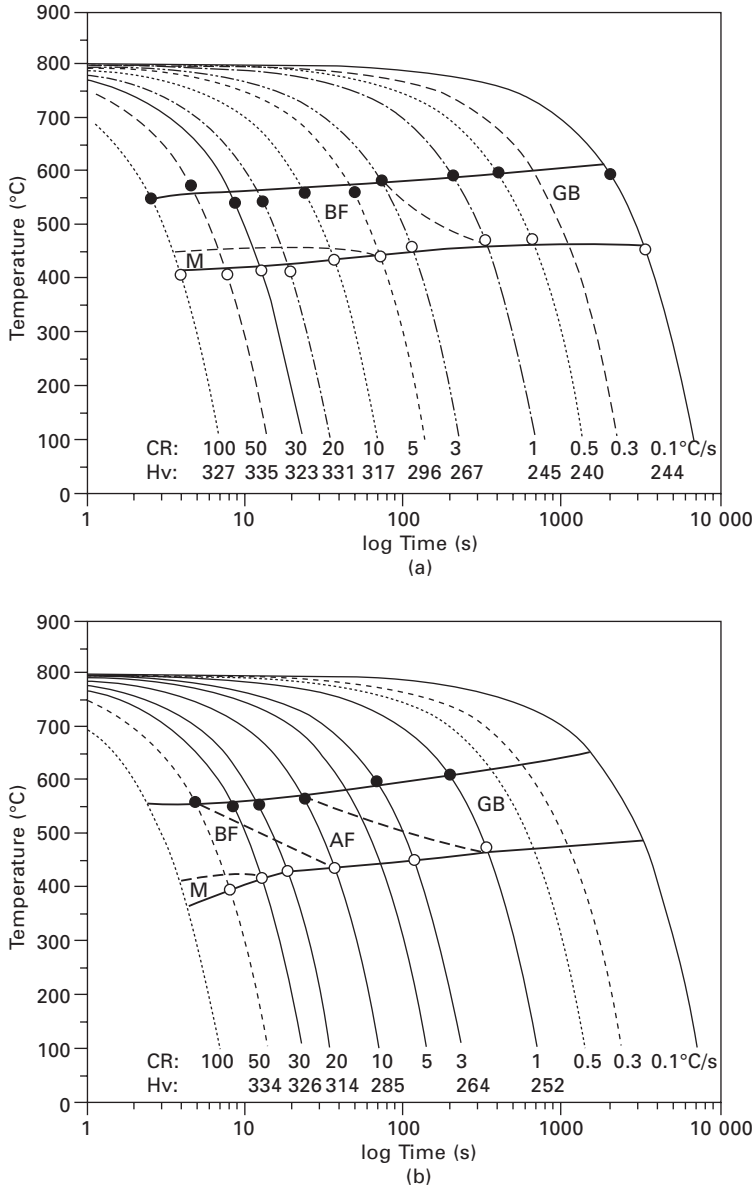
© Woodhead Publishing Limited, 2012

6.8 Conclusions and future trends

While the microalloying concept has proved of great benefit in terms of producing steels capable of satisfying the mechanical property requirements demanded by users, the process of developing new steels still succeeds on an empirical basis although guided by the metallurgical principles described. The increasing need to validate models to predict microstructure will expose some shortcomings in the understanding of the details of the austenite to ferrite phase transformation, specifically nucleation. Austenite grain size prediction from knowledge of the rolling operation and the steel composition already gives realistic results for laboratory simulations used for studying controlled rolling. The role of Nb in the development of the deformation substructures is also approaching a stage where it can realistically be anticipated that the 'conditioned' state of the austenite at a relevant length scale can be predicted for some commercial rolling operations. There seems, however, no simple method of predicting ferrite grain size directly from the state of the austenite. Almost all of the current approaches rely on empirical relationships between the final ferrite grain size and the state of the 'conditioned' austenite. Given the complexity of the ferrite grain coarsening which is evident from more recent studies, it is unlikely, in the author's opinion, that this task will be an easy one. Moreover, the development of the 'ultra-fine', quasi-polygonal, 'bainitic' or acicular ferrite microstructures characteristic of the recent generation of low carbon TMCP steels has yet to be clarified and related in detail to the transformation behaviour. It would appear that there is a much greater spread in grain mis-orientation in these TMCP steels than is observed in more conventional TMCR steels, suggesting that the features noted for ferrite grain coarsening may operate at lower transformation temperatures. Furthermore, the observation of groups of laths with characteristics of bainite together with groups of grains of appreciably larger mis-orientations might imply the diffusional ferrite transformation is promoted or accelerated at particular austenite grain mis-orientations or within the grain interiors by retained deformation. There have been studies on the effects of deformation of weld metals which show an acceleration of the AF reaction, but in one case it was judged that strain accumulation around inclusions raised the AF transformation start temperature (Yang *et al.*, 1995). This finding seems compatible with the microstructural changes noted in some HSLA steels where retained deformation appears to promote AF over GB (granular bainite) in a temperature range where displacive transformation predominates (Jun *et al.*, 2006) (Fig. 6.44).

There are new approaches which should shed some light on the mechanisms responsible for the microstructures found in TMCP steels noted above. Applying molecular dynamics (MD) and Monte Carlo (MC) computational methods to the dynamics of clusters of solute atoms of the type detected

© Woodhead Publishing Limited, 2012



6.44 Effect of deformation (b) in replacing bainitic ferrite (BF) by acicular ferrite (AF) over the cooling rate range ~1–20°C/sec. GB: grain boundary ferrite, M: martensite. Boron treated 0.05%C-0.25%Si-1.92%Mn-0.067Nb+Ti-1.1 total Mo+Cr+Ni. From Jun *et al.* (2006).

© Woodhead Publishing Limited, 2012

by atom probe studies should lead to a better understanding of the events leading to ferrite nucleation (see Tateyama *et al*., 2010; Nagano and Enomoto, 2010). It can be argued, for instance, that strong interactions between Fe and solutes in alloy systems showing intermetallic formation, Fe-V, Fe-Ti, Fe-Nb or Fe-Al, would change the Fe-X(any solute)-Fe cluster dynamics leading to nucleation, both in the austenite matrix but also at grain boundaries, hence influencing nucleation rates of ferrite. The question over the significance of epitaxial nucleation events for acicular ferrite nucleation may also be clarified by such processes; some relevant studies have been carried out on Al alloys (Bunn *et al*., 1998), where similar epitaxial events are thought to be implicated in grain refinement from the as-cast state (Schumacher *et al*., 1998).

6.9 Acknowledgements

The author would like to thank the editors for the opportunity to review a field of literature vast in its scope and application to 'real' materials. In the field of microalloyed steels, to attempt to survey and summarise some 50 years of metallurgical endeavour, both academic and industrial, has meant there will, inevitably, be omissions of very many significant contributions. All of these are of the author's making and are sincerely regretted.

6.10 References

Abad R, Fernandez A I, Lopez B, Rodriguez-Ibabe J M (2001), *ISIJ Int*., 41, 1373–1382.

Adrian H (1992), *Mat. Sci. Tech*., 8, 406–419.

Al-Hajeri K F, Garcia C I, Hua M, DeArdo A J (2006), *ISIJ Int*., 46(8), 1233–1240.

Andrade H L, Akben M G, Jonas J J (1983), *Mat. Trans*., 14A, 1967–1977.

Armstrong R, Codd I, Douthwaite R M, Petch N J (1962), *Phil. Mag*., 7, 45–58.

Avrami M (1939), *J. Chem. Phys*., 7, 1103–1112.

Avrami M (1940), *J. Chem. Phys*., 8, 212.

Avrami M (1941), *J. Chem. Phys*., 9, 177–184.

Axelsen O M, Grong O, Solberg J K (1987), *Mat. Sci. Tech*., 1, 649–655.

Baker R G, Nutting J (1959), 'Precipitation Processes in Steels', Special Report 64, Iron and Steel Institute, London.

Baker T N (2009), *Mat. Sci. Tech*., 25, 1083–1107.

Barbacki, Honeycombe R W K (1976), *Metallography*, 9, 277–291.

Barbaro F J, Kaukis P, Easterling K E (1989), *Mat. Sci. Tech*., 5, 1057–1066.

Basabe V, Jonas J J (2010), *ISIJ Int*., 50(8), 1185–1192.

Beladi H, Kelly G H, Hodgson P D (2007), *Int. Met. Rev*., 52, 15–28.

Beynon J H, Sellars C M (1992), *ISIJ Int*., 32, 359–367.

Bojarski Z, Bold T (1974), *Acta Met*., 22, 1223–1234.

Bunn A M, Evans, P V, Bristow D J, Greer A L, (1998), *Symposium 'Light Metals 1998'*, Canadian Institute of Mining, Metals and Petroleum, Calgary, Canada, pp. 963–968.

© Woodhead Publishing Limited, 2012

Cahn J (1956), *Acta Met*., 4, 449.
Chen Z, Loretto M J, Cochrane R C (1987), *Mat. Sci. Tech*., 3, 836–844 (www.maney.co.uk/journals/mst; www.ingentaconnect.com/content/maney/mst).
Choquet C, Fabrègue P, Guisti J, Chamont B, Pezant J N, Blanchet F (1990), in S. Yue (ed.), *Int. Symp. 'Mathematical Modeling of Hot Rolling of Steel'*, MetSoc-CIM, Montreal, QC, Canada, pp. 34–43.
Cochrane R C (1976), Presented at Institute of Mechanical Engineering Symposium on 'Stress Relieving of Pressure Vessel Steels', London.
Cochrane R C (1979), British Steel Technical Report, internal communication, unpublished.
Cochrane R C (2000), International Conference, 'Thermomechanical Processing of Steels', IOM, London, pp. 15–28.
Cochrane R C, Morrison W B (1979a), International Conference 'Strength of Metals and Alloys', Paper 23, Aachen, West Germany.
Cochrane R C, Morrison W B (1979b), Phase Transformations, Inst. of Metallurgists Conference 3(11), pp. 11–17.
Cochrane R C, Morrison W B (1981a), International Conference 'Steels for Linepipe and Pipeline Fittings', VANITEC & Metals Society Conference, London, Paper 7.
Cochrane R C, Morrison W B (1981b), *Met. Tech*., 12, 481 (www.maney.co.uk/journals/mst; www.ingentaconnect.com/content/maney/mst).
Cochrane R C, Mintz B, Ward J L (1989), *Mat. Sci. Tech*., 5(2), 523–529.
Cotrina E, Argüelles A, Bengochea R, López B, Gutiérrez I (2000), *Int. Conf. on Thermomechanical Processing of Steels*, IOM, London, pp. 255–264.
Cotrina E, Iza-mendia A, López B, Gutiérrez I (2004), *Met. Mater. Trans*., 35A, 93–103.
Couch A J (2001), PhD thesis, University of Leeds.
Craven A J, McKenzie M, Cerezo C, Godfrey T, Clifton P N (2008), *Mat. Sci. Tech*., 24(2), 641–650.
Cuddy L J (1984), *Met. Trans*., 15A, 87–98.
Davenport A T, Honeycombe R W K (1971), *Proc. Roy. Soc. A*, 322, 191–205.
Davies C L, Strangwood M (2009), *Mat. Sci. Tech*., 25(9), 1126–1133.
DeArdo A J (2003), *Int. Mater. Rev*., 48(6), 371–408.
DeArdo A J (2009), *Mat. Sci. Tech*., 25, 1074–1082 (www.maney.co.uk/journals/mst; www.ingentaconnect.com/content/maney/mst).
DeKazinczy F, Axnas A, Pachleitner P (1963), *Jernkont. Ann*., 147, 408.
De Meyer M, Vanderschueren D, De Cooman B C (2000), International Conference. 'Thermomechanical Processing of Steels', IOM, London, pp. 505–514.
Dippenaar R J, Honeycombe R W K (1973), *Proc. Roy. Soc. A*, 333, 455–467.
Dutta B, Palmiere E J (2003), *Metall. Mater. Trans. A*, 34A, 1237–1247.
Dutta B, Sellars C M (1987), *Mat. Sci. Tech*., 3, 197–206.
Dutta B, Valdes E, Sellars C M (1992), *Acta Mater*., 40, 653–662.
Edmonds D V (2004), 'Designing with microalloyed and interstitial-free steels', in G E Totten, L Xie and K Funatani (eds), *Handbook of Mechanical Alloy Design*, Marcel Dekker, New York, pp. 321–353.
Egner D J (1999), PhD thesis, University of Leeds.
Egner D J, Cochrane R C, Brydson, R (1999), Inst. Phys. Conf. No 161 (EMAG'99), Sheffield, IOP Publishing, London, pp. 447–450.
Eldis G, Hagel W C (1978), in *Hardenability Concepts with Applications to Steels*, TMS-AIME, Chicago, IL, pp. 397–420.

© Woodhead Publishing Limited, 2012

Eldridge M F (2000), PhD thesis, University of Leeds.
Enomoto M, Nojiri N, Sato Y (1994), *Mat. Trans. JIM*, 35, 859–867.
Essadiqi E, Jonas J J (1989), *Met. Trans.*, 20A, 987–998.
Faulkner R G (1985), *Mater. Sci. Tech.*, 1, 442–447.
Faulkner R G, Song S-H, Flewitt P J (1996), *Mat. Sci. Tech.*, 12, 818–822.
Fosseart C, Rees G, Maurickx T, Bhadeshia H K D H (1995), *Met. Trans.*, 26A, 21–30.
Fujita S, Bhadeshia H K D H (2001), *Mat. Sci. Tech.*, 17, 403–408.
Garbarz B, Pickering F B (1988), *Mat. Sci. Tech.*, 4, 967–975 (www.maney.co.uk/journals/mst; www.ingentaconnect.com/content/maney/mst).
Garcia de Andres C, Capdevila C, Cabellero F G (1998), *Met. Sci. Forum*, 231, 284–286.
Garcia-Mateo C, Cornide J, Capedevila C, Caballero F G, Garcia de Andres C (2008a), Pt I, *ISIJ Int.*, 48(9), 1270–1275.
Garcia-Mateo C, Cornide J, Capedevila C, Caballero F G, Garcia de Andres C (2008b), Pt II, *ISIJ Int.*, 48(9), 1276–1279.
Gladman T (1966), *Proc. Roy. Soc. A*, 294A, 298–309.
Gladman T (1997), *The Physical Metallurgy of Microalloyed Steels*, IOM, London.
Goldschmidt H J (1967), *Interstitial Alloys*. Butterworths, London.
Gomez M, Medina S F, Valles P (2005), *ISIJ Int.*, 45, 1711–1720.
Grange R A (1971), *Met. Trans.*, 2, 65–78.
Gray J M, Yeo R (1968), *Trans. ASM*, 61, 255–269.
Grong O, Kluken A G, Nylund H K, Don A L, Helen J (1995), *Met. Mat. Trans.*, 26A, 525–533.
Guo A, Mistra R D K, Xoa J, Guo B, Jansto J G (2010), *Mat. Sci. Eng.*, 527A, 3886–3892.
Gupta S (1993), *Steel Research*, 64(12), 623–629.
Han S Y, Shin S Y, Seo C-H, Lee H, Bae J-H, Kim K, Lee S, Kim N J (2009), *Metall. Mater. Trans.*, 40A, 1851–1863.
Hart P H M, Mitchell P S (1995), *Weld. J.*, 74, 239–243.
He K, Edmonds D V (2002), *Mat. Sci Tech.*, 18(2), 289–296.
Heikkinen V K (1974), *Scand. J. Met.*, 3, 41–45.
Heller T, Engl B, Theimann G, Stich G (2000), International Conference, 'Thermomechanical processing of steels', IOM, London, pp. 438–445.
Hellman P, Hillert M (1975), *Scand. J. Met.*, 4, 211–219.
Hickson M R, Gibbs R K, Hodgson P D (1999), *ISIJ Int.*, 39, 1176–1180.
Hillert M (1965), *Acta Met.*, 13, 227–238.
Hillert M (1988), *Acta Met.*, 36(12), 3177–3181.
Hillert M (1999), *Acta Mater.*, 57, 4481–4505.
Hillert M, Staffanson L I (1970), *Acta Chem. Scand.*, 24, 3618–3626.
Hin C, Brechet Y, Maugis P, Soisson F (2008a), *Acta Mater.*, 56, 5653–5667.
Hin C, Brechet Y, Maugis P, Soisson F (2008b), *Acta Mater.*, 56, 5535–5543.
Hodgson P D, Gibbs R K (1992), *ISIJ Int.*, 32, 1329–1336.
Hodgson P D, Trail R M, Gibbs R K, Grace J, Davies C H J (1996), in *Modelling of Metal Rolling Processes*, IOM, London, pp. 345–354.
Honeycombe R W K (1976), *Metall. Trans.*, 7A, 915–936.
Hong C, Lim S H, Lee K L, Shin D H, Lee K S (2003), *ISIJ Int.*, 43, 394–399.
Houghton D C (1993), *Acta Met.*, 41(10), 2293–3006.
Houghton D C, Weatherly G C, Embury J D (1982), in *Thermomechanical Processing of Austenite*, Pittsburgh, PA, AIME, pp. 267–292.

© Woodhead Publishing Limited, 2012

Howe A A (2009), *Mat. Sci. Tech.*, 25, 815–819.
Hudd R C, Jones A, Kale M N (1971), *J. Iron & Steel Institute*, 209, 121–125.
Hulka K, Gray J M, Heisterkamp F (1990), Niobium Technical Report NbTR-16/90, CBMM, Brazil.
Hutchinson W B (2000), in *Thermomechanical Processing of Steels*, IOM, London, pp. 233–244.
Ilman M N (2001), PhD thesis, University of Leeds.
Ilman M N, Evans GM, Cochrane R C (2011) *International Institute of Welding Conference*, Chennai, India.
Irvine K J, Pickering F B, Gladman T (1967), *J. Iron & Steel Institute*, 205, 161–182.
Irvine K J, Gladman T, Orr J, Pickering F B, (1970), *J. Iron & Steel Institute*, 208, 717–726.
Isasti N, Jorge-badiola D, Taheri M H, Lopez B, Uranga P (2011), *Metall. Mater Trans.*, 42A, 3729–3742.
Jachym V, Horky P, Prnka T (1978), *Trans ISIJ*, 18, 181–184.
Jun H I, Kang J S, Seo D H, Kang K B, Park C G (2006), *Mat. Sci. Eng.*, 427A, 157–162.
Kim Y M, Lee H, Kim N J (2008), *Mat. Sci. Eng.*, 478A, 362–370.
Kirkaldy J S, Baganis E A (1978), *Met. Trans.*, 9A, 495–501.
Kozasu I *et al.* (1980), adapted from Nippon Kokan K K, internal report.
Kwon O, DeArdo A J (1991), *Acta Metall. Mater.*, 39, 529–538.
Lagneborg R, Siwecki T, Zajac S, Hutchinson W B (1999), *Scand. J. Met.*, 28(5), 186–241.
Law N C, Parsons S A, Howell P R, Edmonds D V (1987), *Mat. Sci. Tech.*, 3, 642–648.
LeBon A, Rofes-Vernis J, Rossard C (1975), *Met. Sci.*, 9, 36–41 (www.maney.co.uk/journals/mst; www.ingentaconnect.com/content/maney/mst).
Lee J L (1994), *Acta Mater.*, 42, 3291–3298.
Lee S, Chun B, Kwon D (1992), *Met. Trans.*, 23A, 2803–2816.
Li Y, Wilson J A, Craven A J, Mitchell P S, Crowther D N, Baker T N (2007), *Mat. Sci. Tech.*, 23(5), 509–518.
Liu S K, Zhang G Y (1990), *Met. Trans.*, 21A, 1509–1515.
Mannerkoski M (1964), *Acta Politechnia Scand.*, 26.
Martin I W (1983), British Steel Corporation, internal report, unpublished.
Medina S F (1997), *J. Mater. Sci.*, 32, 1487–1492.
Medina S F, Mancilla J E (1994), *Acta Metall. Mater.*, 42, 3945–3951.
Militzer M, Hawbolt E B, Meadowcroft T R (2000), *Metall. Mater. Trans.*, 31A, 1247–1255.
Mills A R, Thewlis G, Whiteman J A (1987), *Mat. Sci. Tech.*, 3, 1051–1061.
Mintz B, Morrison W B, Jones A R (1979), *Met. Technol.*, 6(6), 252–260.
Moon J, Lee C (2009), *Acta Mater.*, 57, 2311–2320.
Morrison W B (2009), *Mat. Sci. Tech.*, 25, 1066–1073 (www.maney.co.uk/journals/mst; www.ingentaconnect.com/content/maney/mst).
Nagano T, Enomoto M (2010), *Met. Mat. Trans.*, 37A, 929–932.
Nagarajan V, Palmiere E J, Sellars C M (2009), *Mat. Sci. Tech.*, 25(9), 1168–1174.
Nakata N, Militzer M (2005), *ISIJ Int.*, 45, 82–90.
Narita K (1975), *Trans. ISIJ*, 15, 145–152.
Okamoto R, Ågren J (2010), *Acta Mater.*, 58, 4791–4803.
Okamoto R, Borgenstam A, Ågren J (2010), *Acta Mater.*, 58, 4783–4790.

© Woodhead Publishing Limited, 2012

Ouchi C, Sampei T, Kosazu T (1982), *Trans. ISIJ*, 22, 214.
Palmiere E J, Garcia C I, DeArdo A J (1994), *Metall. Mater. Trans.*, 25A, 277–86.
Park J S, Lee J K (2007), *Scripta Mater.*, 57, 109–112.
Park J S, Ha Y S, Lee S J, Lee Y K (2009), *Met. Mat. Trans.*, 40A, 560–568.
Pereloma E V, Bayley C, Boyd J D (1996), *Mat. Sci. Eng. A*, 210, 16–24.
Pereloma E V, Crawford B R, Hodgson P D (2001), *Mater. Sci. Eng.*, A299, 27–37.
Pereloma E V, Timokhina I B, Russell K F, Miller M K (2006), *Scripta Mater.*, 54, 471–476.
Pickering F B (1978), *Physical Metallurgy and Design of Steels*, Applied Science Publishers, Barking.
Priestner R, Ali L (1993), *Mater. Sci. Technol.*, 9, 135–141.
Priestner R, de los Rios E (1980), *Met. Technol.*, 7, 309–315.
Quispe A, Medina S F, Valles P (1997), *ISIJ Int.*, 37, 783–788.
Raison J M (1982), MSc thesis, University of Birmingham.
Randerson K (1994), 'Rolling trials at Dalzell Plate Mill', Corus internal communication.
Ricks R A, Howell P R (1983), *Acta Met.*, 31(6), 853–861.
Rios P R (1987), *Acta Met.*, 35, 2805–2814.
Rios P R (1995), *J. Mat. Sci.*, 30, 1872–1878.
Sakuma T, Honeycombe R W K H. (1985), *Mat. Sci. Tech.*, 1, 351–356.
Sarkar S, Militzer M (2009), *Mat. Sci. Tech.*, 25, 1134–1146.
Schumacher P, Greer A L, Worth J, Evans P V, Kearns M A, Fisher P, Green A H, (1998), *Mat. Sci. Tech.*, 14(5), 394–404.
Sellars C M, Palmiere E J (2005), *Mater. Sci. Forum*, 500–501, 3–14.
Sellars C M, Whiteman J A (1979), *Met. Sci.*, 13, 187–194.
Shercliff H, Ashby M F (1990), *Acta Metall. Mater.*, 38, 1789–1807.
Shim J H, Cho Y W, Chung S H, Shim J D, Lee D N (1999), *Acta Mater.*, 47(9), 2751–2760.
Shokouchi A, Hodgson P D (2009), *Mat. Sci. Tech.*, 25(1), 30–34.
Speer J G, Micheal J R, Hansen S S (1987), *Met. Trans.*, 18A, 211–222.
Suzuki H, Sato T, Tanino M (1971), *Trans. ISIJ*, 14, 1082–1086.
Tamura I, Sekine H, Tanaka T, Ouchi C (1988), *Thermomechanical Processing of High Strength Low Alloy Steels*, Butterworths, London.
Tanaka T (1981), *Int. Met. Rev.*, 26, 185–209.
Tanino M (1974), Private communication.
Tateyama S, Shibuta Y, Suzuki T (2010), *ISIJ Int.*, 50(8), 1211–1216.
Thewlis G (2006), *Mat. Sci. Tech.*, 22(2), 153–166.
Timokhina I B, Hodgson P D, Ringer S P, Zheng R K, Pereloma E V (2007), *Scripta Mater.*, 56, 601–604.
Timokhina I B, Hodgson P D, Ringer S P, Zheng R K, Pereloma E V (2011), *Mat. Sci. Tech.*, 27, 305–309.
Todd J A, Li P, Copley S M (1988), *Met. Trans.*, 19A, 2133–2138.
Tomita Y, Saito N, Tsuzuki T, Tokunaga Y, Okamoto K (1994), *ISIJ Int.*, 34(10), 829–835.
Trowsdale A J (1999), *Modelling of Metal Rolling Processes*, IOM, London.
Turnbull D, Fisher J C (1949), *J. Chem. Phys.*, 17, 71–73.
Uhrenius B (1978), in *Hardenability Concepts with Applications to Steels*, TMS-AIME, Chicago, IL, pp. 28–81.
Van Dijk N H, Offerman S E, Sietsma J, van de Zwaag S (2007), *Acta Mater.*, 55, 4489–4498.

© Woodhead Publishing Limited, 2012

Wang W, Shan Y, Yang K (2008), *Mat. Sci. Eng.*, 502A, 38–44.
Weiss I, Jonas J J (1980), *Metall. Trans. A*, 11A, 403–410.
Wilson J A, Craven A J, Li Y, Baker T N (2009), *Mat. Sci. Tech.*, 23(5), 519–526.
Xu Y B, Yu Y M, Xiao B L, Liu Z Y (2009), *J. Mater. Sci.*, 44, 3928–3935.
Yang J R, Huang C Y, Huang C F (1995), *J. Mat. Sci.*, 30, 5036–5041.
Zajac S, Siwecki T, Hutchinson W B, Attlegard M (1991), *Met. Trans.*, 22A, 2681–2694.

© Woodhead Publishing Limited, 2012

7

Phase transformations in transformation induced plasticity (TRIP)-assisted multiphase steels

P. J. JACQUES, Université Catholique de Louvain (UCL), Belgium

Abstract: TRIP-assisted multiphase steels constitute one of the most recent categories of advanced high strength automotive steels. The present chapter will first show how the successive phase transformations needed to shape their microstructures rely on previous solutions of the physical metallurgy of low alloys steels. A general overview of the main features of their thermomechanical processing will then be presented.

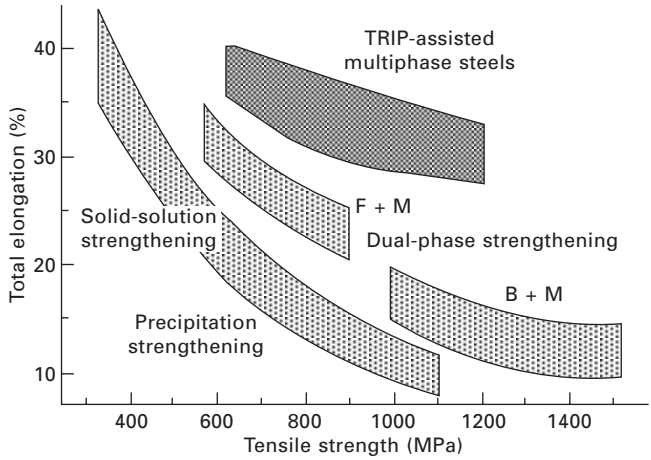
Key words: advanced high strength steels, dual-phase steels, ferritic transformation, bainite transformation, martensitic transformation, retained austenite, thermomechanical processing, microstructure.

7.1 Introduction

Over recent decades, several solutions have been conceived to improve the mechanical properties of iron and steel. These solutions were, and still are, mostly responding to the pressures of the automotive industry which is continually seeking new materials with an improved strength–ductility balance in order to meet, in an effective way, the objectives of reduction of fuel consumption by weight saving whilst increasing safety and crashworthiness. To meet these requirements, Fe and Fe-C-based alloys present the exceptional feature that the processing route can be adapted to lead to various phases that present mechanical properties ranging from soft and ductile ferrite to ultra-high strength martensite. Furthermore, these phases can be combined within finely grained microstructures, thus constituting *in situ* composites.

Pressures from the automotive sector have brought about the rapid development of new steel families. At the end of the 1990s, new steel grades called *TRIP-assisted multiphase steels* were *the* solution proposed by the steel industry for the improvement of the strength–ductility balance as sketched in Fig. 7.1. Since that time, newer solutions have been constantly proposed. The International Iron and Steel Institute published in June 2009 its fourth report on *Advanced High Strength Steel (AHSS) Application Guidelines* (Worldsteel, 2009), demonstrating the worldwide interest in new or advanced

© Woodhead Publishing Limited, 2012



7.1 Typical combinations of strength and ductility exhibited by different steel grades; situation at the end of the 1990s (Jacques, 1999).

or ultra-high strength steels. This report starts with useful definitions that clarify the ways of classifying these different grades:

> Automotive steels can be classified in several different ways. One is by a metallurgical designation. Common designations include low-strength steels (interstitial-free and mild steels); conventional HSS (carbon-manganese, bake hardenable, high-strength interstitial-free, and high-strength low-alloy steels); and the newer types of AHSS (dual phase, transformation-induced plasticity, complex phase, and martensitic steels). Additional higher strength steels for the automotive market include ferritic-bainitic, twinning-induced plasticity, hot-formed, and post-forming heat-treated steels.

These different families are most of the time related to each other through modifications of their chemical compositions or processing routes, e.g. dual-phase steels and TRIP-assisted multiphase steels.

Section 7.2 shows how TRIP-assisted multiphase steels historically derive from various previously developed iron-based alloys. In fact, the name 'TRIP-assisted multiphase steels' recalls the two physical origins of their exceptional mechanical properties, i.e. the multiphase nature of their microstructure and the occurrence of a TRIP effect (i.e. the mechanically induced martensitic transformation of metastable retained austenite). The word 'assisted' (which is often forgotten in the literature) means that these two features interact and influence each other. TRIP-assisted multiphase steels are thus clearly related to the dual-phase steels thoroughly studied since the end of the 1970s. They are also related to the highly alloyed fully

© Woodhead Publishing Limited, 2012

austenitic steels for which it had been shown that mechanically triggered martensitic transformation can contribute very effectively to plasticity and work hardening improvement. Furthermore, bainite transformation can be a very powerful means that could lead to large amounts of retained austenite when particular conditions are fulfilled. Finally, it is worth noting that the TRIP-aided steels actually correspond to a mutation in the way of looking at retained austenite. Indeed, whilst large efforts were customarily made to avoid the presence of retained austenite, particularly in welds, for embrittlement and fracture reasons, the optimisation of the TRIP-assisted multiphase steel properties relies on maximisation of the amount of retained austenite presenting the right stability (Jacques, 2003a).

Section 7.3 deals with the influence of several parameters of the thermomechanical process on the formation and shaping of multiphase microstructures containing retained austenite. Indeed, besides their resemblance with other steels, TRIP-assisted multiphase steels also exhibit unique features that dictate how the successive phase transformations leading to their particular microstructures have to be conducted. This section will focus, in particular, on chemical, geometrical and mechanical features influencing the formation of ferrite, bainite, retained austenite and martensite.

7.2 Historical perspectives on the emergence of transformation induced plasticity (TRIP)-assisted multiphase steels

7.2.1 Dual-phase steels – a new process practice

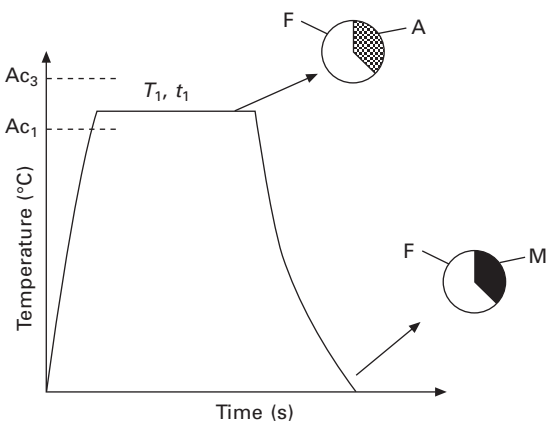
Thermomechanical processing of low- and medium-carbon steels commonly involves cooling from above the upper critical temperature (A_3) where only austenite is stable (Davies and Magee, 1979; Matlock *et al.*, 1982). Thanks to proper control of alloy content and cooling rate, desirable microstructures and resulting properties can be obtained. For example, low-carbon steel sheets used in applications where good ductility is required are cooled at such a rate that microstructures consist primarily of ferrite and only small amounts of pearlite or carbides. Microalloying and/or controlled hot-rolling have dramatically increased the strength of low-carbon steel sheets primarily by refining grain size in what is referred to as 'high strength low alloy' (HSLA) steels.

With the dual-phase steel grade, the forerunner of TRIP-assisted steel, other processing approaches than those which produce exclusively either ferrite/pearlite *or* martensite (in the case of ultra-strength steel) microstructures have been developed. These new approaches resulted in microstructures consisting of ferrite *and* martensite, therefore combining in the same microstructure phases with largely different mechanical properties in order to give rise to

© Woodhead Publishing Limited, 2012

a synergetic composite-type strengthening effect. Dual-phase steels have been thoroughly studied after the early work of Rashid (1976, 1977) who showed that a microstructure consisting of a dispersion of martensite grains in a ferrite matrix can bring about enhanced mechanical properties. Figure 7.2 indicates how the ferrite-martensite microstructure of dual-phase steels is generated by intercritical annealing, i.e. by heating between A_1 and A_3 and subsequently cooling at a rate compatible with austenite transformation to martensite. In industrial practice, steel compositions were adjusted without too large an increase in costs, in order to reach the hardenability compatible with sheet thickness and quenching capabilities of industrial process lines. As a consequence, dual-phase steels typically contain low levels of carbon (from 0.05 to 0.15 wt%), manganese (from 1 to 1.5 wt%), silicon (around 0.4 wt%) and sometimes other elements such as Cr, Mo or V (Speich, 1981). During intercritical annealing, carbon migrates towards austenite but the intercritical annealing times are too short (of the order of a few minutes) to allow any significant redistribution of substitutional alloying elements (Speich, 1981; Speich *et al.*, 1981; Wycliffe *et al.*, 1981; Matlock *et al.*, 1982).

Numerous studies have been devoted to the relationship between microstructure and mechanical properties in dual-phase steels (Davenport, 1977; Kot and Morris, 1979; Kot and Bramfitt, 1981; Matlock *et al.*, 1982). Thus, how the volume fraction, composition, size and distribution of phases influence in an effective way the mechanical properties is well documented. The strength of dual-phase steels increases with increasing volume fraction of martensite, whilst uniform elongation (and more globally the ductility) decreases. More recently, it was shown that the martensite plasticity (and thus its carbon content) and morphology (Mazinani and Poole, 2007) as well as the ferrite grain size (Delince *et al.*, 2006, 2007) also influence the



7.2 Typical heat-treatment scheme of cold-rolled dual-phase steels (Jacques, 1999).

© Woodhead Publishing Limited, 2012

mechanical properties, particularly the product of the uniform strain by the uniform stress (which is an indicator of the energy absorption capacity). As a consequence, it is generally concluded that better strength–ductility combinations are obtained when martensite constitutes a dispersed phase in the ferrite matrix, i.e. when its volume fraction is around 20–40%.

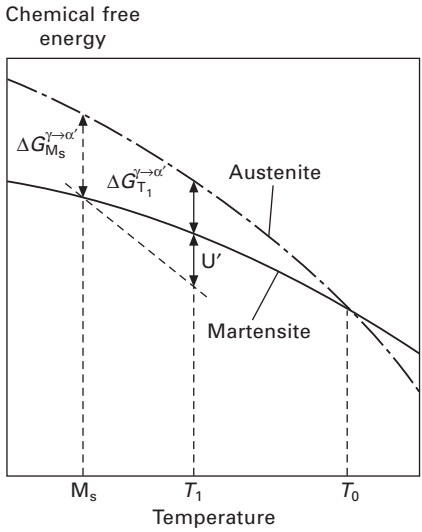
One of the characteristic features of the mechanical properties of dual-phase steels is the occurrence of continuous yielding instead of the appearance of Lüders bands and the associated 'yield point elongation' generally observed in low alloy steels. This continuous yielding is reported to result from the presence of internal stresses allowing dislocations to remain unpinned by interstitial solutes. These dislocations are generated by the austenite to martensite transformation on cooling. As a result, both a high dislocation density and residual stresses are generated in the ferrite phase immediately surrounding martensite particles (Furukawa *et al.*, 1979; Rigsbee *et al.*, 1979; Speich, 1981; Rizk and Bourell, 1982; Bourell and Rizk, 1983). In addition, martensite induces an increase in the dislocation density of ferrite, and this dislocation strengthening of ferrite determines the high work-hardening rate of dual-phase steels.

Finally, several studies have shown that retained austenite with contents up to around 10% can be found adjacent to ferrite and martensite in the microstructure of dual-phase steels (Rigsbee and VanderArend, 1977; Yi *et al.*, 1983; Sachdev, 1983). Consequently, the question was raised as to whether this retained austenite can improve the mechanical properties of dual-phase steels through a TRIP effect.

7.2.2 Mechanically induced martensitic transformation and the TRIP effect

In order to proceed, the martensite transformation needs to be accompanied by a decrease in free energy. Figure 7.3 shows schematically the evolution of the chemical free energy of parent austenite and the martensite product as a function of temperature. For temperatures lower than T_0 (for which the free energies of both phases with identical compositions are identical), the transformation from austenite to martensite is accompanied by a decrease in free energy. However, austenite will not decompose into martensite unless a well-defined activation energy, i.e. an excess of free energy of austenite over that of martensite, corresponding to the activation barrier, is available. As a consequence, martensitic transformation of austenite only occurs at M_s, below a well-defined undercooling ΔT from T_0. As indicated in Fig. 7.3, a driving force of $\Delta G_{M_s}^{\gamma\text{-}\alpha'}$ attained for an undercooling down to M_s is needed to trigger martensitic transformation. This means that in the absence of any other competing phase transformation, austenite cooled at temperatures ranging from M_s to T_0 stays in a metastable state. However, since martensitic

© Woodhead Publishing Limited, 2012



7.3 Schematic illustration showing chemical free energies of austenite and martensite as a function of temperature.

transformation is achieved by a cooperative shear movement of atoms, it can easily be envisioned that the mechanical state of the microstructure may influence the transformation. The chemical driving force $\Delta G_{T_1}^{\gamma\text{-}\alpha'}$ at temperature T_1 in Fig. 7.3, which is insufficient for the onset of martensitic transformation, can be complemented by a mechanical driving force, U, resulting from an externally applied stress which may be added to the chemical driving force in order to attain the required critical driving force $\Delta G_{M_s}^{\gamma\text{-}\alpha'}$. Consequently, martensitic transformation can be mechanically induced when mechanical work supplements the insufficient thermal driving force for triggering the transformation (Olson, 1982; Tamura, 1982; Tamura and Wayman, 1992).

Since martensitic transformation can occur thanks to mechanical activation, its consequences on the deformation process have been thoroughly studied. It was shown that the aftermath of the martensitic transformation, such as the dilatational and shear deformations arising from the change in crystal structure, the formation of preferential variants of martensite and the abrupt change in strength (Patel and Cohen, 1953; Olson and Cohen, 1975, 1982; Onodera *et al*., 1976; Stringfellow *et al*., 1992; Tamura and Wayman, 1992) improve strength and ductility by influencing the work-hardening rate (Angel, 1954; Zackay *et al*., 1967; Ludwigson and Berger, 1969; Olson and Azrin, 1978; Olson, 1982). In fully austenitic steels, the balance of tensile strength and elongation exhibit an overall optimum when testing is carried out in the temperature range between the M_s temperature of spontaneous martensitic transformation on cooling and the M_d temperature at the end of

© Woodhead Publishing Limited, 2012

mechanically induced martensitic transformation. Tensile strength increases with decreasing test temperature, and this increase almost corresponds to the increase in martensite content observed in the specimen after fracture. Total elongation exhibits a maximum at a temperature just above M_s^{σ}, i.e. the temperature at which the stress needed to induce the transformation of austenite corresponds to the austenite yield strength. As a consequence, this TRIP effect was found to be very beneficial to the deformation properties of a wide variety of fully austenitic Fe-Ni-Cr (Angel, 1954; Fahr, 1971; Bhandarkar *et al*., 1972), Fe-Ni (Yeo, 1963; Fahr, 1971) or other highly alloyed steels (Tamura and Wayman, 1992).

The austenite present in dual-phase steels is found either as interlath films within martensite or as very small isolated grains (Yi *et al*., 1983; Rigsbee *et al*., 1979). Since dual-phase steels do not contain strong austenite stabiliser elements, other stabilising effects such as a size effect and a matrix constraint effect were asserted to play a role in austenite retention. Furthermore, it was shown that martensitic transformation of this retained austenite can be mechanically induced during straining so that a TRIP effect occurs in dual-phase steels.

While some studies considered this austenite as a minor phase without any effect on the mechanical properties of dual-phase steels because of its small volume fraction (Speich and Miller, 1979), other works argued that martensitic transformation of retained austenite during deformation improves mechanical properties of dual-phase steels by increasing the work-hardening rate thanks to the generation of a greater dislocation density in ferrite (Rigsbee and VanderArend, 1977). However, this retained austenite transforms very rapidly in the early stage of straining in such a way that after only a few percent of plastic strain, austenite content is completely exhausted and the TRIP effect can no longer affect the work-hardening rate. It was therefore concluded that the unique strength–ductility combinations of dual-phase steels could be further enhanced if retained austenite (inevitably present in their microstructures) would exhibit a higher mechanical stability in such a way that its transformation occurs throughout plastic deformation (Sachdev, 1983; Goel *et al*., 1985a, 1985b). However, this increase in stability should not be obtained at the expense of increasing costs by the addition of costly austenite stabiliser alloying elements such as Ni or Mn. Nevertheless, dual-phase steels contain enough carbon (which is a very strong austenite stabiliser element) for adequate mechanical stability of substantial amounts of austenite at room temperature if further carbon enrichment of this austenite can be achieved following the first enrichment that occurs during intercritical annealing. Such further enrichment can result from the intrinsic characteristics of bainite transformation (despite this being a most complex mechanism of phase change in steels).

© Woodhead Publishing Limited, 2012

7.2.3 Austenite retention through bainite transformation

In plain carbon steels, bainitic microstructures consist of packets of lath- or plate-shaped ferrite, generally associated with carbide particles. The bainite transformation occurs in a temperature range situated between that where pearlite is first formed by the cooperative growth of ferrite and cementite and the temperature below M_s where austenite transforms into martensite. Even though bainitic microstructures present relatively high strength, they are not widely used in technological applications since the presence of coarse carbides reduces ductility and toughness. It has been observed (Hehemann, 1970; Christian and Edmonds, 1984; Bhadeshia and Christian, 1990; Ohmori and Maki, 1991; Takahashi and Bhadeshia, 1991; Bhadeshia, 1992a), that silicon strongly retards the precipitation of cementite during the bainite reaction, therefore bringing about a microstructure consisting of laths/plates of bainitic ferrite and carbon-rich austenite; a 'carbide-free' bainite. This combination of high-strength bainitic ferrite and ductile austenite was reported to drastically enhance strength and toughness properties of bainitic steels (Sandvik and Nevalainen, 1981; Bhadeshia and Edmonds, 1983a, 1983b; Miihkinen and Edmonds, 1987a, 1987b, 1987c; Edmonds and Cochrane, 1990; Tomita and Okawa, 1993) when heat-treatment was conducted in such a way that mechanical stability of austenite was well adjusted. Large contents of retained austenite can thus be found in the microstructure of steels with rather simple compositions containing elements like silicon that inhibit carbide precipitation. The presence of this retained austenite is not fortuitous but results from the intrinsic mechanisms of the bainite transformation.

It is well established now that bainite transformation can be divided into two separable stages: a stage of growth of ferrite and a stage of precipitation of carbides. However, the detailed mechanisms intervening in the bainite transformation still provide opportunities for study. These derive from its intermediate position between the reconstructive pearlite reaction and the displacive martensite reaction, apparently exhibiting features commonly attributed to both. Nonetheless, the intensive interest in bainite developing from the phase transformation issues involved has led not just to improved understanding but perhaps, equally importantly, the confidence to develop potential commercial irons and steels based upon the reliable reproducibility of specific bainite microstructures, one example being TRIP steels.

The main feature of bainite transformation helpful for the retention of austenite at room temperature is this redistribution of carbon accompanying the progress of the transformation. From this point of view, cementite precipitation during the formation of bainitic ferrite is detrimental and has to be avoided. Cementite precipitation is effectively inhibited in iron-based alloys containing substantial amounts of silicon. The effect of silicon is generally attributed to the fact that silicon solubility in cementite is negligibly small.

© Woodhead Publishing Limited, 2012

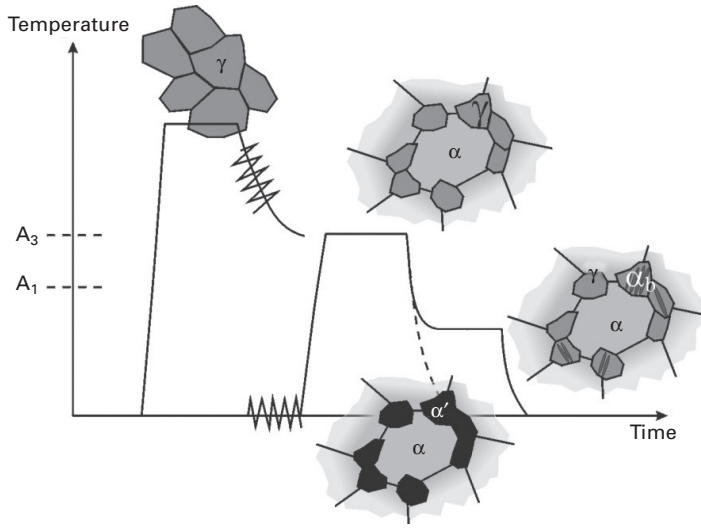
It is therefore proposed that, in the absence of relevant silicon diffusion due to the low temperature, silicon trapping dramatically reduces the driving force for the cementite precipitation.

Carbon enrichment of residual austenite therefore accompanies the progress of the bainite transformation in high silicon steels in such a way that this austenite can be retained at room temperature. However, this process stops before the complete consumption of austenite and at an austenite volume fraction that depends on the bainite transformation temperature. This is known as the *incomplete reaction phenomenon* exhibited by the bainite reaction, which is analogous to the austenite to martensite reaction between the M_s and M_f temperatures (Bhadeshia, 1992b). This means that, in the absence of cementite precipitation 'draining' some of the carbon out of the untransformed austenite, bainitic ferrite platelets nucleate and grow from increasingly carbon-enriched austenite (and further increase this enrichment by rejecting excess carbon) until the carbon content of the residual untransformed austenite reaches the value dictated by the thermodynamic condition for further growth. When this carbon content reaches a certain level, the transformation stops, leaving the residual austenite untransformed. Further holding at the same temperature does not lead to any further progress of bainite transformation.

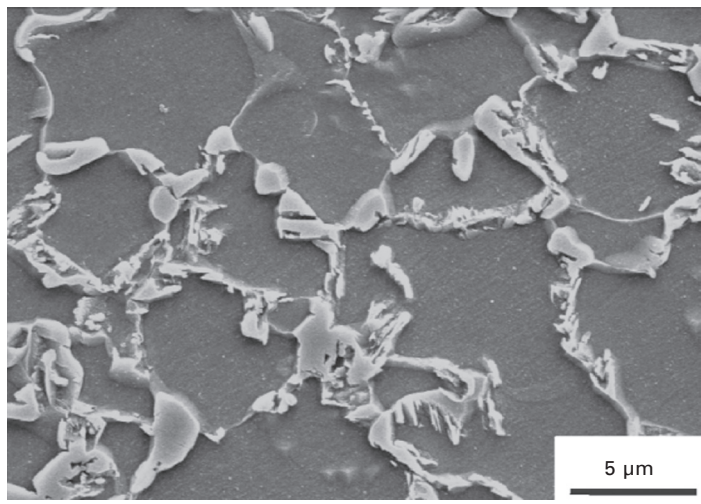
7.2.4 Conjunction of different concepts for the emergence of TRIP-assisted multiphase steels

The characteristics of the TRIP-assisted multiphase steels results from the conjunction of the positive effects of each phenomenon presented above. Like dual-phase steels, TRIP-assisted multiphase steels present a microstructure consisting of more than one phase as a result of the intercritical annealing dwell. As shown in Fig. 7.4, whereas dual-phase steels are directly quenched to room temperature after intercritical annealing, TRIP-aided steels are quenched to an intermediate temperature range, classically 350–450°C, for an isothermal partial bainitic transformation. As for carbide-free bainitic steels, this transformation allows carbon enrichment of residual austenite larger than the level reached during intercritical annealing so that the stability of austenite at room temperature is enhanced in comparison with the retained austenite present in dual-phase steels. In order to promote this enhanced carbon enrichment, TRIP-assisted multiphase steels commonly contain large concentrations of an element leading to the inhibition of cementite precipitation during the bainite transformation, customarily from 1.5 to 2.5 wt% of silicon, i.e. about 1.5 wt% larger than in typical dual-phase steels (Speich, 1981). Furthermore, as for dual-phase steels, TRIP-aided steels also contain from 0.1 to 0.4 wt% of carbon and from 1.5 to 2.5 wt% of manganese. With these chemical compositions and the two-stage heat-treatment described in Fig. 7.4(a), contents of austenite of the order of 5–20% (Sakuma *et al.*,

© Woodhead Publishing Limited, 2012



(a)



(b)

7.4 (a) Schematic representation of the evolution of the microstructure of dual-phase and TRIP-assisted multiphase steels during their respective thermal or thermomechanical treatments (γ: austenite, α: ferrite, α': martensite, α_b: bainite); (b) SEM micrograph illustrating the microstructure of a typical TRIP-assisted multiphase steel.

1991; Akisue and Hada, 1995; Jacques, 2004; De Cooman, 2004) can be retained in the microstructure. As shown by the SEM micrograph in Fig. 7.4(b), besides this austenite, TRIP-assisted multiphase steels also contain intercritical polygonal ferrite, bainitic ferrite and sometimes martensite.

© Woodhead Publishing Limited, 2012

Furthermore, the bainite–austenite grains are located at the grain boundaries of the intercritical polygonal ferrite grains.

7.3 Influence of parameters of the thermomechanical process on the formation of multiphase microstructures containing retained austenite

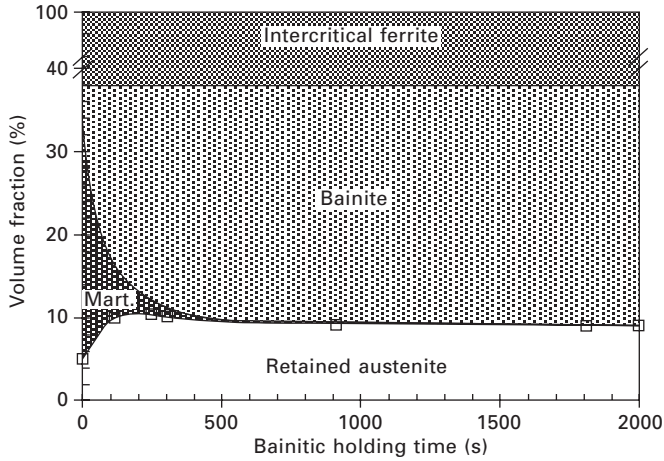
While the previous section showed that the emergence of TRIP-assisted multiphase steels relied upon several previously existing solutions and hypotheses of the physical metallurgy of high performance bainitic, and also martensitic, steels, numerous studies were subsequently conducted to refine the understanding of the successive phase transformations shaping their complex microstructures. Some general trends concerning these phase transformations are described in this section. In particular, it will focus on the *chemical*, *geometrical* and *mechanical* features influencing the phase transformations occurring after cold or hot rolling. Furthermore, even though the bainite transformation has been extensively studied, some issues remain when it is used for the retention of austenite at room temperature. The morphology of the bainitic ferrite could be different from what is classically reported. Furthermore, the transformation kinetics can be strongly dependent on the temperature and prior austenite grain size.

7.3.1 Influence of alloying elements on austenite retention through bainite transformation

Besides carbon (from 0.1 to 0.4 wt%), and manganese (0.5 to 1.5 wt%, providing some hardenability), a real challenge is to find the right alloying element that delays or suppresses cementite precipitation during the bainite transformation. As already described above, it is known that silicon inhibits cementite precipitation. However, the high silicon levels that are needed do not fit well with the industrial practice of galvanised flat products (Vanden Eynde *et al.*, 2003). Aluminium has also been shown to inhibit effectively the cementite precipitation and thus also to promote austenite carbon enrichment (Jacques *et al.*, 2001a; Girault *et al.*, 2001; De Meyer *et al.*, 1999). Some studies have dealt with other elements such as Cu (Traint *et al.*, 2002), P (Chen *et al.*, 1989; Traint *et al.*, 2002) or Ni (Sakuma *et al.*, 1992). However, hardly anything can be found in the literature on the mechanism by which the common steel alloying elements, other than those mentioned already, inhibit cementite precipitation.

Figure 7.5 illustrates the evolution of the nature of the phases constituting the room temperature microstructure of a typical Si-alloyed TRIP-aided steel

© Woodhead Publishing Limited, 2012



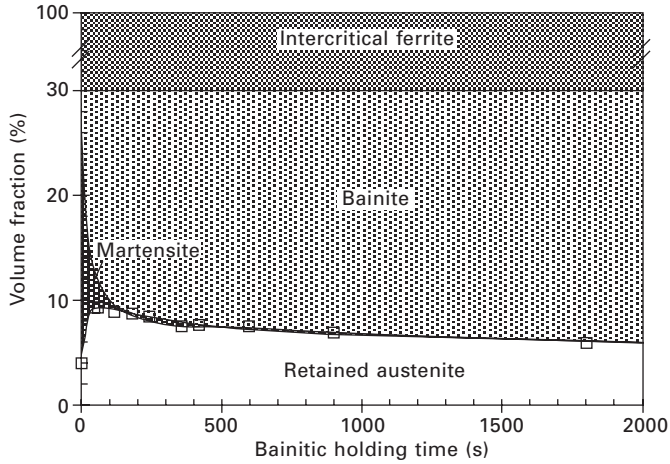
7.5 Transformation map of a typical Si-alloyed TRIP-aided steel indicating the evolution of the room temperature microstructure with progress of the bainite transformation (Jacques *et al.,* 2001a).

as a function of the progress of the bainite transformation. Depending upon the bainitic hold time, various mixtures of bainite, martensite and retained austenite can be found in the microstructure after quenching. Austenite which is carbon enriched during the intercritical anneal progressively transforms to bainite, bringing about its further stabilisation at room temperature at the expense of martensite, which completely disappears after a given time. Finally, it is noteworthy that the bainite transformation stops before the complete consumption of the 'intercritical' austenite.

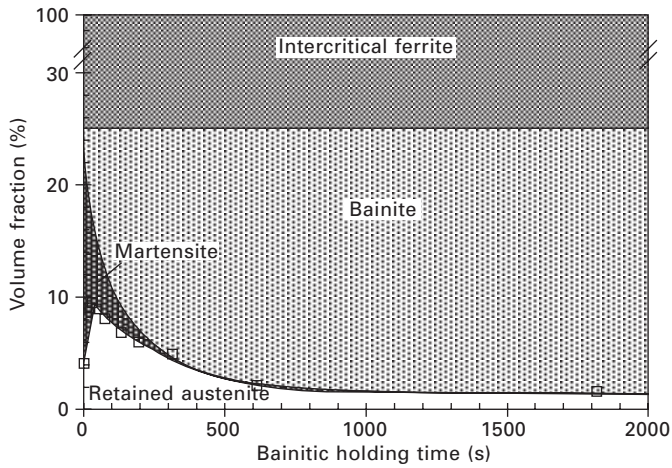
For the sake of comparison, the same transformation map has been established for a steel in which silicon has been substituted by aluminium. The resulting transformation map (Fig. 7.6) demonstrates that the behaviour of Al-alloyed TRIP-aided steel is similar to the behaviour of the Si-alloyed steels. However, comparison of Figs 7.5 and 7.6 shows that the transformation kinetics are faster for steel containing Al. Figure 7.6 also shows that the transformation of the austenite to bainite does not stop completely during 'transformation stasis' in the case of Al-alloyed steel, confirming that silicon is definitely the most effective carbide precipitation inhibitor. Furthermore, the stronger ferrite stabilising effect of Al results in an impossibility to transform fully to austenite steel grades that contain levels of Al needed for sufficient austenite retention through partial bainite transformation.

Figure 7.7 summarises the relative proportions of the different phases present in the room temperature microstructure during bainite transformation of a steel containing the low level of 0.4 wt% Si, which is much smaller than in conventional TRIP-aided steels. Up to 10% of austenite can be retained after very short holding times (from 15 s to 3 min) together with martensite.

© Woodhead Publishing Limited, 2012



7.6 Transformation map of an Al-alloyed TRIP-aided steel indicating the evolution of the room temperature microstructure with bainitic hold time (Jacques *et al.*, 2001a).

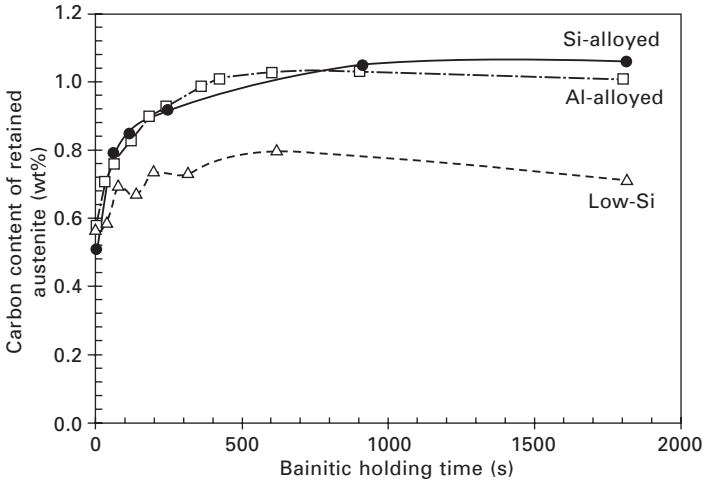


7.7 Transformation map of a steel containing 0.4 wt% of silicon indicating the evolution of the room temperature microstructure with bainitic hold time (Jacques *et al.*, 2001b).

For longer times, the bainite transformation goes to completion and only bainite can be found in the microstructure.

Figure 7.8 presents the evolution of the carbon content of the retained austenite as a function of the bainitic holding time for different steel grades alloyed with silicon or aluminium. This figure clearly shows that the progressive stabilisation of austenite at room temperature at the expense of martensite

© Woodhead Publishing Limited, 2012

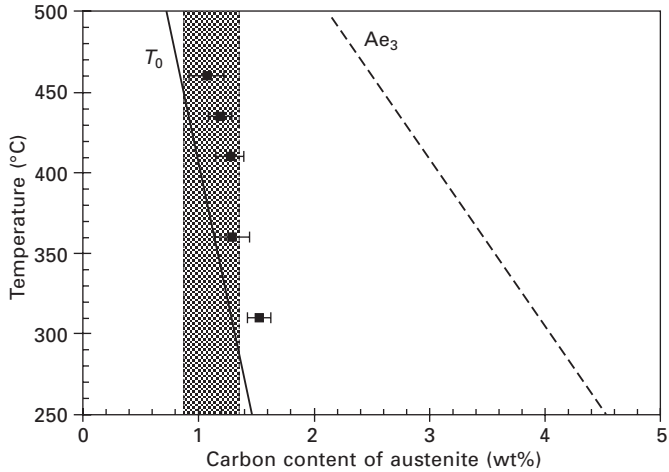


7.8 Evolution of the carbon content of retained austenite with the bainitic hold time for different TRIP-aided steels.

results from its carbon enrichment. Si- and Al-alloyed TRIP-aided steels present the same behaviour with respect to the austenite carbon enrichment up to a maximum level rather similar for the different steel grades. On the other hand, retained austenite in steels with a low Si content present a lower carbon enrichment due to cementite precipitation, as illustrated below.

As already mentioned, an incomplete reaction phenomenon is observed during the bainite transformation for steel grades containing large enough Si or Al levels for the inhibition of cementite precipitation. The austenite carbon content measured after holding times corresponding to the transformation stasis at different temperatures, in the case of a Si-alloyed steel (Jacques *et al.*, 2001a, 2001b), are given in Fig. 7.9 together with the T_0 and Ae_3 curves calculated by the Calphad method. The T_0 curve represents the upper bound of the austenite carbon content allowing diffusionless transformation of austenite to ferrite (i.e. where austenite and ferrite present the same chemical free energy). Perfect agreement between the T_0 curve and the maximum carbon content of retained austenite is found, and this is also the case for Al-alloyed TRIP-aided steels (Jacques *et al.*, 2001a). This behaviour thus tends to support a transformation model for these Si- and Al-alloyed steels which fits with a displacive mechanism for the formation of bainitic ferrite, followed by carbon partitioning between the bainitic ferrite and untransformed residual austenite, coupled with the inhibition of cementite precipitation from austenite (Girault *et al.*, 1999; Jacques, 1999; Ohmori and Maki, 1991). It is also worth mentioning that mixing Al and Si also provides an effective inhibition of carbide precipitation and thus austenite retention (Jacques *et al.*, 2001a). In contrast, low silicon levels (around 0.38 wt%) are not large

© Woodhead Publishing Limited, 2012



7.9 Comparison with the calculated T_0 and Ae_3 curves of the measured maximum carbon content of retained austenite of a Si-alloyed steel held at several temperatures. The shaded box corresponds to the range of carbon content bringing about an optimised mechanical stability of the retained austenite (Jacques *et al.*, 2007a, 2007b).

enough to avoid cementite precipitation during bainite transformation (Jacques *et al.*, 1998, 1999).

A shaded box has also been presented in Fig. 7.9. It corresponds to the range of carbon content bringing about an optimised mechanical stability of austenite for uniaxial tension (Jacques *et al.*, 2007a, 2007b). Indeed, it is worth remembering that the bainite transformation aims at 'meta-stabilising' the remaining austenite so that it will transform during the subsequent forming operations and thus improve the mechanical properties through the TRIP effect. Several studies (Jacques *et al.*, 2001c; Jacques, 2003a, 2003b) showed that the austenite carbon content must lie within the given range for the right effectiveness of the mechanically activated martensitic transformation in these TRIP-assisted multiphase steels. As a consequence, carbon enrichment also delineates the temperature range in which the bainite transformation can be conducted as a function of the T_0 curve and thus of the chemical composition of the steel grade.

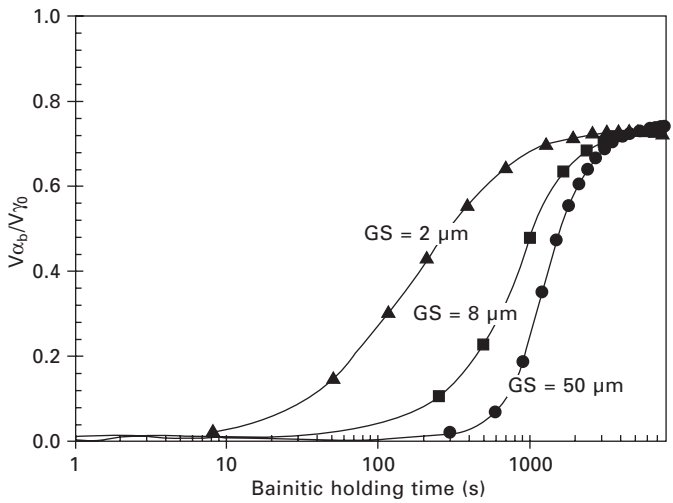
7.3.2 Influence of austenite grain size

Besides specific chemical compositions, another characteristic feature of the bainite transformation occurring in TRIP-aided steels is the austenite grain size. At the end of the intercritical annealing stage, the austenite grain size is of the order of 1–2 μm, which is generally much smaller than in the

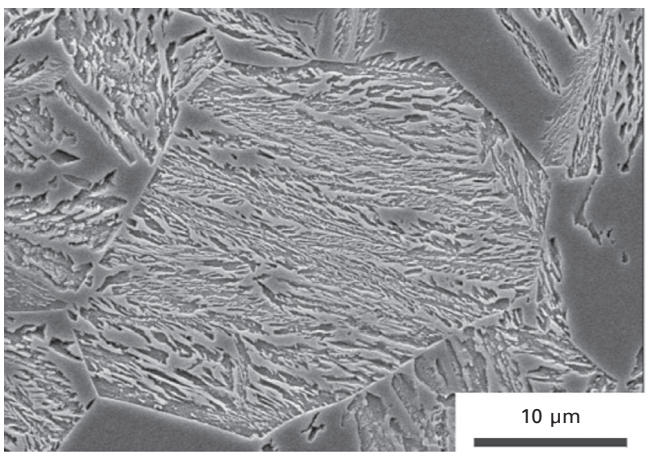
© Woodhead Publishing Limited, 2012

case of initially fully austenitic microstructures that are then transformed to bainite. Figure 7.10 presents the evolution of the normalised bainite content as a function of transformation times for several austenite grain sizes. It shows that for smaller grains, the transformation starts earlier but proceeds at a slower rate.

The scanning electron microscopy (SEM) micrograph in Fig. 7.11 shows that a typical sheaf structure constituted of parallel platelets of bainitic ferrite



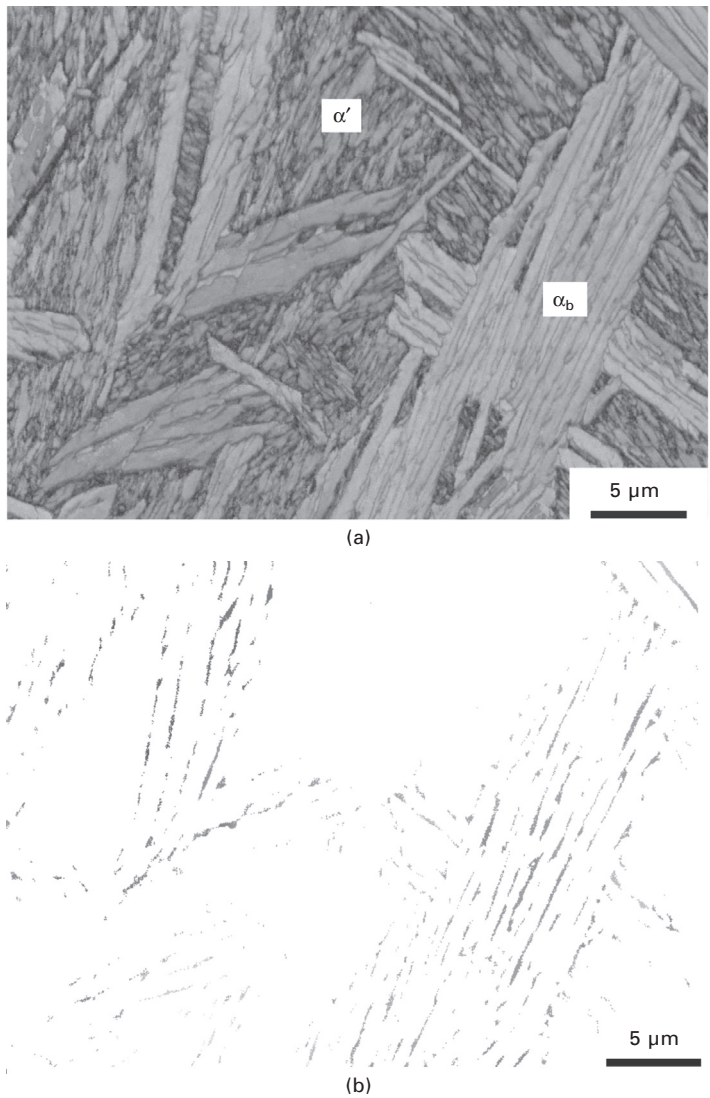
7.10 Evolution of the normalised bainite volume fraction (bainite content with respect to the initial amount of austenite) as a function of the isothermal bainitic hold time (Jacques, 2004).



7.11 SEM micrograph illustrating the sheaf morphology of classical bainite (nital etching).

© Woodhead Publishing Limited, 2012

separated by films of retained austenite is found in the case of initially fully austenitic samples presenting a large grain size. In order to identify more clearly the constitutive units of a bainitic architecture and to assess its mode of formation, Fig. 7.12 presents the electron back-scattered diffraction (EBSD) maps of a partially transformed specimen. The microstructure is constituted



7.12 EBSD maps showing the partial bainite transformation of an initially fully austenitic grade: (a) band contrast map illustrating the difference in morphology between bainite (α_b) and martensite (α'); (b) map showing the location of the FCC phase along the bainitic platelets.

© Woodhead Publishing Limited, 2012

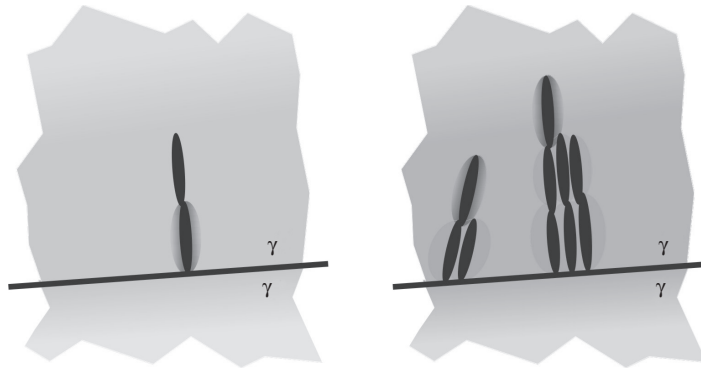
of bainite (the long plates), martensite (the small grains which appear darker due to smaller indexing rate resulting from blurred Kikuchi patterns) and austenite. It is apparent that retained austenite is located adjacent to the plates of bainitic ferrite, indicating that chemical stabilisation of the austenite results from the carbon rejected from these bainitic ferrite plates. The residual austenite not transformed to bainite prior to quenching to room temperature transforms to martensite since its carbon content is not large enough to lower its M_s temperature to below room temperature. Finally, Fig. 7.13 presents a transmission electron microscopy (TEM) micrograph of the early stage of the bainite transformation. This image clearly shows that the first bainitic ferrite sub-units nucleate at the austenite grain boundary and grow towards the interior of the austenite grain. New sub-units then nucleate and grow from the tips of the previous ones, bringing about the sheaf structure. This process has been schematically represented in Fig. 7.14.

Figures 7.11–7.14 indicate a proposed bainitic ferrite growth process and the resulting sheaf morphology in these TRIP-aided steel microstructures, i.e. the successive and repetitive nucleation and growth of platelets of bainitic ferrite at the tip of the previous ones (Bhadeshia, 2001a). This process is valid as long as tip nucleation is possible, i.e. as long as the austenite grains

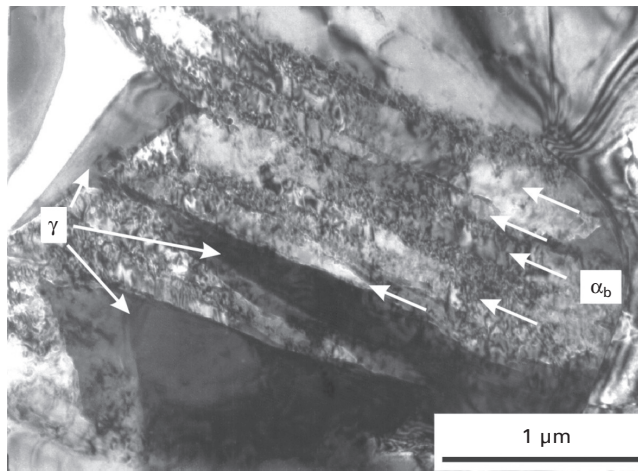


7.13 TEM micrograph showing the first platelets of bainitic ferrite surrounded by martensite.

© Woodhead Publishing Limited, 2012



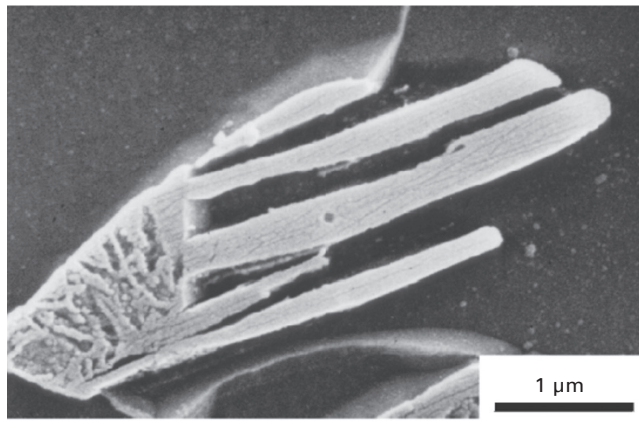
7.14 Schematic representation of the growth process of bainite in the case of austenite grain size larger than the length of the platelets of bainitic ferrite.



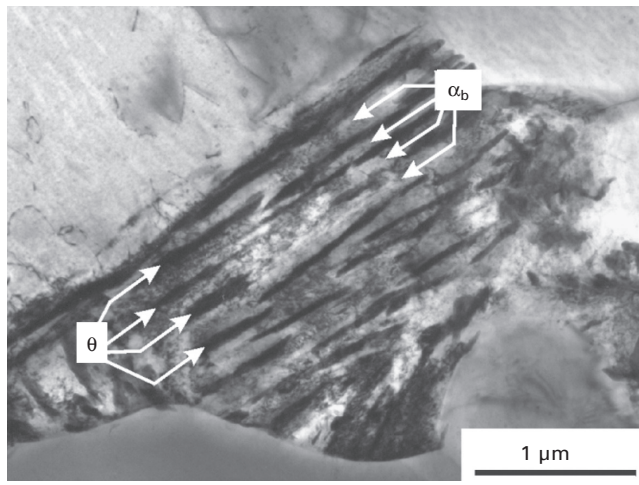
7.15 TEM micrograph of the microstructure of a Si-alloyed TRIP-aided steel (α_b: bainitic ferrite, γ: austenite).

are larger than the platelets' length. In contrast, the bainite morphology is completely different when the austenite grains are only a few μm large, as in the case of the intercritical austenite. Indeed, the TEM micrograph in Fig. 7.15 shows that in the case of small grains of intercritical austenite, bainitic ferrite platelets are lying side by side with remaining zones of untransformed retained austenite or cementite (when the content of silicon is not large enough). Figure 7.16 confirms the morphology of parallel platelets; this micrograph also demonstrates that the carbon rejection must occur mainly from the broad face of the platelets and not from the tip. Indeed, the austenite present along the platelets is retained at room temperature, whilst the

© Woodhead Publishing Limited, 2012



7.16 SEM micrograph illustrating the parallel configuration of platelets of bainite observed in the case of small austenite grains (nital etching).

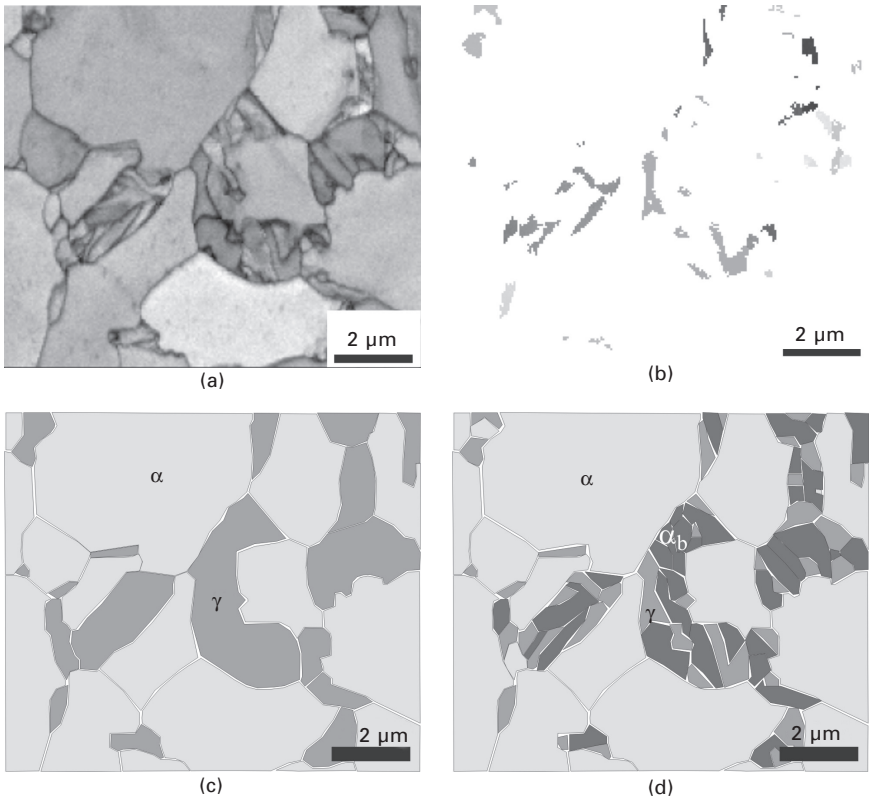


7.17 TEM micrograph of a low silicon (0.4 wt%) TRIP-aided steel showing that cementite (θ) precipitates between the platelets of bainitic ferrite (α_b).

remainder of the intercritical austenite grain is transformed into martensite upon quenching. Finally, when the silicon content is insufficiently large to avoid cementite precipitation, the TEM micrograph in Fig. 7.17 shows that cementite precipitates along the platelets of bainitic ferrite.

As in the case of fully austenitic microstructures, the use of EBSD brings about an easier understanding of the way the different phases form during the course of heat treatment. Figure 7.18 corresponds to several maps obtained

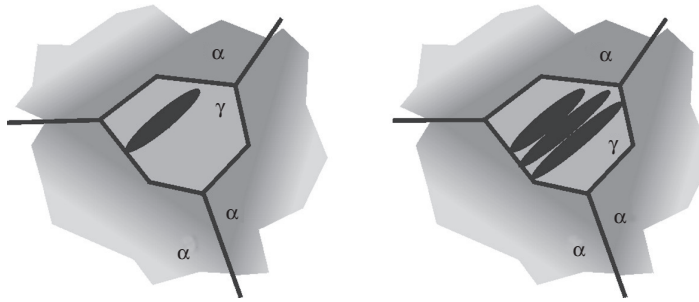
© Woodhead Publishing Limited, 2012



7.18 EBSD maps illustrating the sequence of construction of the microstructure of TRIP-assisted multiphase steels: (a) band contrast map; (b) location of the grains of austenite; (c) and (d) schematically reconstructed microstructures prior to, and after, the bainite transformation stage (α: intercritical ferrite, α_b: bainitic ferrite, γ: austenite).

by EBSD showing that intermingled body-centred cubic (BCC) and face-centred cubic (FCC) grains can be found along the grain boundaries of larger BCC grains, which correspond to the intercritical ferrite. By combining the crystallographic and morphological characteristics of these grains, it is possible to reconstruct the prior intercritical austenite grains and to identify the bainite platelets grown in each of them. Figures 7.18(c) and (d) present such reconstructed microstructures. In the present case, no sheaf composed of successive sub-units can be found. Each platelet of bainitic ferrite completely crosses the intercritical austenite grains. It is worthwhile noting that the partial bainite transformation divides the initial intercritical austenite grains into smaller regions, bringing about some grain refinement. As schematically illustrated in Fig. 7.19, the mechanism of bainite formation in very small

© Woodhead Publishing Limited, 2012



7.19 Schematic representation of the growth process of the bainitic ferrite in the case of small austenite grains with sizes of the order of the length of the platelets (α: intercritical ferrite, γ: austenite).

austenite grains brings about adjacent platelets that completely cross these austenite grains.

These differences in the bainite morphology as a function of the austenite grain size can explain the observed changes in the bainite transformation kinetics. The reduction in grain size brings about an increase in grain boundary area that accelerates the rate of transformation due to an enhanced nucleation rate. This influence was already shown and modelled by Rees and Bhadeshia (1992). However, other mechanisms have to be taken into account when the austenite grain size is reduced to the length of one platelet. In this case, growth by repetitive nucleation at the tip by an autocatalytic process is no longer possible. The kinetics of bainite transformation in very small grains is therefore controlled only by the grain boundary nucleation rate.

Furthermore, it can also be shown that the holding temperature has a strong influence on the bainite transformation rate when the grain size is reduced, while this influence disappears for large grains (Jacques, 2003b). This effect results from the fact that the platelets have to grow adjacent to the previous ones where the carbon redistribution occurs (Figs 7.16 and 7.19). This redistribution is strongly influenced by the holding temperature. There is thus an impingement between the growth of platelets and the carbon diffusion for very small grains. This effect was not postulated for large grains (Rees and Bhadeshia, 1992; Bhadeshia, 2001a) for which the new platelets appear at the tip of previous ones and grow in austenite free from prior C enrichment.

7.3.3 Influence of austenite prior deformation

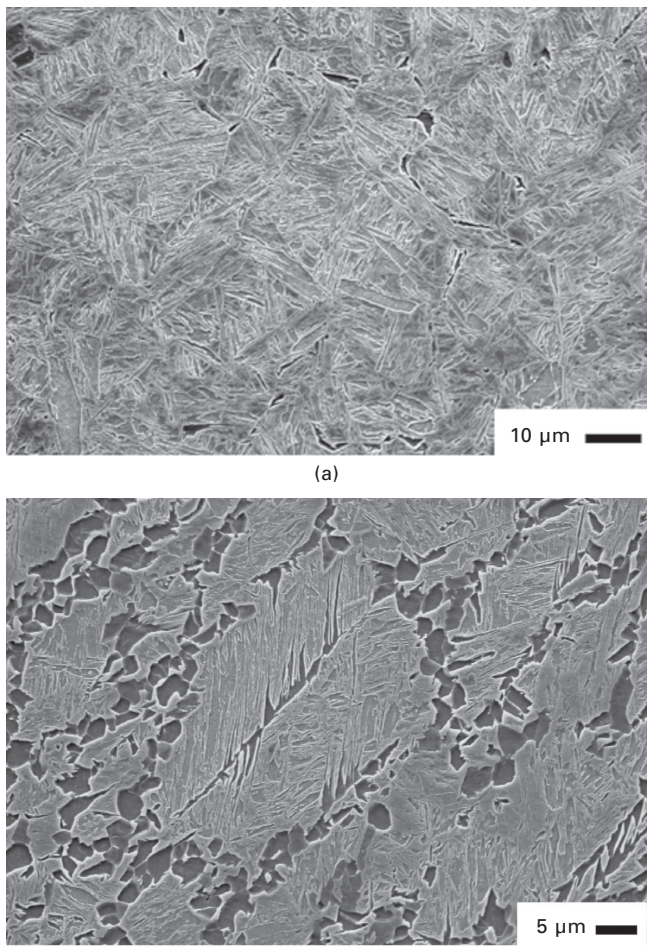
Effect of austenite deformation on its transformation into pro-eutectoid ferrite

As already reported by various authors (Bengochea *et al.*, 1998; Khlestov *et al.*, 1998; Lacroix *et al.*, 2005), the major effect of the deformation of austenite

© Woodhead Publishing Limited, 2012

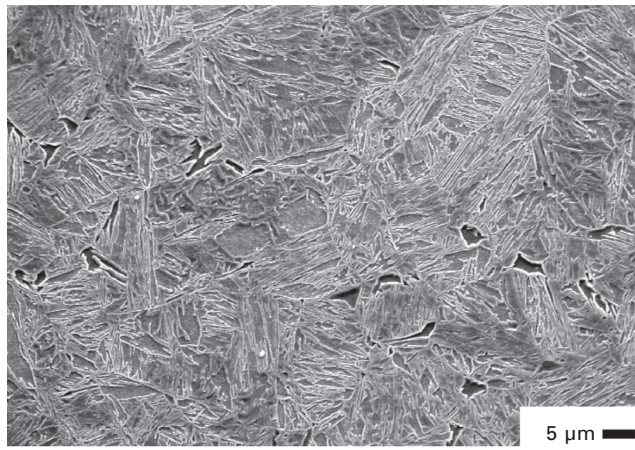
consists in the acceleration of the pro-eutectoid ferrite transformation. Figure 7.20 illustrates the influence of the austenite prior deformation on the ferrite transformation kinetics. In the case of undeformed austenite, almost no ferrite grain nucleates, bringing about a fully martensitic structure after quenching to room temperature. On the other hand, ferrite appears at grain boundaries and within the deformed grains of austenite. This so-called deformation-induced ferrite nucleates at austenite grain boundaries, but also on intragranular defects such as the shear bands formed during the deformation.

The ferrite growth rate is also completely modified when the austenite was deformed as shown in Fig. 7.21. During holding following the deformation

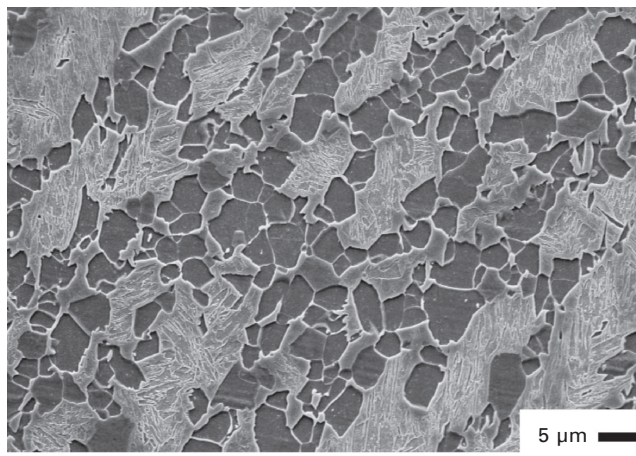


7.20 SEM micrographs illustrating the influence of prior deformation of austenite on its transformation to ferrite: (a) no prior deformation; (b) with prior deformation.

© Woodhead Publishing Limited, 2012



(a)



(b)

7.21 SEM micrographs illustrating the influence of prior deformation of austenite on the growth rate of ferrite: (a) no prior deformation; (b) with prior deformation. Isothermal hold time of 5 s.

stage, deformation-induced ferrite grains grow and transformation proceeds further at a much faster rate than from undeformed austenite. This complete modification of the nucleation and growth process of the ferrite phase is of primary importance in the case of TRIP-assisted multiphase steels. Indeed, the connectivity of the microstructure, i.e. the dispersion of the austenite and ferrite phases within the microstructure, influences the work-hardening rate by the dislocation strengthening resulting from the TRIP effect.

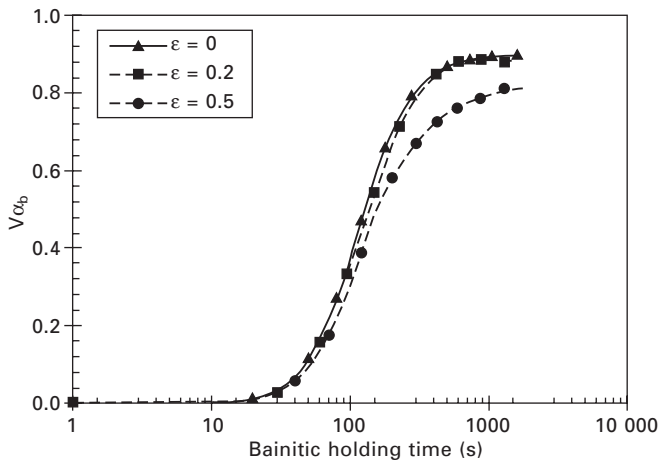
© Woodhead Publishing Limited, 2012

Effect of austenite deformation on its transformation into bainite

Figure 7.22 presents the evolution of the bainite volume fraction as a function of the transformation time for specimens that were deformed to different levels at high temperature (750°C) in the fully austenitic range. Austenite prior deformation causes mainly a change to the amount of untransformed austenite at the end of the bainite transformation. Furthermore, no modification of the incubation time can be observed with the level of hot deformation.

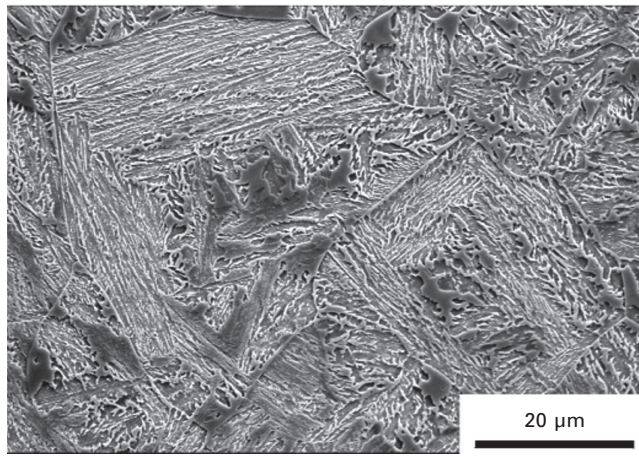
The SEM micrographs in Fig. 7.23 correspond to samples bainitically transformed after different levels of austenite deformation at higher temperature. The austenite prior deformation has a strong influence on the general bainitic morphology. While Fig. 7.23(a) exemplifies once again the typical sheaf structure of bainite that appears when no deformation was previously applied, Fig. 7.23(b) shows that the prior plastic deformation of the austenite results in a decrease in the sheaf size and in the shift to a random, interwoven mixture of bainitic ferrite platelets and retained austenite islands. As a consequence, the resulting microstructure seems finer and less directional. It is worth mentioning that necklaces of allotriomorphic ferrite are present in Fig. 7.23(b).

The SEM micrographs of Figs 7.24 and 7.25 demonstrate that the alteration of the general morphology of bainite results from the consequences of the prior plastic deformation of the austenite on the nucleation of the bainitic ferrite. Indeed, the deformation defects act as potent nucleation sites (Bhadeshia, 2001b). Instead of a few sheaves growing from platelets nucleated on the austenite grain boundaries when no prior deformation is applied (Fig. 7.24), the bainite transformation of previously deformed austenite proceeds by the

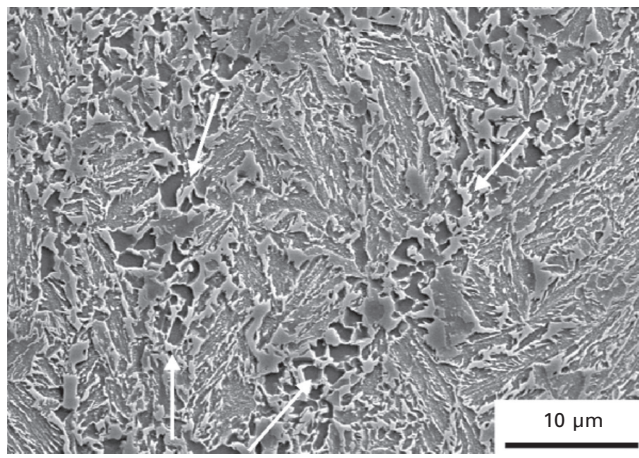


7.22 Evolution of the bainite volume fraction as a function of the holding time after different levels of prior deformation of austenite.

© Woodhead Publishing Limited, 2012



(a)



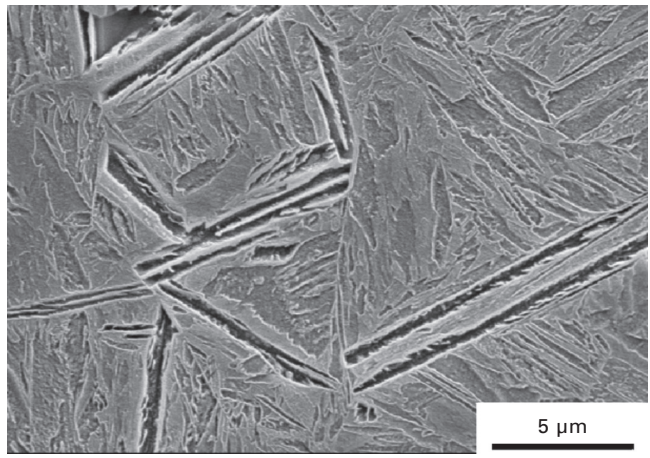
(b)

7.23 SEM micrographs illustrating the change in morphology of bainite when austenite was previously deformed: (a) no prior deformation; (b) with prior deformation of 0.5 (the arrows indicate the position of the prior austenite grain boundaries) (nital etching).

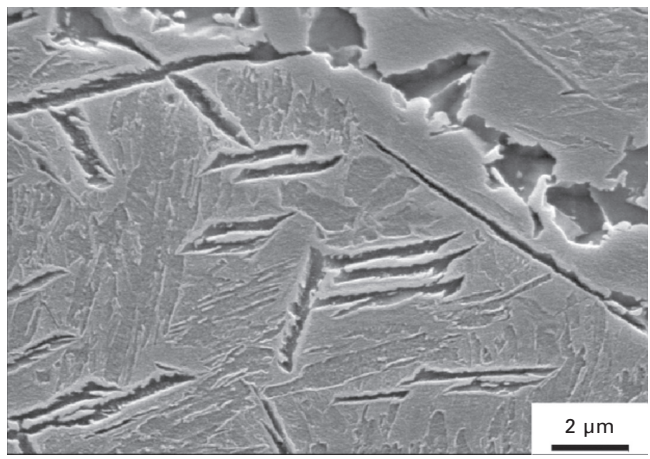
nucleation of platelets more homogeneously distributed within the grains (Fig. 7.25). Figure 7.26 summarises schematically the mode of nucleation and growth of the bainitic ferrite in the case of deformed austenite.

Due to the smaller austenite grain size (resulting from the shape change accompanying the deformation) together with this extended nucleation, the autocatalytic effect typical of bainite growth cannot take place so easily. It can also be postulated that the harder deformed austenite brings about a smaller size for the platelets of bainitic ferrite (Fujiwara and Okaguchi,

© Woodhead Publishing Limited, 2012



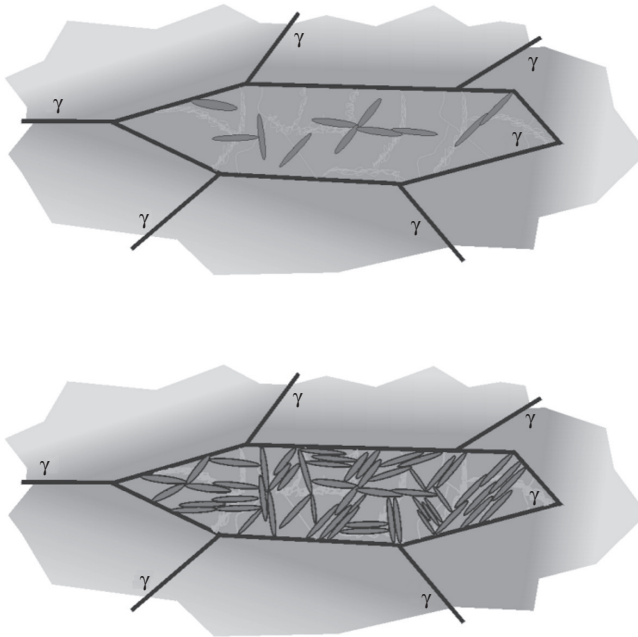
7.24 SEM micrograph showing the typical sheaf bainite structure growing from the austenite grain boundaries when no deformation was applied before the bainite transformation stage.



7.25 SEM micrograph illustrating intragranular nucleation of bainitic platelets when austenite was deformed prior to the bainite transformation stage.

1998). As a consequence, the accelerated nucleation and decelerated growth compensate each other so that no change in the transformation rate can be seen as a function of the hot deformation amplitude at the beginning of the transformation. However, the randomly distributed bainitic platelets cause some kind of geometrical impingement that retards the end of the transformation. As postulated by Bhadeshia (2001b), this slower end of transformation could also result from the transformation of more deformed zones within the austenite grains.

© Woodhead Publishing Limited, 2012



7.26 Schematic representation of the growth process of the bainitic ferrite in the case of deformed austenite grains.

Prior deformation of the austenite is also expected to influence the level at which incomplete reaction phenomena occur. As previously observed, deformation of the austenite hinders its transformation to martensite, which is well known, but also to bainite. This phenomenon is known as 'mechanical stabilisation' (Tsuzaki *et al.*, 1991; Shipway and Bhadeshia, 1995; Yang *et al.*, 1996; Larn and Yang, 2000; Bhadeshia, 2001b). Clearly, the explanation relates to a phase transformation proceeding by a displacive mechanism, in which case defects are inherited by the growing phase and do not supplement the driving force. Moreover, the defects hinder the advance of the glissile interface which can be rendered sessile when it encounters dislocation debris. As a consequence, the transformation stops at an earlier stage.

Effect of austenite deformation on its transformation into martensite

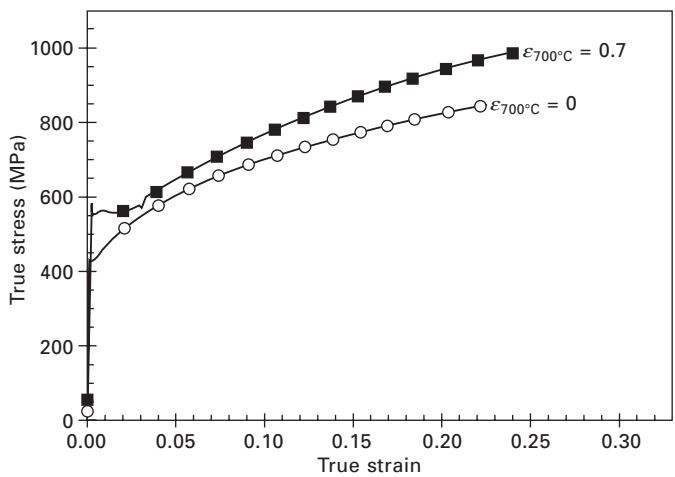
Besides its transformation to ferrite and bainite at elevated temperatures, austenite can transform into martensite, either as a remnant of the bainite-retained austenite conditioning, or more importantly, as a mechanically induced phase transformation during deformation of these TRIP-assisted multiphase steels.

© Woodhead Publishing Limited, 2012

The stress–strain curves of specimens either not deformed, or intercritically rolled, and then bainitically transformed, are shown in Fig. 7.27. Intercritical deformation leads to an increase in the yield strength of more than 100 MPa. This increase results from the hot deformation and recovery of the intercritical ferrite. However, the true stress at necking and the uniform true strain are also larger in the case of the intercritically deformed specimen. This result was not anticipated since it is well known that recovered microstructures generally exhibit deterioration of their work-hardening capabilities (Réglé, 2001).

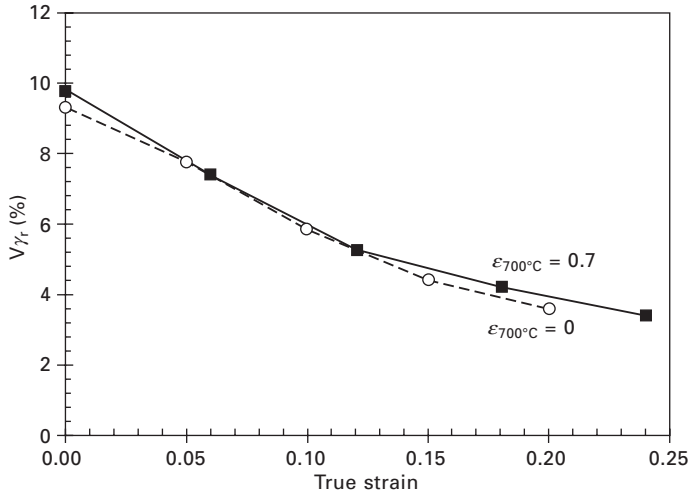
Figure 7.28 presents the variation in retained austenite volume fraction with plastic strain measured in both specimens. They exhibit comparable initial and final volume fractions of retained austenite. The transformation rates during straining are also comparable. This result shows that intercritical rolling and the resulting austenite prior deformation does not influence the strain-induced transformation of austenite into martensite at room temperature. However, the mechanical consequences of this intercritical rolling are quite remarkable.

The improvement in the work-hardening properties is thus related to the occurrence of the TRIP effect within a deformed and recovered ferritic matrix (Godet, 2003). Indeed, the enhancement of properties cannot be attributed to a larger TRIP effect or to a difference in the transformation kinetics. The enhancement of the mechanical properties of the intercritically rolled TRIP-assisted multiphase steels results thus from the interaction between the TRIP effect and the consequences of intercritical deformation. It has



7.27 True stress–true strain curves of specimens of TRIP-aided steels either not deformed or intercritically rolled to ε = 0.7 at 700°C and then bainitically transformed for 30 min at 400°C.

© Woodhead Publishing Limited, 2012



7.28 Evolution of the content of retained austenite during tensile straining of specimens either not deformed or intercritically rolled to ε = 0.7 at 700°C and bainitically transformed for 30 min at 400°C.

been shown that the TRIP effect acts as a dislocation source external to the ferrite (Jacques *et al.*, 2001c). The interactions of this external source with the recovered arrangements of dislocations improve the work-hardening capabilities so that recovered ferrite work-hardens in a more substantial way than recrystallised ferrite.

7.4 Conclusion and future trends

This chapter has given an overview of the phase transformations occurring in the case of TRIP-assisted multiphase steels. Section 7.2 attempted to show how building a historical perspective of the successive steps in the founding of scientific knowledge or 'discoveries' in the general context of various iron-based alloys can give a first insight into the characteristics of currently investigated alloys like the TRIP-assisted multiphase steels. Thus, some relevant results concerning dual-phase steels were first discussed. This led to the TRIP effect being briefly described as a supplementary strengthening mechanism. However, owing to the poor mechanical stability of the retained austenite found in dual-phase steels, it was shown how the intrinsic features of the bainite transformation can bring about stabilisation of austenite through a redistribution of carbon.

Section 7.3 investigated the results of varying several parameters of the microstructure of the TRIP-assisted multiphase steels on the austenite retention at room temperature and, consequently, on the efficiency of the TRIP effect. In particular, the consequences of chemical, geometrical and

© Woodhead Publishing Limited, 2012

mechanical features of TRIP-aided steels on the bainite transformation were scrutinised. The correlation between the heat-treatment conditions and the alloying elements used to inhibit carbide precipitation during the bainite transformation was established for the case of Si- and Al-alloyed TRIP-assisted multiphase steels. The impact of the austenite grain size on the mechanism of bainite transformation and on the resulting isothermal transformation kinetics was then demonstrated. Finally, it was shown that prior hot deformation of austenite also influences in a large way its phase transformations and its retention at room temperature.

This history proceeds relentlessly, since new and more stringent requirements are continuously requested so that new 'hot topics' in the 'steels-for-cars' community are continuously (re-)emerging. This is, for example, the case with the recent twinning-induced plasticity (TWIP) steels, related to the 'old-timers' – the Hadfield steels (Idrissi *et al*., 2010; Bouaziz *et al*., 2011). In parallel also is the current interest emerging in so-called quenched and partitioned (Q&P) steels (Edmonds *et al*., 2006; Santofimia *et al*., 2008).

7.5 References

Akisue O, Hada T (1995), *Nippon Steel Tech. Rep*., 64, 1–6

Angel T (1954), *J. Iron and Steel Inst*., 177, 165–174

Bengochea R, Lopez B, Gutierrez I (1998), *Metall. Mater. Trans. A*, 29, 417–426

Bhadeshia H K D H (1992a), *Bainite in Steels*, The Institute of Materials, London, 124–194

Bhadeshia H K D H (1992b), *Bainite in Steels*, The Institute of Materials, London, 1–19

Bhadeshia H K D H (2001a), *Bainite in Steels*, 2nd edn, The Institute of Materials, London, 129–187

Bhadeshia H K D H (2001b), *Bainite in Steels*, 2nd edn, The Institute of Materials, London, 207–214

Bhadeshia H K D H, Christian J W (1990), *Metall. Trans. A*, 21, 767–797

Bhadeshia H K D H, Edmonds D V (1983a), *Metal Science*, 17, 411–419

Bhadeshia H K D H, Edmonds D V (1983b), *Metal Science*, 17, 420–425

Bhandarkar D, Zackay V F, Parker E R (1972), *Metall. Trans*., 3, 2619–2631

Bouaziz O, Allain S, Scott C P, Cugy P, Barbier D (2011), *Curr Opin Solid St M*, 15, 141–168

Bourell D L, Rizk A (1983), *Acta Metall*., 31, 609–617

Chen H C, Era H, Shimizu M (1989), *Metall Trans A*, 20, 437–445

Christian J.W., Edmonds D V (1984), in *Phase Transformations in Ferrous Alloys*, A R Marder and J I Goldstein (eds), AIME, Warrendale, PA, 293–325

Davenport A T (ed) (1977), *Formable HSLA and Dual-Phase Steels*, TMS-AIME, Warrendale, PA

Davies R G, Magee C L (1979), in *Proc. Conf. Structure and Properties of Dual-Phase Steels*, R A Kot and J W Morris (eds), TMS-AIME, Warrendale, PA, 1–19

De Cooman B C (2004), *Curr Opin Solid St M*, 8, 285–303

De Meyer M, Vanderschueren D, De Cooman B C (1999), *ISIJ Int*, 39, 813–822

© Woodhead Publishing Limited, 2012

Delince M, Jacques P J, Pardoen T (2006), *Acta Mater*, 54, 3395–3403
Delince M, Brechet Y, Embury J D, Geers M G D, Jacques P J, Pardoen T (2007), *Acta Mater*, 55, 2337–2350
Edmonds D V, Cochrane R C (1990), *Metall. Trans. A*, 21A, 1527–1540
Edmonds D V, He K, Rizzo F C, De Cooman B C, Matlock D K, Speer J G (2006), *Mater Sc Eng* A, 438–440, 25–34
Fahr D (1971), *Metall. Trans.*, 2, 1883–1892
Fujiwara K, Okaguchi S (1998), *Mater. Sc. Forum*, 284–286, 271–278
Furukawa T, Morikawa H, Takechi H, Koyama K (1979), in *Proc. Conf. Structure and Properties of Dual Phase Steels*, R A Kot and J W Morris (eds), TMS-AIME, Warrendale, PA, 281–303
Girault E, Jacques P J, Ratchev P, Van Humbeeck J, Verlinden B, Aernoudt E (1999), *Mater. Sc. Eng. A*, 273–275, 471–474
Girault E, Mertens A, Jacques P, Houbaert Y, Verlinden B, Van Humbeeck J (2001), *Scripta Mater*, 44, 885–892
Godet S (2003), PhD thesis, Université catholique de Louvain, Louvain-la-Neuve, Belgium
Goel N C, Sangal S, Tangri K (1985a), *Metall. Trans. A*, 16A, 2013–2021
Goel N C, Sangal S, Tangri K (1985b), *Metall. Trans. A*, 16A, 2023–2029
Hehemann R F (1970), *Phase Transformations*, ASM, Metals Park, OH, 397–432
Idrissi H, Renard K, Ryelandt L, Schryvers D, Jacques P J (2010), *Acta Mater*, 58, 2464–2476
Jacques P J (1999), On the Physics and Mechanics of TRIP-Assisted Multiphase Steels, PhD thesis, Université catholique de Louvain, Louvain-la-Neuve, Belgium
Jacques P J (2003a), in *Thermodynamics, Microstructures and Plasticity*, A Finel, D Mazière, M Veron (eds), Kluwer Academic, Amsterdam, 241–250
Jacques P J (2003b), *J de Phys*, 112, 297–300
Jacques P J (2004), *Curr Opin Solid St M*, 8, 259–265
Jacques P J, Cornet X, Harlet Ph, Ladrière J, Delannay F (1998), *Metall. Mater. Trans. A*, 29, 2383–2393
Jacques P J, Girault E, Catlin T, Geerlofs N, Kop T, van der Zwaag S, Delannay F (1999), *Mater. Sc. Eng. A*, 273–275, 475–479
Jacques P J, Girault E, Mertens A, Verlinden B, Van Humbeeck J, Delannay F (2001a), *ISIJ Int*, 41, 1068–1074
Jacques P J, Girault E, Harlet Ph, Delannay F (2001b) *ISIJ Int*, 41, 1061–1067
Jacques P J, Furnémont Q, Mertens A, Delannay F (2001c), *Phil. Mag. A*, 81, 1789–1812
Jacques P J, Furnemont Q, Lani F, Pardoen T, Delannay F (2007a), *Acta Mater*, 55, 3681–3693
Jacques P J, Lani F, Furnemont Q, Van Rompaey T, Delannay F, Pardoen T (2007b), *Acta Mater*, 55, 3695–3705
Khlestov V M, Konopleva E V, McQueen H J (1998), *Mater. Sc. Technol.*, 14, 783–792
Kot R A, Bramfitt B L (eds) (1981), *Fundamentals of Dual-Phase Steels*, TMS-AIME, Warrendale, PA
Kot R A, Morris J W (eds) (1979), *Proc. Conf. Structure and Properties of Dual-Phase Steels*, TMS-AIME, Warrendale, PA
Lacroix S, Quidort D, Brechet Y, Veron M, Kandel M, Iung T (2005), *Mater. Sc. Forum*, 500–501, 329–338

© Woodhead Publishing Limited, 2012

Larn R H, Yang J R (2000), *Mater. Sci. Eng. A*, 278, 278–291
Ludwigson D C, Berger J A (1969), *J. Iron and Steel Inst.*, 63–69
Matlock D K, Zia-Ebrahimi F, Krauss G (1982), in *Deformation, Processing and Structures*, G. Krauss (ed.), ASM, Metals Park, OH, 47–87
Mazinani M, Poole W J (2007), *Metall Mater Trans A*, 38, 328–339
Miihkinen V T T, Edmonds D V (1987a), *Mater. Sc. Technol.*, 3, 422–431
Miihkinen V T T, Edmonds D V (1987b), *Mater. Sc. Technol.*, 3, 432–440
Miihkinen V T T, Edmonds D V (1987c), *Mater. Sc. Technol.*, 3, 441–449
Ohmori Y, Maki T (1991), *Mater. Trans. JIM*, 32, 631–641
Olson G B (1982), in *Deformation, Processing and Structures*, G. Krauss (ed.), ASM, Metals Park, OH, 391–424
Olson G B, Azrin M (1978), *Metall. Trans. A*, 9A, 713–721
Olson G B, Cohen M (1975), *Metall. Trans. A*, 6A, 791–795
Olson G B, Cohen M (1982), *Metall. Trans. A*, 13A, 1907–1914
Onodera H, Goto H, Tamura I (1976), *Proc. 1st JIM Int. Symp. New Aspects of Martensitic Transformations*, Kobe, Japan, 327–338
Patel J R, Cohen M (1953), *Acta Metall.*, 1, 531–538
Rashid M S (1976), SAE Preprint 760202, SAE Technical Paper, Warrendale, PA
Rashid M S (1977), SAE Preprint 770211, SAE Technical Paper, Warrendale, PA
Rees G I, Bhadeshia H K D H (1992), *Mater. Sc. Technol.*, 8, 985–993
Réglé H (2001), in *Proc. 1st Int. Conf. Recrystallisation & Grain Growth*, G Gottstein and D A Molodov (eds), Aachen, 695–706
Rigsbee J M, VanderArend P J (1977), in *Formable HSLA and Dual-Phase Steels*, A T Davenport (ed.), TMS-AIME, Warrendale, PA, 56–86
Rigsbee J M, Abraham J K, Davenport A T, Franklin J E, Pickens J W (1979), in *Proc. Conf. Structure and Properties of Dual Phase Steels*, R A Kot and J W Morris (eds), TMS-AIME, Warrendale, PA, 304–329
Rizk A, Bourell D L (1982), *Scripta Metall.*, 16, 1321–1324
Sachdev A K (1983), *Acta Metall.*, 31, 2037–2042
Sakuma Y, Matsumura O, Akisue O (1991), *ISIJ Int.*, 31, 1348–1353
Sakuma Y, Matlock D K, Krauss G (1992), *Metall Trans A*, 23, 1221–1232
Sandvik B P J, Nevalainen H P (1981), *Metals Technol.*, 213–220
Santofimia M J, Zhao L, Petrov R, Sietsma J (2008), *Mater Charac*, 59, 1758–1764
Shipway P H, Bhadeshia H K D H (1995), *Mater. Sc. Technol.*, 11, 1116–1128
Speich G R (1981), in *Fundamentals of Dual-Phase Steels*, R A Kot and B L Bramfitt (eds), TMS-AIME, Warrendale, PA, 3–45
Speich G R, Miller R L (1979), in *Proc. Conf. Structure and Properties of Dual Phase Steels*, R A Kot and J W Morris (eds), TMS-AIME, Warrendale, PA, 145–182
Speich G R, Demarest V A, Miller R L (1981), *Metall. Trans. A*, 12, 1419–1428
Stringfellow R G, Parks D M, Olson G B (1992), *Acta Metall. Mater.*, 40, 1703–1716
Takahashi M, Bhadeshia H K D H (1991), *Mater. Trans. JIM*, 32, 689–696
Tamura I (1982), *Metal Sc.*, 16, 245–253
Tamura I, Wayman C M (1992), in *Martensite*, G B Olson and W S Owen (eds), ASM, Metals Park, OH, 227–242
Tomita Y, Okawa T (1993), *Mater. Sc. Eng. A*, 172, 145–151
Traint S, Pichler A, Hauzenberger K, Stiaszny P, Werner E (2002), *Steel Res Int*, 73, 259–266
Tsuzaki K, Fukasu S, Tomota Y, Maki T (1991), *Mater. Trans. JIM*, 32, 222–228
Vanden Eynde X, Servais J P, Lamberigts M (2003), *Surf Int Anal*, 35, 1004–1014

© Woodhead Publishing Limited, 2012

Worldsteel (2009), *Advanced High Strength Steel (AHSS) Application Guidelines*, available at: www.worldautosteel.org
Wycliffe P, Purdy G R, Embury J D (1981), in *Fundamentals of Dual-Phase Steels*, R A Kot and B L Bramfitt (eds), TMS-AIME, Warrendale, PA, 59–84
Yang J R, Huang C Y, Hsieh W H, Chou C S (1996), *Mater. Trans. JIM*, 37, 579–585
Yeo R B G (1963), *Trans. Metall. Soc. AIME*, 227, 884–890
Yi J J, Yu K J, Kim I S, Kim S J (1983), *Metall. Trans. A*, 14, 1497–1504
Zackay V F, Parker E R, Fahr D, Busch R (1967), *Trans. Am. Soc. Met.*, 60, 252–259

© Woodhead Publishing Limited, 2012

8

Phase transformations in quenched and partitioned steels

J. G. SPEER, Colorado School of Mines, USA

Abstract: This chapter introduces the quenching and partition process, a new thermal treatment designed to employ carbon partitioning from martensite into untransformed austenite, with the purpose of generating austenite-containing microstructures in low alloy steels with attractive performance characteristics. The early development of the process and associated mechanisms are reviewed, including models to incorporate thermodynamic aspects, microstructure development principles, and more recently, kinetic factors. Experimental progress is also discussed, including alloy design and microstructure. Encouraging mechanical properties are reported, and some potential applications to different steel product families are highlighted.

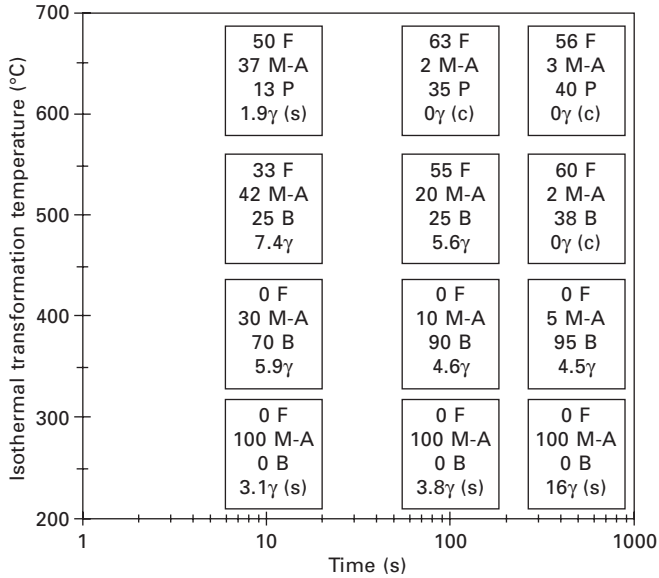
Key words: martensite, diffusion, equilibrium, microstructure, carbon, interface, Q&P, tempering, mechanical properties.

8.1 Introduction to the quenching and partitioning concept

8.1.1 Genesis

The quenching and partitioning concept followed initially from isothermal transformation studies on Si-containing transformation-induced plasticity (TRIP) sheet steels, aimed particularly at examining the bainite transformation and the 'development' of retained austenite (Gallagher *et al.*, 2002). In these studies, it was noticed that isothermal holding at temperatures below M_s led to the retention of small amounts of austenite, without the formation of any 'carbide-free bainite'. Figure 8.1 shows the constituent fractions measured in a 0.15C–1.4Mn–1.5Si (wt%) steel that was fully austenited at 905°C and isothermally transformed for different times and temperatures (Gallagher *et al.*, 2002). For holding times prior to the onset of bainite transformation at 300°C (below M_s), the unexpected presence of measurable retained austenite is noted in this steel containing only 0.15 C. Carbon partitioning from martensite was hypothesized to have contributed to austenite stabilization, and x-ray diffraction showed that the austenite was enriched with carbon to a level of 1.22 wt% after the 10 s holding treatment at 300°C (Gallagher, 2003). Carbon enrichment of retained austenite had also been identified in earlier work (Sarikaya *et al.*, 1982), and the quenching and partitioning, or

© Woodhead Publishing Limited, 2012



8.1 Microstructural constituents in a 0.15C–1.4Mn–1.5Si steel measured after isothermal treatments for 10, 100 or 1000 s at 300, 400, 500 or 600°C following austenitization. F, B, and M-A represent ferrite, bainite and martensite-austenite fractions measured by point counting of SEM images; γ represents the austenite fraction measured by x-ray diffraction. The symbols 's' and 'c' represent x-ray diffraction evidence indicating the presence of a martensite 'shoulder' (tetragonality), or the presence of cementite, respectively (Gallagher *et al.*, 2002).

Q&P, process was conceived to employ this enrichment mechanism in an intentional fashion to develop new steel microstructures with controlled fractions and stabilities of retained austenite. While the austenite fractions discovered in the initial work were rather modest, much progress has since been made to develop microstructures of considerable interest.

Efforts to develop the Q&P process focused first on understanding the potential for carbon partitioning into austenite following transformation to martensite. The partitioning kinetics for some similar processes had been examined by others (Hillert *et al.*, 1993; Mujahid and Bhadeshia, 1993), and the first task was to understand the expected endpoint of carbon partitioning, which would define whether the partitioning mechanism should be capable of stabilizing large austenite fractions, or only small ones. Thermodynamic analysis ensued, to define the conditions under which the carbon potential became equal in martensite and austenite, and thus to understand the expected carbon transport between as-quenched martensite and untransformed austenite. It became immediately clear that other, competing, mechanisms could also occur, such as conventional tempering reactions, and these mechanisms were

© Woodhead Publishing Limited, 2012

ignored in the initial analyses, for simplicity. Quantitatively, it was recognized that the fractions of martensite and austenite present in the microstructure may have a controlling influence on the level of austenite carbon enrichment achieved at the end of partitioning.

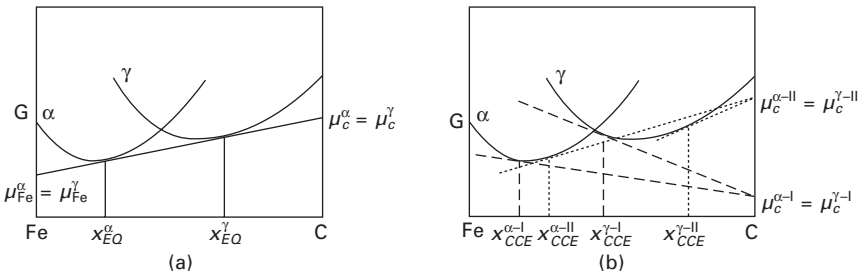
Early calculations assumed that fixed fractions of martensite and austenite would be established prior to partitioning, and that the martensite and austenite fractions might not change much during partitioning, as the mobility of interstitial carbon may be much higher than the mobility of the martensite/austenite interface at partitioning temperatures that are much lower than temperatures more typical of diffusional austenite decomposition. The assumption of a completely immobile interface was incorporated into the equilibrium calculations, allowing quantification of the possible levels of carbon enrichment. The particular conditions where the martensite and austenite fractions are fixed (i.e. the interface is constrained), and the chemical potential of carbon is uniform in the two phases, were initially termed 'constrained paraequilibrium' and later 'constrained carbon equilibrium' or CCE, defining the endpoint of equilibrium partitioning (Speer *et al.*, 2003a, 2005; Hillert and Ågren, 2004). A useful comparison is illustrated in Fig. 8.2 between metastable martensite/austenite equilibrium and CCE which provides schematic Gibbs free energy vs. composition diagrams. The equilibrium condition (Fig. 8.2(a)) is uniquely defined by the common tangent construction, but the CCE condition (Fig. 8.2(b)) is not unique, and two examples are shown with equal carbon potentials (tangents intersecting the carbon axis at the same point).

The CCE condition that applies to a particular situation is understood to be dependent on the phase fractions to satisfy mass balance constraints.[1] As an example, Fig. 8.3 shows the calculated CCE conditions for a 0.5% carbon alloy over a range of temperatures. The phase compositions are strongly influenced by the fraction of martensite, and very high levels of carbon enrichment are predicted in austenite in some cases. The calculated carbon concentration in the ferrite (i.e. carbon depleted martensite) is much lower. Most importantly, the thermodynamic models indicated that almost all of the carbon would prefer to be resident in the austenite, rather than in the martensite where it is much less soluble (Speer *et al.*, 2003a, 2004).

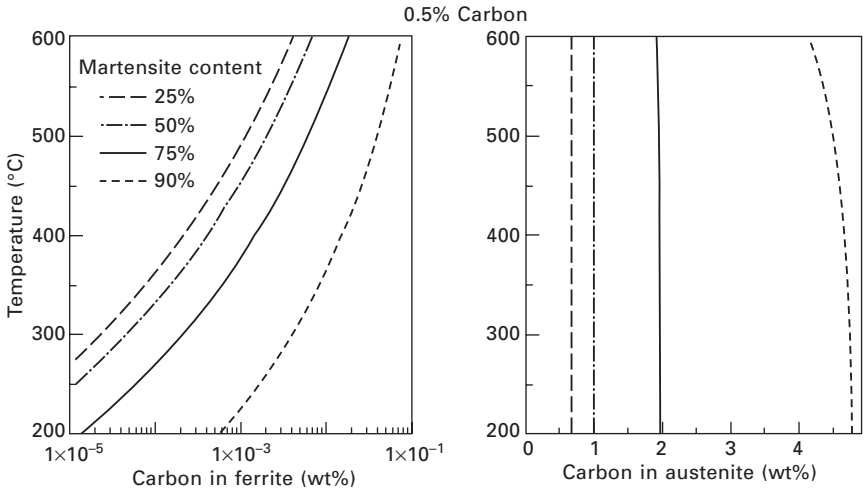
The next step in the development of the Q&P process involved experimental verification of the concept. The process was conceived to involve interrupted

[1] A variation of this analysis also showed that a particular set of ferrite/austenite compositions having equal carbon potentials could also represent a possible interface boundary condition during a hypothesized bainitic transformation occurring by a fully martensitic mechanism under full carbon diffusion control (Speer *et al.*, 2003a, 2004). However, this hypothesis has not yet been evaluated fully by the bainite transformation community.

© Woodhead Publishing Limited, 2012



8.2 Schematic molar Gibbs free energy vs. composition diagrams illustrating equilibria at a particular temperature between martensite and austenite in the Fe-C binary system: (a) equilibrium (EQ), and (b) two possible metastable constrained carbon equilibrium conditions (I and II) (Speer *et al.*, 2004).



8.3 Constrained carbon equilibrium calculations for an Fe-0.5C (wt%) alloy, showing the dependence of CCE ferrite and austenite compositions on temperature and initial martensite fraction (molar basis) (Speer *et al.*, 2003a). In these thermodynamic calculations, carbon-depleted martensite is modeled using free energy data for ferrite.

quenching, to control the fractions of austenite and martensite, followed by a thermal treatment to allow carbon partitioning. The well-known relationship of Koistinen and Marburger was used as a simple means to estimate the expected phase fractions for a given austenite chemical composition, both during the initial quenching step, and then during final cooling to room temperature following carbon partitioning. The Koistinen–Marburger relationship relates the extent of martensite transformation to the amount of undercooling below

© Woodhead Publishing Limited, 2012

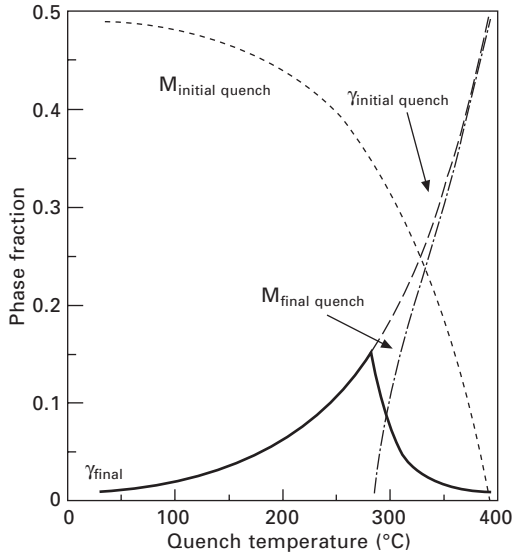
the M_s temperature (Koistinen and Marburger, 1959) through the following expression:

$$f_m = 1 - e^{-1.1\times10^{-2}(M_s - QT)} \quad [8.1]$$

where f_m is the fraction of austenite that transforms to martensite upon quenching to a temperature QT below the M_s temperature. M_s can be predicted for the applicable austenite composition using empirical relations. The models provided a useful means of predicting the amount of austenite that could be stabilized in a particular steel, as a function of the initial quenching temperature, and were employed to design experiments aimed at verifying the Q&P concept. The process design models ignored competing mechanisms such as carbide formation, carbon trapping at dislocations, decomposition of the austenite by other means (such as bainite formation), etc. The 'constrained carbon equilibrium' condition was estimated based on the earlier models showing that nearly all of the carbon is expected to partition to austenite in steels with reasonable carbon concentrations. Hence, the models ignored competing mechanisms, and avoided thermodynamic calculations, simply assuming, as a first approximation, that all of the carbon resides in the austenite after partitioning is complete. These simple models (Speer *et. al.*, 2003b) provided important guidance to early Q&P process designs, identifying an expected 'peak' in the final retained austenite fraction at a certain quenching temperature (QT), designated the 'optimum' quenching temperature. The relationship between the quenching temperature and the microstructure that develops under ideal partitioning conditions (where all of the carbon partitions to the austenite) is illustrated in Fig. 8.4, for a 0.19C steel intercritically annealed to produce 50% ferrite prior to quenching and partitioning. The amount of martensite that forms during the initial quench increases at lower quench temperatures, thereby reducing the amount of austenite that remains before partitioning. Following full partitioning, the austenite stability increases, which influences the final austenite fraction as shown in the figure. At high quench temperatures, the amount of austenite is relatively high, and thus it is less stable upon final cooling to room temperature, having received a lesser amount of carbon available from the smaller martensite fraction.

Development of the early models was occurring simultaneously with the earliest efforts to verify the concept with experimental data. Silicon was considered a potentially important alloying addition because of its ability to suppress cementite precipitation (a competing reaction that 'consumes' carbon which otherwise could be available for austenite stabilization), and early research focused on automotive steels with ~0.2% (by weight) carbon, as potential high strength replacements for bainitic TRIP products (Streicher *et al.*, 2004). A higher carbon (0.6%) Si-containing steel was also examined

© Woodhead Publishing Limited, 2012



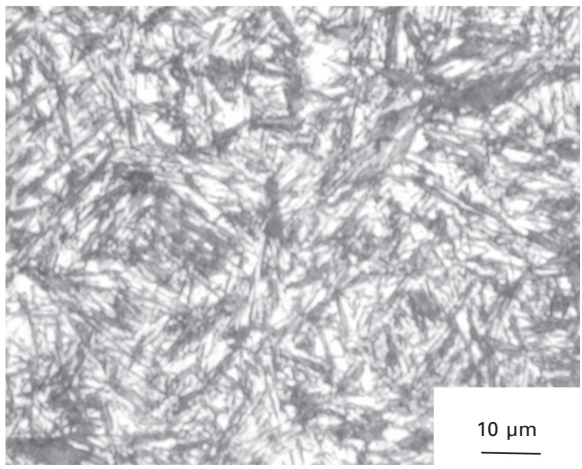
8.4 Predicted Q&P microstructure components for 0.19C steel containing 50% intercritical ferrite, vs. quench temperature, assuming full partitioning prior to final quenching to room temperature. The final austenite fraction at room temperature is given by the solid bold line. Dashed lines represent the austenite and martensite (M) present at the initial quench temperature, and the additional martensite formed during the final quench to room temperature. For this example, $M_{initial\ quench} + M_{final\ quench} + \gamma_{final} = 0.5$, and the intercritical ferrite fraction is 0.5 (Speer *et al.*, 2003b).

in this work, and provided strong support for the partitioning mechanism, and an excellent illustration of austenite stabilization via the Q&P process, owing to its higher carbon level and associated austenite-stabilizing character (Gerdemann *et al.*, 2004). The light optical micrograph in Fig. 8.5 shows the presence of a substantial quantity of retained austenite (approximately 25 vol% based on x-ray diffraction) interspersed with partitioned martensite. The retained austenite fraction is much greater than would be achieved if a steel of this composition was quenched directly to room temperature (appearing more similar to a case carburized microstructure at a much higher carbon level), reflecting powerful stabilization resulting from the carbon partitioning mechanism.

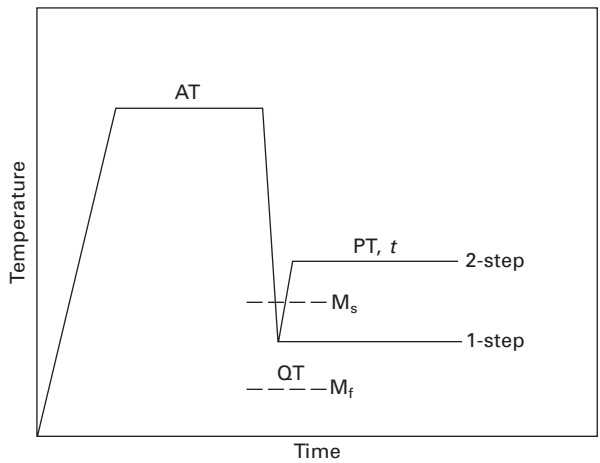
8.2 Microstructure development fundamentals and alloy designs

The basic elements of quenching and partitioning are quite simple, involving partial transformation to martensite (at a carefully controlled temperature

© Woodhead Publishing Limited, 2012



8.5 Light optical micrograph from 0.6 C, 2.0 Si steel after austenitizing, quenching to 190°C, and partitioning for 30 s at 400°C (Gerdemann *et al.*, 2004).



8.6 Schematic illustration of the Q&P thermal processing concept. AT, QT and PT are austenitizing, quenching and partitioning temperature, respectively, M_s and M_f are martensite start and finish temperatures, and *t* is time.

between M_s and M_f), and austenite stabilization via carbon transport from martensite to austenite. The thermal profile is shown schematically in Fig. 8.6. The partitioning treatment is usually accomplished at the same temperature as the quench ('one-step' Q&P) or at a higher temperature ('two-step' Q&P). The basic microstructure is believed to consist of lath martensite with thick films of retained austenite, or plate martensite with carbon enriched

© Woodhead Publishing Limited, 2012

pools. However, the base microstructure may be overlaid with a variety of other important features associated with different mechanisms that may occur during the partitioning step, and each has important or profound implications with respect to the final product behavior. These different mechanisms are associated with competing processes such as trapping of carbon atoms at dislocations, transition carbide or cementite precipitation, bainite transformation, etc. The competing processes are well known to occur under appropriate alloying/processing conditions, and have been more widely accepted than the carbon 'partitioning' mechanism, which was not as well established in the tempering literature. Thus, much of the research on microstructure development in the emergent field of Q&P steels has been devoted to assessing the importance of competing mechanisms and developing strong evidence supporting the operation of the carbon partitioning mechanism. In addition, some studies of partitioning kinetics, (martensite/austenite) interface migration, and alloying effects on austenite stabilization have been conducted.

One of the important assumptions employed in early models of the Q&P process, that 'all of the carbon partitions to the austenite,' has unfortunately led to some confusion. It should be clearly understood that this assumption provides important insight as to the main effects of the partitioning mechanism, but in reality other competing reactions have been:

- an important factor in the earliest conceptual discussions of the concept,
- identified to clearly operate in some instances, and
- understood to have important implications to product and process design.

The competing reactions also create a rich complexity that further enhances the opportunity to create varying microstructures and steel products, while at the same time magnifying the number of fundamental issues that still remain to be fully understood. To the extent that competing reactions are suppressed, then it is correct to presume that nearly all of the carbon will reside in the untransformed austenite. Conversely, to the extent that carbon enrichment of austenite cannot account for the total mass of carbon in a steel, then either partitioning is incomplete or competing reactions have occurred. Some examples may be found in Q&P studies where the mass balance indicates that nearly full partitioning of carbon into austenite has occurred, but in general, *all* of the carbon is not typically found to reside in the retained austenite.

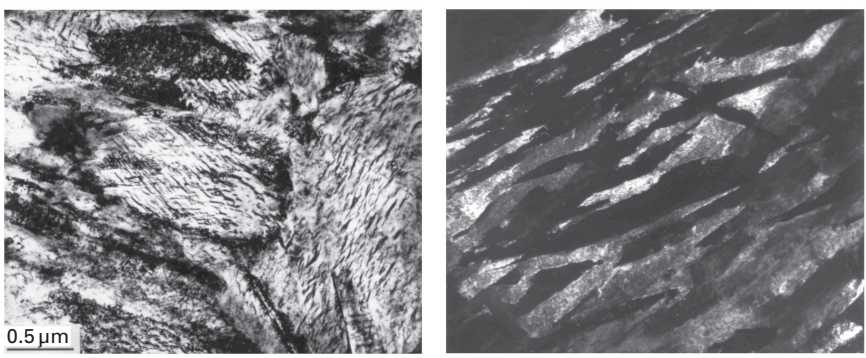
Suppression of carbide formation was understood in early Q&P studies to be critical to austenite stabilization (Speer *et al.*, 2003a) and silicon and/or aluminum were added at levels typical of TRIP sheet steels, where carbide-free bainitic microstructures with interlath retained austenite are

© Woodhead Publishing Limited, 2012

readily obtained through austempering. It was discovered in the 0.6 C, 2% Si steel that austenite stabilization was less effective at a lower partitioning temperature of 250°C in comparison to 400°C, and extensive precipitation of transition carbides occurs at the lower temperature, as shown in Fig. 8.7 (Edmonds *et al.*, 2006). The difference in partitioning response between these two conditions is ascribed to strong suppression of cementite (which forms at high temperatures) by silicon, and weak suppression of transition carbide (which forms at lower temperatures). Since partitioning at higher temperatures usually involves first quenching to lower temperatures to provide sufficient martensite at the quenching step (i.e. two-step processing), the potential for transition carbide precipitation at lower temperatures, followed by dissolution during heating (above the transition carbide solvus) appears likely (Edmonds *et al.*, 2006).

While the majority of Q&P studies have focused on Si-containing grades, aluminum additions have also been explored because of their ability to promote carbon enriched retained austenite in some bainitic TRIP steels. Aluminum promotes bainite and has been found by different investigators to be less effective than silicon for stabilizing austenite in Q&P steels (Santofimia *et al.*, 2008a; De Moor *et al.*, 2009a). Molybdenum, on the other hand, has been found to effectively stabilize austenite for longer times at higher partitioning temperatures in Si-added steels, potentially of importance in hot-dip coated sheet products (where partitioning is accomplished in conjunction with coating) (De Moor *et al.*, 2008). Effective alloying approaches to suppress transition carbide precipitation (during low temperature partitioning) and/or replace Si have yet to be identified.

Recent models predicting aspects of Q&P microstructures have relaxed



8.7 (a) Bright-field TEM micrograph showing extensive transition carbide precipitation in 0.6 C, 2 Si steel after quenching to 150°C and partitioning at 250°C. (b) Dark-field TEM micrograph showing austenite following quenching to 190°C and partitioning at 400°C (Edmonds *et al.*, 2006).

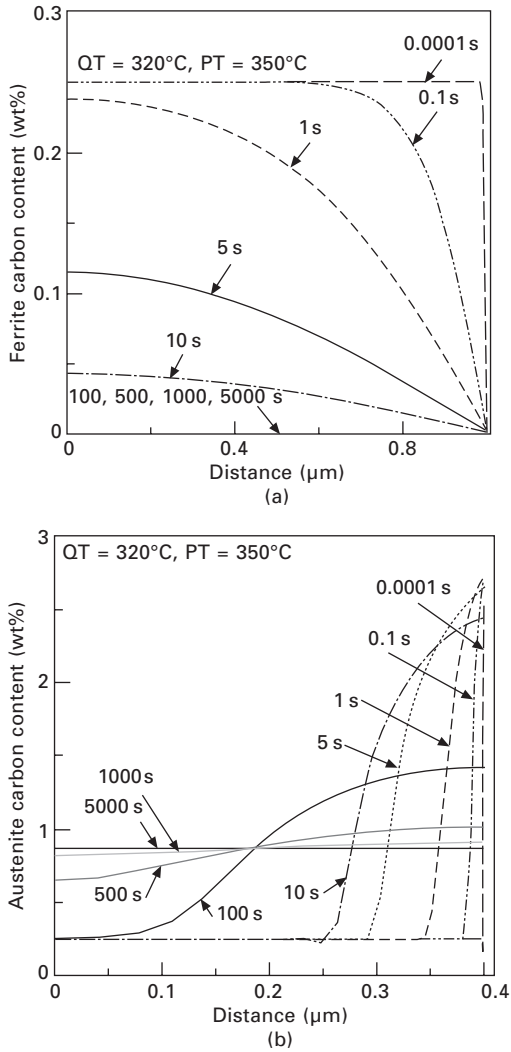
© Woodhead Publishing Limited, 2012

some of the simplifying assumptions made in the earlier models described above. In particular, kinetics were incorporated into the modeling approaches (Rizzo *et al.*, 2005; Clarke *et al.*, 2005), as well as mobility of the martensite/austenite interface, leading to some interesting perspectives (Speer *et al.*, 2007; Santofimia *et al.*, 2008b, 2009). Figures 8.8(a) and (b) show calculated carbon diffusion profiles in the martensite and austenite during partitioning, assuming equilibrium for carbon at the interface, and representing carbon mobility in martensite through better characterized carbon diffusivity data in ferrite. The figure applies to a 0.25 C alloy at 350°C, and was developed for specific dimensions of the adjacent martensite and austenite crystals (Clarke, 2006; Clarke *et al.*, 2009). Figure 8.8(c) also shows the amount of final austenite (after cooling from the partitioning temperature to room temperature), using the carbon profile to define the 'local' austenite stability. This model applies the Koistinen–Marburger expression presented above, based on bulk behavior, to predict microstructural features that may extend over length scales that are significant relative to the carbon gradient, and indicates the need for additional fundamental understanding of transformation behavior under these conditions. The kinetic models suggest that partitioning should occur very rapidly, and may not match experimental observations, perhaps indicating the need for better characterization of carbon mobility through defect-laden martensitic microstructures. Moreover, the models suggest that the retained austenite fractions can be greater in some cases after incomplete partitioning, than would be expected after full partitioning.

Figure 8.9 shows final austenite fractions plotted vs. quench temperature and partitioning time at 400°C, calculated based on the method presented in Fig. 8.8, integrating the local austenite stability across the width of the austenite, thereby accounting for the carbon gradient that exists prior to equilibrium. The results show the expected increase in austenite fraction as partitioning time increases early in the process, and the eventual agreement with the values predicted assuming ideal partitioning. At intermediate times, however, there are some interesting behaviors associated with the carbon gradients that develop during partitioning. At quench temperatures above the optimum temperature, representing the peak in the theoretical curve (also shown), the amount of austenite after initial quenching is greater than the final amount that can be stabilized at room temperature. At these quench temperatures, it is apparent that the final austenite fraction is maximized at intermediate values of partitioning time, and then decreases at longer times, indicating that greater austenite fractions may be possible than predicted under ideal partitioning conditions. The increased austenite associated with incomplete partitioning at high quench temperatures is a consequence of the greater austenite stability in the carbon-enriched regions of austenite when there is a composition gradient in the austenite, relative to the lower overall austenite stability when the carbon is uniformly distributed at a low

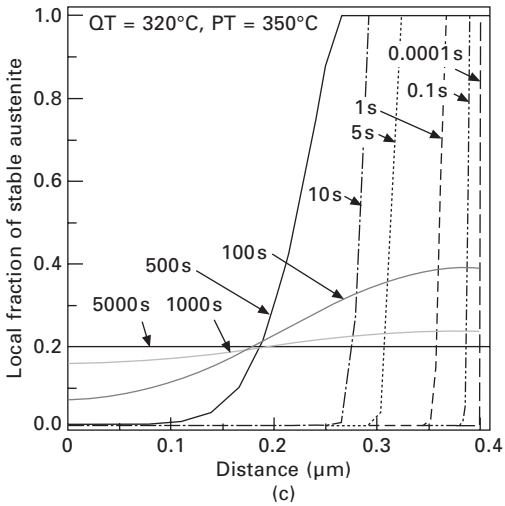
© Woodhead Publishing Limited, 2012

level throughout a larger volume of austenite. The influence of kinetics on the quench temperature dependence of the austenite fraction may have some important industrial relevance, with respect to sensitivity of microstructure/

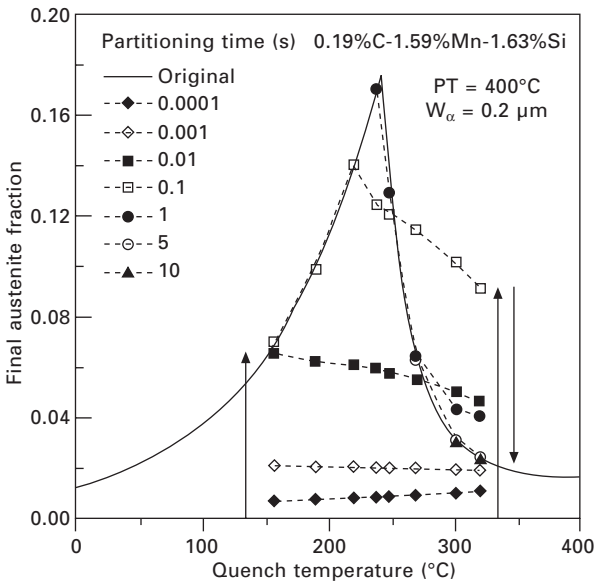


8.8 Calculated carbon concentration in ferrite (a) or austenite (b) as a function of distance for a Fe-0.25 C alloy containing ~29 vol% austenite at a quench temperature of 320°C, for partitioning times at 350°C as indicated. The distance from the center of a ferrite lath to the interface is assumed to be 1 μm for this simulation, while the distance from the center of the austenite film to the interface is ~0.4 μm. The 'local fractions' of austenite stable at room temperature are shown in (c) (Clarke, 2006; Clarke *et al.*, 2009).

© Woodhead Publishing Limited, 2012



8.8 Continued



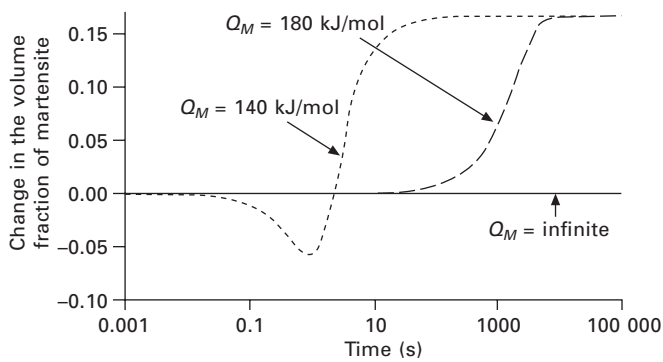
8.9 Calculated final austenite fraction as a function of quench temperature for a 0.19C-1.59Mn-1.63Si alloy. Individual points that incorporate the kinetics of carbon partitioning are also shown for selected partitioning times. A ferrite width of W_α = 0.2 μm was used for the partitioning temperature of 400°C. Arrows highlight austenite fraction behaviors with increasing partitioning time for quench temperatures above and below the peak (optimum) quench temperature (Clarke *et al.*, 2009). A final austenite fraction curve (solid curve) is also shown that does not incorporate carbon partitioning kinetics, but rather assumes complete ideal partitioning.

© Woodhead Publishing Limited, 2012

properties to process variability. The sharp peak, reflecting high sensitivity to quench temperature under equilibrium partitioning conditions, may not be generally applicable to other processing conditions.

In the most recent kinetic models, the assumption of an immobile martensite/austenite interface was relaxed, and the coupling between interface migration and carbon partitioning was incorporated (Santofimia *et al.*, 2008b, 2009). The interface mobility is not well quantified, so different values were used in the models, with profoundly different implications. One example from this work is shown in Fig. 8.10, calculated using three different assumed values of the activation energy for interface migration. In Fig. 8.10, the predicted movement of the martensite/austenite interface is reflected through changes in the martensite volume fraction, shown as a function of partitioning time at 350°C following quenching to 300°C. Corresponding changes in the austenite fraction would be of equal magnitude and opposite sign. One activation energy was selected to represent an immobile interface ($Q_M = \infty$), and the other two were selected, based on a review of the literature, to reflect migration of an incoherent ferrite/austenite interface ($Q_M = 140$ kJ mol^{-1}) or a semi-coherent ferrite/austenite interface ($Q_M = 180$ kJ mol^{-1}). The results in the figure clearly confirm the possibility under some conditions that the transformation interface might move in one direction, and then reverse itself as a consequence of particular coupling between carbon partitioning and interface migration (Speer *et al.*, 2007; Santofimia *et al.*, 2008b, 2009).

The endpoint of partitioning is also dependent on the assumptions made relative to interface mobility. If the interface is stationary, then



8.10 Changes in the martensite fraction during partitioning, calculated based on three assumed values of the activation energy (Q_M) for migration of the martensite/austenite interface. The example was calculated for a 0.19C–1.59Mn–1.63Si steel, quenched to 300°C and partitioned at 350°C for a 0.2 μm martensite lath width (Santofimia *et al.*, 2009).

© Woodhead Publishing Limited, 2012

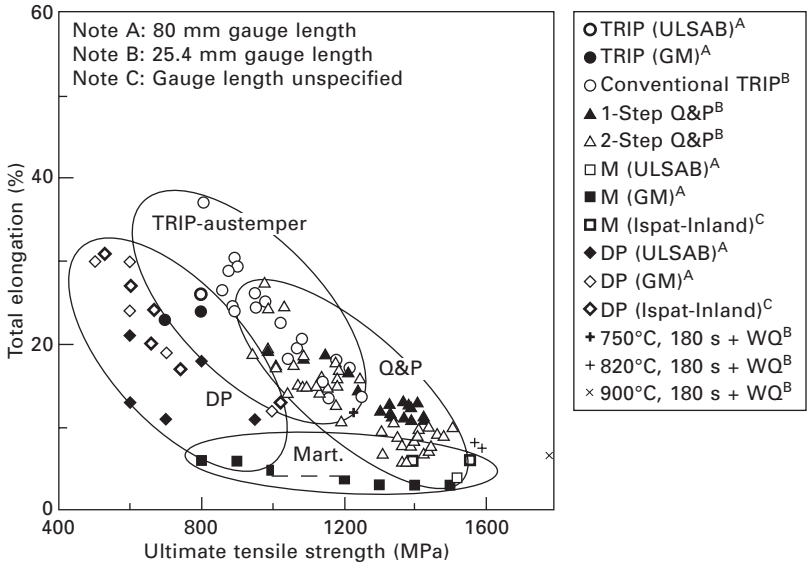
partitioning ends under constrained carbon equilibrium conditions, whereas a mobile interface would allow the phase fractions/compositions to adjust eventually to their metastable paraequilibrium values (Speer *et al.*, 2003; Santofimia *et al.*, 2009). The interface mobility is therefore relevant from a microstructure design standpoint, as it influences both the volume fraction and the carbon concentration of the austenite resulting from Q&P processing. Experimentation related to interface migration remains at an early stage. Some studies have suggested that the fractions of austenite and martensite may increase or decrease during partitioning, while others have indicated that the phase fractions are largely unchanged (De Moor *et al.*, 2008; Kim *et al.*, 2009; Bigg *et al.*, 2011; Thomas, 2011).

8.3 Mechanical behavior, potential applications, and implementation status

High strength steels containing significant fractions of retained austenite are the subject of growing commercial interest. Carbon-enriched metastable retained austenite is considered beneficial because transformation plasticity during deformation, i.e. the TRIP phenomenon, can contribute to work hardening, formability and fracture toughness. Q&P should be of potential interest whenever retained austenite is considered to offer enhanced performance characteristics, and has been applied to a variety of product concepts including cold-rolled and coated sheet steel, heat-treated bar products, plate and hot-rolled sheet steel, and ductile cast iron (Speer *et al.*, 2004). The primary intent is usually to obtain metastable retained austenite in combination with a strong martensitic matrix. High strength is thus achieved in combination with transformation-induced plasticity (TRIP) behavior to enhance an important property for the application of interest, such as ductility/formability, resistance to brittle fracture, damage tolerance in rolling contact, etc.

The initial attention and industrial interest in Q&P has perhaps involved automotive sheet steel applications, where the market demands higher strength products with better formability to achieve improved fuel economy and crashworthiness. As illustrated in Fig. 8.11, Q&P offers the potential to increase the available strength/formability balance in comparison to dual-phase (DP) or martensitic steels, and essentially extends the property range of austempered TRIP steels through higher strength levels as a consequence of the substitution of martensite for bainite. For ultra-high strength sheet steels, hole-expansion formability and shear fracture resistance are factors of increasing importance, and research has also indicated that Q&P may offer some improvements in this regard, when compared to other microstructures at the same strength level (DeMoor *et al.*, 2009b). The early work illustrated in Fig. 8.11 showed that the strength of Q&P steels can be quite high, although tensile strengths near or above 2 GPa have been reported more recently in

© Woodhead Publishing Limited, 2012



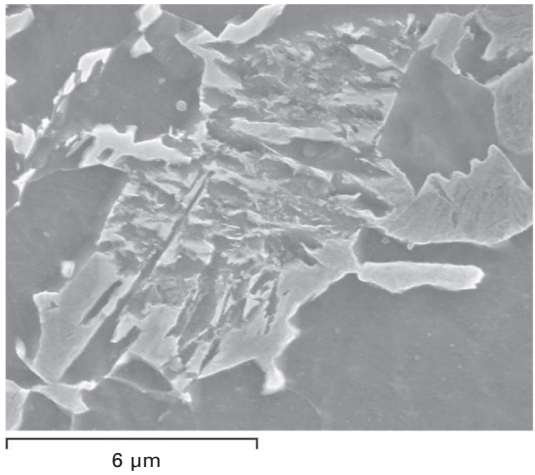
8.11 Tensile ductility plotted as a function of tensile strength for a 0.19C–1.59Mn–1.63Si steel processed by austempering or Q&P, and compared to literature data for DP and martensitic steels (Streicher *et al.*, 2004; Clarke, 2006; Speer and Matlock, 2009).

some low alloy steels with impressive tensile ductility levels exceeding 10% (Rizzo *et al.*, 2007; Li *et al.*, 2010; De Moor *et al.*, 2011). Additional efforts are needed to understand the microstructure contributions to the observed strength levels, including the contributions from substructure, dislocations, carbides, solute, etc., in the partitioned (carbon-depleted) martensite, and even the full influences of austenite fraction and stability, although these subjects are outside the scope of the present discussion.

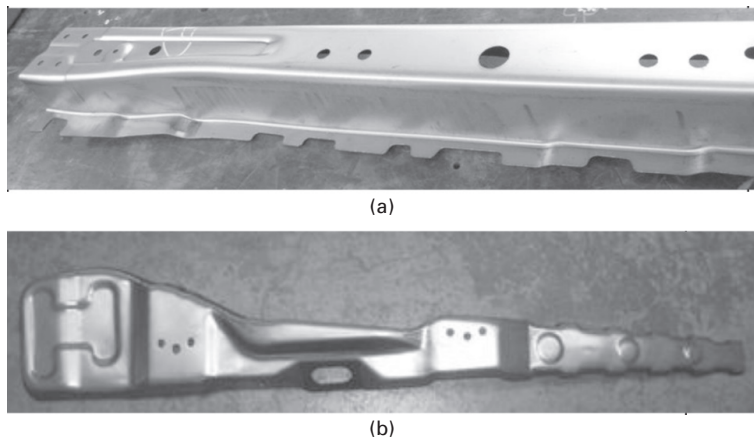
At the time of writing, the Q&P process is at an early stage of industrial implementation, with industrial trials having been conducted to produce advanced high strength automotive sheet material on special processing facilities (Wang and Feng, 2011). Figure 8.12 shows an example of a Q&P microstructure found in an industrially produced Q&P coil (Feng, 2011). The microstructure exhibits equiaxed ferrite formed during intercritical annealing after cold rolling, mixed with martensite and thick austenite films similar to the microstructures published in many Q&P laboratory studies. Some early examples of components produced successfully using Q&P steel are shown in Fig. 8.13.

As mentioned above, retained austenite is considered to offer improved fracture toughness in structural applications, and an investigation related to API linepipe application was undertaken with encouraging results (Hong *et al.*, 2007). Figure 8.14 shows a comparison of Charpy V-notch absorbed

© Woodhead Publishing Limited, 2012



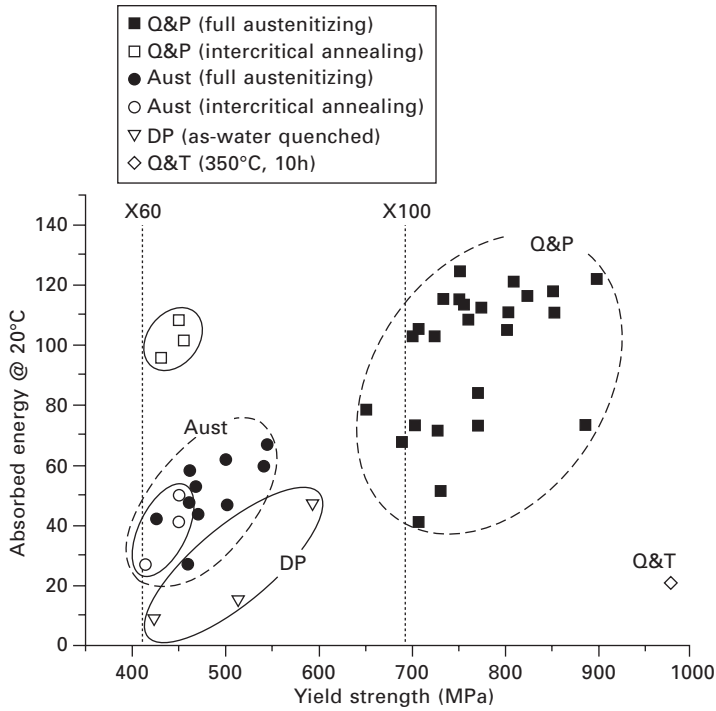
8.12 Scanning electron micrograph of etched Q&P cold-rolled sheet steel, processed using industrial facilities (Feng, 2011).



8.13 Photographs of automotive components produced from Q&P sheet steel, including (a) a 1.8 mm thick floor beam, and (b) a 2.0 mm thick B-pillar reinforcement. Courtesy of Baosteel (Feng, 2011).

impact energy at 20°C plotted against yield strength for a modified X100 type linepipe steel processed via Q&P in comparison to conventional quenched and tempered martensite, austempered bainite, or a dual-phase mixture of ferrite and martensite. The plates were laboratory melted and rolled to a thickness of 12.5 mm before heat treating, followed by a variety of time/temperature profiles to generate a range of properties from each microstructure family. The Q&P condition appears to offer an enhanced combination of strength and toughness when compared to other heat treatments. In contrast to sheet applications, thermal gradients are likely to play a more important role in plate or other bulk applications, but this issue has not been explored to date.

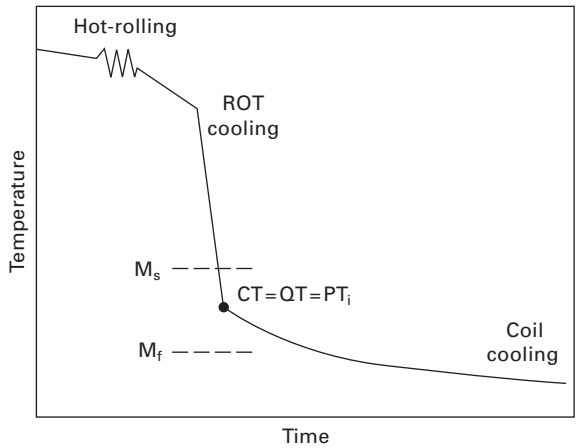
© Woodhead Publishing Limited, 2012



8.14 Comparison of yield strength and Charpy impact toughness of different microstructures, produced by varied processing using a 0.1 C modified X100 steel composition. X60 and X100 linepipe yield strength levels are shown for reference (Hong *et al.*, 2007).

In the long-products area, one attribute for which retained austenite is considered to be beneficial involves improved damage tolerance in rolling contact fatigue, such as in bearing or perhaps gear applications. Initial studies on a 0.6 C, 2% Si alloy showed that Q&P offered improved rolling contact fatigue performance when compared to a conventional quench and tempered microstructure at the same hardness level (Shutts *et al*., 2006; Shutts, 2006; Kim *et al*., 2011). Fine transition carbides are prevalent in this steel at (low) partitioning temperatures where appropriately high levels of hardness are maintained (Shutts *et al*., 2006; Kim *et al*., 2011). The formation of these transition carbides is one example of a mechanism that 'competes' with carbon partitioning. The competing reactions are often considered detrimental in that they limit the extent of austenite stabilization that may be possible, but in the present example may be beneficial via their likely contribution to the desired matrix strength. Some research groups have more recently employed the terminology Q-P-T, or 'quenching, partitioning and tempering' to emphasize the operation of these additional mechanisms during Q&P processing (Zhong *et al*., 2009; Hsu and Jin, 2011).

© Woodhead Publishing Limited, 2012

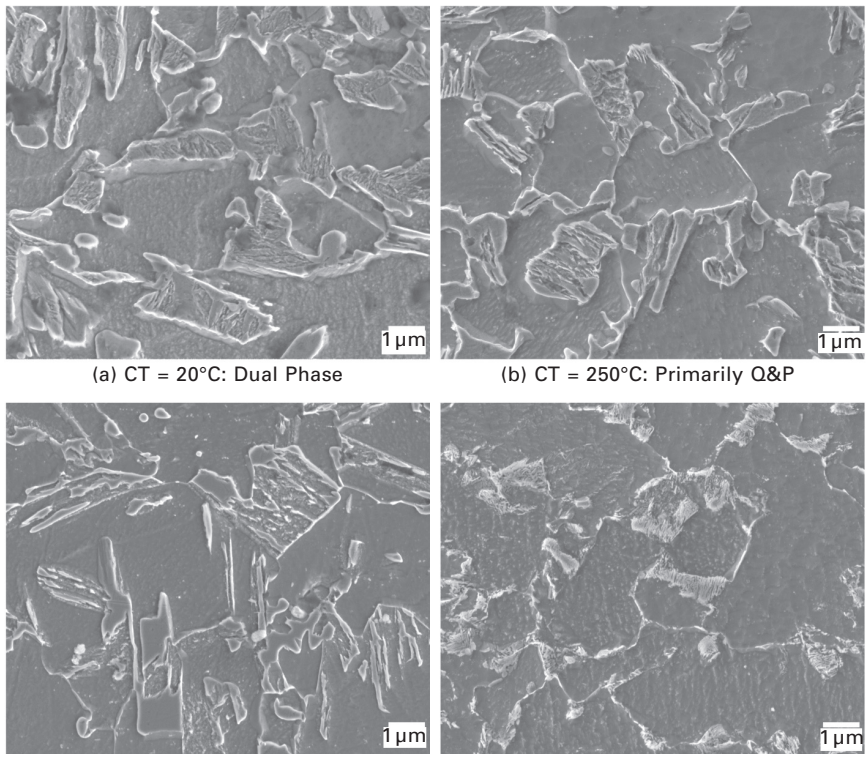


8.15 Schematic thermomechanical processing sequence suggesting application of the quenching and partitioning concept to hot-rolled sheet steel production (Thomas *et al.,* 2008).

The Q&P concept might also be extended to applications beyond heat treating, such as hot-rolling or forging. For example, the first austenitizing step could be incorporated into a sheet hot-rolling process for some applications, with quenching and partitioning occurring on the runout table (ROT) or after coil winding. Such a concept was recently proposed, and is shown schematically in Fig. 8.15 for the case of hot-strip mill sheet rolling, where the quenching step is intended to occur during ROT cooling, and partitioning occurs during coil cooling. The partitioning step is accomplished under non-isothermal conditions in this instance, where the coiling temperature (CT) represents both the quenching temperature (QT) and the initial partitioning temperature (PT_i). The quenching and partitioning steps are somewhat less than ideal in this application, as carbon partitioning occurs over a range of temperatures, and further martensite transformation may not be precluded after coiling. The extent of martensite formation and the extent of carbon partitioning are *both* controlled by the coiling temperature, which creates an additional constraint when compared to the schematic Q&P process signature in Fig. 8.6 where the two processes were controlled independently. However, calculations confirmed that such a scenario may be workable (Thomas *et al*., 2008, 2011).

The processing path implied in Fig. 8.15 is similar to those employed in the production of hot-rolled martensite-containing DP or bainite-containing TRIP sheet steels, and is somewhat intermediate between them. A transition in microstructure with coiling temperature resulting from initial hot-rolled sheet simulations is illustrated in Fig. 8.16. At high coiling temperature, the austenite present transforms to pearlite (Fig. 8.16(a)). Lower coiling temperatures in this Si-containing steel lead to carbide-free bainitic TRIP

© Woodhead Publishing Limited, 2012



(a) CT = 20°C: Dual Phase (b) CT = 250°C: Primarily Q&P

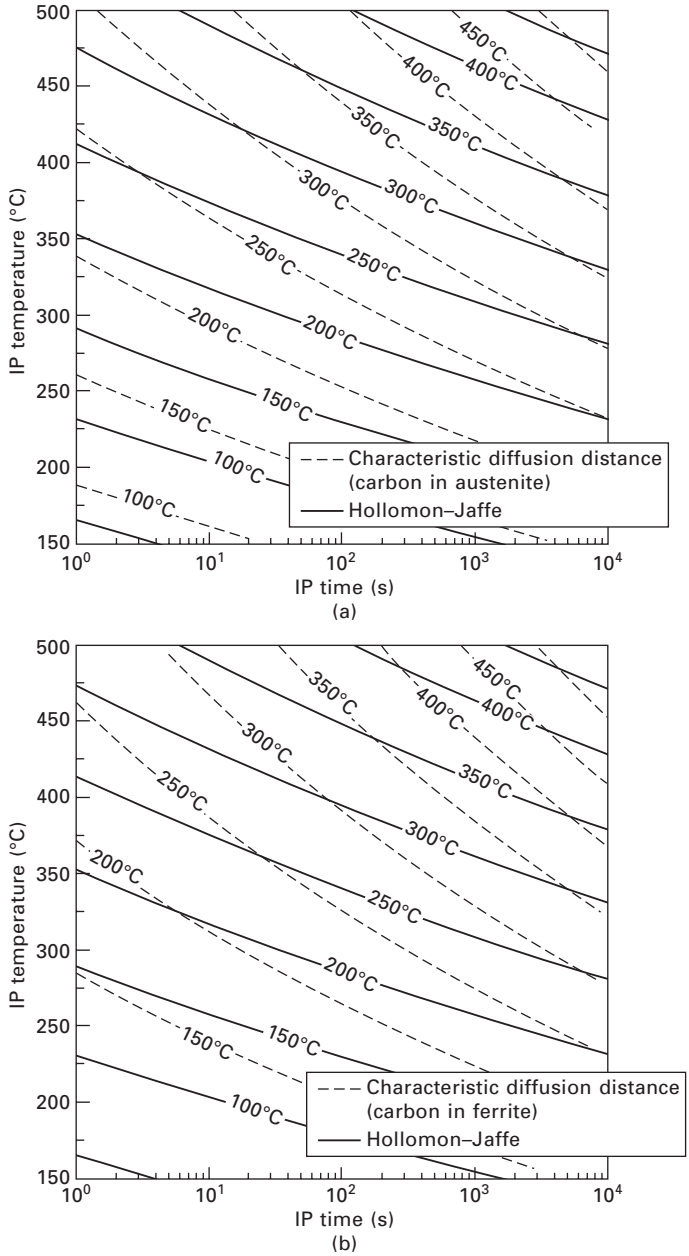
(c) CT = 325°C: Primarily TRIP (d) CT = 475°C: Ferrite/Pearlite

8.16 Microstructures observed after intercritical annealing and slow coil cooling to simulate hot-strip mill processing of 0.19C-1.59Mn-1.63Si alloy, showing the influence of coiling temperature on microstructures at coiling temperatures of (a) 20°C, (b) 250°C, (c) 325°C, or (d) 475°C. SEM (secondary electron) images, nital etched (Thomas *et al.*, 2011).

constituents (Fig. 8.16(b)), then partially transformed martensite/austenite (Q&P) (Fig. 8.16(c)), and finally martensite (Fig. 8.16(d)) in combination with the primary ferrite. Coiling temperature regimes for the different transformation mechanisms appear to overlap, and the Q&P mechanisms operate over a continuum that includes conventional bainitic and martensite microstructures at higher and lower coiling temperature, respectively (Thomas *et al.*, 2011).

In an interesting side-note to model non-isothermal partitioning response during this work, relationships for time–temperature equivalence were explored, and some interesting differences were noted between the traditional Hollomon–Jaffe tempering parameter approach, and one based on equal diffusion distances (Hollomon and Jaffe, 1945; Thomas *et al.*, 2010). The time–temperature equivalence was examined to provide a means to integrate

© Woodhead Publishing Limited, 2012



8.17 Locus of non-isothermal partitioning responses for coil cooling from temperatures ranging between 100 and 500°C (indicated in the figure) that are equivalent to isothermal partitioning (IP) at temperatures and times indicated by the coordinate axes. The solid lines are based on the Hollomon–Jaffe tempering parameter, while the dashed lines are based on carbon diffusion distance in austenite (a) or ferrite (b). Carbon diffusivity in ferrite is based on Do = 2.2 cm^2/s and Q = 123 kJ/mole (Thomas *et al.*, 2008).

© Woodhead Publishing Limited, 2012

expected behaviors over particular cooling profiles, for comparison with isothermal treatments. Figure 8.17 shows the results of calculations for processes occurring in (a) austenite or (b) ferrite, respectively. The axes represent isothermal partitioning times and temperatures, and the plotted curves represent the loci of equivalent non-isothermal partitioning responses for coil cooling from temperatures ranging between 100 and 500°C (indicated in the figure). The solid lines are based on the Hollomon–Jaffe tempering parameter, while the dashed lines are based on carbon diffusion distance in austenite. The results in Fig. 8.17 provide a means to compare isothermal heat treating response with 'equivalent' non-isothermal response during coiling after hot-rolling, and are thus applicable to Q&P partitioning as well as other processes such as bainite formation. There are some differences between the dashed curves and the solid curves, indicating that the classical Hollomon–Jaffe tempering parameter does not accurately match the time–temperature equivalence associated with an approach based on equal carbon diffusion distances. The differences between these approaches were explored further in the context of martensite tempering, where the tempering parameter is most commonly employed, and some interesting implications were found. In particular, the expected sequence of tempering reactions was found to change under different time–temperature scenarios (Thomas *et al.*, 2010), whereby the processes occurring during short-time tempering at elevated temperature may not be identical to those occurring for longer times at lower temperature. Because short-time tempering is possible using induction heating technologies, these behaviors may have important practical implications, so there is a need to understand better the fundamental transformation responses under a wider variety of tempering conditions.

8.4 Conclusions

Phase transformation fundamentals have been critical to the conception and development of the quenching and partitioning process, a new heat treatment aimed at producing high strength steels with enhanced retained austenite fractions via partitioning of carbon from supersaturated martensite. The process has been reviewed, linking the transformation fundamentals to process modeling, microstructure development, properties/application, as well as industrial processing. Several unresolved mechanistic issues are identified, particularly with respect to processes occurring during the 'partitioning' step of the heat treatment. These issues provide fruitful opportunities for additional research, and are needed to guide further progress in development and implementation of the quenching and partitioning process by industry.

© Woodhead Publishing Limited, 2012

8.5 References

Bigg T D, Matlock D K, Speer J G and Edmonds D V (2011), 'Dynamics of the quenching and partitioning (Q&P) process, *Solid State Phenomena*, 172–174, 827–832.

Clarke A (2006), PhD Thesis, Colorado School of Mines.

Clarke A, Speer J G, Matlock D K, Rizzo F C, Edmonds D V and He K (2005), Microstructure and carbon partitioning in a 0.19%C-1.59%Mn-1.63%Si TRIP sheet steel subjected to quenching and partitioning (Q&P), *Solid-to-Solid Phase Transformations in Inorganic Materials 2005 – Volume 2*, TMS, Warrendale, PA, 99–108.

Clarke A J, Speer J G, Matlock D K, Rizzo F C, Edmonds D V and Santofimia M J (2009), Influence of carbon partitioning kinetics on final austenite fraction during quenching and partitioning, *Scripta Mater.*, 61, 149–152.

De Moor E, Penning J, Föjer C, Clarke A J and Speer J G (2008), Alloy design for enhanced austenite stabilization via quenching and partitioning, *Proc. of the Int. Conf. on New Developments in Advanced High-Strength Sheet Steels*, AIST, Warrendale, PA, 199–207.

De Moor E, Speer J G, Matlock D K, Föjer C and Penning J (2009a), Effect of Si, Al and Mo alloying on tensile properties obtained by quenching and partitioning, *Materials Science and Technology (MS&T) 2009*, 1554–1563.

De Moor E, Föjer C, Penning J and Speer J G (2009b), Hole expansion properties of quench and partition steels, *Material Property Data for More Effective Numerical Analysis, Proceedings of International Deep Drawing Research Group 2009 Conference*, IDDRG, 413–424.

De Moor E, Speer J G, Matlock D K, Kwak J H and Lee S B (2011), Effect of carbon and manganese on the quenching and partitioning response of CMnSi steels, *ISIJ Int.*, 51, 137–144.

Edmonds D V, He K, Rizzo F C, De Cooman B C, Matlock D K and Speer J G (2006), Quenching and partitioning martensite – a novel steel heat treatment, *Mater. Sci. Eng.*, A438–440, 25–34.

Feng W (2011), unpublished research, Baosteel Corporation, China.

Gallagher M F (2003), MS Thesis, Colorado School of Mines.

Gallagher M F, Speer J G, Matlock D K and Fonstein N M (2002), Microstructure development in TRIP-sheet steels containing Si, Al, and P, *44th Mechanical Working and Steel Processing Conference Proc.*, XL, 153–172.

Gerdemann F L H, Speer J G and Matlock D K (2004), Microstructure and hardness of steel grade 9260 heat-treated by the quenching and partitioning (Q&P) process, *Proceedings of Materials Science and Technology 2004*, TMS/AIST, Warrendale, PA, 439–449.

Hillert M and Ågren J (2004), On the definitions of paraequilibrium and orthoequilibrium, *Scripta Mater.*, 50, 697–699.

Hillert M, Hoglund L and Ågren J (1993), Escape of carbon from ferrite plates in austenite, *Acta Mater.*, 41, 1951–1957.

Hollomon J H and Jaffe L D (1945), Time-temperature relations in tempering steel, *Trans. AIME*, 162, 223–249.

Hong S C, Ahn J C, Nam S Y, Kim S J, Yang H C, Speer J G and Matlock D K (2007), Mechanical properties of high-Si plate steel produced by the quenching and partitioning process, *Met. Mater. Int.*, 13, 439–445.

Hsu T Y (Xu Z) and Jin X (2011), Ultra-high strength steel treated by using quenching–partitioning–tempering process, *Advanced Steels*, Springer-Verlag, Berlin, 67–73.

© Woodhead Publishing Limited, 2012

Kim D H, Speer J G, Kim H S and De Cooman B C (2009), Observation of an isothermal transformation during quenching and partitioning (Q&P) processing,' *Met. Mat. Trans.*, 40A, 2048–2060.

Kim K H, Lee J S and Lee D L (2011), Improvement of rolling contact fatigue life of bearing steel by quenching and partitioning process, *Proceedings of Thermec 2011*, in press.

Koistinen D P and Marburger R E (1959), A general equation prescribing the extent of the austenite-martensite transformation in pure iron-carbon alloys and plain carbon steels, *Acta Metall.*, 7, 59–60.

Li H Y, Lu X W, Li W J and Jin X J (2010), Microstructure and mechanical properties of an ultrahigh strength 40SiMnNiCr steel during the one-step quenching and partitioning process, *Met. Mat. Trans.*, 41, 1284–1300.

Mujahid S A and Bhadeshia H K D H (1993), Coupled diffusional/displacive transformations: effect of carbon concentration, *Acta Mater.*, 41, 967–973.

Rizzo F, Edmonds D, He K, Speer J, Matlock D and Streicher A M (2005), Carbon enrichment of austenite and carbide precipitation during the quenching and partitioning (Q&P) process, *Solid-to-Solid Phase Transformations in Inorganic Materials 2005 – Volume 1*, TMS, Warrendale, PA, 535–544.

Rizzo F, Martins A R, Speer J G, Matlock D, Streicher A and De Cooman B (2007), Quenching and partitioning process in Ni-added high strength steels, *Mater. Sci. Forum*, 539–543, 4476–4481.

Santofimia M J, Nguyen-Minh T, Zhao L, Hanlon D N, Kop T A and Sietsma J (2008a), Experimental investigation of quenching and partitioning on two low-carbon steels with different silicon contents, *Proc. of the Int. Conf. on New Developments in Advanced High-Strength Sheet Steels*, AIST, Warrendale, PA, 191–198.

Santofimia M J, Zhao L and Sietsma J (2008b), Model for the interaction between interface migration and carbon diffusion during annealing of martensite-austenite microstructures in steels, *Scripta Mater.*, 59, 159–162.

Santofimia M J, Speer J G, Clarke A, Zhao L and Sietsma J (2009), Influence of interface mobility on the evolution of austenite-martensite grain assemblies during annealing, *Acta Mater.*, 57, 4548–4557.

Sarikaya M, Thomas G, Steeds J W, Barnard S J and Smith G D W (1982), Solute element partitioning and austenite stabilization in steels, *Proceedings of an International Conference on Solid to Solid Phase Transformations*, TMS, Warrendale, PA, 1421–1425.

Shutts A (2006), MS Thesis, Colorado School of Mines.

Shutts A J, Speer J G, Matlock D K, Edmonds D V, Rizzo F and Damm E B (2006), Q&P of high carbon bar steel, *International Conference on New Developments in Long and Forged Products: Metallurgy and Applications*, AIST, Warrendale, PA, 191–202.

Speer J G and Matlock D K (2009), Progress in the global development of the quenching and partitioning process, *J. Jap. Soc. Heat Treatment (Special Issue: Proceedings of the 17th IFHTSE Congress)*, 49, 415–422.

Speer J G, Matlock D K, De Cooman B C and Schroth J G (2003a), Carbon partitioning into austenite after martensite transformation, *Acta Mater.*, 51, 2611–2622.

Speer J G, Streicher A M, Matlock D K, Rizzo F and Krauss G (2003b), Quenching and partitioning: a fundamentally new process to create high strength TRIP sheet microstructures, *Austenite Formation and Decomposition*, TMS/ISS, Warrendale, PA, 505–522.

© Woodhead Publishing Limited, 2012

Speer J G, Edmonds D V, Rizzo F C and Matlock D K (2004), Partitioning of carbon from supersaturated plates of ferrite, with application to steel processing and bainite transformation fundamentals, *Curr. Op. Solid State Mater. Sci.*, 8, 219–237.

Speer J G, Matlock D K, De Cooman B C and Schroth J G (2005), Comments on 'On the definitions of paraequilibrium and orthoequilibrium', *Scripta Mater.*, 52, 83–85.

Speer J G, Hackenberg R E, De Cooman B C and Matlock D K (2007), Influence of interface migration during annealing of martensite/austenite mixtures, *Phil. Mag. Lett.*, 87, 379–382.

Streicher A M, Speer J G, Matlock D K and DeCooman B C (2004), Quenching and partitioning response of a Si-added TRIP sheet steel, *Int. Conf. Advanced High-Strength Sheet Steels for Automotive Applications Proceedings*, AIST, Warrendale, PA, 51–62.

Thomas G (2011), unpublished research, Colorado School of Mines.

Thomas G A, Speer J G and Matlock D K (2008), Considerations in the application of the 'Quenching and Partitioning' concept to hot-rolled AHSS production, *AIST Trans.*, 5, 209–217.

Thomas G A, Speer J G, Matlock D K, Krauss G and Hackenberg R E (2010), Time-temperature equivalence in martensite tempering, *Proceedings of ICOMAT-08*, TMS, Warrendale, PA, 595–600.

Thomas G A, Speer J G and Matlock D K (2011), Quenched and partitioned microstructures produced via Gleeble simulations of hot-strip mill cooling practices, *Met. Mater. Trans*, DOI: 10.1007/s11661-011-0648-5, in press.

Wang L and Feng W (2011), Development and application of Q&P sheet steels, *Advanced Steels*, Springer-Verlag, Berlin, 255–258.

Zhong N, Wang X D, Wang L and Rong Y H (2009), Enhancement of the mechanical properties of a Nb-microalloyed advanced high-strength steel treated by quenching–partitioning–tempering process, *Mater. Sci. Eng.*, 506, 111–116.

© Woodhead Publishing Limited, 2012

9
Phase transformations in advanced bainitic steels

F. G. CABALLERO and C. GARCIA-MATEO,
National Centre for Metallurgical Research
(CENIM-CSIC), Spain

Abstract: An innovative design procedure based on phase transformation theory was successfully applied to design a new generation of bainitic steels that transform to bainite at low temperatures (123–335°C). It was possible to achieve a bainitic microstructure with strength of 2.5 GPa and considerable toughness (30 MP $m^{1/2}$). These excellent properties are mainly a consequence of the formation of a nanoscale bainitic microstructure consisting of a mixture of bainitic ferrite and carbon-enriched retained austenite. Such properties have never been achieved before with bainite and the potential use of these nanostructured steels is large.

Key words: high silicon steels, carbide-free bainite, nanostructured steels, mechanical properties.

9.1 Introduction

New high-strength high-toughness bainitic steels have recently been designed and manufactured following conventional thermo-mechanical procedures, and reached significant combinations of strength and toughness, comparable to those of quenched and tempered martensitic steels (Caballero *et al.*, 2006). The microstructure responsible for these mechanical properties is carbide-free bainite. The precipitation of cementite during bainitic transformation can be suppressed by alloying the steel with silicon. The carbon that is rejected from the bainitic ferrite instead enriches the residual austenite, thereby stabilising it down to ambient temperature. The microstructure obtained consists of thin plates of bainitic ferrite separated by carbon-enriched regions of austenite; there may also be some martensite.

There are multiple advantages of this type of microstructure in flat products. Because of the ultrafine grain size of the bainitic ferrite plates, there is a possibility of improving simultaneously both the strength and toughness, while keeping sufficient ductility for forming. The high flow stresses are attributed to the absence of proeutectoid ferrite, present in existing TRIP (transformation-induced plasticity) steels and to the small thickness of the bainitic ferrite plates. The TRIP effect, still expected to operate from the

© Woodhead Publishing Limited, 2012

residual austenite, and the presence of islands of martensite, leads to high instantaneous hardening rates. The in-use properties, such as resistance to damage, fatigue, susceptibility to cut-edge and weldability are also noteworthy.

9.1.1 Theoretical and thermodynamic models for steel design

A theoretical design procedure based upon a displacive theory for the bainite transformation has been successfully applied to design steels with a microstructure consisting of carbide-free bainite (Caballero *et al.*, 2001a,b). In this model the bainite transformation is considered to progress by the diffusionless growth of tiny platelets known as 'sub-units' with the excess carbon in these platelets partitioning into the residual austenite soon after the growth event. According to this idea, diffusionless growth of this kind can only occur if the carbon concentration of the residual austenite is below that given by the T_o' curve. The T_o' curve is a manifestation of the formation of bainitic ferrite with full supersaturation of carbon followed by carbon partitioning between bainitic ferrite and austenite.

It thus follows that the maximum amount of bainite that can be obtained at any temperature is limited by the fact that the carbon content of the residual austenite must not exceed the T_o' curve of the phase diagram. Assuming that no other reaction interacts with the bainitic ferrite formation, the maximum permitted volume fraction of bainitic ferrite, V_b, can be estimated from a simple expression (Bhadeshia and Edmonds, 1983a,b):

$$V_b = \frac{(x_\gamma - \overline{x})}{(x_\gamma - s)} \qquad [9.1]$$

where x_γ is the carbon content of austenite given by the T_o' curve, $\overline{x}$ is the average carbon content of the alloy and s is the amount of carbon trapped in the bainitic ferrite in solid solution ($s = 0.03$ wt%). This equation suggests that there are two main methods of increasing the maximum permitted amount of transformation to bainitic ferrite: by adjusting the T_o' curve to greater carbon concentrations with the use of substitutional solutes, and by reducing the mean carbon concentration (Bhadeshia and Edmonds, 1983a,b).

Apart from controlling the T_o' curve, substitutional solutes also affect hardenability, which is an important design parameter to avoid transformations to proeutectoid ferrite and pearlite during cooling to the bainite range. For this purpose, thermodynamic and kinetic models developed to calculate the isothermal and continuous transformation diagrams, from knowledge of the steel chemical composition, were used (Caballero *et al.*, 2002a; Bhadeshia, 2011). There are other design parameters which need to be considered also,

© Woodhead Publishing Limited, 2012

such as the bainite, Widmanstätten ferrite and martensite start temperatures (García-Mateo and Bhadeshia, 2004).

9.1.2 Earlier approaches in the development of carbide-free bainitic steels

Conventional bainitic steels generally have not been as successful as quenched and tempered martensitic steels, because of the presence of coarse cementite particles in the bainitic microstructure. However, the addition of ~1.5 wt% silicon enables the production of a carbide-free bainitic microstructure. The essential principles governing the optimisation of such microstructures are well established, particularly that an increase in the amount of bainitic ferrite in the microstructure is needed in order to eliminate large regions of untransformed austenite, which under stress can transform to hard, brittle martensite.

In previous research carried out by Bhadeshia and Edmonds (1983a,b) and Miihkinen and Edmonds (1987a,b,c), it was found that carbide-free bainite is in principle an ideal microstructure from many points of view. In particular, the steel has a high resistance to cleavage fracture and void formation due to the absence of carbides. There is a possibility of simultaneously improving the strength and toughness because of the ultrafine grain size of the bainitic ferrite plates, and of further enhancing the toughness by a TRIP effect. These original experiments (Bhadeshia and Edmonds, 1983a,b) were carried out in order to demonstrate the role of the T_o' curve in greatly influencing the mechanical properties of carbide-free bainitic steels. The experimental alloys developed for this purpose are not necessarily the optimum alloys from the point of view of mechanical properties and product development.

More recently, it was demonstrated experimentally that models based on phase transformation theory can be applied successfully to the design of hot-forged carbide-free bainitic steels (Caballero *et al.*, 2001a,b). In this work, steels alloyed with Ni, named Ni1 and Ni2 in Table 9.1, were designed to achieve the highest combination of strength and toughness for bainitic microstructures after air-cooling. Toughness values of ~130 MPa $m^{1/2}$ were obtained for strengths in the range of 1600–1700 MPa.

9.2 Design of third generation of advanced high strength steels

Descriptive terminology on the development of advanced high strength steels (AHSS) for automotive application has evolved to describe the 'first generation' of AHSS as steels that possess primarily ferrite-based microstructures, and the 'second generation' of AHSS as austenitic steels with high manganese contents which include steels that are closely related to austenitic stainless steels. A

© Woodhead Publishing Limited, 2012

Table 9.1 Chemical composition of designed advanced bainitic steels (wt%)

Steel	C	Si	Mn	Ni	Cr	Mo	V
First set of alloys							
Ni1	0.31	1.51	<0.01	3.52	1.44	0.25	0.10
Ni2	0.30	1.51	<0.01	3.53	1.42	0.25	–
Second set of alloys							
CENIM 1	0.29	1.50	2.25	–	–	0.26	–
CENIM 2	0.29	1.46	1.97	–	0.46	0.25	–
CENIM 3	0.29	1.49	1.56	–	1.47	0.25	–
CENIM 4	0.27	1.71	1.53	1.47	0.17	0.24	–
Third set of alloys							
CENIM 5	0.22	1.50	2.23	–	–	0.25	–
CENIM 6	0.21	1.46	1.56	–	1.49	0.24	–

variety of steels including dual-phase (DP), transformation-induced plasticity (TRIP), complex-phase (CP), and martensitic (MART) steels compromise the first generation of AHSS. Second generation austenitic AHSS include twinning-induced plasticity (TWIP) steels, Al-added lightweight steels with induced plasticity (L-IP®), and shear band strengthened steels (SIP steels).

Recently there has been increased interest in the development of a 'third generation' of AHSS; steels with strength/ductility combinations significantly better than exhibited by the first generation, but at a cost significantly less than required for the second generation of AHSS. Recent results from a composite modelling analysis (Matlock and Speer, 2009), have shown that the third generation of AHSS will include materials with complex microstructures consisting of a high strength phase (e.g. ultrafine grained ferrite, martensite or bainite) and significant amounts of a constituent with substantial ductility and work hardening (e.g. austenite).

9.2.1 Advanced bainitic steels for automotive applications

With AHSS, automotive manufacturers can slash the weight of a vehicle's body structure by as much as 25%. But with the third generation of AHSS currently being developed, that figure could one day reach 35% (Steel Market Development Institute, 2010). However, AHSS sheet cannot be applied easily to a wide variety of car components because the formability is relatively poor. In general, in AHSS sheet, if total elongation is increased, the properties governed by local elongation such as stretch flangeability and bendability deteriorate (Mizui *et al.*, 1990). For securing good total elongation, it is beneficial that the microstructure contains ferrite, which is excellent in ductility, and a second hard phase such as bainite and/or martensite (Jacques

© Woodhead Publishing Limited, 2012

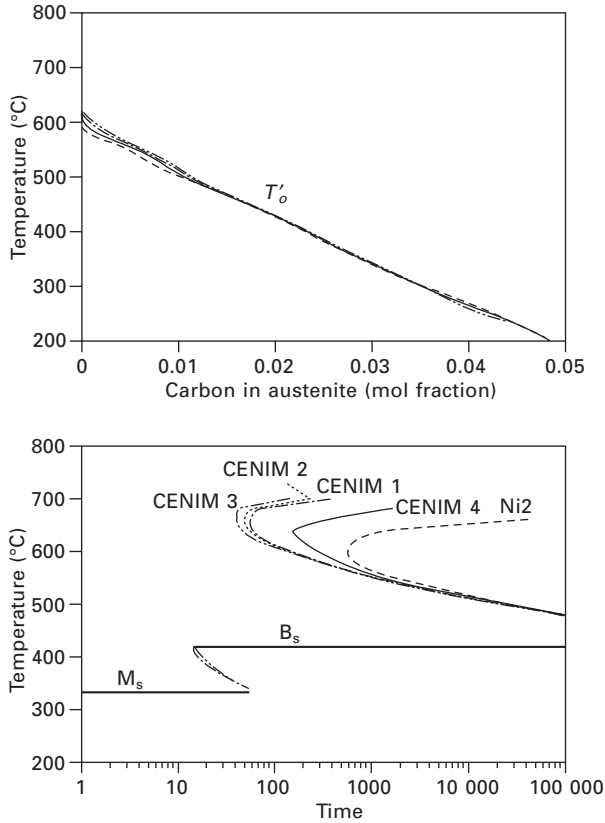
et al., 2001). The presence of retained austenite in the microstructure will enhance even further the total elongation by a TRIP effect (Zackay *et al.*, 1967). By contrast, for good hole expansion and bending behaviour, the microstructure should be homogeneous, otherwise local strain concentration occurs in the soft phase near a hard phase and, as a consequence, leads to the deterioration in stretch flangeability and bendability (Mizui *et al.*, 1990).

An optimum combination of both characteristics is expected to be achieved with a carbide-free bainitic microstructure consisting of a bainitic ferrite matrix and a mixture of austenite and some martensite. The poor stretch flangeability of TRIP-assisted steels may be essentially overcome by replacing the ferrite matrix with bainitic ferrite since bainitic steels generally possess excellent stretch flangeability due to their uniform fine lath structure (Sugimoto *et al.*, 2002). On the other hand, the heterogeneities of hardness due to the presence of martensite in this advanced bainitic microstructure will allow attainment of good deep drawability (Nagasaka *et al.*, 1997). Regarding bendability, it has also been shown that it is not related to ductility, and heterogeneity in the microstructure should be as low as possible (Mizui *et al.*, 1990).

Based on the first successful experience of Caballero *et al.* (2001a,b), a second set of alloys was designed to have the same bainitic transformation region in the time-temperature-transformation (TTT) diagram and the same T_o' curve as those of Ni2 bainitic steel, but avoiding or reducing Ni additions for economical reasons. Moreover, the hardenability of the steel needed to be high enough to avoid the formation of proeutectoid ferrite during cooling. The chemical compositions of the newly designed steels (CENIM 1 to 4) are given in Table 9.1. Figure 9.1 shows calculated T_o' curves and TTT diagrams for the newly designed steels in comparison with those for Ni2 steel. The T_o' curve of the different steels matches perfectly (Fig. 9.1(a)). Moreover, TTT diagrams in Fig. 9.1(b) show that all the new alloys have similar diffusionless curves and B_S and M_S temperatures, but different diffusional noses. This is not surprising since the steels have been designed to have the same maximum volume fraction of bainite at a given temperature. The calculated TTT diagrams suggested that a two-step cooling schedule was the most promising processing route to obtain a fully bainitic microstructure in the new alloys.

The proposed alloys were hot rolled in several passes finishing at 930°C. The bainitic microstructure was obtained in all the steels by air cooling from different temperatures (FCT in Table 9.2) after an initial accelerated cool at 70°C/s. Experimental data on the microstructures are presented in Table 9.2. Some examples of scanning and transmission electron (SEM and TEM) micrographs of carbide-free bainitic microstructures are shown in Figs 9.2 and 9.3. Microstructural characterisation revealed that the CENIM 1 to 4 alloys after air cooling from every temperature tested had the desired

© Woodhead Publishing Limited, 2012



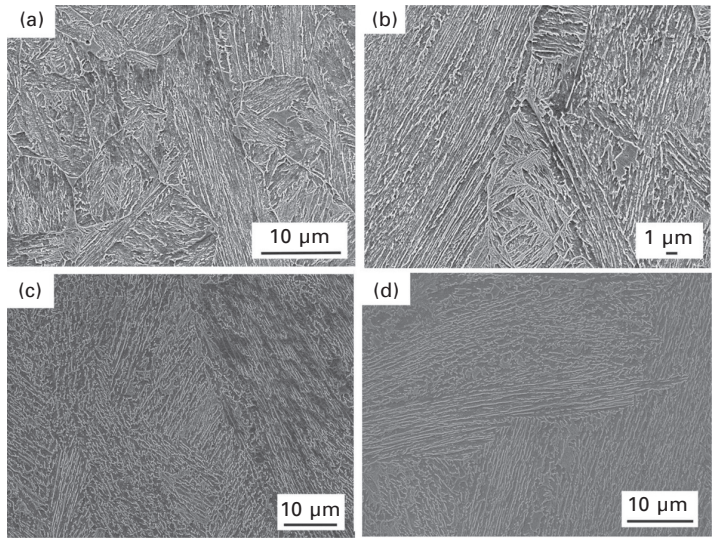
9.1 Calculated (a) T'_o curve and (b) TTT diagram of CENIM 1 to 4 steels. Ni2 is reference steel.

Table 9.2 Quantitative data on microstructure of the second set of designed steels

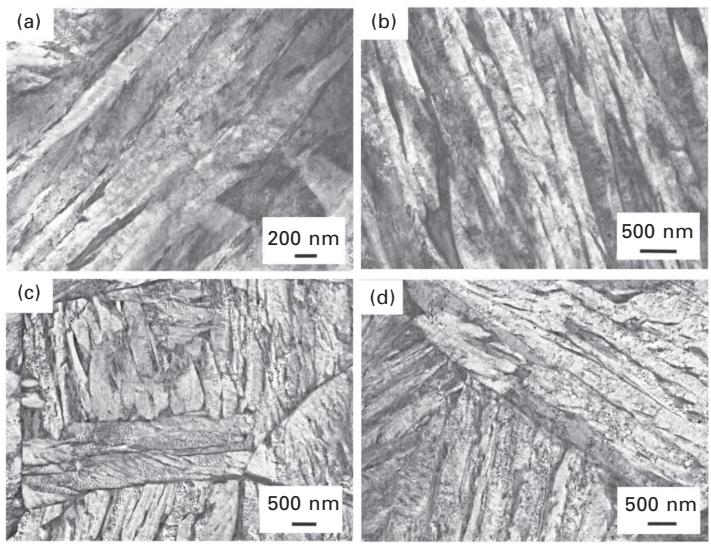
Steel / FCT	V_b	V_M	V_γ	x_γ (wt%)
CENIM 1 / 450°C	0.73 ± 0.04	0.24 ± 0.05	0.03 ± 0.01	0.66 ± 0.06
CENIM 1 / 600°C	0.76 ± 0.03	0.21 ± 0.04	0.03 ± 0.01	0.95 ± 0.01
CENIM 2 / 500°C	0.77 ± 0.04	0.13 ± 0.05	0.10 ± 0.01	1.14 ± 0.03
CENIM 2 / 550°C	0.80 ± 0.04	0.09 ± 0.05	0.10 ± 0.01	1.26 ± 0.07
CENIM 3 / 500°C	0.88 ± 0.02	0.02 ± 0.03	0.11 ± 0.01	1.03 ± 0.05
CENIM 3 / 550°C	0.86 ± 0.02	0.03 ± 0.04	0.11 ± 0.01	1.04 ± 0.04
CENIM 4 / 500°C	0.88 ± 0.02	0.09 ± 0.04	0.03 ± 0.01	1.26 ± 0.07

FCT is interrupted accelerated cooling temperature; V_b is the volume fraction of bainitic ferrite; V_M is the volume fraction of martensite; V_γ is the volume fraction of austenite; x_γ is the carbon content in austenite.

© Woodhead Publishing Limited, 2012



9.2 Scanning electron micrographs of the second set of designed steels (Table 9.1) after air cooling from different temperatures: (a) CENIM 1 / 600°C, (b) CENIM 2 / 500°C, (c) CENIM 3 / 500°C, (d) CENIM 4 / 500°C.



9.3 Transmission electron micrographs of the second set of designed steels (Table 9.1) after air cooling from different temperatures (a) CENIM 1 / 600°C, (b) CENIM 2 / 500°C, (c) CENIM 3 / 500°C and (d) CENIM 4 / 500°C.

© Woodhead Publishing Limited, 2012

microstructure consisting mainly of carbide-free bainitic ferrite, retained austenite and some martensite.

In discussing the morphology of the austenite remaining after partial transformation to bainite, it is necessary to distinguish between the blocky morphology of austenite located between the sheaves of bainite and the films of austenite which are retained between the subunits within a given sheaf of bainite. Film and blocky austenite fractions can be deduced from the total fraction of retained austenite determined by X-ray diffraction (XRD) analysis following equations developed by Bhadeshia and Edmonds (1983a). Due to the high volume fraction of bainitic ferrite in the second set of samples (Table 9.2), retained austenite is mainly present as films between the subunits of bainitic ferrite.

The corresponding mechanical properties are reported in Table 9.3. Plates of bainitic ferrite are typically 10 μm in length and about 0.2 μm in thickness (as shown by TEM micrographs in Fig. 9.3). This gives a rather small mean free path for dislocation glide. Thus, the main microstructural contribution to the strength of bainite is from the extremely fine grain size of bainitic ferrite. It is difficult to separate the effect of retained austenite on strength in these steels from other factors. Qualitatively, austenite can affect the strength in several ways. Residual austenite can transform to martensite during cooling to room temperature, thus increasing the strength. On the other hand, retained austenite interlath films can increase the strength by transforming to martensite during testing, similar to the behaviour of TRIP steels.

The low yield/ultimate tensile strength ratios (YS/UTS) in Table 9.3 are due to the presence of austenite and the generally large dislocation density in the microstructure. Consequently, retained austenite increases the strain-hardening rate of the steel. Likewise, tensile elongation is controlled by the volume fraction of retained austenite. Retained austenite is a ductile phase compared to the bainitic ferrite and would be expected to enhance ductility provided the austenite is homogeneously distributed along lath boundaries

Table 9.3 Tensile properties results at 20°C of the second set of designed steels

Steel / FCT	YS (MPa)	UTS (MPa)	YS/UTS	TE (%)
CENIM 1 / 450°C	1240 ± 31	1796 ± 21	0.69	18 ± 1
CENIM 1 / 600°C	1204 ± 29	1701 ± 9	0.71	16 ± 1
CENIM 2 / 500°C	1187 ± 16	1606 ± 30	0.74	17 ± 2
CENIM 2 / 550°C	1128 ± 32	1539 ± 21	0.73	16 ± 2
CENIM 3 / 500°C	1194 ± 35	1652 ± 6	0.72	18 ± 1
CENIM 3 / 550°C	1204 ± 18	1642 ± 12	0.73	18 ± 1
CENIM 4 / 500°C	1339 ± 16	1763 ± 18	0.76	16 ± 1

FCT is interrupted accelerated cooling temperature; YS yield strength; UTS ultimate tensile strength; TE total elongation.

© Woodhead Publishing Limited, 2012

Table 9.4 Charpy impact test results of the second set of designed steels

Steel / Cooling - FCT	Impact energy (J)						
	–40°C	–20°C	0°C	20°C	50°C	100°C	150°C
CENIM 1 / 450°C	–	–	29	36	–	42	38
CENIM 1 / 600°C	–	–	16	22	–	41	48
CENIM 2 / 500°C	–	–	–	36	39	55	55
CENIM 2 / 550°C	–	–	30	44	47	53	43
CENIM 3 / 500°C	–	32	39	44	–	61	61
CENIM 3 / 550°C	–	–	33	46	–	65	64
CENIM 4 / 500°C	30	–	–	38	47	50	–

FCT is interrupted accelerated cooling temperature.

(film austenite). However, isolated pools of austenite (blocky austenite) would influence unfavourably both elongation and ultimate tensile strength (UTS), presumably because of the strain localization in these areas (Bhadeshia and Edmonds, 1983a). From Table 9.3, it is clear that the steels present an optimum combination of high strength and good ductility.

Impact toughness was measured on standard Charpy notched (10×10 mm^2) samples at temperatures between –40°C and 150°C using a 300 J Charpy testing machine. Charpy impact test results are listed in Table 9.4 for the second set of alloys. High toughness values in these advanced bainitic steels are attributed to the replacement of brittle interlath cementite of the upper bainite structure by very stable interlath films of softer retained austenite. The results also appear to demonstrate that further improvement in the impact toughness was not obtained by adding nickel in CENIM 4 steel. This is consistent with results reported elsewhere for strong steel weld metals (Keehan *et al.*, 2006).

As the results in Tables 9.2 and 9.4 suggest, the relationship between the impact energy and the phase fractions is not significant. However, the optimum combination of strength and toughness in these steels is directly related to the high volume fraction of bainite reached in the microstructure. The results are consistent with the enhancement of toughness expected when the presence of unstable blocky austenite is avoided and the amount of martensite is reduced, in general when the thermal and mechanical stability of residual austenite is increased.

9.2.2 Adjustment of the alloy design to improve in-use properties

Since the designed alloys have to be a reasonable solution from a final customer point of view, an in-use property such as weldability is an important issue in the alloy design procedure. Special adjustments of the chemical

© Woodhead Publishing Limited, 2012

composition of the designed alloys are required to improve this property. In particular, a reduction in the carbon equivalent value is preferable. Former thermodynamic and kinetic calculations performed for the design of bainitic steels with a carbon content of 0.3 wt% are also useful for the development of weldable bainitic steels, since the influence of the average carbon content on the progress of bainite formation is widely known (Hsu and Mou, 1984).

Steels with different carbon content will exhibit the same T_o' curve (Bhadeshia and Edmonds, 1980; Zener, 1946). The driving force for the formation of new plates decreases as the carbon concentration in the untransformed austenite approaches the T_o' composition at which the free energy of ferrite and austenite phases of the same composition become identical. In addition, carbon increases the strength of the parent austenite from which bainite grows, and some approaches have also considered plastic deformation as an additional source of Gibbs energy dissipation during bainite transformation (Quidort *et al.*, 2003). Besides the independence of the T_o' curve with the average carbon content of the steel, the maximum volume fraction of bainite formed at a given transformation temperature will increase as carbon content of the steel is decreased, since the critical T_o' value is reached at a later stage (see Eq. [9.1]) (Bhadeshia and Edmonds, 1983a,b). Moreover, the bainite region in the TTT diagram is expected to be shifted to higher temperatures and shorter times as carbon content is reduced, bearing in mind that carbon is a strong austenite stabiliser. In consequence, the CENIM 5 and 6 steels (Table 9.1) were designed in order to improve the in-use properties of the former advanced bainitic steels.

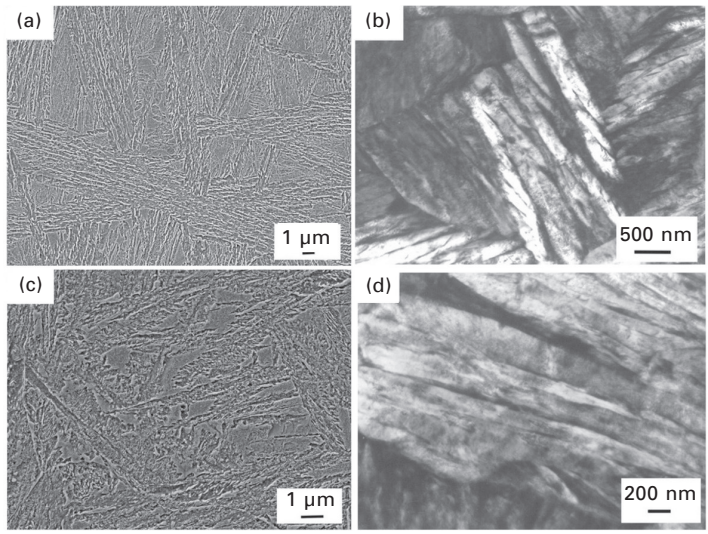
This third set of alloys with a carbon content of 0.2 wt% was manufactured as $180 \times 80 \times 12$ mm^3 plates. Specimens were hot rolled in several passes finishing at 913°C for CENIM 5 and 904°C for CENIM 6. The desired bainitic microstructure was obtained in both steels by air cooling from different temperatures (500 and 550°C; FCT in Table 9.5) after an initial accelerated cool at ~50°C/s. Microstructure data of both steels are presented in Table 9.5. As an example, Fig. 9.4 shows SEM and TEM micrographs of the microstructure obtained after air cooling from 500°C in CENIM 5

Table 9.5 Quantitative data on microstructure of the third set of designed steels

Steel / FCT	V_b	V_M	V_γ	x_γ (wt%)
CENIM 5 / 500°C	0.91 ± 0.02	–	0.09 ± 0.01	1.26 ± 0.06
CENIM 5 / 550°C	0.93 ± 0.02	–	0.09 ± 0.01	1.15 ± 0.03
CENIM 6 / 500°C	0.90 ± 0.02	–	0.11 ± 0.01	1.04 ± 0.07
CENIM 6 / 550°C	0.91 ± 0.02	–	0.12 ± 0.01	1.02 ± 0.06

FCT is interrupted accelerated cooling temperature; V_b is the volume fraction of bainitic ferrite; V_M is the volume fraction of martensite; V_γ is the volume fraction of austenite; and x_γ is the carbon content in austenite.

© Woodhead Publishing Limited, 2012



9.4 Scanning and transmission electron micrographs of the third set of designed steels (Table 9.1) after air cooling from 500°C: (a) and (b) CENIM 5; (c) and (d) CENIM 6.

and 6 steels. Experimental results reveal that both steels have the desired microstructure consisting of mainly bainitic ferrite and retained austenite. Because of the high carbon enrichment in austenite for these alloys (Table 9.5), the majority of residual austenite present after bainite is formed is expected to be retained on cooling to room temperature. In the SEM micrographs, martensite regions are relatively unetched, and appear darker in colour (Fig. 9.4(c)). It is difficult in thin-foil TEM experiments to judge whether any martensite has formed as a result of the thinning process or whether it was present in the original microstructure. To cope with this, the samples were tempered at 200°C for 2 h before making foils. Thus, martensite present in the original sample would contain carbides, whereas any untempered martensite can be interpreted to be austenite which underwent transformation during the foil preparation process. The observation of tempered microstructures showed that the unetched regions in Fig. 9.4(c) are not martensitic; they are blocks of austenite. Note that the low temperature tempering (200°C) heat treatment does not affect bainitic ferrite since the latter does not contain excess carbon.

Finally, the TEM micrographs in Fig. 9.4 show the interlath retained austenite films in carbide-free bainitic microstructure of CENIM 5 and 6 steels. Resultant microstructure of the third set of designed steels is similar to those obtained in the second set of alloys with 0.3 wt% C; however, a reasonable decrease of ~100 HV in hardness was detected for CENIM 5 and 6 steels due to their lower carbon content.

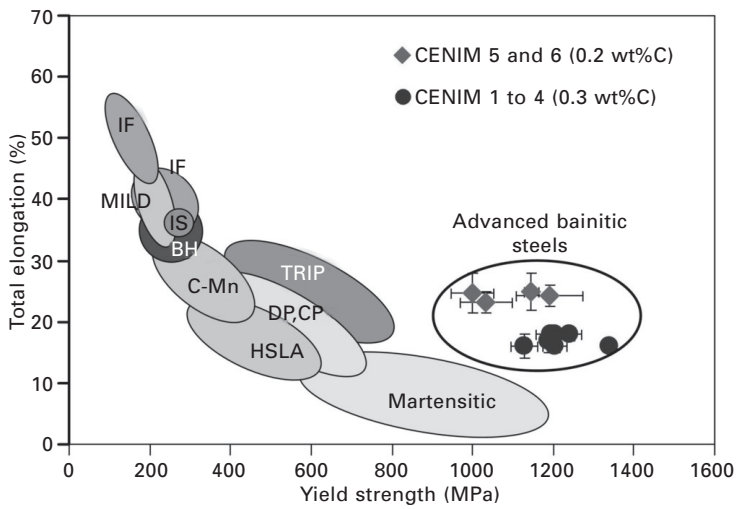
© Woodhead Publishing Limited, 2012

The tensile test results of CENIM 5 and 6 steels are reported in Table 9.6 and represented in Fig. 9.5 in comparison with CENIM 1 to 4 steels as well as other commercial steels. In general, the results suggest that CENIM 5 and 6 steels have considerable potential for automotive application since they can reach very high tensile strength levels, above 1300 MPa, whilst retaining significant ductility. Their total elongations are comparable to those in TRIP steels, very impressive for such high YS and UTS. Regarding the product of UTS and total elongation reached by these steels (higher than 30,000 MPa %), the properties are higher than the ferritic TRIP steels under development (typically 22,500 MPa %) (Jacques *et al.*, 2002). In terms of formability assessment, additional investigations should be performed. However, the present results suggest that the YS/UTS ratio is low and comparable to those obtained in DP steels (polygonal ferrite and martensite as hard phase) which can be beneficial to drawability.

Table 9.6 Tensile test results at 20°C of the third set of designed steels

Steel / FCT	YS (MPa)	UTS (MPa)	YS/UTS	TE (%)
CENIM 5 / 500°C	1192 ± 82	1382 ± 31	0.86	24 ± 2
CENIM 5 / 550°C	1146 ± 17	1347 ± 8	0.85	25 ± 3
CENIM 6 / 500°C	1033 ± 64	1319 ± 12	0.78	23 ± 2
CENIM 6 / 550°C	999 ± 54	1306 ± 16	0.76	25 ± 3

FCT is interrupted accelerated cooling temperature; YS yield strength; UTS ultimate tensile strength; TE total elongation.



9.5 Yield strength and total elongation of advanced bainitic steels in comparison with other commercial steels.

© Woodhead Publishing Limited, 2012

9.3 Carbide-free bainitic steels: a material ready for the nanocentury

In this section, a novel method for making extremely strong and inexpensive nanocrystalline steels without using severe deformation, rapid heat-treatment or mechanical processing is reviewed. Furthermore, the material can be produced in a form which is large in all three dimensions, and has a plethora of other properties useful in engineering design. This new generation of ultra-high strength steels with desirable levels of toughness has awakened great interest in the technical (Defence CODEX, 2008; DSTL, 2008; Chakraborty *et al*., 2009; Putatunda *et al*., 2010; Yoozbashi *et al*., 2011; Zhang *et al*., 2011) and scientific communies (Zhang and Kelly, 2006; Chen *et al*., 2007; Kundu *et al*., 2007; Beladi *et al*., 2009; Timokhina *et al*., 2010). The excellent properties achieved are mainly a consequence of the formation of nanoscale bainitic ferrite plates at very low temperatures.

9.3.1 Processing nanostructured steels by bainite reaction at low temperature

Low transformation temperatures are associated with fine microstructures which in turn generally possess both strength and toughness. There is, in principle, no lower limit to the temperature at which bainite can be generated according to bainite transformation theory (García-Mateo and Bhadeshia, 2004). Thermodynamics calculations by Caballero and Bhadeshia (2004) showed that it should be possible to obtain bainite at room temperature, but kinetics predicted that the transformation time would be approximately 100 years. An appropriate alloy was made in 2004 to test this theory. Two samples have been archived; one at Cambridge University and the other at the Science Museum in London. The samples are sealed in quartz tubes containing pure argon. The tubes will be broken in 2104 to see whether bainite has formed and to conduct detailed characterisation. The samples have been polished to a mirror finish so that any phase change will be evident in the meantime, through surface rumples caused by transformation.

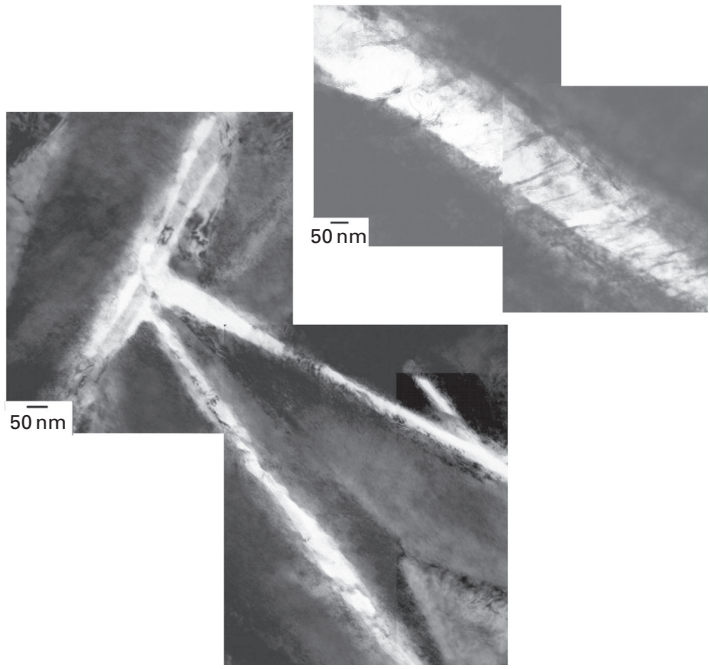
The theoretical design procedure described in Section 9.1.1 was used to produce, in a reasonable time, the finest possible bainitic structure by transformation at the lowest possible temperature (Caballero and Bhadeshia, 2004). From the models, the so-called NANOBAIN steel compositions in Table 9.7 were defined to decrease bainite transformation temperature, increase the maximum volume fraction of bainite in the final microstructure, and improve the hardenability of the steels. The carbon concentration was selected from calculations to suppress the B_S temperature and to make austenite stronger, with the aim of obtaining extremely thin platelets of bainite.

Samples were supplied as 30 kg cast ingots. They were firstly homogenised

© Woodhead Publishing Limited, 2012

Table 9.7 Chemical composition of nanostructured bainitic steels (wt%)

Steel	C	Si	Mn	Cr	Mo	V	Co	Al
NANOBAIN 1	0.79	1.59	1.94	1.33	0.30	0.11	–	–
NANOBAIN 2	0.83	1.57	1.98	1.02	0.24	–	1.54	–
NANOBAIN 3	0.78	1.49	1.95	0.97	0.24	–	1.60	0.99



9.6 Transmission electron micrographs of microstructure obtained at 125°C for 60 days in NANOBAIN 1 steel (Table 9.7).

at 1200°C for 2 days and cooled to room temperature inside the furnace. The homogenised specimens were then austenitised for 15 min. at 1000°C, and then isothermally transformed at temperatures ranging from 125 to 350°C for different times before quenching into water.

Bright-field TEM images of NANOBAIN 1 steel transformed at 125°C for 60 days is presented in Fig. 9.6. Some of the plates of bainite are incredibly long and thin (20–40 nm), giving an ultrafine scale structure consisting of an intimate mixture of austenite and ferrite. Dislocation debris is evident in both the bainitic ferrite and the surrounding austenite. Extensive TEM failed to identify significant carbide precipitation in this low temperature bainite; only a few extremely fine (20 nm wide and 175 nm long) cementite particles in the bainitic ferrite were found in samples after extensive ageing at 200°C for 14 days (Caballero *et al.*, 2002b). Bainite reaction in NANOBAIN

© Woodhead Publishing Limited, 2012

1 steel was found to take between 2 and some 90 days to complete the transformation within the temperature range 125–325°C (Caballero and Bhadeshia, 2004).

9.3.2 Accelerating bainite reaction at low temperature

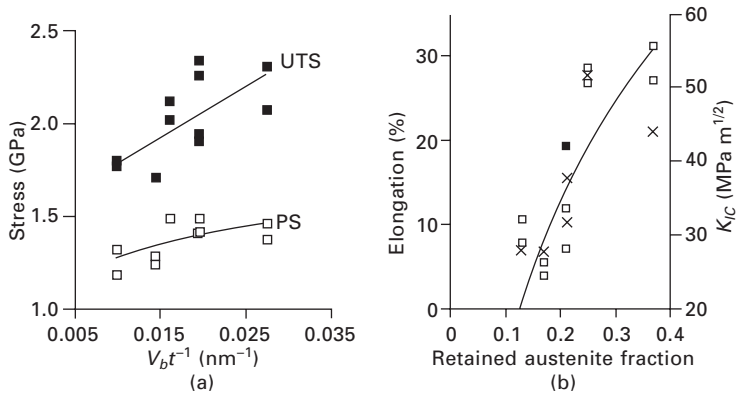
Slow reactions give the ability to transform large components to a uniform microstructure free from residual stresses or complex processing. However, in a commercial scenario, there may be a need for more rapid heat treatment. Anything which enhances the nucleation rate will accelerate transformation, and the most common way of doing this is by refining the austenite grain size. The number density of nucleation sites increases inversely with the austenite grain size. A method to increase further the amount of austenite grain boundary area per unit volume is to deform the austenite, often referred to as 'pancaking' the austenite grains; the increase in grain surface can be predicted quantitatively (Zhu *et al.*, 2007). If the austenite is left in the deformed state, then other defects such as shear bands and dislocations may also contribute to the nucleation rate. However, such defects can, in the case of displacive transformations, retard kinetics by a phenomenon known as mechanical stabilisation (Chatterjee *et al.*, 2006).

Another technique is to increase the magnitude of the free energy change accompanying the decomposition of austenite ($\Delta G^{\gamma\alpha} = G^{\alpha} - G^{\gamma}$), i.e. the driving force for transformation, by making controlled additions of substitutional solutes to the steel. Both the nucleation and the growth rates can be expected to increase as a function of $|\Delta G^{\gamma\alpha}|$. The addition of cobalt and aluminium (detailed compositions are given in Table 9.7), boosts $|\Delta G^{\gamma\alpha}|$, causing the rate of transformation to increase (García-Mateo *et al.*, 2003). The transformation was significantly accelerated to complete the processing within hours (as opposed to days), by making controlled additions of aluminium and cobalt, in concentrations less than 2 wt%. A further rate increment was possible by refining the prior austenite grain size (García-Mateo *et al.*, 2003).

9.3.3 Origin of the mechanical properties in nanostructured bainitic steels

The bainite obtained by low temperature transformation is harder than ever previously achieved for this microstructure, with values in excess of 700 HV. Some strength, ductility and toughness data are illustrated in Fig. 9.7. Much of the strength and hardness of the structure comes from the incredibly thin platelets of bainitic ferrite. For a true thickness t, the mean lineal intercept $\overline{L} \cong 2t$ (Mack and Bartlett, 1956; Bhadeshia, 1997), the resulting strengthening is given by $\Delta\sigma \cong 115\,(\overline{L})^{-1}$ MPa where $\overline{L}$ is in micrometers (Langford and Cohen, 1969, 1970). The inverse dependence on $\overline{L}$, which does not follow

© Woodhead Publishing Limited, 2012



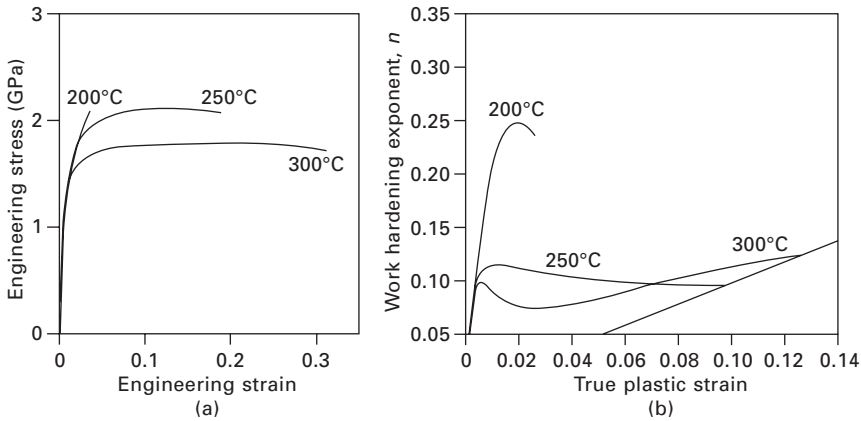
9.7 Mechanical properties of nanostructured bainitic steels (Table 9.7): (a) the ultimate tensile strength (UTS) and 0.2% proof strength (PS) as a function of the volume fraction of bainitic ferrite (V_b) divided by the ferrite platelet thickness (t); (b) ductility (points and curve) and toughness K_{IC} represented as crosses.

the Hall–Petch relation, is because the transmission of slip across boundaries is determined by the energy required to expand dislocation loops rather than by the pile-up of the dislocations obstructed by boundaries (Langford and Cohen, 1970). With $t = 35$ nm, $\Delta\sigma = 1642$ MPa, which decreases to 311 MPa for $t = 185$ nm. Figure 9.7(a) illustrates the strength plotted as a function of the volume fraction of bainitic ferrite, against which the strength scales linearly (Bhadeshia and Edmonds, 1983b), and t^{-1}.

The residue of strength after accounting for the plate thickness comes from dislocation forests, the intrinsic strength of the iron lattice and solution strengthening. It is known from XRD (Caballero and Bhadeshia, 2004) that bainitic ferrite contains much more carbon than is consistent with equilibrium or paraequilibrium. It has been confirmed using atom probe tomography that some of the carbon is trapped at the dislocations (Caballero *et al.*, 2007) created during the growth of the bainite. The strengthening contributions of the carbon and dislocations cannot therefore be independently calculated, but are small in comparison with that due to plate size. This explains why the hardness of the nanostructure is insensitive to tempering, until the onset of plate coarsening at temperatures in excess of 500°C (Peet *et al.*, 2004).

Figure 9.8(a) shows typical stress–strain curves (García-Mateo and Caballero, 2005); the apparent gradual yielding in these curves is characteristic of multiphase structures containing a large number density of dislocations, and may also be attributed to the transformation of some austenite during the application of stress. It is remarkable that all of the elongation in the stress–strain curves (Fig. 9.8(a)) is uniform, with hardly any necking. Indeed, the broken halves of each tensile specimen could be neatly fitted together. It is not clear what determines the fracture strain.

© Woodhead Publishing Limited, 2012



9.8 (a) Engineering stress–strain curves at room temperature and (b) corresponding curves of the incremental work hardening exponent, *n*, of microstructures obtained in NANOBAIN 2 steel (Table 9.7) after transformation at the temperatures indicated. The straight line represents the instability criterion.

It is intriguing that the elongation increases as the nanostructure is generated at the higher temperature (Fig. 9.8(a)). This is in fact a general observation in these steels, and might be an outcome of the lower strength obtained following transformation at high temperatures. However, in this instance, the correlation of ductility with strength is not sensible in a statistical sense, because there are similar low-carbon, low-strength steels which do not show the high ductility illustrated in Fig. 9.8(a) (Caballero *et al.*, 2001a,b).

Strain hardening is characterised by the incremental strain hardening exponent defined as $n = d\ (\ln \sigma)/d(\ln \varepsilon_p)$, where $\sigma = k\varepsilon_p^n$ represents the flow curve in the region of uniform true plastic deformation (ε_p) and k is the strength coefficient. The variation of the incremental work hardening exponent n as a function of true strain in NANOBAIN 2 transformed at different temperatures is shown in Fig. 9.8(b). The straight line corresponds to the instability criterion $\varepsilon_p = n$. It appears that the different strength–ductility combinations in these advanced bainitic microstructures are associated with completely different work-hardening behaviours. The large true uniform strains of specimens treated at 300°C are due to a high retained austenite fraction that continuously increases the incremental work-hardening n after a sharp decrease at low plastic strains. In the microstructure obtained by transformation at 250°C, after reaching a maximum, n smoothly decreases until the onset of necking. For the microstructures obtained at 200°C, the situation differs completely from that previously described at higher transformation temperatures; a high increase of n during the first stages of plastic deformation is followed by a drastic drop that ends at low levels of plastic deformation.

© Woodhead Publishing Limited, 2012

The explanation seems to lie in the stress- and strain-induced martensitic transformation of the retained austenite during tensile testing. The decomposition of the austenite in this manner has been calculated and measured in TRIP-assisted steels for a variety of combinations of bainitic ferrite and austenite (Sherif *et al.*, 2004). It is noticeable that fracture occurs when $V_\gamma = 0.1$ according to calculations on the variation in austenite content V_γ with strain (Bhadeshia, 2008). An experimental *in-situ* study using neutron diffraction during the tensile test concurs with this conclusion (Sherif, 2005).

It has been suggested that failure occurs when the austenite, which is the toughest of all the phases present, becomes geometrically isolated, i.e. it loses interconnection (Bhadeshia, 2008). Garboczi *et al.* (1995) have modelled the percolation threshold for ellipsoidal objects placed in a matrix. Assuming that the austenite is subdivided into the form of plates by the bainite, it can be represented by oblate ellipsoids with an aspect ratio r of between 1/10 and 1/100. The percolation threshold is then found to be $p_c \cong 1.27r$, i.e. $0.127 \geq p_c \geq 0.0127$. This is consistent with the observation that tensile failure occurs when $V_\gamma \cong 0.1$.

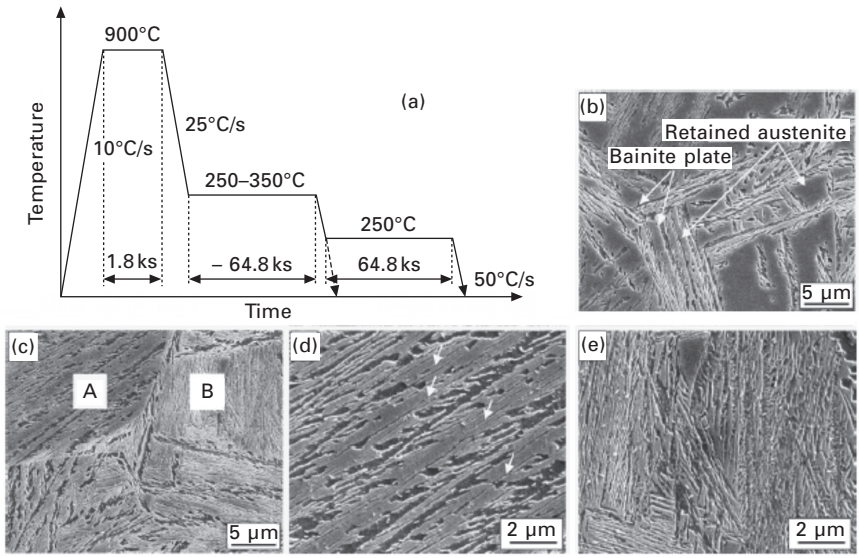
Substantial quantities of brittle martensite which forms during deformation can exist in the microstructure before failure occurs. This is because the tendency of the martensite to crack under stress depends on its absolute size, with coarse regions being most susceptible (Chatterjee and Bhadeshia, 2006). It is the fine scale of the retained austenite that permits the martensite that forms during deformation to be tolerated without compromising the ductility until the percolation threshold is reached. Although the occurrence of high-carbon, untempered martensite causes failure only when the percolation threshold is reached, its presence must influence the toughness.

It seems that the fracture toughness of nanostructured bainitic steels as measured using K_{IC} is reasonably high (Fig. 9.7(b)), but the Charpy impact properties of these nanostructured steels are poor, with only about 5 J of impact energy absorbed at room temperature (García-Mateo and Caballero, 2005). This must be attributed to the fracture of martensite at the high strain rates associated with the impact test. It seems probable that the poor Charpy impact toughness is an intrinsic characteristic of steels containing brittle martensite in microstructures where softer phases that can accommodate the imposed strain rate are absent. After all, much greater absorbed energies are obtained in the similarly strong Aermet 100 steel where the martensite is toughened by severe tempering (Novotny, 1992).

9.3.4 Improving mechanical properties of nanostructured bainitic steels by a new two-step heat treatment

By adopting a two-stage heat treatment, as illustrated in Fig. 9.9(a), in which coarse bainite is produced by isothermal transformation at a high temperature,

© Woodhead Publishing Limited, 2012



9.9 (a) Schematic diagram of two-step heat treatment. (b)–(e) Scanning electron micrographs of bainite transformed at (b) 350°C, 5 h in a single-stage isothermal treatment, (c) 350°C, 5 h followed by 250°C, 18 h using a two-stage isothermal treatment. (d) and (e) are magnified views of the regions marked A and B in (c) (Hase *et al.*, 2006).

followed by isothermal transformation at a lower temperature, it was possible to eliminate blocks of austenite that may influence unfavourably ductility and toughness (Hase *et al.*, 2006). Figures 9.9(b) and (c) show the SEM micrographs following single- and two-step heat treatments. Both the size and the amount of blocky austenite were decreased in the second isothermal treatment. On the other hand, a bimodal size distribution of bainite plates is observed. The size of the thick plates and thin plates in the microstructure of two-stage samples correspond to those obtained in the 350°C and 250°C single-stage treatments, respectively. The major observation is that the two-stage treatment reduced the amount of blocky austenite when compared with the single-stage treatment. In Figs 9.9(c)–(e), the region marked 'A' contains the thick plates generated at 350°C and 'B' is the region without thick bainite plates. In Fig. 9.9(d), a low number-density of thin plates (arrowed) is observed within the film-like retained austenite left untransformed at 350°C. On the other hand, large numbers of fine bainite plates are observed in Fig. 9.9(e), in regions which represented blocks of austenite following the 350°C treatment (Fig. 9.9(b)). This is because the thin regions of austenite are known to contain more carbon than the blocks (Bhadeshia and Waugh, 1982); a higher carbon content in the austenite would lead to a smaller fraction of finer bainite during

© Woodhead Publishing Limited, 2012

the 250°C treatment, as is observed. The non-uniform distribution of carbon results from the trapping of some regions of austenite.

The use of this two-stage isothermal heat treatment has been found beneficial to the mechanical properties of NANOBAIN 3 steel (Table 9.7). An incredible ductility of 40% of total elongation and a toughness of 63 MPa $m^{1/2}$ at an ultimate tensile strength of 1.5 GPa have been achieved, better than was possible with microstructure generated using a single isothermal heat treatment. The double isothermal treatment lead to a bimodal distribution of bainite plate size and a geometrical division of residual austenite in such a manner that the mechanical stability of the austenite is improved, thereby enabling it to compensate for critical damage expected during the late stages of deformation in a tensile test.

Putatunda *et al*. (2010) also studied the influence of a two-step heat treatment on microstructure and mechanical properties of an Fe-0.42C-2.03Si-0.40Mn-0.97Ni-0.82Cr-0.50Cu-0.29Mo (in wt%) steel. In their work, the two-step heat treatment involves first quenching the steel to a lower temperature after austenisation and then immediately raising the temperature of the salt bath to a higher temperature. This resulted in a combination of exceptionally high yield strength (1.6 GPa) as well as very high fracture toughness (87 MPa $m^{1/2}$).

9.4 Conclusions and future trends

It is clear that bainite can be obtained by transforming at very low temperatures. A consequence of the low transformation temperature is that the plates of bainite are extremely fine, 20–40 nm thick, making the material very strong. This is a bulk nanocrystalline material that can be obtained without severe deformation processing. When this feature is combined with the fact that the plates of bainitic ferrite are interspersed with austenite, it becomes possible to create novel strong and tough steels. In this regard, the potential for industrial application is large because the alloys are routinely manufactured.

As is always the case, there remain many parameters that have yet to be characterised, for example, the fatigue and stress corrosion properties. Moreover, the alloys designed so far either transform slowly over a period of many days, or have to be alloyed with cobalt and aluminium in order to accelerate transformation. In the future, it is possible that rapid transformation could be engineered by controlling the manganese concentration. The key will be to do this without compromising properties.

Finally, high carbon steels are difficult to weld because of the formation of untempered, brittle martensite in the coarse grained heat affected zones of the joints. The martensite fractures easily, leading to a gross deterioration in the structural integrity of the joint. For this reason, the vast majority of weldable steels have low carbon concentrations. Low temperature bainitic steels could

© Woodhead Publishing Limited, 2012

in principle be welded maintaining the temperature of the component above the M_S temperature during welding, and then without cooling, transferring it into an oven to allow the austenite to transform into low temperature bainite. This would avoid the formation of martensite, but it is not practical for large components. Therefore, it would be desirable to make the low temperature bainite with a much reduced carbon concentration.

Preliminary calculations indicate that carbon is much more effective in maintaining a difference between the M_S and B_S temperatures than are substitutional solutes which reduce $\Delta G^{\gamma\alpha}$ simultaneously for martensite and bainite. Substitutional solutes do not partition at any stage in the formation of martensite or bainite; therefore, both transformations are identically affected by the way in which the substitutional solute alters the thermodynamic driving force. It is the partitioning of carbon at the nucleation stage that is one of the distinguishing features of bainite when compared with martensite. This carbon partitioning allows bainite to form at a higher temperature than martensite. This advantage is diminished as the overall carbon concentration is reduced. These results are discouraging from the perspective of designing a low carbon bainite with a fine microstructure obtained by transforming at low temperatures. However, the issue is worth investigating further since the original theory has a number of approximations. In the future, the Fe-Mn-Ni-C system should be explored in the context of these calculations, bearing in mind the desire to design low carbon alloys in which the B_S temperature is suppressed.

9.5 Acknowledgement

It is a special pleasure to acknowledge Professor H.K.D.H. Bhadeshia for his collaboration on the design and development of nanostructured bainitic steels.

9.6 References

Beladi H, Adachi Y, Timokhina I and Hodgson P D (2009), 'Crystallographic analysis of nanobainitic steels', *Scripta Mater*, 60, 455–458.

Bhadeshia H K D H (1997), 'Models for the elementary mechanical properties of steel welds', in Cerjak H and Bhadeshia H K D H, *Mathematical Modelling of Weld Phenomena*, *vol. 3*, London, Institute of Materials, 235–255.

Bhadeshia H K D H (2008), 'Properties of fine-grained steel generated by displacive transformation', *Mater Sci Eng A*, 481–482, 36–39.

Bhadeshia (2011), Materials Algorithms Project (MAP), Cambridge, UK, Department of Materials Science and Metallurgy, University of Cambridge. Available at http://www.msm.cam.ac.uk/map (accessed 14 April 2011).

Bhadeshia H K D H and Edmonds D V (1980), 'The mechanism of bainite formation in steels', *Acta Metall*, 28, 1265–1273.

© Woodhead Publishing Limited, 2012

Bhadeshia H K D H and Edmonds D V (1983a), 'Bainite in silicon steels: a new composition–property approach. Part I', *Met Sci*, 17, 411–419.

Bhadeshia H K D H and Edmonds D V (1983b), 'Bainite in silicon steels: a new composition–property approach. Part II', *Met Sci*, 17, 420–425.

Bhadeshia H K D H and Waugh A R (1982), 'Bainite: an atom-probe study of the incomplete-reaction phenomenon', *Acta Metall*, 30, 775–784.

Caballero F G and Bhadeshia H K D H (2004), 'Very strong bainite', *Curr Opin Solid State Mater Sci*, 8, 251–257.

Caballero F G, Bhadeshia H K D H, Mawella K J A, Jones D G and Brown P (2001a), 'Design of novel high strength bainitic steels. Part 1', *Mater Sci Technol*, 17, 512–516.

Caballero F G, Bhadeshia H K D H, Mawella K J A, Jones D G and Brown P (2001b), 'Design of novel high strength bainitic steels. Part 2', *Mater Sci Technol*, 17, 517–522.

Caballero F G, Capdevila C and García de Andrés C (2002a), 'Evaluation and review of the simultaneous transformation model in high strength low alloy steels', *Mater Sci Technol*, 18, 534–540.

Caballero F G, Bhadeshia H K D H, Mawella K J A, Jones D G and Brown P (2002b), 'Very strong low temperature bainite', *Mater Sci Technol*, 18, 279–284.

Caballero F G, Santofimia M J, Capdevila C, García-Mateo C and García de Andrés C (2006), 'Design of advanced bainitic steels by optimization of TTT diagrams and T_0 curves', *ISIJ Int*, 46, 1479–1488.

Caballero F G, Miller M K, Babu S S and García-Mateo C (2007), 'Atomic scale observations of bainite transformation in a high carbon high silicon steel', *Acta Mater*, 55, 381–390.

Chakraborty J, Bhattacharjee D and Manna I (2009), 'Development of ultrafine bainite and martensite duplex microstructure in SAE 52100 bearing steel by prior cold deformation', *Scripta Mater*, 61, 604–607.

Chatterjee S and Bhadeshia H K D H (2006), 'TRIP-assisted steels: cracking of high-carbon martensite', *Mater Sci Technol*, 22, 645–649.

Chatterjee S, Wang H S, Yang J R and Bhadeshia H K D H (2006), 'Mechanical stabilisation of austenite', *Mater Sci Technol*, 22, 641–644.

Chen C Y, Yen H W and Yang J R (2007), 'Nanostructure investigation on a tempered super bainitic steel', in Furuhara T and Tsuzaki K, *The 1st international Symposium on Steel Science*, Kyoto, ISIJ, 123–126.

Defence CODEX (2008), *Super fast, super strong, super steel*, London, MOD. Available at http://www.science.mod.uk/codex/issue1/news/news3.aspx (accessed 27 May 2011).

DSTL (2008), *Super Armour – Made in the UK*, London, MOD.

Garboczi E J, Snyder K A, Douglas J F and Thorpe M F (1995), 'Geometrical percolation threshold of overlapping ellipsoids', *Phys Rev*, E52, 819–828.

García-Mateo C and Bhadeshia H K D H (2004), 'Nucleation theory for high carbon bainite', *Mat Sci Eng*, 378A, 289–292.

García-Mateo C and Caballero F G (2005), 'The role of retained austenite on mechanical properties of novel bainitic microstructures', *Mater Trans*, 46, 1839–1846.

García-Mateo C, Caballero F G and Bhadeshia H K D H (2003), 'Acceleration of low-temperature bainite', *ISIJ Int*, 43, 1821–1825.

Hase K, Garcia-Mateo C and Bhadeshia H K D H (2006), 'Bimodal size-distribution of bainite plates', *Mat Sci Eng A*, 438–440, 145–148.

© Woodhead Publishing Limited, 2012

Hsu T Y and Mou Y (1984), 'Thermodynamics of the bainitic transformation in Fe-C alloys', *Acta Metall*, 32, 1469–1481.

Jacques P J, Girault E, Harlet P H and Delannay F (2001), 'The developments of cold-rolled TRIP-assisted multiphase steels. Low silicon TRIP-assisted multiphase steels', *ISIJ Int*, 41, 1061–1067.

Jacques P, Petein A and Harlet P (2002), 'Improvement of mechanical properties through concurrent deformation and transformation'. In *International conference on TRIP-aided high strength ferrous alloys*, Ghent, Belgium, 281–285.

Keehan E, Karlsson L and Andrén H O (2006), 'Influence of carbon, manganese and nickel contents on microstructure and properties of strong steel weld metals. Part 1 – Effect of nickel content', *Sci. Technol. Weld. Joining*, 11, 1–8.

Kundu S, Hase K and Bhadeshia H K D H (2007), 'Crystallographic texture of stress-affected bainite', *Proc. R. Soc. A*, 463, 2309–2328.

Langford G and Cohen M (1969), 'Strain hardening of iron by severe plastic deformaton', *ASM Trans Quart*, 62, 623–638.

Langford G and Cohen M (1970), 'Calculation of cell size strengthening of wire-drawn iron', *Metall Trans*, 1, 1478–1480.

Mack C and Bartlett M S (1956), 'On clumps formed when convex laminae or bodies are placed at random in two or three dimensions', *Proc Camb Philos Soc*, 52, 246–250.

Matlock D K and Speer J G (2009), 'Third generation of AHSS: microstructure design concepts', in Haldar A, Suwas S and Bhattacharjee D, *Proceedings of the international conference on microstructure and texture in steels and other materials. Part II*, London, Springer, 185–205.

Miihkinen V T T and Edmonds D V (1987a), 'Microstructural examination of two experimental high-strength bainitic low-alloy steels containing silicon', *Mater Sci Technol*, 3, 422–431.

Miihkinen V T T and Edmonds D V (1987b), 'Tensile deformation of two experimental high-strength bainitic low-alloy steels containing silicon', *Mater Sci Technol*, 3, 432–440.

Miihkinen V T T and Edmonds D V (1987c), 'Fracture toughness of two experimental high-strength bainitic low-alloy steels containing silicon', *Mater Sci Technol*, 3, 441–449.

Mizui M, Takechi H and Sekine T (1990), 'Effects of strengthening mechanisms on fatigue damage for 600 MPa class hot-rolled high strength sheet steels', *Tetsu-to-Hagané*, 76, 414–421.

Nagasaka A, Sugimoto K, Kobayashi M and Hashimoto S (1997), 'Effects of warm forming on stretch-flangeability of a TRIP-aided dual-phase sheet steel', *Tetsu-to-Hagané*, 83, 335–340.

Novotny P M (1992), 'Fundamentals of aging and tempering in bainitic and martensitic steel products', in Speich G R, *Symp. 34th Mechanical Working and Steel Processing*, Warrendale, PA, Iron and Steel Society of AIME, 215–236.

Peet M, García-Mateo C, Caballero F G and Bhadeshia H K D H (2004), 'Tempering of hard mixture of bainitic ferrite and austenite', *Mater Sci Technol*, 20, 814–818.

Putatunda K, Deokar A and Bingi G (2010), 'Mechanical properties of a medium carbon low alloy steel processed by two step austempering process', *Materials Science Forum*, 638–642, 3453–3458.

Quidort D, Bouaziz O and Brechet Y (2003), 'The role of carbon on the kinetics of bainite transformation in steels', in Buddy D E and Merwin M J, *Austenite Formation and Decomposition*, Warrendale, PA, TMS.

© Woodhead Publishing Limited, 2012

Sherif M Y (2005), *Characterisation and Development of Nanostructured, Ultrahigh Strength, and Ductile Bainitic Steels*, Cambridge, University of Cambridge.

Sherif M, García-Mateo C, Sourmail T and Bhadeshia H K D H (2004), 'Stability of retained austenite in TRIP-assisted steels', *Mater Sci Technol*, 20, 319–322.

Steel Market Development Institute (2010), *Advanced high-strength steel applications,* Southfield, Michigan, Auto/Steel Partnership. Available at: http://www.autosteel.org/en/Research/Lightweighting.aspx (accessed 14 April 2011).

Sugimoto K, Nakano K, Song S and Kashima T (2002), 'Retained austenite characteristics and stretch-flangeability of high-strength low-alloy TRIP type bainitic sheet steels', *ISIJ Int*, 42, 450–455.

Timokhina I B, Beladi H, Xiong X, Pereloma E V and Hodgson P D (2010), 'Nano-scale analysis of nano-bainite formed in advanced high strength steels', *Mater Sci Forum*, 654–656, 102–105.

Yoozbashi M N, Yazdani S and Wang T S (2011), 'Design of a new nanostructured, high-Si bainitic steel with lower cost production', *Materials and Design*, 32, 3248–3253.

Zackay V F, Parker E R, Fahr D and Bush R (1967), 'The enhancement of ductility in high-strength steels', *Trans Am Soc Met*, 60, 252–259.

Zener C (1946), 'Kinetics of the decomposition of austenite', *Trans AIME*, 167, 550–595.

Zhang M X and Kelly P M (2006), 'Crystallography of carbide-free bainite in a hard bainitic steel', *Mater Sci Eng A*, A438–440, 272–275.

Zhang P, Zhang F C, Wang T S (2011), 'Preparation and microstructure characteristics of low-temperature bainite in surface layer of low carbon gear steel', *Appl Surf Sci*, 257, 7609–7614.

Zhu Q, Sellars C M and Bhadeshia H K D H (2007), 'Quantitative metallography of deformed grains', *Mater Sci Technol*, 23, 757–766.

© Woodhead Publishing Limited, 2012

10

Phase transformations in high manganese twinning-induced plasticity (TWIP) steels

B. C. DE COOMAN, Pohang University of Science and Technology, South Korea

Abstract: The present chapter reviews the recent development of high Mn twinning-induced plasticity (TWIP) steel. These steels can achieve high tensile strengths in excess of 1 GPa and large tensile elongations. The strain hardening behavior of TWIP steels makes them particularly attractive for use in automotive body-in-white manufacturing. The physical metallurgy of TWIP steel is introduced and the influence of the stacking fault energy (SFE) on the deformation mechanism of TWIP steel is discussed. In addition the materials design challenges that remain to be solved are reviewed.

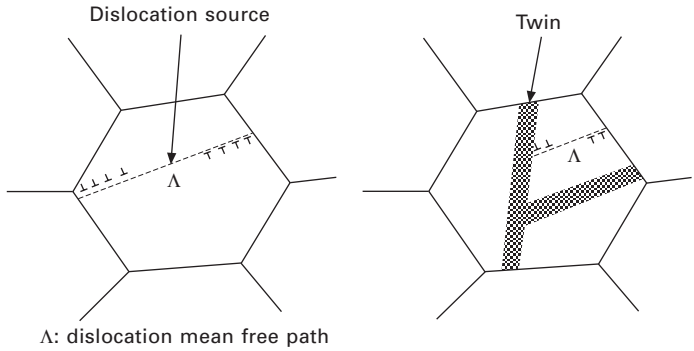
Key words: twinning, stacking fault energy, advanced high strength steel.

10.1 Introduction

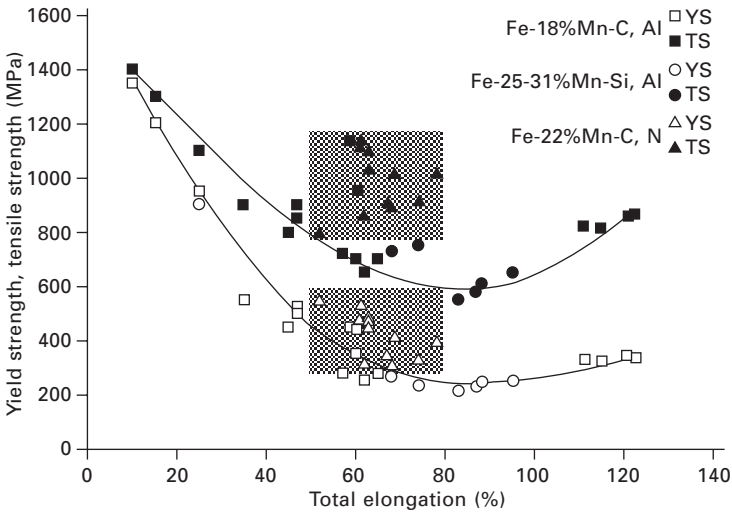
High manganese twinning-induced plasticity (TWIP) steels are highly ductile, high strength Mn austenitic steels characterized by a high rate of work hardening resulting from the generation of deformation-nucleated twins [1–4]. Their Mn content is in the range of 15–30 mass%. Alloying additions of C, Al and/or Si are needed to obtain the high strength and the large uniform elongation associated with strain-induced twinning. Depending on the alloy system, the carbon content is either low, i.e. less than 500 ppm, or high, typically in the range of 0.5–1.0 mass%. Si and Al may be added to achieve a stable fully austenitic microstructure with low stacking fault energy in the range of 15–30 mJ/m^2. High Mn alloys characterized by strength–ductility products 40,000–60,000 MPa% have reached the stage of large-scale industrial testing, and the industrial focus is mainly on TWIP steels with the following compositional ranges: 15–25 mass% Mn, with 0–3% Al, 0–3% Si and 200–6000 ppm C. The dominant deformation mode in TWIP steel is dislocation glide, and the deformation-induced twins gradually reduce the effective glide distance of dislocations. This results in a 'dynamical Hall–Petch effect' illustrated in the schematic of Fig. 10.1. The mechanical properties of typical TWIP steels are reviewed in Fig. 10.2.

TWIP steels have received attention only recently. The pioneering work on high Mn ferrous alloys by Schuman [5] in Germany, Remy and Pineau [6] in France and Kim and co-workers [7, 8] in South Korea did not receive

© Woodhead Publishing Limited, 2012



10.1 Illustration of the dynamical Hall–Petch effect responsible for the strain hardening in twining-induced plasticity (TWIP) steel. Mechanical twins are formed due to the low stacking fault energy. They gradually reduce the effective glide distance of dislocations, resulting in the very high strain hardening observed in TWIP steel.



10.2 Typical ranges for the mechanical properties of TWIP steel.

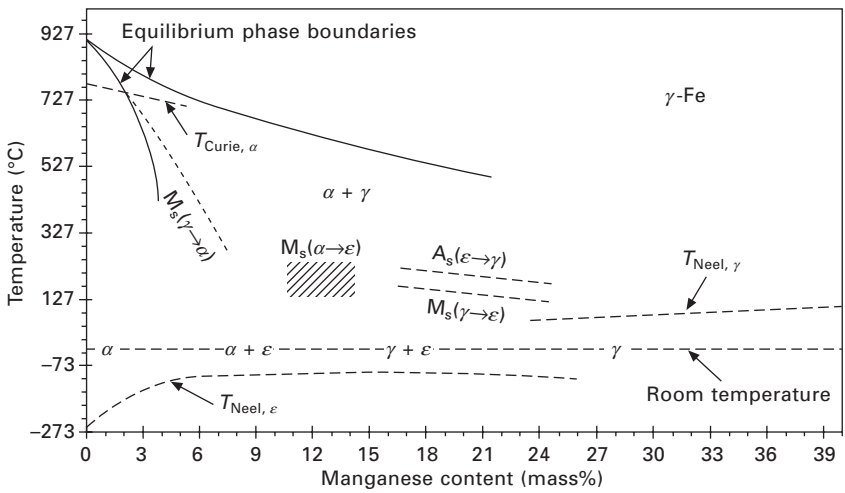
much attention originally. The work carried out by G. Frommeyer and his research group at the Max Planck Institute in Dusseldorf, Germany [1–3], and the interest in advanced high strength steels from the automotive industry has renewed the interest in the properties of high Mn TWIP steels. Mainly three TWIP steel compositions have been extensively investigated: Fe-22%Mn-0.6%C [9], Fe-18%Mn-0.6%C, Fe-18%Mn-0.6%C-1.5%Al [10] and the low carbon Fe-25-30%Mn-3%Si-3%Al [1].

© Woodhead Publishing Limited, 2012

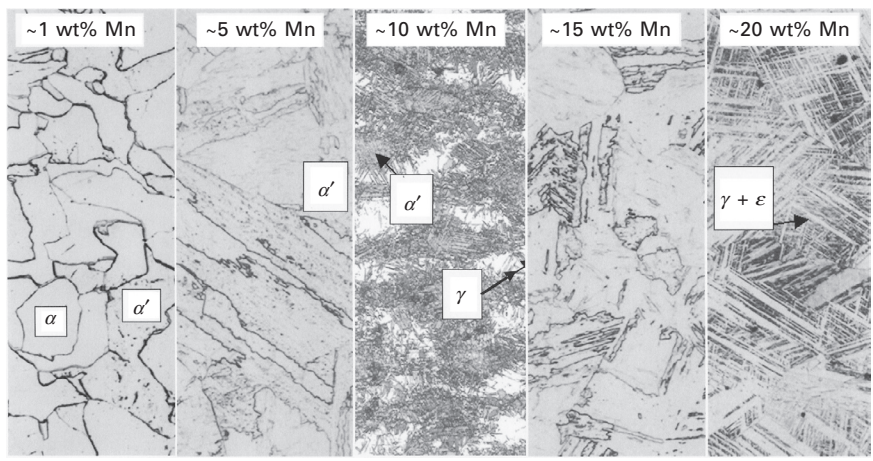
10.2 Fe-Mn-X alloys

10.2.1 Thermodynamic properties

The Fe-Mn equilibrium phase diagram has recently been revised [11]. On the Fe-rich side of the diagram, the binary system would appear to be relatively simple with an open γ-loop. The metastable Fe-Mn diagram (Fig. 10.3), however, reveals much more of the information which is required to understand the microstructures observed in practical non-equilibrium conditions (Fig. 10.4). Small Mn additions have a pronounced hardenability effect. This results



10.3 The metastable Fe-Mn phase diagram.



10.4 Microstructure of Fe-Mn binary alloys.

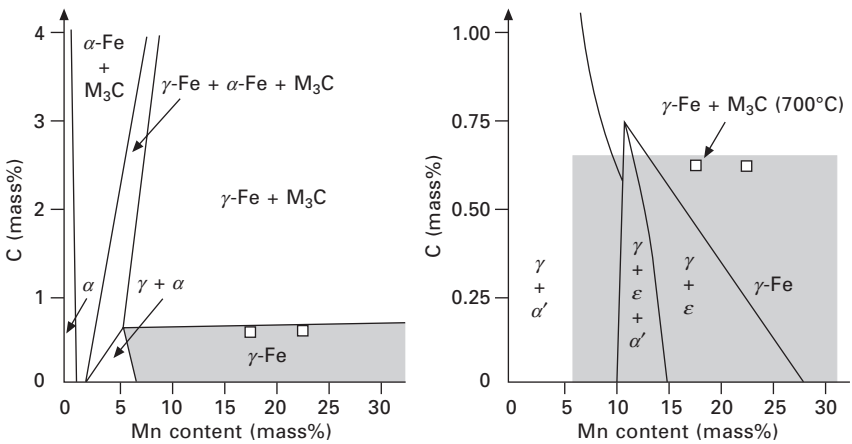
© Woodhead Publishing Limited, 2012

in the formation of cubic α′ martensite. At higher Mn contents hexagonal close-packed (hcp) ε-martensite is formed. Both types of martensite are also generated by stress- and strain-induced transformations of the retained austenite phase. Stabilizing the austenite at room temperature in the binary Fe-Mn alloy system requires Mn contents in excess of 27 mass%.

In order to obtain a stable room austenite phase in alloys with less than 25 mass% of Mn, the formation of α′ and ε-martensite must be suppressed. This can be done by carbon additions. Figure 10.5 illustrates that carbon additions of approximately 0.6 mass% make it possible to obtain uniform, carbide-free, austenitic microstructures and avoid the formation of ε-martensite [5]. Higher carbon additions result in M_3C carbide formation.

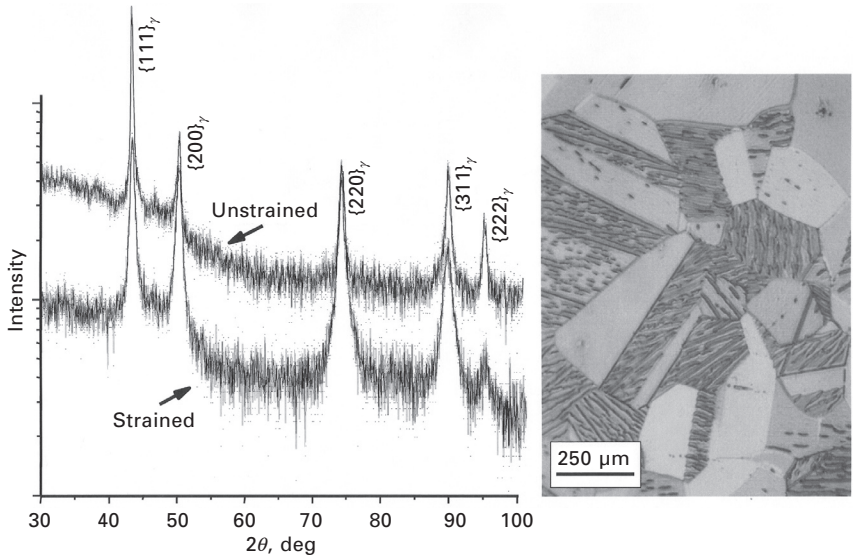
Figure 10.6 illustrates the microstructure of a Fe-18%Mn-0.6%C TWIP steel. The structure is single phase austenitic, with relatively coarse grains, which often contain wide recrystallization twins. The XRD results also illustrate the fact that this TWIP steel does not transform to martensite during straining.

An alternative approach to obtain TWIP steel with uniform, carbide-free, austenitic microstructures is to use a high Mn content and no carbon additions. This TWIP steel composition concept usually requires Al and Si additions to control the stacking fault energy. The importance of the Al additions cannot be underestimated and needs further attention as it results in much improved TWIP properties. It has been shown by Jung *et al.* [12] that even a small amount of Al facilitates the TWIP effect. They show that the suppression of ε-martensite is possible even for Fe-15%Mn-0.6%C TWIP



10.5 Fe-rich corner of the Fe-Mn-C equilibrium phase diagram at 700°C showing the austenite stability range in grey (left). Superposition of the 700°C austenite stability range and the microstructure observed after quenching to room temperature from 950°C (right).

© Woodhead Publishing Limited, 2012



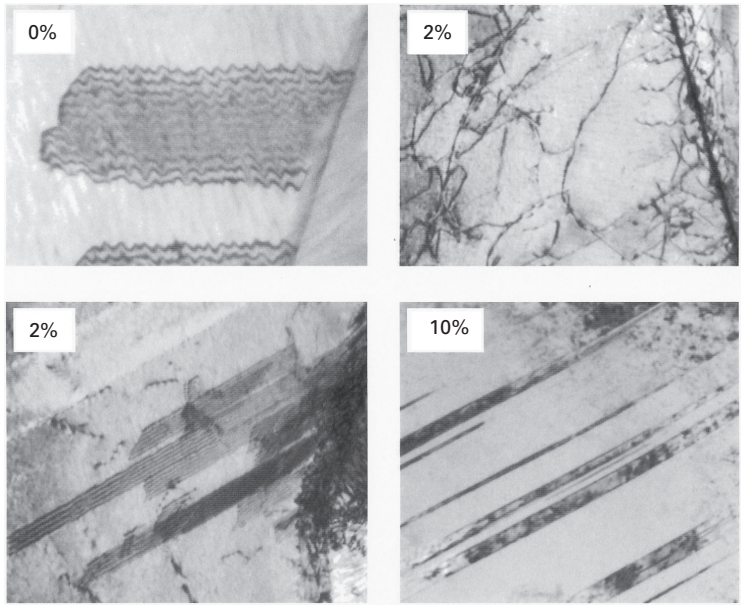
10.6 XRD data for unstrained and strained Fe-18%Mn-0.6%C TWIP steel (left). The log scale was used for the intensity to emphasize the possible presence of small α' and ε diffraction peaks, which are both clearly absent. Corresponding optical metallography obtained by color etching in a solution containing 5 wt% $CuCl_2$, 47.5 wt% HCl and 47.5 wt% ethanol (right). The etch time was 20 s.

steel with 1.5% Al additions. The addition of Al was also found to increase the elongation.

10.2.2 Mechanical properties

TWIP steel research currently focuses on the influence of the alloy composition on the microstructure evolution during deformation and the resulting mechanical properties. In TWIP steel, deformation is by dislocation motion and twinning. The TWIP effect is believed to be due mainly to a dynamic Hall–Petch effect. As the formation of mechanical twins involves the sudden creation of new crystal orientations, the twins will progressively reduce the effective mean free path of dislocations and increase the flow stress, resulting in a high strain hardening behavior. The best way to gain insight into the deformation behavior of TWIP steels is by TEM studies, as the twinning microstructure is very fine. For example, most SEM micrographs will reveal bundles of twins rather than the individual twin lamellas. Typical TEM observations are illustrated in Figs 10.7 and 10.8. In the undeformed material, the dislocations are clearly widely dissociated. In addition, wide stacking faults, often in combination with grain boundaries, are common.

© Woodhead Publishing Limited, 2012

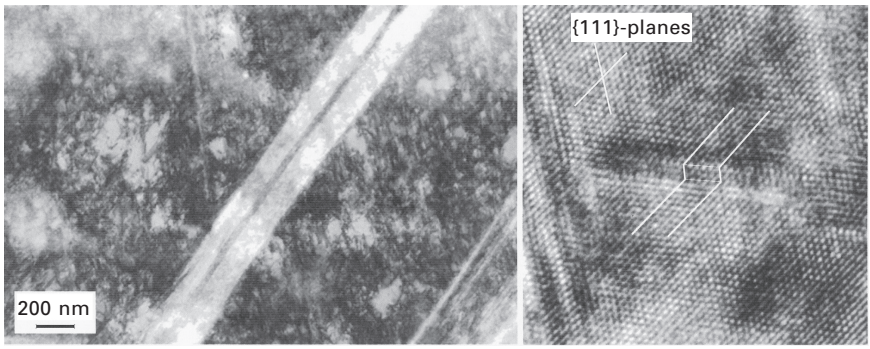


10.7 TEM micrographs of TWIP steel after 0%, 2% and 10% of pre-straining showing an initial increase in the dislocation density without formation of twins. Some grain boundaries reveal the emission of bundles of stacking faults at 2% of strain. The early twins cross the entire grain. The twins often have an internal dislocation sub-structure.

At low strains, the dislocation density increases and the grain boundaries seem to be a particularly effective source of isolated stacking faults. Twins are formed at an engineering strain of about 2–5%. The onset of twinning requires multiple slip within deformed grains. At 10% strain, most grains contain twins. Frequently a single twinning system is activated, together with dislocation glide. These high aspect ratio twins cross the entire grain. High resolution TEM clearly reveals their very narrow width. The twins are very thin and there seems to be a continuous nucleation of new deformation twins of increasingly smaller size. In addition, the twins are internally faulted. The twin volume fraction does not represent a large portion of the total volume. This observation seems to be in agreement with recent constitutive models of TWIP steels.

It is now generally accepted that the SFE plays an essential role in the occurrence of the TWIP effect. Although mainly the role of deformation-induced twins will be discussed in the following paragraphs, it is important to note that the rate of dislocation accumulation will automatically increase when an alloy has a low SFE, independently of twin formation, as the larger dissociation width will more effectively reduce the cross-slip and result in a higher rate of dislocation accumulation.

© Woodhead Publishing Limited, 2012



10.8 (a) TEM micrograph of a TWIP steel deformed at high strains close to fracture. (b) High resolution lattice image of a short secondary twin impinging on a larger primary twin located on the left-hand side of the micrograph.

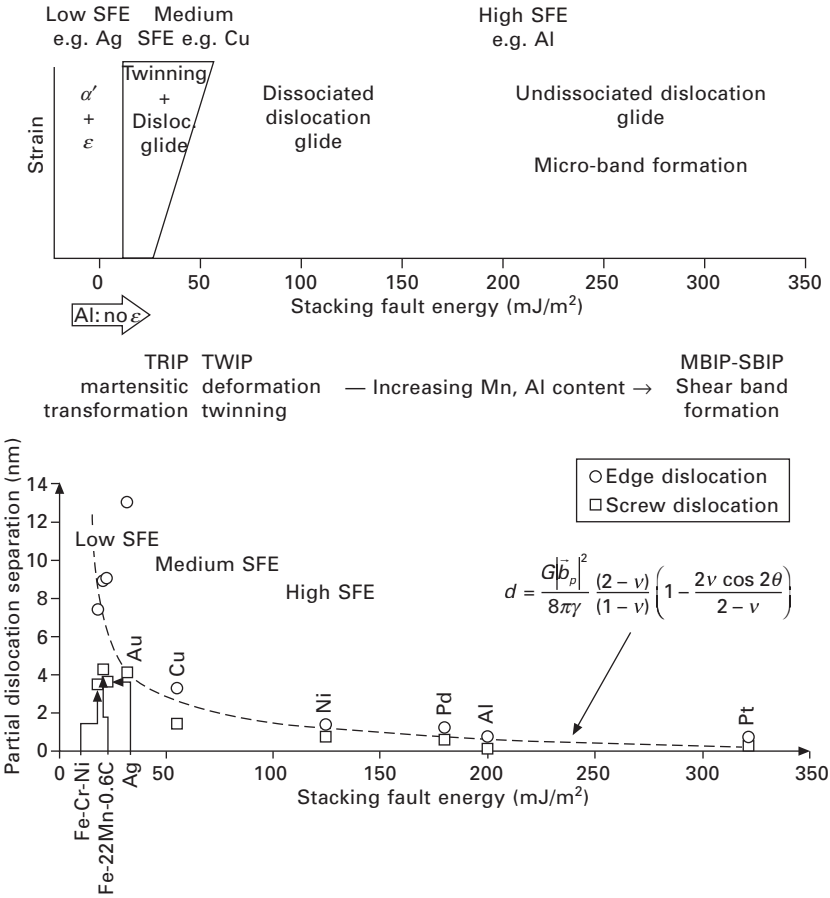
As shown in Fig. 10.9, it is essential for the occurrence of the strain-induced twinning that the SFE be within a very specific range, i.e. 10–40 mJ/m^2, in order to observe mechanical twin formation. Very low SFEs result in strain-induced transformation to either α' or ε martensite. A low SFE, i.e. less than 20 mJ/m^2, has been reported to favor the $\gamma \rightarrow \varepsilon$ transformation.

As the SFE is an essential parameter, there has been considerable interest in the determination of its value for TWIP steels. There is still uncertainty about the exact value of the SFE in Mn alloys and, whereas the theoretical evaluations agree in broad terms, there is still considerable scatter in the actual reported SFE values.

There are currently very few experimental SFE values available for most TWIP alloy systems, but a considerable number of theoretical calculations are available in the literature. From a theoretical point of view, the SFE is proportional to the fcc γ-phase and hcp ε-phase free energies difference. The hcp ε-phase is the high pressure allotropic form of Fe: at room temperature it requires the considerable pressure of 130 kbar to transform α-Fe to ε-Fe. Alloying can, however, stabilize the hcp phase at room temperature in the absence of high pressure. In TWIP steels, a stacking fault may be considered a thin layer of this high pressure phase embedded in the fcc alloy matrix. For a pure metal, the stacking fault energy can be considered the same as the difference between the fcc and the hcp structure for one atomic layer per unit area assuming that the stacking fault is an intrinsic stacking fault [13], i.e.

$$\mathrm{SFE} = \frac{\Delta G_X^{\gamma \rightarrow \varepsilon}}{V^{2/3} \cdot N_o^{1/3}}$$

© Woodhead Publishing Limited, 2012



10.9 Schematic showing the relation between the SFE and the operating deformation mechanism in fcc metals and alloys (top) and the relation between the partial dislocation separation and the SFE (below).

where V is the molar volume and N_o, Avogadro's number. The stacking fault energy can therefore in principle be computed by a thermodynamic approach. In practice, the γ–ε interfacial energy $\sigma^{\gamma-\varepsilon}$ should also be considered. The interfacial energy can be taken as the coherent twin boundary energy and the energy of the twinning dislocations. In Fe-Mn alloys, $\sigma^{\gamma-\varepsilon}$ is in the range 13–20 mJ/m^2 [14]. Usually $\sigma^{\gamma-\varepsilon}$ is considered to be approximately 10 mJ/m^2. Additionally, one takes into account that the stacking fault is on the $\{111\}_\gamma/\{0001\}_\varepsilon$ crystallographic planes [15, 16], to obtain:

$$\mathrm{SFE} = \frac{4}{\sqrt{3}\cdot a_\gamma^2 \cdot N_o}\cdot \Delta G_X^{\gamma\to\varepsilon} + 2\sigma^{\gamma/\varepsilon}$$

© Woodhead Publishing Limited, 2012

where a_γ is the composition and temperature-dependent lattice parameter of the γ-phase. Using the regular solution model, the effect of alloying elements on the relative stability of the fcc γ-phase and the hcp ε-phase can be computed for the ternary Fe-Mn-C and quaternary Fe-Mn-Al-C TWIP alloys. The regular solution model is a model for non-ideal solutions. It is characterized by a non-zero enthalpy of formation, $\Delta H_i^{\mathrm{M}} \neq 0$, and an ideal entropy of formation, $\Delta S_i^M = \Delta S_i^{M,id} = -R\ln X_i$. In the regular solution model, the activity coefficients γ_i, are represented by the quadratic term only, i.e. $\ln \gamma_i = \alpha X_i^2$. Applying this model to the binary Fe-Mn alloy, the free energy of the γ and ε phase, and their relative phase stability, is given by:

$$\begin{aligned}
G^{\varepsilon} &= G^{\varepsilon}_{Mn}\cdot X^{\varepsilon}_{Mn} + G^{\varepsilon}_{Mn}\cdot X^{\varepsilon}_{Mn} + RT \\
&\quad \times (X^{\varepsilon}_{Mn}\cdot \ln X^{\varepsilon}_{Fe} + X^{\varepsilon}_{Mn}\cdot \ln X^{\varepsilon}_{Mn}) + X^{\varepsilon}_{Fe}\cdot X^{\varepsilon}_{Mn}\cdot \Omega^{\varepsilon}_{FeMn} \\
G^{\gamma} &= G^{\gamma}_{Fe}\cdot X^{\gamma}_{Fe} + G^{\gamma}_{Mn}\cdot X^{\gamma}_{Mn} + RT \\
&\quad \times (X^{\gamma}_{Fe}\cdot \ln X^{\gamma}_{Fe} + X^{\gamma}_{Mn}\cdot \ln X^{\gamma}_{Mn}) + X^{\gamma}_{Fe}\cdot X^{\gamma}_{Mn}\cdot \Omega^{\gamma}_{FeMn} \\
\Delta G^{\gamma\to\varepsilon} &= G^{\varepsilon} - G^{\gamma} = (G^{\varepsilon}_{Fe} - G^{\gamma}_{Fe})\cdot X^{\gamma}_{Fe} \\
&\quad + (G^{\varepsilon}_{Mn} - G^{\gamma}_{Mn})\cdot X^{\gamma}_{Mn} + X^{\gamma}_{Fe}\cdot X^{\gamma}_{Mn}\cdot (\Omega^{\varepsilon}_{FeMn} - \Omega^{\gamma}_{FeMn}) \\
\Delta G^{\gamma\to\varepsilon} &= \Delta G^{\gamma\to\varepsilon}_{Fe}\cdot (1 - X^{\gamma}_{Mn}) + \Delta G^{\gamma\to\varepsilon}_{Mn}\cdot X^{\gamma}_{Mn} \\
&\quad + (1 - X^{\gamma}_{Mn})\cdot X^{\gamma}_{Mn}\cdot \Delta\Omega^{\gamma\to\varepsilon}_{FeMn}
\end{aligned}$$

where G_{Fe} and G_{Mn} are the molar free energies of pure Fe and Mn, and Ω_{FeMn} is the interaction parameter in each phase. In the case of TWIP steels, two additional terms must be taken into account, ΔG_{MAG} and ΔG_{GS}, resulting from the effects of the Néel anti-ferromagnetic to paramagnetic transition [17–20], and the grain size effect [21–23], respectively. The temperature for anti-ferromagnetic ordering occurs at relatively high temperatures in both the γ and the ε phase for most TWIP steels. The transition has a clear effect on the SFE and can therefore not be ignored. The high value of the stacking fault energy at the fcc→hcp transition temperature in austenitic stainless steels has been explained by consideration of magnetic effects. In addition, the ordering results in a spontaneous volume magneto-striction. As a consequence elastic stresses are generated. These considerations yield the final form of the equation for the SFE:

$$\mathrm{SFE} = \frac{4}{\sqrt{3}\cdot a_\gamma^2\cdot N_o}\cdot \Delta G^{\gamma\to\varepsilon} + \Delta G^{\gamma\to\varepsilon}_{MAG} + \Delta G^{\gamma\to\varepsilon}_{GS} + 2\,\sigma^{\gamma/\varepsilon}$$

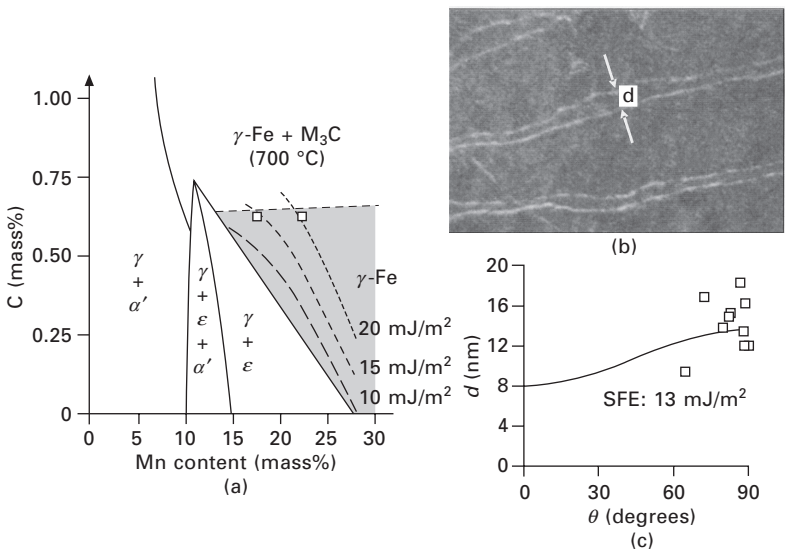
For the Fe-Mn-Al-C system, one has:

$$\Delta G^{\gamma\to\varepsilon} = \sum_{i=Fe,Mn,Al,C} X_i\cdot \Delta G_i^{\gamma\to\varepsilon} + \sum_{i,j=Fe,Mn,Al,C} X_{i,j}\cdot \Delta\Omega_{i,j}^{\gamma\to\varepsilon}$$

© Woodhead Publishing Limited, 2012

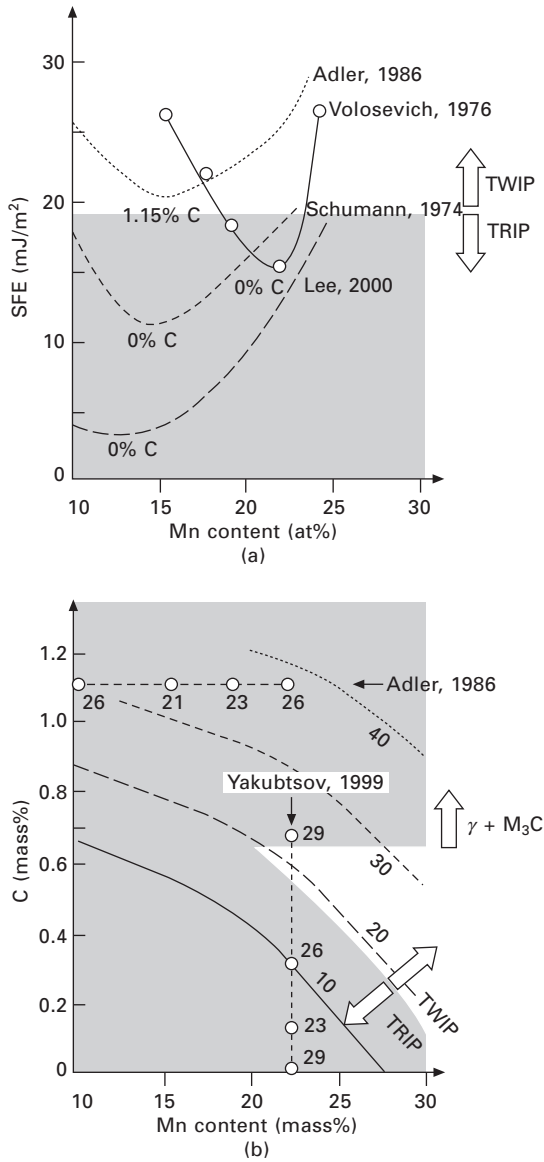
This approach has been used by Saeed-Akbari *et al*. [24] to obtain composition-dependent maps of the SFE for Fe-Mn-Al-C alloys. Figure 10.10 illustrates the relatively good agreement between their results and the stacking fault energy experimentally determined by weak beam dark field transmission electron microscopy [25]. In contrast to a similar thermodynamic analysis of the stacking fault energy of austenitic stainless steels [26, 27], the approach taken so far does not take into account the possibility of Suzuki segregation of carbon at the stacking fault, and the Suzuki segregation appears to have been largely ignored in the literature on TWIP steel containing interstitial carbon.

An essential aspect of the modeling is the choice of the numerical values and functions required in the calculations. This is by no means an easy task [28, 29]. Figure 10.11 reviews some of the SFE determinations for TWIP steels. It is based on the available data for the Fe-Mn-C system [5, 15, 27, 30]. It illustrates the range of composition for Fe-Mn-C TWIP steels based on the assumption that a SFE > 20 mJ/m^2 is required to have a stable TWIP effect. Whereas most authors report that a stable fully austenitic microstructure



10.10 (a) Comparison of the room temperature phases observed in Fe-Mn-C alloys and the calculated SFE. The squares correspond to the Fe-18%Mn-0.6%C (SFE ≈ 13 mJ/m^2) and Fe-22%Mn-0.6%C (SFE ≈ 20 mJ/m^2) TWIP steels. Note that the boundary for the stability of γ-Fe at low carbon and manganese contents is very close to the iso-SFE line for a SFE of 10 mJ/m^2. (b) Weak-beam dark field TEM micrograph of a dissociated dislocation in a Fe-18%Mn-0.6%C TWIP steel. (c) Experimental determination of the SFE of Fe-18%Mn-0.6%C by analysis of the experimentally measured partial dislocation separation.

© Woodhead Publishing Limited, 2012



10.11 Influence of the carbon and manganese content on the SFE of austenitic Fe-Mn-C steel according to literature data.

with TWIP properties must have a SFE in the range of 20–30 mJ/m^2, there is some discrepancy between the reported SFEs. TWIP alloy compositions within the small white wedge-shaped region (Fig. 10.11(b)) are suitable. Carbon additions are absolutely required to obtain a low SFE but the addition of carbon is limited by the formation of M_3C carbide.

© Woodhead Publishing Limited, 2012

Some data on the effect of the carbon content in Fe-22%Mn-C alloys has been reported by Yakubtsov *et al*. [27]. They report that the SFE of a Fe-22%Mn alloy is approximately 30 mJ/m^2. Carbon additions less than 1 mass% reduce the SFE to approximately 22 mJ/m^2. The SFE increases at higher carbon contents.

The critical stacking fault region to achieve twinning-induced plasticity is still unclear. Frommeyer *et al*. [3] indicate that, whereas a SFE larger than about 25 mJ/m^2 will result in the twinning effect in a stable γ phase, a SFE smaller than about 16 mJ/m^2 results in ε phase formation. Allain *et al*. [16] give a much narrower range. According to them the SFE should be at least 19 mJ/m^2 to obtain mechanical twinning. They mention that a SFE less than 10 mJ/m^2 results in ε phase formation. Dumay *et al*. [31] mention that below a SFE of 18 mJ/m^2, twinning tends to disappear and that twinning is replaced by the formation of ε-platelets. They mention that a SFE of about 20 mJ/m^2 is needed for the best hardening rate. Jin and Lee [32] mention that a SFE value of 33 mJ/m^2 is required to obtain twinning in Fe-18%Mn-0.6%C-1.5%Al.

The effect of Al addition to TWIP steel has received much attention as it has resulted in TWIP steels with improved properties and a lower sensitivity to delayed fracture. As Al increases the SFE, it also lowers the strain hardening resulting in TWIP steels with slightly lower tensile strengths. Al also very effectively suppresses the γ→ε transformation. Instead, Al favors the formation of twins. Similar observations have been made for N. Both Al and N reduced the stacking fault formation probability. The SFE for Fe-Mn-Si-Al TWIP steel has been studied by Huang *et al*. [33]. They have also studied the effect of 0.011–0.052% nitrogen on the SFE of Fe-20.24–22.57%Mn-2–3%Si-0.69–2.46%Al containing 100 ppm carbon, by means of XRD. Although they do not report actual SFE values, their results indicate that both Al and N are favorable for the formation of twins. Similarly Dumay *et al*. [31] calculate that Al increases the SFE by about 5 mJ/m^2 per added mass% of Al, whereas Si is also found to increase the SFE by about 1 mJ/m^2 per mass% of Si.

Their results are not confirmed by the experimental measurements of Tian *et al*. [34] who measured the SFE for Fe-25%Mn-0.7%C-Al steel with 1.16–9.77% of Al. They report a much smaller effect of Al on the increase in the SFE, about 1.4 mJ/m^2 per added mass% of Al. Tian *et al*. [34] have compared their measurements with SFE calculations for the paramagnetic case. Their results show an increase in the SFE by about 5.1 mJ/m^2 per added mass% of Al, in agreement with the data of Dumay *et al*. [31]. The extrapolation of their SFE measurements to Al-free Fe-25%Mn-0.7%C is, however, much lower at about 5 mJ/m^2.

In the thermodynamic calculations of the SFE which take into account the anti-ferromagnetic ordering, the configurational entropy is taken into account.

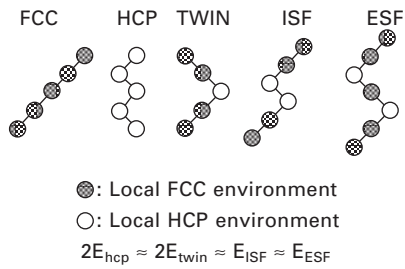
© Woodhead Publishing Limited, 2012

The anti-ferromagnetic transition is, however, also the source of the 'ΔE-effect' a reduction of the modulus occurring due to the anti-ferromagnetic ordering. In the paramagnetic state, the shear modulus is higher than in the anti-ferromagnetic state. This effect does not seem to have been taken into account in all the SFE calculations. As Mn increases the Néel temperature and Al decreases it, the modulus of Fe-18%Mn-0.6%C-1.5%Al is expected to be higher than Fe-22%Mn-0.6%C at room temperature, as they are not in the same magnetic state.

Although there is a general consensus that the stacking fault energy plays an essential role in the mechanical properties of TWIP steel, it is by no means proven that it is the single most important parameter controlling the TWIP mechanism. In fact, Wang *et al*. [35] have made a significant comment about the TWIP effect in high Mn steels. They note that only a very small difference in SFE of the order of 5–10 mJ/m^2 causes an apparently very sharp transition from strain-induced ε-martensite formation to strain-induced twinning. Recent experimental measurements on the nature of the stacking faults have resulted in the suggestion that ε-martensite formation and mechanical twinning is mediated by extrinsic stacking faults (ESF) and intrinsic stacking faults (ISF) respectively. Idrissi *et al*. [36] studied the deformation mechanism of a two-phase α+γ Fe-19.7%Mn-3.1%Al-2.9%Si steel. Deformation at 86°C and 160°C resulted in ε-martensite and twinning at low temperature, and exclusively mechanical twinning at the high temperature. At room temperature only ε-martensite was observed. They argue that this was due to the presence of ESFs at lower temperatures acting as precursors to ε-martensite formation and ISFs at higher temperatures acting as twin precursors.

10.3 Strain-induced twinning

Figure 10.12 compares the structure and the energy of the various planar faults which can occur in fcc metals and alloys. It illustrates the relation between the hcp structure and the extrinsic stacking faults and the relation between the coherent twin and the intrinsic stacking fault. Similar to the



10.12 Comparison of the structure and energy of the planar faults in fcc metals and alloys.

© Woodhead Publishing Limited, 2012

dislocation glide process, twinning is an evolving process. As the stresses increase, the volume fraction of twins increases steadily, continuously dividing grains into smaller units. It can be considered a dynamic Hall–Petch effect as the effective grain size is continuously being decreased. The nucleation of twins in TWIP steel does not seem to be a homogeneous process. Instead, the nucleation stage in deformation twinning is closely related to prior dislocation activity, as the process always occurs after some amount of prior dislocation generation and dislocation–dislocation interactions on different slip systems. Twins are initiated in special dislocation configurations created by these interactions, generally resulting in multi-layer stacking faults which can act as twin nuclei.

The effect of the deformation twinning process is twofold: the twinning shear contributes to the deformation, and the twin boundaries, which act as barriers to dislocation motion, reduce the dislocation mean free path [37].

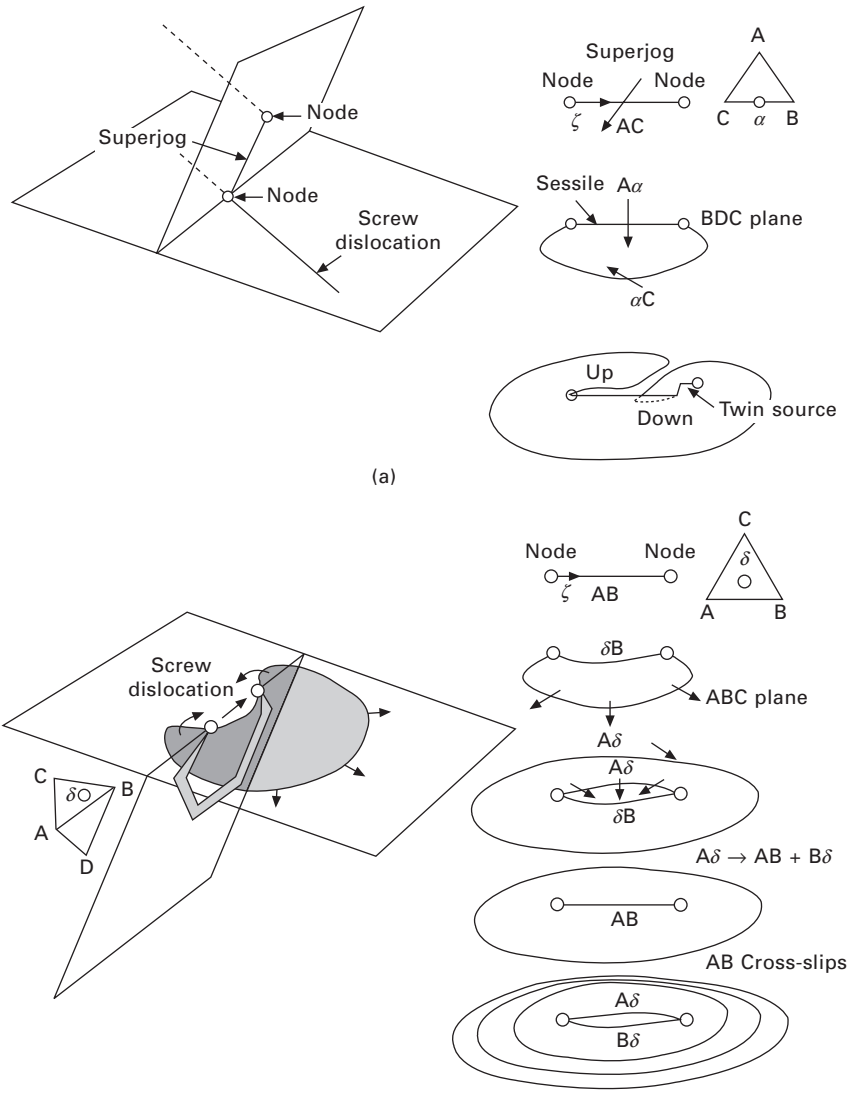
The most likely mechanisms for strain-induced twinning have been proposed by Venables [38–40] and Pirouz [41, 42]. These mechanisms are illustrated in Fig. 10.13. The standard Thompson notation for the description of dislocations in fcc metals applies. In the Venables pole mechanism, the first stage consists of the creation of a jog on a dislocation, with Burgers vector AC, by dislocation intersection. This jog dissociates in a sessile Frank partial dislocation and a Shockley partial dislocation:

$$AC \rightarrow A\alpha + \alpha C$$

When the partial dislocation αC moves under the influence of an externally applied force, it trails an intrinsic stacking fault. The partial dislocation αC rotates repeatedly around the pole dislocation and generates a twin in the process. In the Pirouz double cross-slip mechanism, a screw dislocation segment, having cross-slipped on the ABC plane, dissociates into a low mobility trailing partial and a mobile leading partial dislocation. Under the influence of the applied stress, the leading partial reaches the unstable semi-circular configuration. A new configuration consisting of the original screw segment within a stacking fault region is obtained. After cross-slip of the screw segment, the process can repeat and lead to the formation of a twinned region. Note that there are no direct observations for these mechanisms in TWIP steel.

Glide type deformation-induced twinning mechanisms have also been proposed. In glide mechanisms, the passage of identical a/6<112> type partials on successive {111} planes is assumed. This process requires very high stresses with specific orientations. Glide sources are therefore a less probable source of twins, but Bracke *et al*. [43], who studied twinning in Fe-22%Mn-0.5%C TWIP steel by means of TEM, support the model for the creation of a three-layer stacking fault acting as a twin nucleus. They report a critical shear stress for twinning to be 89 MPa.

© Woodhead Publishing Limited, 2012



10.13 (a) Schematic showing the stages of the Venables pole mechanism for strain-induced twinning. (b) Schematic showing the stages of the Pirouz double cross-slip mechanism for strain-induced twinning.

As there is no agreed model for twin formation, the twinning stress required to nucleate a twin is difficult to compute without making some essential simplifications. The nucleating stress is very likely due to a local stress concentration, as externally applied tensile stresses result in homogeneous

© Woodhead Publishing Limited, 2012

stresses that are too low to nucleate twins. The twinning stress tends to be temperature and strain rate independent. The twinning stress, however, increases with increasing SFE, and the stress required to nucleate a twin is classically related to the intrinsic stacking fault energy in a quadratic or linear manner [40, 42, 44–46]:

$$\tau_T \sim \sqrt{\frac{\gamma_{ISF}}{|\vec{b}_p|}}$$

$$\tau_T \sim \frac{\gamma_{ISF}}{|\vec{b}_p|}$$

Using arguments based on the stress dependence of the dislocation separation, Byun [46] proposed that the critical stress for twinning was the same stress needed to achieve an infinite partial dislocation separation. He derived the following equation for the case of uniaxial stress, assuming that partial dislocation breakaway was the mechanism for the initiation of deformation twinning:

$$\tau_T = 6.14 \cdot \frac{\gamma_{ISF}}{|\vec{b}_p|}$$

The result of the theory is illustrated in Fig. 10.14 for a SFE of 20 mJ/m^2.

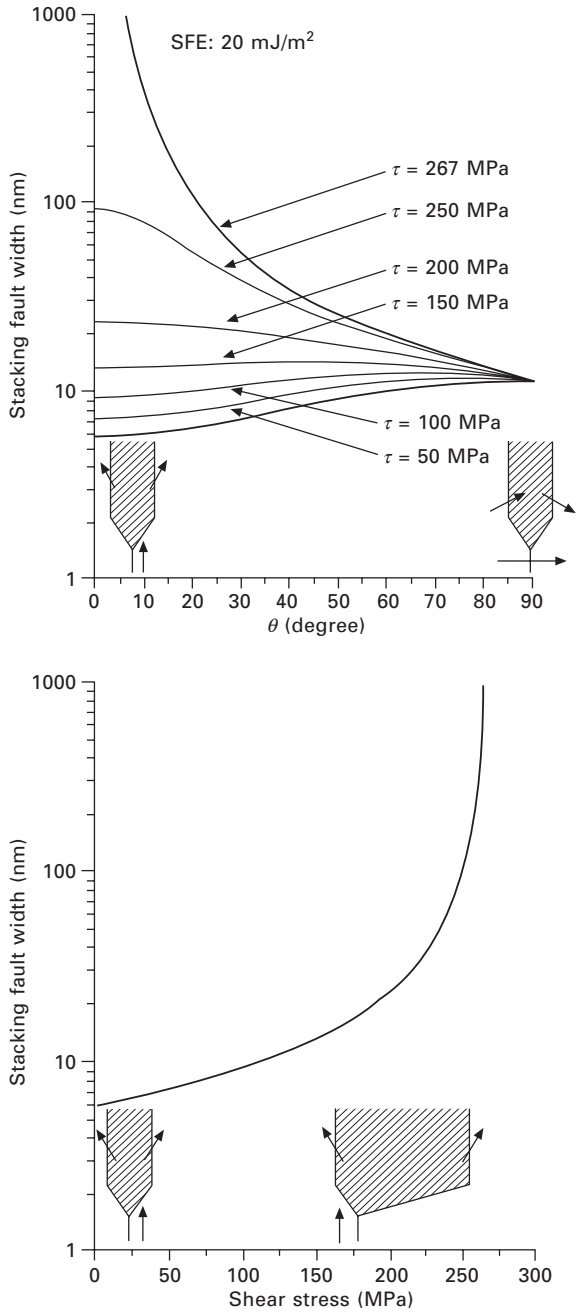
Recently Kibey *et al*. [47, 48] have used a generalized planar fault energy (GPFE) approach, shown schematically in Fig. 10.15, to determine the twinning stress for a three-layer twin nucleus. They found that the critical stress for twinning depended not only on the intrinsic stacking fault energy but also on γ_{ut}, the unstable stacking fault energy, which is considered to be the twin nucleation barrier. It is equal to the sum of the twin boundary migration energy and the twin boundary formation energy, i.e. the coherent twin boundary energy. They do, however, not report applying their model to TWIP steels.

Meyers *et al*. [44] report a model where twins are formed at grain boundaries where they are present in pile-ups. He reports the following equation for the twinning stress:

$$\sigma_T = M \cdot \left(\frac{n \cdot l \cdot E}{M \cdot A_0}\right)^{1/(1+m)} \cdot \dot{\varepsilon}^{1/(1+m)} \cdot e^{Q/[(m+1)\cdot R\cdot T]}$$

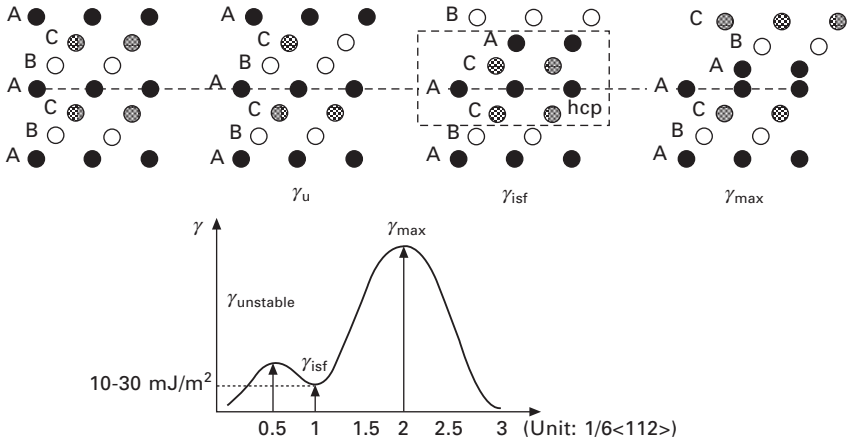
The parameter m relates the dislocation velocity to the applied shear stress $v \sim \tau^m$. n is the number of dislocations in the grain boundary pile-up causing a local stress increase. The parameter l is the distance between the dislocation source and the grain boundary. E is Young's modulus. Q is the activation energy for dislocation motion, and M is an orientation factor.

© Woodhead Publishing Limited, 2012



10.14 Illustration of the Byun analysis for partial dislocation breakaway for dislocations in the screw orientation. For a SFE of 20 mJ/m^2, a tensile stress of approximately 820 MPa is required. This is achieved at 20–25% of strain, i.e. at a much higher stress than is needed to experimentally observe twinning.

© Woodhead Publishing Limited, 2012



10.15 Schematic illustrating the generalized planar fault energy concept, which is the energy required to form a fault by a shearing process.

In the absence of preferred crystallographic orientations and assuming the orientation factors for twinning and slip are equal, the transition from slip only deformation to slip and twinning deformation occurs when the slip stress reaches the twinning stress.

The grain size D may play a role in the value of the twinning stress. Data is not directly available for ferrous TWIP systems, but the k_T value is usually much larger than the k_y value for dislocation slip in the standard Hall–Petch relation:

$$\sigma_T = \sigma_{T0} + \frac{k_T}{\sqrt{D}}$$

As a result, larger grains will tend to expand the twinning domain. Note that whereas the twinning stress may be high, the growth of a twin requires a much lower stress.

Sevillano [49] has recently proposed a strain-hardening model for TWIP steels by considering its behavior similar to that of a plastically heterogeneous composite. He argues that the observation of an important Bauschinger effect, the back stress contributing as much as half of the total stress, by Bouaziz *et al*. [50], is due to the fact that the simultaneous deformation of the grains and their twinned parts requires the presence of a forward internal stress operating on the twin and a backward internal stress operating on the untwinned matrix. This is due to the fact that the twins must share similar strain components with their matrix. The twins must, however, have an important contribution to the strength, which can only be based on their small nanometer thickness. Bouaziz *et al*. [50] link the back-stress to dislocations of a given slip system being stopped at grain and twin boundaries and developing a stress which prevents similar dislocations from moving ahead.

© Woodhead Publishing Limited, 2012

Jin and Lee [32] have studied the strain hardening of Fe-18%Mn-0.6%C-1.5%Al in detail and report that, at large strains, the deformation twinning rate greatly decreases deformation twins with different growth directions, and that the amount of twinned volume is controlled not by the lateral growth of the deformation twins, but by the increase in the number of new deformation twins.

10.3.1 TWIP-effect modeling

Various models have been proposed to model the TWIP effect in high Mn steel in order to understand the parameters controlling their pronounced work hardening. Bouaziz and Geulton [51] and Allain *et al*. [52] were the first to attempt to model the effect of the strain-induced twinning on the work hardening of TWIP steel on a physical basis using the Kocks–Mecking [53] approach. In their description, the twins act as impenetrable obstacles. The model computes uniaxial tensile stress–strain curves on the basis of the evolution of the dislocation density and the twin volume fraction. Their description of the evolution of the dislocation density is given by:

$$\frac{d\rho}{d\gamma} = \frac{1}{b} \cdot \left(\frac{1}{d} + \frac{1}{t} + k \cdot \sqrt{\rho} \right) - f \cdot \rho$$

$$t = 2 \cdot e \cdot \frac{1 - F}{F}$$

The twin volume fraction is given by:

$$F = 1 - e^{-m \cdot \varepsilon}$$

In the Bouaziz–Allain model, the SFE enters indirectly in the value of the *m*-parameter. They applied their model to Fe-22%Mn-0.6%C TWIP steel, and found the following values for the main model parameters: $k = 0.011$, $f = 3$ and $m = 1.95$. Interestingly k and f are exactly the same as for the stainless steel grades AISI 409 and 304L. The m parameter was 1.35 for AISI 304L. The same authors described an extension to their original model using a visco-plastic description and a homogenization law to deal with a randomly oriented polycrystal. These results support the fact that the total volume fraction of the twins is very low and that plastic deformation is mainly achieved by dislocation glide.

In contrast to recrystallization twins, deformation twins tend to be very thin. The twins are estimated to be 15 nm thick. Allain *et al*. [54] also proposed a mechanism for the twinning behavior of the deformation-induced twins whereby in a first stage twins, which are a few tens of a nanometer thick, will move until they reach a strong boundary, i.e. a grain boundary or a twin

© Woodhead Publishing Limited, 2012

boundary. In the second stage the twins thicken. The authors also notice that two twinning systems are sequentially activated in most grains. The first twins develop across the entire grain. The twins of the second system develop between the primary twins and are much shorter and thinner.

Shiekhelsouk *et al*. [55] developed a physically based, micro-mechanical model incorporating elasto-visco-plasticity, to obtain a constitutive model for Fe-22%Mn-0.6%C TWIP steel using a randomly oriented representative volume element of 800 grains. They report that the twinned volume fraction is dependent on the grain orientation, and less than 0.08 for a macroscopic strain of 0.4.

Kim and De Cooman [56] used the Kubin–Estrin model [57] to compute the strain hardening from the evolution of the coupled densities of the mobile dislocations, ρ_m, and immobile forest dislocations, ρ_f. In this model the two dislocation densities saturate at large strains and two dislocation densities are coupled via terms which simultaneously appear as annihilation terms in the evolution equation for ρ_m and as production terms in the evolution equation for ρ_f. The following set of differential equations was used:

$$\frac{d\rho_m}{d\varepsilon_g} = M\left[\frac{C_1}{b^2}\left(\frac{\rho_f}{\rho_m}\right) - C_2\rho_m - \frac{C_3}{b}\rho_f^{1/2}\right]$$

$$\frac{d\rho_f}{d\varepsilon_g} = M\left[C_2\rho_m + \frac{C_3}{b}\rho_f^{1/2} - C_4\rho_f\right]$$

In these equations C_1 is a production term, with forest obstacles acting as pinning points for fixed dislocation sources. C_2 takes into account the mobile density decrease by interactions between mobile dislocations. C_3 describes the immobilization of mobile dislocations with a mean free path proportional to $\rho_f^{1/2}$, assuming a spatially organized forest structure. C_4 is associated with the rearrangement and annihilation of forest dislocations by climb or cross-slip. The Bouaziz and Geulton [51] expression for the twin spacing was modified to take into account the fact that, as a set of parallel planar twins of identical thickness transverses a grain, the areal fraction and the volume fraction of twins are the same and the factor of 2, used by Bouaziz, should not be considered, hence:

$$t = e\frac{1-F}{F}$$

where t is the average twin spacing, e is the average twin thickness which is independent of strain, and F is the twin volume fraction. Combining the three previous equations, the dislocation density evolution was expressed as:

$$\frac{d\rho}{d\varepsilon_g} = M\left[\frac{1}{b}\left(\frac{1}{d} + \frac{1}{t} + k\sqrt{\rho}\right) - k_2\rho\right] = M\left[\frac{1}{b}\left(\frac{1}{d} + \frac{1}{e}\cdot\frac{F}{1-F} + k\sqrt{\rho}\right) - k_2\rho\right]$$

© Woodhead Publishing Limited, 2012

The twinning-related term results in a remarkable increase in the strain hardening behavior compared to the classical strain hardening behavior. A modification to these equations taking into account dynamic strain aging (DSA) should also be included. Results for a Fe-18%Mn-0.6%C-1.5%Al TWIP steel are shown in Fig. 10.16. The model correctly predicts that the strain hardening $d\sigma/d\varepsilon$ has a more or less flat behavior in the intermediate strain levels, rather than a continuously decreasing behavior as in the case of high SFE metals. This sustained strain hardening level is due to the gradual decrease in the dislocation mean free path.

Dini *et al*. [58] analyzed the dislocation density evolution in Fe-31%Mn-3%Al-3%Si TWIP steel during straining by means of XRD. They calculate a large twin volume fraction of 0.56 at a strain of 0.4. They report a value of 18 nm for the twin lamella thickness.

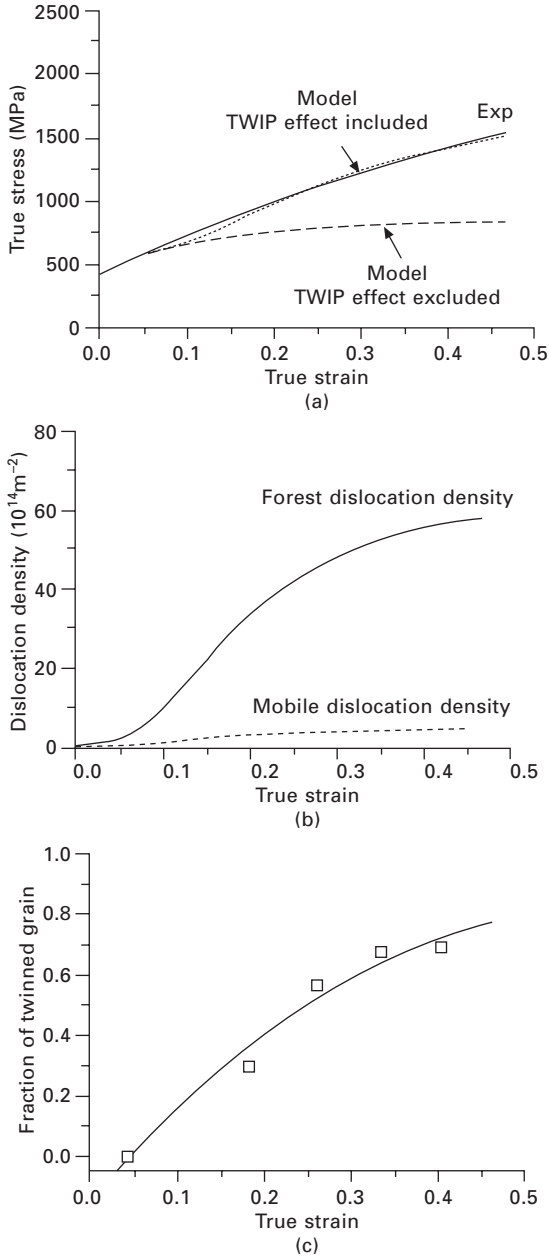
10.3.2 Crystallographic texture evolution

Figure 10.17 gives a broad overview of the most important aspects of rolling deformation texture development in fcc metals and alloys as a function of their SFE. Texture evolution models typically predict a brass component dominated texture for low SFE metals. The mechanism for the development of this texture is unclear and very likely due to the fact that the twinning is locally inhomogeneous and depends on the grain orientation, due to the local activation of slip or twinning system and the kinetics of the process for a specific grain. One possibility is that first the Cu twin orientation, which is a consequence of the twinning of the Cu component, slips into the Goss orientation and eventually to the Brass orientation. Measurements for TWIP steel, however, show an important Goss component, along with the $\{101\}\langle 1\bar{1}1\rangle$ component, and the Cu component as an additional texture component in TWIP steels [4].

An essential aspect of the intensity of the brass component is the volume fraction affected by twinning. Considerably different values have been reported. The amount of twinning was reported to saturate at a value smaller than 30% by Kim and De Cooman [56]. According to Bouaziz and Geulton [51], this figure is 20%. According to Barbier *et al*. [59], the twin volume fraction in an Fe-22%Mn-0.6%C TWIP steel deformed along the TD direction can be as low as 9% at fracture, with the twinning having little influence on the final texture. In contrast, Kim *et al*. [10] have reported twin volume fractions in the range of 60–70% for Fe-Mn-C and Fe-Mn-C-Al TWIP steel. This high value is very likely due to their use of a low resolution microstructural analysis method. Note that if the volume fraction of twins is as low as the most recent data would tend to suggest, the twins themselves, being very thin, do probably not contribute to the overall texture.

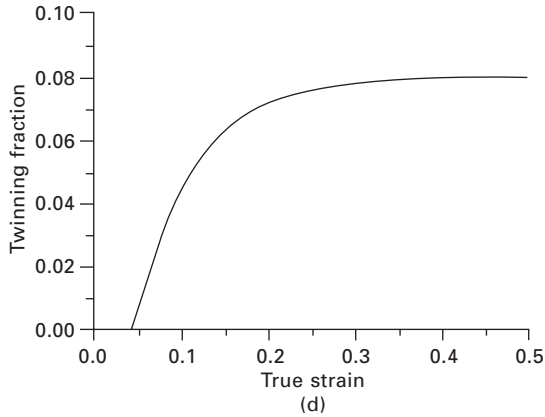
Orientation distribution function (ODF) analysis of an Fe-18%Mn-1.5%Al-

© Woodhead Publishing Limited, 2012

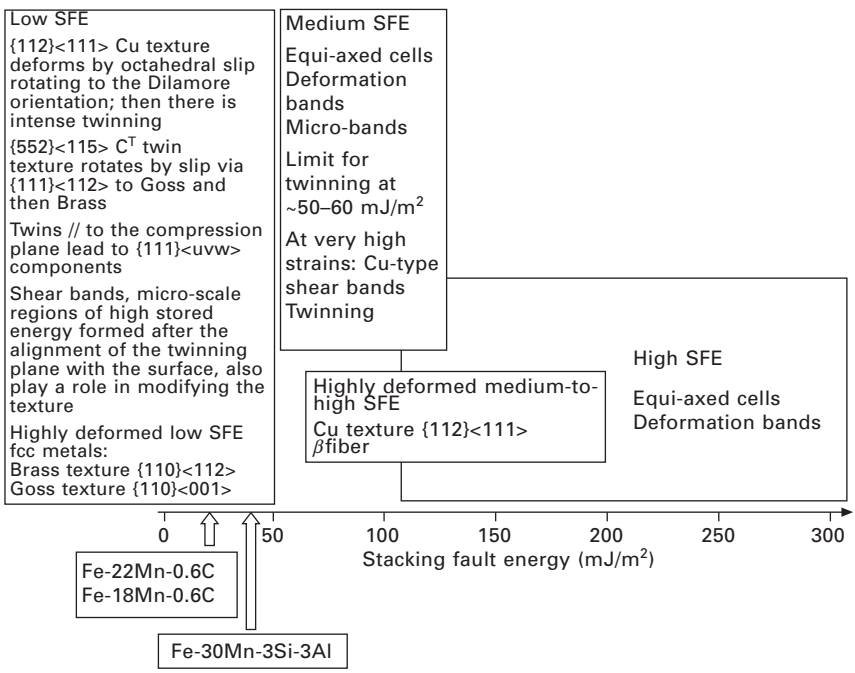


10.16 (a) Comparison of the experimental true stress–true strain curves and the model calculation. (b) Mobile and forest dislocation density for twinned grains as a function of true strain. (c) Fraction of twinned grains as a function of true strain. (d) The average volume fraction of twins inside a twinned grain as a function of true strain (Courtesy of Mr Junkyung Kim, Pohang University of Science and Technology).

© Woodhead Publishing Limited, 2012



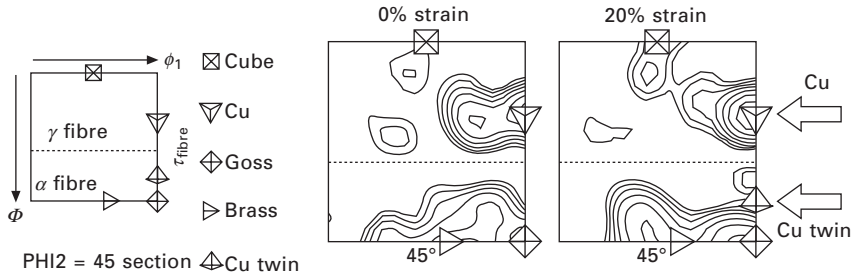
10.16 Continued



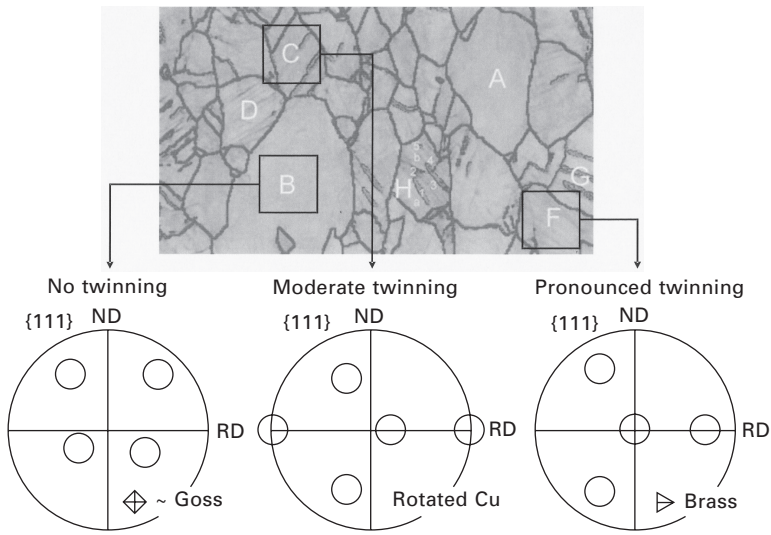
10.17 Texture evolution during rolling of fcc alloys as a function of their SFE.

0.6%C TWIP steel after tensile deformation to moderate strains results in a strengthening of the Cu texture and S components as shown in Fig. 10.18. This is due to a re-orientation of <111> into the rolling direction (RD) of the Fe-18%Mn-1.5%Al-0.6%C TWIP steel caused by the moderate tensile

© Woodhead Publishing Limited, 2012



10.18 PHI = 45° section of the orientation distribution function (ODF) measured at 0% strain and 20% strain.



10.19 Orientation analysis of grains in Fe-Mn-Al-C TWIP steel at 50% engineering strain. The data shows the orientation difference between a twin-free grain, a moderately twinned grain and a grain with pronounced twinning (Courtesy of Dr H. Beladi, Deakin University).

deformation. The <111>//RD fiber orientations are well suited for twinning and reinforce the twinning activity.

Evidence for twinning-related orientations is mainly observed in highly strained conditions. This is shown for 50% strain in Fig. 10.19, which shows that a large tensile deformation results in the presence of the Brass texture component only in grains associated with pronounced twinning [56].

Yang *et al*. [60, 61] have also reported the influence of the grain orientation on the twinning in an Fe-33%Mn-2.93%Al-3%Si TWIP steel during tensile deformation. According to them, multi-slip and dislocation pile-ups are

© Woodhead Publishing Limited, 2012

essential requirements to start the twinning process. Slip favors grain rotation towards <111> and grains with a <111> direction oriented parallel to the tensile direction have three twin variants. Their predictions, based on a Schmid factor analysis, are in agreement with their observations. Twin variants will of course interact and contribute to work hardening. After twinning, strong slip within the twin bands should be favored. The same authors reported the influence of the grain orientation on twinning in the case of axial compression of the same TWIP steel. During tensile deformation, grains containing twins rotated towards <111> directions, favoring twinning. In compression, grains containing twins were brought in <110> directions, thus suppressing further twinning. Karaman *et al*. [62] report that the critical shear stress for twinning is 9.3% higher than glide for <111> oriented grains.

In Fe-30Mn-3Si-3Al, the texture evolution is similar to the texture evolution in low to moderate SFE alloys according to Vercammen *et al*. [63]. They report that the presence of extrinsic SF is uncommon despite the fact that they may be acting as twin nuclei. In this type of TWIP steel, the twinning seems to start at an early stage. The pronounced twinning at an early stage seems to be in agreement with the weak intensity of the Cu orientation, which usually initiates the formation of the Brass orientation. The reduction in the Cu orientation is caused by mechanical twinning. The Cu orientation is transformed to a position near the Goss orientation and the Cu twin orientation rotates into the Goss orientation. Goss and Cu twin orientations are therefore expected to increase in intensity as the twinning proceeds. They report observing shear bands at very high strain.

The texture evolution during deformation of a Fe-22%Mn TWIP steel containing carbon and nitrogen, where the N was apparently added to suppress the DSA effect, was reported by Bracke *et al*. [64]. They showed that both twinning and slip contribute to the formation of the brass texture. Deformation textures, in particular the {114}<172> texture component, play an important role in the development of the Brass texture, as they are twin related. Micro and macro shear bands were not clearly involved in the formation of the brass component. They report a remarkably retained rolling texture after recrystallization annealing, which they ascribe to the absence of preferred nucleation sites within a very homogeneously deformed microstructure.

Barbier *et al*. [59] have analyzed the texture evolution during tensile testing. They also observed a pronounced <111> fiber in the tensile direction, to which they ascribe the high level of strain hardening as a result of the sustained mechanical twinning. Yan *et al*. [65] reported detailed results on the genesis of the deformation texture obtained by the *in situ* synchrotron XRD characterization of Fe-25%Mn-3%Si-3%Al TWIP steel. They also report that the texture strengthening is dominated by the contribution of slip which strengthens the {111} poles in the tensile direction. They conclude that the texture is mainly controlled by dislocation glide and not by the twinning,

© Woodhead Publishing Limited, 2012

which is responsible for impeding the reinforcement of the texture. They report that the twinning activity is of the order of 10%.

10.3.3 High strain rate properties

High strain rate properties of TWIP steels have been reported by Frommeyer *et al*. [3] for a Fe-25%Mn-3%Si-3%Al-0.03%C TWIP steel for which the formation of α and ε was fully suppressed, even after straining. This TWIP steel had a moderate strain hardening, and dislocation glide was the main deformation mechanism. As the temperature was reduced, the amount of twinning was found to increase. There was extensive twin formation during the high strain rate deformation, but no brittle fracture occurred, even at temperatures as low as –200°C.

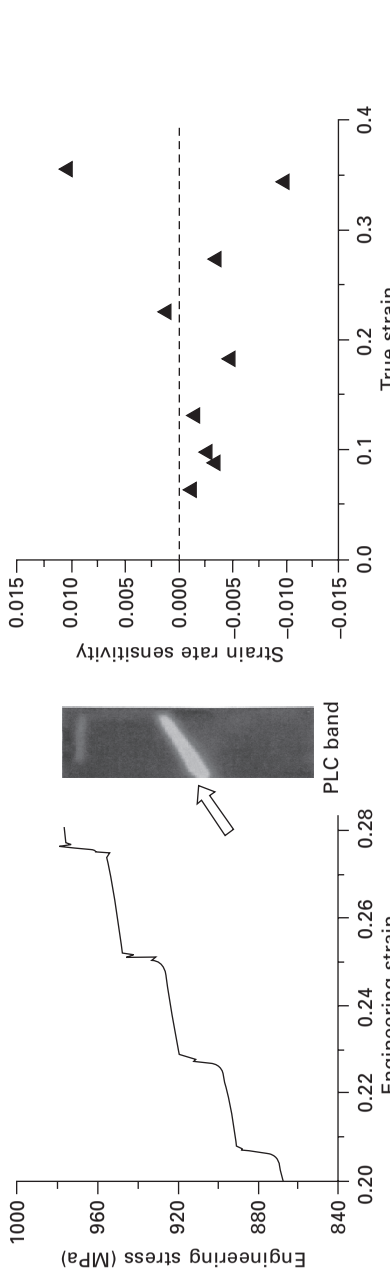
Ueji *et al*. [66] report the mechanical properties of Fe-31%Mn-3%Si-3%Al TWIP steel in the strain rate range of 10^{-3}–10^{+3} s^{-1}. The steel had different grain sizes, in the range of 1.1–35.5 μm. In contrast to the observation made for ferritic steels, there was still a large elongation at small grain sizes. They explained their observations by the limited dynamic recovery in TWIP steels due to a low SFE. The elongation was only slightly smaller at higher strain rates.

Sahu *et al*. [67] have studied the mechanical behavior of two Fe-24%Mn-0.5%Si-(0.11–0.14)%C TWIP steels with 0.91% and 3.5% Al additions in the strain rate range of 10^{-4}–4000 s^{-1}. In the TWIP steel with 0.91% Al, the transformation of austenite to martensite took place up to a strain rate of 1000 s^{-1}. Transformation of the TWIP steel with 3.5% Al was limited to the strain rate range of 10^{-3} s^{-1} to 720 s^{-1}. The TWIP steel with 3.5% Al was therefore more stable. Irrespective of the Al content, the transformation of the austenite phase at high strain rates is suppressed for both TWIP steels due to the adiabatic heating of the sample. Based on the observation of serrated grain boundaries, they also argue that dynamic recrystallization may be taking place during the high strain rate tests.

10.3.4 Strain localization

Room temperature DSA occurs in the most commonly studied carbon-alloyed TWIP steels: Fe-22%Mn-0.6%C and Fe-18%Mn-0.6%C. DSA-related type A serrations are shown in Fig. 10.20. As will be explained later in the section, this is very likely due to the presence of point-defect pairs involving interstitial carbon atoms, which reorient in the presence of dislocations via a single diffusional jump of the carbon atom. This mechanism is similar to a model recently developed by Curtin *et al*. [68]. The reorientation does not require long range diffusion, only a single diffusional jump to achieve a suitable orientation with respect to the strain field of the partial dislocation.

© Woodhead Publishing Limited, 2012



10.20 Direct evidence for dynamic strain aging (DSA) in TWIP steel: type A serrations due to the passage of individual Portevin–LeChatelier (PLC) bands (left). IR thermography of an isolated PLC band (middle). Measurement showing negative values for the strain rate sensitivity (right).

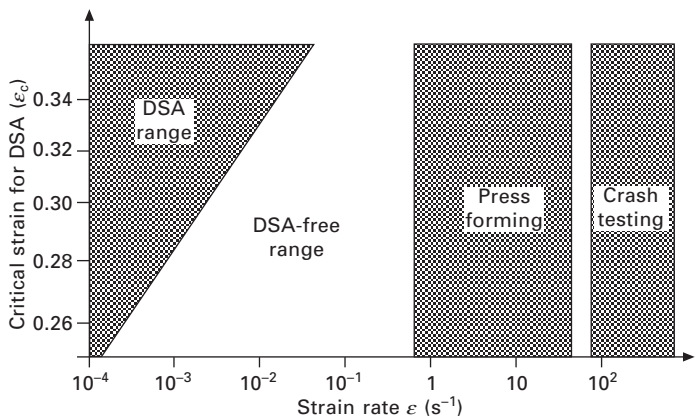
© Woodhead Publishing Limited, 2012

Alternatively, the fast dislocation core diffusion has been proposed to explain the widely observed room temperature DSA [69].

Detailed DSA studies have been carried out by Chen *et al*. [70], Kim *et al*. [71] and Zavattieri *et al*. [72]. The properties of the Portevin–LeChatelier (PLC) bands have been determined for Fe-17-18Mn-0.6%C-1-1.5%Al. The band velocity was found to decrease with strain, and the local PLC band strain rate was 15–100 times the applied value. Localization may in principle result in press forming difficulties, but PLC bands have been reported to have no negative impact on the press forming performance of Fe-22Mn-0.6C TWIP steels [69]. This is due to the fact that the occurrence of DSA-related surface defects are stress state and strain rate dependent. Based on data for the critical strain from Bracke [73], the schematic in Fig. 10.21 is proposed. The other aspects of DSA should, however, not be overlooked; it leads to a negative strain rate sensitivity and hence a very limited post-uniform elongation, as illustrated in Fig. 10.22.

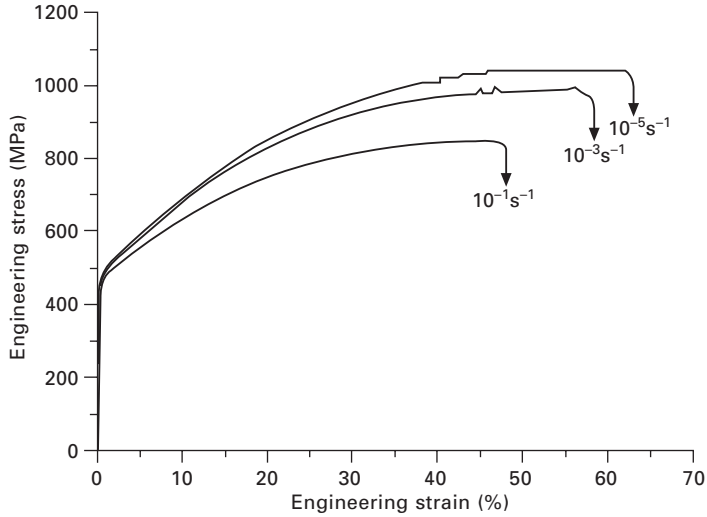
In carbon alloyed fcc alloys, the room temperature DSA cannot be explained by long-range diffusion of carbon. Instead, it results from the presence of point-defect pairs involving interstitial carbon atoms which reorient themselves in the stress field of dislocations. Possible defect complexes are carbon–vacancy, carbon–carbon, and carbon–Mn complexes (Fig. 10.23). The first two complexes may be less likely in TWIP steel due to the very low vacancy concentration and the strong repulsive nearest-neighbor carbon–carbon interaction. The carbon–Mn complexes are more likely due to the strong attractive interaction between interstitial carbon and the substitutional Mn.

Isolated carbon interstitials in fcc metals and alloys do not result in a strain ellipsoid, but point-defect pairs involving interstitial C atoms can result in

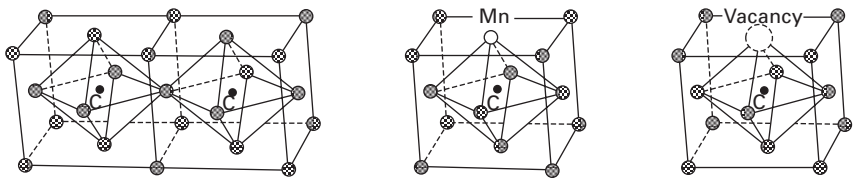


10.21 Schematic showing the approximate strain rate and critical strain region for DSA.

© Woodhead Publishing Limited, 2012



10.22 Stress–strain curves for Fe-Mn-Al-C TWIP steels showing clearly the negative strain rate sensitivity of this material.

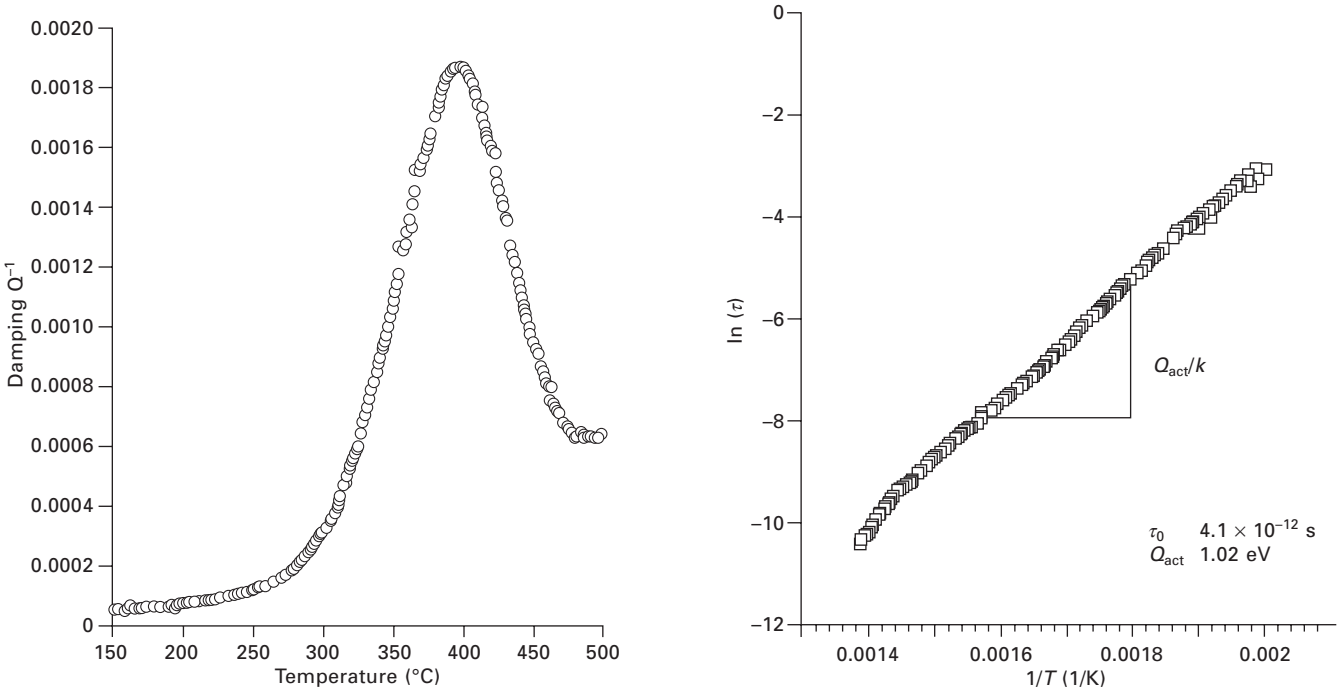


10.23 The three possible point-defect pairs involving interstitial carbon atoms in a Fe-Mn-C TWIP steel.

a strain ellipsoid [74]. Direct evidence for point-defect pairs in austenitic TWIP steels comes from the observation of a Finkelstein–Rosin peak (FR) in internal friction (IF) measurements (Fig. 10.24). Isolated interstitial atoms have a symmetric strain field in austenite, and there is no equivalent for the ferrite Snoek peak for austenite. The stress-induced reorientation of the point-defect pair is, however, possible. The activation energy is 1.02 eV, i.e. about half the value of the activation energy for carbon diffusion in γ-Fe.

The question of the identification of the physical phenomenon responsible for the relaxation peak observed in the internal friction spectrum of TWIP steel is complex. In view of the information available in the literature on the subject, there is currently no general agreement on the nature of the point-defect pairs responsible for the observed IF peak in austenitic steel, and more systematic work needs to be done before a firm conclusion can be formulated. Anelasticity due to the stress-induced reorientation of point-defect complexes in fcc steels has been ascribed to interstitial-substitutional

© Woodhead Publishing Limited, 2012



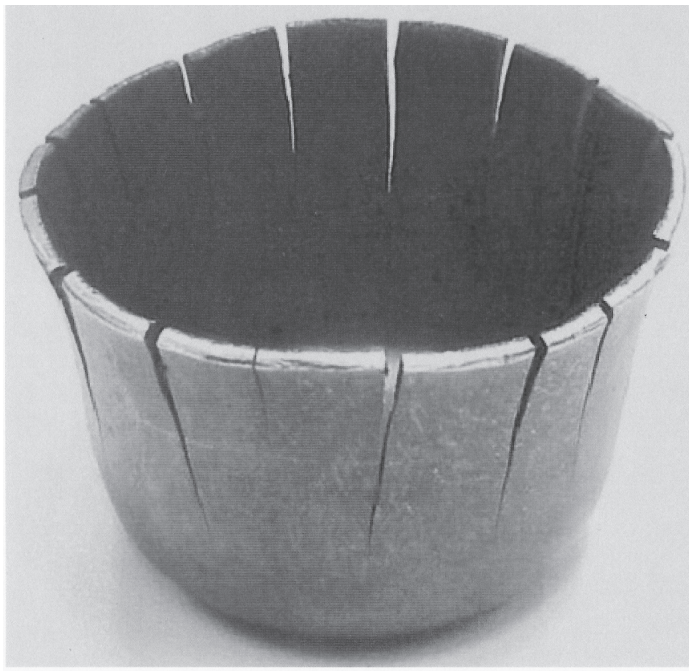
10.24 IF spectrum for a Fe-Mn-C TWIP steel (left). The large, broadening-free, single relaxation Debye peak has a maximum at 393°C for measurements at a resonance frequency of 898 Hz. The peak is direct evidence of the stress-induced reorientation of point-defect pairs involving interstitial C atoms. Analysis of the FR peak to determine the activation energy (right).

© Woodhead Publishing Limited, 2012

solute pairs [75–77], second-neighbors interstitial–interstitial solute pairs [78], and interstitial solute–vacancy pairs [79–83]. There have been several reports indicating that the C-Mn interaction [84, 85] in austenitic alloys was attractive. The observed FR relaxation peak is therefore likely related to the stress-induced reorientation of point-defect pairs involving interstitial C and substitutional Mn atoms. DSA in TWIP steel could thus be linked to the reorientation of point-defect pairs involving interstitial C atoms by the stress field of dislocations. A similar mechanism has been proposed to explain DSA in Hadfield steel [86, 87]. It is, however, not excluded that point-defect pairs involving interstitial C atoms have a direct effect on the SFE as suggested by Fujita *et al*. [88].

10.3.5 Delayed fracture

Delayed fracture has been identified as the major problem for Fe-22%Mn-0.6%C TWIP steel. The effect appears readily in deep drawn cup as deep edge cracks a certain time after the cup has been drawn. A typical example of delayed fracture is shown in Fig. 10.25. The exact mechanism has not yet been identified, but Kim *et al*. [89] have proposed that delayed fracture



10.25 Example of delayed fracture in a deep drawn Fe-22%Mn-0.6%C TWIP steel. Note that the edge of the cup has a residual tensile stress after deep drawing.

© Woodhead Publishing Limited, 2012

is related to martensitic transformation in the presence of residual stresses and possibly hydrogen. They investigated the influence of the $\gamma \rightarrow \alpha'$ and $\gamma \rightarrow \varepsilon$ martensitic transformations. In tensile tests martensite was formed in Fe-18%Mn-0.6%C but Fe-18%Mn-0.6%C-1.5%Al TWIP steels remained free of martensite. Both TWIP steels contained martensite after cup drawing, however, and the amount of martensite was slightly less for the Al-alloyed TWIP steel. Jung *et al*. [90] compared the hydrogen embrittlement of different types of TRIP steels and TWIP steels after cathodic hydrogen charging. They report that the Fe-15%Mn-0.45%C-1%Al and Fe-18%Mn-0.6%C-type TWIP steels, with and without Al additions, contained less hydrogen and were much more resistant to embrittlement after U-bend and cup drawing tests.

10.3.6 Fatigue properties

The performance of 1160 MPa tensile strength Fe-22%Mn-0.52%C TWIP steel [91] during cyclic loading has been reported to be influenced by pre-straining. A significant longer fatigue life was achieved when the TWIP steel was pre-deformed. This was explained by the formation of new twins during the pre-deformation and the fact that these twins were hindering the dislocation motion. This lead to a stable deformation response in cyclic loading and a longer fatigue life. When tested in the as-received state, the dislocation density decreased and the existing twins widened, leading to a cyclic softening due to a lack of dislocation-twin interaction, and a lack of nucleation of new twins. Hamada *et al*. [92] studied the high cycle fatigue behavior of Fe-22.3%Mn-0.6C (SFE: 26 mJ/m^2), Fe-17.8%Mn-0.6%C with a 200 ppm Nb addition (SFE: 23 mJ/m^2) and Fe-16.4%Mn-0.29%C-1.54%Al (SFE: 19 mJ/m^2). The TWIP steels were studied in bending fatigue using a zero mean stress. They report that the three steels had the same 2×10^6 cycles fatigue stress limit of 400 MPa, i.e. well above the yield stress of the steels. The ratio of fatigue limit to tensile strength was in the range 0.42–0.48, i.e. common to austenitic steels. No twins or ε-martensite was formed during the fatigue test, but fatigue cracks nucleated at intersections of slip band and grain boundaries and annealing twin boundaries.

10.3.7 Ultrafine grained (UFG) TWIP steel

Ueji *et al*. [93] have reported that UFG Fe-31%Mn-3%Al-3%Si TWIP steel retained a considerable ductility in contrast to Al or IF steel. Bouaziz *et al*. [94] have studied the properties of nano-structured Fe-22%Mn-0.6%C TWIP steel obtained by a combination of cold deformation and recovery annealing. The process decreases the dislocation density and retains the very dense nano-scale twin microstructure, leading to very high yield stresses and adequate elongations.

© Woodhead Publishing Limited, 2012

10.4 Twinning-induced plasticity (TWIP) industrialization

The considerable interest in high Mn TWIP steels is due to their superior mechanical properties. Compared to standard low carbon steels, TWIP steels have high C and Mn contents. When Al is added, the content also tends to be high. It is clear that the cost issue will be important in addition to remaining technical problems. Ferro-manganese is reportedly rich in P. This will require more attention during steelmaking. Whereas TWIP steels have demonstrated their formability in complex shapes despite their high strength, the behavior in stretch forming, in particular during hole expansion, is not as good as expected, when compared, for example, to that of an IF steel. This is mainly due to the absence of post-uniform strain, which is related to the strain rate sensitivity.

The application of Zn and Zn alloy coatings is currently not being considered, but there are indications that a MnO surface layer is formed during continuous annealing. This MnO surface layer will very likely prevent coating adhesion, and electrolytic Zn deposition will probably remain the preferred route for coating TWIP steels.

The need to study delayed fracture remains important. It is very likely related to hydrogen-induced cracking but this will require further fundamental analysis.

Not much has been reported with regard to welding of TWIP steels. In addition to the technical aspects, the possible health hazards related to Mn-containing welding fumes should be considered [95, 96]. Mn has a low vapor pressure, and adequate ventilation for the removal of Mn-rich fumes should be installed. Whereas Mn is an important trace element required for normal metabolic processes, Mn overexposure may be the cause of Mn-induced Parkinson-like symptoms which have been well documented.

10.5 Conclusions

The present review on the properties of high Mn twinning-induced plasticity steels clearly shows that the Fe-15-30%Mn alloy system with additions of C, Al and/or Si to fully stabilize the fcc phase and control the SFE within the narrow range of 15–30 mJ/m^2, results in steels with a very wide range of mechanical properties which may make this relatively new class of steels of interest for many applications. The physical metallurgy of TWIP steels is still relatively limited and the following aspects need to receive an in-depth analysis: the twinning mechanism, texture evolution, and delayed fracture. The determination of the twinned volume fraction remains a challenge and is needed to evaluate the different models proposed to explain the mechanical behavior of TWIP steels. The distribution of the twinning as it relates to the

© Woodhead Publishing Limited, 2012

formation of texture components must also be given a clear analysis. The delayed fracture problem is still not understood. In particular, the complex interaction of factors related to transformation, residual stresses, and the influence of hydrogen has made the issue particularly difficult to address.

The review has also highlighted the lack of fundamental knowledge on the effect of the anti-ferromagnetic transition on the properties of TWIP steel. There are clear indications that it may be of major importance. In addition, secondary issues of less fundamental and scientific nature, but critically related to the possibility that these steels may find widespread use, must be addressed.

10.6 Acknowledgements

This research was supported by the World Class University (WCU) program through the National Research Foundation of Korea funded by the Ministry of Education, Science and Technology (R32-2009-000-10147-0). The author gratefully acknowledges the contributions of Dr Gwangeun Chin of the POSCO Technical Laboratories in Gwangyang, South Korea, Mr Jinkyung Kim and Ms Lei Chen both of POSTECH-GIFT, in Pohang, South Korea. The collaboration with Dr H. Beladi Dr I. B. Timokhina, both of Deakin University in Geelong, Australia, and Professor Y. Estrin of Monash University and the CSIRO Division of Process Science and Engineering in Australia was also much appreciated.

10.7 References

[1] O. Grässel, L. Kruger, G. Frommeyer, L. Meyer, *Int. J. Plasticity*, 16, 2000, 1391
[2] O. Grässel, G. Frommeyer, C. Derder, H. Hofman, *J. Phys. IV France*, 60, 1997, 383
[3] G. Frommeyer, U. Brux, P. Neumann, *ISIJ International*, 43, 2003, 438
[4] A. Prakash, T. Hochrainer, E. Reisacher, H. Riedel, *Steel Research International*, 79, 2008, 645
[5] H. Schuman, *Neue Hutte*, 17, 1971, 605
[6] L. Remy, A. Pineau, *Mat. Sci. Eng.*, 28, 1977, 99
[7] T.W. Kim, *Mat. Sci. Eng. A*, 160, 1993, 13
[8] Y.G. Kim, T.W. Kim, S.B. Hong, *Proceedings of the ISATA*, Aachen, Germany, 1993, 269
[9] S. Allain, PhD Thesis, INPL, Nancy, 2004
[10] S.K. Kim, J. Choi, S.C. Kang, I.R. Shon, K.G. Chin, POSCO technical report, vol. 10, 2006, 106
[11] V.T. Witusiewicz, F. Sommer, E.J. Mittemeijer, *J. Phase Equilib. Diff.*, 25, 2004, 346
[12] J.K. Jung, O.Y. Lee, Y.K. Park, D.E. Kim, K.G. Jin, S.K. Kim, K.H. Song, *J. Korean Inst. Met. and Mater.*, 46, 2008, 627

© Woodhead Publishing Limited, 2012

[13] J.P. Hirth, *Metallurgical Transactions*, 1, 1970, 2367
[14] S.M. Cotes, A. Fernandez Guillerment, M. Sade, *Metall. Trans. A*, 35A, 2004, 83
[15] P.H. Adler, G.B. Olson, W.S. Owen, *Metall. Trans. A*, 17A, 1986, 1725
[16] S. Allain, J.-P. Chateau, O. Bouaziz, S. Migot, N. Guelton, *Mater. Sci. Eng. A*, 387–389, 2004, 158
[17] M. Hillert, M. Jarl, *CALPHAD*, 2, 1978, 227
[18] G. Inden, *Physica B*, 103, 1981, 82
[19] X.J. Jin, T.Y. Hsu, *Mater. Chem. Phys.*, 61, 1999, 135
[20] L. Li, T.Y. Hsu, *CALPHAD*, 21, 1997, 443
[21] J. Jun, C. Choi, *Mater. Sci. Eng. A*, 257, 1998, 353
[22] S. Takaki, H. Nakatsu, Y. Tokunaga, *Mater. Trans. JIM*, 34, 1993, 489
[23] Y.K. Lee, C.S. Choi, *Metall. Mater. Trans. A*, 31A, 2000, 355
[24] A. Saeed-Akbari, J. Imlau, U. Prahl, W. Bleck, *Metall. Mater. Trans. A*, 40A, 2009, 3076
[25] J. Kim, S.-J. Lee, B.C. De Cooman, Unpublished results, 2011
[26] S. Curtze, V.-T. Kuokkala, A. Oikari, J. Talonen, H. Hänninen, *Acta Mater.*, 59, 2011, 1068
[27] I.A. Yakubtsov, A. Aripour, D.D. Perovic, *Acta Materialia*, 4714, 1999, 1271
[28] A.P. Miodownik, *Z. Metallkunde*, 89, 1998, 840
[29] J. Nakano, P.J. Jacques, *CALPHAD*, 34, 2010, 167
[30] P.H. Adler, G.B. Olson, W.S. Owen, *Metall. Trans. A*, 17, 1986, 1725
[31] A. Dumay, J.-P. Chateau, S. Allain, S. Migot, O. Bouaziz, *Mater. Sci. Eng. A*, 483–484, 2008, 184
[32] J.-E. Jin, Y.-K. Lee, *Mater. Sci. Eng. A*, 527, 2009, 157
[33] B.X. Huang, X.D. Wang, L. Wang, Y.H. Rong, *Metall. Mater. Trans. A*, 39A, 2008, 717
[34] X. Tian, H. Li, Y. Zhang, *J. Mater. Sci.*, 43, 2008, 6214
[35] X.D. Wang, B.X. Huang, Y.H. Rong, *Phil. Mag. Letters*, 88, 2008, 845
[36] H. Idrissi, L. Ryelandt, M. Veron, D. Schryvers, P.J. Jacques, *Scripta Mater.*, 60, 2009, 941
[37] M.A. Meyers, O. Vohringer, V.A. Lubarda, *Acta Mater.*, 49, 2001, 4025
[38] J.A.Venables, *Phil. Mag.*, 6, 1961, 379
[39] J.A.Venables, *Phil. Mag*, 30, 1974, 1165
[40] J.A. Venables, *J. Phys. Chem. Solids*, 1964, 25, 693
[41] P. Pirouz, *Scripta Metall.*, 21, 1987, 1463
[42] K.P.D. Lagerhöf, J. Castaing, P. Pirouz, A.H. Heuer, *Phil. Mag. A*, 82, 2002, 2841
[43] L. Bracke, L. Kestens, J. Penning, *Scripta Mater.*, 61, 2009, 220
[44] M.A. Meyers, O. Vöhringer, V.A. Lubarda, *Acta Mater.*, 49, 2001, 4025
[45] S. Muira, J.I. Takamura, N. Narita, *Trans. J. Inst. Met. Suppl.*, 9, 1968, 555
[46] T.S. Byun, *Acta Mater.*, 51, 2003, 3063
[47] S. Kibey, J.B. Liu, D.D. Johnson, H. Sehitoglu, *Acta Mater.*, 55, 2007, 6843
[48] S. Kibey, L.L. Wang, J.B. Liu, H.T. Johnson, H. Sehitoglu, D.D. Johnson, *Phys. Rev. B*, 79, 2009, 214202
[49] J.G. Sevillano, *Scripta Mater.*, 60, 2009, 336
[50] O. Bouaziz, N. Geulton, C. Scott, *Scripta Mater.*, 58, 2008, 484
[51] O. Bouaziz, N. Geulton, *Mater. Sci. Eng. A*, 319–321, 2001, 246
[52] S. Allain, J.-P. Chateau, O. Bouaziz, *Mater. Sci. Eng. A*, 387–389, 2004, 143

© Woodhead Publishing Limited, 2012

[53] U.F. Kocks, H. Mecking, *Acta Metall*., 32, 1981, 1865
[54] S. Allain, J.-P. Chateau, D. Dahmoun, O. Bouaziz, *Mater. Sci. Eng. A*, 387–389, 2004, 272
[55] M.N. Shiekhelsouk, V. Favier, K. Inal, M. Cherkaoui, *Int. J. Plasticity* 25, 2009, 105
[56] J. Kim, B.C. De Cooman, Unpublished results, 2010
[57] Y. Estrin, L.P. Kubin, *Acta Metall*., 34, 1986, 2455
[58] G. Dini, R. Ueji, A. Najafizadeh, S.M. Monir-Vaghefi, *Mater. Sci. Eng. A*, 527, 2010, 2759
[59] D. Barbier, N. Gey, S. Allain, N. Bozzolo, M. Humbert, *Mater. Sci. Eng. A*, 500, 2009, 196
[60] P. Yang, Q. Xie, L. Meng, H. Ding, Z. Tang, *Scripta Mater.*, 55, 2006, 629
[61] L. Meng, P. Yang, Q. Xie, H. Ding, Z. Tang, *Scripta Mater.*, 56, 2007, 931
[62] I. Karaman, H. Sehitoglu, Y.I. Chumlyakov, H.J. Maier, I.V. Kireeva, *Scripta Mater.*, 44, 2001, 337
[63] S. Vercammen, B. Blanpain, B.C. De Cooman, P. Wollants, *Acta Mater.*, 52, 2004, 2005
[64] L. Bracke, K. Verbeken, L. Kestens, J. Penning, *Acta Mater.*, 57, 2009, 1512
[65] K. Yan, D.G. Carr, M.D. Callaghan, K.-D. Liss, H. Li, *Scripta Mater.*, 62, 2010, 246
[66] R. Ueji, K. Harada, N. Tsuchida, K. Kunishige, *Mater. Sci. Forum*, 561–565, 2007, 107
[67] P. Sahu, S. Curtze, A. Das, B. Mahato, V.-T. Kuokkala, S. Gosh Chowdhury, *Scripta Mater*., 62, 2010, 5
[68] W.A. Curtin, D.L. Olmsted, L.G. Hector Jr, *Nature Materials*, 5, 2006, 875
[69] S. Allain, P. Cygy, C. Scott, J.-P Chateau, A. Rusinek, A. Deschamps, *Int. J. Mat. Res*., 99, 2008, 734
[70] L. Chen, H.-S. Kim, S.-K. Kim, B.C. De Cooman, *ISIJ Int*., 47, 2007, 1804
[71] J.-K. Kim, L. Chen, H.-S. Kim, S.-K. Kim, Y. Estrin, B.C. De Cooman, *Metall. Mater. Trans. A*, 40A, 2009, 3147
[72] P.D. Zavattieri, V. Savic, L.G. Hector Jr, J.R. Fekete, W. Tong, Y. Xuan, *Int. J. Plasticity*, 25, 2009, 2298
[73] L. Bracke, PhD Thesis, Ghent University, Ghent, Belgium, 2006
[74] B.S. Berry, *Acta Metall*., 10, 1962, 271
[75] H. Numakura, K. Kashiwazaki, H. Yokoyama, M. Koiwa, *J. Alloys Compounds*, 310, 2000, 344
[76] M.S. Blanter, I.S. Golovin, R. De Batist, S.A. Golovin, *Physica Status Solidi* (a), 178, 2000, 621
[77] S.M. Teus, V.N. Shyvanyuka, V.G. Gavriljuk, *Acta Mater.*, 54, 2006, 3773
[78] G.V. Serzhantova, N.Ya. Matveeva, I.S. Golovin, A.A. Golovin, *Met. Sci. Heat Treat*., 39, 1997, 376
[79] K.S.B. Rose, S.G. Glover, *Acta Metall*., 14, 1966, 1505
[80] M.G. Ulitchny, R. Gibala, *Metall. Trans. A*, 4A, 1973, 497
[81] C. Godoy, E.M. Paula E Silva, *Metall. Mater Trans. A*, 32A, 2001, 2271
[82] J.A. Slane, C. Wolverton, R. Gibala, *Mater. Sci. Eng. A*, 370, 2004, 64
[83] J.A. Slane, C. Wolverton, R. Gibala, *Metall. Mater. Trans. A*, 35, 2004, 2239
[84] K. Oda, H. Fujimura, H. Ino, *J. Phys.: Condens. Matter*, 6, 1994, 679
[85] A. Biscarini, R. Campanella, B. Coluzzi, F.M. Mazzolai, *J. Phys. IV*, 6, 1996, C8-51

© Woodhead Publishing Limited, 2012

[86] Y.N. Dastur, W.C. Leslie, *Metall. Trans. A*, 12A, 1981, 749
[87] W.S. Owen, M. Grujicic, *Acta Mater.*, 47, 1999, 111
[88] M. Fujita, Y. Kaneko, A. Nohara, H. Saka, R. Zauter, H. Mughrabi, *ISIJ Int.*, 34, 1994, 697
[89] Y. Kim, N. Kang, Y. Park, G. Kim, S. Kim, K. Cho, *J. Korean Inst. Met. Mater.*, 46, 2008, 780
[90] J.K. Jung, O.Y. Lee, Y.K. Park, D.E. Kim, K.G. Jin, *Korean J. Mater. Res.*, 18, 2008, 394
[91] T. Niendorf, C. Lotze, D. Canadinc, A. Frehn, H.J. Maier, *Mater. Sci. Eng. A*, 499, 2009, 518
[92] A.S. Hamada, L.P. Karjalainen, J. Puustinen, *Mater. Sci. Eng. A*, 517, 2009, 68
[93] R. Ueji, N. Tsuchida, H. Fujii, A. Kondo, K. Kunishige, *J. Japan Inst. Metals*, 71, 2007, 815
[94] O. Bouaziz, C.P. Scott, G. Petitgrand, *Scripta Mater.*, 69, 2009, 714
[95] Y. Kim, *Korean J. Occup. Environ. Med.*, 21, 2009, 87
[96] K.M. Erikson, K. Thompson, J. Aschner, M. Aschner, *Pharmacol. Ther.*, 113, 2007, 369

© Woodhead Publishing Limited, 2012

11

Phase transformations in maraging steels

W. SHA, Queen's University Belfast, UK, H. LEITNER, University of Leoben, Austria, Z. GUO, Sente Software Ltd, UK and W. XU, ArcelorMittal Global R&D Gent, Belgium

Abstract: Research on the kinetics of precipitate formation and austenite reversion in maraging steels has received great attention due to their importance to steel properties. Judging from the literature in recent years, research into maraging steels has been very active, mainly extending to new types of steels, for new applications beyond the traditional strength requirements. This chapter provides an in-depth overview of the literature in this area. In addition, the kinetics of precipitate formation are analysed using the Johnson–Mehl–Avrami (JMA) theory.

Key words: precipitation kinetics, austenite, Johnson–Mehl–Avrami theory, computer modelling.

11.1 State of the art of ultra high strength steels

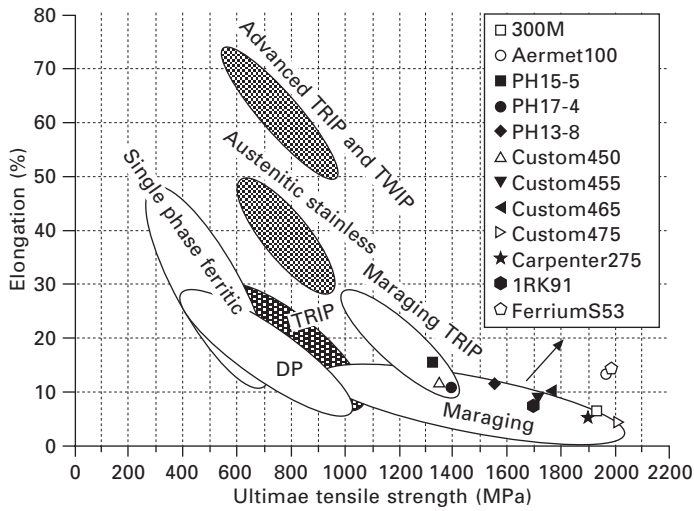
Steels combining properties of ultra high strength (UHS) and good ductility are of great importance in automotive, aerospace, nuclear, gear, bearing and other industries. They are the future key materials for lightweight engineering design strategies and corresponding CO_2 savings. Driven by the development of metallurgy and in response to commercial demands, both academia and industry have made great efforts to develop a large variety of steel grades and processing technology, and hence achieved continuous improvement for some decades.

Conventionally produced bulk high strength steels are known as high-strength low-alloy (HSLA) or microalloyed steels. This family of steels usually has a strength not exceeding 700–800 MPa and possesses a microstructure of fine grained ferrite that has been strengthened with carbon and/or nitrogen precipitates of titanium, vanadium or niobium. These steels can be manufactured under relatively well-established processing conditions and have been widely applied for weight reduction in automotive and general construction applications. In order to further enhance the combination of strength and ductility, more alloying elements have been added and more sophisticated alloy systems have been designed employing various mechanisms including dual-phase (DP) steels, transformation-induced plasticity (TRIP)

© Woodhead Publishing Limited, 2012

steels, twinning-induced plasticity (TWIP) steels and maraging steels. Typical strength–ductility profiles of those steel families are shown in Fig. 11.1.

Dual-phase steels have a microstructure of mainly soft ferrite, with islands of hard martensite dispersed throughout. The strength level of these grades is related to the amount of martensite in the microstructure along with its distribution and morphology. TRIP steels are multiphase grades that involve special alloying and heat treatments to stabilise some amount of austenite at room temperature embedded in a primary ferritic matrix. During plastic deformation and straining, the retained austenite progressively transforms to martensite with increasing strain. This leads to a volume and shape change within the microstructure, which accommodates the strain and increases the ductility. Unlike DP and TRIP steels, TWIP steels generally possess a fully austenitic microstructure at room temperature. The formation of mechanical twins during deformation generates high strain hardening, preventing necking and thus maintaining a very high strain capacity and achieving a better combination of strength and ductility. Another important category of UHS steels is maraging steels, in which martensite is formed upon quenching following solution treatment and consequently further strengthened by the formation of various strengthening precipitates such as Cu clusters, Ni_3Ti, NiAl and other types of intermetallics at a moderate temperature of about 500°C. The superior properties of maraging steels, such as ultra high strength, high ductility, good hardenability, good weldability, simple heat treatment without deformation steps, sometimes in combination with good corrosion resistance, have led to widespread application of maraging steels



11.1 The strength–ductility profile of various steels. The symbols indicate the properties of existing high-end maraging steel grades.

© Woodhead Publishing Limited, 2012

for demanding applications. The composition and mechanical properties of some successful maraging steel grades are summarised in Table 11.1. All steels in this table except 300M and Aermet 100 are stainless grades.

In applications of UHS steels, such as in the automotive, aerospace and nuclear industries, the materials are usually subjected to extreme mechanical loads and harsh environmental conditions in which corrosion is an important issue. However, the most commonly used steels for these applications, such as maraging 300M for aircraft landing gear, and DP/TRIP in the automotive industry, are non-stainless steel grades. Consequently, a specialised and costly coating or plating process has to be employed for corrosion protection. From manufacturing, environmental and reliability considerations, a stainless steel with equivalent mechanical properties but not requiring a corrosion protective coating would be an attractive alternative. Among existing stainless steels, the majority are austenitic, ferritic or duplex (austenite and ferrite) grades. Therefore, much effort for developing ultra high strength stainless steels has been undertaken, employing martensite as the matrix and strengthening further by various precipitates, while a high Cr content is imposed to ensure corrosion resistance. Some successful grades of these maraging stainless steels are shown in Table 11.1. Notwithstanding the efforts to develop high strength and high ductility stainless steels, Table 11.1 shows that few stainless steels meet the properties of their non-stainless counterparts in terms of strength and ductility, because of the nature of ferrite and austenite.

11.2 Types of maraging steels

Precipitation hardening is one of the most effective mechanisms for increasing the strength of metallic high performance materials. The chemical and crystallographic relations of particles and matrix determine the precipitation behaviour and consequently the material's properties. Precipitation hardening was discovered a century ago by Alfred Wilm (1911) in aluminium alloys. The principle of particle strengthening is hindering of dislocation movement by the precipitation of nanometre-sized particles. In steels, particle strengthening can either be caused by the precipitation of carbides, e.g., in so-called secondary hardening low-alloy steels, or intermetallic phases, e.g. in so-called maraging steels. Secondary hardening steels are also the major steel grade for today's tool steels. Generally, secondary hardening steels exhibit a complex microstructure depending on alloy composition and the heat treatment applied. The heat treatment consists of hardening, which denotes austenitising in the gamma phase field followed by quenching and tempering, usually several times. The precipitation of the nanometre-sized carbides has been the focus of numerous studies, and is still a subject of research activities.

The second group of particle-strengthened steels, the maraging steels, was

© Woodhead Publishing Limited, 2012

Table 11.1 Compositions (wt%), yield strength (YS), ultimate tensile strength (UTS) and elongation (El) of some successful grades of maraging steels

Alloy	C	Cr	Ni	Mo	Cu	Mn	Si	Others	YS (MPa)	UTS (MPa)	El
300M	0.4	0.8	1.8	0.4		0.8	1.6	V (0.05)	1586	1995	0.10
Aermet 100	0.23	3.10	11.1	1.2				Co (13.4)	1724	1965	0.14
PH15-5	<0.07	14–15.5	3.5–5.5		2.5–4.5	<1.0			1228	1325	0.16
PH17-4	<0.07	15.5–17.5	3.0–5.0		3.0–5.0	<1.0	<1.0		1275	1399	0.11
PH13-8	<0.05	12.3–13.3	7.5–8.5	2.0–2.5		<0.1		Al (0.90–1.35)	1448	1551	0.12
Custom450	<0.05	14.0–16.0	5.0–7.0	0.5–1.0	1.3–1.8	<1.0	<1.0		1296	1351	0.12
Custom455	<0.05	11.0–12.5	7.5–9.5		1.5–2.5	<0.5	<0.5	Ti (0.8–1.4), Nb (0.1–0.5)	1689	1724	0.10
Custom465	<0.02	11.0–12.5	10.8–11.3	0.75–1.25		<0.25		Ti (1.5–1.8)	1707	1765	0.11
Custom475	<0.01	10.5–11.5	7.5–8.5	4.5–5.5		<0.5		Co (8.0–9.0), Al (1.0–1.5)	1972	2006	0.05
Carpenter275	<0.02	11.0–12.5	10.8–11.3	0.75–1.25		<0.25		Ti (1.55–1.80), Nb (0.15–0.30)	1758	1896	0.06
1RK91	0.01	12.2	9.0	4.0	1.95	0.32	0.15	Ti (0.87)	1500	1700	0.08
FerriumS53	0.20	10.0	5.5	2.0				Co (14.0), W (1.0), V (0.3)	1517	1986	0.15

© Woodhead Publishing Limited, 2012

developed over the past 70 years. The term 'maraging' refers to the ageing of martensite, but specifically a martensite that is easily obtained at *low* cooling rates due to a high Ni content in the steel. In addition, these steel grades possess very low carbon content and, as implied above, can belong to the wider group of ultra high strength steels. Their development started in the 1940s in the USA with the work of Clarence Bieber, when he noticed that magnetic Fe-Ni-Ti-Al alloys could be hardened significantly by heat treatment (Mihalisin and Bieber, 1966). After an initial development period and the addition of Co and Mo, the first applications of maraging steels were set out in the 1960s. Then, the primary goal was to develop high strength steels for submarine hulls, but maraging steels proved unsuitable for these applications. However, in addition to a developing market for specialised aerospace and military applications of these first maraging grades, applications for tools and dies (Shackson, 1991) also became common. Due to the sharp drop in availability and rising cost of Co in the late 1970s, alternatives to cobalt-containing maraging steels were in demand. Thus, much effort was made on developing Co-free maraging steels with appropriate mechanical properties (Wilson, 1989; Sha and Guo, 2009). This resulted in a variety of steels with different precipitating elements, e.g. Al, Ti and Cu, and additionally, alloys with lowered Ni contents. One example of these developments is the PH13-8Mo types (Sha and Guo, 2009). These cobalt-free alloys generally have inferior properties to the cobalt-containing grades, but their properties appear satisfactory for their designed applications, and the absence of cobalt is a distinctive cost advantage.

Intermetallic phases have many specific features in which they differ from carbides, and thus materials that are strengthened by intermetallic precipitates are of great interest for industrial applications. Specifically, they differ from carbides in the following ways:

- Intermetallic phases are formed during primary crystallisation without eutectic transformation, because of which they distribute much more evenly in the cast steel and consequently also in the deformed steel than carbides do. Because of the primary crystallisation we already have a homogeneous distribution in the as-cast state, which is not the case for eutectic solidification. When such a material is deformed the distribution is still homogeneous. In contrast, eutectic carbides, which actually form a network, become more or less homogeneously distributed by deformation (forging or rolling) which is always worse. Intermetallic particle size is usually also smaller, up to 2–3 μm in diameter. Because of this, intermetallic phases have a less detrimental effect on the strength and ductility and on the variations of these properties depending upon the degree of deformation.
- Intermetallic phases precipitate from supersaturated solution during

© Woodhead Publishing Limited, 2012

ageing to result in precipitation hardening. The composition of these precipitated phases does not differ from that of the phases mentioned above, i.e., appearing during solidification and present in hot rolling, etc. Precipitation of intermetallic phases is characterised by the following essential features:

  - The dispersion of intermetallic particles being formed is significant: at the maximum hardness, their size is less than 5–20 nm and the distances between particles around 100 nm, which is lower than the respective values for carbides.
  - The distribution of precipitated particles is relatively uniform, since they form in low-carbon or carbon-free martensite (or austenite), especially when Ni is present in the solution. For that reason, the embrittlement effect of the precipitation hardening, even with fine particles, is weaker than that of carbides. However, the embrittling effect of intermetallics does increase with increasing volume fraction.
  - The strengthening effect of precipitated intermetallics is very high, greater than with carbides. It is a function of the structure of the matrix, being greater for a martensitic matrix when compared to an austenitic one. Precipitation hardening increases the hardness by 20–40 HRC for carbon-free martensite (against 3–10 HRC with carbides) and by ~30 HRC for austenite. This is due to the more refined dispersion of intermetallic phases precipitated, with higher volume fractions than carbides.

- The temperatures of precipitation hardening which produce the maximum rise in hardness depend on the composition of the metallic matrix and the type of precipitated intermetallic compounds. For martensitic steels, they are lower when intermetallic compounds $(Fe,Ni,Co)_7(Mo,W)_6$ and $(Fe,Cr)_3(Ti,Al)$ precipitate, around 500–550°C, and higher for the intermetallic phase $(Fe,Co)_7(W,Mo)_6$, around 580–650°C. In austenitic alloys, these processes are shifted towards still higher temperatures, 750–800°C and higher. For that reason, steels based on carbon-free martensite can acquire a very high hardness, up to 68–69 on the Rockwell hardness scale (HRC), and an increased thermal stability, up to 600–720°C, depending on the type of intermetallic phase. Austenitic steels have a still higher thermal stability, but a lower hardness.
- During precipitation hardening of nickel-containing steels, their hardness rises intensively during the first 10–15 minutes, but then attains its maximum only after a long holding, 5–10 hours, instead of 30–40 minutes required in carbide strengthening.
- Coarsening of precipitated phases and, therefore, reduction in hardness, occur at correspondingly higher temperatures of ageing.

© Woodhead Publishing Limited, 2012

Generally, there are different ways as to how steel grades can be classified, e.g., according to their composition or strength levels. Such a classification is also possible for maraging steels. In the authors' opinion, a classification according to the main alloy system gives the best overview for maraging steels. The Fe-Ni-Mo system is briefly described in the following.

The first alloys, e.g. Fe-28Ni-4Ti-4Al, identified by Bieber (1960) and further work with the Co-Mo hardening system led to the development of the well-known maraging steels based on the Fe-Ni-Mo system, namely the 18Ni (200), 18Ni (250) and 18Ni (300) alloys (Table 11.2). The numbers in parentheses refer to the nominal yield strengths in ksi (pound-force per square inch, lbf/in^2) in the aged condition. Titanium was also added to this group of alloys as a supplemental hardener. In these alloys, hardening is produced by the combination of Co and Mo, as Co lowers the solubility of Mo and thus increases the amount of Mo-rich precipitates that form during ageing. A number of studies have been conducted on the precipitation behaviour of these maraging steels. Overall, the following precipitation reactions take place during ageing. Strengthening in the underaged conditions is caused by Mo-rich zones. With further ageing, the metastable orthorhombic Ni_3Mo forms which transforms into $Fe_2(Mo,Ti)$ hexagonal Laves phase after longer ageing. The formation of Ni_3Mo is accelerated by Co. However, it is suggested that higher Ti contents (alloy 350) lead to the formation of Ni_3Ti instead of Ni_3Mo.

As mentioned above, around 1978–1980, development of cobalt-free grades was promoted (Wilson, 1989; Sha and Guo, 2009). Considering that the goal was the development of high fracture toughness in cobalt-free maraging steel, various elements that might successfully substitute for Co were considered. An analysis of a number of variants revealed that the alloy should contain 3% Mo and 1.4% Ti to achieve the desired yield strength of 250 ksi (1700 MPa) with good transverse ductility. Ni_3Ti was found to be the major precipitation-hardening phase in cobalt-free maraging steels, whereas the achieved yield strength rises with increased Mo- and Ti-contents (up to 2400 MPa). The mechanism of strengthening and toughening is the same in low and high Mo- and Ti-containing alloys. However, the high Mo and Ti alloys additionally contain a large number of coarse particles of type

Table 11.2 Nominal compositions (wt%) and the respective yield strength (YS) of commercial maraging steels (Inco)

Alloy designation	Ni	Mo	Co	Ti	Al	YS (MPa)
18Ni (200)	18	3.3	8.5	0.2	0.1	1400
18Ni (250)	18	5.0	8.5	0.4	0.1	1700
18Ni (300)	18	5.0	9.0	0.7	0.1	2000
18Ni (350)	18	4.2	12.5	1.6	0.1	2400
18Ni (cast)	17	4.6	10.0	0.3	0.1	1650

© Woodhead Publishing Limited, 2012

Fe_2Ti and $Fe_2(Mo,Ti)$ embedded in the martensite lath boundary or within the lath. Those particles produce a detrimental effect on fracture toughness and ductility.

Other maraging systems include broadly Fe-Ni-Cr and Fe-Ni-Mn, which will be discussed in the following sections.

11.3 Microstructure and precipitates in maraging steels

11.3.1 PH13-8Mo maraging steels

The microstructural constituents that were observed in PH13-8Mo maraging steels include the following:

- δ ferrite
- cubic martensite
- retained and reverted austenite
- nanometre-sized precipitates of intermetallic type
- Laves phase.

A phase that is sometimes present in PH13-8Mo maraging steels is δ ferrite, the high temperature body-centred cubic (bcc) ferrite. The presence of this phase is associated with the alloy composition and production route. Although the solidification path of the PH13-8Mo steel grades is known to be fully ferritic via the δ phase, the transformation of $\delta \rightarrow \gamma$ strongly depends on cooling rate. Thus, large cast sizes and an appropriate composition can provoke the incomplete transformation of $\delta \rightarrow \gamma$.

PH13-8Mo maraging steels receive their excellent combination of strength and ductility by a heat treatment which consists of a first step solution annealing in the temperature range 900–1000°C and subsequent air-cooling to room temperature. When quenched from the austenitic single-phase field after solution annealing, the austenite transforms into a soft, but heavily dislocated Ni-martensite, exhibiting a cubic structure. The martensite in this steel grade is of lath type and it forms a packet that consists of many similar sized laths arranged parallel to each other. Each prior austenite grain includes several lath packets.

Depending mainly upon the Ni content, but also on all other alloying elements, a certain amount of austenite can be retained after quenching to room temperature. Besides this retained austenite, which is the result of a martensite finish temperature below room temperature, a so-called ‘reverted austenite’ can also be present in maraging steels. The occurrence of this reverted austenite also depends upon chemical composition but additionally the applied ageing temperature and time play decisive roles. The reverted austenite emerges from martensite during ageing at temperatures below

© Woodhead Publishing Limited, 2012

the global $\alpha \rightarrow \gamma$ transformation temperature. This is the temperature where the entire material transforms, which is significantely higher than the local temperature because of Ni-enrichment.

Ageing, which is typically carried out in a temperature range of 400–600°C, leads to the precipitation of the strengthening nanometre-sized intermetallic particles. Laves phase formed at higher ageing temperatures has also been observed in this steel grade. However, the nanometre-sized precipitates and the austenite phase fraction have the strongest effect on the mechanical properties of maraging steels and, thus, a more detailed survey of the literature for these aspects is given in the following.

11.3.2 Precipitates

The precipitation behaviour and strengthening mechanisms in cobalt-free maraging steels have been extensively studied by employing a variety of characterisation techniques. It has been shown that maraging steels containing Ni and Al are strengthened by the formation of the ordered β'-NiAl phase with B2 (CsCl) superlattice structure (Sha and Guo, 2009). This structure consists of two interpenetrating primitive cubic cells, where the Al atoms occupy the cube corners of the first sublattice and the Ni atoms occupy the cube corners of the second sublattice. The lattice constant of the stoichiometric composition is 0.2887 nm (Kitabjian and Nix, 1998). This is very close to the lattice constant for ferrite, which has a value of 0.28664 nm (Self *et al.*, 1981). Because of this, the NiAl precipitates are coherent with the matrix and even remain coherent after long ageing times (Seetharaman *et al.*, 1981). Precipitation takes place immediately after heating the material to the ageing temperature. Sha and Guo (2009) reported Ni- and Al-rich clusters after just 6 min of ageing at 593°C and after 40 min of ageing at 510°C. However, the composition of the precipitates, even after longer ageing times, is far from stoichiometric NiAl phase, the precipitates containing a significant amount of Fe (Sha and Guo, 2009). The shape of the precipitates is a matter of debate in the literature. In general, the NiAl phase is believed to be of spherical shape, but some authors assume a change of morphology from spherical to needle- and plate-shaped forms at longer ageing times. However, it is generally thought that their formation proceeds via solute-rich clusters within the martensitic matrix. Out of these nuclei, the coherent NiAl precipitates are formed and distributed uniformly within the matrix (Leitner *et al.*, 2010).

In contrast, it has been reported that strengthening in Ti-containing maraging steels is caused by the precipitation of the η-phase ($Ni_3(Ti,Al)$) (Leitner *et al.*, 2010). The η-phase exhibits a hexagonal lattice with $a = 0.255$ nm and $c = 0.42$ nm. In the literature, some debate exists on the mechanism of formation of the η-phase. In most studies, heterogeneous nucleation on

© Woodhead Publishing Limited, 2012

dislocations is proposed, with subsequent growth taking place via pipe diffusion (Dutta *et al.*, 2001). Others advance the theory that formation of coherent zones on dislocations in the martensitic matrix takes place first, acting as nucleation sites for the η precipitates (Leitner *et al.*, 2010). There is also some discrepancy on the dominating strengthening mechanism in this kind of maraging steels. While the majority of studies attributed strengthening to the formation of Ni_3Ti, others proposed an additional contribution from some B2-type ordering of Fe and Ni atoms in the matrix (Leitner *et al.*, 2010).

A further type of precipitate phase, called G-phase, was found by Gemperle *et al.* (1992) in Ti-containing maraging steels alloyed with Si. The G-phase exhibits the chemical composition $Ti_6Si_7Ni_{16}$ and precipitates primarily on grain boundaries. Depending upon the chemical composition of the alloy, the G-phase ($Ti_6Si_7Ni_{16}$) and the η-phase (Ni_3Ti) can precipitate either simultaneously or separately (Gemperle *et al.*, 1992). The shape of the Ni_3Ti-phase was thought to be rod-like, whereas the G-phase shows a spherical morphology. Later studies revealed that both the spherical G-phase and the rod-shaped η-phase are formed independently out of an undefined precursor phase, which is responsible for strengthening up to peak hardness. Atom probe tomography (APT) was used to follow the precipitation sequence in a Si-free Fe-Cr-Ni-Al-Ti stainless steel during ageing at 525°C (Schober *et al.*, 2009). In that work, instead of splitting into G-phase ($Ti_6Si_7Ni_{16}$) and η-phase (Ni_3Ti), the formation of spherical NiAl particles and elongated $Ni_3(Ti,Al)$ particles out of an undefined precursor phase in the early stages was found.

A further age-hardener in maraging steels is copper. It is used in PH15-5 and PH17-4 alloys as a precipitating hardening element, but also in alloy systems such as 1RK91 (Sandvik in-house grade designation) and C455 (Custom455, a registered trademark of Carpenter Technology Corporation) (for compositions see Table 11.1) as nucleation site for the precipitation of the strengthening causing phase (Schnitzer *et al.*, 2010a).

In the case of 1RK91, the precipitation sequence starts with the formation of a Ni, Ti and Al-rich phase nucleating on Cu-rich clusters (Schnitzer *et al.*, 2010a). During further ageing, $Ni_3(Ti,Al)$ precipitates develop adjacent to Cu-rich precipitates. The C455, which contains less Al and no Mo, forms clusters of Cu, Ti and Ni at the early stages, and they are thought to be a precursor phase of η-Ni_3Ti (Schnitzer *et al.*, 2010a). An extended ageing treatment then leads to the separation of Ni-rich (η-Ni_3Ti) and Cu-rich precipitates. The effect of Cu on the precipitation evolution in PH13-8Mo type maraging steel, which exhibits NiAl and η-phase precipitates, was recently investigated by Schnitzer *et al.* (2010a). This study revealed the formation of NiAl out of a Cu-containing precursor phase and the nucleation of η-phase on independent Cu clusters.

There exists an almost complete picture of precipitation behaviour in

© Woodhead Publishing Limited, 2012

PH13-8Mo type maraging steels. Only the influence of Cu on the formation of G-phase is missing.

Additionally to the strengthening precipitates, the formation of carbides has been observed in maraging steels, although the carbon content is generally very low in such steels. These carbides precipitate adjacent to or inside reverted austenite because of the higher carbon solubility in austenite. The carbides were found to be of type $Cr_{23}C_6$ and $(Cr,Mo)_2C$.

11.4 Reverted austenite and mechanical properties

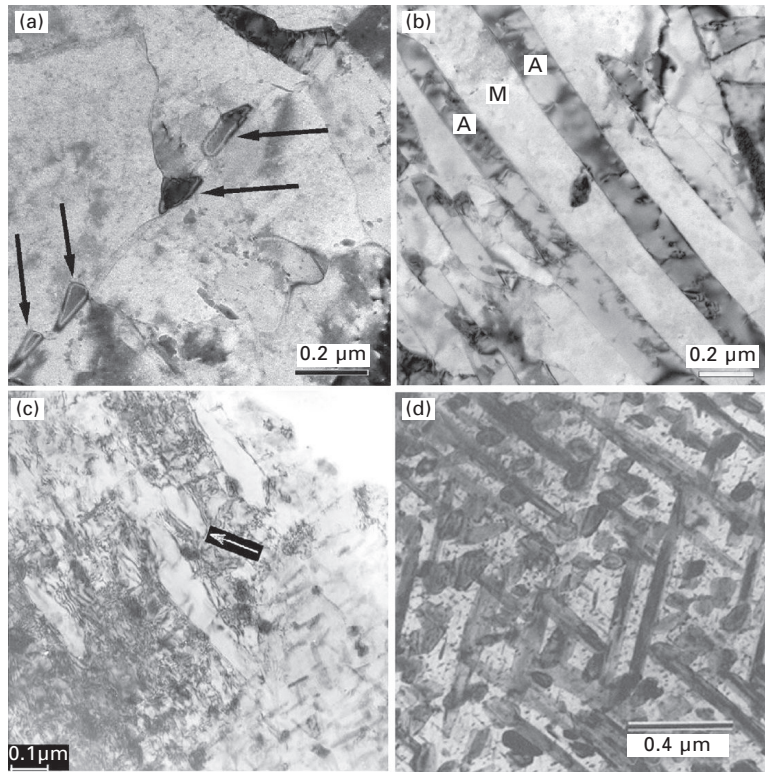
11.4.1 Reverted austenite

In maraging steels, partial reversion from martensite to austenite can take place during ageing below the global $\alpha \rightarrow \gamma$ temperature (Schober *et al.*, 2009). The amount of reverted austenite present after ageing depends on the ageing temperature as well as ageing time (Sha and Guo, 2009). The formation of reverted austenite is reported to be the result of local Ni-enrichment, which arises during ageing. As Ni, one of the major alloying elements in maraging steels, is an austenite stabilising element, the local transition temperature of martensite to austenite is lowered. In this area, the applied ageing temperature is, therefore, higher than the transition temperature from martensite to austenite. Due to this Ni enrichment, this austenite remains stable even when the material is cooled back to room temperature. This type of austenite has to be distinguished from retained austenite, which can also be present in maraging steels after cooling from the solution annealing temperature (Perkas, 1968). Depending on the alloy composition and the applied heat treatment, different morphologies of reverted austenite have been observed in maraging steels, shown in Fig. 11.2. Shiang and Wayman (1988) classified the observed reverted austenite morphologies into three types:

- matrix austenite,
- lath-like austenite, and
- recrystallised austenite.

Matrix austenite (Fig. 11.2(a)) grows either from retained austenite with the same orientation, or nucleates on prior austenite grain boundaries and then forms a single grain. Lath-like austenite (Fig. 11.2(b)) can develop within the martensite lath or grow along the lath boundaries of martensite. The growing direction of the austenite laths is parallel to the martensite lath resulting in a lamellar structure of austenite and martensite. The elongated shape is supposed to be caused by a growth impediment of the adjacent martensite laths. Recrystallised austenite (Fig. 11.2(c)) forms at higher ageing temperatures or longer ageing times, and is characterised by a very low density of defects and dislocations (Viswanathan *et al.*, 2005). In addition, a fourth morphology

© Woodhead Publishing Limited, 2012



11.2 Morphologies of reverted austenite in maraging steels: (a) matrix austenite (Schnitzer *et al.*, 2010b); (b) lath-like austenite (A = austenite, M = martensite) (Schnitzer *et al.*, 2010b); (c) recrystallised austenite (Viswanathan *et al.*, 2005) (reprinted from *Materials Science and Engineering: A*, 398, U.K. Viswanathan, G.K. Dey, V. Sethumadhavan, Effects of austenite reversion during overageing on the mechanical properties of 18 Ni (350) maraging steel, 367–372, 2005, with permission from Elsevier); (d) Widmanstätten austenite (Kim and Wayman, 1990) (reprinted from *Materials Science and Engineering: A*, 128, Sung-Joon Kim, C. Marvin Wayman, Precipitation behavior and microstructural changes in maraging Fe-Ni-Mn-Ti alloys, 217–230, 1990, with permission from Elsevier).

found in maraging steels is Widmanstätten (Fig. 11.2(d)), only evidenced in high Ni-alloyed and Ti-containing maraging steels (Schnitzer *et al.*, 2010b). The morphology of the reverted austenite developed depends on the applied heating rate and the ageing temperature (Schnitzer *et al.*, 2010c).

Independently of morphology, the orientation relationship between austenite and martensite was found to be either of Kurdjumov–Sachs type, with $(110)_{bcc}$ // $(111)_{fcc}$ and $[111]_{bcc}$ // $[110]_{fcc}$, or Nishiyama-Wassermann type with $(110)_{bcc}$ // $(111)_{fcc}$ and $[100]_{bcc}$ // $[110]_{fcc}$ (Schnitzer *et al.*, 2010b).

© Woodhead Publishing Limited, 2012

An important finding for the understanding of the formation of reverted austenite is the fact that the regions of reverted austenite are free of the precipitates causing strengthening. Only carbides precipitate inside the austenite or adjacent to it, due to the higher solubility for carbon in austenite compared to martensite. The formation mechanism of reverted austenite in maraging steels is supposed to be a diffusion-controlled process. It is assumed that the formation of reverted austenite is connected to the dissolution of precipitates, resulting in a local enrichment of austenite stabilising elements (Sha and Guo, 2009). This was also reported for 18% Ni steels, where the formation of reverted austenite was encouraged by the dissolution of Ni_3(Mo,Ti) precipitates. It was also found that the formation of reverted austenite is accompanied by the precipitation of Fe_2Mo (Vasudevan *et al*., 1990). This leads to the assumption that the Ni of the dissolved Ni_3(Mo,Ti) precipitates contributes to the formation of reverted austenite, while the released Mo is used to form Fe_2Mo precipitates.

Others exclude the theory that the formation of reverted austenite is related to the dissolution of precipitates. For example, Sinha *et al*. (1995) suppose that Ni diffuses to dislocations and other defects, resulting in microsegregation of the austenite stabilising elements in localised areas. Hsiao *et al*. (2002) reported that in Cu-containing maraging alloys, such as PH17-4, fine Cu precipitates act as nucleation sites for austenite formation since both copper and austenite exhibit the same crystallographic structure with similar lattice parameter. Kim and Wayman (1990) suggested that the formation of lath-like austenite in high Ni-containing maraging alloys is shear dominated, but assisted by a diffusion-controlled process. Schnitzer *et al*. (2010b) investigated the formation of reverted austenite in PH13-8Mo type maraging steel. The interpretation of the experimental data was supported by thermodynamic and kinetic calculations using the software package MatCalc (Kozeschnik and Buchmayr, 2001). It was shown that the formation of NiAl precipitates and reverted austenite starts from the very beginning of ageing widely independent of each other, i.e. the formation of both, austenite and NiAl nuclei, is thermodynamically possible in the virgin martensitic matrix. Thus, dissolution of precipitates is not necessarily the initial driving factor for the formation of reverted austenite. Consequently, a formation mechanism was proposed as follows: beginning from lath martensite with high dislocation density after solution annealing, NiAl precipitates and reverted austenite nucleate independently. The NiAl precipitates are homogeneously distributed in the martensitic matrix and reverted austenite forms preferentially on prior austenite grain boundaries or on martensite lath boundaries. Growth of reverted austenite is related to dissolution of adjacent NiAl precipitates, whereas the reverted austenite incorporates Ni stemming from the dissolved precipitates. In contrast, the released Al content is transferred to the NiAl precipitates left in the matrix.

© Woodhead Publishing Limited, 2012

11.4.2 Mechanical properties

Maraging steels belong to the group of high-strength steels, i.e. tensile strength >1000 MPa. The achieved strength values range from 1000 MPa up to 3000 MPa. The stress–strain behaviour is characterised by a yield strength that is above 80% of the ultimate tensile strength, i.e., the work hardening is small. The reason for this behaviour is proposed to be as follows. The coherent precipitates introduce a friction stress acting on dislocations, which raises the level of the stress–strain curve without markedly altering the dislocation interactions leading to work hardening.

The following microstructural features were reported to have an influence on the mechanical properties, whereas their influence is different:

- nanometre-sized precipitates
- retained or reverted austenite
- prior austenite grain size.

The required strength and toughness is reached after an ageing treatment, which conforms to the application (Sha and Guo, 2009). Of course, the chemical composition, but also the applied ageing temperature and time, influence types, size and volume fraction of precipitates as well as the amount of austenite and thus the mechanical properties. In maraging alloys, the main strengthening contribution stems from the precipitation of nanometre-scale precipitates (Sha and Guo, 2009). The high strength of maraging steels, thereby, is the result of dense and homogeneous distributed precipitates in the martensitic matrix (Sha and Guo, 2009). Depending upon their size and coherency, they are either sheared or circumvented by dislocations.

Retained and reverted austenite also show a strong influence on the mechanical properties of maraging steels. Reverted austenite is free of precipitates and possesses a much lower yield strength compared to the martensitic matrix (Sha and Guo, 2009). Reverted austenite influences the mechanical properties. Viswanathan *et al*. (2005) observed a pronounced decrease in the yield strength with increasing amount of reverted austenite. Reverted austenite is supposed to increase the ductility and impact toughness (Viswanathan *et al*., 2005). Therefore, for high toughness requirements, increased amounts of reverted austenite are beneficial and the material is subjected to higher ageing temperatures (Squires and Wilson, 1972). On prolonged ageing, coarsening of precipitates also results in an increase in ductility but loss of strength. However, it was reported that the influence of austenite reversion is much more pronounced on softening than the influence of precipitate coarsening (Schnitzer *et al*., 2010b). In the literature, there are also investigations that report a detrimental effect of reverted austenite. Viswanathan *et al*. (2005) showed that the ductility is only increased in the early stages of ageing. Severe embrittlement was noticed in samples subjected

© Woodhead Publishing Limited, 2012

to prolonged ageing (Viswanathan *et al*., 2005). Vylezhnev *et al*. (1993) stated that reverted austenite in a Co-containing maraging steel led to deterioration in ductility at low temperatures as fracture occurs along the boundaries of the martensite packets. However, it is known that the austenite phase in maraging steels is not stable during deformation (Schnitzer *et al*., 2010c), which results in transformation to martensite (the so-called transformation-induced plasticity, TRIP effect). This transformation behaviour also strongly influences the mechanical properties of maraging steels.

Normally, the amount of austenite is associated with the size of precipitates. Schnitzer *et al*. (2010c) performed a study on PH13-8Mo type maraging steel to judge the individual influence of precipitates and reverted austenite on mechanical properties. Calculation revealed that approximately 40% of the loss in yield strength during ageing could be attributed to the influence of higher amounts of reverted austenite. The remaining amount of the observed decrease in strength is due to coarsening of NiAl precipitates.

A further microstructure constituent in maraging steels, which may affect the mechanical properties, is the martensitic matrix and thus, the prior austenite grain size. The grain size depends on the solution treatment temperature as well as time, whereas the martensite lath spacing in maraging steels is independent of the solution treatment temperature (Schnitzer *et al*., 2010c). The influence of the grain size on mechanical properties depends on the nucleation size of the precipitates. When precipitates nucleate homogeneously in the martensitic matrix, no influence of grain size was observed (Schnitzer *et al*., 2009). In contrast, others found that the relationship between yield strength and grain size follows the Hall–Petch equation after ageing when the precipitates nucleate on grain boundaries.

11.5 Evolution of precipitates and the overall process

Adapted from a recent research monograph on maraging steels (Sha and Guo, 2009), Sections 11.5 and 11.6 describe recent theoretical research on the two main types of phase transformation in maraging steels, *precipitation* and *austenite reversion*. Before either of these transformations happen in these steels (during heating), there is a third transformation, which is the martensitic transformation (during cooling). Precipitation and austenite reversion occur in this martensite matrix, the former generally desirable as long as it is not too complete and the latter usually undesirable. In simple terms, precipitation leads to hardening and austenite reversion leads to softening. Although martensitic transformation is a pre-requisite of the functioning of maraging steels, it is easily achievable and its details do not strongly determine the final steel properties, at least to a far lesser extent than precipitation and austenite reversion. For this reason, these sections will not consider the details of the martensitic transformation in maraging steel.

© Woodhead Publishing Limited, 2012

Section 11.5.1 gives a brief discussion of the evolution of precipitates in maraging steels, with particular reference to its complexity in inter-particle spacing. This is followed by the short Section 11.5.2 on the overall transformation process.

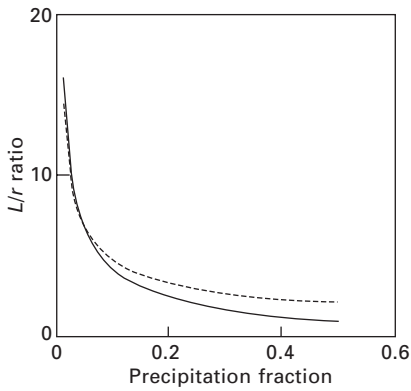
11.5.1 Calculation of inter-particle spacing

When precipitation fraction increases, the particle size should not be ignored when calculating the inter-particle spacing L. Assuming that the precipitates are spherical, the relationship between precipitate fraction f, inter-particle spacing and particle radius r is given by Sha and Guo (2009), which reference also contains the equations developed in the remainder of this chapter:

$$L = (1.23\sqrt{2\pi/(3f)} - 2\sqrt{2/3})r \qquad [11.1]$$

When precipitation fraction increases, the L/r ratio decreases dramatically (Fig. 11.3). L and r become very much comparable when f increases to about 0.1. The simple formula significantly overestimates the inter-particle spacing when the precipitation fraction is large. In addition to Eq. [11.1] for spherical precipitates, there are equations for plate-like particles, which is the case for Ni_3Ti-type precipitates in maraging steels. If the volume fraction can be estimated using the Johnson–Mehl–Avrami (JMA) equation (Section 11.6.1), then particle spacing as a function of time will be known. Such a procedure allows the quantification of age hardening to be carried out accurately.

The size increment of particles during the early ageing period may follow a slower procedure than the classical parabolic growth law would allow, regardless of whether the phase separation follows classical nucleation or



11.3 Comparison of L/r ratio as a function of precipitation fraction, between Eq. [11.1] (solid line) and the simple formula $L/r = \sqrt{2\pi/3f}$ (dotted line).

© Woodhead Publishing Limited, 2012

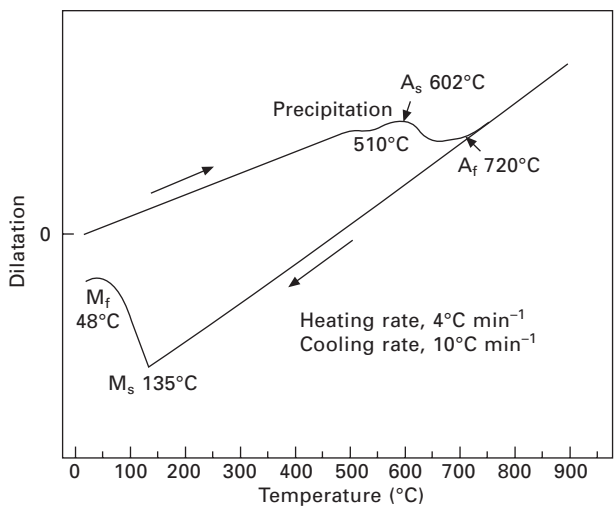
spinodal decomposition. Although sometimes it is difficult to determine the controlling step, and in turn the operating coarsening law, Lifshitz–Slyozov–Wagner (LSW) theory (Lifshitz and Slyozov, 1961; Wagner, 1961) may be used for practical purposes. The LSW theory is the first statistical mechanical formulation of the kinetics of precipitate ageing, for diffusion-limited as well as interface-limited precipitate coarsening. The prediction of LSW theory that the cube of the average length scale of particles increases linearly with time was validated by numerous experiments, even in cases where there was a finite volume fraction of the dispersed phase. In LSW theory, the coarsening rate of a precipitate particle is given by the linear form

$$\frac{dr}{dt} = \frac{K_{LSW}}{r}\left(\frac{1}{r^*} - \frac{1}{r}\right) \qquad [11.2]$$

where r and r^* are the radius of the particle, and the critical radius of the precipitate population, respectively. K_{LSW} is the kinetic coefficient and is independent of the volume fraction of the precipitates.

11.5.2 The overall process

The overall transformation curve can be recorded using dilatometry (Fig. 11.4) measured for a cobalt-free maraging steel as an example. The steel composition is Fe-18.9Ni-4.1Mo-1.9Ti (wt%). Uniform expansion continues until 510°C when a small contraction starts to occur, indicating the start of precipitation at this temperature. This is followed by a small period of linear



11.4 Dilatometry curve of the 2000 MPa grade cobalt-free maraging steel.

© Woodhead Publishing Limited, 2012

expansion with increasing temperature. When the temperature is raised to 602°C, a large contraction appears in the dilatometry curve, which can be taken as the start of austenite formation (A_s). At 660°C, this contraction starts to slow down, until 720°C when the curve resumes linear expansion. Therefore, the austenite transformation ends at around 720°C (A_f). Complete solution is ensured by heating continuously to 900°C and holding at this temperature for 30 minutes. During cooling to room temperature, there is drastic expansion at approximately 135°C, due to the sudden start of rapid transformation from austenite to martensite, corresponding to the martensite start temperature, M_s. Martensite finish temperature (M_f) is about 48°C. Thus, the cobalt-free maraging steel should have a single-phase structure upon cooling to room temperature that is martensite.

A discrepancy in dilatation at room temperature is apparent in Fig. 11.4. In dilatometry curves for T300 (Fe-18Ni-2.4Mo-2.2Ti, wt%) and C350 (Fe-18.77Ni-10.8Co-4.2Mo-1Ti, wt%) (He *et al.*, 2003) recorded in the literature, the cooling curve normally does not return to zero but to below the original point. This residual strain may be induced by the martensite phase transformation, due to both thermal and transformation changes. The yield strength level (2000 MPa) of the commercial cobalt-free T300 steel is the same as the experimental cobalt-free maraging steel used in Fig. 11.4, although the experimental steel, due to its very low impurity levels, has better toughness. The C350 steel is also an ultra-purified steel, reaching a yield strength level of 2400 MPa. The transformation-induced plasticity in the free dilatometry cycle is seen in the martensitic transformation in many experiments (He *et al.*, 2003; Coret *et al.*, 2004). However, the exact mechanism is not clear. It is possible that the lattice has been sheared and it could not return to the original position.

Cobalt raises the martensitic phase transformation temperature. In general, the martensitic transformation temperature in 18Ni maraging steels is 50–100°C higher than in their cobalt-free counterparts. However, controlling correctly the amount of nickel and molybdenum in cobalt-free maraging steels can still ensure complete martensitic transformation upon cooling to room temperature after solution treatment.

11.6 Precipitation kinetic theory in Fe-12Ni-6Mn maraging type alloy

This section concentrates on the quantification or modelling of the precipitation transformation in Fe-12Ni-6Mn maraging steel. In order to develop cheaper alternatives than the classical 18Ni maraging steels (Table 11.2), research was carried out in Russia and Japan, studying maraging in a series of experimental Fe-Ni-Mn alloys. Research with a Fe-12Ni-6Mn alloy showed that age hardening is achieved due to precipitation of θ-NiMn in the lath

© Woodhead Publishing Limited, 2012

martensite, the quenched structure before ageing, as observed using electron microscopy.

11.6.1 Theoretical analysis of the early-stage ageing process

Coherent zones, possibly with a bcc structure, form at the early stages of ageing. After these, e.g. 0.2 hours at 450°C, θ-NiMn forms well before peak hardness. Deformation occurs by dislocations cutting through these coherent zones (or precipitates). Because the increase in yield stress is proportional to the increase in hardness (ΔH) for maraging steels, and applying a coherency-strengthening mechanism, one may get:

$$\Delta H = Ar^{1/2}f^{1/2} \qquad [11.3]$$

where r is radius of the particle, f is volume fraction of the transformed particles, and A is a coefficient relating the increase in hardness to precipitate size and fraction:

$$A = \frac{M_T}{q}(\kappa\varepsilon)^{3/2}\mu\left(\frac{3}{2\pi b}\right)^{1/2} \qquad [11.4]$$

where M_T is the Taylor factor, q is a conversion constant between Vickers hardness and yield strength, κ is a numerical constant between 3 and 4, taken as 3.5, ε is a strain energy constant, μ is the shear modulus of the matrix, taken as 81 GPa, and b is the dislocation Burgers vector.

Since κ, ε, μ and b are all material constants and can be obtained from the literature, the quantification of ΔH is now switched to the determination of the particle size r and precipitation fraction f.

The relationship between ageing time t and radius r of zone or precipitate (assumed spherical) is given by Zener's parabolic relationship:

$$r = \alpha\,(Dt)^{1/2} \qquad [11.5]$$

where α is a constant related to the solid solubility of the precipitate and the matrix and the composition of the alloy, and D is the diffusion coefficient.

When time t is small for the early ageing stage, α can be considered as a constant and calculated following Christian's suggestion for a spherical precipitate and small degree of supersaturation (Christian, 2002):

$$\alpha = \frac{2^{1/2}(c_0 - c_\alpha)^{1/2}}{(c_\theta - c_0)^{1/2}} \qquad [11.6]$$

where c_0 is concentration of the precipitating elements in the matrix before ageing, taken as the sum of Ni and Mn, equal to the composition of the alloy, c_α is the solid solubility of the controlling elements in the parent

© Woodhead Publishing Limited, 2012

phase, and c_θ is the concentration of the elements in the new phase, that is, the θ-NiMn precipitate.

The Johnson–Mehl–Avrami (JMA) equation can be used to describe the relationship between transformation fraction and time at a certain temperature:

$$\frac{f}{f_{eq}} = 1 - \exp[-(kt)^m] \quad [11.7]$$

where f_{eq} is the equilibrium fraction of the precipitation (temperature dependent), k is a reaction rate constant, and m is the Avrami index.

At an early ageing stage, that is, when $kt << 1$, the above equation reduces to the following:

$$f = f_{eq}(kt)^m \quad [11.8]$$

Combining Eqs [11.3], [11.5] and [11.8], one obtains:

$$\Delta H = A(\alpha f_{eq})^{1/2} D^{1/4} k^{m/2} t^{(m/2+1/4)} = (Kt)^n \quad [11.9]$$

where n is the time exponent in the relationship between the increase in hardness and ageing time in the early stage of ageing, $n = (2m + 1)/4$, and K is a temperature-dependent rate constant.

Assuming that K follows the Arrhenius type of equation:

$$K = K_0 \exp\left(-\frac{Q}{RT}\right) \quad [11.10]$$

where K_0 is a pre-exponential term, R is the gas constant, T is temperature (in Kelvin), and the activation energy Q for the precipitation process during ageing can be calculated. Using Eq. [11.10] to replace K in Eq. [11.9] and then taking natural logarithms of both sides, one may get:

$$\ln \Delta H = n\left(\ln K_0 - \frac{Q}{RT} + \ln t\right) \quad [11.11]$$

For a constant increase in hardness ΔH_0 at different temperatures, one will have:

$$\ln t = \frac{Q}{RT} + \frac{\ln \Delta H_0}{n} - \ln K_0 \quad [11.12]$$

Assuming that n is constant, the activation energy Q can be obtained by plotting $\ln t$ versus $1/T$, where t is the time to reach ΔH_0 at temperature T. The slope of the straight line is Q/R as can be seen from the above equation. K_0 can be obtained simultaneously from the interception of the straight line with the $\ln t$ axis. When the activation energy Q and K_0 are known, ΔH during the age hardening can be calculated using Eq. [11.9], in conjunction with Eq. [11.10].

© Woodhead Publishing Limited, 2012

11.6.2 Overall ageing process

There are a few assumptions in the above theory that may prohibit its application to the overall ageing process:

(A1) coherent precipitate strengthening mechanism;
(A2) spherical precipitate (zone or particle);
(A3) constant activation energy;
(A4) $kt << 1$, which allows the simplification from Eq. [11.7] to Eq. [11.8];
(A5) constant α for precipitate growth.

The strengthening is due to coherent precipitates before peak hardness is reached, and the particles do not change to platelets until overageing takes place. These allow assumptions A1 and A2 to be applied to describe the overall ageing period. As to the activation energy, assumption A3, this may change during the ageing process. However, when ΔH_0 takes different values, the calculations to be shown later imply that the activation energy does not vary very much. Therefore, the activation energy will be considered as a constant value in the current model.

Assumptions A4 and A5 will not be acceptable when ageing proceeds beyond the early stage. The growth constant α in Eq. [11.5] is no longer constant when the precipitates continue to form and grow, because the composition of the matrix changes significantly when more precipitates form from the matrix. Consequently, a more accurate way to calculate r is formulated below, considering α as a function of t through the change of c_0, the composition of the matrix. Before ageing takes place, c_0 is the concentration of the precipitating elements in the alloy. Both are considered as the total amount of Ni and Mn.

From Eq. [11.5], the growth rate of particles is given by:

$$\frac{\mathrm{d}r}{\mathrm{d}t} = \frac{1}{2} D^{1/2} \alpha(t) t^{-1/2} + D^{1/2} \frac{\mathrm{d}\alpha(t)}{\mathrm{d}t} t^{1/2} \qquad [11.13]$$

so

$$r = \int D^{1/2} \left(\frac{1}{2} \alpha(t) t^{-1/2} + \frac{\mathrm{d}\alpha(t)}{\mathrm{d}t} t^{1/2} \right) \mathrm{d}t \qquad [11.14]$$

where α can still be calculated from Eq. [11.6]. However, it should be noted that the concentration in the matrix c_0, taken as the sum of Ni and Mn, changes during the ageing process simultaneously with the fraction of the precipitation f, denoted as c_0', therefore:

$$c_0' = c_0 - c_\theta f \qquad [11.15]$$

Thus, for the overall ageing process, we have:

© Woodhead Publishing Limited, 2012

$$\Delta H = AD^{1/4} f_{eq}^{1/2} \left(\int \left(\frac{1}{2} \alpha(t) t^{-1/2} + \frac{d\alpha(t)}{dt} t^{1/2} \right) dt \right)^{1/2} (1 - \exp(-(kt)^m))^{1/2} \quad [11.16]$$

where A is as defined in Eq. [11.4].

In Eq. [11.16], if the transformation fraction f is known (i.e. k is known), the precipitate size r can be calculated (assuming D is known), through the calculation of c_0' and α. As a result, ΔH as a function of time and temperature can be quantitatively described.

11.6.3 Parameter determination

Strengthening

In Eq. [11.16], A can be calculated when parameters M_T, q, κ, ε, μ, b in Eq. [11.4] are known. The strain energy constant ε for precipitation of θ-NiMn in the α-iron matrix is:

$$\varepsilon = \frac{3K_\theta(1 + \nu_\alpha)\delta}{3K_\theta(1 + \nu_\alpha) + 2E_\alpha} \quad [11.17]$$

where K_θ is the bulk modulus of the θ-NiMn precipitate, ν_α is Poisson's ratio of ferrite in pure iron, taken as 0.282, E_α is the Young's modulus of ferrite in pure iron, taken as 206 GPa (Ledbetter and Reed, 1973), and δ is the linear strain accompanying precipitation from the matrix:

$$\delta = \frac{2(\Omega_\theta - \Omega_\alpha)}{(3\Omega_\theta + \Omega_\alpha)} \quad [11.18]$$

where Ω_α and Ω_θ are the atomic volumes of the ferrite (0.01176 nm^3/atom) and the θ-NiMn precipitate (0.01224 nm^3/atom), respectively. Alternatively, δ can be determined from $(1 + \delta)^3 = \Omega_\theta/\Omega_\alpha$, which gives a value close to that from Eq. [11.18]. The above parameters are summarised in Table 11.3. The Taylor factor M_T is taken as 2.75 (Hosseini and Kazeminezhad, 2009) for bcc materials, and κ is assigned as 3.5.

Activation energy and Avrami index

The activation energy Q is calculated using Eq. [11.12], based on early ageing data. When ΔH_0 takes different values 70, 100, 150 HV, Q is determined

Table 11.3 Values of parameters involved in the calculation of precipitation strengthening in Fe-12Ni-6Mn maraging type alloy

M_T	q (MPa/HV)	κ	Ω_α (nm^3)	Ω_θ (nm^3)	δ	ε	μ (GPa)	b (nm)
2.75	2.5	3.5	0.01176	0.01224	0.01333	0.0084	81	0.248

© Woodhead Publishing Limited, 2012

as 141, 133, and 125 kJ mol^{-1}, respectively. It is reasonable to treat it as a constant. In the following calculation, Q is taken as 133 kJ mol^{-1}, the average of the above three values. Growth-related constants n and m are 0.475 and 0.45, respectively.

Reaction rate constant in the Johnson–Mehl–Avrami equation

Experimental research shows that peak hardness is reached either by holding at 400°C for 16 hours, at 450°C for 1.4 hours, or at 500°C for 0.24 hours. Assuming that the precipitate fraction corresponding to peak hardness at 400°C or 450°C is known, f/f_{eq} is known, one can obtain the value of the pre-exponential term k_0, if the reaction rate constant in the Johnson–Mehl–Avrami equation k is assumed to follow an Arrhenius type equation with the same activation energy as K:

$$k = k_0 \exp\left(-\frac{Q}{RT}\right) \qquad [11.19]$$

Combining Eqs [11.19] and [11.7], one will obtain:

$$k_0 = \frac{(-\ln(1 - f/f_{eq}))^{1/m}}{t_p} \exp\left(\frac{Q}{RT}\right) \qquad [11.20]$$

where t_p is the time to reach peak hardness.

The percentage of the precipitate formed at peak hardness will be determined later. As will also be shown later, the precipitation fraction corresponding to peak hardness at 400°C is higher than that at 450°C, which partially contributes to the stronger age hardening effect at 400°C than at 450°C.

Growth and diffusion constants

Equation [11.6] shows that α is a function of c_0, c_θ and c_α. In the calculations below, as discussed earlier, c_0 will be replaced by c_0', calculated from Eq. [11.15]. Both c_θ and c_α are to be considered as the sum of Ni and Mn in atomic fraction. Since NiMn only contains Ni and Mn, c_θ always equals 1. The values of c_α at different temperatures are calculated using Thermo-Calc with the Kaufman binary (KP) database (Table 11.4, together with the equilibrium amount of NiMn precipitate). The value for c_0 is 0.1728 in atomic fraction, which is the equivalent of 0.1765 in weight fraction, that is the sum of 11.9 wt% Ni and 5.75 wt% Mn, the precise composition of the alloy studied.

At 450°C, the average diameter of precipitates is around 3 nm after 0.2 hour ageing, and 6 nm after 2 hours (peak hardness). Based on these, the

© Woodhead Publishing Limited, 2012

Table 11.4 Results calculated with Thermo-Calc using Kaufman binary database related to precipitation in Fe-12Ni-6Mn maraging type alloy

Temperature (°C)	350	375	400	425	450
Ni in ferrite (at%)	6.6	6.7	6.8	7.0	7.2
Mn in ferrite (at%)	0.4	0.5	0.7	0.9	1.1
c_α (at%)	7.0	7.2	7.5	7.9	8.3
f_{eq} (vol%)	11.4	11.1	10.8	10.5	9.7

diffusion coefficient can be estimated. One may assume that D follows an Arrhenius-type equation with the same activation energy as K:

$$D = D_0 \exp\left(-\frac{Q}{RT}\right) \quad [11.21]$$

Then, the pre-exponential term D_0 can be obtained by combining Eqs [11.21] and [11.14]:

$$D_0 = \left(\frac{r}{\int\left(\frac{1}{2}\alpha(t)t^{-1/2} + \frac{\mathrm{d}\alpha(t)}{\mathrm{d}t}t^{1/2}\right)\mathrm{d}t}\right)^2 \exp\left(\frac{Q}{RT}\right) \quad [11.22]$$

Critical nucleus size

Critical nucleus size (R_c) is the size of the precipitate above which the nucleus is stable and able to grow. It can be calculated as (Porter and Easterling, 1981):

$$R_c = \frac{-2\sigma N_A \Omega_\theta}{\Delta G_v} \quad [11.23]$$

where σ is the interface energy per unit area between precipitate and matrix, taken as 0.2 J m^{-2}, N_A is Avogadro's number, and the Gibbs energy difference between the precipitate and ferrite, ΔG_v, can be calculated using Thermo-Calc software with the KP database.

Rivera-Díaz-del-Castillo and Bhadeshia (2001) calculated the critical nucleus size taking into account the Gibbs–Thomson capillarity effect, which influences the equilibrium compositions at the particle/matrix boundary:

$$R_c = \frac{2c_\alpha \Gamma}{c_0 - c_\alpha} \quad [11.24]$$

where the capillarity constant Γ is given by:

© Woodhead Publishing Limited, 2012

Table 11.5 Driving force and the critical nucleus radius of precipitation in Fe-12Ni-6Mn maraging type alloy

Temperature (°C)	350	375	400	425	450
Driving force ($-\Delta G_v/RT$)	0.97	0.86	0.77	0.67	0.59
R_c (nm) (Eq. [11.23])	1.05	1.10	1.16	1.24	1.34
R_c (nm) (Eq. [11.24])[a]	0.39	0.39	0.41	0.43	0.46

[a]Rivera-Díaz-del-Castillo and Bhadeshia (2001).

Table 11.6 Values of parameters obtained by best fitting

Temperature (°C)	k_0 (s^{-1})	D_0 (m^2s^{-1})	f_p/f_{eq}	f_{eq} (vol%)	f_p (vol%)	r_p (nm)
400	2.392×10^5	2.532×10^{-10}	0.56	10.8	6.1	3.9
450	2.392×10^5	2.532×10^{-10}	0.44	9.7	4.3	3.0
500	2.392×10^5	2.532×10^{-10}	0.39	8.7	3.4	2.2

$$\Gamma = \frac{\sigma N_A \Omega_\theta}{RT} \frac{1 - c_\alpha}{c_\theta - c_\alpha} \quad [11.25]$$

ΔG_v and R_c calculated from both methods at various temperatures are listed in Table 11.5. When calculating the incubation period, the larger R_c values calculated from Eq. [11.23] are used. It should be noted that even for sizes smaller than the critical radius, a parabolic growth law described by Eq. [11.5] is assumed.

Precipitation fraction at peak hardness

The determination of precipitation fraction f at peak hardness, f_p, as a percentage of the equilibrium fraction f_{eq} at different temperatures involves an optimisation procedure. Using the various transformation fraction values, the age hardening curves at various temperatures can be obtained. One may therefore obtain the transformation fraction value to best fit the calculated hardness curves with the experimental curves (Table 11.6). In general, peak hardness increases with decreasing temperature due to greater supersaturation giving a greater volume fraction of precipitate.

11.7 Research trends

Although research in maraging steels usually involves the quantification of phase transformation kinetics, this section will expand beyond this theme, to the general developments in this type of steel. These can be roughly divided into the following areas.

© Woodhead Publishing Limited, 2012

11.7.1 Ultrafine-grained Fe-Ni-Mn steels

The research includes the study of behaviour during isothermal ageing (Nedjad *et al.*, 2009a), the effects of chromium addition (Meimandi *et al.*, 2008) and further alloying (Nedjad *et al.*, 2008a, 2009b) on microstructure and mechanical properties including tensile behaviour (Nedjad *et al.*, 2009c), and the correlation between intergranular brittleness and precipitation reactions (Nedjad *et al.*, 2008b). Transmission electron microscopy studies have been carried out on grain boundary precipitation (Nedjad *et al.*, 2006, 2008c). X-ray diffraction, including peak profile analysis (Garabagh *et al.*, 2008a) and microstructural study (Mobarake *et al.*, 2008), have been carried out on a nanostructured 18Ni maraging steel prepared by equal-channel angular pressing (Garabagh *et al.*, 2008b), aimed at better understanding of the deformation process and deformed structure. This equal-channel angular pressing is a natural extension after studying the extent and mechanism of nanostructure formation during cold rolling and ageing of lath martensite (Nedjad *et al.*, 2008d).

11.7.2 Development of novel maraging steels and atom probe tomography

These include their characterisation using advanced equipment and techniques, the most recent example being of the precipitation behaviour of intermetallic NiAl particles in Fe-6at%Al-4at%Ni by small angle neutron scattering (SANS) and three-dimensional atom probe (3DAP) (Schober *et al.*, 2010). Transformation during continuous-to-isothermal ageing applied on a maraging steel has been studied (Primig and Leitner, 2010), as has the effect of Cu on the evolution of precipitation in an Fe-Cr-Ni-Al-Ti maraging steel (Schnitzer *et al.*, 2010a) and the splitting phenomenon (Leitner *et al.*, 2010). In addition, reverted austenite in a PH13-8Mo maraging steel has been investigated (Schnitzer *et al.*, 2010b), in particular its influence on static and dynamic mechanical properties (Schnitzer *et al.*, 2010c). Modelling work has also been carried out on the yield strength of a stainless maraging steel (Schnitzer *et al.*, 2010d). The latest techniques of atom probe tomography have been used in this field (Pereloma *et al.*, 2004, 2009; Shekhter *et al.*, 2004).

11.7.3 Computer-aided alloy design approach to new steel compositions

Design is always followed by characterisation of the steels manufactured on a laboratory scale. Studies include real-time martensitic transformation kinetics in maraging steel under high magnetic fields (San Martín *et al.*,

© Woodhead Publishing Limited, 2012

2010). A novel ultra-high strength stainless steel, strengthened by various coexisting and multi-species (Xu *et al.*, 2008) nanoprecipitates including Ni_3Ti intermetallic, has been designed (Xu *et al.*, 2010a) based on a genetic algorithm and thermokinetics, and has been characterised (Xu *et al.*, 2010b). This genetic computational design of novel ultra-high strength maraging precipitation hardenable stainless steels has incorporated alloy composition as well as austenitisation and ageing temperatures as combined optimisation parameters (Xu *et al.*, 2009a,b); the model description and first experimental validation have been given (Xu *et al.*, 2009c).

Traditionally, new alloys have been developed through an empirical 'trial-and-error' approach, which is based on systematic experimental investigations. This semi-empirical approach is very dependent on intuition, experience and, to some extent, luck. Depending on the matrix type and the strengthening system, modern high-end UHS steels possess intentionally, and with specified amounts, a range of elements such as C, Cr, Ni, Al, Ti, Mo, V, Mn, Nb, Co, Cu, W, Si, B and N in wide ranges of concentrations. The interactions of alloying elements display complex cross effects. To understand the competition, conflict and synergy among various alloying elements experimentally, it would be necessary to systematically produce a large number of alloys with different compositions. Apart from the alloy composition, the heat treatment plays a paramount role in determining mechanical properties as well. After producing trial alloys, processing parameters need to be optimised via a tremendous amount of experimental work to achieve the best mechanical properties. Therefore, the conventional trial-and-error approach has been recognised to have low success rate, and to be very costly and time consuming.

With the improved understanding of processing/structure/property/performance relationships, and with the advent of more powerful and reliable computer hardware and software, alloy design philosophies are now increasingly oriented in the goal/means direction as demonstrated by the chain design model by Olson (1997). The goal/means oriented alloy design approach starts with defining the target properties required by the applications. This first link between performance and properties is based mainly on mechanical engineering. In the second step, the target microstructures are subsequently designed to obtain the desired properties, according to metallurgical and mechanical principles. The last link, attaining the tailored microstructures, is the key and most sophisticated process in the goal/means alloy design strategy. The alloy composition and heat treatment parameters are designed and optimised, employing various approaches, to obtain the desired microstructures.

Following fully or partially the goal/means oriented alloy design methodology, computational methods of different types have become a more efficient and powerful tool in providing guidance for designing new alloys as

© Woodhead Publishing Limited, 2012

well as for process development. Thermodynamics aided design approaches have been applied, in different degrees, to various systems such as maraging. Another popular computational approach is artificial neural networks (ANN) which extracts empirical trends from exploring large databases. The neural networks are often coupled with genetic algorithms (GA) for alloy design to fulfil the multi-objective optimisation goals. More recently, atomic level *ab initio* calculations are also applied to provide theoretical guidance in selecting and optimising the composition of Ti-based alloys, stainless steels and UHS steels. With respect to the process development, the experimental approach can also be better guided by extracting information from computational thermodynamics and artificial neural networks.

11.8 References

Bieber C G (1960), 'Progress with 25% nickel steels for high-strength applications', *Met Prog*, 78, 99–100.

Christian J W (2002), *The theory of transformations in metals and alloys*, Pergamon, Oxford.

Coret M, Calloch S, Combescure A (2004), 'Experimental study of the phase transformation plasticity of 16MND5 low carbon steel induced by proportional and non-proportional biaxial loading paths', *Eur J Mech A-Solid*, 23, 823–842.

Dutta B, Palmiere E J, Sellars C M (2001), 'Modelling the kinetics of strain induced precipitation in Nb microalloyed steels', *Acta Mater*, 49, 785–794.

Garabagh M R M, Nedjad S H, Shirazi H, Mobareke M I, Ahmadabadi M N (2008a), 'X-ray diffraction peak profile analysis aiming at better understanding of the deformation process and deformed structure of a martensitic steel', *Thin Solid Films*, 516, 8117–8124.

Garabagh M R M, Nedjad S H, Ahmadabadi M N (2008b), 'X-ray diffraction study on a nanostructured 18Ni maraging steel prepared by equal-channel angular pressing', *J Mater Sci*, 43, 6840–6847.

Gemperle A, Gemperlova J, Sha W, Smith G D W (1992), 'Aging behaviour of cobalt free chromium containing maraging steels', *Mater Sci Technol*, 8, 546–554.

He Y, Liu K, Yang K (2003), 'Effect of solution temperature on fracture toughness and microstructure of ultra-purified 18Ni(350) maraging steel', *Acta Metall Sin*, 39, 381–386.

Hosseini E, Kazeminezhad M (2009), 'Dislocation structure and strength evolution of heavily deformed tantalum', *Int J Refract Met Hard Mater*, 27, 605–610.

Hsiao C N, Chiou C S, Yang J R (2002), 'Aging reactions in a 17-4 PH stainless steel', *Mater Chem Phys*, 74, 134–142.

Kim S J, Wayman C M (1990), 'Precipitation behavior and microstructural changes in maraging Fe-Ni-Mn-Ti alloys', *Mater Sci Eng A*, 128, 217–230.

Kitabjian P H, Nix W D (1998), 'Atomic size effects in Ni–Al based solid solutions', *Acta Mater*, 46, 701–710.

Kozeschnik E, Buchmayr B (2001), 'MATCALC – a simulation tool for multicomponent thermodynamics, diffusion and phase transformations', in *Fifth International Seminar on the Numerical Analysis of Weldability*, Schloss Seggau, Austria, 349–361.

Ledbetter H M, Reed R P (1973), 'Elastic properties of metals and alloys, I. Iron, nickel, and iron-nickel alloys', *J Phys Chem Ref Data*, 2, 531–617.

© Woodhead Publishing Limited, 2012

Leitner H, Schober M, Schnitzer R (2010), 'Splitting phenomenon in the precipitation evolution in an Fe-Ni-Al-Ti-Cr stainless steel', *Acta Mater*, 58, 1261–1269.

Lifshitz I M, Slyozov V V (1961), 'The kinetics of precipitation from supersaturated solid solutions', *J Phys Chem Solids*, 19, 35–50.

Meimandi S H, Nedjad S H, Yazdani S, Ahmadabadi M N (2008), 'Effect of chromium addition on the microstructure and mechanical properties of Fe-10Ni-6Cr-2Mn maraging steels', in *New Developments on Metallurgy and Applications of High Strength Steels*, TMS, Warrendale, PA, 1151–1157.

Mihalisin J R, Bieber C G (1966), 'Progress toward attaining theoretical strength with iron-nickel maraging steels', *J Metals*, 18, 1033–1036.

Mobarake M I, Ahmadabadi M N, Poorganji B, Fatehi A, Shirazi H, Furuhara T, Parsa H, Nedjad S H (2008), 'Microstructural study of an age hardenable martensitic steel deformed by equal channel angular pressing', *Mater Sci Eng A*, 491, 172–176.

Nedjad S H, Ahmadabadi M N, Mahmudi R, Furuhara T (2006), 'Analytical transmission electron microscopy study of grain boundary precipitates in an Fe-Ni-Mn maraging alloy', *Mater Sci Eng A*, 438, 288–291.

Nedjad S H, Garabagh M R M, Ahmadabadi M N, Shirazi H (2008a), 'Effect of further alloying on the microstructure and mechanical properties of an Fe-10Ni-5Mn maraging steel', *Mater Sci Eng A*, 473, 249–253.

Nedjad S H, Ahmadabadi M N, Furuhara T (2008b), 'Correlation between the intergranular brittleness and precipitation reactions during isothermal aging of an Fe-Ni-Mn maraging steel', *Mater Sci Eng A*, 490, 105–112.

Nedjad S H, Ahmadabadi M N, Furuhara T (2008c), 'Transmission electron microscopy study on the grain boundary precipitation of an Fe-Ni-Mn maraging steel', *Metall Mater Trans A*, 39A, 19–27.

Nedjad S H, Ahmadabadi M N, Furuhara T (2008d), 'The extent and mechanism of nanostructure formation during cold rolling and aging of lath martensite in alloy steel', *Mater Sci Eng A*, 485, 544–549.

Nedjad S H, Ahmadabadi M N, Furuhara T (2009a), 'Annealing behavior of an ultrafine-grained Fe-Ni-Mn steel during isothermal aging', *Mater Sci Eng A*, 503, 156–159.

Nedjad S H, Teimouri J, Tahmasebifar A, Shirazi H, Ahmadabadi M N (2009b), 'A new concept in further alloying of Fe-Ni-Mn maraging steels', *Scr Mater*, 60, 528–531.

Nedjad S H, Meimandi S, Mahmoudi A, Abedi T, Yazdani S, Shirazi H, Ahmadabadi M N (2009c), 'Effect of aging on the microstructure and tensile properties of Fe-Ni-Mn-Cr maraging alloys', *Mater Sci Eng A*, 501, 182–187.

Olson G B (1997), 'Computational design of hierarchically structured materials', *Science*, 277, 1237–1242.

Pereloma E V, Shekhter A, Miller M K, Ringer S P (2004), 'Ageing behaviour of Fe-20Ni-1.8Mn-1.6Ti-0.59Al (wt%) maraging steel: clustering, precipitation and hardening', *Acta Mater*, 52, 5589–5602.

Pereloma E V, Stohr R A, Miller M K, Ringer S P (2009), 'Observation of precipitation evolution in Fe-Ni-Mn-Ti-Al maraging steel by atom probe tomography', *Metall Mater Trans A*, 40A, 3069–3075.

Perkas M D (1968), 'High-strength maraging steels', *Met Sci Heat Treat*, 10, 415–425.

Porter D A, Easterling K E (1981), *Phase transformations in metals and alloys*, Van Nostrand Reinhold, New York.

Primig S, Leitner H (2010), 'Transformation from continuous-to-isothermal aging applied on a maraging steel', *Mater Sci Eng A*, 527, 4399–4405.

Rivera-Díaz-del-Castillo P E J, Bhadeshia H K D H (2001), 'Theory for growth of spherical precipitates with capillarity effects', *Mater Sci Technol*, 17, 30–32.

© Woodhead Publishing Limited, 2012

San Martín D, van Dijk N H, Jiménez-Melero E, Kampert E, Zeitler U, van der Zwaag S (2010), 'Real-time martensitic transformation kinetics in maraging steel under high magnetic fields', *Mater Sci Eng A*, 527, 5241–5245.

Schnitzer R, Zickler G A, Zinner S, Leitner H (2009), 'Structure-properties relationship of a PH 13-8 Mo maraging steel', in Beiss P, Broeckmann C, Franke S, Keysselitz B (eds), *Tool Steels – Deciding Factor in Worldwide Production*, Proceedings of the 8th International Tooling Conference, vol. I, Aachen, Germany, 491–503.

Schnitzer R, Schober M, Zinner S, Leitner H (2010a), 'Effect of Cu on the evolution of precipitation in an Fe-Cr-Ni-Al-Ti maraging steel', *Acta Mater*, 58, 3733–3741.

Schnitzer R, Radis R, Nöhrer M, Schober M, Hochfellner R, Zinner S, Povoden-Karadeniz E, Kozeschnik E, Leitner H (2010b), 'Reverted austenite in PH 13-8 Mo maraging steels', *Mater Chem Phys*, 122, 138–145.

Schnitzer R, Zickler G A, Lach E, Clemens H, Zinner S, Lippmann T, Leitner H (2010c), 'Influence of reverted austenite on static and dynamic mechanical properties of a PH 13-8 Mo maraging steel', *Mater Sci Eng A*, 527, 2065–2070.

Schnitzer R, Zinner S, Leitner H (2010d), 'Modeling of the yield strength of a stainless maraging steel', *Scr Mater*, 62, 286–289.

Schober M, Schnitzer R, Leitner H (2009), 'Precipitation evolution in a Ti-free and Ti-containing stainless maraging steel', *Ultramicroscopy*, 109, 553–562.

Schober M, Lerchbacher C, Eidenberger E, Staron P, Clemens H, Leitner H (2010), 'Precipitation behavior of intermetallic NiAl particles in Fe-6 at.%Al-4 at.%Ni analyzed by SANS and 3DAP', *Intermetallics*, 18, 1553–1559.

Seetharaman V, Sundararaman M, Krishnan R (1981), 'Precipitation hardening in a PH 13-8 Mo stainless steel', *Mater Sci Eng*, 47, 1–11.

Self P G, Bhadeshia H K D H, Stobbs W M (1981), 'Lattice spacings from lattice fringes', *Ultramicroscopy*, 6, 29–40.

Sha W, Guo Z (2009), *Maraging steels: Modelling of microstructure, properties and applications*, Woodhead Publishing, Cambridge.

Shackson R H (1991), *Marketing research for E.E.&G. Mound Applied Technologies' heat treatment process of high strength materials*, The Industrial Technology Institute, Ann Arbor, MI.

Shekhter A, Aaronson H I, Miller M K, Ringer S P, Pereloma E V (2004), 'Effect of aging and deformation on the microstructure and properties of Fe-Ni-Ti maraging steel', *Metall Mater Trans A*, 35A, 973–983.

Shiang L T, Wayman M (1988), 'Maraging behavior of an Fe-19.5Ni-5Mn alloy II: Evolution of reverse-transformed austenite during overaging', *Metallography*, 21, 425–451.

Sinha P P, Sivakumar D, Babu N S, Tharian K T, Natarajan A (1995), 'Austenite reversion in 18 Ni Co-free maraging steel', *Steel Res*, 66, 490–494.

Squires D R, Wilson E A (1972), 'Aging and brittleness in an Fe-Ni-Mn alloy', *Metall Trans*, 3, 579–585.

Vasudevan V K, Kim S J, Wayman C M (1990), 'Precipitation reactions and strengthening behavior in 18 Wt Pct nickel maraging steels', *Metall Trans A*, 21, 2655–2668.

Viswanathan U K, Dey G K, Sethumadhavan V (2005), 'Effects of austenite reversion during overageing on the mechanical properties of 18 Ni (350) maraging steel', *Mater Sci Eng A*, 398, 367–372.

Vylezhnev V P, Sukhikh A A, Bragin V G, Kokovyakina S A (1993), 'Mechanical properties of grade N18K9M5T maraging steel containing retained and reversed austenite', *Phys Met Metall*, 75, 448–452.

© Woodhead Publishing Limited, 2012

Wagner C (1961), 'Theory of the ageing of precipitates by redissolution (Ostwald maturing)', *Z Elektrochem*, 65, 581–591.

Wilm A (1911), 'Physikalisch-metallurgische Untersuchungen über agnesiumhaltige Aluminiumlegierungen', *Metallurgie: Zeitschrift für de gesamte Hüttenkunde*, 8(8), 225–227.

Wilson R K (ed.) (1989), *Maraging steels: Recent development and applications*, TMS, Warrendale, PA.

Xu W, Rivera-Díaz-del-Castillo P E J, van der Zwaag S (2008), 'Computational design of UHS stainless steel strengthened by multi-species nanoparticles combining genetic algorithms and thermokinetics', in *New developments on metallurgy and applications of high strength steels*, TMS, Warrendale, PA, 1167–1181.

Xu W, Rivera-Díaz-del-Castillo P E J, van der Zwaag S (2009a), 'Computational design of UHS maraging stainless steels incorporating composition as well as austenitisation and ageing temperatures as optimisation parameters', *Phil Mag*, 89, 1647–1661.

Xu W, Rivera-Díaz-del-Castillo P E J, van der Zwaag S (2009b), 'A combined optimization of alloy composition and aging temperature in designing new UHS precipitation hardenable stainless steels', *Comput Mater Sci*, 45, 467–473.

Xu W, Rivera-Díaz-del-Castillo P E J, Yang K, Yan W, van der Zwaag S (2009c), 'Genetic computational design of novel ultra high strength stainless steels: model description and first experimental validation', in *TMS 2009 138th Annual Meeting & Exhibition – Supplemental Proceedings*, Vol 2: Materials Characterization, Computation and Modeling, TMS, Warrendale, PA, 319–326.

Xu W, Rivera-Díaz-del-Castillo P E J, Yan W, Yang K, San Martín D, Kestens L A I, van der Zwaag S (2010a), 'A new ultrahigh-strength stainless steel strengthened by various coexisting nanoprecipitates', *Acta Mater*, 58, 4067–4075.

Xu W, Rivera-Díaz-del-Castillo P E J, Wang W, Yang K, Bliznuk V, Kestens L A I, van der Zwaag S (2010b), 'Genetic design and characterization of novel ultra-high-strength stainless steels strengthened by Ni_3Ti intermetallic nanoprecipitates', *Acta Mater*, 58, 3582–3593.

© Woodhead Publishing Limited, 2012

12

First principles in modelling phase transformations in steels

M. H. F. SLUITER, Delft University of Technology, The Netherlands

Abstract: Simulating materials behaviour and designing materials to meet prerequisite properties increasingly require insight at the atomistic level. First-principles modelling, through a quantum mechanical description of the electronic structure, provides insight in bonding at the atomic level without needing experimental data. In this chapter applications of first-principles modelling relevant to iron and its alloys are reviewed and summarized.

Key words: first-principles modelling, iron phase stability, iron carbides, atomic diffusion, solute–vacancy binding.

12.1 Introduction

In recent years the first-principles modelling of steel has begun in earnest. For steel, research started somewhat later than in other alloys, such as aluminium alloys, for a number of reasons: the presence of magnetism in steel presents a formidable challenge that is not present in aluminium alloys; interstitial solutes such as carbon in steel mean that computations require more memory and more computer time compared to most other alloys; displacive structural phase transformations play an essential role in steel while such transformations are absent or of much lesser importance to other alloys where transformations might be of order-disorder type. Hence, first-principles modelling of steel provides a great challenge.

The earliest work started with pure iron, and gradually more complex compositions, structures and phenomena were studied. The field is still in full development and many controversies, even on very basic questions, remain. As such the present chapter must be regarded as a status report that reflects on the current state of the art. First, a brief historical overview of the field of first-principles modelling of alloy phase stability will be presented. Secondly, the *ab initio* studies of pure iron will be summarized, as it gives a good impression of the challenges that are posed by the strong coupling between atomic structure and magnetic order that is inherent in all low alloy steels. The various crystalline forms of iron carbide are examined, because they are ubiquitous in steels. Thirdly, the role of alloying elements in steel and then, in particular, the (de)stabilization of carbides will be examined

© Woodhead Publishing Limited, 2012

because it has important applications for steels in which carbide formation is suppressed, such as transformation-induced plasticity (TRIP) steels. Next, the role of the common interstitial solutes carbon and nitrogen in the ferrite matrix is considered. Fourthly, impurity diffusion of interstitial and substitutional alloying elements is discussed, and an outlook is given on further developments.

12.1.1 First-principles electronic structure of alloys

First-principles modelling in this chapter refers to the application of density functional electronic structure methods for the calculation of total energies and all the properties that can be derived from these energies. Although the fundamental principles of density functional theory (DFT) were already derived in the 1960s (Hohenberg and Kohn, 1964; Kohn and Sham, 1965) and the spin-polarization treatment, which is the basis for treating magnetic properties, dates from the early 1970s (van Barth and Hedin, 1972; Rajagopal and Callaway, 1973), first-principles calculations entered the realm of materials modellers in earnest with the publication of the book *Calculated Electronic Properties of Metals* (Moruzzi *et al.*, 1978). In this book, for the first time, many computed properties, such as lattice parameters, bulk moduli, electronic contribution to the heat capacity, electronic density of states, magnetic state and magnetization, of all metallic elements were listed.

Although many of the properties were already known from experiments, the great utility was immediately evident because these properties could be computed for many structures and for many (metallic) compounds, even in the absence of experimental data, and even for hypothetical or metastable compounds. Initially, limitations in computer hardware and software were important impediments. Even more important were certain theoretical limitations such as the ability to efficiently reach charge self-consistency[1] (Johnson, 1988), to efficiently optimize structures through the direct calculation of forces (Yu *et al.*, 1991; Kresse and Hafner, 1993) and stresses (Nielsen and Martin, 1983; Hamann *et al.*, 2005), and algorithmic developments such as ultrasoft pseudopotentials[2] (Vanderbilt, 1990) and projector augmented-wave

[1]Density functional calculations typically start with an estimated electronic charge density, which is used to compute an electrostatic potential that in turn influences the state, and thus density, of electrons. Obviously in a stationary state the charge density that gives rise to the potential, and the charge density that results from this potential must be the same. This identity is called charge self-consistency.

[2]Pseudopotentials take advantage of the fact that bonding in materials is due to valence electrons. Electrons in the atomic core are hardly affected by chemical bonding and therefore can be considered frozen when the atomic neighbourhood is changed. There are various procedures by which core electrons can be frozen which give rise to various types of pseudopotentials for each element in the periodic table.

© Woodhead Publishing Limited, 2012

pseudopotentials (Blöchl, 1994) as well as increasingly accurate exchange correlation functionals (Perdew and Wang, 1986; Perdew *et al*., 1996).

More empirical electronic structure formalisms were developed in the same time period. The Slater–Koster tight-binding method (Slater and Koster, 1954) proved a fruitful basis for further development, such as the computationally highly efficient recursion method (Haydock *et al*., 1975), and the fitting of the so-called Slater–Koster parameters (Papaconstantopoulos and Mehl, 2003) allowed tight-binding calculations to reproduce certain first-principles results at a fraction of computational effort. The tight-binding was also an efficient platform for further theoretical developments, such as for the description of random solid solutions or alloys via the coherent potential approximation (CPA) (Soven, 1967; Velický, 1969) which then could also be implemented in more rigorous first-principles methods (Faulkner and Stocks, 1980; Abrikosov and Johansson, 1998). Later, it was realized that composition fluctuations could be treated analytically in the CPA via the so-called generalized perturbation method (GPM) (Ducastelle and Gautier, 1976; Bieber *et al*., 1981). This led to the first treatments of the thermodynamics and order-disorder phenomena in alloys firmly based on electronic structure.

12.1.2 Order–disorder and its coupling with first-principles electronic structure

Order–disorder transitions had also drawn the interest from the side of statistical mechanics. The so-called Ising model (Lenz, 1920; Ising, 1925), in which magnetization is described through assigning a local spin moment to each atom of either up or down type, and where spins interact with an applied field and short-range interactions with other spins in the vicinity, proved to be extremely difficult to solve exactly. In fact, determining the partition function for such a model for a square two-dimensional lattice with nearest-neighbour interactions only between spins proved to be a mathematical tour-de-force (Onsager, 1944; Yang, 1952; Kac and Ward, 1952). In fact the three-dimensional Ising model remains unsolved, and may be unsolvable (Istrail, 2000), although at times reports of its solution surface (Zhang, 2007), which then typically are rebuked soon after (Wu *et al*., 2008; Perk, 2009).

The difficulty to arrive at exact solutions to the Ising model inspired Kikuchi to devise one of the presently best known approximate solutions via the so-called cluster variation method (CVM) (Kikuchi, 1951), later reformulated by Hijmans and de Boer (1954). The CVM was shown to produce classical critical exponents which quickly led to a loss of interest, although Suzuki (1986) later showed that through an application of the CVM, namely the coherent-anomaly method, non-classical scaling behaviours of cooperative systems can be explored efficiently. Van Baal (1973) revived the method

© Woodhead Publishing Limited, 2012

through the awareness that the Ising model, with atomic sites being occupied by up and down spins, is identical to a simple alloy model where atomic sites are occupied by two types of atomic species, say Fe and Ni, and the realization that alloy phase diagrams, certainly those of the first order type, do not require knowledge of the precise values of the critical exponents. This led to the first topologically correct composition–temperature phase diagrams for solid solutions undergoing order–disorder transformations (van Baal, 1973; Kikuchi, 1974).

The cluster algebra required for efficient CVM calculations was developed by Sanchez and de Fontaine (1978), and this in turn led to more sophisticated phase diagram calculations (Sanchez and de Fontaine, 1982) and, more significantly, to the structure inversion method for cluster expanding alloy properties (Connolly and Williams, 1983; Laks *et al.*, 1992; Sluiter and Kawazoe, 2005; Drautz and Diaz-Ortiz, 2006; Mueller and Ceder, 2009) initially often referred to as the Connolly–Williams method (1983, Terakura *et al.*, 1987, Sluiter *et al.*, 1990). While initially there were many reservations concerning the validity of the structure inversion method because expansion coefficients were shown to be dependent on structure selection and cluster cut-off criteria (Sluiter and Turchi, 1989), gradually by using essentially statistical methods (Garbulsky and Ceder 1995; Sluiter *et al.*, 1996; van de Walle and Ceder, 2002; van de Walle *et al.*, 2002) cluster expansions were shown to be much more versatile than the earlier theory based on perturbation of the coherent potential (CPA-GPM theory). This is particularly relevant to modelling of steels because lattice relaxations around interstitials such as C and N, and larger solute atoms such as Nb, couple with the magnetic local order, thereby having significant consequences for the phase stability (Friak *et al.*, 2001; Marsman and Hafner, 2002; Boukhvalov *et al.*, 2007; Urtsev *et al.*, 2010).

In spite of its limited application (Turchi *et al.*, 1991; Sluiter *et al.*, 1992; Ruban *et al.*, 2004) to phase stability studies of alloys, the CPA-GPM theory has had a strong impact because it provides analytic expression for interactions (Ducastelle, 1991; Sluiter and Kawazoe, 1995) that can be connected rather easily with well understood alloy parameters, such as valence electron per atom ratio. Moreover, the CPA-GPM calculations gave a clear indication of the type of interactions that are likely to contribute significantly to the alloy energetics (Bieber *et al.*, 1981; Turchi *et al.*, 1987; Ducastelle, 1991).

Another significant development based on cluster expansions is the so-called special quasi-random structure (SQS) concept (Zunger *et al.*, 1990) for simulating global properties of random solid solutions. The special feature of these structures is that, by assuming that short-ranged few-body interactions are the most significant, it is possible to approximate the random state with rather small periodic cells containing only a small number of atoms. This makes these structures amenable to *ab initio* electronic structure calculations,

© Woodhead Publishing Limited, 2012

unlike the conventional randomly assembled large cells. Initially the SQSs were used to extract mixing energies (Sluiter and Kawazoe, 2002; Jiang *et al*., 2004; Wang *et al*., 2009) and electronic band gaps (Hass *et al*., 1990; Wei and Zunger, 1996) for solid solutions. More recently SQSs have been used also to predict other properties of random alloys such as the elastic tensor (Jiang *et al*., 2005a; von Pezold *et al*., 2010; Zhang *et al*., 2010a, Friak *et al*., 2011).

For most alloys it has become apparent that a highly accurate description of the thermodynamics of order–disorder processes requires rather long-ranged interactions (Garbulsky and Ceder, 1995) that are challenging for the CVM (Sluiter *et al*., 1996) and often go beyond the practical range of the CVM. For that reason, and because of the much greater ease of coding, Monte Carlo methods have become more common (van de Walle and Ceder, 2002; van de Walle *et al*., 2002).

12.1.3 *Ab initio* prediction of atomic diffusion in alloys

While thermodynamic equilibrium addresses many important aspects of materials behaviour, it does not answer the question how and how fast equilibrium is being approached. Kinetics gives insights into the timescale for changes occurring in materials. The most basic process in a material is probably atomic diffusion.

Already half a century ago a sophisticated analysis of atomic diffusion was formulated, known as transition state theory (Vineyard, 1957). However, the formalism required many parameters that could be reliably computed only with the advent of *ab initio* methods. While in chemistry the earliest applications date from the mid-1990s (Truong and Duncan, 1994), the *ab initio* diffusivity predictions in alloys occurred a little later (Bester *et al*., 1999). Transition state theory requires knowledge of the minimum energy path (MEP) during the atomic jump process. A complication is that, during the atomic jump, (distant) neighbours also move so that the computation of the MEP is not trivial. Only about a decade ago, with the development of the nudged elastic band method by Henkelman and Jónsson (2000) transition state theory could finally be used fully (Windl *et al*., 2001; Siegel and Hamilton, 2003; Janotti *et al*., 2004; Krčmar *et al*., 2005). Study of impurity diffusivity in bcc Fe has received considerable attention: interstitial diffusion by H, He, C and O, and substitutional diffusion by P, Cr, Co, Cu, Mo, W, Hf, Ta and self-diffusion have already been studied (Jiang and Carter, 2003, 2004b; Slane *et al*., 2004; Perez and Weissmann, 2004; Barashev, 2005; Domain and Becquart, 2005; Barashev and Arokiam, 2006, 2007; Vincent *et al*., 2006; Djurabekova *et al*., 2007; Ortiz *et al*., 2007; Tapasa *et al*., 2007; Soisson and Fu, 2007; Fu *et al*., 2007; Borodin and Vladimirov, 2009; Huang *et al*., 2010). In the cases examined so far, impurity diffusion is considered. In

© Woodhead Publishing Limited, 2012

concentrated alloys, and in alloys where short- and long-range order play a role, Van der Ven and Ceder found diffusion to be a much more complex process (2005a, 2005b) that cannot be described by a simple scalar Arrhenius function of the temperature (Kehr *et al*., 1989).

Ab initio studies of the kinetics of martensitic transformations are possible for highly idealized modalities only, such as the Bain transformation path (Friak *et al*., 2001; Tsetseris, 2005; Okatov *et al*., 2009). However, in actual steels features at the microstructural length scale are essential and these are generally not yet computationally feasible, although much progress is being made with empirical potentials (Bos *et al*., 2006) based on *ab initio* data through a so-called multiscale approach. *Ab initio* approaches to study amorphous steel are not treated here, although some work in this area has started (Kazimirov *et al*., 2008; Gu *et al*., 2008). Likewise, the very extensive literature on modelling of complex crystal defects, such as interfaces and dislocation cores, will not be reviewed here. In this chapter a very brief mention of *ab initio* grain boundary segregation studies will be made only in the context of the effect of alloying species on steel.

12.2 *Ab initio* description of phase stability of pure iron

Although the early local density approximation modelling by Moruzzi *et al*. (1978) gave very good results for most elements in the periodic table, this was not the case for iron. The experimentally observed ground state of iron is ferromagnetic bcc, but local spin density approximation (LSDA) calculations wrongly indicate fcc iron to be more stable than bcc Fe (Bagno *et al*., 1989; Leung *et al*., 1991; Singh *et al*., 1991). Moreover, the LSDA-computed cohesive energy of iron is 2 eV/atom larger than the experimental value (Philipsen and Baerends, 1996). Fortunately, exchange-correlation potentials that account for the effect of gradients in the charge density, the so-called generalized gradient approximation (GGA), perform much better than the LSDA implementation of DFT. In particular, the GGA due to Perdew and Wang (1992) performs significantly better for the ground state properties of iron (Bagno *et al*., 1989; Leung *et al*., 1991; Singh *et al*., 1991; Asada and Terakura, 1992) and other transition metals (Ozolins and Körling, 1993). Attempts to further improve the agreement with experiment have proven quite difficult with many efforts still ongoing (Cococcioni and de Gironcoli, 2005; Sánchez-Barriga *et al*., 2009; Katanin *et al*., 2010).

The phase stability of iron as a function of temperature and pressure has been intensively investigated, both experimentally and theoretically, because of the important implications for the understanding of the earth's core (Boehler, 1993; Saxena *et al*., 1994; Söderlind *et al*., 1996; Shen *et al*., 1998; Laio *et al*., 2000; Luo *et al*., 2010; Tateno *et al*., 2010).

© Woodhead Publishing Limited, 2012

Experiments indicate that pure iron at ambient pressure undergoes a series of transformations when the temperature is increased from 0 K: the ferromagnetic bcc ground state, usually indicated by α, magnetically disorders around 1043 K to a paramagnetic bcc state; at about 1184 K the paramagnetic bcc state gives way to a paramagnetic fcc state, referred to by the symbol γ; while at a still higher temperature of 1665 K the paramagnetic bcc state reappears, now named δ, and at 1811 K iron melts to form a paramagnetic liquid (Massalski and Laughlin, 2009).

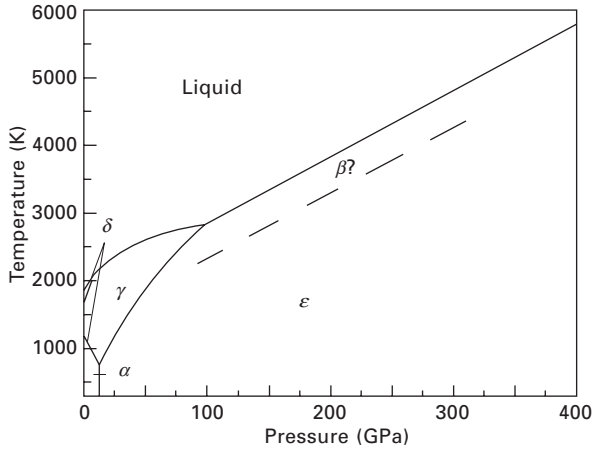
It has been argued that the ground state of pure iron is not bcc but bct (Falicov and Ruvalds, 1968; Cracknell, 1969; Massalski and Laughlin, 2009) because the magnetization aligns with one particular direction of the set of directions <100>, say [100], so that the [010] and [001] directions are no longer equivalent to [100]. For reasons of consistency the paramagnetic bcc state between 1043 K and 1184 K ought to be called δ, although it is customary to refer to this state as α. Experimentally, it is evident also that beyond pressures of about 10 to 13 GPa the ferromagnetic bcc ground state gives way to hcp, usually designated with the symbol ε. The fcc paramagnetic state is stabilized also by hydrostatic pressure over the bcc ferromagnetic and bcc paramagnetic states so that in the neighbourhood of 8.2 GPa and 678 K (Klotz *et al.*, 2008), a triple point exists where ferromagnetic bcc (α), paramagnetic fcc (γ) and paramagnetic hcp (ε) iron co-exist.

At high pressure and temperature, the hcp allotrope was believed to undergo a transformation to dhcp (so-called β) before melting at still higher temperatures (Brown and McQueen, 1986; Boehler, 1993; Saxena *et al.*, 1993); however, recently there have been other interpretations based on simulations (Vocadlo *et al.*, 2003; Belonoshko *et al.*, 2009) and experiments (Mikhaylushkin *et al.*, 2007; Tateno *et al.*, 2010).

The magnetic disordering in the bcc phase is found to be rather insensitive to pressure (Leger *et al.*, 1972; Zhang and Guyot, 1999), which is not easy to understand or reproduce theoretically (Moran *et al.*, 2003; Körmann *et al.*, 2009). On the theoretical side, there are a plethora of studies attempting to reproduce the known features of the pressure–temperature phase diagram (see Fig. 12.1) of which here only a few recent examples are listed (Lavrentiev *et al.*, 2010a; Sha and Cohen, 2010; Toledano *et al.*, 2010; Luo *et al.*, 2010; Katanin *et al.*, 2010; Zhang *et al.*, 2010b).

The magnetic disordering of bcc Fe has been modelled a number of times with LSDA (Staunton and Gyorffy, 1992; Halilov *et al.*, 1997; Rosengaard and Johansson, 1997; Pajda *et al.*, 2001; Lichtenstein *et al.*, 2001) and GGA (Wang *et al.*, 2006; Körmann *et al.*, 2008) or both LSDA and GGA (Körmann *et al.*, 2009) exchange correlation functionals. While the LSDA exchange correlation functionals give much larger magnetic energies than most GGA functionals, and while LSDA exchange correlation functionals do not properly reproduce the ferromagnetic bcc ground state, nevertheless

© Woodhead Publishing Limited, 2012



12.1 Experimental pressure–temperature phase diagram of pure iron. α ferromagnetic bcc, β presumed dhcp, γ paramagnetic fcc, δ paramagnetic bcc, ε paramagnetic hcp.

the earlier LSDA studies appear to have given Curie temperatures that agreed just as well with experiment as the later GGA work (Körmann *et al.*, 2008). Much progress has been made in modelling the thermodynamic properties of bcc iron, including vibrational, electronic and magnetic free-energy contributions (Körmann *et al.*, 2008, 2010).

It is worthwhile to mention that there are two main conceptual frameworks to represent the magnetic (dis)order: the atomic local moment framework of Heisenberg and the itinerant electron framework of Bloch and Stoner. The Heisenberg model is the most widely applied because of its conceptual simplicity. However, for many systems delocalized electron states play non-negligible roles and, even for transition metal magnetism, important aspects are well described by the itinerant picture. Fortunately, it has been proven possible to link the two frameworks (Niu *et al.*, 1999).

Above the Curie temperature the two frameworks give rise to two distinct representations as well:

- the disordered local moment picture (Pindor *et al.*, 1983; Pinski *et al.*, 1986; Akai and Dederichs, 1993; Niu *et al.*, 1999; Bansil *et al.*, 1999), which has been generalized to non-collinear spin configurations (Stocks *et al.*, 1998; Lounis *et al.*, 2005), arises naturally in the context of multiple scattering theory (Faulkner, 1979; Strange *et al.*, 1989; Zeller *et al.*, 1995) in analogy with disordered alloys with atom centred scatterers;
- an approach drawing on an analogy with phonons is the magnon picture where with increasing temperature increasing numbers of magnetic disordering wave packets, so-called magnons, are generated (Collins *et al.*, 1969; Shastry *et al.*, 1981; Bylander *et al.*, 2000; Körmann *et al.*, 2008).

© Woodhead Publishing Limited, 2012

Finally, we can mention that classical Heisenberg representations, where the effective interatomic exchange interactions are extracted from a limited number of ferro- and antiferromagnetic configurations (Sluiter and Kawazoe, 1995; Bergqvist *et al*., 2005; Drautz and Fähnle, 2005; Bose and Kudrnovsky, 2010), have also proven to be very useful.

The magnetic state of densely packed crystal structures of Fe remains an area of intense research (Toledano *et al*., 2010; Ayuela and March, 2010; Lavrentiev *et al*., 2010a; Soulairol *et al*., 2010; Ono *et al*., 2010; Mohammed *et al*., 2010). In order to experimentally study fcc iron, which is stable only between 1183 and 1663 K, much effort has gone into artificially stabilizing it at lower temperatures. There are several methods to achieve this: precipitation of fcc Fe from Cu-rich Cu-Fe solid solutions (Smith, 1940), epitaxial growth of Fe thin films on Cu substrates (Macedo and Keune, 1988), laser induced decomposition of carbonyl $Fe(CO)_5$ (Haneda *et al*., 1992), and alloying with so-called austenite-formers, i.e. alloying elements that stabilize fcc at the expense of bcc, such as Ni. The important questions are then the nature of the magnetic ordering, the degree of spin polarization, and the transition temperature. Experimentally, the general consensus is that an anti-ferromagnetic (AFM) ground state develops below a Neel temperature of about 60 K (Gonser *et al*., 1963; Johanson *et al*., 1970; Sakuma, 1999; Chen and Sundman, 2001; Hines *et al*., 2009), with local moments of about 1.8 μ_B per iron atom (Matsui *et al*., 1980; Hines *et al*., 2009), and a wave vector for the spin density wave at, or very near, the X-point (Tsunoda, 1988, 1989; Naono and Tsunoda, 2004).

As γ-Fe is the simplest itinerant electron system with a non-collinear spin structure and as iron is of great interest in its own right, there have been many theoretical studies aimed at reproducing and understanding the magnetic structure. In early LSDA studies a spiral spin density wave ground state could be obtained (Uhl *et al*., 1992; Mryasov *et al*., 1992) for a specific range of lattice parameters, but the wave vector did not agree with values from experiments. The GGA gave a better agreement on the wave vector (Körling and Ergon, 1996). Various improvements to the theory of non-collinear magnetism then led to still better agreement with experiments using LSDA (Bylander and Kleinman, 1999) and GGA (Knopfle *et al*., 2000). Still more advanced GGA calculations (Sjöstedt and Nordström, 2002), however, gave a double-layered AFM structure and incorrect equilibrium lattice parameter (Marsman and Hafner, 2002). It has become evident that the results of these calculations are very sensitive to the lattice parameter (Acet *et al*., 1994; Kong and Liu, 2004) and details of the calculations. Another factor is that magnetic ordering would break the fcc crystal symmetry, a factor that is usually neglected in the theoretical calculations, although a detailed study of the Bain transformation path connecting bcc and fcc structures has been performed (Wang *et al*., 2006). However, a recent experiment has argued

© Woodhead Publishing Limited, 2012

that the tetragonal distortion effect is rather insignificant (Tsunoda *et al.*, 2007). Thus, it appears that a final theoretical understanding of the fcc Fe magnetic ground state is still lacking.

For the high pressure hcp structure, the situation is equally confused: experiments generally suggest that hcp Fe is non-magnetic (Taylor *et al.*, 1991; Nasu *et al.*, 2002), while DFT calculations give AFM (Steinle-Neumann *et al.*, 1999) with the wave vector being in the basal plane at, or near, the M-point.[3] Recent work (Steinle-Neumann *et al.*, 2004) suggests that the local moments in hcp Fe are rather small and difficult to observe and, moreover, they might vanish altogether at pressures near 60 GPa, and recent experiments seem to confirm this (Ono *et al.*, 2010).

12.3 *Ab initio* phase stability of iron carbides

As almost all steels contain carbon, and carbon has a tendency to form carbides with transition metals, particularly with those early in the transition metal series, carbides are almost always present. Alloying elements often have stronger chemical affinity towards carbon than iron but their concentration is usually too low to prevent the formation of iron carbides. The iron–carbon composition–temperature phase diagram indicates that bcc and fcc iron-rich solid solutions and pure carbon are the only stable solid phases (Ågren, 1979; Okamoto, 1990); however, in practice pure elemental carbon is not found in steel, instead, iron carbides are formed. The Fe-C phase diagram assessments in the literature (Ågren, 1979; Okamoto, 1990) based on experimental data, typically show one type of iron carbide only, Fe_3C cementite. Furthermore, although long known to exist over a range of compositions (Petch, 1944), cementite is typically erroneously represented as a line-compound. However, detailed experiments and first-principles calculations indicate a more varied phase stability.

Early *ab initio* studies of iron carbides have shown that Fe_3C cementite has a formation enthalpy that is quite similar to that of other carbide structures (Widom and Mihalkovic, 2005; Sluiter, 2006), later confirmed in more detailed studies by Fang *et al.* (2010a,b,c,d). Experimentally, oftentimes cementite Fe_3C only is reportedly observed in steel. However, already in the early 1950s Hofer and Cohn (1951) found that η-Fe_2C carbide forms first in quenched steels at temperatures between 370 and 470 K. Around the same time Manes *et al.* (1952) observed that ε-Fe_2C is the only carbide forming up to 520 K, while it can form together with cementite at temperatures as high as 600 K and that it then is a precursor for Hägg carbide (Fe_5C_2) (Hirotsu and Nagakura, 1972). A very long aging study at 300 K followed

[3]The hcp M-point is located at the middle of the rectangular face of the first Brillouin zone.

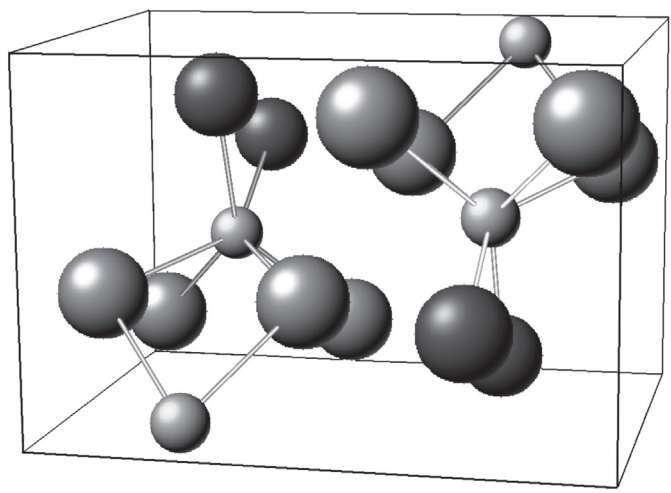
© Woodhead Publishing Limited, 2012

by a brief 405 K anneal has revealed both η-Fe_2C and ε-Fe_2C (Van Genderen *et al.*, 1993). At temperatures above 720 K cementite is formed exclusively (Hofer and Cohn, 1951). The actual situation may be more complex still, because very small iron carbide precipitates in an iron matrix are difficult to structurally characterize and it is possible that in fact many other carbides can be formed as well, possibly stabilized by coherency strains with the surrounding iron-rich matrix (Fang *et al.*, 2010a).

Iron carbides are of interest also for planetary science, as they have been considered candidate earth core materials (Wood, 1993; Vocadlo *et al.*, 2002; Fiquet *et al.*, 2009; Lord *et al.*, 2009; Ono and Mibe, 2010), as a catalyst for Fischer–Tropsch synthesis (Steynberg *et al.*, 2008; Cheng *et al.*, 2010; de Smit *et al.*, 2010) and other reactions (Gracia *et al.*, 2009), and potentially for their Invar properties (Shigematsu, 1975; Umemoto *et al.*, 2001; Wood *et al.*, 2004; Duman *et al.*, 2005; Khmelevskyi *et al.*, 2005a).

Cementite, the most common metastable carbide in steel, is ferromagnetic at room temperature with a Curie temperature, T_c, of about 483 K (Umemoto *et al.*, 2001; Zhao *et al.*, 2009). Cementite has an orthorhombic crystal structure represented by Pearson symbol oP16, space group number 62, with 12 Fe and 4 C atoms per unit cell (Petch, 1944; Fasiska and Jeffrey, 1965). There are two inequivalent Fe positions with Wyckoff notations, 8d and 4c, respectively. Carbon atoms occupy a 4c Wyckoff site also (see Fig. 12.2). Its structural and elastic properties have been studied in detail (Faraoun *et al.*, 2006; Jiang *et al.*, 2008a; Nikolussi *et al.*, 2008).

Cementite is often assumed to be stoichiometric (Ågren, 1979; Okamoto, 1990), but older X-ray measurements (Petch, 1944) as well as recent neutron



12.2 Crystal structure of cementite, small spheres: carbon; dark medium-sized spheres: iron 4c; large spheres: iron 8d positions.

© Woodhead Publishing Limited, 2012

scattering experiments have shown cementite in steel to be carbon depleted to about $Fe_3C_{0.75}$ near 1070 K and *ab initio* calculations have confirmed low formation energies for carbon vacancies in cementite (Jiang *et al.*, 2008b; Voronin *et al.*, 2010). This finding appears very plausible considering that much stronger carbide formers than iron, e.g. vanadium (Ozolins and Häglund, 1993; Rafaja *et al.*, 1998), titanium (Hugosson *et al.*, 2001; Korzhavyi *et al.*, 2002; Tsetseris and Pantelides, 2008), niobium (Rempel and Gusev, 2000), and hafnium (Gusev and Zyryanova, 2000) are all known to form carbon deficient carbides (Sourmail, 2001; Henriksson *et al.*, 2008). Strong carbon depletion has been observed also in cementite under intense plastic deformation (Hong *et al.*, 1999). Thus, other iron carbides might also be carbon deficient when formed in steel. Surprisingly, there is also an iron carbide $Fe_{23}C_6$ for which the Fe vacancy has been calculated to require little energy (Fang *et al.*, 2010c).

From a phase stability perspective, cementite competes most prominently with η-Fe_2C, ε-Fe_2C and Hägg Fe_5C_2 carbides. Various models for η-Fe_2C and ε-Fe_2C were recently reviewed (Faraoun *et al.*, 2006; Lv *et al.*, 2008; Fang *et al.*, 2010a). It was concluded that ε-Fe_2C is rather stable and that it can form relatively easily from fcc Fe through rearrangement of densely packed planes. The most stable hexagonal ε-carbide was argued to be carbon deficient at a composition $Fe_{2.4}C$, and these carbides with somewhat variable carbon concentrations could lower their energy further by transforming to orthorhombic η-Fe_2C, Hägg carbide Fe_5C_2, and cementite Fe_3C, depending on temperature and other possible factors (Fang *et al.*, 2010a). It was argued that the rather low energy iron carbide Fe_7C_3 was less likely to occur because it could not so easily be derived from a hexagonal ε-carbide precursor and also because of poor matching with the ferrite matrix (Fang *et al.*, 2010a).

The reason that cementite is usually seen in steels has been argued on the basis of finite temperature thermodynamic factors. Cementite has relatively large local moments per iron atom which disorder at relatively low temperature which makes for a larger magnetic entropy for cementite than other competing carbides and, furthermore, cementite is favoured also by vibrational effects. As a consequence, cementite is predicted to be more stable than mixtures of other carbides with ferrite at temperatures above 330 K (Fang *et al.*, 2010d). Recently, the non-zero temperature thermodynamic properties of cementite were analysed in detail (Hallstedt *et al.*, 2010). Cementite can be present in various forms in steel, e.g. as pearlite, a fine eutectoid mixture of cementite and ferrite, or as fine discrete precipitation in annealed martensite, and cementite strongly affects the properties of steel.

The (de)stabilization of cementite plays an important role in the secondary hardening of steel (Kwon *et al.*, 1998; Lee *et al.*, 2001), and the suppression of cementite by alloying elements is of utmost interest for transformation-induced plasticity (so-called TRIP) steels (Tamura, 1982; Timokhina *et*

© Woodhead Publishing Limited, 2012

al., 2004; see also Chapter 7) and for steels based on the quenching and partitioning process (Speer *et al*., 2003, Santofimia *et al*., 2010; see also Chapter 8).

12.4 Substitutional alloying elements

Once *ab initio* calculations reproduced the correct Fe ground state crystal structure, it is relatively straightforward to apply methods developed earlier for other alloys to binary Fe-M alloys, especially for those cases where the alloying element M is substitutional in bcc Fe. We focus first on the bcc case because of its relatively better understood ferromagnetic state.

As initially the computational methods were based on the CPA, which did not allow for lattice relaxations, at first alloys were selected in which relaxation effects could be anticipated to be fairly small, such as Fe-Co (Sluiter and Kawazoe, 1995; Abrikosov *et al*., 1996), Fe-Mn, Fe-Cr (Kulikov and Demangeat, 1997), Fe-V and Fe-Al (Staunton *et al*., 1997). In Fe-Co the CsCl-type ordering on the bcc lattice near equiatomic composition could be linked to magnetic effects (Sluiter and Kawazoe, 1995; Abrikosov *et al*., 1996). These magnetic effects also inspired others (Drautz *et al*., 2004; Diaz-Ortiz *et al*., 2006) to investigate this alloy in detail. Other alloys with bcc superstructures or solid solutions have also been analysed, such as Fe-Al (Gonzales-Ormeño *et al*., 2002, 2006; Smirnov *et al*., 2005; Adebambo *et al*., 2010), Fe-Be (Ohtani *et al*., 2004), and Fe-V (Kissavos *et al*., 2006).

However, Fe-Cr is by far the most extensively studied alloy in this context, partially because of its potential application under high radiation fluxes in fusion reactors (Lavrentiev *et al*., 2010b) and also because of its intriguing reversal of ordering and phase separation tendencies near $Fe_{0.9}Cr_{0.1}$ (Akai and Dederichs, 1993; Moroni and Jarlborg, 1993; Olsson *et al*., 2003; Klaver *et al*., 2006; Ackland, 2006; Lavrentiev *et al*., 2007, 2010a; Tarafder *et al*., 2008; Ruban *et al*., 2008; Xiong *et al*., 2010). The issues surrounding radiation damage in Fe-Cr spurred extensive *ab initio* calculations for lattice defects and their mutual interactions, and the influence they exert on materials properties (Klaver *et al*., 2007, 2010; Sandberg *et al*., 2008; Terentyev *et al*., 2008; Becquart and Domain, 2010). Surface segregation (Wille *et al*., 1998; Geng, 2003), grain boundaries (Lu *et al*., 2010; Wachowicz *et al*., 2010), carbon dissolution and diffusion (Sandberg *et al*., 2008) in Fe-Cr have been considered as well.

A number of ternary bcc-based alloys have been studied by *ab initio* modelling, such as Fe-Al-C (Maugis *et al*., 2006), Fe-Ni-Al (Eleno *et al*., 2006), Fe-Nb-B (Yoshitomi *et al*., 2008), Fe-Zr-B (Tokunaga *et al*., 2008), Fe-Al-Ti (Alonso *et al*., 2009) and Fe-Al-Mo (Sodre *et al*., 2009).

Some of the earliest work on fcc iron alloys focused on stainless steels, on the role of electronic structure on the chemical short range order (Gavriljuk *et*

© Woodhead Publishing Limited, 2012

al., 2000). Gavriljuk *et al*. (2000) argued that short range order in austenitic alloys is correlated with the free electron concentration, whereas clustering of alloy atoms was associated with enhanced localization of electrons at the atomic sites. Alloying with transition metals to the left of Fe in the periodic table (Cr, Mn, Mo) and carbon lead via enhanced localization to clustering, whereas elements such as Ni, Cu, Si, Al and N promoted a more homogeneous distribution of solute atoms in CrNiMn austenitic steels.

Other early work focused on optimizing the ductility as a function of the composition of austenitic Fe-Cr-Ni alloys (Vitos *et al*., 2002, 2003, 2006b). Although austenitic stainless steels are not ferromagnetic, magnetism is known to play an important role (Vitos *et al*., 2006a; Pitkanen *et al*., 2009). Magnetic storage applications lead to an early interest in Fe-Pd (Shi *et al*., 2002; Mohri and Chen, 2004; Barabash *et al*., 2009) and Fe-Pt (Mohri and Chen, 2002; Zotov and Ludwig, 2008; Barabash *et al*., 2009) alloys featuring CuAu-type ordering.

Among fcc alloys, Fe-Ni (Mohn *et al*., 1991; Podgorny, 1992; Akai and Dederichs, 1993; Abrikosov *et al*., 1995, 2007; Wang *et al*., 1997; Entel *et al*., 2000; Crisan *et al*., 2002; Ruban *et al*., 2007; Liot and Abrikosov, 2009; Barabash *et al*., 2009; Xiong *et al*., 2011) is of significance for the occurrence of the Invar effect, generally understood to be due to the volume contraction associated with magnetic (e.g. high-spin to low-spin; Moruzzi, 1992) transformation compensating for the vibrational anharmonicity caused by thermal expansion. Lagarec *et al*. (2001) have challenged this view. They argue that the high to low moment transition is separate from the Invar effect, and might not even occur at all. In Fe-Ni rather, local moments do not change in magnitude so much as that they become disordered. In their view the electronic changes that are associated with this magnetic disordering are responsible for the vanishing of thermal expansion. Invar effects in similar alloys, such as Fe-Pt, have also been studied (Podgorny, 1992; Uhl *et al*., 1994; Uhl and Kübler, 1997; Khmelevskyi *et al*., 2005b; Barabash *et al*., 2009).

Alloying elements can also give rise to complex intermetallic phases such as the so-called σ phase that can form in Cr bearing steels upon annealing. In steels alloyed with high levels of transition metals, such phases can be very detrimental to mechanical and other properties. *Ab initio* methods have been applied to better understand the factors that stabilize these phases, such as electronic d-band filling and atomic size. Particularly for the FeCr σ phase, there is a rich *ab initio* literature (Sluiter *et al*., 1995; Havrankova *et al*., 2001; Vrestal, 2001; Korzhavyi *et al*., 2005; Vrestal *et al*., 2006; Cieslak *et al*., 2008; Kabliman *et al*., 2009; Ackland, 2009; Pavlu *et al*., 2010, Kabliman *et al*., 2011). Other σ phases in Fe-based alloys studied by *ab initio* methods are Fe-V (Korzhavyi *et al*., 2005; Cieslak *et al*., 2010), Fe-W and Fe-Cr-W (Chvatalova *et al*., 2007), Fe-Mo (Korzhavyi *et al*., 2005; Vrestal *et al*.,

© Woodhead Publishing Limited, 2012

2006; Joubert, 2008), Fe-Cr-Mo (Vrestal *et al.*, 2006). As these complex phases occur mostly in highly alloyed steels, we will consider it sufficient here to refer to a recent review of experimental data (Joubert, 2008).

Alloying elements in steel cannot usually be understood in terms of binary phase diagrams because the interaction with carbon plays an important role. This interaction can result in the precipitation of carbides, such as NbC and many others (Sourmail, 2001; Henriksson *et al.*, 2008). As the number of carbides actually occurring in alloyed steel is very large, and as some of these carbides may not incorporate iron, the focus here will be on how alloying elements affect the carbides that are naturally occurring in the binary Fe-C alloy. The most apparent approach then is to consider whether and where alloying elements are incorporated in iron carbides such as cementite.

Typically, Fe atoms in the carbide structure are substituted by other elements and subsequently the resulting changes in the electronic structure and the energetics are evaluated (Mizuno *et al.*, 1997; Shein *et al.*, 2007; Medvedeva *et al.*, 2008; Konyaeva and Medvedeva, 2009; Gutina *et al.*, 2009; Zhou *et al.*, 2009; Ande and Sluiter, 2010; von Appen *et al.*, 2010; Jang *et al.*, 2009, 2010b). In some cases substitution of the carbon site in cementite by boron (Medvedeva *et al.*, 2007), or alternative iron carbide structures, have been considered (Widom and Mihalkovic, 2005; Ohodnicki *et al.*, 2008; Jang *et al.*, 2010a).

In the case of metal substitution on the Fe sites in cementite, it has become apparent that generally the lower symmetry site with Wyckoff designation 8d is favoured over the 4c site, most probably because the former site allows for more advantageous structural relaxation as most metal species are larger than Fe (Ande and Sluiter, 2010). In many of these studies the formation enthalpy of the mixed carbide relative to unalloyed stoichiometric iron carbide and the pure alloying element in its standard state is used to evaluate whether that alloying element stabilizes the iron carbide (Shein *et al.*, 2007; Medvedeva *et al.*, 2008; Konyaeva and Medvedeva, 2009; Gutina *et al.*, 2009; Zhou *et al.*, 2009; Jang *et al.*, 2009, 2010a, 2010b). This criterion has been challenged (Ande and Sluiter, 2010) because in reality the pure alloying element in its standard state plays no role in the actual thermodynamic equilibrium. Instead it is argued that both ferrite and iron carbide, and possibly even other phases, compete for the dissolution of the alloying element.[4] Then

[4]Alloying elements that do not dissolve in cementite destabilize it for several reasons: (a) the ferrite free energy is lowered relative to that of cementite; imagining austenite to remain unchanged, we see that thermodynamically a two-phase mixture of ferrite and carbon-supersaturated austenite becomes more favourable than a ferrite and cementite mixture; (b) nucleation of cementite is more difficult because alloying elements need to be expelled from the nucleus; (c) growth of cementite is hindered because alloying elements need to be repelled and redistributed.

© Woodhead Publishing Limited, 2012

it follows that an alloying element stabilizes the iron carbide only if it is the more favourable phase for its dissolution, in other words the solution enthalpy in carbide should be more exothermic than in ferrite. While this thermodynamic argument could resolve the earlier reports that incorrectly identified Al as a cementite stabilizer (it is not!), nevertheless some other relatively weak cementite stabilizers, such as V, Cr and Mo, were computed to be inert or even ferrite formers (Ande and Sluiter, 2010). Currently it is thought that the magnetic disordering in cementite and other iron carbides plays an important role for the more subtle alloying elements.

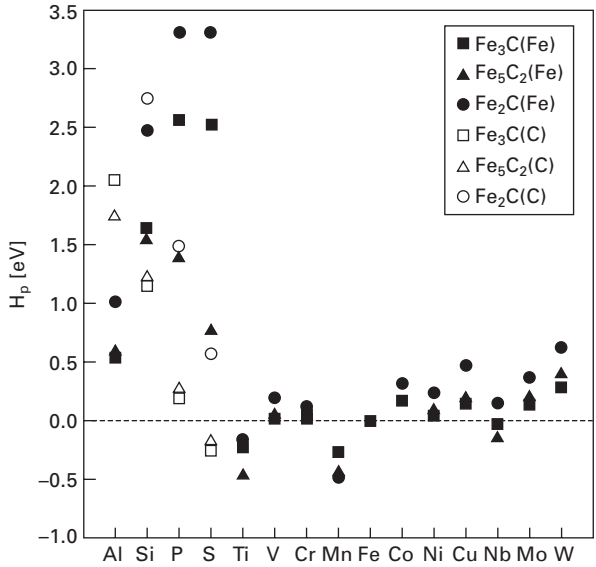
Experimentally and theoretically it has been shown that Si is the strongest cementite destabilizer, followed by Al and P, whilst Mn, in particular, stabilizes the iron carbides (Ande and Sluiter, 2010, 2011). The role of Si is of great interest for Q&P processes and for bainitic steels. *Ab initio* calculations have shown that, while Si prefers dissolution in the ferrite phase for any of the carbides considered (cementite Fe_3C, Hägg Fe_5C_2 and η-carbide Fe_2C), dissolution in η-carbide is least favoured. Another surprising finding is that in Fe_3C and Fe_5C_2, Si would replace C rather than Fe, while in Fe_2C it replaces Fe (see Fig. 12.3). Current *ab initio* calculations do not yet address the role that Si plays in nucleation and diffusion during austenite transformation.

In the solid solution phases too, alloying elements that substitute for Fe interact with carbon (Sawada *et al*., 2005; Simonovic *et al*., 2010) and other interstitial species such as N (Kamminga *et al*., 2003), and lattice defects such as vacancies and interstitials (Olsson *et al*., 2007, 2010). At grain boundaries, where due to segregation impurity concentrations may be much enhanced, and grain boundary cohesion affected, the mechanical properties can be strongly affected (Wu *et al*., 1994, 1996; Zhong *et al*., 1997; Geng *et al*., 2000; Jiang and Carter, 2004a; Kim *et al*., 2004; Braithwaite and Rez, 2005; Gesari *et al*., 2006; Wachowicz and Kiejna, 2008; Wachowicz *et al*., 2010; Yuasa and Mabuchi, 2010). Calculations show that the interactions between impurity, or alloying species themselves can be very significant and can result in expulsion from a boundary of a weaker segregating species by a stronger segregating species (Viefhaus and Richarz, 1995).

Interstitial species have also been shown to strongly interact with other free volume type defects, particularly with vacancies (Domain *et al*., 2004; Legris, 2004; Fu *et al*., 2007). It has been computed that under near equilibrium conditions the vast majority of vacancies in ferrite would be trapping several carbon atoms per vacancy (Legris, 2004; Forst *et al*., 2006; Fu and Willaime, 2008). It should be emphasized that carbon remains in a relaxed octahedral interstice, and does not actually take the centre position in an Fe vacancy in ferrite (Simonetti *et al*., 2007).

In austenite, where the magnetic local moments are disordered at all but the lowest temperatures, it has been attempted to determine the carbon–vacancy interaction by sampling various local moment configurations (Slane *et al*.,

© Woodhead Publishing Limited, 2012



12.3 Partitioning enthalpy between ferrite and carbides (as defined by Ande and Sluiter, 2010) for various alloying elements. Three stoichiometric carbides were considered: cementite Fe_3C, Hägg Fe_5C_2 and η-carbide Fe_2C. ε-carbide $Fe_{2.4}C$ derives from η-carbide by introduction of vacancies on the carbon sites. Si has a positive partitioning enthalpy indicating preference for the ferrite phase over any of the three carbides. In Fe_3C and Fe_5C_2, computations show Si substitution on the Fe sites (filled symbols) to be even more disadvantageous than Si substitution on the C sites (open symbols), while in Fe_2C the Fe sites (filled circles) are less disadvantageous than the C sites (open circles) for Si substitution (Ande and Sluiter, 2011).

2004). A weak attraction of about 0.35 eV was computed, in agreement with experimental evidence. The vacancy–carbon attraction in austenite is less than half as strong as in ferrite, but nevertheless because of generally higher carbon concentations can be expected to have significant effects, such as introduction to Snoek-like internal damping, reduction of the apparent activation energy for Fe self-diffusion by increasing C content (and associated effects on high-temperature steady state creep), as well as hardening due to vacancy–carbon complexes.

12.5 *Ab initio* description of diffusivity in bcc Fe

As mentioned already, carbon and nitrogen are interstitial species in both ferritic and austenitic steel. The situation for boron is more complex because a substitutional boron has about the same energy as an interstitial boron and a vacancy (Fors and Wahnström, 2008). Therefore, a boron atom can

© Woodhead Publishing Limited, 2012

jump relatively easily between a substitutional site and an interstitial site while leaving a vacancy behind, and as the activation energy for interstitial diffusion is rather low (0.2 eV) this makes boron a highly mobile species in ferrite (Baik *et al.*, 2010).

The diffusion of carbon in ferrite is well understood and excellent agreement between experiment and *ab initio* calculations exists (Jiang and Carter, 2003, 2005; Domain *et al.*, 2004; Simonovic *et al.*, 2010). However, the strong carbon–vacancy interaction suggests that carbon might strongly affect the diffusion of substitutional alloy species (Legris, 2004; Tapasa *et al.*, 2007; Fu *et al.*, 2008). *Ab initio* modelling of diffusion of substitutional alloying species is still generally limited to ferritic alloys in the dilute limit due to the magnetic complications in austenite.

Activation energies for substitutional impurity diffusion can generally be separated in a vacancy formation term, a solute-vacancy binding term, and activation energies for various vacancy jumps. In ferrite, it is well established that the vacancy formation energy is a little in excess of 2 eV (Jiang and Carter, 2003; Domain *et al.*, 2004; Fors and Wahnström, 2008). The solute-vacancy binding energies have been computed also for a number of elements (Vincent *et al.*, 2005; Ohnuma *et al.*, 2009; Olsson *et al.*, 2010) (see Table 12.1). Generally, impurities are bound to vacancies because almost all impurities are too large to fit well in the ferrite matrix. For transition metals (TM), the attraction to vacancies is quite regular with the strongest attraction occurring at the ends of the TM series, and the weakest attraction at the middle (Olsson *et al.*, 2010). Mn is the only element that breaks this tendency by being more attracted to a vacancy than its neighbours Cr and V.

Recently, the Fe self-diffusivity and the diffusivities of Hf, Ta, Mo and W were computed including the pre-exponential frequency factor (Huang *et al.*, 2010). Some *ab initio* computed impurity diffusion parameters in ferromagnetic bcc Fe are listed in Table 12.2. Even in ferrite, it was shown to be important to make a (semi-empirical) correction for the loss of magnetic order above the Curie temperature (Perez and Weissmann, 2004; Fähnle and Schimmele, 2005; Huang *et al.*, 2010).

For other elements also, with various methodologies such as being applicable to materials under irradiation, diffusivities have been computed: Cu (Barashev and Arokiam, 2006; Vincent *et al.*, 2006, 2007; Soisson and Fu, 2007; Djurabekova *et al.*, 2007), H (Jiang and Carter, 2004b; Sorescu, 2005; Sanchez *et al.*, 2008; Kimizuka *et al.*, 2011), He (Ortiz *et al.*, 2007; Borodin and Vladimirov, 2009; Terentyev *et al.*, 2009), P (Domain and Becquart, 2005; Barashev, 2005; Meslin *et al.*, 2007), Mn, Ni and Si (Vincent *et al.*, 2006, 2007).

© Woodhead Publishing Limited, 2012

Table 12.1 Binding energies (meV) for vacancy–subsitutional solute atom pairs as a function of the distance (in units of the bcc lattice parameter) in ferromagnetic bcc Fe

	[½ ½ ½]	[100]	[110]	[1½ ½ ½]	[111]	Reference
Sc	–630	–	–	–	–	Ohnuma *et al.*, 2009
Ti	–237	174	–10	–1	–12	Olsson *et al.*, 2010
Ti	–220	–	–	–	–	Ohnuma *et al.*, 2009
Ti*	–160	–	–	–	–	Doyama, 1986
V	–56	86	5	5	–18	Olsson *et al.*, 2010
V	–40	–	–	–	–	Ohnuma *et al.*, 2009
V*	>–105	–	–	–	–	Doyama, 1986
Cr	–57	–14	–4	7	–20	Olsson *et al.*, 2010
Cr	–50	–	–	–	–	Ohnuma *et al.*, 2009
Cr*	>–105	–	–	–	–	Doyama, 1986
Mn	–206	–140	–65	–32	–53	Olsson *et al.*, 2010
Mn	–120	–70	–	–	–	Vincent *et al.*, 2005
Mn	–160	–	–	–	–	Ohnuma *et al.*, 2009
Mn*	–150	–	–	–	–	Doyama, 1986
Co	12	–96	–6	7	–10	Olsson *et al.*, 2010
Co	–100	–	–	–	–	Ohnuma *et al.*, 2009
Co*	–140	–	–	–	–	Doyama, 1986
Ni	–115	–197	–35	–1	–22	Olsson *et al.*, 2010
Ni	–30	–180	–	–	–	Vincent *et al.*, 2005
Ni	–190	–	–	–	–	Ohnuma *et al.*, 2009
Ni*	–215	–	–	–	–	Doyama, 1986
Cu	–270	–162	–33	38	–25	Olsson *et al.*, 2010
Cu	–170	–190	–	–	–	Vincent *et al.*, 2005
Cu	–240	–	–	–	–	Ohnuma *et al.*, 2009
Cu	–170	–280	–40			Becquart and Domain, 2003
Cu*	–140	–	–	–	–	Doyama, 1986
Zn	–330	–	–	–	–	Ohnuma *et al.*, 2009
Zr	–734	74	–69	–32	–25	Olsson *et al.*, 2010
Nb	–367	144	–42	–13	–28	Olsson *et al.*, 2010
Mo	–165	109	–21	–2	–22	Olsson *et al.*, 2010
Mo	–330	–	–	–	–	Ohnuma *et al.*, 2009
Mo	–170	–	–	–	–	Huang *et al.*, 2010
Tc	–134	37	–33	2	–21	Olsson *et al.*, 2010
Ru	–114	–16	–47	2	–15	Olsson *et al.*, 2010
Rh	–154	–96	–58	0	–15	Olsson *et al.*, 2010
Pd	–299	–183	–90	–8	–30	Olsson *et al.*, 2010
Pd*	–210	–	–	–	–	Doyama, 1986
Ag	–530	–212	–117	–17	–33	Olsson *et al.*, 2010
Hf	–610	153	–63	–21	–24	Olsson *et al.*, 2010
Hf	–650	–	–	–	–	Huang *et al.*, 2010
Ta	–309	178	–32	–5	–25	Olsson *et al.*, 2010
Ta	–320	–	–	–	–	Huang *et al.*, 2010
W	–141	130	–20	2	–26	Olsson *et al.*, 2010
W	–140	–	–	–	–	Huang *et al.*, 2010
Re	–105	56	–25	5	–23	Olsson *et al.*, 2010
Os	–117	–19	–46	7	–21	Olsson *et al.*, 2010
Ir	–145	–89	–57	8	–13	Olsson *et al.*, 2010
Pt	–268	–186	–81	3	–24	Olsson *et al.*, 2010

© Woodhead Publishing Limited, 2012

Table 12.1 Continued

	[½ ½ ½]	[100]	[110]	[1½ ½ ½]	[111]	Reference
Au	–494	–265	–121	–10	–33	Olsson *et al.*, 2010
Au*	–270	–	–	–	–	Doyama, 1986
Si	–240	–140	–	–	–	Vincent *et al.*, 2005
Si*	–230	–	–	–	–	Doyama, 1986
Si	–290	–	–	–	–	Ohnuma *et al.*, 2009
Si*	–230	–	–	–	–	Doyama, 1986
P	–360	–	–	–	–	Ohnuma *et al.*, 2009
Sb*	–455	–	–	–	–	Doyama, 1986
S	–530	–	–	–	–	Ohnuma *et al.*, 2009

Note: Negative binding energies indicate attraction. The binding energies tend to zero for large distances the vacancy and the solute atom. Experimentally determined binding energies (Doyama, 1986), marked with asterisk, are not pair-specific. Therefore the data from Doyama (1986) are listed in the [½½½] column but actually must be interpreted to represent the strongest binding pair (e.g. [100] pair for Ni).

Table 12.2 First-principles computed substitutional impurity diffusion in ferromagnetic bcc Fe

	D_0 (m^2/s)	Q (eV)	Reference
Fe	6.7×10^{-5}	2.87	Huang *et al.*, 2010
Mo	6.3×10^{-5}	2.60	Huang *et al.*, 2010
W	1.4×10^{-4}	2.80	Huang *et al.*, 2010
Ta	–	2.35	Huang *et al.*, 2010
Hf	–	1.75	Huang *et al.*, 2010
H	–	0.046	Jiang and Carter, 2004b
H		0.047	Sorescu, 2005
H	3.23×10^{-8}	0.037	Kimizuka *et al.*, 2011
He		0.06	Borodin and Vladimirov, 2009
He		0.05	Terentyev *et al.*, 2009
Cu	5.86×10^{-4}	0.64	Djurabekova *et al.*, 2007

12.6 Future trends

Sometimes it is suggested that advancing capabilities in *ab initio* modelling of materials is driven largely by improvement in computational hardware. However, our limitations are often more of a theoretical and algorithmic nature. For example, a proper description of the Fe ground state was possible only when the GGA was formulated; having better computer hardware played no role. Likewise, without the development of the nudged elastic band method, it would have remained impractical to compute the minimum energy paths required for modelling atomic diffusion; and without analytic force and stress calculations within DFT codes, it would have remained impractical to optimize complex and low symmetry structures. Therefore, the

© Woodhead Publishing Limited, 2012

most promising future developments are those where our current limitations are most apparent:

- The magnetic state in austenite and in ferrite and various iron carbides above their Curie temperatures: current methodology of sampling a few antiferromagnetic local moment configurations with frozen moments as an approximation for a disordered local moment state is rather ineffective.
- Bridging length- and timescale through multi-scale physics: the methodology that we currently have for extracting effective interatomic potentials from *ab initio* data is highly cumbersome and mostly art rather than science.
- While the GGA generally has given improvements over the local density approximation, accuracy is still limited and even qualitative incorrect results can occur for some classes of materials (strongly correlated electron systems: actinides) and for certain electronic structure features (band gaps).

Future developments that address these issues most probably will have the greatest impact in the near future.

Finally, on the hardware side, significant help may be underway: general-purpose computing on graphics processing units may revolutionize large-scale computing efforts once software has been recoded to take advantage of the abundant parallelization offered, coupled with the hardware bottlenecks, such as bus bandwidth and latency between the CPU and the GPU, and the peculiarities of the programming resources.

12.7 References

Abrikosov IA and Johansson B (1998), 'Applicability of the coherent-potential approximation in the theory of random alloys', *Physical Review B*, 57, 14164–14173.

Abrikosov IA, Eriksson O, Söderlind P, Skriver HL and Johansson B (1995), 'Theoretical aspects of the Fe_cNi_{1-c} Invar alloy', *Physical Review B*, 51, 1058–1063.

Abrikosov IA, James P, Eriksson O, Söderlind P, Ruban AV, Skriver HL and Johansson B (1996), 'Magnetically induced crystal structure and phase stability in $Fe_{1-c}Co_c$', *Physical Review B*, 54, 3380–3384.

Abrikosov IA, Kissavos AE, Liot F, Alling B, Simak SI, Peil O and Ruban AV (2007), 'Competition between magnetic structures in the Fe rich fcc FeNi alloys', *Physical Review B*, 76, 014434.

Acet M, Zähres H, Wassermann EF and Pepperhoff W (1994), 'High-temperature moment-volume instability and anti-Invar of γ-Fe', *Physical Review B*, 49, 6012–6017.

Ackland GJ (2006), 'Magnetically induced immiscibility in the Ising model of FeCr stainless steel', *Physical Review Letters*, 97, 015502.

Ackland GJ (2009), 'Ordered σ-type phase in the Ising model of Fe-Cr stainless steel', *Physical Review B*, 79, 094202.

Adebambo PO, Bamgbose KM, Olowofela JA, Oguntuase JA and Adebayo GA (2010),

© Woodhead Publishing Limited, 2012

'Electronic structure and optical properties of α-Fe-Al alloy from *ab initio* calculations', *Physica B – Condensed Matter*, 405, 4578–4581.
Ågren J (1979), 'A thermodynamic analysis of the Fe-C and Fe-N phase diagrams', *Metallurgical Transactions Section A*, 10, 1847–1852.
Akai H and Dederichs PH (1993), 'Local moment disorder in ferromagnetic alloys', *Physical Review B*, 47, 8739–8747.
Alonso PR, Gargano PH, Ramirez-Caballero GE, Balbuena PB and Rubiolo GH (2009), 'First principles calculation of $L2_1$+A2 coherent equilibria in the Fe-Al-Ti system', *Physica B: Condensed Matter*, 404, 2845–2847.
Ande CK and Sluiter MHF (2010), 'First-principles prediction of partitioning of alloying elements between cementite and ferrite', *Acta Materialia*, 58, 6276–6281.
Ande CK and Sluiter MHF (2011), 'First-principles calculations on stabilization of iron carbides (Fe_3C, Fe_5C_2 and η-Fe_2C) in steels by common alloying elements', *Metallurgical and Materials Transactions A*, submitted (E-TP-11-555-A).
Asada T and Terakura K (1992), 'Cohesive properties of iron obtained by use of the generalized gradient approximation', *Physical Review B*, 46, 13599–13602.
Ayuela A and March NH (2010), 'The magnetic moments and their long-range ordering for Fe atoms in a wide variety of metallic environments', *International Journal of Quantum Chemistry*, 110, 2725–2733.
Bagno P, Jepsen O and Gunnarsson O (1989), 'Ground-state properties of third-row elements with nonlocal density functionals', *Physical Review B*, 40, 1997–2000.
Baik SS, Min BI, Kwon SK and Koo YM (2010), 'Boron solution and distribution in α-Fe: application to boron steel', *Physical Review B*, 81, 144101.
Bansil A, Kaprzyk S, Mijnarends PE and Tobola J (1999), 'Electronic structure and magnetism of $Fe_{3-x}V_xX$ (X = Si, Ga, and Al) alloys by the KKR-CPA method', *Physical Review B*, 60, 13396–13412.
Barabash SV, Chepulskii RV, Blum V and Zunger A (2009), 'First-principles determination of low-temperature order and ground states of Fe-Ni, Fe-Pd, and Fe-Pt', *Physical Review B*, 80, 220201.
Barashev AV (2005), 'Monte Carlo simulation of phosphorus diffusion in α-iron via the vacancy mechanism', *Philosophical Magazine*, 85, 1539–1555.
Barashev AV and Arokiam AC (2006), 'Monte Carlo modelling of Cu atom diffusion in α-Fe via the vacancy mechanism', *Philosophical Magazine Letters*, 86, 321–332.
Becquart CS and Domain C (2003), '*Ab initio* contribution to the study of complexes formed during dilute FeCu alloys radiation', *Nuclear Instruments and Methods in Physics Research B*, 202, 44–50.
Becquart CS and Domain C (2010), 'Introducing chemistry in atomistic kinetic Monte Carlo simulations of Fe alloys under irradiation', *Physica Status Solidi B*, 247, 9–22.
Belonoshko AB, Derlet PM, Mikhaylushkin AS, Simak SI, Hellman O, Burakovsky L, Swift DC and Johansson B (2009), 'Quenching of bcc-Fe from high to room temperature at high-pressure conditions: a molecular dynamics simulation', *New J. Phys.*, 11, 093039.
Bergqvist L, Eriksson O, Kudrnovsky J, Drchal V, Bergman A, Nordström L and Turek I (2005), 'Magnetic properties and disorder effects in diluted magnetic semiconductors', *Physical Review B*, 72, 195210.
Bester G, Meyer B and Fähnle M (1999), '*Ab initio* calculation of the activation energy for Ni self-diffusion in $D0_3$ Ni_3Sb', *Physical Review B*, 59, 3274–3275.
Bieber A, Gautier F, Treglia G and Ducastelle F (1981), 'Electronic structure, pairwise interactions and ordering energies in binary f.c.c. transition metal alloys', *Solid State Communications*, 39, 149–153.

© Woodhead Publishing Limited, 2012

Blöchl PE (1994), 'Projector augmented-wave method', *Physical Review B*, 50, 17953–17979.

Boehler R (1993), 'Temperatures in the Earth's core from melting-point measurements of iron at high static pressures', *Nature*, 363, 534–536.

Borodin VA and Vladimirov PV (2009), 'Kinetic properties of small He–vacancy clusters in iron', *J. Nucl. Mat.*, 386–388, 106–108.

Bos C, Sietsma J and Thijsse BJ (2006), 'Molecular dynamics simulation of interface dynamics during the fcc-bcc transformation of a martensitic nature', *Physical Review B*, 73, 104117.

Bose SK and Kudrnovsky J (2010), 'Exchange interactions and Curie temperatures in Cr-based alloys in the zinc blende structure: volume- and composition-dependence from first-principles calculations', *Physical Review B*, 81, 054446.

Boukhvalov DW, Gornostyrev YN, Katsnelson MI and Lichtenstein AI (2007), 'Magnetism and local distortions near carbon impurity in γ-iron', *Physical Review Letters*, 99, 247205.

Braithwaite JS and Rez P (2005), 'Grain boundary impurities in iron', *Acta Materialia*, 53, 2715–2726.

Brown JM and McQueen RG (1986), 'Phase transitions, Grüneisen parameter, and elasticity for shocked iron between 77 GPa and 400 GPa', *J. Geophys. Res.*, 91, 7485–7494.

Bylander DM and Kleinman L (1999), 'Spiral spin-density-wave ground state of γ-Fe calculated with spin stiffness correction to the local-spin-density approximation', *Physical Review B*, 60, R9916–R9918.

Bylander DM, Niu Q and Kleinman L (2000), 'Fe magnon dispersion curve calculated with the frozen spin-wave method', *Physical Review B*, 61, R11875–R11878.

Chen QL and Sundman B (2001), 'Modeling of thermodynamic properties for bcc, fcc, liquid, and amorphous iron', *Journal of Phase Equilibria*, 22, 631–644.

Cheng J, Hu P, Ellis P, French S, Kelly G and Lok CM (2010), 'Density functional theory study of iron and cobalt carbides for Fischer–Tropsch synthesis', *Journal of Physical Chemistry C*, 114, 1085–1093.

Chvatalova K, Vrestal J, Houserova J and Sob M (2007), 'First-principles calculations of energetics of σ phase formation and thermodynamic modelling in the Cr-Fe-W system', *Materials Science and Engineering A*, 462, 153–158.

Cieslak J, Tobola J, Dubiel SM, Kaprzyk S, Steiner W and Reissner M (2008), 'Electronic structure of a σ-FeCr compound', *Journal of Physics: Condensed Matter*, 20, 235234.

Cieslak J, Tobola J and Dubiel SM (2010), 'Electronic structure of the σ phase of paramagnetic Fe-V alloys', *Physical Review B*, 81, 174203.

Cococcioni M and de Gironcoli S (2005), 'Linear response approach to the calculation of the effective interaction parameters in the LDA+U method', *Physical Review B*, 71, 035105.

Collins MF, Minkiewicz VJ, Nathans R, Passell L and Shirane, G (1969), 'Critical and spin-wave scattering of neutrons from iron', *Physical Review*, 179, 417–430.

Connolly JWD and Williams AR (1983), 'Density-functional theory applied to phase transformations in transition-metal alloys', *Physical Review B*, 27, 5169–5172.

Cracknell AP (1969), 'Group theory and magnetic phenomena in solids', *Rep. Prog. Phys.*, 32, 633–707.

Crisan V, Entel P, Ebert H, Akai H, Johnson DD and Staunton JB (2002), 'Magnetochemical origin for Invar anomalies in iron-nickel alloys', *Physical Review B*, 66, 014416.

de Smit E, Cinquini F, Beale AM, Safonova OV, van Beek W, Sautet P and Weckhuysen

© Woodhead Publishing Limited, 2012

BM (2010), 'Stability and reactivity of ε-χ-θ iron carbide catalyst phases in Fischer–Tropsch synthesis: controlling mu C', *J. Am. Chem. Soc.*, 132, 14928–14941.

Díaz-Ortiz A, Drautz R, Fähnle M, Dosch H and Sanchez JM (2006), 'Structure and magnetism in bcc-based iron-cobalt alloys', *Physical Review B*, 73, 224208.

Djurabekova FG, Malerba L, Domain C and Becquart CS (2007), 'Stability and mobility of small vacancy and copper-vacancy clusters in bcc-Fe: an atomistic kinetic Monte Carlo study', *Nuclear Instruments & Methods in Physics Research B*, 255, 47–51.

Domain C and Becquart CS (2005), 'Diffusion of phosphorus in α-Fe: an *ab initio* study', *Physical Review B*, 71, 214109.

Domain C, Becquart CS and Foct J (2004), '*Ab initio* study of foreign interstitial atom (C, N) interactions with intrinsic point defects in α-Fe', *Physical Review B*, 69, 144112.

Doyama M (1986), 'Study of metallic properties by positive muons – crystalline defects', *Nihon Kinzoku Gakkai Kaihou (Bulletin of the Japan Institute of Metals)*, 25, 808–815 (in Japanese).

Drautz R and Díaz-Ortiz A (2006), 'Obtaining cluster expansion coefficients in *ab initio* thermodynamics of multicomponent lattice-gas systems', *Physical Review B*, 73, 224207.

Drautz R and Fähnle M (2005), 'Parametrization of the magnetic energy at the atomic level', *Physical Review B*, 72, 212405.

Drautz R, Díaz-Ortiz A, Fähnle M and Dosch H (2004), 'Ordering and magnetism in Fe-Co: dense sequence of ground-state structures', *Physical Review Letters*, 93, 067202.

Ducastelle F (1991), *Order and Phase Stability in Alloys*, (Cohesion and Structure, Vol. 3), North-Holland/Elsevier Science Publishers, Amsterdam.

Ducastelle F and Gautier F (1976), 'Generalized perturbation theory in disordered transitional alloys: application to the calculation of ordering energies', *J. Phys. F: Metal Phys.*, 6, 2039–2062.

Duman E, Acet M, Wassermann EF, Itié JP, Baudelet F, Mathon O and Pascarelli S (2005), 'Magnetic instabilities in Fe_3C cementite particles observed with Fe K-edge X-ray circular dichroism under pressure', *Physical Review Letters*, 94, 075502.

Eleno L, Frisk K and Schneider A (2006), 'Assessment of the Fe-Ni-Al system', *Intermetallics*, 14, 1276–1290.

Entel P, Hoffmann E, Herper HC, Wassermann EF, Crisan V, Ebert H and Akai H (2000), 'Collinear and noncollinear magnetism in transition-metal alloys', *Journal of the Physical Society of Japan*, 69, 112–118.

Fähnle M and Schimmele L (2005), 'The influence of magnetism on atomic defects and diffusion: model calculations and *ab initio* electron theory', *Defect and Diffusion Forum Series*, 237–240, 19–29.

Falicov LM and Ruvalds J (1968), 'Symmetry of the wave functions in the band theory of ferromagnetic metals', *Physical Review*, 172, 498–507.

Fang CM, van Huis MA and Zandbergen HW (2010a), 'Structure and stability of Fe_2C phases from density-functional theory calculations', *Scripta Materialia*, 63, 418–421.

Fang CM, van Huis MA and Zandbergen HW (2010b), 'Stability and structures of the ε-phases of iron nitrides and iron carbides from first principles', *Scripta Materialia*, 64, 296–299.

Fang CM, van Huis MA, Sluiter MHF and Zandbergen HW (2010c), 'Stability, structure and electronic properties of γ-$Fe_{23}C_6$ from first-principles theory', *Acta Materialia*, 58, 2968–2977.

Fang CM, Sluiter MHF, van Huis MA, Ande CK and Zandbergen HW (2010d), 'Origin

© Woodhead Publishing Limited, 2012

of predominance of cementite among iron carbides in steel at elevated temperature', *Physical Review Letters*, 105, 055503.

Faraoun HI, Zhang YD, Esling C and Aourag H (2006), 'Crystalline, electronic, and magnetic structures of θ-Fe_3C, χ-Fe_5C_2, and η-Fe_2C from first principle calculation', *J. Appl. Phys.*, 99, 093508.

Fasiska EJ and Jeffrey GA (1965), 'On the cementite structure', *Acta Crystallography*, 19, 463–471.

Faulkner JS (1979), 'Multiple-scattering approach to band theory', *Physical Review B*, 19, 6186–6206.

Faulkner JS and Stocks GM (1980), 'Calculating properties with the coherent-potential approximation', *Physical Review B*, 21, 3222–3244.

Fiquet G, Badro J, Gregoryanz E, Fei Y and Occelli F (2009), 'Sound velocity in iron carbide (Fe_3C) at high pressure: implications for the carbon content of the Earth's inner core', *Physics of the Earth and Planetary Interiors*, 172, 125–129.

Fors DHR and Wahnström G (2008), 'Nature of boron solution and diffusion in α-iron', *Physical Review B*, 77, 132102.

Forst CJ, Slycke J, Van Vliet KJ and Yip S (2006), 'Point defect concentrations in metastable Fe-C alloys', *Physical Review Letters*, 96, 175501.

Friak M, Sob M and Vitek V (2001), '*Ab initio* calculation of phase boundaries in iron along the bcc-fcc transformation path and magnetism of iron overlayers', *Physical Review B*, 63, 052405.

Friak M, Hickel T, Kormann F, Udyansky A, Dick A, von Pezold J, Ma D, Kim O, Counts WA, Sob M, Gebhardt T, Music D, Schneider J, Raabe D and Neugebauer J (2011), 'Determining the elasticity of materials employing quantum-mechanical approaches: from the electronic ground state to the limits of materials stability', *Steel Research Int.*, 82, 86–100.

Fu CC and Willaime F (2008), 'First principles calculations in iron: structure and mobility of defect clusters and defect complexes for kinetic modelling', *Comptes Rendus Physique*, 9, 335–342.

Fu CL, Krčmar M, Painter GS and Chen XQ (2007), 'Vacancy mechanism of high oxygen solubility and nucleation of stable oxygen-enriched clusters in Fe', *Physical Review Letters*, 99, 225502.

Fu CC, Meslin E, Barbu A, Willaime F and Oison V (2008), 'Effect of C on vacancy migration in α-iron', *Solid State Phenomena*, 139, 157–164.

Garbulsky GD and Ceder G (1995), 'Linear-programming method for obtaining effective cluster interactions in alloys from total-energy calculations: application to the fcc Pd-V system', *Physical Review B*, 51, 67–72.

Gavriljuk VG, Shanina BD and Berns H (2000), 'On the correlation between electron structure and short range atomic order in iron-based alloys', *Acta Materialia*, 48, 3879–3893.

Geng WT (2003), 'Cr segregation at the Fe-Cr surface: a first-principles GGA investigation', *Physical Review B*, 68, 233402.

Geng WT, Freeman AJ, Wu R and Olson GB (2000), 'Effect of Mo and Pd on the grain-boundary cohesion of Fe', *Physical Review B*, 62, 6208–6214.

Gesari S, Irigoyen B and Juan A (2006), 'Segregation of H, C and B to Σ = 5 (013) α-Fe grain boundary: a theoretical study', *Applied Surface Science*, 253, 1939–1945.

Gonser U, Meechan CJ, Muir AH and Wiedersich H (1963), 'Utilization of Mossbauer effect to determine the Neel temperatures of 304 stainless steel and γ-Fe precipitates stabilized in copper lattice', *Journal of Applied Physics*, 34, 2373–2378.

© Woodhead Publishing Limited, 2012

Gonzales-Ormeño PG, Petrilli HM and Schön CG (2002), '*Ab-initio* calculations of the formation energies of bcc-based superlattices in the Fe-Al system', *Calphad-Computer Coupling of Phase Diagrams and Thermochemistry*, 26, 573–582.

Gonzales-Ormeño PG, Petrilli HM and Schön CG (2006), '*Ab initio* calculation of the bcc Fe-Al phase diagram including magnetic interactions', *Scripta Materialia*, 54, 1271–1276.

Gracia JM, Prinsloo FF and Niemantsverdriet JW (2009), 'Mars-van Krevelen-like mechanism of CO hydrogenation on an iron carbide surface', *Catalysis Letters*, 133, 257–261.

Gu XJ, Poon SJ, Shiflet GJ and Widom M (2008), 'Ductility improvement of amorphous steels: roles of shear modulus and electronic structure', *Acta Materialia*, 56, 88–94.

Gusev AI and Zyryanova AN (2000), 'Ordering and magnetic susceptibility of non-stoichiometric hafnium carbide', *Physica Status Solidi A*, 177, 419–437.

Gutina OY, Medvedeva NI, Shein IR, Ivanovskii AL and Medvedeva JE (2009), 'Electronic structure and magnetic properties of Fe_3C with 2p and 3p impurities', *Physica Status Solidi B*, 246, 2167–2171.

Halilov SV, Perlov AY, Oppeneer PM and Eschrig H (1997), 'Magnon spectrum and related finite-temperature magnetic properties: a first-principle approach', *Europhysics Letters*, 39, 91–96.

Hallstedt B, Djurovic D, von Appen J, Dronskowski R, Dick A, Körmann F, Hickel T and Neugebauer J (2010), 'Thermodynamic properties of cementite (Fe_3C)', *Calphad-Computer Coupling of Phase Diagrams and Thermochemistry*, 34, 129–133.

Hamann DR, Wu X, Rabe KM and Vanderbilt D (2005), 'Metric tensor formulation of strain in density-functional perturbation theory', *Physical Review B*, 71, 035117.

Haneda K, Zhou ZX, Morrish AH, Majima T and Miyahara T (1992), 'Low-temperature stable nanometer-size fcc-Fe particles with no magnetic ordering', *Physical Review B*, 46, 13832–13837.

Hass KC, Davis LC and Zunger A (1990), 'Electronic structure of random $Al_{0.5}Ga_{0.5}As$ alloys: test of the special-quasirandom-structures description', *Physical Review B*, 42, 3757–3760.

Havrankova J, Vrestal J, Wang LG and Sob M (2001), '*Ab initio* analysis of energetics of σ-phase formation in Cr-based systems', *Physical Review B*, 63, 174104.

Haydock R, Heine V and Kelly MJ (1975), 'Electronic structure based on the local atomic environment for tight-binding bands II', *Journal of Physics C: Solid State Physics*, 8, 2591–2605.

Henkelman G and Jónsson H (2000), 'Improved tangent estimate in the nudged elastic band method for finding minimum energy paths and saddle points', *J. Chem. Phys.*, 113, 9978–9985.

Henriksson KOE, Sandberg N and Wallenius J (2008), 'Carbides in stainless steels: results from *ab initio* investigations', *Applied Physics Letters*, 93, 191912.

Hijmans J and de Boer J (1954), 'An approximation method for order-disorder problems', *Physica*, 21, 471–484; 485–498; 499–516.

Hines WA, Shanthakumar P, Huang T, Budnick JI, Miller RL, Pease DM and Perry DM (2009), 'Magnetic and structural study of fcc γ-Fe precipitates in Cu', *Physica Status Solidi B*, 246, 2154–2158.

Hirotsu Y and Nagakura S (1972), 'Crystal structure and morphology of the carbide precipitated from martensitic high carbon steel during the first stage of tempering', *Acta Metallurgica*, 20, 645–655.

Hofer LJE and Cohn EM (1951), 'Some reactions in the iron-carbon system: application to the tempering of martensite', *Nature (London)*, 167, 977–978.

© Woodhead Publishing Limited, 2012

Hohenberg P and Kohn W (1964), 'Inhomogeneous electron gas', *Physical Review*, 136, B864–B871.

Hong MH, Reynolds WT, Tarui T and Hono K (1999), 'Atom probe and transmission electron microscopy investigations of heavily drawn pearlitic steel wire', *Metallurgical and Materials Transactions A*, 30, 717–727.

Huang SY, Worthington DL, Asta M, Ozolins V, Ghosh G and Liaw PK (2010), 'Calculation of impurity diffusivities in α-Fe using first-principles methods', *Acta Materialia*, 58, 1982–1993.

Hugosson HW, Korzhavyi P, Jansson U, Johansson B and Eriksson O (2001), 'Phase stabilities and structural relaxations in substoichiometric TiC_{1-x}', *Physical Review B*, 63, 165116.

Ising E (1925), 'Beitrag zur Theorie des Ferromagnetismus', *Z. Phys.*, 31, 253–258.

Istrail S (2000), 'Statistical mechanics, three-dimensionality and NP-completeness: I. Universality of intractability for the partition function of the Ising model across non-planar surfaces', *Proceedings of the 32nd annual ACM symposium on Theory of Computing*, pp. 87–96.

Jang JH, Kim IG and Bhadeshia HKDH (2009), 'Substitutional solution of silicon in cementite: a first-principles study', *Computational Materials Science*, 44, 1319–1326.

Jang JH, Kim IG and Bhadeshia HKDH (2010a), 'ε-Carbide in alloy steels: first-principles assessment', *Scripta Materialia*, 63, 121–123.

Jang JH, Kim IG and Bhadeshia HKDH (2010b), 'First-principles calculations and the thermodynamics of cementite', *Materials Science Forum*, 638–642, 3319–3324.

Janotti A, Krčmar M, Fu CL and Reed RC (2004), 'Solute diffusion in metals: larger atoms can move faster', *Physical Review Letters*, 92, 085901.

Jiang C, Wolverton C, Sofo J, Chen LQ and Liu ZK (2004), 'First-principles study of binary bcc alloys using special quasirandom structures', *Physical Review B*, 69, 214202.

Jiang C, Chen LQ and Liu ZK (2005), 'First-principles study of constitutional point defects in B2 NiAl using special quasirandom structures', *Acta Materialia*, 53, 2643–2652.

Jiang C, Srinivasan SG, Caro A and Maloy SA (2008a), 'Structural, elastic, and electronic properties of Fe_3C from first principles', *Journal of Applied Physics*, 103, 043502.

Jiang C, Uberuaga BP and Srinivasan SG (2008b), 'Point defect thermodynamics and diffusion in Fe_3C: a first-principles study', *Acta Materialia*, 56, 3236–3244.

Jiang DE and Carter EA (2003), 'Carbon dissolution and diffusion in ferrite and austenite from first principles', *Physical Review B*, 67, 214103.

Jiang DE and Carter EA (2004a), 'First principles assessment of ideal fracture energies of materials with mobile impurities: implications for hydrogen embrittlement of metals', *Acta Materialia*, 52, 4801–4807.

Jiang DE and Carter EA (2004b), 'Diffusion of interstitial hydrogen into and through bcc Fe from first principles', *Physical Review B*, 70, 064102.

Jiang DE and Carter EA (2005), 'Carbon atom adsorption on and diffusion into Fe(110) and Fe(100) from first principles', *Physical Review B*, 71, 045402.

Johanson GJ, McGirr MB and Wheeler DA (1970), 'Determination of the Néel temperature of face-centered-cubic iron', *Physical Review B*, 1, 3208–3208.

Johnson DD (1988), 'Modified Broyden's method for accelerating convergence in self-consistent calculations', *Physical Review B*, 38, 12807–12813.

Joubert JM (2008), 'Crystal chemistry and Calphad modeling of the σ phase', *Progress in Materials Science*, 53, 528–583.

Kabliman EA, Mirzoev AA and Udovskii AL (2009), 'First-principles simulation of an

© Woodhead Publishing Limited, 2012

ordered σ phase of the Fe-Cr system in the ferromagnetic state', *Physics of Metals and Metallography*, 108, 435–440.

Kabliman E, Blaha P, Schwarz K, Ruban AV and Johansson B (2011), '*Ab initio*-based mean-field theory of the site occupation in the Fe-Cr σ-phase', *Physical Review B*, 83, 092201.

Kac M and Ward JC (1952), 'A combinatorial solution of the two-dimensional Ising model', *Physical Review*, 88, 1332–1337.

Kamminga JD, Klaver TPC, Nakata K, Thijsse BJ and Janssen GCAM (2003), 'The interaction of N with atomically dispersed Ti, V, Cr, Mo, and Ni in ferritic steel', *Journal of Computer-aided Materials Design*, 10, 1–11.

Katanin AA, Poteryaev AI, Efremov AV, Shorikov AO, Skornyakov SL, Korotin MA and Anisimov VI (2010), 'Orbital-selective formation of local moments in α-iron: first-principles route to an effective model', *Physical Review B*, 81, 045117.

Kazimirov VY, Louca D, Widom M, Gu XJ, Poon SJ and Shiflet GJ (2008), 'Local organization and atomic clustering in multicomponent amorphous steels', *Physical Review B*, 78, 054112.

Kehr KW, Binder K and Reulein SM (1989), 'Mobility, interdiffusion, and tracer diffusion in lattice-gas models of two-component alloys', *Physical Review B*, 39, 4891–4910.

Khmelevskyi S, Ruban AV and Mohn P (2005a), 'Electronic structure analysis of the pressure induced metamagnetic transition and magnetovolume anomaly in Fe_3C-cementite', *Journal of Physics – Condensed Matter*, 17, 7345–7352.

Khmelevskyi S, Ruban AV, Kakehashi Y, Mohn P and Johansson B (2005b), '*Ab initio* investigation of the Invar anomaly in ordered fcc Fe-Pt alloys', *Physical Review B*, 72, 064510.

Kikuchi R (1951), 'A theory of cooperative phenomena', *Physical Review*, 81, 988–1003.

Kikuchi R (1974), 'Superposition approximation and natural iteration calculation in cluster-variation method', *Journal of Chemical Physics*, 60, 1071–1080.

Kim M, Geller CB and Freeman AJ (2004), 'The effect of interstitial N on grain boundary cohesive strength in Fe', *Scripta Materialia*, 50, 1341–1343.

Kimizuka H, Mori H and Ogata S (2011), 'Effect of temperature on fast hydrogen diffusion in iron: a path-integral quantum dynamics approach', *Physical Review B*, 83, 094110.

Kissavos AE, Simak SI, Olsson P, Vitos L and Abrikosov IA (2006), 'Total energy calculations for systems with magnetic and chemical disorder', *Computational Materials Science*, 35, 1–5.

Klaver TPC, Drautz R and Finnis MW (2006), 'Magnetism and thermodynamics of defect-free Fe-Cr alloys', *Physical Review B*, 74, 094435.

Klaver TPC, Olsson P and Finnis MW (2007), 'Interstitials in FeCr alloys studied by density functional theory', *Physical Review B*, 76, 214110.

Klaver TPC, Bonny G, Olsson P and Terentyev D (2010), 'Benchmarking FeCr empirical potentials against density functional theory data', *Modelling and Simulation in Materials Science and Engineering*, 18, 075004.

Klotz S, Le Godec Y, Strässle Th and Stuhr U (2008), 'The α-γ-ε triple point of iron investigated by high pressure-high temperature neutron scattering', *Appl. Phys. Letters*, 93, 091904.

Knopfle K, Sandratskii LM and Kübler J (2000), 'Spin spiral ground state of γ-iron', *Physical Review B*, 62, 5564–5569.

Kohn W and Sham LJ (1965), 'Self-consistent equations including exchange and correlation effects', *Physical Review*, 140, A1133–A1138.

© Woodhead Publishing Limited, 2012

Kong LT and Liu BX (2004), 'Correlation of magnetic moment versus spacing distance of metastable fcc structured iron', *Applied Physics Letters*, 84, 3627–3629.

Konyaeva MA and Medvedeva NI (2009), 'Electronic structure, magnetic properties, and stability of the binary and ternary carbides (Fe, $Cr)_3C$ and (Fe, $Cr)_7C_3$', *Physics of the Solid State*, 51, 2084–2089.

Körling M and Ergon J (1996), 'Gradient-corrected *ab initio* calculations of spin-spiral states in fcc-Fe and the effects of the atomic-spheres approximation', *Physical Review B*, 54, R8293–R8296.

Körmann F, Dick A, Grabowski B, Hallstedt B, Hickel T and Neugebauer J (2008), 'Free energy of bcc iron: integrated *ab initio* derivation of vibrational, electronic, and magnetic contributions', *Physical Review B*, 78, 033102.

Körmann F, Dick A, Hickel T and Neugebauer J (2009), 'Pressure dependence of the Curie temperature in bcc iron studied by *ab initio* simulations', *Physical Review B*, 79, 184406.

Körmann F, Dick A, Hickel T and Neugebauer J (2010), 'Rescaled Monte Carlo approach for magnetic systems: *ab initio* thermodynamics of bcc iron', *Physical Review B*, 81, 134425.

Korzhavyi PA, Pourovskii LV, Hugosson HW, Ruban AV and Johansson B (2002), '*Ab initio* study of phase equilibria in TiC_x', *Physical Review Letters*, 88, 015505.

Korzhavyi PA, Sundman B, Selleby M and Johansson R (2005), 'Atomic, electronic, and magnetic structure of iron-based σ-phases', *Materials Research Society Proc*, 842, 517–522.

Krčmar M, Fu CL, Janotti A and Reed RC (2005), 'Diffusion rates of 3d transition metal solutes in nickel by first-principles calculations', *Acta Materialia*, 53, 2369–2376.

Kresse G and Hafner J (1993), '*Ab initio* molecular dynamics for liquid metals', *Physical Review B*, 47, 558–561.

Kulikov NI and Demangeat C (1997), 'Spin polarization of disordered Fe-Cr and Fe-Mn alloys', *Physical Review B*, 55, 3533–3542.

Kwon H, Lee JH, Lee KB, Kwon H, Kim CM and Yang HR (1998), 'Effects of Co and Ni on secondary hardening and fracture behavior of martensitic steels bearing W and Cr', *Metallurgical and Materials Transactions A*, 29, 397–401.

Lagarec K, Rancourt DG, Bose SK, Sanyal B and Dunlap RA (2001), 'Observation of a composition-controlled high-moment/low-moment transition in the face centered cubic Fe-Ni system: Invar effect is an expansion, not a contraction', *Journal of Magnetism and Magnetic Materials*, 236, 107–130.

Laio A, Bernard S, Chiarotti GL, Scandolo S and Tosatti E (2000), 'Physics of iron at Earth's core conditions', *Science*, 287, 1027–1030.

Laks DB, Ferreira LG, Froyen S and Zunger A (1992), 'Efficient cluster expansion for substitutional systems', *Physical Review B*, 46, 12587–12605.

Lavrentiev MY, Drautz R, Nguyen-Manh D, Klaver TPC and Dudarev SL (2007), 'Monte Carlo study of thermodynamic properties and clustering in the bcc Fe-Cr system', *Physical Review B*, 75, 014208.

Lavrentiev MY, Nguyen-Manh D and Dudarev SL (2010a), 'Magnetic cluster expansion model for bcc-fcc transitions in Fe and Fe-Cr alloys', *Physical Review B*, 81, 184202.

Lavrentiev MY, Nguyen-Manh D and Dudarev SL (2010b), 'Cluster expansion models for Fe-Cr alloys, the prototype materials for a fusion power plant', *Computational Materials Science*, 49, S199–S203.

Lee KB, Kwon H, Kwon H and Yang HR (2001), 'Effects of alloying additions and

© Woodhead Publishing Limited, 2012

austenitizing treatments on secondary hardening and fracture behavior for martensitic steels containing both Mo and W', *Metallurgical and Materials Transactions A*, 32, 1659–1670.

Leger JM, Loriers-Susse C and Vodar B (1972), 'Pressure effect on the Curie temperatures of transition metals and alloys', *Physical Review B*, 6, 4250–4261.

Legris A (2004), 'Recent advances in point defect studies driven by density functional theory', *Defect and Diffusion Forum*, 233, 77–86.

Lenz W (1920), 'Beitrag zum Verständnis der magnetischen Erscheinungen in festen Körpern', *Physikalische Zeitschrift*, 21, 613–615.

Leung TC, Chan CT and Harmon BN (1991), 'Ground-state properties of Fe, Co, Ni, and their monoxides: results of the generalized gradient approximation', *Physical Review B*, 44, 2923–2927.

Lichtenstein AI, Katsnelson MI and Kotliar G (2001), 'Finite-temperature magnetism of transition metals: an *ab initio* dynamical mean-field theory', *Physical Review Letters*, 87, 067205.

Liot F and Abrikosov IA (2009), 'Local magnetovolume effects in $Fe_{65}Ni_{35}$ alloys', *Physical Review B*, 79, 014202.

Lord OT, Walter MJ, Dasgupta R, Walker D and Clark SM (2009), 'Melting in the Fe-C system to 70 GPa', *Earth and Planetary Science Letters*, 284, 157–167.

Lounis S, Mavropoulos P, Dederichs PH and Blügel S (2005), 'Noncollinear Korringa–Kohn–Rostoker–Green function method: application to 3d nanostructures on Ni(001)', *Physical Review B*, 72, 224437.

Lu S, Hu QM, Yang R, Johansson B and Vitos L (2010), 'First-principles determination of the α-α' interfacial energy in Fe-Cr alloys', *Physical Review B*, 82, 195103.

Luo W, Johansson B, Eriksson O, Arapan S, Souvatzis P, Katsnelson MI and Ahuja R (2010), 'Dynamical stability of body center cubic iron at the Earth core conditions', *Proceedings of the National Academy of Sciences of the USA*, 107, 9962–9964.

Lv ZQ, Sun SH, Jiang P, Wang BZ and Fu WT (2008), 'First-principles study on the structural stability, electronic and magnetic properties of Fe_2C', *Computational Materials Science*, 42, 692–697.

Macedo WAA and Keune W (1988), 'Magnetism of epitaxial fcc-Fe (100) films on Cu (100) investigated *in situ* by conversion-electron Mössbauer spectroscopy in ultrahigh vacuum', *Physical Review Letters*, 61, 475–478.

Manes M, Damick AD, Mentser M, Cohn EM and Hofer LJE (1952), 'Hexagonal iron carbide as an intermediate in the carbiding of iron Fischer–Tropsch catalysts', *Journal of the American Chemical Society*, 74, 6207–6215.

Marsman M and Hafner J (2002), 'Broken symmetries in the crystalline and magnetic structures of γ-iron', *Physical Review B*, 66, 224409.

Massalski TB and Laughlin DE (2009), 'The surprising role of magnetism on the phase stability of Fe (Ferro)', *Calphad-Computer Coupling of Phase Diagrams and Thermochemistry*, 33, 3–7.

Matsui M, Adachi K and Chikazumi S (1980), 'Magnetic and thermal anomalies of Invar alloys', *Journal of Applied Physics*, 51, 6319–6325.

Maugis P, Lacaze J, Besson R and Morillo J (2006), '*Ab initio* calculations of phase stabilities in the Fe-Al-C system and CALPHAD-type assessment of the iron-rich corner', *Metallurgical and Materials Transactions A*, 37, 3397–3401.

Medvedeva NI, Shein IR, Gutina OY and Ivanovskii AL (2007), 'Simulation of the structural, electronic, and magnetic properties of $Fe_3C_{1-x}B_x$ borocementites', *Physics of the Solid State*, 49, 2298–2302.

© Woodhead Publishing Limited, 2012

Medvedeva NI, Shein IR, Konyaeva MA and Ivanovskii AL (2008), 'Effect of chromium on the electronic structure and magnetic properties of cementite', *Physics of Metals and Metallography*, 105, 568–573.

Meslin E, Fu CC, Barbu A, Gao F and Willaime F (2007), 'Theoretical study of atomic transport via interstitials in dilute Fe-P alloys', *Physical Review B*, 75, 094303.

Mikhaylushkin AS, Simak SI, Dubrovisnky LS, Dubrovinskaia N, Johansson B and Abrikosov IA (2007), 'Pure iron compressed and heated to extreme conditions', *Physical Review Letters*, 99 165505.

Mizuno M, Tanaka I and Adachi H (1997), 'Effect of solute atoms on the chemical bonding of Fe_3C (cementite)', *Philosophical Magazine B*, 75, 237–248.

Mohammed YS, Yan Y, Wang HX, Lia K and Du X (2010), 'Stability of ferromagnetism in Fe, Co, and Ni metals under high pressure with GGA and GGA+U', *Journal of Magnetism and Magnetic Materials*, 322, 653–657.

Mohn P, Schwarz K and Wagner D (1991), 'Magnetoelastic anomalies in Fe-Ni Invar alloys', *Physical Review B*, 43, 3318–3324.

Mohri T and Chen Y (2002), 'First-principles investigation of L1(0)-disorder phase equilibrium in Fe-Pt system', *Materials Transactions*, 43, 2104–2109.

Mohri T and Chen Y (2004), 'First-principles calculation of $L1_0$-disorder phase boundary in Fe-Pd system', *Materials Transactions*, 45, 1478–1484.

Moran S, Ederer C and Fähnle M (2003), '*Ab initio* electron theory for magnetism in Fe: pressure dependence of spin-wave energies, exchange parameters, and Curie temperature', *Physical Review B*, 67, 012407.

Moroni EG and Jarlborg T (1993), 'Electronic structure, ordering effects, phase stability, and magnetism in $Fe_{1-x}Cr_x$ systems', *Physical Review B*, 47, 3255–3267.

Moruzzi VL (1992), 'Theory of Invar', *Solid State Communications*, 83, 739–743.

Moruzzi VL, Janak JF and Williams AR (1978), *Calculated electronic properties of metals*, Pergamon Press, New York.

Mryasov ON, Gubanov VA and Liechtenstein AI (1992), 'Spiral-spin-density-wave states in fcc iron: linear-muffin-tin-orbitals band-structure approach', *Physical Review B*, 45, 12330–12336.

Mueller T and Ceder G (2009), 'Bayesian approach to cluster expansions', *Physical Review B*, 80, 024103.

Naono T and Tsunoda Y (2004), 'The particle size effect of the spin-density wave in cubic γ-Fe precipitates in Cu', *Journal of Physics: Condensed Matter*, 16, 7723–7732.

Nasu S, Sasaki T, Kawakami T, Tsutsui T and Endo S (2002), 'Mössbauer study of ε-Fe under an external magnetic field', *Journal of Physics: Condensed Matter*, 14, 11167–11171.

Nielsen OH and Martin RM (1983), 'First-principles calculation of stress', *Physical Review Letters*, 50, 697–700.

Nikolussi M, Shang SL, Gressmann T, Leineweber A, Mittemeijer E, Wang Y and Liu ZK (2008), 'Extreme elastic anisotropy of cementite, Fe_3C: first-principles calculations and experimental evidence', *Scripta Materialia*, 59, 814–817.

Niu Q, Wang XD, Kleinman L, Liu WM, Nicholson DMC and Stocks GM (1999), 'Adiabatic dynamics of local spin moments in itinerant magnets', *Physical Review Letters*, 83, 207–210.

Ohnuma T, Soneda N and Iwasawa M (2009), 'First-principles calculations of vacancy-solute element interactions in body-centered cubic iron', *Acta Materialia*, 57, 5947–5955.

Ohodnicki PR, Cates NC, Laughlin DE, McHenry ME and Widom M (2008), '*Ab initio* theoretical study of magnetization and phase stability of the $(Fe, Co, Ni)_{23}B_6$ and

© Woodhead Publishing Limited, 2012

(Fe, Co, Ni)$_{23}$Zr$_6$ structures of $Cr_{23}C_6$ and $Mn_{23}Th_6$ prototypes', *Physical Review B*, 78, 144414.

Ohtani H, Takeshita Y and Hasebe M (2004), 'Effect of the order-disorder transition of the bcc structure on the solubility of Be in the Fe-Be binary system', *Materials Transactions*, 45, 1499–1506.

Okamoto H (1990), 'C-Fe (Carbon-Iron)', in *Binary Alloy Phase Diagrams*, *vol. 1*, 2nd edn, Ed. TB Massalski, ASM International, Materials Park, OH, 842–848.

Okatov SV, Kuznetsov AR, Gornostyrev YN, Urtsev VN and Katsnelson MI (2009), 'Effect of magnetic state on the γ-α transition in iron: first-principles calculations of the Bain transformation path', *Physical Review B*, 79, 094111.

Olsson P, Abrikosov IA, Vitos L and Wallenius J (2003), '*Ab initio* formation energies of Fe-Cr alloys', *Journal of Nuclear Materials*, 321, 84–90.

Olsson P, Domain C and Wallenius J (2007), '*Ab initio* study of Cr interactions with point defects in bcc Fe', *Physical Review B*, 75, 014110.

Olsson P, Klaver TPC and Domain C (2010), '*Ab initio* study of solute transition-metal interactions with point defects in bcc Fe', *Physical Review B*, 81, 054102.

Ono S and Mibe K (2010), 'Magnetic transition of iron carbide at high pressures', *Physics of the Earth and Planetary Interiors*, 180, 1–6.

Ono S, Kikegawa T, Hirao N and Mibe K (2010), 'High-pressure magnetic transition in hcp-Fe', *American Mineralogist*, 95, 880–883.

Onsager L (1944), 'Crystal statistics. I. A two-dimensional model with an order-disorder transition', *Physical Review*, 65, 117–149.

Ortiz CJ, Caturla MJ, Fu CC and Willaime F (2007), 'He diffusion in irradiated α-Fe: an *ab-initio*-based rate theory model', *Physical Review B*, 75, 100102(R).

Ozolins V and Häglund J (1993), 'First-principles study of effective cluster interactions and enthalpies of formation of substoichiometric VC_{1-x}', *Physical Review B*, 48, 5069–5076.

Ozolins V and Körling M (1993), 'Full-potential calculations using the generalized gradient approximation: structural properties of transition metals', *Physical Review B*, 48, 18304–18307.

Pajda M, Kudrnovský J, Turek I, Drchal V and Bruno P (2001), '*Ab initio* calculations of exchange interactions, spin-wave stiffness constants, and Curie temperatures of Fe, Co, and Ni', *Physical Review B*, 64, 174402.

Papaconstantopoulos DA and Mehl MJ (2003), 'The Slater–Koster tight-binding method: a computationally efficient and accurate approach', *Journal of Physics: Condensed Matter*, 15, R413–R440.

Pavlu J, Vrestal J and Sob M (2010), '*Ab initio* study of formation energy and magnetism of σ phase in Cr-Fe and Cr-Co systems', *Intermetallics*, 18, 212–220.

Perdew JP and Wang Y (1986), 'Accurate and simple density functional for the electronic exchange energy: generalized gradient approximation', *Physical Review B*, 33, 8800–8802.

Perdew JP and Wang Y (1992), 'Accurate and simple analytic representation of the electron-gas correlation energy', *Physical Review B*, 45, 13244–13249.

Perdew JP, Burke K and Ernzerhof M (1996), 'Generalized gradient approximation made simple', *Physical Review Letters*, 77, 3865–3868.

Perez RA and Weissmann M (2004), '*Ab initio* study of magnetic effects on diffusion in α-Fe', *Journal of Physics: Condensed Matter*, 16, 7033–7043.

Perk JHH (2009), 'Rejoinder to the response to the comment on "Conjectures on exact solution of three-dimensional (3D) simple orthorhombic Ising lattices"', *Philosophical Magazine*, 89, 769–770.

© Woodhead Publishing Limited, 2012

Petch NJ (1944), 'The interpretation of the crystal structure of cementite', *Journal of the Iron and Steel Institute*, 149, 143–150.

Philipsen PHT and Baerends EJ (1996), 'Cohesive energy of 3d transition metals: density functional theory atomic and bulk calculations', *Physical Review B*, 54, 5326–5333.

Pindor AJ, Staunton J, Stocks GM and Winter H (1983), 'Disordered local moment state of magnetic transition metals: a self-consistent KKR CPA calculation', *Journal of Physics F: Metal Physics*, 13, 979–989.

Pinski FJ, Staunton J, Gyorffy BL, Johnson DD and Stocks GM (1986), 'Ferromagnetism versus antiferromagnetism in face-centered-cubic iron', *Physical Review Letters*, 56, 2096–2099.

Pitkanen H, Alatalo M, Puisto A, Ropo M, Kokko K, Punkkinen MPJ, Olsson P, Johansson B, Hertzman S and Vitos L (2009), '*Ab initio* study of the phase stability in paramagnetic duplex steel alloys', *Physical Review B*, 79, 024108.

Podgorny M (1992), 'Magnetic instabilities in $PtFe_3$ and in the fcc Ni-Fe system', *Physical Review B*, 46, 6293–6302.

Rafaja D, Lengauer W, Ettmayer P and Lipatnikov VN (1998), 'Rietveld analysis of the ordering in V_8C_7', *Journal of Alloys and Compounds*, 269, 60–62.

Rajagopal AK and Callaway J (1973), 'Inhomogeneous electron gas', *Physical Review B*, 7, 1912–1919.

Rempel AA and Gusev AI (2000), 'Preparation of disordered and ordered highly nonstoichiometric carbides and evaluation of their homogeneity', *Physics of the Solid State*, 42, 1280–1286.

Rosengaard NM and Johansson B (1997), 'Finite-temperature study of itinerant ferromagnetism in Fe, Co, and Ni', *Physical Review B*, 55, 14975–14986.

Ruban AV, Shallcross S, Simak SI and Skriver HL (2004), 'Atomic and magnetic configurational energetics by the generalized perturbation method', *Physical Review B*, 70, 125115.

Ruban AV, Khmelevskyi S, Mohn P and Johansson B (2007), 'Magnetic state, magnetovolume effects, and atomic order in $Fe_{65}Ni_{35}$ Invar alloy: a first principles study', *Physical Review B*, 76, 014420.

Ruban AV, Korzhavyi PA and Johansson B (2008), 'First-principles theory of magnetically driven anomalous ordering in bcc Fe-Cr alloys', *Physical Review B*, 77, 094436.

Sakuma A (1999), 'First principles study on the exchange constants of the 3d transition metals', *Journal of the Physical Society of Japan*, 68, 620–624.

Sanchez JM and de Fontaine D (1978), 'The fcc Ising model in the cluster variation approximation', *Physical Review B*, 17, 2926–2936.

Sanchez JM and de Fontaine D (1982), 'Ising model phase diagram calculations in the fcc lattice with first- and second-neighbor interactions', *Physical Review B*, 25, 1759–1765.

Sanchez J, Fullea J, Andrade C and de Andres PL (2008), 'Hydrogen in α-iron: stress and diffusion', *Physical Review B*, 78, 014113.

Sánchez-Barriga J, Fink J, Boni V, di Marco I, Braun J, Minár J, Varykhalov A, Rader O, Bellini V, Manghi F, Ebert H, Katsnelson MI, Lichtenstein AI, Eriksson O, Eberhardt W and Dürr HA (2009), 'Strength of correlation effects in the electronic structure of iron', *Physical Review Letters*, 103, 267203.

Sandberg N, Henriksson KOE and Wallenius J (2008), 'Carbon impurity dissolution and migration in bcc Fe-Cr: first-principles calculations', *Physical Review B*, 78, 094110.

© Woodhead Publishing Limited, 2012

Santofimia M, Zhao L, Takahama Y and Sietsma J (2010), 'The complexity of the microstructural changes during the partitioning step of the quenching and partitioning process in low carbon steels', *Mater Sci Forum*, 638–642, 3485–3490.

Sawada H, Kawakami K and Sugiyama M (2005), 'Interaction between substitutional and interstitial elements in α iron studied by first-principles calculation', *Materials Transactions*, 46, 1140–1147.

Saxena SK, Shen G and Lazor P (1993), 'Experimental evidence for a new iron phase and implications for Earth's core', *Science*, 260, 1312–1314.

Saxena SK, Shen G and Lazor P (1994), 'Temperatures in Earth's core based on melting and phase transformation experiments on iron', *Science*, 264, 405–407.

Sha XW and Cohen RE (2010), 'First-principles thermal equation of state and thermoelasticity of hcp Fe at high pressures', *Physical Review B*, 81, 094105.

Shastry BS, Edwards DM and Young AP (1981), 'The paramagnetic state of bcc iron', *Journal of Physics C – Solid State Physics*, 14, L665–L670.

Shein IR, Medvedeva NI and Ivanovskii AL (2007), 'Electronic structure and magnetic properties of Fe_3C with 3d and 4d impurities', *Physica Status Solidi B*, 244, 1971–1981.

Shen GY, Mao HK, Hemley RJ, Duffy TS and Rivers ML (1998), 'Melting and crystal structure of iron at high pressures and temperatures', *Geophysical Research Letters*, 25, 373–376.

Shi YS, Qian D, Dong GS, Jin XF and Wang DS (2002), 'Electronic structure and magnetism of $Fe_{1-x}Pd_x$ alloys', *Physical Review B*, 65, 172410.

Shigematsu T (1975), 'Invar properties of cementite $(Fe_{1-X}Me_X)_3C$, Me=Cr, Mn, Ni', *Journal of the Physical Society of Japan*, 39, 915–920.

Siegel DJ and Hamilton JC (2003), 'First-principles study of the solubility, diffusion, and clustering of C in Ni', *Physical Review B*, 68, 094105.

Simonetti S, Pronsato ME, Brizuela G and Juan A (2007) 'The C-C pair in the vicinity of a bcc Fe bulk vacancy: electronic structure and bonding', *Physica Status Solidi B*, 244, 610–618.

Simonovic D, Ande CK, Duff AI, Syahputra F and Sluiter MHF (2010), 'Diffusion of carbon in bcc Fe in the presence of Si', *Physical Review B*, 81, 054116.

Singh DJ, Pickett WE and Krakauer H (1991), 'Gradient-corrected density functionals: full-potential calculations for iron', *Physical Review B*, 43, 11628–11634.

Sjöstedt E and Nordström L (2002), 'Noncollinear full-potential studies of γ-Fe', *Physical Review B*, 66, 014447.

Slane JA, Wolverton C and Gibala R (2004), 'Carbon-vacancy interactions in austenitic alloys', *Materials Science and Engineering A*, 370, 67–72.

Slater JC and Koster GF (1954), 'Simplified LCAO method for the periodic potential problem', *Physical Review*, 94, 1498–1524.

Sluiter M (2006), 'Phase stability of carbides and nitrides in steel', *Mat. Res. Soc. Proc. Vol. 979E*, pp 43–48, eds. DN Seidman, P Bellon, C Abromeit, J-L Boquet, MRS Fall meeting, Boston 2006, symposium HH.

Sluiter M and Kawazoe Y (1995), 'Magnetic and chemical interactions in metallic alloys', *Sci. Rep. RITU, Ser. A*, 40, 301–306.

Sluiter M and Kawazoe Y (2002), 'Prediction of the mixing enthalpy of alloys', *Europhys. Letters*, 57, 526–532.

Sluiter MHF and Kawazoe Y (2005), 'Invariance of truncated cluster expansions for first-principles alloy thermodynamics', *Physical Review B*, 71, 212201.

Sluiter M and Turchi PEA (1989), 'Electronic theory of phase stability in substitutional

© Woodhead Publishing Limited, 2012

alloys: the generalized perturbation method versus the Connolly–Williams method', *Physical Review B*, 40, 11215–11228.

Sluiter M, de Fontaine D, Guo XQ, Podloucky R and Freeman AJ (1990), 'First-principles calculation of phase equilibria in the aluminum lithium system', *Physical Review B*, 42, 10460–10476.

Sluiter M, Turchi PEA, Pinski FJ and Stocks GM (1992), 'A first-principles study of phase stability in Ni-Al and Ni-Ti alloys', *Journal of Materials Science and Engineering A*, 152, 1–8.

Sluiter M, Esfarjani K and Kawazoe Y (1995), 'Site occupation reversal in the Fe-Cr σ phase', *Physical Review Letters*, 75, 3142–3145.

Sluiter MHF, Watanabe Y, de Fontaine D and Kawazoe Y (1996), 'First-principles calculation of the pressure dependence of phase equilibria in the Al-Li system', *Physical Review B*, 53, 6137–6151.

Smirnov AV, Shelton WA and Johnson DD (2005), 'Importance of thermal disorder on the properties of alloys: origin of paramagnetism and structural anomalies in bcc-based $Fe_{1-x}Al_x$', *Physical Review B*, 71, 064408.

Smith CS (1940), 'Structure and ferromagnetism of cold-worked copper containing iron', *Physical Review*, 57, 337.

Söderlind P, Moriarty JA and Wills JM (1996), 'First-principles theory of iron up to earth-core pressures: structural, vibrational, and elastic properties', *Physical Review B*, 53, 14063–14072.

Sodre N, Gonzales-Ormeño PG, Petrilli HM and Schön CG (2009), '*Ab initio* calculation of the bcc Fe-Al-Mo (iron-aluminum-molybdenum) phase diagram: implications for the nature of the tau(2) phase', *Calphad-Computer Coupling of Phase Diagrams and Thermochemistry*, 33, 576–583.

Soisson F and Fu CC (2007), 'Cu-precipitation kinetics in α-Fe from atomistic simulations: vacancy-trapping effects and Cu-cluster mobility', *Physical Review B*, 76, 214102.

Sorescu DC (2005), 'First principles calculations of the adsorption and diffusion of hydrogen on Fe(100) surface and in the bulk', *Catalysis Today*, 105, 44–65.

Soulairol R, Fu CC and Barreteau C (2010), 'Structure and magnetism of bulk Fe and Cr: from plane waves to LCAO methods', *Journal of Physics – Condensed Matter*, 22, 295502.

Sourmail T (2001), 'Precipitation in creep resistant austenitic stainless steels', *Materials Science and Technology*, 17, 1–14.

Soven P (1967), 'Coherent-potential model of substitutional disordered alloys', *Physical Review*, 156, 809–813.

Speer JG, Matlock DK, DeCooman BC, Schroth JG (2003), 'Carbon partitioning into austenite after martensite transformation', *Acta Mater*, 51, 2611–2622.

Staunton JB and Gyorffy BL (1992), 'Onsager cavity fields in itinerant-electron paramagnets', *Physical Review Letters*, 69, 371–374.

Staunton JB, Ling MF and Johnson DD (1997), 'A theoretical treatment of atomic short-range order and magnetism in iron-rich bcc alloys', *Journal of Physics – Condensed Matter*, 9, 1281–1300.

Steinle-Neumann G, Stixrude L and Cohen RE (1999), 'First-principles elastic constants for the hcp transition metals Fe, Co, and Re at high pressure', *Physical Review B*, 60, 791–799.

Steinle-Neumann G, Stixrude L and Cohen RE (2004), 'Magnetism in dense hexagonal iron', *Proceedings of the National Academy of Sciences of the USA*, 101, 33–36.

Steynberg PJ, van den Berg JA and Janse van Rensburg W (2008), 'Bulk and surface

© Woodhead Publishing Limited, 2012

analysis of Hägg Fe carbide (Fe_5C_2): a density functional theory study', *Journal of Physics – Condensed Matter*, 20, 064238.

Stocks GM, Ujfalussy B, Wang XD, Nicholson DMC, Shelton WA, Wang Y, Canning A and Gyorffy BL (1998), 'Towards a constrained local moment model for first principles spin dynamics', *Philosophical Magazine B*, 78, 665–673.

Strange P, Ebert H, Staunton JB and Gyorffy BL (1989), 'A relativistic spin-polarised multiple-scattering theory, with applications to the calculation of the electronic structure of condensed matter', *Journal of Physics – Condensed Matter*, 1, 2959–2975.

Suzuki M (1986), 'Statistical mechanical theory of cooperative phenomena. I. General theory of fluctuations, coherent anomalies and scaling exponents with simple applications to critical phenomena', *Journal of the Physical Society of Japan*, 55, 4205–4230.

Tamura I (1982), 'Deformation-induced martensitic transformation and transformation-induced plasticity in steels', *Metal Science*, 16, 245–253.

Tapasa K, Barashev AV, Bacon DJ and Osetsky YN (2007), 'Computer simulation of carbon diffusion and vacancy-carbon interaction in α-iron', *Acta Materialia*, 55, 1–11.

Tarafder K, Ghosh S, Sanyal B, Eriksson O, Mookerjee A and Chakrabarti A (2008), 'Electronic and magnetic properties of disordered FeCr alloys using different electronic structure methods', *Journal of Physics – Condensed Matter*, 20, 445201.

Tateno S, Hirose K, Ohishi Y and Tatsumi Y (2010), 'The structure of iron in Earth's inner core', *Science*, 330, 359–361.

Taylor RD, Pasternak MP and Jeanloz R (1991), 'Hysteresis in the high pressure transformation of bcc- to hcp-iron', *Journal of Applied Physics*, 69, 6126–6128.

Terakura K, Oguchi T, Mohri T and Watanabe K (1987), 'Electronic theory of the alloy phase stability of Cu-Ag, Cu-Au, and Ag-Au systems', *Physical Review B*, 35, 2169–2173.

Terentyev D, Olsson P, Klaver TPC and Malerba L (2008), 'On the migration and trapping of single self-interstitial atoms in dilute and concentrated Fe-Cr alloys: atomistic study and comparison with resistivity recovery experiments', *Computational Materials Science*, 43, 1183–1192.

Terentyev D, Juslin N, Nordlund K and Sandberg N (2009), 'Fast three dimensional migration of He clusters in bcc Fe and Fe-Cr alloys', *Journal of Applied Physics*, 105, 103509.

Timokhina IB, Hodgson PD and Pereloma EV (2004), 'Effect of microstructure on the stability of retained austenite in transformation-induced-plasticity steels', *Metallurgical and Materials Transactions A*, 35, 2331–2341.

Tokunaga T, Terashima K, Ohtani H and Hasebe M (2008), 'Thermodynamic analysis of the phase equilibria in the Fe-Zr-B system', *Materials Transactions*, 49, 2534–2540.

Toledano P, Katzke H and Machon D (2010), 'Symmetry-induced collapse of ferromagnetism at the α-ε phase transition in iron', *Journal of Physics – Condensed Matter*, 22, 466002.

Truong TN and Duncan W (1994), 'A new direct *ab initio* dynamics method for calculating thermal rate constants from density functional theory', *Journal of Chemical Physics*, 101, 7408–7414.

Tsetseris L (2005), 'Noncollinear magnetism of iron along the tetragonal Bain transformation', *Physical Review B*, 72, 012411.

Tsetseris L and Pantelides ST (2008), 'Vacancies, interstitials and their complexes in titanium carbide', *Acta Materialia*, 56, 2864–2871.

Tsunoda Y (1988), 'Spin density wave in fcc FeCo', *Journal of Physics F: Metal Physics*, 18, L251–L255.

© Woodhead Publishing Limited, 2012

Tsunoda Y (1989), 'Spin-density wave in cubic γ-Fe and γ-$Fe_{100-x}Co_x$ precipitates in Cu', *Journal of Physics: Condensed Matter*, 1, 10427–10438.

Tsunoda Y, Nogami H and Takasaka M (2007), 'Lattice symmetry of the spiral spin-density-wave state in γ-Fe precipitates in Cu', *Physical Review B*, 76, 054419.

Turchi P, Sluiter M and de Fontaine D (1987), 'Prototype fcc-based binary-alloy phase diagrams from tight-binding electronic-structure calculations', *Physical Review B*, 36, 3161–3174.

Turchi PEA, Sluiter M, Pinski FJ, Johnson DD, Nicholson DM, Stocks GM and Staunton JB (1991), 'A first principles description of phase stability in Cu-Zn substitutional alloys', *Physical Review Letters*, 67, 1779–1782; and erratum: *Physical Review Letters*, 68, 418 (1992).

Uhl M and Kübler J (1997), 'Exchange-coupled spin-fluctuation theory: calculation of magneto-elastic properties', *Journal of Physics – Condensed Matter*, 9, 7885–7902.

Uhl M, Sandratskii LM and Kübler J (1992), 'Electronic and magnetic states of γ-Fe', *Journal of Magnetism and Magnetic Materials*, 103, 314–324.

Uhl M, Sandratskii LM and Kübler J (1994), 'Spin fluctuations in γ-Fe and in Fe_3Pt Invar from local-density-functional calculations', *Physical Review B*, 50, 291–301.

Umemoto M, Liu ZG, Matsuyama K and Tsuchiya K (2001), 'Influence of alloy additions on production and properties of bulk cementite', *Scripta Mater.*, 45, 391–397.

Urtsev VN, Gornostyrev YN, Katsnelson MI, Shmakov AV, Korolev AV, Degtyarev VN, Mokshin ED and Voronin VI (2010), 'Relation between the magnetic and lattice degrees of freedom in the Fe-C system', *Steel in Translation*, 40, 671–675.

van Baal CM (1973), 'Order-disorder transformations in a generalized Ising alloy', *Physica*, 64, 571–586.

van de Walle A and Ceder G (2002), 'Automating first-principles phase diagram calculations', *Journal of Phase Equilibrium*, 23, 348–359

van de Walle A, Asta M and Ceder G (2002), 'The alloy theoretic automated toolkit: a user guide', *Calphad-Computer Coupling of Phase Diagrams and Thermochemistry*, 26, 539–553.

Van der Ven A and Ceder G (2005a), 'First principles calculation of the interdiffusion coefficient in binary alloys', *Physical Review Letters*, 94, 045901.

Van der Ven A and Ceder G (2005b), 'Vacancies in ordered and disordered binary alloys treated with the cluster expansion', *Physical Review B*, 71, 054102.

van Genderen MJ, Böttger A, Cernik RJ and Mittemeijer EJ (1993), 'Early stages of decomposition in iron-carbon and iron-nitrogen martensites: diffraction analysis using synchrotron radiation', *Metallurgical Transactions A*, 24, 1965–1973.

Vanderbilt D (1990), 'Soft self-consistent pseudopotentials in a generalized eigenvalue formalism', *Physical Review B*, 41, 7892–7895.

Velický B (1969), 'Theory of electronic transport in disordered binary alloys: coherent-potential approximation', *Physical Review*, 184, 614–627.

Viefhaus H and Richarz B (1995), 'Phosphorus in iron and steel – an overview of surface analytical investigations of the segregation behaviour of phosphorus on internal and external iron and steel surfaces', *Materials and Corrosion*, 46, 306–316.

Vincent E, Becquart CS and Domain C (2005), '*Ab initio* calculations of vacancy interactions with solute atoms in bcc Fe', *Nuclear Instruments and Methods in Physics Research B*, 228, 137–141.

Vincent E, Becquart CS and Domain C (2006), '*Ab initio* calculations of self-interstitial interaction and migration with solute atoms in bcc Fe', *Journal of Nuclear Materials*, 359, 227–237.

© Woodhead Publishing Limited, 2012

Vincent E, Becquart CS and Domain C (2007), 'Atomic kinetic Monte Carlo model based on *ab initio* data: simulation of microstructural evolution under irradiation of dilute Fe-CuNiMnSi alloys', *Nuclear Instruments and Methods in Physics Research B*, 255, 78–84.

Vineyard GHJ (1957), 'Frequency factors and isotope effects in solid state rate processes', *Phys. Chem. Solids*, 3, 121–127.

Vitos L, Korzhavyi PA and Johansson B (2002), 'Elastic property maps of austenitic stainless steels', *Physical Review Letters*, 88, 155501.

Vitos L, Korzhavyi PA and Johansson B (2003), 'Stainless steel optimization from quantum mechanical calculations', *Nature Materials*, 2, 25–28.

Vitos L, Korzhavyi PA and Johansson B (2006a), 'Evidence of large magnetostructural effects in austenitic stainless steels', *Physical Review Letters*, 96, 117210.

Vitos L, Nilsson JO and Johansson B (2006b), 'Alloying effects on the stacking fault energy in austenitic stainless steels from first-principles theory', *Acta Materialia*, 54, 3821–3826.

Vocadlo L, Brodholt J, Dobson DP, Knight K, Marshall W, Price G and Wood IG (2002), 'The effect of ferromagnetism on the equation of state of Fe_3C studied by first-principles calculations', *Earth Planet Science Letters*, 203, 567–575.

Vocadlo L, Alfé D, Gillan MJ, Wood IG, Brodholt JP and Price GD (2003), 'Possible thermal and chemical stabilization of body-centred-cubic iron in the Earth's core', *Nature*, 424 536–539.

von Appen J, Eck B and Dronskowski R (2010), 'A density-functional study of the phase diagram of cementite-type $(Fe, Mn)_3C$ at absolute zero temperature', *Journal of Computational Chemistry*, 31, 2620–2627.

von Barth U and Hedin L (1972), 'A local exchange-correlation potential for the spin polarized case: I', *J. Phys. C: Solid State Phys.*, 5, 1629–1642.

von Pezold J, Dick A, Friák M and Neugebauer J (2010), 'Generation and performance of special quasirandom structures for studying the elastic properties of random alloys: application to Al-Ti', *Physical Review B*, 81, 094203.

Voronin VI, Berger IF, Gornostyrev YN, Urtsev VN, Kuznetsov AR and Shmakov AV (2010), 'Composition of cementite in the dependence on the temperature. *In situ* neutron diffraction study and *ab initio* calculations', *JETP Letters*, 91, 143–146.

Vrestal J (2001), 'Recent progress in modelling of σ-phase', *Archives of Metallurgy*, 46, 239–247.

Vrestal J, Kroupa A and Sob M (2006), 'Application of *ab initio* electronic structure calculations for prediction of phase equilibria in superaustenitic steels', *Computational Materials Science*, 38, 298–302.

Wachowicz E and Kiejna A (2008), 'Effect of impurities on grain boundary cohesion in bcc iron', *Computational Materials Science*, 43, 736–743.

Wachowicz E, Ossowski T and Kiejna A (2010), 'Cohesive and magnetic properties of grain boundaries in bcc Fe with Cr additions', *Physical Review B*, 81, 094104.

Wang A, Zhou L, Kong Y, Du Y, Liu ZK, Shang SL, Ouyang Y, Wang J, Zhang L and Wang J (2009), 'First-principles study of binary special quasirandom structures for the Al-Cu, Al-Si, Cu-Si, and Mg-Si systems', *Calphad-Computer Coupling of Phase Diagrams and Thermochemistry*, 33, 769–773.

Wang JT, Wang DS and Kawazoe Y (2006), 'Finite-temperature magnetism of tetragonal iron', *Applied Physics Letters*, 88, 132513.

Wang Y, Stocks GM, Nicholson DMC, Shelton WA, Antropov VP and Harmon BN (1997), 'Noncollinear magnetic structure in $Ni_{0.35}Fe_{0.65}$', *Journal of Applied Physics*, 81, 3873–3875.

© Woodhead Publishing Limited, 2012

Wei SH and Zunger A (1996), 'Giant and composition-dependent optical bowing coefficient in GaAsN alloys', *Physical Review Letters*, 76, 664–667.

Widom M and Mihalkovic M (2005), 'Stability of Fe-based alloys with structure type C_6Cr_{23}', *Journal of Materials Research*, 20, 237–242.

Wille LT, Nonas B, Dederichs PH and Dreysse H (1998), 'Growth mode of Cr on Fe(001) described by *ab-initio* interactions', *Philosophical Magazine B*, 78, 643–652.

Windl W, Stumpf R, Liu XY and Masquelier MP (2001), '*Ab initio* modeling study of boron diffusion in silicon', *Computational Materials Science*, 21, 496–504.

Wood BJ (1993), 'Carbon in the core', *Earth Planet Science Letters*, 117, 593–607.

Wood IG, Vocadlo L, Knight KS, Dobson DP, Marshall WG, Price GD and Brodholt J (2004), 'Thermal expansion and crystal structure of cementite, Fe_3C, between 4 and 600K determined by time-of-flight neutron powder diffraction', *Journal of Applied Crystallography*, 37, 82–90.

Wu FY, McCoy BM, Fisher ME and Chayes L (2008), 'Comment on a recent conjectured solution of the three-dimensional Ising model', *Philosophical Magazine*, 88, 3093–3095.

Wu RQ, Freeman AJ and Olson GB (1994), 'First principles determination of the effects of phosphorus and boron on iron grain boundary cohesion', *Science*, 265, 376–380.

Wu RQ, Freeman AJ and Olson GB (1996), 'Effects of carbon on Fe-grain-boundary cohesion: first-principles determination', *Physical Review B*, 53, 7504–7509.

Xiong W, Selleby M, Chen Q, Odqvist J and Du Y (2010), 'Phase equilibria and thermodynamic properties in the Fe-Cr system', *Critical Reviews in Solid State and Materials Sciences*, 35, 125–152.

Xiong W, Zhang H, Vitos L, Selleby M (2011), 'Magnetic phase diagram of the Fe-Ni system', *Acta Materialia*, 59, 521–530.

Yang CN (1952), 'The spontaneous magnetization of a two-dimensional Ising model', *Physical Review*, 85, 808–816.

Yoshitomi K, Nakama Y, Ohtani H and Hasebe M (2008), 'Thermodynamic analysis of the Fe-Nb-B ternary system', *ISIJ International*, 48, 841–850.

Yu R, Singh D and Krakauer H (1991), 'All-electron and pseudopotential force calculations using the linearized-augmented-plane-wave method', *Physical Review B*, 43, 6411–6422.

Yuasa M and Mabuchi M (2010), 'Effects of segregated Cu on an Fe grain boundary by first-principles tensile tests', *Journal of Physics – Condensed Matter*, 22, 505705.

Zeller R, Dederichs PH, Ujfalussy B, Szunyogh L and Weinberger P (1995), 'Theory and convergence properties of the screened Korringa–Kohn–Rostoker method', *Physical Review B*, 52, 8807–8812.

Zhang HL, Punkkinen MPJ, Johansson B, Hertzman S and Vitos L (2010a), 'Single-crystal elastic constants of ferromagnetic bcc Fe-based random alloys from first-principles theory', *Physical Review B*, 81, 184105.

Zhang HL, Lu S, Punkkinen MPJ, Hu QM, Johansson B, Vitos L (2010b), 'Static equation of state of bcc iron', *Physical Review B*, 82, 132409.

Zhang J and Guyot F (1999), 'Thermal equation of state of iron and $Fe_{0.91}Si_{0.09}$', *Physics and Chemistry of Minerals*, 26, 206–211.

Zhang ZD (2007), 'Conjectures on exact solution of three-dimensional (3D) simple orthorhombic Ising lattices', *Philosophical Magazine*, 87, 5309–5419.

Zhao F, Tegus O, Fuquan B and Brück E (2009), 'Magnetic properties of $Fe_{3(1-x)}Cr_{3x}C$ alloys', *International Journal of Minerals, Metallurgy, and Materials*, 16, 314–316.

© Woodhead Publishing Limited, 2012

Zhong LP, Wu RQ, Freeman AJ and Olson GB (1997), 'Effects of Mn additions on the P embrittlement of the Fe grain boundary', *Physical Review B*, 55, 11133–11137.

Zhou CT, Xiao B, Feng J, Xing JD, Xie XJ, Chen YH and Zhou R (2009), 'First principles study on the elastic properties and electronic structures of $(Fe,Cr)_3C$', *Computational Materials Science*, 45, 986–992.

Zotov N and Ludwig A (2008), 'First-principles calculations of the elastic constants of Fe-Pt alloys', *Intermetallics*, 16, 113–118.

Zunger A, Wei SH, Ferreira LG and Bernard JE (1990), 'Special quasirandom structures', *Physical Review Letters*, 65, 353–356.

© Woodhead Publishing Limited, 2012

13

Phase field modelling of phase transformations in steels

M. MILITZER, The University of British Columbia, Canada

Abstract: Phase field models are powerful tools to simulate the evolution of microstructures with complex morphologies. This chapter provides first a brief overview on the phase field methodology itself. Then its application to phase transformations in steels is described. Both austenite formation and austenite decomposition are considered. The pearlite-to-austenite transformation is discussed as an example where phase field simulations capture the formation of complex finger-type morphologies of the growing austenite. Phase field simulations are then analysed for austenite decomposition into polygonal, massive and Widmanstätten ferrite as well as pearlite.

Key words: simulation of transformation products with complex morphology, Ginzburg–Landau free energy functional, austenite formation, austenite decomposition,

13.1 Introduction

Over the past two decades, the phase field model (PFM) approach has been developed into a powerful tool to model microstructure evolution. Initially, PFMs were used to simulate solidification but more recently they have also been applied to solid-solid phase transformations in steels (Böttger *et al.*, 2008).

In general, multi-phase materials contain domains of well-defined phases of different composition and crystal structure. If the system is not in equilibrium, the microstructure evolves to reduce the total free energy of the system. The classical approach to model microstructure evolution treats the region between these different domains with an interface of zero thickness. These sharp interface models require the solution of diffusion equations with moving boundary conditions at the interface, i.e. the so-called free boundary problem. The free-boundary approach has been successfully implemented for phase changes with simple geometries – one-dimensional thickening of a ferrite film, or ferrite growth in a spherical austenite grain, are classical examples. Unfortunately, the free-boundary approach becomes impractical for more complex two- or three-dimensional systems. Phase field models are an alternative and more convenient way of modelling microstructure evolution with complex geometries.

© Woodhead Publishing Limited, 2012

In this chapter, the status of the application of PFMs to austenite-ferrite transformations in steels will be critically reviewed. First, a brief general introduction to the PFM methodology will be given. Subsequently, PFM simulations of the austenite formation in eutectoid and low carbon steels will be described. This is followed by analysing the application of PFMs to austenite decomposition. Here, the formation of polygonal ferrite will be considered first before discussing PFM simulations of more complex transformation products, i.e. massive ferrite, Widmanstätten ferrite and pearlite. The chapter is concluded with a short commentary on future trends in phase field modelling and its application to steels.

13.2 Phase field methodology

13.2.1 Background

Before examining the application of PFMs to the austenite-ferrite transformations in steels, it is useful to provide a brief overview of the methodology itself. For an in-depth description of the phase field methodology and its underlying physics, the reader is referred to a number of recent reviews. Karma (2001) gives a brief introduction to the general phase field methodology. The review papers of Moelans *et al*. (2008) as well as Singer-Loginova and Singer (2008) provide excellent general introductions to phase field modelling of microstructures. Steinbach (2009) emphasizes in his review the multi-phase field approach and its application to solidification. Provatas and Elder (2010) describe in their monograph the detailed physics, as well as the mathematical and numerical aspects, of PFMs. They also give a comprehensive overview on phase field crystal models that have recently emerged as a modelling tool to study systems on atomistic length scales but with diffusional timescales.

The phase field approach considers both bulk and interface regions of the system in an integral manner based on the construction of a Ginzburg–Landau free energy functional (Ginzburg and Landau, 1950). A functional is a function whose input is a vector function rather than individual values. One or more continuous field variables are introduced to describe at any time, t, in each position, r, the different domains present in the system. Typically, these phase field parameters are constant in the bulk regions but change continuously over a diffuse interface of thickness, l.

The simplest representation of the free energy functional that combines the bulk thermodynamics with a minimal description of the interfacial energy is given by

$$F(\phi, T) = \int_V \left[\frac{1}{2} |\kappa \nabla \phi|^2 + f(\phi(r), T(r)) d^3 r \right] \qquad [13.1]$$

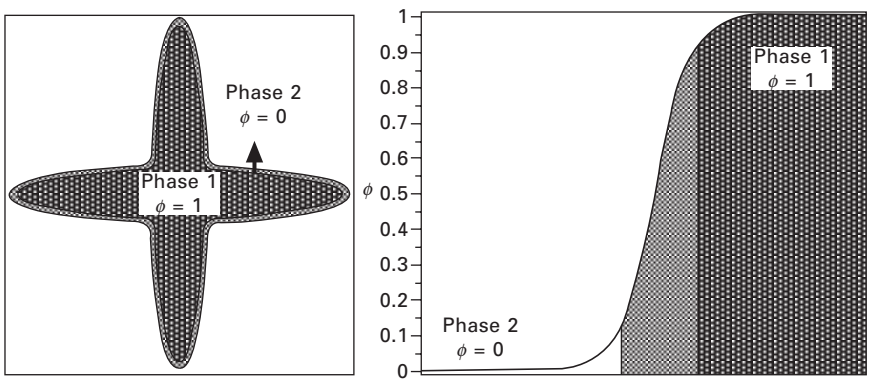
© Woodhead Publishing Limited, 2012

where ϕ is the phase field parameter, f is the bulk free energy density and κ is a parameter that is related to the interfacial energy – the gradient term in Eq. [13.1] accounts for the energy penalty of the interface through which the phase field parameter, ϕ, changes gradually, as shown in Fig. 13.1. Figure 13.1 gives a schematic representation of a two-phase structure where one phase (e.g. liquid) is characterized by $\phi = 0$ and the other (e.g. solid) by $\phi = 1$. A classical example of this situation is the Ising model to describe ferromagnetism where the bulk free energy is given by

$$f = a_0(T) + \frac{a_2(T)}{2}\phi^2 + \frac{a_4(T)}{4}\phi^4 \qquad [13.2]$$

Here the a_i's are suitable functions of temperature. Minimization of this free energy density implies $\phi = 0$ above a critical temperature, i.e. the Curie temperature, and $\phi = \sqrt{(-a_2)/a_4}$ to account for spin ordering below the Curie temperature. The Ising model is the simplest example for a non-conserved order or phase field parameter that is used in the PFM methodology to describe phase transformations. In phenomenological PFMs ϕ is, for convenience, usually normalized to assume values from 0 to 1 (see Fig. 13.1). For the situation of the Ising model, the gradient term in Eq. [13.1] describes the microscopic zone (i.e. interface) where the local magnetization changes abruptly between two magnetic domains. Equation [13.1] serves as the starting point for modelling the microstructure evolution using the PFM methodology. In general, f can be a complex function of the phase field parameters characterizing the system or phenomena to be simulated.

In order to simulate the evolution of the system from a non-equilibrium state, the time-dependent Ginzburg–Landau equation, also known as the Allen–Cahn equation (Allen and Cahn, 1979), is employed, i.e.



13.1 Schematics of a 2D phase field and the continuous change of the phase field parameter ϕ through the diffuse interface.

© Woodhead Publishing Limited, 2012

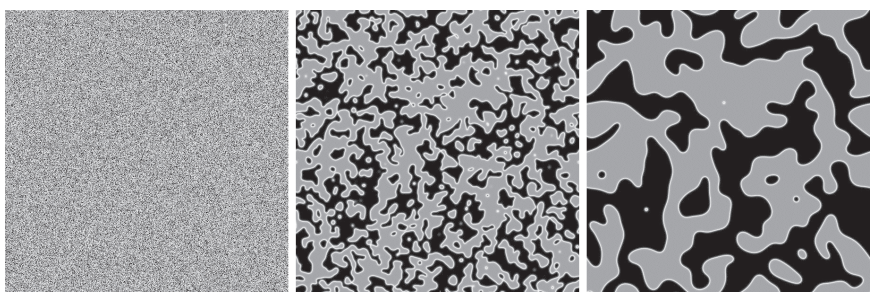
$$\frac{d\phi}{dt} = -L\frac{\delta F(\phi, T)}{\delta \phi} = L\left(\kappa\nabla^2\phi - \frac{\partial f}{\partial \phi}\right) \quad [13.3]$$

where L is related to the timescale of atomic re-arrangements at the interface. For the Ising model, combining Eqs [13.2] and [13.3] yields

$$\frac{d\phi}{dt} = L(\kappa\nabla^2\phi - a_2\phi - a_4\phi^3) \quad [13.4]$$

which can be viewed as the simplest form of a phase field equation. Figure 13.2 shows a sequence of time slices in the evolution of magnetic domains simulated according to the dynamics of Eq. [13.4]. Despite the simplicity of the model it is striking that complex pattern formation and the coarsening of magnetic domains (or any other microstructure feature) can be dealt with. The evolution of the domains, i.e. the position of the interfaces, is implicitly given by the evolution of the phase field.

One drawback of the PFM methodology is its computational expense. As a result, the development of PFMs is inherently linked to the advances made in computer technology and can be traced back about two decades. Since then the phase field methodology has become ubiquitous and is increasingly gaining popularity as the method of choice in modelling microstructures in solidification and solid-solid transformations. Even though PFMs offer a deeper connection to fundamental thermodynamics than larger-scale engineering or sharp interface models, the emergence of a mesoscopic, i.e. diffuse, interface leads to significant challenges from both fundamental and numerical points of view. To minimize computational expense in modelling microstructures on the length scales of micrometers or centimetres, interface thicknesses are employed that can be orders of magnitude larger than those of the actual interfaces. Thus, thin-interface asymptotic analysis methods are critical to validate PFM simulations. New mathematical and numerical techniques have recently been developed to face these challenges as eloquently summarized



13.2 Time sequence of magnetic domain formation and coarsening in a 2D phase field simulation using the Ising model free energy density.

© Woodhead Publishing Limited, 2012

by Provatas and Elder (2010). Here, only a brief account of the PFM methodology development is provided to assist the reader in appreciating its application to phase transformations in steels.

13.2.2 Phase field model approaches

Broadly speaking, there are two types of phase field models that have been formulated independently. The first type was developed by Chen and Khachaturyan (1991) and Wang Y *et al*. (1993) based on the microscopic theory of Khachaturyan (1968, 1983). Here, the phase field variables are related to microscopic parameters, e.g. order parameters reflecting the crystal symmetry relations between two phases. An example of this type of PFM is the above described simulation of the evolution of a ferromagnetic domain structure based on the Ising model. In general, the PFMs of this family are applied to solid-solid transformations.

The second PFM type is phenomenological in nature and was developed primarily to avoid tracking the interface – an idea that was first proposed by Langer (1986). This phase field technique was originally used to simulate dendritic growth in pure undercooled melts (Wheeler *et al*., 1992; Kobayashi, 1993) before extending its application to solidification of alloys (Caginalp and Xie, 1993; Warren and Boettinger, 1995). Many of the phenomenological PFMs are based on the classical approach proposed by Wheeler, Boettinger and McFadden – the WBF model (Wheeler *et al*., 1992) that starts from a double-well description of the free energy density for pure materials, i.e.

$$f = (1 - p(\phi))f^{\alpha} + p(\phi)f^{\beta} + wg(\phi) \qquad [13.5]$$

where f^{α} and f^{β} are the free energy expressions for the α and β phases, respectively, w is a constant and $g(\phi)$ is the double-well potential

$$g(\phi) = \phi^2(1 - \phi)^2 \qquad [13.6]$$

Assuming ϕ equals 1 in the β phase and 0 in the α phase, the interpolation function $p(\phi)$ is a smooth function that is 1 for $\phi = 1$ and 0 for $\phi = 0$, and has local extrema at $\phi = 1$ and $\phi = 0$. Frequently, the expression (Wang S L *et al*., 1993)

$$p(\phi) = \phi^3(6\phi^2 - 15\phi + 10) \qquad [13.7]$$

is employed.

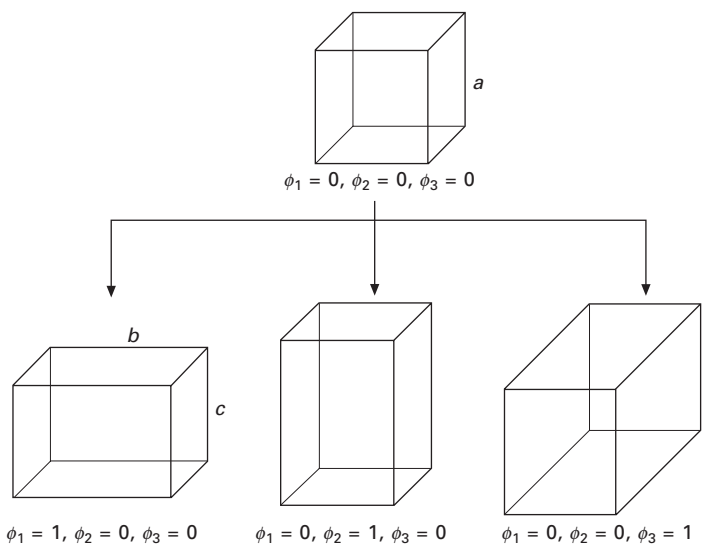
To extend this model to binary alloys, a continuous composition profile is considered through the interface where the free energy density is constructed using the linear law of mixtures for the free energy densities of the pure systems at the given composition. However, in the diffuse interface, two (or more) phases coexist and, since only a single composition field is considered, all coexisting phases then have the same composition. The problem with this

© Woodhead Publishing Limited, 2012

approach is that the interfacial parameters depend on the interface thickness of the numerical simulations. As an alternative, the interface region can be considered as a mixture of the two phases with different compositions that are defined by a constant ratio for each element (Steinbach *et al.*, 1996; Tiaden *et al.*, 1998). Kim *et al.* (1998) provided a thermodynamically consistent derivation for this approach to treating the interface region.

13.2.3 Multi-phase field models

In general, the proper simulation of microstructures may require introducing more than one phase field variable. To illustrate this, one may consider the transition from a cubic to a tetragonal lattice structure – the austenite-to-martensite transformation in steels is an important example of this transition. As shown in Fig. 13.3, the tetragonal structure has less symmetry than the cubic structure but can be oriented in three equivalent ways with respect to the cubic structure. In the first type of PFMs, i.e. the Chen–Wang approach, this situation can be depicted by introducing three order parameters to describe the free energy that must have six minima with equal depth, ϕ_{eq}, at $(\phi_1,\phi_2,\phi_3) = (\pm\phi_{eq},0,0)$, $(0,\pm\phi_{eq},0)$, $(0,0,\pm\phi_{eq})$. The following sixth-order expression may be used for the required free energy density (Wang and Khachaturyan, 1997):



13.3 Transition from a cubic structure with lattice parameter *a* to a tetragonal structure with lattice parameters *b* and *c* where three order parameters (ϕ_1, ϕ_2, ϕ_3) can be used to distinguish the three tetragonal variants with respect to the cubic structure.

© Woodhead Publishing Limited, 2012

$$f = \frac{a_2}{2}\sum_{i=1}^{3}\phi_i^2 - \frac{a_4}{4}\sum_{i=1}^{3}\phi_i^4 + \frac{a_6}{6}\left(\sum_{i=1}^{3}\phi_i^2\right)^3 \quad [13.8]$$

where the a_i's are positive constants that determine the value of ϕ_{eq}. Equation [13.8] replicates for each phase field parameter ϕ_i the double-well function of the Ising model.

The free energy density of Eq. [13.8] with three order parameters can be generalized for the case of N phase field parameters. The evolution of what is now a phase field vector instead of a scalar phase field parameter is described by a coupled set of differential equations that has the general form of

$$\frac{d\phi_i}{dt} = -L_i \frac{\delta F(\phi_1,\ldots,\phi_i,\ldots,\phi_N,T)}{\delta\phi_i} \quad [13.9]$$

For the phenomenological PFMs, the multi-phase field approach was introduced by Steinbach *et al*. (1996). Here, each grain and/or microstructure constituent is characterized by its own phase field parameter and can thus be tracked throughout the simulation domain to predict the evolution of an assembly of grains and/or phases. Each grain can be characterized by a number of attributes, e.g. its phase and crystallographic orientation. For a simulation domain with N grains, ϕ_i $[i = 1,\ldots, N]$, ϕ_i is equal to 1 inside grain i and 0 elsewhere. At the interface between two grains, there is a gradual change of the two corresponding phase field parameters from 0 to 1 such that $\sum_{i=1}^{N}\phi_i(r,t) = 1$ holds.

The phenomenological multi-phase field model is commonly used to describe the austenite-ferrite transformations, in particular to capture the resulting grain size and phase distributions. A significant body of this simulation work employs the commercially available code MICRESS® (microstructure evolution simulation software, www.access.rwth-aachen.de/MICRESS/), which is based on the multi-phase PFM of Steinbach *et al*. (1996). Here, the system of coupled differential equations for the phase field vector is given by

$$\frac{d\phi_i}{dt} = \sum_{i\neq j}\mu_{ij}\left[\sigma_{ij}\left\{\phi_j\nabla^2\phi_i - \phi_i\nabla^2\phi_j + \frac{\pi^2}{2l_{ij}^2}(\phi_i - \phi_j)\right\} + \frac{\pi}{l_{ij}}\sqrt{\phi_i\phi_j}\Delta G_{ij}\right] \quad [13.10]$$

where μ_{ij} is the interface mobility, σ_{ij} is the interfacial energy, l_{ij} is the interface thickness and ΔG_{ij} is the driving pressure. An advantage of MICRESS® is its versatility and ease of use for applications of the phase field method. However, the application potential of PFMs is not limited to this particular

© Woodhead Publishing Limited, 2012

software, and alternative PFM methods (Yeon *et al.*, 2001; Loginova *et al.*, 2003; Li *et al.*, 2005; Huang *et al.*, 2006) have also been applied to steel.

The phase field equations can be coupled with the diffusion equations, e.g. for carbon to describe phase transformations in the Fe-C system. The evolution of the carbon concentrations, C, for two neighbouring grains i and j with carbon diffusivities D_i and D_j, respectively, is given by

$$\frac{\partial C}{\partial t} = \nabla[\phi_i D_i \nabla C_i + \phi_j D_j \nabla C_j] \qquad [13.11]$$

where C_i and C_j are the carbon concentration in grains i and j, respectively. Provided both grains are of the same phase, Eq. [13.11] reduces to the classical diffusion equation $\partial C/\partial t = \nabla(D\nabla C)$. The driving pressures for solving the phase field equations can be obtained from thermodynamic databases, e.g. Thermo-Calc® (www.thermocalc.com). Further, elastic strain contributions to the free energy can be considered and the phase field equations can be coupled with the equations describing the temperature evolution throughout the simulation domain (Böttger *et al.*, 2008).

The multiplicity of interfacial properties (μ_{ij}, σ_{ij}, l_{ij}) must be provided as an input and, in principle, this permits incorporation of potential anisotropy in these properties. Unfortunately, exact knowledge of interfacial parameters, in particular mobilities, and their potential anisotropy is rather limited. Since the PFM is derived as a growth model, nucleation of grains of a new phase is another phenomenon that must be specified as input information. PFM simulation results depend markedly on the assumed density and distribution of nuclei as well as the rate of nucleation, as will be shown in more detail below for the austenite-ferrite transformations. As a result, interfacial mobilities, anisotropy factors and nucleation scenarios are usually employed as adjustable parameters when a quantitative description of experimental observations is sought.

Overall, phase field models provide a powerful methodology to describe phase transformations. This technique can easily handle time-dependent growth geometries with complex pattern formations, as illustrated above for magnetic domains (see Fig. 13.2). Thus, PFMs are very suitable to simulate phase transformations in steels where morphological complexities are common, e.g. for austenite formation as well as austenite decomposition into, say, Widmanstätten ferrite and bainite.

13.2.4 Benchmarking of phase field models

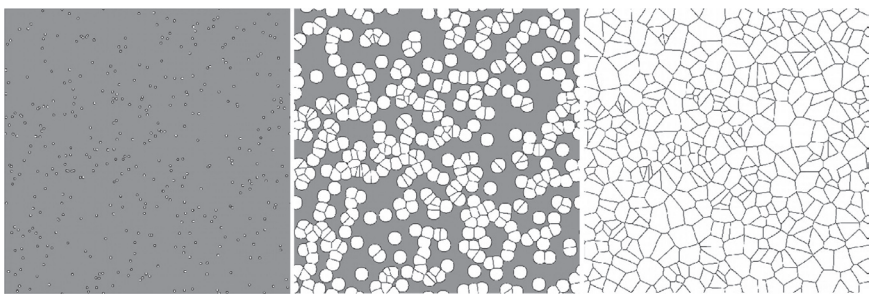
Before discussing these applications in more detail, it is useful to benchmark the phase field model with the Johnson–Mehl–Avrami–Kolmogorov (JMAK) model (Kolmogorov, 1937; Johnson and Mehl, 1939; Avrami, 1939). This fundamental transformation model has been widely used, at least in a semi-

© Woodhead Publishing Limited, 2012

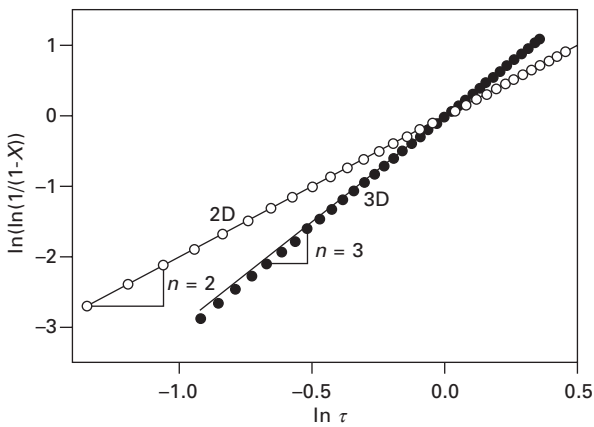
empirical manner, to describe phase transformations in steels even though its simplified assumptions are usually not fulfilled. Let us consider the JMAK scenario with nucleation site saturation, where N randomly distributed nuclei grow at a constant rate, v, i.e. with constant driving pressure, ΔG. According to the JMAK theory, the fraction transformed, X, is given by

$$X = 1 - \exp(-\tau^n) \qquad [13.12]$$

where τ is the dimensionless normalized isothermal holding time and the exponent n is equal to the dimensionality of the system: two in 2D and three in 3D, respectively. Using the concept of mobility, $v = \mu\Delta G$, the normalized time can be related to the actual time by $\tau = (Ns_n)^{1/n}\mu\Delta G t$, where s_n is a shape factor ($4\pi/3$ for spheres and π for circles). Figure 13.4 shows the evolution of the system as predicted with a 2D phase field simulation. As summarized in Fig. 13.5, the PFM replicates the idealized JMAK exponents $n = 2$ and $n = 3$, respectively. In order for the kinetics to agree quantitatively in both



13.4 Time sequence of a 2D PFM simulation of the JMAK transformation scenario with nucleation site saturation.



13.5 Comparison of idealized JMAK kinetics (lines) with PFM simulations (symbols) in 2D and 3D.

© Woodhead Publishing Limited, 2012

models, a mobility term had to be taken in these PFM simulations that was by a factor of 1.3 larger than in the JMAK model. This is a consequence of the diffuse nature of the interface whereas the JMAK approach is a sharp interface model. This benchmarking exercise is a further justification for the application of PFMs to austenite (γ)–ferrite (α) transformations in steels for both austenite formation and austenite decomposition, as described below.

13.3 Austenite formation

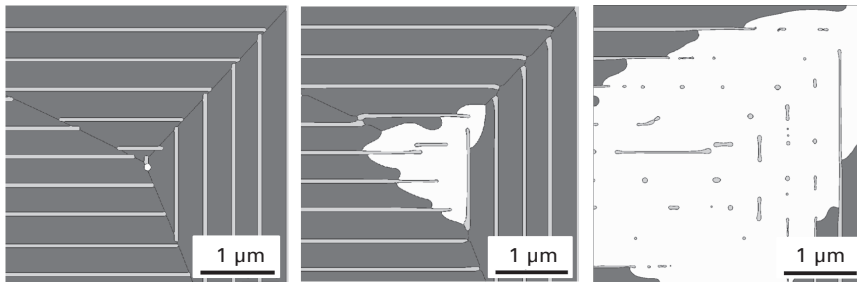
When processing steel, e.g. hot rolling starting from continuous cast slabs, or intercritical annealing of sheet steels for automotive applications, austenite formation (usually from a ferrite or ferrite-pearlite microstructure) precedes the otherwise much more studied austenite decomposition. Here, we will first examine phase field modelling of the austenite formation. The interest in this phase formation has recently been rekindled because intercritical annealing is an essential, if not critical, processing step in manufacturing dual-phase steels that have become one of the materials of choice for car makers.

The formation of austenite was much studied in the 1970s and 1980s when dual-phase steels where first considered for potential commercialization. These studies showed that the austenite formation kinetics occurs in three stages (Speich *et al.*, 1981):

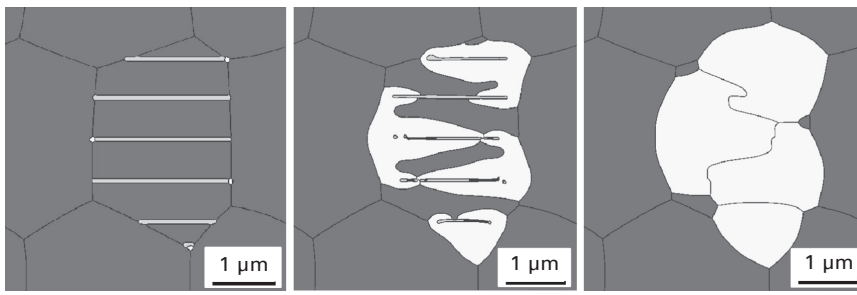
- very rapid growth of austenite into pearlite to completely dissolve pearlite,
- slower growth of austenite into ferrite governed primarily by C diffusion,
- even slower redistribution of substitutional alloying elements (e.g. Mn) to attain equilibrium.

In Fe-C alloys, both the pearlite-to-austenite and ferrite-to-austenite transformations are controlled by C diffusion. Assuming a sufficiently large interface mobility (e.g. 10^{-11} cm^4 J^{-1} s^{-1} at 750°C) 2D PFM simulation can be benchmarked with analytical solutions of the diffusion problem for planar and radial growth of austenite from cementite (Azizi-Alizamini and Militzer, 2010; Militzer and Azizi-Alizamini, 2011). Militzer and Azizi-Alizamini (2011) used their PFM approach to simulate the pearlite-to-austenite transformation in a eutectoid 0.96 wt% C steel where experimental data of Speich *et al.* (1969) confirmed C diffusion-controlled transformation kinetics. Figure 13.6 shows the sequence of austenite formation simulated at 750°C for an interlamellar spacing of 0.4 μm that is consistent with the measurements of Speich *et al.* (1969). Assuming symmetrical boundary conditions, an austenite nucleus is located at the triple point of three pearlite colonies and grows preferentially along the cementite lamellae before consuming all of the parent pearlite. Remnants of carbides within the newly formed austenite are predicted, i.e.

© Woodhead Publishing Limited, 2012



13.6 Time sequence from 2D PFM simulations of the pearlite-to-austenite transformation in a eutectoid 0.96 wt% C steel at 750°C (austenite: white, cementite: light grey, ferrite: dark grey); adapted from Militzer and Azizi-Alizamini (2011).

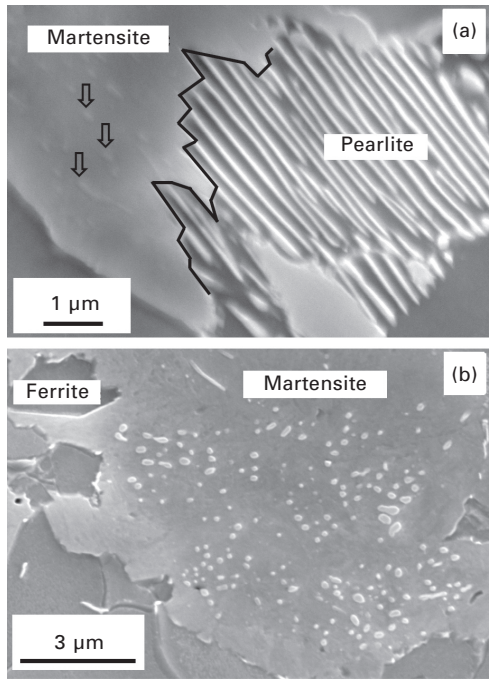


13.7 Time sequence of 2D phase field simulation of austenite formation in Fe-0.17 wt% C at an intercritical annealing temperature of 750°C (ferrite: dark grey, cementite: light grey, austenite: white).

the dissolution of cementite occurs at a slower rate than the progression of the austenite-pearlite transformation front. The predicted average austenite growth rate of 6 μm/s is close to the experimental rate of 2 μm/s and this is consistent with a reaction controlled by C diffusion in austenite (Militzer and Azizi-Alizamini, 2011). Further, Militzer and Azizi-Alizamini (2011) applied 2D PFM simulations to intercritical austenite formation at 750°C in a ferritic-pearlitic Fe-0.17 wt% C alloy, as shown in Fig. 13.7. Nucleation of austenite was assumed to occur at the boundary of the pearlite colony. These simulations confirm the morphological aspects of the pearlite-to-austenite formation, as discussed above for the eutectoid steel. These predictions are in agreement with experimental observations. Figure 13.8 shows two micrographs of an intercritically annealed plain carbon steel (0.17 wt% C–0.74 wt% Mn) that confirm the finger-type preferential growth of austenite (i.e. martensite after quenching) along the cementite lamellae (Fig. 13.8(a)) as well as the presence of carbides within austenite (Fig. 13.8(b)).

Systematic PFM simulations for intercritical austenite formation from ultrafine ferrite-cementite aggregates with circular (2D) and spherical particles

© Woodhead Publishing Limited, 2012

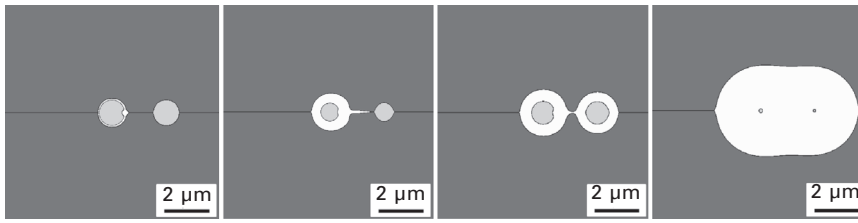


13.8 Micrographs from experimental studies of the pearlite-to-austenite transformation in a ferritic-pearlitic 0.17 wt% C–0.74 wt% Mn steel: (a) intercritically annealed at 735°C with partially transformed pearlite (martensite indicates austenite at the transformation temperature, arrows indicate carbides), (b) carbides (light grey areas) after completion of the pearlite transformation at 740°C.

(3D) showed, in the diffusion-controlled limit, a tendency for preferential growth of austenite towards carbides as they are sources of carbon. This again results in the development of finger-type structures, as illustrated in Fig. 13.9 (Azizi-Alizamini and Militzer, 2010). In this simulation series, carbide particle sizes of about 100 nm were resolved. In the situation depicted in Fig. 13.9, two cementite particles are present – one with an austenite nucleus, the other one without a nucleus. The austenite spike that forms in the early transformation stages towards the cementite particle without an austenite nucleus is promoted by eliminating the ferrite grain boundary but no fast grain boundary diffusion had been considered in these simulations. Further, the degree of the morphological complexity depends significantly on spacing and distribution of cementite particles.

The above simulations deal with Fe-C alloys and only some very initial PFM studies have been reported on austenite formation in steels containing substitutional alloying elements. Thiessen *et al.* (2006, 2007) conducted

© Woodhead Publishing Limited, 2012



13.9 Time sequence of a 2D austenite formation simulation in Fe-0.17 wt% C from circular cementite particles located at a ferrite grain boundary when at only one of the two cementite particles an austenite nucleus present (ferrite: dark grey, cementite: light grey, austenite: white); adapted from Azizi-Alizamini and Militzer (2010).

2D phase field simulations for austenite formation from ferrite-pearlite and ferrite-martensite structures during heat treatment cycles that replicate those in the weld heat affected zone (HAZ). To reduce computational cost, cementite lamellae were not resolved and pearlite was approximated as supersaturated ferrite with eutectoid carbon content. Using this approach, Savran (2009) described austenite formation during continuous heating in a number of C-Mn steels with C concentrations in the range of 0.2–0.6 wt%. By adjusting the interface mobilities, agreement with experimentally observed transformation kinetics can be obtained. For very slow heating (0.05 K/s) a mobility value was found that is a factor of 10 lower than for more rapid heating (3 K/s). This behaviour of the effective mobility was attributed to the potential for spheroidization of pearlite and/or Mn redistribution during very slow heating. The mobility values are sufficiently low such that the transformation kinetics are not solely controlled by C diffusion but depend also on the interface reaction, i.e. the kinetics are of mixed-mode character.

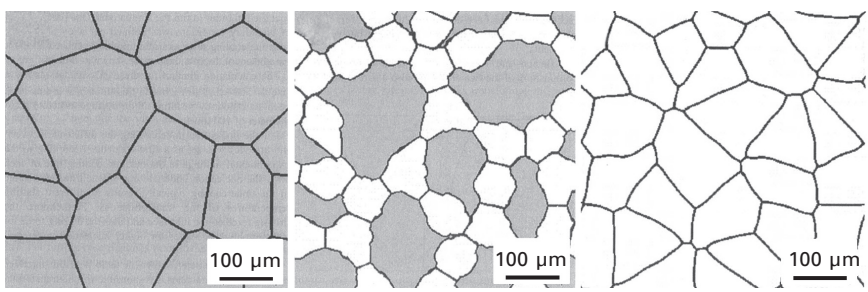
These PFM simulations provide insight into the evolution of austenite-ferrite dual-phase structures that are relevant for intercritical annealing of advanced high strength steels. Given the morphological complexity, it is of paramount importance to validate the presented 2D simulations with a rigorous series of 3D simulations. To date, just one 3D simulation result of austenite formation from spherical cementite particles has been reported (Azizi-Alizamini and Militzer, 2010). Further, in order to obtain a quantitative description of austenite formation in advanced high strength steels, the role of substitutional alloying elements needs to be considered in PFM simulations. The 'effective mobility' approach (Thiessen *et al*., 2006, 2007; Savran, 2009) appears to be a likely methodology to be employed in future simulations that explicitly incorporate the lamellar structure of pearlite. Subsequently, it may be possible to rationalize these mobility values and their temperature dependence with more physically based models, as proposed for the widely investigated austenite-to-ferrite transformation.

© Woodhead Publishing Limited, 2012

13.4 Austenite decomposition

13.4.1 Formation of polygonal ferrite

The austenite-to-ferrite transformation is arguably the most widely studied phase transformation as it is the key metallurgical tool to manipulate the properties of steels. Consequently, there is an extensive body of PFM simulations available for the decomposition of austenite. Yeon *et al.* (2001) and Pariser *et al.* (2001) were the first to employ PFM simulations to describe the formation of ferrite from austenite. With 1D simulations of ferrite growth, Yeon *et al.* (2001) analysed local equilibrium conditions for an Fe-Cr-Ni alloy and para-equilibrium conditions for the Fe-C-Mn system. Using Steinbach's multi-phase field model (Steinbach *et al.*, 1996), Pariser *et al.* (2001) conducted 2D simulations of the overall austenite-to-ferrite transformation during continuous cooling in two steels with ultra low carbon content – one ultra low carbon grade (22 wt.ppm C) and one interstitial-free grade (33 wt.ppm C). Nucleation was assumed to occur at austenite grain boundaries for an undercooling of 20 K and interfacial parameters were assumed to depend only on the phases of the neighbouring grains, i.e. α-α, α-γ, γ-γ. An α-γ interface mobility of 5×10^{-4} cms^{-1} K^{-1} was selected to replicate the experimental transformation kinetics for intermediate cooling rates of about 0.3 K/s. For other cooling rates, in particular for very slow cooling at 0.04 K/s, simulation results did show some discrepancies with the experiments. This was primarily attributed to the restrictive assumptions made for nucleation – for very slow cooling the transformation closely follows equilibrium, i.e. the transformation starts essentially at the Ae_3 temperature rather than at a prescribed undercooling. Figure 13.10 shows the simulated evolution of the austenite-to-ferrite transformation in the ultra low carbon grade cooled at 0.35 K/s. The nuclei density at austenite grain boundaries



13.10 2D simulated microstructure development in an ultra low carbon steel (22 wt.ppm C) cooled at 0.35 K/s (ferrite: white, austenite: grey, interfaces: black) (reproduced from Pariser *et al.*, 2001). Reproduced with permission of Wiley-VCH Verlag GmbH & Co. KGaA.

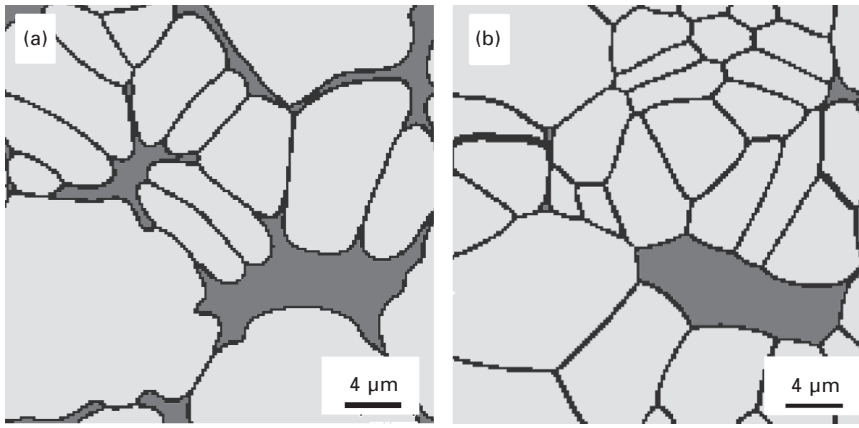
© Woodhead Publishing Limited, 2012

was taken such as to yield a final ferrite grain size of approximately 50 μm that is comparable to the average measured grain size of 60 μm.

These simulations employed, at least implicitly, the paradigm of adjusting interface mobilities and nucleation scenarios to match a reference or measured kinetics and this has now become a standard in PFM simulations of the overall austenite-to-ferrite transformation. Whilst for the ultra low carbon steels referred to above the reaction was shown to be essentially interface controlled, long range carbon diffusion acquires a crucial role when describing ferrite formation in steels with higher carbon content. At sufficiently high carbon content (>0.3 wt%), the reaction is controlled by long range carbon diffusion as discussed earlier for the reverse transformation of austenite formation. For intermediate carbon levels, i.e. for low carbon steels, the transformation is of mixed-mode character, i.e. the transformation kinetics depend on both the interface reaction and long range diffusion (Sietsma and van der Zwaag, 2004). By coupling the phase field equations with the diffusion equations, the PFM methodology naturally replicates the mixed-mode philosophy. In practice, only carbon diffusion is usually included in the simulations and the much slower redistribution of substitutional alloying elements is not considered. Thus, para-equilibrium is then commonly adopted to calculate the driving pressure for the transformation. To reduce computational cost, linearized phase diagrams are employed in many simulations. A detailed analysis of the mixed-mode character indicates a gradual change from an interface-controlled to a carbon diffusion-controlled reaction as confirmed with PFM simulations by Mecozzi *et al*. (2005a, 2005b, 2006). They conducted 2D simulations to describe continuous cooling transformation kinetics in low carbon steels including a Nb microalloyed grade.

Militzer *et al*. (2006) extended the above 2D austenite-ferrite phase field simulations to 3D space. Comparing 2D and 3D simulation results shows that faster transformation rates are predicted in 2D for a given interface mobility. This is a reasonable finding as 2D simulations can be viewed as cylindrical growth, whereas for the cases studied, formation of equiaxed ferrite in 3D is more consistent with spherical growth. Thus, to match experimental kinetics, the apparent 2D mobilities are smaller than those obtained with 3D simulations. The details of these mobility differences depend on topological aspects of the simulated transformation cases, but the values of the apparent 2D and 3D mobilities are usually of the same order of magnitude. Further, 3D simulations lead to more realistic microstructure topologies as compared to 2D simulations. As shown in Fig. 13.11, grain shapes in the 2D cuts from 3D simulations are similar to those observed in micrographs, whereas 2D simulations may yield a number of unrealistic grain shapes. For example, the remaining austenite develops long-elongated channels with a number of narrow inlet-type features between ferrite grains that often appear as squashed circles (see Fig. 13.11(a)).

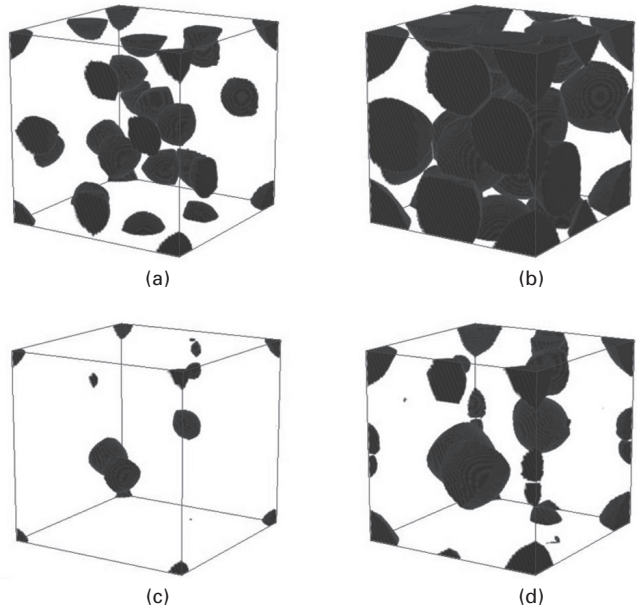
© Woodhead Publishing Limited, 2012



13.11 Comparison of PFM simulated 2D (a) vs. 3D (b) microstructures for continuous cooling transformation in a 0.1 wt% C–0.49 wt% Mn steel at 10 K/s (ferrite: light grey, austenite: dark grey, interfaces: black); adapted from Militzer *et al.* (2006).

The role of nucleation behaviour was also more rigorously analysed with these 3D simulations (Militzer *et al.*, 2006; Mecozzi *et al.*, 2008). The general simulation approach had been to assume a reasonable nucleation condition (nuclei density) to obtain a reference ferrite grain size. Then, the α-γ interface mobility, μ, was used to fit experimentally observed transformation kinetics. However, the magnitude of the mobility values depends on the detail of the selected nucleation scenario (nuclei density, spatial distribution of nuclei, nucleation temperature range). In the 3D simulations (Militzer *et al.*, 2006; Mecozzi *et al.*, 2008), the ferrite grain size distribution was used to conclude a likely nucleation scenario. In these simulations all nuclei formed at the austenite grain boundary with grain edges between three austenite grains as preferred nucleation sites. Sufficiently small grain boundary mobilities were assumed such that each nucleus leads to a ferrite grain in the final microstructure. The nuclei density determines the average ferrite grain size while the temperature range, δT, of nucleation can be used to change the width of the grain size distribution. Figure 13.12 shows an example of the effect of δT on the progression of ferrite formation for a given interface mobility where earlier nuclei formation increases transformation rates. Further, when all nuclei form at the same temperature ($\delta T = 0$ K) the resulting ferrite grains are of similar size (see Fig. 13.12(a)), whereas in the case where nucleation occurs over a temperature range (e.g. $\delta T = 24$ K), a significant spread in the ferrite grain sizes is obtained (see Fig. 13.12(d)). This general methodology provides a tool to determine the μ-δT combination that best replicates the experimental (or reference) transformation kinetics and resulting ferrite grain size distribution.

© Woodhead Publishing Limited, 2012



13.12 Effect of the nucleation temperature range, δT, on the simulated 3D microstructure (ferrite shown in dark) in Fe-0.1 wt% C–0.49 wt% Mn during cooling at 0.4 K/s for δT = 0 K at (a) 807°C and (b) 797°C; for δT = 24 K at (c) 807°C and (d) 797°C; adapted from Mecozzi *et al.* (2008).

A concern with this approach is that simulations do not account for ferrite grain coarsening. Ferrite grain coarsening during the austenite-to-ferrite transformation was analysed with 2D phase field simulations (Huang *et al.*, 2006; Huang and Browne, 2006). Substantial ferrite grain coarsening was predicted for simulations of continuous cooling transformation in a 0.17 wt% C–0.74 wt% Mn steel – about 50% of the initially nucleated ferrite grains have been consumed at the completion of transformation (Huang *et al.*, 2006). In addition to classical grain growth, grain rotation was also considered in these simulations. Then, both grain growth and grain coalescence contribute to the predicted coarsening of the ferrite grains. Even though the assumption that not all nuclei will lead to a ferrite grain in the final microstructure is very reasonable, the selection of the appropriate mobility parameters for ferrite grain coarsening is a challenge. Further, Huang *et al.* (2006) proposed that for sufficiently fast cooling, nucleation occurs also in the grain interior. Alternatively, Thiessen *et al.* (2006) employed classical nucleation theory to introduce ferrite nuclei into their 2D PFM simulations of phase transformations in a low carbon steel (0.05 wt% C–0.31 wt% Mn–0.18 wt% Si). In this approach, six empirical parameters were required to describe nucleation at three different grain boundary sites (corners, edges, faces). The geometric factor describing the potency of a particular nucleation mode, i.e.

© Woodhead Publishing Limited, 2012

the difference between added and removed interfacial energy, was adopted using literature values. The density of ferrite nuclei formed at different sites was selected in order to replicate the measured average ferrite grain size.

As outlined above, a number of approaches have been employed to introduce ferrite nuclei into the simulation domain. Unfortunately, there is a multiplicity of nucleation parameters that are not known exactly. Some of these parameters can be estimated from experimental data, e.g. nucleation temperature range δT (Offerman *et al.*, 2002), whereas other assumptions may only be qualitatively motivated, e.g. not all nuclei will lead to a ferrite grain in the as-transformed microstructure. The selection of the α-γ interface mobility depends in detail on the assumed nucleation conditions but remains a critical issue in its own right. The independent quantification of the interfacial mobilities is thus a task that has yet to be accomplished from a more fundamental perspective. It may be speculated that atomistic simulations could provide insight into the physics of interface mobilities. In the current PFM simulations of the austenite-ferrite transformations, interface mobilities are adopted as effective values. An Arrhenius relationship is usually assumed to account for the temperature dependence of the mobility with a generally accepted activation energy in the range of 140–160 kJ/mol (Mecozzi *et al.*, 2005b; Militzer *et al.*, 2006; Thiessen *et al.*, 2006) and the pre-exponential mobility term is employed as an adjustable parameter. To match experimental data, this factor was found to increase with cooling rate. For example, to simulate continuous cooling transformation in an Fe-0.1 wt% C-0.49 wt% Mn alloy, the pre-exponential mobility term increases by a factor of approximately seven when increasing the cooling rate from 0.4 to 10 K/s (Militzer *et al.*, 2006). This reflects the larger transformation rates at lower transformation temperatures – the cooling rate increase considered lowers the average transformation temperature by approximately 70 K. Similarly, Huang *et al.* (2006) modified the Arrhenius relationship of their interface mobility with a correction term that increases linearly as the transformation temperature decreases.

In essence, physical models have to be developed to account for this temperature dependence of the effective mobility that does not follow the initially proposed Arrhenius law. Takahama and Sietsma (2008) analysed the mobility values obtained in simulations of the austenite-to-ferrite transformation in a Nb microalloyed steel (0.136 wt% C–1.2 wt% Mn–0.02 wt% Nb) cooled at 0.3 K/s from different austenitization temperatures that range from 900 to 1200°C. Austenite grain size and Nb content in solution increase with the austenitization temperature. As a result, lower transformation temperatures are observed when increasing the reheating temperature. Using the procedures of Mecozzi *et al.* (2005a, 2005b, 2006), the pre-exponential mobility values were obtained and increase with decreasing transformation temperature. An explanation for this trend was proposed in terms of solute

© Woodhead Publishing Limited, 2012

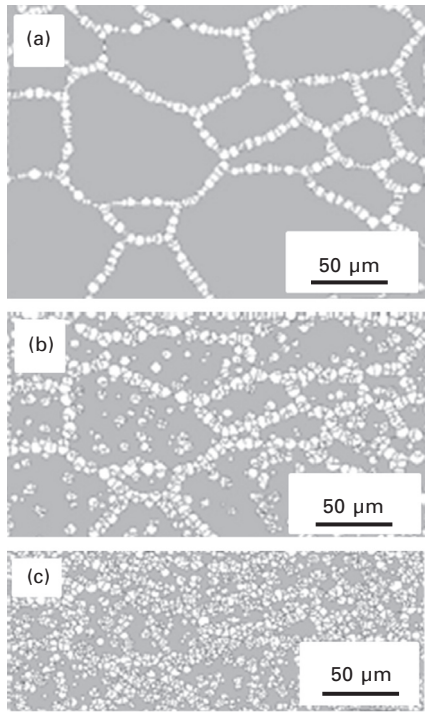
drag and pinning by NbC. Because of dissolution of NbC, the Nb content in solution increases with reheating temperature, as experimentally quantified for the steel investigated. But it remains a challenge to de-convolute the effects of pinning and solute drag on the effective mobility. To obtain an interpretation of their mobility values, Takahama and Sietsma (2008) suggested a decrease in solute drag for the case with the lowest transformation temperature where the highest velocities of the α-γ interface were observed. This velocity dependence is consistent with solute drag theories, but this could not be included in a more rigorous way in the proposed analysis. As a result, all these phenomenological phase field models are descriptive in nature and have yet to be brought to a level such that reliable quantitative predictions can be made for microstructure evolution during processing of commercial steels. To advance the field, a multi-scale modelling approach may be considered by coupling PFMs to atomistic simulations of the interface properties. However, at least currently, atomistic simulations, both truly *ab initio* techniques (density functional theory) and molecular dynamics, do not provide the required quantitative information (Moelans *et al.*, 2008).

Nevertheless, application of the PFM methodology is progressing towards a description of ferrite formation in advanced low carbon steels. Employing 2D PFM simulations, Suwanpinij *et al.* (2009) considered the decomposition of pancaked, i.e. non-recrystallized, austenite in a dual-phase steel (0.073 wt% C–1.43 wt% Mn–0.13 wt% Mo) with different levels of applied strain up to 0.6. Comparing with isothermal transformation data at 680°C, mobility values, nuclei densities and the sequence of introducing nuclei during the transformation were selected to obtain reasonable agreement with the experimental observations in terms of transformation rates and ferrite grain size distributions at intermediate transformation stages. Three potential nucleation sites were considered, i.e. grain corners/edges, grain boundary faces and grain interiors. Nucleation is increasingly activated at less favourable sites, i.e. grain faces and interiors, when the applied strain is increased (i.e. increased degree of 'pancaking'), as illustrated in Fig. 13.13. Similarly, Thiessen *et al.* (2007) used a 2D phase field model to simulate ferrite formation during continuous cooling at 10 K/s from a fully austenitic and a partially austenitic, i.e. intercritical, structure in another dual-phase steel (0.09 wt% C–1.72 wt% Mn–0.26 wt% Si). Selecting suitable nucleation scenarios and mobility terms enabled the simulations to match the transformation rates and resulting microstructures observed experimentally.

13.4.2 Formation of pearlite and non-polygonal transformation products

The early work on phase field modelling of the austenite-to-ferrite transformation emphasized already the transition between different transformation modes.

© Woodhead Publishing Limited, 2012

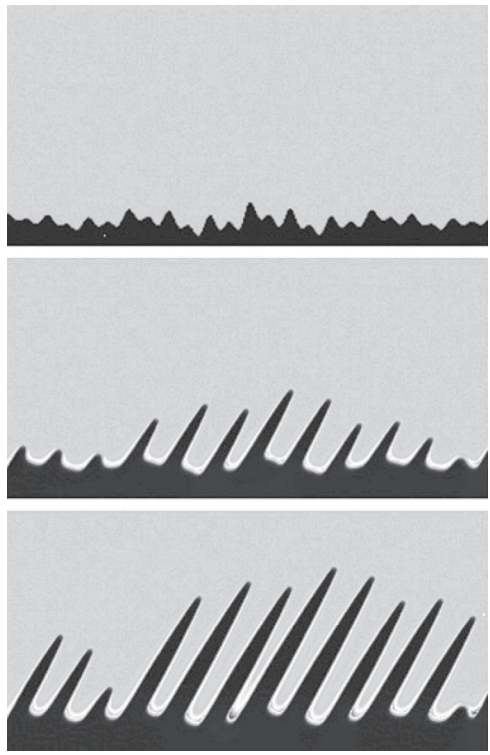


13.13 Effect of applied strain, ε, on the 2D simulated ferrite formation in a 0.073 wt% C–1.43 wt% Mn–0.013 wt% Mo steel after holding 7 s at 680°C: (a) ε = 0.2, (b) ε = 0.4, (c) ε = 0.6 (austenite: grey, ferrite: white) (reproduced from Suwanpinij *et al.*, 2009). Reproduced with permission of Wiley-VCH Verlag GmbH & Co. KGaA.

Loginova *et al.* (2003) evaluated with 1D PFM simulations the transition between diffusion-controlled and massive transformation in a binary Fe-C alloy. The computational cost of 1D simulations is low such that an interface thickness can be employed approaching that of the physical interface, e.g. 1 nm (Loginova *et al.*, 2003). In qualitative agreement with experimental observations, a transition to the partitionless, massive transformation was predicted at sufficiently high undercooling.

Loginova *et al.* (2004) then extended their PFM simulations to 2D with the aim of evaluating the conditions for the formation of Widmanstätten ferrite. For this purpose, the α-γ interfacial energy and the interface thickness were assumed to depend on the orientation of the growth direction. This anisotropy was described with an amplitude that is based upon the ratio of maximum and minimum interfacial energies to mimic high-energy incoherent and low-energy coherent interfaces, respectively. Figure 13.14 illustrates how this approach permitted prediction of Widmanstätten ferrite growth in an Fe-0.22 wt% C alloy at 720°C for a sufficiently large anisotropy amplitude. The critical

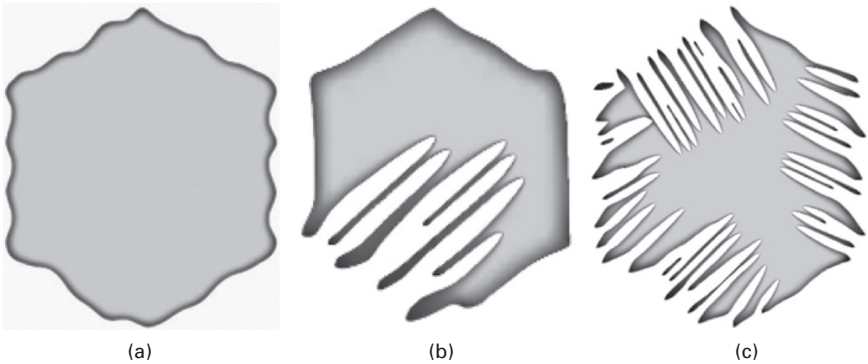
© Woodhead Publishing Limited, 2012



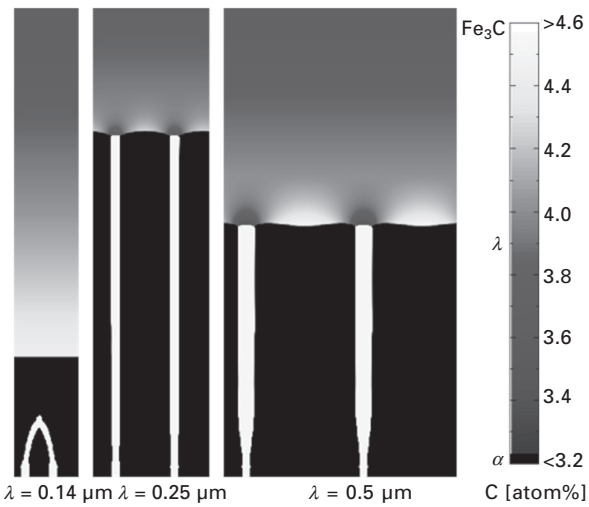
13.14 2D phase field simulations of Widmanstätten ferrite growth (ferrite: black, austenite: grey) (Loginova *et al.*, 2004). Reprinted from *Current Opinion in Solid State and Materials Science* Vol. 15, Matthias Militzer, Phase field modeling of microstructure evolution in steels, pp. 106–115 (2011) with permission from Elsevier.

amplitude value was found to increase with decreasing interface thickness and, extrapolating to a realistic interface thickness of 1 nm, implied a rather high value of 100, but the authors suggested that this critical value may be lower at a higher undercooling. Yamanaka *et al*. (2008) employed an alternative approach to account for the anisotropy of the interfacial energy. Similarly to the methodology of Loginova *et al*. (2004), the anisotropy magnitude was described by a strength factor. The transition from allotriomorphic to Widmanstätten ferrite formation was predicted for isothermal austenite-ferrite transformation in Fe-0.44 wt% C at 727°C when the anisotropy strength is increased, as shown in Fig. 13.15. Increasing the anisotropy magnitude further refines the Widmanstätten structure. The studies by Loginova *et al*. (2003, 2004) and Yamanaka *et al*. (2008) are superb examples that illustrate the potential of PFMs to predict complex transformations from austenite into a number of transformation products including massive and Widmanstätten ferrite.

© Woodhead Publishing Limited, 2012



13.15 2D PFM simulations of ferrite growth into a hexagonal austenite grain surrounded by a ferrite matrix assuming different anisotropy factors (a): 0.1, (b) 0.35, (c) 0.5 (Yamanaka *et al.*, 2008). Reprinted from *Current Opinion in Solid State and Materials Science* Vol. 15, Matthias Militzer, Phase field modeling of microstructure evolution in steels, pp. 106–115 (2011) with permission from Elsevier.



13.16 2D PFM simulations of austenite-to-pearlite transformation in a eutectoid Fe-C alloy with different interlamellar spacing, λ, considering C diffusion in austenite only. The grey level denotes the carbon concentration; adapted from Steinbach and Apel (2007).

Nakajima *et al*. (2006) were the first to simulate the cooperative growth of pearlite from austenite in an eutectoid Fe-0.77 wt% C alloy using the multi-phase field method. Nucleation was not treated in these simulations. Instead, initial lamellae were introduced with a prescribed spacing in the range of 0.1 and 1 μm. Sufficiently large interfacial mobilities were employed such that pearlite formation is controlled by carbon diffusion. These simulations provided

© Woodhead Publishing Limited, 2012

a systematic study on the effects of interlamellar spacing and undercooling on the transformation rate. An example of these 2D simulations is presented in Fig. 13.16, suggesting that medium spacing (here 250 nm) shows the highest growth rate. Further, when decreasing the interlamellar spacing to 145 nm (and below), the lamellar structure becomes unstable because of the large curvature and ferrite overgrows cementite. Only carbon diffusion in austenite was considered in these simulations and the results compare favourably to the classical Zener–Hillert model (Zener, 1947; Hillert, 1957). In detail the predicted growth rates were somewhat smaller than in the Zener–Hillert model and this was attributed to the finite interface mobility that had to be assumed in the PFM simulations. More importantly, the predicted growth rates were about a factor of 10 smaller than those observed experimentally. Including carbon diffusion in ferrite increased the predicted pearlite growth rates by a factor of four due to a decreased supersaturation of austenite. To close the gap with experimental growth rates, Steinbach and Apel (2007) incorporated also the effect of strain and stress on the pearlite formation into their PFM simulations. Further, to obtain a stable growth solution they had to assume anisotropic properties (interface energy, mobility) for the austenite–cementite interface. Their simulation results indicated that the transformation strain inhibits the lamellar growth with a smooth transformation front. Instead, staggered growth of cementite needles ahead of the ferrite front was predicted, i.e. cementite platelets grow into austenite followed by ferrite within a distance that is comparable to the width of the cementite lamellae. The growth velocities predicted with this approach are in agreement with experimental data. Some indications for the experimental observation of the staggered growth mode can be inferred from the classical paper of Mehl and Hagel (1956, p. 120), where they state that 'indeed Fe_3C platelets often extend separately into the parent austenite'. Unfortunately, the corresponding figure in their paper is inconclusive to unambiguously confirm this staggered growth mode. Further, the structure of the transformation front may change during quenching. Steinbach and Apel (2007) suggested that cementite quickly ceases to grow during the quench whereas ferrite can still grow significantly to overgrow the cementite platelets – a picture that is commonly observed metallographically, i.e. conclusive metallographic proof of the existence of the proposed staggered growth mode remains elusive.

As indicated in Section 13.2, PFMs were also developed to describe the displacive martensitic transformation, but no specific applications to steel have been reported so far. An Fe-Ni alloy (Fe-31%Ni), however, was considered in 3D simulations of martensite formation (Artemev *et al.*, 2001). Thus, the potency of PFMs for simulating austenite decomposition has been demonstrated for all but bainitic transformation products.

An interesting attempt to use PFM simulations for a more complex transformation scenario has recently been made to describe the transformation

© Woodhead Publishing Limited, 2012

mechanisms for the new quenching and partitioning (Q&P) heat treatment route in a low carbon–high aluminium steel (Santofimia *et al.*, 2008). A partially austenitized microstructure was assumed as initial condition that is consistent with the as-received microstructure. Then epitaxial ferrite growth and the associated carbon redistribution were simulated during rapid cooling at 100 K/s to a number of quench temperatures below the martensite start temperature. Employing an activation energy of 140 kJ/mol, the pre-exponential term of the interfacial mobility was adjusted to obtain agreement with the as-quenched microstructures. Based on the carbon content and the quench temperature, the austenite portions in the simulation domain were assigned that transform to martensite and remain as austenite, respectively. Then simulations of the partitioning step at 350°C suggested that, depending on the quench temperature, austenite may either grow or shrink. Even though experimental investigations showed some bainite formation during the partitioning step, this was not included into these initial PFM simulations of the Q&P process.

13.5 Future trends

Overall, PFMs are a very promising tool for the modelling of phase transformations in steels. PFM simulations can provide invaluable qualitative and semi-quantitative insight into phase transformation mechanisms in steels with complex microstructure morphologies. The use of PFMs as modelling tools with predictive capabilities hinges on the availability of quantitative data for interfacial parameters and nucleation scenarios. Currently, this information must be inferred in an empirical fashion from experimental data. An important advantage of PFMs is that they provide a single modelling tool to track the microstructure evolution from casting to the final processing step, e.g. either coiling or annealing for sheet production. A particular strength of the phase field approach is that the formation of morphologically complex features can be readily simulated, for example, as illustrated for Widmanstätten ferrite.

In part owing to the ongoing debate about the reaction mechanisms, bainite is the only transformation product that has yet to be considered with phase field modelling. However, the complexity of the bainite reaction also in terms of the morphology of bainitic transformation product seems to suggest that PFMs would in principle be suitable simulation tools. The progress in applying phase field models to describe phase transformations in advanced high strength steels may be taken as an indication that initial phase field simulations of the bainite transformation will be conducted in the near future. It is likely that these first attempts will employ approaches that are similar to those adopted for modelling Widmanstätten ferrite, i.e. suitable anisotropy factors may be assumed for interfacial properties.

© Woodhead Publishing Limited, 2012

Further, PFM simulations would be very useful for conditions where different microstructure features evolve simultaneously, e.g. spheroidization, recrystallization and austenite formation during annealing of cold-rolled steels. A challenge here may be that potentially individual microstructure processes can have different length scales. The pearlite-to-austenite transformation is an important example in this regard, where the lamellar pearlite structure has a much smaller length scale than the austenite grains. Suitable approximations, e.g. describing pearlite as ferrite with eutectoid carbon concentration (Thiessen *et al*., 2006; Savran, 2009), may be adopted in PFM simulations to bridge these length scales rather than employing a more rigorous, but potentially computationally prohibitive, approach.

Another field where PFMs may provide significant impact in the near future is modelling phase transformations in the weld HAZ where microstructure evolution occurs in steep temperature gradients. Even though the PFM work of Thiessen *et al*. (2006, 2007) was aimed at describing microstructure evolution in the HAZ, they used a more traditional approach of simulating selected positions in the HAZ according to their time–temperature paths but without considering the spatial gradients throughout the HAZ. The associated constraints can be naturally simulated with PFMs as recently shown by Toloui and Militzer (2010) for austenite grain growth. It is reasonable to expect that similar simulations will be conducted in the foreseeable future to predict austenite decomposition in the spatial temperature gradient of the HAZ.

13.6 References

Allen S M and Cahn J W (1979), 'A microscopic theory for antiphase boundary motion and its application to antiphase domain coarsening', *Acta Metall*, 27, 1085–95.

Artemev A, Jin Y and Khachaturyan A G (2001), 'Three-dimensional phase field model of proper martensitic transformation', *Acta Mater*, 49, 1165–77.

Avrami M (1939), 'Kinetics of phase change I – general theory', *J Chem Phys*, 7, 1103–12.

Azizi-Alizamini H and Militzer M (2010), 'Phase field modelling of austenite formation from ultrafine ferrite-carbide aggregates in Fe-C', *Int J Mater Res*, 101, 534–41.

Böttger B, Apel M, Eiken J, Schaffnit P and Steinbach I (2008), 'Phase-field simulation of solidification and solid-solid transformations in multicomponent steels', *Steel Res Int*, 79, 608–16.

Caginalp G and Xie W (1993), 'Phase-field and sharp-interface alloy models', *Phys Rev E*, 48, 1897–909.

Chen L Q and Khachaturyan A G (1991), 'Computer simulation of structural transformations during precipitation of an ordered intermetallic phase', *Acta Metall Mater*, 39, 2533–51.

Ginzburg V and Landau L D (1950), 'On the theory of superconductivity', *Zh Eksp Teor Fiz*, 20, 1064–82. (English translation in *Collected papers by L.D. Landau*, Pergamon, Oxford, 1965, 546–68.)

© Woodhead Publishing Limited, 2012

Hillert M (1957), 'The role of interfacial energy during solid state phase transformations', *Jernkont Ann*, 147, 757–89.

Huang C J and Browne D J (2006), 'Phase-field model prediction of nucleation and coarsening during austenite/ferrite transformation in steels', *Metall Mater Trans A*, 37, 589–98.

Huang C J, Browne D J and McFadden S (2006), 'A phase-field simulation of austenite to ferrite transformation kinetics in low carbon steels', *Acta Mater*, 54, 11–21.

Johnson W A and Mehl R F (1939), 'Reaction kinetics in processes of nucleation and growth', *Trans AIME*, 135, 416–42.

Karma A (2001), 'Phase-field methods', in Buschow K H J, Cahn R W, Flemings M C, Ilschner B, Kramer E J and Mahajan S, *Encyclopedia of materials science and technology*, Oxford, Elsevier, 6873–86.

Khachaturyan A G (1968), 'Microscopic theory of diffusion in crystalline solid solutions and the time evolution of the diffuse scattering of X-rays and thermal neutrons', *Sov Phys Solid State*, 9, 2040–46.

Khachaturyan A G (1983), *Theory of structural transformations in solids*, New York, Wiley.

Kim S G, Kim W T and Suzuki T (1998), 'Interfacial compositions of solid and liquid in a phase-field model with finite interface thickness for isothermal solidification in binary alloys', *Phys Rev E*, 58, 3316–23.

Kobayashi R (1993), 'Modeling and numerical simulations of dendritic crystal growth', *Physica D*, 63, 410–23.

Kolmogorov A N (1937), 'Statistical theory of crystallization of metals', *Izv Akad Nauk USSR – Ser Matemat*, 1, 355–59 (in Russian).

Langer J (1986), 'Models of pattern formation in first-order phase transitions', in Grinstein G and Mazenko G, *Directions in condensed matter physics*, Singapore, World Scientific, 165–85.

Li J, Brooks G and Provatas N (2005), 'Kinetics of scrap melting in liquid steel', *Metall Mater Trans B,* 36, 293–302.

Loginova I, Odqvist J, Amberg G and Ågren J (2003), 'The phase-field approach and solute drag modeling of the transition to massive γ-α transformation in binary Fe-C alloys', *Acta Mater*, 51, 1327–39.

Loginova I, Ågren J and Amberg G (2004), 'On the formation of Widmanstätten ferrite in binary Fe-C – phase-field approach', *Acta Mater*, 52, 4055–63.

Mecozzi M G, Sietsma J and van der Zwaag S (2005a), 'Phase field modelling of the interfacial condition at the moving interphase during the $\gamma \rightarrow \alpha$ transformation in C-Mn steels', *Comput Mater Sci*, 34, 290–97.

Mecozzi M G, Sietsma J, van der Zwaag S, Apel M, Schaffnit P and Steinbach I (2005b) 'Analysis of the $\gamma \rightarrow \alpha$ transformation in a C-Mn steel by phase field modeling', *Metall Mater Trans A*, 36, 2327–40.

Mecozzi M G, Sietsma J and van der Zwaag S (2006), 'Analysis of $\gamma \rightarrow \alpha$ transformation in a Nb micro-alloyed C-Mn steel by phase field modelling', *Acta Mater*, 54, 1431–40.

Mecozzi M G, Militzer M, Sietsma J and van der Zwaag S (2008), 'The role of nucleation behavior in phase-field simulations of the austenite to ferrite transformation', *Metall Mater Trans A*, 39, 1237–47.

Mehl R F and Hagel W C (1956), 'The austenite:pearlite reaction', *Prog Metal Phys*, 6, 74–134.

Militzer M and Azizi-Alizamini H (2011), 'Phase field modelling of austenite formation in low carbon steels', *Solid State Phenomena*, 172–174, 1050–59.

© Woodhead Publishing Limited, 2012

Militzer M, Mecozzi M G, Sietsma J and van der Zwaag S (2006), 'Three-dimensional phase field modelling of the austenite-to-ferrite transformation', *Acta Mater*, 54, 3961–72.

Moelans N, Blanpain B and Wollants P (2008), 'An introduction to phase-field modeling of microstructure evolution', *Comp Coupling Phase Diagrams Thermochem*, 32, 268–94.

Nakajima K, Apel M and Steinbach I (2006), 'The role of carbon diffusion in ferrite on the kinetics of cooperative growth of pearlite: a multi-phase field study', *Acta Mater*, 54, 3665–72.

Offerman S E, van Dijk N H, Sietsma J, Grigull S, Lauridsen E M, Margulies L, Poulsen H F, Rekveldt M T and van der Zwaag S (2002), 'Grain nucleation and growth during phase transformations', *Science*, 298, 1003–05.

Pariser G, Shaffnit P, Steinbach I and Bleck W (2001), 'Simulation of the γ-α transformation using the phase-field method', *Steel Res*, 72, 354–60.

Provatas N and Elder K (2010), *Phase field methods in materials science and engineering*, Weinheim, Wiley-VCH.

Santofimia M J, Takahama Y, Zhao L and Sietsma J (2008), 'Analysis of the quenching and partitioning (Q&P) process with partial austenitisation in a low-carbon steel by phase field modelling', in *New developments on metallurgy and applications of high strength steels*, Warrendale, PA, TMS, 777–86.

Savran V I (2009), *Austenite formation in C-Mn steel*, PhD Thesis, TU Delft.

Sietsma J and van der Zwaag S (2004), 'A concise model for mixed-mode phase transformations in the solid state', *Acta Mater*, 52, 4143–52.

Singer-Loginova I and Singer H M (2008), 'The phase field technique for modeling multiphase materials', *Rep Prog Phys*, 71, 106501.

Speich G R, Szirmae A and Richards M J (1969), 'Formation of austenite from ferrite and ferrite-carbide aggregates', *Trans Metall Soc AIME*, 245, 1063–73.

Speich G R, Demarest V A and Miller R L (1981), 'Formation of austenite during intercritical annealing of dual-phase steels', *Metall Trans*, 12, 1419–28.

Steinbach I (2009), 'Phase-field models in materials science', *Modelling Simul Mater Sci Eng*, 17, 073001.

Steinbach I and Apel M (2007), 'The influence of lattice strain on pearlite formation in Fe-C', *Acta Mater*, 55, 4817–22.

Steinbach I, Pezzola F, Nestler B, Seeßelberg M, Prieler R, Schmitz G J and Rezende J L L (1996), 'A phase field concept for multiphase systems', *Physica D*, 94, 135–47.

Suwanpinij P, Rudnizki J, Prahl U and Bleck W (2009), 'Investigation of the effect of deformation on $\gamma \rightarrow \alpha$ phase transformation kinetics in hot-rolled dual phase steel by phase field approach', *Steel Res Int*, 80, 616–22.

Takahama Y and Sietsma J (2008), 'Mobility analysis of the austenite to ferrite transformation in Nb microalloyed steel by phase field modelling', *ISIJ Int*, 48, 512–17.

Thiessen R G, Richardson I M and Sietsma J (2006), 'Physically based modelling of phase transformations during welding of low-carbon steel', *Mater Sci Eng A*, 427, 223–31.

Thiessen R G, Sietsma J, Palmer T A, Elmer J W and Richardson I M (2007), 'Phase-field modelling and synchrotron validation of phase transformations in martensitic dual-phase steel', *Acta Mater*, 55, 601–14.

Tiaden J, Nestler B, Diepers H J and Steinbach I (1998), 'The multiphase-field model with an integrated concept for modelling solute diffusion', *Physica D*, 115, 73–86.

© Woodhead Publishing Limited, 2012

Toloui M and Militzer M (2010), 'Phase field simulation of austenite grain growth in the HAZ of a microalloyed linepipe steel', *Int J Mater Res*, 101, 542–48.

Wang S L, Sekerka R F, Wheeler A A, Murray B T, Coriell S R, Braun R J and McFadden G B (1993), 'Thermodynamically-consistent phase-field models for solidification', *Physica D*, 69, 189–200.

Wang Y and Khachaturyan A G (1997), 'Three-dimensional field model and computer modeling of martensitic transformations', *Acta Mater*, 45, 759–73.

Wang Y, Chen L Q and Khachaturyan A G (1993), 'Kinetics of strain-induced morphological transformation in a cubic alloy with a miscibility gap', *Acta Metall Mater*, 41, 279–96.

Warren J A and Boettinger W J (1995), 'Prediction of dendritic growth and microsegregation patterns in a binary alloy using the phase-field method', *Acta Metall Mater*, 43, 689–703.

Wheeler A A, Boettinger W J and McFadden G B (1992), 'Phase-field model for isothermal phase-transitions in binary-alloys', *Phys Rev A*, 45, 7424–39.

Yamanaka A, Takaki T and Tomita Y (2008), 'Coupled simulation of microstructural formation and deformation behavior of ferrite-pearlite steel by phase-field method and homogenization method', *Mater Sci Eng A*, 480, 244–52.

Yeon D H, Cha P R and Yoon J K (2001), 'A phase field study for ferrite-austenite transitions under para-equilibrium', *Scr Mater*, 45, 661–68.

Zener C (1947), 'Kinetics of the decomposition of austenite', *Trans AIME*, 167, 550–95.

© Woodhead Publishing Limited, 2012

14

Molecular dynamics modeling of martensitic transformations in steels

H. M. URBASSEK and L. SANDOVAL, Universität Kaiserslautern, Germany

Abstract: Molecular dynamics simulation constitutes an appealing method to study, on an atomistic basis, the processes and mechanisms of martensitic phase transformations. Its use requires the existence of reliable interatomic potentials which adequately describe the properties of the phases. In this review we present a few recent examples demonstrating the application of this method to the study of the martensitic phase transition in iron. Besides phase changes in bulk materials, transformations in small systems (nanowires) are also considered.

Key words: solid-solid phase transitions, molecular dynamics simulation, interatomic interaction potentials.

14.1 Introduction

Molecular dynamics simulation has been used for around 20 years to study martensitic phase transformations, and the application of this technique to transformations in ferrous alloys reaches back more than a decade. In molecular dynamics simulation, each individual atom in the system is described by a point mass which interacts via interatomic forces with the other atoms in the system. The dynamics of the system then simply follow Newton's laws which may be supplemented by constraints to control temperature and/or pressure as appropriate. Since the system evolves 'by itself', the method has been found appealing to learn on an atomistic basis about details of solid-solid phase transformations. In particular, the method allows a study of the dynamics of the system as well as the influence of various effects on the transformation, such as the presence of defects or external constraints (e.g. stress).

On the other hand, computational restrictions limit such studies to systems containing $\sim 10^6$–10^7 atoms with length scales of up to ~100 nm; similarly, timescales are restricted to a few ns. These limits will certainly extend in the course of time due to the progress in computational hardware and software. A more severe restriction is the availability and reliability of the interatomic potential from which the forces exerted on each atom are calculated. Since (free) energy differences between the phases are small (of the order of tens

© Woodhead Publishing Limited, 2012

of meV/atom) the interatomic potential must be carefully tuned in order to reproduce free energies.

Molecular dynamics simulation studies of phase transformations in iron and its alloys started with a series of papers by Meyer, Entel, Kadau and coauthors, who studied the $Fe_{1-x}Ni_x$ system; for reviews see Entel *et al*. (1998, 2000a, 2000b). They succeeded in generating a potential which allowed application of molecular dynamics simulation to the α/γ phase transition of iron (Meyer and Entel, 1998); even though the transition temperature is at T_c = 600 K rather than at 1184 K, this potential allowed study of the austenitic and martensitic transformations for this alloy system. Most of the simulations on Fe/Ni, and also on pure Fe, have up to now been performed with this potential. A more recent potential reported by Müller *et al*. (2007), which incorporates the α/γ transition at 1030 K (and even the γ/δ transition) does not appear to have been used yet in molecular dynamics simulations studying these phase transformations. We note that the generation of a reliable interatomic potential is all the more complicated by the influence of the electronic magnetism on the bonding properties in Fe.

The earliest simulations of martensitic phase transitions in metallic materials have been performed in the NiAl system, both in the ordered B2 NiAl phase and the disordered Ni_xAl_{1-x} alloy (Yu and Clapp, 1989; Rubini and Ballone, 1993). In these materials the martensitic transformation has been studied most extensively, and homogeneous and heterogeneous nucleation of the martensitic phase, as well as the relationship of the transition to soft modes, have been discussed (Shao *et al*., 1996; Lazarev *et al*., 2006). Zirconium, which transforms from a high-temperature bcc to a low-temperature hcp phase by a martensitic transformation, has also been studied recently (Ackland *et al*., 2008). Here, molecular dynamics simulation contributed to understanding the formation of martensitic microstructure and found a precursor long wavelength instability in the austenite phase. Also for this material, the generation of a new interatomic potential which allowed application of molecular dynamics simulation to the transition was an important prerequisite to study this system (Mendelev and Ackland, 2007).

In the following we shall describe briefly the potentials which are used in the molecular dynamics simulation of iron and present a few recent examples of this method to the study of phase transitions in elemental iron.

14.2 Interatomic interaction potentials

14.2.1 Available interaction potentials for iron

Due to the industrial and scientific importance of iron, a large number of potentials have been set up to describe its properties. While it is not the place here to discuss these potentials in an exhaustive way, we wish to present

© Woodhead Publishing Limited, 2012

several established potentials since they form the basic ingredients of a molecular dynamics simulation; more details and comparisons can be found in Nordlund *et al*. (2006), Müller *et al*. (2007) and Engin *et al*. (2008).

The interatomic interaction potential describes the total potential energy of a system of particles i as

$$E_{\text{tot}} = \sum_i E_i \qquad [14.1]$$

E_i is the energy of one particle (i) in the system. The simplest approach describes the interatomic interaction by pair potentials ϕ, which depend only on the interatomic distance $r_{i,j}$ between atoms i and j,

$$E_i = \frac{1}{2} \sum_j \phi(r_{i,j}) \qquad [14.2]$$

Such a description is usually not adequate for metals. Nevertheless, a fit of the properties of iron to a Morse potential has been given by Girifalco and Weizer (1959) and may be appropriate in certain applications. We note that the potential by Osetsky and Serra (1998), which is able to describe the γ/δ transition of iron, is a pure pair potential based on pseudopotential theory.

Usually, metallic bonding is implemented by adding a many-body term to the pair potential assumption of Eq. [14.2]. In the so-called embedded-atom method (EAM) (Daw *et al*., 1993; Finnis, 2003), this is achieved by introducing a nonlinear embedding function G, which depends on the local 'electron density' ρ_i felt by atom i,

$$E_i = \frac{1}{2} \sum_j \phi(r_{i,j}) + G(\rho_i) \qquad [14.3]$$

The local electron density at atom i is the superposition of the contributions g imparted by the surrounding atoms j:

$$\rho_i = \sum_j g(r_{i,j}) \qquad [14.4]$$

The various potentials that have been set up to describe iron differ from each other in the details of the functions ϕ, G, and g; these have usually been generated with different applications in mind. The Finnis and Sinclair (1984) and the Johnson and Oh (1989) potentials are often employed and are thus well established. The so-called Voter–Chen potential, devised by Harrison *et al*. (1989), is used in studies of Fe under high pressure since it represents well the high pressure α/ε phase transition in Fe (Kadau *et al*., 2005). Simonelli *et al*. (1993) and Ackland *et al*. (1997) focus on defects in pure iron and its alloys, Pasianot *et al*. (1991) explicitly include a many-body contribution to the crystal elastic shear, Ackland *et al*. (2004) describe P impurities in α-Fe, and Wallenius *et al*. (2005) model Fe-Cr alloys in the

© Woodhead Publishing Limited, 2012

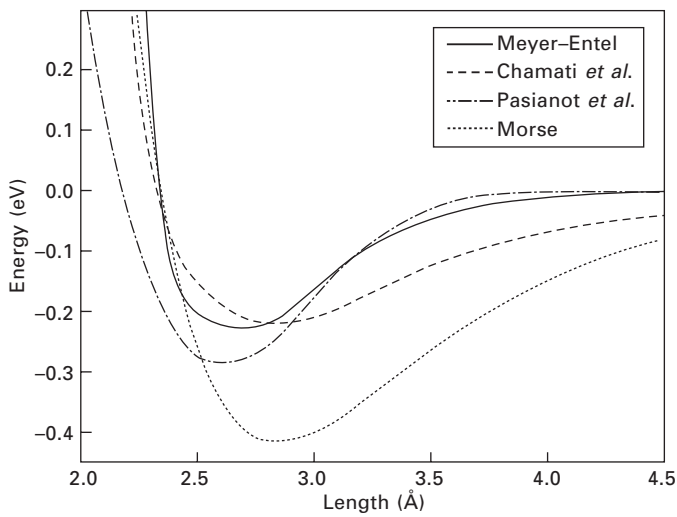
ferromagnetic state. The Meyer and Entel (1998) potential mentioned above has been constructed to describe the martensite–austenite transition in $Fe_{1-x}Ni_x$ alloys. The potential by Mendelev *et al*. (2003) describes both crystalline and liquid Fe, while the recent Dudarev and Derlet (2005) potential incorporates the magnetic contribution of the electronic system for different crystal phases. For the fitting of the Chamati *et al*. (2006) potential, experimental data obtained both for the low-temperature bcc and the high-temperature fcc phases have been included.

Recently, Müller *et al*. (2007) proposed a so-called bond-order potential for Fe; this is of a different form than Eq. [14.3], and computationally more time-expensive. Due to their careful fitting, this potential is able to describe both the α/γ and the γ/δ transition; the latter occurs in this potential at 2210 K, just before the melting point at 2270 K.

The various many-body potentials of the EAM type (and pair potentials) may be compared with each other in the vicinity of the equilibrium bcc structure. If we denote by ρ_0 the equilibrium electron density at an atomic site, linearization of the embedding energy G gives an effective potential (Foiles, 1985; Carlsson, 1990)

$$\phi_{\text{eff}}(r) = \phi(r) + 2g(r_{i,j})\, G'(\rho_0) \qquad [14.5]$$

where G' denotes the derivative of the embedding function G with respect to its argument. Figure 14.1 demonstrates that the various potentials generated for Fe differ considerably from each other. We list several of the properties of interest for the solid-solid phase transition behavior in Table 14.1. It is



14.1 Effective pair potential, Eq. [14.5], for various potentials: Morse (parameters as provided by Girifalco and Weizer, 1959), Pasianot *et al*. (1991), Meyer and Entel (1998), and Chamati *et al*. (2006).

© Woodhead Publishing Limited, 2012

Table 14.1 Potential energy difference ΔE between bcc and fcc phase at 0 K, and phase transition temperature T_C calculated for several interatomic potentials and compared to experimental data

Potential	ΔE (meV/atom)	T_c (K)
Experiment	50[a]	1184
Theory	60[b]	–
	122[c]	
	110[d]	
Finnis and Sinclair (1984)	50	none
Mendelev *et al.* (2003)	121	none
Chamati *et al.* (2006)	99	none
Dudarev and Derlet (2005)	86	none
Meyer and Entel (1998)	38	600
Müller *et al.* (2007)	30	1030

[a]Bendick and Pepperhoff (1982)
[b]Chen and Sundman (2001)
[c]Mendelev *et al.* (2003)
[d]Müller *et al.* (2007)
Note: Entry 'none' means that bcc phase is stable in this potential up to the melting point. Data are from Engin *et al.* (2008) and Müller *et al.* (2007), if not stated otherwise.

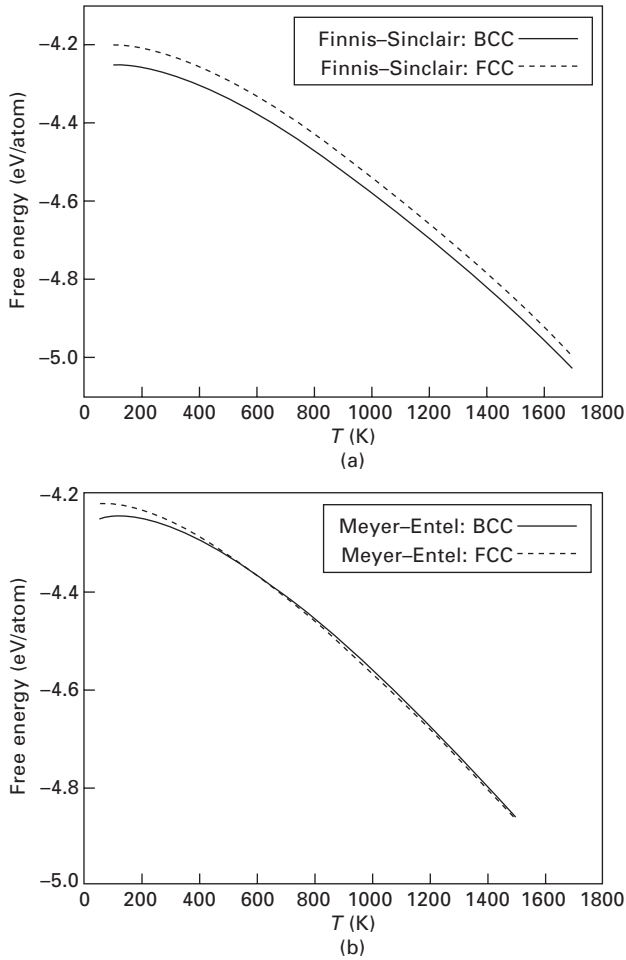
seen that the potentials often give only a poor representation of the energy difference of the bcc and fcc phases, and differ by up to 100% or even more from the experimental values. This is, of course, because in the list of data to which the potential was fitted this structural information was sometimes not included, or was not given a high weighting.

14.2.2 Free energy calculation

In order to determine the ground-state phase at finite temperatures, the free energy F of the relevant phases needs to be calculated and compared with each other. This information also allows us to find the phase transition temperature. The calculation of F is not easy in atomistic simulation, and several methods have been devised for this purpose. We mention the methods of thermodynamic integration (Frenkel and Smit, 2002) and metric scaling (Miller and Reinhardt, 2000; Hoy and Robbins, 2004). Detailed information on the application of these methods to iron crystals can be found in Engin and Urbassek (2008) and Engin *et al.* (2008).

Using these methods, the stability of the fcc and the bcc phases has been determined for several potentials (Müller *et al.*, 2007; Engin *et al.*, 2008). Figure 14.2 shows the free energies for two potentials investigated in the fcc and bcc structures as calculated with the method of thermodynamic integration. The calculations, which have been performed between 100 K and 1700 K, show that the bcc phase is the only stable phase of Fe for the

© Woodhead Publishing Limited, 2012

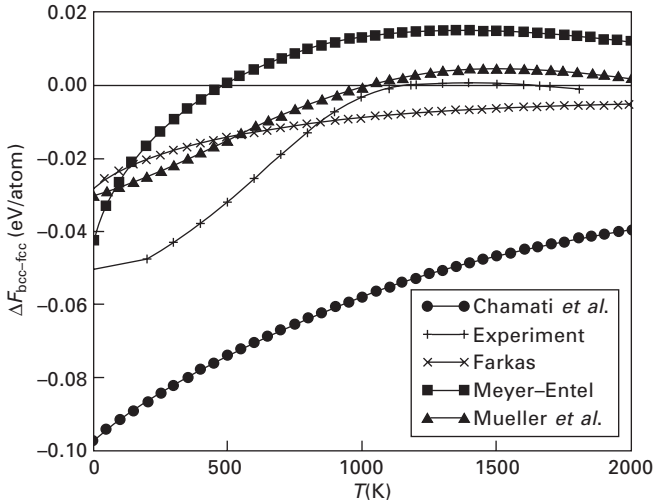


14.2 Temperature dependence of the free energies of the fcc and bcc phases of Fe for (a) the Finnis and Sinclair (1984) and (b) the Meyer and Entel (1998) potentials. From Engin *et al.* (2008).

Finnis and Sinclair (1984) potential; this applies similarly to almost all other Fe potentials investigated. In contrast the Meyer and Entel (1998) potential features a phase transition from the bcc to the fcc phase at $T_c = 600$ K. Note that the actual behavior of Fe is even more complex and shows several phase transitions: the bcc-fcc transformation from α- to γ-Fe at 1184 K, the transformation from fcc γ- to bcc δ-Fe at 1665 K, and melting at 1811 K. The data of the free-energy difference between the bcc and the fcc phase at 0 K, as well as the predicted bcc/fcc phase transition temperatures, if any, of several potentials are assembled in Table 14.1.

Figure 14.3 shows the free energy difference for several potentials as a

© Woodhead Publishing Limited, 2012



14.3 Free energy differences between the fcc and bcc phases compared to experimental data (Bendick and Pepperhoff, 1982) for Fe. Data taken from Engin *et al.* (2008) and Müller *et al.* (2007).

function of temperature and compares these to experimental data (Bendick and Pepperhoff, 1982). Note that the experimental free-energy differences are rather small, ≤50 meV/atom. Figure 14.3 demonstrates that among the potentials investigated, it is only the potentials due to Müller *et al.* (2007) and to Meyer and Entel (1998) which show a phase transition from the bcc to the fcc phase. In all the other potentials the bcc phase is stable up to the melting point.

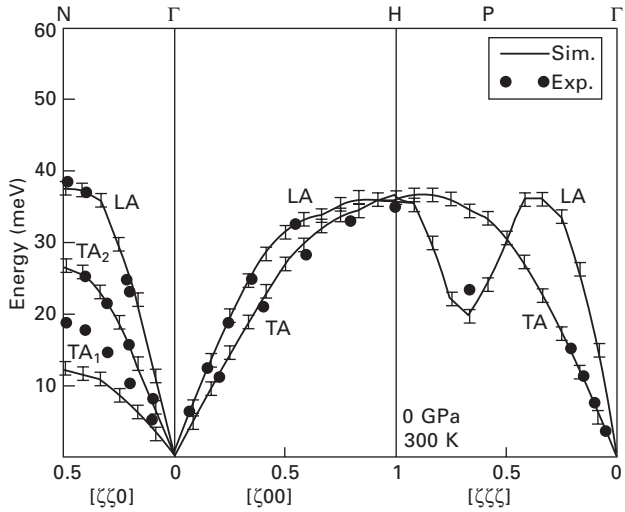
In the following, we shall show molecular dynamics results which have been obtained exclusively with the Meyer and Entel (1998) potential. An exception is made only for Section 14.3, which is based on the Finnis and Sinclair (1984) potential.

14.2.3 Phonon softening

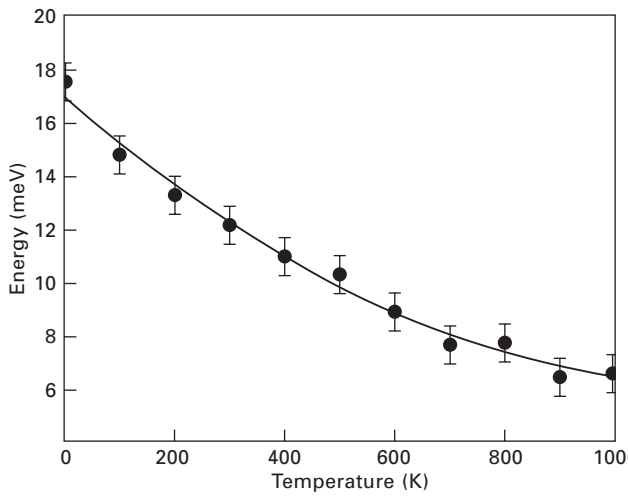
In Fig. 14.4, we show the phonon dispersion curves at 300 K obtained at vanishing pressure for the Meyer and Entel (1998) potential and compared to experimental data (Klotz and Braden, 2000). Both the longitudinal (LA) and the transverse acoustical (TA) branches are shown. Due to the symmetry of the crystal lattice, the TA branch splits into two distinct branches, labeled TA_1 and TA_2, for phonon propagation in the [110] direction. Since this potential was fitted to some selected phonon modes (Meyer and Entel, 1998), the agreement with the experimental values is quite satisfactory.

Let us concentrate on the ½TA_1 [110] phonon mode, whose temperature dependence is shown in Fig. 14.5. The potential exhibits a progressive

© Woodhead Publishing Limited, 2012



14.4 Phonon dispersion curves of bcc Fe at 300 K at zero pressure, evaluated for the Meyer and Entel (1998) potential (Sandoval *et al.*, 2009b). Both the longitudinal (LA) and the transverse acoustical (TA) branches are shown. The dispersion curves show the dependence of the phonon energy with respect to the phonon wave vector ***q***. Variation of ***q*** along the three high-symmetry directions – [100], [110] and [111] – is shown and is parameterized by ζ in units of $2\pi/a$, where a is the lattice constant of bcc Fe. Experimental data taken from Klotz and Braden (2000).



14.5 ½TA_1 [110] phonon mode in bcc Fe evaluated for the Meyer and Entel (1998) potential as a function of temperature (Sandoval *et al.*, 2009b).

© Woodhead Publishing Limited, 2012

softening of this mode; however, it does not vanish in the temperature range considered. This behavior is in agreement with *ab initio* (Ekman *et al*., 1998) and experimental (Neuhaus *et al*., 1997) results, which also show that the $\frac{1}{2}TA_1$ [110] phonon mode does not vanish at the α/β transition point. These results, as well as other predictions of the Meyer and Entel (1998) potential (Meyer and Entel, 1998; Sandoval *et al*., 2009b) demonstrate that the Meyer and Entel (1998) potential is well able to describe (at least semi-quantitatively) the bcc/fcc phase transition of Fe.

14.2.4 Transformation path

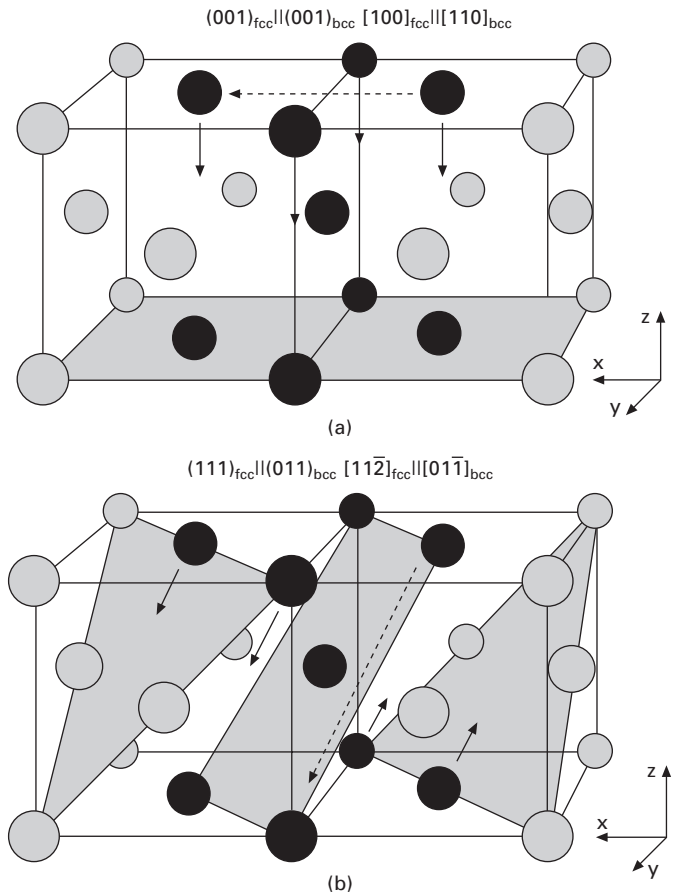
A realistic potential may allow one to obtain information on the transformation path taken during the transition; moreover, it may differentiate between different paths and provide data to learn why a particular path is followed in reality. We shall present results on the Bain and the Nishiyama–Wassermann path for the Meyer and Entel (1998) potential.

From a structural point of view, the martensitic transformation is characterized by the orientation relationship between the two phases, which can be characterized by an associated transformation path. The most intuitive transformation path from the fcc to the bcc crystal structure was proposed by Bain (1924). After defining a bct unit cell in the fcc crystal (see Fig. 14.6(a)), the z-axis is contracted by about 21% and the x and y axes are expanded by about 12%. In spite of its simplicity, the orientation relationship between the fcc (parent) and the bcc (martensite) phases, $(001)_{fcc}\|(001)_{bcc}$ and $[100]_{fcc}\|[110]_{bcc}$, is not observed experimentally. Closer to what has been experimentally reported for many iron-based alloys is the Nishiyama–Wassermann path (Nishiyama, 1978; Entel *et al*., 2000a; Tateyama *et al*., 2010), which satisfies the orientation relationship $(111)_{fcc}\|(011)_{bcc}$ and $[11\bar{2}]_{fcc}\|[0\bar{1}1]_{bcc}$. For the Nishiyama–Wassermann path the entire transformation may be visualized in two steps (see Fig. 14.6(b)). In the first step, a $\{111\}_{fcc}$ plane is fixed and the two neighboring $\{111\}_{fcc}$ planes are shifted in opposite directions with a common uniform shear of 19°28' in the $[11\bar{2}]_{fcc}$ direction. The second step consists of an orthogonal expansion/contraction in order to obtain the desired atomic density.

Sandoval *et al*. (2009a) showed that the evolution of the free energy along the two paths is very similar and also that the transformation barriers for the two paths coincide. This is astonishing and indicates that for processes occurring in thermodynamic equilibrium, the two paths are equivalent.

However, in reality the transformation does not occur in equilibrium, but in a strained and stressed environment as well as in the presence of other martensitic variants. Therefore, it is appropriate to calculate also the variation of the elements of the stress tensor, σ_{ij}, along the transformation paths, and of the total pressure p. The corresponding data are shown in Fig. 14.7. They

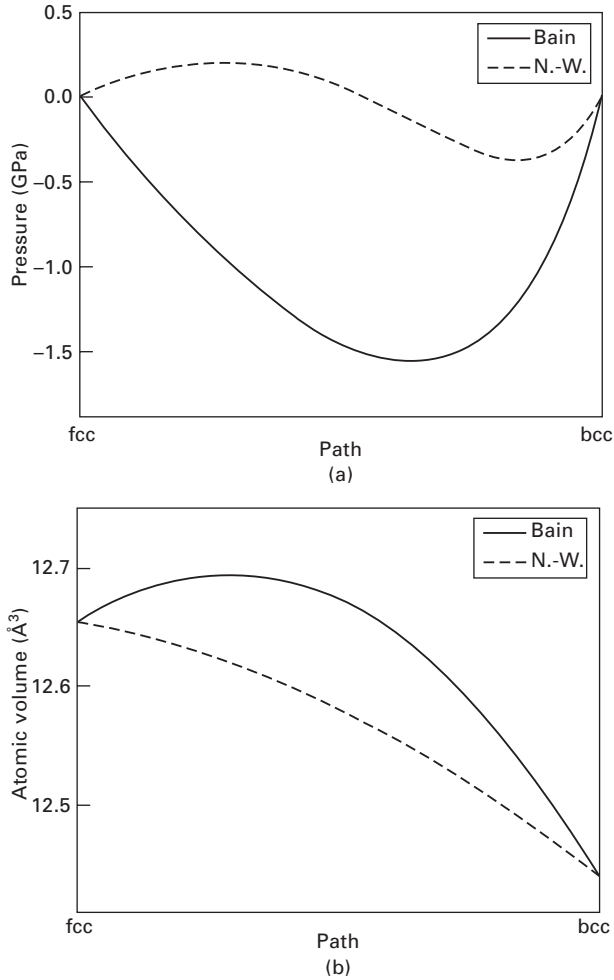
© Woodhead Publishing Limited, 2012



14.6 Orientational relationship between the parent (fcc) and martensite (bcc) phases for (a) the Bain and (b) the Nishiyama–Wassermann paths. The black atoms indicate a bcc unit cell. The full arrows indicate part of the motion initiating the transformation. The dashed arrows indicate the invariant direction which is shared by the parent and martensite phases. From Sandoval *et al.* (2009a).

reveal a distinct difference between the two paths. The total pressure – and also the shear components (Sandoval *et al.*, 2009a) – is considerably larger along the Bain path than along the Nishiyama–Wassermann path. For the Bain path, the compressive pressure is higher by a factor of five than for the Nishiyama–Wassermann path. For the Nishiyama–Wassermann path, the diagonal elements of the stress tensor partially compensate, leading to a small hydrostatic pressure, while for the Bain path, the diagonal elements add up to a sizeable pressure. This behavior can be rationalized by considering the evolution of the atomic volume in Fig. 14.7(b), which shows a considerably smoother variation for the Nishiyama–Wassermann path.

© Woodhead Publishing Limited, 2012



14.7 Evolution of (a) the total pressure and (b) the atomic volume along the Bain path and the Nishiyama–Wassermann path evaluated for the Meyer and Entel (1998) potential. From Sandoval *et al.* (2009a).

14.3 Martensitic transformations in iron: case studies

The simplest way to induce a solid-solid phase transformation in a molecular dynamics simulation is to start it with the crystal in a metastable crystal structure (here the fcc structure). If the temperature is sufficiently high (and no volume or other constraints hinder the transition), the crystal will spontaneously transform to the stable (bcc) structure; this can be considered as an example of a martensitic transformation. This process will even work if

© Woodhead Publishing Limited, 2012

the potential employed has no temperature regime where the fcc structure is stable. We shall give an example of such a transformation in Section 14.3.1 where the Finnis and Sinclair (1984) potential is employed.

An alternative procedure to study the martensitic transition is to prepare in the simulation an fcc/bcc interface and to study its dynamics at elevated temperature. Again, since the fcc structure is metastable, the bcc phase will grow and the interface will start moving. Such studies have been performed (Bos *et al.*, 2006a; Tateyama *et al.*, 2008, 2010), using the Finnis and Sinclair (1984) and Johnson and Oh (1989) potentials, respectively, and results on the structure and dynamics of the moving interface could be obtained. Due to the importance of the fcc/bcc interface for the phase transition, also the (kinetic) Monte Carlo method has been employed to study the interface energetics (Nagano and Enomoto, 2006) and kinetics (Bos *et al.*, 2006b).

It is evident that the simulation of an austenitic (bcc→fcc) transition needs more care and, in particular, a reliable potential featuring a stable high-temperature phase.

Another set of simulations studied strain- or stress-induced transformations. The strain-induced nucleation of the martensite phase from austenite was investigated by Sinclair and Hoagland (2008) using the Ackland *et al.* (1997) potential; they focused on the martensite nucleation at the interface of stacking-fault bands in the austenite. Latapie and Farkas (2003) considered the action of a crack tip in nanocrystalline α-iron using the Simonelli *et al.* (1993) potential and found that the stress field locally transforms the material to the fcc phase.

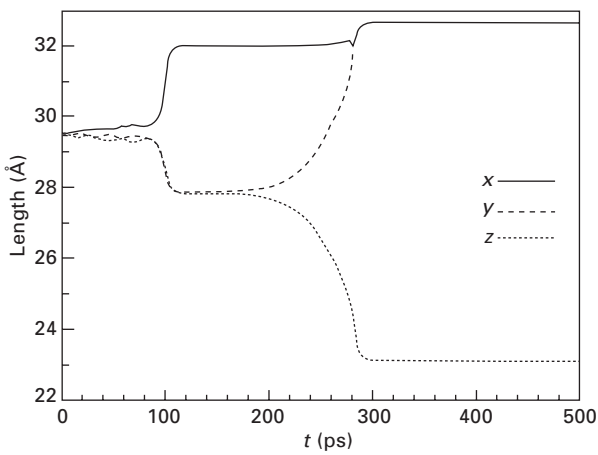
Transformations may also be induced by strong shock waves. Molecular dynamics studies using both the Meyer and Entel (1998) and the Voter–Chen potential (Harrison *et al.*, 1989) investigated the α/ε transition occurring in shocked Fe (Kadau *et al.*, 2002b, 2005). At shock strengths immediately above the threshold, the shock wave splits into an elastic precursor and a lagging transformation wave. These studies report that the observed transformations have martensitic character and that the orientation of the resulting close-packed grains obey Nishiyama–Wassermann orientational relations, or their analogue for hcp grains.

Finally, due to the importance of Fe for understanding the earth's core, molecular dynamics simulations have been performed to understand the high-temperature/high-pressure behavior of Fe. As a recent example, we mention the work by Belonoshko *et al.* (2009) which is based on the Belonoshko *et al.* (2000) potential; they employ atomistic simulation to show that a high-temperature/high-pressure bcc phase of Fe (stable above 3000 K and 100 GPa) transforms to a mixture of hcp and fcc grains upon quenching to room temperature.

© Woodhead Publishing Limited, 2012

14.3.1 Temperature-induced transformation at zero pressure: homogeneous nucleation

In this simulation (Engin and Urbassek, 2008), based on the Finnis and Sinclair (1984) potential, an fcc crystallite containing 2048 atoms is set up initially. This is kept at a fixed temperature T while allowing the pressure to equilibrate and relax to $p = 0$. In the ensuing simulation, the edges of the simulation crystallite are allowed to adjust their lengths so as to keep the components of the stress tensor close to zero. Figure 14.8 demonstrates that at $T = 1400$ K, the crystal spontaneously undergoes a phase transformation. The complicated changes of the edges of the simulation volume displayed in the figure are necessary to prevent the build-up of strong stresses that might be induced as a result of the deformation. At $t \cong 100$ ps, around 80% of the material has transformed, and at around 280 ps, the transformation is complete. When repeating the simulation with different numbers of atoms and different initial configurations, qualitatively, the same behavior always results: an induction period of the order of around 100 ps and then a spontaneous decay which transforms the entire volume either in one step or in several steps, as shown in Fig. 14.8. Since the crystal is initially homogeneous, the new phase nucleates homogeneously in the crystallite. The transformation may be initiated by a thermal fluctuation of the simulation volume, which leads to a deformation from the cubic shape. This may be effected by the excitation of a lattice vibration whose cooperative motion initiates the transformation and induces the spontaneous transformation. After start of



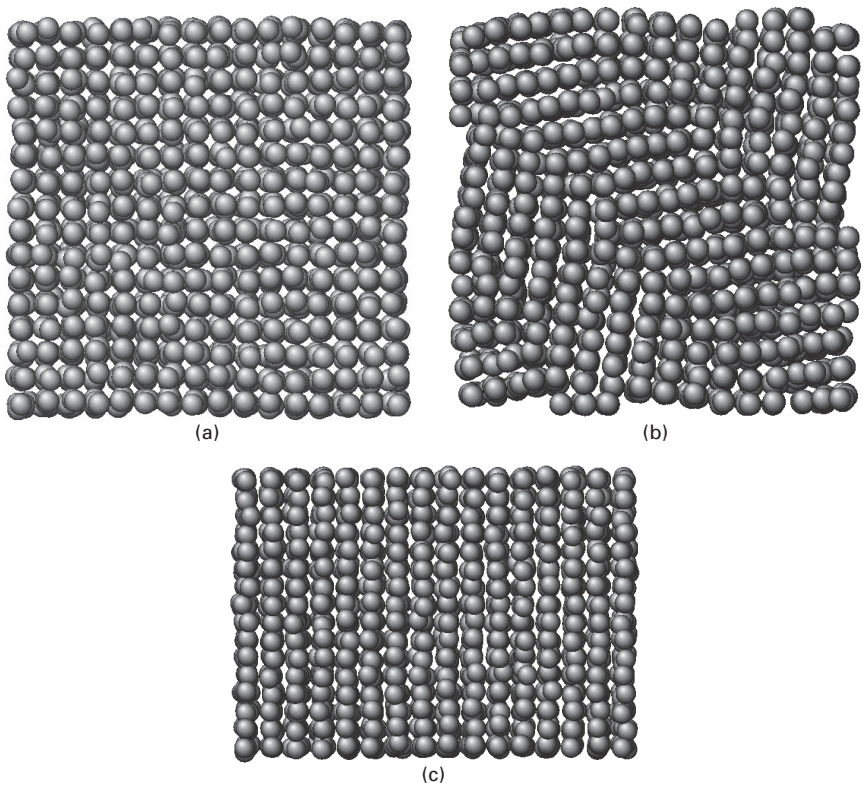
14.8 Temporal evolution of the lengths of the edges of the simulation volume. Initially the iron was in the metastable fcc state. During the evolution under the Finnis and Sinclair (1984) potential at constant temperature $T = 1400$ K and vanishing pressure, it spontaneously decays to the bcc phase. From Engin and Urbassek (2008).

© Woodhead Publishing Limited, 2012

the transformation, the resulting strain and stress field in the material assists the continuation of the transformation.

Figure 14.9 gives cross-sectional views of the crystallite before, during and after the transformation. At 50 ps, the initial fcc structure extends homogeneously throughout the crystal. After the transformation has started, at 200 ps, however, typical twin structures are formed, which are characteristic of the transforming metal. This structure is only an intermediate stage and continues transforming until 300 ps. The martensite transition in real steel shows similar structures, which are stable, since the austenitic matrix constrains the volume of the martensitic phase such that the phase transformation cannot be complete. In the simulation presented here, however, the entire simulation volume can transform, such that at 400 ps the crystal is entirely in its bcc state and all twin boundaries have vanished.

Such simulations demonstrate that the metastable phase decays on a timescale amenable to atomistic simulations to the ground-state bcc structure; however, sufficiently high temperatures are needed. Note that, in contrast to the situation



14.9 Cross-sectional view through the transforming crystallite (Fig. 14.8) at various stages of the transformation process: (a) 50 ps, (b) 200 ps, (c) 400 ps. From Engin and Urbassek (2008).

© Woodhead Publishing Limited, 2012

encountered in experiment, the transformation nucleates *homogeneously*, i.e., without nucleation centers such as extended defects, dislocations, or grain boundaries. The transformation itself need not necessarily occur in one step, but can be split into several steps, as seen in the results presented above (Fig. 14.9). The transformation proceeds quickly, i.e., with the speed of sound, and thus incorporates the cooperative motion of a multitude of atoms. It does not start immediately at the beginning of the simulation, but after an incubation period, which is interpreted as the time necessary for a large thermal fluctuation to bring the system into a favorable condition for the cooperative movement of many atoms.

14.3.2 Influence of external constraints

In reality, the transformation will not occur at vanishing pressure and the volume will not adapt to the transforming crystal, as was supposed in the previous section. Rather, the volume will be fixed by the surrounding material, and stresses will take time to relax. In molecular dynamics, the simulation reacts very sensitively to such external constraints (fixed volume, external stress fields, etc.).

Typically, the martensitic transformation will not happen when the simulation is performed at fixed volume, not even at high temperatures (Engin and Urbassek, 2008). This is understandable, since the coordinated atom motion during the transformation needs space to allow it to happen. Meyer and Entel (1998) found that a high concentration of vacancies – of the order of a few percent – is necessary for the transformation. Here again, it is obviously the free volume offered by the vacancies, which is decisive, but also the potential energy of these point defects may help in the transformation. In the next section, we shall show that extended defects, such as grain boundaries, play the same role in making the transformation possible.

Another route to facilitate the transformation is offered by free surfaces. In the extreme case, on an isolated nanoparticle or cluster in vacuum, the transformation occurs quickly. Thus it was found by Engin and Urbassek (2008) that in an entirely free cubic cluster, the transformation occurs spontaneously without an incubation period, at times $t \lesssim 5$ ps, and even at zero temperature; here the transformation is driven exclusively by the potential energy of the surfaces. The role of free surfaces to induce or facilitate the transformation will be further discussed in Section 14.4.

14.3.3 Grain boundaries: heterogeneous nucleation

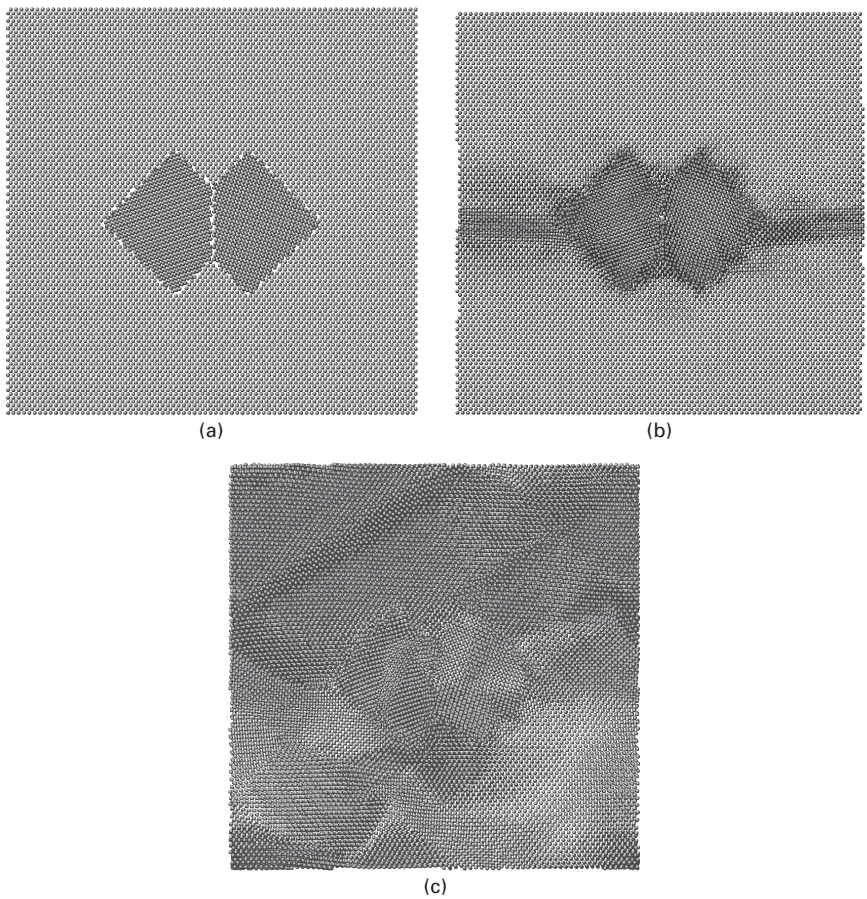
Extended defects strongly affect the occurrence and dynamics of phase transformations. As an example, we consider the effect of a grain boundary

© Woodhead Publishing Limited, 2012

on the martensitic transformation; such simulations have been performed by Gornostyrev *et al*. (2005) and Engin and Urbassek (2008).

Consider a metastable fcc crystal in thin-plate geometry; we note that for the Finnis and Sinclair (1984) potential, even at elevated temperatures, no phase transformation will occur. However, when introducing grain boundaries into the thin plate such as displayed in Fig. 14.10(a), the transformation will happen.

In the situation discussed here (Engin and Urbassek, 2008), the thin plate has free (110) surfaces and is constrained laterally by periodic boundary conditions. Two further fcc grains are embedded into it with (100) surfaces in a twin geometry ($\sum 5$ grain boundary). The structure is then relaxed until



14.10 Cross-sectional view through the simulation crystallite containing several fcc grains during the transformation to the bcc phase: (a) initial configuration, (b) 3 ps, (c) 15 ps. From Engin and Urbassek (2008).

© Woodhead Publishing Limited, 2012

its potential energy has decreased to an average value of only 4 meV/atom; this energy corresponds to the potential energy stored in the grain boundaries. While the average pressure vanishes, stresses still occur locally, at the grain boundaries, but disappear in the homogeneous regions.

After starting the simulation, the system spontaneously transforms to the bcc phase. This occurs without an induction period. Certainly, the potential energy input into the system (interface energy of 4 meV/atom) aids in the transformation. But in addition, the free volume provided by the grain boundary gives the atoms the mobility to start the transformation. It may thus be concluded that it is the combination of the interface energy and the free volume that exists at the grain boundaries which facilitates atomic motion and hence starts the transformation process right from the beginning of the simulation.

Figures 14.10(b) and (c) show cross sections through the transforming crystallite at times $t = 3$ ps and 15 ps. As Fig. 14.10(b) shows, the transformation starts heterogeneously at the location where the two grains meet; the resulting strain field lets the transformation propagate horizontally sideways. Figure 14.10(c) demonstrates that, in contrast to Fig. 14.9, the transformation does not result in an homogeneous final state. The strongly heterogeneous structure is due to the fact that the transformation may now start at many locations at the grain boundary more or less simultaneously. Figure 14.10(c) looks very irregular, since the thin film is no longer viewed along a low-indexed direction.

14.4 Transformations in ferrous nanosystems

The simulation of transformations occurring in nanosystems has recently gained considerable interest. These systems are characterized by the strong influence which the surface may exert on the transition; it is strongest in nanoparticles (clusters), but also influences nanowires and thin-film systems.

The investigation of solid-solid phase transitions in Fe and Fe/Ni nanoparticles has initially focused mainly on nanoclusters (Kadau *et al.*, 2002a; Kadau and Entel, 2002). In Fe nanoclusters both the martensitic and the austenitic transformations have been investigated (Entel *et al.*, 2004). For the austenitic transformation, it was found that the transition temperature scales inversely proportional with the nanocluster diameter, analogous with the melting temperature (Entel *et al.*, 2004). The martensitic transformation, however, only proceeds when an (unphysically high) number of defects exist in the nanoclusters, because the fcc phase possesses a high metastability under cooling. The martensitic transformation could also be detected in sintered Fe-Ni nanoparticles (Kadau *et al.*, 2002a).

Also thin Fe films – both free-standing films and thin films grown epitaxially on a substrate – were studied. The structural stability of thin fcc

© Woodhead Publishing Limited, 2012

Fe films grown epitaxially on Cu (001) and (111) was investigated by Kadau *et al*. (1999) and Kadau and Entel (1999), and a structural transformation to bcc was found with decreasing temperature and increasing film thickness. More recently, Lai and Zhao (2004) studied free bcc Fe thin films using the Ackland *et al*. (1997) potential and found a spontaneous transformation to fcc structure. They argue that it is due to the change in the elastic moduli in these thin films, induced by the surface stress.

Nanowires have been studied particularly in fcc metals. Here, no phase transition was found, but a different kind of transformation; a reorientation process. It has been investigated by atomistic simulation for several fcc metals (Liang *et al*., 2005; Park *et al*., 2005; Liang and Zhou, 2006; Ji and Park, 2007). Some metallic fcc nanowires exhibit pseudo-elasticity or shape memory. These phenomena have been explained by the formation of defect-free twins during the ⟨100⟩ to ⟨110⟩/{111} reorientation process (Park *et al*., 2005).

In the following, we concentrate on Fe nanowires and present a few examples of phase transition and reorientation processes in order to exemplify the rich array of phenomena occurring. In these simulations the Meyer and Entel (1998) potential was used. The nanowires are cylindrical and are characterized by their diameter D and their axial orientation. By using periodic boundary conditions along the axis, they can be considered to be infinitely long.

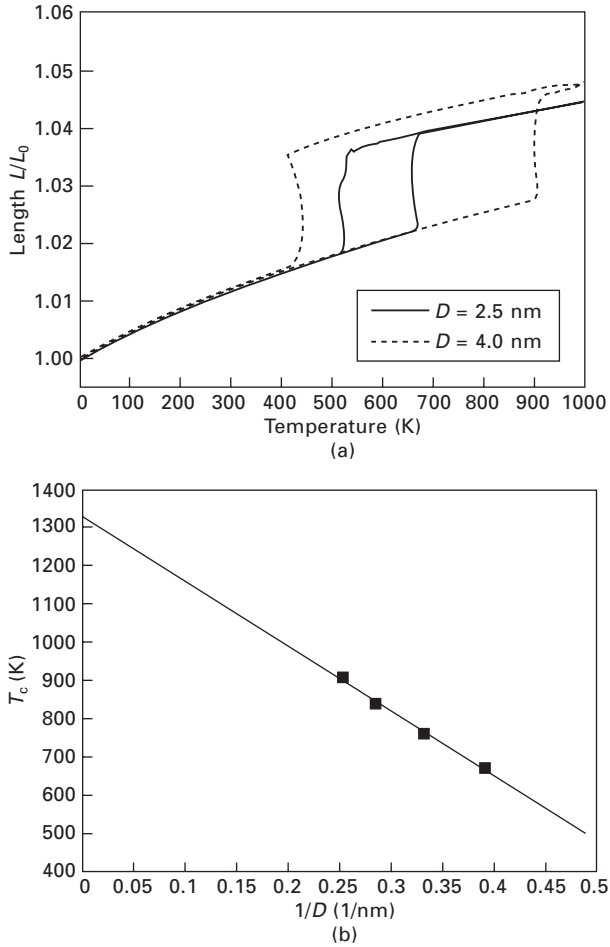
14.4.1 Temperature-induced transformation

Figure 14.11(a) shows how the length L of a nanowire changes upon heating and cooling with a rate of 1 K/ps. Apart from thermal expansion, the length shows a sudden increase and decrease, respectively, which is indicative of a first-order phase transition. A considerable hysteresis is observed which becomes stronger for thicker wires. The phase transition temperature – taken to be the average of the transition temperatures upon heating and cooling – increases with wire diameter.

The nature of the phase transition can be analyzed by determining the local atomic structure in the wire. Figure 14.12 displays several snapshots of the transforming nanowire for different temperatures. The transition temperature is 760 ± 5 K. Figure 14.12(a) proves that at 10 K below the transition temperature, the nanowire is still entirely in its bcc state, even though a considerable thermal disorder has already developed. Above the transition (Fig. 14.12(b)), the nanowire is a mixture of fcc and hcp phases. The cross-sectional view shows a triangular symmetry, which is nearly constant along the nanowire.

We note that the energy difference between the fcc and the hcp phase in the Meyer and Entel (1998) potential amounts to only 2.9 meV/atom, while

© Woodhead Publishing Limited, 2012

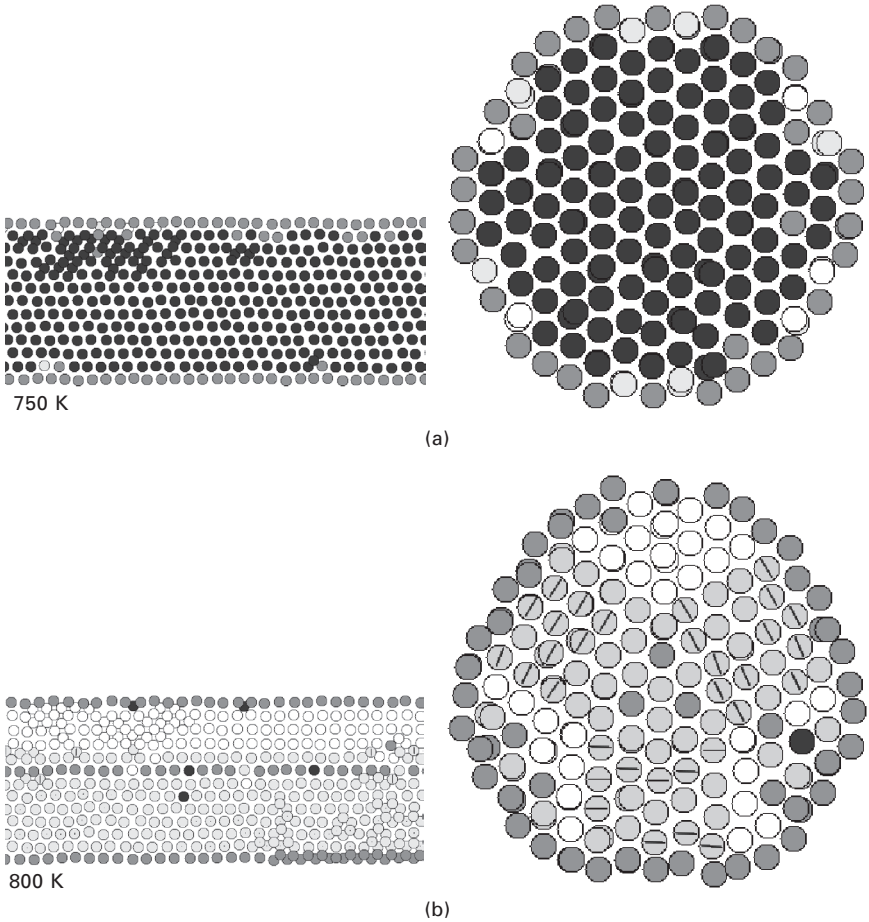


14.11 Temperature dependence of the nanowire length for various diameters *D*. The wires are oriented along the ⟨111⟩ axis. (a) Length vs temperature hysteresis curves for a heating/cooling cycle. (b) Transformation temperature T_c vs the inverse of the diameter *D*, Eq. [14.6]. Data taken from Sandoval and Urbassek (2009a).

the bcc phase has a smaller energy by 40 meV/atom. This fcc-hcp energy difference is negligible at room temperature and above; this may explain why the transformed crystal is not found in a single (fcc) phase.

Figure 14.11(b) displays a clear dependence of the transition temperature on the wire diameter. This finding is analogous to that found for nanoclusters, both in the austenitic (bcc→fcc) transformation (Entel *et al*., 2004) and in the melting process (Chushak and Bartell, 2001; Shibuta and Suzuki, 2008). The dependence can be described by a law (Sandoval and Urbassek, 2009a)

© Woodhead Publishing Limited, 2012



14.12 Local atomic structure in an axial (left) and cross-sectional (right) slice through the nanowire (diameter D = 3 nm, oriented along ⟨111⟩) (a) before and (b) after the transformation process. Grey-shade denotes local structure (Ackland and Jones, 2006): black: bcc, white: fcc, light grey: hcp, dark grey: unidentified. From Sandoval and Urbassek (2009a).

$$T_c(D) = T_c^{\text{bulk}}\left[1 - \frac{4(\sigma_{\text{bcc}} v_{\text{bcc}}^{\text{at}} - \sigma_{\text{fcc}} v_{\text{fcc}}^{\text{at}})}{DL_{\text{bcc}\to\text{fcc}}}\right] \qquad [14.6]$$

which follows from a decomposition of the wire free energy into its bulk and surface contributions and an expansion around the bulk transition temperature T_c^{bulk}. Besides the atomic volume v^{at} and the specific surface free energies (σ) of the fcc and bcc phase, the latent heat per atom, $L_{\text{bcc}\to\text{fcc}}$, enters this expression.

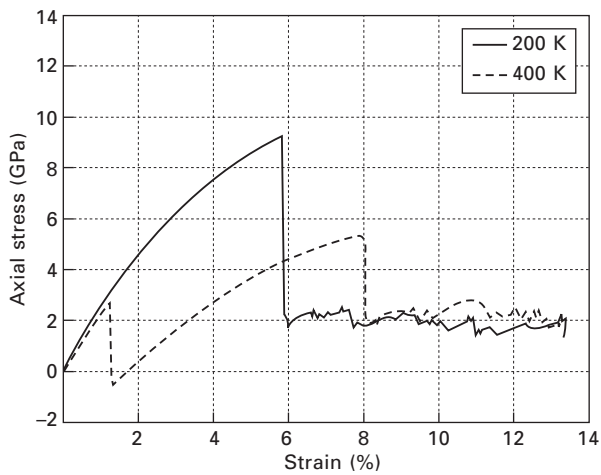
© Woodhead Publishing Limited, 2012

The extrapolation of the results shown in Fig. 14.11(b) to $D \rightarrow \infty$ gives a prediction for T_c^{bulk} of 1330 ± 30 K. While this value agrees satisfactorily with the experimental value, 1184 K, it is too high for the interatomic potential employed, which predicts 600 K. There are two reasons for this discrepancy. Firstly, for nanowires, the transformation is heterogeneous, starting from the surface, while in the bulk, it is homogeneous. Secondly, as Fig. 14.11(a) demonstrates, the length–temperature hysteresis widens considerably with increasing wire diameter, demonstrating that in thick nanowires, considerable overheating is possible. The bulk phase transition, as calculated using free energy calculations, however, is sharp, and hence must occur at a temperature which is considerably lower than the upper transition temperature for a wire.

14.4.2 Stress-induced transformation

Besides temperature, stresses may induce solid-solid phase transitions. In the case of nanowires, such stresses can be applied by straining the wire along its axis. Here we show results obtained for nanowires under tensile axial stress (Sandoval and Urbassek, 2009b).

Figure 14.13 displays the variation of the axial tensile stress as a function of the strain for two different temperatures. At the lower temperature (200 K), the wire shows a simple behavior, characterized by an elastic regime, which becomes nonlinear for higher strains, until at a well-defined strain, the metal yields and then deforms plastically. For the higher temperature

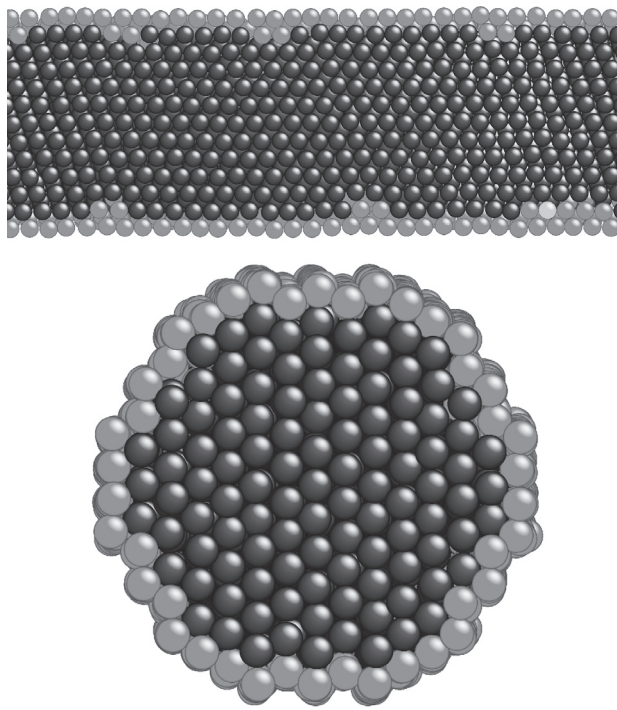


14.13 Axial stress as a function of the applied strain for a ⟨111⟩ oriented Fe nanowire of D = 3 nm diameter for two temperatures. Data from Sandoval and Urbassek (2009b).

© Woodhead Publishing Limited, 2012

(400 K), however, the behavior is more complex. Two elastic regimes are found, which are separated by a critical strain of around 1.5%.

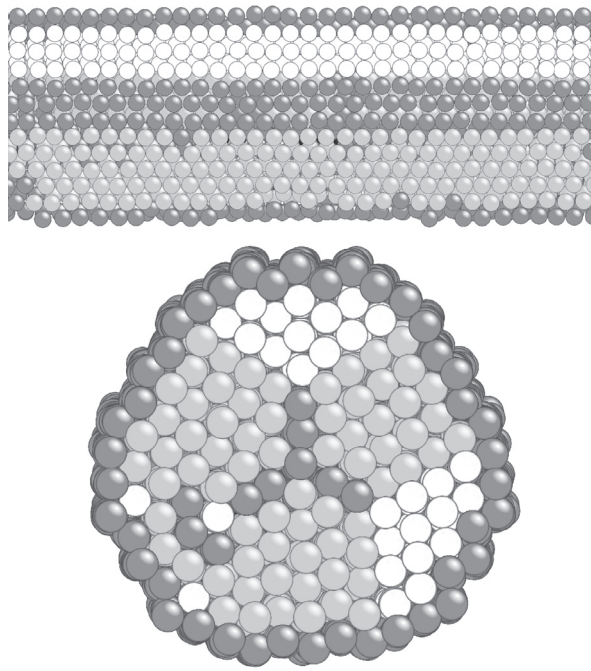
An inspection of the local atomic structure reveals that the occurrence of the second elastic regime coincides with a phase transition of the Fe nanowire from the bcc to a close-packed phase, consisting of a mixture of fcc and hcp coordinations. As an example, Fig. 14.14 visualizes the crystal structure via representative snapshots for a nanowire strained at 600 K. The elastic bcc, the elastic close-packed and the plastic regime are displayed. After the phase transformation, the transformed wire is in a phase mixture of hcp and fcc domains. At the wire axis, several phases meet; this indicates that the transformation did not nucleate in the wire volume, but at its surface. A roughly threefold symmetry is visible both in the core region and in the cross-sectional shape. The transformed fcc phase is oriented in ⟨111⟩ direction



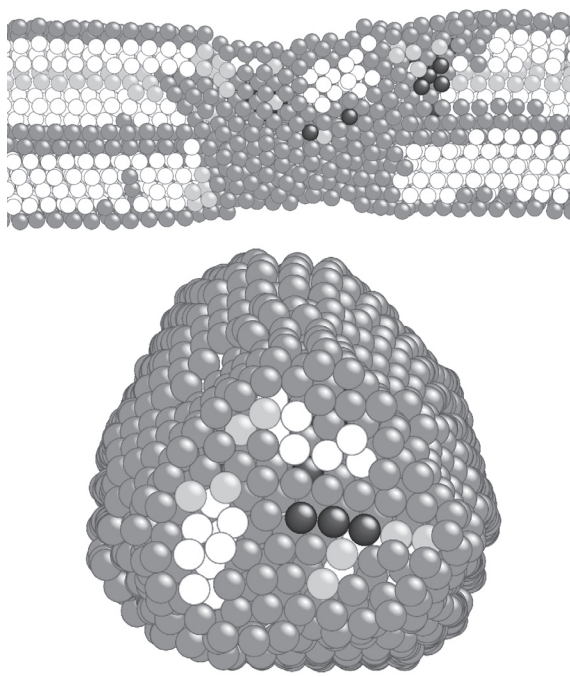
(a)

14.14 Local structure in a ⟨111⟩ oriented Fe nanowire of D = 3 nm diameter strained at 600 K. (a) Elastic regime in bcc phase (strain ε = 0%). (b) Elastic regime in close-packed phase (ε = 4%). (c) Plastic regime (ε = 10%). Top: side view of the cut wire. Bottom: cross-sectional view. Grey shade denotes local crystal structures: black: bcc, white: fcc, light grey: hcp, dark grey: unidentified. From Sandoval and Urbassek (2009b).

© Woodhead Publishing Limited, 2012



(b)



(c)

14.14 Continued

© Woodhead Publishing Limited, 2012

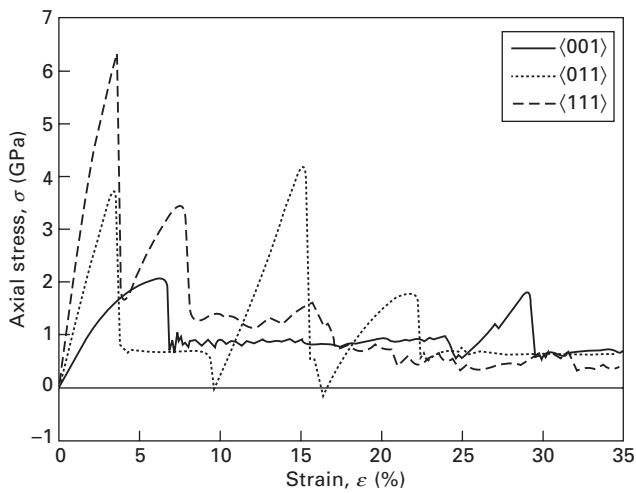
towards the wire axis. At the largest strain, Fig. 14.14(c), the non-elastic wire has yielded to the increased tensile stress; a neck has formed by plastic deformation, in which the crystal structure has been destroyed.

14.4.3 Dependence on orientation

Not surprisingly, the transformation behavior of nanowires shows a strong dependence on the wire orientation. Sandoval and Urbassek (2009c) investigated this dependence by straining Fe nanowires with three different axial orientations – ⟨001⟩, ⟨011⟩ and ⟨111⟩ – and found a rich variety of phenomena exhibiting series of elastic parts and phase transformation parts.

Figure 14.15 gives an overview of the phenomena encountered with the help of stress versus strain plots. The behavior for the ⟨111⟩ orientation has already been discussed in Fig.14.13. The two other orientations also display an intriguing behavior, which can be summarized as follows.

1. For small strains, the wire exhibits in all three orientations an elastic regime in a bcc structure. The Young's modulus depends on the orientation, as in the bulk: the ⟨001⟩ orientation is the softest and ⟨111⟩ is the stiffest.
2. The ⟨001⟩ oriented nanowire shows a highly nonlinear elastic behavior, losing its elasticity at a strain of $\varepsilon = 6.4\%$. A local structure analysis shows that at this point, the crystal starts transforming; between $\varepsilon = 7\%$



14.15 Stress vs strain curves for three different axial crystal orientations. Nanowires had a diameter of $D = 5$ nm and a temperature of 400 K. Data taken from Sandoval and Urbassek (2009c).

© Woodhead Publishing Limited, 2012

and 24%, the bcc crystal structure transforms continuously to a mixture of fcc and hcp phases. After this transformation period, at $\varepsilon = 24\%$, a purely close packed nanowire is obtained; it exhibits a second elastic regime until at $\varepsilon = 28\%$, elasticity is lost again and the wire presents a second phase transition back to the bcc structure.

3. The ⟨001⟩ oriented nanowire exhibits a series of phase transitions between the bcc and the close-packed structures. Three elastic regimes can be identified: the first corresponds to the initial bcc structure; the second, after a transition region, to an hcp elastic region at strains between 10 and 15%; and the last one again to a bcc crystal structure.
4. The phenomenon of the re-occurrence of the original bcc phase at higher strains is puzzling. The analysis by Sandoval and Urbassek (2009c) reveals that it is connected to a reorientation of the wire axis. For the initially ⟨011⟩ oriented nanowire, the high-strain bcc phase shows a wire orientation close to the ⟨001⟩ axis. However, the initially ⟨001⟩ oriented wire is reoriented in its high-strain bcc phase to ⟨011⟩. We note that the phenomenon of reorientation in nanowires has been observed also in fcc metals (Liang *et al.*, 2005; Park *et al.*, 2005). In these materials the situation is simpler as no polymorphic transition occurs. It was found that the reorientation happens when under the high tensile uniaxial stress, lattice planes in the wire shift coherently to produce a new orientation.

14.4.4 Transformation path

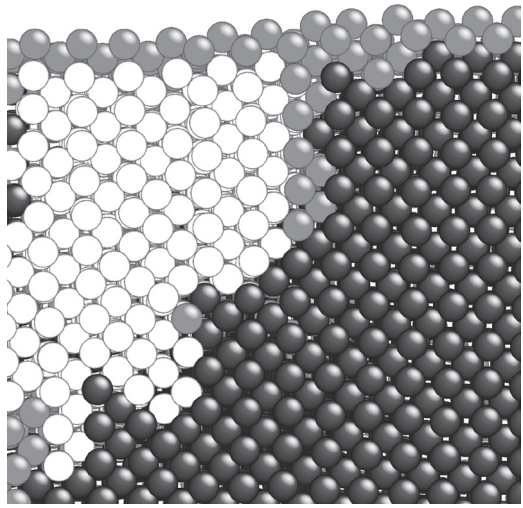
Atomistic simulation allows identification of the path that the transforming system takes. This analysis has been undertaken for transforming nanowires; due to the existence of free surfaces, the system has considerable freedom in atom motion and to choose the appropriate transformation path with few external constraints.

Figures 14.16(a) and (b) analyze the transformation paths by zooming into the transforming regions for the ⟨001⟩ and ⟨011⟩ oriented nanowires, respectively.

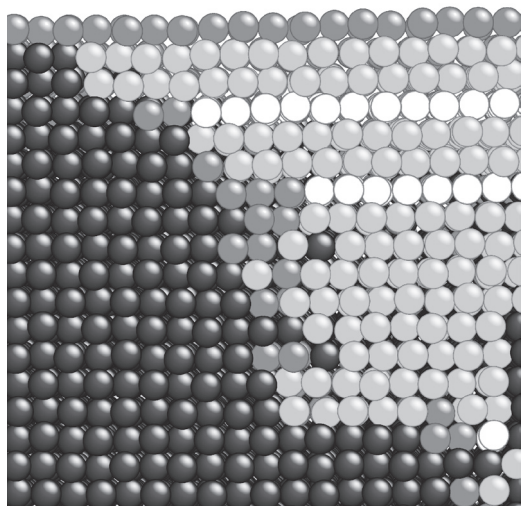
- In Fig. 14.16(a), the plotted plane is a $(100)_{bcc}$ plane. The horizontal direction is $[010]_{bcc}$ and the vertical direction corresponds to $[001]_{bcc}$. The fcc region is a $(\bar{1}10)_{fcc}$ plane. The snapshot demonstrates that there exist clear orientational relationships between the phases: $(111)_{fcc}\|(011)_{bcc}$ and $[11\bar{2}]_{fcc}\|[01\bar{1}]_{bcc}$. These are the relations satisfied by the Nishiyama–Wassermann transformation path (see Section 14.2.4).
- For a ⟨011⟩ oriented nanowire, Fig. 14.16(b) shows that the strain facilitates the opposite displacement of adjacent $(110)_{bcc}$ planes $[110]_{bcc}$ in directions. These define the Burgers' mechanism for the bcc

© Woodhead Publishing Limited, 2012

to hcp phase transition (Burgers, 1934; Ekman *et al.*, 1998; Friák and Šob, 2008), with orientational relationships of $(100)_{bcc}||(001)_{hcp}$ and $[111]_{bcc}||[110]_{hcp}$.



(a)



(b)

14.16 Side view of an axial slice (10 Å thick) in a transforming Fe nanowire. Grey shade denotes local atomic structure: black: bcc, white: fcc, light grey: hcp, dark grey: unidentified. (a) ⟨001⟩ oriented nanowire. (b) ⟨011⟩ oriented nanowire. Atomistic data from Sandoval and Urbassek (2009c).

© Woodhead Publishing Limited, 2012

14.5 Conclusions and future trends

Besides NiAl (and Ni_xAl_{1-x} alloys) and Zr, the investigation of the martensitic transformation by molecular dynamics simulation has evolved farthest in the Fe (and $Fe_{1-x}Ni_x$) system.

The simplest way to study the dynamics of the phase transformation consists in monitoring the decay of the metastable (fcc) phase towards the minimum-free-energy (bcc) phase. Such simulations showed the homogeneous nucleation of the new phase, and also the heterogeneous nucleation near extended defects (grain boundaries). An alternative simulation method consists in setting up a bi-system consisting of the two phases to be studied, and to analyze the dynamics and the motion of the interface. Results obtained using this procedure include the structure of the evolving interface and its velocity (Bos *et al*., 2006a; Tateyama *et al*., 2010). Such studies may be performed even if one of the phases is only metastable. Under these circumstances it is not even necessary to employ an interatomic interaction potential which has the austenite phase as its high-temperature stable phase, but it can be metastable.

For more detailed studies, and in particular to model the austenitic transition, the interatomic potential needs to incorporate reliable information on the (temperature dependent) free energy difference between the two phases, and must, in particular, allow for a high-temperature austenitic (fcc) phase. In such studies only the Meyer and Entel (1998) potential has been employed which – at least qualitatively correct – predicts the existence of a high-temperature fcc and a low-temperature bcc phase. Due to its complexity, the quantitatively more reliable Müller *et al*. (2007) potential does not appear to have been used for such studies up to now. As a result, both the austenitic and the martensitic transformation as a function of temperature could be studied. In all of these studies it turns out that the role of external constraints on the system is essential in controlling the transformation. Thus, point defects or extended defects (such as grain boundaries) can act as a source of potential energy and/or allow for free volume to trigger and mediate the transformation.

In particular, the role of free surfaces was found to influence most deeply the occurrence, the dynamics and the results of phase transformations in iron. Thus the study of ‘small’ systems – here nanowires were presented as an example – yielded a number of intriguing results. These include the spontaneous austenitic transformation during heating, the stress-induced occurrence of multiple phase transformations under tensile axial stress, and the crystallographic reorientation of the wire axis under tensile stress.

© Woodhead Publishing Limited, 2012

14.6 Acknowledgement

We acknowledge support by the Deutsche Forschungsgemeinschaft via the Graduiertenkolleg 814 and the Sonderforschungsbereich 926.

14.7 References

Ackland G.J. and Jones A.P. (2006): Applications of local crystal structure measures in experiment and simulation. *Phys Rev B* **73**, 054104

Ackland G.J., Bacon D.J., Calder A.F. and Harry T. (1997): Computer simulation of point defect properties in dilute Fe-Cu alloy using a many-body interatomic potential. *Philos Mag A* **75**, 713

Ackland G.J., Mendelev M.I., Srolovitz D.J., Han S. and Barashev A.V. (2004): Development of an interatomic potential for phosphorus impurities in α-iron. *J Phys: Condens Matter* **16**, S2629

Ackland G.J., Jones A.P. and Noble-Eddy R. (2008): Molecular dynamics simulations of the martensitic phase transition process. *Mat Sci Eng A* **481–482**, 11

Bain E.C. (1924): The nature of martensite. *Trans AIME* **70**, 25

Belonoshko A.B., Ahuja R. and Johansson B. (2000): Quasi-*ab initio* molecular dynamic study of Fe melting. *Phys Rev Lett* **84**, 3638

Belonoshko A.B., Derlet P.M., Mikhaylushkin A.S., Simak S.I., Hellman O., Burakovsky L., Swift D.C. and Johansson B. (2009): Quenching of bcc-Fe from high to room temperature at high-pressure conditions: a molecular dynamics simulation. *New J Phys* **11**, 093039

Bendick W. and Pepperhoff W. (1982): On the α/γ stability of Fe. *Acta Metall* **30**, 679

Bos C., Sietsma J. and Thijsse B.J. (2006a): Molecular dynamics simulation of interface dynamics during the fcc-bcc transformation of a martensitic nature. *Phys Rev B* **73**, 104117

Bos C., Sommer F. and Mittemeijer E.J. (2006b): Multi-lattice kinetic Monte Carlo simulation of interphase kinetics for an iron fcc to bcc transformation. *Model Simul Mater Sci Eng* **14**, 273

Burgers W.G. (1934): On the process of transition of the cubic-body-centered modification into the hexagonal-close-packed modification of zirconium. *Physica* **1**, 561

Carlsson A.E. (1990): Beyond pair potentials in elemental transition metals and semiconductors. In H. Ehrenreich and D. Turnbull, editors, *Solid State Physics*, vol. 43, 1. Academic Press, Boston, MA

Chamati H., Papanicolaou N.I., Mishin Y. and Papaconstantopoulos D.A. (2006): Embedded-atom potential for Fe and its application to self-diffusion on Fe(100). *Surf Sci* **600**, 1793

Chen Q. and Sundman B. (2001): Modeling of thermodynamic properties for bcc, fcc, liquid, and amorphous iron. *J Phase Equilibria* **22**, 631

Chushak Y.G. and Bartell L.S. (2001): Melting and freezing of gold nanoclusters. *J Phys Chem B* **105**, 11605

Daw M.S., Foiles S.M. and Baskes M. (1993): The embedded-atom method: a review of theory and applications. *Mat Sci Rep* **9**, 251

Dudarev S.L. and Derlet P.M. (2005): A 'magnetic' interatomic potential for molecular dynamics simulations. *J Phys: Condens Matter* **17**, 7097

Ekman M., Sadigh B., Einarsdotter K. and Blaha P. (1998): *Ab initio* study of the martensitic bcc-hcp transformation in iron. *Phys Rev B* **58**, 5296

© Woodhead Publishing Limited, 2012

Engin C. and Urbassek H.M. (2008): Molecular dynamics investigation of the fcc → bcc phase transformation in Fe. *Comput Mater Sci* **41**, 297

Engin C., Sandoval L. and Urbassek H.M. (2008): Characterization of Fe potentials with respect to the stability of the bcc and fcc phase. *Model Simul Mater Sci Eng* **16**, 035005

Entel P., Meyer R., Kadau K., Herper H.C. and Hoffmann E. (1998): Martensitic transformations: first-principles calculations combined with molecular-dynamics simulations. *Eur Phys J B* **5**, 379

Entel P., Kadau K., Meyer R., Crisan V., Ebert H., Germann T.C., Lomdahl P.S. and Holian B.L. (2000a): Molecular-dynamics simulations of martensitic transformations. *Adv Solid State Phys* **40**, 345

Entel P., Meyer R. and Kadau K. (2000b): Molecular dynamics simulations of martensitic transformations. *Philos Mag B* **80**, 183

Entel P., Kreth M., Meyer R. and Kadau K. (2004): Simulation of structural transformations in nanoparticles. In P. Vincenzini and F. Zerbetto, editors, *Advances in Science and Technology*, vol. 44, 101. Techna Group, Faenza, Italy

Finnis M. (2003): *Interatomic forces in condensed matter*. Oxford University Press, Oxford

Finnis M.W. and Sinclair J.E. (1984): A simple empirical N-body potential for transition metals. *Philos Mag A* **50**, 45. Erratum: **53** (1986) 161

Foiles S.M. (1985): Application of the embedded-atom method to liquid transition metals. *Phys Rev B* **32**, 3409

Frenkel D. and Smit B. (2002): *Understanding molecular simulation,* 2nd edn. Academic Press, San Diego

Friák M. and Šob M. (2008): *Ab initio* study of the bcc-hcp transformation in iron. *Phys Rev B* **77**, 174117

Girifalco L.A. and Weizer V.G. (1959): Application of the Morse potential function to cubic metals. *Phys Rev* **114**, 687

Gornostyrev Y.N., Urtsev V.N., Zalalutdinov M.K., Entel P., Kaptsan A.V. and Kuznetsov A.R. (2005): Reconstruction of grain boundaries during austenite-ferrite transformation. *Scr Mater* **53**, 153

Harrison R.J., Voter A.F. and Chen S.P. (1989): An embedded atom potential for bcc iron. In V. Vitek and D.J. Srolovitz, editors, *Atomistic Simulation of Materials: Beyond Pair Potentials*, 219. Plenum Press, New York

Hoy R.S. and Robbins M.O. (2004): Fcc-bcc transition for Yukawa interactions determined by applied strain deformation. *Phys Rev E* **69**, 056103

Ji C. and Park H.S. (2007): The coupled effects of geometry and surface orientation on the mechanical properties of metal nanowires. *Nanotechnology* **18**, 305704

Johnson R.A. and Oh D.J. (1989): Analytic embedded atom method model for bcc metals. *J Mater Res* **4**, 1195

Kadau K. and Entel P. (1999): Atomistic study of the structural transformation in thin iron films on copper. *J Magn Magn Mater* **198–199**, 531

Kadau K. and Entel P. (2002): Atomistic investigations of the thermodynamical stability and martensitic nucleation of $Fe_{80}Ni_{20}$ nanoparticles. *Phase Trans* **75**, 59

Kadau K., Meyer R. and Entel P. (1999): Molecular-dynamics study of thin iron films on copper. *Surf Rev Lett* **6**, 35

Kadau K., Entel P. and Lomdahl P.S. (2002a): Molecular dynamics study of martensitic transformations in sintered Fe-Ni nanoparticles. *Comput Phys Commun* **147**, 126

© Woodhead Publishing Limited, 2012

Kadau K., Germann T.C., Lomdahl P.S. and Holian B.L. (2002b): Microscopic view of structural phase transitions induced by shock waves. *Science* **296**, 1681

Kadau K., Germann T.C., Lomdahl P.S. and Holian B.L. (2005): Atomistic simulations of shock-induced transformations and their orientation dependence in bcc Fe single crystals. *Phys Rev B* **72**, 064120

Klotz S. and Braden M. (2000): Phonon dispersion of bcc iron to 10 GPa. *Phys Rev Lett* **85**, 3209

Lai W.S. and Zhao X.S. (2004): Strain-induced elastic moduli softening and associated fcc ↔ bcc transition in iron. *Appl Phys Lett* **85**, 4340

Latapie A. and Farkas D. (2003): Molecular dynamics simulation of stress-induced phase transformations and grain nucleation at crack tips in Fe. *Model Simul Mater Sci Eng* **11**, 745

Lazarev N.P., Abromeit C., Schäublin R. and Gotthardt R. (2006): Temperature-controlled martensitic phase transformations in a model NiAl alloy. *J Appl Phys* **100**, 63520

Liang W. and Zhou M. (2006): Atomistic simulations reveal shape memory of fcc metal nanowires. *Phys Rev B* **73**, 115409

Liang W., Zhou M. and Ke F. (2005): Shape memory effect in Cu nanowires. *Nano Lett* **5**, 2039

Mendelev M.I. and Ackland G.J. (2007): Development of an interatomic potential appropriate for simulation of phase transformations in zirconium. *Philos Mag Lett* **87**, 349

Mendelev M.I., Han S., Srolovitz D.J., Ackland G.J., Sun D.Y. and Asta M. (2003): Development of new interatomic potentials appropriate for crystalline and liquid iron. *Philos Mag* **83**, 3977

Meyer R. and Entel P. (1998): Martensite-austenite transition and phonon dispersion curves of $Fe_{1-x}Ni_x$ studied by molecular-dynamics simulations. *Phys Rev B* **57**, 5140

Miller M.A. and Reinhardt W.P. (2000): Efficient free energy calculations by variationally optimized metric scaling: concepts and applications to the volume dependence of cluster free energies and to solid-solid phase transitions. *J Chem Phys* **113**, 7035

Müller M., Erhart P. and Albe K. (2007): Analytic bond-order potential for bcc and fcc iron – comparison with established EAM potentials. *J Phys: Condens Matter* **19**, 326220

Nagano T. and Enomoto M. (2006): Calculation of the interfacial energies between α and γ iron and equilibrium particle shape. *Metall Mater Trans A* **37A**, 929

Neuhaus J., Petry W. and Krimmel A. (1997): Phonon softening and martensic transformation in α-Fe. *Physica B* **234–236**, 897

Nishiyama Z. (1978): *Martensitic transformation*. Academic Press, New York

Nordlund K., Wallenius J. and Malerba L. (2006): Molecular dynamics simulations of threshold displacement energies in Fe. *Nucl Instrum Meth B* **246**, 322

Osetsky Y.N. and Serra A. (1998): Computer-simulation study of high-temperature phase stability in iron. *Phys Rev B* **57**, 755

Park H.S., Gall K. and Zimmerman J.A. (2005): Shape memory and pseudoelasticity in metal nanowires. *Phys Rev Lett* **95**, 255504

Pasianot R., Farkas D. and Savino E.J. (1991): Empirical many-body interatomic potential for bcc transition metals. *Phys Rev B* **43**, 6952

Rubini S. and Ballone P. (1993): Quasiharmonic and molecular-dynamics study of the martensitic transformation in Ni-Al alloys. *Phys Rev B* **48**, 99

Sandoval L. and Urbassek H.M. (2009a): Finite-size effects in Fe-nanowire solid-solid phase transitions: a molecular dynamics approach. *Nano Lett* **9**, 2290

Sandoval L. and Urbassek H.M. (2009b): Solid-solid phase transitions in Fe nanowires induced by axial strain. *Nanotechnology* **20**, 325704

© Woodhead Publishing Limited, 2012

Sandoval L. and Urbassek H.M. (2009c): Transformation pathways in the solid-solid phase transitions of iron nanowires. *Appl Phys Lett* **95**, 191909

Sandoval L., Urbassek H.M. and Entel P. (2009a): The Bain versus Nishiyama–Wassermann path in the martensitic transformation of Fe. *New J Phys* **11**, 103027

Sandoval L., Urbassek H.M. and Entel P. (2009b): Solid-solid phase transitions and phonon softening in an embedded-atom method model for iron. *Phys Rev B* **80**, 214108

Shao Y., Clapp P.C. and Rifkin J.A. (1996): Molecular dynamics simulation of martensitic transformations in NiAl. *Metall Mat Trans A* **27A**, 1477

Shibuta Y. and Suzuki T. (2008): A molecular dynamics study of the phase transition in bcc metal nanoparticles. *J Chem Phys* **129**, 144102

Simonelli G., Pasianot R. and Savino E.J. (1993): EAM interatomic potentials for bcc Fe. *Mater Res Soc Symp Proc* **291**, 657

Sinclair C.W. and Hoagland R.G. (2008): A molecular dynamics study of the fcc → bcc transformation at fault intersections. *Acta Mater* **56**, 4160

Tateyama S., Shibuta Y. and Suzuki T. (2008): A molecular dynamics study of the fcc-bcc phase transformation kinetics of iron. *Scr Mater* **59**, 971

Tateyama S., Shibuta Y. and Suzuki T. (2010): Orientation relationship in fcc-bcc phase transformation kinetics of iron: a molecular dynamics study. *ISIJ Int* **50**, 1211

Wallenius J., Olsson P. and Lagerstedt C. (2005): Relation between thermal expansion coefficient and interstitial formation energy in Fe and Cr. *Nucl Instrum Meth B* **228**, 122

Yu Z.Z. and Clapp P.C. (1989): Growth dynamics study of the martensitic transformation in Fe-30 Pct Ni alloys: Part II. Computer simulation of martensitic growth. *Metall Trans A* **20A**, 1617

© Woodhead Publishing Limited, 2012

15

Neural networks modeling of phase transformations in steels

C. CAPDEVILA, National Centre for Metallurgical Research (CENIM-CSIC), Spain

Abstract: This chapter deals with the applications of neural networks to the specific problem of solid-solid phase transformations in steels. The first part of this chapter is devoted to an introduction of the essence of the method, highlighting useful concepts such as 'evidence' and 'uncertainty' to take advantage in the designing of new experiments to fill gaps in the data distribution in the input space. The following section deals with applications of neural network modeling to calculate the transformation temperatures and the evolution of microstructural parameters, such as interlamellar spacing of pearlite, bainite plate thickness, etc., of key importance to the mechanical behavior of the resulting microstructure. Finally, the last section describes attempts to deal with an important issue: continuous cooling transformation (CCT) diagrams, effectively, a map of steel transformation, of practical importance for optimizing the steel product from the point of view of the final microstructure and properties.

Key words: neural networks, mathematical modeling, data mining, critical temperatures, CCT diagrams.

15.1 Introduction

Neural networks are a powerful tool, which permit the development of quantitative expressions without compromising the known complexity of the problem. It is a mathematically transparent technique which is able to capture complex relationships without the need to fix the mathematical form at the outset. These capabilities are enhanced by a proper consideration of errors and uncertainties. This makes them ideal in circumstances where simplification of the problem, in order to make it mathematically tractable, would lead to an unacceptable loss of information. As pointed out by Ziman (1979), there is a fine balance between over-idealizing the initial hypothesis in order to make it amenable to mathematical analysis, and abandoning reality.

Materials science has always been an interdisciplinary affair, but the introduction of new techniques frequently causes perturbations. Some regard neural networks with suspicion whereas others unashamedly embrace them as facilities which help cope with difficult problems. The suspicion arises because the method has been shown to thrive in complexity. This goes against

© Woodhead Publishing Limited, 2012

intuition. Strangely enough, the very same ability to deal with complexity delights those who exploit the technique. The truth is that the technique is one of the panoply of tools now available to deal with the quantitative design of materials and processes. Neural networks have had a liberating effect on materials science because, for the first time, they have enabled the creation of complete models, essential in any design problem (Fujii and Bhadeshia, 1996; Bhadeshia, 1999, 2009; Bhadeshia *et al.*, 2009).

15.2 Essence of the method

Modeling techniques are sometimes classified as white, gray or black boxes, with the implication that the white-box model is completely transparent and comprehensible in its construction, whereas the black box is simply a magical instrument which relates a set of inputs to the output without giving insight into how the conversion is achieved. A neural network is a mathematical function which is fitted to experimental data; the trained network cannot therefore contain more knowledge than the data used in its creation. The function and its associated coefficients are precisely defined and hence transparent to observation; there are no black boxes! When fed with the same inputs, the network produces precisely the same outputs.

15.2.1 Linear regression

Linear regressions are a simple example, but none the less very useful to grasp the basic concepts of the neural network method. Linear regressions are used to fit a set of data $\{x, y\}$. The problem is to find two parameters $\{a, b\}$ so that the equation $y = ax + b$ represents the closest fit to the set of data $\{x, y\}$. 'Closest' is translated, in mathematics, by minimizing an error function (a function of a and b which takes large values if a and b provide a poor fit, smaller values when a and b provide a better fit and is a minimum when the fit is optimal). As an example, the temperature at which the martensite reaction starts (i.e. M_s) in steels may be written as (Andrews, 1965):

$$\begin{aligned} M_s(^\circ\mathrm{C}) &= \sum_{j=1}^{5} w_j X_j + \theta \\ &= 539 - 423X_\mathrm{C} - 30.4X_\mathrm{Mn} - 17.7X_\mathrm{Ni} - 12.1X_\mathrm{Cr} - 7.5X_\mathrm{Mo} \end{aligned} \quad [15.1]$$

where X_C, X_Mn, X_Ni, X_Cr and X_Mo indicate the element, in wt%, which is in solid solution in austenite. The term w_i is then the best-fit value of the weight by which the concentration is multiplied; and θ is a constant. In this particular case of Eq. [15.1], $\theta = 539$; $W_\mathrm{C} = -423$; $W_\mathrm{Mn} = -30.4$; $W_\mathrm{Ni} =$

© Woodhead Publishing Limited, 2012

–17.7; $W_{Cr} = -12.1$ and $W_{Mo} = -7.5$. This relationship between the start of transformation M_s and the steel composition has been investigated by Grange and Stewart (1946), Payson and Savage (1944), Steven and Haynes (1956) and Andrews (1965). Andrews used the largest sample size, 184 data, for M_s and reported the simple linear formula expressed in Eq. [15.1] where 92% of the M_s values were within 25°C of the predicted values. Of course, there is no justification for the choice of the particular form of relationship. This, and other difficulties associated with ordinary linear regression analysis, can be summarized in three main points: first, a relationship has to be chosen before analysis; second, the relationship chosen tends to be linear, or with non-linear terms added together to form a pseudo-linear equation; and third, the regression equation, once derived, applies across the entire span of the input space, which might not be reasonable for certain regions of the input space.

15.2.2 Neural networks

A general method of regression which avoids the above-mentioned difficulties is neural network analysis. Neural networks provide a tool to perform similar operations to linear regression, but in a far more general context. They can perform non-linear, multiple regressions, that is, they do not assume a linear relationship between y and x; they also allow for multiple inputs, and can deal with interactions between them.

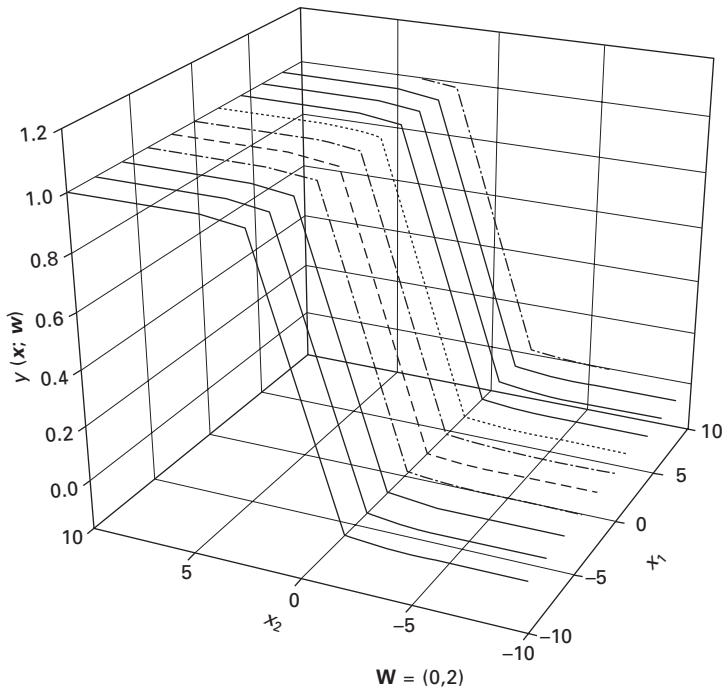
A very simple neural network, which is described by two inputs $\boldsymbol{x} = (x_1,x_2)$ and two weights $\boldsymbol{w} = (w_1,w_2)$, produces an output between 0 and 1 as the following function of $\mathbf{x}$:

$$y(\boldsymbol{x}:\boldsymbol{w}) = \frac{1}{1 + e^{-(w_1x_1 + w_2x_2)}} \qquad [15.2]$$

This example has two important features: (a) linear operation, $a = (w_1x_1 + w_2x_2)$; followed by (b) non-linear function, $f(a) = 1/(1 + e^{-a})$. Most neural network models share these features, having multiple linear operations alternating with non-linear functions. Figure 15.1 shows the output of the neuron as a function of the input vector, for $\mathbf{w} = (0,2)$. The two horizontal axes of this figure are the inputs x_1 and x_2, with the output y on the vertical axis. Notice that on any line perpendicular to $\mathbf{w}$, the output is constant, and along a line in the direction of $\mathbf{w}$, the output is a 'sigmoid' function. Thus each *point* in $\mathbf{w}$ space corresponds to a *function* of $\mathbf{x}$. Notice that the gain of the sigmoid function (the gradient to the ramp) increases as the magnitude of $\mathbf{w}$ increases.

Now, the central idea of the neural network method is this. Given examples of a relationship between an input vector $\mathbf{x}$, and a 'target' t, we hope to make the neural network '*learn*' a model of the relationship between $\mathbf{x}$ and t. A

© Woodhead Publishing Limited, 2012



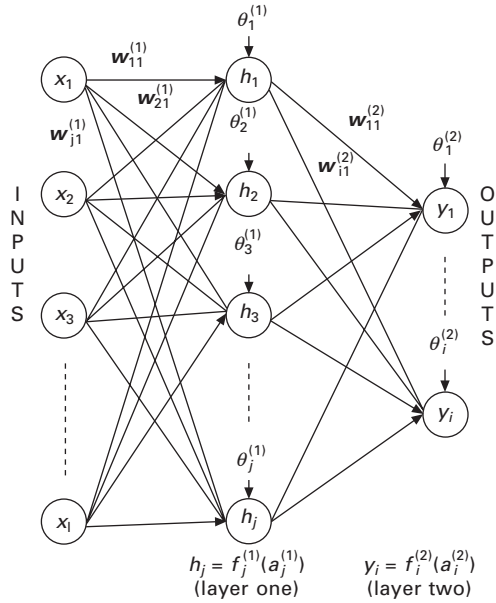
15.1 Output of a simple neural network as a function of its input.

successfully 'trained' network will, for any given **x**, give an output *y* that is close (in some sense) to the target value *t*. '*Training*' the network involves searching in the weight space of the network for a value of **w** that produces a function that fits the provided training data well.

As an example, if we wished to predict the toughness of a weld with a given chemical composition, then we might define the inputs **x** to be the chemical composition, and the output *y* to be the predicted toughness. The training data would be a set $\{\boldsymbol{x},t\}$ of measured weld compositions **x** and measured toughness *t*. The hope would be that a trained network would extract a non-linear relationship between toughness and the input variables.

However, in comparison with the example described before, the toughness of a weld, as a function of the composition, is a more complex function than the one described in Eq. [15.2]. It is necessary, therefore, to turn to more complex networks. The standard feed-forward networks used in this type of analysis consists of two layers of neurons interconnected as described in Fig. 15.2. The first layer of neurons is often referred to as a '*hidden layer*' and its neurons as hidden units. The mapping for the two layer network has the form:

© Woodhead Publishing Limited, 2012



15.2 A two-layer feed-forward network similar to the one used in this work. The activation function of the neurons in the first layer (hidden layer) is hyperbolic tangent (tanh) and is linear in the second one (output layer). The complexity of the model is controlled by the number of neurons in the first layer, also called hidden units.

Hidden layer:

$$a_j^{(1)} = \sum_l \boldsymbol{w}_{jl}^{(1)} x_l + \theta_j^{(1)}; \quad \boldsymbol{h}_j = f^{(1)}(a_j^{(1)}) \qquad [15.3]$$

Output layer:

$$a_i^{(2)} = \sum_j \boldsymbol{w}_{ij}^{(2)} \boldsymbol{h}_j + \theta_i^{(2)}; \quad y_i = f^{(2)}(a_i^{(2)}) \qquad [15.4]$$

The activation functions used in most of the models dealing with phase transformations in steels (MacKay, 1992a) are $f^{(1)}(a) = \tanh(a)$, and $f^{(2)}(a) = a$. Here l runs over the inputs $x_1 \ldots x_L$, j runs over the hidden units, and i runs over the outputs. The 'weights' w and 'biases' θ together make up the parameter vector $\mathbf{w}$. The non-linear 'sigmoid' function $f^{(1)}$ at the hidden layer gives the neural network greater computational flexibility than a standard linear regression model. Graphically, we can represent the neural network as a set of layers of connected neurons (as shown in Fig. 15.2). This is called a two-layer network because it has two layers of weights. In terms of layers of neurons, it has one input layer, one hidden layer and one output layer.

The neural network can capture interactions between the inputs because the hidden units are non-linear. The nature of these interactions is implicit in the

© Woodhead Publishing Limited, 2012

values of the weights, but the weights may not always be easy to interpret. For example, there may exist more than just pair-wise interactions, in which case the problem becomes difficult to visualize from an examination of the weights. A better method is to use the network to make predictions and to see how these depend on various combinations of inputs.

15.2.3 How a neural network is traditionally trained

A network as defined in Eqs [15.3] and [15.4] is trained using a data set $D = \{\mathbf{x}^{(m)},\mathbf{t}^{(m)}\}$ by adjusting $\mathbf{w}$ so as to minimize an error function, e.g.,

$$E_D(w) = \frac{1}{2}\sum_m\sum_i (t^{(m)} - y_i(\boldsymbol{x}^{(m)};\boldsymbol{w}))^2 \qquad [15.5]$$

The objective function is a sum of terms, one for each input/target pair $\{\boldsymbol{x},t\}$, measuring how close the output $\boldsymbol{y}(\boldsymbol{x};\boldsymbol{w})$ is to the target t. This minimization is based on repeated evaluation of the gradient of E_D using 'back-propagation' (Rumelhart *et al*., 1986). The backpropagation algorithm computes for each input–output pair m the gradient $\frac{1}{2}(t_i^{(m)} - y_i(\boldsymbol{x}^{(m)};\boldsymbol{w}))^2$ by following the 'forward pass' of Eqs [15.3] and [15.4] by a 'backward pass', in which information about errors $(t_i^{(m)} - y_i(\boldsymbol{x}^{(m)};\boldsymbol{w}))$ propagates back through the network by the chain rule. Therefore, 'training the network' is achieved by altering the parameters to fit the functions to the data using backpropagation optimization procedures (MacKay, 1992c) to minimize an objective function. Extra care has to be taken to avoid fitting to local minima (MacKay, 1997).

15.2.4 The Bayesian framework

In MacKay's Bayesian treatment (MacKay, 1992b, 1992c) over-complex and under-regularized models are automatically inferred to be less probable, even though the flexibility of Eq. [15.3] allows them to fit the data better. This is achieved by calculating and optimizing an objective function $M(w) = \beta E_D + \alpha E_w$ (regularization method) which combines an error term (E_D) to assess how good the fitting is and regularization term ($E_w = \frac{1}{2}\sum_i w_i^2$) to penalize large weights. This additional term favors small values of $\mathbf{w}$ and thus encourages the model to find simpler solutions with less tendency to 'overfit' noise in the training data. The terms α and β are complexity parameters described in the following paragraphs.

MacKay described the above-mentioned learning process of neural networks following a probabilistic interpretation. The error function is interpreted as defining the probability distribution of a noise model (H):

© Woodhead Publishing Limited, 2012

$$P(D|\mathbf{w},\beta,H) = \frac{1}{Z_D(\beta)} \exp(-\beta E_D) \quad [15.6]$$

Thus, the use of the sum-squared error described in Eq. [15.5], e.g. E_D, corresponds to an assumption of Gaussian noise on the target variables, and the parameter β defines the noise level $\sigma_v^2 = 1/\beta$. Similarly, the regularizer (E_w) is interpreted in terms of the logarithm of prior probability distribution over the parameters:

$$P(\mathbf{w}|\alpha,H) = \frac{1}{Z_w(a)} \exp(-aE_w) \quad [15.7]$$

If E_w is quadratic as defined above, then the corresponding prior distribution is a Gaussian with variance $\sigma_w^2 = 1/\alpha$. The probabilistic model H specifies the functional form of the network, the likelihood (see Eq. [15.6]), and the prior probability distribution (see Eq. [15.7]). The objective function $M(\mathbf{w})$ then corresponds to the inference of the parameters $\boldsymbol{w}$, given the data. By Bayes' theorem (Jaynes, 2003):

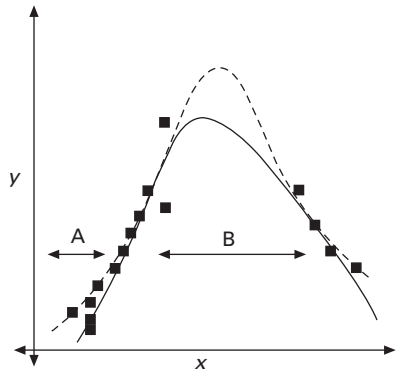
$$P(\mathbf{w}|D,\alpha,\beta,H) = \frac{P(D|\mathbf{w},\alpha,\beta,H)P(\mathbf{w}|\alpha,H)}{P(D|\alpha,\beta,H)} = \frac{1}{Z_M} \exp(-M(\mathbf{w})) \quad [15.8]$$

The $\mathbf{w}$ found by (locally) minimizing $M(\mathbf{w})$ is then interpreted as the (locally) most probable parameter vector, $\mathbf{w}_{\mathbf{MP}}$.

In summary, in the traditional way of learning, a single parameter vector $\mathbf{w}$ evolves under the learning rule from an initial starting point to a final optimum one that minimizes $M(\mathbf{w})$. In contrast, given the Bayesian interpretation of $M(\mathbf{w})$ as a logarithm of probability, the product of learning is an ensemble of plausible parameter values. There are a number of useful consequences with this view of neural network learning, relating to automatic control of neural network complexity, and to quantification of the uncertainty of a model's predictions.

The main consequence that can be derived from this treatment is the *uncertainty determination*. The above-mentioned neural networks treatment developed by MacKay in a Bayesian framework (MacKay, 1992b) allows the calculation of error bars representing the uncertainty in the fitting parameters. The method recognizes that there are many functions which can be fitted or extrapolated into uncertain regions of the input space, without unduly compromising the fit in adjacent regions which are rich in accurate data. Instead of calculating a unique set of weights, a probability distribution of sets of weights is used to define the fitting uncertainty. Figure 15.3 illustrates the problem; the practice of using the best-fit function (i.e. the most probable values of the weights) does not adequately describe the uncertainties in

© Woodhead Publishing Limited, 2012



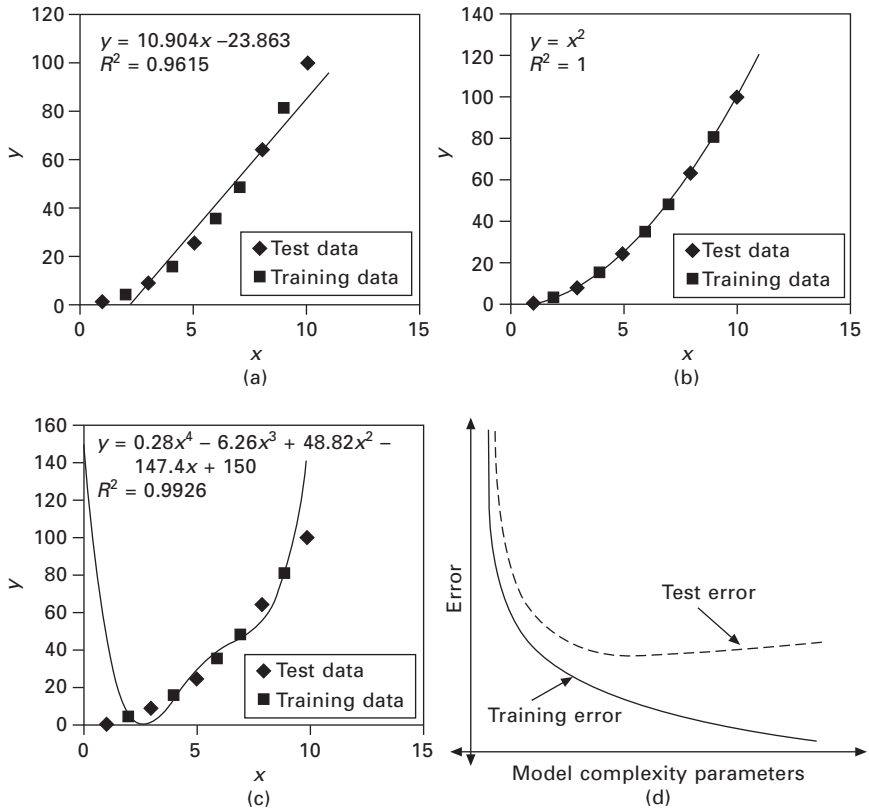
15.3 Schematic illustration of the uncertainty in defining a fitting function in regions where data are sparse (B) or where they are noisy (A). The lines represent error bounds due to uncertainties in determining the weights.

regions of the input space where data are sparse (B), or where the data are noisy (A). The error bars therefore become large when data are sparse or locally noisy, as illustrated in Fig. 15.3. This methodology has proved to be extremely useful in materials science where properties need to be estimated as a function of a vast array of inputs.

15.2.5 Complexity control: overfitting problem

Finally, the other main advantage of the neural network treatment developed by MacKay could be the way of dealing with overfitting. Consider a control parameter which influences the complexity of a model (for example, a regularization constant α). As the control parameter is varied to increase the complexity of the model, the best fit to the training data that the model can achieve becomes increasingly good. However, the empirical performance of the model, the test error, has a minimum as a function of the control parameters. An over-complex model overfits the data and generalizes poorly. To avoid this difficulty, the experimental data can be divided into two sets, a training dataset and a test dataset. The model is produced using only the training data. The test data are then used to check that the model behaves itself when presented with previously unseen data. This is illustrated in Fig. 15.4 which shows three attempts at modeling noisy data for a case where y should vary with x^2. A linear model (Fig. 15.4(a)) is too simple and does not capture the real complexity in the data. An over-complex function such as that illustrated in Fig. 15.4(c) accurately models the training data but generalizes badly. The optimum model is illustrated in Fig. 15.4(b). The training and test errors are shown schematically in Fig. 15.4(d); not surprisingly, the training error tends to decrease continuously as the model complexity increases. It is

© Woodhead Publishing Limited, 2012



15.4 Variations in the test and training errors as a function of model complexity, for noisy data in a case where y should vary with x^2. The square points were used to create the models (i.e., they represent training data), and the diamonds constitute the test data. (a) A linear function which is too simple. (b) A quadratic polynomial with optimum representation of both the training and test data. (c) A fourth order polynomial which generalizes poorly. (d) Schematic illustration of the variation in the test and training errors as a function of the model complexity.

the minimum in the test error which enables that model to be chosen which generalizes best to unseen data.

15.3 On the quest of critical temperatures

Determination of allotropic transformation temperatures is an important issue in the design of heat treatments for optimizing microstructure and hence the final mechanical properties for a particular application. Because of its readiness and the large number of variables that can be considered

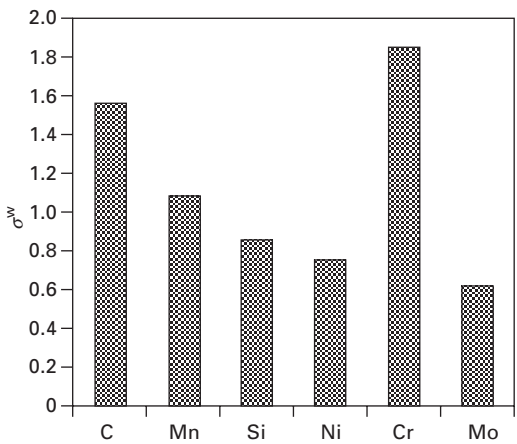
© Woodhead Publishing Limited, 2012

simultaneously, neural network modeling has been extensively used to determine the transformation temperatures. A review of the application of neural network models to the determination of phase transformation temperatures in steel is presented in this section.

15.3.1 Transformation during heating: austenite formation

One of the most important factors to take into account in designing a steel is the temperature at which austenite is the only stable phase present (Ae_3). This matter has been an objective of research for a long time, and the best known study, by Andrews (1965), proposed an empirical formula that works extremely well in a limited range of compositions. Artificial neural networks, based on a Bayesian framework, can be used to rationalize the published data on austenitizing temperature, Ae_3, in steels (Capdevila *et al.*, 2004). The Ae_3 model created in such a way allows the evolution of Ae_3 to be described with chemical composition. The analysis is empirical, but after appropriate training it is found to reproduce reliably known metallurgical experience. The method is useful because the optimized network summarizes knowledge in a quantitative manner and can be retrained as new data become available. The results predicted by the neural network model were validated from a thermodynamic perspective using the latest assessed thermodynamic data for steels from the MTDATA database (MTDATA, 1995).

Figure 15.5 illustrates the significance (σ_w) of each of the input variables, as perceived by the Ae_3 model, in influencing the Ae_3 temperature, within the limitations of the dataset. A high value of σ_w for a given input implies that this variable explains a relatively large amount of the variation in



15.5 Histogram showing the significance (σ_w) of input variables influencing the Ae_3 temperature as perceived by the model.

© Woodhead Publishing Limited, 2012

transformation temperature in the dataset (rather like a partial correlation coefficient in multiple regression analysis). It follows that the carbon content together with chromium content clearly has a large intrinsic effect, which is consistent with experimental evidence reported in the literature for decades. The manganese content in steel also has a significant effect on Ae_3 temperature, also as well established in the literature (US Steel, 1959), whilst the influence of silicon and nickel are moderate. By contrast, molybdenum has only a small effect.

The evolution of Ae_3 with varying compositions of carbon, chromium, silicon, manganese and nickel is shown in Fig. 15.6. The solid line represents the model predictions whilst the dashed lines represent the error bounds. It is clear from Fig. 15.6(b) that no phase transition from α to γ is possible for chromium content higher than 14 wt% since error bounds increase considerably. Likewise, a similar effect with increasing molybdenum content is detected, i.e. no $\alpha \rightarrow \gamma$ transformation for molybdenum content higher than 3.8 wt% is produced, which is in accordance with phase diagram assessments. Likewise, it is worth mentioning the change in tendency in Ae_3 temperature in Fig. 15.6(b) with chromium content. In this sense, a decrease in Ae_3 temperature is expected as chromium content increases up to 8 wt%, while a rise in Ae_3 temperature values is obtained for further addition of chromium, which is consistent with Fe-Cr binary phase diagram predictions. Figure 15.6(e) shows evolution of Ae_3 temperature with Mn content, while Fig. 15.6(f) shows the evolution of Ae_3 with increase in the nickel content. It is shown that Ae_3 temperature monotonically decreases as Mn and/or Ni content increase, which is in agreement with the respective binary phase diagrams.

The neural network model reported allows extension of the range of chemical compositions where the Andrews' formula (1965) is applicable. Therefore, the Ae_3 model could be used to derive an expression more general than the Andrews' one, as well as to account for the change of tendency when an eutectoid point is present. A paraboloid type equation, rather than linear, is found to be a better approximation to take into account the different tendency of the Ae_3 temperature once the eutectoid point is passed:

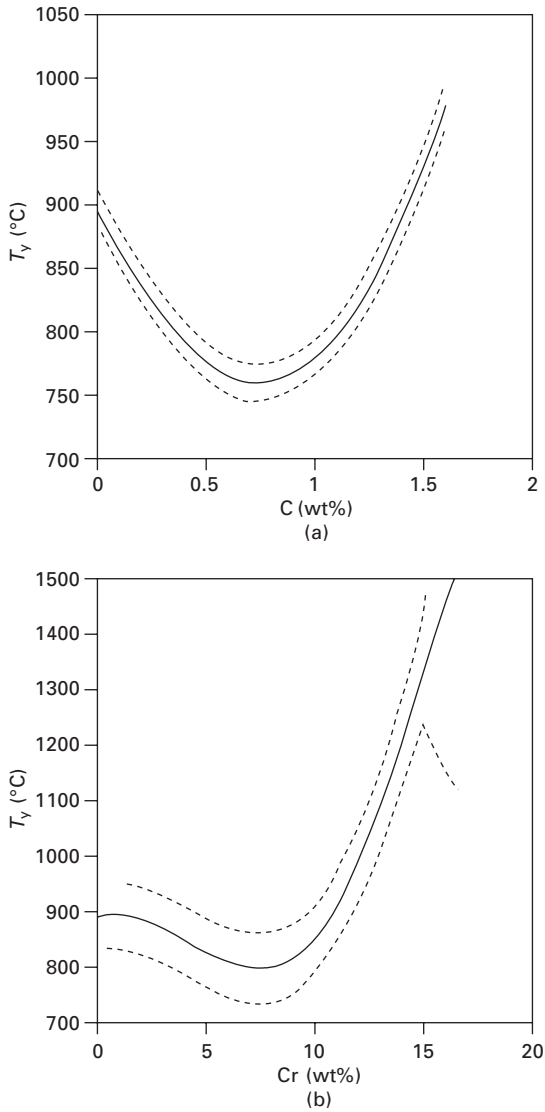
$$Ae_3 = To_I\, t_1\sqrt{C} + t_2X + t_3\,(CX) + t_4(C^2) + t_5(X^2) \qquad [15.9]$$

where To stands for the Ae_3 temperature for pure-iron, C and X stand for the mass percentage of carbon and other alloying elements, and t_i ($i = 1 \ldots 5$) represent fitting constants. The equation keeps the square root dependence for carbon proposed by Andrews, and it also includes terms that take into account the interaction of C-alloying element, CX, and a square dependence of both. The values of t_i are listed in Table 15.1.

So far, only the equilibrium ferrite–austenite transformation temperature

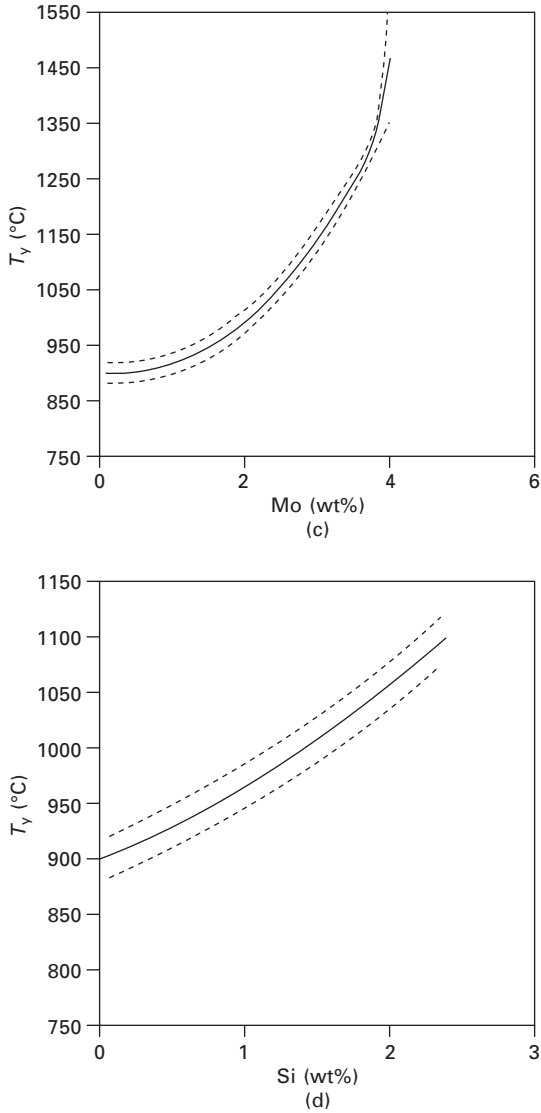
© Woodhead Publishing Limited, 2012

has been considered. The temperature at which austenite begins to form during the continuous heating of steel is termed the Ac_1 temperature, and that at which the steel becomes fully austenitic is the Ac_3 temperature, with $Ac_1 \geq Ae_1$ (equilibrium temperature at which austenite starts forming) and $Ac_3 \geq Ae_3$. There is another important difference between the transformation



15.6 Evolution of Ae_3 with (a) carbon, (b) chromium, (c) molybdenum, (d) silicon, (e) manganese and (f) nickel content.

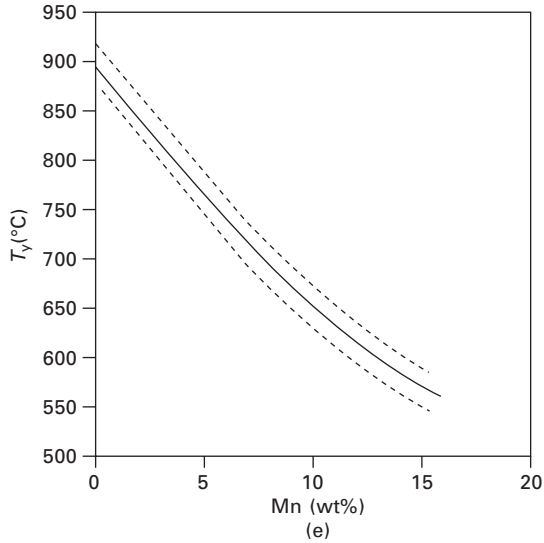
© Woodhead Publishing Limited, 2012

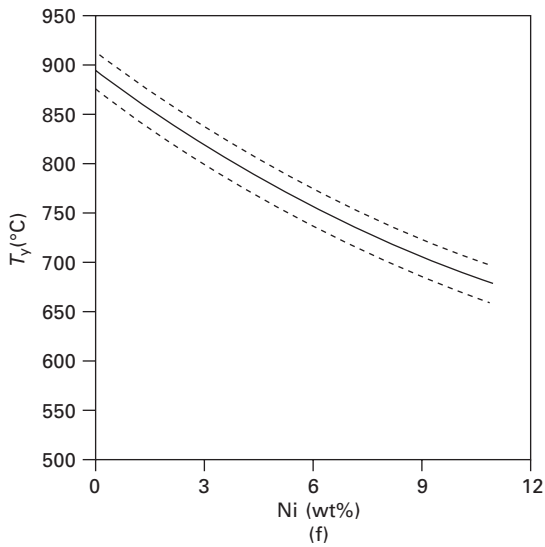


15.6 Continued

of austenite and the transformation to austenite. In the former case, the kinetics of transformation can be described completely in terms of the alloy composition and the austenite grain size. By contrast, the microstructure from which austenite may grow can be varied infinitely. Many more variables

© Woodhead Publishing Limited, 2012





15.6 Continued

are therefore needed to describe the kinetics of austenite formation. The extent to which the starting microstructure has to be specified remains to be determined, but factors such as the distribution and chemistry of individual phases, their size and homogeneity, the presence of non-metallic inclusions, should all be important. This discussion highlights the complexity of the

© Woodhead Publishing Limited, 2012

Table 15.1 Fitting parameters obtained for Eq. [15.9]

X	t_2	t_3	t_5
Cr	–5.7	30.2	1.3
Ni	–26.3	34.2	0.5
Si	64.7	–65.7	4.1
Mo	41.9	–4.2	10.9
Mn	–14.3	32.7	–8.4

Note: To = 922, t_1 = –233 and t_5 = 67.5 were fixed values.

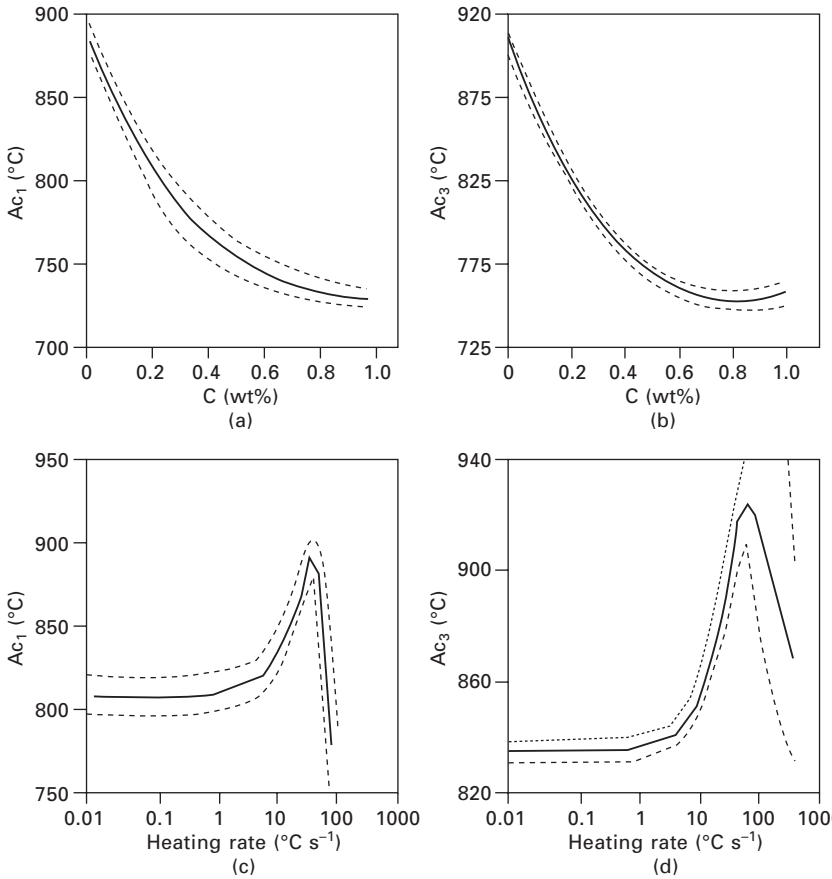
problem, and hence it is the sort of problem where the application of neural networks is potentially profitable.

Bailer-Jones *et al*. (1999) and Gavard *et al*. (1996) described this problem in Gaussian and neural network models, respectively. The models developed are found to be capable of estimating the transformation temperatures to an accuracy of about ± 40 K (95% confidence limits). Figure 15.7 illustrates the possibilities of a neural network approach through the predicted effects of the carbon concentration and heating rate on the Ac_1 and Ac_3 temperatures of plain carbon steel. The data presented as a function of carbon are calculated for a heating rate of 1 K s^{-1}. As might be expected, the Ac_1 temperature decreases with carbon concentration, reaching a limiting value which is very close to the eutectoid temperature of about 723°C. This limit is expected because of the slow heating rate and the fact that the test steel does not contain any substitutional solutes. Note that there is a slight under prediction of the Ac_1 temperature for pure iron, although the expected temperature of about 910°C is within the 95% confidence limits of the prediction (twice the width of the error limits illustrated in Fig. 15.7).

By contrast, the Ac_3 temperature appears to go through a minimum at about the eutectoid carbon concentration. This is also expected because the Ae_3 temperature also goes through a minimum at the eutectoid composition (see Fig. 15.6(a)). Furthermore, unlike the Ac_1 temperature, the minimum value of the calculated Ac_3 never reaches the eutectoid temperature; even at the slow heating rate it is expected that the austenite transformation finishes at some superheat above the eutectoid temperature, the superheat being reasonably predicted to be about 25 K.

Figure 15.8 shows the σ_w results as perceived by the model. The σ_w value for manganese is larger for the Ac_1 data than for the corresponding Ac_3 data. This is confirmed by the predicted effect of manganese on the transformation temperatures (Fig. 15.9), since the Ac_1 temperature is indeed found to be more sensitive to manganese than the Ac_3 temperature. This behavior is also expected from the Fe-C-Mn phase diagram. Whereas the effect of manganese on the Ac_3 temperature is simply to lower the $(\alpha + \gamma)/\gamma$ phase boundary on the temperature scale (via the thermodynamic effect of manganese on austenite

© Woodhead Publishing Limited, 2012



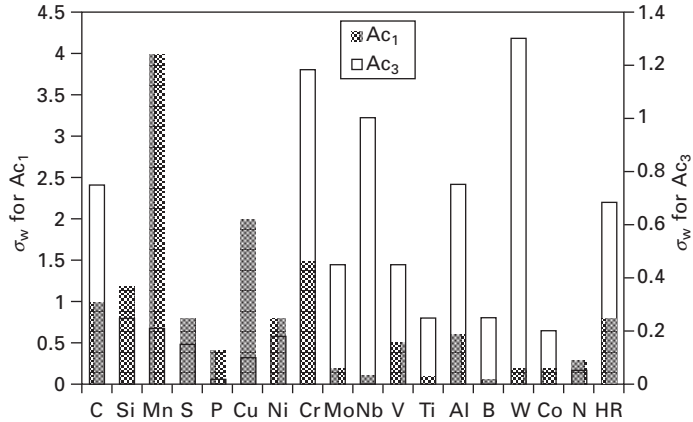
15.7 Predicted variation in Ac_1 (a,c) and Ac_3 (b,d) temperatures with carbon concentration (a) and (b), and heating rate (c) and (d). Lines represent ±1°′ error bars about calculated points (after Gavard *et al.*, 1996). Heating rate for (a) and (b) is 1°C s^{-1}.

stability), the influence on Ac_1 is much larger since a three-phase $\alpha + \gamma + M_3C$ field develops, as was confirmed by phase diagram calculations carried out using the MTDATA thermodynamic package (MTDATA, 1995).

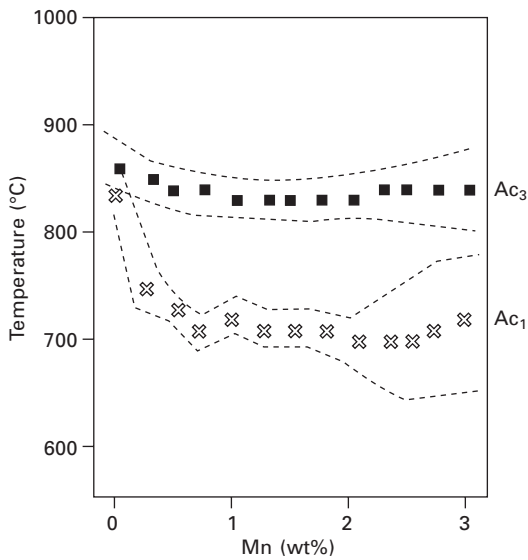
15.3.2 Bainite formation

Both for their mechanical properties and low costs, bainitic steels are finding an increasing number of applications, ranging from railway track to Formula 1 racing car gearboxes. A common observation is that the bainite start temperature is very sensitive to the chemical composition (Bhadeshia, 1992), indicating that the influence of solutes is more than just thermodynamic. The bainitic structure develops at temperatures between that for pearlite

© Woodhead Publishing Limited, 2012



15.8 Significances σ_w perceived by the model of each input variable influencing either Ac_1 or Ac_3 temperatures (after Gavard *et al.,* 1996).



15.9 Model predictions for varying Mn content in a Fe-0.2C steel. Heating rate of 1 K s^{-1} (after Bailer-Jones *et al.,* 1999). Squares and crosses represent predictions and dashed lines the error.

formation and the martensite start temperature. The exact value of these temperatures strongly depends on the elements present in the steel, and considerable work has been devoted to developing quantitative models for their compositional dependency.

Early approaches for predicting the bainite start temperature (B_s) essentially consisted in the fitting of simple linear empirical relationships

© Woodhead Publishing Limited, 2012

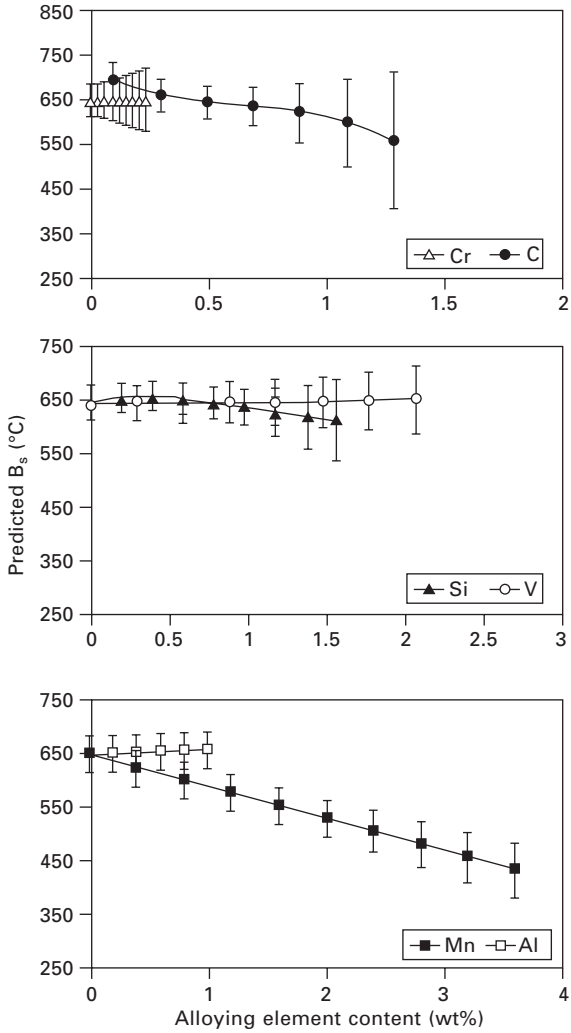
(Kunitake and Okada, 1998; Lee, 2002). Though easily communicated and interpreted, such methods often have very limited ranges of applicability because of their inability to incorporate interactions or non-linear effects. With the development of calculation frameworks such as CALPHAD, which allow prediction of thermodynamic properties of complex systems from data collected on simpler ones, more physically relevant approaches relying on the satisfaction of some thermodynamic criteria have gained importance (Olson and Cohen, 1976). In general, such models extrapolate considerably better than the earlier empirical approaches. They do, however, still suffer a number of drawbacks:

- Being essentially self-consistent, these approaches require that identical thermodynamic databases be used in the predictions as those which were used for the derivation of the criteria. With the multiplication of databases (SGTE SSOL (MTDATA, 1995), NPL plus (MTDATA, 1995), TCFE (Thermo-Calc, 1984)), this is increasingly becoming a problem.
- Such approaches rely on the availability of expensive thermodynamic calculation software, the costs of which are hardly justified for such an application alone.
- The empirical component is not eliminated but displaced to lower levels of the model.

The model reported by Garcia-Mateo *et al*. (2005) takes advantage of neural network analysis to offer attractive advantages such as covering arbitrarily large ranges of data, and a feature unique to the method employed, which is the ability of the model to accompany its predictions by an indication of their reliability. As was illustrated in Fig. 15.3, where sufficient data is available, the uncertainty is small, and it becomes larger where there is a lack of it. Very illustrative of this is the influence of Cr, Mo, W and C at high concentrations (see Fig. 15.10).

The results presented in Fig. 15.10 allow us to distinguish the alloying elements according to their influence on the bainite start temperature (B_s). Thus, the general lineal trend of reducing transformation temperature for the elements C, Mn, Ni, W and Mo is that also observed by other authors (Steven and Haynes, 1956; Bodnar *et al*., 1989). Another group of elements that increase the bainitic transformation temperature would be those of Co, Al and V; in this case, the only reference found to record this influence (Zhao *et al*., 2001) is opposite to that just described. There is only one element, Cu, that has no influence on B_s, in the limited range of compositions studied. Finally, there is a group of elements that cannot be described in terms of a simple linear relationship. Up to additions of about 0.5 wt% of Si, the B_s increases, above that concentration a decrease in this temperature is predicted. This behavior would explain the fact that in different empirical formulae, in the fitting of simple linear relationships the influence of Si is either neglected

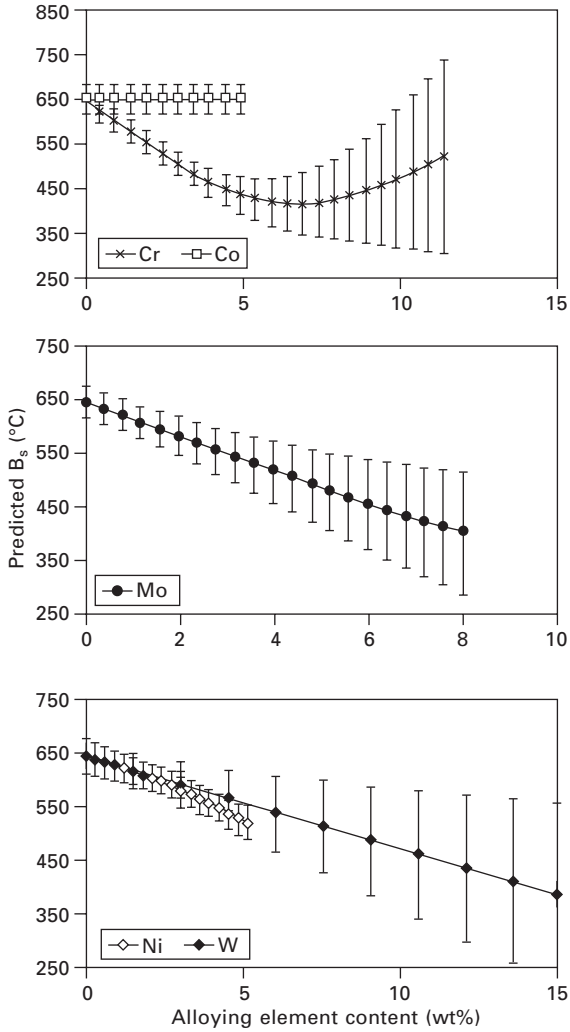
© Woodhead Publishing Limited, 2012



15.10 Effect of alloying elements on the B_s temperature in Fe-0.4 C-X wt% steels and the binary system Fe-C for C influence, according to the neural network model created by Garcia-Mateo *et al.* (2005).

or it has different signs. Another case of non-linear behavior is shown by Cr, although the error bars become larger as the concentration increases and in consequence no accurate description of the effect can be predicted; the general trend is a reduction in Cr influence above concentrations of 3–4 wt%.

© Woodhead Publishing Limited, 2012



15.10 Continued

15.3.3 Martensite start temperature

There is considerable industrial interest in being able to predict reliably the temperature at which austenite transforms to martensite (M_s). For this reason, a significant amount of work has been devoted to obtaining quantitatively accurate models for predicting M_s. This temperature is typically a function of a number of variables which may include stress or magnetic field. From a material's point of view, the M_s temperature is essentially controlled by the composition of the steel, although the austenitizing state, external stresses and stored deformation energy may sometimes play an important role as well.

© Woodhead Publishing Limited, 2012

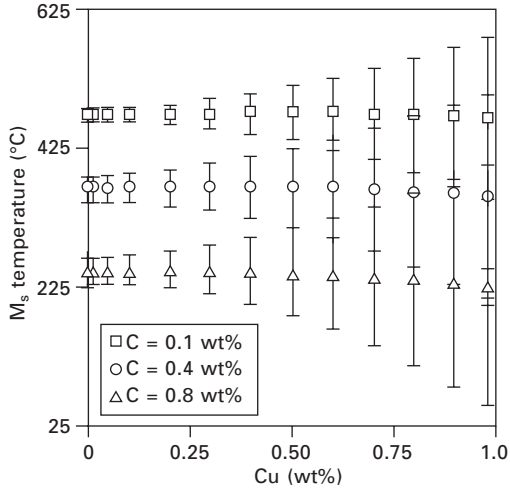
Martensite start temperatures are usually relatively easy to calculate as long as the steels have low alloy content (Kung and Rayment, 1978; Wang *et al.*, 2000). Even though empirical equations exist for high alloy steels, they are not sufficiently general and are known to provide inaccurate answers for the new steels which contain different alloying elements, or their compositional ranges are out of bounds of those used to formulate the equations.

Capdevila *et al.* (2002, 2003) outlined the use of an artificial neural network to model the calculation of M_s temperature in engineering steels from their chemical composition (M_s model). In a recent assessment of the existing models for predicting the M_s temperature of steels as a function of their compositions, Sourmail and Garcia-Mateo (2005) showed that, from an applied point of view, the neural network model proposed by Capdevila *et al.* (2002, 2003) performed at least as well as the thermodynamic models proposed by Ghosh and Olson (1994a, 1994b, 2002). Furthermore, the former is freely available as a standalone computer program (Capdevila *et al.*, 2000).

The M_s model can be used to disclose the role of certain elements that are added to steel grades looking for an improvement of in-use properties. For instance, the interest in copper additions to the chemical composition of steels has increased in recent years. Copper-bearing low carbon steels are used in heavy engineering applications which demand combinations of strength, toughness and weldability (Foularis *et al.*, 1996; Pereloma and Boyd, 1996; Thompson *et al.*, 1996; Banerjee *et al.*, 2001). Strength is achieved by precipitation of fine copper precipitates during aging, instead of the precipitation of carbide particles (Depaul and Kitchen, 1970). Therefore, copper is not in this respect different from any secondary hardening element in steels. Likewise, it has been demonstrated that copper sulfide strongly enhances acicular ferrite formation, which induces a good combination of mechanical properties as compared to conventional bainite and, especially, to ferrite-pearlite microstructures (Madariaga and Gutierrez, 1999; Madariaga *et al.*, 1999; García de Andrés *et al.*, 2001). Figure 15.11 shows the prediction of the evolution of M_s with copper additions according to the M_s model.

Likewise, some power plant steels are in the near future required to operate with steam temperatures in excess of 873 K. The steels currently being developed to cope with these requirements contain a total solute concentration which is often in excess of 14 wt%. The main solutes include carbide-forming elements such as chromium and molybdenum. Chromium also provides the necessary corrosion and oxidation resistance for prolonged elevated temperature service. The main alloys under consideration include numerous variants of the classical 12Cr-1Mo and 9Cr-1Mo steels (Sikka *et al.*, 1983). An important variant of the 9Cr-1Mo steel is that in which tungsten is added to induce precipitation hardening (Abe, 2001). Gustafson and Ågren (2001) reported that Co has a remarkable influence on coarsening

© Woodhead Publishing Limited, 2012



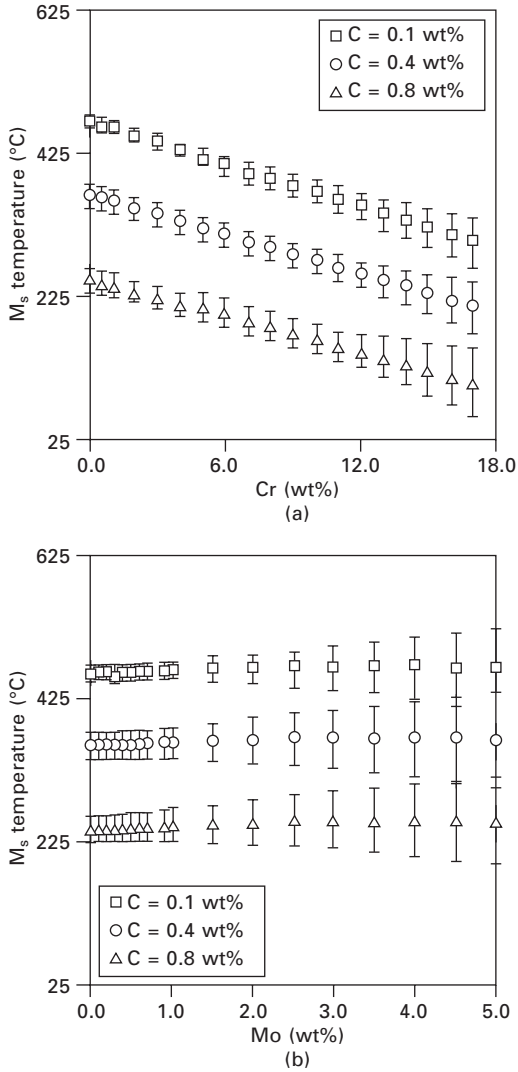
15.11 Influence of Cu on M_s temperature for different carbon grades (after Capdevila *et al.*, 2002, 2003).

of $M_{23}C_6$ carbides in the 9Cr-1Mo steel. Their results show that a final average radius of the carbides after 30 000 h at 873 K decreases by 30% with a Co addition of 10 mass%. This raises the Orowan stress by 30%. Moreover, it is assumed that slower particle coarsening also leads to a retardation in the coarsening of the martensite lath structure. Thus, an improvement in creep life of the steels is expected (Gustafson and Ågren, 2001). Likewise, it has been reported that the combined additions of cobalt and tungsten to the chemical composition strengthen the steel by precipitation of tungsten-cobalt (WC-Co) cemented carbides (Lisovskii, 2001). These new power plant steels are also widely used as tool steels where a good combination of abrasion resistance and corrosion resistance is required (Kwok *et al.*, 2001).

The M_s temperature of Cr-Mo steels is of considerable importance for the exact welding conditions necessary to avoid cracking (Abe, 2001; Kwok *et al.*, 2001). It then follows that how molybdenum, tungsten, and cobalt additions affect the M_s temperature is an important issue. The M_s model can be used to disclose the role of each of these elements on M_s temperature. In this sense, Fig. 15.12 illustrates the variation of M_s with combinations of Cr, Mo and W.

Since M_s temperature can thus be a key design parameter in new steel grades, it is interesting to derive a generalized equation similar to that obtained by Andrews (1965) and expressed in Eq. [15.1]. Although the relationship between the martensite start transformation and steel composition was investigated previously by Grange and Stewart (1946), Payson and Savage (1944) and Kung and Rayment (1978), it was the study by Andrews (1956)

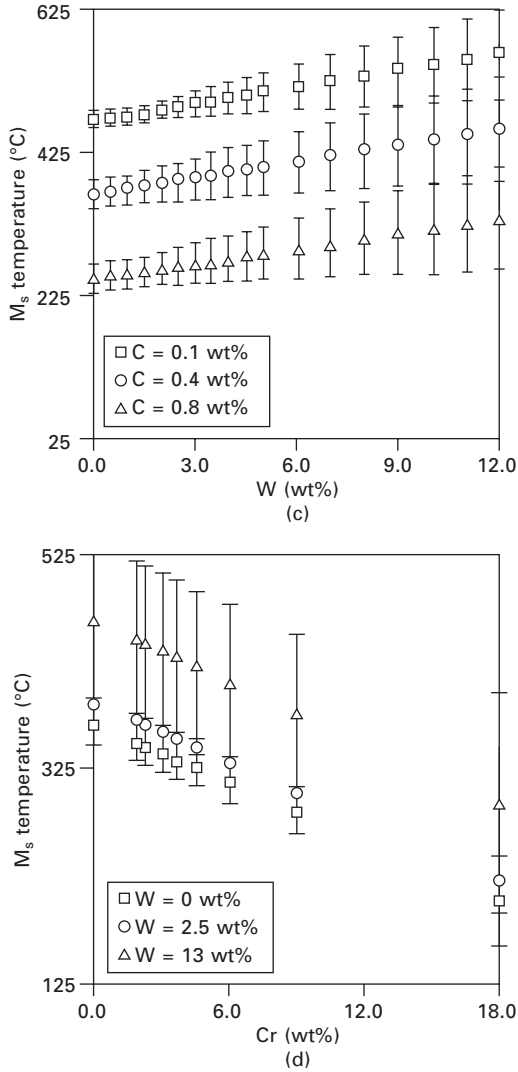
© Woodhead Publishing Limited, 2012



15.12 Influence of (a) Cr, (b) Mo, (c) W and (d) Cr-W on M_s temperature for different carbon grades (after Capdevila *et al.*, 2002, 2003).

which has proved most reliable because it considered the largest number of samples. In order to find a similar linear dependence of M_s upon chemical composition to that obtained by Andrews (1956), the results from the M_s model were plotted by pairs of elements (C-Mn, C-Ni, C-Cu, C-W, C-Co, C-Cr, and C-Mo). These values are fitted to a plane regression equation ($M_s = y_o + ax + by$, where x corresponds to carbon concentration values in

© Woodhead Publishing Limited, 2012



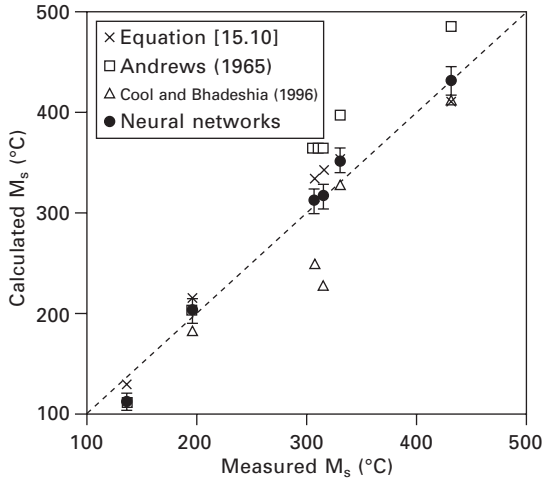
15.12 Continued

wt%, and y corresponds to the alloying element) by non-linear regression analysis. Therefore, the relative effect of other alloying elements is indicated in the following empirical relationship obtained from the neural network analysis:

$$M_s(K) = 764.2 - 302.6w_C - 30.6w_{Mn} - 16.6w_{Ni} - 8.9w_{Cr} + 2.4w_{Mo} - 11.3w_{Cu} + 8.58w_{Co} + 7.4w_W - 14.5w_{Si} \quad [15.10]$$

Figure 15.13 shows a comparison between the predictions from Andrews'

© Woodhead Publishing Limited, 2012



15.13 Comparison between results predicted by Eq. [15.10], Andrews (1965) Eq. [15.1], Cool and Bhadeshia (1996) model and M_s model reported by Capdevila *et al.* (2002, 2003).

Table 15.2 Chemical composition of the six steels analyzed

	C	Mn	Si	Cr	Ni	W	Co	Mo	V	Al	Cu	Nb	Ti
S1	0.45	0.4	0.32	13.0	0.38	0	0	0	0	0	0	0	0
S2	0.8	3.52	1.67	1.1	0	0.99	1.44	0.24	0	0.01	0	0	0
S3	0.07	1.5	0.37	0.039	0.49	0	0	0.021	0.004	0.045	0.04	0.03	0.01
S4	0.31	1.22	0.253	0.138	0.098	0	0	0.03	0.004	0	0	0	0
S5	0.09	1.03	0.16	9.1	0.99	0	0	0.99	0.19	0	0	0.04	0
S6	0.09	0.99	0.18	8.94	0	0.98	1.87	0.96	0.18	1.87	0	0.05	0

empirical equation (Eq. [15.1]), Cool and Bhadeshia (1996) for M_s temperature, and from Eq. [15.10]. This analysis is performed in six very different alloys whose actual compositions are listed in Table 15.2. S1 is a commercial martensitic stainless steel, S2 is a high carbon high strength steel, S3 is a low carbon HSLA steel, S4 is a medium carbon forging steel, and S5 and S6 are both power plant ferritic steels. All of these steels are used for commercial purposes, and therefore, the M_s temperature is a critical parameter whose accurate determination is very important in the processing route of the steel. It could be concluded from the figure that the neural network model provides the most accurate M_s temperature predictions.

15.4 Determining microstructural parameters

Several models are reported in the literature to deal with microstructural parameters resulting from phase transformations in steels. In this section,

© Woodhead Publishing Limited, 2012

neural network models dealing with the microstructural parameters of the interlamellar spacing of pearlite and bainite plate thickness are described.

15.4.1 Interlamellar spacing of pearlite

Interlamellar spacing is one of the most fundamental parameters which characterize a pearlitic microstructure. The wide range of mechanical properties of pearlitic microstructures, and hence a main reason as to why ferrite-pearlite steels are by far the most utilized structural alloys in the world, are intrinsically related to the pearlite interlamellar spacing. It is therefore not surprising that the influence of alloying elements and cooling conditions on the interlamellar spacing of pearlite has been reported upon for decades (Zener, 1946; Munirajulu *et al.*, 1994). In addition, the role of interlamellar spacing on austenite formation during isothermal and continuous heating has also been reported more recently (Caballero *et al.*, 2001a, 2001b). Thus, the study of factors affecting the interlamellar spacing during transformation to pearlite remains an interesting topic. Implementation of the neural networks models allow the role of parameters to be evaluated individually.

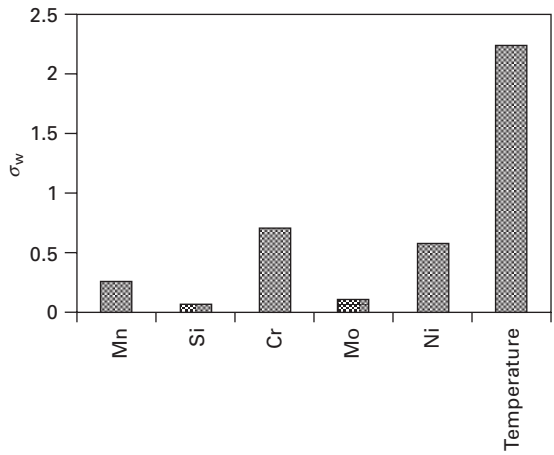
The first caution for neural network modeling of the interlamellar spacing of pearlite is the definition of interlamellar spacing itself, and the concomitant database considered. There is experimental evidence for pearlites produced under isothermal conditions that the true spacing is not the minimum spacing observed in metallographically prepared surfaces. The average minimum observed spacing (S_o), taken from several colonies, is a perpendicular distance across two adjacent lamellae, i.e. ferrite and cementite. The true spacing does not have a constant value but is a distribution of spacings about a mean true value. It is clear that the factor which relates the minimum and mean true spacing is not constant and may vary from system to system, and with temperature in a given system. It is because of the uncertainty in the relationship between the minimum and mean true spacing that the minimum spacing which can be both readily and reproducibly measured, is the most representative to characterize the structure. Assuming these considerations a neural network model based on compiled data for minimum interlamellar spacings has been described recently (Capdevila *et al.*, 2005a, 2005b). It was also considered that the interlamellar spacing of pearlite ideally requires a complete description of the chemical composition and the isothermal transformation temperature. Table 15.3 shows the list of six input variables considered in the S_o model.

Figure 15.14 illustrates the significance (σ_w) of each of the input variables, as perceived by the S_o model, in influencing the interlamellar spacing of pearlite. The temperature clearly has a large intrinsic effect, which is consistent with experimental evidence reported in the literature for decades. The content of chromium and nickel in the steel also have a large effect on

© Woodhead Publishing Limited, 2012

Table 15.3 Variables that influence pearlite growth rate

	Minimum	Maximum	Average	Standard deviation
Mn (wt%)	0.00	1.80	0.4460	0.6695
Si (wt%)	0.00	1.94	0.1179	0.4210
Cr (wt%)	0.00	9.00	3.4975	0.7441
Mo (wt%)	0.00	0.48	0.0473	0.1319
Ni (wt%)	0.00	3.00	1.4085	0.8897
T (°C)	567.00	802.00	660.6986	40.9968
Log S_o (μm/s)	–1.4473	–0.0969	–0.9082	0.3082



15.14 Histogram showing measure of model's perceived significance of input variables in influencing interlamellar spacing.

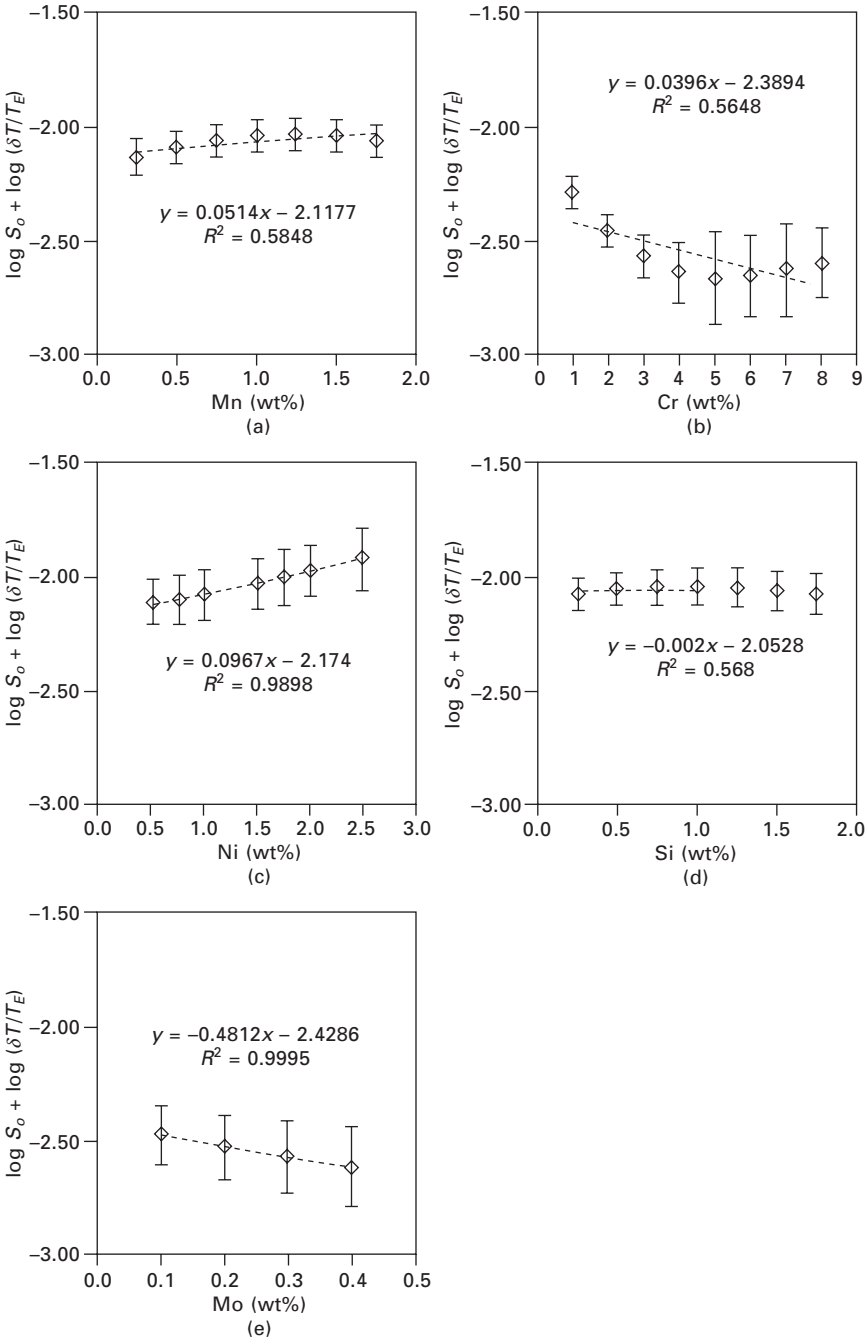
pearlite interlamellar spacing, as has been well established in the literature (Al-Salman *et al.*, 1979; Sharma *et al.*, 1979; Hashiguchi and Kirkaldy, 1984), whereas the influence of manganese is more moderate. On the other hand, silicon and molybdenum have only a small effect. It is also possible that the effects of silicon and molybdenum are higher at concentration levels above those considered in Fig. 15.14.

The straightforward application of the S_o model is to determine an empirical expression for the interlamellar spacing as a function of the chemical composition, which, following the Zener criterion (Zener, 1946; Hillert, 1957) for Fe-C-X steels, could be expressed as:

$$y \equiv \log S_o + \log\left(\frac{T_E - T}{T_E}\right) = c + \sum_i b_i[X_i] \qquad [15.11]$$

where $[X_i]$ is the alloy content in wt%, and c and b are constants. Figure 15.15 shows the evolution of the factor $\log S_o + \log(T_E - T/T_E)$ with different

© Woodhead Publishing Limited, 2012



15.15 Evolution of the factor log S_o + log(T_E – T/T_E) (Eq. [15.11]) with (a) Mn, (b) Cr, (c) Ni, (d) Si, and (e) Mo.

© Woodhead Publishing Limited, 2012

contents of Mn, Cr, Ni, Si and Mo. The fitting of the data presented in Fig. 15.15 to a straight line leads to an equation for the interlamellar spacing which represents the dependence of such a parameter on the chemical composition of the steel:

$$\ln S_o = -2.212 + 0.0514 \times [\text{Mn}] - 0.0396 \times [\text{Cr}] + 0.0967 \times [\text{Ni}] - 0.002 \times [\text{Si}] - 0.4812 \times [\text{Mo}] - \ln\left(\frac{T_E - T}{T_E}\right) \quad [15.12]$$

where S_o is measured in μm, and [Mn], [Cr], [Ni], [Si], and [Mo] are the alloy content in wt%, respectively. It is noted that the addition of Cr or Mo decreases the interlamellar spacing as observed in many other alloys, whereas additions of Mn and Ni cause an increase in interlamellar spacing. Silicon, however, has a slight influence on interlamellar spacing, although the tendency indicates a decrease with increasing silicon content.

On the other hand, Eq. [15.12] could be rewritten as,

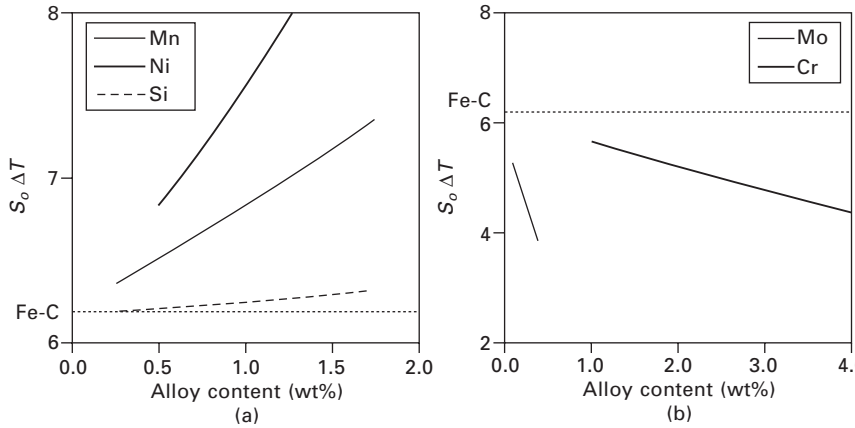
$$S_o \Delta T = T_E \left(10^{-2.212 + \sum_i b_i [X_i]}\right) \quad [15.13]$$

where $[X_i]$ represents the concentrations of alloying elements, and b_i is a constant. This equation leads to a value of $S_o\Delta T = 6.23$ for plain carbon steels, which is in excellent agreement with that proposed by Cheetham and Ridley (1973) ($S_o\Delta T = 6.19$). Figure 15.16 presents the evolution of the $S_o\Delta T$ factor as a function of alloy composition for those elements which are strong carbide formers, such as Cr and Mo, and those which stabilize the austenite, such as Mn and Ni. Likewise, Fig. 15.16 presents the evolution of reciprocal spacing values with temperature for different alloy compositions. Values for plain carbon steels are also plotted for comparison. In general, it is clear from this figure that strong carbide formers, such as Cr and Mo, tend to decrease the $S_o\Delta T$ factor, and therefore induce lower values of spacing. On the other hand, austenite stabilizer elements, such as Mn and Ni, tend to increase the $S_o\Delta T$ factor, and thus induce higher values of spacing.

15.4.2 Bainite plate thickness

The microstructure of bainite consists of fine plates of ferrite, growing in clusters known as sheaves. Within each sheaf, the plates are parallel and in identical crystallographic orientation, each with a well-defined crystallographic habit plane. Their thickness is typically a fraction of a micrometer. Since it is the thickness rather than the plate length that primarily determines the mean free slip distance (Daigne *et al.*, 1982), there is considerable technological interest in understanding and controlling the scale of the microstructure.

© Woodhead Publishing Limited, 2012



15.16 Evolution of $S_o \Delta T$ factor as content of (a) Mn, Ni and Si increases, and (b) Cr and Mo increases. Dotted lines indicate the plain carbon steel.

It was noticed during early studies that the growth of bainite causes displacements which can, on a macroscopic scale, be described by an invariant plane strain (IPS). The invariant plane is the habit plane of the plate (Ko and Cottrell, 1952; Srinivasan and Wayman, 1968). From these observations, taking one description of the transformation gives a basis for developing a neural network model to predict the plate thickness dimension. The strain is a large shear deformation (≈ 0.26) on the habit plane and a smaller dilatational strain (≈ 0.03) directed normal to the habit plane. The magnitude of these strains is so large that this description requires the transformation product to be constrained in the form of a thin plate, a shape which minimizes the strain energy when the plate is elastically accommodated. The shape change is not expected to be fully elastically accommodated, particularly when the bainite transformation occurs at an elevated temperature where the austenite has lower yield strength and plastic relaxation can thus occur in the austenite adjacent to the plate. But the dislocation debris associated with the plastic deformation is expected to resist the further advance of the interface, the resistance being largest when the austenite is strong. Consequently, it follows that the strength of austenite must be an important factor in controlling the ultimate thickness of bainite plates.

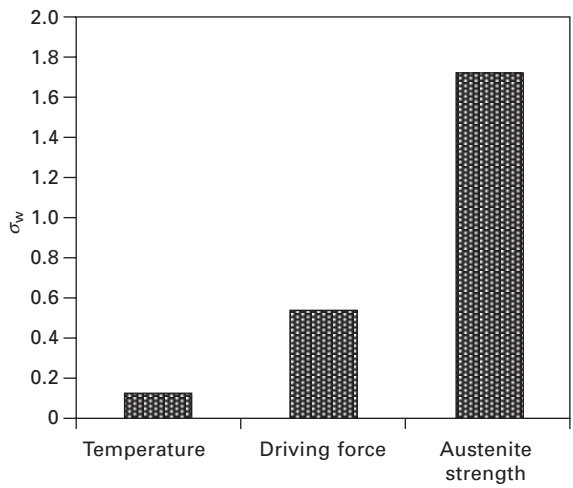
The plates are expected to be thicker at higher temperatures, when the yield strength of the austenite remains low in spite of the plastic relaxation. Dynamic recovery may also play a role but since this can only weaken the austenite, its effect will be similar to that of the temperature dependence of the yield strength. On the other hand, if the austenite is sufficiently strong, then the plates are expected to be more fully elastically accommodated. They may then, in the limit, maintain elastic equilibrium with the matrix, continuing

© Woodhead Publishing Limited, 2012

to thicken until the strain energy balances the available free energy. If the plates were allowed to grow freely (i.e., without impingement) they would then be expected to be thicker at lower temperatures, where the driving force is largest. Not surprisingly, this contradicts the experimental data which therefore suggests that bainite is certainly not in thermoelastic equilibrium with the matrix. There is a further effect concerned with impingement models between adjacent plates of growing new phase which might determine the size of bainite plates; a large nucleation rate must naturally refine the microstructure.

From the above description it follows that the three most important factors that influence the bainite thickness are the austenite strength, temperature, and driving force. But, the explicit dependence of the thickness on these variables is not known. The usual regression methods do not help in this respect since they require an assumed relationship to begin the analysis. Therefore, the neural network approach can be adopted as it does not require a prior choice of the relationship between the input and output variables. This approach was taken by Mukherjee and Singh (2009) who reported a neural network model to predict the bainite plate thickness as a function of the aforementioned variables; austenite strength, temperature and driving force.

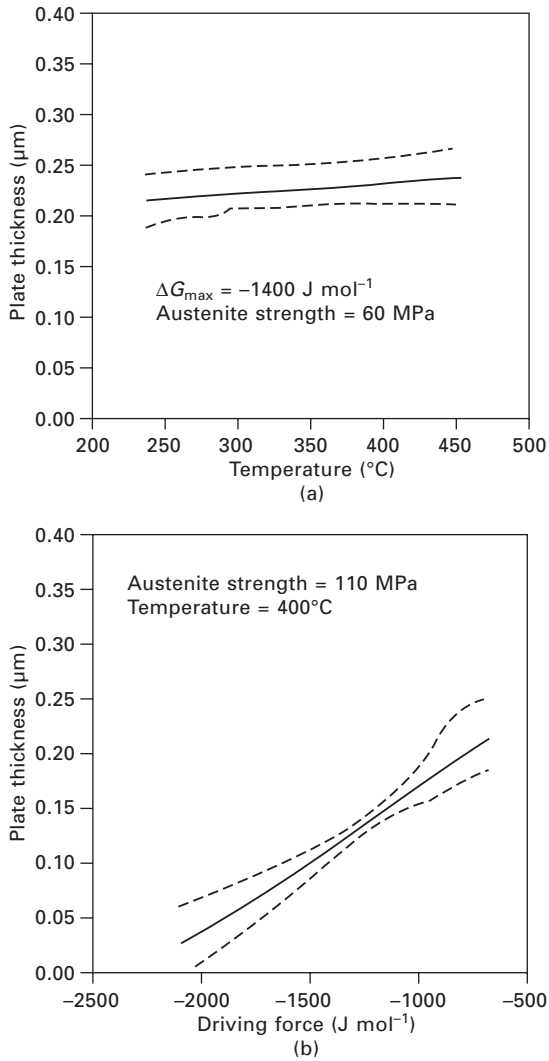
Figure 15.17 illustrates the significance (σ_w) of each of the variables, as perceived by the neural network, in influencing the plate thickness of bainite. Thus, it is interesting to note that a large part of the variation in the bainite plate thickness dataset can be explained by the variation in the



15.17 The model's perceived significance of the input variables in influencing the bainite plate thickness (after Singh and Bhadeshia, 1998).

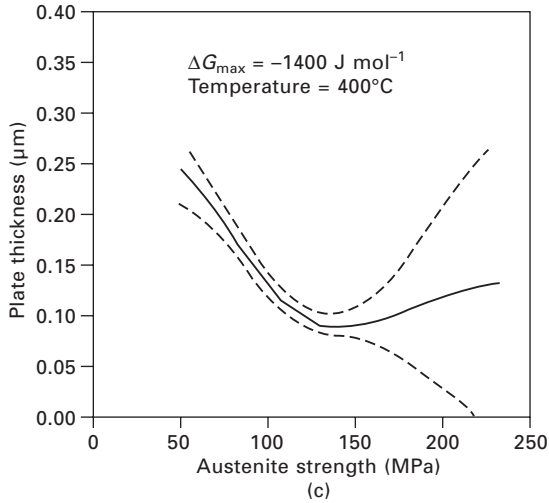
© Woodhead Publishing Limited, 2012

austenite strength. The sensitivity of plate thickness to these three variables is illustrated for silicon-rich steels (Singh and Bhadeshia, 1998); Fig. 15.18 shows that the thickness of bainite plates in silicon-rich steels depends primarily on the strength of the austenite at the transformation temperature, and the chemical free energy change accompanying transformation. This conclusion applied specifically when the shape deformation causes plastic



15.18 Variation of bainite plate thickness with (a) transformation temperature, (b) transformation driving force, and (c) austenite strength. Dashed lines indicate error bars about calculated points (after Singh and Bhadeshia, 1998).

© Woodhead Publishing Limited, 2012



15.18 Continued

strain in the adjacent austenite. It indicates that strong austenite or a large driving force results in finer plates, the former because there is a larger resistance to interface motion and the latter because an increased nucleation rate leads to microstructural refinement. Temperature does not, in its own right, seem to have a significant effect over the range 260–460°C, but it is possible that this situation could change if dynamic recovery effects become prominent.

15.5 Development of continuous cooling transformation (CCT) diagrams

For common heat treatment practice, knowledge of the phase transformation behavior of steels is crucial, since it enables the control of the structure and properties of the final product. This transformation behavior is commonly summarized in a continuous cooling transformation (CCT) diagram, which, for a single steel composition, gives the phase regions, as well as the fractions of microstructural components and hardness after cooling as a function of the cooling path followed. The cooling takes place at an approximately constant cooling rate, i.e. tests are performed in such a way that the effects of the heat release due to the transformations are small.

The measurement of a CCT diagram is a complex task. For one CCT diagram a large number of experiments (usually dilatometric or calorimetric) is needed, and the specimens need to be examined metallographically after cooling. Hence the full determination of a CCT diagram is time consuming and difficult. Additionally, large measurement errors can occur, since the

© Woodhead Publishing Limited, 2012

experimental results (dilatometer and calorimeter measurements) are indirect and not straightforward to interpret unambiguously. To be able to quantify aspects of the steel transformation behavior as described by a CCT diagram without performing the actual measurements, significant efforts have been undertaken to model the steel transformation behavior. Both physical and statistical approaches have been followed, yet both approaches have not yet yielded sufficiently accurate results. The two major difficulties in modeling are the fact that the metallurgical phenomena are only partially understood due to their complexity and mutual interactions, and the large measurement errors present in the CCT diagrams. Artificial neural networks have thus been established as a potential method for predicting austenite transformation using the chemical composition, the austenitization temperature and cooling rate as input (van der Wolk *et al*., 2002; Dobrzanski and Trzaska, 2003; Ghosh *et al*., 2008).

Ghosh *et al*. (2008) presented a neural network model to predict the effect of Ti, B, Cu and Ni on CCT diagrams of low carbon (0.04–0.05 wt%) steels. The predicted results were validated with dilatometric and metallographic studies to compare the phase fields in different CCT diagrams, demonstrating that in Ni containing 1.5 wt% Cu-added Ti–B microalloyed steel, it is possible to achieve dual-phase (ferrite–martensite) microstructures in the directly air-cooled condition (i.e., at cooling rates close to 1°C/s) by suppressing pearlite formation. It was also demonstrated that Cu addition remarkably improves the hardness of the directly air-cooled Cu-added Ti–B microalloyed steel.

Additionally, Dobrzanski and Trzaska (2003) have reported a method of forecasting CCT diagrams for steels by the use of neural network modeling. Input data are chemical composition and austenitizing temperature. Results of the neural networks calculation consist of the temperature of beginning and end of transformation as a function of cooling rate. Dobrzanski and Trzaska (2003) took advantage of two applications of neural networks: classification and regression. Thus the CCT diagram calculation process was divided into two stages. In the first stage the austenite decomposition products formed during cooling were determined, i.e. if ferrite, pearlite, bainite, and/or martensitic transformation took place. The range of the cooling duration time, characteristic range of cooling times for particular transformations, and types of microstructure constituents occurring in the steel after cooling were determined as a result of the classification process. Further, temperature values were calculated for the beginning and end of the particular transformations for each of the analyzed cooling rates. Information regarding the types of microstructure constituents that formed in the steel as a result of cooling at a particular rate was used to determine steel hardness and volume fraction: for ferrite, pearlite, bainite, and martensite with retained austenite. The method consists of: determining the types of transformations occurring at given cooling rates (classification), calculating the critical temperatures of

© Woodhead Publishing Limited, 2012

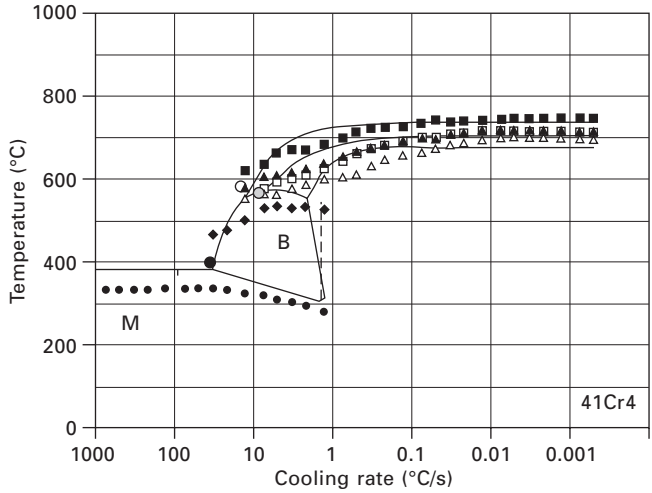
transformations (Ac_1, Ac_3, M_s, B_s), calculating time to the beginning and the end of the particular transformations as functions of cooling rate, and calculating hardness and volume fraction of the particular microstructural constituents as functions of cooling rate. The outputs feature data that unequivocally define the form of the CCT diagram and are the basis of its graphical representation.

Vermeulen *et al*. (1996) has shown for vanadium-containing steels that neural networks are a type of statistical model very suitable for predicting transformation start and end lines in CCT diagrams. However, his model is based on a small amount of data only, which limits its application range. This limitation was alleviated by the model presented by van der Wolk (1994) and van der Wolk *et al*. (2002). They reported a CCT diagram model consisting of two neural networks: a phase region network and a critical cooling rate network. Both neural networks were three-layered feed-forward hierarchical neural networks (van der Wolk, 1994). The networks were adapted to cope with 'undefined' output values in the fit procedure by defining the difference between a calculated output value and a 'not defined' value to be zero for such a parameter, so that the fit parameters in the model are not adjusted for these 'not defined' output values. Since the number of independent parameters is large compared to the number of experimental CCT diagrams available for the model, a special fit procedure was used for the calibration of both networks which uses all available data. The steel compositions of the available diagrams were examined to determine which alloying elements were present at a sufficient level to be used as input parameters. Furthermore, the range of input parameters has been limited. The alloying elements Nb, W, B, Ti, N, S, P, and rare earth elements were not used in the model. On the other hand, the phase region network has as the input parameters austenitizing temperature and the alloying contents of C, Si, Mn, Cr, Mo, Ni, V, Al and Cu. The output parameters are start and end temperature for ferrite, pearlite, and bainite formation, and the martensite start temperature for 32 cooling rates. The comparison for 41Cr4 steel (0.41%C- 0.25%Si-0.71%Mn-0.22%Ni) is shown in Fig. 15.19, where the model also corresponds rather well with the original data; all predicted temperature values are slightly lower than the original data; the largest error, approximately 50°C, is in the martensite start temperature.

15.6 Conclusions and future trends

Neural networks have had a significant impact on predicting the phase transformation in steels and in the subsequent implementation of steel processing. This is because they represent a transparent and quantitative method which is able to deal with sophisticated problems typical in materials science. There are therefore efforts to estimate the influence of chemical composition

© Woodhead Publishing Limited, 2012



15.19 The CCT diagram used for calibration (solid lines) and the calculated CCT diagram (ferrite is indicated by squares, pearlite by triangles, bainite start by diamonds, and martensite by circles) for a 0.41%C-0.25%Si-0.71%Mn-0.22%Ni steel (41Cr4 steel) with an austenitizing temperature of 880°C. The nose positions of ferrite, pearlite and bainite are indicated by a large open, grey and black circle, respectively; the dashed line is the bainite end line (after van der Wolk, 1994).

and cooling path on the austenite decomposition processes. Most of these efforts include as many variables in the analysis as the availability of the data will permit, on the grounds that Bayesian methods are robust enough to minimize the influence of irrelevant variables, thus avoiding the risk of preconceived bias. Because of the risk of wild predictions, neural network methods should not be relied on unless a Bayesian framework is used.

It is also important to study the behavior of the network in domains where knowledge does not exist, i.e. to use the models to make bold predictions which form the basis for experiments and the discovery of new phenomena. Indeed, the performance of a network is most useful to researchers in domains where the modeling uncertainty is greatest. An alternative way of stating this is that new experiments are only necessary when the network predicts that the uncertainty is large.

Reviewed in this chapter have been the combined and individual predicted effects of cooling path and alloying elements such as C, Cr, Mn, Mo or W on the transformation temperatures (Ae_3, Ae_1, B_s and M_s), fractions of microstructural components and microstructural parameters such as bainite lath thickness and pearlite interlamellar spacing, on a wide range of steels. The neural network models produced reveal new detailed quantitative information, in line with common metallurgical knowledge. It is obvious, however, that

© Woodhead Publishing Limited, 2012

to exploit the full potential of the neural network technique, it is necessary to think about the best method for publishing the results, with particular attention being paid to dissemination and modeling uncertainties. Neither of these is difficult to achieve. The consistency of the models originates from the consistency of the original database and the small modeling error.

Finally, the future trend in the application of neural networks on predicting phase transformations in steels relies on a different approach aimed at 'dimensionality reduction', i.e. simplification of the problem prior to creating models. Steels contain a myriad of solutes and an attempt to use linear combinations of solutes to reduce the number of input variables is necessary. The difference between the calculated values of these test data and actual measurements could be used as a measure of success.

15.7 References

Abe F (2001), 'Creep rates and strengthening mechanisms in tungsten-strengthened 9Cr steels', *Mater. Sci. Eng. A*, 319–321, 770–773.

Al-Salman A, Lorimer G W and Ridley N (1979), 'Partitioning of silicon during pearlite growth in a eutectoid steel', *Acta Metall.*, 27, 1391–1400.

Andrews K W (1965), 'Empirical formulae for the calculation of some transformation temperatures', *JISI*, 203, 721–727.

Bailer-Jones C A L, Bhadeshia H K D H and MacKay D J C (1999), 'Gaussian process modelling of austenite formation in steel', *Mat. Sci. Technol.*, 15, 287–294.

Banerjee M K, Banerjee P S and Datta S (2001), 'Effect of thermomechanical processing on the microstructure and properties of a low carbon copper bearing steel', *ISIJ Int.*, 41, 257–261.

Bhadeshia H K D H (1992), *Bainite in Steels*, London, The Institute of Materials.

Bhadeshia H K D H (1999), 'Neural networks in materials science', *ISIJ Int.*, 39, 966–979.

Bhadeshia H K D H (2009), 'Neural networks and information in materials science', *Statistical Analysis and Data Mining*, 1, 296–305.

Bhadeshia H K D H, Dimitriu R C, Forsik S, Pak J H and Ryu J H (2009), 'Performance of neural networks in materials science', *Mat. Sci. Technol.*, 25, 504–510.

Bodnar R L, Ohhashi T and Jaffee R I (1989), 'Effects of Mn, Si and purity on the design of 3.5NiCrMoV, 1CrMoV and 2.25Cr-lMo bainitic alloy steels', *Met. Trans. A.*, 20, 1445–1460.

Caballero F G**,** Capdevila C and García de Andrés C (2001a), 'Modelling of kinetics of austenite formation in steels with different initial microstructures', *ISIJ Int.*, 41, 1093–1102.

Caballero F G, Capdevila C and García de Andrés C (2001b), 'Influence of pearlite morphology and heating rate on the kinetics of continuously heated austenite formation in a eutectoid steel', *Metall. Trans. A*, 32, 1283–1291.

Capdevila C, Caballero F G and García de Andrés C (2000), 'Estimation of the Ms temperature in steels', Materials Algorithm Project (MAP) Library, University of Cambridge, Available from: http://www.msm.cam.ac.uk/map/steel/programs/MS.neural.htm

Capdevila C, Caballero F G and García de Andrés C (2002), 'Determination of Ms temperature in steels: a Bayesian neural network model', *ISIJ Int.*, 42, 894–902.

© Woodhead Publishing Limited, 2012

Capdevila C, Caballero F G and García de Andrés C (2003), 'Analysis of effect of alloying elements on martensite start temperature of steels', *Mat. Sci. Technol.*, 19, 581–586.

Capdevila C, Garcia-Mateo C, Caballero F and García de Andrés C (2004), 'Proposal of an empirical formula for the austenitising temperature', *Mat. Sci. Eng. A*, 386, 354–361.

Capdevila C, Caballero F G and García de Andrés C (2005a), 'Neural network model for isothermal pearlite transformation. Part I: Interlamellar spacing', *ISIJ Int.*, 45, 229–237.

Capdevila C, Caballero F G and García de Andrés C (2005b), 'Neural network model for isothermal pearlite transformation. Part II: Growth rate', *ISIJ Int.*, 45, 238–247.

Cheetham D and Ridley N (1973), 'Isovelocity and isothermal pearlite growth in a eutectoid steel', *J. Iron Steel Inst.*, 211, 648–652.

Cool T and Bhadeshia H K D H (1996), 'Carbide precipitation in some secondary hardening steels', *Mat. Sci. Technol.*, 12, 40–44.

Daigne J, Guttmann M and Naylor J P (1982), 'The influence of lath boundaries and carbide distribution on the yield strength of 0.4% C tempered martensitic steels', *Mater. Sci. Eng. A*, 56, 1–10.

Depaul R A and Kitchen A L (1970), 'The role of nickel, copper, and columbium (niobium) in strengthening a low-carbon ferritic steel', *Metall. Trans.*, 1, 389–393.

Dobrzanski L A and Trzaska J (2003), 'Application of neural networks for prediction of hardness and volume fractions of structural components in constructional steels cooled from the austenitizing temperature', *Mater. Sci. Forum*, 437–438, 359–362.

Foularis G, Baker A J and Papadimitriou G D (1996), 'Effect of copper additions on the isothermal bainitic transformation in hypereutectoid copper and copper-nickel steels', *Acta Mater.*, 12, 4791–4805.

Fujii H and Bhadeshia H K D H (1996), 'Bayesian neural network analysis of fatigue crack growth rate in nickel base superalloys', *ISIJ Int.*, 36, 1373–1382.

García de Andrés C, Capdevila C, Madariaga I and Gutiérrez I (2001), 'Role of molybdenum in acicular ferrite formation under continuous cooling in a medium carbon microalloyed forging steel', *Scr. Mater.*, 45, 709–716.

Garcia-Mateo C, Sourmail T, Caballero F G, Capdevila C and García de Andrés C (2005), 'New approach for the bainite start temperature calculation in steels', *Mat. Sci. Technol.*, 21, 934–940.

Gavard L, Bhadeshia H K D H, MacKay D J C and Suzuki S (1996), 'Bayesian neural network model for austenite formation in steels', *Mat. Sci. Technol.*, 12, 453–463.

Ghosh G and Olson G B (1994a), 'Kinetics of fcc → bcc heterogeneous martensitic nucleation – I. The critical driving force for athermal nucleation', *Acta Mat.*, 42, 3361–3370.

Ghosh G and Olson G B (1994b), 'Kinetics of fcc → bcc heterogeneous martensitic nucleation – II. Thermal activation', *Acta Mat.*, 42, 3371–3379.

Ghosh G and Olson G B (2002), 'The isotropic shear modulus of multicomponent Fe-base solid solutions', *Acta Mat.*, 50, 2655–2675.

Ghosh S K, Chattopadhyay P, Haldar A, Ganguly A and Datta A (2008), 'Design of the directly air-cooled pearlite-free multiphase steel from CCT diagrams developed using ANN and dilatometric methods', *ISIJ Int.*, 48, 649–657.

Grange R A and Stewart H M (1946), 'The temperature range of martensite formation', *Trans. AIME*, 167, 467–490.

Gustafson A and Ågren J (2001), 'Possible effect of Co on coarsening of $M_{23}C_6$ carbide and Orowan stress in a 9% Cr steel', *ISIJ Int.*, 41, 356–360.

© Woodhead Publishing Limited, 2012

Hashiguchi K and Kirkaldy J S (1984), 'Pearlite growth by combined volume and phase boundary diffusion', *Scand. J. Metall*, 13, 240–248.
Hillert M (1957), 'The role of interfacial energy during solid-state phase transformations', *Jernkont. Ann.*, 141, 757–789.
Jaynes E T (2003), *Probability Theory: the Logic of Science*, Cambridge, Cambridge University Press.
Ko T and Cottrell S A (1952), 'The formation of bainite', *JISI*, 172, 307–313.
Kung C Y and Rayment J J (1978), *Hardenability Concepts with Applications to Steels*, Warrendale, PA, TMS–AIME.
Kunitake T and Okada Y (1998), 'The estimation of bainite transformation temperatures in steels by the empirical formulas', *J. Iron and Steel Inst. Japan*, 84, 137–141.
Kwok C T, Cheng F T and Man H C (2001), 'Laser-fabricated Fe-Ni-Co-Cr-B austenitic alloy on steels. Part II. Corrosion behaviour and corrosion-erosion synergism', *Surf. Coat. Technol.*, 145, 206–214.
Lee Y K (2002), 'Empirical formula of isothermal bainite start temperature of steels', *J. Mater. Sci. Lett.*, 21, 1253–1255.
Lisovskii A F (2001), 'Mesostructuring in sintered hard alloys', *Powder Metall. Met. Ceram.*, 40, 71–76.
MacKay D J C (1992a), 'Information-based objective functions for active data selection', *Neural Comput.*, 4, 590–604.
MacKay D J C (1992b), 'Practical Bayesian framework for backpropagation networks', *Neural Comput.*, 4, 448–472.
MacKay D J C (1992c), 'Comparison of approximate methods for handling hyperparameters', *Neural Comput.*, 4, 1035–1072.
MacKay D J C (1997), 'Bayesian non-linear modeling with neural networks', in H Cerjak and H K D H Bhadeshia, *Mathematical Modeling of Weld Phenomena 3*, London, Institute of Materials.
Madariaga I and Gutierrez I (1999), 'Role of the particle matrix interface on the nucleation of acicular ferrite in a medium carbon microalloyed steel', *Acta Mater.*, 47, 951–960.
Madariaga I, Gutierrez I, García de Andrés C and Capdevila C (1999), 'Acicular ferrite formation in a medium carbon steel with a two stage continuous cooling', *Scr. Mater.*, 41, 229–235.
MTDATA (1995), *Metallurgical Thermochemical Data*, Teddington, National Physical Laboratory.
Mukherjee M and Singh S B (2009), 'Artificial neural network: some applications in physical metallurgy of steels', *Materials and Manufacturing Processes*, 24, 198–208.
Munirajulu M, Dhindaw B K, Biswas A and Roy A (1994), 'Modelling of eutectoid transformation in plain carbon steel', *ISIJ Int.*, 34, 355–358.
Olson G B and Cohen M (1976), 'General mechanism of martensitic nucleation', *Metall. Trans.*, 7A, 1897–1923.
Payson P and Savage C H (1944), 'Martensite reactions in alloy steels', *Trans. ASM*, 33, 261–275.
Pereloma E V and Boyd J D (1996), 'Effects of simulated on line accelerated cooling processing on transformation temperatures and microstructure in microalloyed steels', *Mater. Sci. Technol.*, 12, 1043–1052.
Rumelhart D E, Hilton G E and Williams R J (1986), 'Learning representations by backpropagating errors', *Nature*, 323, 533–536.
Sharma R C, Purdy G C and Kirkaldy J S (1979), 'Thermodynamics and phase equilibria for the Fe–C–Cr system in the vicinity of the eutectoid temperature', *Metall. Trans. A*, 10, 1119–1127.

© Woodhead Publishing Limited, 2012

Sikka V K, Ward C T and Thomas K C (1983), *Ferritic steels for high temperature applications*, Metals Park, OH, ASM.

Singh S B and Bhadeshia H K D H (1998), 'Estimation of bainite plate-thickness in low-alloy steels', *Mater. Sci. Eng. A*, 245, 72–79.

Sourmail T and Garcia-Mateo C (2005), 'A model predicting Ms temperature in steels', *Comp. Mat. Sci.*, 34, 213–218.

Srinivasan G R and Wayman E M (1968), 'The crystallography of the bainite transformation', *Acta Metall.*, 16, 621–636.

Steven W and Haynes A G (1956), 'The temperature formation of martensite and bainite in low-alloyed steels', *JISI,* 183, 349–359.

Thermo-Calc (1984), *Thermodynamic Database*, Stockholm, The Royal Institute of Technology, Sweden.

Thompson S W, Colvin D J and Krauss G (1996), 'Austenite decomposition during continuous cooling of an HSLA-80 plate steel', *Metall. Trans. A*, 27, 1557–1571.

US Steel (1959), *Atlas of Isothermal Transformation Diagrams*, Pittsburgh, PA, United States Steels (USS) Corporation.

van der Wolk P J (1994), 'Modelling material production processes using hierarchical artificial neural networks', Delft, TU Delft.

van der Wolk P J, Wang J, Sietsma J and van der Zwaag S (2002), 'Design of the directly air-cooled pearlite-free multiphase steel from CCT diagrams developed using ANN and dilatometric methods', *Z. Metallkd.*, 93, 1208–1216.

Vermeulen W G, van der Wolk P J, de Weijer A P, van der Zwaag S (1996), 'Prediction of Jominy hardness profiles of steels using artificial neural networks', *Journal of Materials Engineering and Performance*, 5, 57–63.

Wang J, van der Wolk P J and van der Zwaag S (2000), 'Determination of martensite start temperature in engineering steels, Part 1: Empirical relations describing the effect of steel chemistry', *Mater. Trans. JIM*, 41, 761–768.

Zener C (1946), 'Kinetics of decomposition of austenite', *Trans. AIME*, 167, 550–583.

Zhao Z, Liu C, Liu Y and Northwood D O (2001), 'A new empirical formula for the bainite upper temperature limit of steel', *J. Mater. Sci.*, 36, 5045–5056.

Ziman J M (1979), *Models of Disorder*, Cambridge, Cambridge University Press.

© Woodhead Publishing Limited, 2012

© Woodhead Publishing Limited, 2012

16

Application of modern transmission electron microscopy (TEM) techniques to the study of phase transformations in steels

D. BOYD and Z. YAO, Queen's University, Canada

Abstract: Transmission electron microscopy (TEM) is the most widely used technique for studying all aspects of phase transformations in steels over the length scale range 1–100 nm. The capabilities of modern TEM include aberration correction (spherical and chromatic), energy-filtered imaging (EFTEM), convergent beam diffraction (CBED), annular dark field imaging (ADF) and microchemical analysis by X-ray energy dispersive spectroscopy (XEDS) and electron energy loss spectroscopy (EELS). Nevertheless, the majority of TEM studies on phase transformations in steels continue to be conventional TEM (CTEM). This chapter reviews the wide application of TEM to this subject. It includes brief descriptions of sample preparation techniques and CTEM. The main body of the chapter considers modern TEM techniques and emerging TEM techniques, which offer new capabilities. For complete characterization of microstructures at all relevant length scales, complementary techniques such as atom probe tomography (APT), electron back scattered diffraction (EBSD) and bulk diffraction techniques (synchrotron X-ray and neutron) must be utilized, in addition to TEM.

Key words: transmission electron microscopy, sample preparation, conventional TEM imaging and microanalysis, high resolution TEM, energy filtered imaging, annular dark field imaging, X-ray energy dispersive spectroscopy, electron energy loss spectroscopy, convergent beam electron diffraction, *in-situ* TEM, electron tomography.

16.1 Introduction

Transmission electron microscopy (TEM) is the most powerful tool for characterizing solid state phase transformations. There are other complementary techniques for studying phase transformations (see Chapters 17–19). However, it should be evident from the preceding chapters in this book that TEM is the most widely used technique for studying all aspects of phase transformations in steels over the length scale range 1–100 nm. As stated in a comprehensive review of the contributions of TEM to materials science, no theory of alloy behaviour is complete without TEM observations to support it (Newbury and Williams, 2000).

The power of TEM lies in its ability to determine microstructure (phase

© Woodhead Publishing Limited, 2012

morphology and size distribution), structure (crystalline, quasi-crystalline or amorphous) and chemical composition (uniform and gradients) of individual phases in a single instrument at a particular sample location. In addition to basic information on phase microstructure/crystal structure/chemical composition, it is possible to characterize nucleation sites (dislocations, grain boundaries (GB), stacking faults (SF), vacancy and solute clusters), transformation interfaces (ledges, steps, dislocations, chemical segregation, local strains), structural and chemical changes during growth, and particle coarsening/dissolution. It follows then that TEM has been widely applied in support of research on all types of phase transformations in steels, including studies of diffusion-controlled transformations, martensite, bainite and precipitates.

The capabilities of a modern TEM include aberration correction (spherical and chromatic), energy-filtered imaging (EFTEM), convergent beam diffraction (CBED), annular dark field imaging (ADF) and microchemical analysis by X-ray energy dispersive spectroscopy (XEDS) and electron energy loss spectroscopy (EELS). All of these techniques were available in 2000, when the review by Newbury and Williams (2000) was published, but there have been continuing advances and extensive application over the past decade. Nevertheless, these modern TEM techniques remain a minor part of all the research published on phase transformations in steels. The majority of the TEM results reported in these publications are conventional TEM (CTEM).

This chapter begins with a brief description of TEM sample preparation techniques, followed by a summary of the techniques of CTEM. In the main body of the chapter, the techniques of modern TEM are described with recent examples of their application. We conclude this chapter with some comments on currently emerging TEM techniques, which we anticipate will impact the study of phase transformations in steels in future years.

16.2 Transmission electron microscopy (TEM) sample preparation

The ability to exploit the capabilities of modern TEM techniques for image resolution and micro-chemical analysis is strongly influenced by the condition of the sample which is inserted into the transmission electron microscope. The time and effort required to produce high quality TEM samples of steels likely explains why steels are under-represented in total numbers of publications of TEM studies compared with other metals and materials. Ideally, a TEM sample is a perfectly planar slice 100 nm thick, or less, and is perfectly representative (at this scale) of the bulk material. i.e., it contains no artefacts resulting from the sample preparation procedure. The techniques available for TEM sample preparation are listed in Table 16.1, along with brief comments on advantages and disadvantages of each.

© Woodhead Publishing Limited, 2012

Table 16.1 Summary of TEM sample preparation methods

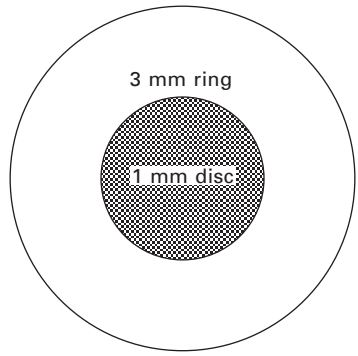
Method	Advantages	Disadvantages
Electropolishing	Well-established procedure for all common steels Fast	Inferior results with large 2nd-phase particles
Ion milling	Uniform thinning of multiphase samples	Slow Ion damage
Extraction replicas	Accurate chemical analysis of precipitates	No matrix information
Focused ion beam	Uniformly thin samples Precise location of area imaged	Slow Ion damage

Source: Williams and Carter (2004).

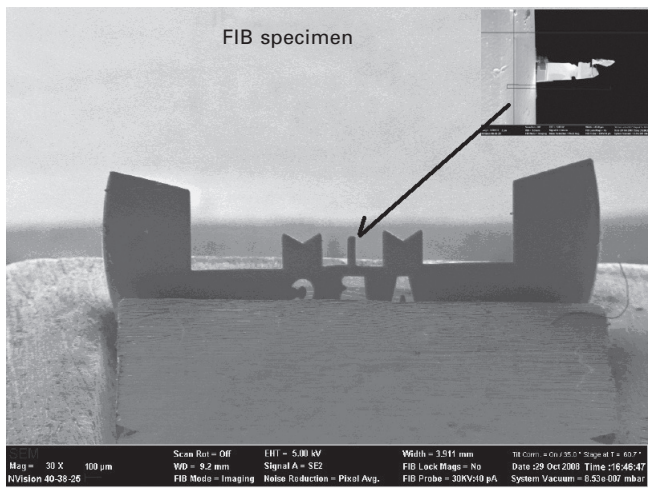
For TEM studies of bulk steel, the traditional electropolished disc method remains the most widely used technique. Extraction replicas are used for accurate chemical analysis of small precipitates, but they have a lower size limit of 2–5 nm. Aluminum substrates have been employed to determine C/N ratios of carbonitride precipitates in microalloyed steels, but they suffer from poor contrast due to their crystalline structure. Amorphous alumina (Al_2O_3) replicas have been developed, which alleviate this problem (Scott *et al*., 2002). Focused ion beam (FIB) technology is advancing rapidly, and its application to TEM sample preparation should increase in the future. FIB milling has the advantages over all other techniques of producing thin (~100 nm), parallel sided and (where desired) site-specific TEM samples. It has also facilitated study of surface layers on steels, including oxidation (Liu *et al*., 2009), galvanizing (Yu *et al*., 2007) and nitriding (Zhou *et al*., 2010). The limitations of FIB are long milling times (3–10 h per sample) and creation of artefacts by ion bombardment damage, which includes chemical change, structural change and introduction/modification of crystal defects near the surface (Sugiyama and Sigesato, 2004).

In addition to the normal challenges of sample preparation, TEM of ferritic/martensitic steels poses the additional problem of ferromagnetism. At the least, this requires much additional effort to perform re-alignments after each sample translation/rotation, and it limits the resolution that can be achieved in the TEM image and associated microchemical analysis. The only approach to this problem is to reduce the volume of the TEM sample (and hence reduce the volume of ferromagnetic metal). Some benefit is achieved by pre-thinning the sample to say 50 μm prior to electropolishing. Another approach is to fabricate a composite sample, comprising an inner 1 mm diameter disc of the test material and an outer 3 mm ring of stainless steel (Fig. 16.1(a)). The composite sample is then pre-thinned and electropolished in the usual way. A much smaller sample of ferromagnetic steel can be cut

© Woodhead Publishing Limited, 2012



(a)



(b)

16.1 Sample preparation for minimizing effects of ferromagnetic metals: (a) composite disc sample; (b) FIB micro-sample mounted on 3 mm grid (Yao, 2010).

from a FIB-thinned sample and attached to a special 3 mm TEM grid by 'platinum deposition' in a dual-beam FIB, as shown in Fig. 16.1(b). This represents the current state-of-the-art sample preparation method for TEM of ferritic/martensitic steels.

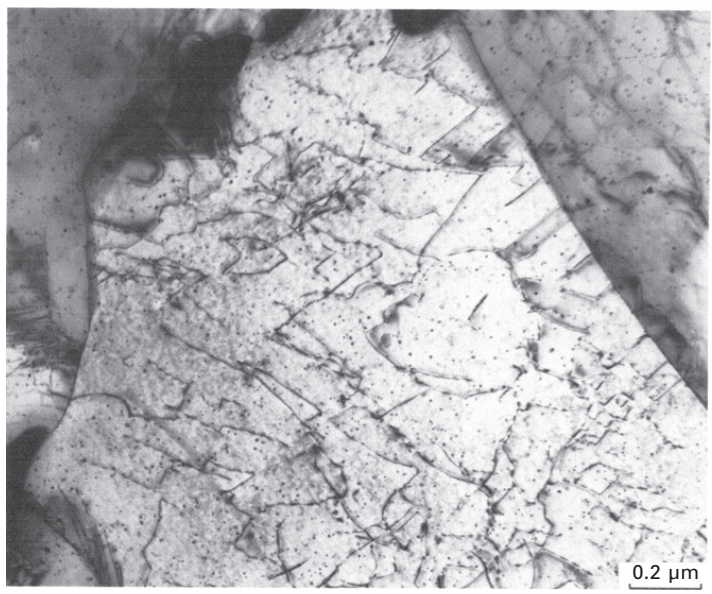
16.3 Conventional transmission electron microscopy (CTEM) of steels

In TEM, a high energy electron beam (typically 200 kV) is focused on the thin foil sample parallel to the optic axis of the microscope with a beam diameter of 1–25 μm. The transmitted beam undergoes coherent elastic

© Woodhead Publishing Limited, 2012

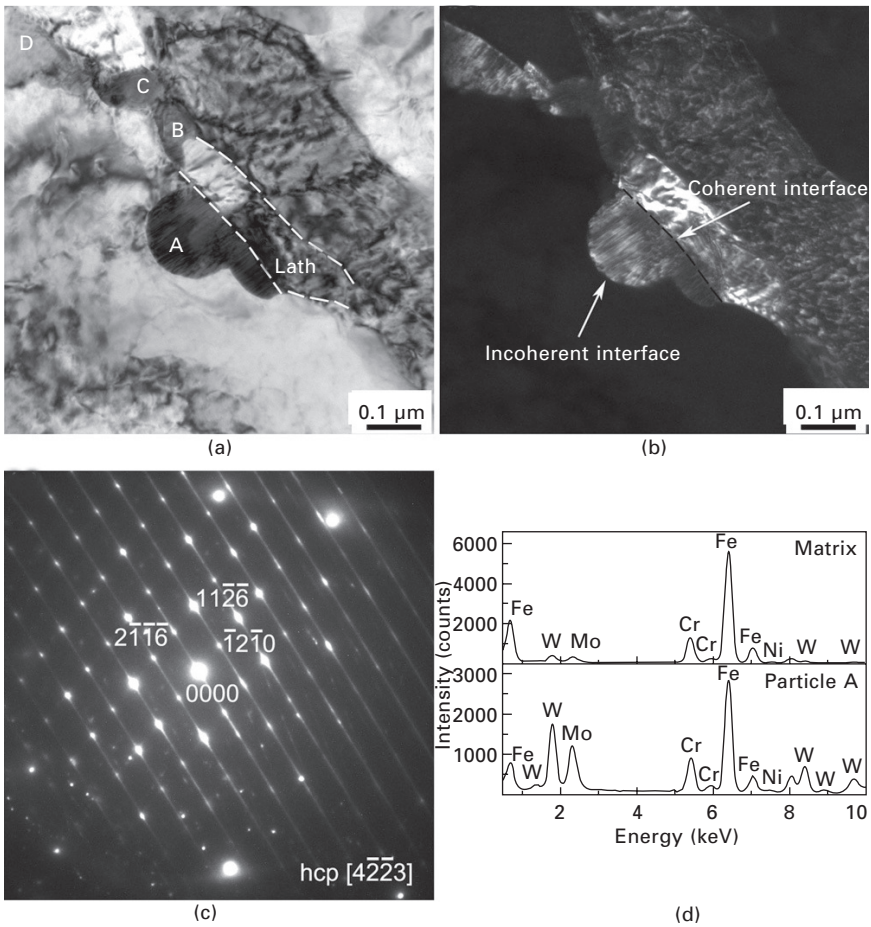
('Bragg') diffraction and the emerging beams can be focused to form either an electron diffraction pattern or a highly magnified image. Because the diffracted beams can be collected from a particular area of the specimen, they are called selected area diffraction patterns (SADP). A bright field (BF) image is formed by excluding all the diffracted intensity by means of an objective aperture, and using only the transmitted beam. Contrast arises from local differences in diffracted intensity, hence these are diffraction contrast images. Both SADPs and images can be viewed directly on a fluorescent screen in the microscope column, or electronic images can be produced via an electron detector and a CCD camera. The 2D DP represents the symmetry of the crystal planes parallel to the electron beam ('zone axis'). If more than one grain or phase are present in the volume of material sampled by the electron beam, each will produce a DP superimposed in the correct orientation relationship. The image is a 2D projection of the volume sampled (typically 10 μm × 10 μm × 100 nm). The electron intensity in the image depends precisely on the diffraction conditions. The contrast of specific features varies with orientation changes on the order of 0.5° (~10 mrad). Thus, to interpret diffraction contrast images, it is necessary to know the exact diffraction conditions, as determined from the SADP, and to utilize the well-established dynamical theory of electron diffraction (Hirsch *et al.*, 1977).

Figures 16.2–16.4 illustrate the scale and variety of the information that can be obtained from CTEM. Figure 16.2 is a CTEM image which shows details



16.2 CTEM image of a thermomechanically processed microalloyed steel (Boyd, 1976).

© Woodhead Publishing Limited, 2012



16.3 Laves phase precipitates in a 12% Cr steel: (a) CTEM image, (b) DF image of same area in (a), (c) SADP, (d) XEDS spectra from matrix and particle A (Cui *et al.*, 2010).

of dislocations, subgrains and Nb(C,N) precipitates in a thermomechanically processed microalloyed steel. The image in Fig. 16.3(a) shows the formation of particles of a $(Fe,Cr)_2(W,Mo)$ Laves phase during creep exposure of a 12% Cr steel (particles A–D). It is seen that the Laves phase particles nucleate in the tempered martensite matrix at martensite lath boundaries or subgrain boundaries. Images can also be formed using the intensity in a particular diffracted beam. Figure 16.3(b) is such a dark field (DF) image showing the strongly diffracting regions of particle A and adjacent martensite laths. From such images it is observed that the Laves phase particle forms a coherent interface with the substrate martensite lath, and grows into the adjacent lath by movement of an incoherent interface. The internal structure of the Laves phase particle indicates a high density of stacking faults. The corresponding

© Woodhead Publishing Limited, 2012

SADP (Fig. 16.3(c)) shows the [4 $\bar{2}$ $\bar{2}$ 3] zone axis diffraction pattern (ZAP) of the hexagonal Laves phase and some matrix diffraction maxima. The streaking of the Laves phase diffraction maxima is due to the thin stacking faults within the particle.

The third capability of CTEM is chemical analysis of phases in the thin foil specimen, which involves analysing the characteristic X-rays emitted by the inelastic scattering of the high energy electrons. The energy (wavelength) of the emitted X-rays is characteristic of the scattering atom, and the atom species can be identified by measuring this energy. Regions for analysis are selected by focusing the incident beam, and the emitted X-rays are detected and their energies identified by a solid-state X-ray energy-dispersive spectrometer (XEDS). The output of this procedure is an XEDS spectrum, which is a plot of X-ray counts vs. energy. Examples of such spectra are shown in Fig. 16.3(d), which give qualitative chemical compositions of the martensite matrix and the Laves particle A. It can be seen that the $(Fe,Cr)_2(W,Mo)$ precipitate is enriched in W and Mo.

In addition to phase identification and characterization (as shown in Figs 16.2 and 16.3), the other main use of CTEM is to characterize lattice defects, which exhibit distinct contrast in BF and DF images due to local lattice strain or rotation. Figure 16.4 is a BF image of a duplex stainless steel aged at 475°C, showing a characteristic 'cross-stitch' arrangement of dislocations in the δ phase. In this case, the image was recorded under conditions which produced one strong diffraction beam from (112) planes ('two-beam conditions'). By recording several images of the same area under two-beam conditions, it would be possible to determine the dislocation type (Burgers vector and line direction).

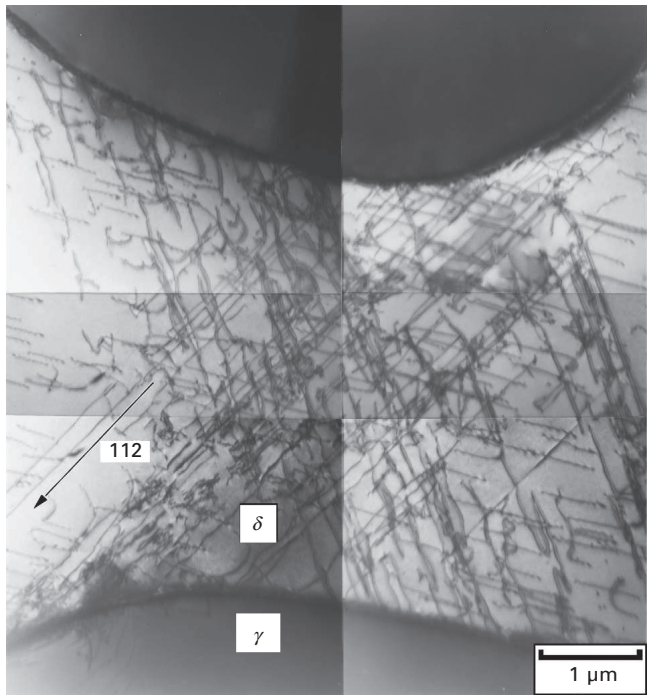
All of the three basic techniques of CTEM (imaging, diffraction, microanalysis) were available 35 years ago when the image in Fig. 16.2 was recorded. Since then, there have been major advances in the accuracy, spatial resolution, limits of detection and speed of recording and measurement for CTEM, as represented by Figs 16.3 and 16.4. In addition, significant new TEM techniques have been developed during this period, which are described in the next section. However, it must be emphasized that the majority of TEM studies published in support of research on phase transformations in steels utilize CTEM.

16.4 Modern transmission electron microscopy (TEM) of steels

16.4.1 Imaging techniques

With spherical aberration correction (Cs), a monochromator and a field emission source up to 300 kV, it is possible to achieve sub-angstrom image

© Woodhead Publishing Limited, 2012

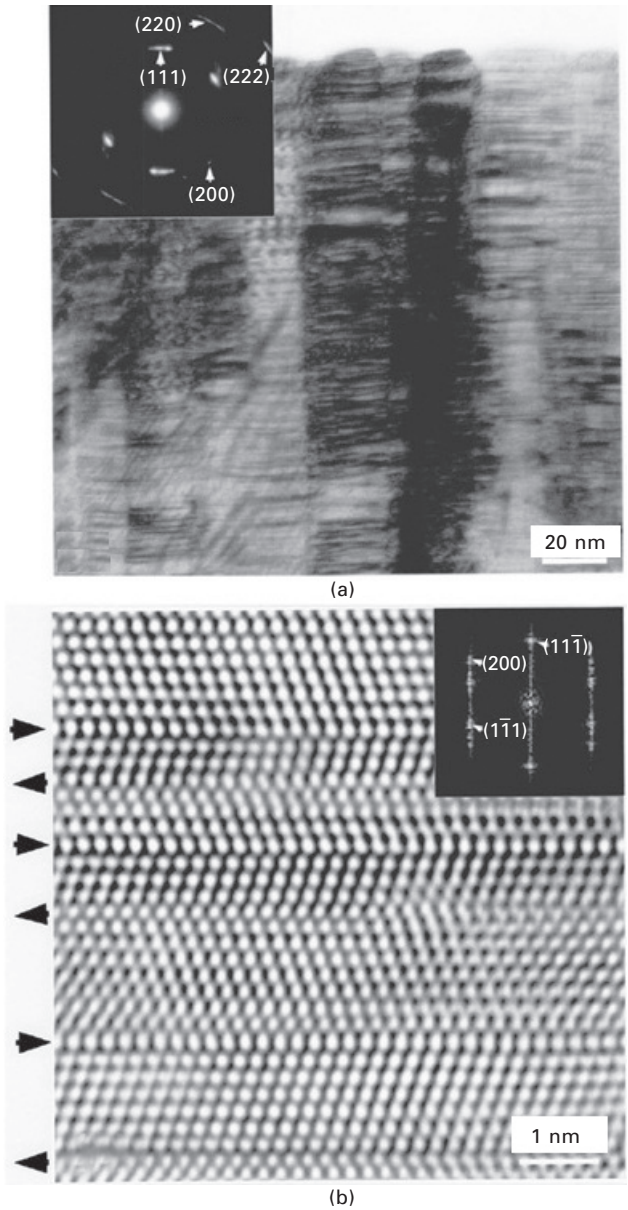


16.4 Dislocation structure in δ ferrite of an aged duplex stainless steel. Observation under two-beam conditions γ = (112) (Weng *et al.*, 2004).

resolution and concomitant atom-position information, for both austenitic and ferritic steel samples (Figs 16.5 and 16.6). These advances in microscope technology have significantly improved the spatial resolution of conventional diffraction contrast TEM images (described in Section 16.3). However, they have also improved the resolution of phase contrast TEM images, whereby more than one beam contribute to the image, as illustrated by the striking lattice images in Figs 16.5 and 16.6. The terminology 'high resolution TEM (HRTEM)' now refers exclusively to phase contrast lattice images. With modern TEMs, it is relatively straightforward to obtain HRTEM images, but the quantitative interpretation of such images is difficult, requiring significant image simulation calculations.

The atomic structure information obtained by high resolution TEM (HRTEM) can provide valuable insights into phase transformation mechanisms. Figure 16.7 shows an HRTEM image of a twinned 9R precipitate in an Fe-Cu alloy, which revealed details of the bcc-to-9R martensite transformation. Figure 16.8 shows an HRTEM image of the $\gamma \rightarrow \alpha$ transformation interface in a transformation-induced plasticity (TRIP) steel, which confirms the Nishiyama–Wassermann (N-W) orientation

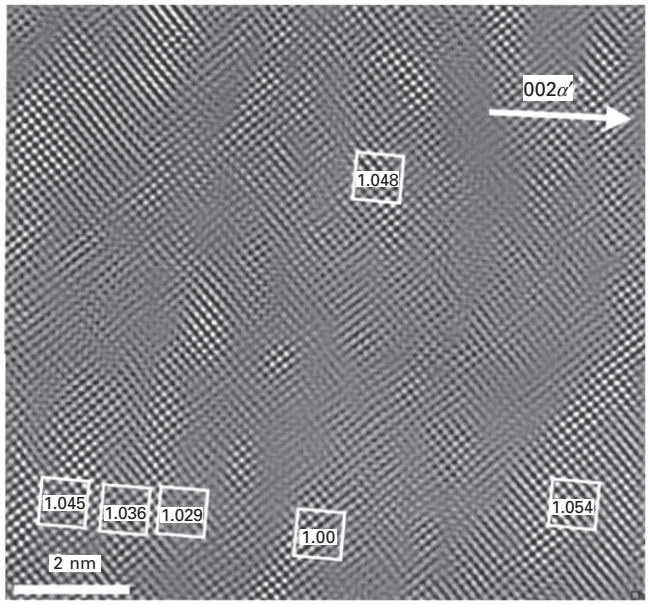
© Woodhead Publishing Limited, 2012



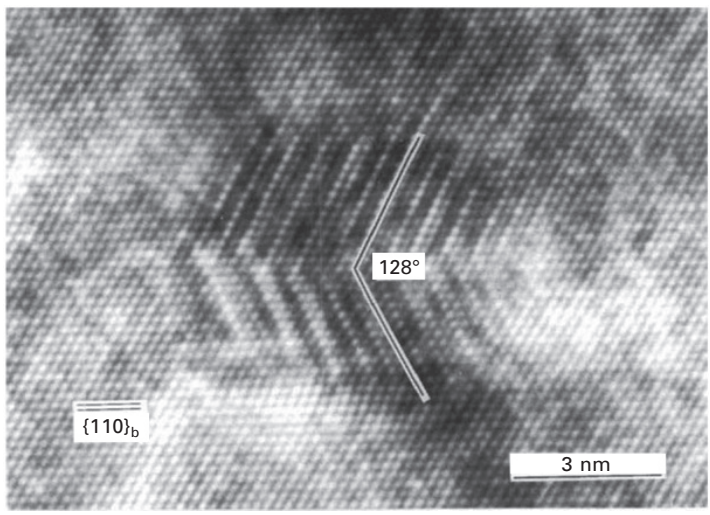
16.5 Sputter-deposited austenitic stainless steel thin film: (a) BF-CTEM showing heavily twinned 30 nm columnar grains; (b) HRTEM image showing nanoscale growth twins on {111} (Zhang *et al.,* 2004).

relationship, i.e., $(111)_{fcc}//(011)_{bcc}$, $[110]_{fcc}//[100]_{bcc}$ and displays local lattice rotations. Figure 16.9 is a fast Fourier transform (FFT) image, which reveals the details of the ledge structure of the bainite–austenite interface in an Fe-Si-C alloy.

© Woodhead Publishing Limited, 2012



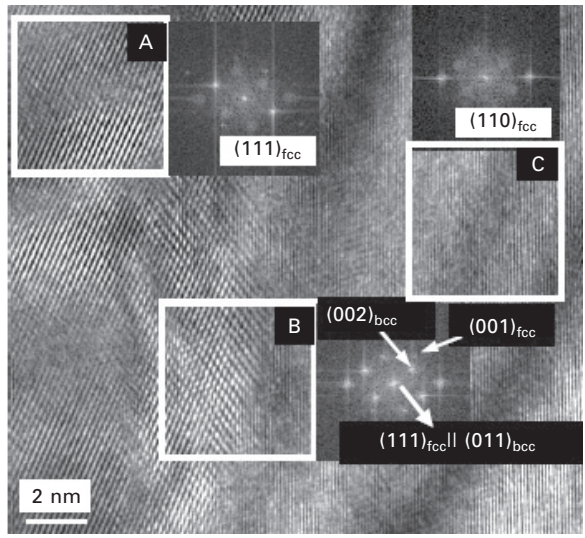
16.6 HRTEM image of Fe-C martensite (α') aged < 6 h at room temperature, showing regions of varying tetragonality (Han *et al.*, 2001).



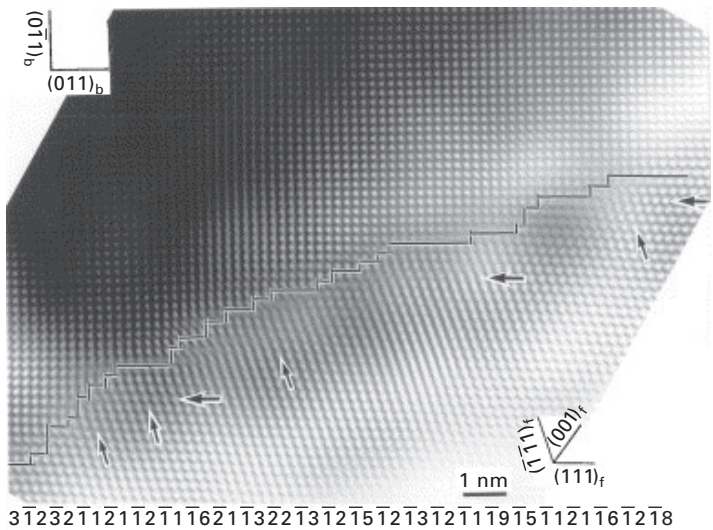
16.7 HRTEM image of a precipitate in Fe-1.5 wt% Cu, showing twinned 9R structure (Monzen *et al.*, 2000).

These examples of insightful HRTEM images notwithstanding, it is the ability to combine specialized imaging techniques such as HRTEM, energy-filtered imaging (EFTEM) and high angle annular dark field (HAADF)

© Woodhead Publishing Limited, 2012



16.8 HRTEM image of two differently oriented austenite regions (A and C) separated by a narrow ribbon of ferrite (region B) in a TRIP steel (Borisova *et al.*, 2010).



16.9 Fast Fourier transform of HRTEM image of an Fe-Si-C alloy, showing details of the $\{110\}_{bcc}$ ledge structure of a bainite–austenite interface (highlighted) and dislocations in austenite (arrows) (Ogawa and Kajiwara, 2006).

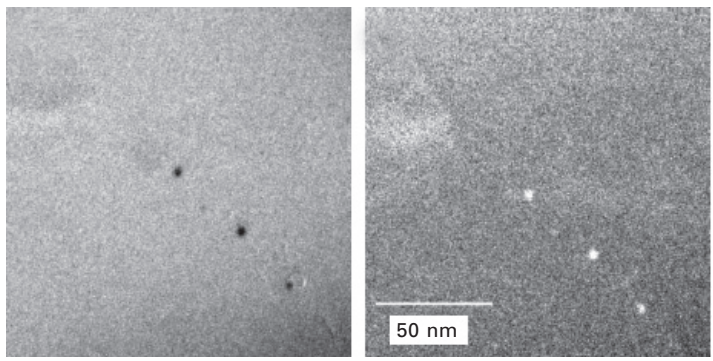
© Woodhead Publishing Limited, 2012

with conventional diffraction contrast imaging (CTEM) that makes TEM the most powerful tool for phase transformation studies in steels and other materials.

Energy-filtered images are obtained by means of a filter, which selects electrons with a specific energy loss range. These are also called 'EELS maps' or 'core-loss' images. (Since EFTEM is based on electron energy loss spectroscopy (EELS) of inelastically scattered electrons, it might be helpful to first read the brief description of EELS in Section 16.4.2.) EFTEM images can be obtained using a post-column imaging filter (GIF) or with an in-column filter ('Ω filter'). It is currently possible to achieve spatial resolution in core-loss EFTEM images better than 1 nm for embedded particles (Lozano-Perez *et al.*, 2006). The characterization of nanometre-scale precipitate phases in steels provides excellent examples of the application of these techniques. Figures 16.10 and 16.11 show EFTEM images of NbC precipitates on grain



16.10 Montage of Nb-$N_{2,3}$ EFTEM images of 5 nm NbC precipitates in an Fe-C-Nb alloy, showing grain boundary precipitates in upper part of figure and dislocation-nucleated precipitates at the left side (Courtois *et al.*, 2006).



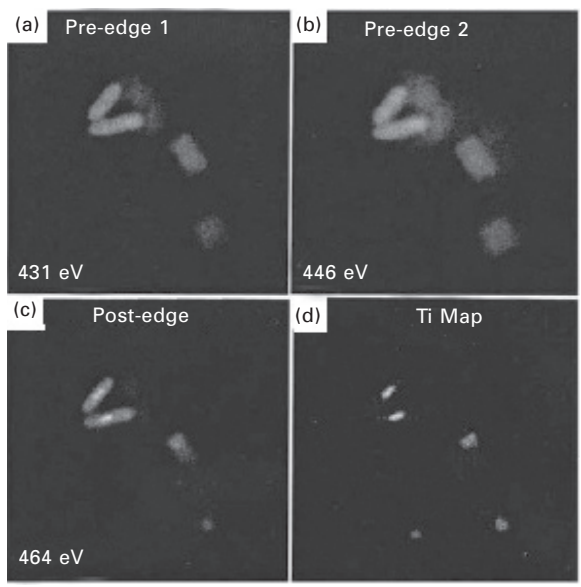
16.11 EFTEM images of NbC precipitates on deformation microbands in a model austenitic steel: (a) Fe-$M_{2,3}$ edge jump ratio image; (b) Nb-$M_{4,5}$ edge jump ratio image (Rainforth *et al.*, 2002).

© Woodhead Publishing Limited, 2012

boundaries and dislocations, and on deformation microbands, respectively. In these cases, it was necessary to employ EFTEM to obtain sufficiently uniform imaging of the smallest particles (e.g., for quantitative measurements of size, volume fraction, etc.).

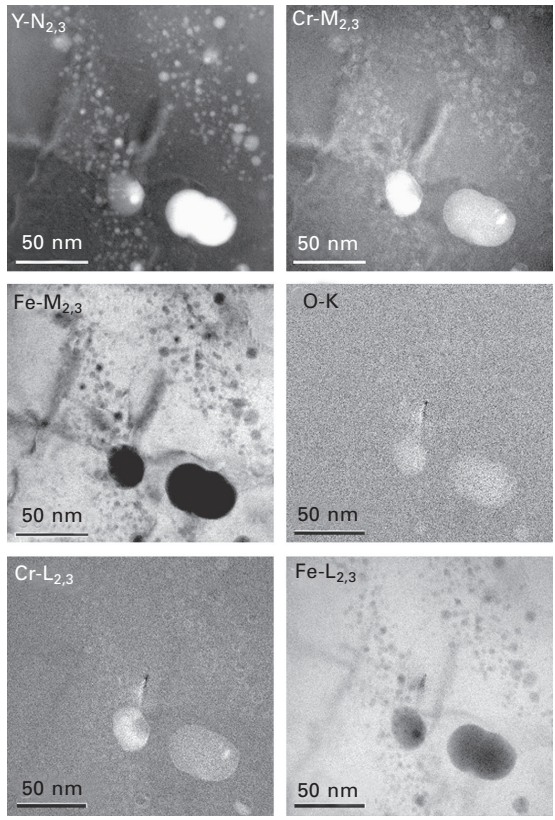
Figure 16.12 shows EFTEM images of 10–20 nm AlN precipitates in a Fe-Al-N alloy, where it was determined that the AlN precipitates nucleate on small $Al_xTi_{1-x}N$ core particles. In this case the crystal structures of AlN and TiN are too close to distinguish, even with HRTEM, but the Ti-rich nuclei are clearly revealed in EFTEM images.

EFTEM has also been widely applied to the characterization of nanometer-sized oxide particles in oxide dispersion strengthened steels, in particular reduced activation ferritic/martensitic steels (ODS-RAFMS) for potential fusion reactor applications. The work of Lozano-Perez *et al*. (2009) represents the current state-of-the-art for EFTEM characterization of fine particles at high spatial resolution and good signal-to-noise ratio. Figure 16.13 illustrates these results for 1–35 nm Y-Cr-O particles in an ODS-RAFMS, obtained by employing two C_s correctors (for probe and image mode), an Ω filter and a multivariate statistical analysis procedure. Two yttria (Y_2O_3) phases were recognized, having either monoclinic or cubic structures, and the particles had a Cr-rich outer shell. The Cr-O shell could be detected down to the smallest particles, where its width was 1.2 nm! Such high resolution characterization of phase composition can be compared directly with the



16.12 EFTEM images of cubic AlN precipitates in a Fe-Al-N alloy, showing Ti-rich nuclei (Sennour and Esnouf, 2003).

© Woodhead Publishing Limited, 2012



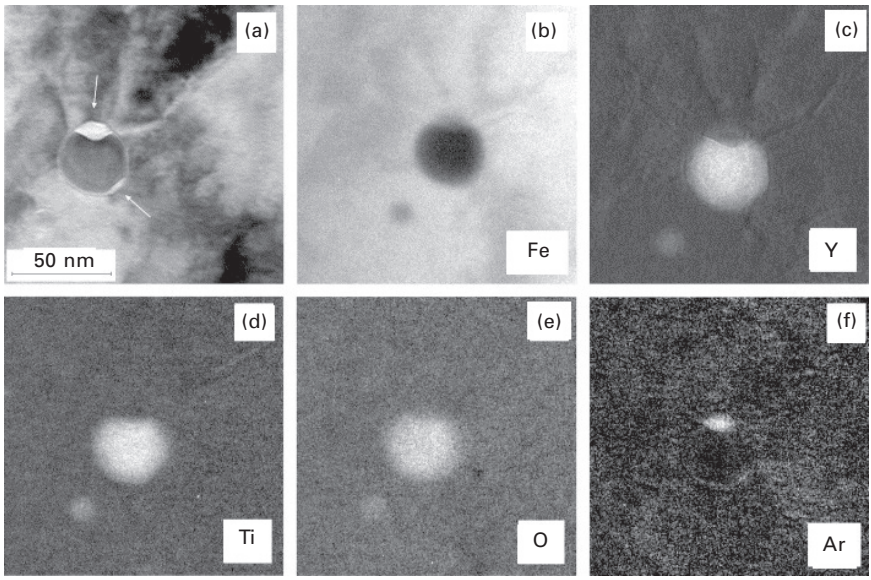
16.13 EFTEM elemental images, following multiple linear least squares (MLLS) fitting for Y-Cr-O particle in an ODS-RAFMS. Note presence of Cr-O shell on particles (Lozano-Perez *et al.*, 2009).

results of atom probe tomography of the same material, where the Cr-rich shell on Y-Cr-O particles has been observed (Williams *et al.*, 2010).

Another EFTEM study of ODS-RAFMS was carried out using a post-column imaging filter (GIF) (Klimiankou *et al.*, 2005). Figure 16.14 shows CTEM and EFTEM images of 10–25 nm $Ti_2Y_2O_7$ particles for various elemental EEL edges. The presence of small (5 nm) Ar-containing cavities is clearly seen in Figs 16.14(a) and (f). The details of an energy loss spectrum (see Section 16.4.2) immediately above a sharp ionization edge can also be analysed. This energy-loss near-edge structure (ELNES) is sensitive to the bonding or valence state of the ionized atom. For example, the dissolution of Fe_3C during extreme plastic deformation of pearlite has been monitored by combining EFTEM imaging with ELNES observations (Wetscher *et al.*, 2006).

High angle annular dark field (HAADF) imaging is obtained in a scanning

© Woodhead Publishing Limited, 2012



16.14 (a) CTEM and (b)–(f) EFTEM elemental images of the same $Ti_2Y_2O_7$ particle in an ODS-RAFMS. EFTEM 3-window method with Fe $L_{3,2}$, Y $M_{5,4}$, Ti $L_{3,2}$, O K and Ar $L_{3,2}$ edges (Klimiankou *et al.*, 2005).

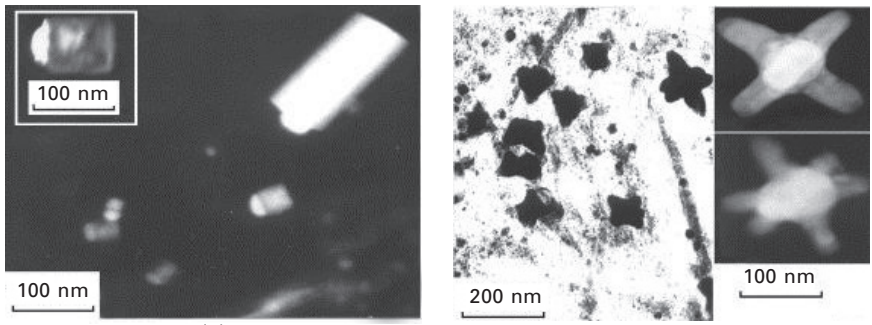
transmission electron microscope (STEM) by detecting only high angle (>~50 mrad) incoherently scattered electrons (Nellist and Pennycook, 1998). Since the scattering angle is a function of atomic number, the DF image is chemistry-specific (as compared with crystallography-specific for a CTEM-DF image), and is also called a 'Z-contrast' image. In comparison with EFTEM, annular dark field (ADF) and high angle annular dark field (HAADF) imaging has been employed much less frequently in TEM studies of steels. It has been used to characterize duplex precipitates, where the phases have different composition but similar crystal structure (Fig. 16.15), and to provide more uniform contrast from precipitates for quantitative measurements (Fig. 16.16). It has also been employed to determine the dissociation of Fe_3C in drawn pearlitic wire (Park *et al.*, 2011).

16.4.2 Microchemical analysis

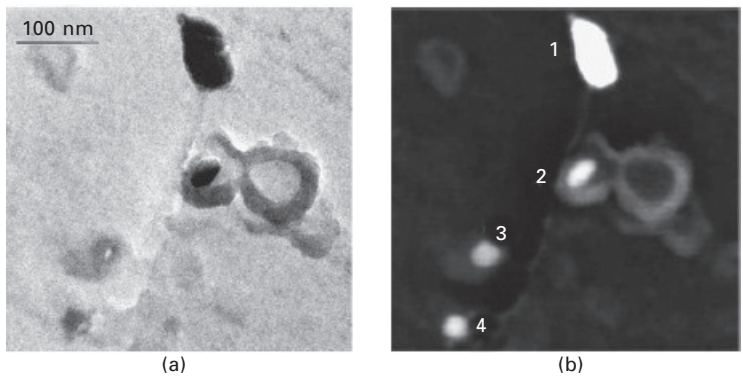
X-ray microanalysis (XEDS) continues to be the predominant technique for determining phase composition and spatial distribution of alloy elements. It is possible to obtain elemental mapping at the atomic level with a state-of-the-art silicon-drift XEDS detector (Botton *et al.*, 2010), although this has not yet been reported for any steels.

Electron energy loss spectroscopy (EELS) is now an important

© Woodhead Publishing Limited, 2012



16.15 STEM ADF images of duplex (Ti,Nb)(C,N) precipitates in a Ti-Nb microalloyed steel showing Ti-rich 'cores' and Nb-rich 'caps': (a) plate and cuboid morphology; (b) cruciform morphology (Craven *et al.*, 2000).



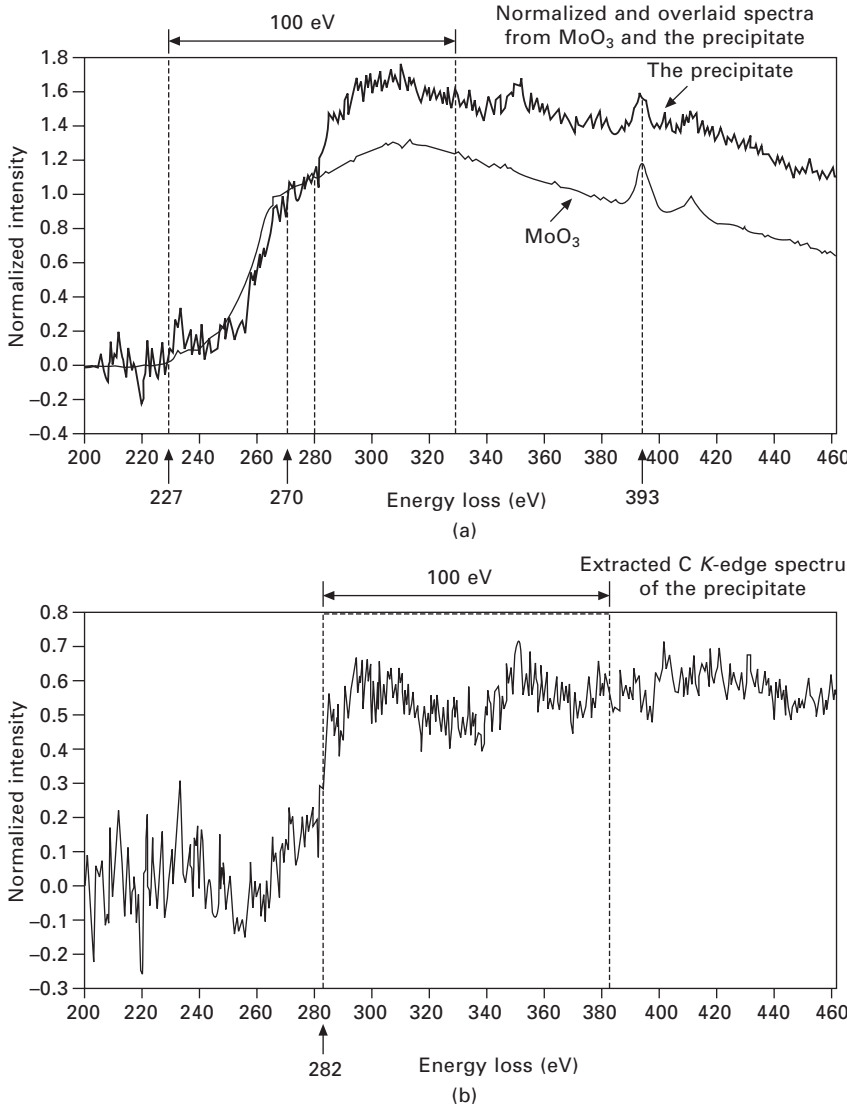
16.16 Same NbC precipitates as in Fig. 16.10, on Al_2O_3 extraction replicas: (a) CTEM-BF, (b) HAADF.

complementary microanalysis technique. EELS developed as a TEM technique to measure the energy of inelastically scattered electrons and hence obtain chemical information, mainly by identifying inner-shell ionization events. A major incentive in the development of EELS was the ability to detect light elements, since it is not limited by fluorescence yield as is the case with XEDS (Egerton, 2011). Hence, EELS is widely used for the characterization of carbonitride phases in steels. An EEL spectrum is obtained with the magnified image of the specimen on the viewing screen, which is coincident with the spectrometer entrance aperture ('TEM image mode'). The emerging electrons enter a magnetic prism spectrometer below the microscope column and the energies of all the electrons are measured simultaneously ('parallel EELS' – PEELS). An EELS spectrum is a plot of counts vs. energy loss, which appears as a series of discrete edges on a smoothly varying background

© Woodhead Publishing Limited, 2012

(e.g., Fig. 16.17). Qualitative chemical analysis involves identifying the ionization edges on the EELS spectrum, and is limited mainly by the edge height-to-background ratio ('jump ratio').

Quantitative EELs analysis involves background subtraction, removal of multiple scattering effects by deconvolution and determination of 'k



16.17 (a) Normalized and overlaid EEL spectra of a precipitate particle in a cast + heat treated duplex stainless steel and for a MoO_3 powder standard. (b) The extracted C *K*-edge EEL spectrum of the precipitate (Kuimalee *et al.,* 2010).

© Woodhead Publishing Limited, 2012

factors' using standards. Again, characterization of the microchemistry of small precipitates in steels provides examples of the application of these techniques. The compositions of the 'cap' and 'core' phases for the duplex precipitates in Fig. 16.15 were determined by EELS on C-extraction replica samples to be $(Ti_xNb_{1-x})N$ and $Nb(C_yN_{1-y})$, respectively, where x and y are in the range 0.8–1. (Note: it was necessary to collect spectra from particles overhanging the C-replica substrate.) The metal contents were confirmed by XEDS and the quantitative analyses were assisted by measurements of lattice parameters of the various phases on Al extraction replicas. Figure 16.17(a) shows the normalized EEL spectrum (following background subtraction and Fourier deconvolution) of a precipitate particle in a cast + heat treated duplex stainless steel, and that of MoO_3 powder used as a standard. The resultant C *K*-edge spectrum of the precipitate is given in Fig. 16.17(b). (Note: in this case, the TEM specimens were electropolished thin foils and spectra were collected from 'overhanging' 100 nm particles.) The integrated intensities under each spectrum within the 100 eV windows (shown) were used to obtain the Mo:C ratio. Combining this with an estimate of the metallic elements in the precipitate obtained by spot XEDS produced a precipitate composition of $Cr_{1.52}Fe_{2.33}Mo_{1.25}Ni_{0.17}Si_{0.46}$, i.e., $\sim M_6C$.

16.4.3 Convergent beam electron diffraction (CBED)

CBED is a powerful, but underutilized, TEM technique for determining the three-dimensional crystal structure of complex phases at high spatial resolution. The capability of this technique is evident from the work of Liu (2003), where the complete space group (L10, P4/mmm, a = 3.52, c = 3.63, A and Z = 2) was determined for ~50 nm 'L-phase' (MNi) particles in a 12Cr-9Ni-4Mo-2Cu maraging steel by CBED, XEDS and HRTEM. Accurate measurements of specimen thickness and phase lattice parameter can also be obtained from the HOLZ line patterns within CBED diffraction maxima. A procedure for determining the lattice parameter, and hence the C concentration of retained austenite in a TRIP steel, to a precision of 0.2 wt% is described by Scott and Drillet (2002).

16.5 *In-situ* transmission electron microscopy (TEM)

16.5.1 Heating/cooling experiments

Direct observation of phase transformations in the transmission electron microscope can provide unique insights with respect to transformation mechanisms and kinetics. For example, Khalid and Edmonds (1993) reported observations on the defect concentration in austenite associated with pearlite growth. In this case, the pearlite growth took place during 90 s heating increments at 500°C, followed by cooling and TEM observations at room

© Woodhead Publishing Limited, 2012

temperature. With currently available double-tilt hot-stage specimen holders (±45° tilt), it is possible to conduct *in-situ* heating experiments up to 1000°C with a temperature accuracy of ±15°C. Furthermore, images can be recorded at temperature individually or by high speed video camera. The series of images in Fig. 16.18 shows the progress of the martensite (dark) → austenite (light) transformation in a Fe-Ni-Mn alloy at 580°C, over a time interval of ~2 s. The austenite/lath-martensite interface was observed to move by the migration of 12–54 nm high ledges at velocities up to 0.79 μm/s, with 'stop-start' behaviour. The pre-existing martensite laths transformed on one side only, and preferentially receded at the locations of transformation twins. The thermal stability of yttria particles in an ODS-RAFMS is demonstrated by the series of *in-situ* TEM observations shown in Fig. 16.19. Note that the authors were able to record images of exactly the same area, under the same diffraction contrast conditions, at 100°C temperature intervals up to 1000°C, with 15 min hold at each temperature. (See row of particles located by arrow in each micrograph.) There was no change in the size or shape of the yttria particles over this temperature range, whereas the chromium carbides ($Cr_{23}C_6$) completely dissolved above 800°C.

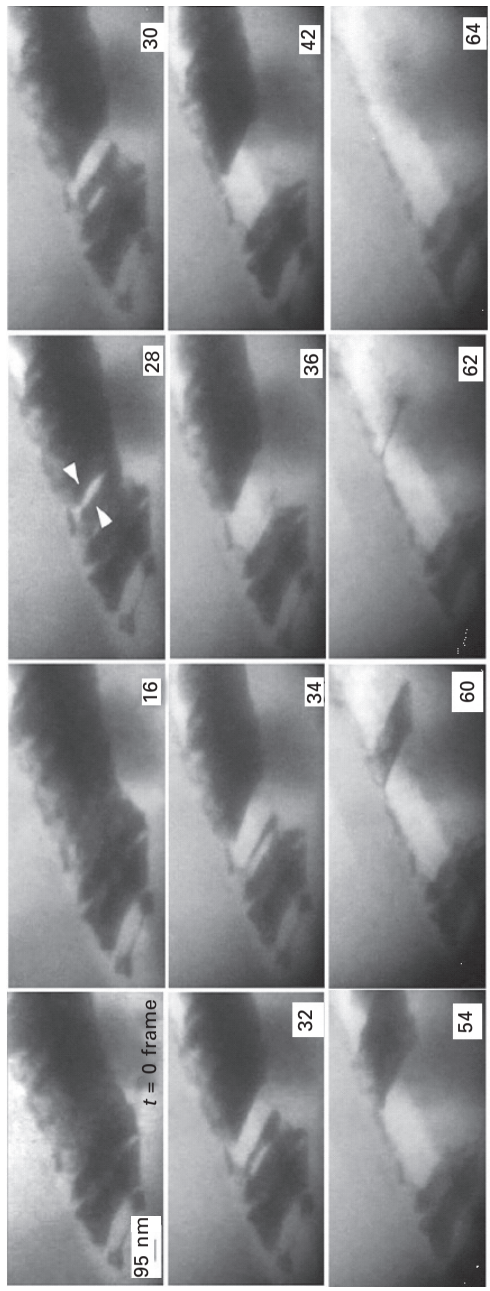
16.5.2 Straining experiments

In-situ deformation experiments can be employed to study the effects of (i) a (static) deformation substructure and (ii) (dynamic) deformation on phase transformations in steels. Early work was reported by Rao and Rashid (1997) on a V-microalloyed dual-phase (DP) steel employing a single-tilt (±45°) specimen holder and an elongation rate of ~ 0.00035 mm/s. (Note: owing to the irregular specimen geometry, it is difficult to estimate the deformation strain.) In this steel the 'non-ferritic phase' was a mixture of martensite and retained austenite (RA). With increasing deformation strain, the stacking faults in large (2–6 μm) RA particles nucleate the transformation to twinned plate martensite (Fig. 16.20(b,c)), accompanied by increased dislocation density in ferrite close to transformed austenite (Fig. 16.20(d)). Small (<1 μm) RA particles do not contain stacking faults and resist transforming to martensite until high strain is reached. More recently, Datta *et al.* (2009) have reported TEM observations on a metastable austenitic stainless steel, deformed *in-situ* to 5% strain, which show evidence of both $\delta \rightarrow \alpha'$ and $\delta \rightarrow \varepsilon$ strain-induced martensite transformations (Fig. 16.21).

16.6 Future trends: emerging transmission electron microscopy (TEM) techniques

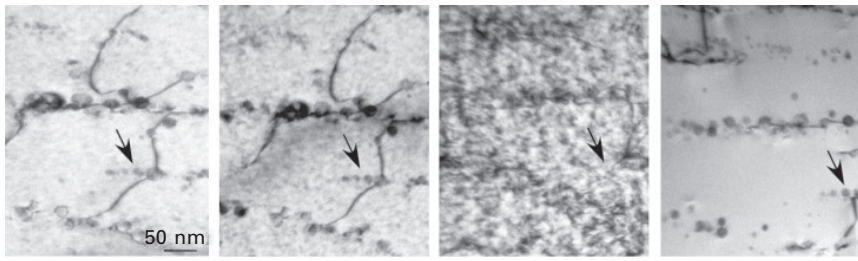
The output of all of the TEM techniques and applications described in this chapter are two-dimensional (2D) projections of the 3D structure. It

© Woodhead Publishing Limited, 2012

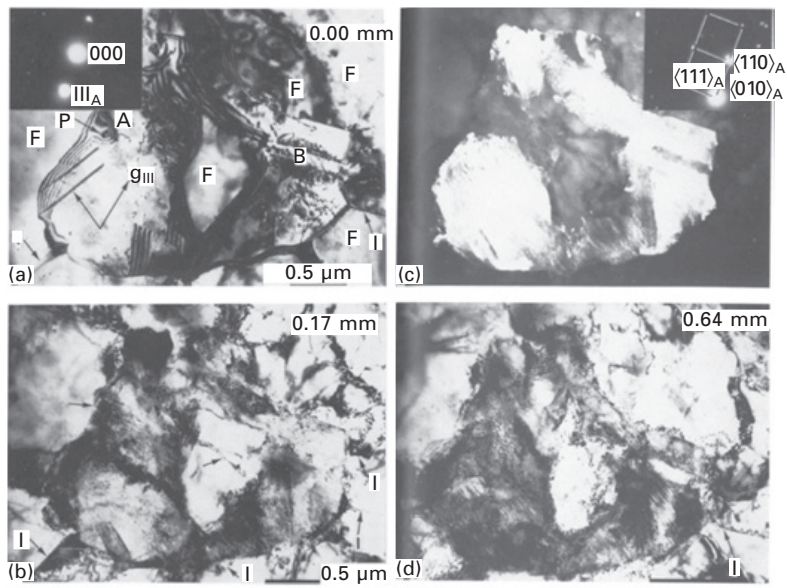


16.18 A sequence of images showing the migration of austenite (light)/martensite (dark) interface at ~ 580°C in a Fe-Ni-Mn alloy. Note migration of lower interface of martensite lath by ledge motion and splitting of the martensite at pre-existing transformation twins (arrows) (Wu *et al.*, 2011).

© Woodhead Publishing Limited, 2012



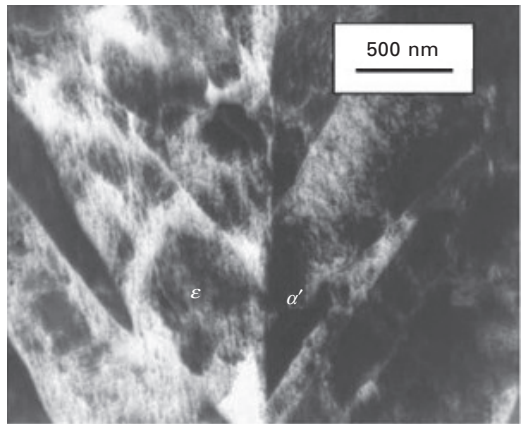
16.19 Yttria particles in an ODS-RAFMS at various temperatures during *in-situ* heating (Ramar *et al.*, 2008).



16.20 In-situ straining TEM of a V-microalloyed dual-phase (DP) steel: (a) before deformation, (b) after elongation to 0.17 mm, (c) DF of (b), (d) after elongation to 0.64 mm (F – ferrite, B – bainite, P – precipitate) (Rao and Rashid, 1997).

is possible to reconstruct 3D images from a series of conventional 'thin slice' TEM images recorded every 1–2° about a tilt axis over a large tilt range (70–80°). Electron tomography is a well-established technique, which has been widely applied in the study of biological materials and other soft materials (Midgley and Dunin-Borkowski, 2009). In electron tomography of crystalline materials STEM-HAADF imaging mode is used because the contrast is monotonic with specimen thickness. 3D EFTEM reconstructions and 3D EELS or XEDS maps can also be produced. 3D reconstructions of

© Woodhead Publishing Limited, 2012



16.21 CTEM BF image of austenitic stainless steel deformed *in-situ* to ~ 5% strain, showing α' and ε martensite (Datta *et al.*, 2009).

precipitate distributions (in non-ferrous alloys) (Kaneko *et al.*, 2008; Hata *et al.*, 2008) and dislocation networks (Barnard *et al.*, 2006) have been reported. It could be said that the ultimate in microscopy has been reached, now that 3D structure and chemical information can be obtained over all length scales by the complementary techniques of atom probe tomography, transmission electron tomography and scanning electron microscopy.

The capabilities of modern TEM instruments are truly amazing. The wide range of available TEM characterization techniques is crucial to advancing our understanding of structures and transformations in steels and all other materials. Unfortunately, these powerful experimental capabilities are not conveniently accessible to many researchers. As pointed out by Newbury and Williams (2000), TEM development has always focused on innovative design to achieve new plateaus of image resolution and chemical detection, which leads to the resulting high cost to purchase, operate and maintain these instruments. Hence, state-of-the-art TEMs are found only in specialized TEM centres, which must be accessed by the majority of researchers. This should stimulate progress in 'remote-access TEM', whereby all TEM operations can be carried out at the specialty TEM centre, without the need to travel there.

16.7 Sources of further information and advice

To encourage and assist readers to utilize the power of TEM to the utmost in their research, the following list of comprehensive references is provided:

de Graef, M (2003), *Introduction to conventional transmission electron microscopy*, Cambridge University Press, Cambridge.

© Woodhead Publishing Limited, 2012

Egerton, RF (2011), *Electron energy-loss spectroscopy in the electron microscope*, 3rd edn, Springer, New York.
Hirsch, PB, Howie, A, Nicholson, RB, Pashley, DW & Whelan, MJ (1977), *Electron microscopy of thin crystals*, R.E. Krieger Pub. Co., Huntington, NY.
Pennycook, SJ & Nellist, PD (eds) (2011), *Scanning transmission electron microscopy: imaging and analysis*, Springer, New York.
Spence, JCH (2003), *High-resolution electron microscopy* (monographs on the physics and chemistry of materials), Oxford University Press, Oxford.
Williams, DB & Carter, CB (2004), *Transmission electron microscopy: a textbook for materials science*, 2nd edn, Springer, New York.

16.8 Conclusions

This chapter is an overview of the techniques of TEM, with comment on their applicability to research on phase transformations and microstructure evolution in steels. It is evident that the information produced by state-of-the-art TEM techniques is necessary for the complete understanding of any material's behaviour at the 1–100 nm length scale. This is evident from the TEM examples cited in the other chapters in this book to support the current understanding of the various phase transformations in steels. For complete characterization of microstructures at all relevant length scales, complementary techniques such as atom probe tomography (APT), electron back scattered diffraction (EBSD) and bulk diffraction techniques (synchrotron X-ray and neutron) must be utilized, in addition to TEM. The reader is referred to Chapters 17–19 of this book for more detailed information on these techniques.

16.9 References

Barnard, JS, Sharp, J, Tong, JR & Midgley, PA (2006), 'High-resolution three-dimensional imaging of dislocations', *Science*, vol. 303, p. 319.
Borisova, D, Schimpf, C, Jahn, A, Klemm, V, Shreiber, G, Simek, D & Rafaja, D (2010), 'Microstructure investigations of the phase boundaries in the Bridgman TRIP steel crystal', *Solid State Phenomena*, vol. 160, pp. 211–216.
Botton, GA, Lazar, S & Dwyer, C (2010), 'Elemental mapping at the atomic scale using low accelerating voltages', *Ultramicroscopy*, vol. 110, pp. 926–934.
Boyd, JD (1976), 'A note on the microstructure of reheated, quenched, and tempered low carbon-manganese-niobium steel', *Metall. Trans. A*, vol. 7A, pp. 1604–1609.
Courtois, E, Epicier, T & Scott, C (2006), 'EELS study of niobium carbo-nitride nano-precipitates in ferrite', *Micron*, vol. 37, pp. 492–502.
Craven, AJ, He, K, Garvie, AJ & Baker, TN (2000), 'Complex heterogeneous precipitation in titanium-niobium microalloyed Al-killed HSLA steels – I. (Ti,Nb)(C,N) particles', *Acta Mater.*, vol. 48, pp. 3857–3868.

© Woodhead Publishing Limited, 2012

Cui, H, Sun, F, Chen, K, Zhang, L, Wan, R, Shan, A & Wu, J (2010), 'Precipitation behaviour of Laves phase in 10%Cr steel X12CrMoWVNbN10-1-1 during short-term creep exposure', *Mater. Sci. and Eng. A*, vol. 527, pp. 7505–7509.

Datta, K, Delhez, R, Bronsveld, PM, Beyer, J, Geijselaers, HJM & Post, J (2009), 'A low-temperature study to examine the role of ε-martensite during strain-induced transformations in metastable austenitic stainless steels', *Acta Mater.*, vol. 57, pp. 3321–3326.

Egerton, RF (2011), *Electron energy-loss spectroscopy in the electron microscope*, 3rd edn, Springer, New York.

Han, K, van Genderens, MJ, Bottger, A, Zandbergen, HW & Mittemeijer, EJ (2001), 'Initial stages of Fe-C martensite decomposition', *Phil. Mag. A*, vol. 81, pp. 741–757.

Hata, S, Kimura, K, Gao, H, Matsumura, S, Doi, M, Moritani, T, Barnard, JS, Tong, JR, Sharp, JH & Midgely, PA (2008), 'Electron tomography imaging and analysis of γ' and γ domains in Ni-based superalloys', *Adv. Mater.*, vol. 20, pp. 1905–1909.

Hirsch, PB, Howie, A, Nicholson, RB, Pashley, DW & Whelan, MJ (1977), *Electron microscopy of thin crystals*, R.E. Krieger Pub. Co., Huntingdon, NY.

Kaneko, K, Inoke, K, Sato, K, Kitawaki, K, Higashida, H, Arslan, I & Midgely, PA (2008), 'TEM characterization of Ge precipitates in an Al-1.6 at% Ge alloy', *Ultramicroscopy*, vol. 108, pp. 210–220.

Khalid, FA & Edmonds, DV (1993), 'Observations concerning transformation interfaces in steels', *Acta Metal. Mater.*, vol. 41, pp. 3421–3434.

Klimiankou, M, Lindau, R & Moslang, A (2005), 'Energy-filtered TEM imaging and EELS study of ODS particles and argon-filled cavities in ferritic-martensitic steels', *Micron*, vol. 36, pp. 1–8.

Kuimalee, S, Chairuangsri, T, Pearce, JTH, Edmonds, DV, Brown, AP & Brydson, RMD (2010), 'Quantitative analysis of a complex metal carbide formed during furnace cooling of cast duplex stainless steel using EELS and EDS in the TEM', *Micron*, vol. 41, pp. 423–429.

Liu, F, Tang, JE, Asteman, H, Svensson, J-E, Johansson, L-G & Halvarsson, M (2009), 'Investigation of the evolution of the oxide scale formed on 310 stainless steel oxidized at 600°C in oxygen with 40% water vapour using FIB and TEM', *Oxid. Met.*, vol. 71, pp. 77–105.

Liu, P (2003), 'Space-group and atomic structure determination of a nano-sized ordered phase derived from a f.c.c. structure in maraging steel 12Cr-9Ni-4Mo-2Cu using transmission electron microscopy', *Acta Cryst.*, vol. B59, pp. 167–174.

Lozano-Perez, S, Titchmarsh, JM & Jenkins, ML (2006), 'Determination of the Fe content of embedded Cu-rich particles in ferritic alloys using energy-filtered TEM', *Ultramicroscopy*, vol. 106, pp. 75–91.

Lozano-Perez, S, de Castro Bernal, V & Nicholls, RJ (2009), 'Achieving sub-nanometre particle mapping with energy-filtered TEM', *Ultramicroscopy*, vol. 109, pp. 1217–1228.

Midgley, PA & Dunin-Borkowski, RE (2009), 'Electron tomography and holography in materials science', *Nature Materials*, vol. 8, pp. 271–280.

Monzen, R, Jenkins, ML & Sutton, AP (2000), 'The bcc-to-9R martensitic transformation of Cu precipitates and the relaxation process of elastic strains in an Fe-Cu alloy', *Phil. Mag. A*, vol. 80, pp. 711–723.

Nellist, PD & Pennycook, SJ (1998), 'Subangstrom resolution by underfocused incoherent transmission electron microscopy', *Phys. Rev. Letts.*, vol. 81, pp. 4156–4159.

Newbury, DE & Williams, DB (2000), 'The electron microscope: the materials characterization tool of the millenium', *Acta Mater.*, vol. 48, pp. 323–346.

© Woodhead Publishing Limited, 2012

Ogawa, K & Kajiwara, K (2006), 'Basic differences between martensitic and bainitic transformations revealed by high resolution electron microscopy', *Mater. Sci. and Eng. A*, vols 438–440, pp. 90–94.

Park, J, Kim, S-D, Hong, S-P, Baik, S-I, Ko, D-S, Lee, CY, Lee, D-K & Kim, Y-W (2011), 'Quantitative measurement of cementite dissociation in drawn pearlitic steel', *Mater. Sci and Eng. A*, vol. 528, pp. 4947–4952.

Rainforth, WM, Black, MP, Higginson, RL, Palmiere, EJ, Sellars, CM, Prabst, I, Warbichler, P & Hofer, F (2002), 'Precipitation of NbC in a model austenitic steel', *Acta Mater.*, vol. 50, pp. 735–747.

Ramar, A, Spatig, P & Schaublin, R (2008), 'Analysis of high temperature deformation mechanism in ODS EUROFER97 alloy', *J. Nucl. Mater.*, vol. 382, pp. 210–216.

Rao, BVN & Rashid, MS (1997), 'Direct observations of deformation-induced retained austenite transformation in a vanadium-containing dual phase steel', *Mater. Character.*, vol. 39, pp. 435–453.

Scott, C & Drillet, J (2002), 'Quantitative analysis of local carbon concentrations in TRIP steels', *Int. Conf. on TRIP-Aided High Strength Ferrous Alloys, GRIPS*, Bad Harzburg, 2002, pp. 97–102.

Scott, CP, Chaleix, D, Barges, P & Rebischung, V (2002), 'Quantitative analysis of complex carbo-nitride precipitates in steels', *Scripta Mater.*, vol. 47, pp. 845–849.

Sennour, M & Esnouf, C (2003), 'Contribution of advanced microscopy techniques to nano-precipitates characterization: case of AlN precipitation in low-carbon steel', *Acta Mater.*, vol. 51, pp. 943–957.

Sugiyama, M & Sigesato, G (2004), 'A review of focused ion beam technology and its applications in transmission electron microscopy', *J. Electron Microscopy*, vol. 53, pp. 527–536.

Weng, KL, Chen, HR & Yang, JR (2004), 'The low-temperature aging embrittlement in a 2205 duplex stainless steel', *Mater. Sci. and Eng. A*, vol. 379, pp. 119–132.

Wetscher, F, Pippan, R, Sturm, S, Kauffmann, F, Scheu, C & Dehm, G (2006), 'TEM investigations of the structural evolution in a pearlitic steel deformed by high-pressure torsion', *Metall. and Mater. Trans. A*, vol. 37A, pp. 1963–1968.

Williams, C, Marquis, EA, Cerezo, A & Smith, GDW (2010), 'Nanoscale characterization of ODS Eurofer97 steel: an atom-probe tomography study', *J. Nucl. Mater.*, vol. 400, pp. 37–45.

Williams, DB & Carter, CB (2004), *Transmission electron microscopy: a textbook for materials science*, 2nd edn, Springer, New York.

Wu, J, Howe, JM & Zhang, W-Z (2011), 'An *in-situ* transmission electron microscopy study of interface growth during martensitic transformation in an Fe-Ni-Mn alloy', *Acta Mater.*, vol. 59, pp. 3297–3303.

Yao, Z (2010), Queen's University, Kingston, ON, Canada, unpublished research.

Yu, J, Liu, J, Zhou, W, Zhang, J & Wu, J (2007), 'Cross-sectional TEM observation of iron-zinc intermetallic Γ and Γ_1 phases in commercial galvannealed IF steel sheets', *Materials and Design*, vol. 28, pp. 249–253.

Zhang, X, Misra, A, Wang, H, Nastasi, M, Embury, JD, Mitchell, TE, Hoagland, RG & Hirth, JP (2004), 'Nanoscale-twinning-induced strengthening in austenitic stainless steel thin films', *App. Phys. Letts.*, vol. 84, pp. 1096–1098.

Zhou, Z, Rainforth, WM, Luo, Q, Hovsepian, PEh, Ojeda, JJ & Romero-Gonzalez, ME (2010), 'Wear and friction of TiAlN/VN coatings against Al_2O_3 in air at room and elevated temperatures', *Acta Mater.*, vol. 58, pp. 2912–2925.

© Woodhead Publishing Limited, 2012

17

Atom probe tomography for studying phase transformations in steels

M. K. MILLER, Oak Ridge National Laboratory, USA

Abstract: Atom probe tomography is a three-dimensional micro- or nano-characterization technique that is routinely used to visualize and quantify the microstructure of materials at the atomic level. In this chapter, an overview of the technique of atom probe tomography is presented as it pertains to phase transformation in steels. The electropolishing and focused-ion beam-based methods used to fabricate the needle-shaped specimens of steels are summarized. The typical methods, such as atom maps and isoconcentration surfaces, used to visualize the phases and other fine scale microstructural features are outlined. The common methods used to analyze and quantify the various types of phase transformations in steels, including the early stages of nucleation and spinodal decomposition, are discussed.

Key words: atom probe tomography, three-dimensional atom probe, nucleation, spinodal decomposition, phase separation, local electrode atom probe.

17.1 Introduction

Atom probe tomography (APT) is an atomic scale microstructural characterization technique (Miller *et al*., 1996a; Miller, 2000; Kelly, 2007; Kelly and Miller, 2007; Seidman, 2007; Miller and Forbes, 2009; Seidman and Stiller, 2009) that has played a major role in understanding phase transformations in steels and many other materials. The atomic spatial resolution in three dimensions enables the finest scale and amplitude features and therefore, the earliest stages of phase transformations, such as nucleation and spinodal decomposition, to be characterized. In state-of-the-art three-dimensional atom probes, the volume of analysis can contain millions to billions of atoms. Therefore, even relatively coarse microstructural features can be characterized with atomic precision, especially when combined with

This submission was sponsored by a contractor of the United States Government under contract DE-AC05-00OR22725 with the United States Department of Energy. The United States Government retains, and the publisher, by accepting this submission for publication, acknowledges that the United States Government retains, a nonexclusive, paid-up, irrevocable, worldwide license to publish or reproduce the published form of this submission, or allow others to do so, for United States Government purposes.

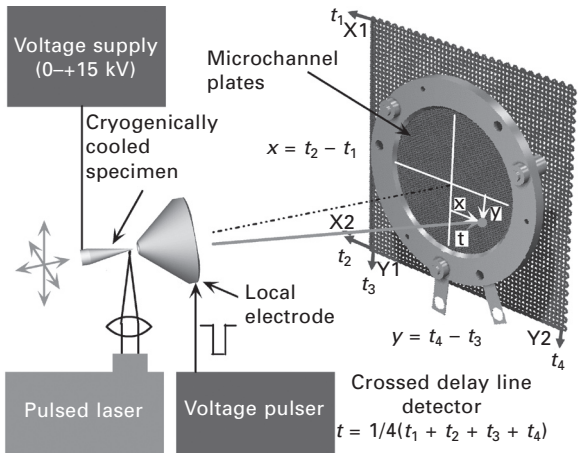
Published by Woodhead Publishing Limited, 2012

state-of-the-art focused ion beam-based, site-specific specimen preparation methods. As the time-of-flight mass spectrometer used in the technique has equal sensitivity to all elements and an unrestricted mass range, atom probe tomography is particularly useful for determining the distribution of light elements, such as carbon, nitrogen and boron. The technique is also used routinely to quantify the partitioning of the elements between co-existing phases, and solute segregated to interphase interfaces, grain boundaries, dislocations, etc. As the technique determines the local solute concentrations from the relative numbers of the atoms of each element present, the complex microstructures of multi-element steels are amenable to study. In addition to the element quantification, the technique also provides information on the three-dimensional morphology and topology of phases, and surface roughness of internal interfaces and boundaries.

In this chapter, an overview of atom probe tomography is presented, as it pertains to the atomic scale characterization of phase transformations in steels.

17.2 Outline of the technique

In atom probe tomography, atoms are removed from the surface of the apex region of the needle-shaped, cryogenically-cooled specimen by a field evaporation mechanism (Gomer, 1993). Two different but related methods may be used to field evaporate atoms from the specimen. Until recently, the predominant method was to superimpose a short duration, high voltage pulse on a standing voltage. Voltage pulsing is restricted to electrically conducting materials, including most steels, due to the attenuation of the amplitude of the pulse along the specimen in poor electrical conductors. More recently, laser pulsing was introduced in which a ~50–100 K temperature rise produced by a ~0.1– ~10 picosecond laser pulse that enables field evaporation on the standing voltage only during the duration of the heat pulse. Laser pulsing has the advantage of applying less mechanical stress to the specimen and therefore is useful for very brittle materials and poor electrical conductors. However, care is required in that the temperature rise during the pulse does not promote surface segregation or alter the microstructure. After the ions are removed from the specimen and pass through the counter electrode, they travel in a time-of-flight mass spectrometer, as shown in Fig. 17.1. The ions are detected on a position-sensitive, single atom, crossed delay line detector positioned at the end of the time-of-flight mass spectrometer. The identity of each ion is determined from its mass-to-charge state ratio, $m/n = cVt^2/d^2$, which is derived from the flight time, t, flight distance, d, a conversion constant, c, and total applied voltage, V. This relationship is derived from the equivalence of the potential energy of the ion on the surface of the specimen just prior to field evaporation and its kinetic energy just after leaving the



17.1 The components of a local electrode atom probe. Either voltage or laser pulses may be used to field evaporate atoms from the cryogenically cooled needle-shaped specimen. The ions pass through the counter electrode that is the entrance aperture to the time-of-flight mass spectrometer and are detected on position-sensitive, crossed delay line single atom detector.

specimen ($neE = \frac{1}{2}m(d/t)^2$). In voltage-pulsed instruments, an electrostatic reflectron lens, an ion mirror with a series of lens elements with increasing potential, is often used in the time-of-flight mass spectrometer to improve the mass resolution by compensating for small variations in the energy of the ions during the field evaporation process (Poschenrieder, 1972; Müller and Krishnaswamy, 1974). The lateral positions of the atoms in the specimen (x and y) are determined from the impact coordinates on the position-sensitive detector, and the distance along the specimen axis, z, is derived from the order in which the atoms are collected (Bas *et al.*, 1995; Gault *et al.*, 2008). Small uncertainties and errors in the reconstruction of the atom positions, such as trajectory aberrations and local magnification effects from different phases (Miller and Hetherington, 1991), limit the spatial resolution of each atom to ~0.1– ~0.3 nm.

The concentration of element i, in atomic percent, is estimated from the number of atoms of each element, n_i, in the volume compared to the total number of atoms in the volume, n_T, i.e., $c_i = n_i/n_T$. The standard error on the concentration estimate is given by $\sigma = \sqrt{c_i(1 - c_i)/n_T}$. Therefore, as the sample size decreases, the magnitude of the error increases. The minimum sensitivity is dictated by the number of atoms in the sample or feature of interest. For large sample sizes, the minimum sensitivity is in the parts per million range for all elements. However, in small precipitates it is considerably higher and the exact position of the precipitate–matrix interface becomes a critical parameter.

All information and data visualizations are derived from the ordered list of the atomic coordinates and mass-to-charge state ratios of the atoms in the volume analyzed. This list is an interrupted time series due to the less than ideal detection efficiency of the position-sensitive detector. Typically only 40–60% of the ions are collected with the current generation of instruments. In practice, this random loss of atoms is only a concern in analysis routines that are based on nearest neighbor arrangements, such as short range order. As atom probe tomography is a destructive technique, it is not possible to continuously watch the development of the microstructure. Instead, snapshots of the microstructure as a function of time are obtained. As the data are stored in a computer, the same data may be repeatedly analyzed by different methods after the experiment is concluded.

17.3 Specimen requirements

The goal of specimen preparation for atom probe tomography is to produce a sharp needle that contains the region of interest in the analyzable apex region of the specimen. This specimen should have a circular cross section with no protrusions, an end diameter of less than ~100 nm, and a taper angle of 1–10°. Ideally, the specimen should also be free of surface films or contamination. However, field evaporation at the start of the experiment can normally remove these surface layers and produce a pristine sample. These specimen parameters are important to acquire high quality data and also minimize the introduction of artifacts during the reconstruction of the atom positions. The thickness of the specimen in the apex region is amenable to examination in standard transmission electron microscopes so that it is possible to identify and characterize the features in the specimen prior to analysis by atom probe tomography.

Traditionally, field ion microscopy and atom probe tomography specimens are fabricated by cutting a small bar from bulk material with typical dimensions of ~0.2 × ~0.2 × 5–10 mm and electropolishing it into a sharp needle (Miller *et al.*, 1996a, p. 476; Miller, 2000, p. 28). This procedure is generally performed in two stages. The first stage rapidly removes material when the blank is immersed into an electrolyte (e.g., 25% perchloric acid in acetic acid for most steels) such that the top of the bar is in air and the lower part of the bar is in an inert liquid (e.g., a polyfluorinated polyether). As the top and bottom regions of the blank are protected from the electrolyte, material is only removed from the central region and naturally forms a necked region. As electropolishing continues, the diameter of the neck is progressively reduced until the point where the weight of the lower part of the specimen cannot be supported, as in a miniature tensile test. Just before separation, the blank is normally transferred to the second stage in which a slower and more precisely controllable electrolyte (e.g., 2% perchloric acid

in 2-butoxyethanol for most steels) is used so that a high quality surface finish and suitable end radius are achieved.

More recently, focused ion beam (FIB) methods have been widely adopted to fabricate atom probe tomography specimens. In these lift-out methods, a small bar is cut out with the gallium ion beam, mounted on a needle or multi-tip array with platinum or tungsten deposit, and then annular milled into a sharp needle (Miller *et al.*, 2007; Thompson *et al.*, 2007). Major advantages of this method for the analysis of steels are that the specimen may be cut out of a site-specific location, such as a particular precipitate, grain boundary, or interphase interface and the resulting cross section of the specimen is circular. Care is required in choosing appropriate milling parameters so as not to change the microstructure by introducing damage by gallium implantation (Knipling *et al.*, 2010). Therefore, low accelerating voltages (2–5 keV) are generally used for the final stages of annular milling to eliminate or reduce the depth of gallium implantation. It is also becoming increasingly common to perform a final annular ion mill on electropolished specimens to ensure that the cross section is circular and that the end radius is suitable for atom probe tomography.

The correct choice of analysis conditions in the three-dimensional atom probe is critical for steels, as steels normally contain several elements with different evaporation fields (Miller *et al.*, 1996a). The standing and pulse voltages (pulse fraction of 0.2), specimen temperature (typically 40–60 K), pulse repetition rate (200 kHz), and evaporation/collection rate (1–2%) should be selected to prevent preferential field evaporation or retention of all the elements in the steel. The new generation of atom probes with high pulse repetition rates minimizes the time spent at the standing voltage, and therefore helps to minimize preferential evaporation between the field evaporation pulses. The selection of specimen temperature is particularly important in laser-pulsed mode, where surface migration of carbon may occur even at cryogenic temperatures, and the local heating produced from the laser pulse may significantly affect the microstructure. Therefore, the lowest practical base temperature, typically less than 30 K, and minimum laser power that are consistent with no preferential field evaporation or retention of all elements in the steel should be used in laser-pulsed mode. It should be noted that holding a specimen at these cryogenic temperatures may transform any retained austenite present into martensite, thereby altering the microstructure, especially when the same specimen is resharpened for additional analyses. Specimen analysis procedures should also take into account the possibility of natural aging that may occur in some steels.

17.4 Recent developments

Several major improvements in instrumentation have been introduced over the last few years that have developed this methodology into a routine

microanalytical technique to complement light optical microscopy and the various forms of electron microscopy. A major breakthrough was made with the introduction of a local electrode positioned 30–40 μm from the apex of the specimen and with a similarly sized circular central aperture (Kelly *et al.*, 1995, 1996). This configuration enables a higher field to be generated for a given applied voltage on the specimen compared to the original remote electrode configuration. In order to maintain the same evaporation field, $F = V/kr$, during the experiment, the voltages are increased to accommodate the increase in radius, r, of the specimen as atoms are removed from the apex region (where k is a geometrical factor typically between 3 and 5). In general, a factor of two lower voltages (typically 1 to ~14 kV) is used to field evaporate specimens with the local electrode configuration. This configuration also enables lower voltage pulses to be used. These pulses can be generated by solid-state devices at substantially higher pulse repetition rates (up to 200 kHz), thereby significantly increasing the data acquisition rate. This change also requires improved (crossed delay line) single atom detectors and better timing systems to be used, which enhances the discrimination and deconvolution of multiple ions striking the detector on the same field evaporation pulse. Although energy-compensating torroidal sections and reflectron lenses were common in the time-of-flight mass spectrometers of previous generations of atom probe field ion microscopes and the early narrow field-of-view 3D atom probes to improve the mass resolution, they are not compatible with the wide field-of-view position-sensitive detectors used in the latest generations of 3D atom probes. Recently, Panayi (2006) developed a wide angle reflectron lens for these instruments and enabled mass resolutions to be obtained that were sufficient to fully resolve the mass peaks in steels that were 1/6 Da (or amu) or less apart. As mentioned above, the re-adoption of laser pulsing both enables more brittle materials to be examined and also improves the mass resolution to approximately the same level. Finally, FIB-based specimen preparation methods have enabled atom probe tomography specimens to be made from site-specific regions and also non-metallic phases, such as carbides, that were previously impossible to fabricate into APT specimens.

17.5 Interpretation of data

Several different forms of data processing are generally used for the visualization of microstructural features and the quantification of their size, morphology, and compositions. A library of analysis methods has been developed to extract quantitative information from most types of microstructural features found in steels (Miller *et al.*, 1996a, p. 271; Miller, 2000, p. 157). Some of the common types of representations and analyses are illustrated in the examples below.

The identification of each phase present is normally determined indirectly from the composition of the different regions of the data rather than from its crystal structure, as the spatial resolution of atom probe tomography is not currently sufficient to position each atom on its exact lattice site. There are several factors that influence the composition estimates, especially for nanoscale features, in which the phase composition may be far from its equilibrium or stoichiometric value and the position of the matrix-feature interface may be difficult to establish with sufficient precision due to solute concentration profiles and the various methods used to estimate the concentration, etc. In addition, carbon can field evaporate with several charge states and commonly as complex and molecular ions, i.e., C_i^{+}, C_i^{++}, C_i^{+++}, C_i^{++++} (i = 1..4), and MC_i^{n+} species, depending on the specimen temperature, evaporation rate, phase, phase composition, etc. This can lead to element assignment issues, e.g., the overlap of C^{+} and C_2^{++} at 12 Da (or u). In some cases, the ratio of the charge states can be estimated through the small (1.11% abundance) $_{13}C$ isotope and the relative abundances of $_{12}C^{+}$, $_{13}C^{+}$ $_{12}C_{12}C^{++}$, $_{12}C_{13}C^{++}$ and $_{13}C_{13}C^{++}$ mass peaks. This issue can only be unambiguously resolved through the determination of the charge state, n, e.g., via the measurement of the kinetic energy of each ion (see Section 17.7). Correct assignment is especially important for the C_2^{n+} and C_3^{n+} peaks due to the multiplying factor (2 and 3) for each ion. Therefore, there can be significant uncertainties in the concentration estimates. The presence of MC_i^{n+}, MB_i^{n+}, MN_i^{n+} and MO_i^{n+} species are common in steels that contain refractory elements, such as Ti, Mo, Nb, Ta, and W.

17.6 Characterizing and understanding phase transformations in various steels

Atom probe tomography and atom probe field ion microscopy have been used for over 40 years to understand many phenomena related to the phase transformations that occur in steels. In order to identify the microstructural features in complex steels, their morphology, size, composition and distribution are determined. This information must be interpreted correctly and then related to the correct phase, such as ferrite, martensite, austenite, cementite, ε-carbide, refractory carbides, oxides, silicides, etc., or other types of microstructural features, such as Cottrell atmospheres at dislocations and segregation to interfaces and grain boundaries. It is important to ascertain where all the solutes are located to ensure the correct mass balance and to identify grain or lath boundaries and dislocations, because they are common locations for heterogeneous nucleation and regions of enhanced solute diffusion. In this section, some examples of the different microstructures found in steels are presented to illustrate the types of analyses that are possible by atom probe tomography.

Published by Woodhead Publishing Limited, 2012

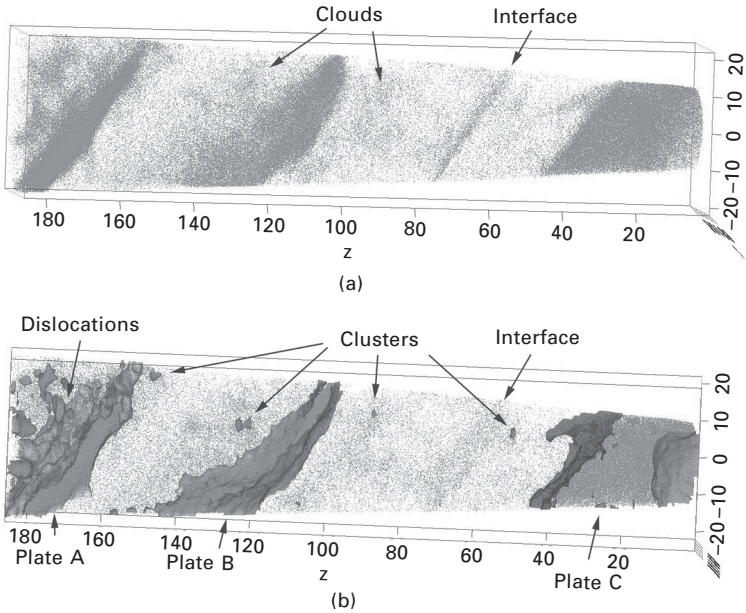
17.6.1 Precipitation and cluster formation

Atom probe tomography is well suited to the characterization of small features, such as precipitates and solute clusters. Typical uses are to follow the nucleation and growth of precipitates during tempering or aging behavior of steels. The spatial resolution of atom probe tomography enables the earliest stages of the process to be studied, including detecting and characterizing embryos. As the microstructure is characterized at different specific aging times, it is not possible to determine whether a detected embryo is smaller or larger than the critical nucleus and, therefore, whether it will dissolve or grow.

The effectiveness of the method for this analysis is primarily dictated by the number density of the precipitates. If the number density is less than approximately 10^{18} m^{-3}, the likelihood of randomly encountering precipitates in a dataset is small. For lower number densities, selected area FIB-based lift-out methods can be used to extract and fabricate a specimen containing ~20 nm diameter or larger precipitates. However, this method is not generally effective for smaller precipitates due to the difficulty in resolving them.

For datasets containing precipitates that are larger than ~2 nm in diameter, isoconcentration surfaces and atom maps are effective in revealing the distribution of the precipitates and whether they are homogeneously distributed or heterogeneously located at dislocations or interfaces. The solute partitioning between phases and solute enrichments at interfaces can be determined by a variety of methods, such as a proximity histogram (Hellman *et al.*, 2000), one-dimensional concentration profile, and radial concentration profile for spherical precipitates.

The most common initial form of data visualization is the *atom map* in which selected colored spheres or dots are used to represent the coordinates of one or more selected type of atom or element. The major element, i.e., iron, is normally omitted for clarity. Generally, atom maps provide insight regarding the presence and partitioning of solutes to precipitates and clusters and solute segregation to interfaces. The information derived from atom maps is used to decide on subsequent analysis methods. A carbon atom map of a high carbon, high silicon, nanocrystalline steel (Caballero *et al.*, 2009, 2010) that transformed to bainite during an isothermal heat treatment at 300°C is shown in Fig. 17.2(a). In this example, several different microstructural features are evident from the distribution of carbon atoms. There are three high carbon regions evident in the atom map, an interface that exhibits an enrichment of carbon, and some other regions with a carbon level higher than the low carbon ferrite matrix. The upper view is oriented so that the carbon-enriched interface is viewed exactly edge-on. In the lower view, the carbon-enriched interface is no longer clearly defined, as the volume has been rotated slightly away from the edge-on view. The ability to orient



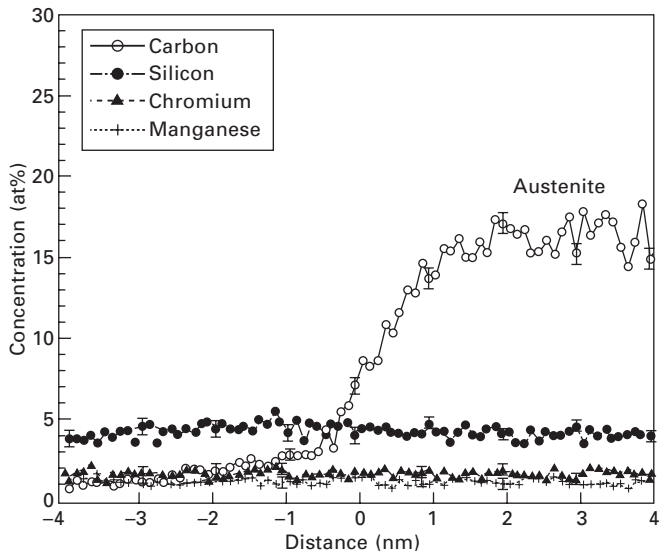
17.2 (a) Carbon atom map showing the distribution of carbon atoms, and (b) isoconcentration surfaces showing the outlines of phases and other solute-enriched microstructural features in a high carbon, high silicon, nanocrystalline bainitic steel. (a) is shown exactly edge-on to the interface, whereas the volume has been rotated in (b).

freely the volume in three dimensions provides a more complete view of the microstructure, as image overlap of different features in the thickness of the volume can be detected and avoided. Trajectory aberrations, local magnification effects, and the different atomic densities of phases can produce misleading interpretations on the extent of partitioning and segregation.

The three-dimensional morphology and distribution of phases may also be visualized by plotting isoconcentration surfaces to reveal the outline of phases and other solute-enriched microstructural features, as shown for an 8 at% C surface in Fig. 17.2(b). The concentration used for the isoconcentration surface is selected by the user to be intermediate to the concentrations of the phases of interest, e.g., precipitate and matrix. These isoconcentration surfaces are more synonymous with traditional micrographs and more intuitive than the atom maps. In this view, the extent and morphology of the three high carbon plate-shaped regions are more clearly defined. The carbon-enriched interface is not detected in this isoconcentration surface, indicating that its maximum carbon level is less than 8 at% C. As labeled in Fig. 17.2(b), plates A and B are thin high carbon 'plates' and the thicker plate-shaped region C is lower in carbon and most likely austenite. In addition, small spheroidal carbon-enriched regions or clusters and a dislocation tangle are visualized in

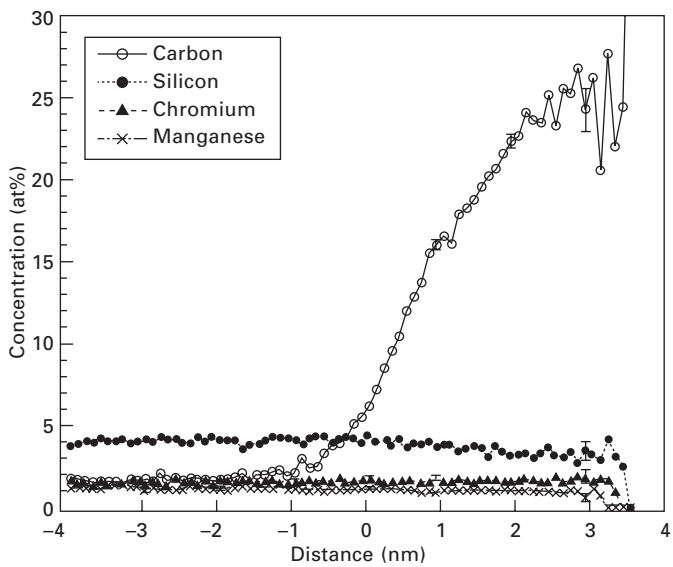
Fig. 17.2(b). The dislocation tangle is inferred from the linear morphology of the individual sections, the enhanced carbon level, and supporting evidence from a transmission electron microscopy characterization of this material. In this bainitic steel, transmission electron microscopy has revealed bainitic ferrite, α, thin austenite, γ, plates with average thicknesses of ~120 nm, ε-carbide $Fe_{2.4}C$, cementite Fe_3C, dislocations (in the form of isolated lines, loops, and tangles), and possibly carbon clusters and the products of spinodal decomposition after different heat treatments. Dislocation debris was often observed close to the austenite–bainitic ferrite interface. In addition to providing the visualization, the isoconcentration surface may be used to define the extent of the precipitates or phases so that the number of different types of atoms within or outside the surface(s) can be counted to estimate their individual compositions.

The isoconcentration surface is also used as the reference surface in two-phase materials, or volumes restricted to two phases, to investigate solute segregation and partitioning with a proximity histogram (Hellman *et al.*, 2000). The proximity histogram assumes or is constructed such that the interface is between only two phases, otherwise an averaged value is obtained. In this method, the closest distance of each atom to this reference surface is calculated and accumulated into a histogram. The solute concentration may then be calculated from the number of different ions in each bin and plotted as a function of distance from the interface, as shown in Fig. 17.3 for the



17.3 Proximity histogram across the austenite–ferrite interface (plate C) shown in Fig. 17.2. The carbon had partitioned between the austenite and ferrite phases but the chromium, silicon and manganese showed no partitioning consistent with para-equilibrium.

ferrite–austenite interface (plate C) shown in Fig. 17.2. The ~25 nm thick austenite plate exhibits a sharp interface with the ferrite and a uniform carbon content of 16.1 ± 1.1 at% C. The proximity histogram revealed that in this bainitic steel, the carbon had partitioned between the austenite and ferrite phases, but the transition elements, chromium, silicon and manganese, showed no partitioning, i.e., after the low temperature heat treatment, the bainite was in para-equilibrium. The proximity histogram of the leftmost, ~10 nm thick plate A exhibited a gradual increase in the carbon level over 2 nm from the bainitic ferrite, as shown in Fig. 17.4, and a maximum carbon level in its core of 26.7 ± 2.4 at% C. The maximum carbon level in the core of the central ~20 nm thick plate B was slightly lower at 24.4 ± 2.0 at% C. The overall average carbon concentrations over the full extent of the A and B plates, as estimated from the atoms within the isoconcentration surfaces, are much lower, 17.8 and 18.9 at% C, respectively. It is likely from the morphology and core compositions that both these features are cementite plates, possibly slightly sub-stoichiometric due to the low formation temperature. However, the low average carbon level could be interpreted as austenite without the supporting evidence from the transmission electron microscope. The carbon levels in the small spheroidal features reach ~16 at% C and exhibit no clear evidence of partitioning of the other solutes. These levels are significantly lower than the 25% or 29.4% for stoichiometric cementite or ε-carbide. Therefore, these features are probably carbon-enriched clusters. As the carbon level is similar to the carbon content of the austenite phase, they

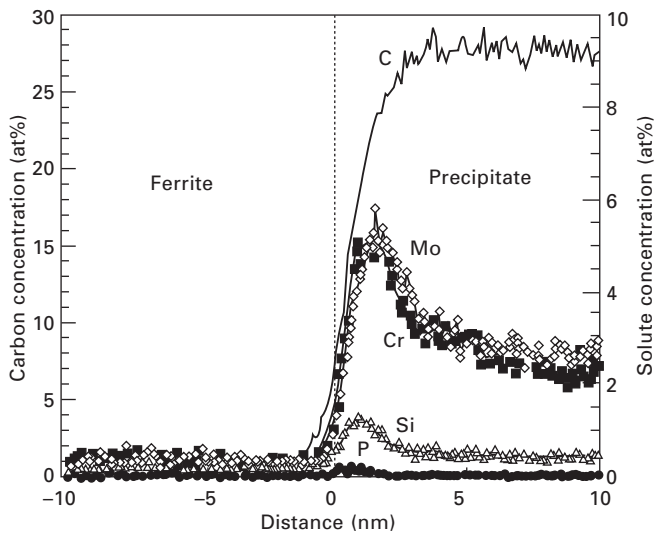


17.4 Proximity histogram across the cementite–ferrite interface (plate A) shown in Fig. 17.2.

could also be interpreted as austenite. However, the austenite interpretation is not supported by the transmission electron microscopy results. Note also the carbon-enriched clouds in the matrix, especially close to the designated features.

Interfacial segregation of all the solutes can often be visualized in atom maps, as shown in Fig. 17.2. The level of solute segregation or depletion can be quantified with the use of proximity histogram or concentration profiles. An example of chromium, silicon, molybdenum, and phosphorus enrichment to the precipitate side of the precipitate–ferrite matrix interface in a proximity histogram is shown in Fig. 17.5. The solute-enriched zone is approximately 2 nm in extent. The interfacial excess, Γ_i, is determined from the difference between the total number of solute atoms in the volume containing the interface and the numbers of solute atoms in the adjoining regions (i.e., the ferrite and precipitate), $n_{i(\alpha)}$ and $n_{i(\beta)}$, and the area of the interface, A, i.e., $\Gamma_i = (n_i - n_{i(\alpha)} - n_{i(\beta)})/A$ (Gibbs, 1948).

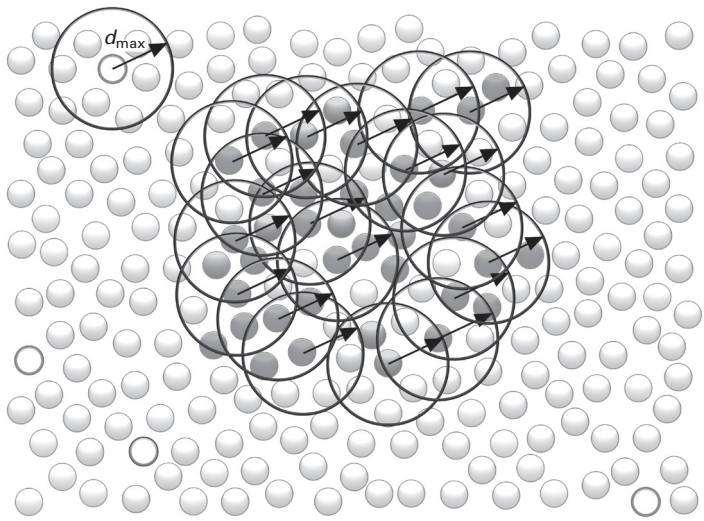
Due to the large datasets, data mining methods are often used to detect solute clusters and precipitates, especially for those features that are less than ~2 nm in diameter. For low solute (<1–5%) alloys, 'friend-of-friends' or 'cluster' search methods have been found to be effective approaches (Hyde and English, 2001; Stephenson *et al.*, 2007). In these algorithms, the data are searched for an individual or a specific set of solute atoms. Then, the data are searched for additional solute atoms that are within a user-specified maximum separation distance, typically 0.2–1 nm depending on the solute



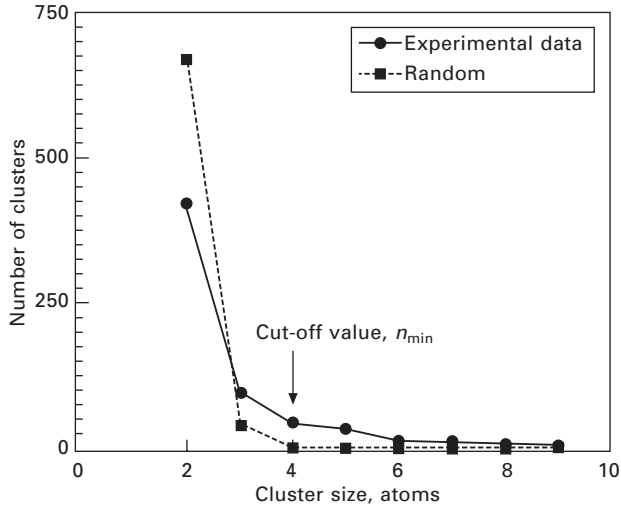
17.5 Proximity histogram across a ferrite–precipitate interface showing enrichments of Cr, Mo, Si and P on the precipitate side of the interface.

level in the matrix, from this identified solute atom, as shown in Fig. 17.6. If no other solute atoms are found within this distance, the solute atom is considered to belong to the matrix. If another solute atom is found within this distance, this recursive search is continued until the positions and types of all solute atoms within the cluster are identified. The search is continued for all clusters in the data. The data are then randomized with respect to the identity of the atom at each location and searched again to produce a comparative random solid solution condition.

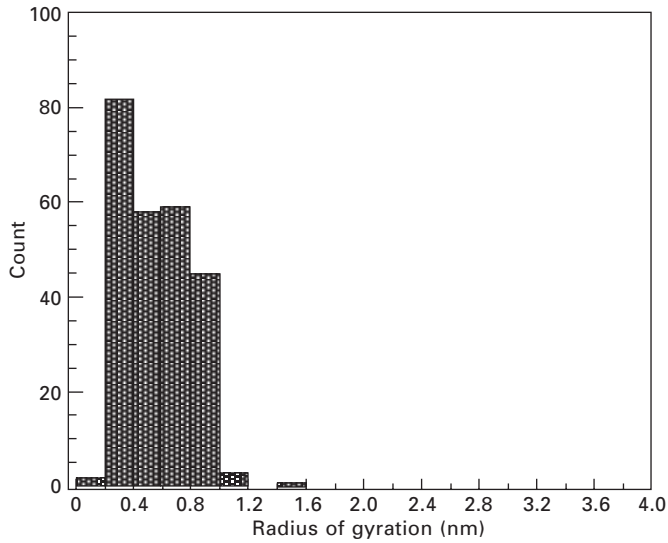
The two histograms of the number of clusters at each cluster size, as defined by the number of atoms comprising the cluster, are compared to differentiate between the solute agglomerations due to a random distribution of solute and clusters and precipitates produced by phase separation, as shown in Fig. 17.7. In this example of copper-enriched precipitates in steel, the maximum separation method did not detect any clusters in randomly distributed solute with more than three atoms, whereas the experimental data had 226 clusters/precipitates above this cut-off limit. The size distribution of the radii of gyration of these clusters is shown in Fig. 17.8. The method is able to detect clusters containing more than five solute atoms in low solute steels and may also be used to hide the solute atoms in the matrix to enhance the visibility of clusters and precipitates. The coordinates of the solutes within



17.6 The number of clusters of different sizes, as estimated from the maximum separation method. The randomized distribution indicates the number of clusters of each size expected in a random distribution in a solid solution. Deviations from the random distribution are due to clusters and precipitates. A total of 124 clusters was detected at larger sizes in the non-randomized data.



17.7 Size distribution of the clusters in the data shown in Fig. 17.5 that were larger than the cut-off limit of three atoms.



17.8 Size distribution of the copper-enriched precipitates detected by the maximum separation method.

the cluster are used to estimate the center of mass, radius of gyration, l_g, and the Guinier radius (for spherical particles, the Guinier radius is $\sqrt{(5/3)}\, l_g$) of each cluster or precipitate (Miller, 2000, pp. 160, 184). The number density of clusters in the volume is estimated from the number of clusters detected in the volume. As some of the finer precipitates will intersect the edge of

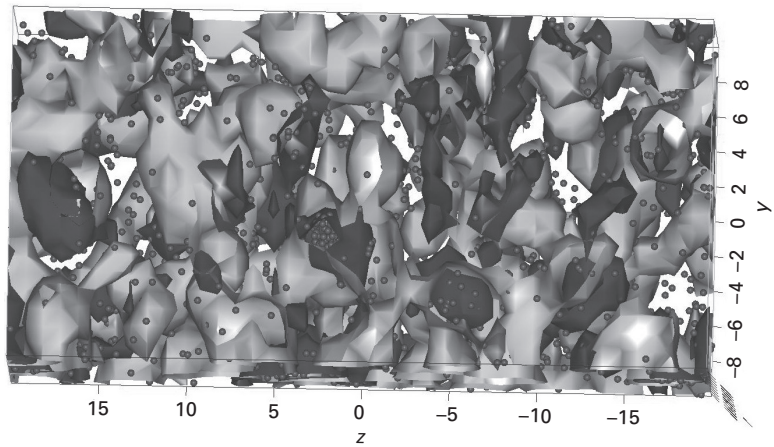
the analysis volume, a systematic methodology has to be used to eliminate those particles whose center of mass is not located within the volume of analysis. The volume is normally estimated from the number of atoms in the analysis volume, detection efficiency of the mass spectrometer, and the atomic densities of the matrix and precipitate phases. The composition of the clusters may also be estimated.

As the field-of-view of the atom probe is relatively limited, it is possible that some larger phases extend beyond the edge of the volume, such as the austenite and cementite plate-shaped regions shown in Fig. 17.2. In these cases, it is generally not possible to estimate the maximum thickness or extent of the 'plate'. The field-of-view also limits the area of a grain boundary that can be characterized.

17.6.2 Spinodal decomposition and phase separation within a miscibility gap

Phase separation in steels is not restricted to nucleation and growth of different carbides. For example, in the δ-ferrite phase of duplex stainless steels (Miller and Bentley, 1990; Miller *et al*., 1995a), high chromium oxide dispersion strengthened (ODS) ferritic alloys such as PM 2000™ (Capdevila *et al*., 2008) and maraging steels, spinodal decomposition and non-classical nucleation can occur within the low temperature miscibility gap leading to the formation of a chromium-enriched α' phase and an iron-rich α matrix. An example of this α–α' decomposition in the PM 2000 alloy aged within the miscibility gap is shown in Fig. 17.9. Under these low temperature aging conditions, almost all of the α' phase in this view is a single particle indicating a percolated, interconnected network structure. The other regions of the α' phase are on the edge of the analysis volume where the connection cannot be determined. In addition to this α–α' decomposition, a second distribution of titanium- and aluminium-enriched particles of the Fe(Ti,Al) β' phase is also evident. The lower volume fraction of isolated particles of the β' phase is located on the surfaces of the α' phase.

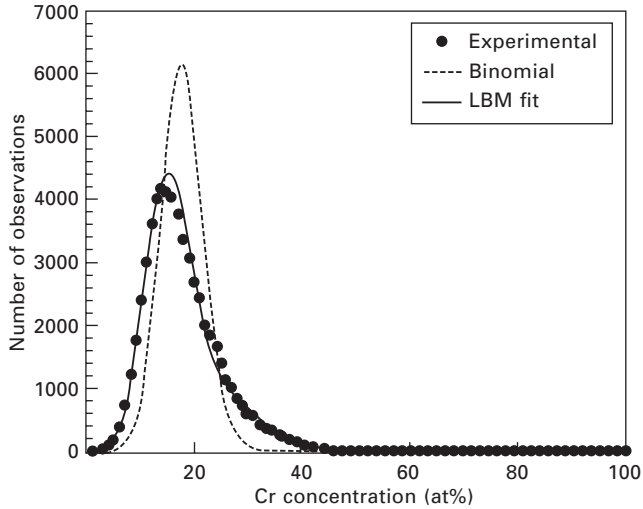
Atom probe field ion microscopy, the forerunner to atom probe tomography, was the first experimental technique to correctly identify the microstructure responsible for the so-called 475° embrittlement that occurs in Fe-Cr alloys (Brenner *et al*., 1982). This embrittlement was due to spinodal decomposition of the ferrite into an interconnected network of a chromium-enriched α' and an iron-rich α phase. Atom probe tomography can follow the evolution of the composition, morphology, and size of these phases from the earliest stages of formation and provide the necessary experimental evidence for the confirmation of spinodal decomposition (Hyde *et al*., 1992). As the chromium content of the parent phase increases (from the low solute edge towards the center of the miscibility gap), the lever rule indicates that the volume fraction of the



17.9 Example of the percolated, interconnected network structure of the α' phase (light grey) and isolated titanium- and aluminum-enriched particles of the Fe(Ti,Al) β' phase (dark grey) in the PM 2000 alloy aged for 24 h at 435°C. The α matrix phase is the volume between these phases. Titanium atoms (small grey spheres) are also shown.

α' phase produced at a given temperature increases. Atom probe tomography has shown that the morphology of the α' phase progressively changes from isolated particles to a fully interconnected network structure as its volume fraction increases (Miller *et al.*, 1995b; Hyde *et al.*, 1995a, 1995b).

Phase separation can be detected at the earliest stages by fitting the experimental results to models, such as the binomial distribution to test for a random distribution of solute, or the Langer, Bar-on, Miller (LBM) model (Langer *et al.*, 1975), to the frequency distribution of the concentrations of fixed size voxels (Hetherington *et al.*, 1991; Miller *et al.*, 1996a; Moody *et al.*, 2008) to estimate the concentrations and the volume fraction of the phases, as shown in Fig. 17.10. As with the proximity histogram, the standard double Gaussian LBM approach should be limited to two-phase systems. In this example, the experimental chromium frequency distribution of 100 atom voxels is significantly broader than the binominal distribution and the χ^2 value is extremely large, ~600 000 with 28 degrees of freedom, indicating a rejection of the hypothesis of a random solid solution, and therefore, that phase separation has occurred. The fit with the double Gaussian distributions of the LBM model is significantly better – the χ^2 value is ~1182 with 44 degrees of freedom. At the later stages where the scale of the microstructure is coarser, selected volume measurements, 1D concentration profiles, or proximity histograms can be used. The scale of the solute-enriched regions can be estimated from autocorrelograms (Miller *et al.*, 1996a, p. 315) for



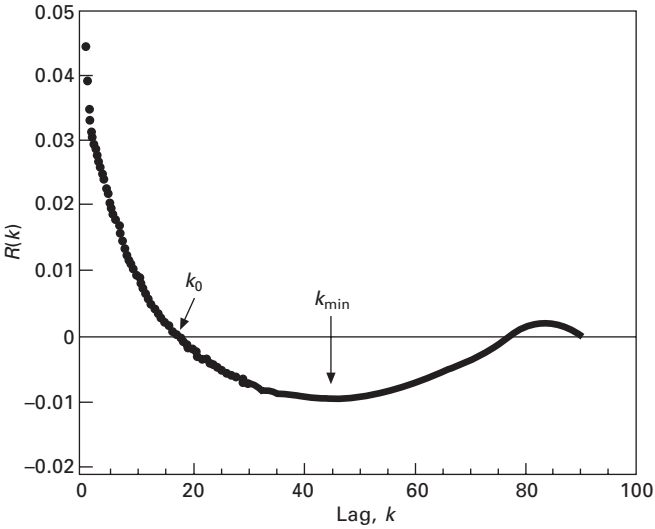
17.10 A comparison of an experimental concentration frequency distribution and a binomial distribution of the chromium concentrations of 100 atom voxels from the PM 2000 alloy aged for 24 h at 435°C. A maximum likelihood fit of the experimental data based on the Langer, Bar-on, Miller (LBM) model is also shown. The common doubly-charged $_{54}Cr/_{54}Fe$ isobar has not been included in this analysis.

both isolated particles and the interconnected network structure, as shown in Fig. 17.11. The lags, k, at the first minimum, k_{min}, and the zero crossing value, k_0, provide estimates of the size of the features present. In the latter case, the wavelength of the modulations can also be estimated. Another phase separation involving the titanium and aluminum atoms is also evident in the data shown in Fig. 17.9 for the PM 2000 alloy. The high spatial resolution of the atom probe can be used to investigate whether the titanium- and aluminium-enriched particles of the Fe(Ti,Al) β' phase are due to rejection of these solutes from the α' phase and nucleation on the surface of the α' phase, or an independent nucleation event in the solute-enriched α matrix.

17.6.3 Phase transformation and stability under extreme conditions

The behavior and susceptibility of steels towards phase transformations can be significantly influenced by the environment, particularly under extreme conditions, such as irradiation, and extreme deformation as in mechanical alloying or cold rolling. Under these conditions, higher than equilibrium concentrations of vacancies are present and the alloy is far from equilibrium. These regimes can accelerate the kinetics of phase transformations and also influence the position of the phase boundaries (Miller *et al.*, 1996b).

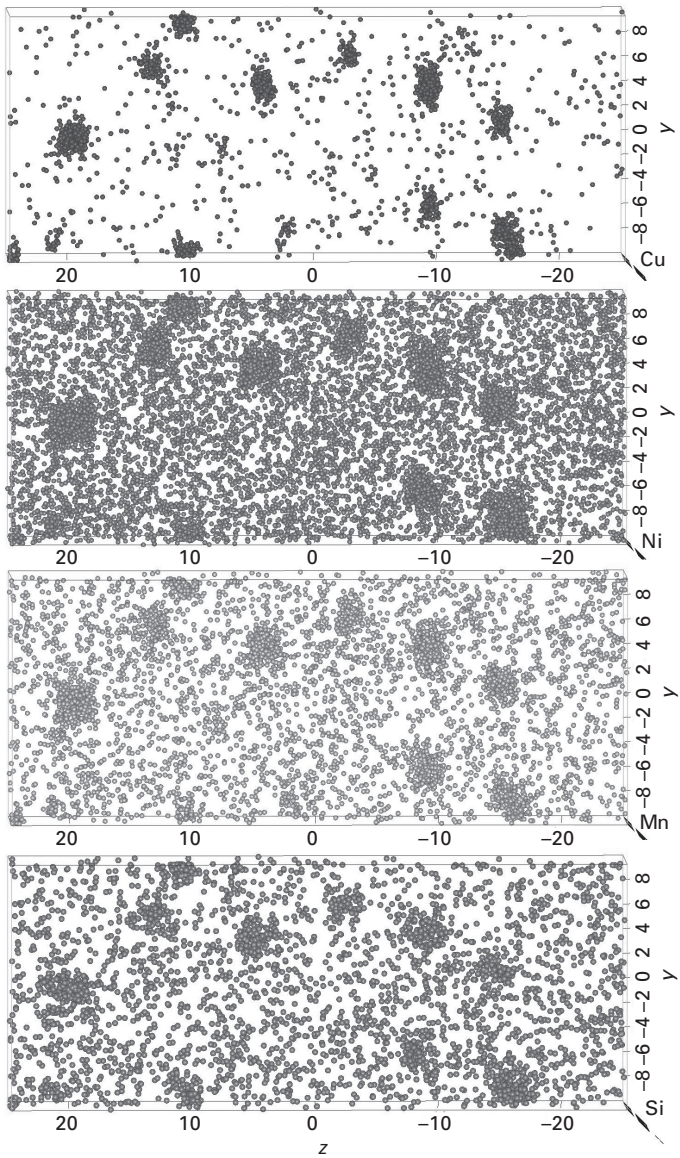
Published by Woodhead Publishing Limited, 2012



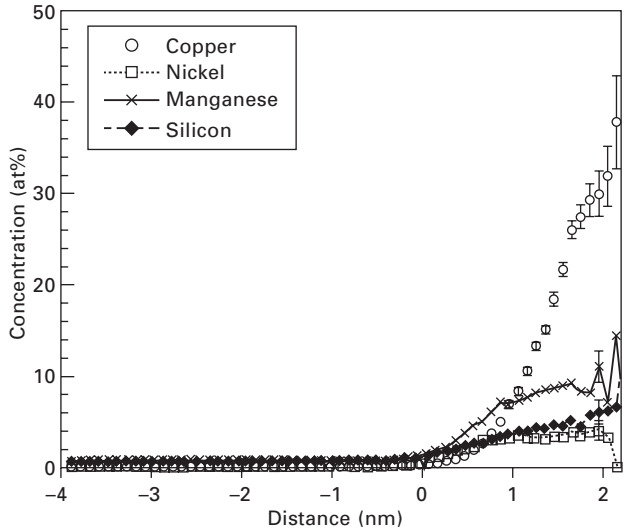
17.11 Autocorrelation of the Cr-enriched α' phase in the PM 2000 alloy. The lags at k_{min} and k_0 provide estimates of the size of the features present.

A classic example of phase transformation under extreme conditions is the embrittlement of pressure vessel steels during long-term service in a nuclear reactor when they are subjected to neutron irradiation. Atom probe tomography established that the copper that was introduced into the welds from the protective copper coating on the welding rods can nucleate ultrafine (1–2 nm in diameter) copper-enriched precipitates in the steels if the copper content exceeds the modified solubility limit (Miller and Russell, 2007). These precipitates produce embrittlement and alter the ductile-to-brittle transformation temperature. Atom maps and proximity histograms (Figs 17.12 and 17.13) revealed that the solute distributions in and around the precipitate are complex and are best described as a copper-enriched core with significant manganese, nickel, and silicon enrichments at the precipitate–matrix interface and extending into the matrix (but not a core-shell structure in the strict sense of that structure). Under these extreme conditions, classical nucleation behavior is not expected and the solute profiles are likely due to kinetically limited diffusion of the solutes. By matching the continuation of the atomic planes in the matrix and the precipitates, the precipitates were found to have a body centered cubic structure rather than the face centered cubic structure of the equilibrium ε-copper phase. In some high nickel, high manganese pressure vessel steels in which the copper level is low or absent, such as the steels used in VVER 1000 reactors, phase separation at high doses can still occur. In these materials, atom probe tomography has demonstrated that

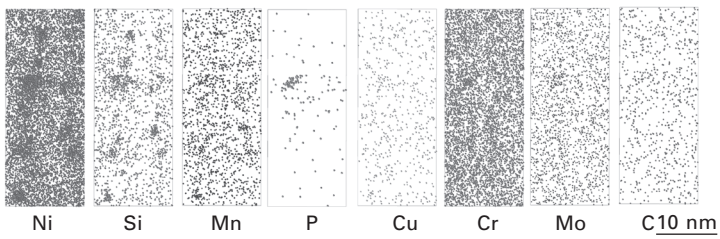
ultrafine nickel-manganese-silicon-enriched nanoclusters are formed (Miller *et al.*, 2009), as shown in Fig. 17.14. The phosphorus enrichment is due to the intersection of a dislocation with this selected volume.



17.12 Atom maps of copper-enriched precipitates in a neutron irradiated pressure vessel steel. Enrichments of copper, nickel, manganese and silicon are evident. The extent of the copper atoms is smaller than the other solutes.



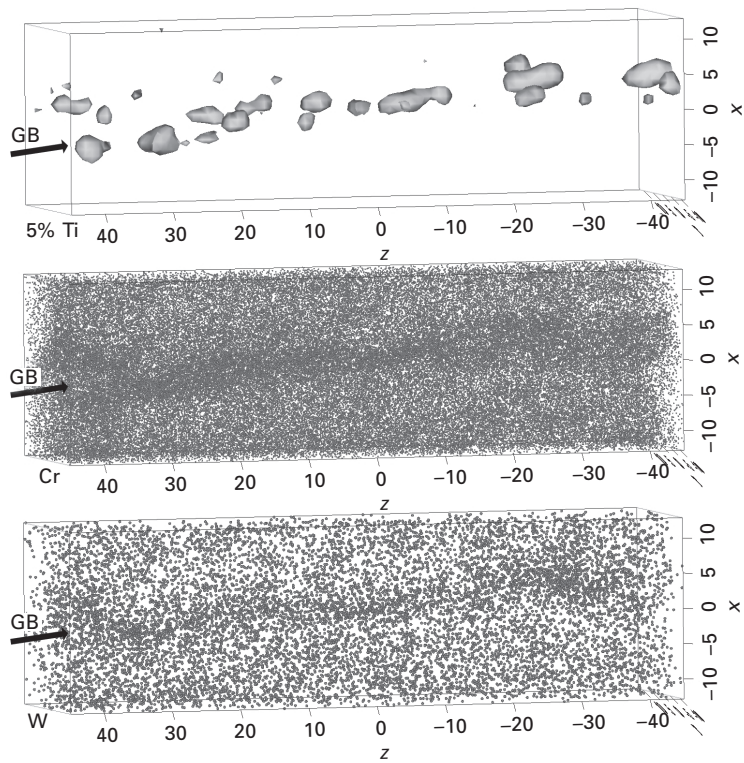
17.13 Proximity histograms of ~2 nm diameter, copper-enriched precipitates in a neutron irradiated pressure vessel steel. Enrichments of copper, nickel, manganese and silicon are evident. The vertical line indicates the position of the isoconcentration surface used to define the interface.



17.14 Phase separation of ultrafine nickel-manganese-silicon-enriched nanoclusters at high doses in a high nickel, high manganese pressure vessel steel used in VVER 1000 reactors.

Atom probe tomography has played a key role in understanding the behavior of ODS steels and nanostructured ferritic alloys, which are being developed for extreme conditions in future generations of advanced reactors. These mechanically alloyed, ultrafine grain size alloys exhibit remarkable creep properties at high temperatures (Klueh *et al.*, 2002) and tolerance to high dose radiation (Miller *et al.*, 2010). The reason for these unique properties is the underlying non-classical nucleation involving high levels of vacancies that are introduced in these steels during the mechanical alloying process and the interaction of the vacancies with the solute atoms. Atom probe

tomography characterization has revealed that the microstructure consists of high number densities, up to 10^{24} m^{-3}, of 2 nm diameter titanium-yttrium-oxygen-enriched nanoclusters in the grain interiors and coarser variants of the nanoclusters and other types of precipitates, including $Y_2Ti_2O_7$ and Ti(N,C,O), on the grain boundaries. An example of heterogeneous nucleation on grain boundaries is shown in Fig. 17.15. The combination of a high areal density of intergranular precipitates, together with solute segregation of chromium and tungsten effectively pin the grain boundary, thereby preventing grain growth. This grain boundary pinning together with the interaction of the vacancies with the oxygen, titanium and yttrium atoms that retards all diffusional processes, also minimizes grain boundary sliding and results in the superior creep properties despite the fine grain size.



17.15 Heterogeneous distribution of ~2–5 nm diameter titanium-yttrium-oxygen-enriched nanoclusters and $Y_2Ti_2O_7$ precipitates decorating a grain boundary in a 14YWT nanostructured ferritic steel. Chromium and tungsten atoms are also segregated to the grain boundary segments between the nanoclusters and precipitates.

17.7 Future trends

Currently, the atom probe tomography technique has several weaknesses that limit the performance with respect to phase transformations. The quality of the reconstruction of atom positions is not accurate enough to place the atoms on their lattice sites. The limitation is partially due to some assumptions in the reconstruction algorithm in current use and partially due to subtle changes in the surface of the specimen at zone lines, crystallographic poles and interfaces, as well as local magnification and atomic density changes that occur when a phase emerges onto the surface. Some exploratory attempts have been made to place each reconstructed atom on its correct lattice site (Camus *et al.*, 1995; Moody *et al.*, 2011). Some suggestions have been proposed to improve the quality of the reconstruction by integrating a local electrode atom probe into a scanning transmission electron microscope to take advantage of the two streams of data (Miller and Kelly, 2010).

The use of kinetic energy measurement for resolving charge state overlaps has recently been suggested by Kelly (2011). This additional information would permit the correct identification of isobar overlaps such as $_{28}Si^{++}/_{14}N^{++}$, $_{48}Ti^{+++}/_{16}O^{+}$, $_{32}S^{++}/_{16}O^{+}$, $C^{+}/C_2{}^{++}$, etc., and thereby improve the accuracy of compositional determinations. In addition, if the kinetic energy resolution is sufficiently high, it would enable the background noise to be identified and eliminated from the mass spectrum and thereby improve compositional determinations. Instead, the background noise could be used to construct a field ion image in between the field evaporation pulses and possibly be used to assist in the reconstruction of the atom positions (Kelly, 2010).

Improvement of the detection efficiency of the microchannel plates in the single atom detector or the development of new types of high detection efficiency position-sensitive single atom detectors will enable the detection of smaller clusters and embryos and, together with improved spatial resolution, will enable nearest neighbor interactions and short range order to be investigated. The additional ions collected would also improve the statistics of all compositional determinations and lower the minimum level of solute that can be quantified.

In addition to these instrument improvements, developments are in progress to improve the data analysis and data mining methods. Currently, data analysis methods are lagging behind the hardware developments. One type of method that is being adapted and developed for atom probe tomography is multivariate statistical analysis to automatically determine and then quantify the microstructural components in the sample (Parish and Miller, 2010). There is no doubt that more sophisticated data analysis methods could extract more detailed information from existing data. One important goal for the atom probe tomography community is to introduce standards and terminology for the data analysis procedures.

Published by Woodhead Publishing Limited, 2012

17.8 Conclusion

Atom probe tomography can provide atomic level information for the understanding of phase transformations in a wide range of steels from the initial stages of the phase separation, whether by nucleation or spinodal decomposition. The technique can characterize and quantify the changes in the size, morphology, number density, and compositions of the co-existing phases during subsequent aging or tempering. The atomic resolution of the technique enables the earliest stages of phase transformations to be detected and quantified.

17.9 Acknowledgments

The author thank Drs F. G. Caballero and C. Capdevila of CENIM, Dr T. F. Kelly of Cameca Instruments, Ms K. F. Russell, Ms K. A. Powers and Dr D. T. Hoelzer of Oak Ridge National Laboratory for their contributions. This research was sponsored by the Materials Sciences and Engineering Division, Office of Basic Energy Sciences, US Department of Energy. Atom probe tomography was supported by ORNL's Shared Research Equipment (SHaRE) User Facility, which is sponsored by the Office of Basic Energy Sciences, US Department of Energy.

17.10 References

Bas P, Bostel A, Deconihout B, Blavette D (1995), 'A general protocol for the reconstruction of 3D atom probe data', *Appl Surf Sci*, 87–88, 298–304

Brenner S S, Miller M K, Soffa W A (1982), 'Spinodal decomposition of iron-32 at.% chromium at 470°C', *Scr Metall*, 16, 831–6

Caballero F G, Garcia-Mateo C, Santofimia M J, Miller M K, de Andrés C G (2009), 'New experimental evidence on the incomplete transformation phenomenon in steel', *Acta Mater*, 57 (1), 8–17

Caballero F G, Miller M K, Garcia-Mateo C (2010), 'Carbon supersaturation of ferrite in a nanocrystalline bainitic steel', *Acta Mater*, 58, 2338–2343

Camus P P, Larson D J, Kelly K F (1995), 'A method for reconstructing and locating atom on the crystal-lattice in 3-dimensional atom-probe data', *Appl Surf Sci*, 87–88, 305–310

Capdevila C, Miller M K, Russell K F, Chao J, González-Carrasco (2008), 'Phase separation in PM 2000 Fe-base ODS alloy: experimental study at the atomic level', *Mater Sci Eng A*, 490, 277–288

Gault B, de Geuser F, Stephenson L T, Moody M P, Muddle B C, Ringer S P (2008), 'Estimation of the reconstruction parameters for atom probe tomography', *Microsc Microanal*, 14, 296–305

Gibbs J W (1948), *The collected works of J. Willard Gibbs*, Vol 1, New Haven, CT, Yale University Press

Gomer R (1993), *Field emission and field ionization*, Woodbury, NY, American Institute of Physics

Hellman O C, Vandenbrouck J A, Rüsing J, Isheim D, Seidman D N (2000), 'Analysis of three-dimensional atom-probe data by the proximity histogram', *Microsc Microanal*, 6, 437–444

Hetherington M G, Hyde J M, Miller M K, Smith G D W (1991), 'Measurement of the amplitude of a spinodal', *Surf Sci*, 246, 304–314

Hyde J M, English C A (2001), 'An analysis of the structure of irradiation-induced Cu-enriched clusters in low and high nickel welds', in 'Microstructural processes in irradiated materials – 2000', *Proceedings of the Material Research Society Symposium*, Pittsburgh, PA, MRS, p. R6.6.1

Hyde J M, Cerezo A, Hetherington M G, Miller M K, Smith G D W (1992), 'Three dimensional characterization and modeling of spinodally decomposed iron-chromium alloys', *Surf Sci*, 266, 370–377

Hyde J M, Miller M K, Hetherington M G, Cerezo A, Smith G D W, Elliott C M (1995a), 'Spinodal decomposition in Fe-Cr alloys: experimental study at the atomic level and comparison with computer models, II. Development of domain size and composition amplitude', *Acta Metall Mater*, 43, 3403–3413

Hyde J M, Miller M K, Hetherington M G, Cerezo A, Smith G D W, Elliott C M (1995b), 'Spinodal decomposition in Fe-Cr alloys: experimental study at the atomic level and comparison with computer models, III. Development of morphology', *Acta Metall Mater*, 43, 3415–3426

Kelly T F (2007), 'Atom probe tomography of electronic materials', *Annu Rev Mater Sci*, 37, 681–727

Kelly T F (2010), private communication

Kelly T F (2011), 'Kinetic energy discrimination for atom probe tomography', *Microsc Microanal*, 17, 1–14

Kelly T F, Miller M K (2007), 'Atom probe tomography', *Rev Sci Instrum*, 78, 031101

Kelly T F, Camus P P, Larson D J, Holzman L M, Bajikar S S (1995), 'High mass resolution local-electrode atom probe', US Patent 5440124

Kelly T F, Camus P P, Larson D J, Holzman L M, Bajikar S S (1996), 'On the many advantages of local-electrode atom probes', *Ultramicroscopy*, 62, 29–42

Klueh R L, Maziasz P J, Kim I S, Heatherly L, Hoelzer D T, Hashimoto N, Kenik E A, Miyahara K (2002), 'Tensile and creep properties of an oxide dispersion strengthened ferritic steel', *J Nucl Mater*, 307–311, 773–777

Knipling K E, Rowenhorst D J, Fonda R W, Spanos G (2010), 'Effects of focused ion beam milling on austenite stability in ferrous alloys', *Mater Charact*, 61, 1–6

Langer J S, Bar-on M, Miller H D (1975), 'New computational method in the theory of spinodal decomposition', *Phys Rev*, A 11, 1417–1429

Miller M K (2000), *Atom probe tomography; analysis at the atomic level*, New York, Kluwer Academic/Plenum

Miller M K, Bentley J (1990), 'APFIM and AEM investigation of CF8 and CF8M primary coolant pipe steels', *Mater Sci Technol*, 6, 285–292

Miller M K, Forbes R G (2009), 'Atom probe tomography', *Mater Charact*, 60, 461–469

Miller M K, Hetherington M G (1991), 'Local magnification effects in the atom probe', *Surf Sci*, 246, 442–449

Miller M K, Kelly T F (2010), 'The atom tomography (ATOM) concept', *Microsc Microanal*, 16(suppl 2), 1856–1857

Miller M K, Russell K F (2007), 'Embrittlement of RPV steels: an atom probe tomography perspective', *J Nucl Mater*, 371, 145–160

Miller M K, Hyde J M, Cerezo A, Smith G D W (1995a), 'Comparison of low temperature decomposition in Fe-Cr and duplex stainless steels', *Appl Surf Sci*, 87/88, 323–328

Miller M K, Hyde J M, Hetherington M G, Cerezo A, Smith G D W, Elliott C M (1995b), 'Spinodal decomposition in Fe-Cr alloys: experimental study at the atomic level and comparison with computer models. I. Introduction and methodology', *Acta Metall Mater*, 43, 3385–3401

Miller M K, Cerezo A, Hetherington M G, Smith G D W (1996a), *Atom probe field ion microscopy*, *monographs on the physics and chemistry of materials*, 52, Oxford, Oxford University Press

Miller M K, Stoller R E, Russell K F (1996b), 'Effect of neutron-irradiation on the spinodal decomposition of Fe-32% Cr model alloy', *J Nucl Mater*, 230, 219–225

Miller M K, Russell K F, Thompson K, Alvis R, Larson D J (2007), 'Review of atom probe FIB-based specimen preparation methods', *Microsc Microanal*, 13(6), 428–436

Miller M K, Chernobaeva A A, Shtrombakh Y I, Russell K F, Nanstad R K, Erak D Y, Zabusov O O (2009), 'Evolution of the nanostructure of VVER-1000 RPV materials under neutron irradiation and post irradiation annealing, *J Nucl Mater*, 385, 615–622

Miller M K, Hoelzer D T, Russell K F (2010), 'Towards radiation tolerant nanostructured ferritic alloys', *Mater Sci Forum*, 654–656, 23–28

Moody M P, Stephenson L T, Ceguerra A V, Ringer S P (2008), 'Quantitative binomial distribution analyses of nanoscale like-solute atom clustering and segregation in atom probe tomography data', *Microsc. Res. Tech*, 71, 542–550

Moody M P, Gault B, Stephenson L T, Marceau R K W, Powles R C, Ceguerra A V, Breen A J, Ringer S P (2011), 'Lattice rectification in atom probe tomography: towards true 3D atomic microscopy', *Microsc Microanal*, 17, 226–239

Müller E W, Krishnaswamy S V (1974), 'Premature field evaporation in the atom probe', *Rev Sci Instrum*, 45, 1049–1052

Panayi P (2006), 'Atom probe', Patent WO 2006/134380

Parish C M, Miller M K (2010), 'Multivariate statistical analysis of atom probe tomography data', *Ultramicroscopy*, 110, 1362–1373

Poschenrieder W P (1972), 'Multiple-focusing time-of-flight mass spectrometers. Part II: TOFMS with equal energy acceleration', *Int J Mass Spectrum Ion Phys*, 9(4), 357–373

Seidman D N (2007), 'Three-dimensional atom-probe tomography: advances and applications', *Annu. Rev Mater Res*, 37, 127–158

Seidman D N, Stiller K (2009), 'An atom-probe tomography primer', *MRS Bulletin*, 34, 717–724

Stephenson L T, Moody M P, Liddicoat P V, Ringer S P (2007), 'New techniques for the analysis of fine-scaled clustering phenomena with atom probe tomography (APT) data', *Microsc Microanal*, 13, 448–463

Thompson K, Lawrence D, Larson D J, Olson J D, Kelly T F, Gorman B (2007), '*In situ* site-specific specimen preparation for atom probe tomography', *Ultramicroscopy*, 107, 131–139

18

Electron backscatter diffraction (EBSD) techniques for studying phase transformations in steels

S. ZAEFFERER, N.-N. ELHAMI and P. KONIJNENBERG, Max Planck Institute for Iron Research, Germany

Abstract: The electron backscatter diffraction (EBSD) technique and EBSD-based orientation microscopy (ORM) are very powerful techniques for the comprehensive characterization of crystalline microstructures in the scanning electron microscope. ORM delivers accurate and quantitative data about the morphology and crystallography of a material, e.g. shape, size and neighbourhood relations of crystals, crystallographic phases, and crystallographic texture and misorientation distribution. By combining two-dimensional EBSD-based ORM with serial sectioning the technique can be extended to a three-dimensional technique. In addition to the morphological description of microstructures, this technique allows the comprehensive crystallographic characterization of grain boundaries and the quantification of deformation structures in terms of densities of geometrically necessary dislocations. The present text gives an overview on EBSD applications to the study of phase transformations in steels and briefly describes future developments of the technique.

Key words: EBSD, 3D EBSD, misorientations, orientation relationships, plastic strain, grain boundaries, martensite variants, ferrite, bainitic ferrite.

18.1 Introduction

Diffraction techniques are generally used to obtain information on the crystalline state of matter, for example crystallographic structure, orientation and defects. Electron diffraction in transmission electron microscopy (TEM) is a frequently used and well-established technique which allows study of crystal structures in thin foils down to a few hundred nm^3.[1] In contrast, diffraction techniques used in scanning electron microscopy (SEM) work on the surface of bulk samples. The most prominent of these is the electron backscatter diffraction (EBSD) technique which currently reaches a spatial resolution in the order of several thousand nm^3. We will describe the physical

[1] Note that we use here a volume description of spatial resolution indicating the total electron-matter interaction volume that leads to the measured signal.

© Woodhead Publishing Limited, 2012

basics of this technique in Section 18.2. EBSD became particularly popular and powerful when the fully automated evaluation of EBSD patterns was introduced (Krieger-Lassen *et al*., 1992) and led to a new form of microscopy called 'orientation microscopy' (here called 'ORM') (Adams *et al*., 1993). This technique is based on the EBSD-based measurement of crystal orientations and crystallographic phases on a regular grid on the surface of a sample followed by representing these measurements in the form of maps. These mappings display an accurate and quantitative representation of the measured microstructure, including details about the morphology of crystals (size, shape, neighbour relations), defects (grain boundaries, dislocations, phases) and texture. A number of overview papers on the technique are available, e.g. Dingley and Field (1997), Schwarzer (1997), Humphreys (2001), Baba-Kishi (2002), Dingley (2004) and Randle (2008). The most comprehensive of these are the collections of articles in the books by Schwartz *et al*. (2000, 2009). An overview with particular focus on phase transformation in steels has been published by Gourgues-Lorenzon (2009). In the present text, the 2D EBSD technique will be introduced in Section 18.3 by means of some applications on a low-alloyed TRIP steel.

It is, in principle, straightforward to extend the two-dimensional (2D) orientation microscopy technique to a three-dimensional (3D) technique by combining the 2D mapping with serial sectioning, e.g. by mechanical or chemical polishing or sputtering with a focused ion beam (FIB). Particularly the latter has resulted in a fully automated system for high resolution 3D orientation microscopy. 3D ORM offers a number of unique features, in particular the full, five-parameter grain boundary description but also the description of connectivity of phases, 3D morphology of crystals and the determination of geometrically necessary dislocation densities. In Section 18.4 we will take up some aspects of 3D EBSD including the measurement process and the description of grain boundaries. Section 18.5, finally, concludes the text and briefly presents some further interesting new developments in the field of EBSD.

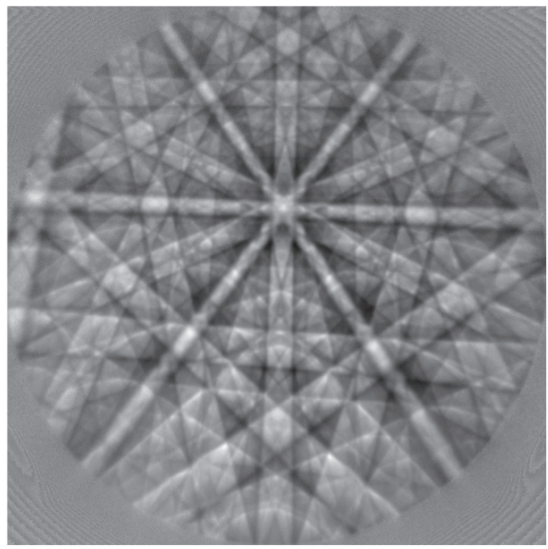
18.2 Fundamentals of the electron backscatter diffraction (EBSD) technique

Figure 18.1 shows a typical EBSD pattern, obtained on a Fe 36% Ni crystal with 15 keV electrons together with a sketch of its generation geometry in a scanning electron microscope. The pattern formation may be understood as a two-step process. The first step consists of an incoherent[2] quasi-elastic, large angle scattering process of the primary electrons on the atoms of the crystal, producing a point-like electron source inside the crystal. This

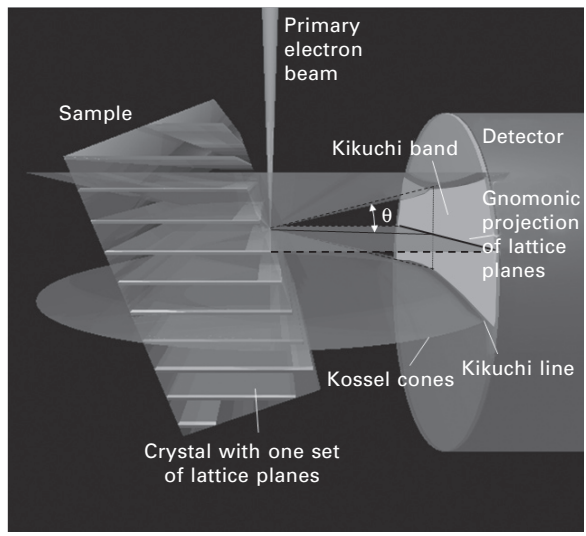
[2] The term 'incoherent' means that the scattered electron wave has no fixed phase relation with the incoming wave.

© Woodhead Publishing Limited, 2012

incoherent scattering determines the spatial resolution of the technique (i.e. the interaction volume leading to the formation of a pattern). In the second step the incoherently scattered electrons are coherently scattered about a



(a)



(b)

18.1 (a) EBSD pattern of Fe 36% Ni (fcc crystal structure), acquired at 15 kV. (b) Sketch of the geometry of EBSD patterns. Only one bright Kikuchi band is displayed which corresponds to just one of the bright bands in (a). The Bragg angle, θ, between the Kossel cones is displayed much larger than it is in the pattern in (a).

© Woodhead Publishing Limited, 2012

small angle creating Kikuchi cones. This second step is responsible for the geometry of the pattern and its intensity distribution. The geometry of an EBSD pattern, as sketched in Fig. 18.1(b), is in principle quite simple. In the most simple picture, the centre line inside each of the bright bands in the pattern may be understood as the gnomonic projection of one of the lattice planes of the crystal, i.e. simply as the trace of the lattice plane extended through the point of pattern formation to the detector plane. The width of the band is approximately proportional to twice the Bragg angle. The geometric simplicity of the patterns makes the determination of crystal orientation straightforward, provided the crystallographic phase is known (e.g., Dingley, 1984; Krieger-Lassen, 1994; Zaefferer, 2000). Furthermore, from the sharpness of the pattern (the 'pattern quality', PQ), a qualitative value for the defect density at the point of observation can be obtained. Note that while the geometry of the pattern is simple, understanding its intensity distribution imperatively requires the application of the dynamical theory of electron diffraction (see, e.g., Winkelmann *et al.*, 2007).

For EBSD-based orientation microscopy, the electron beam is scanned across the surface of a flat sample. For optimum observation conditions, the sample must have a flat and artefact-free surface. It is tilted such that the primary beam hits the surface at an angle of approximately 20°. The EBSD patterns are acquired on a retractable semi-transparent phosphor screen combined with a highly sensitive CCD camera, which is positioned close to the sample (usually at a distance of few cm). The image is transmitted to a computer for orientation determination. The same computer also controls the beam and stage positioning.

A few key parameters of the technique shall be briefly mentioned here. The *lateral resolution* of the technique is in the order of 20–200 nm, depending on the sample material (lower density or lower atomic number lead to larger values), the type of microscope (field emission gun results in smaller values than a tungsten filament gun) and the primary beam energy (higher energy results in higher values). More accurately the *spatial resolution* is determined by the size of the electron-matter interaction volume as was mentioned above. For standard conditions the *angular resolution*, i.e. the smallest orientation difference between two crystals that can still be determined, is in the order of 0.5–1° (e.g., Brough *et al.*, 2006). Using special measurement parameters and dedicated analysis algorithms (e.g., Wilkinson *et al.*, 2006a) these values can be reduced to 0.1 or even less than 0.01°. The pattern acquisition rate on an SEM currently reaches up to over 500 patterns per second. Nevertheless, compared to other SEM techniques, EBSD-ORM is still rather slow. Orientation maps which usually consist of several hundred thousand pixels still require measurement times in the order of half an hour or more. It is to be noted, of course, that in this time much more data are collected than with any other SEM technique.

© Woodhead Publishing Limited, 2012

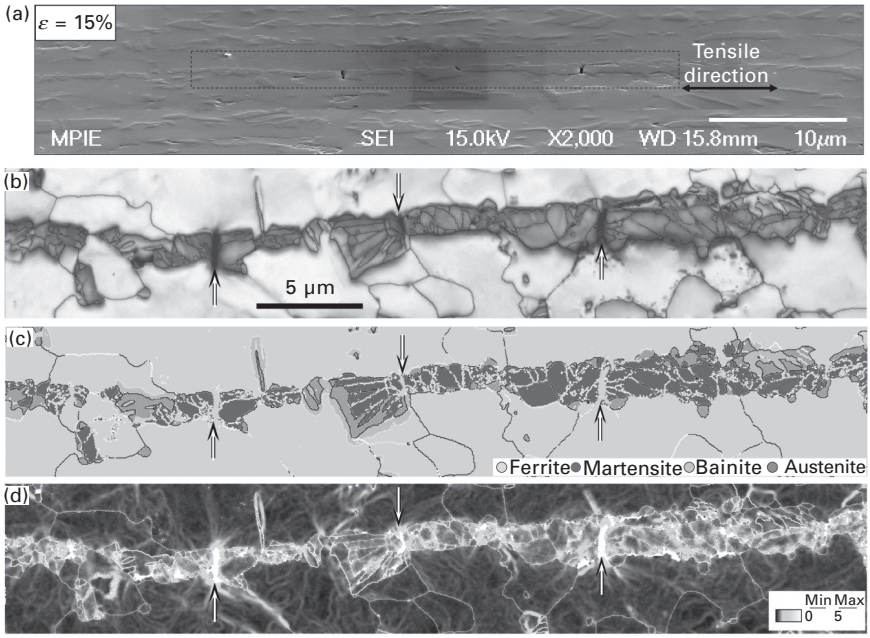
18.3 The current standard of 2D electron backscatter diffraction (EBSD) applications

18.3.1 Microstructure characterization by orientation microscopy

The strength of EBSD-based orientation microscopy for the investigation of microstructures and phase transformations will be illustrated in the following by an example from a study on damage mechanisms in a low-alloyed steel with transformation-induced plasticity (TRIP) (composition approx. (in mass%) 0.2 C, 1.5 Al, 1.5 Mn, bal. Fe). These steels consist of a ferritic matrix which includes, in the undeformed state, about 10 vol% of metastable, residual austenite and 10–20 vol% of bainitic ferrite. During deformation an increasing amount of austenite transforms into martensite. The transformation stresses are accommodated by dislocations which effectively increase the hardening rate and, consequently, the tensile elongation of the material (see, e.g., Jacques, 2004, for a description of TRIP steels). At the same time, the transformation also creates highly localized stresses which may lead to the formation of decohesions and fracture nuclei which then finally limit the total elongation to fracture. All 2D measurements presented here were measured on a JEOL 6500 F field emission gun SEM with a TSL OIM EBSD system and a Digiview II camera. The EBSD mapping was carried out at an acceleration voltage of 15 kV and working distance of 15 mm.

Figure 18.2(a) shows an EBSD-based measurement of the microstructure of this material displaying a band of former austenite which, during straining, partially transformed into martensite. The four microstructural constituents ferrite, martensite, bainitic ferrite and austenite are indicated by different grey values in Fig. 18.2(b). Austenite is distinguished by its different crystal structure. In contrast, ferrite, martensite and bainitic ferrite all have bcc crystal structure (the slight tetragonal distortion of martensite cannot be detected by EBSD) and other means need to be taken to separate them. Martensite is recognized by its, on average, significantly lower pattern quality compared to ferrite. Using the grain-average pattern quality value, a clear distinction between ferrite and martensite can be made. Bainitic ferrite, in contrast, is more difficult to recognize (Gourgues *et al*., 2000; Wu *et al*., 2005; Petrov *et al*., 2007). Its pattern quality is usually less than that of ferrite but better than that of martensite. Furthermore, bainitic ferrite always appears in conjunction with a plate-shaped, carbon supersaturated austenite, with which it has a well-defined orientation relationship, e.g. the Kurdjumov–Sachs (KS) type (Zaefferer *et al*., 2004). Zaefferer *et al*. (2008a) proposed an automatic method to determine bainite in these structures, based on the orientation gradients that are created by the shear-type transformation. However, this method only works reliably on undeformed material which is why in the present case some of the areas of bainitic ferrite were marked manually.

© Woodhead Publishing Limited, 2012



18.2 Microstructure of a martensite–austenite band in a low-alloyed TRIP steel after 15% of tensile deformation. (a) Secondary electron image, showing several decohesions along the band. (b) Pattern quality map obtained by EBSD-based ORM. Darker grey corresponds to lower quality of the EBSD patterns. The arrows indicate the position of decohesions. (c) Microstructure constituent map (see text for details). Grain boundaries with Kurdjumov–Sachs (KS) orientation relation (OR) between austenite and martensite are coloured in black, large angle grain boundaries ($\omega >$ 15°) inside of one phase are coloured in black. All bright grey coloured boundaries indicate typical misorientations between those martensite variants that formed from one austenite grain according to the KS OR (Shibata *et al.,* 2005).
(d) Next-nearest neighbour kernel average misorientation (KAM) maps indicating the rotation gradient and thus the strain gradient in the material.

18.3.2 Description of orientation relationships

EBSD is an ideal tool to determine orientation relationships between different phases, e.g. martensite and austenite, first because of its inherently good angular resolution (0.1–0.5°), and second because of the possibility to measure a large amount of boundaries and therefore obtain data of high statistical significance. Note that other techniques, e.g. TEM Kikuchi pattern or convergent beam diffraction, may reach up to one order better values, and some carefully executed X-ray diffraction techniques up to two orders better values. These techniques, however, suffer either from too small observable

© Woodhead Publishing Limited, 2012

areas or a too poor spatial resolution (see Table 18.1). For the present example, the misorientation between austenite and ferrite is displayed in Fig. 18.3 as rotation-axis rotation-angle pairs. The axis corresponds to the crystallographic direction in the austenite crystal about which the martensite crystal co-ordinate system has to be rotated to superimpose with the crystal co-ordinate system of the parent austenite crystal. The angle is the required rotation angle about that axis. Note that when calculating the misorientation, each of the crystal coordinate systems can be rotated by any of its n crystal symmetry elements. Thus the misorientation beween two crystals 1 and 2 is calculated according to

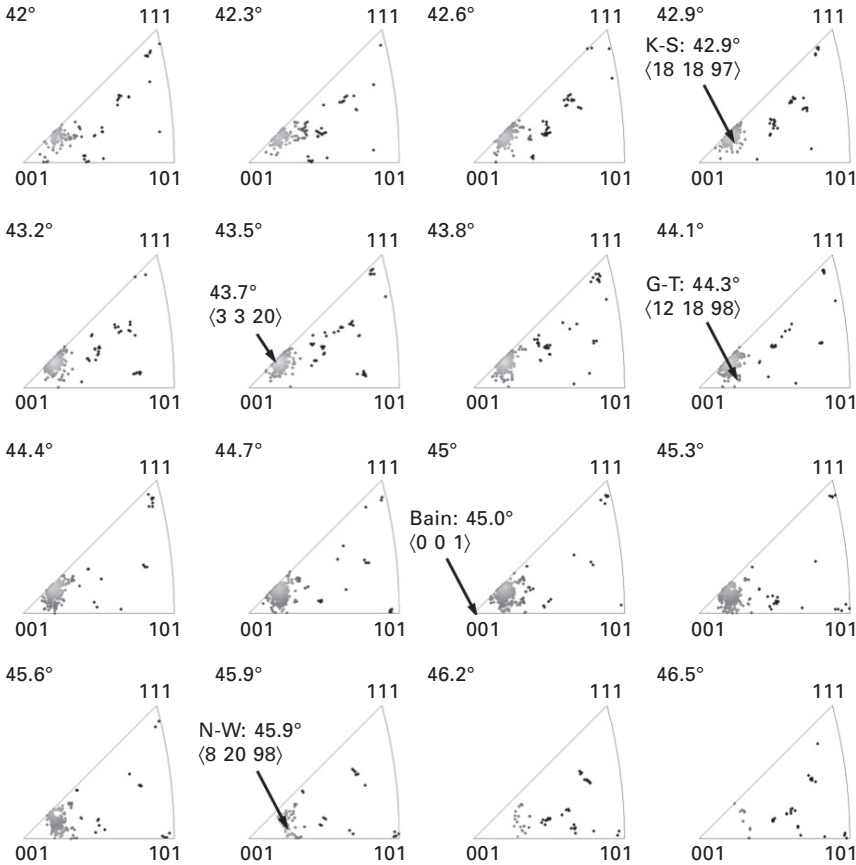
$$\Delta\mathbf{g}_{1,2}^{(i,j)} = \mathbf{g}_2\mathbf{g}_1^{-1} = \mathbf{S}_{2j}\mathbf{g}_2(\mathbf{S}_{1i}\mathbf{g}_1)^{-1} \qquad i = 1,\ldots m,\ j = 1\ldots n \qquad [18.1]$$

where $\mathbf{g}_k$ indicates the crystal orientation of crystal k and $\mathbf{S}_{ji}$ indicates the n different symmetry operations for this crystal. As a result a misorientation can be expressed by $2 \times n \times m$ physically identical descriptions ($n = m = 24$ for the symmetry of fcc and bcc crystals). By convention the misorientation with the smallest rotation angle and the rotation axis in the standard orientation triangle is selected to represent the respective misorientation. From the misorientation distribution, the orientation relationship (OR) between austenite and martensite can be deduced. In the present case the most frequent misorientation is 43.7° about the <3 3 20> axis of the austenite. This OR is about 2.2° away from the KS OR, expressed as 42.85° <18 18 97>. The ideal KS OR is deduced from the parallelism of densely packed planes and

Table 18.1 Comparison of some characteristics of diffraction techniques for orientation determination

	EBSD	TEM, micro-bean spot diffraction	TEM, Kikuchi diffraction	TEM, CBED	3D micro-x-ray diffraction
Spatial resolution (volume (nm^3))	$2 \cdot 10^4$ ... 10^3, depends on material and acc. voltage	$5 \cdot 10^3$...$1 \cdot 10^2$, on thin foils	$1 \cdot 10^4$ ... $1 \cdot 10^3$ depends on material and acc. voltage	$5 \cdot 10^3$ ... $1 \cdot 10^2$, on thin foils	$2 \cdot 10^8$, on bulk material
Max. observable volume and area	10^6 μm^3 (10×10 mm^2, 10 nm thickness)	10^3 μm^3 (100×100 μm^2, 50 ... 100 nm thickness)	10^3 μm^3 (100×100 μm^2, 100 ... 200 nm thickness)	10^3 μm^3 (100×100 μm^2, 50 ... 100 nm thickness)	10^9 μm^3 (10×10 mm^2, 10 μm thickness)
Angular resolution (°)	0.5 ... 0.1	2 ... 0.5	0.2 ... 0.02	0.1 ... 0.01	0.1 ... 0.001
Sample	Semi-infinite, bulk	Thin foil	Thin foil	Thin foil	Bulk

© Woodhead Publishing Limited, 2012



18.3 Some sections out of the complete misorientation distribution plot across the austenite–martensite boundaries in Fig. 18.2. The position of a point inside a standard triangle indicates the position of the misorientation rotation axis. The number on top of each triangle indicates the misorientation rotation angle about the marked rotation axis. The most frequent misorientation is 43.7° <3 3 20>. Marked are some ideal orientation relationships (OR): the Kurdjumov–Sachs (K-S) OR, the Nishiyama–Wassermann (N-W) OR, the Greninger–Trojano (G-T) OR and the Bain OR.

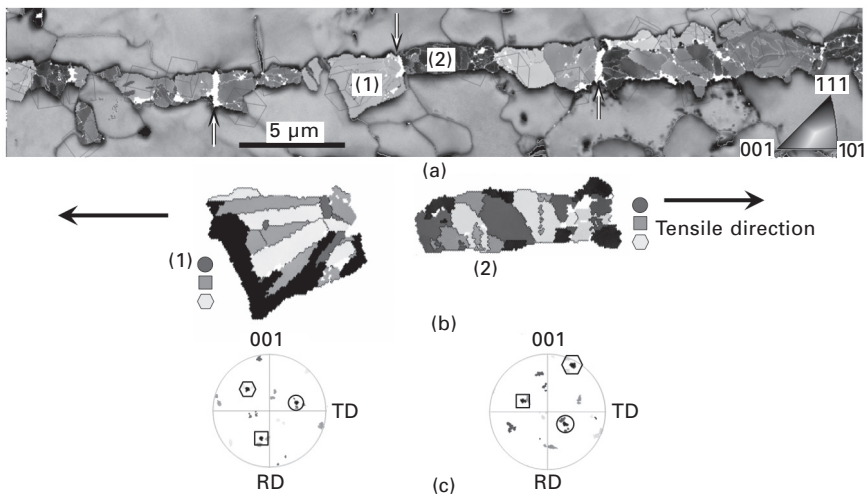
directions, $(111)_\gamma \parallel (011)_\alpha$ and $[110]_\gamma \parallel [111]_\alpha$. In the present example, in contrast, the OR corresponds to deviations of 2° between the close packed planes and 1.3° between the close packed directions. Cayron *et al*. (2010) proposed that an intermediate transformation to ε-martensite would be an explanation for the observed deviation of OR from the ideal KS OR. In the present example, the misorientation furthermore shows a certain distribution with a spread of about 1.5° around the determined OR. This spread may have two possible reasons. The first is the deformation due to the tensile testing,

© Woodhead Publishing Limited, 2012

which may lead to different lattice rotations of austenite and martensite. The second is the deformation of the crystal lattices due to the transformation itself. The martensitic transformation may lead to a significant deformation of the austenite matrix (Shibata *et al*., 2005) which may cause a large variability in the observed OR even along one single phase interface (e.g., Sato and Zaefferer, 2009). This effect is, however, most severe when only one martensite variant appears. Usually, however, the transformation strain is reduced by the appearance of several variants.

18.3.3 Description of martensite variants

When describing martensitic transformations, the original austenite microstructure is of great importance. For the present example, the residual austenite and the known nature of the martensite–austenite and martensite–martensite variant boundaries were used to reconstruct the original austenite grains. This reconstruction is displayed for our example in Fig. 18.4. Note that all observed decohesions appear at former austenite–austenite grain boundaries. For larger areas and particularly when no residual austenite is present, mathematical algorithms for austenite reconstruction may be applied

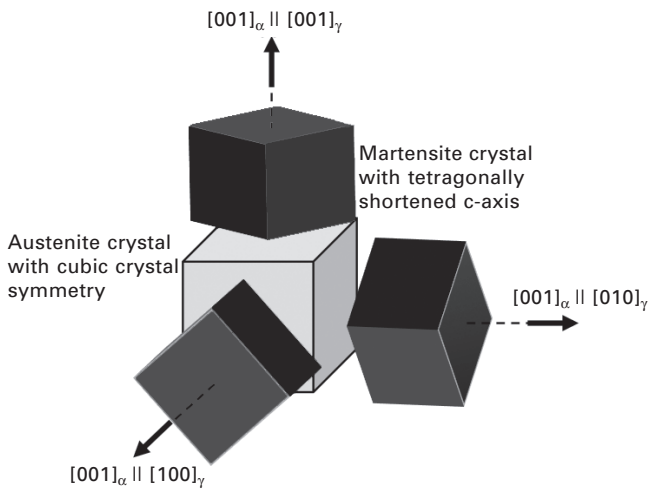


18.4 (a) Reconstructed austenite IPF map. Crystal orientations are described by lattice cell plots in each grain. (b) Bain variant maps of two austenite grains (1) and (2) in (a). The grey values correspond to the directions of the martensite c-axis as indicated in the pole figures in (c). Austenite is displayed in black. Note that the c-axis is the direction of maximum contraction during the martensitic transformation. (c) Pole figures of the (001) poles of martensite variants (grey) and of austenite (black). The austenite poles are the poles in the centre of the symbols.

© Woodhead Publishing Limited, 2012

(e.g., Cayron *et al.*, 2006; Cayron, 2007; Germain *et al.*, 2007; Humbert *et al.*, 2011; Miyamoto, 2010).

Once the austenite has been reconstructed it is possible to classify the martensite variants occurring in more detail. Classically, the martensite structures that are formed from one individual austenite grain are separated into packets, i.e. variants that have the same habit plane, and blocks, i.e. variants that have the same Bain correspondence (see, e.g., Morito *et al.*, 2006). According to the Bain correspondence, martensite is described as a contraction of the lattice along one of the a-axes of the original austenite and an expansion of the axes perpendicular to it parallel to the respective $\{110\}_\gamma$ axes. Bain variants are consequently those variants that have been created by contraction along the same a-axis of the austenite. In martensite, this direction corresponds to the c-axis of the tetragonally distorted lattice. The distortion of the austenite lattice during transformation can be significant and may lead to high residual stresses. It is therefore interesting to determine the direction of maximum distortion. EBSD is usually not able to determine the small tetragonal distortion (maximum 2%) of martensite directly (see, however, Zambaldi *et al.*, 2009). Rather, martensite is described as cubic lattice and the direction of its c-axis is determined in an indirect way. As indicated in Fig. 18.5, the c-axis of martensite is almost parallel to one of the a-axes of austenite. With this knowledge, the appropriate direction can easily be



18.5 Sketch of the Bain correspondence between a parent austenite (γ) crystal unit cell (in light grey) and the three different Bain variants of the martensite (α') unit cell. The unit cell of α' is slightly shorter in the direction parallel to the corresponding <001> direction of the γ crystal (the distortion is shown larger here than it is in reality). In real ORs, the different Bain variants may split up into further, slightly misoriented variants.

© Woodhead Publishing Limited, 2012

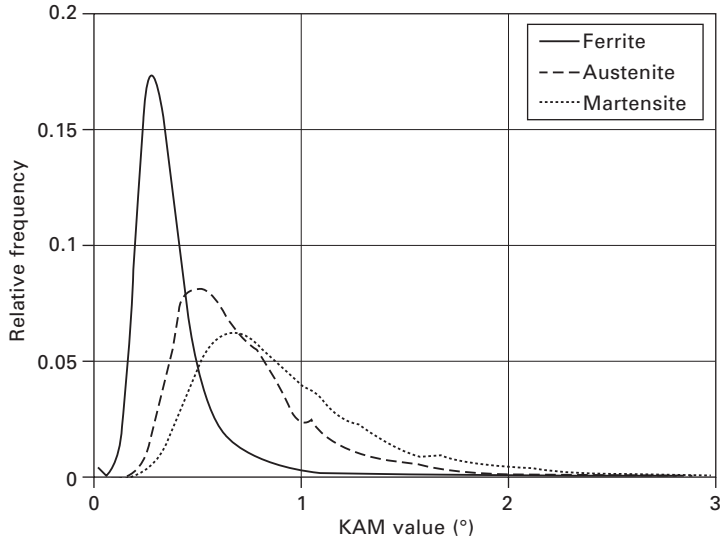
determined. This is done for two of the former austenite grains in Fig. 18.4. Here the three different Bain variants are indicated by three different grey values and the c-axis of the different variants are marked by three different symbols in the corresponding pole figure. For the present example, the figure suggests that those martensite variants that create a lattice expansion in the tensile direction are dominant. Nevertheless, the strain incompatibility of different martensite variants meeting at former austenite grain boundaries may lead to the observed decohesion of these boundaries. This can, however, not be decisively determined as long as the three-dimensional arrangement and volume fraction of the martensite crystallites are not known.

18.3.4 Description of plastic strain

The description of the distribution of plastic strain, i.e. the local dislocation density, in a sample is one of the strong features of EBSD-based ORM. Nevertheless, still most of the descriptions remain on a qualitative level. Frequently the EBSD pattern quality has been used to qualitatively describe the distribution of plastic strain (e.g., Choi and Jin, 2004; Gerber *et al.*, 2004; Baudin *et al.*, 2007). However, without additional processing (e.g. dynamic pattern background subtraction), the pattern quality depends also on parameters other than the defect density, for example the quality of surface preparation and the surface inclination. Pattern quality is therefore not an ideal choice for the description of plastic strain. A more quantitative measure is, for example, the so-called kernel average misorientation (KAM) which is determined as the average over all misorientation angles calculated between the centre pixel of a kernel and all of its nearest or next nearest neighbour pixels. The KAM value approximately indicates the magnitude of orientation change at every point, i.e. it is a simple form of a gradient. Figure 18.2(c) shows a KAM map for the above selected example. It is interesting to note that the areas close to microstructure decohesions show particularly large orientation gradients in the neighbouring ferrite grains. This indicates that the decohesions most probably formed at significantly lower strain and deformation concentrated at these weak points. A more quantitative description of strain distribution is obtained when plotting the frequency of KAM values for the different microstructural constituents (Fig. 18.6). This plot shows that martensite has the highest local gradients and therefore the highest amount of dislocations. These dislocations arise from the shear transformation of austenite to martensite. Also austenite shows relatively high local gradients, most probably also created during the transformation process. Ferrite, in contrast, is much softer and contains on average comparatively fewer dislocations.

Despites its power for indicating and comparing strain gradients, the KAM is only an angular measure and does not tell anything about the number

© Woodhead Publishing Limited, 2012



18.6 Frequency distribution of the kernel average misorientation (KAM) values in the different constituents, austenite, ferrite and martensite measured in Fig. 18.2(d).

of dislocations that cause these orientation gradients. However, using the formalisms developed by Nye (1953), Kröner (1981) and Christian (1975), it is possible to calculate the density of geometrically necessary dislocations (GND) from the orientation gradient tensor:

$$\begin{aligned} &\alpha = rot\beta_{el}. \\ &\alpha_{ij} = e_{ikl}\mathbf{g}_{jl,k} \\ &\alpha_{ij} = \sum_{k=1}^{K} \varphi^k \mathbf{b}_i^k \otimes \mathbf{t}_j^k \end{aligned} \qquad [18.2]$$

Here α is the 'dislocation tensor' calculated over all slip systems k, where φ^k is the density of these dislocations, and $\mathbf{b}^k$ and $\mathbf{t}^k$ their Burgers vectors and line direction vectors, respectively. β is the elastic strain gradient tensor, which, in the absence of long range elastic stress fields, can be expressed by the components of the orientation gradient tensor $\mathbf{g}_{jl,k} = \dfrac{\partial \mathbf{g}_{jl}}{\partial x_k} \cdot \mathbf{g}$ is the orientation tensor and e the Levi–Civita permutation symbol.

Note, that the full orientation gradient tensor requires knowledge of the three-dimensional distribution of orientations. Results will therefore be presented in Section 18.4 about 3D measurements. With two-dimensional orientation measurements, only that part of the geometrically necessary dislocations can be determined that create rotations in the x-y plane (El-Dasher *et al.*, 2003; Pantleon, 2008), which may, nevertheless indicate trends in activation of certain types of dislocations (e.g., Wheeler *et al.*, 2009; Britton *et al.*, 2010).

© Woodhead Publishing Limited, 2012

It should be remarked that the concept of GNDs is a rather artificial one: it considers only the fraction of all dislocations that make up an orientation change that can be *measured* with the respective technique. This means the GND density strongly depends on spatial and angular resolution of the measurement technique and on the particular form of orientation gradients (long or short range). Furthermore, GNDs do not correspond to a particular kind of dislocations but may be composed out of mobile dislocations (i.e. pile-ups in front of obstacles) or sessile dislocations (i.e. subgrain boundaries). Finally, Field *et al*. (2011) pointed out that GNDs constitute only a small fraction of all dislocations in the order of 10%.

To conclude, two-dimensional EBSD-based orientation microscopy is ideal to determine a number of characteristics of phase transformation microstructures. This includes morphology, nature and distribution of phases, misorientations and orientation relationships between phases, distribution of strain and the classification of transformation variants. It cannot, however, determine the exact morphology of non-spherical grains (e.g. plate vs. lath shape of martensite), the exact volume fraction of certain local features (statistical data can be given, however) and, very importantly, the nature of grain boundaries. This information can be obtained using a three-dimensional EBSD technique.

18.4 3D electron backscatter diffraction (3D-EBSD)

18.4.1 Measurement of 3D data by FIB-EBSD tomography

In principle, 3D characterization of microstructures can be performed by two different approaches, either by serial sectioning (destructive) or, in a non-destructive manner, by observation with some sort of transmissive radiation, e.g. synchrotron radiation. We focus here on the serial sectioning approach. Sectioning techniques simply comprise the removal of slices of material with some cutting technique followed by the recording of the structure of the thus-exposed material surface with an appropriate microscopic technique. Finally the 3D structure is reconstructed by stacking of the recorded images. Serial sectioning techniques are applicable to a wide range of materials and material problems, with the only serious disadvantage that they are destructive. For an overview on 3D serial sectioning techniques, see the viewpoint set in *Scripta Materialia* (Spanos, 2006), Uchic *et al*. (2004) and Groeber *et al*. (2006).

The combination of serial sectioning with a focused ion beam (FIB) and EBSD-based orientation microscopy in a combined FIB-SEM constitutes, for certain applications, an ideal technique. Sectioning with the ion beam allows the creation of parallel and equally spaced sections; due to its numerical description of microstructures, EBSD enables a much better and quantitative

© Woodhead Publishing Limited, 2012

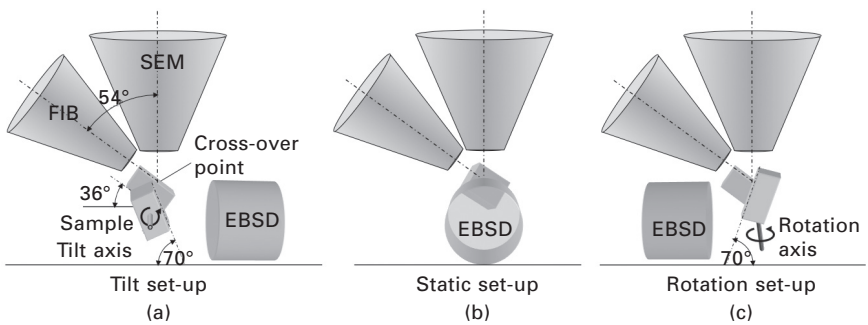
3D reconstruction than that which can be achieved for example by optical micrographs. Both techniques reach a comparable lateral resolution in the order of some 10 nm and the technique can easily be fully automated. 3D orientation microscopy systems combining FIB and EBSD have been developed in the last few years by Mulders and Day (2005), Zaefferer *et al*. (2005), Rollett *et al*. (2007) and several others.

Technical set-up

Typical geometrical set-ups for FIB-EBSD tomography are sketched in Fig. 18.7. Figure 18.7(a) displays the 'tilt' set-up where the sample needs to be tilted in order to change between the EBSD and FIB position (Zaefferer *et al*., 2005, 2008b). Figure 18.7(c) is the 'rotation' set-up which requires a 180° sample normal rotation for this change (Mulders and Day, 2005). A third set-up which, to the authors' knowledge, has not been realized yet but probably offers the most powerful arrangement for 3D EBSD, is sketched in Fig. 18.7(b): here the EBSD detector is mounted at 90° to both the electron beam and ion beam direction. If the sample is positioned appropriately, no sample movement between the milling and EBSD position is necessary at all. This set-up is therefore called the 'static' set-up. The accuracy and advantages and disadvantages of the different set-ups are discussed in more detail in Zaefferer and Wright (2009).

Limitations by resolution and volume

The spatial resolution of a 3D measurement system results from the lateral resolution achieved on the 2D sections, the accuracy of alignment of the



18.7 Three different set-ups for 3D orientation microscopy using a combination of EBSD and FIB sputtering. For changing between EBSD and milling position the tilt set-up (a) requires a 36° rotation about the indicated tilt axis and the rotation set-up (c) a 180° rotation about the indicated rotation axis. The static set-up (b) requires no movement.

© Woodhead Publishing Limited, 2012

sections and the depth resolution. For FIB-EBSD tomography, 50 nm seems to represent the best resolution currently achievable. Most of the studies performed so far have been carried out with 100 nm step sizes in all dimensions which give satisfactory section alignment.

The maximum size of the observable volume is an important limiting factor for the technique. It depends mainly on the material and on the time investment one wants to make. To date, the largest smooth areas that can be prepared with acceptable efforts are in the order of 100 μm × 100 μm (by the present author on Fe 36% Ni). On other materials, e.g. ferritic steels, much smaller smoothly milled depths of only approximately 30 μm were reached. Number and maximum thickness of milled sections are, in principle, unlimited. However, with increasing milling depth the milled volume has to be increased in order to prevent shadowing on the EBSD screen and serious re-depositing of milled material. It can be estimated that the largest volume accessible with the method presented here is in the order of 50 × 50 × 50 μm^3 (if using special sample geometries, see, e.g., Groeber *et al.*, 2006). Note that a volume of 30^3 μm^3, measured with a step size of 100 nm already contains almost 30 million data points, which represents a serious challenge to the post processing.

Materials issues

On many materials the surfaces created by FIB milling show sufficiently low radiation damage to preserve the crystal structure close to the surface (see, e.g., Prasad *et al.*, 2003; Matteson *et al.*, 2002). Therefore, many metals and intermetallics investigated so far (various ferritic, austenitic and martensitic steels, nickel, copper, aluminium, FeAl, CuZnAl) allow creation of excellent diffraction patterns from milled surfaces and the microstructures observed on these are similar to those prepared by other methods. Nevertheless, various problems exist. One is the amorphization of certain materials. It has been observed, for example, that hard intermetallics, e.g. Laves phases, do not give any patterns when prepared by milling (Konrad *et al.*, 2006). Problems also arise when milling steels containing metastable residual austenite, for example low-alloyed TRIP steels or iron-nickel alloys. Here, all of the austenite transforms into the stable ferrite during milling.

18.4.2 Voxel-based description of 3D data

Data processing

After measurement, 3D EBSD data exist first as unconnected volume pixels, hence called ‘voxels’. When describing crystalline microstructures it is important to group these voxels into crystallites. To this end the

© Woodhead Publishing Limited, 2012

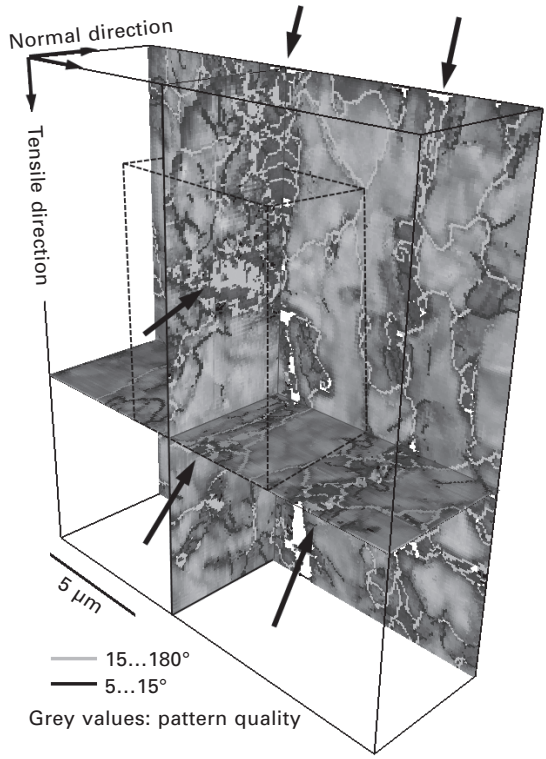
measured sections first have to be aligned such that subsequent sections fit together in an optimum manner. Alignment of complete sections is easily accomplished using cross-correlation techniques which identify a minimum of the average misorientation between neighbouring slices. It is significantly more complicated, however, to correct for misalignments which do not concern the full slice. These misalignments may occur, for example, due to thermally or electrostatically induced drift during the EBSD measurements. Also imperfections in the milling process may contribute to such unsystematic misalignments. To our knowledge no proper approach to this problem has yet been proposed in the literature. We have implemented a simple Monte-Carlo (MC) Potts-model algorithm which cleans up the microstructure effectively while conserving most of the sub-structure inside the grains.

Voxel-based mapping

After slice alignment, a segmentation algorithm is used to group voxels into grains. This algorithm performs a three-dimensional search for voxels that are within a certain threshold misorientation (e.g. 5°) with respect to their neighbours. Usually groups of voxels that are smaller than a certain minimum number of voxels (e.g. 10) are excluded from the grain arrangement. An example for a rendered voxel-based microstructure is displayed in the form of a PQ map in Fig. 18.8 for the above example of a tensile-deformed low-alloyed TRIP steel. Due to the reduction of pattern quality caused by milling, the positions of the martensite bands, marked by arrows in the figure, are, unfortunately, not as clear as in the 2D case. In Fig. 18.9(a) the area that is outlined by dashed lines in Fig. 18.8 is rendered as an inverse pole figure (IPF) map. One deformed ferrite grain is randomly picked out and displayed in Fig. 18.9(b). The graph shows, more than 2D maps, how large and heterogeneous orientation changes may occur in one single grain.

Voxel-oriented displays allow a one-to-one correspondence of crystal orientation and position in space which is of great use for deformed structures. A particularly interesting analysis with respect to deformation and phase transformation is the calculation of GND densities according to Eq. [18.2]. Figure 18.9(c) displays the total GND density determined for a fraction of the volume displayed in Fig. 18.9(a), in comparison to a 3D KAM map of the same volume, displayed in Fig. 18.9(d). The similarity between both graphics with respect to the main features is obvious, although the GND map shows a real dislocation density in contrast to the KAM map, which shows only a rotation angle. The calculated density of GNDs depends critically on the angular resolution of the measurement. The orientation noise, that is the variation in orientation below the angular resolution of the technique, introduces a spurious dislocation density below which any discrimination becomes meaningless (He *et al.*, 2008). In particular, 3D EBSD data suffer

© Woodhead Publishing Limited, 2012



18.8 3D EBSD pattern quality mapping obtained from a low-alloyed TRIP steel shortly before fracture (measurement: 60 slices @ 100 nm distance). The position of martensite is visible as dark bands through the structure. At the same time, the position of the bands is indicated by arrows. Bright grey boundaries are large-angle (>15°) grain boundaries, black boundaries are medium-angle (5–15°) boundaries.

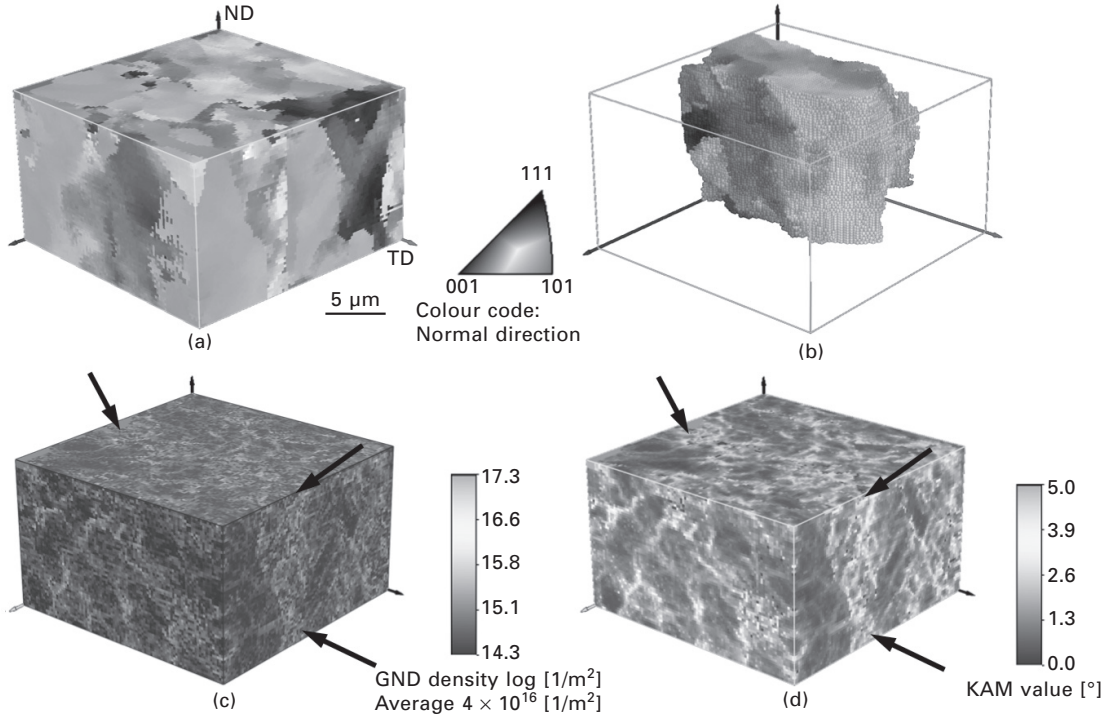
from a relatively high orientation noise, in consequence the spurious GND density is high as well. Assuming an orientation noise of about 1° and a step size of 80 nm, one obtains in the present case a spurious density of about 8×10^{14} m^{-2}.

The GND calculation is one particularly powerful feature of voxel-based 3D ORM. Other examples of voxel-based analysis use only morphological information, for example, on recrystallization of a particle containing alloy (Xu *et al.*, 2007), on microbands in a Ni single crystal (Afrin *et al.*, 2011), and on the deformation gradients around particles (Konrad *et al.*, 2006).

18.4.3 Five-parameter grain boundary characterization

Using the orientation information given by the EBSD technique, one can go one step further and describe the crystallographic nature of interfaces.

© Woodhead Publishing Limited, 2012



18.9 A voxel-based display of the area marked by dashed lines in Fig. 18.8. (a) Inverse pole figure (IPF) plot indicating the crystallographic direction parallel to the normal direction (ND) of the sheet. TD indicates the tensile direction. (b) One of the grains in (a) created by grain reconstruction with 5° misorientation threshold. (c) 3D plot of the density of geometrically necessary dislocations (GND) (in log 1/m²) calculated according to Eq. [18.2]. The arrows on the surface indicate the position of one of the austenite–martensite bands. (d) 3D plot of the kernel average misorientation (°) with direct neighbours. Note that the spatial distribution of KAM values is very similar to that of the GND density values but the difference between small and large values is stronger.

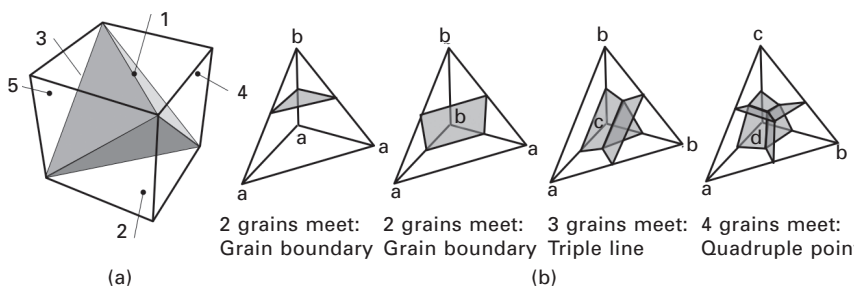
© Woodhead Publishing Limited, 2012

If one disregards the atomistic level, grain boundaries are comprehensively described by five parameters, that is the misorientation across the boundary (three parameters) and the crystallographic orientation of one of the interface normals (two parameters). All five parameters can be determined unambiguously only if a 3D technique is employed. Rohrer (2011) presents a good overview of the possibilities of 3D EBSD-based ORM and other techniques. For a comprehensive treatment of grain boundaries, see Sutton and Balluffi (2009). In the following we will briefly outline algorithms for grain boundary reconstruction and description.

Boundary meshing

Boundary reconstruction is composed of two sequential steps; identifying the boundary surface and subsequently translating this surface into a mesh of discrete geometric surface facets, the latter usually being triangles.

A well-known method for boundary reconstruction is the Marching Cubes (MC) algorithm, as introduced originally by Lorensen and Cline (1987), which has previously been applied to boundary reconstruction from orientation voxels (Dillon *et al.*, 2008). The standard MC algorithm suffers from several inherent ambiguities. These ambiguities can be solved by disassembling each cube into unambiguous tetrahedra, which, at the same time, has the advantage of generating a finer mesh. In the so-called Marching Tetrahedra (MT) algorithm (Dillard *et al.*, 2007), every marching cube is split into five tetrahedra, one central and four peripheral ones as shown in Fig. 18.10(a). Neighbouring cube cells are split mirror symmetrically, such that adjoining tetrahedra match properly. In each tetrahedron up to four different grains (i.e. voxels belonging to four different grain classes) can meet. Therefore,



18.10 Schematic display of the basic units used for the marching tetrahedra approach. (a) displays how every measurement voxel is split into five equal-sized tetrahedra. (b) describes the four different boundary cases that may occur depending on how many grains meet across the corners of the tetrahedra (slightly modified from Dillard *et al.*, 2007). For complete triangulation of a surface, the splitted cube in (a) needs to move across all measurement voxels of the dataset.

© Woodhead Publishing Limited, 2012

any resulting boundary structure can be described in terms of grain or phase boundaries, triple lines and quadruple junctions. Any higher order components will automatically be disassembled into a combination of the previous three. The four possible situations are displayed in Fig. 18.10(b).

Mesh smoothing

An as-meshed surface structure still exhibits an undesirable degree of inherent roughness and, more importantly, artifacts due to a poor slice alignment of the 3D datasets. Smoothing strategies are therefore essential to obtain artifact-free surfaces. In the field of 3D-orientation data meshing, only a few dedicated methods exist. Rowenhorst *et al*. (2006b, 2010) employed a method based on a long-range alignment by fiducial markers and a sub-pixel alignment. Dillon and Rohrer (2009) proposed another approach based on sub-pixel alignment of triple junctions. We developed a smoothing strategy (Konijnenberg *et al*., 2011) which is inspired by computer models for grain growth simulation as implemented in a vertex model by Barrales Mora (2008) and others (Weygand *et al*., 1999). In conventional grain growth processes, the main driving force for grain boundary motion comes from a lowering of the system's Gibbs free enthalpy by reducing grain boundary curvature. As a result grain boundaries move under the action of a driving force towards their local centre of curvature,

$$v = m_{eff} F_{sum} \qquad [18.3]$$

where v is the velocity, m_{eff} the effective boundary mobility and F_{sum} the net driving force pointing towards the curvature centre of the boundary. The driving force is calculated from

$$F_{sum} = \frac{\gamma_{GB}}{2} \sum_{i=1}^{n} \frac{s_{0i} \times (s_{1i} \times s_{0i})}{\| s_{1i} \times s_{0i} \|} \qquad [18.4]$$

where γ_{GB} is the grain boundary energy of the n surface facets meeting a given vertex point. s_{0i} and s_{1i} are the two vectors spanning each of the different surface facets.

Due to the increasing driving force with increasing curvature, local protrusions will straighten out first. Our model, however, differs from a classical vertex model in several notable ways. The number of grains must stay constant (thus no topological changes) and quadruple junctions are not allowed to move. All boundaries and triple lines are treated each with a uniform mobility and surface energy. We refer to this approach as a constrained vertex model (CVM) method.

© Woodhead Publishing Limited, 2012

Application example

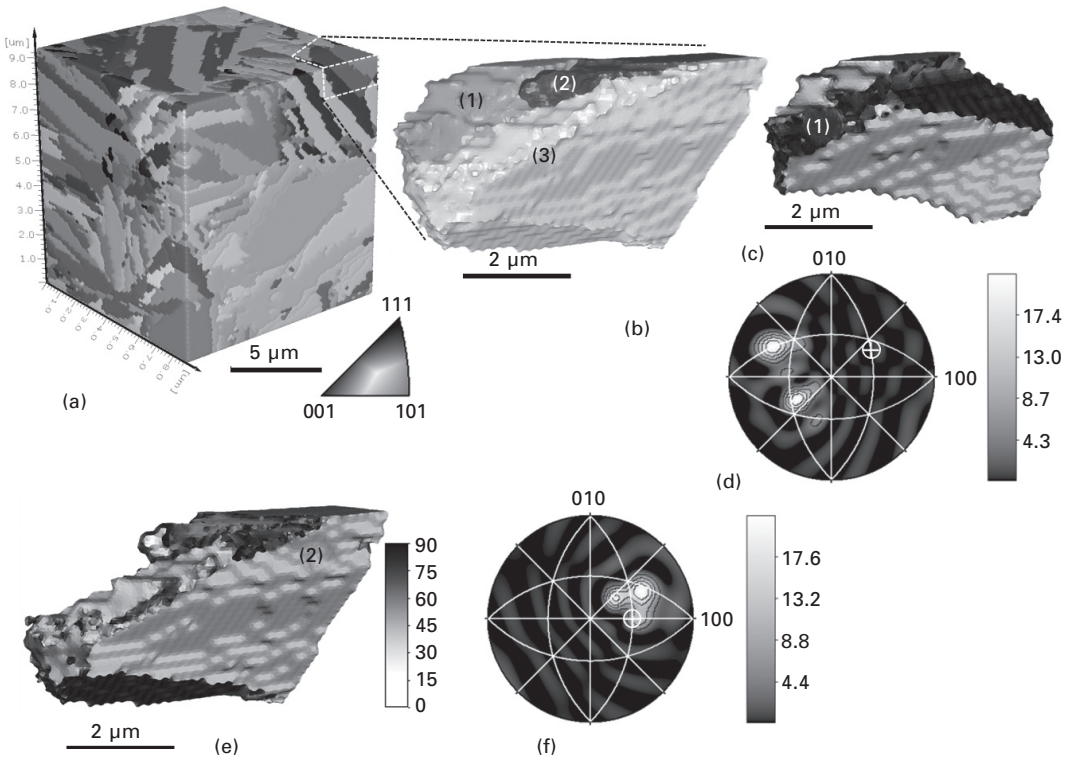
The described algorithms have been employed for the analysis of some selected grain boundaries in an Fe 28% Ni alloy (Kitahara *et al.*, 2005). The microstructure of this material consists almost entirely of lenticular martensite, exhibiting intricately developed habit planes (Fig. 18.11(a)). After the grain structure was established with a critical angle of 2° (1st neighbours only), the boundary structure was meshed with the MT method and smoothed in 20 smoothing cycles at an arbitrary but constant mobility and surface energy.

In In order to describe the grain boundary character three adjoining grains, (1), (2) and (3) are isolated from the microstructure (Fig. 18.11(b)). The mean disorientation between the grains amounts to about 55° [101] between grains (2) and (3) and 53° [323] between grains (1) and (2). Both grain boundaries can be identified to be close to typical disorientations between two Nishiyama-Wassermann variants. The grain boundaries are shown in Fig. 18.11(c) and (e), where the grey values indicate the boundary character in terms of the angle between the disorientation rotation axis and the grain boundary normal. The boundary character is twist if both vectors are parallel (e.g. they include an angle of 0°); the boundary has tilt character if both vectors are perpendicular (they include an angle of 90°). This situation is shown more quantitatively in the pole figures of the boundary normal vectors (Fig. 18.11(d) and (f)). The misorientation axis is marked by a cross in a circle and the boundary normal distribution is indicated by grey values. The grain boundary between (1) and (2) (Fig. 18.11(c)) is thus a tilt boundary, the one between (2) and (3) (Fig. 18.11(e)) a twist boundary.

Alternative approaches

The approach to grain boundary characterization by 3D EBSD-based ORM presented above allows a comprehensive and accurate description of grain boundaries. The technique has, however, significant limitations in terms of volume and resolution. The relatively small observable volume allows either the accurate observation of a small number of grain boundaries only (at high spatial resolution) or, if the grain size is small, a large number of boundaries may be observed but the accuracy of description decreases (see, e.g., Khorashadizadeh *et al.*, 2011). It is therefore desirable to combine high resolution and large observable volumes in one technique. One possible approach is the combination of EBSD with mechanical serial sectioning, as has been done by, for example, Rowenhorst *et al.* (2006a) and Morito *et al.* (2012) and others. Particularly interesting in this regard is the work of Saylor *et al.* (2003) who prepared only a few serial sections but observed very large areas. This allowed collection of a large amount of boundary

© Woodhead Publishing Limited, 2012



18.11 3D surface-based display of the microstructure of an Fe-28% Ni alloy (material supplied by N. Tsuji, Kyoto University). The material is fully transformed into lenticular martensite. (a) The full block of material displayed as IPF map of the sample normal direction. (b) Three neighbouring plates, (1), (2) and (3), of lenticular martensite taken from (a). (c) Twist-tilt character plot of the interface between the grains (1) and (3). For a legend to the grey values see (e) (see text for further information). (d) Grain boundary normal pole figure of the interface from (c) indicating the position of the misorientation rotation axis (white cross in a circle) and the position of the surface normals (peak maxima). Two surface normal maxima are visible which correspond to the interface normals with respect to grain (2) and grain (3). Both are almost pure tilt boundaries. (e) Twist-tilt plot of the interface between grains (2) and (3). (f) Grain boundary normal pole figure of the grains in (e) indicating a pure twist boundary.

© Woodhead Publishing Limited, 2012

segments with quite acceptable accuracy. An important condition for this approach is, however, that grain boundaries are truly faceted.

Another approach is to fall back on the 2D EBSD technique, which allows probing a much larger grain ensemble than the 3D technique. When grain boundaries show a statistical preference for certain crystallographic planes, for example low energy planes in a recrystallized material, the boundary distribution may be obtained from a stereological analysis of grain boundary traces as has been proposed by Saylor *et al*. (2004a). In this paper and in Saylor *et al*. (2004b) the authors applied their method to the measurement of grain boundary densities in recrystallized aluminium. Khorashadizadeh *et al*. (2011) performed, on a fine grained fcc Cu-Zr alloy with a large amount of twin boundaries, a detailed comparison of the stereological and the 3D-based determination of boundaries. They found, as pointed out already by Saylor *et al*. (2004a,b), that the occurrence of a sharp crystallographic fibre texture may significantly influence the 2D results. If this is properly corrected for, however, the 2D method may, due to its higher statistical relevance, finally be more informative than local 3D grain boundary descriptions.

18.5 Conclusions and future development of the technique

18.5.1 A comparison between EBSD, TEM diffraction and X-ray diffraction

EBSD is a powerful SEM-based diffraction and microscopy technique, well suited to study a large number of aspects of crystalline microstructures, including phase transformations. Compared to competing diffraction techniques in TEM and with X-rays (XRD), it has a number of advantages (see Table 18.1). With respect to TEM, the EBSD technique works on bulk samples and may cover very large areas or volumes, respectively. It does not require thin foils which eases sample preparation and reduces the risk of artefact formation. Its spatial resolution, though currently not as good as TEM, approaches that of TEM diffraction techniques when working at low acceleration voltages. It may be assumed that with more sensitive detectors, an interaction volume of $30 \times 10 \times 5$ nm^3 may be achievable at 5 kV acceleration voltage (Steinmetz and Zaefferer, 2010). In TEM the volume contributing to diffraction patterns is not much smaller, since even the thinnest TEM samples are not much thinner than 30 nm and a reasonable beam size is in the order of 2–10 nm in diameter. Furthermore, areas that are that thin are very limited in size. Nevertheless, low acceleration voltages also cause problems, for example, concerning the sensitivity to any kind of surface layers such as contamination or oxide films. Furthermore, as EBSD requires incoherent scattering, it generally needs a higher beam current than

© Woodhead Publishing Limited, 2012

those TEM techniques that work only with coherent, elastic scattering. EBSD might therefore be less suited for electron-beam sensitive materials.

With respect to XRD the EBSD technique also has a number of advantages. One is the significantly better spatial resolution, even when compared to the best micro-XRD technique. The statistical relevance of XRD data is also not necessarily better than that of EBSD because the latter can be applied to very large areas at competitive measurement times (see, e.g., Davut and Zaefferer, 2010). In terms of texture determination, EBSD offers the advantage that orientations are measured directly (see, e.g., Wright *et al.*, 2007). XRD techniques, in contrast, only measure pole densities from which the orientation distribution function (ODF) has to be calculated in a rather complicated procedure (see, e.g., Bunge, 1987). With EBSD, consequently, techniques like pole figure inversion and pole figure corrections are not required to determine the ODF. On multiphase materials, no peak overlaps occur as they frequently do in XRD. Together with texture measurements, microscopic or macroscopic information is also delivered which may allow quantitative description of misorientation distribution functions (MODFs). In terms of phase determination, EBSD-based techniques have made great progress. Compared to XRD, much smaller volumes can be investigated. The missing peak overlaps here are also a great advantage. Finally, with the advent of new pattern simulation techniques based on dynamic electron diffraction theory (Winkelmann *et al.*, 2007), it appears that in the not too distant future it may be possible to perform even structure determination from EBSD patterns. The combination of EBSD with X-ray spectroscopy techniques, i.e. EDX and WDX, particularly at low acceleration voltage for increased resolution, may further support effective structure determination (Dingley, 2004; Nowell and Wright, 2004).

The fact that EBSD is a bulk (or semi-bulk) technique makes *in-situ* observations of processes such as thermally or mechanically induced phase transformations more realistic and more feasible than is the case with TEM of thin foils. A number of observations of phase transformations have been made, e.g. by Seward *et al*. (2004) and Fukino *et al*. (2011) on thermally induced, diffusive transformations and Karlsen *et al*. (2009) and Sato and Zaefferer (2009) on deformation induced martensite. It should be noted, however, that the results of such investigations have to be observed with caution because the free surface may significantly modify the usual bulk behaviour.

With respect to 3D observations, the EBSD technique is complementary to 3D techniques available in TEM (TEM tomography) and XRD (mainly as synchrotron-based tomography techniques) as it covers exactly the lateral length scales between these two techniques. The synchrotron-based techniques are of particular interest because they are non-destructive and therefore

© Woodhead Publishing Limited, 2012

well suited to observe processes during thermal or mechanical loading of materials.

18.5.2 New EBSD-based techniques

Two further tools that make use of EBSD measurements shall be mentioned briefly, the electron channelling contrast imaging (ECCI) technique and the measurement of elastic lattice strain using a pattern cross-correlation technique.

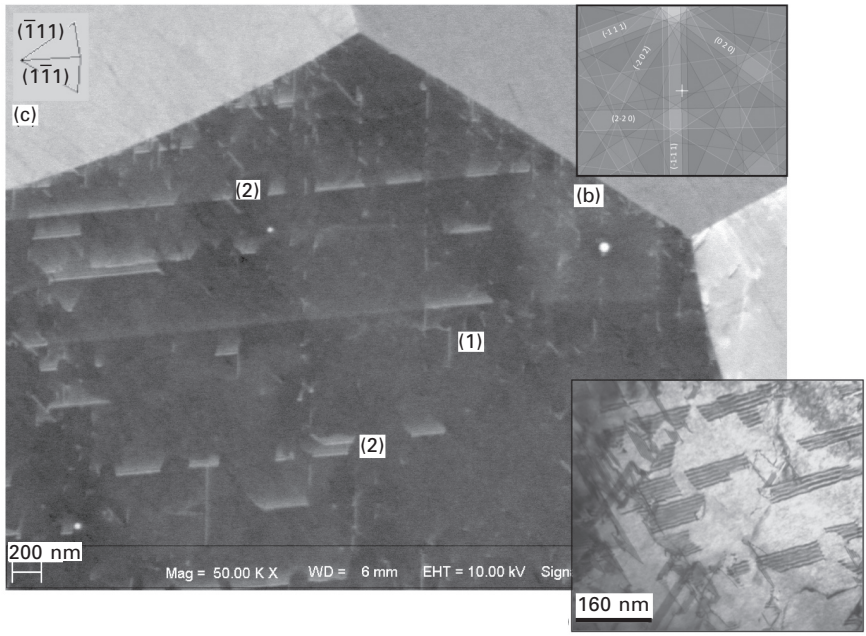
The ECCI technique enables direct observation of dislocations, stacking faults and fine twins or martensite crystals within the SEM using the backscattered electron mode. The technique is similar to dark field imaging in TEM. The proper sample tilt to obtain two-beam conditions (which means that the primary beam impinges on the sample under Bragg conditions with respect to one of the lattice planes in the illuminated crystal) is traditionally established using electron channelling patterns (ECP) (e.g., Simkin and Crimp, 1999). With dedicated pattern simulation techniques (Zaefferer, 2002), the tilt can now be determined on the basis of EBSD measurements (Gutierrez-Urrutia *et al*., 2009). One resulting image is shown in Fig. 18.12.

The determination of lattice strain by EBSD has been promoted mainly by Wilkinson *et al*. (2006a, 2006b). It makes use of the fact that the elastic distortion of a lattice unit cell leads to a similar distortion of the EBSD pattern. This distortion, although very small (resulting shifts of diffraction features on the EBSD detector are of only subpixel size), can be determined by comparing the pattern with a very similar but non-distorted one, which is taken at a lattice strain-free location nearby. The technique has been employed to determine residual stresses in semi-conductor materials. For ductile materials, the technique very sensitively yields lattice rotations caused by GNDs. Rotation angles smaller than 0.01° can be determined. Residual stress measurements in such materials are not yet well established but several groups are working on it.

18.5.3 Future applications of EBSD to steels

With respect to investigations of steels, EBSD has proven to be extremely useful. Nevertheless, the increasingly smaller structures of modern steels require improved spatial resolution of the EBSD technique by moving to lower acceleration voltages and more sensitive detectors. The increasing structural complexity of steels also requires improved tools that prove the representativeness of microscopic measurements or observations for the investigated material. Davut and Zaefferer (2010) have worked in this direction. *In-situ* EBSD-based observations of thermally induced phase transformation

© Woodhead Publishing Limited, 2012



18.12 Electron channelling contrast image (ECCI) taken on a slightly deformed TWIP steel (~22 mass% Mn, 0.6% C, bal. Fe) under well-controlled diffraction conditions (so-called cECCI) in a Zeiss FEG-SEM with Gemini column at high beam current and 10 kV acceleration voltage. (a) Positions (1) and (2) indicate dislocations and stacking faults, respectively. (b) Diffraction pattern simulated based on EBSD measurements indicating the required tilt angles for optimum visibility of the defects (two-beam conditions). (c) Position of the (111) planes for the current observation conditions. (d) TEM image of a similar area with stacking faults and dislocations. Note that the intense fringe contrast visible in TEM can also be observed in the cECC image, though with weaker contrast.

processes have had little success because the free surface frequently changes the behaviour of nucleation or growth processes. Also strain-induced *in-situ* processes should be regarded with caution because of the free surface.

Understanding more details about martensitic transformations, e.g. variant selection and martensite morphology, requires the measurement of elastic stresses around progressing martensite structures. EBSD-based measurements might become extremely helpful for these subjects. Diffusive transformations always occur in conjunction with partitioning processes, particularly of carbon but also of other elements. These processes may be very effectively observed by a combination of EBSD, EDX and WDX at low acceleration voltages. Nevertheless, the small structures that play a role here (for example in quench-and-partition (QP) steels) imperatively require the application

© Woodhead Publishing Limited, 2012

of further tools, for example of atom probe tomography (APT). A good example has been published by Dmitrieva *et al*. (2011) on a lean maraging TRIP steel. To this aim EBSD is extremely helpful in selecting the correct area of observation which is subsequently prepared for TEM and APT by focused ion beam milling.

18.6 References

Adams B L, Wright S I, Kunze K (1993), Orientation imaging: the emergence of a new microscopy, *Metall. Trans*. 24A, 819–831

Afrin N, Quadir M Z, Bassman L, Driver J H, Alboud A, Ferry M (2011), The three-dimensional nature of microbands in a channel die compressed Goss-oriented Ni single crystal, *Scripta Mater*. 64, 221–224

Baba-Kishi K Z (2002), Review – electron backscatter Kikuchi diffraction in the scanning electron microscope for crystallographic analysis, *J. Mater. Sci*. 37, 1715–1746

Barrales Mora L A (2008), 2D and 3D Grain Growth Modeling and Simulation, PhD thesis, Cuvillier Verlag, Göttingen

Baudin T, Etter A L, Penelle R (2007), Annealing twin formation and recrystallization study of cold-drawn copper wires from EBSD measurements, *Mat. Char*. 58, 947–952

Britton T B, Birosca S, Preuss M, Wilkinson A J (2010), Electron backscatter diffraction study of dislocation content of a macrozone in hot-rolled Ti–6Al–4V alloy, *Scripta Mater*. 62, 639–642

Brough I, Bate P S, Humphreys F J (2006), Optimising the angular resolution of EBSD, *Mater. Sci. Technol*. 22 1279–1287

Bunge H J (1987), Three-dimensional texture analysis, *Int. Mat. Rev*. 32, 265–291

Cayron C (2007), ARPGE: a computer program to automatically reconstruct the parent grains from electron backscatter diffraction data, *J. Appl. Crystall*. 40, 1183–1188

Cayron C, Artaud B, Briottet L (2006), Reconstruction of parent grains from EBSD data, *Mat. Char*. 57, 386–401

Cayron C, Barcelo F, Carlan Y (2010), The mechanisms of the fcc–bcc martensitic transformation revealed by pole figures, *Acta Mater*. 58, 1395–1402

Choi S-H, Jin Y-S (2004), Evaluation of stored energy in cold-rolled steels from EBSD data, *Mat. Sci. Eng*. A371, 149–159

Christian J W (1975), *The Theory of Transformations in Metals and Alloys*, 2nd edn, Pergamon Press, Oxford

Davut K, Zaefferer S (2010), Statistical reliability of phase fraction determination based on EBSD investigations on the example of an Al-TRIP steel, *Mater. Trans*. 41A, 2187–2996

Dillard S, Bingert J, Thoma D, Hamann B (2007), Construction of simplified boundary surfaces from serial-sectioned metal micrographs, *IEEE TVCG* 13 (6), 1528–1535

Dillon S, Rohrer G (2009), Three-dimensional FIB-OIM of ceramic materials, *J. Am. Ceram. Soc*. 92, 1580–1585

Dillon S J, Lee S, Rollett A D, Rohrer G S (2008), Measuring the five parameter grain boundary character distribution from three-dimensional orientation maps, *Microsc. Microanal*. 14 (S2), 978–979

Dingley D J (1984), On-line determination of crystal orientation and texture determination in an SEM, *Proc. Royal Microsc. Soc*. 19, 74–75

© Woodhead Publishing Limited, 2012

Dingley D J (2004), Progressive steps in the development of electron backscatter diffraction and orientation imaging microscopy, *J. Microscopy* 213, 214–224

Dingley D J, Field D P (1997), Electron backscatter diffraction and orientation imaging microscopy, *Mater. Sci. Technol.* 13, 69–78

Dmitrieva O, Ponge D, Inden G, Millán J, Choi P, Sietsma J, Raabe D (2011), Chemical gradients across phase boundaries between martensite and austenite in steel studied by atom probe tomography and simulation, *Acta Mater.* 59, 364–374

El-Dasher B S, Adams B L, Rollett A D (2003), Viewpoint: experimental recovery of geometrically necessary dislocation density in polycrystals, *Scripta Mater.* 48, 141–145

Field D P, Merriman C C, Allain-Bonasso N, Wagner F (2011), Quantification of dislocation structure heterogeneity in deformed polycrystals by EBSD, *Modelling and Simulation in Mater. Sci. Eng.*, in press

Fukino T, Tsurekawa S, Morizono Y (2011), *In-situ* scanning electron microscopy/electron backscattered diffraction observation of microstructural evolution during α to γ phase transformation in deformed Fe-Ni alloy, *Metall. Mater. Trans. A* 42A, 587–593

Gerber Ph, Baudin T, Jakani S, Mathon M H, Bacroix B (2004), Estimation of stored energy distribution from EBSD measurements, *Mat. Sci. Forum* 467–470 51–56

Germain L, Dey S R, Humbert M, Gey N (2007), Determination of parent orientation maps in advanced titanium-based alloys, *J. Microscopy* 227, 284–291

Gourgues-Lorenzon A-F (2009), Application of electron backscatter diffraction to the study of phase transformations: present and possible future, *J. Microscopy* 233, 460–473

Gourgues A-F, Flower H M, Lindley T C (2000), Electron backscattering diffraction study of acicular ferrite, bainite, and martensite steel microstructures, *Mater. Sci. Technol.* 16, 26–40

Groeber M A, Haley B K, Uchic M D, Dimiduk D M, Gosh S (2006), 3D reconstruction and characterization of polycrystalline microstructures using a FIB-SEM system, *Mat. Char.* 57, 259–273

Gutierrez-Urrutia I, Zaefferer S, Raabe D (2009), Electron channeling contrast imaging of twins and dislocations in twinning-induced plasticity steels under controlled diffraction conditions in a scanning electron micro-scope, *Scripta Mater.* 61, 737–740

He W, Ma W, Pantleon W (2008), Microstructure of individual grains in cold-rolled aluminium from orientation inhomogeneities resolved by electron backscattering diffraction, *Mater. Sci. Eng. A* 494, 21–27

Humbert M, Blaineau P, Germain L, Gey N (2011), Refinement of orientation relations occurring in phase transformation based on considering only the orientations of the variants, *Scripta Mater.* 64, 114–117

Humphreys F J (2001), Grain and subgrain characterisation by electron backscatter diffraction, *J. Mater. Sci.* 36, 3833–3854

Jacques P J (2004), Transformation-induced plasticity for high strength formable steels, *Curr. Opin. Solid State Mater. Sci.* 8, 259–265

Karlsen M, Grong Ø, Søfferud M, Hjelen J, Rørvik G, Chiron R (2009), Scanning electron microscopy/electron backscatter diffraction-based observations of martensite variant selection and slip plane activity in supermartensitic stainless steels during plastic deformation at elevated, ambient, and subzero temperatures, *Metall. Mater. Trans. A* 40A, 310–320

Khorashadizadeh A, Raabe D, Zaefferer S, Rohrer G S, Rollett A D, Winning M (2011), Five-parameter grain boundary analysis by 3D EBSD of an ultra-fine grained CuZr alloy processed by equal channel angular pressing, *Adv. Eng. Mater.* 13, 237–244

© Woodhead Publishing Limited, 2012

Kitahara H, Ueji R, Ueda M, Tsuji N, Minamino Y (2005), Crystallographic analysis of plate martensite in Fe–28.5 at.% Ni by FE-SEM/EBSD, *Mat. Char.* 54, 378–386

Konijnenberg P J, Zaefferer S, Lee S-B, Rollett A D, Rohrer G S, Raabe D (2011), Advanced methods and tools for reconstruction and analysis of grain boundaries from 3D-EBSD data sets, *Proceedings ICOTOM* 16, in press

Konrad J, Zaefferer S, Raabe D (2006), Investigation of orientation gradients around a hard Laves particle in a warm-rolled Fe3Al-based alloy using a 3D EBSD-FIB technique, *Acta Mater.* 54, 1369–1380

Krieger-Lassen N C (1994), Automated determination of crystal orientations from electron backscattering patterns, PhD thesis, Danmarks Tekniske Universitet, Lyngby

Krieger-Lassen N C, Jensen D J, Conradsen K (1992), Image processing procedures for analysis of electron diffraction patterns, *Scanning Microscopy* 6, 115–121

Kröner E (1981), Continuum theory of defects, in Balian R, Kleman M, Poirer J P (eds) *Physics of Defects*, North-Holland, Amsterdam, 215–315

Lorensen W E, Cline H E (1987), Marching cubes: a high resolution 3D surface construction algorithm. ACM SIGGRAPH, *Computer Graphics* 21, 163–169

Matteson T L, Schwarz S W, Houge E C, Kempshall B W, Gianuzzi L A (2002), Electron backscattering diffraction investigation of focused ion beam surfaces, *J. Electronic Mater.* 31, 33–39

Miyamoto G, Iwata N, Takayama N, Furuhara T (2010), Mapping the parent austenite orientation reconstructed from the orientation of martensite by EBSD and its application to ausformed martensite, *Acta Mater.* 58, 6393–6403

Morito S, Huang X, Furuhara T, Maki T, Hansen N (2006), The morphology and crystallography of lath martensite in alloy steels, *Acta Mater.* 54, 5323–5331

Morito S, Edamatsu Y, Ichinotano K, Ohba T, Hayashi T, Adachi Y, Furuhara T, Miyamoto G, Takayama N (2012), Quantitative analysis of three-dimensional morphology of martensite packets and blocks in iron-carbon-manganese steels, *J. Alloys Compounds*, to be published

Mulders J J L, Day A P (2005), Three-dimensional texture analysis, *Mat. Sci. Forum* 495–497, 237–242

Nowell M M, Wright S I (2004), Phase differentiation via combined EBSD and XEDS, *J. Microscopy* 213, 296–305

Nye J F (1953), Some geometrical relations in dislocated crystals, *Acta Metall.* 1, 153–162

Pantleon W (2008), Resolving the geometrically necessary dislocation content by conventional electron backscattering diffraction, *Scripta Mater.* 58, 994–997

Petrov R, Kestens L, Wasilkowska A, Houbaert Y (2007), Microstructure and texture of a lightly deformed TRIP-assisted steel characterized by means of the EBSD technique, *Mater. Sci. Eng. A.* 447, 285–297

Prasad S V, Michael J R, Christenson T R (2003), EBSD studies on wear-induced subsurface regions in LIGA nickel, *Scripta Mater.* 48, 255–260

Randle V (2008), Recent developments in electron backscatter diffraction, *Adv. Imag. Electron Phys* 151, 363–416

Rohrer G S (2011), Measuring and interpreting the structure of grain-boundary networks, *J. Am. Ceram. Soc.* 94, 633–646

Rollett A D, Lee S-B, Campman R, Rohrer G S (2007), Three-dimensional characterization of microstructure by electron back-scatter diffraction, *Annu. Rev. Mater. Res.* 37, 627–658

© Woodhead Publishing Limited, 2012

Rowenhorst D J, Gupta A, Feng C R, Spanos G (2006a), 3D crystallographic and morphological analysis of coarse martensite: combining EBSD and serial sectioning, *Scripta Mater*. 55, 11–16

Rowenhorst D J, Kuang J P, Thornton K, Voorhees P W (2006b), Three-dimensional analysis of particle coarsening in high volume fraction solid–liquid mixtures, *Acta Mater.* 54, 2027–2039

Rowenhorst D J, Lewis A C, Spanos G (2010), Three-dimensional analysis of grain topology and interface curvature in a b-titanium alloy, *Acta Mater.* 58, 5511–5519

Sato H, Zaefferer S (2009), A study on the formation mechanisms of butterfly-type martensite in Fe-30%Ni alloy using orientation microscopy, *Acta Mater.* 57, 1931–1937

Saylor D M, Morawiec A, Rohrer G S (2003), Distribution of grain boundaries in magnesia as a function of five macroscopic parameters, *Acta Mater.* 51, 3663–3674

Saylor D M, El-Dasher B S, Adams B L, Rohrer G S (2004a), Measuring the five-parameter grain-boundary distribution from observations of planar sections, *Metall. Mater. Trans. A* 35A (7), 1981–1989

Saylor D M, El-Dasher B S, Rollett A D, Rohrer G S (2004b), Distribution of grain boundaries in aluminum as a function of five macroscopic parameters, *Acta Mater.* 52, 3649–3655

Schwartz A J, Kumar M and Adams B L (eds) (2000), *Electron Backscatter Diffraction in Materials Science*, Kluwer Academic/Plenum Publishers, New York

Schwartz A J, Kumar M, Adams B L and Field D P (eds) (2009), *Electron Backscatter Diffraction in Materials Science*, 2nd edn, Springer, New York

Schwarzer R A (1997), Automated crystal lattice orientation mapping using computer controlled SEM, *Micron* 28, 249–265

Seward G G E, Celotto S, Prior D J, Wheeler J, Pond R C (2004), *In situ* SEM-EBSD observations of the hcp to bcc phase transformation in commercially pure titanium, *Acta Mater.* 52, 821–832

Shibata A, Morito S, Furuhara T, Maki T (2005), Local orientation change inside lenticular martensite plate in Fe-33Ni alloy, *Scripta Mater*. 53, 597–602

Simkin B A, Crimp M A (1999), An experimentally convenient configuration for electron channeling contrast imaging, *Ultramicroscopy* 77, 65–75

Spanos G (2006), Viewpoint set no. 41 '3D characterization and analysis of materials', *Scripta Mater*. 55, 3

Steinmetz D, Zaefferer S (2010), Towards ultra-high resolution EBSD by low accelerating voltage, *Mater. Sci. Technol*. 26, 640–645

Sutton A P, Balluffi R W (2009), *Interfaces in Crystalline Materials*, Clarendon Press, Oxford

Uchic M D, Groeber M, Wheeler R, Scheltens F, Dimiduk D M (2004), Augmenting the 3D characterization capability of the dual beam FIB-SEM, *Microsc. Microanal.* 10, 1136–1137

Weygand D, Bréchet Y, Lépinoux J, Gust W (1999), Three-dimensional grain growth: a vertex dynamics simulation, *Phil. Mag*. 79, 703–716

Wheeler J, Mariani E, Piazolo S, Prior D J, Trimby P, Drury M R (2009), The weighted Burgers vector: a new quantity for constraining dislocation densities and types using electron backscatter diffraction on 2D sections through crystalline materials, *J. Microscopy* 233, 482–494

Wilkinson A J, Meaden G, Dingley D J (2006a), High resolution mapping of strains and rotations using electron backscatter diffraction, *Mater. Sci. Technol*. 22, 1271–1278

© Woodhead Publishing Limited, 2012

Wilkinson A J, Meaden G, Dingley D J (2006b), High-resolution elastic strain measurement from electron backscatter diffraction patterns: new levels of sensitivity, *Ultramicroscopy* 106, 307–313

Winkelmann A, Trager-Cowan C, Sweeney F, Day A P, Parbrook P (2007), Many-beam dynamical simulation of electron backscatter diffraction patterns, *Ultramicroscopy* 107, 414–421

Wright S I, Nowell M M, Bingert J F (2007), A comparison of textures measured using X-ray and electron backscatter diffraction, *Met. Mat. Trans. A*, 38A, 1845–1855

Wu J, Wray P J, Garcia C I, Hua M, Deardo A J (2005), Image quality analysis: a new method of characterizing microstructures, *ISIJ Int.* 45, 254–262

Xu W, Ferry M, Cairney J M, Humphreys F J (2007), Application of FIB-EBSD tomography for understanding annealing phenomena in a cold rolled particle-containing nickel alloy, *Mater. Sci. Forum* 558–559, 413–418

Zaefferer S (2000), New developments of computer-aided crystallographic analysis in transmission electron microscopy, *J. Appl. Crystall.* 33, 10–25

Zaefferer S (2002), Computer-aided crystallographic analysis in the TEM, *Adv. Imaging Electron Phys.* 125, 355–415

Zaefferer S, Wright S I (2009), 3D-orientation microscopy by serial sectioning and EBSD-based orientation mapping in a FIB-SEM, in *EBSD in Materials Science*, ed. A. Schwartz, J. Kumar, B. Adams, Springer, New York

Zaefferer S, Ohlert J, Bleck W (2004), A study of microstructure, transformation mechanisms and correlation between microstructure and mechanical properties of a low alloyed TRIP steel, *Acta Mater.* 52, 2765–2778

Zaefferer S, Konrad J, Raabe D (2005), 3D-orientation microscopy in a combined focused ion beam (FIB)-scanning electron microscope: a new dimension of microstructure characterisation, *Microscopy Conference 2005*, Davos, 63

Zaefferer S, Romano P, Friedel F (2008a), EBSD as a tool to identify and quantify bainite and ferrite in low alloyed Al-TRIP steels, *J. Microscopy* 230, 499–508

Zaefferer S, Wright S I, Raabe D (2008b), 3D-orientation microscopy in a FIB SEM: a new dimension of microstructure characterisation, *Metall. Mater. Trans.* 39A, 374–389

Zambaldi C, Zaefferer S, Wright S I (2009), Characterization of order domains in gamma-TiAl by orientation microscopy based on electron backscatter diffraction, *J. Appl Crystall* 42, 1092–1101

© Woodhead Publishing Limited, 2012

19

Application of synchrotron and neutron scattering techniques for tracking phase transformations in steels

S. S. BABU, The Ohio State University, USA

Abstract: This chapter reviews the role of synchrotron and neutron scattering techniques for measurement of transformation kinetics in steels and understanding of phase transformation mechanisms. In the first part of the chapter, various techniques are introduced. In the second part of the chapter, the use of these techniques are demonstrated by published examples. These examples include non-equilibrium phase transformations during liquid to solid as well as solid-solid phase transformations. As a part of solid-state transformation, austenite formation during heating as well as the decomposition of austenite to various ferrite morphologies are considered. Extensions of these techniques for describing phase transformation during thermo-mechanical transients are also described.

Key words: phase transformations in steels, X-ray diffraction, neutron scattering, time-resolved techniques.

19.1 Introduction

Even with many centuries of experience in treating, making, shaping and usage of steels (Fruehan, 1998), there is ongoing research to understand the details of phase transformations in steels for different length- and time-scales (Offerman *et al*., 2002; Wong *et al*., 2003; Kelly and Miller, 2007; Elmer, 2008). This continued research is driven by a number of factors. With increased demand for low-temperature (e.g. strength, toughness, corrosion resistance), high-temperature (e.g. creep strength, oxidation resistance) and dynamic (e.g. ballistic resistance) properties, new generations of steels are required. To meet this need, microstructures are being engineered through careful design of alloying element concentration and innovative heat treatments. Some of these developments are already discussed elsewhere in this book, but in order to provide context to the present chapter, some examples are introduced briefly here.

Saha and Olson (2007) and Saha *et al*. (2007) have developed ballistic resistance steel by using multi-scale modeling technologies. In this steel, nano-scale bcc-Cu precipitates and M_2C carbides are distributed within a low-carbon martensitic matrix. In addition, a dispersion of nano-scale nickel

© Woodhead Publishing Limited, 2012

enriched γ-phase was triggered by selection of heat treatment temperature. This unique distribution of nanoscale precipitates within a low-carbon martensitic matrix lead to an optimum combination of strength and toughness. In another example, Caballero *et al*. (2002) and Bhadeshia (2010) have developed a nano-scale bainitic microstructure by austempering a silicon-containing high-carbon steel. In this development, the steel is austenitized and isothermally transformed at temperatures in between the bainitic start (B_s) and martensitic start (M_s) temperatures. The addition of silicon retards the cementite precipitation from both austenite and ferrite and thereby promotes a mixture of very thin low-carbon bainitic ferrite laths (2–3 nm thick) interspersed in a high-carbon austenitic matrix. Following a similar trend of leveraging low-temperature transformation, researchers at Colorado School of Mines (Speer *et al*., 2003; Clarke *et al*., 2008) have developed an innovative steel heat treatment they have called quenching and partitioning (Q&P). In Q&P steels, the steel is quenched to low temperature to induce incomplete transformation of austenite to martensite (i.e. a quench temperature between M_s and M_f) before heating to a temperature at which the carbon partitions from martensite to the residual untransformed austenite. This high carbon austenite then becomes stable at room temperature. This combination of low-carbon martensite and high-carbon austenite provides good combinations of strength and toughness. Recently, steel researchers have also proven that the unique microstructure evolution in steels can be obtained by introducing high magnetic field (> 10 tesla) as the steel cools from austenite phase field to room temperature (Enomoto *et al*., 2001; Ludtka *et al*., 2004; Jaramillo *et al*., 2005; Ohtsuka, 2008). For example, the kinetics of the austenite to pearlite transformation were accelerated in conjunction with a reduction in interlamellar spacing to nanoscale (~70 nm) levels.

It is noteworthy that researchers behind the above examples leveraged the computational thermodynamic and kinetic models to reduce development cycle time. However, optimization of the heat treatment conditions (temperature and time) was still achieved by trial-and-error kinetic experimentations. These experiments included dilatometry and microscopy (optical, electron, atom probe) of samples obtained by interrupted heat treatments. This leads to an important question: Why are we unable to leverage existing computational models to predict the kinetics of microstructural evolution in steels for any alloying element concentration and arbitrary thermo-mechanical history? The answer is partly the lack of robust computational models that *predict* the kinetics to greater accuracy. Many of these models are descriptive and based on data measured by post-process (*ex-situ*) characterization methods. As a result, these data do not have the fidelity to extract the fundamental characteristics (e.g., non-equilibrium partitioning of carbon between bainitic ferrite and austenite) during the (*in-situ*) transformations. Phase transformations in steels are accompanied by many changes in properties including physical

© Woodhead Publishing Limited, 2012

(expansion coefficient), modulus, crystal structure, molar volume, enthalpy, magnetic, resistance, defect density, compositional differences and mechanical properties. All of the above changes can be tracked by one or more *in-situ* techniques, e.g. change in molar volume and thermal expansion coefficient during the austenite to ferrite reaction can be tracked by dilatometry.

The present chapter introduces the role of synchrotron and neutron scattering techniques to track the kinetics, as well as indicate phase transformation mechanisms. In the first part of the chapter, these techniques are introduced. In the second part, the use of these techniques to understand phase transformations in steels is demonstrated by selected examples. This will span both liquid-to-solid and solid-to-solid phase transformations, and the importance of these data in understanding the fundamental physical processes that occur will be discussed. In addition, the role of these *in-situ* measurements in the development of robust kinetic models will also be presented.

19.2 X-ray and neutron scattering techniques

The goal of this section is to introduce briefly the techniques of X-ray and neutron scattering measurement. For more comprehensive details, readers are referred to standard reference books on X-ray (Cullity and Stock, 2001) and neutron scattering (Kostorz, 1996); a good understanding of the techniques and their limitations from these reference books is necessary for proper interpretation of the data. Graduate students and researchers who are contemplating following this research direction are also recommended to attend the workshops organized by different beam line facilities (LANSCE, Los Alamos National Laboratory, 2010). Recent advancements in these techniques are also being addressed by symposia organized by Barabash, Wang and Liaw (Barabash *et al*., 2008; Cheng *et al*., 2008; Choi *et al*., 2008; Dai *et al*., 2008; Huang, 2008; Ice, 2008; Jensen and Godisken, 2008; Jia *et al*., 2008; Muansky *et al*., 2008; Pereloma *et al*., 2008; Wang *et al*., 2008). The papers in the symposium were published in a special issue of *Metallurgical and Materials Transactions A* in 2008. In addition, publications with a specific focus on *in-situ* investigations have been compiled by Kannengiesser *et al*. (2010).

19.2.1 Theoretical basis

The atoms in a given material scatter the incoming radiation, if their wavelengths (λ) are equal to or smaller than the interatomic spacing (Kostorz, 1996). Basic premises for describing this atom–radiation scattering are given by kinematical diffraction theory. A good introduction to this theory is given by Ruhle and Wilkens (2006). The theory states the following:

© Woodhead Publishing Limited, 2012

1. scattering at individual atoms are elastic (λ (incoming) = λ (scattered));
2. scattering of the atoms occurs coherently, and as a result there is no phase difference between incoming and scattered waves
3. due to its low strength, the second scattering of the scattered wave is negligible; and
4. total scattering of the atoms in a sample is weak and the intensity of the incoming wave is the same within the irradiated volume.

Under diffraction conditions, coherent superpositions of scattered waves from atom centers occurs. Using this basis, the scattering and diffraction equations can be derived. The diffraction depends on the scattering factor (F_{hkl} = function of atomic scattering factor and structure of the crystal (fcc or bcc)) and the spacing of diffracting *hkl* planes (d_{hkl}). This leads to Bragg's law:

$$2d_{hkl} \sin \theta_{hkl} = \lambda \qquad [19.1]$$

In the above equation, θ_{hkl} is the angle between the incident beam and the diffraction planes, referred to as the Bragg angle. By measuring θ_{hkl} at constant wavelength, it is possible to measure the interatomic spacing (d_{hkl}). The intensity of the diffraction peak is proportional to the square of the structure factor, F_{hkl}:

$$I_{hkl} = | F_{hkl} |^2 \qquad [19.2]$$

Methods to calculate the structure factors and the intensity of diffracted beams are outlined in textbooks (e.g. Thomas, 1962). The definition of a diffraction pattern is given by Kostorz (1996): 'A diffraction pattern, after all instrument corrections, reflects the distribution of scattering matter within the (average) unit cell of a substance and the atomic coordinates (location of the centers of scattering objects) as well as the scattering-length distribution (electrons with X-rays, nuclei and magnetic moments with neutrons) can be determined from an analyses of Bragg Peaks'. By analyzing the diffraction patterns, we can identify the type of crystal structure. It is noteworthy that the diffraction peaks are not sharp and the width of these peaks depends upon the crystallite size. The peak broadening ($\Delta\theta_{hkl}$) can be correlated to the crystallite size (L) and wavelength:

$$2(\Delta\theta_{hkl}) = \frac{\lambda}{L \cos \theta_{hkl}} \qquad [19.3]$$

With suitable models, the peak broadening can also be correlated with defect density (Barabash *et al.*, 2004). With changes in peak locations at a given temperature, it is also possible to evaluate the partitioning of interstitial element concentrations in steels between austenite and ferrite (Babu *et al.*, 2005a). Peak shifts in a well characterized material (i.e. knowledge of the

© Woodhead Publishing Limited, 2012

strain-free lattice parameter) can also be used to measure the residual stress in the samples (Withers and Bhadeshia, 2001a, 2001b). In addition, it is also possible to predict the lattice structure and its elemental composition using peak fitting techniques including Rietveld methods (Rietveld, 1969; Hill and Howard, 1987; Bish and Howard, 1988).

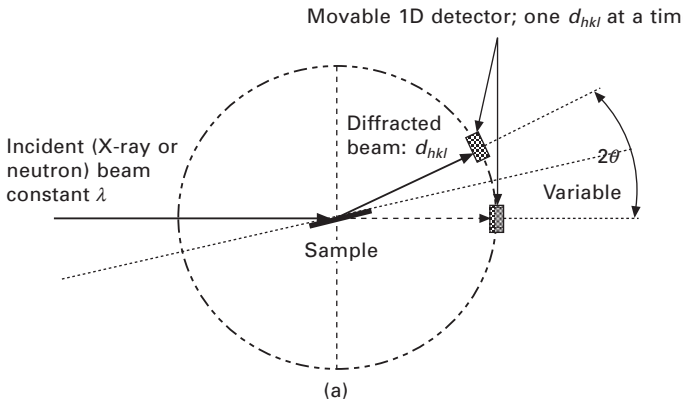
Steel phase transformations have been investigated by both X-rays and neutron scattering. X-ray scattering occurs by interaction with the electron cloud and is very sensitive to the atomic number. In contrast, neutrons are scattered by nuclei and do not scale with the atomic number (Dianoux and Lander, 2003). Although one can perform X-ray diffraction using laboratory cathode tube based X-ray sources, the experiments are very slow. For example, to obtain one diffraction measurement, the time taken may range from a few minutes to several hours. However, these time resolutions are not compatible with the rate of phase transformations in steels. In this regard, the use of synchrotrons as an X-ray source has become popular (Elmer, 2008). The main advantage is related to brightness (photons/sec/mm^2/m.rad^2) of the synchrotron X-ray sources (10^{15}) that are many orders of magnitude greater than laboratory sources (10^7), and allow rapid measurements in the order of microseconds. In the case of neutron diffraction, traditional reactor sources are used routinely as a source (Root *et al.*, 1993). With careful diffraction geometries, it is indeed possible to get rapid measurements even with these sources. Recently, pulsed neutron sources allow for much more rapid measurements (Bourke *et al.*, 2002; Matthies *et al.*, 2005; Liaw, 2006; Santisteban *et al.*, 2006; Wang *et al.*, 2006). In addition, the neutron beams also sample large volumes and therefore are not sensitive to surface conditions of the samples. The impact of these techniques will be described in later sections.

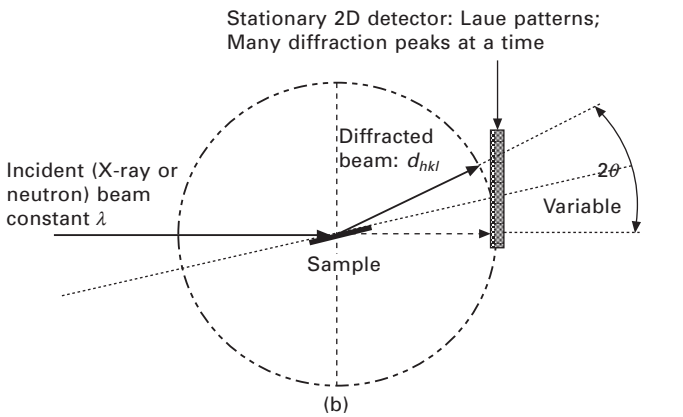
19.2.2 Experimental methods

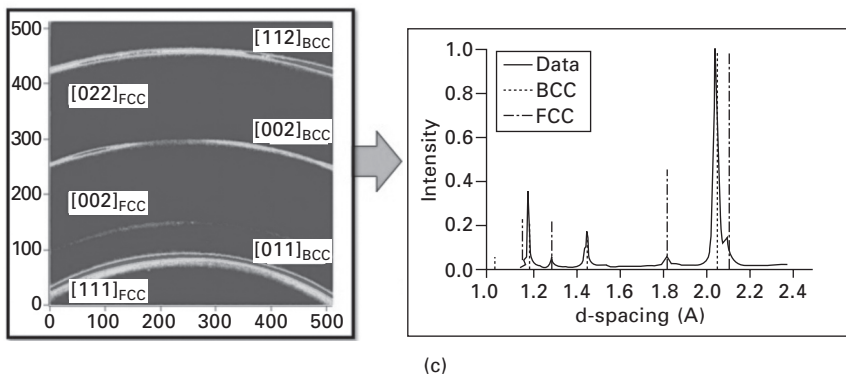
Angular dispersive method

The most common method to measure diffraction peaks is the angular method (see Fig. 19.1(a)). In this method, the incident (neutron or X-ray) beam impinges on the surface of the sample at an angle θ and the diffracted beam is measured at angle 2θ. Samples are placed in the center of the goniometer allowing for rotation at different angles without any linear translation. With the incident beam direction fixed, the sample is tilted to various θ, while the detector moves along a constant circle radius. The diffraction peaks are measured at 2θ angles. In this configuration, the detector (1D geometry) will remain stationary at prescribed 2θ intervals, for a fixed amount of time to gain good measurement counts (high signal-to-noise ratio). This set-up is ideal for slow phase transformations in fine-grained materials. If the grain

© Woodhead Publishing Limited, 2012







19.1 Schematic representation of the sample and detector position for angular diffraction set-up: (a) movable detector; (b) stationary detector; (c) typical image from a stationary detector and diffraction spectrum after integrating the image along the Debye rings.

© Woodhead Publishing Limited, 2012

size is large, the diffraction geometry may not allow for the detection of diffraction peaks by these linear detectors during its rotational movement along the radius of the circle. In addition, the time resolution is also limited due to the need for mechanical movement of these detectors.

In order to address this limitation, 2D CCD detectors have been introduced which allows for simultaneous recording of diffraction peaks similar to Laue diffraction geometry (see Fig. 19.1(b)). The above arrangement can operate in a reflection (from surface) or a transmitted (through the sample) mode (Offerman *et al.*, 2002). Some of the recent detectors are capable of taking snapshot images at intervals of 0.3 seconds or less (Offerman *et al.*, 2002; Eikenberry *et al.*, 2003). A typical image obtained by 2D CCD detectors with diffraction Debye rings from both austenite (fcc) and ferrite (bcc) phases in steel is shown in Fig. 19.1(c). These diffraction images can be calibrated using standard samples. After calibration, the diffraction rings can be integrated to obtain the classical intensity versus d-spacing data as shown in Fig. 19.1(c).

Energy dispersive method

In the energy dispersive method (Genzer *et al.*, 2007), the incoming X-ray radiation produced by a synchrotron is a white beam (having a wide range of wavelength or energy distribution ranging from 20 to 150 keV). The detector position is fixed at a given 2θ angle (see Fig. 19.2(a)). The experimental methodology can be understood by Bragg's law (Eq. [19.1]) and energy relation (Eq. [19.4]):

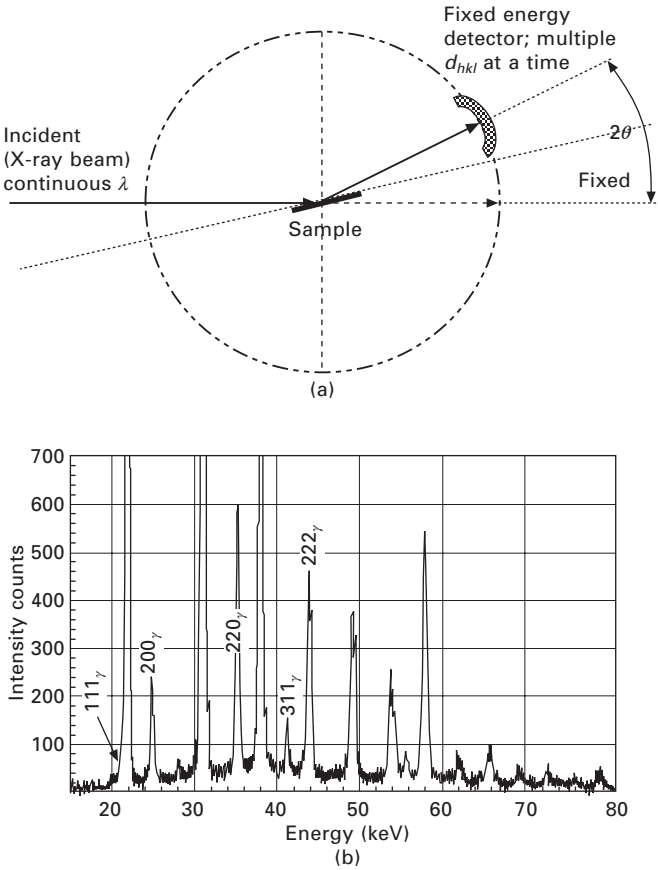
$$E = \frac{hc}{\lambda} \qquad [19.4]$$

In the above equation, E is energy of the X-ray beam, h is Planck's constant, c is the speed of light and λ is the wavelength. By replacing λ in Eq. [19.1] with the above relation, Bragg's law can be rewritten as follows:

$$d_{hkl} = \frac{hc}{2\sin\theta}\frac{1}{E(hkl)} = const.\ \frac{1}{E(hkl)} \qquad [19.5]$$

Since the detector is capable of resolving diffraction peaks based on their energy or wavelength, we can now detect the diffraction peaks from *hkl* planes. Similar to other methods, the constant in Eq. [19.5] can be obtained from calibration with standard samples. The advantage of this technique is that it is possible to obtain a wide range of *hkl* diffraction peaks with each measurement (see Fig. 19.2(b)). As a result, the above data are compatible with full spectrum fitting analysis techniques (e.g. Rietveld methods) (Rietveld, 1969; Bish and Howard, 1988). The time-resolution for this technique will be decided by the collection time at the detector.

© Woodhead Publishing Limited, 2012



19.2 (a) Schematic representation of the sample and detector position for energy dispersive diffraction set-up. (b) Typical diffraction spectra from austenite in steel for the same experimental set-up. The figures were reproduced with permission from authors.

Time-of flight diffraction

Another method similar to the energy dispersive technique is time-of-flight (TOF) diffraction. This pertains only to neutron diffraction using white beams (continuous wavelengths) produced by pulsed sources (Dianoux and Lander, 2003). This is based on the de Broglie relationship (Eq. [19.6]) that states that neutrons with different energy (or different wavelength) travel at different velocities (v):

$$\lambda = \frac{h}{mv} \qquad [19.6]$$

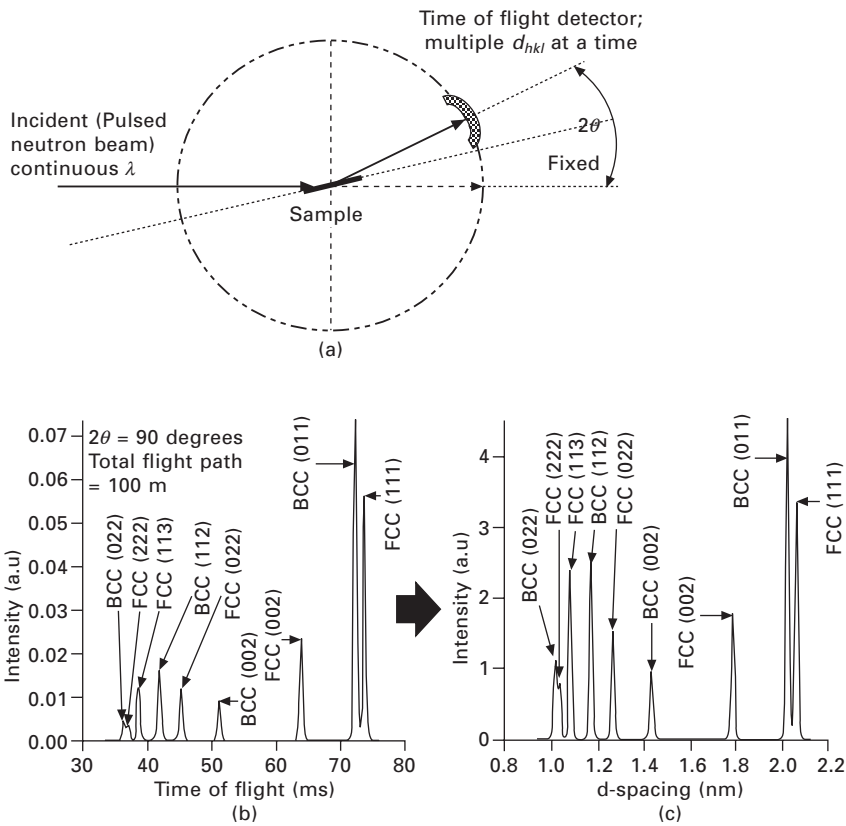
In the above equation, m is the mass and v is the velocity of the neutrons.

© Woodhead Publishing Limited, 2012

In a pulsed neutron source, all the neutrons with different wavelengths are produced at the same time, t_o. If we place a neutron detector at a distance (total flight path distance (L_f)), the neutrons with higher energy will travel faster and arrive at this detector more quickly than the neutrons with lower energy (see Fig. 19.3). Using Eq. [19.6] and time of flight (TOF), it is now possible to detect the wavelength of the diffracted neutron beam using Eq. [19.7]:

$$\lambda = \frac{h \cdot TOF}{m \cdot L_f} \qquad [19.7]$$

Substituting this relation into Eq. [19.1], we obtain a relationship between *TOF* and d_{hkl}, as given by Eq. [19.8]:



19.3 (a) Schematic representation of the sample and detector position for time-of-flight (TOF) neutron diffraction. (b) Calculated TOF diffraction spectra for austenite and ferrite. (c) Corresponding diffraction spectra in terms of intensity vs d-spacing.

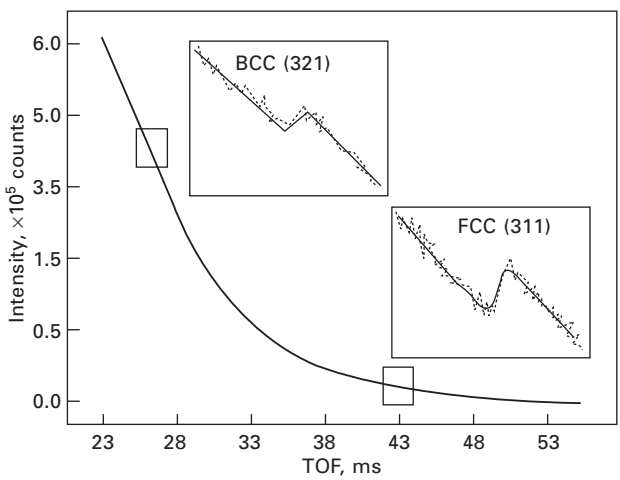
© Woodhead Publishing Limited, 2012

$$2d_{hkl}\sin\theta = \frac{h \cdot TOF}{m \cdot L_f} \quad [19.8]$$

In this experimental configuration, the angle between the incident beam and the detector (2θ) is kept constant. Therefore, it is now possible to measure the TOF and calculate the diffraction spectra. Similar to energy dispersive X-ray diffraction, the TOF neutron diffraction method allows for measurement of diffraction spectra with a wide range of interplanar spacing. Readers are referred to some of the on-line information for details of this technique (ISIS, 2010). A typical calculated TOF dataset (assuming a 100 m flight path) for austenite and ferrite in steel and corresponding interplanar spacings is shown in Fig. 19.3(b).

Bragg edge technique

In the Bragg edge technique (BET), the transmitted beam is analyzed to evaluate the diffraction conditions that exist within the sample (Santisteban *et al.*, 2002; Huang *et al.*, 2007). In this case, the incident beam, the sample and the detector are located on the same axis. From Bragg's law we know that radiation with wavelength greater than $2d_{hkl}$ cannot be diffracted. As a result, after each given $2d_{hkl}$ value, the intensity of the transmitted beam rises rapidly. This technique is appropriate for high symmetry, high scattering length and low absorption materials, and therefore ideal for steels. Typical Bragg edge data from TOF neutron scattering are shown in Fig. 19.4. Using the Rietveld approach (Rietveld, 1969), the data can be analyzed to extract



19.4 Typical data from transmission Bragg edge spectrum showing the edge data from bcc and fcc phases is shown here. The data are reproduced from Huang *et al.* (2007).

© Woodhead Publishing Limited, 2012

useful information such as phase fraction and lattice parameter. The Bragg edge height is correlated to the phase fractions. The lattice parameter can be extracted from the Bragg edge locations and edge width parameters. The only challenge is that the data analyses should be able to extract this small change in intensity from the large background signals of the transmitted beams. The time resolution of such experiments has been reported to be 12 s. Santisteban *et al*. (2002) have used this technique and pixelated detectors to map the phase transformation and strain distribution in welds.

Small angle scattering methods

In addition to the diffraction information, valuable information about clustering and precipitation can be attained by evaluating the scattering cross-sections near the origin (see Fig. 19.5(a)) of the reciprocal lattice (close to the direction of the incident beam), also known as small angle scattering (SAS) (Dianoux and Lander, 2003; NIST, 2010; Kostorz, 1996). The expression for SAS containing a certain number (N_p) of second-phase particles of volume (V_p) and scattering length density (ρ_p) in a matrix of scattering length density (ρ_m) is given by the following equation:

$$\frac{d\sigma}{d\Omega} = N_p(\rho_p - \rho_m)^2 V_p^2 S\{k\} \qquad [19.9]$$

In the above equation, $S\{k\}$ is the single particle scattering function, which is related to particle shape and their orientation in space. Given the atomic number density of the material N/V (atomic scattering nuclei/cm^3) macroscopic cross section is also defined as

$$\Sigma_s = \frac{N}{V}\frac{d\sigma_s}{d\Omega} \qquad [19.10]$$

The SAS data are often represented in absolute values, independent of instrumental set-up sample volume by

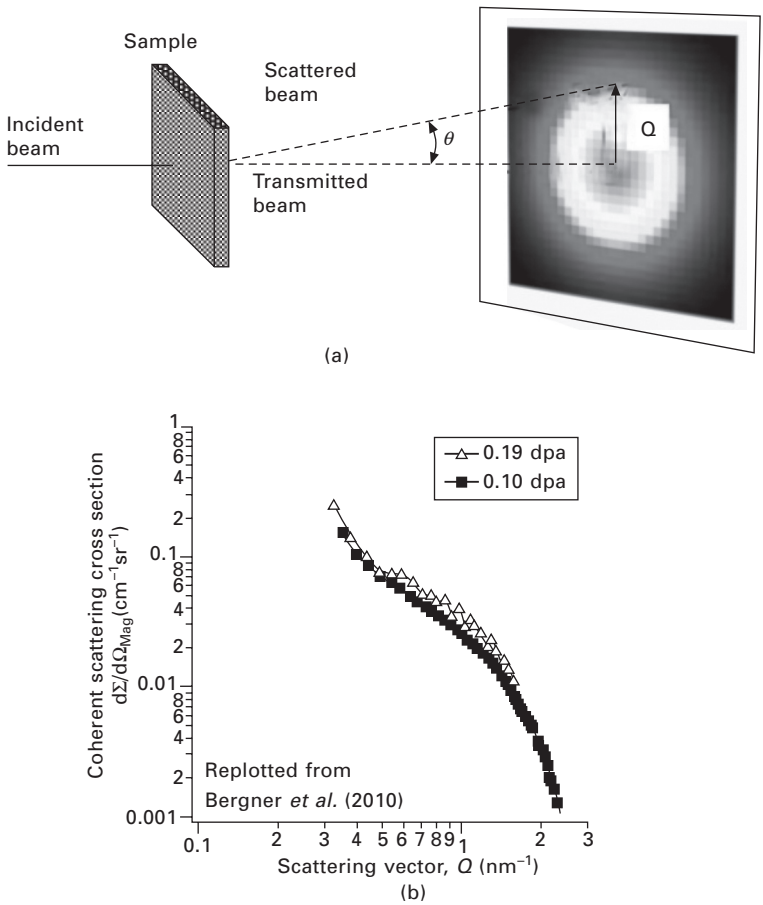
$$\frac{d\Sigma_s}{d\Omega} = \frac{N}{V}\frac{d\sigma_s}{d\Omega} \qquad [19.11]$$

The small angle scattering measurements on steels using neutrons are often carried out while they are immersed in a magnetic field. Typical data from an (0.19 displacement per atom (dpa)) irradiated Fe-0.1 wt% Cu alloy (Bergner *et al*., 2010) are shown in Fig. 19.5(b). In this plot, Q corresponds to the scattering vector (4π sin (θ)). The above data are then correlated to a microstructure distribution containing a size distribution of non-magnetic particles (dilute two-phase matrix with inclusion microstructure) distributed in an iron matrix. For the above condition, the scattering cross section for Eq. [19.11] is modified to the form given by:

© Woodhead Publishing Limited, 2012

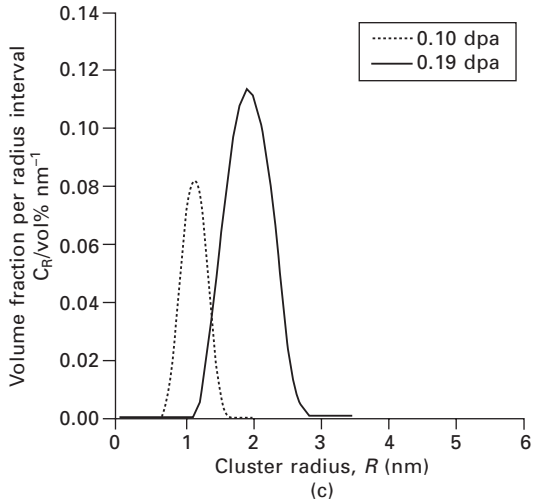
$$\left(\frac{d\Sigma}{d\Omega}\right)_{coherent} = \frac{N}{V_s}\Delta\eta^2 V_p^2 |F(Q,R)|^2 \qquad [19.12]$$

where V_s is the probed volume, N is the number of spherical particles with a radius distribution of R, F is the form factor, which is related to size distribution, and $\Delta\eta^2$ is the scattering contrast, which is related to nuclear and magnetic scattering. It is now possible to calculate the size distribution of particles (see Fig. 19.5(c)) corresponding to the data shown in Fig. 19.5(b), using numerical methods. These measurements were performed under



19.5 Schematic illustration of the experimental set-up for small angle neutron scattering (adopted from NIST website for SAS). (b) Typical SANS data (redrawn from data in Bergner *et al.*, 2010) from an iron alloy containing irradiation induced copper precipitates. (c) Calculated precipitate distribution corresponding to the data shown in (b).

© Woodhead Publishing Limited, 2012



19.5 Continued

different irradiation conditions to describe the evolution of precipitate size distributions with radiation dosage.

Auxiliary instruments and methods

The above sections provided different methodologies for performing scattering/diffraction experiments. In the context of steel phase transformations, there is a requirement for auxiliary instruments for imposing thermo-mechanical conditions. For imposing thermal cycles and to do *in-situ* measurements, furnace designs (Offerman and Sharma, 2010; Sharma *et al.*, 2009) that are compatible with synchrotron or neutron measurement methods are required. Some of the important parameters that must be considered during the design of such furnaces include minimal thermal gradients, minimal sample movement due to thermal expansion, ensuring free stress state, accuracy in temperature measurements, avoidance of diffraction data from the furnace and heating elements, as well as avoiding decarburization and oxidation during experimentation. Although one could accelerate the progress made in heat treatment furnace designs, the incorporation of the same within the synchrotron or neutron beam line prove to be difficult. Elmer *et al.* (1996) used a gas tungsten arc-welding set-up that is enclosed in an aluminum container with shielding gas to perform welding-related experiments. Specht *et al.* (2004) have used simple resistance-heating instead of a furnace. To avoid oxidation they enclosed the sample heating stage within an aluminum cylinder. Two holes were cut from the cylinder to allow for the entry of incident beam and exit of diffracted beams. To allow for maintaining the protective environment, these holes were sealed with Kapton films. (Kapton

© Woodhead Publishing Limited, 2012

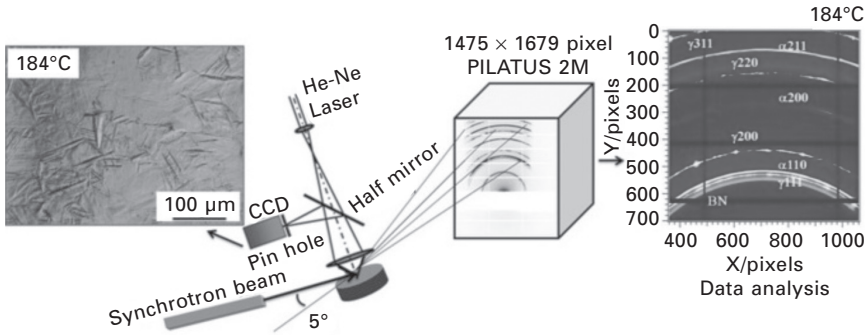
is a polyimide film originaly developed by DuPont.) In addition, the samples were mounted on a stage equipped with a spring, which allows the sample height to be maintained when the steel samples change in volume during the phase transformation.

Recently, thermo-mechanical testing has been achieved within the synchrotron beamlines (Liss and Yan, 2010). For example, Stone *et al.* (2008b) have deployed a closed loop thermo-mechanical tester that allows for loading of samples whilst subjected to any thermal cycle. By measuring the external loading conditions and lattice parameter and phase fractions, comprehensive information on steel phase transformations under complex elastic and plastic stress states can be measured. Similar conditions are also available within neutron beam lines (Santisteban *et al.*, 2006; ENGIN-X, 2010; SMARTS, 2010; VULCAN, 2010; Tomota *et al.*, 2009). Recently, NIST has also developed machines to impose bi-axial stress states (Gnaeupel-Herold *et al.*, 2005, 2007).

In addition, there is great interest in evaluating the effect of pressure (0.25 GPa to 22 GPa) and temperature on phase transformations in iron (to induce a bcc to hcp transition). This is made possible by using diamond anvil cells and laser heating (Miyagi *et al.*, 2008) in a dedicated synchrotron beam line. There has been a preliminary attempt at *in-situ* measurement of magnetic field induced transformations in steels (Ludtka *et al.*, 2007). In principle, this can be done with existing beam line facilities. For example, Liu *et al.* (2010) have measured the stress and magnetic field aided transformation in Ni-Co-Mn-In alloys.

In addition to the above auxiliary instruments for thermo-mechanical magnetic loading of samples, it is often useful to measure many microstructural (e.g. morphology, composition) features at the same time. This is indeed possible with some innovative experimentation. For example, Specht *et al.* (2003) used X-ray fluorescence with an energy dispersive detector for measuring composition, while measuring the diffraction data using 2D CCD detectors. This allowed for direct correlation of structure and chemistry in an Fe-Cr-Ni system. Although the diffraction information (reciprocal space) can provide the transformation kinetic data, it is desirable to correlate the same with morphology (real space) of the microstructure evolution. In order to achieve this, Terasaki and Komizo (2011) have developed a hybrid system that couples the *in-situ* diffraction using a synchrotron beam line with a laser confocal microscopy system (see Fig. 19.6). Details of this technique will be presented in the later sections. Following a similar trend, Brauser *et al.* (2010) have used *in-situ* diffraction (phase change) with digital image correlation (strains) to understand transformation-induced plasticity in steels. Koo *et al.* (2009) also used neutron diffraction and dilatometry simultaneously to rationalize the bainitic transformations. Readers are referred to these references for more details.

© Woodhead Publishing Limited, 2012



19.6 Hybrid experimental set-up for tracking microstructure evolution (real-space) using laser scanning confocal microscopy and diffraction from phases (reciprocal space). Image courtesy of Prof. Terasaki, JUWRI, Osaka, Japan.

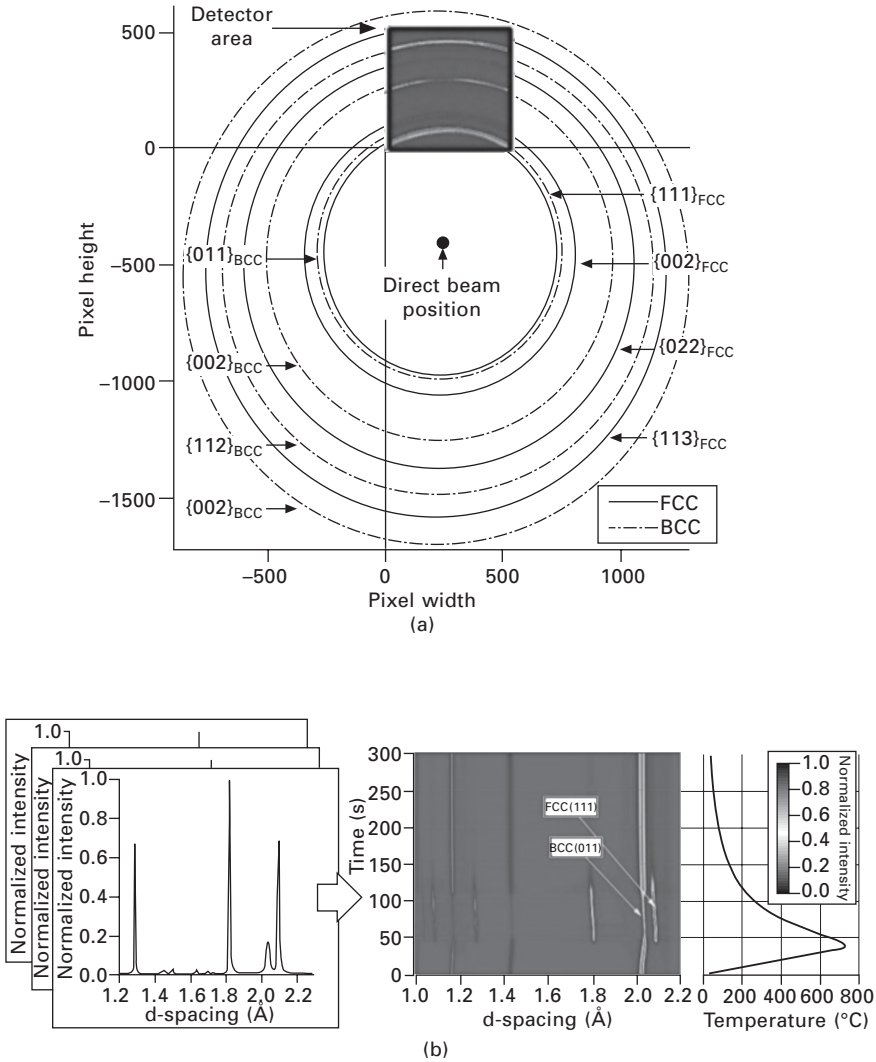
Typical steps involved in in-situ *tracking of phase transformation kinetics*

In this section, typical steps used to measure phase transformation kinetics using *in-situ* time-resolved diffraction methods are discussed briefly. This will allow the readers to follow results to be presented in the next section.

The first step involves the calibration of the diffraction experimental set-up using the Debye rings obtained at room temperature. This can be done either by using the ferrite lattice parameter measured by traditional high-resolution diffraction methods in the laboratory or in a synchrotron beam line. The same calibration can also be carried out by using standard reference samples like platinum or niobium. For example, the diffraction set-up parameters for the experimental condition shown in Fig. 19.1(b) are obtained by the following steps. Since the 2D detector (see Fig. 19.7(a)) samples only part of the Debye rings, the geometry of the detector with reference to the diffraction geometry has to be calibrated. This calibration is done by fine-tuning the distance from detector to sample, X-ray wavelength, virtual location of the direct beam position with reference to the detector coordinates, rotation angle of the tilting plane, and angle of the detector in that plane. These calibrations can be made by user-defined programs or by public domain software, Fit2D (Hammersley *et al*., 1996). The importance of the calibration step in interpreting the diffraction data was stressed by Stone *et al*. (2008a).

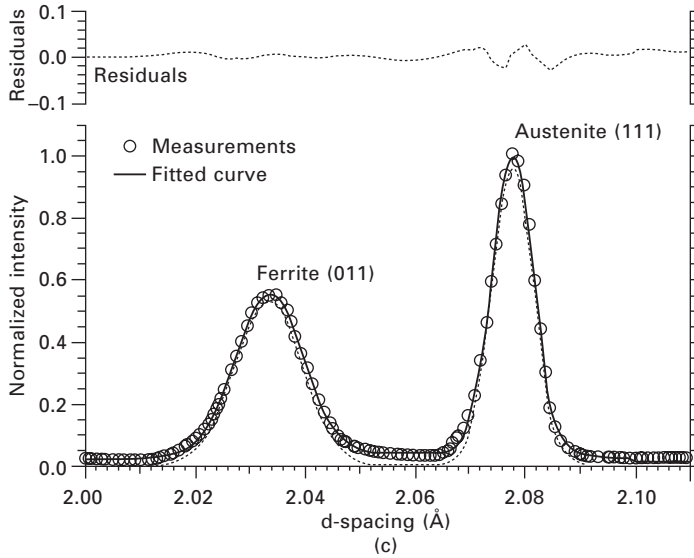
After the calibration is completed, the diffraction images are obtained sequentially as a function of thermo-mechanical history. Each of these images is then integrated along these Debye rings to produce standard intensity vs. d-spacing plots. These integrations are also made by user-defined programs or using Fit2D software. Once the integration is made, the data can be collated into an image format showing the diffraction intensity of different peaks as

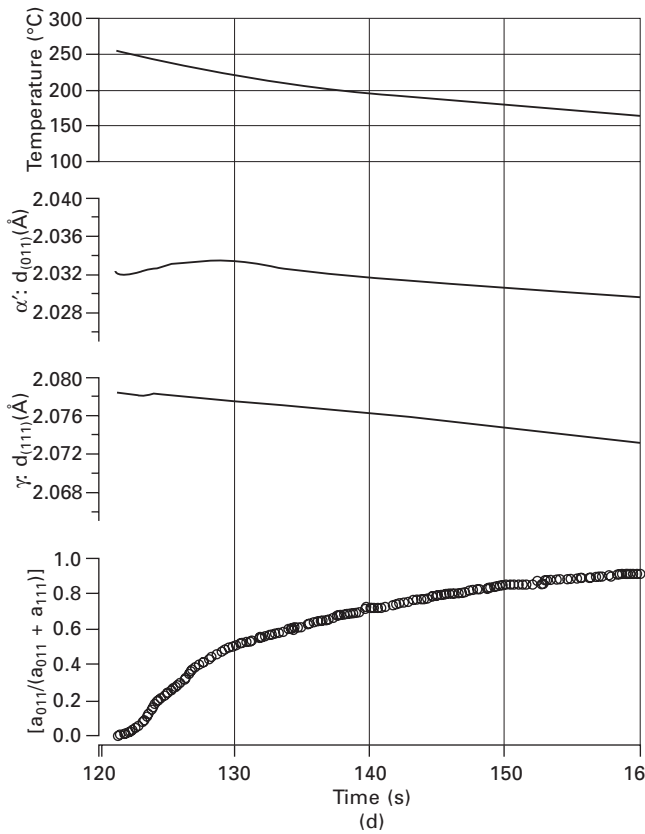
© Woodhead Publishing Limited, 2012



19.7 Steps involved in a typical *in-situ* time-resolved X-ray diffraction experiment. (a) Typical image from 2D CCD detector shows that the detector is tracking only a small quadrant of the Debye diffraction circle. (b) Sequence of CCD images are then converted to text files containing intensity vs d-spacing and then stacked together in an image format to provide an overview of the whole experiment. (c) Each diffraction spectra at a given time is analyzed by peak fitting algorithms to extract the integrated peak areas for all the phases. (d) The analyzed data as a function of temperature and time are compiled to show the variation of phase fraction as well as lattice parameter of austenite and ferrite.

© Woodhead Publishing Limited, 2012





19.7 Continued

© Woodhead Publishing Limited, 2012

a function of temperature and time (see Fig. 19.7(b)). This image format allows for an overview of transformation kinetics in a given experiment.

In the next step, the area under each diffraction peak is analyzed using peak fitting algorithms (see Fig. 19.7(c)). Since a typical phase transformation experiment may involve thousands of spectra, it is necessary to develop automated peak fitting and analysis routines (Babu *et al.*, 2005b). Finally, the analyzed data can be used to track the lattice parameter of ferrite, austenite, and volume fraction of bcc as a function of temperature and time (see Fig. 19.7(d)).

The above procedure is more or less the same for all *in-situ* time-resolved experimentation, except for the calibration steps and file formats used by different beam lines. In the case of neutron diffraction data, public domain software GSAS (VonDreele, 1997), which also performs Rietveld analyses, is used by researchers. The following section provides some tangible examples of measuring phase transformations in steels using the above techniques.

19.3 Measurements of phase transformation in steels

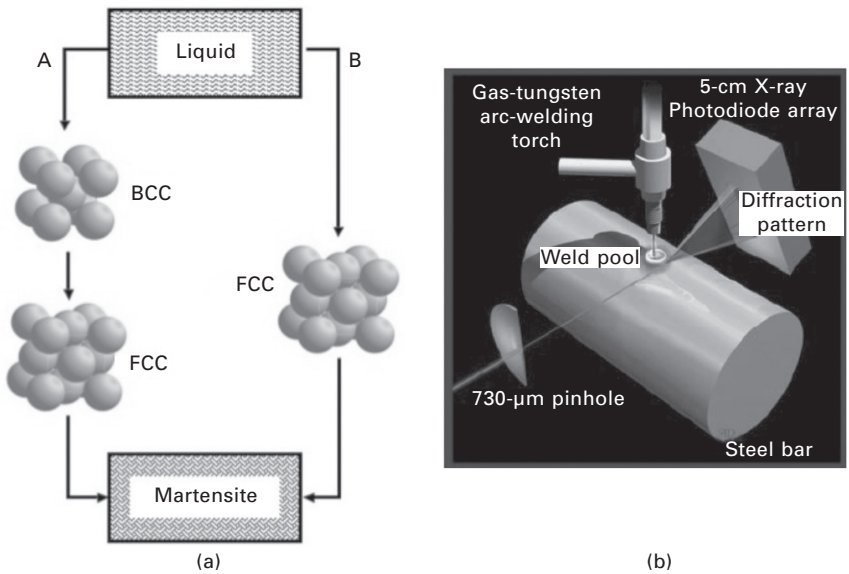
The following examples of microstructure evolution in steels, during both solidification and solid-state transformation, are discussed with reference to characterizing the phase transformations under isothermal, non-isothermal and thermo-mechanical conditions. It is noteworthy that the use of synchrotron and neutron techniques for these examples are justified only because the traditional methods were incapable of providing the fundamental information required.

19.3.1 Non-equilibrium phase transformations during solidification

Fundamental understanding of physical processes during steel solidification is a mature field (Kurz and Fisher, 1998). It is quite possible to predict the first phase to form using computational thermodynamic tools. In addition, it is also possible to predict the transition from planar to cellular to dendritic and back to planar solidification as a function of thermal gradient and liquid-solid interface velocity, using interface response function theories (Trivedi and Kurz, 1994). Most of these theories have been developed by characterizing the microstructure at room temperature using optical microscopy, electron microscopy and transmission electron microscopy, as well as thermal techniques (differential scanning calorimetry, differential thermal analyses). The above theories have also been extended to welding and rapid solidification conditions (David and Vitek, 1989). In a routine evaluation of spot-weld solidification microstructure in Fe-C-Mn-Al weld (Babu *et al.*, 2002), the room temperature

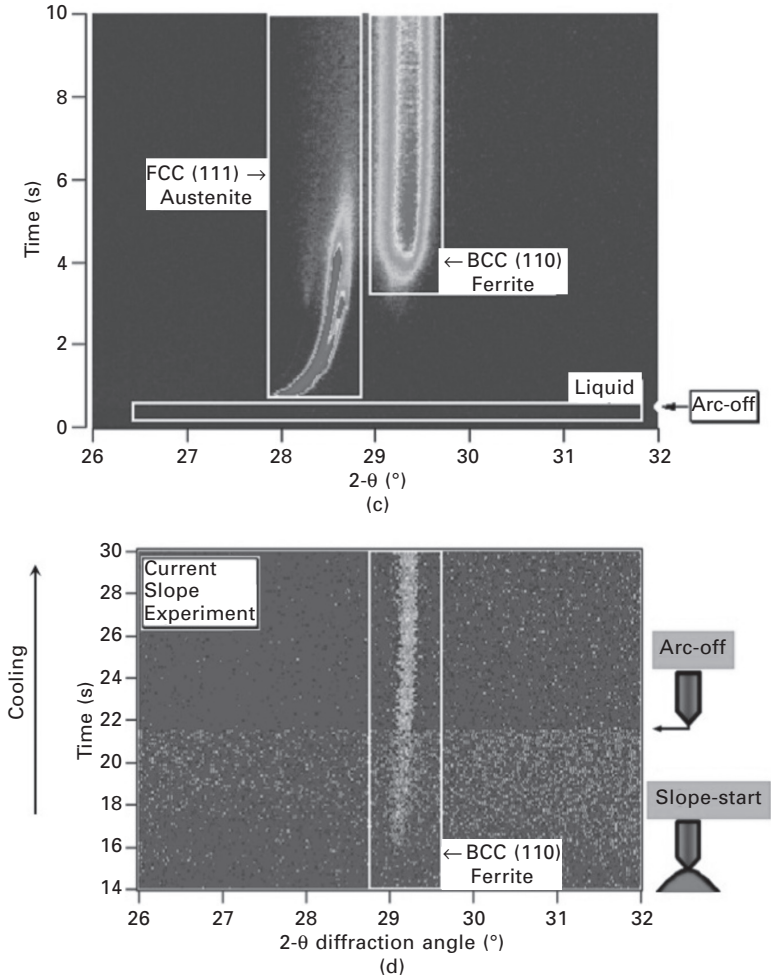
© Woodhead Publishing Limited, 2012

microstructure contained 100% martensitic microstructure. However, using the above theories, the predicted microstructure was a mixture of δ-ferrite and bainite for most of the welding conditions. This is predominantly due to increased stability of δ-ferrite with aluminum additions. With increased aluminum addition, this alloy is not expected to form 100% austenite. As a result, 100% martensite microstructure is also not expected. The above phenomenon can be interpreted by two mechanisms as shown in Fig. 19.8(a). In one of the mechanisms (denoted A), the liquid solidifies to 100% δ-ferrite and then transforms to 100% austenite, followed by transformation to martensite. In the other mechanism (denoted B), the liquid may transform to 100% austenite by non-equilibrium phase selection during solidification, followed by transformation to martensite. It is impossible to delineate the real mechanism by performing post-process characterization or thermal analyses since the solidification structure is destroyed by the martensitic transformation. Therefore, we need an *in-situ* technique that is capable of tracking the phase evolution during solidification.



19.8 (a) Possible paths to obtain martensite microstructure in Fe-C-Al-Mn steel welds are shown. (b) *In-situ* time-resolved X-ray diffraction experimental set-up for spot welding experiment. The arc is struck for a given time to form a small spot weld pool. After reaching this time, the arc is extinguished. This leads to rapid solidification. (c) Measured data from the rapid cooling experiment showing non-equilibrium solidification from melt. (d) Equilibrium δ-ferrite phase forms on slow cooling of the weld pool. The slow cooling rate was achieved by ramping down the welding current.

© Woodhead Publishing Limited, 2012



19.8 Continued

The welding experiment was performed by *in-situ* time-resolved X-ray diffraction in the Stanford Synchrotron Radiation Laboratory. The set-up is shown in Fig. 19.8(b). For more details of these experiments, readers are referred to a paper by Elmer (2008). A cylindrical steel sample with the surface composition of Fe-C-Mn-Al alloy was made. In the next step, the sample is enclosed in a chamber that contains a gas-tungsten arc welding set-up and 1-d linear photodiode array for measurement of the diffraction spectrum. The detector is capable of recording at a time resolution of 0.05 seconds and the overall 2θ range was 30°. The measurements during weld solidification are shown in Fig. 19.8(c) in an image format. Measurements of diffraction data started just before the extinction of the welding arc. Due to

© Woodhead Publishing Limited, 2012

the presence of liquid, no diffraction peaks were observed at $t = 0$ seconds. As soon as the arc was extinguished, the diffraction peaks appeared. The analyses of the data showed that the first phase to appear from the liquid is indeed austenite. This is proved by the appearance of fcc (111) peaks. With subsequent cooling, the fcc diffraction peak moves towards higher 2θ values indicating a reduction in lattice parameter. On continued cooling to a lower temperature, the weld metal transforms from austenite to martensite. This is indicated by the appearance of bcc (110) peaks. Due to the low-carbon concentrations and limited resolution of the detector, the split in diffraction due to the tetragonal distortion is not resolved. This experiment clearly proved that mechanism B is operative under spot welding conditions. The results were then interpreted based on interface response function theories. The phase selection of austenite from liquid, instead of δ-ferrite, is driven by the rapid increase in liquid–solid interface velocity under spot welding conditions. Confirmatory experiments to prove this hypothesis were performed by slowing down the liquid–solid interface velocity. The measurements (see Fig. 19.8(d)) showed the re-emergence of δ-ferrite as the primary solidification mode, under these modified conditions. It is noteworthy that the above fundamental information could not have been obtained by any other technique.

One of the problems with the use of a linear detector (see Fig. 19.8(b)) is the inability to track diffraction from coarse grain sizes. Since 1D detectors sample only a thin sliver of the Debye rings, it is quite possible to miss the diffraction information. This problem has been addressed by using two-dimensional detectors (Yonemura *et al*., 2010). In principle, it is also possible to couple the diffraction technique with laser confocal microscopy (Zhang *et al*., 2010) and will be discussed later. It is noteworthy that Matsumiya *et al*. (1987) tracked the morphology of steel solidification by synchrotron radiation topography. It would be interesting to couple this technique with diffraction in the future.

19.3.2 Phase transformations during solid-state transformations

Ferrite/martensite to austenite transformations

The heating transformation of pearlite to austenite in Fe-0.4 wt%C steel has been analyzed using thermodynamic and kinetic models (Reed *et al*., 1998). The models were validated by experimental measurements using dilatometry and neutron diffraction. Neutron diffraction data were instrumental in defining the lattice parameter of cementite and other phases that are critical in the model. Some of the recent *in-situ* neutron diffraction studies and *ab-initio* calculations suggest that the cementite composition may not be stoichiometric

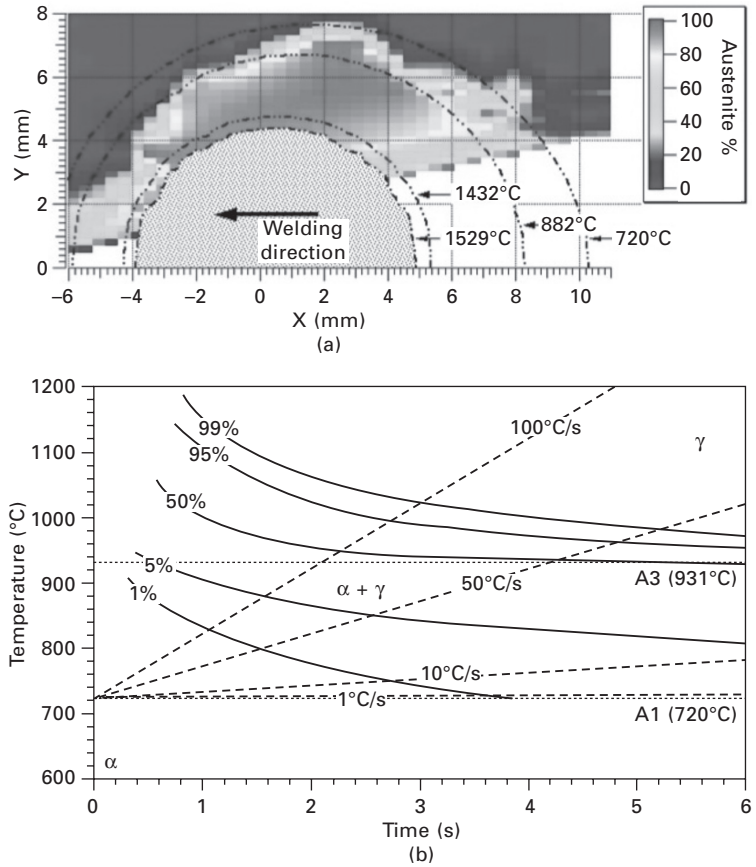
© Woodhead Publishing Limited, 2012

(Voronin *et al.*, 2010). The *in-situ* neutron diffraction data indicated that the carbon concentration of the cementite lattice decreases. Based on these results, the authors argue that the cementite must be denoted as interstitial solid solution as Fe_3C_x ($0 < x < 1$) and the empty carbon sites in the lattice must be occupied by vacancies. The dissolution kinetics of carbides in high carbon steel was also tracked by using *in-situ* diffraction (using laboratory sources). In this case, the authors used the austenite lattice parameter (i.e. carbon concentration of austenite) as a way to track the dissolution of carbides. The above research demonstrates that if the kinetics are slow, one can use the laboratory X-ray sources to perform the *in-situ* time-resolved studies (Epp *et al.*, 2007). Comprehensive tracking of reverse transformation from a martensitic microstructure to austenite and the cooling transformation was made by Tomota *et al.* (2009). Although the data has poor time resolution, this paved the way for the comprehensive evaluation of steel transformations under thermo-mechanical conditions to be described later.

Although the above work has shown the reverse transformation to austenite in an averaged fashion, the data is not capable of delineating the nucleation and growth stage. In this regard, the 3D XRD microscopy technique developed at the European Synchrotron Radiation Facility is very powerful. With 2D detectors (1 second time resolution) and diffraction geometry, Savran *et al.* (2010) have decoupled the measurements of austenite nucleation and growth from the initial pearlite microstructure on heating (10°C/min). This technique is similar to the method used to track ferrite formation from austenite published by the same group (Offerman *et al.*, 2002). The data shows the two-stage mode of growth due to different nucleation rates at the pearlite/ferrite interface and at the ferrite/ferrite grain boundaries. In addition, phase field modeling of austenite formation in a martensitic duplex steel has been validated recently by *in-situ* synchrotron diffraction methods (Thiessen *et al.*, 2007).

During welding, reverse transformation of ferrite to austenite occurs under non-equilibrium conditions. Elmer *et al.* (2003) used spatially resolved X-ray diffraction to track the phase boundaries around a weld pool, under steady state conditions. Typical data from a low-alloy steel is shown in Fig. 19.9(a). The figure also shows the calculated isotherms for Ac_1 (720°C) and Ac_3 (882°C). The data show some interesting features. In the heating side of the coordinates (e.g. $x = -4$ mm, $y = 4$ mm), there is no evidence for the formation of austenite in between Ac_1 and Ac_3. The delay in complete austenitization is related to the rapid heating rates achieved during welding. The above experiments were repeated for a low-carbon (specification: AISI 1005) steel. The data was then used to calibrate an overall transformation kinetic model. Using this calibrated model, continuous heating transformation diagrams were developed (see Fig. 19.9(b)). Model calculations clearly demonstrate that under slow heating conditions, the transformation

© Woodhead Publishing Limited, 2012



19.9 (a) Map of the austenite phase fraction as a function of location around the weld pool was measured by spatially resolved X-ray diffraction set-up. (b) Using similar data from AISI 1005 (Fe-0.05C-0.3Mn-0.18Si-0.11Ni-0.1Cr wt%) steel and fitting the data to JMAK equations, continuous heating transformation (CHT) diagrams were calculated. Figures are adopted from Elmer *et al.* (2003).

temperatures will be closer to equilibrium temperature, which is similar to the data presented by Savran *et al.* (2010). However, for rapid heating rates (> 100°C/s), the majority of ferrite to austenite transformations occur far above the equilibrium Ac_3 temperature. The heating rate effects have been addressed by other researchers using computational models (Bailer-Jones *et al.*, 1999). Extensive experimental work on this topic are addressed in Chapter 17 of volume 1. It will be of interest to compare the relative stability of carbides under rapid heating conditions. For example, it has been shown that Cr containing cementite dissolves slowly far above the equilibrium Ac_3 temperature (Liu *et al.*, 1991; Lolla *et al.*, 2011).

© Woodhead Publishing Limited, 2012

Reverse transformation (α' to γ) in stainless steel has been studied by neutron Bragg edge diffraction. First, the martensite was formed in type-304 stainless steels (Fe-0.051C-18.29Cr-8.22Ni-0.19Mo-0.085 wt%) by deforming them at 77 K. At this temperature, the mode of transformation is expected to be displacive with no long-range diffusion of either substitutional or interstitial elements. Then, the reverse transformation of martensite to austenite was tracked on heating to 550°C (Bourke *et al.*, 1996). The diffraction data showed sluggish kinetics of reverse transformation to austenite at this temperature. On heating the sample to 670°C and holding at that temperature for 9 h, nearly 90% of austenite was achieved. Due to the sluggish kinetics, transformation may be attributed to a reconstructive mechanism. Although the data includes the Bragg edge positions, the lattice parameter calculations were not done. It will be interesting to calculate the lattice parameter variation and compare these results with transformation driven by a para- or local-equilibrium mode.

Austenite to high-temperature δ-ferrite and δ-ferrite stability

The formation of high temperature δ-ferrite from austenite on heating is often ignored in low-alloy steel phase transformation studies, since it transforms back to austenite on cooling. However, the formation of δ-ferrite is an important phenomenon during welding of 9 wt% Cr steel. At high peak temperatures in the heat-affected zone, it is indeed possible to form small amounts of δ-ferrite. However, on cooling, this δ-ferrite phase does not transform back to austenite and is retained at room temperature. This is not ideal for the creep rupture properties of these steels. However, it is often difficult to delineate this phase at room temperature from the background martensitic matrix.

In order to prove the tendency for the formation of δ-ferrite, Mayr *et al.* (2010) used *in-situ* time-resolved X-ray diffraction (with the same set-up as the one shown in Fig. 19.1(b)). The data show that, on heating to a temperature above 1300°C, 19% of δ-ferrite is formed. However, on cooling, 17% of δ-ferrite is transformed back to austenite and 2% δ-ferrite remained at room temperature. Based on the above experiments, the authors proposed a two-stage cooling cycle (rapid cooling from 1300°C and slow cooling/annealing in the 100% austenite phase field) to avoid the retention of δ-ferrite. The stability of δ-ferrite has also been studied by Babu *et al.* in an attempt to understand the microstructure memory in Fe-C-Al-Mn multipass steel welds (Babu *et al.*, 2005a). In addition, the phase stability of δ-ferrite in duplex stainless steel welds has been studied by Palmer *et al.* (2002, 2004). In this classic and sustained work, Palmer *et al.* (2002, 2004) and Zhang *et al.* (2005) analyzed the isothermal and non-isothermal growth and dissolution of δ-ferrite with respect to the austenite phase and

© Woodhead Publishing Limited, 2012

compared this with models. The above data has been rationalized based on paraequilibrium transformation mechanisms. In addition, extensive data with reference to kinetics of σ phase growth and dissolution within the δ-phase were also collected (Elmer *et al*., 2007a, 2007b). The above data are yet to be used for evaluation of computational thermodynamic and kinetic models (Babu, 2009).

Austenite to low-temperature α-ferrite and/or pearlite

In the literature, the austenite to α-ferrite phase transformation has been studied extensively by using post-characterization techniques (Bhadeshia, 1985) and by many groups lead by Johnson and Mehl (1939, reprinted in 2010), Aaronson (2005) and Hillert (1997). Even after these extensive works, there are still unanswered questions including, activation energy for nucleation, transition from local equilibrium to paraequilibrium, competition between nucleation rate and growth of grain boundary allotriomorphs, interface structure and partitioning, and mixed mode (interface and diffusion-controlled growth) transformation. Some of the above questions are being answered by careful experimentation involving selective field ion beam machining and atom probe field ion microscopy. However, the *in-situ* tracking of these transformations has only been performed using resistance, magnetic and dilatometry methods, the latter being the most popular. In this regard, direct tracking of crystal structure and its carbon concentration would be ideal. Offerman *et al*. (2002) have used *in-situ* synchrotron diffraction to track the nucleation and growth states under slow cooling conditions. Based on the data, they concluded that the experimentally measured activation energy for nucleation of ferrite is much lower than that predicted by thermodynamic models. Such data are influencing the development of robust austenite to ferrite transformation models (Van Dijk *et al*., 2007). Offerman *et al*. (2003) also used neutron depolarization techniques to evaluate the nucleation and growth rate of pearlite. Readers are referred to these classic papers for more details.

Austenite to bainite

Other extensively researched topics in the steel phase transformation literature, especially more recently, are related to bainitic transformations. Note that the current section pertains only to the investigation of the above transformation using neutron and X-ray scattering tools. Therefore, this section is not a comprehensive review of bainitic transformation mechanisms. The readers are referred to other chapters in this book as well as the vast amount of data and papers published on this topic. Readers are also referred to extensive information on bainite by Prof. Bhadeshia at the following website: http://www.msm.cam.ac.uk/phase-trans/newbainite.html

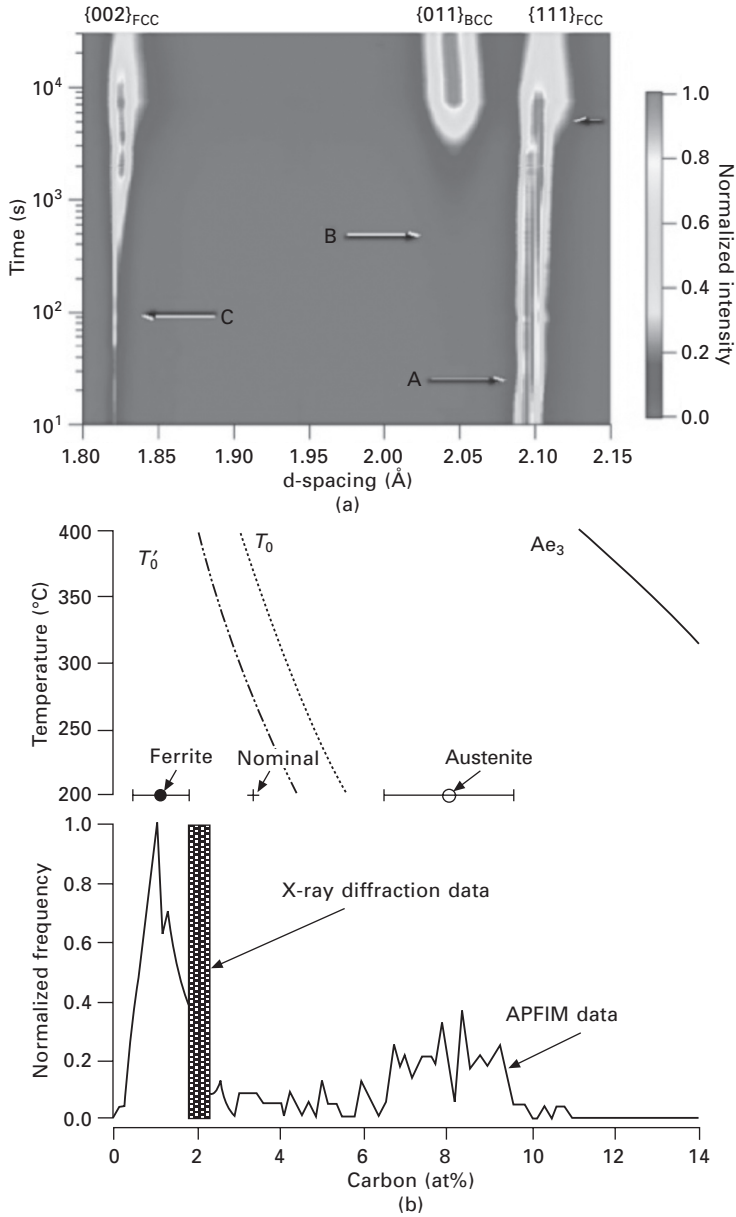
© Woodhead Publishing Limited, 2012

To rationalize austenite to bainitic phase transformation, it is important to track the morphology, concentration of carbon and other elements, dislocation density, ferrite/austenite interface structure, orientation relationships, surface relief, and strength under *in-situ* conditions. Most of the theories of bainitic transformation have been developed based upon post-process characterization involving optical microscopy, electron back scattered diffraction, transmission electron microscopy, and atom probe field ion microscopy. The *in-situ* studies have been limited to thermal and dilatation analyses. One of the key questions in bainitic transformation is whether bainitic ferrite grows with the same carbon concentration as that of the austenite followed by subsequent partitioning of carbon to austenite. If this is the case, the bainitic transformation stops at the T_o' line (where free energy of austenite = free energy of ferrite + strain energy) in a paraequilibrium Fe-C phase diagram.

Using *in-situ* time-resolved X-ray diffraction technique with synchrotron radiation, Babu *et al*. (2005a) tracked the isothermal kinetics of bainitic ferrite, as well as the lattice parameter of ferrite and austenite (see Fig. 19.10(a)). The data show that the ferrite lattice parameter is higher in the early stages of transformation and slowly reduces with time. These data confirm earlier evidence of carbon supersaturation in ferrite (Bhadeshia, 2001). With partitioning of carbon from ferrite to austenite, the austenite carbon concentration is expected to increase. In agreement with this hypothesis, the position of austenite diffraction peaks shifts to higher d-spacing. Using published relationships relating the lattice parameter of ferrite and austenite to their composition, the above data were analyzed to extract the carbon concentration of bainitic ferrite and austenite. The data were then compared to atom probe measurements (see Fig. 19.10(b)). Again, there is general agreement of measurements made by these two different techniques. During the above analyses, Babu *et al*. (2005a) also found some spurious splitting of austenite diffraction peaks before the onset of the bainite transformation. However, the above phenomenon could not be rationalized using existing theories.

Stone *et al*. (2008b) repeated the same experiment after making three modifications. First, to improve the signal-to-noise ratio, the austenitization was done at 832°C, instead of 1000°C. Second, by using higher energy X-rays and rotating the sample, the measurements were made from the total volume of the sample. This is in contrast to the surface measurements made by Babu *et al*. (2005a). Although Stone *et al*. (2008b) found the same results with reference to bainitic transformation and lattice parameter shifts of austenite and ferrite, there was no splitting of austenite before the onset of the bainitic transformation. Using some new Fe-Ni-C data attained by Babu *et al*. (2007), Stone *et al*. (2008b) showed that the appearance of peak splitting could be related to instrument resolution and parameters used in the integration procedures. Although Stone *et al*. (2008b) demonstrated that

© Woodhead Publishing Limited, 2012



19.10 (a) Measured diffraction peak positions and intensity of austenite and bainitic ferrite are shown as a function of time during isothermal holding. (b) The data are interpreted to extract the carbon concentration of ferrite and compared with atom probe data. The top plot shows the calcualted paraequilibrium phase diagram showing the Ae_3, T_o and T'_o lines, as well as the concentration of carbon measured by atom probe. The bottom plot overlays the calculated carbon composition of ferrite from X-ray diffraction data on top of the carbon frequency distribution calculated from atom probe data.

© Woodhead Publishing Limited, 2012

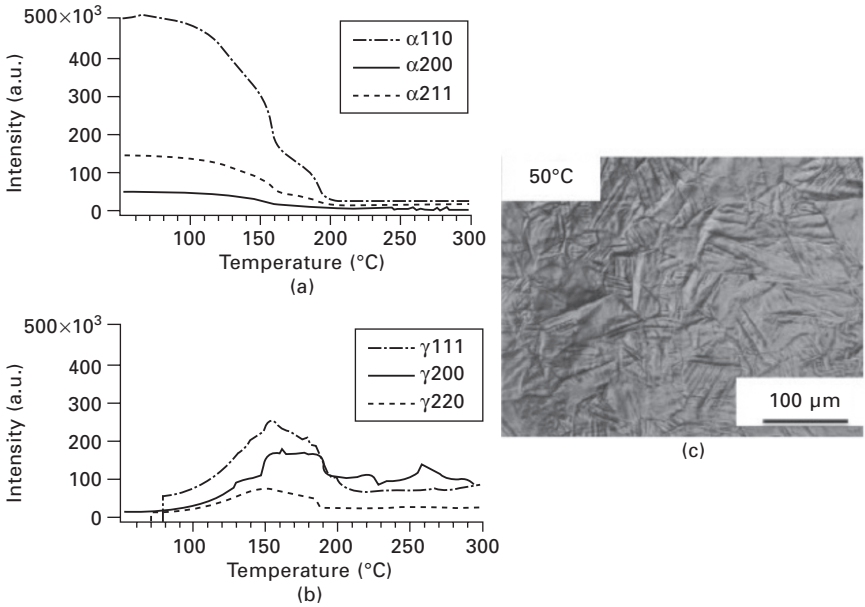
such splitting could be rationalized based on the diffraction geometry and integration errors, it is of interest to reconfirm the same with other independent measurements.

Recently, Koo *et al*. (2009) used *in-situ* dilatometry and neutron diffraction methods to track the austenite to bainite transformation in a similar high-carbon steel alloy. Increase in volume fraction of bainite at isothermal temperature conditions measured as a function of time using dilatometry correlated very well with integrated intensity from neutron diffraction peaks. Moreover, the data showed that the peak broadening and shift to higher d-spacing occurred only after the onset of bainitic transformation. These results are in agreement with the data from Stone *et al*. (2008b) and consistent with the existing austenite to bainite transformation theories. As mentioned earlier, Huang *et al*. (2007) used Bragg edge transmission techniques to understand the bainitic transformation and indicated an increase in austenite lattice parameter only after the initiation of bainitic transformation.

Austenite to martensite

Since the speed of the martensitic transformation approaches the velocity of sound in steels, it is currently impossible to track the pre-martensitic behavior in austenite using the methods discussed in this chapter. Nevertheless, useful information related to kinetics and the morphology of transformation can be measured using synchrotron and neutron diffraction techniques. Austenite to martensite transformation has been extensively studied in low-temperature-transformation filler metals. This is mainly because of its beneficial effect in introducing compressive stresses in the toe of the weld, resulting in increased fatigue life. Kromm and Kannengiessser (2009) studied the transformation of low temperature transformation (LTT) wire using synchrotron diffraction measurements. These measurements were also coupled with single-sensor differential thermal analysis. Recently, the transformations in LTT wire have been tracked with *in-situ* diffraction and laser scanning confocal microscopy (Terasaki and Komizo, 2011). The peak intensity from coarse austenite grains is expected to be very low during *in-situ* time-resolved X-ray diffraction measurements. In recent studies, the onset of martensitic transformation is shown to increase the intensity of austenite peaks (see Fig. 19.11). The data show that intensities of [(111), (200), and (220)] austenite peaks are very low before the onset of martensitic transformation. As soon as the austenite cools below 210°C, the bcc peaks corresponding to martensite formation are observed. Surprisingly, even with small volume fractions of martensite formation, the peak intensity increases 200%. With continued cooling below 150°C, eventually the austenite peak intensities decrease due to an increase in martensite fraction. This early rise in the diffraction intensity of austenite is related to subdivision of the original relatively coarse austenite grains

© Woodhead Publishing Limited, 2012



19.11 (a) and (b) Measured peak intensity of austenite and martensite as a function of cooling from single-phase austenite phase field. (b) Corresponding laser scanning confocal microscopy at low temperature shows the martensite laths subdividing coarse (~ 100 μm) austenite grains into small regions (<10 μm). Figures adopted from Zhang *et al.* (2010).

into finer ones by martensite laths. The concurrent laser scanning confocal microscopy observations support this hypothesis (Terasaki *et al.*, 2010). Such a sudden increase in austenite peak intensity has also been observed in the studies involving welds (Zhang *et al.*, 2010).

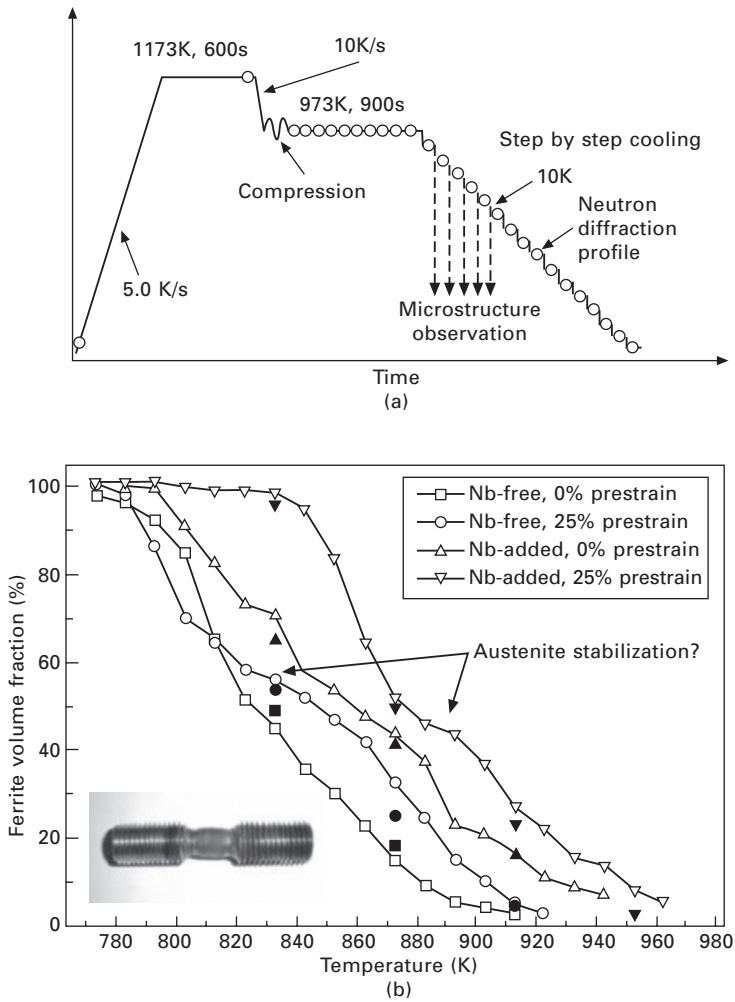
19.3.3 Phase transformations during thermo-mechanical loading

Austenite to ferrite

Another long-standing problem in steel phase transformation is related to the effect of thermo-mechanical processing on the kinetics of the austenite to ferrite transformation. It is indeed very difficult to interrogate the state of austenite and ferrite phases during hot deformation process under *in-situ* conditions. To address this need, Tomota *et al.* (2010) have carried out pioneering research on this topic by employing both traditional and high flux pulsed neutron sources. Some of the salient results from their publication are discussed below.

© Woodhead Publishing Limited, 2012

In one of the experiments, a compressive strain of 25% was introduced in the austenite phase region of two different low-alloy steels with and without niobium additions (see Fig. 19.12(a)). After the compressive deformation, the steel was cooled to low temperature through a step cooling method (hold for 120 s after each 10 K temperature decrease). During the holding time, the diffraction measurements were taken. The data were then interpreted to evaluate the lattice parameter of austenite, ferrite and phase fractions. The



19.12 (a) Schematic illustration of the thermomechanical processing history of two low-alloy steels and *in-situ* neutron diffraction data collection times. (b) Calculated phase fraction from the diffraction data shows the sensitivity to Nb concentration and compressive pre-strain. Data adopted from Tomota *et al.* (2010).

© Woodhead Publishing Limited, 2012

kinetics of ferrite formation as a function of temperature is shown in Fig. 19.12(b). The data clearly show that the pre-straining of the austenite does promote the kinetics in both steels with and without Nb addition. In addition, the steels subjected to deformation showed a reduction in transformation kinetics (marked by arrows in Fig. 19.12(b)). This reduction is attributed to the stabilization of austenite by carbon partitioning. Similar experiments were repeated in a pulsed neutron source. In addition, the concurrent measurement of lattice parameter and phase fraction during compressive deformation has also been performed. Separation of plastic strain and austenite enrichment effects are performed by simultaneous measurement of the shape of the sample during the above experiments.

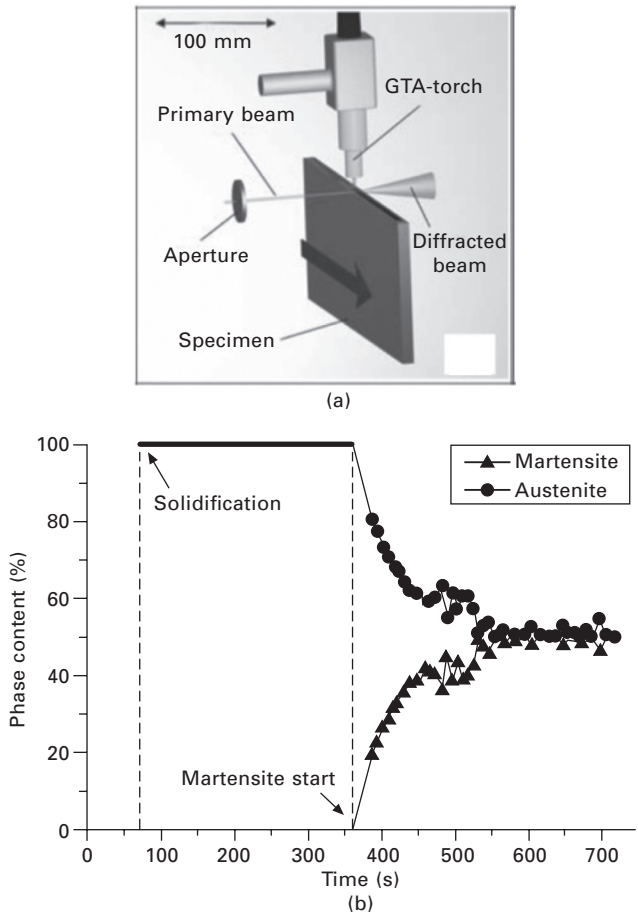
Austenite to martensite

Transformation of austenite to martensite under thermo-mechanical loading is relevant to residual stress development in welding. As mentioned earlier, LTT wires lead to a large thermal expansion at low temperature and thereby modify the residual stress distribution. Kromm *et al*. (2010) studied the transformation kinetics of these wires and associated changes in the residual stresses. Specifically they measured the residual stresses in both the martensite and austenite phases. Their experimental set-up is shown in Fig. 19.13(a) in which an energy dispersive diffraction technique was used (Kromm *et al*., 2010). To allow for the penetration of X-rays through the sample at different distances from the fusion line, thin plate geometry was employed and the welding was performed at the edge of the sample. The transformation kinetics were measured during welding and the measurements showed 50% of martensite formed on cooling to room temperature. Finally, using the diffraction techniques, phase-specific residual stresses were calculated and compared with traditional steels (European Standard S690 Q&T steel). The data showed that the use of LTT wire leads to compressive stresses very close to the fusion line of the weld. This result is in agreement with similar research by Dai *et al*. (2008). Relating the transformation kinetics to residual stress is still an active field and extensive progress has been made in recent times by using simple tests such as the Satoh Test (Shirzadi and Bhadeshia, 2010; Dai *et al*., 2008) and other special instrumentation within a neutron or diffraction beam line (James *et al*., 2006). For more relevant information, the reader is referred to a review on residual stress by Withers (2007). Correlation of residual stress development to microstructure evolution after carburization has been performed by Bourke *et al*. (1998), using X-ray and neutron diffraction studies. In this work, they stress the importance of lattice parameter measurement from strain-free crystals on the accuracy of the residual stress development.

Nanostructured austenitic steels have been attained by repeated strain-

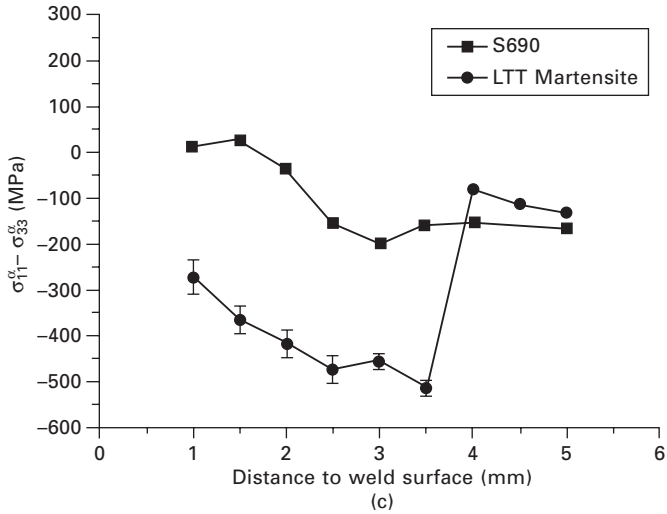
© Woodhead Publishing Limited, 2012

induced transformation of austenite to martensite at low temperature and reverse transformation of martensite to austenite at high temperature (Cheng *et al.*, 2010). The stability of this nanostructured austenite during loading was studied by high-energy synchrotron diffraction. The data showed initial loading of the austenite phase and transfer of the load to martensite, once the transformation of austenite to martensite occurs. Such data will be valuable in designing steel compositions for high ductility and strength. Thermal stability of ultrafine-grained austenitic stainless steels was also evaluated using traditional techniques by Etienne *et al.* (2010). They observed intriguing



19.13 (a) Schematic illustration of the welding set-up to measure the phase fraction using energy dispersive X-ray diffraction method. (b) Measured variation of austenite and martensite in the weld region during weld cooling. (c) For the same conditions, the residual stress in the heat-affected-zone was measured and compared with welds made with S690 filler wire. Data adopted from Kromm *et al.* (2010).

© Woodhead Publishing Limited, 2012



19.13 Continued

stability of ε and α' martensite depending on the stainless steel (type 304 or type 316)[1] composition. The authors found the formation of ε martensite only in type 304 stainless steels.

Strain-induced martensitic transformation in austenitic steels has also been studied with multiple techniques including neutron diffraction, electron back scattered diffraction (EBSD), magnetic measurements and acoustic emission (Hausild *et al.*, 2010). Although neutron diffraction studies were made under *ex-situ* conditions, the authors concluded that neutron diffraction provides the volumetric information and is more desirable. In addition, the authors also suggest that these measurements can be used to calibrate the magnetic and acoustic emission measurements. This clearly suggests a future path for the challenge of accommodating a wide range of experimental measurements in the limited beam line instruments in the world. Evaluations of the transformation-induced plasticity (TRIP) effect are of great importance to a new generation of steels. The TRIP effects has been extensively studied by various researchers (e.g., Datta *et al.*, 2009; Jimenez, 2009) and the reader is referred to a classic review paper on the same (De Cooman, 2004). The role of different thermo-mechanical processing on the stability of austenite in TRIP steel was studied by neutron diffraction under *in-situ* loading conditions (Zrnik *et al.*, 2008). The data showed that the austenite is stronger compared to ferrite for these conditions. This was related to the

[1] Type 316: Fe-0.05C-0.68Si-16.6Cr-10.6Ni-2.25Mo-1.12Mn-0.24Cu-0.12Co (wt%). Type 304: Fe-0.022C-0.36Si-18.61Cr-9.86Ni-0.0Mo-1.79Mn-0.25Cu-0.06Co (wt%).

© Woodhead Publishing Limited, 2012

enhanced carbon concentrations in the austenite. The effects of strain-induced martensitic transformation and internal stresses on the overall mechanical response have also been studied by neutron diffraction (Spencer *et al.*, 2009; Zickler *et al.*, 2009). The stability of reverted austenite to external loading in a maraging steel was also studied by high-energy synchrotron diffraction. This work showed that the reverted austenite in a Ph 13-8 maraging steel was not stable under mechanical loading conditions.

19.3.4 Characterization of precipitations

The small angle neutron scattering (SANS) in conjunction with neutron diffraction allows for bulk analyses and removes the sampling bias associated with transmission electron microscopy measurements (e.g. replica techniques). For example, Seong *et al.* (2008) used diffraction and two-dimensional SANS to investigate the 60 nm sized precipitates which showed core-shell structures of MnS/CuS and BN, respectively. This data was used to explain the improved ductility in this low-carbon steel due to a reduction in free carbon and nitrogen. This is attributed to the formation of boron-rich carbides and nitrides on the sulfide inclusions. Similarly to the above research, the evolution of precipitation in tool steels has also been studied by SANS (Bischof *et al.*, 2008). Through combined techniques including TEM and X-ray diffraction, the authors have measured differences in the coarsening and dissolution rates of MC, M_2C, $M_{23}C_6$ and M_6C carbides. A similar approach has been adopted by Michaud *et al.* (2007) to track the carbide formation in 5 wt% Cr martensitic steel. The data were used to rationalize the secondary hardening and its relationship to the final properties (Michaud *et al.*, 2007). The SANS technique has also been used to evaluate the stability of MnS and Nb(CN) precipitates in the austenite phase of a low-alloy steel. The data shows that the MnS particles coarsen, whilst the Nb(CN) particles dissolve in the austenite (Van Dijk, 2002).

Copper precipitation in steels under irradiated conditions has attracted a lot of interest with reference to property degradation. Research on this topic has been pursued by many researchers using atom probe and SANS (Bergner *et al.*, 2010), but often discrepancies appear in the composition estimation of these copper precipitates by these two different techniques. The question revolves mainly around the extent of iron in these precipitates. Recently, Bergner *et al.* (2010) used results from different techniques including transmission electron microscopy, atom probe, positron annihilation spectroscopy, and SANS to arrive at a self-consistent interpretation of copper precipitates through defect-cluster interactions. The data from pure iron alloys and reactor pressure vessel steels after different radiation dosage have been compared (Bergner *et al.*, 2010; Ulbricht *et al.*, 2007). The square root of volume fraction change from 0 to 0.8 measured by SANS was correlated to

© Woodhead Publishing Limited, 2012

an increase in yield strength from 50 to 350 MPa, respectively. The readers are referred to reviews by Odette and Nanstad (2009), as well as Lucas (2010), for more details on this topic.

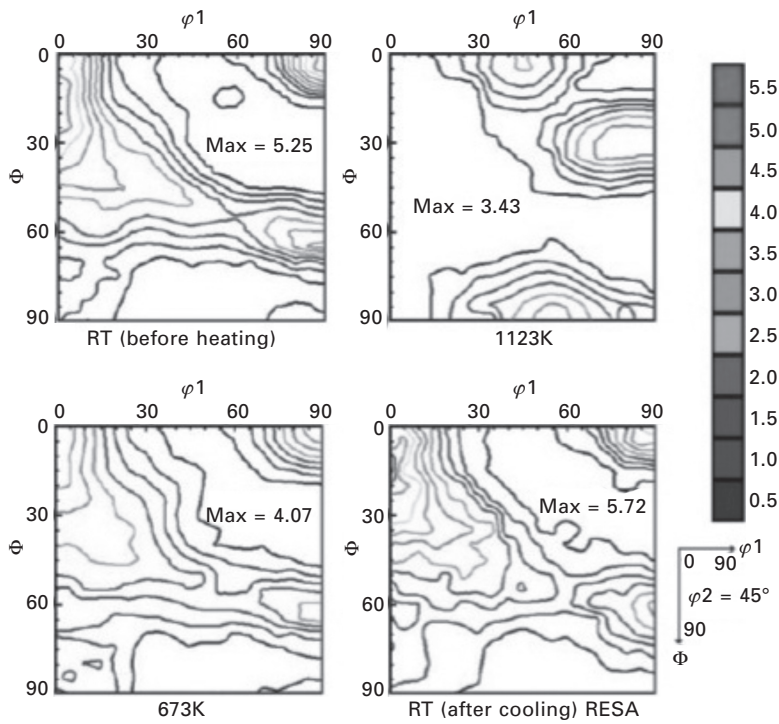
Nickel aluminide (NiAl) precipitate evolution in an iron alloy (Fe-6at%Al-4at%Ni) was characterized by using *in-situ* small angle neutron scattering (SANS) measurement (Shober *et al*., 2010) followed by 3D atom probe (3DAP) measurements. This data showed that the precipitates do not attain the equilibrium value at the early stage of tempering. The data show slow and steady cross-diffusion of Fe and Ni between the precipitates and matrix. The paper also discussed the importance of characterization methodologies in reconciling the differences between 3DAP and SANS data. It is noteworthy that the earliest use of neutron diffraction to a study of nanoscale phase transformations can be credited to Spooner *et al*. as early as 1971! They used neutron scattering to measure diffuse scattering and relate this to the early stages of decomposition. The use of small angle X-ray scattering and high-angle X-ray diffraction has also been combined to understand the coalescence of oxide particles in oxide dispersion strengthened iron alloys (Kim *et al*., 2009).

19.3.5 Characterization of texture in steels

Another important factor that controls the properties of steels is related to crystallographic texture that evolves from solid-state phase transformations during thermal and/or thermo-mechanical processing (Jay and Jonas, 1990). Texture in steel surfaces can be obtained by EBSD and traditional X-ray diffraction. However, neutron diffraction offers a unique advantage since it samples a larger volume. In addition, with pulsed neutron sources, these measurements can be done under *in-situ* conditions by maintaining the sample in a furnace while texture measurements (either by step heating or continuous heating) are made continuously. Thus, dynamic recovery and recrystallization in a cold-rolled ultra low carbon steel plate was investigated by Brand *et al*. (1995). Iordanova *et al*. (1989) studied the recrystallization texture under *in-situ* conditions and argued that this is more accurate than off-line measurements. However, the extensions of these techniques are necessary to understand the texture evolution during $\alpha \rightarrow \gamma$ and $\gamma \rightarrow \alpha$ transformations. Bruckner *et al*. (2001) used EBSD and innovative experimental methods to understand the texture of austenite that forms from the ferrite. In this study, a nickel foil was wrapped around the ferritic sample before the heat treatment. As the austenite forms, the nickel diffuses into the austenite and stabilizes it. As the sample cools to room temperature, the nickel-enriched austenite remains stable at room temperature. The EBSD measurements on these samples showed predominantly a Kurdjumov–Sachs (KS) relationship between ferrite and austenite. It is indeed important to reconfirm these results without the

© Woodhead Publishing Limited, 2012

special nickel alloying, and *in-situ* neutron diffraction is the ideal approach (Wenk *et al*., 2007). Recently, Tomota *et al*. (2010) performed *in-situ* texture analyses using neutron diffraction on a low alloy steel at room temperature, 673 K, 1123 K, and after cooling to room temperature (see Fig. 19.14). Comparison of texture from before heating at room temperature, at 673 K, and after thermal processing, showed a strong memory effect. This memory effect is in agreement with work by Wenk *et al*. (2007). It is interesting to note that such memory effects are also observed in 9Cr steels (Shirane *et al*., 2009) during $\alpha \rightarrow \gamma \rightarrow$ martensite transformations, typical to that of the heat-affected-zone. However, these measurements were performed by EBSD analyses. It will be of interest to evaluate these effects using modern texture instruments such as the high-pressure preferred orientation (HIPPO) instrument (Wenk *et al*., 2010). Additional references realted to texture memory effect in steel can also be found in Chapter 17 of Volume 1.

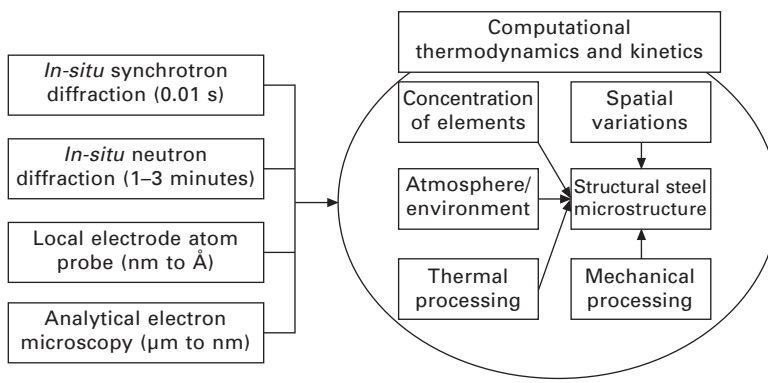


19.14 Results from *in-situ* texture evolution in a low-alloy steel during heating and cooling using neutron diffraction show a memory effect. Data adopted from Tomota *et al*. (2010).

© Woodhead Publishing Limited, 2012

19.4 Conclusions and future trends

In this chapter, the synchrotron and neutron scattering techniques for investigation of phase transformations in steels have been introduced. Some of the basic experimental approaches were presented with references to published literature. Tangible examples related to the study of phase transformations in steels were presented. The examples and techniques discussed clearly show that *in-situ* analyses of phase transformations in steel can now be readily performed using different synchrotron and neutron beam lines. In addition, auxiliary tools (e.g. fusion welding, friction stir welding, thermal, thermo-mechanical, magnetic) are also available to subject any new steels to desired external loading conditions. Although *in-situ* analyses of phase transformations of steels have been studied earlier under nominal heating and cooling conditions (Televich and Prikhod'ko,1994a, 1994b, 1994c, 1994d; Televich *et al*., 1994), the use of high flux synchrotron and neuton beam line under *in-situ* processing conditions was pioneered by Elmer and his group (Elmer *et al*., 1996) and researchers from ESRF facilities (Offerman *et al*., 2002). As a result the *in-situ* characterization using the neutron and synchtrotron beam lines are generally available in all beam line facilities across the world. It is expected that within two decades, we will have ready-made auxiliary tools that can be loaded into synchrotron and neutron beam lines to perform thermo-mechanical-magnetic processing under different environments (see Fig. 19.15). With these *in-situ* scattering tools coupled with digital image correlations, thermal analyses, laser scanning confocal microscopy, spectroscopy methods and *ex-situ* techniques (electron



19.15 Future research that leverages both *ex-situ* and *in-situ* characterization data to develop a comprehensive computational thermodynamic and kinetic model to predict the steel phase transformation under a wide range of boundary conditions is envisioned.

© Woodhead Publishing Limited, 2012

microscopy and atom probe), many of the challenges associated with steel phase transformations can be addressed.

19.5 Acknowledgements

The author acknowledges the collaboration with researchers on this exciting topic of *in-situ* analyses of steel transformation using synchrotron and neutron diffraction. Researchers from Oak Ridge National Laboratory are as follows: Drs E. D. Specht, S. A. David, J. M. Vitek, M. L. Santella, and E. A. Payzant. Collaborators from Lawrence Livermore National Laboratory are Drs John Elmer, J. Wong, and T. Palmer. Collaborators from Los Alamos National Laboratory are Drs D. Brown and S. C. Vogel. In addition, the author acknowledges collaboration with Prof. H. K. D. H. Bhadeshia, M. Peet and H. Stone from the University of Cambridge. Collaboration on hybrid synchrotron diffraction and laser scanning confocal microscopy is credited to Prof. Y. Komizo and Dr H. Terasaki from JWRI, Osaka University. In addition, special thanks go to Dr Thomas Kannengiesser (BAM, Berlin), Prof. Komizo (Osaka University), and Dr A. Ramirez (Brazilian Synchrotron Radiation Laboratory) for initiating the workshop on *in-situ* studies with photons, neutrons and electrons. The author also gratefully acknowledges many of the above collaborators and Prof. Y. Tomota (Ibaraki University, Japan) and Dr F. Bergner (Institute of Safety Research, Dresden, Germany) for providing permission to use the figures and data from their research. Finally, the author thanks Dr Linda Horton (ORNL) and Dr J. W. Elmer who were instrumental in directing his foray into this area. He also acknowledges unfettered access and help from many scientists from the UNICAT beam line, the Argon Photon Source and SSRL.

19.6 References

Aaronson, H. I. (2005), 'Diffusional-displacive phase transformations and related issues,' *Proceedings of Intl. Conf. on Solid-Solid Phase Transformations in Inorganic Materials*, May, Phoenix, AZ

Babu, S. S. (2009), 'Thermodynamic and kinetics models for describing microstructure evolution during joining of advanced materials,' *International Materials Reviews*, Vol. 54, pp. 333–367

Babu, S. S., *et al*. (2002), 'Time-resolved X-ray diffraction investigation of primary weld solidification in Fe-C-Al-Mn steel welds,' *Acta Materialia*, Vol. 50, pp. 4763–4781

Babu, S. S., *et al*. (2005a), '*In-situ* observations of lattice parameter fluctuations in austenite and transformation to bainite,' *Metall. Mater. Trans. A*, Vol. 36A, pp. 3281–3289

Babu, S. S., *et al*. (2005b), 'Modeling and characterization of nonequilibrium weld microstructure evolution,' in *Mathematical Modeling of Weld Phenomena 7*, Eds. H. Cerjak, H. K. D. H. Bhadeshia, E. Kozeschnik, Technical University of Graz, 179–205

© Woodhead Publishing Limited, 2012

Babu, S. S., *et al*. (2007), 'Time resolved X-ray diffraction investigation of austenite and transformation to bainite,' *Proceedings of 1st international symposium on steel science (IS^3 2007)*, The Iron and Steel Institute of Japan, May, pp. 93–99

Bailer-Jones, C. A. L., Bhadeshia, H. K. D. H., and Mackay, D. J. C. (1999), 'Gaussian process modeling of austenite formation in steel,' *Materials Science and Technology*, Vol. 15, pp. 287–294

Barabash, O. M., *et al*. (2004), 'Evolution of dislocation structure in the HAZ of a nickel based single crystal,' *J. Appl. Physics*, Vol. 96, pp. 3673–3679

Barabash, R. I., Wang, Y., and Liaw, P. (2008), 'Neutron and X-ray studies for probing materials behavior: foreword', *Metall. Mater. Trans. A*, Vol. 39A, p. 3057

Bergner, F., *et al*. (2010), 'Comparative small-angle neutron scattering study of neutron-irradiated Fe, Fe-based alloys and a pressure vessel steel,' *J. Nuclear Materials*, Vol. 399, pp. 129–136

Bhadeshia, H. K. D. H. (1985), 'Diffusional formation of ferrite in iron and its alloys,' *Progress in Materials Science*, Vol. 29, pp. 321–386

Bhadeshia, H. K. D. H. (2001), *Bainite in Steels*, Institute of Materials, London

Bhadeshia, H. K. D. H. (2010), 'Nanostructured bainite,' *Proc. Royal. Soc. A. Math. Phys. Engg. Sci*., Vol. 466, pp. 3–18

Bischof, M., *et al*. (2008), 'On the overaging behavior of tool steel X38 CrMoV 5-3,' *Materials Science and Engineering A*, Vol. 472, pp. 148–156

Bish, B., and Howard, S. (1988), 'Quantitative phase analysis using the Rietveld method,' *J. Appl. Cryst*., Vol. 21, pp. 86–91

Bourke, M. A. M., *et al*. (1996), 'Real time measurement by Bragg edge diffraction of the reverse (α' to γ) transformation in a deformed 304 stainless steel,' *Materials Science and Engineering*, Vol. A221, pp. 1–10

Bourke, M. A. M. *et al*. (1998), 'Complementary X-ray and neutron strain measurements of a carburized surface,' *Materials Science and Engineering*, Vol. A257, pp. 333–340

Bourke, M. A. M., Dunand, D. D., and Ustundag, E. (2002), 'SMARTS – a spectrometer for strain measurements in engineering materials,' *Applied Physics A – Materials Science and Processing*, Vol. 74, pp. S1707–S1709

Brand, P. C., *et al*. (1995), 'Dynamic recovery and recrystallization in a cold rolled ultra low carbon steel plate: a neutron and X-ray diffraction study,' *J. Materials Science*, Vol. 30, pp. 1307–1312

Brauser, S., *et al*. (2010), '*In-situ* synchrotron diffraction and digital image correlation technique for characterization of retained austenite stability in low-alloyed transformation induced plasticity steel,' *Scripta Materialia*, Vol. 63, pp. 1149–1152

Bruckner, G., *et al*. (2001), 'Orientation correlation during diffusional α-γ phase transformation in a ferritic low carbon steel,' *Scripta Materialia*, Vol. 44, pp. 2635–2640

Caballero, F. G., *et al*. (2002), 'Very strong low temperature bainite,' *Materials Science and Technology*, Vol. 18, pp. 279–284

Cheng, S., *et al*. (2008), 'Probing the characteristic deformation behaviors of transformation-induced plasticity steels,' *Metall. Mater. Trans. A*, Vol. 39A, pp. 3105–3112

Cheng, S., *et al*. (2010), 'An assessment of the contributing factors to the superior properties of a nanostructured steel using *in situ* high energy X-ray diffraction,' *Acta Materialia*, Vol. 58, pp. 2419–2429

Choi, K. S., *et al*. (2008), 'Advanced micromechanical model for transformation-induced plasticity steels with application of *in-situ* high energy diffraction method,' *Metall. Mater. Trans. A*, Vol. 39A, pp. 3089–3096

© Woodhead Publishing Limited, 2012

Clarke, A. J., *et al*. (2008), 'Carbon partitioning to austenite from martensite or bainite during the quench and partition (Q&P) process: a critical assessment,' *Acta Materialia*, Vol. 56, pp. 16–22

Cullity, B. D., and Stock, S. R. (2001), *Elements of X-ray Diffraction*, 3rd edn, Prentice Hall, Englewood Cliffs, NJ

Dai, H., *et al*. (2008), 'Characterizing phase transformations and their effects on ferritic weld residual stresses with X-rays and neutrons,' *Metall. Mater. Trans. A*, Vol. 39A, pp. 3070–3078

Datta, K. *et al*. (2009), 'A low-temperature study to examine the role of ε-martensite during strain-induced transformations in metastable austenitic stainless steels,' *Acta Materialia*, Vol. 57, pp. 3321–3326

David, S. A., and Vitek, J. M. (1989), 'Correlation between solidification parameters and weld microstructures,' *International Materials Reviews*, Vol. 34, pp. 213–245

De Cooman, B. C. (2004), 'Structure-properties relationship in TRIP steels containing carbide-free bainite,' *Current Opinions in Solid State and Materials Sciences*, Vol. 8, pp. 285–303

Dianoux, A.-J., and Lander, G. (eds) (2003), *Neutron Data Booklet*, 2nd edn, ILL Neutrons for Science, Grenoble

Eikenberry, E. F., *et al*. (2003), 'PILATUS: a two dimension X-ray detector for macromolecular crystallography,' *Nuclear Instruments and Method in Physics Research: Section A – Accelerators, Spectrometers, Detectors, and Associated Equipment*, Vol. 501, pp. 260–266

Elmer, J. W. (2008), 'A new path forward for understanding microstructural evolution during welding,' *Welding Journal*, Vol. 87, pp. 149s–166s

Elmer, J. W., *et al*. (1996), 'Analysis of heat affected zone phase transformations using *in situ* spatially resolved X-ray diffraction with synchrotron radiation,' *Metall. Mater. Trans. A*., Vol. 27, pp. 775–783

Elmer, J. W., *et al*. (2003), 'Kinetic modeling of phase transformations occurring in the HAZ of C-Mn steel welds based on direct observations,' *Acta Materialia*, Vol. 51, pp. 3333–3349

Elmer, J. W., Palmer, T. A., and Specht, E. D. (2007a), 'Direct observations of sigma phase formation in duplex stainless steels using *in-situ* synchrotron X-ray diffraction,' *Metall. Mater. Trans. A*., Vol. 38A, pp. 464–475

Elmer, J. W., Palmer, T. A., and Specht, E. D. (2007b), '*In situ* observations of sigma phase dissolution in 2205 duplex stainless steel using synchrotron X-ray diffraction,' *Materials Science and Engineering*, Vol. 459, pp. 151–155

ENGIN-X, ISIS (2010), Instrument, http://www.isis.stfc.ac.uk/instruments/engin-x/

Enomoto, M., *et al*. (2001), 'Influence of magnetic field on the kinetics of pro-eutectoid ferrite transformation in iron alloys,' *Metall. Mater. Trans. A*., Vol. 32, pp. 445–453

Epp, J., *et al*. (2007), '*In-situ* X-ray phase analysis and computer simulation of carbide dissolution of ball bearing steel at different austenitizing temperatures,' *Acta Materialia*, Vol. 55, pp. 5959–5967

Etienne, A., *et al*. (2010), 'Thermal stability of ultrafine-grained austenitic stainless steels,' *Materials Science and Engineering A*, Vol. 527, pp. 5805–5810

Fruehan, R. J. (1998), *The Making, Shaping and Treating of Steel*, United States Steel Company, ASM, AISE

Genzer, Ch., *et al*. (2007), 'The materials science synchrotron beamline EDDI for energy dispersive diffraction analyses,' *Nuclear Instruments and Methods in Physics Research*, Vol. A578, pp. 23–33

© Woodhead Publishing Limited, 2012

Gnaeupel-Herold, T., *et al*. (2005), 'An investigation of springback stresses in AISI-1010 deep drawn cups,' *Materials Science and Engineering*, Vol. A 399, pp. 26–32

Gnaeupel-Herold, T., *et al*. (2007), 'Biaxial loading effects: low-cycle fatigue, yield surfaces and more,' presented at the ORNL Users week, October (presentations downloadable at: http://neutrons.ornl.gov/workshops/users2007/T1/Gnaupel-Harold.pdf)

Hammersley, A. P., *et al*. (1996), 'Two-dimensional detector software: from real detector to idealized image or two-theta scan,' *High Pressure Research*, Vol. 14, pp. 235–248

Hausild, P., *et al*. (2010), 'Characterization of strain-induced martensitic transformation in a metastable austenitic stainless steel,' *Materials and Design*, Vol. 31, pp. 1821–1827

Hill, E., and Howard, C. (1987), 'Quantitative phase analysis from neutron powder diffraction data using the Rietveld method,' *J. Appl. Cryst.*, Vol. 20, pp. 467–474

Hillert, M. (1997), 'Prediction of alloy constitution and phase transformations by computer modeling: an aid in alloy design and materials processing,' *Scandinavian Journal of Metallurgy*, Vol. 26, pp. 215–223

Huang, E. (2008), 'Slip-system-related dislocation study from *in-situ* neutron measurements,' *Metall Mater. Trans. A*, Vol. 39A, pp. 3079–3088

Huang, J., Vogel, S. C., Poole, W. J., Militzer, M., and Jacques, P. (2007), 'The study of low-temperature austenite decomposition in a Fe-C-Mn-Si steel using the neutron Bragg edge transmission technique,' *Acta Materialia*, Vol. 55, pp. 2683–2693

Ice, G. E. (2008), 'The future of spatially-resolved polychromatic neutron and X-ray microdiffraction,' *Metall. Mater. Trans. A*, Vol. 39A, pp. 3058–3064

Iordanova, I., *et al*. (1989), 'Investigation using neutron diffraction of changes of deformation texture in low carbon cold rolled steel during recrystallization annealing,' *Materials Science and Technology*, Vol. 5, pp. 665–673

ISIS Laboratory (2010), http://www.isis.stfc.ac.uk/learning/learning2114.html

James, M. N., *et al*. (2006), 'Correlating weld process conditions, residual strain and stress, microstructure and mechanical properties for high strength steel – the role of neutron strain scanning,' *Materials Science and Engineering*, Vol. A427, pp. 16–26

Jaramillo, R. A., *et al*. (2005), 'Effect of 30 T magnetic field on transformations in a novel bainitic steel,' *Scripta Materialia*, Vol. 52, pp. 461–466

Jay, R. K., and Jonas, J. J. (1990), 'Transformation textures in steels,' *International Materials Reviews*, Vol. 35, pp. 1–36

Jensen, D. J., and Godisken, R. B. N. (2008), 'Neutron and synchrotron X-ray studies of recrystallization kinetics,' *Metall. Mater. Trans. A.*, Vol. 39A, pp. 3065–3069

Jia, N., *et al*. (2008), 'Tensile deformation behavior of duplex stainless steel studied by *in-situ* time-of-flight neutron diffraction,' *Metall. Mater. Trans. A*, Vol. 39A, pp. 3134–3140

Jimenez, J. A. (2009), 'Effect of testing temperature and strain rate on the transformation behavior of retained austenite in low-alloy multiphase steel,' *Materials Science and Engineering A*, Vol. 508, pp. 195–199

Johnson, W. A., and Mehl, R. F. (2010), 'Reaction kinetics of nucleation and growth' (reprinted from *Transactions of the American Institute of Mining and Metallurgical Engineers*, Vol. 135, pg. 416, 1939),' *Metall. Mater. Trans. A.*, Vol. 41A, pp. 2713–2775

Kannengiesser, Th., Babu, S. S., Komizo, Y., and Ramirez, A. J. (eds) (2010), *In-situ Studies with Photons, Neutrons and Electrons Scattering*, Springer, Berlin

Kelly, T. F., and Miller, M. K. (2007), 'Invited review article – atom probe tomography,' *Review of Scientific Instruments*, Vol. 78, 031101

© Woodhead Publishing Limited, 2012

Kim, S.-W., *et al*. (2009), 'Kinetic approach for growth and coalescence of nano-size oxide particles in 9Cr-ODS steel using high-energy synchrotron radiation X-rays in Spring-8,' *Materials Transactions*, Vol. 50, pp. 917–921

Koo, M., *et al*. (2009), 'Bainitic transformation behavior studied by simultaneous neutron diffraction and dilatometric measurement,' *Scripta Materialia*, Vol. 61, pp. 797–800

Kostorz, G. (1996), 'X-ray and neutron scattering,' in R. W. Cahn and P. Haasen (eds), *Physical Metallurgy*, 4th edn, Elsevier Science, Amsterdam

Kromm, A., and Kannengiesser, T. (2009), '*In-situ* phase analyses using synchrotron radiation of a low temperature transformation temperature (LTT) welding material,' *Soldagem and Inspecao*, Vol. 14, pp. 82–88

Kromm, A., Kannengiesser, Th., and Gibmeier, J. (2010), '*In-situ* studies of phase transformation and residual stresses in LTT alloys,' in Th. Kannengiesser, S. S. Babu, Y. Komizo, A. J. Ramirez (eds), *In-situ Studies with Photons, Neutrons and Electrons Scattering*, Springer, Berlin

Kurz, W., and Fisher, D. J. (1998), *Fundamentals of Solidification*, Trans Tech Publications, Zurich

LANSCE Neutron School (2010), http://lansce.lanl.gov/neutronschool/

Liaw, P. K. (2006), 'Development of an *in situ* neutron scattering facility for research and education in the mechanical behavior of materials,' *Materials Science and Engineering A*, Vol. 437, pp. 126–133

Liss, K.-D., and Yan, K. (2010), 'Thermo-mechanical processing in a synchrotron beam,' *Materials Science and Engineering A*, Vol. 528, pp. 11–27

Liu, D. M., *et al*. (2010), '*In-situ* studies of stress- and magnetic field induced phase transformation in a polymber-bonded Ni-Co-Mn-In composite,' *Materials Science and Engineering*, Vol. 527, pp. 3561–3571

Liu, Z.-K., *et al*. (1991), 'An experimental and theoretical study of cementite dissolution in an Fe-Cr-C alloy,' *Metall. Mater. Trans. A*., 22A, 1745–1752

Lolla, T., *et al*. (2011), 'Development of rapid heating and cooling (flash processing) process to produce advanced high strength steel microstructures,' *Materials Science and Technology*, Vol. 27, pp. 863–875

Lucas, G. E. (2010), 'An evolution of understanding reactor pressure vessel steel embrittlement,' *Journal of Nuclear Materials*, Vol. 407, pp. 59–69

Ludtka, G. M., *et al*. (2004), '*In situ* evidence of enhanced transformation kinetics in a medium carbon steel due to a high magnetic field,' *Scripta Materialia*, Vol. 51, pp. 171–174

Ludtka, G. M., *et al*. (2007), 'Time-resolved analyses of microstructures in advanced materials under magnetic field at elevated temperatures using neutrons,' *Proceedings of Symposium on Materials Processing under the Influence of External Fields*, TMS 2007 Annual Meeting, pp. 3–8

Matsumiya, T., *et al*. (1987), '*In situ* observation of solidification of silicon steel by synchrotron radiation X-ray topography,' *Metall. Trans. A*, Vol. 18, pp. 723–727

Matthies, S., *et al*. (2005), 'Quantitative texture analysis with HIPPO neutron TOF diffractometer,' *J. Appl. Cryst*., Vol. 38, pp. 462–475

Mayr, P., *et al*. (2010), 'Formation of delta ferrite in 9 wt.% Cr steel investigated by *in-situ* X-ray diffraction using synchrotron radiation,' *Metall. Mater. Trans. A*, Vol. 41A, pp. 2462–2465

Michaud, P., *et al*. (2007), 'The effect of the addition of alloying elements on carbide precipitation and mechanical properties in 5% chromium martensitic steels,' *Acta Materialia*, Vol. 55, pp. 4877–4889

© Woodhead Publishing Limited, 2012

Miyagi, L., *et al*. (2008), '*In situ* phase transformation and deformation of iron at high pressure and temperature,' *Journal of Applied Physics*, Vol. 104, 103510

Muansky, O. *et al*. (2008), 'The structure dependence of deformation behavior of transformation-induced plasticity-assisted steel monitoring by *in-situ* neutron diffraction,' *Metall. Mater. Trans. A*, Vol. 39A, pp. 3097–3104

NIST (2010), http://www.ncnr.nist.gov/programs/sans/tutorials/index.html

Odette, G. R., and Nanstad, R. K. (2009), 'Predictive reactor pressure vessel steel irradiation embrittlement models: issues and opportunities,' *JOM*, Vol. 61, pp. 17–23

Offerman, S. E., and Sharma, H. (2010), 'Grain nucleation and growth of individual austenite and ferrite grain studied by 3DXRD microscopy at the ESRF,' in Th. Kannengiesser, S. S. Babu, Y. Komizo, A. J. Ramirez (eds), *In-situ Studies with Photons, Neutrons and Electrons Scattering*, Springer, Berlin

Offerman, S. E., *et al*. (2002), 'Grain nucleation and growth during phase transformations,' *Science*, Vol. 298, pp. 1003–1005

Offerman, S. E., *et al*. (2003), '*In-situ* study of pearlite nucleation and growth during isothermal austenite decomposition in nearly eutectoid steel,' *Acta Materialia*, Vol. 51, pp. 3927–3928

Ohtsuka, H. (2008), 'Structural control of Fe-based alloys through diffusion solid/solid phase transformations in a high magnetic field,' *Science and Technology of Advanced Materials*, Vol. 9, 013004

Palmer, T. A., Elmer, J. W., and Wong, J. (2002), '*In-situ* observations of ferrite-austenite transformations in duplex stainless steel weldments using synchrotron radiation,' *Science and Technology of Welding and Joining*, Vol. 7, pp. 159–171

Palmer, T. A., *et al*. (2004), 'Observations of ferrite/austenite transformations in the heat affected zone of 2205 duplex stainless steel spot welds using time resolved X-ray diffraction,' *Materials Science and Engineering A*, Vol. 374, pp. 307–321

Pereloma, E. V., Miller, M. K., and Timokhina, I. B. (2008), 'On the decomposition of martensite during bake hardening of thermo mechanically processed transformation-induced plasticity steels,' *Metall. Mater. Trans. A.*, Vol. 39A, pp. 3210–3216

Reed, R. C., *et al*. (1998), 'Determination of reaustenitization kinetics in a Fe-0.4C steel using dilatometry and neutron diffraction,' *Materials Science and Engineering*, Vol. A256, pp. 152–165

Rietveld, H. M. (1969), 'A profile refinement method for nuclear and magnetic structures,' *J. Appl. Crystallography*, Vol. 2, pp. 65–71

Root, J. H., *et al*. (1993), 'Residual stress mapping in multipass ferritic steel weld,' *Materials Science and Technology*, Vol. 9, pp. 754–759

Ruhle, M., and Wilkens, M. (1996), 'Transmission electron microscopy,' in R. W. Cahn and P. Haasen (eds) *Physical Metallurgy*, 4th edn, Elsevier Science, Amsterdam, 1033–1114

Saha, A., and Olson, G. B. (2007), 'Computer aided design of transformation toughened blast resistance naval hull steels: Part I,' *Journal of Computer Aided Materials Design*, Vol. 14, pp. 177–200

Saha, A., Jung, J., and Olson, G. B. (2007), 'Computer aided design of transformation toughened blast resistance naval hull steels: Part II,' *Journal of Computer Aided Materials Design*, Vol. 14, pp. 201–203

Santisteban, J. R., *et al*. (2002), 'Engineering applications of Bragg-edge neutron transmission,' *Applied Physics A*, Supplemental Issue, pp. S1443–S1446

Santisteban, J. R., *et al*. (2006), 'ENGIN-X: a third generation neutron strain scanner,' *J. Appl. Cryst.*, Vol. 39, pp. 812–825

© Woodhead Publishing Limited, 2012

Savran, V. I., Offerman, S. E., and Sietsma, J. (2010), 'Austenite nucleation and growth observed on the level of individual grains by three-dimensional X-ray diffraction microscopy,' *Metall. Mater. Trans. A*, pp. 583–591

Seong, B. S., *et al*. (2008), 'Study of the effect of nano-sized precipitates on the mechanical properties of boron added low-carbon steels by neutron scattering techniques,' *J. Appl. Cryst*., Vol. 41, pp. 906–912

Sharma, H., *et al*. (2009), 'Multipurpose furnace for *in situ* studies of polycrystalline materials using synchrotron radiation,' *Review of Scientific Instruments*, Vol. 80, 123301

Shirane, T., *et al*. (2009), 'Ferrite to austenite reverse transformation process in B containing 9%Cr heat resistant steel HAZ,' *Science and Technology of Welding and Joining*, Vol. 14, pp. 698–707

Shirzadi, A. A., and Bhadeshia, H. K. D. H. (2010), 'Accumulation of stress in constrained assemblies: novel Satoh test configuration,' *Science and Technology of Welding and Joining*, Vol. 15, pp. 497–499

Shober, M., *et al*. (2010), 'Precipitation behavior of intermetallic NiAl particles in Fe-6 at% Al-4 at%Ni analyzed by SANS and 3DAP,' *Intermetallics*, Vol. 18, pp. 1553–1559

SMARTS, LANL (2010), http://lansce.lanl.gov/lujan/instruments/SMARTS/index.html

Specht, E. D., *et al*. (2003), 'Rapid structural and chemical characterization of ternary phase diagrams using synchrotron radiation,' *Journal of Materials Research*, Vol. 18, pp. 2522–2527

Specht, E. D., Tortorelli, P. F., and Zschack, P. (2004), '*In situ* measurement of growth stress in alumina scale,' *Powder Diffraction*, Vol. 19, pp. 69–73

Speer, J. G., *et al*., (2003), 'Quenching and partitioning: a fundamentally new process to create high strength TRIP sheet microstructures,' in E. B. Damm and M. J. Merwin (eds), *Proceedings of a Symposium on Austenite Formation and Decomposition*, pp. 505–522

Spencer, K., *et al*. (2009), 'The strain induced martensitic transformation in austenitic stainless steels, Part 2 – Effect of internal stresses on mechanical response,' *Materials Science and Technology*, Vol. 25, pp. 18–28

Spooner, S., *et al*. (1971), 'Neutron diffraction analysis of atomic arrangements in a maraging steel,' *Metall. Trans*., Vol. 2, pp. 2306–2307

Stone, H. J., Bhadeshia, H. K. D. H., and Withers, P. J. (2008a), '*In situ* monitoring of weld transformations to control weld residual stresses, stress evaluation in materials using neutrons and synchrotron radiation,' *Materials Science Forum*, Vol. 571–572, pp. 393–398

Stone, H. J., *et al*. (2008b), 'Synchrotron X-ray studies of austenite and bainitic ferrite,' *Proc. Roy. Soc. A – Math. Physics Engg. Sci.*, Vol. 464, pp. 1009–1027

Televich, R. V., and Prikhod'ko, S. V. (1994a), 'Crystallography of austenite formation in quenched carbon steel,' *Phys. Metals*, Vol. 13, pp. 332–344

Televich, R. V., and Prikhod'ko. S. V. (1994b), 'Formation of austenite structure in prequenched alloy steels,' *Phys. Metals*, Vol. 13, pp. 749–757

Televich, R. V., and Prikhod'ko, S. V. (1994c), 'Crystallographic features of $\alpha \rightarrow \gamma$ transformation in a tempered structural steel. II The effect of preliminary tempering on the crystallography of fine-grained austenite,' *Phys. Metals*, Vol. 13, pp. 1126–1132

Televich, R. V., and Prikhod'ko, S. V. (1994d), 'Crystallography of austenite formation in hypoeutectoid steel with ferrite-pearlite microstructure,' *Metal Phys. Adv. Techn*., Vol. 16, pp. 28–33

© Woodhead Publishing Limited, 2012

Televich, R. V., Prikhod'ko, S. V. and Kocherga, O. V. (1994), 'Crystallographic features of $\alpha \rightarrow \gamma$ transformation in a tempered structural steel. I The effect of preliminary tempering of martensite on structural heredity on rapid heating,' *Phys. Metals*, Vol. 13, pp. 984–991

Terasaki, H., and Komizo, Y. (2011), 'Diffusional and displacive transformation behavior in low carbon-low alloy steels studied by a hybrid *in-situ* observation system,' *Scripta Materialia*, Vol. 64, pp. 29–32

Terasaki, H., Shouyuan, Z., and Komizo, Y. (2010), '*In-situ* analyses of effects of transformation strain on the austenite phase during martensitic transformation of Cr-Ni steel,' *Proceedings of International Conference on Solid-Solid Phase Transformations 2010*.

Thiessen, R. G., *et al*. (2007), 'Phase-field modeling and synchrotron validation of phase transformations in martensitic dual-phase steels,' *Acta Materialia*, Vol. 55, pp. 607–614

Thomas, G. (1962), *Transmission Electron Microscopy of Metals*, Wiley, Chichester

Tomota, Y., *et al*. (2009), '*In-situ* TOF neutron diffraction during phase transformation in an engineering steel,' *Nuclear Instruments and Methods in Physics Research A*, Vol. 600, pp. 313–315

Tomota, Y., *et al*. (2010), '*In-situ* neutron diffraction during thermo-mechanically controlled processes for low alloy steels,' in Th. Kannengiesser, S. S. Babu, Y. Komizo, A. J. Ramirez (eds), *In-situ Studies with Photons, Neutrons and Electrons Scattering*, Springer, Berlin

Trivedi, R., and Kurz, W. (1994), 'Dendritic growth,' *International Materials Reviews*, Vol. 39, pp. 49–74

Ulbricht, A., *et al*. (2007), 'SANS response of VVER440-type weld material after neutron irradiation, post-irradiation annealing and re-irradiation,' *Philosophical Magazine*, Vol. 87, pp. 1855–1870

Van Dijk, N. H. (2002), 'High temperature SANS experiments on Nb(C,N) and MnS precipitates in HSLA steel,' *Metall. Mater. Trans. A*, Vol. 33A, pp. 1883–1891

Van Dijk, N. H., *et al*. (2007), 'Barrier-free heterogeneous grain nucleation in polycrystalline materials: the austenite to ferrite phase transformation in steel,' *Acta Materialia*, Vol. 55, pp. 4489–4498

VonDreele, R. B. (1997), 'Quantitative texture analysis by Rietveld refinement,' *J. Appl. Cryst*., Vol. 30, pp. 517–525

Voronin, V. I., *et al*. (2010), 'Composition of cementite in the dependence on the temperature: *in-situ* neutron diffraction study and *ab initio* calculations,' *JETP Letters*, Vol. 91, pp. 143–146

VULCAN, ORNL (2010), http://neutrons.ornl.gov/instruments/SNS/VULCAN/

Wang, G., *et al*. (2008), '*In-situ* high-energy X-ray diffuse scaterring study of the phase transition in a Ni_2MnGa ferromagnetic shape-memory crystal,' *Metall. Mater. Trans. A*, Vol. 39A, pp. 3184–3190

Wang, X.-L., *et al*. (2006), 'VULCAN – The engineering diffractometer at the SNS,' *Physica – B*, Vol. 385–386, pp. 673–675

Wenk, H.-R., *et al*. (2007), '*In-situ* observation of texture changes during phase transformations in ultra-low-carbon steel,' *Metall. Mater. Trans. A*, Vol. 38A, pp. 261–267

Wenk, H.-R., Lutterotti, L., and Vogel, S. C. (2010), 'Rietveld texture analysis from TOF neutron diffraction data,' *J. Powder Diffraction*, Vol. 25, pp. 283–296

© Woodhead Publishing Limited, 2012

Withers, P. J. (2007), 'Residual stress and its role in failure,' *Reports on Progress in Physics*, Vol. 70, pp. 2211–2264

Withers, P. J., and Bhadeshia, H. K. D. H. (2001a), 'Overview – residual stresses Part 1 – Measurement techniques,' *Materials Science and Technology*, Vol. 17, pp. 355–365

Withers, P. J., and Bhadeshia, H. K. D. H. (2001b), 'Overview – residual stresses Part 2 – Nature and origins,' *Materials Science and Technology*, Vol. 17, pp. 366–375

Wong, J., *et al*. (2003), 'Dynamics of phase transformations and microstructure evolution in carbon-manganese steel arc welds using time-resolved synchrotron X-ray radiation,' *Journal of Synchrotron Radiation*, Vol. 10, pp. 154–167

Yonemura, M., *et al*. (2010), 'Two-dimensional time-resolved X-ray diffraction study of dual phase rapid solidification in steels,' *Journal of Applied Physics*, Vol. 107, 013523

Zhang, D., *et al*. (2010), '*In-situ* observation on the formation of intragranular acicular ferrite at non-metallic inclusions in C-Mn steel,' *Acta Materialia*, Vol. 58, pp. 1369–1378

Zhang, W., *et al*. (2005), 'Modeling of ferrite formation in a duplex stainless steel weld considering non-uniform starting microstructure,' *Acta Materialia*, Vol. 53, pp. 4441–4453

Zickler, G. A., *et al*. (2009), 'Transformation of reverted austenite in a maraging steel under external loading: an *in-situ* X-ray diffraction study using high-energy synchrotron radiation,' *International Journal of Materials Research*, Vol. 100, pp. 1566–1573

Zrnik, J., *et al*. (2008), 'Effect of processing conditions on the structure development and mechanical response of Si-Mn "TRIP" steel,' *Materials Science and Engineering*, Vol. 483–484, pp. 71–75

© Woodhead Publishing Limited, 2012

Index

aberration correction, 508
acicular ferrite steels, 202–4
  acceleration of acicular ferrite formation, 204
  ferrite plates nucleating at TiO inclusions, 203
Ackland potential, 444
advanced bainitic steels, 271–91
  carbide-free bainitic steels, 283–90
    accelerating bainite reaction at low temperature, 285
    chemical composition of nanostructured bainitic steels, 284
    engineering stress-strain curves, 287
    improving mechanical properties, 288–90
    mechanical properties of nanostructured bainitic steels, 286
    microstructure obtained in NANOBAIN 1 steel, 284
    origin of mechanical properties, 285–8
    processing by bainite reaction at low temperature, 283–5
    two-step heat treatment schematic diagram, 289
  chemical composition, 274
  earlier approaches in development of carbide-free bainitic steels, 273
  future trends, 290–1
  second set of designed steels after air cooling
    scanning electron micrographs, 277
    transmission electron micrographs, 277
  theoretical and thermodynamic models for steel design, 272–3
  third generation design, 273–82
    adjustment to improve in-use properties, 279–82
    automotive applications, 274–9
    calculated T'_o curve and TTT diagram of CENIM 1 to 4 steels, 276
    Charpy impact test results of second set of designed steels, 279
    micrographs of third set of designed steels, 281
    quantitative data on microstructure of second set of designed steels, 276
    quantitative data on microstructure of third set of designed steels, 280
    tensile properties results of second set of designed steels, 278
    tensile test results of third set of designed steels, 282
    yield strength and total elongation vs other commercial steels, 282
ageing
  classification of tempering stages, 130–1
    resistivity curve of martensite in an iron-nickel-carbon alloy, 131
  martensitic fine structure changes, 131
AISI 1005 steel, 609
Allen–Cahn equation, 407
allotropic transformation temperature, 472–3
alloying element, 140–4
  iron-carbon alloys
    retardation of softening relative after tempering at 540°C, 143
    retardation of softening relative after tempering 260°C, 144
  tempering response, 141
  transition metal carbides, 142
α′ martensite, 34–5
Andrew's model, 474
angular dispersive method, 592–4
angular resolution, 560
annular dark field imaging (ADF), 508, 521
artificial neural network, 359, 484, 497
athermal behaviour, 62–3
atom map, 539, 543, 549
atom probe tomography, 520, 528
  data interpretation, 537–8
  developments, 536–7
  phase transformation in steels, 532–54
    future trends, 553–4
    transformation characterisation and understanding, 538–552
  specimen requirements, 535–6
  technique outline, 533–5
    local electrode atom probe, 534
austenite
  precipitation kinetics in strain induced precipitation, 167–71
    electrolytic extraction of NbC, 169
    NbCN in a 0.08%C-0.039%Nb steel, 170
    Ti-Nb-N in a simulated weld heat affected zone, 172

© Woodhead Publishing Limited, 2012

role in ferrite formation and 'dynamic strain-induced' ferrite, 198–9
presence of an additional size group of ferrite grains after treatment, 199
solubility of microalloying elements, 157–61
relative solubilities of microalloy carbides and nitrides, 159–60
austenite/ferrite transformation, 185–6
precipitation during 'row' or interphase precipitation, 171–4
complex fibrous carbide morphologies in Nb-Mo X80, 175
formation of interphase precipitates by ledge migration, 173
isothermal Nb precipitation kinetics, 175
'row' spacing vs cooling rate for Nb treated steels, 173
transformation temperature, particle size and sheet spacing, 174
austenite formation, 473–9
Ac_1 and Ac_3 influencing input variables significance histogram, 480
Ac_1 and Ac_3 variation prediction, 479
Ae_3 evolution with C, Cr, Mo, Si, Mg, and Ni content, 475–7
Fe-0.2C steel Mn content predictions, 480
fitting parameters for Ae_3 temperature, 478
variables influencing Ae_3 significance histogram, 473
austenite-formers, 373
austenite strengthening factor, 104
austenitic stainless steels, 99–100
autocorrelograms, 548–9
automotive steels, 214

back-propagation algorithm, 469
Bain correspondence, 566
Bain path, 442
Bain strain **B,** 13, 14, 15
bainite formation, 479–83
bainite plate thickness, 492–6
variables significance histogram, 494
variation with temperature, driving force and austenite strength, 495–6
bainitic transformation, 613
ballistic resistance steel, 588
Bauschinger effect, 312
Bayesian framework, 469–71, 499
Belonoshko potential, 444
black-box model, 465
body-centered cubic (bcc), 6, 8, 62
body-centered tetragonal (bct), 6, 8
bond-order potential, 436
Bouaziz–Allain model, 313
Bragg diffraction, 511
Bragg edge technique, 597–8, 615
Bragg's law, 591, 594
bright field image, 511
bulk phase transition, 453
Burgers' mechanism, 457–8

C455, 341
CALPHAD framework, 481
Calphad method, 226
cap phase, 524
carbide
tempering third stage considerations, 137–8
intralath distributions of fine cementite plates, 138
carbon atom segregation
during quenching and room temperature ageing, 128–30
electrical resistivity of as-quenched martensite, 129
carbon equivalent value (CEV), 157
carbon steels
martensite tempering, 126–45
classification of ageing stages, 130–1
fine structure changes due to ageing, 131
microstructures prior to heat treatments, 127–30
stages, 132–44
cast steels
precipitation
dendritic Nb-Ti-V particles, 162
Nb microsegregation mapping of a 0.042Nb-0.05%V, 164
'Star' shaped particles in as-cast Nb-V-Ti steels, 163
CCD camera, 560, 594, 601
cementite, 375–6
formation during quenching, 128
CENIM 1 to 4 alloys, 275
Chamati potential, 436
Charpy testing machine, 279
Chen–Wang approach, 410
closed loop thermomechanical tester, 601
cluster search method, 543
cluster variation method (CVM), 367
Co-free ternary alloys, 98
coherent-anomaly method, 367
coherent potential approximation (CPA), 367
cold rolling, 108, 110
Connolly–Williams method, 368
constrained carbon equilibrium (CCE), 249, 251
constrained paraequilibrium, 249
constrained vertex model (CVM) model, 576
continuous cooling transformation diagrams, 496–8
controlled rolled ferrite/pearlite steels, 191–8
CCT diagrams for Nb steel, 194–5
changes in ferrite grain numbers in unit volume, 196–7
changes in relative austenite grain size and shape, 191
ferrite formation at intragranular sites in austenit, 193
ferrite grain size and the surface area/unit volume, 193
controlled rolled steels, 156
precipitation
dark field images centred on precipitates, 167
precipitate distribution in a commercial C-Mn-Nb steel, 166
region of 'random' VC precipitation in normalised C-Mn-V-N steel, 168
'Row' or interphase precipitation in a 0.45%V steel, 168

© Woodhead Publishing Limited, 2012

convergent beam diffraction (CBED), 508, 524
copper precipitation, 621
core-loss images *see* EELS maps
core phase, 524
Cottrell atmospheres, 538
CPA-GPM theory, 368
Cr-Mo steels, 485
crystallography
  Eshelby/Christian model and infinitesimal deformation (ID), 24–5
  future trends, 28–9
  interfacial dislocation models, 26–7
  martensite transformations in steels, 3–29
  overview, 4–10
    martensite transformation characteristics, 8–10
    observable effects associated with a martensite transformation in steels, 5
    theories, 8–10
  phenomenological theory of martensite crystallography (PTMC), 10–19
  post PTMC period, 19–24
Cu-Zr alloy, 579
Curie temperature, 407

dark field image, 512, 521
de Broglie relationship, 595
Debye rings, 594, 602
defect-cluster interactions, 621
defect dissociation
  heterogeneous nucleation, 61–3
    discrete-dislocation model of martensitic interface, 61
    nucleating defect, interfacial coherency dislocation and dislocation arrays, 62
deformation-induced martensitic transformation, 66
density functional theory (DFT), 366
diamond anvil cells, 601
diffraction pattern, 591
diffusion-controlled transformation, 8
Digiview II camera, 561
dilatometry, 589–90, 601, 608, 615
dimensionality reduction, 500
direct hot rolling, 108
dislocation density, 313
dislocation tangle, 541
dislocation tensor, 568
domain-specific manner (DSM), 103
double shear, 22
dual-phase steels, 333
Dudarev and Derltet potential, 436
dynamic Hall–Petch effect, 295, 308
dynamic strain ageing (DSA), 315
dynamic strain-induced ferrite
  deformed austenite role in ferrite formation, 198–9
    presence of an additional size group of ferrite grains after DSIT treatment, 199
dynamic strain-induced transformation (DSIT), 198

EELS maps, 518
EELS spectrum, 522–3
effective mobility approach, 417
elastic strain gradient tensor, 568
electron backscatter diffraction (EBSD)
  2D applications, 561–9
    kernel average misorientation values frequency distribution, 568
    martensite variants description, 565–7
    microstructure characterisation, 561
    orientation relationships description, 562–5
    plastic strain description, 567–9
    TRIP steel martensite-austenite band microstructure, 562
  3D EBSD, 569–79
    five-parameter grain boundary characterisation, 573, 575–9
    measurement by FIB-EBSD tomography, 569–71
    voxel-based description, 571–3
  fundamentals, 558–60
    Fe 36% Ni crystal patterns, 559
  future developments, 579–83
    EBSD vs TEM diffraction vs X-ray diffraction, 579–81
    future applications to steels, 581–3
    new techniques, 581
    TWIP steel electron channelling contrast image, 582
  phase transformations in steels, 557–83
electron chanelling contrast imaging (ECCI), 581
electron energy loss spectroscopy (EELS), 158, 508, 521–2
electropolished disc methods, 509
energy dispersive method, 594
  set-up and sample spectra, 595
energy-filtered imaging (EFTEM), 508, 516, 518
energy-loss near-edge structure, 520
ε martensite, 37
Eshelby/Christian model, 24–5
η-phase, 340–1
European Synchotron Radiation Facility, 609
extraction replicas, 509
extrinsic stacking faults (ESF), 307

face-centered cubic (fcc), 6, 8, 62
Fe-0.1 wt% Cu alloy, 598
Fe-Al-N alloy, 519
Fe-C-Mn-Al alloy, 605–6, 607, 611
Fe-C-Mn phase diagram, 478
Fe-Cr phase diagram, 474
Fe films, 449–50
Fe-Mn alloys, 100–15
  applications, 114–15
  developments, 100–4
  precipitate particles effect, 111–14
  silicon effect, 104–7
  thermo-mechanical treatment, 107–11
Fe-Mn-X alloys, 297–307
  mechanical properties, 299–307
    carbon and manganese content on the SFE of austenitic Fe-Mn-C steel, 305
    relation between SFE and the operating deformation mechanism, 302

© Woodhead Publishing Limited, 2012

room temperature phases and calculated SFE, 304
TWIP steel after pre-straining, 300
TWIP steel deformed at high strains close to fracture, 300
thermodynamic properties, 297–9
Fe-rich corner of the Fe-Mn-C equilibrium phase diagram, 298
metastable Fe-Mn phase diagram, 297
microstructure of Fe-Mn binary alloys, 297
unstrained and strained Fe-18%Mn-0.6%C TWIP steel, 299
Fe nanoclusters, 449
Fe-Ni alloys, 93–6
Fe-Ni-C alloys, 93–6
Fe-Ni-Co alloys, 96–9
deformation temperature effect on percentage shape recovery, 98
Fe-Ni-Mn alloy, 525
Fe-Pt alloys, 89–93
electrical resistance curves, 90
self-accommodating group of martensite plates, 92
ferrite
deformed austenite role and 'dynamic strain-induced' ferrite, 198–9
additional size group of ferrite grains after DSIT treatment, 199
nucleation and growth, 186–7
effects of Nb and V on ferrite nucleation, 186
precipitation
effect of cooling rate and transformation temperature, 177
elemental maps of C, Mo and Nb, 176
strengthening in normalised V steels, 178
stress relief heat treatment, 179
solubility of microalloying elements, 157–61
relative solubilities of microalloy carbides and nitrides, 159–60
ferrite/bainite steels
controlled processed acicular ferrite steels, 199–204
'bainitic' microstructure of a controlled rolled 890 MPa linepipe steel, 201
microstructure of X80 type HSLA steels, 200
partially transformed acicular ferrite (AF), 202
role of alloying on transformation characteristics, 200
ferrite-carbide aggregate, 88
ferrite-pearlite steel, 489
ferrite Snoek peak, 323
ferromagnetism, 509
ferrous alloys
martensite morphology and crystallographic feature, 34–7
formation range of various α' types, 36
lath, lenticular and ε types, 35
substructure, habit plane, and orientation relationship of α' types, 37
shape memory, 83–117
austenitic stainless steels with low stacking fault energy (SFE), 99–100
Fe-Mn alloys, 100–15
Fe-Ni and Fe-Ni-C alloys, 93–6
Fe-Ni-Co alloys, 96–9
Fe-Pt alloys, 89–93
future trends, 115–17
overview, 83–9
ferrous martensite, 6
ferrous nanosystems, 449–58
orientation dependence, 456–7
crystal orientations stress vs strain curves, 456
stress-induced transformation, 453–6
Fe nanowire local structure, 454–5
nanowire axial stress vs applied strain, 453
temperature-induced transformation, 450–3
nanowire atomic structure before and after transformation, 452
nanowire length temperature dependence, 451
transformation path, 457–8
transforming Fe nanowire axial slice, 458
field evaporation mechanism, 533, 537
field ion/atom probe microscopy, 129
field ion beam technology, 612
field ion microscopy, 535, 538, 546
finish rolling temperature (FRT), 192
Finkelstein–Rosin peak (FR), 323
Finnis and Sinclair potential, 444–5, 448
first-order phase transition, 450
first principles modelling
diffusivity in bcc Fe, 381–4
binding energies for vacancy-substitutional solute atom pairs, 383–4
computed substitutional impurity diffusion in ferromagnetic bcc Fe, 384
first-principles electronic structure of alloys, 366–7
future trends, 384–5
order-disorder and its coupling with first-principles electronic structure, 367–9
phase stability of iron carbides, 374–7
crystal structure of cementite, 375
phase stability of pure iron, 370–4
experimental pressure-temperature phase diagram of pure iron, 372
phase transformations in steels, 365–85
prediction of atomic diffusion in alloys, 369–70
substitutional alloying elements, 377–81
partitioning enthalpy between ferrite and carbides, 381
Fischer–Tropsch synthesis, 375
Fit2D software, 602
focused ion beam-electron backscatter diffraction (FIB-EBSD) tomography, 569–71
limitations by resolution and volume, 570–1
materials issues, 571

© Woodhead Publishing Limited, 2012

technical set-up, 570
set-ups schematic, 570
focused ion beam (FIB) technology, 509, 533, 536
475° embrittlement, 546
fracture toughness
transformation plasticity applications, 77–9
computed stress–strain curves for crack tip cell model, 79
measured J_{IC} of 12Cr and 4Cr austenitic alloy, 78
Frank partial dislocation, 308
free-boundary approach, 405
functional, 406

G-phase, 341
gas tungsten arc-welding set-up, 600, 607
generalised gradient approximation (GGA), 370
generalised perturbation method (GPM), 367
generalised planar fault energy (GPFE), 310
genetic algorithms (GA), 359
Gibbs–Thomson capillarity effect, 355
Ginzburg–Landau free energy functional, 406
gnomonic projection, 560
grain boundary, 573, 575–9
alternative approaches, 577–9
Fe 28% Ni alloy 3D surface-based display, 578
application example, 577
boundary meshing, 575–6
marching tetrahedra approach schematic, 575
mesh smoothing, 576
pinning, 552
Greninger–Troiano orientation relationship, 7, 9, 36
GSAS software, 605
Guinier radius, 545

Hadfield steels, 243
Hall–Petch equation, 346
Hall–Petch relation, 286
HCP martensite, 34
Heisenberg model, 372
heterogeneous nucleation, 552
defect dissociation, 61–3
discrete-dislocation model of martensitic interface, 61
nucleating defect, interfacial coherency dislocation and interfacial dislocation arrays, 62
hexagonal close-packed (hcp), 6
high angle annular dark field imaging (HAADF), 516, 520–1
high-energy synchrotron diffraction, 619
high manganese twinning-induced plasticity (TWIP) steels, 295–328
dynamical Hall–Petch effect responsible for strain hardening in TWIP steel, 296
Fe-Mn-X alloys, 297–307
mechanical properties, 299–307
thermodynamic properties, 297–9
strain-induced twinning, 307–26
crystallographic texture evolution, 315–20
delayed fracture, 325–6
fatigue properties, 326
high strain rate properties, 320
strain localisation, 320–5
TWIP-effect modelling, 313–15
ultrafine grained TWIP steel, 326
twinning-induced plasticity industrialisation, 327
typical ranges for mechanical properties, 296
high-pressure preferred orientation instrument, 623
high resolution transmission electron microscopy (HRTEM), 158, 514
high strength low alloy, 215, 332
controlled processed ferrite/bainite and acicular ferrite steels, 199–204
development of microalloyed steels, 155–7
effect of microalloying on transformation kinetics, 177–85
CCT diagrams for a 0.03%C-1.78%Mn-0.26%Cu-0.17%Ni-0.29%Cr steel, 182
changes in Ar_3 temperatures for microalloying, 181
effect of deformation on the CCT transformation behaviour, 183
effect of Nb on the transformation behaviour of a C-Mn steel, 180
effects of Mo and V on the ferrite transformation, 184
effects of near-stoichiometric additions, 184
future trends, 205–7
deformation effect in bainitic ferrite by acicular ferrite, 206
microalloyed phase transformations, 153–207
overview, 153–5
phase transformation during processing, 185–99
austenite to ferrite transformation, 185–6
controlled rolled ferrite/pearlite steels, 191–8
deformed austenite in ferrite formation and ‘dynamic strain-induced’ ferrite, 198–9
normalised steels, 187–90
nucleation and growth of ferrite, 186–7
precipitation, 161–77
solubility of microalloying elements in austenite and ferrite, 157–61
Hollomon–Jaffe tempering parameter, 265–6
homogeneous nucleation, 445–7
simulation volume edges evolution, 445
transforming crystallite cross-section, 446
hot rolling, 108, 109, 110

imaging techniques
modern TEM, 513–21
Al_2O_3 replicas NbC precipitates CTEM-BF and HAADF images, 522
austenite regions HRTEM image, 517

© Woodhead Publishing Limited, 2012

austenitic steel NbC precipitates EFTEM image, 518
duplex precipitates in Ti-Nb steel STEM ADF images, 522
duplex stainless steel δ ferrite dislocation structure, 514
fast Fourier transformed Fe-Si-C alloy HRTEM image, 517
Fe-1.5 wt% Cu precipitate HRTEM image, 516
Fe-Al-N alloy AIN precipitates EFTEM images, 519
Fe-C martensite HRTEM image, 516
Fe-C-Nb alloy NbC precipitates EFTEM image, 518
sputter-deposited austenitic stainless steel thin film:, 515
$Ti_2Y_2O_7$ particle CTEM and EFTEM elemental images, 521
Y-Cr-O particle EFTEM elemental images, 520
in-column imaging filter, 518
in-situ diffraction, 601
in-situ time-resolved X-ray diffraction, 613
in-situ transmission electron microscopy, 524–5
heating/cooling experiments, 524–5
austenite migration images, 526
yttria particles ODS-RAFMS, 527
straining experiments, 525
austenitic stainless steel CTEM BF image, 528
V-microalloyed dual-phase *in-situ* straining TEM, 527
infinitesimal deformation (ID), 24–5
infinitesimal strains, 25
input layer, 468
interatomic interaction potentials, 434–43
free energy calculation, 437–9
fcc and bcc free energy differences, 439
fcc and bcc free energy temperature dependence, 438
iron interaction potentials, 434–7
bcc and fcc phase potential energy difference, 437
effective pair potential for various potentials, 436
phonon softening, 439–41
bcc Fe 1/2 TA_1 phonon mode, 440
bcc Fe phonon dispersion curves, 440
transformation path, 441–3
fcc and bcc phases orientation relationships, 442
parameters evolution in Bain and Nishiyama–Wassermann paths, 443
interfacial dislocation model, 26–7
interlamellar spacing
pearlite, 489–92
factors influencing pearlite growth rate, 490
$\log S_o + \log(T_E - T/T_E)$ vs Mn, Cr, Ni, Si, and Mo, 491
$S_o\Delta T$ factor vs Mn, Ni, Si, Cr, and Mo, 493
variables significance histogram, 490
intermetallic phases, 336–7
interphase precipitation *see* row precipitation
intrinsic stacking faults (ISF), 307
Invar effect, 378
invariant plane strain, 9, 10, 13–14, 16, 86, 106, 493
inverse pole figure map, 572
Ising model, 367, 407, 408
isoconcentration surface, 540–1
isothermal behaviour, 62–3

Jaswon–Wheeler theoretical analysis, 9
JEOL 6500 F gun, 561
Johnson and Oh potential, 444
Johnson–Mehl–Avrami (JMA) equation, 347, 351
Johnson–Mehl–Avrami–Kolmogorov (JMAK) model, 412

Kapton film, 600–1
Kaufman binary database, 354
kernel average misorientation (KAM) value, 567
Kikuchi cones, 560
kinematical diffraction theory, 590–1
Kocks–Mecking approach, 313
Koistinen–Marburger relationship, 250, 256
Kubin–Estrin model, 314
Kurdjumov–Sachs relationship, 6, 7, 8, 36, 561, 577, 622
Kurdjumov–Sachs type, 343

Langer, Bar-on, Miller model, 547
laser confocal microscopy, 608, 616
laser heating, 601
laser pulsing, 533
lateral resolution, 560
lath-like austenite, 342
lath martensite
morphology and substructure, 38–45
block structure, 42
change in microstructure at the scale of the optical microscope, 39
characteristics in an austenite grain, 38
crystallographic features, 38–43
dislocation density, 43–5
dislocation density change with carbon and Ni content in Fe-C and Fe-Ni alloys, 45
orientation relationship between K-S variants, 41
twenty-four variants in the K–S relationship, 40
variation of packet size and block width with austenite grain size, 43
lattice correspondence, 11
lattice invariant shear, 7, 17, 20, 23
lattice invariant strain, 15
lattice strain **S,** 87
Laves phase, 512
lenticular martensite, 94
morphology and substructure, 46–9
development during growth, 48
Fe-Ni alloy and areas of observation, 47
Fe-Ni alloy and internal structure, 46
tangled and uniformly straight dislocations, 49

© Woodhead Publishing Limited, 2012

lever rule, 546–7
Levi-Civita permutation symbol, 568
Lifshitz–Slyozov–Wagner (LSW) theory, 348
light optical microscopy, 537
linear detector, 608
linear regression, 465–6
local electrode configuration, 537
local spin density approximation (LSDA), 370
long range order (LRO), 91, 95
longitudinal acoustical branch, 439
low carbon steel, 497
low temperature transformation wire, 615

magnetically-induced martensitic transformation, 117
magnons, 372
maraging, 336
maraging steels, 332–59
  composition and mechanical properties, 335
  evolution of precipitates and the overall process, 346–9
    dilatometry curve of 2000 MPa grade cobalt-free maraging steel, 348
    inter-particle spacing calculation, 347–8
    L/*r* ratio as function of precipitation fraction, 348
    overall process, 348–9
  microstructure and precipitates, 339–42
    PH13-8Mo maraging steels, 339–40
    precipitates, 340–2
  parameter determination, 353–6
    activation energy and Avrami index, 353–4
    critical nucleus size, 355–6
    driving force and the critical nucleus radius of precipitation, 356
    growth and diffusion constants, 354–5
    precipitation fraction at peak hardness, 356
    reaction rate constant in the Johnson–Mehl–Avrami equation, 354
    results calculated with ThermoCalc using Kaufman binary database, 355
    strengthening, 353
    values of parameters involved in precipitation strengthening calculation, 353
    values of parameters obtained by best fitting, 356
  precipitation kinetic theory in Fe-12Ni-6Mn maraging type alloy, 349–56
    overall ageing process, 352–3
    theoretical analysis of early-stage ageing process, 350–1
  research trends, 356–9
    computer-aided alloy design approach to new steel compositions, 357–9
    development of novel maraging steels and atom probe tomography, 357
    ultrafine-grained Fe-Ni-Mn steels, 357
  reverted austenite and mechanical properties, 342–6
    mechanical properties, 345–6
    morphologies in maraging steels, 343
    reverted austenite, 342–4
  state of the art ultra high strength steels, 332–4
    strength-ductility profile of various steels, 333
  types, 334–9
    nominal compositions and respective yield strength of commercial maraging steels, 338
Marching Cubes algorithm, 575
Marching Tetrahedra algorithm, 575, 577
martensite
  classification of ageing and tempering stages, 130–1
    resistivity curve of martensite in an iro-nickel-carbon alloy, 131
  crystallographic feature in ferrous alloys, 34–7
  fine structure changes due to ageing, 131
  lath, 38–45
  lenticular, 46–9
  microstructures prior to tempering heat treatments, 127–30
    carbon atom segregation during quenching and room temperature ageing, 128–30
    cementite formation during quenching, 128
    M_S temperatures and morphologies as function of carbon content, 128
  morphology and substructure in steels, 34–55
  start temperature, 483–8
    analysed steels chemical compositions, 488
    Andrews vs Cool and Bhadeshia model vs M_s model, 488
    Cu, Cr, Mo, W, and Cr-W influence for different carbon grades, 486–7
    Cu influence for different carbon grades, 485
  tempering in carbon steels, 126–45
  tempering stages, 132–44
    eta transition carbides, 134
    first stage, 132
    fourth stage, 140–4
    interlath cementite formation, 136
    retained austenite and cementite in various as-quenched medium-carbon steels, 135
    second stage, 132–6
    third stage, 136–40
    transformation of retained austenite in the martensitic microstructure, 135
    transition carbide formed in a crystal of martensite, 133
  thin plate, 50–4
  transformation and shape memory, 86–9
martensite transformation, 346
  crystallography of steels, 3–29
  Eshelby/Christian model and infinitesimal deformation (ID), 24–5
  future trends, 28–9
  interfacial dislocation models, 26–7
  kinetics in steels, 59–80
  mechanically induced transformations, 63–5

© Woodhead Publishing Limited, 2012

interrelationships between stress-assisted and strain-induced transformation, 64
strain-assisted transformations mechanism, 65
stress-assisted transformations mechanism, 64–5
mechanism and kinetics, 60–3
heterogeneous nucleation by defect dissociation, 61–3
molecular dynamics modelling, 433–59
case studies in iron, 443–9
ferrous nanosystems, 449–58
future trends, 459
interatomic interaction potentials, 434–43
overview, 4–10
characteristics, 4–8
crystallography theories, 8–10
observable effects associated with a martensite transformation in steels, 5
phenomenological theory of martensite crystallography (PTMC), 10–19
plasticity constitutive relations and applications, 66–79
post PTMC period, 19–24
martensite variants, 565–7
austenite and martensite unit cells Bain correspondence, 566
austenite grains reconstruction illustration, 565
MatCalc, 344
materials science, 464
matrix
third stage tempering considerations, 138–40
nital etch of microstructure of lath martensite, 139
matrix austenite, 342
maximum separation method, 544
mechanical stabilisation, 240
memory effect, 623
memory elements, 99
metric scaling, 437
Meyer and Entel potential, 436, 438–9, 441, 444, 450, 459
MICRESS, 411–12
microalloyed steels, 332
microalloying
phase transformations in high strength low alloy steels, 153–207
controlled processed ferrite/bainite and acicular ferrite steels, 199–204
development, 155–7
during HSLA processing, 185–99
effect on transformation kinetics, 177–85
future trends, 205–7
overview, 153–5
precipitation, 161–77
solubility of elements in austenite and ferrite, 157–61
miscibility gap
spinodal decomposition and phase separation in miscibility gap, 546–8
Cr concentration frequency vs binomial distribution, 548
Fe(Ti,Al) and PM2000 alloy network structure, 547
PM 2000 alloy Cr-enriched α' phase autocorrelation, 549
misorientation distribution, 563, 580
molecular dynamics modelling
case studies in iron, 443–9
external constraints, 447
heterogeneous nucleation, 447–9
homogeneous nucleation, 445–7
simulation crystallite cross section, 448
ferrous nanosystems, 449–58
orientation dependence, 456–7
stress-induced transformation, 453–6
temperature-induced transformation, 450–3
transformation path, 457–8
interatomic interaction potentials, 434–43
free energy calculation, 437–9
iron interaction potentials, 434–7
phonon softening, 439–41
transformation path, 441–3
martensitic transformations, 433–59
future trends, 459
Monte-Carlo (MC) Potts-model algorithm, 572
Monte Carlo method, 444
Morse potential, 435
M_s model, 484
MTDATA database, 473, 479
multivariate statistical analysis, 519

nano-scale bainitic microstructure, 589
NANOBAIN 2 steel, 287
NANOBAIN 3 steel, 290
NANOBAIN steel, 283
nanowires, 450
network 'training,' 467
neural networks, 466–9
feed-forward network schematic, 468
output vs input, 467
neural networks modeling
continuous cooling transformation diagrams, 496–8
calibration and calculated CCT diagram, 499
critical temperature determination, 472–88
austenite formation, 473–9
bainite formation, 479–83
Fe-0.4 C-X steels alloying elements effect on B_s temperature, 482–3
martensite start temperature, 483–8
essence of methods, 465–72
Bayesian framework, 469–71
fitting function uncertainty schematic, 471
linear regression, 465–6
neural networks, 466–9
neural networks traditional training, 469
overfitting problem, 471–2
test variations and training errors vs model complexity, 472
future trends, 498–500
microstructural parameters determination, 488–96
bainite plate thickness, 492–6

© Woodhead Publishing Limited, 2012

pearlite interlamellar spacing, 489–92
phase transformation in steels, 464–500
neutron diffraction, 592, 601, 608–9, 615, 621, 623
neutron irradiation, 549
neutron scattering techniques
angular dispersive method, 592–4
sample and detector position schematic, 593
auxiliary instruments and methods, 600–1
microstructure evolution tracking set-up, 602
Bragg edge technique, 597–8
transmission data, 597
energy dispersive method, 594
experimental methods, 592–605
phase transformation kinetics *in-situ* tracking, 602–5
in-situ time-resolved X-ray diffraction, 603–4
phase transformation tracking in steels, 588–625
future trends, 624–5
phase transformation measurement in steels, 605–23
research for *ex-situ* and *in-situ* characterisation data, 624
small angle scattering methods, 598–600
set-up schematic and sample data, 599–600
time-of flight diffraction, 595–7
set-up schematic and sample spectra, 596
X-ray scattering, 590–605
theoretical basis, 590–2
New Materials Group of Nippon Steel, 115
Newton's laws, 433
Ni-Co-Mn-In alloys, 601
NiAl system, 434
nickel aluminide precipitate evolution, 622
Nishiyama–Wasserman orientation relationship, 6–7, 36
Nishiyama–Wassermann path, 441–2, 444, 457, 514
Nishiyama–Wassermann type, 343
non-thermoelastic transformation, 97
normalised steels, 187–90
changes in Jominy hardenability of a V-Al-N steel, 190
effect of prior as-rolled ferrite grain size on the final ferrite grain size, 189
effect of transformation temperature on the efficiency of austenite grain boundaries, 189
influence of soluble Al/N ratio, 188
nucleus transformation strain (IPS), 60

one-dimensional concentration profile, 539
optical microscopy, 589
orientation, 6, 562–5
austenite–martensite boundaries misorientation distribution, 564
diffraction techniques for orientation determination, 563
orientation distribution function (ODF), 315, 317
orientation microscopy, 558
output layer, 468
overfitting, 471–2

pancaking, 285
partially transformed acicular ferrite, 202
Patel–Cohen model, 64
pearlite, 376
interlamellar spacing, 489–92
factors influencing pearlite growth rate, 490
log S_o + log($T_E - T/T_E$) vs Mn, Cr, Ni, Si, and Mo, 491
$S_o\Delta T$ factor vs Mn, Ni, Si, Cr, and Mo, 493
PH17-4, 344
PH 13-8 maraging steel, 621
PH13-8Mo maraging steels, 336, 339–40
phase field modelling (PFM), 405–29
austenite decomposition, 418–28
applied strain on the 2D simulated ferrite formation, 424
2D simulated microstructure development in ultra low carbon steel, 418
2D simulations of austenite-to-pearlite transformation, 426
2D simulations of ferrite growth into hexagonal austenite grain, 426
2D simulations of Widmanstätten ferrite growth, 425
nucleation temperature range on simulated 3D microstructure, 421
pearlite and non-polygonal transformation products formation, 423–8
polygonal ferrite formation, 418–23
simulated 2D vs 3D microstructures, 420
austenite formation, 414–17
2D austenite formation simulation in Fe-0.17 wt% C, 417
2D simulation of austenite formation, 415
2D simulations of pearlite-to-austenite transformation, 415
micrographs of pearlite-to-austenite transformation, 416
future trends, 428–9
phase field methodology, 406–14
background, 406–9
benchmarking of phase field models, 412–14
comparison of idealised JMAK kinetics with PFM simulations, 413
2D phase field and continuous change of phase field parameter, 407
2D simulation of JMAK transformation scenario, 413
multiphase field models, 410–12
phase field model approaches, 409–10
time sequence of magnetic domain formation and coarsening, 408
transition from a cubic structure to tetragonal structure, 410

© Woodhead Publishing Limited, 2012

phase transformation
advanced bainitic steels, 271–91
carbide-free bainitic steels, 283–90
design of third generation of advanced high strength steels, 273–82
future trends, 290–1
atom probe tomography in steels, 532–54
data interpretation, 537–8
developments, 536–7
future trends, 553–4
specimen requirements, 535–6
technique outline, 533–5
characterisation and understanding, 538–52
copper-enriched precipitates atom maps, 550
copper-enriched precipitates proximity histograms, 551
Ni-Mn-Si-enriched nanoclusters phase separation, 551
precipitation and cluster formation, 539–46
spinodal decomposition and phase separation in miscibility gap, 546–8
stability under extreme conditions, 548–52
Ti-Y-O-enriched nanoclusters distribution, 552
controlled processed ferrite/bainite and acicular ferrite steels, 199–204
development of microalloyed steels, 155–7
during high strength low alloy steels processing, 185–99
austenite to ferrite transformation, 185–6
controlled rolled ferrite/pearlite steels, 191–8
deformed austenite in ferrite formation and dynamic strain-induced ferrite, 198–9
normalised steels, 187–90
nucleation and growth of ferrite, 186–7
effect of microalloying on kinetics, 177–85
CCT diagrams for a 0.03%C-1.78%Mn-0.26%Cu-0.17%Ni-0.29%Cr steel, 182
changes in Ar_3 temperatures for microalloying, 181
deformation on the CCT transformation behaviour, 183
Mo and V effect on the ferrite transformation, 184
Nb effect on the transformation behaviour of a C-Mn steel, 180
near-stoichiometric additions, 184
electron backscatter diffraction (EBSD) of steels, 557–83
3D EBSD, 569–79
2D EBSD applications, 561–9
EBSD fundamentals, 558–60
future developments, 579–83
first principles in modelling, 365–85
diffusivity in bcc Fe, 381–4
future trends, 384–5
phase stability of iron carbides, 374–7
phase stability of pure iron, 370–4
substitutional alloying elements, 377–81
future trends, 205–7
deformation effect in bainitic ferrite by acicular ferrite, 206
high manganese twinning-induced plasticity steels, 295–328
Fe-Mn-X alloys, 297–307
strain-induced twinning, 307–26
twinning-induced plasticity industrialisation, 327
maraging steels, 332–59
evolution of precipitates and the overall process, 346–9
microstructure and precipitates in maraging steels, 339–42
precipitation kinetic theory in Fe-12Ni-6Mn maraging type alloy, 349–56
research trends, 356–9
reverted austenite and mechanical properties, 342–6
state of the art ultra high strength steels, 332–4
types of maraging steels, 334–9
measurements in steels, 605–23
in-situ texture evolution results, 623
martensite microstructure formation and XRD set-up, 606–7
non-equilibrium transformations during solidification, 605–8
precipitations characterisation, 621–2
texture characterisation, 622–3
transformations during solid-state transformations, 608–16
transformations during thermo-mechanical loading, 616–21
microalloyed high strength low alloy steels, 153–207
neural networks modeling in steels, 464–500
continuous cooling transformation diagrams, 496–8
critical temperature quest, 472–88
essence of methods, 465–72
future trends, 498–500
microstructural parameters determination, 488–96
overview, 153–5
phase field modelling, 405–29
austenite decomposition, 418–28
austenite formation, 414–17
future trends, 428–9
phase field methodology, 406–14
precipitation, 161–77
quenched and partitioned steels, 247–67
mechanical behaviour, potential applications and implementation status, 260–7
microstructure development fundamentals and alloy designs, 252–60
quenching and partitioning concept, 247–52
solubility of microalloying elements in austenite and ferrite, 157–61

© Woodhead Publishing Limited, 2012

synchotron and neutron scattering applications for tracking, 588–625
future trends, 624–5
research for *ex-situ* and *in-situ* characterisation data, 624
X-ray and neutron scattering techniques, 590–605
TEM applications in steels, 507–28
conventional TEM, 510–13
future trends, 525, 527–8
in-situ TEM, 524–5
modern TEM, 513–24
sample preparation, 508–10
transformation-induced plasticity-assisted multiphase steels, 213–43
future trends, 242–3
historical perspectives, 215–23
thermomechanical process parameters, 223–42
phenomenological theory of martensite crystallography (PTMC), 3–4, 9, 10–19
key features, 10–15
Bain correspondence for martensite in steels, 12
rectangular block of fcc austenite, 14
post period, 19–24
alternative theories, 21–4
theory experiments and trials, 19–21
process, 15–19
martensite plate formation showing two types of lattice invariant shear (LIS), 16
stepped interface used in the Topological Model (TM), 18
phonon softening, 439–41
Pirouz double cross-slip mechanism, 308
plain carbon steels, 492
plane regression equation, 486–7
plastic flow
stability, 73–4
ideal exponential hardening vs power law hardening behaviour, 74
plate-type martensite, 94
platinum deposition, 510
PM 2000 alloy, 546
point defects, 98
Portevin–LeChatelier (PLC) bands, 322
position-sensitive single atom detectors, 553
post-column imaging filter, 518
precipitate particles, 111–14
shape recovery of particle-free and particle-containing alloys, 112
precipitation, 161–77
cast steels, 161–5
dendritic Nb-Ti-V particles, 162
Nb microsegregation mapping of a 0.042Nb-0.05%V, 164
'Star' shaped particles in as-cast Nb-V-Ti steels, 163
controlled rolled steels, 165–7
dark field images centred on precipitates, 167
precipitate distribution in a commercial C-Mn-Nb steel, 166
region of 'random' VC precipitation in normalised C-Mn-V-N steel, 168
'Row' or interphase precipitation in a 0.45%V steel, 168
during austenite/ferrite transformation, 'row' or interphase precipitation, 171–4
ferrite, 174–7
effect of cooling rate and transformation temperature on precipitation strengthening, 177
elemental maps of C, Mo and Nb, 176
strengthening in normalised V steels, 178
stress relief heat treatment, 179
kinetics in austenite and strain induced precipitation, 167–71
precipitation hardening, 334
proximity histogram, 539, 541–3, 549
pseudo-elasticity, 83, 84, 450
pseudo-linear equation, 466
pseudo-strain, 85
pseudopotential theory, 435

quantum jump, 156
quasi-polygonal ferrite, 154
quenched and partitioned steels, 243, 247–67
mechanical behaviour, potential applications and implementation status, 260–7
automotive components produced from Q&P sheet steel, 262
etched Q&P cold-rolled sheet steel, 262
locus of non-isothermal partitioning response for coil cooling, 266
microstructures observed after intercritical annealing and slow coil cooling, 265
tensile ductility plotted as function of tensile strength, 261
thermomechanical processing sequence, 264
microstructure development fundamentals and alloy designs, 252–60
calculated carbon concentration in ferrite and austenite, 257–8
calculated final austenite fraction, 258
changes in martensite fraction during partitioning, 259
extensive transition carbide precipitation, 255
Q&P thermal processing concept, 253
quenching and partitioning concept, 247–52, 253
constrained carbon equilibrium calculations, 250
light optical micrograph after austenitizing, quenching and partitioning, 253
microstructural constituents in steel after isothermal treatment, 248
predicted Q&P microstructure components, 252
schematic molar Gibbs free energy vs composition diagrams, 250
quenching

© Woodhead Publishing Limited, 2012

carbon atom segregation during room temperature ageing, 128–30
cementite formation, 128
quenching, partitioning and tempering (Q-P-T), 263
quenching and partitioning process, 247–9, 427, 589

radial concentration profile, 539
recovery annealing, 108, 109, 110
recrystallised austenite, 342
reflectron lens, 534
regulariser, 470
retained austenite, 342
reverse transformation, 101, 611
reverted austenite, 339
Rietveld analysis, 592, 605
rolling schedules, 192
room temperature ageing, 128–30
row precipitation
precipitation during austenite/ferrite transformation, 171–4
complex fibrous carbide morphologies in Nb-Mo X80 controlled rolled steel, 175
formation of interphase precipitates by ledge migration, 173
isothermal Nb precipitation kinetics, 175
relationship between 'row' spacing and cooling rate for Nb treated steels, 173
transformation temperature, particle size and sheet spacing relationship, 174

Satoh Test, 618
scanning electron microscopy (SEM), 528, 557
scanning transmission electron microscopy (STEM), 520–1, 553
Schmid factor analysis, 319
secondary hardening steels, 334
segmentation algorithm, 572
selected area diffraction patterns, 511
serial sectioning, 569
shape memory, 450
austenitic stainless steels with low stacking fault energy (SFE), 99–100
Fe-Mn alloys, 100–15
Fe-Ni and Fe-Ni-C alloys, 93–6
Fe-Ni-Co alloys, 96–9
Fe-Pt alloys, 89–93
ferrous alloys, 83–117
future trends, 115–17
overview, 83–9
behaviour definition, 84–6
martensitic transformation, 86–9
steel definition, 84
steels, 83–4
shape memory effect (SME), 83, 84–5, 105, 108, 112–13, 116
shear-type transformation, 561
Shockley partial dislocation, 308
short range ordering (SRO), 94, 95, 116
σ phase, 378
silicon, 104–7
single particle scattering, 598
Slater–Koster parameters, 367
Slater–Koster tight-binding method, 367
small angle neutron scattering (SANS), 357
small angle scattering methods, 598–600, 621
S_o model, 489–90
solid-state transformations
austenite to bainite, 612–15
paraequilibrium phase diagram and ferrite C composition, 614
austenite to high temperature δ-ferrite and δ-ferrite stability, 611–12
austenite to low temperature δ-ferrite and/or pearlite, 612
austenite to martensite, 615–16
martensitic transformation and austenite intensity peaks relationship, 616
ferrite/martensite to austenite transformations, 608–11
continuous heating transformation diagrams, 610
phase transformations, 608–16
spatial resolution, 560
special quasi-random structure (SQS) concept, 368
spherical aberration correction, 513–14
spinodal decomposition, 131
stacking fault energy (SFE), 99–100, 104–5, 295, 301–3
stacking fault nuclei, 100
Stanford Synchrotron Radiation Laboratory., 607
static set-up, 570
static strain-induced ferrite transformation (SSIT), 192
steels
atom probe tomography for phase transformations, 532–54
data interpretation, 537–8
developments, 536–7
future trends, 553–4
specimen requirements, 535–6
technique outline, 533–5
transformation characterisation and understanding, 538–52
crystallography of martensite transformation, 3–29
Eshelby/Christian model and infinitesimal deformation (ID), 24–5
future trends, 28–9
interfacial dislocation models, 26–7
overview, 4–10
phenomenological theory of martensite crystallography (PTMC), 10–19
post phenomenological theory of martensite crystallography (PTMC) period, 19–24
definition, 84
temperature variation of stress to induce martensite, 86
martensite morphology and substructure, 34–55
crystallographic feature in ferrous alloys, 34–7
lath, 38–45
lenticular, 46–9

© Woodhead Publishing Limited, 2012

thin plate, 50–4
martensite transformation kinetics, 59–80
mechanically induced, 63–5
mechanism, 60–3
plasticity constitutive relations and applications, 66–79
martensitic transformations molecular dynamics modelling, 433–59
case studies in iron, 443–9
ferrous nanosystems, 449–58
future trends, 459
interatomic interaction potentials, 434–43
phase transformation measurements, 605–23
phase transformation neural networks modeling, 464–500
continuous cooling transformation diagrams, 496–8
critical temperature determination, 472–88
essence of methods, 465–72
future trends, 498–50
microstructural parameters determination, 488–96
phase transformation tracking by scattering techniques, 588–625
future trends, 624–5
research for *ex-situ* and *in-situ* characterisation data, 624
X-ray and neutron scattering techniques, 590–605
phase transformations electron backscatter diffraction (EBSD), 557–83
3D EBSD, 569–79
2D EBSD applications, 561–9
EBSD fundamentals, 558–60
future developments, 579–83
precipitation and cluster formation, 539–46
austenite-ferrite interface proximity histogram, 541
carbon atom map and isoconcentration surfaces, 540
cementite-ferrite interface proximity histogram, 542
ferrite-precipitate interface proximity histogram, 543
number of clusters in maximum separation method, 544
size distributions of clusters, 545
size distributions of Cu-enriched precipitates, 545
shape memory, 83–4
transmission electron microscopy applications, 507–28
conventional TEM, 510–13
future trends, 525, 527–8
in-situ TEM, 524–5
modern TEM, 513–24
sample preparation, 508–10
step cooling method, 617
strain-assisted transformations, 65
strain-induced martensitic transformation, 620
strain-induced nucleation, 63, 444
strain induced precipitation
precipitation kinetics in austenite, 167–71
electrolytic extraction of NbC, 169
NbCN in a 0.08%C-0.039%Nb steel, 170
Ti-Nb-N in a simulated weld heat affected zone, 172
strain-induced twinning, 307–26
Byun analysis for partial dislocation breakaway for dislocations in screw orientation, 311
comparison of structure and energy of planar faults in fcc metals and alloys, 307
crystallographic texture evolution, 315–20
measured orientation distribution function, 318
orientation analysis of grains in Fe-Mn-Al-C TWIP steel, 318
texture evolution during rolling of fcc alloys, 317
delayed fracture, 325–6
deep drawn Fe-22%Mn-0.6%C TWIP steel, 325
fatigue properties, 326
generalised planar fault energy concept, 312
high strain rate properties, 320
stages of Venables pole mechanism and Pirouz double cross-slip mechanism, 309
strain localisation, 320–5
approximate strain rate and critical strain region for DSA, 322
direct evidence for dynamic strain ageing, 321
IF spectrum for Fe-Mn-C TWIP steel, 324
stress-strain curves for Fe-Mn-Al-C TWIP steels, 323
three possible point-defect pairs involving interstitial carbon atoms, 323
TWIP-effect modelling, 313–15, 316
experimental true stress-true strain curves vs model calculation, 316
ultrafine grained TWIP steel, 326
strength-differential effect, 68
stress-assisted nucleation, 63
stress-assisted transformations, 64–5
stress-induced martensite (SIM), 85, 93, 102, 105, 111–12, 116
stress-induced transformation, 453–6, 459
sum-squared error, 470
super-elasticity, 85
synchotron diffraction, 615
synchotron scattering techniques
phase transformation tracking in steels, 588–625
future trends, 624–5
phase transformation measurement in steels, 605–23
research for *ex-situ* and *in-situ* characterisation data, 624
X-ray and neutron scattering techniques, 590–605
System I transformations, 22

© Woodhead Publishing Limited, 2012

System II transformations, 22

½TA_1 [110] phonon mode, 439, 441
Taylor factor, 353
temperature-induced transformation, 450–3
tempering
  classification of ageing stages, 130–1
    resistivity curve of martensite in an iro-nickel-carbon alloy, 131
  martensite in carbon steels, 126–45
  martensitic fine structure changes due to ageing, 131
  microstructures prior to heat treatments, 127–30
    carbon atom segregation during quenching and room temperature ageing, 128–30
    cementite formation during quenching, 128
    M_S temperatures and morphologies as function of carbon content, 127–30
  stages, 132–44
    eta transition carbides, 134
    first stage, 132
    fourth stage, 140–4
    interlath cementite formation, 136
    retained austenite and cementite in various as-quenched medium-carbon steels, 135
    second stage, 132–6
    third stage, 136–40
    transformation of retained austenite in the martensitic microstructure, 135
    transition carbide formed in a crystal of martensite, 133
Thermo-Calc, 412
thermo-mechanical loading
  phase transformations, 616–21
    austenite to ferrite, 616–18
    austenite to martensite, 618–21
    thermomechanical processing schematic and difffraction data phase fraction, 617
    weld set-up, variations during cooling and S690 residual stress, 619–20
thermo-mechanical treatment (TMT), 107–11
  effect of cold rolling strain and heat treatment on the percentage shape recovery, 110
  effect of recovery annealing temperature following hot rolling, 109
  training cycles effect on recovery of tensile strain Fe-20Mn-6Si-7Cr-1Cu alloy, 108
ThermoCalc, 354
thermodynamic integration, 437
thermoelastic martensitic transformation, 88
thermoelastic transformation, 97
thermomechanical controlled processing (TMCP), 157
thermomechanical controlled rolling (TMCR), 156–7
thin plate martensite
  morphology and substructure, 50–4
    change in twin width and matrix width with carbon content in Fe-Ni-C alloys, 51
    transformation sequence during cooling, 51
    transmission electron micrograph in Fe-Ni alloy, 50
    various morphologies of lenticular martensite, 53
three-dimensional atom probe (3DAP), 357, 532, 536–7
Ti–B microalloyed steel, 497
time-dependent behaviour *see* isothermal behaviour
time-independent behaviour *see* athermal behaviour
time-of flight diffraction, 595–7
time-of-flight mass spectrometer, 533, 537
Topological Model (TM), 26
transformation induced plasticity, 93, 346, 561, 601, 620
transformation induced plasticity (TRIP)-assisted multiphase steels, 213–43
  combinations of strength and ductility exhibited by different steel grades, 214
  future trends, 242–3
  historical perspectives, 215–23
    austenite retention through bainite transformation, 220–1
    chemical free energies of austenite and martensite, 218
    different concepts for TRIP-assisted multiphase steels emergence, 221–3
    dual-phase steels, 215–17
    evolution of dual-phase and TRIP-assisted multiphase steels microstructure, 222
    heat-treatment scheme of cold-rolled dual-phase steels, 216
    mechanically induced martensitic transformation and the TRIP effect, 217–20
  influence of austenite grain size, 227–34
    evolution of normalised bainite volume fraction content, 228
    first platelets of bainitic ferrite surrounded by martensite, 230
    growth process of bainite, 231
    growth process of bainitic ferrite, 234
    low silicon TRIP-aided steel showing cementite, 232
    parallel configuration of platelets of bainite, 232
    partial bainite transformation of an initially fully austenitic grade, 229
    sequence of construction of TRIP-assisted multiphase steels microstructure, 233
    sheaf morphology of classical bainite, 228
    Si-alloyed TRIP-aided steel microstructure, 231
  influence of austenite prior deformation, 234–42

© Woodhead Publishing Limited, 2012

bainite volume fraction evolution, 237
change in morphology of bainite when austenite was previously deformed, 238
effect on its transformation into bainite, 237–40
effect on its transformation into martensite, 240–2
effect on its transformation into pro-eutectoid ferrite, 234–6
evolution of content of retained austenite, 242
growth process of bainitic ferrite in case of deformed austenite grains, 240
intragranular nucleation of bainitic platelets, 239
SEM micrographs, 235, 236
sheaf bainite structure growing from austenite grain boundaries, 239
true stress-true strain curves of TRIP-aided steels specimens, 241
thermomechanical process parameters on multiphase microstructures formation, 223–42
alloying elements on austenite retention through bainite transformation, 223–7
calculated curves of measured maximum carbon content of retained austenite, 227
evolution of carbon content of retained austenite, 226
transformation map
Al-alloyed TRIP-aided steel, 225
Si-alloyed TRIP-aided steel, 224
steel containing 0.4% wt of silicon, 225
transformation plasticity, 64
constitutive relations and applications, 66–79
applications to ductility, 74–7
applications to fracture toughness, 77–9
calculated transformation stresses and measured yield stresses for TRIP steel, 69
calculated vs observed tru σ–ε curves for TRIP steels, 70
flow relations, 66–73
plastic flow stability, 73–4
temperature dependence of yield stress, 67
transformation and flow behaviour of a metastable austenitic stainless steel, 71
transition state theory, 369
transmission electron microscopy (TEM), 541, 557, 579–80
conventional TEM, 510–13
laves phase precipitates in 12% Cr steel, 512
thermomechanically processed microalloyed steel image, 511
future trends, 525, 527–8
in-situ TEM, 524–5
heating/cooling experiments, 524–5
straining experiments, 525
modern TEM, 513–24
convergent beam electron diffraction, 524
EELS spectra illustration, 523
imaging techniques, 513–21
microchemical analysis, 521–4
sample preparation, 508–10
methods summary, 509
minimising ferromagnetic metal effects, 510
steels phase transformation applications, 507–28
transmissive radiation, 569
transverse acoustical branch, 439
TRIP steels, 333
twin volume fraction, 313
twinning-induced plasticity (TWIP) industrialisation, 327
TWIP steels, 333

uncertainty determination, 471
uniform ductility
transformation plasticity applications, 74–7
tensile properties of austenitic TRIP steel, 76
true stress–strain curves of high-strength austenitic TRIP steel, 75

V-microalloyed dual-phase steel, 525
vanadium-containing steel, 498
Venables pole mechanism, 308
VN precipitation, 113
voltage pulsing, 533
Voter–Chen potential, 435, 444
voxel, 571
voxel-based description, 571–3
data processing, 571–2
voxel-based mapping, 572–3
TRIP steel EBSD patttern quality mapping, 573
voxel-based display illustration, 574
VVER 1000, 549

warm rolling, 108, 111
WBF model, 409
white-box model, 465
Widmanstätten, 343

X-ray diffraction microscopy, 609
X-ray diffraction (XRD) analysis, 579–81
X-ray energy dispersive spectroscopy (XEDS), 508, 513, 521, 524
X-ray fluorescence, 601
X-ray scattering, 590–605
X-ray spectroscopy, 580

yield strength, 154

Z-contrast image *see* dark field image
Zener criterion, 490
Zener–Hillert model, 427
Zener's parabolic relationship, 350
zirconium, 434
zone axis diffraction pattern, 513

© Woodhead Publishing Limited, 2012